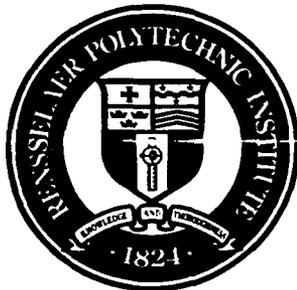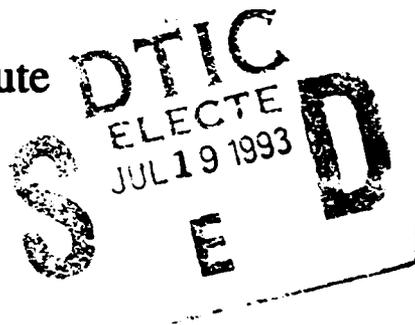# HiTASC

AD-A267 023

High Temperature Advanced Structural Composites

Rensselaer Polytechnic Institute
Troy, N. Y. 12180-3590

DTIC
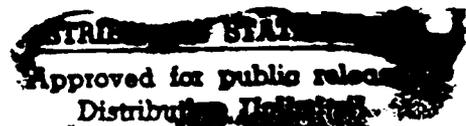ELECTE
JUL 19 1993
S E D

Final Report

Book 2 of 3: *Ceramic Matrix Composites, Fiber Processing and Properties, and Interfaces*

University Research Initiative

Contract No.: N00014-86-K-0770
October, 1986 - June, 1992
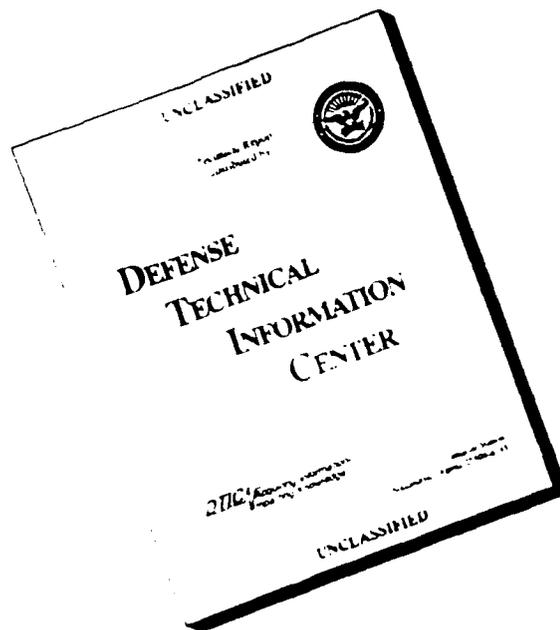
Sponsored by: The Defense Advanced Research Projects Agency

Monitored by: Office of Naval Research

93-16146

93 7 16 053

DISCLAIMER NOTICE

THIS REPORT IS INCOMPLETE BUT IS THE BEST AVAILABLE COPY FURNISHED TO THE CENTER. THERE ARE MULTIPLE MISSING PAGES. ALL ATTEMPTS TO DATE TO OBTAIN THE MISSING PAGES HAVE BEEN UNSUCCESSFUL.

REPORT DOCUMENTATION PAGE

Form Approved
OMB No. 0704-0188

1a. REPORT SECURITY CLASSIFICATION Unclassified		1b. RESTRICTIVE MARKINGS			
2a. SECURITY CLASSIFICATION AUTHORITY		3. DISTRIBUTION / AVAILABILITY OF REPORT Unrestricted			
2b. DECLASSIFICATION / DOWNGRADING SCHEDULE					
4. PERFORMING ORGANIZATION REPORT NUMBER(S)		5. MONITORING ORGANIZATION REPORT NUMBER(S)			

6a. NAME OF PERFORMING ORGANIZATION Center for Composite Materials and Structures Rensselaer Polytechnic Institute	6b. OFFICE SYMBOL (If applicable)	7a. NAME OF MONITORING ORGANIZATION Office of Naval Research
6c. ADDRESS (City, State, and ZIP Code) Rensselaer Polytechnic Institute Troy, NY 12180-3590		7b. ADDRESS (City, State, and ZIP Code) 800 North Quincy Street Arlington, VA 22217-5000
8a. NAME OF FUNDING / SPONSORING ORGANIZATION Advanced Research Projects Agency	8b. OFFICE SYMBOL (If applicable)	9. PROCUREMENT INSTRUMENT IDENTIFICATION NUMBER #N00014-86-K-0770

8c. ADDRESS (City, State, and ZIP Code) 1400 Wilson Blvd. Arlington, Virginia 22209	10. SOURCE OF FUNDING NUMBERS			
	PROGRAM ELEMENT NO.	PROJECT NO.	TASK NO.	WORK UNIT ACCESSION NO.

11. TITLE (Include Security Classification)

High Temperature Advanced Structural Composites

12. PERSONAL AUTHOR(S) George J. Dvorak and R. Judd Diefendorf

13a. TYPE OF REPORT Final	13b. TIME COVERED FROM 861001 TO 920613	14. DATE OF REPORT (Year, Month, Day) 930402	15. PAGE COUNT 748

16. SUPPLEMENTARY NOTATION

17.	COSATI CODES		18. SUBJECT TERMS (Continue on reverse if necessary and identify by block number)
FIELD	GROUP	SUB-GROUP	High temperature composites, Fibers, Matrices, Interfaces,
			Processing, Thermomechanical and Environmental behavior

19. ABSTRACT (Continue on reverse if necessary and identify by block number)

Final results obtained on the High Temperature Advanced Structural Composites Program at Rensselaer Polytechnic Institute are described in three volumes. Volume one contains the Executive Summary and reprints of papers on Intermetallic Compounds. Volume two contains reprints of papers on Ceramic Matrix Composites, Fiber Processing and Properties and on Interfaces. The third volume contains reprints of papers on Mechanics.

20. DISTRIBUTION / AVAILABILITY OF ABSTRACT ☒ UNCLASSIFIED/UNLIMITED ☐ SAME AS RPT. ☐ DTIC USERS	21. ABSTRACT SECURITY CLASSIFICATION Unclassified	
22a. NAME OF RESPONSIBLE INDIVIDUAL	22b. TELEPHONE (Include Area Code)	22c. OFFICE SYMBOL

DD Form 1473, JUN 86 — Previous editions are obsolete.

FINAL REPORT

University Research Initiative
Contract No. N00014—86—K—0770
October 1, 1986 — June 13, 1992

High Temperature Advanced Structural Composites

vol. 2 of 3

sponsored by
**Office of Naval Research and
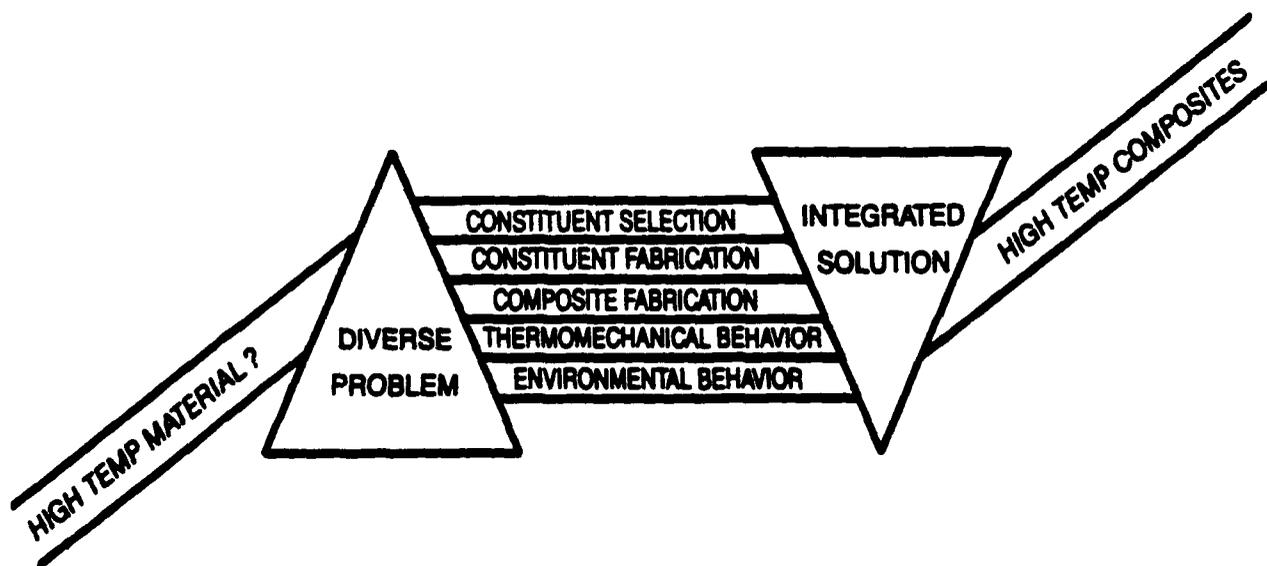Defense Advanced Research Projects Agency**

Accesion For		
NTIS CRA&I	☑	
DTIC TAB	☐	
Unannounced	☐	
Justification		
By		
Distribution /		
Availability Codes		
Dist	Avail and / or Special	
A-1		

DTIC QUALITY INSPECTED 5

HiTASC

HIGH TEMPERATURE ADVANCED STRUCTURAL COMPOSITES

RENSSELAER POLYTECHNIC INSTITUTE
TROY, N.Y. 12180-3590

FINAL REPORT

University Research Initiative
CONTRACT NO. N00014-86-K-0770
OCTOBER 1, 1986 – JUNE 13, 1992

Volume 2 of 3

HiTASC

HIGH TEMPERATURE ADVANCED
STRUCTURAL COMPOSITES

Professor George J. Dvorak
Program Director

Professor R. J. Diefendorf
Program Director (1986–1989)

RENSSELAER POLYTECHNIC INSTITUTE

Troy, N.Y. 12180

SUMMARY

OF

TABLE OF CONTENTS

BOOK 2

TABLE OF CONTENTS

CERAMIC MATRIX COMPOSITES

Wiedemeier, H. and Singh, M., "Thermal Stability of Refractory Materials for High—Temperature Composite Applications," Journal of Materials Science, 26, 2421–2430, (1991).

Singh, M. and Wiedemeier, H., "High Temperature Thermal and Environmental Stabilities of Boron Nitride, Aluminum Nitride and Silicon Nitride Ceramics," Materials at High Temperatures, Vol. 9, 139–144, (1991).

Interrante, L.V., Czekaj, C.L., Hakney, M.L.J., Sigel, G.A., Schields, P.J., and Slack, G.A., "An Investigation into the Preparation, Properties and Processing of SiC/AlN and Si_3N_4/AlN Solid Solutions from Organometallic Precursors," Materials Research Society Symposium Proceedings, Vol. 121, Materials Research Society, Pittsburgh,PA, 1988, pp. 465–470.

Kazmer, A.J. and Diefendorf, R.J., "Oxidative Stabilization of Bulk Carbonceous Materials." Abstract of Am. Carbon Soc. 20th Biennial Conf. on Carbon, 6/23–28/91, pp. 178–179.

Boisvert, R.P. and Diefendorf, R.J., "Siliciumcarbid—Verbundwerkstoffe Aus Polymeren Precursoren," Internationaler Kongress Hochleistungs Verbundwerkstoffe Fur Neue Systeme Proceedings, Demat Exposition Managing, Frankfurt, Germany, 1988, pp. 13.1–13.37.

Boisvert, R.P. and Diefendorf, R.J., "Chemical Vapor Deposition of Silicon Carbide Using Methyltrichlorosilane," Proceedings of the International Ceramic Conference, Vol. 1, AUSTCERAM 92, Melbourne, Australia, 1992, pp. 487–493.

Shinavaski, R.J. and Diefendorf, R.J., "Chemical Vapor Infiltration of Hafnium Diboride Matrix Composites," Proceedings of 16th Annual Conference on Composite Materials & Structures, Cocoa Beach, FL, 1992,(in print), Jan. 1993.

Boisvert, R.P. and Diefendorf, R.J., "Polymeric Precursor SiC Matrix Composites," Proceedings of American Ceramic Society 12th Annual Conference on Composites, Cocoa Beach, FL, 1988, pp. 873–880.

Diefendorf, R.J., "Continuous Carbon Fiber Reinforced Carbon Matrix Composites," Engineered Materials Handbook, Vol. I—Composites, ASM Intl., 911–914, (1987).

Doremus, R.H., "Alumina—Silica System," Handbook of Ceramics and Composites, Vol. 1, Ed., N.P. Cheremisinoff, Marcel Dekker, New York, NY, 1989, pp. 23–34.

Hynes, A.P., Folmsbee, Jr., and Doremus, R.H., "Grain Growth in Mullite and a Mullite/Corundum Composite," Proceedings of the American Ceramic Society for Composites, Sixth Technomic Pub. Co., Lancaster, PA, 1991 pp. 400–408.

Lee, C., Microstructure and Grain Growth of Mullite Prepared by the Sol—Gel Method, Master of Science, Rensselaer Polytechnic Institute, 61 p., 1988.

Czekaj, C.L., Hackney, M.L.J., Hurley, Jr., W.J., Interrante, L.V., and Sigel, G.A., "Preparation of Silicon Carbide/Aluminum Nitride Ceramics Using Organometallic Precursors," Journal of the American Ceramic Society, Vol. 73,352–357, (1990).

Amato, C.C., Hudson, J.B., and Interrante, L.V., "Gas Phase Decomposition of an Organometallic Chemical Vapor Deposition Precursor to AlN: [Al(CH$_3$)$_2$NH$_2$]3," Materials Research Society Symposium Proceedings, Vol. 168, Materials Research Society, Pittsburgh, PA, 1990, pp. 119–124.

Whitmarsh, C.K. and Interrante, L.V., "Synthesis and Structure of a Highly Branched Polycarbosilane Derived from (Chloromethyl)trichlorosilane," Organometallics, 1991, American Chemical Society, 1991, pp. 1336–1344.

Interrante, L.V., Hurley, Jr., W.J., Schmidt, W.R., Kwon, D., Doremus, R.H., Marchetti, P.S., and Maciel, G.E., "Preparation of Nanocrystalline Composites by Pyrolysis of Organometallic Precursors," Ceramic Transactions, Advanced Composite Materials, Vol. 19, M.D. Sooks, ed., American Ceramics Society, 3–17 (1991).

Interrante, L.V., Whitmarsh, C.K., Trout, T.K. and Schmidt, W.R., "Synthesis and Pyrolysis Chemistry of Polymeric Precursors to SiC and Si$_3$N$_4$," Inorganic and Organic Polymers with Special Properties, 243–254, (1992).

Whitmarsh, C.K. and Interrante, L.V., "Synthesis and Characterization of Mono—, Bis—, Tris—, and Tetrakis(trimethylsilylmethyl)silanes: (Me$_3$SiCH$_2$)$_x$SiH$_{4-x}$ (x = 1–4)," Journal of Organometallic Chemistry, 418, 69–77, (1991).

Interrante, L.V., Schmidt, W.R., Shaikh, S.N. and Garcia, R., "Silicon Carbide—Aluminum Nitride Solid Solutions by Pyrolysis of Organometallics." Processing of Advanced Materials, L.L. Hench and J.K. West, eds., J. Wiley & Sons, New York, NY, 1992, pp. 777–789.

Wu, H—J and Interrante, L.V., "Preparation of Poly(dichlorosilaethylene) and Poly(silaethylene) via Ring—Opening Polymerization," Macromolecules, 25, American Chemical Society, 1840–1841 (1992).

Interrante, L.V., Schmidt, W.R., Marchetti, P.S., Maciel, G.E., "Preparation of Non—Oxide Ceramics by Pyrolysis of Organometallic Precursors," Symposium on Better Ceramics Through Chemistry, in press, (1992).

Wu, H—J. and Interrante, L.V., "Poly(silaethylene) the 'Silaethylene' Analog of Polyethylene and a High Yield Precursor to SiC," Polymer Preprints, 33(2) 210–211 (1992).

Whitmarsh, C.K. and Interrante, L.V., "Carbosilane Polymer Precursors to Silicon Carbide Ceramics," U.S. Patent No. 5,153,295, 10/16/92.

Hynes, A.P., Wilenski, M.S. and Doremus, R.H., "Compressive Creep of MoSi$_2$ Matrix and Composite," Proceedings of the American Society for Composites, Sixth Technical Conference, Technomic Pub. Co., Lancaster, PA, 1991, pp. 591–600.

Hynes, A.P. and Doremus, R.H., "High—Temperature Compressive Creep of Polycrystalline Mullite," Journal of the American Ceramic Society, 74, 2469–2475, (1991).

FIBER PROCESSING AND PROPERTIES

Lara–Curzio, E. and Sternstein, S.S., "A High–Temperature Fibre Testing Facility," Meas. Sci. Technol., 2, 358–368, (1991).

Lara–Curzio, E. and Sternstein, S.S., "Thermoelastic Analysis of Composite CVD SiC Fibers," Journal of Composites Science and Technology, (in press).

Lara–Curzio, E. and Sternstein, S.S., "A Methodology for the Elevated Temperature Characterization of High Performance Fibers," Proceedings of the American Society for Composites Sixth Technical Conference, Albany, New York, 1991, pp. 460–470.

Sternstein, S.S., Lara–Curzio, E. and Beale, J., "Characterization of Fibers at High Temperature," Proceedings of the North American Thermal Analysis Society 21st Annual Conference, Atlanta, Georgia, 1992.

Beale, J., Lara–Curzio, E. and Sternstein, S.S., "High Temperature Deformation Studies on CVD Silicon Carbide Fibers," 35th International SAMPE Symposium, 1990, pp. 1193–1204.

Diefendorf, R.J., "Carbon/Graphite Fibers," Engineered Materials Handbook, Vol. I – Composites," ASM Intl., 1987, pp. 49–53.

Tzeng, S.–S., and Diefendorf, R.J., "Cross–Sectional Area Measurement of Single Carbon Fibers," Proceedings of the 19th Biennial Carbon Conference, Penn State University, State College, PA, 1989, pp. 298–299.

Diefendorf, R.J. and Mazlout, L., "High Performance Titanium Diboride Fibers," Proceedings of FIBER–TEX'88, Greenville, SC, 1988, pp. 169–189.

Diefendorf, R.J., "High Temperature, Advanced Structural Composite Reinforcements," Proceedings Veergundwerk '90, International Congress on Fibre Reinforced Tech., Wiesbaden, West Germany, 1990, pp. 31.3–31.13.

Edie, D.D. and Diefendorf, R.J., "Carbon Fiber Manufacturing," Carbon–Carbon Composites, Noyes Publs., J.D., Buckley, Ed., in press.

Kurtz, D.A., D'Abate, G.D, Tzeng, S.S. and Diefendorf, R.J., "Modulus of Mesophase Pitch Carbon Fibers," Proc. 2nd Japan International SAMPE Symposium, Chiba, Japan, 1991, pp. 158–165.

Tzeng, S.–S., Final ONR–DARPA HiTASC Report "Transverse Thermal Expansion and Microstructure Studies of Carbon Fibers," March 31, 1992.

Diefendorf, R.J. and Mazlout, L., "Simplified Dynamic Finite Element Processing Model for the CVD of TiB_2 Fibers," Extended Abstract for "Advances in Inorganic Fibre Technology" Workshop, Melbourne, Australia, 1992 (accepted for publication in Composites Science and Technology).

INTERFACES IN INTERMETALLIC AND CERAMIC MATRIX COMPOSITES

Fischer, H.E., Larkin, D.J. and Interrante, L.V., "Fiber Coatings Derived From Molecular Precursors," MRS Bulletin, 59–65, 1991.

Larkin, D.J. and Interrante, L.V., "Application of Chemical Vapor Deposited Yttria for the Protection of Silicon Carbide Fibers in a SiC/Ni₃Al Composite," Journal of Materials Research, 5, 2706–2717, (1990).

Hudson, J.B. and Sun, B.–X., "Interface Stability in Aluminide Matrix Composites," Proceedings of the Sixth Technical Conference, American Society for Composites, pp. 769–778 (1991).

Lagos, B. and Hudson, J.B., "Hollow Cathode Sputter Deposition of Titanium onto Carbon Fiber Tows," Journal of Vacuum Science and Technology, (submitted for publication).

Singh, M. and Wiedemeier, H., "Chemical Interactions in Diboride–Reinforced Oxide–Matrix Composites," Journal of the American Ceramic Society, 74, 724–727 (1991).

Wiedemeier, H. and Singh, M., "Thermochemical Modelling of Interfacial Reactions in Molybdenum Disilicide Matrix Composites," Journal of Materials Science, 27, 2974–2978 (1992).

Boisvert, R.P., Hutter, R.K., Diefendorf, R.J., "Interface Manipulation in Ceramic Matrix Composites for Improved Mechanical Performance," Proceedings of the 4th Japan–U.S. Conference on Composite Materials, AIME, Washington, D.C., 1988, pp. 789–798.

CERAMIC MATRIX COMPOSITES

Thermal stability of refractory materials for high-temperature composite applications

H. WIEDEMEIER, M. SINGH
Department of Chemistry, Rensselaer Polytechnic Institute, Troy, NY 12180-3590, USA

A computational thermodynamic analysis of the stability of group IV, V, and VI transition metal borides, carbides, nitrides, and oxides is presented. The results of these computations can be employed to assess the stability and decomposition of these materials at high temperatures under different ambient conditions. The thermodynamic stabilities of group IV, V, and VI compounds increase with atomic number of the metal in the same group and decrease with atomic number in the same period. Based on the equilibrium computations of the decomposition reactions considered, V_3B_4, HfC, HfN and Ti_3O_5 are the most stable compounds in each class. In general, the refractory oxides are the most stable compounds followed by the borides, carbides and nitrides.

1. Introduction

In recent years, considerable attention has been focused on the development of high-temperature structural composite materials, which might serve as replacements for superalloys in high-temperature and aerospace applications. These materials should have high melting points, good oxidation resistance, low density, and superior high-temperature creep and other mechanical properties. The thermochemical behaviour and properties of refractory borides, carbides, nitrides, silicides and oxides are being investigated for the above purposes. One of the major requirements for the efficient design and operation of high-temperature components and processes is reliable data about the thermodynamic stabilities, decomposition and oxidation behaviour under different conditions. These data are very useful in estimating the vaporization losses and predicting the lifetime of such materials.

Despite continuing research efforts and the use of advanced experimental techniques, there are still many gaps in the knowledge and understanding of the high-temperature properties of these refractory materials. The considerable lack of reliable experimental data concerning the stability and oxidation under different conditions at elevated temperatures has encouraged us to estimate these properties using thermodynamic data.

The present investigation deals with the stability relative to decomposition (vaporization) of borides, carbides, nitrides and oxides of group IV (titanium, zirconium and hafnium), group V (vanadium, niobium and tantalum), and group VI (chromium, molybdenum and tungsten) metals. Several of these compounds are of current interest for high-temperature structural applications. Hillig [1] discussed various problems and prospects for several of these compounds as constituents (fibre/matrix/coating) for high-temperature composites. Titanium diboride reinforcements are reported to be compatible with and to

improve the mechanical properties of intermetallic (aluminides) and of some ceramic (oxide) matrix composites [2-4]. Pure and partially stabilized zirconia (PSZ) are found to be quite attractive and effective as thermal barrier coatings for high-temperature applications [5]. A number of compounds of this class, i.e. TiC, TiN, TiO_2, TaC, Cr_3C_2 and Cr_2O_3 are widely used for different applications in heat engines [6]. In addition, studies [7] indicate that TiC and TiB_2 are also promising materials for use as limiters (the part of a fusion reactor nearest to the plasma). Other applications of materials containing refractory metal carbides, nitrides and borides include their use as effective wear-resistant materials for cutting tools [8-10]. A number of composite systems containing these compounds as reinforcements (whiskers, particulates and fibres), matrices, and coatings are reported in the literature. The main objectives of this investigation are to evaluate the thermal stabilities of these materials at high temperatures and to provide a data base for further computations. Other more specific analyses of the high-temperature applications and properties of these materials are part of a continuing effort and are being reported elsewhere [11-13].

2. Thermodynamic considerations

Thermodynamic equilibrium calculations represent a powerful tool to assess the chemical reactivities of materials, in particular at elevated temperatures. The free energies of reactions provide guidelines with respect to the dominant direction and extent of processes. However, thermodynamically favourable reactions may not occur owing to reaction kinetics. In such cases the actual physical state of the material, e.g. texture, porosity, stress and strain, may become very important. The rate of a reaction is also affected by the surface area available which, in turn, is related to the porosity of the material. Reactions may be inhibited

by the formation of protective layers. The latter case is of particular interest for the application of many composite materials at high temperatures, where the partial pressures of gaseous reactant or product species may stabilize or destabilize the system.

One of the main problems encountered in the thermochemical analysis of the refractory materials is the lack of reliable thermodynamic data for compounds at high temperatures. In such cases, the estimation of data is required. For the analysis of the decomposition behaviour of a given material, various reactions are considered which may occur in a particular system. Using the available and estimated data, equilibrium thermodynamic computations are performed for all reactions. For a meaningful application and interpretation of thermochemical computations a brief review of the basic relationships and conventions may be desirable.

The equation for chemical equilibrium can be intuitively expressed in terms of activities, namely

$$\mu_i(T, p, \text{comp.}) \equiv \mu_i^0 + RT \ln a_i(T, p, \text{comp.}) \quad (1)$$

where μ_i^0 is the chemical potential of a substance in its standard state in a particular phase. The choice of standard states for a substance is a matter of convenience. Conventionally, the standard state of a component in a gaseous phase is that of unit fugacity, i.e. the pure gas in the hypothetical ideal condition at temperature T and 1 atm pressure. Thus $a_i \rightarrow p_i$ as $\rho_i \rightarrow 0$. For a pure solid or liquid or for a solid or liquid solution, the most convenient standard state is the pure solid or liquid (or pure solvent) at temperature T and 1 atm pressure. For such a substance, $a_1 \rightarrow x_1$ as $x_1 \rightarrow 1$ if the pressure is 1 atm. Unless the pressure is very high, the pressure dependence of μ_i of condensed phases can be neglected because of the small molar volume in the term $v_i dp$ of the modified Gibbs–Duhem equation.

With Equation 1 the change in Gibbs free energy for a chemical reaction is defined as

$$\Delta G \equiv \sum_i v_i \mu_i \equiv \sum_i v_i \mu_i^0 + RT \sum_i v_i \ln a_i, \quad (2)$$

where the stoichiometric coefficients v_i are negative for reactants and positive for products. Introducing the quantity ΔG^0 for $\sum_i v_i \mu_i^0$, Equation 2 can be written in the form

$$\Delta G \equiv \Delta G^0 + RT \ln \prod_i a_i^{v_i}. \quad (3)$$

It is useful to recall that ΔG^0 is the change in Gibbs free energy for a process starting with the stoichiometric number of moles of reactants in their standard states, and ending with the stoichiometric number of moles of products in their standard states. The second term in Equation 3 is the product of activities and/or partial pressures of reactants and products. When the process is at equilibrium, $\Delta G = 0$ and Equation 3 takes the form

$$\Delta G = 0 = \Delta G^0 + RT \ln K_{eq}, \quad (4)$$

where $K_{eq} = \prod_i a_i^{v_i}$ and is the equilibrium constant of the reaction. When gaseous species are involved in the reaction, the symbol K_p is frequently used for K_{eq}. The equilibrium condition is commonly expressed by the equation

$$\Delta G^0 = -RT \ln K_{eq}. \quad (5)$$

The quantity ΔG^0 is related to the reaction enthalpies and entropies of substances in their standard states by the expression

$$\Delta G_T^0 = \Delta H_T^0 - T \Delta S_T^0 \quad (6)$$

For computational purposes Equation 6 can be expanded to

$$\Delta G_T^0 = \Delta H_{298}^0 + \int_{298}^T \Delta C_p^0 dT - T \Delta S_{298}^0$$
$$- T \int_{298}^T \frac{\Delta C_p^0}{T} dT \quad (7)$$

where ΔH_{298}^0 and ΔS_{298}^0 are enthalpy and entropy changes, respectively, of reaction at 298 K. Thus, ΔG^0 can be computed for any reaction and at any temperature for which thermodynamic data (heats of formation, absolute entropies, heat capacities) of reactants and products are available. Assuming that the reaction process involves at least one reactant or product substance in the gaseous state and that the others are in the condensed state, then based on the above definition of ΔG^0 and at equilibrium, the activities of the substances in the condensed phase are unity and of those in the gaseous state are equal to their equilibrium partial pressures.

Under these conditions, the sign of ΔG^0 indicates the endo- or exo-thermicity (direction) of the reaction as written. The magnitude of ΔG^0 is related to the magnitude of the partial pressure(s) of gaseous species present, which, in turn, is related to the amount(s) of gaseous substances in the reaction system. On the other hand, the activity of a pure condensed phase (at 1 atm) is unity by definition and independent of the amount of substance present. Thus, for a process in which only reactants and products in the condensed phase participate, ΔG^0 indicates the direction of a process, but not the "extent" of the reaction. If $\Delta G^0 < 0$, then eventually all reactants must disappear; if $\Delta G^0 > 0$, eventually all products must disappear. Only at one particular temperature is $\Delta G^0 = 0$, and the ratio of activities is unity for condensed-phase reactions. Therefore, generally it is not meaningful to compute equilibrium constants from thermodynamic data for reactions involving only condensed-phase substances. The computation of ΔG^0 values for such reactions provides an indication whether the reaction as written is thermodynamically favourable or not. As indicated above, kinetic factors may have a considerable influence on the actual behaviour of a process under given conditions of temperature, pressure, and of the physical state of the materials involved.

A computer program has been developed to calculate ΔG^0 values for all individual reactions considered in this work over wide temperature ranges. The majority of the chemical reactions employed in the thermodynamic analysis of the different systems contain one or more gaseous reactant(s) and/or product(s). For these condensed-gas phase reactions, based on the

TABLE I Sources of thermochemical data for substances considered in equilibrium calculations of this work

Substance	Ref.	Substance	Ref.	Substance	Ref.	Substance	Ref.
$B(s, l)$	17	$Ta(g)$	16	$ZrC(s)$	17	$CrN(s)$	18
$B(g)$	17	$Cr(s, l)$	15	$HfC(s)$	14	$Cr_2N(s)$	18
$C(s)$	19	$Cr(g)$	16	$VC(s, l)$	15	$TiO(s, l)$	14
$C(g)$	19	$Mo(s, l)$	15	$V_2C(s, l)$	14	$TiO(g)$	14
$C_2(g)$	17	$Mo(g)$	18	$NbC(s)$	18	$TiO_2(s, l)$	14
$C_3(g)$	17	$W(s)$	14	$Nb_2C(s)$	14	$Ti_2O_3(s, l)$	14
$N(g)$	19	$TiB(s, l)$	17	$TaC(s)$	15	$Ti_3O_5(s, l)$	14
$N_2(g)$	19	$TiB_2(s)$	17	$Ta_2C(s)$	15	$ZrO(g)$	14
$O(g)$	19	$ZrB_2(s)$	17	$Cr_3C_2(s)$	18	$ZrO_2(s, l)$	14
$O_2(g)$	19	$HfB_2(s)$[a]	17	$Cr_7C_3(s)$	18	$HfO_2(s, l)$	14
$Ti(s, l)$	17	$V_3B_2(s)$	15	$Mo_2C(s)$[a]	14	$VO_2(s, l)$	14
$Ti(g)$	17	$VB(s)$	15	$WC(s)$	14	$V_2O_5(s, l)$	14
$Zr(s, l)$	17	$V_3B_4(s)$	15	$W_2C(s)$	15	$NbO(s, l)$	14
$Zr(g)$	17	$V_2B_3(s)$	15	$TiN(s)$	17	$NbO_2(s, l)$	14
$Hf(s, l)$	14	$V_5B_6(s)$	15	$ZrN(s)$	17	$Nb_2O_5(s, l)$	14
$Hf(g)$	16	$VB_2(s)$	15	$HfN(s)$[a]	14	$Ta_2O_5(s, l)$	14
$V(s, l)$	15	$NbB_2(s)$	14	$VN(s, l)$	18	$Cr_2O_3(s, l)$	18
$V(g)$	18	$TaB_2(s)$	14	$NbN(s, l)$	14	$MoO_2(s)$	18
$Nb(s, l)$	14	$CrB(s)$[a]	–	$Nb_2N(s)$	14	$MoO_3(s, l)$	18
$Nb(g)$	18	$CrB_2(s)$[a]	–	$TaN(s)$	15	$WO_2(s, l)$	18
$Ta(s)$	14	$TiC(s)$	17	$Ta_2N(s)$	15	$WO_3(s, l)$	18

[a] Extrapolated to higher temperatures.

stoichiometry of the reaction and on Equation 5, equilibrium constants (K_p) for individual reactions and equilibrium partial pressures of different gaseous species are computed. For those reactions containing only substances in the condensed phase, ΔG^0 values are reported. For the representative compound of a given class of materials, the equilibrium constants of individual reactions are given as a function of temperature in graphical representation. In the interest of numerical accuracy and for the convenience of the user, the ΔG^0 and equilibrium constant values of all individual reactions are expressed in the form of linear, two-term equations. The numerical constants a and b of these equations are listed in tables. In this way, the results provided can be used for specific reactions alone, and in combination with other reactions of the same and of other systems.

The sources of the thermochemical values of the elements and compounds used in the present computations are listed in Table I. The heat capacity and entropy values of HfN and HfB₂ are given in the literature [14] only up to 1500 and 1700 K, respectively. Thermochemical data for the molybdenum and tungsten borides and nitrides are not readily available. There are various sources of thermochemical data in the literature for a given material. The selection of the sources used in this work is based on a critical analysis of literature data and on a comparative evaluation of theoretical predictions and experimental evidence.
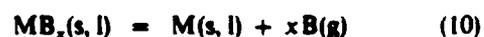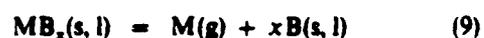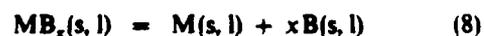
3. Results and discussion

Among the important criteria for the assessment of thermochemical properties and for the application of composite materials at high temperatures is the stability of their constituents with respect to decomposition (volatilization) and their "inertness" with respect to chemical reactivity. Based on common experience and on available literature [1], some stability criteria

of these materials have been established. Vapour pressures or dissociation pressures of about 10^{-6} atm or less present no long-term stability problems. However, vapour pressures of about 10^{-3} atm or higher are considered excessive and may cause serious damage and failure of components of a system. Thus, vapour pressures of about 10^{-5} atm may be taken as an upper-bound safety limit.

These criteria are, of course, qualitative guidelines, and individual materials have to be evaluated under actual conditions. Detailed analyses of the decomposition behaviour of these materials involve specific assumptions about the reaction mechanisms. Thermodynamic analyses of individual chemical reactions have been carried out to estimate their relative importance and that of different vapour species participating in the decomposition process. The chemical stabilities of the refractory borides, carbides, nitrides and oxides will be discussed in separate sections below.

3.1. Stability of metal borides

The decomposition reactions of the refractory metal borides presently considered to yield different product species are represented by the following generalized equations:

$$MB_x(s, l) = M(s, l) + xB(s, l) \tag{8}$$

$$MB_x(s, l) = M(g) + xB(s, l) \tag{9}$$

$$MB_x(s, l) = M(s, l) + xB(g) \tag{10}$$

$$MB_x(s, l) = M(g) + xB(g) \tag{11}$$

where M is a refractory metal of group IV, V, and VI elements and x is the number of boron atoms per metal atom. Because of the large number of compounds and reactions involved, a detailed representation of the K_p values against reciprocal temperature

TABLE II: Values of a and b in the relation $\log K_p = a + (10^4 b/T)$ for different decomposition reactions of refractory borides; the headings indicate the type of reaction products, but not in all cases the stoichiometry

Compound[a]	M(s, l) + B(s, l)[b]	M(s, l) + B(g)	M(g) + B(s, l)	M(g) + B(g)
TiB	$a = 30.86$ $b = 0.4414$	$a = 8.273$ $b = -3.762$	$a = 7.926$ $b = -3.308$	$a = 15.358$ $b = -6.191$
TiB$_2$	$a = 50.89$ $b = 0.8353$	$a = 16.595$ $b = -7.283$	$a = 8.348$ $b = -3.919$	$a = 23.689$ $b = -9.711$
ZrB$_2$	$a = 59.20$ $b = 0.955$	$a = 16.746$ $b = -7.515$	$a = 8.481$ $b = -4.942$	$a = 23.82$ $b = -10.73$
HfB$_2$	$a = 70.48$ $b = 0.4847$	$a = 16.088$ $b = -7.554$	$a = 7.678$ $b = -5.405$	$a = 23.01$ $b = -11.20$
V$_3$B$_2$[a]	$a = 64.56$ $b = 0.3745$	$a = 16.187$ $b = -7.395$	$a = 23.857$ $b = -9.620$	$a = 39.34$ $b = -15.42$
VB[a]	$a = 29.42$ $b = 0.1689$	$a = 8.065$ $b = -3.627$	$a = 7.933$ $b = -3.394$	$a = 15.781$ $b = -6.302$
V$_3$B$_4$[a]	$a = 102.2$ $b = 0.6417$	$a = 32.20$ $b = -14.15$	$a = 24.39$ $b = -10.58$	$a = 55.35$ $b = -22.18$
V$_2$B$_3$[a]	$a = 72.10$ $b = 0.4717$	$a = 24.09$ $b = -10.51$	$a = 16.35$ $b = -7.159$	$a = 39.58$ $b = -15.86$
V$_5$B$_6$[a]	$a = 118.5$ $b = 2.846$	$a = 52.04$ $b = -21.41$	$a = 44.18$ $b = -17.38$	$a = 90.62$ $b = -34.78$
VB$_2$[a]	$a = 41.98$ $b = 0.3029$	$a = 16.066$ $b = -6.868$	$a = 8.293$ $b = -3.741$	$a = 23.786$ $b = -9.544$
NbB$_2$	$a = 36.09$ $b = 0.2555$	$a = 15.766$ $b = -6.701$	$a = 8.304$ $b = -4.738$	$a = 23.64$ $b = -10.53$
TaB$_2$	$a = 43.31$ $b = 0.325$	$a = 15.862$ $b = -6.889$	$a = 7.860$ $b = -5.172$	$a = 23.18$ $b = -10.96$
CrB[a]	$a = 17.21$ $b = 0.0179$	$a = 7.753$ $b = -3.284$	$a = 7.274$ $b = -2.427$	$a = 15.017$ $b = -5.328$
CrB$_2$[a]	$a = 18.25$ $b = 0.1705$	$a = 15.843$ $b = -6.288$	$a = 7.609$ $b = -2.529$	$a = 23.145$ $b = -8.330$

[a] All K_p values are for the temperature range 500 to 3000 K, except for those compounds marked (a) which are for the temperature range 500 to 2500 K.

[b] ΔG^0 values from $\Delta G^0 = a + (10^4 b/T)$ are given in kcal mol^{-1} for the reactions in this column only (1 cal = 4.19 J).

for the individual solid–gas phase reactions of TiB and TiB$_2$ is given in Fig. 1. The temperature dependence of the equilibrium constants of the other group IV, V, and VI borides is represented by the a and b terms of the corresponding linear equations listed in Table II.
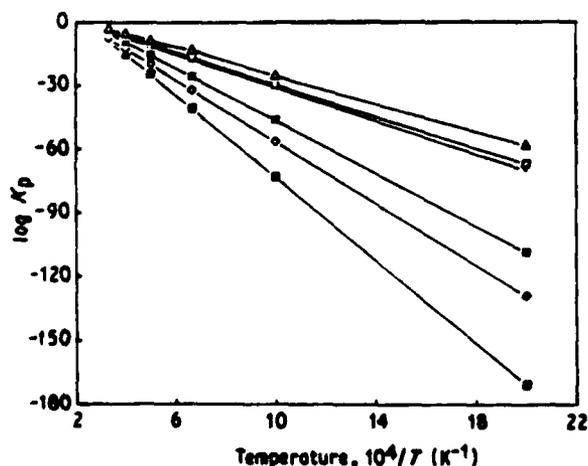

Figure 1 Equilibrium constants as a function of reciprocal temperature for the main solid–gas phase decomposition reactions of TiB(s) and TiB$_2$(s). ($\triangle$) TiB(s) = Ti(g) + B(s, l); ($\square$) TiB(s) = Ti(s, l) + B(g); ($\bullet$) TiB(s) = Ti(g) + B(g); ($\circ$) TiB$_2$(s) = Ti(g) + 2B(s, l); ($\lozenge$) TiB$_2$(s) = Ti(s, l) + 2B(g); ($\blacksquare$) TiB$_2$(s) = Ti(g) + 2B(g).

No reliable thermochemical data for the borides of molybdenum and tungsten are presently available. Therefore, these compounds are not included in the present investigation.

It is evident from Fig. 1 that at lower temperatures the reactions yielding gaseous species are rather insignificant with respect to decomposition of TiB and TiB$_2$. But with increasing temperature and owing to the increasing dominance of the entropy contribution, these reactions may become important for the stability evaluation of the materials. If the gaseous molecules can escape from the reaction interface, even a minor reaction may become critical and become a "runaway reaction". It is also apparent from Fig. 1 that TiB is less stable with respect to decomposition than TiB$_2$. It is intuitively obvious that the decomposition reactions of a given compound yielding condensed-phase products require less energy than those leading to gaseous products. Thus, under given temperature and pressure conditions, the former reactions are more critical with respect to thermal stability of the compound than the latter.

In an attempt to compare the relative thermodynamic stabilities of the metal borides investigated here, the lowest ΔG^0 values at 2000 K, corresponding to the decomposition of a given compound to condensed-phase products, are graphically represented in the
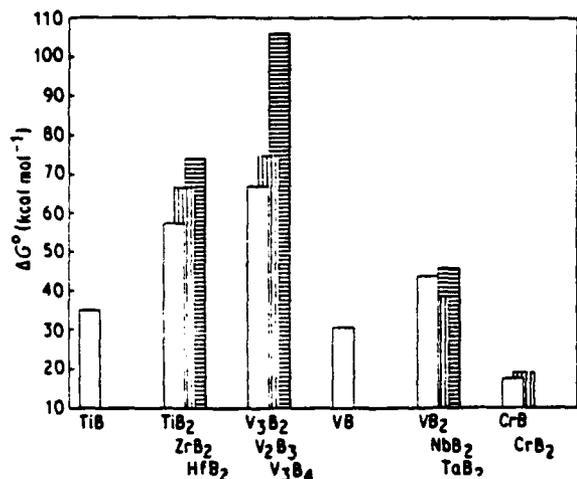
Figure 2 Standard Gibbs free energy changes of the thermodynamically most favourable condensed-phase decomposition reactions of metal borides at 2000 K (1 cal = 4.19 J).

Figure 3 Equilibrium constants as a function of reciprocal temperature for the main solid–gas phase decomposition reactions of TiC(s). (•) TiC(s) = Ti(g) + C(s); (△) TiC(s) = Ti(s, l) + C(g); (□) 2TiC(s) = 2Ti(s, l) + C₂(g); (◇) TiC(s) = Ti(g) + C(g); (+) 3TiC(s) = 3Ti(s, l) + C₃(g); (●) 2TiC(s) = 2Ti(g) + C₂(g); (■) 3TiC(s) = 3Ti(g) + C₃(g).

form of a bar diagram in Fig. 2. In other words, the Gibbs free energy changes (under standard conditions) of the thermodynamically most favourable decomposition reactions of these metal borides are given. Within the constraints of the definition of ΔG^0 and of the meaning of activities for condensed-phase reactions, and assuming that all other conditions (e.g. kinetic limitations) are the same for different compounds, the heights of the bars in Fig. 2 provide a qualitative guideline for the relative stability of the compounds. A larger ΔG^0 value indicates a more stable compound. Apparently, with increasing atomic number of the metal atom, the stabilities of the borides increase within the same group and decrease within the same period of the periodic table for compounds of the same metal to non-metal ratio. In view of the above constraints, a further interpretation of Fig. 2 is not justified. Bolgar et al. [19] measured high-temperature thermodynamic properties (enthalpy and heat capacity) of transition metal refractory borides and has shown that with increasing number of boron atoms per metal atom in the compound, the bond strength of the compounds increases. The same trend is predicted in Fig. 2, based on independent thermochemical computations. These computations suggest that V_3B_4 is the most stable boride followed by V_2B_3 and HfB_2.

3.2. Stability of metal carbides

High-temperature applications of metal carbides require resistance to decomposition and to chemical attack at a free surface. The high melting points and low vapour pressures of group IV, V and VI transition-metal carbides provide the stability in vacuum and inert atmospheres of these materials. For most metal carbides, decomposition occurs by vaporization which may be congruent or incongruent. For some decomposition reactions, product species containing metal–carbon bonds have been reported. The following decomposition reactions of the above metal car-
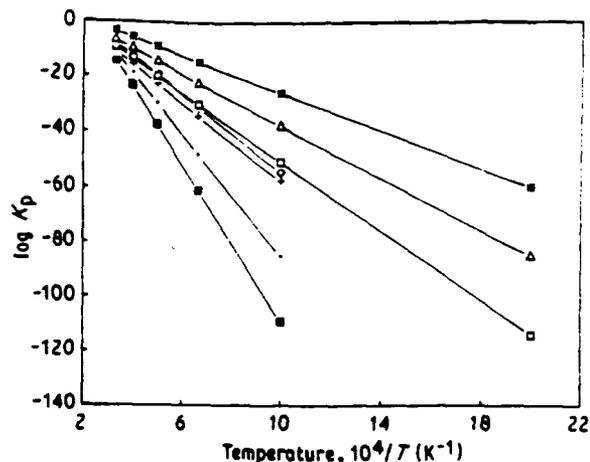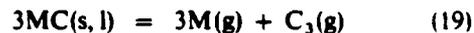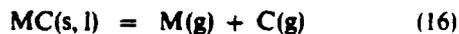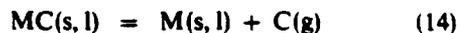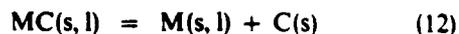
bides are considered for the computational analysis:

$$MC(s, l) = M(s, l) + C(s) \qquad (12)$$

$$MC(s, l) = M(g) + C(s) \qquad (13)$$

$$MC(s, l) = M(s, l) + C(g) \qquad (14)$$

$$2MC(s, l) = 2M(s, l) + C_2(g) \qquad (15)$$

$$MC(s, l) = M(g) + C(g) \qquad (16)$$

$$3MC(s, l) = 3M(s, l) + C_3(g) \qquad (17)$$

$$2MC(s, l) = 2M(g) + C_2(g) \qquad (18)$$

$$3MC(s, l) = 3M(g) + C_3(g) \qquad (19)$$

where M is the same as above. The equilibrium constants as a function of $1/T$ for the most important solid–gas phase decomposition reactions of TiC are graphically represented in Fig. 3. The overall trend of the temperature dependence of the different decomposition reactions and the interpretation are very similar to those of TiB. Again, reactions involving gaseous products can become rather critical at elevated temperatures and seriously affect the stability of the material. The a and b values of the linear equations for the above thermodynamic functions of the other metal carbide decomposition reactions are given in Table III. Reliable thermodynamic data for MoC are presently not available. Drowart et al. [20] reported that at temperatures of about 2500 K and higher, TiC evaporates predominantly as Ti(g) and C₂(g). The different slopes of the decomposition reactions in Fig. 3 are consistent with these observations. For HfC and TaC, Engelke et al. [21] reported that a vapour pressure of carbon higher than that of the metal leads to a loss of carbon at temperatures close to the melting point. A more comprehensive review of the properties of refractory carbides is given by Storms [22] and by Toth [23].

Analogous with the borides, the decomposition reactions of the metal carbides yielding exclusively condensed-phase products are more favourable than

TABLE III Values of a and h in the relation $\log K_p = a + (10^4 b/T)$ for different decomposition reactions of refractory carbides; the headings indicate the type of reaction products, but not in all cases the stoichiometry.

Compounds[a]	M(s, l)→C(s)[z]	M(g)→C(s)	M(s, l)→C(g)	M(s, l)→C₂(g)	M(s, l)→C₃(g)	M(g)+C(g)	M(g)→C₂(g)	M(g)→C₃(g)
TiC	$a = 33.94$	$a = 7.844$	$a = 9.017$	$a = 11.639$	$a = 12.400$	$a = 16.126$	$a = 26.21$	$a = 34.42$
	$h = 0.5072$	$b = -3.401$	$b = -4.727$	$h = -6.300$	$b = -7.051$	$b = -7.147$	$b = -11.25$	$b = -14.44$
ZrC	$a = 39.48$	$a = 7.645$	$a = 8.801$	$a = 11.587$	$a = 12.491$	$a = 15.889$	$a = 25.73$	$a = 33.71$
	$h = 0.3668$	$b = -4.248$	$b = -4.784$	$b = -6.505$	$b = -7.328$	$b = -7.994$	$b = -12.94$	$b = -16.99$
HfC	$a = 48.50$	$a = 7.417$	$a = 8.731$	$a = 11.422$	$a = 12.231$	$a = 15.661$	$a = 25.28$	$a = 33.01$
	$h = 0.3271$	$b = -4.850$	$b = -4.953$	$b = -6.861$	$b = -7.860$	$b = -8.596$	$b = -14.15$	$b = -18.79$
VC[a]	$u = 18.06$	$a = 8.259$	$a = 8.811$	$a = 11.670$	$a = 12.523$	$a = 16.521$	$a = 27.09$	$a = 35.58$
	$h = 0.2933$	$b = -3.212$	$b = -4.293$	$b = -5.529$	$b = -5.857$	$b = -6.968$	$b = -10.88$	$b = -13.87$
V₂C[b]	$a = 33.45$	$a = 15.79$	$a = 8.438$	$a = 11.06$	$a = 11.53$	$a = 24.06$	$a = 42.31$	$a = 58.40$
	$h = 0.0704$	$b = -6.132$	$b = -4.524$	$b = -6.001$	$b = -6.561$	$b = -9.889$	$b = -16.73$	$b = -22.65$
NbC	$a = 31.05$	$a = 8.003$	$a = 8.362$	$a = 10.685$	$a = 11.137$	$a = 16.241$	$a = 26.45$	$a = 34.77$
	$h = 0.0743$	$b = -4.542$	$b = -4.468$	$b = -5.874$	$b = -6.381$	$b = -8.297$	$b = -13.53$	$b = -17.87$
Nb₂C[b]	$u = 39.81$	$a = 16.55$	$a = 8.93$	$a = 12.09$	$a = 12.99$	$a = 24.82$	$a = 43.83$	$a = 60.68$
	$h = 0.2736$	$b = -8.681$	$b = -4.771$	$b = -6.497$	$b = -7.300$	$b = -12.44$	$b = -21.83$	$b = -30.30$
TaC	$a = 35.10$	$a = 7.226$	$a = 8.120$	$a = 10.209$	$a = 10.408$	$a = 15.463$	$a = 24.89$	$a = 32.43$
	$h = -0.0942$	$b = -4.804$	$b = -4.482$	$b = -5.902$	$b = -6.422$	$b = -8.558$	$b = -14.05$	$b = -18.65$
Ta₂C	$u = 47.95$	$a = 14.699$	$a = 8.326$	$a = 10.473$	$a = 10.796$	$a = 22.93$	$a = 39.82$	$a = 54.84$
	$h = -0.0101$	$b = -9.199$	$b = -4.814$	$b = -6.541$	$b = -7.379$	$b = -12.95$	$b = -22.84$	$b = -31.83$
Cr₃C₂[a]	$a = 27.83$	$a = 20.995$	$a = 15.755$	$a = 9.790$	$a = 19.44$	$a = 37.50$	$a = 31.55$	$a = 84.74$
	$h = -0.3679$	$b = -6.551$	$b = -7.934$	$b = -4.876$	$b = -9.755$	$b = -14.06$	$b = -11.01$	$b = -28.15$
Cr·C₃	$a = 54.87$	$a = 49.20$	$a = 23.18$	$a = 14.251$	$a = 9.292$	$a = 73.97$	$a = 65.05$	$a = 60.08$
	$h = -0.7251$	$b = -15.12$	$b = -12.08$	$b = -7.501$	$b = -5.066$	$b = -26.39$	$b = -21.80$	$h = -19.37$
Mo₂C[a]	$a = 13.50$	$a = 14.921$	$a = 8.011$	$a = 10.08$	$a = 10.16$	$a = 23.19$	$a = 40.40$	$a = 55.64$
	$h = -0.0866$	$b = -7.084$	$b = -3.999$	$b = -4.943$	$b = -4.980$	$b = -10.84$	$b = -18.62$	$b = -25.50$
WC	$a = 7.653$	–	$a = 7.989$	$a = 10.84$	$a = 11.30$	–	–	–
	$h = 0.0678$	–	$b = -3.932$	$b = -4.858$	$b = -4.851$	–	–	–
W₂C	$a = 31.64$	–	$a = 6.037$	$a = 6.039$	$a = 4.163$	–	–	–
	$h = -1.397$	–	$b = -3.805$	$b = -4.548$	$b = -4.391$	–	–	–

[a] All K_p values are for the temperature range 500 to 3000 K, except ([a]) for 500 to 2500 K and ([b]) for 500 to 2000 K.

[z] ΔG^0 values from $\Delta G^0 = a + (10^4 b/T)$ given in kcal mol^{-1} for the reactions in this column only (1 cal = 4.19 J).

those yielding gaseous products within a given temperature range. Thus, the thermal stability of the metal carbides is limited by the former reactions. Within the same constraints as discussed above for the metal borides, the relative stabilities of the metal carbides at 2000 K are compared in terms of the ΔG^0 values for the most favourable condensed-phase decomposition reactions in Fig. 4. Under these conditions, it is apparent from Fig. 4 that the stabilities of the mono-carbides increase with atomic number of the metal in groups IV and V and for the di-metal carbides of group V at 2000 K.

For the chromium, molybdenum and tungsten carbides the trend is different owing to the molecularity effect. But on a per-atom basis, the trend is the same. Electronic band calculations for these carbides [24–26] suggest that electron transfer occurs from the metal to the interstitial carbon atoms upon bond formation in the above carbides. This direction of transfer would lead to the formation of a stronger C–M bond associated with a weakened M–M bond in MC relative to the pure metal. Shohoji [27] estimated the carbon–metal interactions in carbides and reported that the C–M bonds in group IV metal carbides tend to strengthen with increasing atomic number of the metal from titanium to hafnium. These theoretical considerations [27] are consistent with our thermochemical predictions concerning the relative

stabilities of TiC, ZrC and HfC based on their decomposition reactions evaluated in this work (Fig. 4).

The metal–carbon bond energy (E_{C-M}) of the vanadium, niobium and tantalum carbides was also estimated by Shohoji [27]. The trend in the E_{C-M} values is the same as that for the titanium, zirconium and hafnium carbides. But the E_{C-M} values of group V
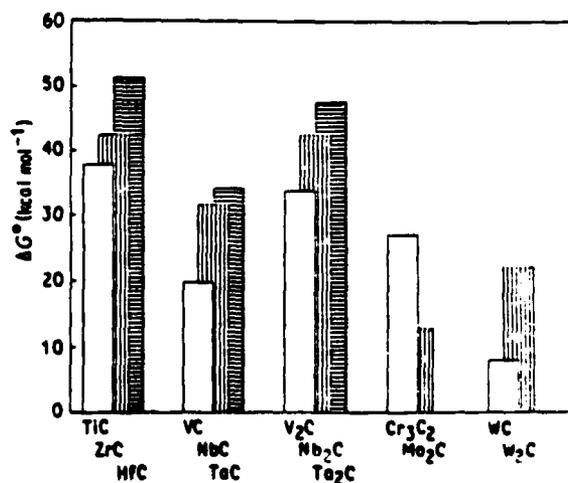

Figure 4 Standard Gibbs free energy changes of the thermodynamically most favourable condensed-phase decomposition reactions of metal carbides at 2000 K (1 cal = 4.19 J).

metal carbides are less negative (i.e. weaker C–M bond strength) than those of the group IV carbides. These trends are also reflected in our thermodynamic estimations. Our predictions are also supported by the suggestion of Storms [22], relating the increases in the melting points of group IV and V metal carbides relative to those of the pure group IV and V metals to the different C–M bond strengths in these metal carbides. Because the metal–carbon bonds in group IV (titanium, zirconium and hafnium) carbides are much stronger than the bonds in titanium, zirconium and hafnium metals, these carbides show a considerable increase in their melting points relative to those of the pure metals.

The corresponding differences in M–C and M–M bond energies in group V (vanadium, niobium and tantalum) carbides and metals, respectively, are less pronounced, which leads to the smaller increases in melting points of group V carbides relative to those of the pure metals. Samsonov et al. [28] presented a configurational model for these materials, according to which the degree of localization of valence electrons in stable configurations of titanium, zirconium and hafnium is not high. Thus, on forming carbides, these metals employ a greater part of their non-localized electrons for M–C bond formation. This leads to stabilization of the sp^3 configuration of carbon atoms, and titanium, zirconium and hafnium carbides are formed with strong metal–carbon bonds.

Based on our thermodynamic estimations, the stabilities of group IV, V and VI carbides are in the order of group IV > group V > group VI, and HfC is the most stable of these carbides.

3.3. Stability of metal nitrides

The main decomposition reactions of the metal nitrides considered in this work are given by the reactions

$$MN(s, l) = M(s, l) + \tfrac{1}{2}N_2(g) \quad (20)$$

$$MN(s, l) = M(g) + \tfrac{1}{2}N_2(g) \quad (21)$$
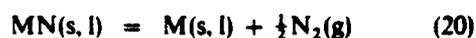
The temperature dependences of the equilibrium constants of the above decomposition reactions of titanium, zirconium and hafnium nitrides are given in Fig. 5. It is apparent from the results that at lower temperatures the reactions leading to M(g) are rather insignificant. At higher temperatures these reactions become increasingly more important, reflecting the increased dominance of the entropy contribution to the free energy of reaction. Combined with a continuous escape of the gaseous products under non-equilibrium conditions from the reaction interface, these reactions may cause catastrophic failure of the materials.

The a and b values of the linear $\log K_p$ against $1/T$ equations of the metal nitride reactions considered here are given in Table IV. The maximum $\log K_p$ values associated with the dominant reactions of group IV, V, and VI metal nitrides at 2000 K are graphically represented in Fig. 6. From this diagram it is evident that the stabilities of group IV and V metal nitrides increase with increasing atomic number of the
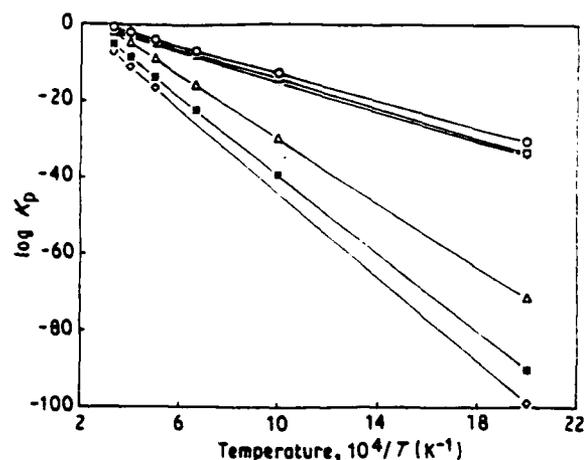

Figure 5 Equilibrium constants as a function of reciprocal temperature for the main solid–gas phase decomposition reactions of TiN(s), ZrN(s) and HfN(s). (○) TiN(s) = Ti(s, l) + ½N₂(g); (□) TiN(s) = Ti(g) + ½N₂(g); (□) ZrN(s) = Zr(s, l) + ½N₂(g); (●) ZrN(s) = Zr(g) + ½N₂(g); (●) HfN(s) = Hf(s, l) + ½N₂(g); (○) HfN(s) = Hf(g) + ½N₂(g).

metal within the same group and with increasing number of metal atoms in the compound. Reliable thermodynamic data for molybdenum and tungsten nitrides are not available. The relative thermodynamic stabilities of group IV, V and VI refractory nitrides are in the order group IV > group V > group VI.

3.4. Stability of metal oxides
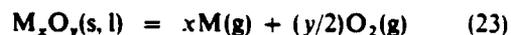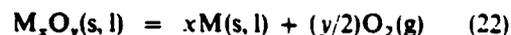The decomposition reactions presently considered for the selected refractory metal oxides are

$$M_xO_y(s, l) = xM(s, l) + (y/2)O_2(g) \quad (22)$$

$$M_xO_y(s, l) = xM(g) + (y/2)O_2(g) \quad (23)$$

TABLE IV Values of a and b in the relation $\log K_p = a + (10^4 b/T)$ for the decomposition reactions of refractory metal nitrides; the headings indicate the type of reaction products, but not in all cases the stoichiometry

Compounds[a]	M(s, l) + ½N₂(g)	M(g) + ½N₂(g)
TiN	a = 4.938	a = 12.031
	b = −1.762	b = −4.190
ZrN	a = 4.847	a = 11.936
	b = −1.091	b = −5.122
HfN	a = 4.409	a = 11.707
	b = −1.901	b = −5.508
VN	a = 4.305	a = 11.910
	b = −1.121	b = −3.789
NbN	a = 3.875	a = 11.753
	b = −1.194	b = −5.203
Nb₂N[a]	a = 4.110	a = 17.064
	b = −1.275	b = −9.069
TaN	a = 4.187	a = 11.491
	b = −1.272	b = −5.352
Ta₂N	a = 4.336	a = 19.199
	b = −1.364	b = −9.526
CrN	a = 3.847	a = 11.667
	b = −0.594	b = −2.669
Cr₂N[a]	a = 3.590	a = −18.104
	b = −0.632	b = −4.719

[a] All K_p values are for the 500 to 3000 K temperature range except (a) which are for the 500 to 2500 K temperature range.

TABLE V Values of a and b in the relation $\log K_p = a + (10^4\, b/T)$ for the decomposition reactions of refractory metal oxides; the headings indicate the type of reaction products, but not in all cases the stoichiometry

Compound[a]	M(s,l) + O₂(g)	M(g) + O₂(g)	MO₂(s,l) + MO(s,l)[c]	MO₂(s,l) + MO(g)	MO(s,l) + O₂(g)	MO(g) + O₂(g)	MO₂(s,l) + O₂(g)
TiO	a = 7.216, b = -5.350	a = 21.40, b = -10.21					
TiO₂	a = 9.159, b = -4.906	a = 16.254, b = -7.334			a = 11.102, b = -4.460	a = 27.030, b = -9.873	
Ti₂O₃	a = 25.96, b = -15.66	a = 54.34, b = -25.37	a = 8.724, b = 0.120	a = 8.180, b = 2.955	a = 5.774, b = -2.480	a = 21.70, b = 7.892	
Ti₃O₅	a = 21.35, b = -12.67	a = 42.63, b = -19.96	a = 15.96[b], b = -0.334	a = 7.466, b = -2.896	a = 10.51, b = -4.647	a = 34.40, b = -12.77	
ZrO₂	a = 9.629, b = -5.709	a = 16.684, b = -8.926				a = 13.30, b = -5.973	
HfO₂	a = 8.958, b = -5.766	a = 15.891, b = -9.409					
VO₂[*]	a = 7.537, b = -3.653	a = 15.250, b = -6.329					
V₂O₃	a = 18.375, b = -7.887	a = 30.74, b = -12.70					a = 3.572, b = -0.599
NbO	a = 4.086, b = -2.104	a = 11.963, b = -5.932					
NbO₂	a = 8.439, b = -4.085	a = 16.321, b = -7.914			a = 4.357, b = -1.981		
Nb₂O₅	a = 20.474, b = -9.770	a = 36.24, b = -17.43			a = 12.554, b = -5.579		a = 3.697, b = -1.607
Ta₂O₅	a = 20.66, b = -10.52	a = 35.340, b = -18.67					
Cr₂O₃	a = 13.562, b = -5.898	a = 27.713, b = -9.961					
MoO₂	a = 8.687, b = -3.011	a = 16.195, b = -6.426					
MoO₃[b]	a = 12.035, b = -3.891	a = 19.679, b = -7.315					
WO₂[*]	a = 8.904, b = -3.034						
WO₃	a = 12.463, b = -4.332						

[a] All K_p values are for the temperature range 500 to 3000 K, except (*) which are for 500 to 2500 K and (b) for 500 to 2000 K.

[b] ΔG^0 values from $\Delta G^0 = a + (10^4\, b/T)$ are in kcal mol⁻¹ for the reactions in this column only (1 cal = 4.19 J).
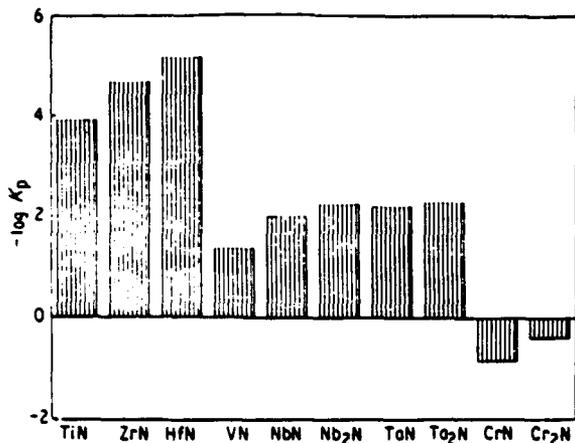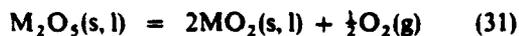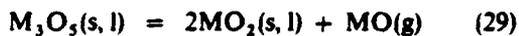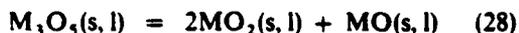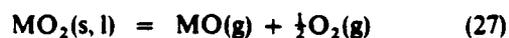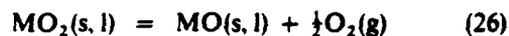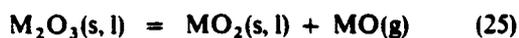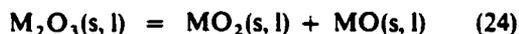
Figure 6 Equilibrium constants of the thermodynamically most favourable decomposition reactions of metal nitrides at 2000 K.

Figure 8 Equilibrium constants of the thermodynamically most favourable decomposition reactions of metal oxides at 2000 K.

$$M_2O_3(s, l) = MO_2(s, l) + MO(s, l) \qquad (24)$$

$$M_2O_3(s, l) = MO_2(s, l) + MO(g) \qquad (25)$$

$$MO_2(s, l) = MO(s, l) + \tfrac{1}{2}O_2(g) \qquad (26)$$

$$MO_2(s, l) = MO(g) + \tfrac{1}{2}O_2(g) \qquad (27)$$

$$M_3O_5(s, l) = 2MO_2(s, l) + MO(s, l) \qquad (28)$$

$$M_3O_5(s, l) = 2MO_2(s, l) + MO(g) \qquad (29)$$

$$MO_3(s, l) = MO_2(s, l) + \tfrac{1}{2}O_2(g) \qquad (30)$$

$$M_2O_5(s, l) = 2MO_2(s, l) + \tfrac{1}{2}O_2(g) \qquad (31)$$

The temperature dependences of the equilibrium constants for the TiO and TiO_2 decomposition reactions are shown in Fig. 7. The a and b values of the linear equations of the $\log K_p$ and ΔG^0 values of the refractory oxides are given in Table V. The maximum $\log K_p$ values associated with the dominant decomposition reactions of the different refractory oxides at
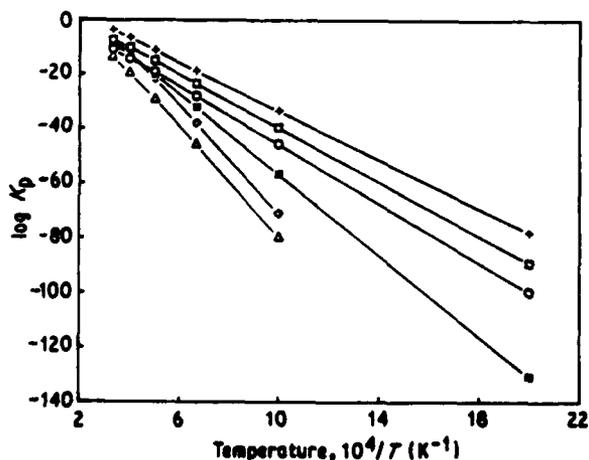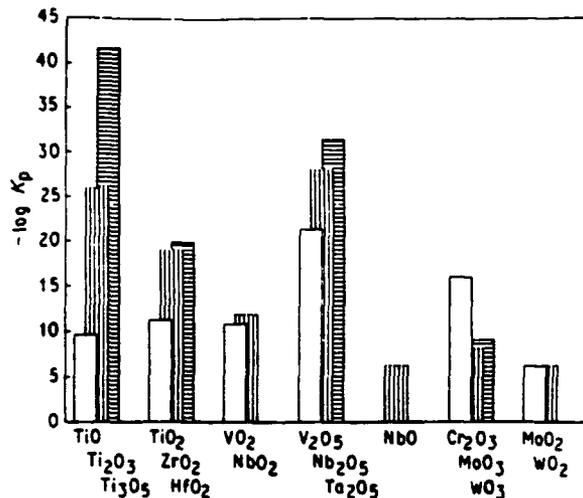
2000 K are shown in Fig. 8. It is apparent from Fig. 8 that for the same composition, the stabilities of group IV, V, and VI oxides increase with increasing atomic number of the metal within the same group. Also, the higher metal oxides are more stable than those of the lower oxidation states.

4. Summary and conclusions

The equilibrium thermodynamic computations suggest that at 2000 K, V_3B_4 is the most stable boride followed by V_2B_3 and HfB_2. Of the refractory carbides and nitrides, HfC and HfN are predicted to be the most stable compounds. In the case of refractory oxides, Ti_3O_5 and Ta_2O_5 are the most stable ones with respect to decomposition at 2000 K. Based on the thermodynamic functions (ΔG^0, K_p), the stabilities of refractory metal borides, carbides, nitrides, and oxides are in the order

oxides > borides > carbides > nitrides

The predictions of our thermodynamic computations agree well with experimental observations and with other theoretical computations reported in the literature. The thermal stability of materials is one of the most important criteria for the selection of constituent materials for high-temperature composites. Other relevant considerations include mechanical properties, density, vaporization (mass loss), oxidation and thermal shock resistance.

The usefulness of our thermochemical computations is multifold. Based on the results obtained, work is in progress to estimate the vaporization (mass loss) rates of these materials under different conditions. In addition, the data produced in this work provide valuable guidelines for the selection of materials and for the prediction of their relative stabilities as constituents (fibre, matrix and coatings) in composite systems. Corresponding computations for selected systems are in progress in our laboratory. Most importantly, these theoretical considerations provide a scientific basis for a meaningful modification of present and design of new high-temperature materials.

Figure 7 Equilibrium constants as a function of reciprocal temperature for the main solid-gas phase decomposition reactions of $TiO(s)$ and $TiO_2(s)$. (O) $2TiO(s) = 2Ti(s, l) + O_2(g)$; (Δ) $2TiO(s) = 2Ti(g) + O_2(g)$; (□) $TiO_2(s) = Ti(s, l) + O_2(g)$; (•) $TiO_2(s) = Ti(g) + O_2(g)$; (+) $2TiO_2(s) = 2TiO(s, l) + O_2(g)$; (◊) $2TiO_2(s) = 2TiO(g) + O_2(g)$.

Acknowledgements

References

1. W. B. HILLIG. in "Tailoring Multiphase and Composite Ceramics", Materials Science Research, Vol. 20, edited by R. E. Tressler, G. L. Messing, C. G. Pantano and R. E. Newnham (Plenum, New York, 1986) p. 697.
2. L. CHRISTODOULOU, P. A. PARISH and C. R. CROWE. *Mater. Res. Soc. Symp. Proc.* **120** (1988) 29.
3. R. K. VISWANADHAM, J. D. WHITTENBERGER, S. K. MANNAN AND B. SPRISSLER, *ibid.* **120** (1988) 89.
4. K. VEDULA, A. ABADA and W. S. WILLIAMS, *ibid.* **120** (1988) 61.
5. Proceedings of 2nd Conference on Advanced Materials for Alternative-Fuel-Capable Heat Engines, Monterey, California, August 1981, EPRI-RD-2369-ST (Electric Power Research Institute, Palo Alto, California, 1982).
6. W. J. LACKEY, D. P. STINTON, G. A. CERNY, A. C. SCHAFFHAUSER and L. L. FEHRENBACHER. *Adv. Ceram. Mater.* **2** (1) (1987) 24.
7. L. H. ROVNER and G. R. HOPKINS, *Nucl. Technol.* **29** (1976) 204.
8. K. SHOBU, T. WATANABE, Y. ENOMOTO, K. UMEDA and Y. TSUYA. *J. Amer. Ceram. Soc.* **70**(5) (1987) C-103.
9. B. L. MORDIKE. *Wear* **3** (1960) 374.
10. Y. G. TKACHENKO, S. S. ORDAN'YAN, D. Z. YURCHENKO, V. K. YULYUGIN and D. V. CHUPOV. *Sov. Powder Metall. Metal Ceram.* (English translation) **22**(1) (1983) 137.
11. M. SINGH and H. WIEDEMEIER, in "Interfacial Phenomena in Composite Materials, '89", edited by F. R. Jones (Butterworths, London, 1989) p. 303.
12. H. WIEDEMEIER and M. SINGH, in Symposium on "High Temperature Chemistry of Composite Materials", 176th Meeting of the Electrochemical Society, Hollywood, Florida (1989) p. 753.
13. *Idem.* in "Interfaces in Metal–Ceramics Composites", edited by R. Y. Lin, R. J. Arsenault, G. P. Martins and S. G. Fishman (The Minerals, Metals and Materials Society, Warrendale, PA, 1989) p. 125.
14. I. BARIN and O. KNACKE. "Thermochemical Properties of Inorganic Substances" (Springer, Berlin, 1973).
15. *Idem.* "Thermochemical Properties of Inorganic Substances", Supplement (Springer, Berlin, 1977).
16. D. R. STULL and H. PROPHET. "JANAF Thermochemical Tables", 2nd Edn (National Bureau of Standards, Washington, DC, 1971).
17. M. W. CHASE Jr, C. A. DAVIES, J. R. DOWNEY Jr, D J FRURIP, R. A. McDONALD and A. N. SYVERUD. "JANAF Thermochemical Tables", 3rd Edn (National Bureau of Standards, Washington, DC, 1985).
18. M. W. CHASE Jr, J. L. CURNUTT, R. A. McDONALD and A. N. SYVERUD. "JANAF Thermochemical Tables", Supplement (National Bureau of Standards, Washington, DC, 1978).
19. A. S. BOLGAR, A. B. LYASHCHENKO, L. A. KLOCHKOV, A. V. BLINDER, Y. B. MURATOV, M. I. SERBOVA and V. V. FESENKO. *J. Less-Common Met.* **117** (1986) 303.
20. J. DROWART, G. DEMARIA and M. G. INGHRAM. *J. Chem. Phys.* **29** (1958) 1015.
21. J. L. ENGELKE, F. A. HALDEN and E. F. FARLEY. US Air Force Report WADC-TR-59-654 (Stanford Research Institute, February 1960).
22. E. K. STORMS. "The Refractory Carbides" (Academic, New York, 1967).
23. L. TOTH. "Transition Metal Carbides and Nitrides" (Academic, New York, 1971).
24. T. HORI, H. ADACHI and S. IMATO. *Trans. Jpn Inst. Met.* **18** (1977) 31.
25. L. P. MOKHRACHEVA, V. A. TSKHAI and P. V. GELD. *Phys. Status Solidi (b)* **84** (1977) 465.
26. *Idem, ibid.* **87** (1978) 49.
27. N. SOHOJI. *Mater. Chem. Phys.* **17** (1981) 391.
28. G. V. SAMSONOV, A. S. BOLGAR, E. A. GUSEVA, L. A. KLOCHKOV, B. A. KOVENSKAYA, T. I. SEREBRYAKOVA, I. I. TIMOFEEVA, A. G. TURCHANIN and V. V. FRESENKO. *High Temp.-High Press.* **5** (1973) 29.

High temperature thermal and environmental stabilities of boron nitride, aluminium nitride and silicon nitride ceramics

M. Singh and H. Wiedemeier

The thermal and environmental stabilities of boron nitride (BN), aluminium nitride (AIN), and silicon nitride (Si_3N_4) ceramics have been evaluated using thermochemical modelling. The volatility diagrams of these materials have been established at 2000 K. Master volatility diagrams with equilibrium pressure of dominant vapour species at 1400, 1600, 1800 and 2000 K have also been constructed. The phase stability diagrams of BN and Si_3N_4 have been established to indicate the stability of various oxide and oxynitride phases in equilibrium with these nitrides at different oxygen and nitrogen pressures. These data show that in order to prevent dissociation and volatilization, nitrogen over-pressures are required during processing and/or operation at higher temperatures. Vaporization rate data indicate that under congruently vaporizing conditions, the mass losses of silicon nitride are greatest, followed by those of aluminium nitride and then boron nitride.

Keywords: ceramics; boron nitride; aluminium nitride; silicon nitride; thermal stability; environmental stability

Introduction

In recent years, there has been a surge of interest in materials containing borides, carbides, nitrides and oxides of refractory metals and of silicon, aluminium and boron for a variety of high temperature and aerospace applications. Some interesting properties of these materials are their high melting points and low densities, their high hardness and strength, and resistance to oxidation and wear[1,2]. Boron and aluminium nitride have high thermal conductivity, low thermal expansion and good thermal shock resistance. Applications for nitride ceramics have emerged because of their increasing use as monolithic and as constituents for high temperature and high performance composites. Boron nitride coatings are quite effective in preventing the chemical interactions of silicon carbide fibres with alumina, mullite, zircon and some other high temperature oxide matrices[3]. In addition, boron nitride toughened oxide matrix composites have also been considered for radome applications[4]. Silicon nitride has been used as matrix and reinforcement (fibres/whiskers) in high temperature composites. However, degradation of these nitride ceramics has been frequently observed at elevated temperatures under different conditions.

The thermal stability and vaporization behaviour of these materials have been the subject of numerous experimental investigations[5–9]. Hildenbrand and Hall[6] have investigated the vaporization behaviour of boron nitride and aluminium nitride and observed that the measured vapour pressures of both materials are strongly affected by the effusion orifice area. Jones and Nicholas[7] reported a weight gain for the aluminium nitride and a weight loss for the boron nitride and silicon nitride ceramics at 1423 K. These observations were attributed to the formation of a stable condensed oxide for aluminium nitride and dissociation and/or reactive formation of volatile oxides for boron nitride and silicon nitride. Sato et al.[8] and Boch et al.[9] observed that the oxidation kinetics of aluminium nitride were promoted by water vapour. Billy and Desmaison[10] reported that the thermomechanical properties (oxidation, creep and strength) are strongly dependent on the nature and amount of residual intergranular glassy phases present owing to the use of densification additives.

Most of these experimental studies could not be conducted at temperatures of current interest because of experimental limitations. For these materials, valuable predictions can be made from thermodynamic modelling and from computations of maximum possible dissociation and oxidation rates at high temperatures. In the present paper, the thermal and environmental stabilities of boron nitride, aluminium nitride and silicon nitride are reported. The volatility and phase stability diagrams of these materials under different environmental conditions are discussed. A detailed understanding of the thermal and environmental stabilities and of the mass loss behaviour is required for the application of these nitrides as high temperature structural materials. This detailed information is presently not available for some of these materials.

Thermochemical considerations

A number of materials are thermodynamically unstable at high temperatures and in a reactive environment. The rate and the extent of the degradation depends on the type(s) and rate(s) of the reaction(s) causing this

instability. We have used thermochemical modelling to predict the occurrence of reactions under different high temperature conditions. Thermodynamic data used in the present investigation have been taken from JANAF Tables[11] and from Barin and Knacke[12]. Based on the free energies and equilibrium constants of reactions, volatility and phase stability diagrams have been constructed at different temperatures. Individual chemical reactions were considered to analyse the effect of different vapour species. For the vaporization rate calculations, the Hertz–Knudsen equation has been used[13]. The combined information obtained from these computations will contribute to the better understanding of the thermal behaviour of these ceramic materials.

Results and discussion

Based on common experience and on available literature data[14], stability criteria for different materials relative to decomposition have been established. Vapour or dissociation pressures of about 10^{-6} atm or less present no long-term problems. However, vapour pressures of about 10^{-3} atm or higher are excessive and may cause damage and failure of the components. Thus, vapour pressures of about 10^{-5} atm may be taken as an upper bound safe limit. However, these criteria are qualitative guidelines and individual materials have to be evaluated under actual application conditions.

Boron nitride

Thermodynamic calculations for the decomposition and vaporization of boron nitride are based on the following dominant reactions:

$$BN(s) = B(s) + \tfrac{1}{2} N_2(g) \qquad (1)$$

$$BN(s) = BN(g) \qquad (2)$$

and

$$BN(s) = B(g) + \tfrac{1}{2} N_2(g). \qquad (3)$$

Because of the relatively low stability of gaseous boron nitride and the very high stability of the nitrogen molecule, solid boron nitride vaporize primarily according to reactions (1) and (3). Schissel and Williams[5] observed the elemental species by using mass spectroscopy. X-ray diffraction analysis of partially decomposed boron nitride samples by Hildenbrand and Hall[6], showed no indication of crystalline boron, and they concluded that the decomposition reaction leading to amorphous boron and nitrogen may be favourable.

The volatility diagram of the B–N system at 2000 K is given in Figure 1. From this diagram it is evident that at nitrogen pressures above 1 atm, BN(g) is the dominant species. At nitrogen pressures below 1 atm, B(g) is dominant. At a nitrogen pressure of about 10^{-4} atm,
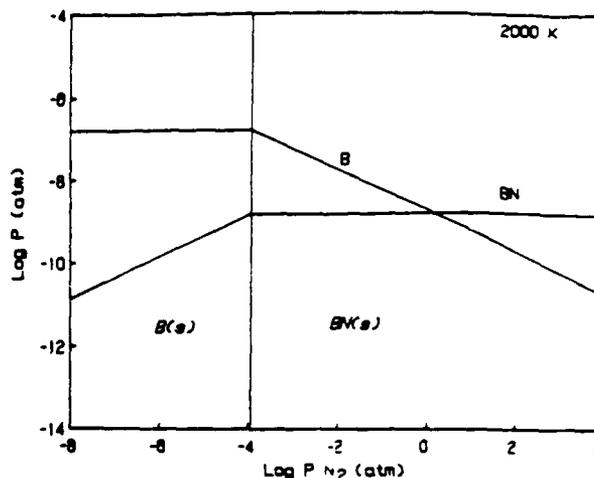

Figure 1. Equilibrium partial pressures of B(g) and BN(g) over BN(s) or B(s) as a function of nitrogen partial pressure at 2000 K
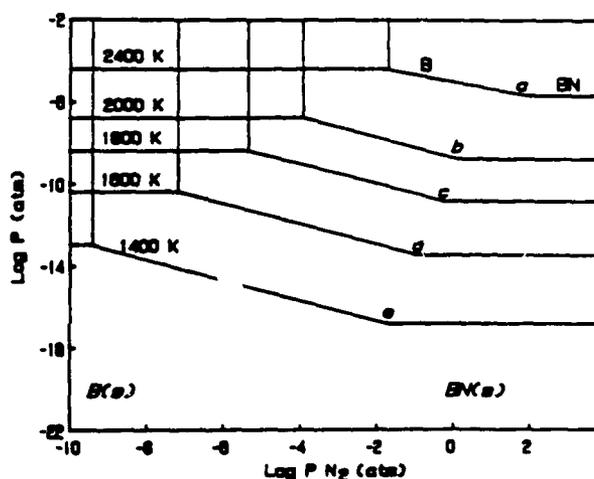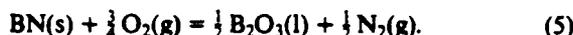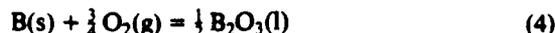

Figure 2. Equilibrium partial pressures of B(g) and BN(g) over BN(s) or B(s) as a function of nitrogen partial pressure at different temperatures

B(g) reaches saturation pressure, and at lower nitrogen pressures, BN(g) decomposes. The equilibrium pressure lines of the dominant species for the vaporization of the B–N system at different temperatures and nitrogen pressures are given in Figure 2. At the points a, b, c, d and e on the partial pressure lines, the dominant vapour species changes from BN to B. The vertical lines in Figures 1 and 2 indicate the saturation pressure of boron at corresponding temperatures. At a given temperature, if the nitrogen pressures are higher than those corresponding to the vertical lines, boron nitride is stable. The partial pressures of BN and B are lower than 10^{-5} atm up to 2000 K and reach critical limits at about 2400 K. This indicates that significant mass losses could occur due to decomposition at about 2400 K.

Another criterion for the use of boron nitride at high temperatures is its reaction with oxygen. Phase stability diagrams are very useful to determine the stability range of various solid phases at different temperatures

and pressures. In the present case, two temperatures (1600 and 2000 K) have been considered. The dominant chemical reactions of boron and boron nitride with oxygen considered here are:

$$B(s) + \tfrac{3}{4} O_2(g) = \tfrac{1}{2} B_2O_3(l) \qquad (4)$$

$$BN(s) + \tfrac{3}{4} O_2(g) = \tfrac{1}{2} B_2O_3(l) + \tfrac{1}{2} N_2(g). \qquad (5)$$

In a three component system, three solid phases can be in equilibrium at a fixed temperature and pressure. There are no thermodynamic data reported in the literature on the boron oxynitride phase. Based on the phase rule, one invariant point exists in the B–N–O system, which involves B, BN and B_2O_3. The phase stability diagram of the B–N–O system in Figure 3 indicates that decomposition and oxidation of BN at 2000 K can be prevented at oxygen pressures lower than 8.7×10^{-15} atm and at nitrogen pressures higher than 1.3×10^{-4}. Boron nitride is also stable at lower temperatures and nitrogen pressures, but at very low oxygen-containing environments. The oxygen pressures required to have stable BN depend on the nitrogen pressures (Figure 3).

Aluminium nitride

The dominant decomposition and vaporization reactions of aluminium nitride considered are:

$$AlN(s) = Al(s,l) + \tfrac{1}{2} N_2(g) \qquad (6)$$

$$AlN(s) = AlN(g) \qquad (7)$$

and

$$AlN(s) = Al(g) + \tfrac{1}{2} N_2(g). \qquad (8)$$
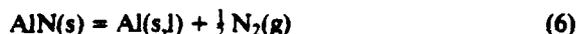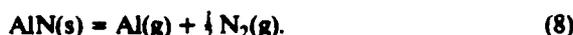
Schissel and Williams[5] observed mass spectrometrically that AlN vaporizes to form gaseous Al and N_2. This observation suggests that the vaporization

Figure 4. Equilibrium partial pressures of Al(g) and AlN(g) over AlN(s) or Al(l) as a function of nitrogen partial pressure at 2000 K

reaction (8) is dominant. Hildenbrand and Hall[6] reported no change in the lattice constants of aluminium nitride with amount vaporized and concluded that the process must be essentially congruent. The volatility diagram of the Al–N system at 2000 K in Figure 4 shows that Al(g) is the major species at all nitrogen pressures. At atmospheric nitrogen pressure (and below), the partial pressure of Al reaches critical limits at 2000 K. The equilibrium pressures of Al(g) at four different temperatures are shown in Figure 5. The vertical lines in Figures 4 and 5 indicate the saturation pressures of aluminium. From the volatility diagram (Figure 5), nitrogen partial pressures required to minimize aluminium mass losses can be estimated at different temperatures. The stability of AlN is determined for a given temperature by the nitrogen pressure.

The dominant reactions of Al(l) and AlN(s) with oxygen are

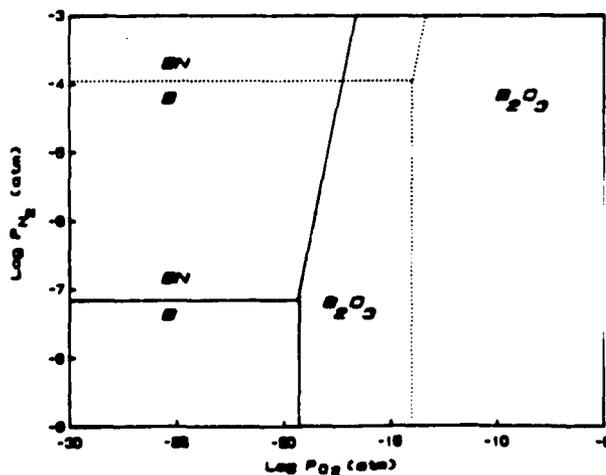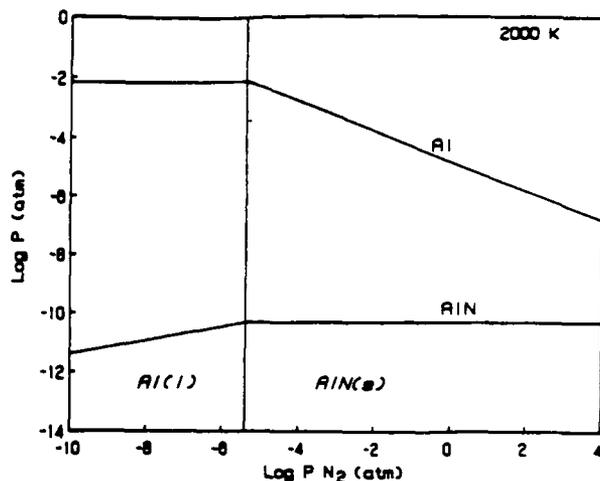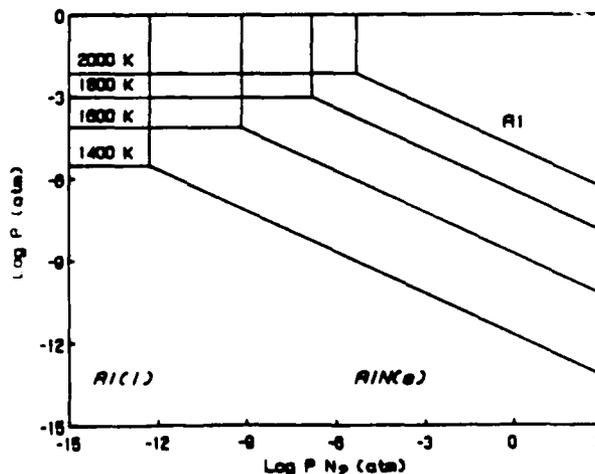$$Al(l) + \tfrac{3}{4} O_2(g) = \tfrac{1}{2} Al_2O_3(s) \qquad (9)$$

Figure 3. The phase stability diagram for the B–N–O system in terms of nitrogen and oxygen partial pressures at 1600 K (solid lines) and 2000 K (dotted lines)

Figure 5. Equilibrium partial pressures of Al(g) over AlN(s) or Al(l) as a function of nitrogen partial pressure at different temperatures

$$AlN(s) + \tfrac{3}{4} O_2(g) = \tfrac{1}{2} Al_2O_3(s) + \tfrac{1}{2} N_2(g). \qquad (10)$$

Some reports in the literature indicate the existence of aluminium oxynitrides. Thermodynamic data for these compounds are not available. The Gibbs free energy changes (ΔG°) or reactions (9) and (10) indicate that these reactions are more favourable than those of boron and boron nitride with oxygen (reactions (4) and (5)).
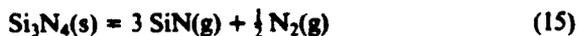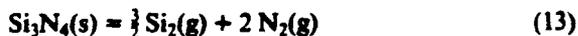
Silicon nitride

Decomposition of silicon nitride occurs during processing and operating conditions at high temperatures. During the sintering of silicon nitride, Lange[15] observed moderate to severe mass losses depending on the temperature, vacuum (oxygen pressure) and nitrogen pressure applied during sintering. The vaporization reactions leading to mass losses can also yield undesirable compositional changes. The dissociation of silicon nitride to condensed silicon and N_2 occurs according to the reaction[16]:

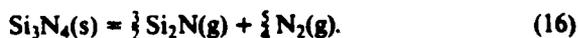$$Si_3N_4(s) = 3 Si(s,l) + 2 N_2(g). \qquad (11)$$

The equilibrium constants of reaction (11) as a function of temperature indicate that the nitrogen pressure reaches 1 atm at about 2150 K.

The vaporization behaviour of silicon nitride is quite complex and the possible reactions include:

$$Si_3N_4(s) = 3 Si(g) + 2 N_2(g) \qquad (12)$$

$$Si_3N_4(s) = \tfrac{3}{2} Si_2(g) + 2 N_2(g) \qquad (13)$$

$$Si_3N_4(s) = Si_3(g) + 2 N_2(g) \qquad (14)$$

$$Si_3N_4(s) = 3 SiN(g) + \tfrac{1}{2} N_2(g) \qquad (15)$$

and

$$Si_3N_4(s) = \tfrac{3}{2} Si_2N(g) + \tfrac{5}{4} N_2(g). \qquad (16)$$

The partial pressures of the various vapour species in reactions (12) to (16) as a function of nitrogen pressure at 2000 K in Figure 6 show that the predominant vapour species over Si_3N_4 are SiN(g) and Si(g). At 2000 K, the partial pressures of Si(g) reach critical limits (Figure 6) based on general criteria[14]. The volatility diagram of the Si–N system for the equilibrium pressures of the dominant species at four different temperatures is given in Figure 7. At the points a, b, c, and d on the partial pressure lines, the dominant vapour species changes from SiN to Si. The vertical lines in Figures 6 and 7 indicate the saturation pressures of silicon. These volatility diagrams indicate that the dissociation and vaporization of silicon nitride can be suppressed at high temperatures by applying high nitrogen pressures.

In addition to the decomposition and volatilization, chemical interactions of silicon nitride with oxygen occur under processing and application conditions at high temperatures[17, 18]. The dominant chemical reactions of silicon nitride with oxygen considered are
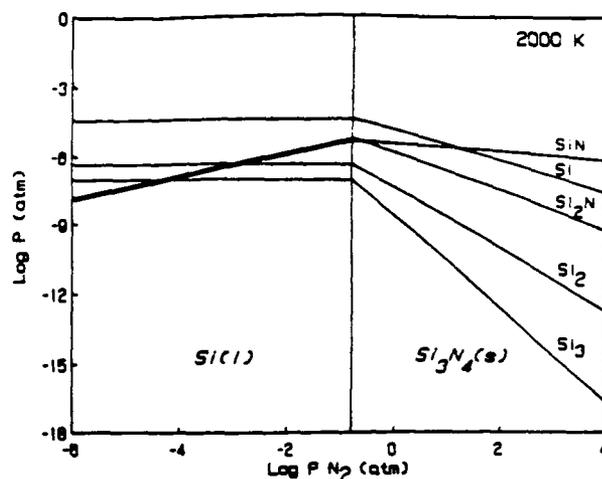
$$Si_3N_4(s) + 3 O_2(g) = 3 SiO_2(s,l) + 2 N_2(g) \qquad (17)$$

Figure 6. Equilibrium partial pressures of various Si-containing species over $Si_3N_4(s)$ or Si(l) as a function of nitrogen partial pressure at 2000 K
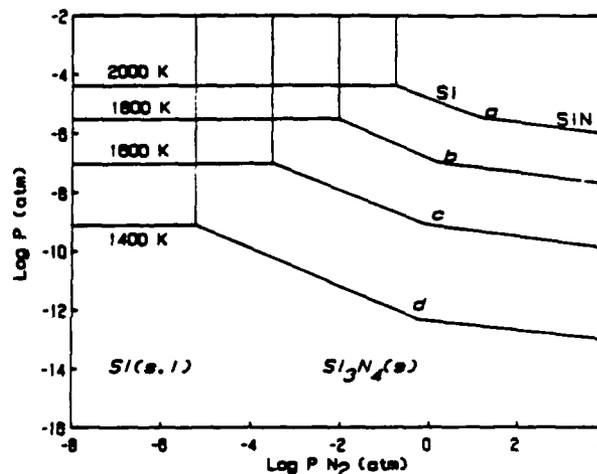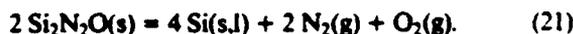

Figure 7. Equilibrium partial pressures of Si(g) and SiN(g) over $Si_3N_4(s)$ or Si(s,l) as a function of nitrogen partial pressure at different temperatures

$$Si_3N_4(s) + \tfrac{3}{2} O_2(g) = 3 SiO(g) + 2 N_2(g) \qquad (18)$$

$$4 Si_3N_4(s) + 3 O_2(g) = 6 Si_2N_2O(s) + 2 N_2(g) \qquad (19)$$

$$2 Si_2N_2O(s) + 3 O_2(g) = 4 SiO_2(s) + 2 N_2(g) \qquad (20)$$

and

$$2 Si_2N_2O(s) = 4 Si(s,l) + 2 N_2(g) + O_2(g). \qquad (21)$$

Thermodynamic data for silicon oxynitride have been taken from Hendry[19]. Based on the phase rule and thermochemical data for reactions (17)–(21), the phase stability diagram of the Si–N–O system has been established at various oxygen and nitrogen partial pressures in Figure 8. Two invariant points exist in the Si–N–O system. One involves Si, Si_3N_4, and Si_2N_2O, and the other involves Si, Si_2N_2O and SiO_2. The solid and dotted lines in Figure 8 correspond to 1600 and 2000 K, respectively. It is evident from Figure 8 that high nitrogen pressures are required to maintain silicon nitride as a stable phase at these temperatures, and to prevent the formation of silicon oxynitride (Si_2N_2O). At 1600 K, silicon nitride is stable at pressures
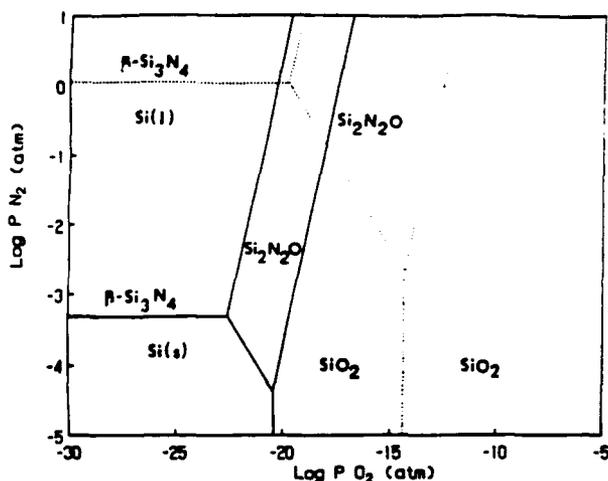
Figure 8. The phase stability diagram for the Si–N–O system in terms of nitrogen and oxygen partial pressures at 1600 K (solid lines) and 2000 K (dotted lines)

of $P_{N_2} = 4.9 \times 10^{-4}$ atm and $P_{O_2} = 2.6 \times 10^{-23}$ atm or higher. These conditions change to $P_{N_2} = 1.12$ atm and $P_{O_2} = 1.6 \times 10^{-20}$ atm at 2000 K. If the oxygen pressure increases, nitrogen overpressures are required to prevent formation of oxynitride and oxide phases.

For comparison purposes, from the equilibrium constants of reactions (1), (6) and (11), the equilibrium partial pressures of nitrogen have been plotted at two B, Al and Si activities ($a = 1$, 0.01) in Figure 9. At both activities of B, Al and Si, the nitrogen partial pressures from the decomposition of silicon nitride are several orders of magnitude higher than the nitrogen partial pressures resulting from the boron nitride and aluminium nitride decomposition. These data indicate that aluminium nitride is more stable than boron nitride and silicon nitride. However, if the activities of B, Al and Si are less than unity ($a = 0.01$), then the nitrogen pressure increases by several orders of magnitude. This indicates that any solid solution or compound formation of B, Al and Si will increase the tendency of these nitrides to decompose.
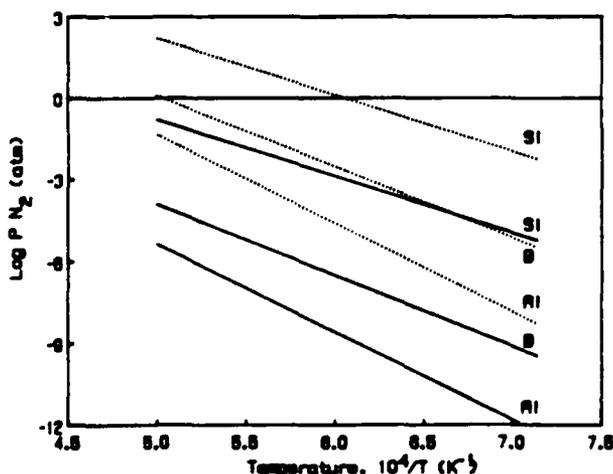

Figure 9. Equilibrium partial pressures of nitrogen as a function of temperature at two activities of B, Al and Si (solid lines ($a = 1$), dotted lines ($a = 0.01$))

The two main reasons for the mass loss of these materials at high temperatures are dissociation to their elemental species and/or formation of volatile oxides in the presence of oxygen. Hildenbrand and Hall[6] reported that the vaporization of AlN is congruent in the temperature range 1780–1970 K. The vaporization behaviour of other nitrides is not available in the literature for the temperature range considered here. The vaporization (mass loss) rates of these nitrides can be computed by using the Hertz–Knudsen equation of classical kinetic theory[13] for free or vacuum evaporation conditions. The present estimations are based on two assumptions; namely, the vaporization of these materials is congruent according to reactions (3), (8) and (12), and equilibrium vapour pressures are exhibited under free vaporization conditions. Because of the latter assumption, the estimated mass losses represent maximum values. Based on the above, the masses of the two elements leaving the surface have the relation

$$\frac{n_B}{n_{N_2}} = \frac{wt.B}{M_B} \frac{M_{N_2}}{wt.N_2} = \frac{2}{1} \tag{22}$$

and the mass of each constituent leaving unit area of the solid in unit time is obtained from the Knudsen equation

$$\text{Mass loss of } B = 44.3 \, P_B \left(\frac{M_B}{T}\right)^{1/2} \tag{23}$$

Hence

$$\frac{n_B}{n_{N_2}} = \frac{P_B}{P_{N_2}} \left(\frac{M_{N_2}}{M_B}\right)^{1/2} = \frac{2}{1} \tag{24}$$

$$P_{N_2} = \frac{P_B}{2} \left(\frac{M_{N_2}}{M_B}\right)^{1/2} \tag{25}$$

$$P_{N_2} = 0.804 \, P_B. \tag{26}$$

Substitution of the value of P_{N_2} in the expression for the equilibrium constant of reaction (3) yields

$$K_3 = 0.897 \, P_B^{3/2}. \tag{27}$$

By using equation (27), P_B can be determined. The total mass loss per unit area of the solid BN is then the sum of the masses of B and N_2 lost during evaporation

$$\text{Total mass loss} = 44.3 \left(\frac{P_B}{T}\right)^{1/2} (M_B^{1/2} + 0.897 \, M_{N_2}^{1/2}). \tag{28}$$

By using the same approach, partial pressures and equilibrium constants for AlN and Si_3N_4, the corresponding expressions are

$$K_8 = 0.713 \, P_{Al}^{3/2} \tag{29}$$

and

$$K_{12} = 0.444 \, P_{Si}^{5}. \tag{30}$$

A plot of the mass loss rates versus temperature is given in Figure 10. The mass loss of silicon nitride is greatest followed by that of aluminium nitride and boron nitride. The experimental mass losses reported by
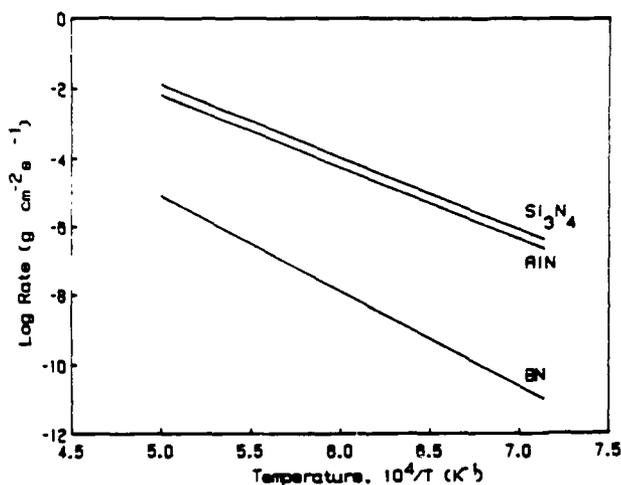
Figure 10. Maximum vaporization rates of BN, AIN, and Si_3N_4 as a function of temperature

Jones and Nicholas[7] at 1423 K for boron nitride and silicon nitride are 6.2×10^{-8} and 4.5×10^{-8} g cm^{-2} s^{-1}, respectively. Based on our estimations, the mass loss of silicon nitride at 1400 K is 2.88×10^{-7} g cm^{-2} s^{-1}, i.e. greater than observed, which is consistent with the above assumptions. For boron nitride, our computed value is a few orders of magnitude lower than the observed one. This discrepancy is not consistent with expectations and could indicate mass losses caused by other than 'pure' vaporization processes in the experimental investigations.

Conclusions

The construction and use of volatility diagrams showing the partial pressures of gaseous species in equilibrium with condensed phases for B-N, Al-N and Si-N systems are discussed. Boron nitride is quite stable at 2000 K with respect to dissociation, but significant mass losses could occur at about 2400 K. For aluminium nitride and silicon nitride, dissociation pressures reach critical limits depending on the nitrogen pressures. The phase stability diagrams of the B-N-O and Si-N-O systems at 1600 and 2000 K indicate that nitrogen overpressures are required to prevent dissociation and oxidation of boron nitride and silicon nitride depending on the processing and operating conditions. In addition, it is estimated that under congruent vaporization conditions, mass loss of silicon nitride is greatest followed by aluminium nitride and boron nitride.

References

1 Corbin, N.D., Resetar, T.M. and McCauley, J.W. In *Innovations in Materials Processing, Sagamore Army Mater Res. Conf.* Vol. 30 (Ed. G. Bruggerman and V Weiss) Plenum Press, New York (1985)

2 Larsen, D.C., Adams, J.W., Johnson, L.R., Teotia, A.P.S. and Hill, L.G. *Ceramic Materials for Advanced Heat Engines* Noyes Publications, Park Ridge, NJ (1985)

3 Cramer, D.C. Fiber coating and characterization. *Ceram. Bull.* 68 2 (1989) pp 415–419

4 Coblenz, W. and Lewis, D. In situ reaction of B_2O_3 with AIN and/or Si_3N_4 to form BN-toughened composites. *J. Am. Ceram. Soc.* 71 12 (1988) pp 1080–1085

5 Schissel, P. and Williams, W.S. Mass spectroscopic studies of the vaporization of certain refractory materials. *Bull. Am. Phys. Soc.* II 4 (1959) p 139

6 Hildenbrand, D.L. and Hall, W.F. The vaporization behavior of boron nitride and aluminum nitride. In *Condensation and Evaporation of Solids* (Ed. E. Rutner, P. Goldfinger and J.P. Hirth) Gordon and Breach, New York (1964) pp 399–415

7 Jones, L.M. and Nicholas, M.G. Thermal stability of nitride ceramics. *J. Mater. Sci. Lett.* 8 3 (1989) pp 265–266

8 Sato, T., Haryu, K., Endo, T. and Shimada, M. High temperature oxidation of hot-pressed aluminium nitride by water vapor. *J. Mater. Sci.* 22 6 (1987) pp 2277–2280

9 Boch, P., Glandus, J.C., Jarrige, J., Lecompte, L.P. and Mexmain, J. Sintering, oxidation and mechanical properties of hot pressed aluminum nitride. *Ceram. Int.* 8 1 (1982) pp 34–40

10 Billy, M. and Desmaison, J.G. High temperature oxidation of silicon based structural ceramics. *High Temp. Technol* 4 3 (1986) pp 131–139

11 Stull, D.R. and Prophet, H.D. *JANAF Thermochemical Tables* National Bureau of Standards, Washington, DC (1971)

12 Barin, I. and Knacke, O. *Thermochemical Properties of Inorganic Substances* Springer Verlag, New York (1973); Suppl. (1977)

13 Turkdogen, E.T. *Physical Chemistry of High Temperature Technology* Academic Press, New York (1980)

14 Wiedemeier, H. and Singh, M. Thermal stability of refractory materials for high-temperature composite applications. *J. Mater. Sci.* 26 (1991) pp 2421–2430

15 Lange, F. Volatilization associated with the sintering of Si_3N_4 materials. *J. Am. Ceram. Soc.* 65 8 (1982) pp C120–121

16 Greskovich, G. and Prochazka, S. Stability of Si_3N_4 and liquid phase(s) during sintering. *J. Am. Ceram. Soc.* 64 7 (1981) pp C96–97

17 Singhal, S.C. Oxidation of silicon nitride and related materials. In *Nitrogen Ceramics* (Ed. F.L. Riley) Noordhoff International, Leyden. The Netherlands (1977) pp 607–626

18 Heuer, A.H. and Lou, V.L.K. Volatility diagrams for silica, silicon nitride and silicon carbide and their application to high temperature decomposition and oxidation. *J. Am. Ceram. Soc.* 73 10 (1990) pp 2785–2803

19 Hendry, A. Thermodynamics of silicon nitride and oxynitride. In *Nitrogen Ceramics* (Ed. F.L. Riley) Noordhoff International, Leyden. The Netherlands (1977) pp 183–185

Authors

The authors are at the Department of Chemistry, Rensselaer Polytechnic Institute, Troy, NY 12180-3590, USA.

AN INVESTIGATION INTO THE PREPARATION, PROPERTIES, AND PROCESSING OF SiC/AlN and Si_3N_4/AlN SOLID SOLUTIONS FROM ORGANOMETALLIC PRECURSORS.

LEONARD V. INTERRANTE[*], CORINNA L. CZEKAJ[*], MICHEAL L.J. HACKNEY[*], GARY A. SIGEL[*], PAUL J. SCHIELDS[**], AND GLEN A. SLACK[**].

 [*] Rensselaer Polytechnic Institute, Troy, NY 12180.

 [**] General Electric Research and Development Center, P.O. Box 8, Schenectady, NY 12301.

Abstract

Solid solutions of SiC and AlN have been prepared by the co-pyrolysis of polysilanes and organoaluminum amides. In the presence of ammonia, Si_3N_4 and AlN are formed. These materials are fully characterized by TEM, SAD, SEM, XRPD, and elemental analyses. The influence of reaction conditions, as well as precursor properties and reactivity, on the composition and morphology of these materials is addressed.

Introduction

A constraint on the use of SiC in high temperature applications is the existence of cubic (β-SiC, 3C), hexagonal (α-SiC, 2H, 4H, 6H), and rhombohedral ("α-SiC", 15R, 21R) polytypes of SiC having one or more phase transformations between 1400 and 2200°C. These phase transformations often result in undesirable changes in microstructure, including exagerated grain growth [1]. AlN is a good candidate for phase stabilization of and solid solution formation with SiC because its only form is isostructural with the wurtzite (hexagonal, 2H) form of SiC and is closely latticed matched.

The prospect of alloying SiC with other covalently bonded refractory materials, such as AlN, to achieve microstructural control or alter properties has previously been noted and realized under certain conditions [1-8]. SiC/AlN solid solutions have been prepared by hot pressing mixtures of α-SiC with AlN [2,3], carbothermal reduction of silica and alumina powders [4], sintering [5], and vapor deposition processes [6].

Several observations regarding the formation and microstructure of SiC/AlN solid solutions emerge from these studies. First, it is difficult to prepare homogeneous single phase SiC solid solutions at "low" temperatures (less than 2300°C). Second, large gradients in composition

typically exist within solid solutions and individual grains. Finally, the microstructure and composition of the resulting materials is highly sensitive to the nature of the starting materials, processing conditions, and impurities, such as oxygen, nitrogen, and metal ions.

The use of organometallic presursors to SiC/AlN composites and solid solutions may overcome some of these difficulties. We have applied this approach to the preparation of SiC/AlN ceramics by the co-pyrolysis of molecularly mixed organometallic presursors to SiC and AlN [9,10]. Slow pyrolysis of a mixture of polysilane or carbosilane with an organoaluminum amide leads to a composite of 2H-AlN with 3C-SiC, which transforms into a single phase 2H-SiC/AlN solid solution on heating to 2000°C. Heating the same precursors and precursor mixtures under ammonia at 1000°C yields Si_3N_4 and mixtures of Si_3N_4 with AlN, respectively. Improved ceramic yields for the mixed precursor systems suggested that chemical interaction of the SiC and AlN precursors or their pyrolysis products may occur at some point in the pyrolysis.

The information obtained from the co-pyrolysis and TGA studies suggested that phase separation might be avoided by carrying out the pyrolysis at elevated temperatures, where the rates of pyrolysis of both precursors were sufficiently high. Herein, we report on our efforts to prepare SiC/AlN solid solutions at temperatures less than 1600°C by a rapid pyrolysis or "hot-drop" approach.

Experimental

Alkylaluminum amide compounds, $[R_2AlNH_2]_3$, where R=ethyl or isobutyl, were employed as the precursor to AlN. These colorless, air-sensitive, oily liquids decompose on heating in an ammonia atmosphere to yield high purity AlN in a two step process. The first step occurs at temperatures between 110 and 200°C and results in the formation of an insoluble aluminum imide polymer and one mole of alkane gas. Subsequent heating of this polymer to 1000°C under an ammonia atmosphere yields AlN containing less than 0.5% residual C and O [11]. A polysilane polymer, provided by C. Schilling at Union Carbide [12], $[(Me_3Si)_{0.85}(CH_2CHSiMe)_{1.0}(Me_2Si)_{0.30}]_x$, served as the source of SiC. Both compounds were handled and stored in a nitrogen filled glove box.

In a typical "hot-drop" experiment, 1.60g of Schilling's polymer (SP) and 2.41 g of $[Et_2AlNH_2]_3$, 9.70×10^{-3} and 8.00×10^{-3} moles respectively, were mixed in a nitrogen filled glove box for 30 minutes at room

temperature. The clear liquid mixture is then transferred to a 5.0 mL syringe, whose tip is covered with a septum. The quartz stage of the reactor was heated to the desired temperature--500 to 700°C--in a sand bath, then flushed with ammonia. The needle was then pushed through the small septum and a septum on the reactor in one motion. The precursor mixture was dropped onto the stage over a 45 minute period, while flowing ammonia into the reactor at a rate of 50 cc/min. A solid white product was obvserved immediately on addition. After two hours of heating under ammonia, nitrogen gas was introduced into the system and heating was continued for four hours. The reactor was then cooled to room temperature and transferred to a nitrogen filled glove box, where the white solid was removed and placed in a molybdenum boat enclosed in a quartz tube for further heating to 1000°C. The products at this stage are poorly crystalline black solids, which required further heat treatment at 1400-1800°C to develop sufficient crystallinity for analysis and remove excess carbon.

Solid products were analyzed by TEM, SAD, SEM, electron microprobe, x-ray diffraction, and chemical analyses [13]. Pyrolysis behavior was studied by TGA and GC analyses of the pyrolysis gases. Variable temperature ^{1}H, ^{13}C, and ^{29}Si NMR studies were carried out on samples of SP, $[Et_2AlNH_2]_3$, SP + $[Et_2AlNH_2]_3$, $(CH_2=CH)_2SiMe_2$ + $[Et_2AlNH_2]$, and $Me_3Si-SiMe_3$ + $[Et_2AlNH_2]_3$ dissolved in benzene-d$_6$ or toluene-d$_8$.

Results and Discussion

Analyses of the solid product of the co-pyrolysis of a 1:1 mixture of Schilling's polymer and $[Et_2AlNH_2]_3$ by the "hot drop" approach indicates direct formation of 2H-SiC/AlN solid solutions. XRD data of the product, after heating to 1790°C under nitrogen, shows only 2H-type lines. These lines are relatively broad, suggesting poor crystallinity or a range of 2H-SiC/AlN compositions. The apparent existence of two peaks in the x-ray intensity region between the 2H-SiC and 2H-AlN reference positions suggests that two main solid solution compositions may be present , as shown in Figure 1. Lines for other SiC polytypes and β-Si$_3$N$_4$ are absent. Similar lines were much broader.

The existence of two separate 2H-SiC/AlN solid solution phases is corroborated by electron microprobe, TEM, and SAD analyses. Electron microprobe indicates a non-uniform distribution of Si and Al within and between individual grains, with Al:Si ratios varying between 1:1.2 and
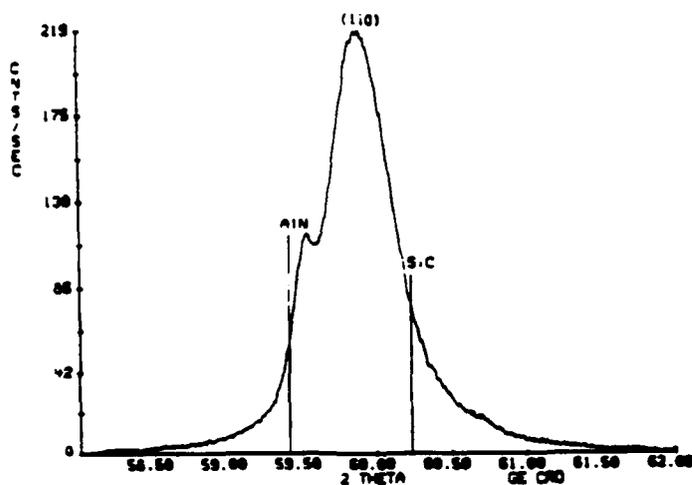
Figure 1.

1:1.6. TEM analyses indicate the presence aluminum and silicon rich
particles, with Si:Al ratios in the range of 1:10 and 2.5:1, respectively.
There are large compositional variations between particles; however,
both exhibit wurtzite diffraction patterns as observed by SAD.

Elemental analyses of the 1790°C sample gave Anal. calcd. for SiC/AlN:
Si, 34.64%; C,14.76%; Al, 33.19%;, N, 17.23%. Found: Si, 39.71%; C, 17.22%;
Al, 27.20%; N, 15.72%. These data suggests that volatile Al and N containing
products are being removed from the reactor during pyrolysis. An
independent analysis for oxygen on the same sample [13], giving a value of
2.98%.

Solid products obtained at 600 and 1000°C were found to be
non-crystalline by x-ray and electron diffraction. TEM analyses show that
the products are featureless. In all cases SEM data indicate that the
products are made up of highly agglomerated, irregularly shaped particles.

The detailed dependence of the product composition and phase
distribution on process variables such as structure, oxygen content, and
relative amount of the two precursors, temperature of the quartz reactor,
and the use of ammonia or nitrogen at various stages of the pyrolysis is
still under investigation. Recent experiments suggest that virtually any
desired phase in the Si-C-Al-O-N system can be obtained by proper control
of these variables. In addtion to our work in the SiC/AlN and Si$_3$N$_4$/AlN
system [12], we have recently discovered that the product of "hot-drop"
reactions, carried out at 640°C under ammonia, using precursors which
apparently contain appreciable oxygen, is β'-SiAlON. This assignment is

based on XRD of the product after heating in nitrogen to 1490°C, and supported by elemental analysis.

A second area of interest has been the exploration of the chemistry associated with the transformation of SP and [Et$_2$AlNH$_2$]$_3$ to a SiC/AlN solid solution. TGA data indicate that mixtures of Schilling's polymer and [Et$_2$AlNH$_2$]$_3$ have a higher ceramic yield than would be predicted based on individual ceramic yields [10]. GC analyses of the pyrolysis products of the precursor mixture, as compared to the pyrolysis products of SP or [Et$_2$AlNH$_2$]$_3$, indicate that the precursors are reacting with one another during pyrolysis.

Variable temperature solution NMR studies were carried out to gain insight into the nature of this reactivity. On heating [Et$_2$AlNH$_2$]$_3$ in tol· ·-d$_8$ solution from 60-120°C in the NMR probe, the conversion of [Et$_2$ ₂]$_3$ to a new but chemically similar species is observed. The conversion is reversible; after allowing the sealed NMR tube to stand overnight at room temperature, the original spectrum of [Et$_2$AlNH$_2$]$_3$ is obtained. This process is not observed when [Et$_2$AlNH$_2$]$_3$ is heated to 120°C as a neat liquid, then dissolved in toluene-d$_8$. This provides evidence for the formation of a solution stabilized intermediate during the conversion, perhaps monomeric Et$_2$AlNH$_2$.

On heating [Et$_2$AlNH$_2$]$_3$ with SP in toluene-d$_8$ between 60 and 120°C, the conversion of the trimer to a new species is observed. This conversion is accompanied by changes in the vinyl region of the ^{1}H NMR and ^{13}C spectra, suggesting the reaction of SP with some "Et$_2$AlNH$_2$" species in solution. Changes in the ^{29}Si spectrum for the Si bound to a vinyl group support this observation. Finally, in a model study for this process, the reaction of the vinyl group of (CH$_2$=CH)$_2$SiMe$_2$ with [Et$_2$AlNH$_2$]$_3$ in benzene-d$_8$ solution was observed.

It is important to note that although GC data suggest that Schilling's polymer and [Et$_2$AlNH$_2$]$_3$ react during pyrolysis, this reactivity was not observed in NMR spectra taken after the precursors were mixed and heated as a neat liquid to 120°C, then dissolved in solution. Solid state and solution NMR studies, aimed at providing insight into these differences in reactivity, are currently in progress.

Acknowledgements

References

1. I.B. Cutler, P.D. Miller, W. Rafaniello, M.K. Park, D.P. Thompson, and K.H. Jack, Nature 275, 434 (1978).

2. R. Ruh and A. Zangvil, J. Amer. Cer. Soc. 65, 260 (1982).

3. R. Ruh and A. Zangvil, presented at the 1981 Meeting of the American Ceramic Society, Washington, D.C., 1981 (unpublished).

4. W. Rafaniello, K. Cho, and A. Vikar, J. Mater. Sci. 16, 349 (1981). 5.

5. G. Irving, Jr., U.S. patent No. 3 492 153 (27 January 1970).

6. S.A. Nurmagomedov, Pis'ma Tekh. Fiz. 12, 1043 (1986).

7. G.K. Safaraliev, G.K. Salchank, Y.M. Tairov, V.F. Tsvetkov, Inorg. Mater. 22, 1610 (1987).

8. K. Tskuma, M. Shimidu, M. Koizami, J. Mater. Sci. Lett. 3, 249 (1984).

9. M.L.J. Hackney, L.V. Interrante, G.A. Slack, P.J. Schields, presented at the Proceedings of the 3rd International Conference on Ultrastructure Processing of Ceramics, Glasses, and Composites, San Diego, CA, 1987.

10. C.L. Czekaj, M.L.J. Hackney, L.V. Interrante, G.A. Sigel, G.A. Slack, and P.J. Schields, submitted to J. Amer. Cer. Soc., 1988.

11. L.V. Interrante, L.E. Carpenter II, C. Whitmarsh, W. Lee, M. Garbauskas, and G.L. Slack in Better Ceramics Through Chemistry II, edited by C.J. Brinker, D.E. Clark, and D.R. Uhlrich (Maters. Res. Soc. Proc. 73, Pittsburgh, PA 1985) pp. 359.

12. C.L. Schilling, Jr., J.P. Wesson, T.C. Williams, Ceram. Bull. 62, 912 (1983).

13. X-ray diffraction was performed using either a Siemens d500 or Rigaku theta-theta diffractometer at General Electric. Elemental Analyses were provided by Multichem and Galbraith Analytical Laboratories. TEM and SAD analyses were carried out on a JEOL-100-X microscope. NMR studies were performed on a Varian XL-200 spectrometer.

OXIDATIVE STABILIZATION OF BULK CARBONCEOUS MATERIALS

A. J. Kazmer[1] and R. J. Diefendorf[2]

1. Rensselaer Polytechnic Institute, Troy, N. Y.
2. Clemson University, Clemson, S. C.

INTRODUCTION

Oxidative stabilization is a process that converts a thermoplastic mesophase pitch into a thermosetting solid. In the past, this thermosetting technique has been used to prevent the melting, viscous flow and microstructural changes in the production of carbon fibers. In order for stabilization to thermoset bulk mesophase pitches, oxygen must diffuse to reaction sites where reaction occurs. In trying to understand the reactions that lead to stabilization the effects of environment, temperature, and time on the diffusion of oxygen in a mesophase pitch system have been quantified.

EXPERIMENTAL PROCEDURE

Particles of a solvent fractionated Ashland A240 petroleum pitch were used in this study. The 350 μm mesophase particles were stabilized in a Mettler TA1 thermogravimetric analyzer (TGA) in oxygen and air environments. 50 mg samples were heated at 10 c/min to temperatures of 220, 240, 260, 280 and 300C. In a later experiment after 4 hours of exposure at 300C in oxygen a vacuum removed the oxidizing environment and was replaced by an argon environment at temperatures of 220, 260, and 300C.

The heat treated samples have been mounted, polished and their oxygen profiles obtained using a JEOL 733 electron microprobe calibrated for oxygen analysis with a probe diameter of 2 μm. The calibration of the microprobe for oxygen analysis was set using a silica standard and verified on polished beads of Poly p-phenylene ether sulphone (20.5 wt% O) and propenoic acid (8.9 wt% O).

RESULTS AND DISCUSSION

The change in weight percent versus time as a function of temperature for air and oxygen environments have been determined by thermogravimetric analysis (Figures 1 and 2). In both environments, the samples heat treated at lower temperatures (220 and 240C) show net weight gains only. The samples heat treated to higher temperatures (260, 280, and 300C) show both net weight gains and losses. At higher temperatures the samples in both cases lose a significant portion of the weight gained while at the lower temperatures the samples maintain their weight over time. The samples treated in the oxygen environment show

increases in the net weight gain and accelerated behavior when compared to samples treated in air (Figure 3).

Two general trends are observed when comparing the oxygen profiles of the oxygen treated versus air treated samples (Figures 4 and 5). The first is that the oxygen environment samples have a higher weight percent oxygen throughout the probed distance. The second is that oxygen is found to greater depths in the oxygen treated sample. Additionally, the higher temperature samples (260, 280, and 300C) in either environments have higher maximum weight percents of oxygen than the lower temperature samples (220 and 240C).

The net weight gain of these samples has been attributed to the diffusion and reaction of oxygen into the samples which stabilizes the microstructure. Two of the processes contributing to the net weight loss of the material are surface oxidation and decomposition. Surface oxidation is the loss of material at the surface due to its reaction with oxygen and occurs where diffusion of oxygen into the material is slow. The oxygen reacts at the surface rather than diffusing into the bulk of the material. Decomposition is the internal oxidation of the material with time. In this case, oxygen diffuses into the sample rather than reacting at the surface. Over time, internal oxidation occurs subsequently releasing gaseous products that must diffuse back out through the material.

In order to separate surface reactions from bulk decomposition, the samples were heat treated to maximum weight gain at 300C in oxygen. The oxidizing environment was removed by vacuum and replaced with argon at each of three temperatures (220 260 and 300C). The samples lost weight in the inert environment indicating that the material had decomposed. Surface oxidation would have been indicated if the material had shown no weight loss in the argon environment.

CONCLUSIONS

Stabilization of bulk carbonaceous materials occurs faster in oxygen than air. In addition, at lower temperatures (220 and 240C) the material maintains its weight rather than losing it due to surface oxidation. Stabilization is being characterized by trying to understand the components of the process.

References

1. White, J. L. and P. M. Sheaffer,
Proceedings of the 17th Biennial
Conference on Carbon, American Carbon
Society, Lexington, Ky, June 16-21, 1985
pp. 161-162

2. Stevens, W. C. and R. J. Diefendorf,
Proceedings of the XVI International
Conference on Carbon, German Ceramic
Society, Baden-Baden, FRG., June 30 -
July 4, 1986 pp. 37-42

3. Kowbel, W., P. G. Wapner, and M. A.
Wright, J. Phys. Chem Solids 49 (1988)
pp. 1279-1285

4. Mochida, I., H. Toshima, and Y. Korai,
J. Mat. Sci. 23 (1988) pp. 670-677

5. Zimmer, J. Private Communication

6. Lin, S., SAMPE 27, No. 1 Jan/Feb
(1991) 9-14

Figure 3: Effect of environment and
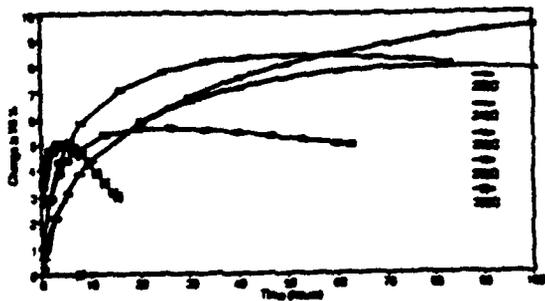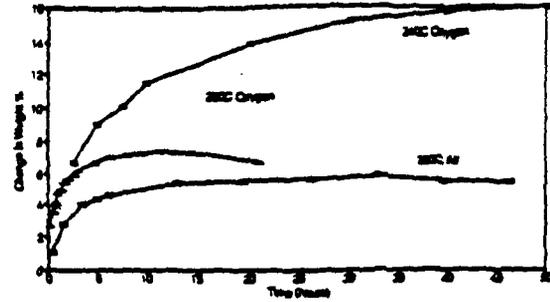temperature on mesophase particles
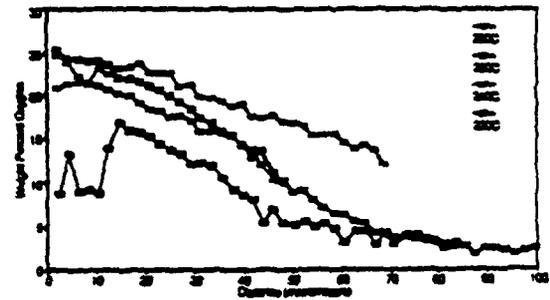
Figure 4: Oxygen profiles of particles
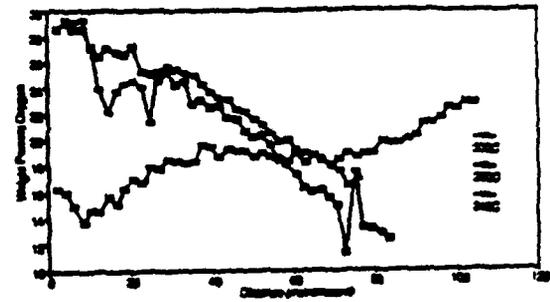stabilized in an air environment

Figure 1: Effect of temperature on
mesophase particles in an oxygen
environment

Figure 5: Oxygen profiles of particles
stabilized in an oxygen environment

Figure 2: Effect of temperature on
mesophase particles in an air environment
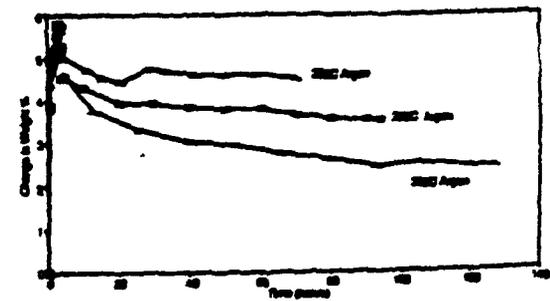
Figure 6: Effect of heat treatment in
argon after stabilization in oxygen

VERBUNDWERK 88

GS

INTERNATIONALER KONGRESS

HOCHLEISTUNGSVERBUNDWERKSTOFFE

FÜR NEUE SYSTEME

19.09.-22.09.198

VERANSTALTER
DEMAT EXPOSITION MANAGING
6 FRANKFURT AM MAIN POSTFACH 10 611
TELEFON 069 234 351

SILICIUMCARBID - VERBUNDWERKSTOFFE
AUS POLYMEREN PRECURSOREN

von

R. P. Boisvert und R. J. Diefendorf
Materials Engineering Department, Rensselaer Polytechnic Institute, Troy, NY, USA

EINLEITUNG

Die Herstellung von keramischen Verbundwerkstoffen durch Pyrolyse von Polymeren ist eine Gruppe von Verfahren, die bei niederen Drucken und niederen Temperaturen arbeitet. Für polymere Precursoren sind Schmelzpunkte unterhalb 400 °C typisch oder sie härten beim Erwärmen aus; dies erlaubt es, keramische Verbundkörper durch eine Lay-up-Technik ähnlich der für Epoxidharzkörper in evakuierten Kapseln vorzuformen. Auf Grund der Natur der Abbaureaktionen, die während der Wärmebehandlung ablaufen, können die Pyrolysebedingungen einen großen Einfluß auf das keramische Produkt haben. Sorgfältiges Studium der Ausgangsmaterialien und die Anwendung geeigneter Umsetzungszyklen sind unerläßlich, um die gewünschten Ausbeuten und Mikrostrukturen zu erhalten. Zu den Faktoren, deren Beachtung für eine erfolgreiche Umwandlung eines Polymers in eine Keramik notwendig ist, gehören: die Pyrolysebedingungen, die Struktur des Polymers und die thermische Beständigkeit des Precursors. Durch die Optimierung dieser Parameter kann die Herstellung nahezu vollkommen dichter, rißfreier keramischer Werkstoffe erreicht werden.

Polymere Precursoren erlauben eine bessere Durchmischung auf molekularer Ebene über einen breiteren Bereich von Atomzahlverhältnissen sowie eine verbesserte Homogenität. Theoretisch kann eine sehr hohe Reinheit erreicht werden, da die Synthese sehr reiner Reaktanden möglich ist. Dennoch sind dem Gebrauch dieser Technik Probleme wie die Stöchiometrie und die Phasenreinheit der keramischen Endprodukte inhärent. Für die Pyrolyse von SiC-Precursoren ist es typisch, große Mengen an gebundenem Kohlenstoff und Sauerstoff im Endprodukt zu hinterlassen. Bei einer Wärmebehandlung bei Temperaturen oberhalb 1000 °C beeinflussen diese beiden Verunreinigungen die mechanischen Eigenschaften keramischer Werkstoffe drastisch. Phasenreinheit muß erreicht werden, um die Vorteile der Pyrolyse von Polymeren gegenüber konventionellen Herstellungsverfahren in vollem Umfang zu nutzen.

Die auftretende Schrumpfung stellt einen der größten Nachteile polymerer Precursoren dar. Sie ist auf geringe Ausbeuten nach der Pyrolyse und auf Dichteunterschiede zwischen Polymer und Endprodukt zurückzuführen. Für die organometallischen Polymere sind Dichten im Bereich von 1 g/cm^3 typisch, während SiC eine Dichte von 3.2 g/cm^3 aufweist. Dieser Dichteunterschied führt zusammen mit der geringen Ausbeute während der Herstellung zur Bildung von Mikrorissen im Verbundwerkstoff. Das führt dazu, daß das Matrixmaterial nicht in der Lage ist, die Verstärkungskomponente unter Einsatzbedingungen so zu schützen, wie das notwendig wäre. Die Schrumpfung kann durch den Einsatz keramischer Füller und langsame Pyrolyse stark herabgesetzt werden. Dennoch ist es notwendig, mehrfach Imprägnierzyklen anzuwenden, um diese Verbundwerkstoffe zu verdichten und ihre mechanischen Eigenschaften zu verbessern.

In der vorliegenden Untersuchung wurden zwei verschiedene Precursoren für SiC, Polycarbosilan und Polyvinylsilan, studiert. Die Probleme durch thermische Instabilität und Schrumpfung während der Wärmebehandlung wurden durch Quervernetzung und Zugabe keramischer

Füller gelöst. Es wurde gefunden, daß durch Vernetzung der Polymere vor der Pyrolyse mittels Einführung von Vinylgruppen, Oxidation oder Zugabe von Brennhilfsmitteln die Ausbeute erhöht und das Aufschäumen vermindert wird. Durch die Zugabe keramischer Füller zu den Polymeren konnten mit Partikeln versehene keramische Verbunde hergestellt werden, die während des Brennens keine Schrumpfung erfuhren; die Zugabe erfolgte vor der Pyrolyse.

Unter Verwendung von Nicalon- und Avco SCS-6 SiC- Fasern wurden zahlreiche Verbundkörper hergestellt. Schlechte mechanische Eigenschaften von Verbundkörpern führten zur Suche nach Methoden, das Bruchverhalten zu beeinflussen und damit ein vertieftes Verständnis der wirksamen Bruchmechanismen zu erhalten. Es wurde angenommen und experimentell bestätigt, daß die Stärke der Bindung an der Grenzfläche zwischen Faser und Matrix das Bruchverhalten bestimmt.

Ein billiges Verfahren zur Aufbringung einer dünnen, gleichförmigen Kohlenstoffschicht auf keramische Fasern, die das Bruchverhalten beeinflussen soll, wurde entwickelt. Auf Grund der Erfolge mit einer Sperrschicht zwischen Faser und Matrix bei der Herstellung von Verbundkörpern mit höherer Leistungsfähigkeit wurden in die Matrix eingebrachte Vielfachsperrschichten verwendet, um die Leistung der Verbunde weiter zu verbessern. An den so erhaltenen Verbundkörpern mit keramischer Matrix wurde die Prüfung der mechanischen Eigenschaften durchgeführt.

EXPERIMENTELLES VORGEHEN

Monolithische Keramik

Für die Herstellung monolithischer keramischer Strukturen aus Polycarbosilanen wurden verschiedene Verfahren angewandt. Polycarbosilanpulver wurde zu verschiedenen Formen verdichtet oder unmittelbar eingesetzt. Polycarbosilan wurde vor der Pyrolyse entweder durch Oxidation oder Zugabe von Brennhilfsmitteln stabilisiert. Die Stabilisierung des Polycarbosilans wurde in einem Rohrofen bei 190 °C an Luft (1 atm, 1 h) durchgeführt. Andere gezielte Oxidationsbehandlungen wurden in einem Autoklaven bei erhöhtem Sauerstoffpartialdruck durchgeführt. Für die Stabilisierung des durch Druck vorverdichteten Polycarbosilans wurde die Oxidation bei 175 °C unter einem Luftdruck von 34.86 bar 24 h lang durchgeführt. Für die Stabilisierung des Polycarbosilans durch Zugabe eines Brennhilfsmittels müssen zuerst beide Stoffe in n-Hexan gelöst werden, das dann verdampft wird, um ein Pulver zu erhalten. Dieses Pulver konnte dann entweder zu einem Grünkörper verdichtet oder unmittelbar pyrolysiert werden. Der Wärmebehandlungszyklus wurde so festgelegt, daß mit einer Geschwindigkeit von 2 K/min auf 1000 °C aufgeheizt und diese Temperatur dann 1 Stunde lang gehalten wurde; die gesamte Behandlung wurde unter Stickstoff durchgeführt.

Verbundstrukturen

Es wurden zwei Arten von Verbundstrukturen untersucht: Verbunde mit dispergierten Teilchen und endlosfaserverstärkte Verbundkörper. Dispersionsverstärkte Keramiken wurden durch Zugabe unterschiedlicher Füller [z.B. SiC- Pulver (325 mesh), SiC- Whisker (Tomax), Al_2O_3- Pulver und Acheson- Graphit (Grade 38)] zum Polycarbosilan vor dem Brennen hergestellt. Die Proben wurden oxidiert und anschließend pyrolysiert. In einigen Fällen wurde das Pulver vor dem Verdichten der Proben 1 Stunde lang bei 190 °C oxidiert. Langfaserverstärkte Proben wurden unter Verwendung von Nicalon-SiC 8-Satingewebe hergestellt. Die keramischen

Fasern wurden mit einer Lösung von Polycarbosilan in Hexan getränkt, 24 Stunden lang an Luft getrocknet, bei 210 °C oxidiert und bei 1000 °C pyrolysiert. Eine andere Verfahrensvariante schloß die Infiltration von Faserbündeln mit geschmolzenem Polycarbosilan ein.

Polysilan ist ein zähflüssiges, durchscheinendes, beim Erwärmen härtendes Polymer. Es wurde mit unterschiedlichen keramischen Füllstoffen [z. B. SiC- Whisker (Tomax), Al_2O_3, SiC- Pulver (800 mesh)] zur Beeinflussung der Schrumpfung und der Bildung von Mikrorissen vermischt. Füller wurden zu Polyvinylsilan zugegeben und bis zum Erreichen einer einheitlichen Mischung gerührt. Danach wurden die so erzeugten Mischungen als Harze für die keramischen Verbundkörper eingesetzt. Da die Polycarbosilane beim Erwärmen aushärten, kann bei der Herstellung der Verbundkörper dieselbe Vakuumkapseltechnik angewendet werden wie bei der Herstellung von Graphit / Epoxidharz- Verbundkörpern. Die für das Lay-up benutzte Apparatur ist in Abb. 1 gezeigt. Die Nicalon- Verstärkungsfasern wurden als gewebtes Tuch, die Avco-Fasern als einzelne Filamente eingesetzt; eine typische Laminatstruktur bestand aus 6 vorgefertigten Schichten. Die Proben wurden unter Vakuum eingekapselt und 6 Stunden lang bei 200 °C unter einem Druck von 34.86 bar gepreßt. Eine andere Herstellungsmethode schloß die Verwendung einer Aluminiummatrize ein, um ein Herauswaschen der Fasern zu verhindern. Nach Beendigung dieser Behandlung wurden die Laminate unter Stickstoff pyrolysiert. Der typische Zyklus für die Umsetzung bestand aus dem Aufheizen auf 800 °C bei einer Geschwindigkeit von 1 K/min und einer Haltezeit von 2 Stunden. Durch wiederholte Imprägnierung und Pyrolyse der bereits pyrolysierten Quader wurde die Dichte der Körper erhöht und ihre mechanischen Eigenschaften verbessert. Das Fließschema in Abb. 2 zeigt den gesamten Prozeß. Zur Beeinflussung der Rißausbreitung wurden auf den Nicalon- Geweben Kohlenstoffschichten aufgebracht. Einzelne keramische Verbundkörper wurden zwischen zwei aufeinanderfolgenden Verdichtungsschritten mit Polycarbosilan und einem polymeren Kohlenstoff-Precursor imprägniert, um das Bruchverhalten zu beeinflussen. Abb. 3 gibt den Ablauf eines derartigen Verfahrens schematisch wieder.

ERGEBNISSE UND DISKUSSION

Polycarbosilane als Precursoren für keramische Matrices

Thermische Stabilität

Die in dieser Arbeit verwendeten Polycarbosilane wurden von Nippon Carbon nach dem von Yajima (1) entwickelter Verfahren hergestellt. Das durch Dampfdruckosmometrie (bei 40 °C unter Verwendung von n-Hexan als Lösungsmittel) bestimmte mittlere Molekulargewicht lag bei 1500. Die thermische Beständigkeit des SiC-Precursors wurde durch simultane Differentialthermoanalyse/Thermogravimetrie (DTA/TG) untersucht. Es wurde gefunden, daß das Polycarbosilan beim Aufheizen bis 800 °C mit einer Aufheizgeschwindigkeit von 2 K/min unter Stickstoff nicht formstabil ist. Die keramische Ausbeute lag bei etwa 63 Ma-%; die Instabilität der Abmessungen wurde aus der Höhe des Schaumes im Tiegel bestimmt. Abb. 4 zeigt eine bei der Pyrolyse von Polycarbosilan entstandene TG- Kurve. Der Massenverlust setzt bei 250 °C ein und erreicht zwischen 350 und 500 °C die größte Geschwindigkeit. Die Herabsetzung der Aufheizgeschwindigkeit auf 0.5 K/min hatte eine Erhöhung der Ausbeute auf 65.5 Ma-% und eine Verringerung der Höhe des Schaumes um 18 % zur Folge. Die Forminstabilität wird auf

das Vorhandensein niedermolekularer Spezies, die die Schaumbildung verursachen, zurückgeführt.

Zur Verbesserung der Formstabilität der Polycarbosilane während der Pyrolyse wurden mehrere Methoden untersucht. Zunächst wurden niedermolekulare Bestandteile durch 2-stündige Vakuumdestillation bei 340 °C unter einem Druck von 5.2 Torr entfernt. Das Molekulargewicht des so erhaltenen Materials betrug 2450. Die Höhe des Schaumes wurde um 75 % herabgesetzt und die zugehörige keramische Ausbeute betrug 75 Ma-%, nachdem 23 % der Spezies mit niederem Molekulargewicht entfernt waren. Für die Pyrolyse unter Stickstoff wurde die Heizgeschwindigkeit auf 0.5 K/min bis zu einer Temperatur von 800 °C festgelegt. Die Entfernung von etwa 50 % der niedermolekularen Bestandteile hatte ein Anwachsen der Schaumbildung um etwa 200 % und eine Erhöhung der Ausbeute auf 83 Ma-% zur Folge. Es wurde beobachtet, daß das Schäumen der Polycarbosilane von der Geschwindigkeit der Entwicklung der Pyrolysegase und von der Viskosität abhängt.

Die Quervernetzung der Polycarbosilane erhöht die Ausbeute und unterdrückt die Schaumbildung. Die Oxidation stellt die gebräuchlichste Methode zur Quervernetzung dar und wird auch bei der Herstellung von Nicalon -Fasern angewendet. Der Nachteil der Oxidation besteht im Einbau von Sauerstoff in den Precursor, der zur Bildung von SiO_2 führt. Dieses kann verheerende Auswirkungen auf die Leistungsfähigkeit des Verbundes bei hohen Temperaturen haben (2). Für die Untersuchung der Oxidation wurde Polycarbosilanpulver verwendet. Der Precursor wurde auf eine vorher festgelegte Temperatur mit 10 K/min erhitzt. Die Massenzunahme setzte bei einer Temperatur von 190 °C ein, was den Beginn der Quervernetzung anzeigt. Polycarbosilan, das an Luft 2 Stunden lang bei 190 °C behandelt wurde, zeigte einen Massenzuwachs von 5 %. Dieses Pulver wurde anschließend bei 1000 °C unter Stickstoff pyrolysiert, wobei der gesamte Massenverlust 20.2 % betrug. Abb. 5 zeigt die TG-Kurven von Polycarbosilanen, die unterschiedlich lange oxidiert wurden. Mit zunehmender Oxidationszeit wurde ein Anstieg der Ausbeute beobachtet und bei diesen Proben wurde kein Anzeichen einer Schaumbildung mehr festgestellt. Es wurde weiter beobachtet, daß eine Massenzunahme des Polycarbosilans während der Oxidation von 2 % genügt, um das Polymer während der Pyrolyse zu stabilisieren.

Größe, Form und Porosität der polymeren Grünkörper spielen bei der Festlegung der optimalen Oxidationsbedingungen eine Rolle. Polycarbosilan wurde zu einer etwa 1.5 mm dicken Scheibe von 12.5 mm Durchmesser verdichtet und an Luft 4 Stunden lang bei 190 °C oxidiert, was zu einer Massenzunahme von 5.3 % führte. Die Oxidation führte zu keiner Verformung der Scheibe. Die oxidierte Scheibe wurde in Stickstoffatmosphäre mit 2 K/min auf 1000 °C aufgeheizt. Die Scheibe verformte sich (schäumte) in der Mitte, was auf unvollständige Oxidation hinweist. Die Ausbeute wurde zu 75 %, die Dichte der Scheibe zu 1.7 g/cm³ berechnet. Scheiben, die 18 Stunden lang bei 190 °C oxidiert wurden, (Massenzunahme 6.5 Ma-%) zeigten dennoch nach dem Aufheizen auf 1000 °C Anzeichen eines teilweisen Schmelzens. Das zeigt, daß der Sauerstoff nicht in die Mitte der Scheibe eingedrungen war und den Precursor nicht stabilisiert hat.

Diese ungenügende Oxidation kann durch partielle Oxidation des Polycarbosilanpulvers vor der Verdichtung zur Scheibe überwunden werden. Der Precursor wurde gesiebt (#100) und anschließend an Luft 2 Stunden lang bei 190 °C oxidiert. Das oxidierte Pulver wurde unter Stickstoff mit einer Aufheizgeschwindigkeit von 2 K/min bis auf 1000 °C aufgeheizt. Die Scheibe zeigte keine Verformung, was auf eine befriedigende Stabilisierung des Polycarbosilans hinweist. Die Ausbeute betrug 80 Ma-%, die mittlere Dichte der Scheibe 2.2 g/cm³.

Anstelle der Oxidation wurden zwei Brennhilfsmittel eingesetzt:
1.) Tricresylphosphat (TCP) und 2.) Tri-n-Butylborat (TNBB). Bei Zusätzen von bis zu 25 Ma-

% TCP wurde eine deutliche Verringerung der Schaumbildung, jedoch keine vollständige Stabilisierung des Precursors beobachtet. Unterschiedliche Mengen TNBB ($C_4H_9O)_3B$) wurden einer Mischung aus Carbosilan und n-Hexan zugesetzt. Das Hexan wurde verdampft. Das so erhaltene Pulver wurde gemahlen, gesiebt und mit 2 K/min bis 1000 °C aufgeheizt. Bei einer Zugabe von 14 Ma-% TNBB zu einer Polycarbosilanfraktion mit hohem Molekulargewicht (MG = 2900) war nach der Pyrolyse bis 1000 °C kein Schäumen erkennbar. Die Dichte der Scheibe betrug 2.28 g/cm^3 bei einer Ausbeute von 78 Ma-%. Diese Ergebnisse sind denen an Proben vergleichbar, die 2 Stunden lang an Luft bei 190 °C oxidiert wurden. Geringere Zusätze an TNBB ergaben höhere Ausbeuten (siehe Abb. 6), aber bei Zugabe von weniger als 5 Ma-% TNBB trat Schaumbildung auf. Wenn diese Brennhilfsmittel zugegeben werden, setzt der Massenverlust bei geringeren Temperaturen ein als bei Proben, die oxidiert wurden.

Schrumpfung

Die Brennschrumpfung während der Pyrolyse stellt das zweite große Hindernis bei der Verwendung von Polycarbosilanen als Precursor für eine keramische Matrix dar. Diese Schrumpfung führt zu Mikrorissen, besonders wenn Hindernisse wie Fasern zugegen sind. An Luft 2 Stunden lang bei 190 °C oxidierte Polycarbosilanpulver wurden zu Scheiben von 12.5 mm Durchmesser gepreßt und unter Stickstoff mit 2 K/min auf 1000 °C erhitzt. Bei einer Ausbeute von etwa 80 Ma-% wurde eine gesamte Volumenschrumpfung von 58 % gemessen. Die theoretisch berechnete Volumenschrumpfung sollte 76.5 % betragen; das bedeutet, daß die Scheibe 18.5 % Porosität enthält, wenn das Produkt reines SiC ist. Als Dichte der Scheibe wurden 2.2 g/cm^3 gemessen. Diese im Vergleich zu reinem SiC geringe Dichte kann auf Abweichungen von der idealen Stöchiometrie und auf geschlossene Porosität zurückgeführt werden. Diese Leerräume bilden sich auf Grund von Pyrolysegasen, die während des Prozesses nicht an die Oberfläche diffundieren können. Längere Oxidationszeiten führten zu einer geringen Abnahme der Schrumpfung infolge einer höheren Ausbeute. Mit 14.5 Ma-% TNBB versetztes Polycarbosilan (MG = 2900) zeigte bei der Pyrolyse bis 1000 °C eine Volumenschrumpfung von 60 %. Die Zugabe von Füllern zu Polycarbosilan vor der Pyrolyse ergab eine drastische Abnahme der Schrumpfung. Unter den verwendeten Füllern waren Acheson-Graphit (#38), Al_2O_3 - Pulver (0.05 µm), SiC- Pulver (325 mesh) und Tomax SiC-Whisker. Im Polycarbosilan gleichmäßig verteilte Füller wurden zu Pulver gemahlen, durch ein #100-Sieb gesiebt und 1 Stunde lang bei 190 °C an Luft oxidiert. Die oxidierten Pulver wurden zu Scheiben von 12.5 mm Durchmesser gepreßt und unter Stickstoff bei einer Heizgeschwindigkeit von 2 K/min bis 1000 °C pyrolysiert.

Die Ausbeute des Polycarbosilans hing nur wenig von Art und Menge des zugesetzten Füllers ab und lag bei etwa 80 Ma-%. Für Graphit und Aluminiumoxid, aber nicht für SiC kann eine lineare Beziehung zwischen dem Massenanteil des Füllers und der Volumenschrumpfung der Scheibe angegeben werden, wie in Abb. 7 gezeigt ist; höhere prozentuale Anteile des Füllers ergeben geringere Schrumpfungen.

Letztendlich wurden als Füller für das Polycarbosilan SiC-Whisker in Volumenanteilen von 40 und 50 % verwendet. Der Abb. 8 kann man entnehmen, daß durch optimale Dosierung der Zugabe von SiC-Whiskern im Prinzip eine Schrumpfung von 0 % erreichbar ist. Um Proben mit höherem Whiskeranteil herzustellen, mußte der Verfahrensablauf geändert werden. Diese Proben wurden vor der Luftoxidation im Autoklaven (24 Stunden bei 175 °C unter einem Druck von 4 atm) in Scheibenform gepreßt. Temperaturen oberhalb 175° C führten zu Verwerfungen und zum Schäumen, bei geringeren Temperaturen nahm die Oxidationszeit unvertretbar zu. Der erhöhte Luftdruck trug dazu bei, die Oxidationszeit herabzusetzen. Bei einem Druck von 4 atm

ergab sich eine Verkürzung der Oxidationszeit um 25%. Die Proben wurden dann unter Stickstoff mit 2 K/min auf 1000 °C erhitzt. Die Proben wurden nach der Verdichtung oxidiert, weil oxidierte Pulver mit hohen Konzentrationen des Füllers keine handhabbaren Grünkörper ergaben. Abb. 9 zeigt, daß für alle Füller ein kritischer Massenanteil gefunden werden kann, bei dem keine Schrumpfung auftritt.

Verbundwerkstoffe mit Partikeleinlagerungen

Polycarbosilanbasierte Verbundkörper wurden im Dreipunkt-Biegetest auf Festigkeit und Elastizitätsmodul geprüft. Alle geprüften Proben zeigten Sprödbruchverhalten und ein linear-elastisches Antwortsignal bis zum Bruch.

Es wurden Proben mit 75, 65 und 56 Ma-% Graphit, SiC-Pulver (800 mesh) und SiC-Whiskern (Tomax) getestet. Mit steigendem Filleranteil ergeben sich schlechtere mechanische Eigenschaften, wie in den Abb. 10 und 11 zu erkennen ist. SiC-whiskerverstärkte Verbundkörper zeigten die besten mechanischen Eigenschaften. Im Gegensatz zur durchgehenden Verstärkung, bei der die Leistung mit steigendem Faservolumenanteil zunimmt, wurde festgestellt, daß Festigkeit und Elastizitätsmodul mit wachsendem Anteil des Füllers fallen: Die Schrumpfung der Matrix und unterschiedliche thermische Ausdehnungen von Füller und pyrolysiertem Polycarbosilan führten mit größter Wahrscheinlichkeit zur Bildung von Mikrorissen beim Abkühlen von der Prozeßtemperatur auf Umgebungstemperatur. Diese Mikrorisse verminderten die Leistungen dieser Körper. Bei whiskerverstärkten Verbundkörpern wurden die besten mechanischen Eigenschaften bei den Proben mit der geringsten Dichte gefunden. Reines pyrolysiertes Polycarbosilan (MG = 2900, 14.5 Ma-% TNBB) zeigte eine Biegefestigkeit von 14 000 Psi (96.5 MPa). Alle getesteten Füller verschlechterten die Eigenschaften der entsprechenden Körper.

Endlosfaserverstärkte Verbundkörper

Polycarbosilan wurde als Matrixprecursor für die Herstellung von durchgehend verstärkten keramischen Verbundkörpern mit Nicalon-SiC-Fasern als Verstärkungsfaser benutzt. Die Nicalonfasern wurden 2 Stunden lang einer Wärmebehandlung bei 700 °C in Argon unterzogen, um die bei der Herstellung aufgebrachte Schlichte zu entfernen.

Die SiC-Fasern wurden mit einer Lösung von Polycarbosilan mit 14.5 Ma-% TNBB getränkt, getrocknet und anschließend einer einstündigen Wärmebehandlung bei 1000 °C unterzogen; die Heizgeschwindigkeit betrug 2 K/min. Alternativ dazu wurden die Nicalonfasern mit geschmolzenem Polycarbosilan getränkt, 10 min lang bei 210 °C oxidiert und dann pyrolysiert. Im Rasterelektronenmikroskop wurde das Vorhandensein zahlreicher Mikrorisse beobachtet, wobei die Bildung von Mikrorissen bei den durch Schmelzimprägnierung hergestellten Verbunden weniger stark ausgeprägt war.

Um möglichst rißfreie Verbundkörper zu erhalten, wurden die Körper mehrfach mit Polycarbosilan imprägniert. In diesen Proben ist wesentlich mehr Matrix enthalten, aber sie zeigen trotzdem noch sehr viele Mikrorisse. Diese Art von Verbundkörpern macht die Aufbringung einer äußeren Oxidationsschutzschicht unerläßlich, da die mikrorissige Matrix der Faser keinen Oxidationsschutz gewährt.

Polyvinylsilane als Precursoren für die keramische Matrix

Thermische Stabilität

Einer der größten Vorteile von Polyvinylsilanen gegenüber Polycarbosilanen besteht darin, daß sie ohne Sauerstoffeintrag thermisch vernetzt werden können. Die Vernetzung erfolgt bei Temperaturen zwischen 100 und 270 °C; bei höheren Temperaturen setzt der Abbau des Precursors ein. Vor einer Behandlung bei 200 °C beträgt die Dichte des Polymers etwa 1 g/cm³, danach 0,75 g/cm³. Abb. 12 zeigt die TG-Kurve eines Polyvinylsilans, das bei 2 K/min unter Stickstoff auf 1000 °C aufgeheizt wurde. Der Abbau erreicht zwischen 400 und 600 °C die größte Geschwindigkeit und bei der Pyrolyse bis 1200 °C beträgt die Ausbeute 60.6 Ma-%. Die geringe Dichte des Produktes wird auf Abweichungen von der stöchiometrischen Zusammensetzung und auf geschlossene Porosität zurückgeführt.

Abhängig vom benutzten Wärmebehandlungszyklus verändert sich die Mikrostruktur. Beim Aufheizen auf 800 °C mit einer Geschwindigkeit von 1 K/min bilden sich in der Matrix zahlreiche Poren. Um die Anzahl der Leerräume zu verringern, muß die Heizgeschwindigkeit herabgesetzt werden, um die für die Diffusion der Abbauprodukte zur Verfügung stehende Zeit zu verlängern. Mit steigender Stärke des Werkstückes muß wegen der zunehmenden Diffusionswege die Heizgeschwindigkeit gesenkt werden. Die Wärmebehandlung der Polysilanproben wurden nach folgendem Programm durchgeführt:

1) 1 K/min bis 250 °C
2) 10 K/h zwischen 250 und 600 °C
3) 1 K/min bis 800 °C

Dies sollte die Anzahl der Leerräume vermindern. Die langsame Heizgeschwindigkeit zwischen 250 und 600 °C wurde gewählt, da in diesem Temperaturbereich der Massenverlust die größte Geschwindigkeit erreicht.

Zur Verbesserung der mechanischen Eigenschaften und zur Verringerung der Schrumpfung wurden dem Polyvinylsilan Füller zugesetzt. SiC-Whisker, Al₂O₃-, BN- und SiC-Pulver wurden, jeweils für sich, dem Polyvinylsilan zugesetzt, anschließend bei 200 °C behandelt und danach unter Stickstoff bis 800 °C mit 1 K/min pyrolysiert. In Tab. 1 sind die Daten für Schrumpfung und mechanische Eigenschaften zusammengefaßt. Die keramischen Füller trugen dazu bei, die Schrumpfung zu verringern, aber die Art des verwendeten Füllers hatte keinen Einfluß auf die Schrumpfung. Im Rasterelektronenmikroskop zeigten die SiC- whisker- und pulververstärkten Proben eine sehr poröse Mikrostruktur, aber in der Oberfläche waren keine Risse erkennbar. Im Gegensatz dazu zeigte die Oberfläche der Al₂O₃-verstärkten Proben starke Mikrorisse. Die wahrscheinlichste Erklärung dafür ist der unterschiedliche thermische Ausdehnungskoeffizient von Füller und Matrix. Diese Risse schlagen sich darin nieder, daß diese Proben die schlechtesten mechanischen Eigenschaften zeigten. Im Gegensatz zu den partikelverstärkten Verbunden verbesserten die Füller die mechanischen Eigenschaften dieser Proben in jedem Fall.

Voruntersuchung der Eigenschaften der Verbundkörper

Unter Verwendung von Polyvinlysilan als Matrixprecursor und Nicalon-8-Satingewebe als Verstärkungskomponente wurden keramische Verbundkörper hergestellt. Man muß erwarten, daß die mechanischen Eigenschaften zweiachsig verstärkter Materialien wesentlich schlechter sind als die unidirektional verstärkter, da der Faservolumenanteil parallel zur Richtung der Beanspruchung geringer ist. Die Eigenschaften von Verbunden, die Tuch als Verstärkungsphase benutzen, werden durch Schädigung der Faser während des Webens und durch die Webanordnung weiter verschlechtert. Der Aufbau der Verbundlaminate erfolgte aus 6 vorgefertigten Schichten, die unter Verwendung eines geeigneten Harzes aus Polysilan und keramischem Füller als Matrixprecursor hergestellt wurden.

Für die zuerst hergestellten Verbundkörper wurde Polysilan mit 25 Ma-% Bornitridpulver oder 15 Ma-% Siliciumcarbidwhisker als Matrixprecursor verwendet. Die Volumenschrumpfung betrug 20 % für die mit BN als Füller hergestellten Proben, aber nur 3 % für die Verbunde aus Gewebe und Füller. Die geringe Schrumpfung der Verbunde mit beiden Füllern hat eine große Porosität und eine starke Bildung von Mikrorissen in der Matrix zur Folge. Ähnlich zur Herstellung von Kohlenstoff/Kohlenstoffverbundwerkstoffen war eine mehrfache Imprägnierung notwendig, um die Porosität zu verringern und die mechanischen Eigenschaften zu verbessern. Abb. 13 zeigt die berechnete Porosität nach jedem Imprägnierschritt für die mit Bornitrid als Füller hergestellten Verbunde. Die Kurve nähert sich asymptotisch einem Wert von etwa 9 Vol-% Porosität, was die im Verbund vorhandene geschlossene Porosität anzeigt. In Abb. 14 sind Daten für die Dichte beider Arten von Verbundkörpern gezeigt. Bei beiden Versuchsreihen wurde gefunden, daß der Elastizitätsmodul mit wachsender Zahl der Imprägnierzyklen steigt; dieser Anstieg ist bei Verwendung von SiC-Whiskern steiler als bei Verwendung von BN-Pulver (Abb. 15). Abb. 16 zeigt, daß die Biegefestigkeit ebenfalls mit jedem Imprägnierzyklus ansteigt. Proben, die nach der ersten Pyrolyse geprüft wurden, zeigten Scherversagen durch Delaminierung. Der Versagenstyp ging nach zwei oder mehr Imprägnierungen in Zugversagen über. In keiner der getesteten Proben wurden Anzeichen von Faser-Pull-out gefunden. Die schlechten mechanischen Eigenschaften können auf eine starke Bindung zwischen Faser und Matrix zurückgeführt werden. Alle untersuchten Proben versagten bei der Bruchdehnung der Matrix. Die höheren Bruchfestigkeiten wurden wegen des höheren Elastizitätsmoduls der Verbunde im Vergleich zur unverstärkten Matrix erzielt. Da die Verbundkörper versagten, bevor die Bruchdehnung der Fasern (1 %) erreicht war, konnten diese nicht viel zur gesamten Festigkeit der Verbundwerkstoffe beitragen. Risse, die in der Matrix entstanden waren, pflanzten sich einfach durch den gesamten Verbund fort.

Beeinflussung des Bruchverhaltens

Das Bruchverhalten keramischer Verbundwerkstoffe unterscheidet sich von dem von Verbunden mit Polymer- oder Metallmatrix auf Grund der Eigenschaften der einzelnen Komponenten. Bei den SiC-Keramiken, über die hier berichtet wird, ist der Elastizitätsmodul der Fasern größer als der der Matrix, aber die Bruchdehnung der Matrix ist geringer. Der Verbund profitiert von der Übertragung von Spannungen aus der Matrix auf die Faser, aber im Gegensatz zu Verbunden mit polymerer Matrix, wo der Bruch durch Versagen der Fasern eingeleitet wird, bricht in unserem Fall die Matrix vor den Fasern. Wenn sich in der Matrix eine Kerbe ausbreitet und eine Faser erreicht, wird die Spannungskonzentration an ihrer Spitze auf die Faser übertragen, wenn eine vollständige Spannungskopplung gegeben ist. Diese Spannungskonzentration ist hoch genug, um unmittelbar einen Bruch der Faser herbeizuführen und dadurch die Festigkeit und Brucharbeit des Verbundwerkstoffs auf die der Matrix zu begrenzen. Eine Optimierung der Eigenschaften der Verbunde muß demnach auf eine Situation führen, in der eine schwache Anbindung zwischen Faser und Matrix gegeben ist, die dazu führt, daß Risse in der Matrix nicht

zum Versagen der Faser führen. Unter der Annahme, daß keine Kopplung zwischen Faser und Matrix existiert und die Festigkeit der Faser keiner Verteilung unterliegt, kann eine Obergrenze für die Festigkeit des Verbundes angegeben werden. Wenn zwischen Faser und Matrix keine mechanische Wechselwirkung stattfindet, können Risse, die sich in der Matrix ausbreiten, die Faser nicht schädigen. Bei nicht gekoppelten unidirektionalen Verbunden beobachtet man beim Wert für die Bruchdehnung der Matrix einen sprunghaften Anstieg der Dehnung, da bei dieser Dehnung die Last von der Faser übernommen wird, wie in Abb. 17 gezeigt ist. Von da an trägt die Faser die gesamte auf dem Werkstoff aufliegende Last. Weitere Steigerung der Spannung führt letztendlich zum Versagen der Fasern, was zum Bruch des Verbundkörpers führt. Der flachere Verlauf der Spannungs-/Dehnungskurve ist darauf zurückzuführen, daß das Diagramm auf dem Gesamtquerschnitt des Verbundes vor dem Bruch der Matrix basiert. Wesentliche Steigerungen von Festigkeit und Brucharbeit sind also durch das Abkoppeln der Faser von der Matrix möglich. Trotzdem ist eine gewisse Verbindung zwischen Faser und Matrix notwendig, um die Spannungsübertragung zu ermöglichen.

Verbundkörpereigenschaften

Es konnte gezeigt werden, daß eine schwache Bindung zwischen Faser und Matrix die mechanische Leistungsfähigkeit von Verbundwerkstoffen mit keramischer Matrix entscheidend verbessert. Bei allen bisher beschriebenen Faser/Matrix-Kombinationen trat Sprödbruchversagen bei der Bruchdehnung der Matrix auf. Um eine Kohlenstoff-Zwischenschicht mit graphitischer Struktur zu erzeugen, wurde ein spezieller Kohlenstoffprecursor entwickelt. Die Biegefestigkeit stieg dadurch gegenüber allen bis dahin getesteten Verbundkörpern um mindestens 50 % an (Abb. 18). Für Verbunde, die bis zu dreimal imprägniert wurden, war ein nichtkatastrophales Versagen typisch. Last-/Durchbiegungskurven, wie sie in Abb. 19 gezeigt sind, zeigen Verbesserungen in Bezug auf Zähigkeit und die Fähigkeit, Belastungen auszuhalten. Proben, die nur einmal imprägniert waren, versagten durch Scherung mit nur wenigen gebrochenen Fasern. Proben mit zwei Imprägnierzyklen zeigten einen gewundenen Bruchweg, wie aus der Durchbiegungskurve ersichtlich ist. Dies ergab einen Verbund, dessen Bruchenergie gegenüber den vorangegangenen Proben wesentlich höher lag. Katastrophales Bruchverhalten trat bei Proben mit vier Imprägnierzyklen auf. Diese Verbunde versagten bei einer höheren Dehnung als die reine Matrix, was zu Verbunden mit höherer Festigkeit führte. Die höhere Bruchdehnung dieser Proben weist darauf hin, daß an der Grenzfläche zwischen Matrix und Kohlenstoff eine gewisse Umlenkung von Rissen eingetreten sein muß. Bei weiterer Imprägnierung wurde eine Verringerung der Biegefestigkeit gefunden; die Werte für den Elastizitätsmodul fielen im Vergleich zu den vorherigen Proben, aber die Dichte blieb konstant, wodurch die spezifische Festigkeit zunahm. Eine Berechnung des Faservolumenanteils ergab Werte von etwa 40 %, die Bruchdehnung wurde mit 0.4 % berechnet, während die Nicalonfaser eine Bruchdehnung von 1 % aufweist. Dieser Unterschied weist darauf hin, daß die Beschichtung nicht jede Rißfortpflanzung in die Faser hinein verhindert und daher eine vollständige Entfaltung des Potentials dieser Verbunde nicht erreicht wird. Die Bruchdehnung des Verbundes liegt höher als die der Matrix; die Beschichtung ist also teilweise wirksam, um Wechselwirkungen zwischen Faser und Matrix auszuschalten.

Bei der letzten Probenreihe wurde ein anderer Precursor für die Abscheidung des Kohlenstoff-coatings verwendet. Die in Abb. 20 zu erkennenden Verbesserungen der Festigkeit waren nicht so ausgeprägt wie in der vorangegangenen Reihe, aber die Durchbiegungskurven deuten auf einen zäheren keramischen Verbund hin. Selbst nach 5 Imprägnierzyklen war das nichtkatastrophale Versagen, durch das die Fläche unter der Kurve, die ein Maß für die aufgewendete Energie darstellt, größer wird, vorherrschend. Nach bis zu 5 Imprägnierzyklen wurde auf Grund des nichtkatastrophalen Versagens kein Zurückgehen der Festigkeit festgestellt. Die geringere

Festigkeit wird auf einen geringeren Faservolumenanteil (33 % gegenüber 40%) zurückgeführt. Während des Beschichtungsprozesses wurde eine dicke Schicht aufgebracht, die eine Verdichtung des Verbundes während der Wärmebehandlung in der Heißpresse verhinderte, was zu dem verringerten Faservolumenanteil in Verbundkörpern führte.

Auf die Faser aufgebrachte Schichten tragen eindeutig dazu bei, die Leistungen keramischer Verbundwerkstoffe zu verbessern. Die wirklich erzielte Verbesserung der Eigenschaften hängt von der Art des verwendeten Kohlenstoffprecursor ab. Precursoren, die die Mesophasenbildung begünstigen, ergaben die größten Gewinne. Eine Schicht aus reinem Graphit dürfte die mechanischen Eigenschaften dieser Verbundsysteme weiter verbessern.

Bis hierher wurden die Versuche, die Leistungsfähigkeit der Verbundkörper zu verbessern, auf die Veränderung der Grenzfläche zwischen Faser und Matrix gegründet. Risse, die in der spröden Matrix entstehen, breiten sich relativ ungehindert aus, bis sie eine Faser erreichen. In dieser Untersuchung wurde eine neue Technik benutzt, um eine Begrenzung der Größe dieser Risse dadurch zu erreichen, daß zusätzliche rißablenkende Schichten in die Matrix des Verbundes eingebracht wurden. Dadurch können Risse nur bis zu einer bestimmten Größe wachsen, bevor sie eine Grenzfläche erreichen, an der sie entweder gestoppt oder in eine andere Richtung abgelenkt werden, wodurch ihre Größe und Spannungsintensität begrenzt werden. Um diese Wirkung der Einführung schwach gebundener Grenzflächen innerhalb der Matrix zu demonstrieren, wurde nach jeder Polysilanimprägnierung eine Imprägnierung mit Kohlenstoffprecursor durchgeführt. Das nichtkatastrophale Versagen trat bei allen getesteten Verbundkörpern ein. Verbundkörper mit einem Faservolumengehalt von 28 Vol-%, bei denen 5 Imprägnierungen mit Polysilan und 5 mit Kohlenstoffpresursor durchgeführt wurden, zeigten eine durchschnittliche Biegefestigkeit von 0.3 GPa. Dieser Wert markiert die höchste während der gesamten Arbeit gemessene Festigkeit (Abb. 21). Die Last-/Durchbiegungskurven in Abb. 22 deuten auf einen zähen Verbundwerkstoff mit hoher Festigkeit hin. Die Einführung von Zwischenschichten hat also die Leistungen der Verbunde verbesssert.

SCHLUSSFOLGERUNGEN

1. Die Temperaturbeständigkeit der Polycarbosilane hängt von Molekulargewicht und Molekulargewichtsverteilung ab.

2. Die Oxidation oder Zugabe von Brennhilfsmitteln stabilisiert Polycarbosilane, was zu Proben mit besserer Formbeständigkeit und höherer Ausbeute nach dem Brennen führt.

3. Die Schrumpfung während der Pyrolyse der Polycarbosilane kann durch Zugabe verschiedener keramischer Füller beeinflußt werden.

4. Die Zugabe von Füllern verschlechtert die mechanischen Eigenschaften dispersionsverstärkter polycarbosilanbasierter Verbundwerkstoffe.

5. Mit Polycarbosilan infiltrierte Nicalon-Faserbündel ergeben nach der Pyrolyse eine sehr rissige Matrix.

6. Mehrere Imprägnierzyklen sind erforderlich, um einen Verbundkörper aus Polycarbosilan und Endlosfasern nachzuverdichten.

7. Zu Polyvinylsilan zugesetzte Füller verbessern die mechanischen Eigenschaften und setzen die Schrumpfung herab.

8. Die Fähigkeit der Polyvinylsilane zur Quervernetzung erlaubt es, zur Vorformung der Verbundkörper die Vakuumkapseltechnik anzuwenden.

9. Mehrfache Imprägnierungen sind erforderlich, um die mechanischen Eigenschaften der Verbundkörper zu verbessern; Ursache hierfür sind die geringen Ausbeuten und die große Schrumpfung der Polyvinylsilane.

10. Die reaktive Oberfläche der Nicalonfasern und die Natur der Abbaureaktionen während der Pyrolyse führen zu einer starken chemischen Bindung zwischen Matrix und Verstärkungskomponente.

11. Eine starke Bindung zwischen Faser und Matrix führt zu Verbunden mit geringer Zähigkeit und Festigkeit.

12. Polymere Kohlenstoffprecursoren können verwendet werden, um schwache Grenzflächen auf der Faser oder schwache Zwischenschichten innerhalb der Matrix einzuführen.

13. Die Entkopplung der Faser von der Matrix führt zu nennenswerten Verbesserungen der Festigkeit und der Brucharbeit der Verbundkörper.

14. Eine aus vielen Schichten aufgebaute Matrix erweist sich als hilfreich bei der Beeinflussung des Bruchverhaltens, wodurch Festigkeit und Brucharbeit des Verbundes verbessert werden.

DANKSAGUNG

LITERATURANGABEN

1. Yajima, S. , Okamura, K., Hayashi, J., and Omori, M., J. Amer. Cer. Soc., 59 (7-8), (1976), 324 - 327.

2. Simon, G. and Bunsell, R.., J. Mater. Sci., 19, (1984).

FIGURE CAPTIONS

FIGURE 1: Vacuum bag lay-up construction.

FIGURE 2: Composite processing flow diagram for polyvinyl-silane.

FIGURE 3: Polysilane composite flow diagram involving carbon impregnations.

FIGURE 4: TGA curve for pyrolysis of polycarbosilane, 2°C/min heating rate under nitrogen gas.

FIGURE 5: TGA curves for pyrolysis of oxidized polycarbosilane, 2°C/min heating rate under nitrogen gas.

FIGURE 6: TGA curves for pyrolysis of polycarbosilane with TNBB, 2°C/min heating rate under nitrogen gas.

FIGURE 7: Shrinkage of pyrolysed, particulate reinforced polycarbosilane.

FIGURE 8: Shrinkage of pyrolysed polycarbosilane as a function of weight percent SiC whiskers added.

FIGURE 9: Volume of percent shrinkage of pyrolysed polycarbo-silane as a function of weight percent ceramic filler.

FIGURE 10: Flexural strength of pyrolysed, particulate reinforced polycarbosilane.

FIGURE 11: Modulus of pyrolysed, particulate reinforced poly-carbosilane.

FIGURE 12: TGA curve for pyrolysis of polyvinylsilane to 1000°C at 2°C/min under nitrogen gas.

FIGURE 13: Porosity versus impregnation number for polyvinyl-silane/nicalon composite. The polyvinylsilane was filled with 25 w/o boron nitride. No carbon fiber/matrix interfacial coating.

FIGURE 14: Density versus impregnation number for polyvinyl-silane/nicalon composites with particulate fibers. No carbon fiber/matrix interfacial coating.

FIGURE 15: Modulus of pyrolysed nicalon fiber/polyvinylsilane matrix composites. The matrix was particulate reinforced, but no fiber/matrix carbon interfacial layer was used to arrest cracks.

FIGURE 16: Flexural strength of pyrolysed nicalon fabric/poly-vinylsilane composites. The matrix was particulate reinforced, but with no crack stopping fiber/matrix interface.

FIGURE 17: Stress-strain response curve for a ceramic matrix composite with 0% coupling between fiber and matrix.

FIGURE 18: Flexural strength of pyrolysed nicalon fabric/par-ticulate reinforced polyvinylsilane with an opti-mized crack arresting fiber/matrix interface.

FIGURE 19: Load/deflection curves for pyrolysed nicalon fabric/ particulate reinforced polyvinylsilane with a crack arresting fiber/matrix interface.

FIGURE 20: Load/deflection curves for pyrolysed nicalon fabric/ particulate reinforced polyvinylsilane with an opti-mized crack arresting fiber/matrix interface.

FIGURE 21: Flexural strength of pyrolysed nicalon fabric/ particulate reinforced polyvinylsilane matrix composites with multiple crack stopping interfaces.

FIGURE 22: Load/deflection curves for pyrolysed nicalon fabric/ particulate reinforced polyvinylsilane matrix with multiple crack stopping interfaces.

TABLE CAPTION

TABLE I: Shrinkage and mechanical properties for pyrolysed, particulate reinforced polyvinylsilane.
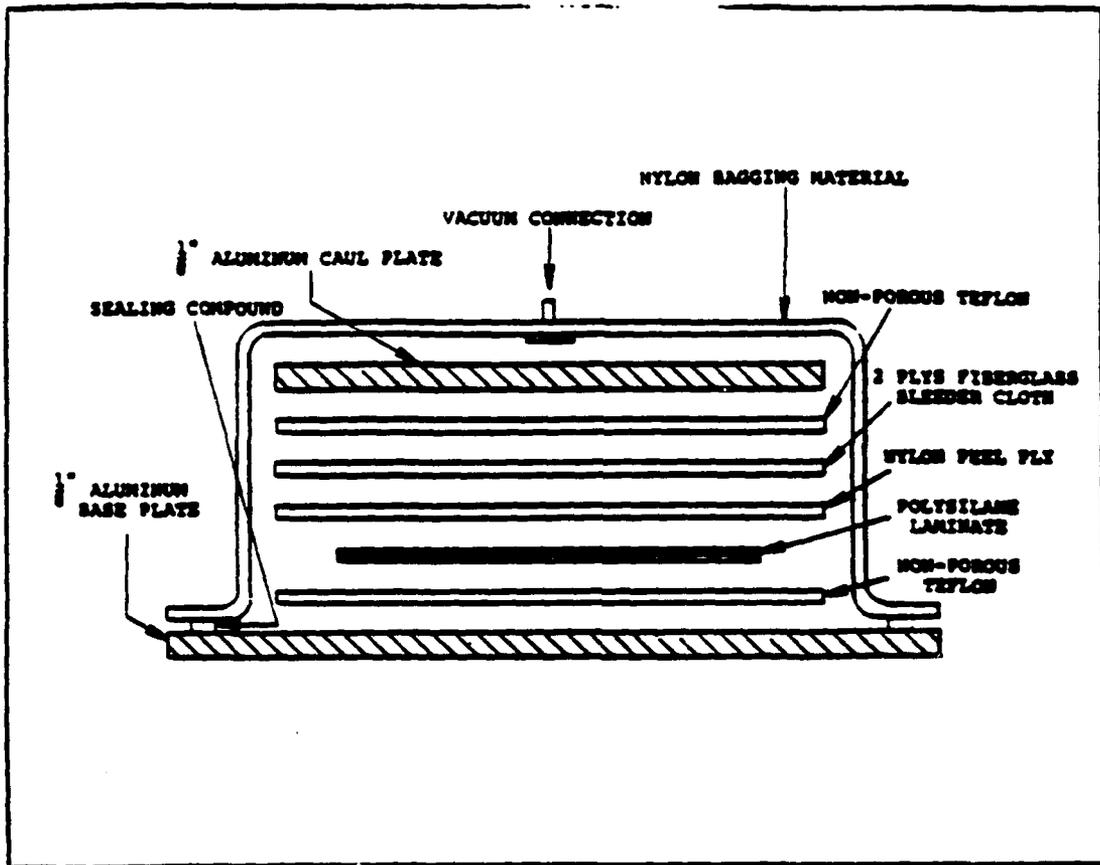
Abbildung 1
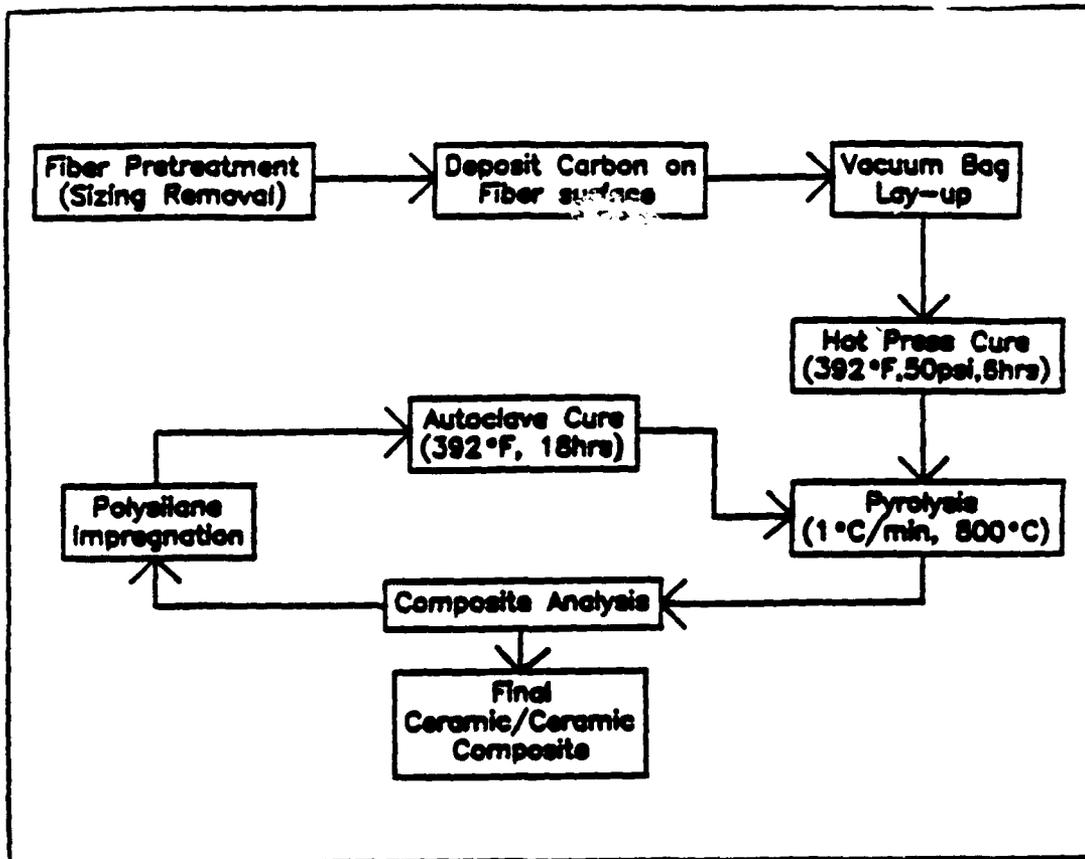
Abbildung 2
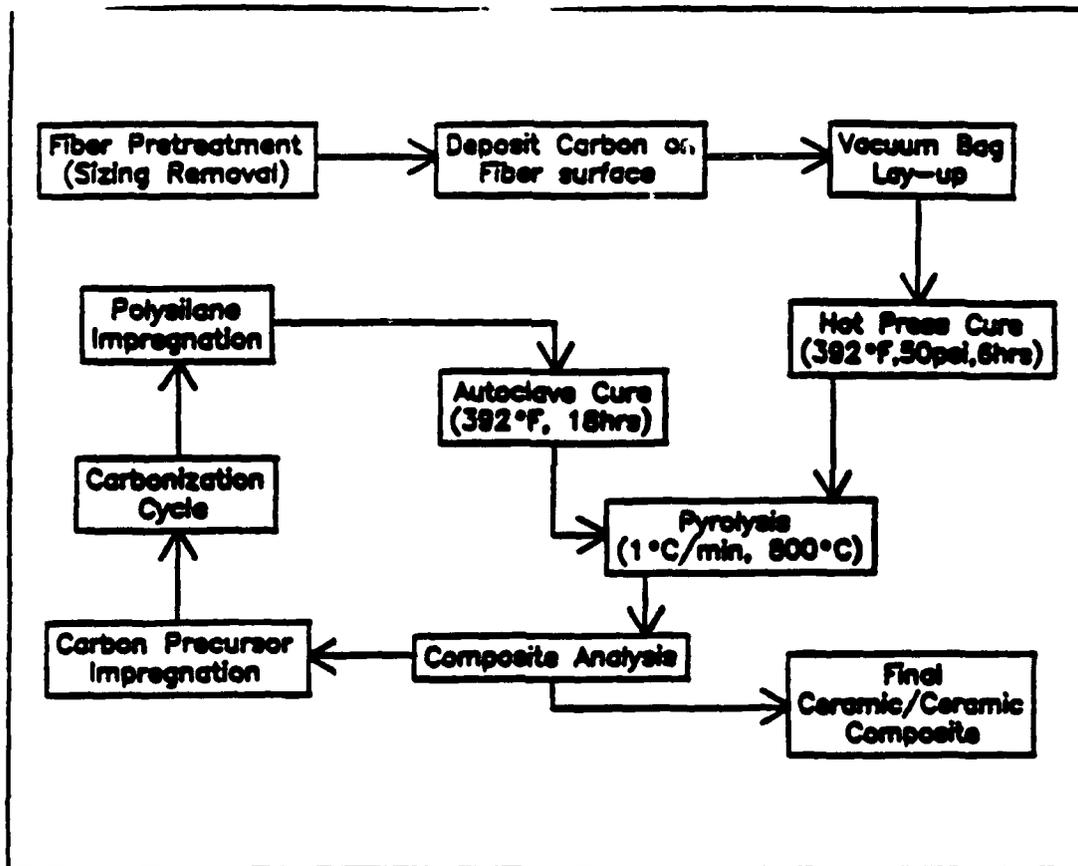
Abbildung 3
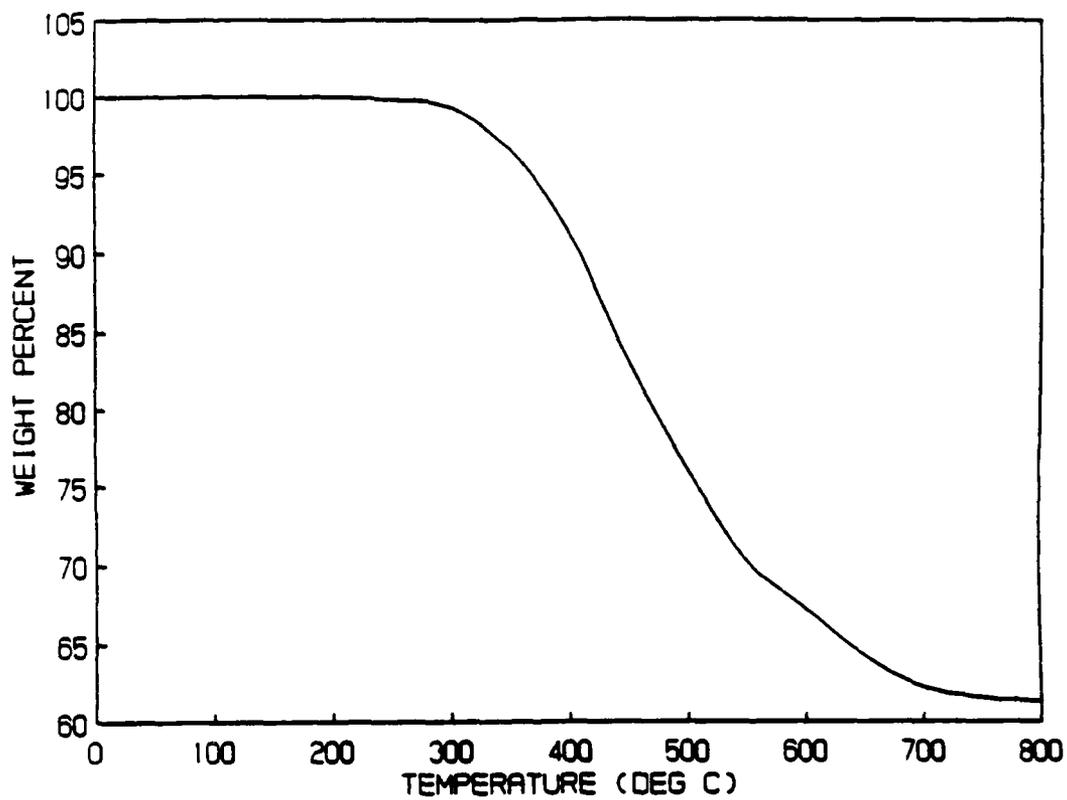
Abbildung 4
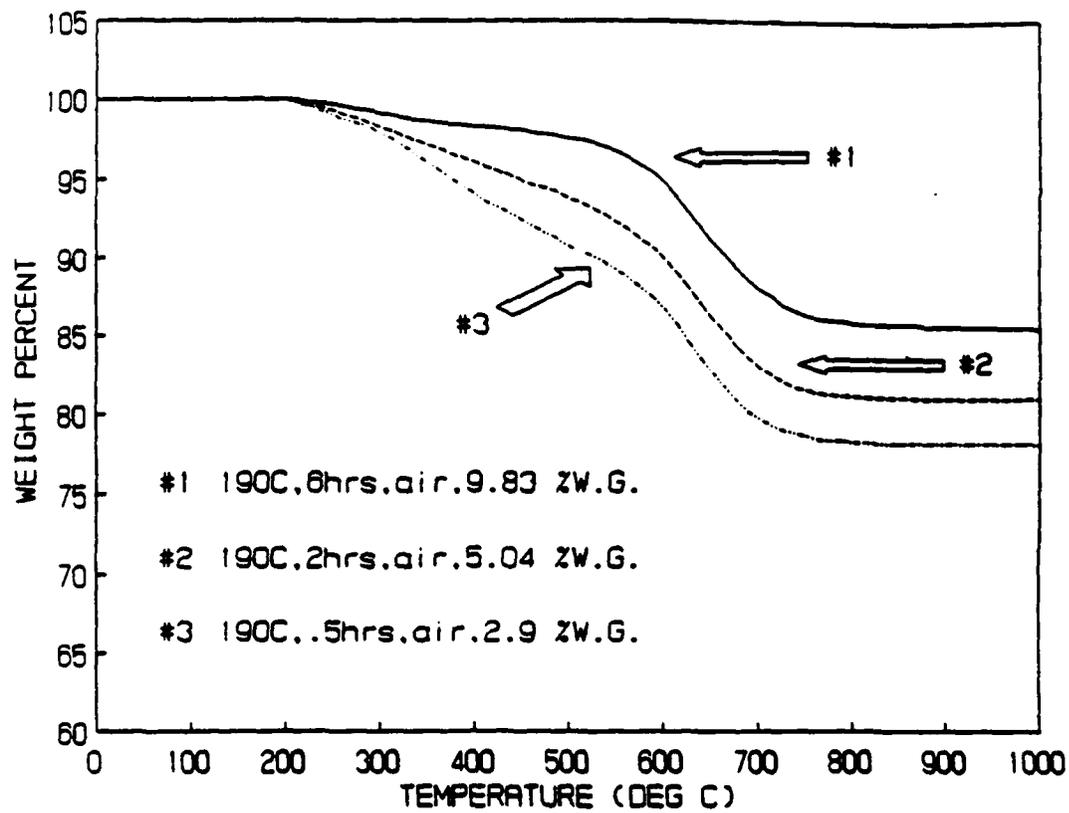
Abbildung 5
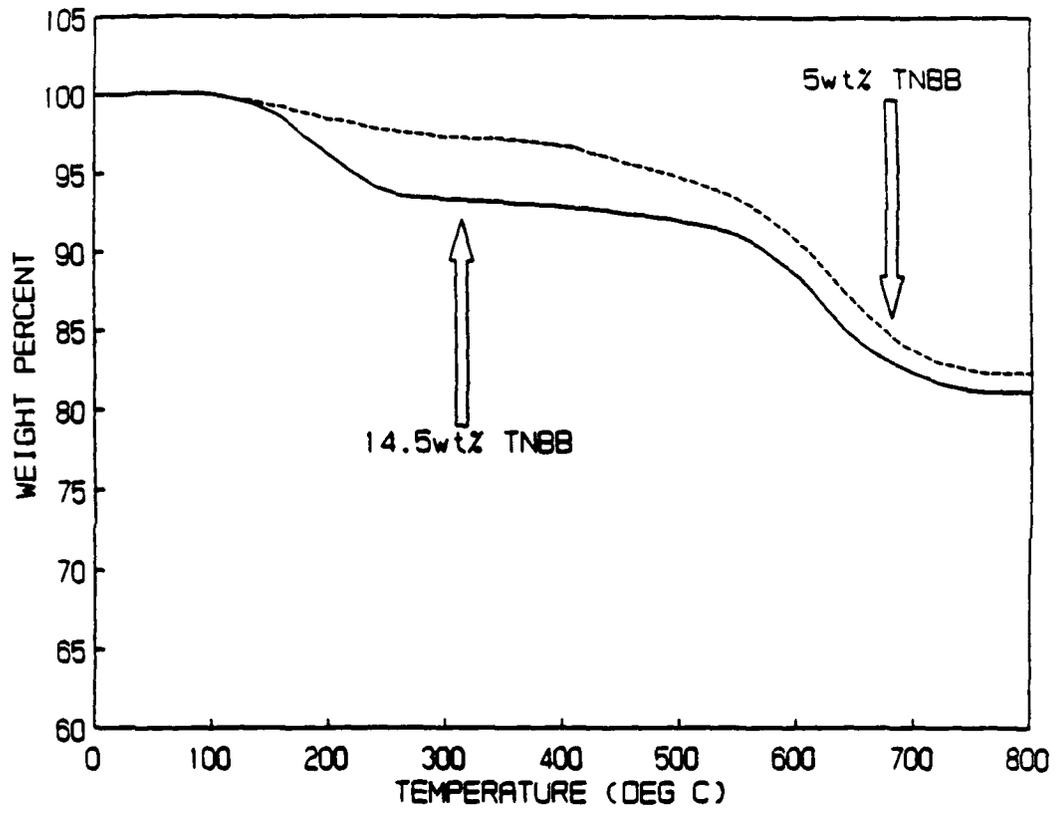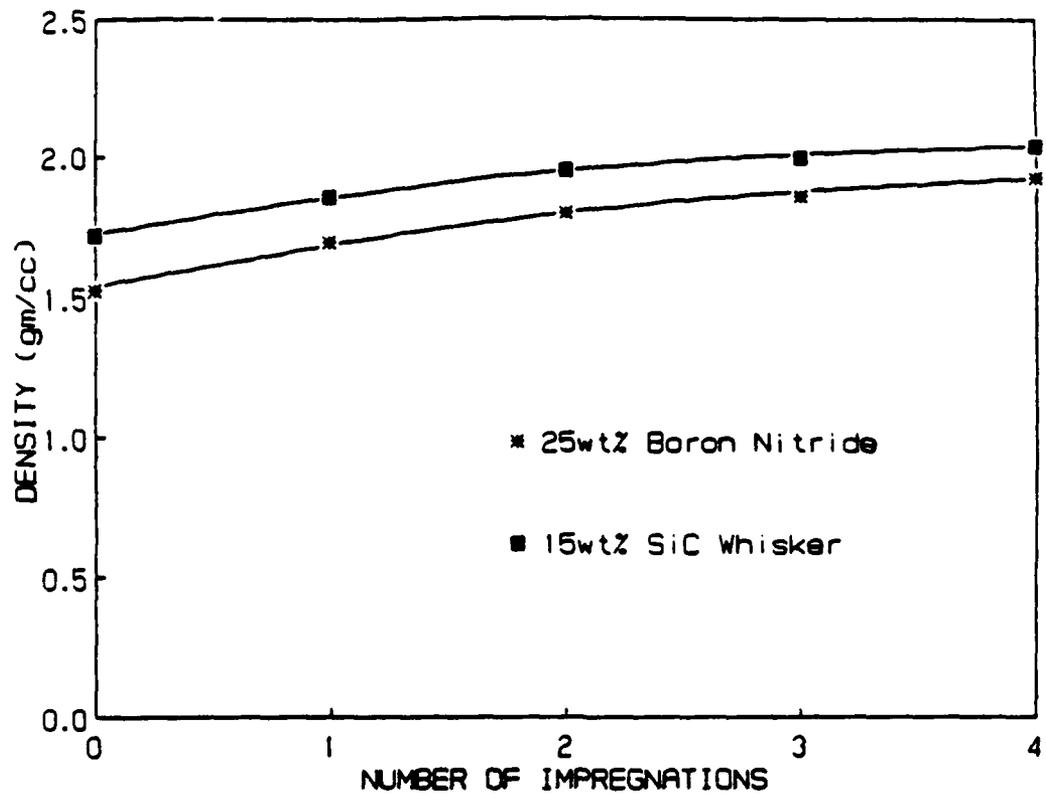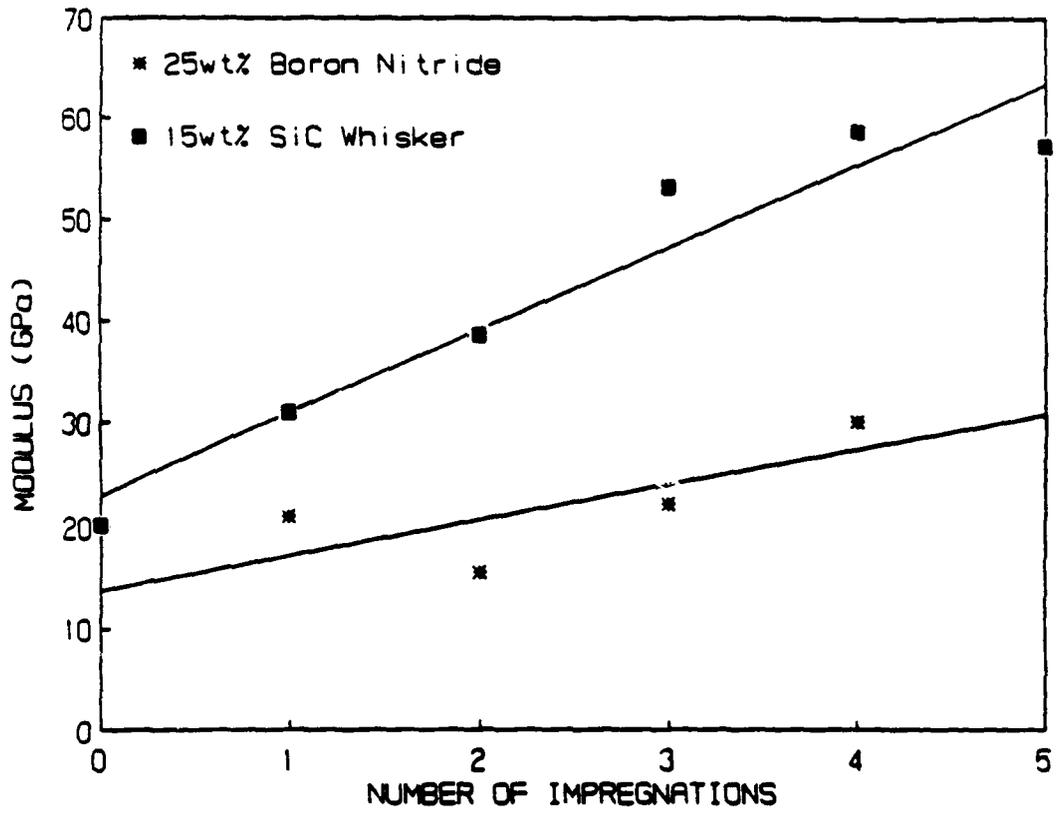
Abbildung 6

Abbildung 7

13.22
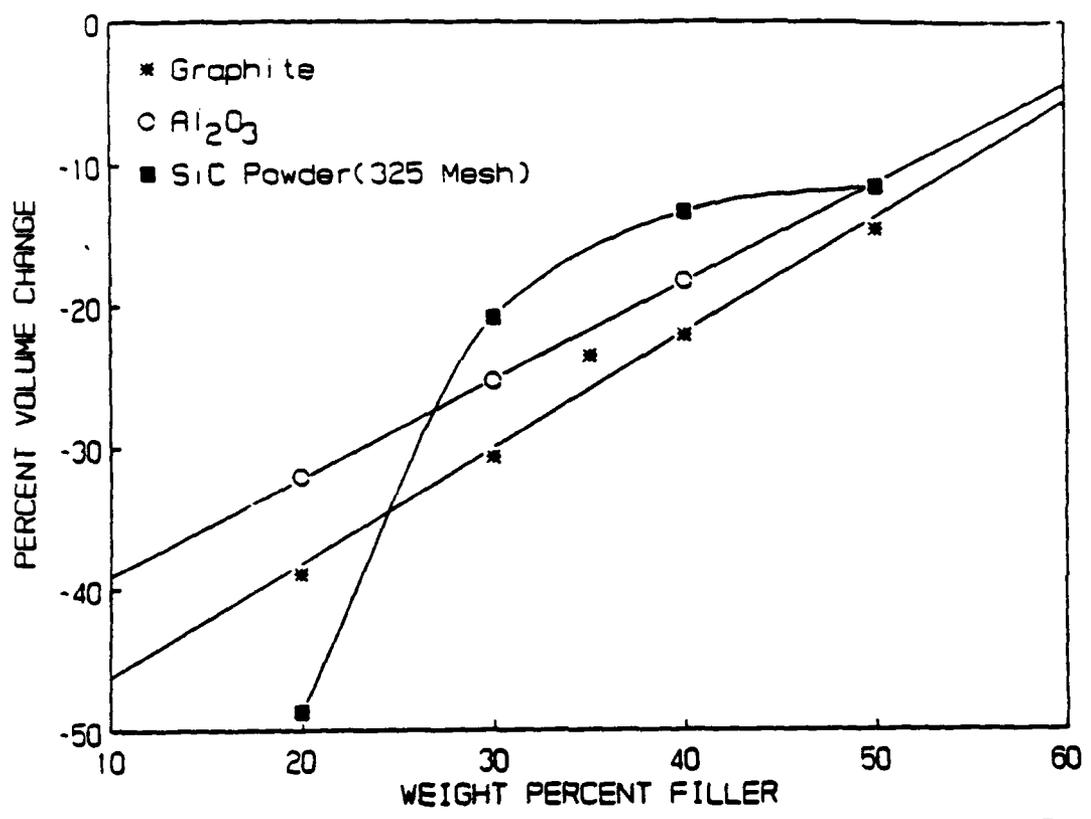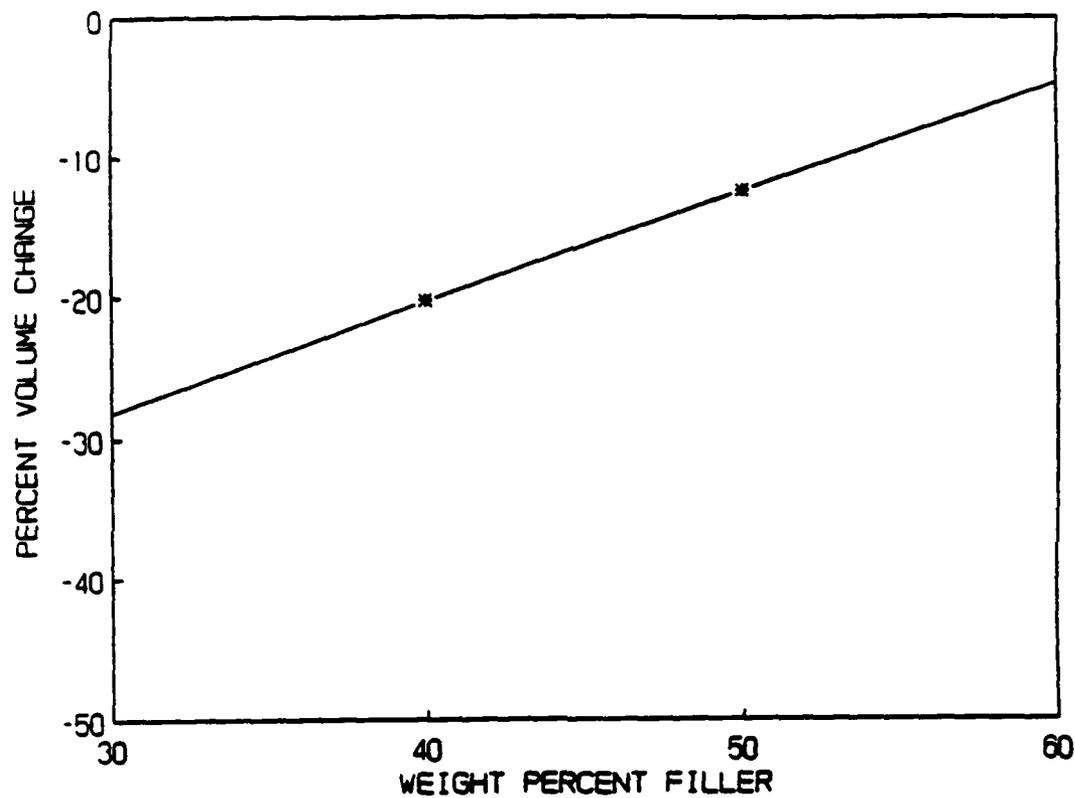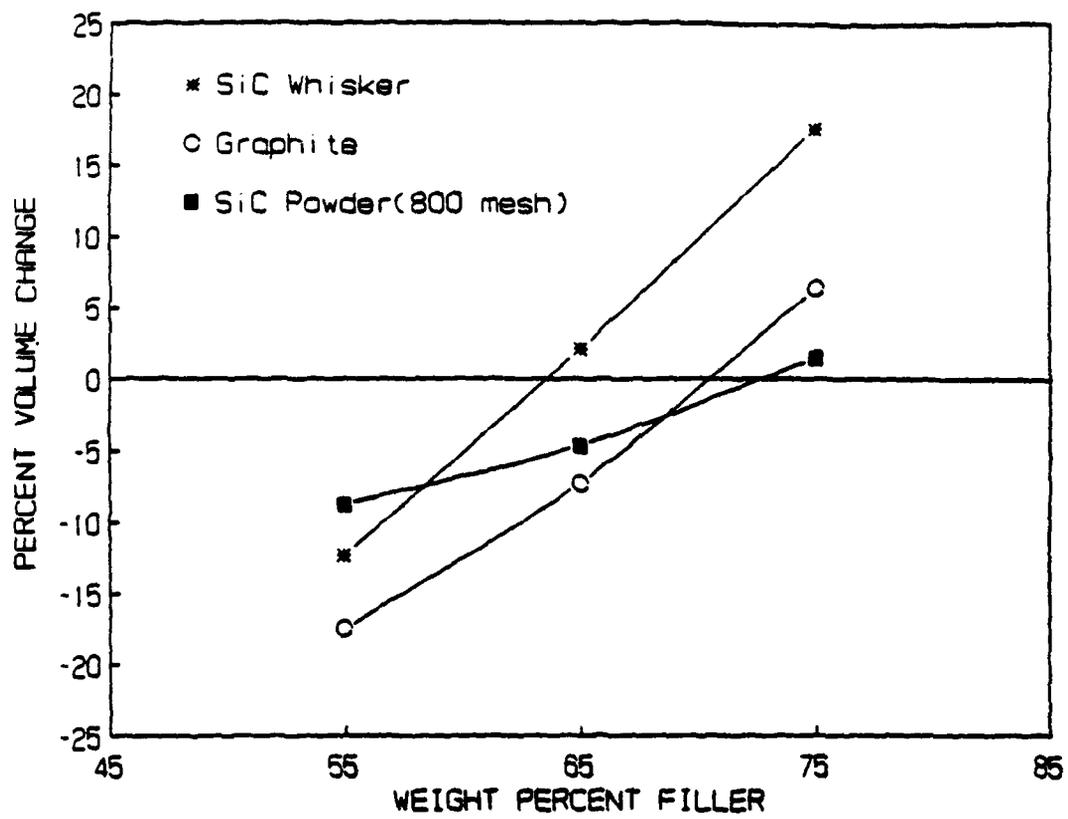
Abbildung 8

Abbildung 9
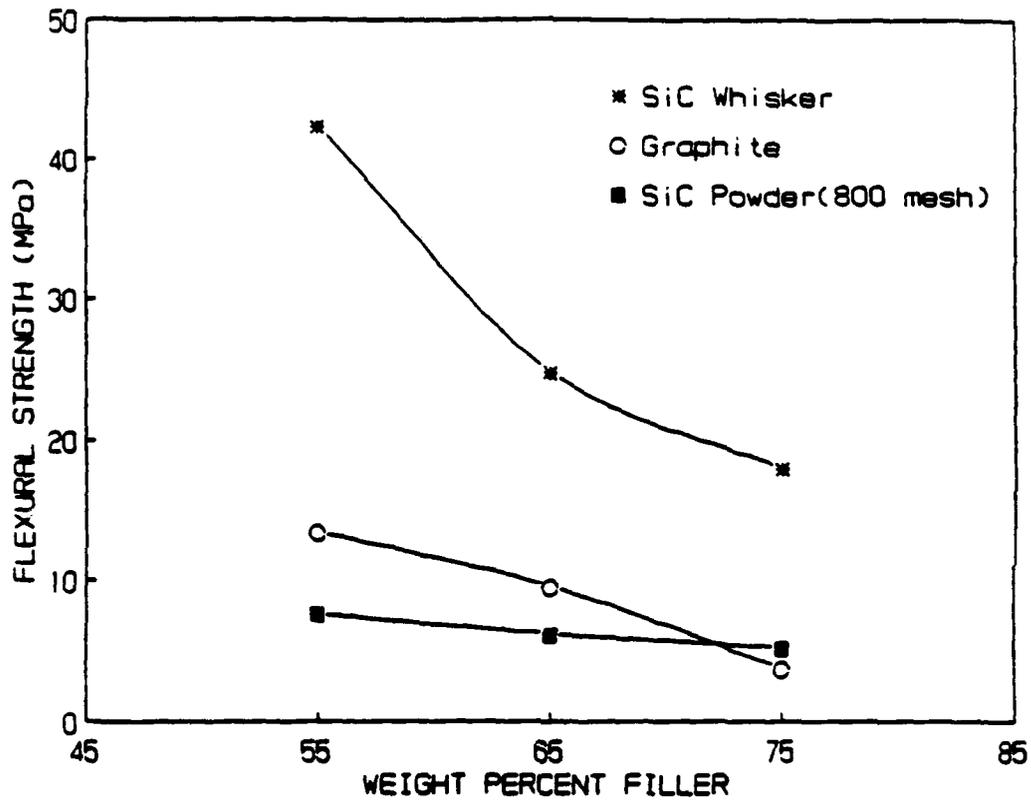
Abbildung 10
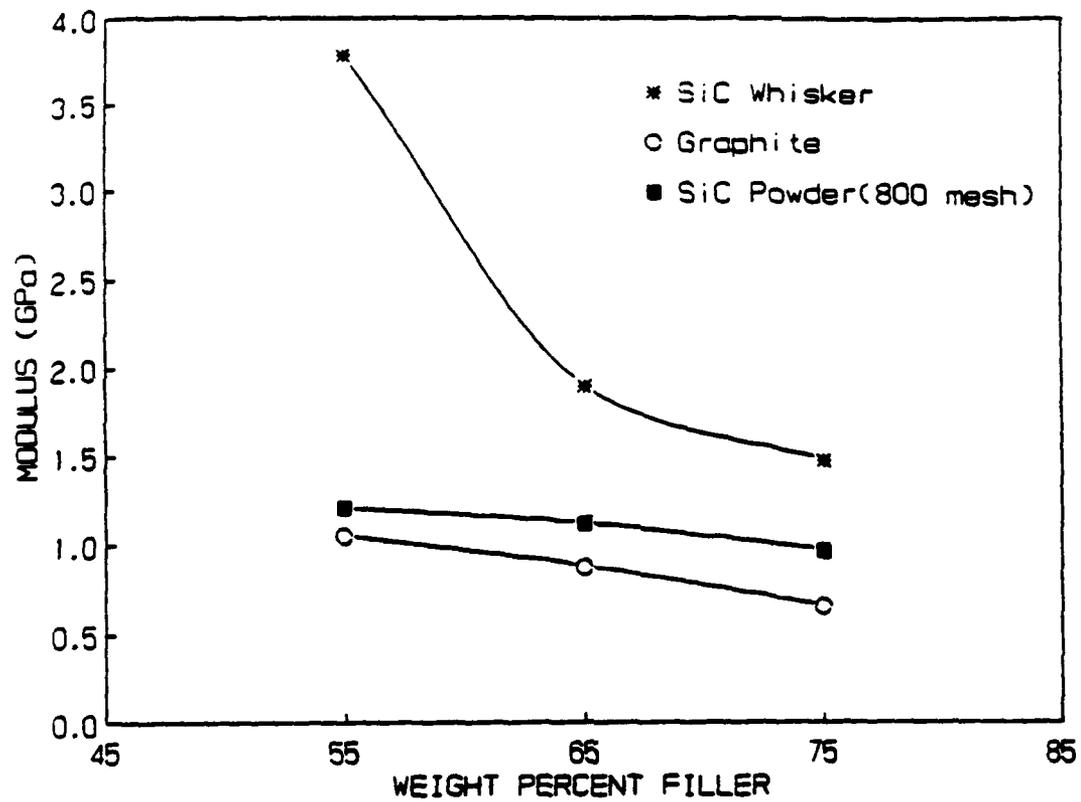
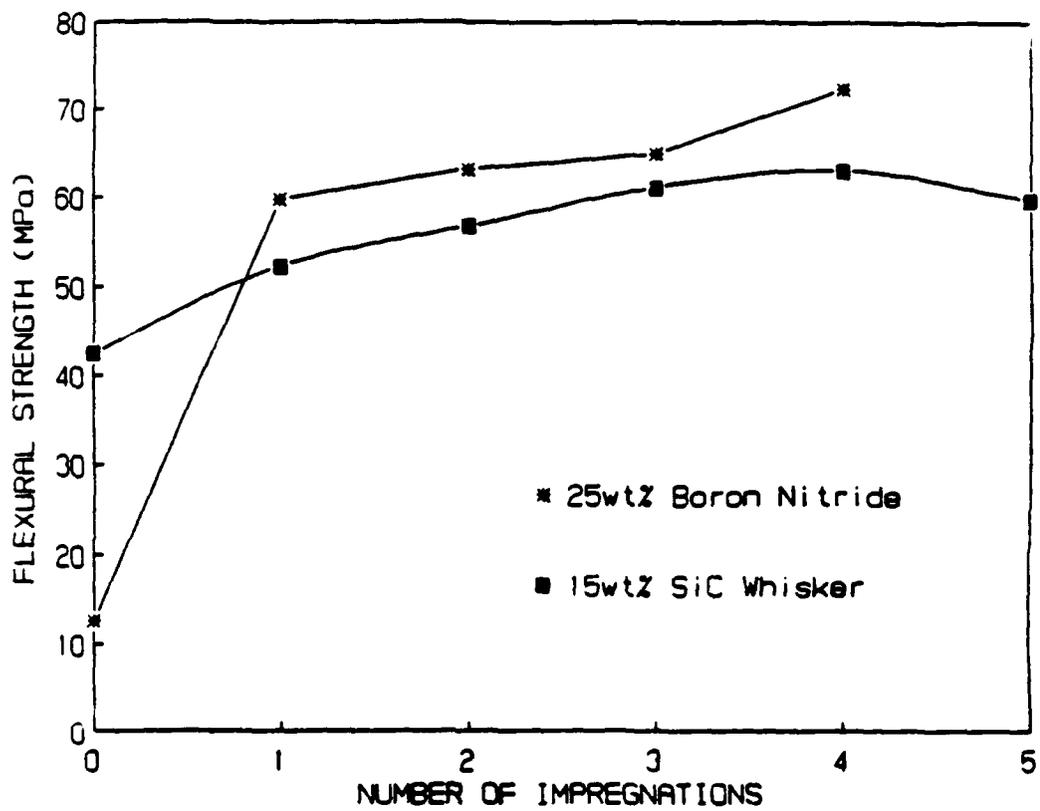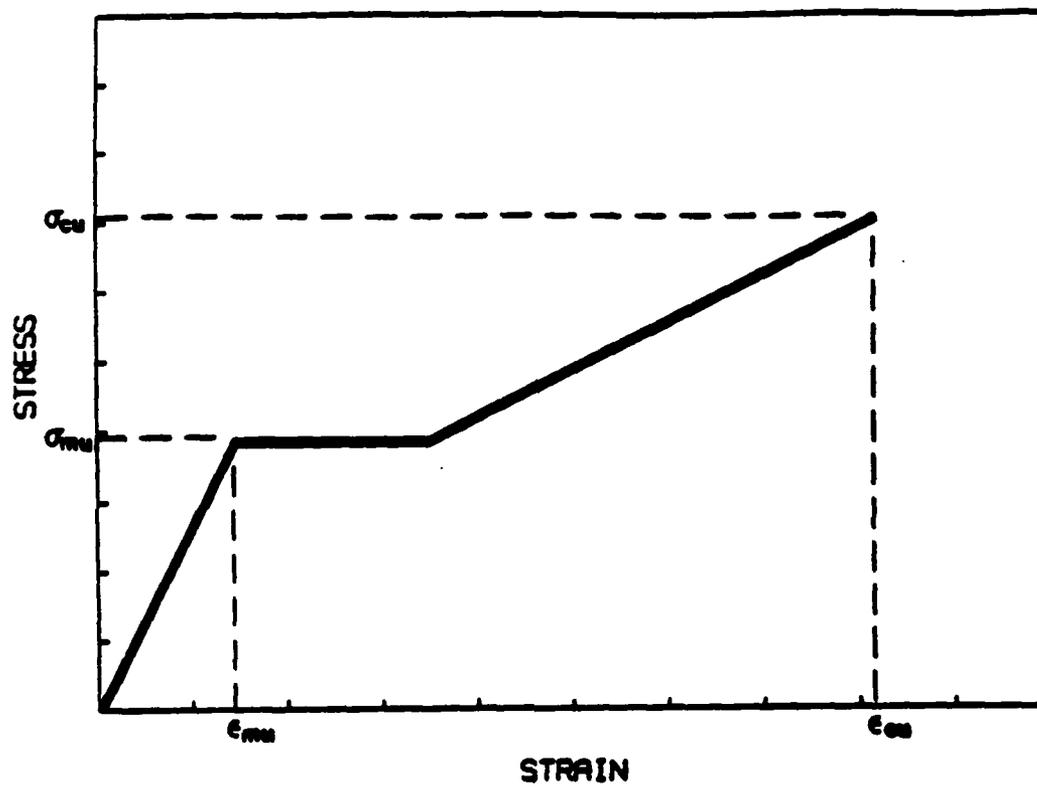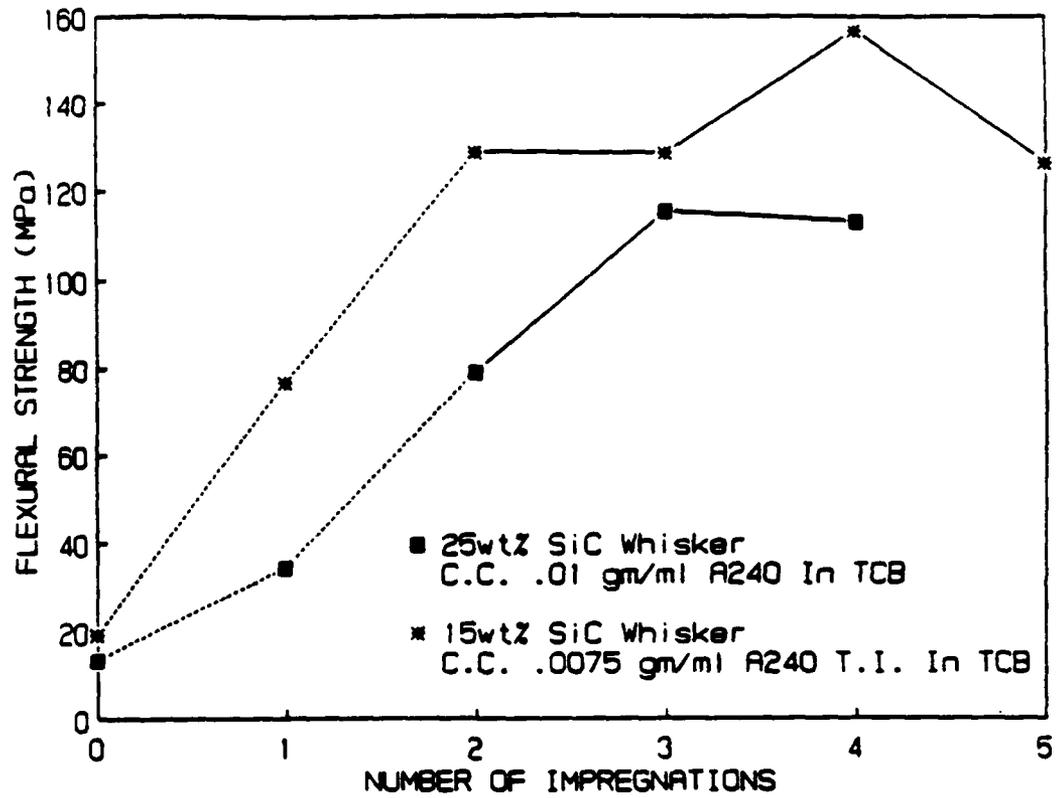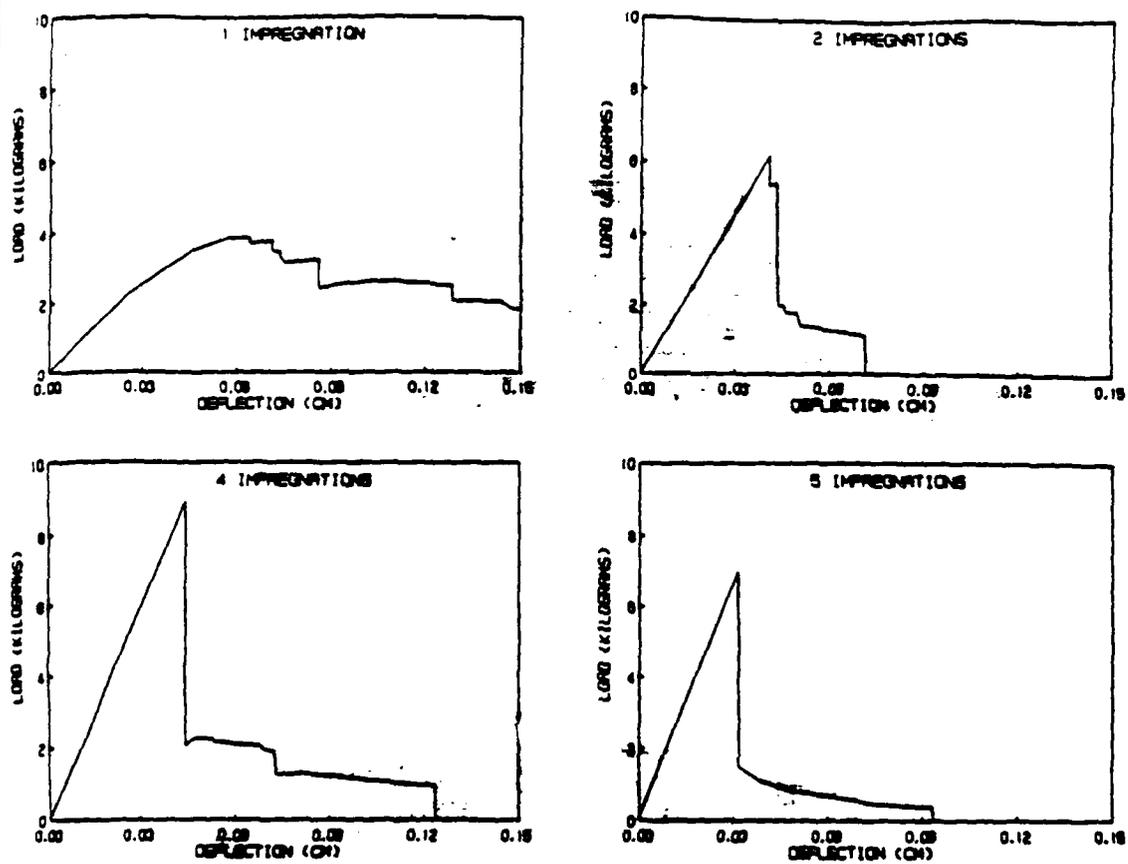Abbildung 11
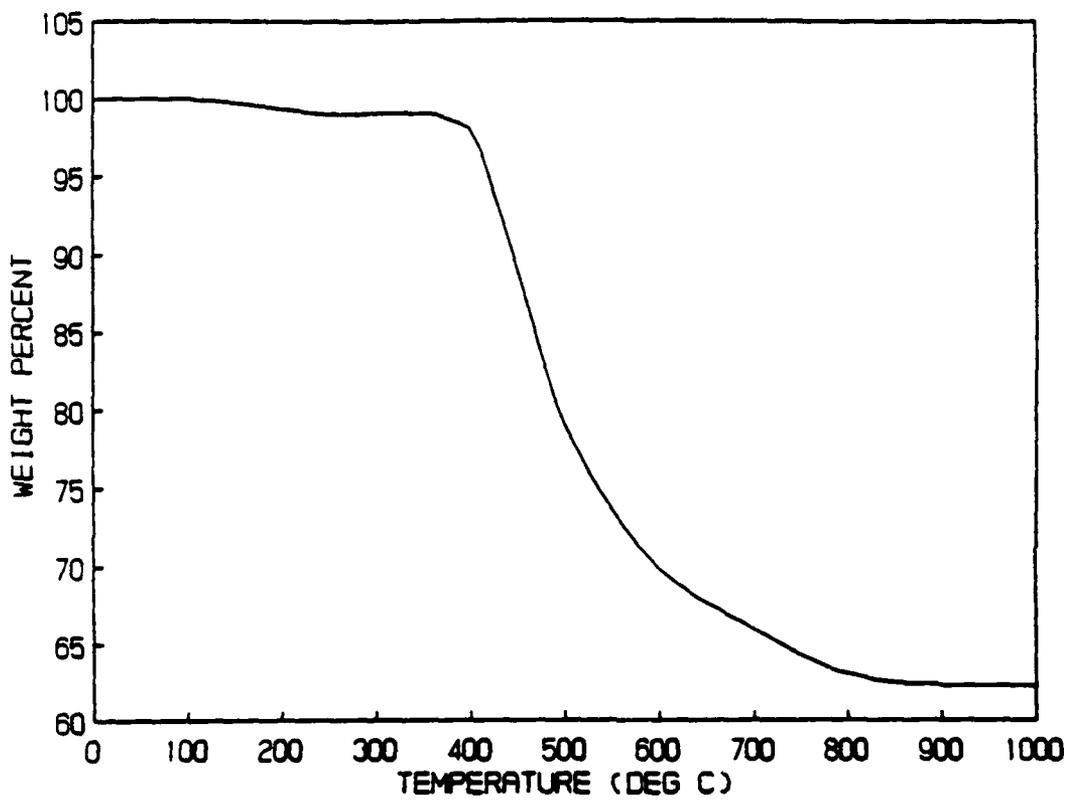
Abbildung 12
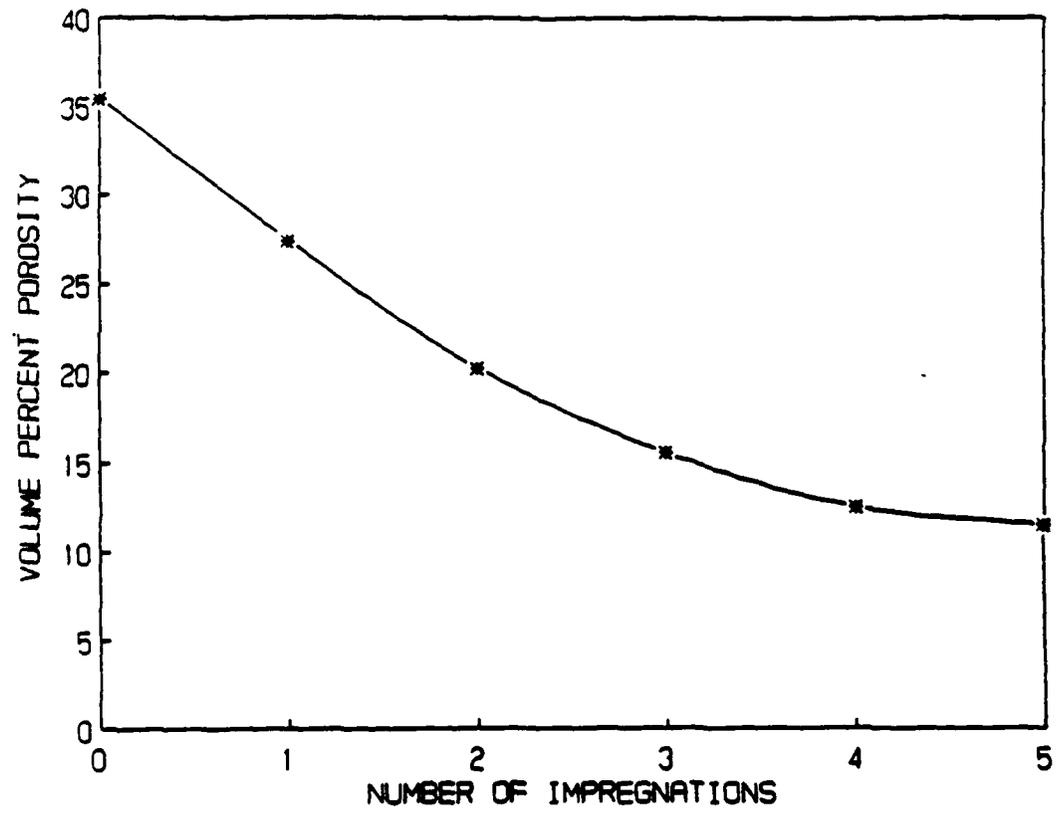
Abbildung 13

Abbildung 14

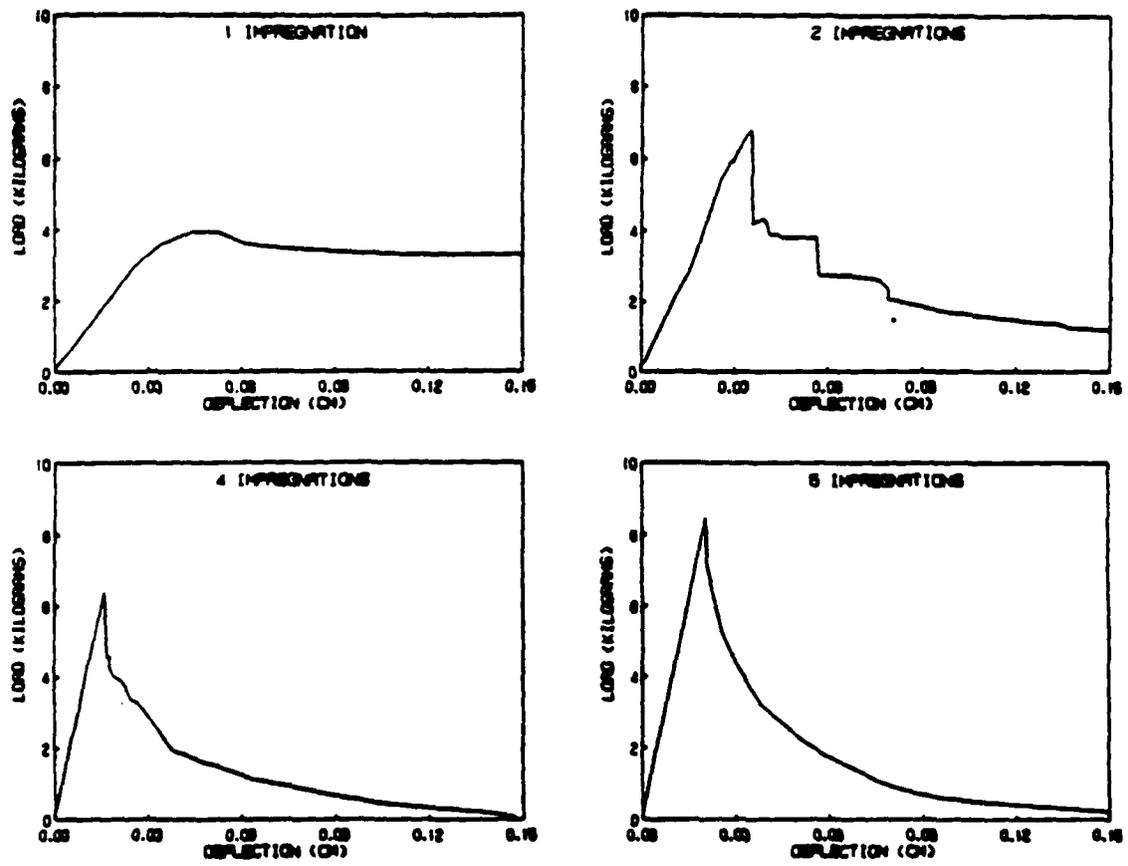Abbildung 15

13.30

Abbildung 16

Abbildung 17

Abbildung 18

Abbildung 19

13.34
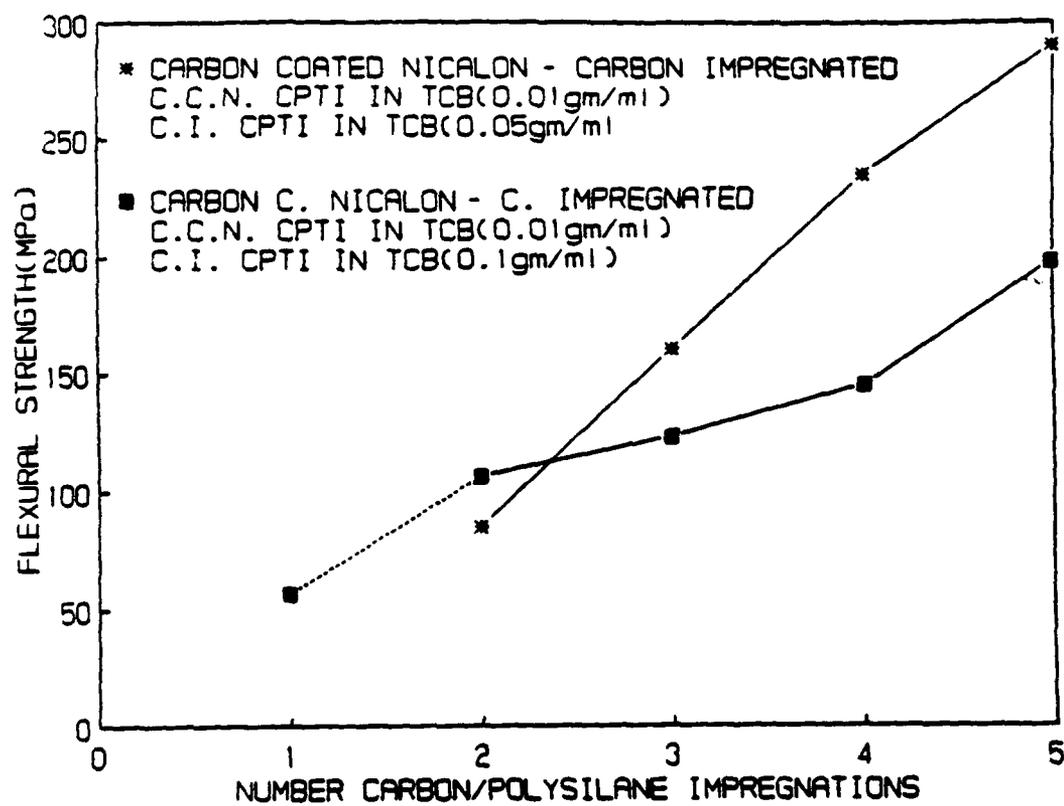
Abbildung 20

Abbildung 21
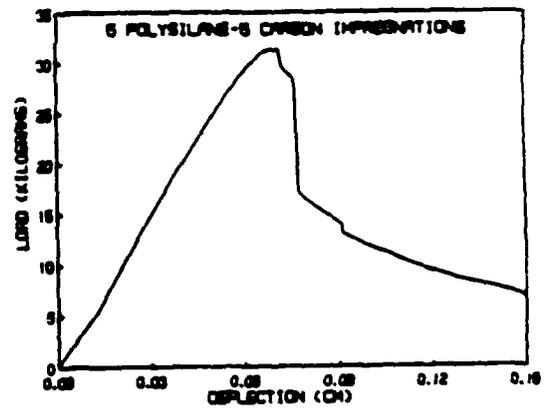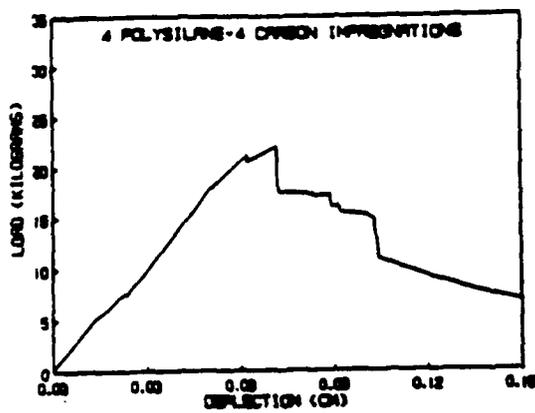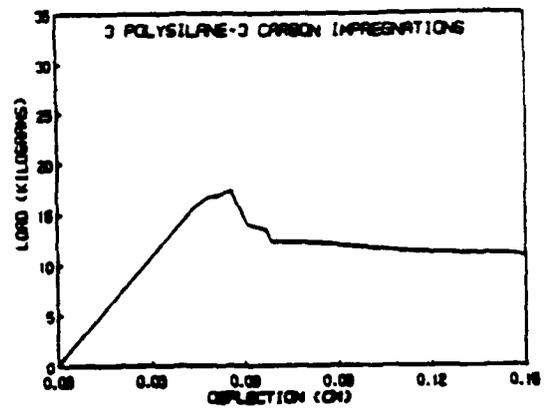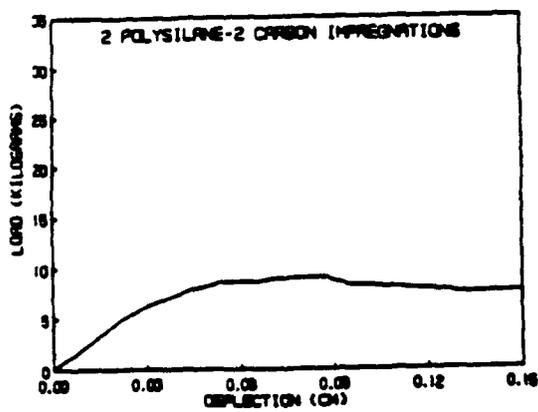
Abbildung 22

	Percent Shrinkage	Strength Bend, MPa	Modulus GPa
Pure Polysilane	28.8	3.30	7.03
25wt% SiC Whisker	20.2	35.23	14.62
15wt% SiC Whisker	21.7	23.51	8.27
5wt% SiC Whisker	27.5	26.61	33.03
25wt% BN Powder	21.0	13.65	6.07
25wt% S3N4 Powder	20.5	5.33	3.31
25wt% SiC Powder	22.5	18.89	10.20

Tafel 1

CERAMICS
adding the value

VOLUME 1

Editor: M.J. Bannister

AUSTCERAM 92

Proceedings of the International Ceramic Conference
Australia 1992

Volumes 1 and 2 – AUSTCERAM 92 manuscripts

CSIRO
AUSTRALIA

CHEMICAL VAPOR DEPOSITION OF SILICON CARBIDE USING METHYLTRICHLOROSILANE

R.P. Boisvert and R.J. Diefendorf

Clemson University, Ceramic Engineering Department
Clemson, SC 29634-0907, USA

INTRODUCTION

Fiber reinforced ceramic matrix composites   a promising clas of
structural materials for applications which require high strength,
high stiffness, low density and most importantly some degree of
damage tolerance. The performance of ceramic matrix composites has
been found to depend critically on the nature of the fiber-matrix
interface.   In general, the strength of the interface must be
sufficiently low to deflect cracks and allow fiber-pullout. While
tensile failure strains often approach one percent for the compos-
ite, matrix microcracking frequently occurs at just a small frac-
tion of the failure strain. Matrix microcracking allows internal
oxidation of the crack deflecting interface layer at high tempera-
ture which subsequently causes embrittlement at room temperature.

Multiple crack-deflecting interfaces were introduced within the
matrix in an effort to increase the strain at which matrix micro-
cracking occurs [1,2]. The concept was to limit the maximum flaw
dimension in the matrix, and also make a tough lamellar composite
matrix. The objective of the present research was to develop a
technique whereby the matrix layering could be simply controlled.
The work is separated into two parts: 1) defining the deposition
conditions to deposit pure SiC uniformly throughout a fiber
preform, and 2) depositing multilayered matrix composites and
determining their structure and properties. This paper reports on
the first part for the chemical vapor infiltration of silicon
carbide from methyltrichlorosilane (MTCS) and hydrogen.

EXPERIMENTAL TECHNIQUES

The silicon carbide deposition studies were carried out over a
temperature range of 750-1300°C, pressure range of 267-1333Pa, and
a $H_2:CH_3SiCl_3$ ratio of 8 to 15:1 in a hot wall tubular reactor held
at constant deposition conditions during the run. In addition to
the Nicalon tow substrates, graphite bars were used for depositing
coatings for x-ray diffraction, and fine diameter (25μm) carbon or
tungsten filament were utilized to determine deposition profiles

within the reactor. The diameter of the coated filaments was
measured with a laser diffraction technique. The last deposited
surfaces and composite fracture surfaces were characterized using
scanning electron microscopy. Matrix layer thicknesses and
microstructure were determined by optical microscopic observation
of polished cross-sections. The purity, crystal structure, crys-
tallite size and preferred orientation were measured by x-ray
diffraction. Tensile tests were performed on the composite
strands.

RESULTS AND DISCUSSION

Thermodynamic Analysis

Thermochemical analysis of CVD systems has proven useful for
selecting deposition conditions. A total of 46 gaseous species and
4 condensed phases were considered in these calculations which used
a modified version of Solgasmix-PV [3,4]. The calculations are
subjected to constraints which include conservation, constant
temperature and constant total pressure. The thermodynamic equi-
librium state that results allows: 1) determination of condensed
phases deposited, 2) the theoretical reaction efficiencies, and 3)
the partial pressures of all the gaseous species.

Figure 1 illustrates the thermodynamically stable phases as a
function of temperature and H_2/MTCS ratio. Only two regions, β-SiC
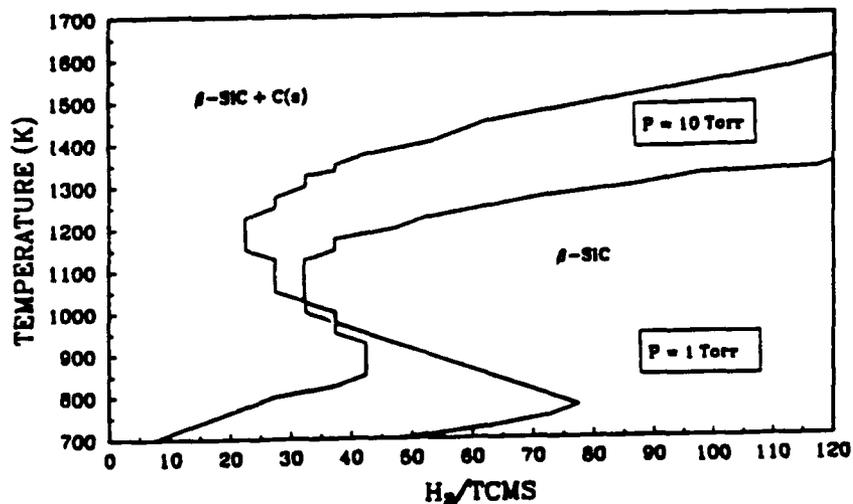and β-SiC+C(s), were identified as stable compositions for the

FIGURE 1

conditions studied. At low H_2/MTCS ratios, carbon was found to co-
deposit with SiC. Increases in total pressure extend the single
phase β-SiC region to higher temperatures and lower H_2/MTCS ratios.

The thermodynamic efficiencies for the deposition of SiC from MTCS
and H_2 were calculated as a function of H_2/MTCS and a temperature
and pressure range of 1075-1475K and 0.133-1.33kPa respectively

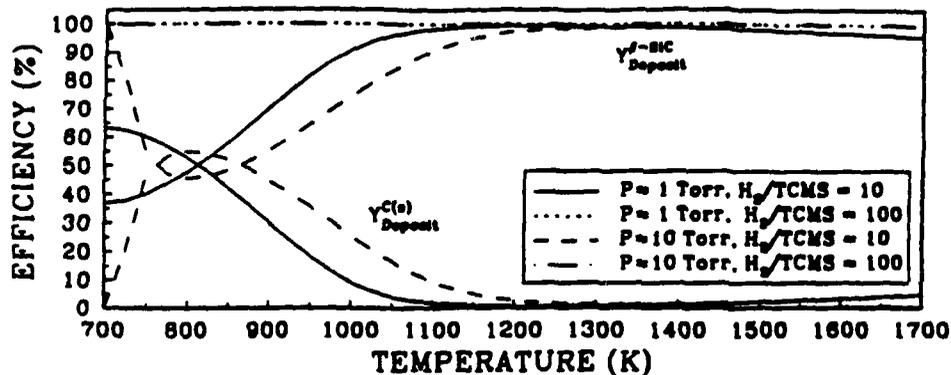(Figure 2). At all ratios of H_2/MTCS, carbon is essentially

FIGURE 2

stripped from the gas phase. Due to the low yields of Si at low H_2/MTCS ratios, excesses of C are co-deposited. Similarly, higher total pressure and/or lower temperature also increase the amount of free carbon that is predicted to co-deposit.

The gas phase composition as a function of H_2/MTCS for heterogeneous equilibrium is illustrated in Figure 3. Hydrogen and
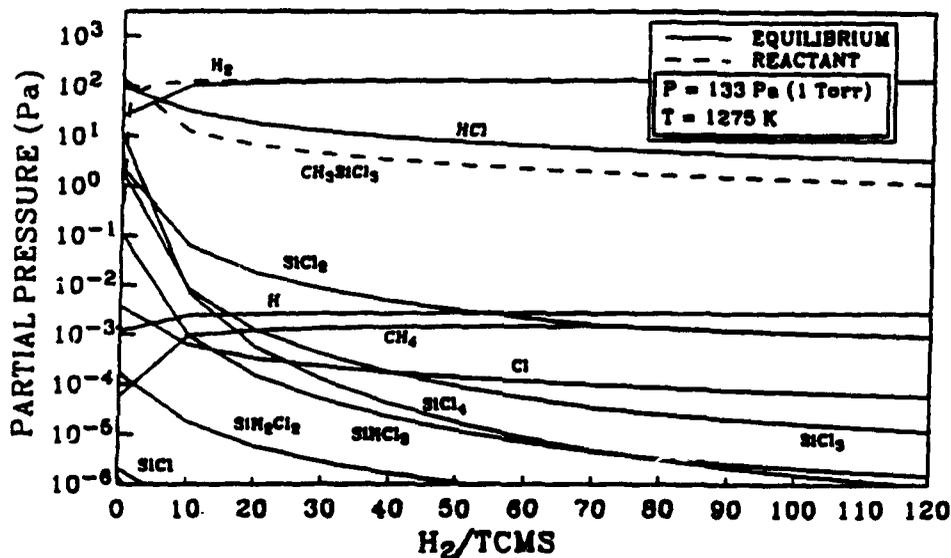

FIGURE 3

hydrogen chloride are the major species. Silicon dichloride is the predominant Si bearing species whereas methane is the main carbon bearing species. The low equilibrium vapor pressure for MTCS is an indication of its low stability. Rapid changes occur in partial pressures of all species when hydrogen is initially added to the system, but decreases as more hydrogen is added.

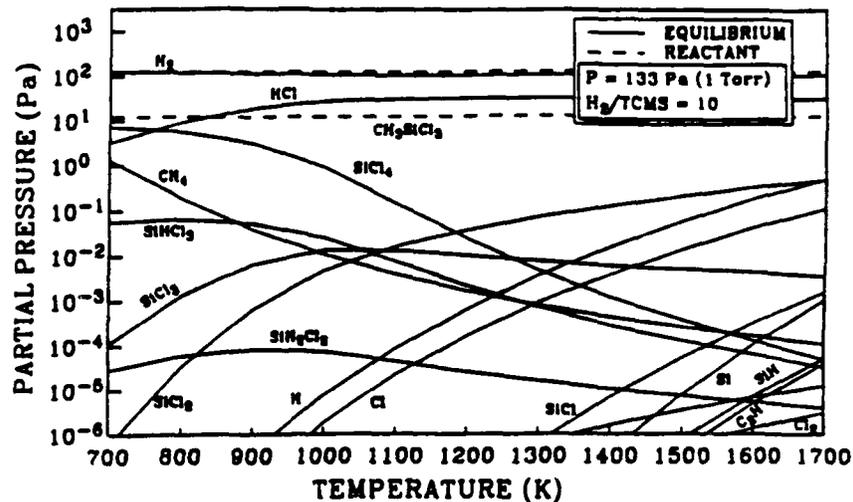Figure 4 illustrates the gas phase composition as a function of

FIGURE 4

temperature. At temperatures below 1100K, $SiCl_4$ is the predominant Si bearing species. Above 1100K, $SiCl_2$ becomes the most abundant species. Methane has the highest partial pressure for carbon bearing species over the whole range of conditions studied. (Page limits permit only the data for 130Pa to be shown.)

Results for the gas phase composition, assuming equilibrium among the gas phase species but not with respect to the solid phases (homogeneous equilibrium), show several differences with respect to the heterogeneous equilibrium values. Methane is significantly more abundant whereas the reaction product HCl is obviously more plentiful for heterogeneous equilibrium.

In summary, thermodynamic calculations indicate that high reaction efficiencies can be obtained, but free carbon is predicted to co-deposit with the silicon carbide at the lower temperatures that would be required for infiltration of a fibrous composite preform.

Deposit Morphology and Structure

Smooth deposit surfaces with rounded growth features, similar to cauliflower, were observed at low temperature. Atoms are expected to have low surface mobility at low temperatures which favors continuous nucleation of new crystals. At high temperatures, higher surface mobility results in larger crystallite sizes [5] which is manifested in the strongly facetted morphologies at temperatures above 1300°C. These faceted deposits were normally multiridged, but occasionally crystals with regular hexagonal cross-sections were observed. X-ray evidence for the presence of α-SiC in the high temperature deposits is documented later.

Increases in the H_2/MTCS ratio or decreases in pressure, both of which decrease supersaturation, increase the faceting of the

deposit surface.   Morphological differences along single deposits
occurred only when the H_2/MTCS ratio was below 12:1.   For example,
ratios of 8:1 and temperatures below 1000°C resulted in uneven
nucleation at the inlet of the reactor, but a rounded columnar
deposit was formed further into the reactor.

X-ray diffraction of the deposits showed them to be β-SiC and in
some instances at high temperature α-SiC.   Elemental carbon or
silicon was not identified in the x-ray patterns.   Deposits were
characterized as polycrystalline with a high degree of preferred
orientation.   The texture was dependent upon temperature, pressure
and MTCS flux.   The (111) texture, with the (111) plane parallel to
the substrate, was the preferred orientation for low temperature,
high pressures and high MTCS flux.   At high temperatures, low
pressures and low MTCS flux, the texture with (220) planes parallel
to the substrate was the preferrec orientation [6-8].

Deposition Profiles

A laser diffraction technique was   i to quantify the potential
for deposition by measuring depositi_ on fine filaments which were
mounted both radially and axially at a number of locations within
the reactor.   A typical curve for an axial filament is shown in
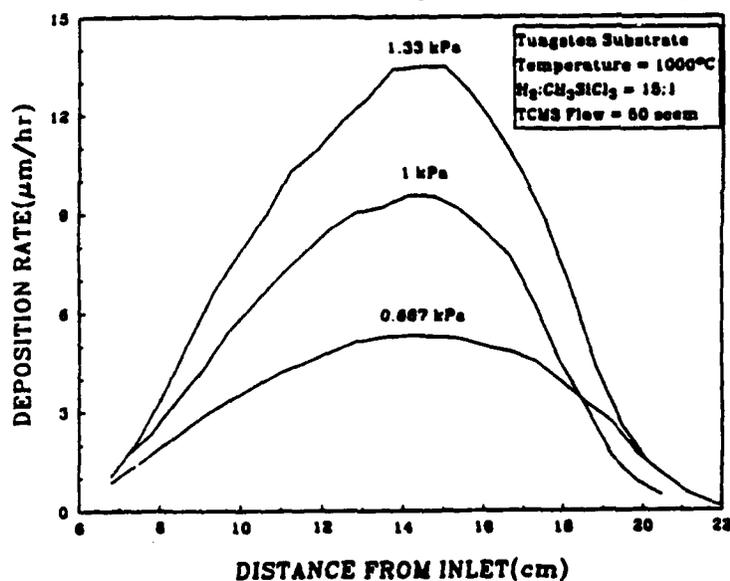Figure 5.   There are three different parts to these deposition rate

DISTANCE FROM INLET(cm)
FIGURE 5

profiles.   The increasing rate at the inlet indicates the distance
necessary to heat the reactant gas stream to temperature and create
the species from which the SiC deposits.   The central region of the
deposition profile provides the relatively uniform rate which is
desirable for deposition.   The decreasing rate in the third region
can be caused by depletion of reactants or decrease in temperature.
A series of runs at different flow rates indicated that depletion
was not a factor for these conditions.   Estimates of the gas tem-

perature, using a fine thermocouple, suggested that the decreasing deposition rate is the result of decreasing temperature.

Deposition Kinetics

The effect of total pressure and H_2/MTCS on deposition rate was studied over the temperature range of 1123-1271K in an effort to define the deposition mechanism. The deposition rate was found to vary linearly with pressure and partial pressure, but neither plot went through the origin. Based on these observations, only the apparent activation energy based on deposition rate could be calculated. The Arrhenius plot of deposition rate versus reciprocal temperature clearly indicates a transition from surface kinetic to mass transport rate limiting processes with increasing temperature, Figure 6. The apparent activation energy for lower
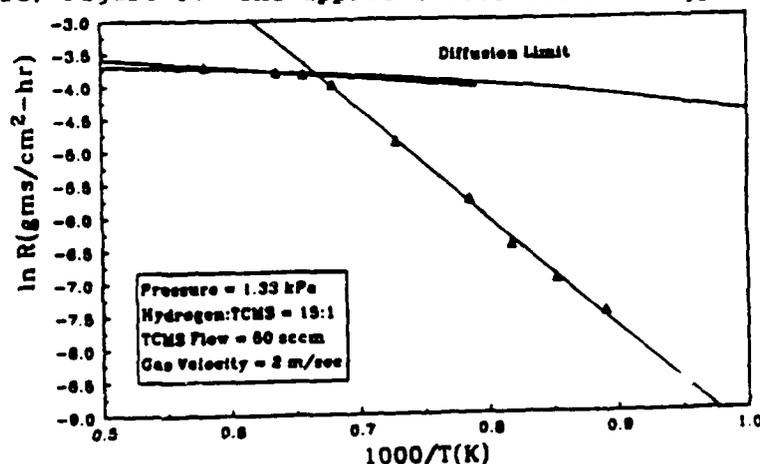

FIGURE 6

temperatures was 138kJ/mole, which is characteristic for a chemical reaction. Above 1473K, the apparent activation energy decreased to 13.4 kJ/mole, which is typical of a gas diffusional process. A calculation for mass transport, assuming equilibrium at the surface, is also shown on the figure.

Ceramic Matrix Composites

The deposition conditions for forming a matrix in a fibrous pre form must uniformly deposit the matrix material throughout the pre form. Hence the mass transport in and out of the preform must be rapid compared to the surface deposition rate such that the concen tration of species is uniform throughout the preform. Single tow of Nicalon SiC fibers were used as a substrate to study the effect of temperature, system pressure and reactant gas flow rate on in filtration. Temperatures between 1023-1573K and pressures betwee 0.33kPa-1.33kPa were studied. Infiltration conditions selected fo producing the composites were temperature = 1273K, pressure = 1.3 kPa and H_2/TCMS ratio = 10, based on deposition rate and uniformity

Specimens were fabricated with and without carbon interfacia

coatings between the fiber and matrix. Best results were obtained for carbon deposition using a propylene to argon ratio of 1:5 at 1373K and 2.66kPa pressure for 2 hours. In addition, specimens with multiple 20μm, 50μm, or 100μm matrix layers were deposited with carbon coatings between the matrix layers. Although the mechanical test results and microstructure will be reported more completely in a subsequent paper, proper multilayering doubled the strength and improved the work of fracture over composites with just a single crack stopping layer between the fiber and matrix. The improvement was not as great as when whisker reinforced polymeric precursors were used to form the matrix. With polymeric precursor matrices, the effective modulus of the matrix is less than that of the fiber, while the CVI matrix modulus is approximately two and one half times greater. Hence, much of the load is carried by a CVI matrix, and a substantial drop in modulus occurs with matrix microcracking. However, thinner matrix lamellae appear to produce higher strength, and also appear to allow thinner crack stopping coatings. Future studies will be performed to determine if improved composites can be fabricated.

CONCLUSIONS

The chemical vapor infiltration conditions required for uniform deposition of pure SiC or carbon throughout a fibrous preform were determined. No excess silicon or carbon was identified by x-ray diffraction of the silicon carbide. Lamellar matrix/continuous fiber reinforced composites have successfully been prepared by CVI, and significant improvements in composite properties were observed.

ACKNOWLEDGEMENTS

REFERENCES

1) Boisvert, R.P. and Diefendorf, R.J.: Proceedings Verbundwerk 88, (Demat, Frankfurt, 1988) pp. 13.1-37.
2) Diefendorf, R.J. and Boisvert, R.P.: Materials Research Society Symposium Proceedings, 1988, Vol. 120, pp. 157-162.
3) Besman, T.M.:"Solgasmix-PV - A Computer Program to Calculate Equilibrium Relationships in Complex Chemical Systems", 1977, ORNL/TM 5775, pp. 1-35.
4) Besman, T.M. provided the authors with an updated (computer disk) version.
5) Spear, K.E. and Tsui, P.: "A Morphological Study of Silicon Carbide Prepared by Chemical Vapor Deposition", Tailoring Multiphase and Composite Ceramics, Eds. Tressler, R.E., et al., (Plenum Press, New York, 1986) pp. 371-380.
6) Chin, J., Gantzel, P.K. and Hudson, R.G.: Thin Solid Films, 1977, 40, pp. 57-72.
7) Kuo, D.H., Cheng, D.J., Shyy, W.J. and Han, M.H.: J. Electrochem. Soc., 1987, Vol. 134, No. 12, pp. 3145-3149.
8) Kuo, D.H., Cheng, D.J. and Shyy, W.J.: J. Electrochem. Soc., 1990, Vol. 137, No. 11, pp. 3688-3692.

CHEMICAL VAPOR INFILTRATION OF
HAFNIUM DIBORIDE MATRIX COMPOSITES

R. J. Shinavski
Rensselaer Polytechnic Institute
Troy, N.Y.

R. J. Diefendorf
Clemson University
Clemson, S.C.

ABSTRACT

Hafnium diboride has been proposed for ultra-high temperature (>1800°C) applications due to its highly refractive nature. HfB_2 was deposited by hydrogen reduction of the chlorides in an isothermal CVI furnace. The thermodynamics and mass transport of the reaction were examined to aid in the understanding of the process. Fine cylindrical capillaries were used to simulate the macroporosity within a fibrous preform. The microporosity was studied by infiltrating carbon fiber bundles. The bundles can be infiltrated to <15% porosity.

INTRODUCTION

The ability to operate materials at higher temperatures has benefits in terms of higher efficiency and performance. These extreme conditions require the development of new material systems capable of performing in oxidative and/or reducing atmospheres at temperatures in excess of 1800°C. Ceramic materials are likely candidates for these conditions; however their inherently low fracture toughness indicates a need for reinforcement with proper interface control to improve damage tolerance.

Given these guidelines, the field of potential materials is rather limited. One of the promising in this group is carbon fiber reinforced hafnium diboride. HfB_2 is a group IVA boride with a hexagon crystal structure. It is the highest melting boride with a melting point of 3380°C.[1] It also has a high elastic modulus of 500 GPa.[2] These properties are indications of a strongly bonded material that would retain its room temperature properties at elevated temperatures. Wiley measured only a 10% decrease in modulus at 1000°C.[2] Creep resistance should be good since hafnium diboride is only at $0.6T_m$ at 1800°C. Other properties of hafnium diboride are listed in Table I.

The oxidation resistance of hafnium diboride is relatively good in the ultra-high temperature regime.[3,4] Its oxide product is adherent and parabolic behavior is observed. Also at lower temperatures B_2O_3 provides a glassy sealant. The material has also been shown to outperform Space Shuttle RCC heat shield samples.[5] However, the recession rates that have been observed, while better than other non-oxide materials, are too high for long term use at ultra-high temperature. Thus the material is restricted to shorter lifetime applications or the oxidation resistance must be improved. A number of researchers have shown that additions of 20 v/o SiC significantly decreases the rate of oxidation to levels below HfB_2 or SiC alone.[6,7]

where M is the molecular weight, T is the absolute temperature, P is the pressure in atmospheres, σ is the collision diameter and Ω is a dimensionless function of temperature and the intermolecular potential field.

The molecular diffusivities were then obtained by extending Hsu and Bird's[10] solution of the Stefan-Maxwell equations from a three component to a four component system. The simplifying assumption that the diffusivity was constant through the boundary layer was made.

The porosity within a fibrous preform can be assumed to consist of a network of cylindrical pores. In calculating effective diffusivities, the effect of capillary diffusion was considered. Knudsen diffusion plays an important role when the mean free path of the gas is significantly larger than the diameter of the capillaries. The mean free path in the CVD/CVI experiments were on the order of 10 - 100 μm. The porosity within a fibrous preform can be considered to be of two orders of magnitude; the micron size pores within a fiber bundle and the pores between fiber bundles that are on the order of several hundred microns. Achieving uniform deposition to full density inside larger pores greatly increases the time for infiltration. The mean free path is approximately the same as the pore size, which places the diffusivity in the transition region between Knudsen and purely molecular. The effective diffusivity can be estimated by:

$$\frac{1}{D_{\textit{eff}}} \approx \frac{1}{D_M} + \frac{1}{D_K} \tag{3}$$

Figure 3 shows that Knudsen diffusion has a significant effect even at pore sizes of several hundred microns, and thus must be considered in any mass transport calculations for CVI.

Relative fluxes to and from the surface can be calculated from the product of the effective diffusivity and the concentration gradient. Figure 4 shows that although a large amount of HCl is produced by the reaction to form HfB_2, its mass transport is significantly greater than that of hafnium tetrachloride. Thus in a mass transport controlled reaction regime, diffusion of hafnium chloride should be limiting.

EXPERIMENTAL

Hafnium diboride was deposited using a 10 kw graphite resistance furnace with a hot zone 8" long and 1.75" in diameter. Pyrolytic graphite disks at the ends provided a very uniform temperature distribution along the length. Substrates used for deposition were Stackpole 2020 graphite bars and cylinders drilled with fine capillaries from 150 μm to 1030 μm in diameter to simulate the larger scale porosity in a preform. Infiltration of carbon fiber bundles were studied to provide information on the fine scale porosity.

All gases were controlled using mass flow controllers except the hafnium species, where a chlorine flow was metered into a bed of hafnium sponge (- 0.75' → ⁺20 mesh) heated to 350°C. The resultant rate of chlorination was measured by weight loss of the sponge. The experiments resulted in an average composition of $HfCl_{3.14\pm0.3}$. The chlorination was highly reproducible allowing flows up to 70 sccm to be predicted within 2.3 sccm with a 95% confidence interval. The possible reactions that could occur were studied by Troyanov et al.[11] and can be summarized as:

occurs within the capillary. The implications of this profile are that under a set of deposition parameters certain size pores can be completely filled at a much higher rate. Capillaries of a number of different sizes were examined under different deposition conditions. The results can be summarized as follows:

1. Penetration depth is greater for lower temperatures and larger diameter capillaries.
2. Deposition maxima occur only inside certain capillary diameters with a given set of deposition conditions.
3. At higher temperatures, deposition maxima occur in larger capillaries.
4. This behavior is present along the entire length of the hot zone.

Another observation was an initial decrease followed by a region of constant deposition rate along the capillary length (Figure 10). This behavior, with a properly controlled gas composition, could also result in more rapid infiltration.

In an effort to understand how a maxima could form, models of infiltration were reviewed to see if any predicted this behavior. The model developed by Middleman[12] incorporates a gas phase reaction and predicts that deposition maxima could occur inside a capillary depending on the magnitudes of the rate of the surface reaction compared to the gas phase reaction. However, this model assumes that the gas phase reaction occurs only within the capillary.

CONCLUSIONS

Hafnium diboride was deposited under a wide range of conditions by the hydrogen reduction of the chlorides. Direct chlorination of hafnium sponge metal proved to be a very reliable technique for introducing $HfCl_x$ into the furnace. CVD surface studies proved to be valuable but insufficient for identifying conditions favorable for infiltration. Studies of deposition within cylindrical pores provided insight into the infiltration process. This allowed conditions to be identified where carbon fiber bundles could be infiltrated to <15% porosity. Observation of deposition maxima and plateaus indicate that with further study it may be possible to infiltrate the macroporosity of a preform very rapidly.

Modeling of the mass transport processes indicate that at higher temperatures, the flux of the hafnium specie to the surface should be limiting. Thermodynamic calculations set an upper limit for reaction efficiency, while providing insight into the equilibrium gas composition. Current work is concentrating on modifying the gas composition to understand the deposition maxima and plateaus.

ACKNOWLEDGEMENTS

REFERENCES

1. Moffat, William G., General Electric Handbook of Binary Phase Diagrams, vol. 1, Genium Publishing, Schenectady, N.Y. 1984.

TABLE I: HfB$_2$ PROPERTIES

Melting Point:	3380°C
Elastic Modulus:	500 GPa
Poisson's Ratio:	0.11
Density:	10.6 g/cc
	11.18 g/cc (x-ray diffraction)
Knoop Hardness:	2900 kg/mm^2 with 30g load.
Crystal Structure:	Hexagonal
	a = 0.314 nm c = 0.348 nm
Thermal Expansion:	α_a = 5.21 x 10^{-6}/K (R.T.)
	α_c = 6.03 x 10^{-6}/K (R.T.)
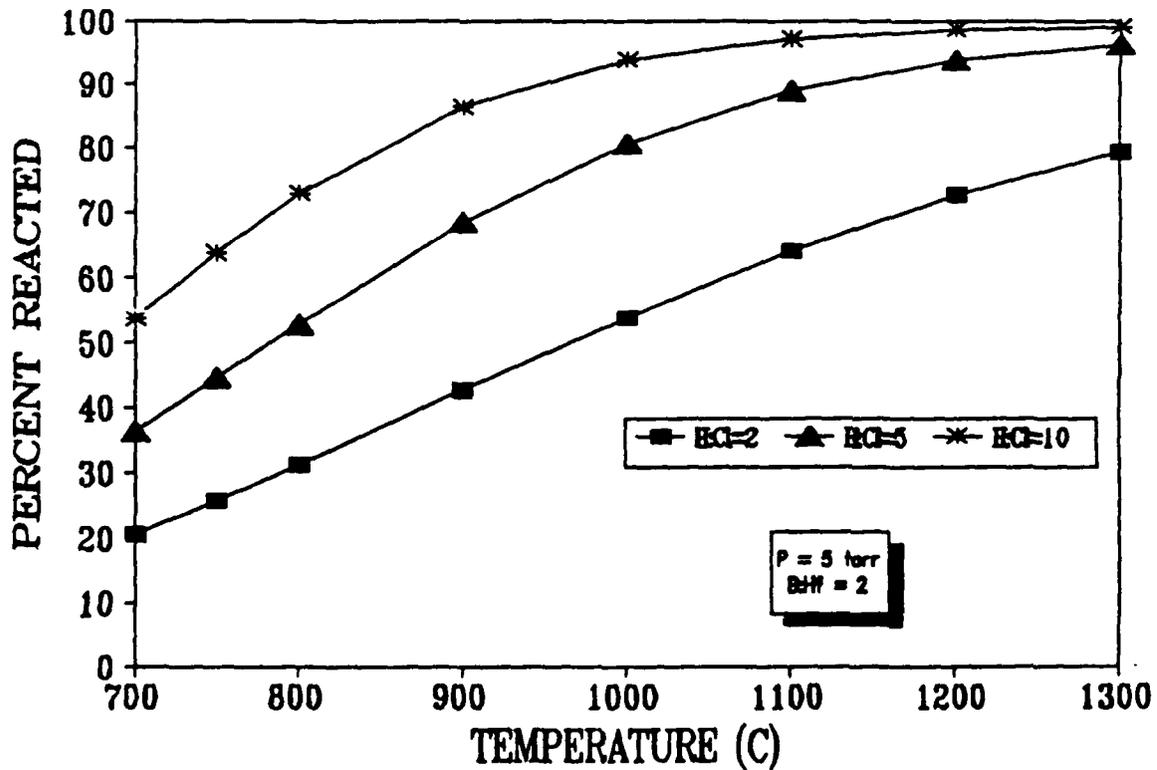
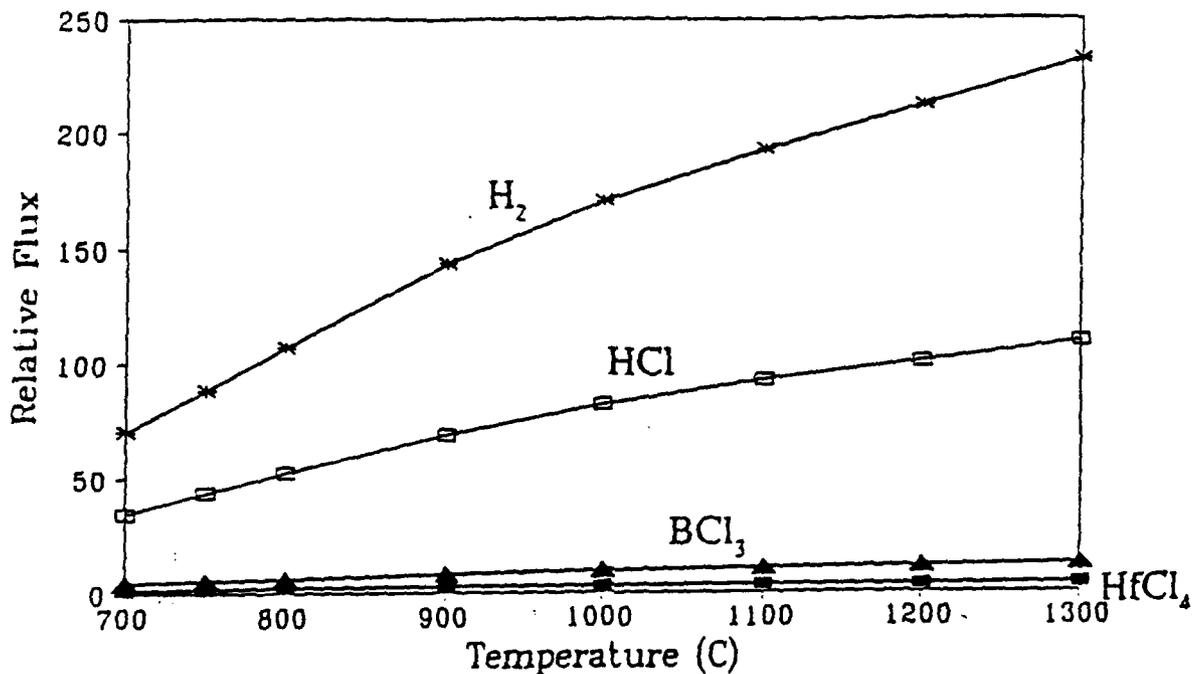FIGURE 1: THERMODYNAMIC EFFICIENCY
OF CVD REACTION

FIGURE 4: RELATIVE RATES OF MASS TRANSPORT TO AND FROM THE SURFACE
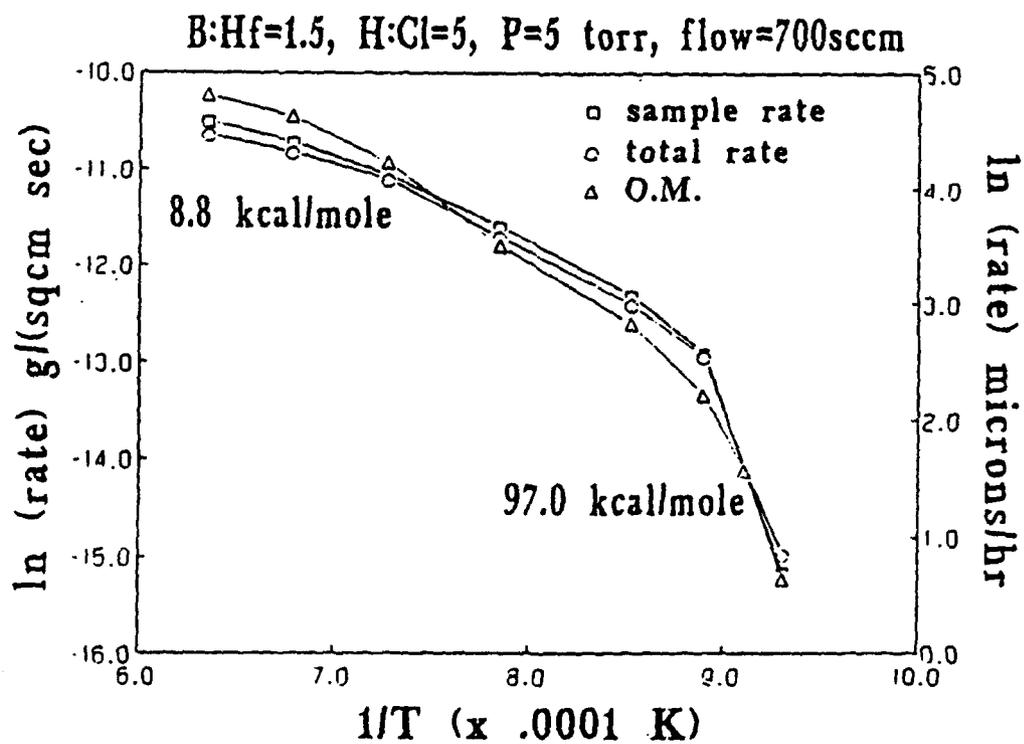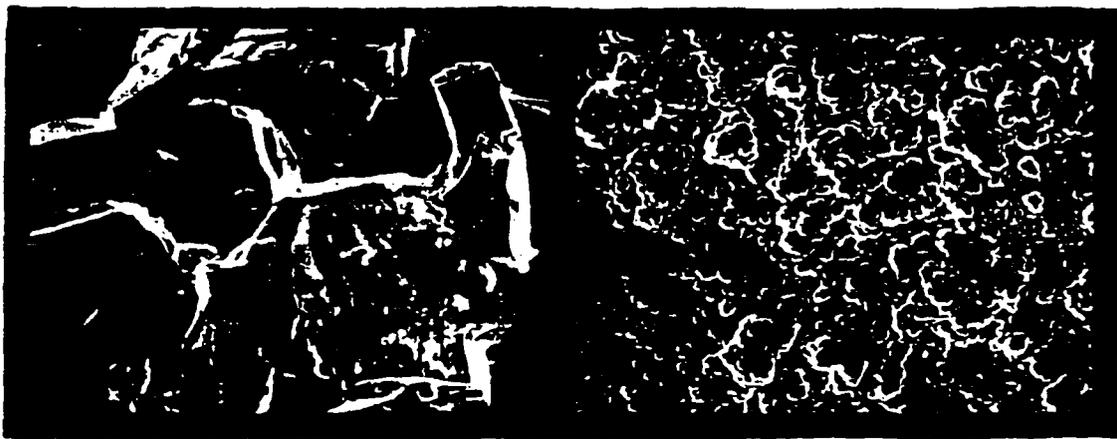

FIGURE 5: ARRHENIUS PLOT SHOWING THE APPARENT ACTIVATION ENERGY OF THE REACTION

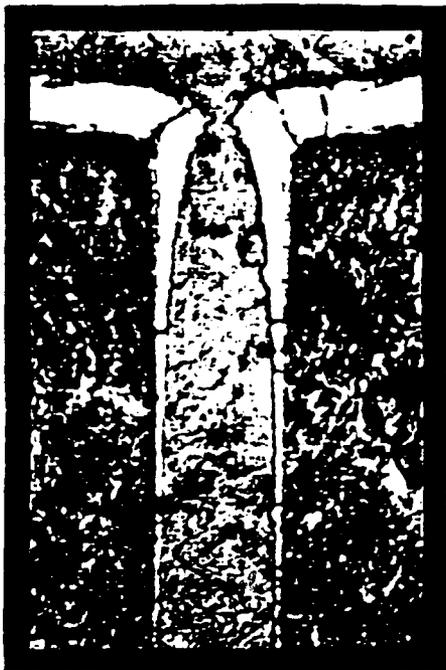a. 900°C   b. 800°C

c. 775°C   d. 725°C

X500   10µm

**FIGURE 7: SEM MICROGRAPHS
OF DEPOSIT MORPHOLOGIES**

T = 1300 C
a.

T = 1000 C
b.

FIGURE 9: LONGITUDINAL CROSS-SECTION
OF 430 μm CAPILLARIES

B:Hf=1.5, H:Cl=5, P=5 torr, flow=700sccm
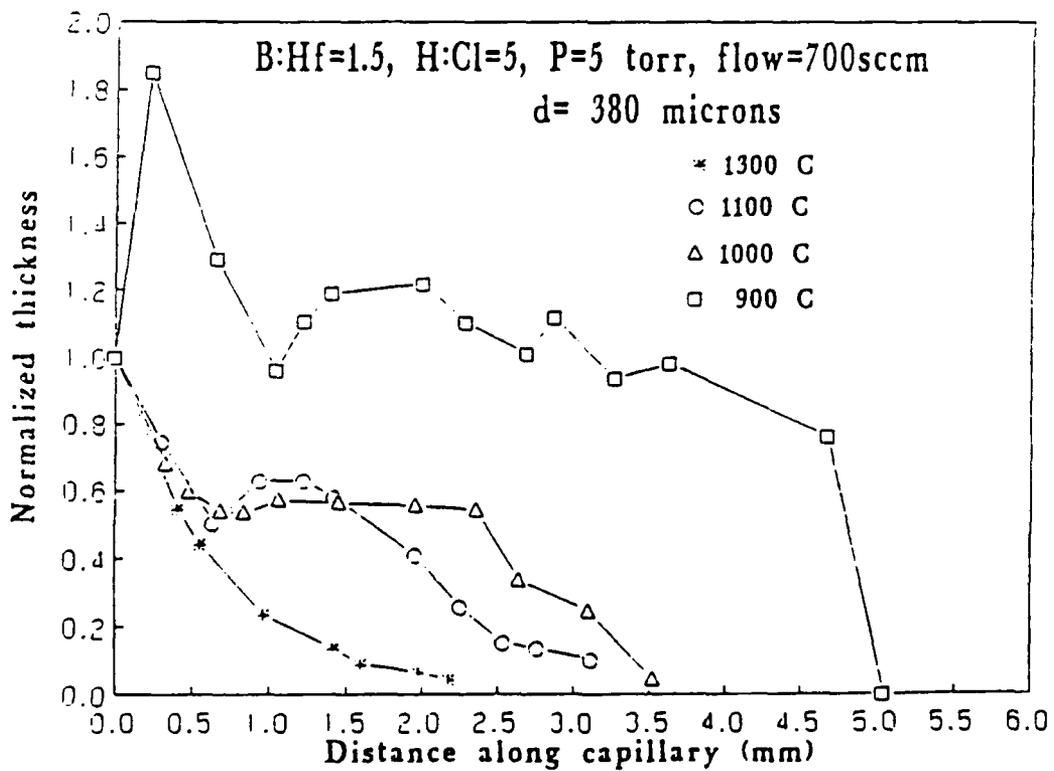d= 380 microns

* 1300 C
○ 1100 C
△ 1000 C
□ 900 C

FIGURE 10: INFILTRATION AS A FUNCTION OF
CAPILLARY DEPTH.

POLYMERIC PRECURSOR SiC MATRIX COMPOSITES*

R. P. Boisvert and R. J. Diefendorf
Materials Engineering Department
Rensselaer Polytechnic Institute
Troy, NY 12180-3590

ABSTRACT

Pyrolysis of organometallic polymers was investigated as a low temperature processing route for the fabrication of ceramic matrix composites. Two polymeric precursors, polycarbosilane (PCS) and polyvinylsilane (PVS), were used in this study. Ceramic yields as high as 85 wt % are possible when PCS is used as the precursor. Dimensional instability and microcracking encountered during pyrolysis can be overcome by the addition of suitable ceramic fillers. Preliminary mechanical testing results of continuous, SiC fiber reinforced ceramic matrix composites indicate the fiber/matrix interface is important.

INTRODUCTION

The conversion of a polymeric precursor into a ceramic artifact has been practised for many years in the carbon and graphite industry. The driving force for developing the polymeric precursor route for carbon bodies stems from the difficulties in attempting to produce such articles by others means, such as casting or sintering. As a result of similar problems associated with other ceramic materials, organometallic precursors have been developed which allow ceramic formation at lower temperatures and pressures than otherwise required. Careful consideration of the starting materials along with appropriate processing cycles is necessary to obtain desirable yields and microstructures. Factors which must be considered for a successful conversion of polymer to ceramic include: pyrolysis conditions, polymer structure and the thermal stability of the precursor.

Much of the revived interest in organometallic polymers as precursors to ceramics is due in part to the success of Yajima and coworkers in producing SiC fibers, and complex ceramic shapes from polycarbosilane.[1-5] Their processing, which is based on the work of Burkhard[6], is a two step process which produces a carbosilane which forms microcrystalline β-SiC upon pyrolysis to temperatures above 1200C. The major processing problems associated with polycarbosilane and other polymeric precursors include shrinkage, low yields and phase purity. These obstacles need to be overcome to fully exploit the benefits of polymer pyrolysis over conventional processing techniques.

EXPERIMENTAL PROCEDURE

Particulate Ceramics via Polycarbosilane

Polycarbosilane was obtained directly from Nippon Carbon. Polycarbosilane is a white solid which can be dissolved in a variety of solvents or crushed and sieved into a fine powder. Particulate reinforced ceramics were produced by adding various fillers (e.g., SiC powder [325 mesh], SiC whiskers [Tomax], and Acheson graphite [Grade 38]) with polycarbosilane before firing. Crushed PCS was dissolved in n-hexane. Then, ceramic filler was added slowly, and the whole solution was stirred to form a homogeneous mixture. Residual n-hexane was removed by stirring at room temperature, followed by air drying for 24 hrs. The resulting powder was crushed, sieved, and then compacted into the desired shape by cold pressing.

Polycarbosilane must be thermoset before pyrolysis by either oxidation or the addition of a charring agent. Oxidation was performed at 190C for a long enough period to thermoset the specimen. Times depended on sample thickness, but was as short as one hour for powders. The thermolysis cycle used a heating rate of 2C/min up to 1000C followed by a 1-hour soak, all under a flow of nitrogen gas.

Polyvinylsilane Ceramic Matrix Composites

A vinylic polysilane, developed by Schilling, et al.[7], was also investigated as a potential SiC precursor. The vinyl and SiH groups of the vinylic polysilane provides an efficient thermal crosslinking mechanism not involving oxygen. Crosslinking occurs via a combination of vinyl/SiH addition and vinyl polymerization between 100C and 270C. The vinylic polysilanes were supplied by the Union Carbide Corporation.

The molecular weight and structure of the polyvinylsilane were controlled to provide a viscous, translucent thermosetting polymer. Vacuum-bag technology was used to manufacture the laminates, which were subsequently pyrolyzed to form a ceramic matrix composite. Typical composite test specimens were composed of 6 fabric layers with dimensions of: 6.35mm wide, 3.18mm thick, and 76.2mm long; but plates as large as 300mm by 300mm were made also. Nicalon in the form of eight harness satin weave was used as the reinforcement for all composites reported in this paper, although other fibers have been used.

The composite processing flow diagram is as follows: the epoxy sizing was removed by subjecting the fibers to a temperature of 700°C under argon for 2 hrs. In some instances a carbon layer was placed on the fiber surface in order to improve fracture behavior. A vacuum-bag process was used to form the laminate and was cured in a press at 200C for 6 hours under 0.3 MPa (50 PSI) pressure. After cure, laminates were removed from the press and cut into specimens with a diamond saw. Pyrolysis was performed in a tube furnace under a nitrogen atmosphere. The typical conversion cycle was 1C/min to 800C, hold 800C for 2 hours.

Reimpregnation of pyrolyzed bars was necessary to increase the density and mechanical properties. Composite samples were submerged in a polysilane bath and placed under vacuum for 24 hours. Then, the specimens were removed and placed in an autoclave which was filled with argon at .83 MPa and heated

to 200C for 18 hrs. Composites were removed from the autoclave, pyrolyzed and analyzed to see if further densifications were required.

RESULTS AND DISCUSSION

Pyrolysis Characteristics

Polycarbosilane shrunk when heat treated to 800C at 2C/min under a nitrogen atmosphere. Ceramic yield was 63 wt %. Crosslinking of polycarbosilane, by oxidation or addition of a charring agent, increases the yield and subdues the formation of porosity (foam) during pyrolysis. The drawback of both methods is the introduction of oxygen into the precursor. At high temperatures, silica and CO form which degrade strength. Figure 1 shows TGA curves generated during the pyrolysis of PCS under various conditions. Oxidation or the addition of tri-n-butylborate not only eliminated foaming but also increased the ceramic yield up to a maximum of 85 wt %.

One of the major advantages of PVS over PCS is the ability to thermally crosslink the polymer without introducing oxygen. Polyvinylsilane crosslinks between the temperatures 100-260C, above which the precursor begins to decompose. The time required to completely cure polysilane is dependent on the temperature and the exotherm. The density of the polymer is $1.0gm/cm^3$ before curing and $.75gm/cm^3$ after curing at 200C. Figure 2 shows the TGA curve for PVS heat treated to 1000C at 2C/min under nitrogen gas. The yield for polysilane is 63, 62, and 61 wt % when heat treated to 800, 1000 and 1200C, respectively. The density of the final ceramic when heat treated to 1000C is $2.05gm/cm^3$. The low density of the final ceramic is attributed to excess carbon along with entrapped fine porosity.

Particulate Composite Properties

Due to low yields and large differences in density between initial polymer and final ceramic shrinkage must occur during pyrolysis. Volume shrinkage of 12.7mm diameter disc of stabilized PCS was measured at 58%. This shrinkage

leads to microcracks especially if any constraints, such as fibers, are present. The addition of ceramic fillers to PCS before pyrolysis was found to drastically reduce shrinkage, Fig. 3. No shrinkage is observed when certain fillers are added in correct proportions.

The modulus and strength of polycarbosilane particulate composites were measured by three point bend testing. Composite test specimens were produced by mixing an appropriate filler with the PCS, pressing into test bar shape, oxidizing in an autoclave for 24 hrs at 175C and 0.3 MPa (50 PSI) air and heat treating to 1000C at 2C/min under an nitrogen atmosphere, Tables I-III. As opposed to continuous reinforcement, where higher fiber volume fraction increases performance, the strength and modulus were found to decline with increasing filler content. Whisker reinforced composites were found to have the best performance, and the lowest density. Stabilized PCS with no filler additions had a flexural strength of 96.5 MPa. All samples tested failed in a brittle manner.

Continuous Reinforced Composite Properties

Ceramic composites were prepared using polyvinylsilane as the matrix precursor and Nicalon SiC fabric as the reinforcement. SiC whiskers (15 wt %) were added to the polysilane to reduce shrinkage and control micro-cracking. Figure 4 shows that substantial porosity still exists within the composite even after 5 impregnation cycles. A large portion of the porosity results from matrix shrinkage. Poor fabric packing and resin flow also generates porosity during lamination.

Ceramic composites were tested mechanically utilizing a three point bend apparatus. Table IV lists the results for composites with no carbon coating on the fiber surface. Flexural strengths increased with each impregnation. Samples tested after the initial pyrolysis cycle failed in a shear mode by delamination between the plies. Failure mode changed to

a tensile failure after two impregnations. Brittle failure occurred for specimens with two or more impregnations. Poor mechanical performance was attributed to good bonding between fiber and matrix. All composites tested at the failure strain of the matrix.

To determine the effect of a weak fiber/matrix interface, composites were produced utilizing Nicalon SiC fibers which were carbon coated using various cuts and concentrations of Ashland 240 pitch in trichlorobenzene, Tables V, VI, & Fig. 5. Altering the fiber/matrix interface significantly improved the mechanical performance of these composite systems. Failures were typically non-catastrophic with large amounts of fiber pull-out evident on the fracture surfaces. Composites composed of fibers coated using the toluene insoluble fraction of A240 had the best performance.

CONCLUSIONS

Polymeric precursors allow the fabrication of various ceramic materials at relatively low temperatures and pressures. Shrinkage, low yields, purity and microcracking are presently limiting their successful application in the fabrication of ceramic matrix composites. However, large panels or complex shapes can be formed via conventional compositing techniques which can be pyrolyzed into a ceramic composite. Mechanical performance of these composites is good when the fiber/matrix interface strength is properly controlled.

REFERENCES

1. Yajima, S., Ceramic Bulletin, 62[8], (1983), 893.
2. Yajima, S. and Nakamura, Y., Ceramic Bulletin, 61[5], (1982), 572.
3. Hasegawa, Y. and Okamura, K., J. Matl. Sci., 4, (1985), 356.
4. Yajima, S., Omori, M., Hayashi, J., Okamura, K., Matsuzawa, T., and Liaw, C., Chem. Lett., (1976), 551.
5. Yajima, S., Hasegawa, Y., Hayashi, J. and Imura, M., J. Matl. Sci., 13, (1978), 2569.
6. Burkhard, C. A., J. Am. Chem. Soc., 71, (1949), 963.
7. Schilling, C. L. and Williams, T. C., Polym. Prepr. (Am. Chem. Soc., Div. Polym. Chem.), 25[1], (1984), 1.

TABLE I

THE EFFECT OF SiC WHISKER ADDITIONS ON THE PROPERTIES OF PCS MATRIX PRECURSOR COMPOSITES

| | Wt % SiC Whisker | | |
	75	65	55
% Volume Change	17.7	2.15	-12.3
Density (gm/cm^3)	1.11	1.27	1.48
Modulus (GPa)	1.48	1.90	3.79
Flexural Strength (MPa)	17.9	24.8	42.4

TABLE II

THE EFFECT OF SiC POWDER ADDITIONS ON THE PROPERTIES OF PCS MATRIX PRECURSOR COMPOSITES

| | Wt % SiC Powder | | |
	75	65	55
% Volume Change	1.50	-4.62	- 8.69
Density (gm/cm^3)	1.58	1.62	1.60
Modulus (GPa)	0.97	1.12	1.21
Flexural Strength (MPa)	5.2	6.2	7.6

TABLE III

THE EFFECT OF GRAPHITE POWDER ADDITIONS ON THE PROPERTIES OF PCS MATRIX PRECURSOR COMPOSITES

| | Wt % Graphite | | |
	75	65	55
% Volume Change	6.39	-7.20	-17.4
Density (gm/cm^3)	1.34	1.49	1.59
Modulus (GPa)	0.56	0.88	1.05
Flexural Strength (MPa)	3.8	9.5	13.4

TABLE IV

THE PROPERTIES OF POLYVINYLSILANE/NICALON COMPOSITES WITH 15 Wt % SiC WHISKERS
(Eight Harness Weave - No Fiber Coating)

	Preform	Impregnation #					
		0	1	2	3	4	5
Density (gm/cm^3)	1.59	1.51	1.72	1.86	1.95	2.00	2.04
Modulus (GPa)	*	20.2	31.1	38.7	53.0	58.7	57.4
Flexural Strength (MPa)	*	42.6	52.3	56.7	61.2	63.2	59.7

TABLE V

THE PROPERTIES OF POLYVINYLSILANE/NICALON COMPOSITES WITH 15 Wt % SiC WHISKERS
(Eight Harness Weave - Fiber Coated Using Ashland 240 Pitch in Trichlorobenzene [.01gm/ml])

	Preform	Impregnation #				
		0	1	2	3	4
Density (gm/cm^3)	1.64	1.55	1.71	1.86	1.95	2.00
Modulus (GPa)	*	*	5.8	11.4	29.0	31.8
Flexural Strength (MPa)	*	13.7	21.6	73.1	91.7	112.4

TABLE VI

THE PROPERTIES OF POLYVINYLSILANE/NICALON COMPOSITES WITH 15 Wt % SiC WHISKERS
(Eight Harness Weave - Fiber Coated Using the Toluene Insolubles of Ashland 240 Pitch in Trichlorobenzene [.0075gm/ml])

	Preform	Impregnation #					
		0	1	2	3	4	5
Density (gm/cm^3)	1.54	1.40	1.60	1.73	1.81	1.89	1.92
Modulus (GPa)	*	6.0	21.2	33.9	36.1	39.0	45.8
Flexural Strength (MPa)	*	19.4	76.5	128.2	128.2	157.2	126.2

*No data available.

LIST OF FIGURE CAPTIONS
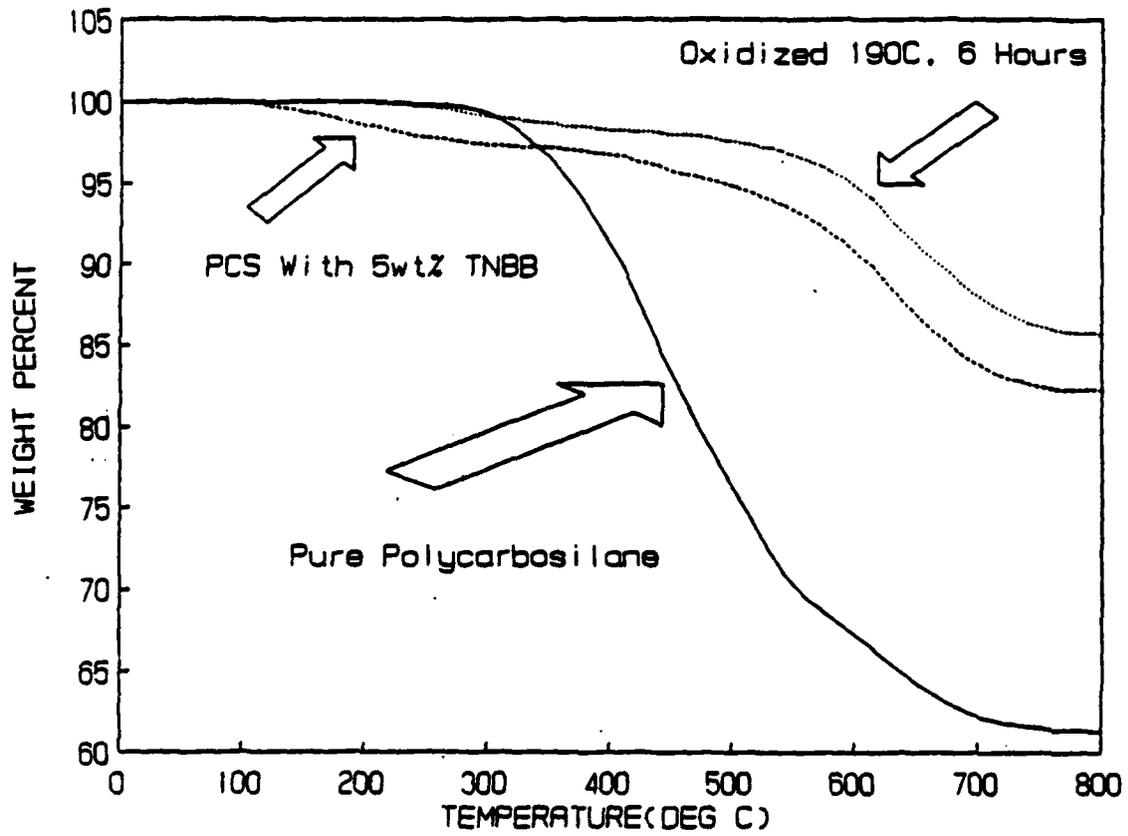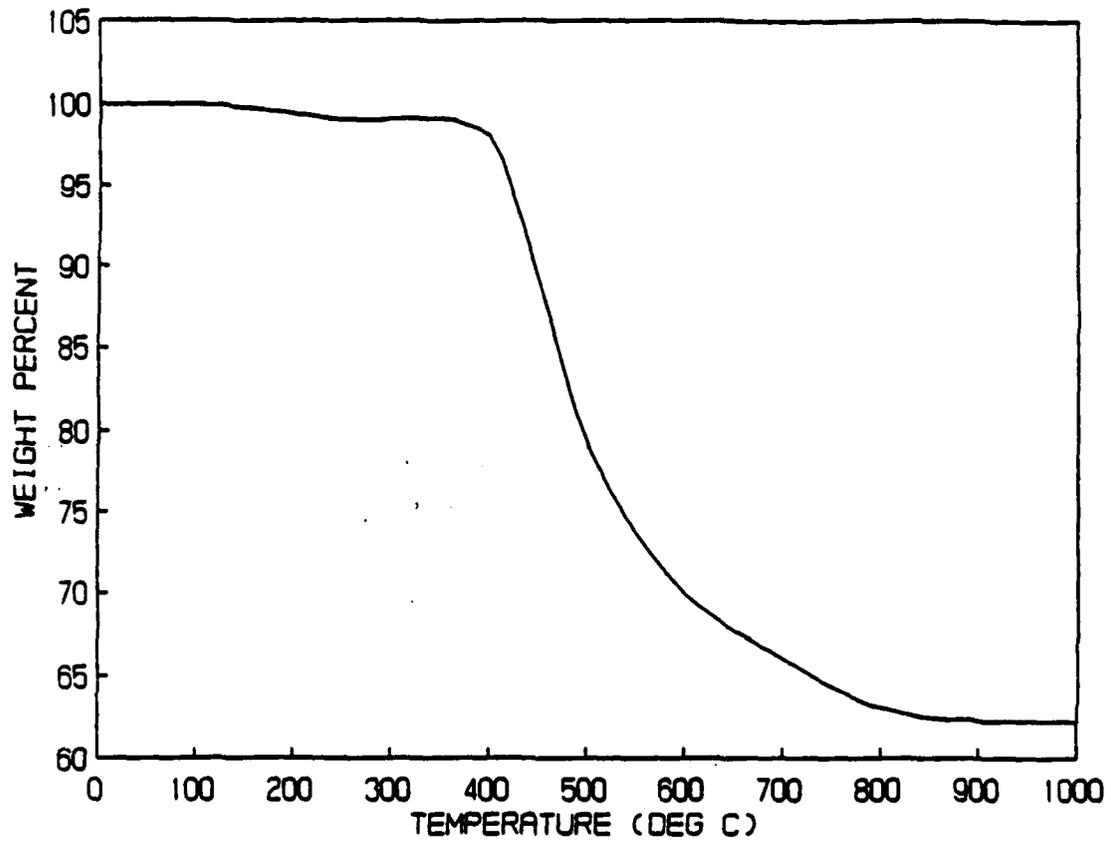
FIGURE 1: TGA Results Comparing Various Stabilization Techniques of Polycarbosilane.

FIGURE 2: TGA Results for the Pyrolysis of Polyvinylsilane.

FIGURE 3: Shrinkage Results for Polycarbosilane Combined with Various Ceramic Fillers.

FIGURE 4: Porosity Level Versus Number of Densification Cycles for a Typical Nicalon/Polyvinylsilane Composite.

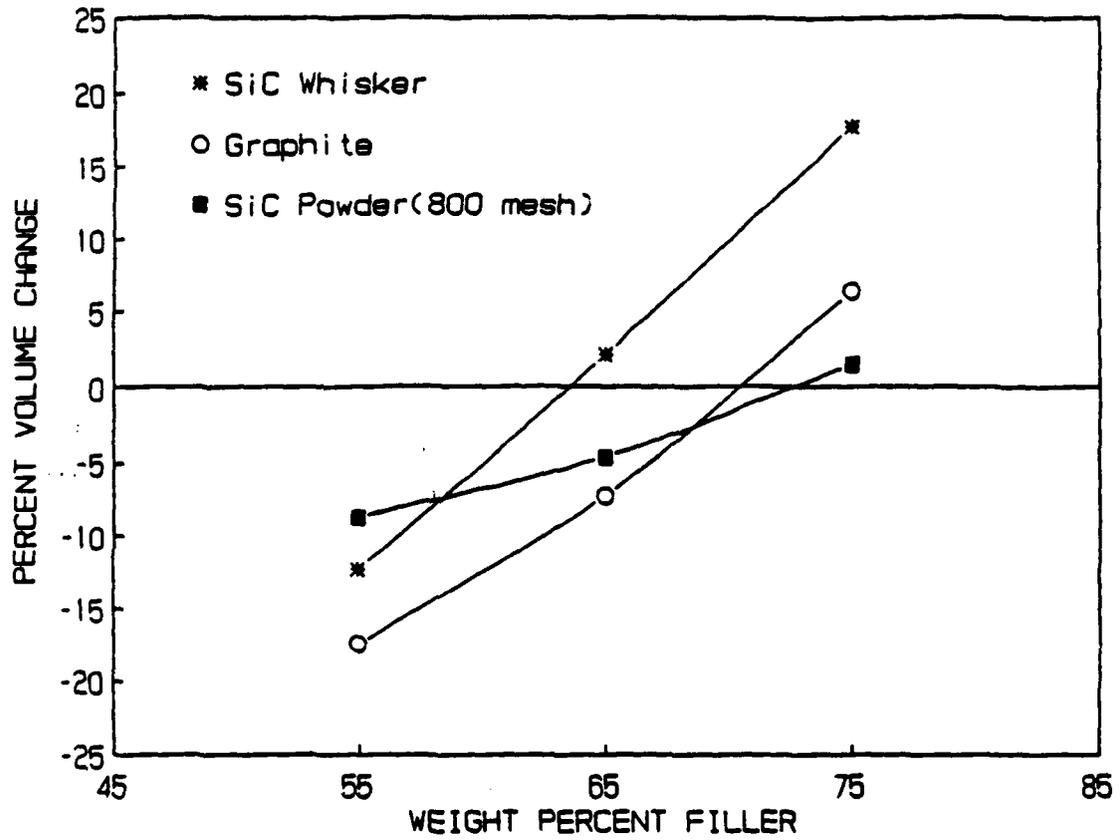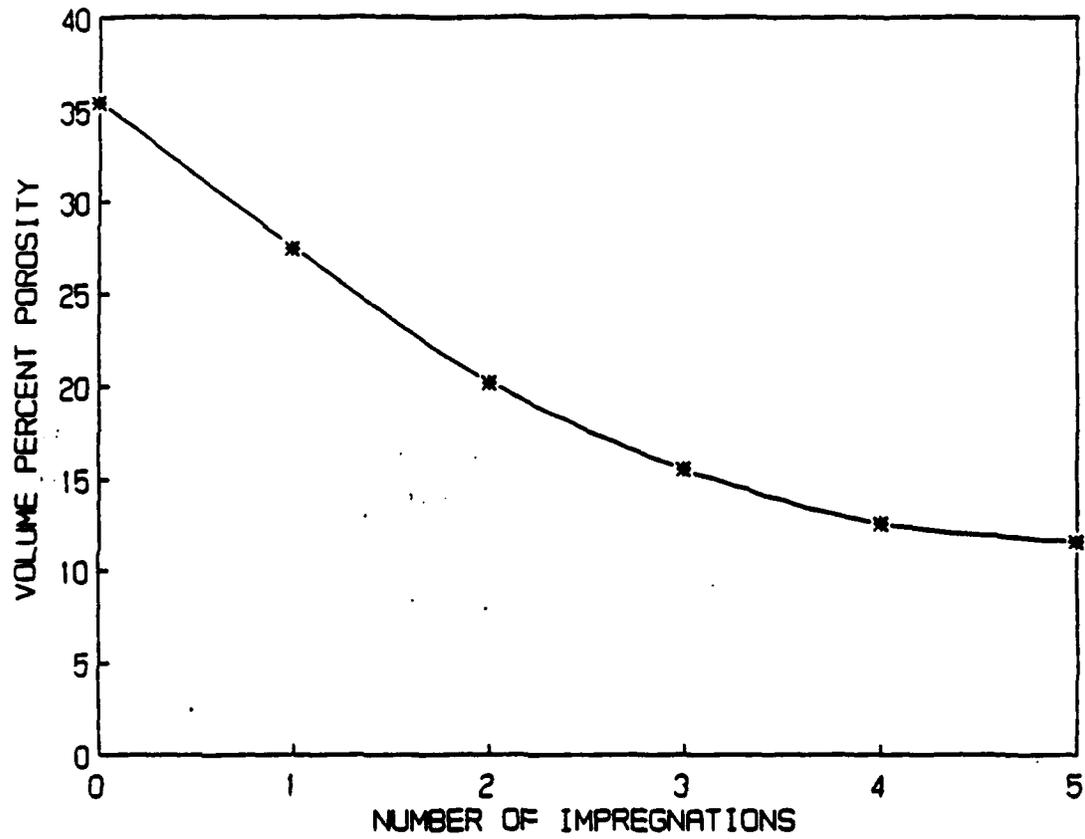FIGURE 5: Mechanical Strength of Nicalon/Polyvinylsilane Composites.

FIGURE 1: TGA Results Comparing Various Stabilization Techniques of Polycarbosilane.
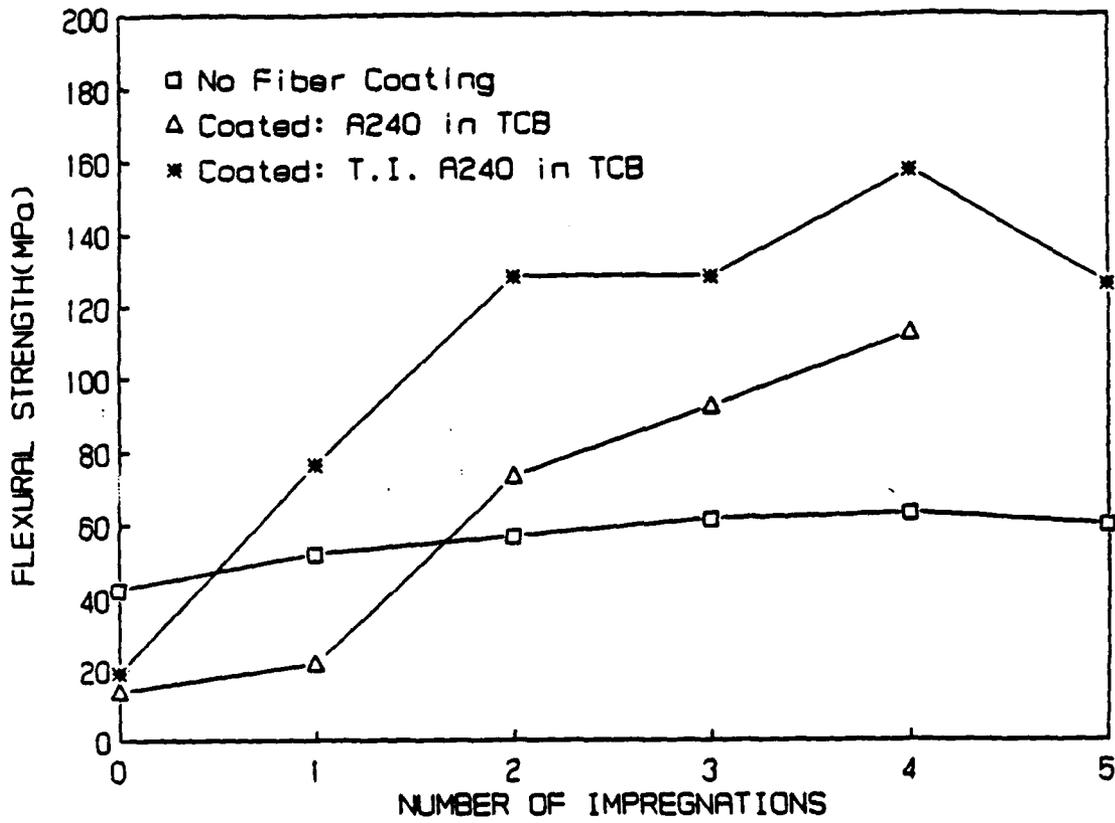
FIGURE 2: TGA Results for the Pyrolysis of Polyvinylsilane.

FIGURE 3: Shrinkage Results for Polycarbosilane Combined with Various Ceramic Fillers.

FIGURE 4: Porosity Level Versus Number of Densification Cycles for a Typical Nicalon/Polyvinylsilane Composite.

FIGURE 5: Mechanical Strength of Nicalon/Polyvinylsilane Composites.

Continuous Carbon Fiber Reinforced Carbon Matrix Composites

Russell J. Diefendorf, Rensselaer Polytechnic Institute

CARBON FIBER REINFORCED CARBON MATRIX composites have many of the desirable high-temperature properties of conventional carbons and graphites, including high strength, high modulus, and low creep. In addition, the high thermal conductivity and low coefficient of thermal expansion, coupled with high strength, produce a material with low sensitivity to thermal shock. Also characteristic of carbon-carbon composites are a high fracture toughness and a pseudoplasticity, the latter of which bears a resemblance to fiber-reinforced polymers. These attributes make carbon-carbon composites uniquely useful at temperatures as high as 2800 °C (5070 °F). The major problems with carbon-carbon composites have been high-temperature oxidation and off-fiber-axis properties.

Unidirectional carbon-carbon composites can approach the same strengths and moduli as those achieved with resin matrix composites. Moreover, because their properties are maintained to 2000 °C (3650 °F), they represent the premier material for inert atmosphere or short-time high-temperature applications.

Carbon-Carbon Processes

Carbon-carbon composites were developed to withstand the harsh but different conditions of reentry, rocket motors, and aircraft brakes. Early work on fiber-reinforced polymers used in ablative heat shields indicated that the lowest ablation rate was achieved with polymers that gave high char yields. Still lower ablation rates were achieved by precharring the matrix polymer to produce what was referred to as "burned toast." At the same time, carbon-carbon composites were produced, inadvertently, in the carbon felt insulation in pyrolytic graphite furnaces. Two processes, liquid impregnation and gaseous infiltration, have been developed to produce the present high-performance carbon-carbon composites.

Liquid Impregnation. Carbon fibers can be laid-up uniaxially, in either two-dimensional fabrics or in three-dimensional woven forms before impregnation with a matrix material (Refer to the article "Multidirectionally Rein-

forced Carbon/Graphite Matrix Composites" in this Section of the Volume for detailed information.) Prepregs with phenolic or other high-char-yield resins are used to fabricate the unidirectional laminates. Preliminary processing is much like that for other carbon fiber reinforced resin matrix composites. The laminate is laid up, vacuum bagged, autoclave or press cured, and postcured. Then, the matrix in the composite is carbonized carefully and, often, heat treated to a higher temperature. The matrix material loses mass and densifies during this process. Bulk shrinkage is constrained by the fibers, and extensive matrix microcracking and void formation occur within the composite. The function of subsequent processing is to convert this composite, consisting of fibers loosely coupled by matrix carbon binder bridges, into a strong matrix.

Carbon precursors used in later processing should have low viscosity as well as good wetting to allow thorough impregnation (Fig. 1). Carbon fiber prepregs are fabricated into a desired shape, or alternatively, dry fiber is laid up into a preform and then impregnated with a liquid resin or pitch. The resin is thermoset and then slowly carbonized. During carbonization, the resin microcracks extensively because of weight loss and densification, although resins with low weight loss are used. To achieve a higher density and stronger matrix, the carbon-

carbon composite is recycled using resin or pitch impregnation and additional slow carbonization cycles. Graphitization may be included also, to encourage porosity for impregnation and to provide structural stability and better thermal shock resistance.

Ideally, the precursor should be thermosetting, to prevent liquid exudation upon subsequent heating, and it also should have a high carbon yield. Thermosetting phenolic, furfural, or acetylenic resins provide simple processing, but generally give lower density carbon matrices. Thermoplastic impregnants, such as coal tar or petroleum pitch, also can be used. They must be carbonized very slowly and usually under 10 MPa (100 bar) pressure, to prevent gaseous products from exuding the impregnant from the body. However, the density of carbonized pitch is usually higher. Multiple pitch or resin impregnations under pressure, followed by carbonization and high-temperature heat treatments, often with five or more cycles, is the most common sequence used to produce carbon-carbon composites.

The **chemical vapor infiltration (CVI)** (Ref 1) of carbon uses gaseous hydrocarbons such as methane, propane/propylene, and benzene to deposit a carbon matrix internally in a carbon fiber preform. The process can be performed using three different methods. In the most commonly used technique (Fig. 2a) natu-
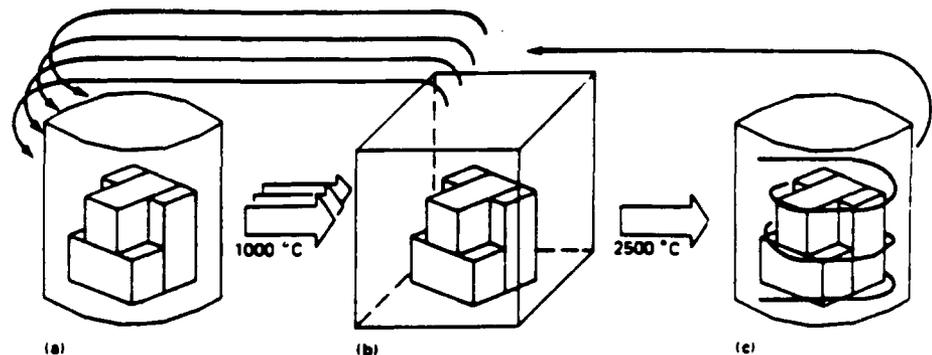

Fig. 1 Composite fabrication of preforms. (a) Impregnation. (b) Carbonization. (c) Graphitization

ral gas or other carbonaceous gases are flowed past and through a carbon fiber preform located in a low-pressure isothermal furnace. Uniform deposition throughout the preform can be achieved by operating at a temperature sufficiently low to permit rapid gaseous diffusion, compared to deposition of carbon. However, the deposition time is usually very long. Mass transfer through the fiber preform can be improved by inducing a pressure gradient through it (Fig. 2b). The deposition rate can be much higher. Enhanced deposition rates can be achieved also by using a temperature gradient deposition process (Fig 2c)

A major problem with CVI is to achieve the uniform deposition of the carbon matrix throughout a thick preform. Mass transfer from the bulk gas must be sufficiently high in the fiber preform to keep a relatively constant concentration of carbon-containing molecules throughout. Hence, the rate at which carbon is deposited must be slow compared to the mass transfer of carbon into and throughout the preform. Mass transfer of carbon-containing molecules into the preform is usually by diffusion, which slowly increases with temperature. The deposition of carbon is complex, but the overall process has a high temperature coefficient. Hence, the relative rates of the two processes can be varied by adjusting the temperature. A temperature of 1000 to 1100 °C (1830 to 2010 °F) is commonly used, along with a pressure of 500 to 3000 Pa (5 to 30 mbar) to achieve a relatively uniform deposition of carbon throughout a part 10 mm (0.40 in.) thick. More rapid mass transfer can be achieved by placing a pressure drop across the fiber preform (Fig. 2b). However, the deposition rate decreases as the pressure decreases, which produces nonuniform deposition through the preform. A pressure gradient process can be used at the end of a conventional cycle when mass transfer through tiny pores is extremely slow. An alternative is to use a temperature gradient such that carbon is deposited at a moving boundary that sweeps through the thickness (Fig. 2c). The deposition time can be significantly decreased because mass transfer of the deposition gases is mostly through parts of the preform that have not yet been deposited upon. Unfortunately, the technique produces a

variation in microstructure because deposition occurs at different temperatures. A problem with all present CVI processes is closed pore formation caused by the sealing off of bottleneck pores, and, more insidiously, delaminated regions. However, high-temperature heat treatment may be employed to induce microcracks in the matrix to be filled in the subsequent CVI process. Using liquid impregnation to produce relatively uniform open pores, followed by CVI, is another attractive alternative.

Unidirectional Properties

The properties of a carbon-carbon composite depends on the fiber and matrix constituent properties and the coupling between them.

The mechanical behavior of carbon-carbon composites in tensile fracture behavior differs from that of resin matrix composites in two major ways. First, the polymers used in many current applications have much higher strains to failure than do the fiber reinforcement. In carbon-carbon systems, the strain-to-failure of the matrix is usually lower than that of the fibers and, indeed, is frequently microcracked from processing stresses. Hence, instead of the fibers initiating failure, as in a polymeric com-

posite, the carbon matrices fail first. The second major difference is that the moduli of fiber and matrix may be similar. Hence, the load will be shared more evenly between matrix and fiber than for the polymeric system

Even though these two differences exist between polymeric and carbon matrix systems, the general approach to increasing the strength and fracture toughness is the same. Namely, when fibers or matrix in a composite begin to fail in a statistical sequence, it is advantageous to prevent these local failures from propagating through the rest of the part and causing catastrophic failure

Fracture Behavior. Generally, the coupling between fibers and matrix that arises from both chemical and mechanical bonding is instrumental in controlling crack propagation and the extent of damage. The fiber type, matrix precursor, and subsequent type of processing determine the strength of the interfacial coupling. Two extreme cases, that of 100% and 0% coupling, describe the limits experimentally observed in carbon-carbon composites

For a strong interfacial bond, the crack which forms in the lower strain-to-failure matrix, propagates across the fiber-matrix interface to cause immediate fiber failure (Fig 3a)
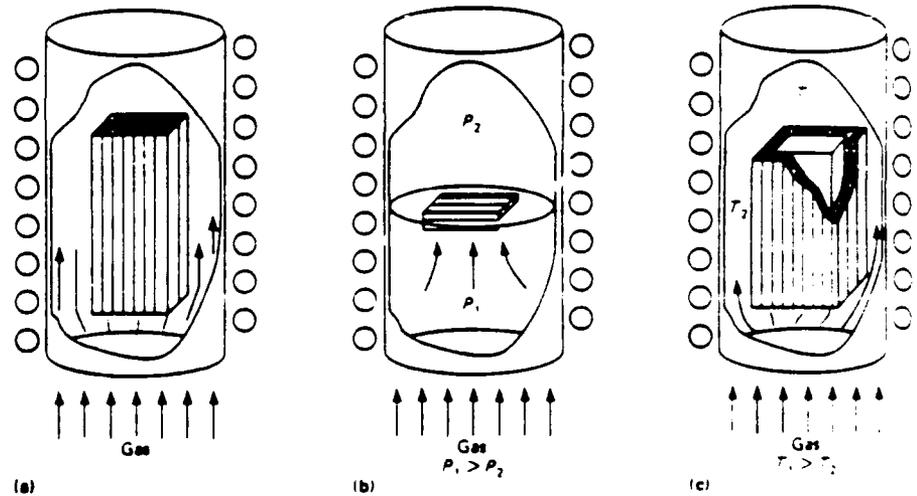

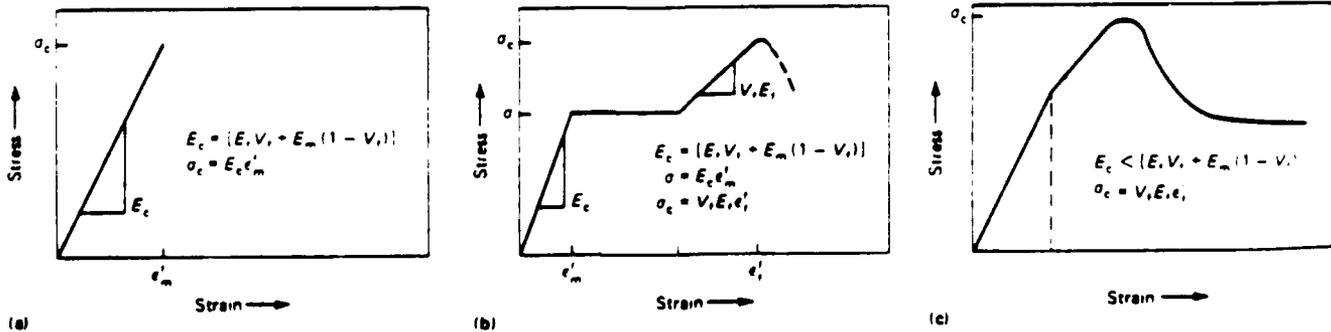**Fig. 2** Chemical vapor infiltration process

Fig. 3 Stress-strain curves. (a) 100% fiber-matrix coupling. (b) 0° fiber-matrix coupling. (c) Precracked matrix

Table 1 Mechanical properties of unidirectional carbon-carbon composites (~55 vol%)

	Parallel		Perpendicular	
	HTU	HMS	HTU	HMS
Modulus, GPa (10⁶ psi)				
Tension	125 (20)	220 (30)		
Compression	10 (1.5)	250 (35)	7.5 (1.1)	
Strength, MPa (ksi)				
Tension	600 (90)	575 (85)	4 (0.60)	5 (0.75)
Compression	285 (40)	380 (55)	25 (4)	50 (7.5)
Bend	1250-1600 (180-230)	825-1000 (120-145)	20 (3)	30 (4.5)
Shear	20 (3)	28 (4)		
Fracture toughness, kJ m⁻² (ft lbf/ft²)	70 (4800)	20 (1370)	0.4 (30)	0.8 (55)

HTU, High tensile untreated surface. HMS, high modulus surface-treated

Table 2 Effect of matrix precursor on composite modulus

	Heat treatment	
	at 1000 °C (1830 °F)	at 2600 °C (4710 °F)
Phenolic resin	110%	140%
Pitch	130%	210%

Note: Fiber stiffening factor assuming all stiffness comes from HM fiber

Therefore, failure is brittle and the strength of the composite is governed by the strain-to-failure of the matrix. Higher-strength composites can be obtained by using higher-modulus fibers, but the strain-to-failure will still remain low (Ref 2). Fibers that are surface treated to promote adhesion and matrices with high carbonization shrinkages both promote this strong coupling between matrix and fiber, in the first case by chemical bonding, and in the second case by compressive stresses normal to the interface (Ref 3, 4).

When poor coupling exists between fiber and matrix, the composite can show a substantial increase in strength and fracture toughness when loaded parallel to the fiber axis. In this case, as the composite is loaded up to the failure strain of the matrix, the matrix cracks cause a debonding between matrix and fiber as the crack approaches the interface. The fiber bridges the crack and maintains load-bearing capability (Fig. 3b). Matrix cracks are often observed to run across the full width of the specimen normal to the stress. Numerous matrix cracks can form, and the effective stiffness of the composite decreases. The exact nature of the stress-strain curve depends on the fiber and matrix moduli and the flaw distributions. Increasing load initiates fiber fracture and failure. If the test is displacement controlled, the load increases to a maximum at which significant fiber fracture occurs, and then decreases slowly as fibers pull out of the matrix (dotted line in Fig. 3b). In many cases with carbon-carbon composites, the matrix is heavily microcracked from processing shrinkages, or from cool-down from a high-temperature heat treatment. Then, the large discontinuity that occurs when the matrix fractures is largely absent (Fig. 3c).

The effect of fiber-matrix coupling on mechanical properties has been documented by studying polyacrylonitrile (PAN)-based carbon fibers of different moduli with and without surface treatments to promote fiber-matrix coupling (Ref 4, 5). The coupling for resin matrix composites is observed to decrease with increasing modulus for both untreated and surface-treated fibers, although the magnitude is higher for surface-treated fibers. C.R. Thomas and E.J. Walker (Ref 5) found that both AU (untreated) and AS (surface-treated) lower modulus (230 GPa, or 35 × 10⁶ psi) fibers in

carbon-carbon composites failed at the failure strain (0.1%) of the matrix, and only low-strength composites were ever produced. When higher-modulus high-tensile (HT) (265 GPa, or 40 × 10⁶ psi) fibers were evaluated, surface-treated fibers still fractured at the matrix failure strain. However, high-tensile untreated surface (HTU) fibers produced much higher strengths and fracture toughness (Table 1). For still higher moduli (400 GPa, or 60 × 10⁶ psi) surface-treated (HMS) fibers, the mechanical properties of the composite depended on the heat treatment temperature. Heat treatment at 1000 °C (1830 °F) produced carbon-carbon composites that failed at 250 MPa (35 ksi) or the failure strain of the matrix (0.1 to 0.2%), and had a fracture toughness of 1 kJ/m² (70 ft · lbf/ft²). Heat treatment to a temperature of 2600 °C (6510 °F) caused microcracking on cool-down and decoupling within the carbon-carbon composite. The strength more than doubled and fracture toughness increased by a factor of 20. High-modulus untreated (HMU) surface (400 GPa, or 60 × 10⁶ psi) composites produced good toughness and strengths even after carbonization (1000 °C or 1830 °F).

The high-temperature properties of HM composites have been measured from room temperature to 2000 °C (3630 °F). The modulus decreases from 180 GPa (26 × 10⁶ psi) at room temperature to 175 GPa (25 × 10⁶ psi) at 2000 °C (3630 °F). Tensile strength is also surprisingly constant, varying from 0.95 GPa (0.14 × 10⁶ psi) at room temperature to 1.2 GPa (0.17 × 10⁶ psi) at 1000 °C (1830 °F) and 1.1 GPa (0.16 × 10⁶ psi) at 2000 °C (3630 °F). However, strain-to-failure increases from 0.48% at room temperature to 0.65% at 1000 °C (1830 °F) and 0.73% at 2000 °C (3630 °F) (Ref 5).

Weak fiber-matrix interfaces allow the fiber strength to dominate the composite strength parallel to the fiber axis and to have a high fracture toughness value because of the fiber pullout from the matrix. However, off-axis strengths such as shear and transverse tension are severely degraded (Ref 6). In many applications, it is these off-axis stresses that limit the design.

Moduli. The type of matrix precursor affects the moduli of the composites as well (Table 2) (Ref 4). Resin precursor binders and impreg-

nants usually yield low-modulus isotropic carbons, and at low volume fractures do not contribute substantially to composite moduli. By comparison, pitch precursors generally transform to a mesophase (liquid-crystalline) state, which most frequently orders parallel to the fiber axis. A highly oriented graphitic matrix is produced upon graphitization and provides a high-modulus contribution parallel to the fiber axis.

Fatigue. The fatigue of carbon-carbon composites might be expected to be a problem because of the extensive matrix microcracking that is present before even the first loading. Matrix cracks do increase during cycling, and decreasing modulus and dusting of the matrix from the composite have been observed. Transverse tensile strength and shear strength are likely to be degraded during fatigue tests loaded parallel to the fiber axis. However, fatigue has been found to be proportionately as good as with resin matrix composites (Ref 7).

Thermal Expansion. The thermal expansion of unidirectional carbon-carbon composites tends to be dominated by the fibers parallel to the fiber axis. Thermal expansion coefficients vary from being slightly negative at room temperature for high-modulus fibers to being slightly positive for low-modulus fibers. The coefficients become positive at higher temperatures but in all cases remain low. The transverse thermal expansion coefficients depend on matrix, fiber, and voids. The anisotropic nature of the graphite crystal thermal expansion causes microcracking between basal planes upon cool-down because of mechanical constraints. The planar voids, which form upon cool-down, are expanded upon reheating. A lower thermal expansion coefficient than might be expected can result. However, the transverse thermal expansion is several times the axial expansion. This difference in the thermal expansion coefficient will generate sufficiently high residual stresses during cool-down from processing so that laminates, such as 0°/90°/0°, cannot be manufactured with good integrity. A partial solution has been the use of fabrics, which minimize this problem.

Oxidation of carbon-carbon composites can begin at temperatures as low as 400 °C (750 °F). The rate of oxidation depends on the perfection of the carbon structure and its purity. Highly disordered carbons, such as carbonized resins given low-temperature heat treatments, will oxidize at appreciable rates at 400 °C (750 °F). Highly graphitic structures,

such as pitch-based carbon fibers, can be heated as high as 650 °C (1200 °F) before extensive oxidation occurs. At these low temperatures, carbons are very susceptible to catalytic oxidation by alkali metals, such as sodium, and multivalent metals, such as iron and vanadium, at extremely low concentrations. Therefore, the oxidation rate often is determined by the initial purity of the carbon-carbon composite or by in service contamination. Borates and particularly phosphates have been found to inhibit oxidation up to about 600 °C (1110 °F) (Ref 8). Oxidation at higher temperatures becomes more rapid and by 1300 °C (2370 °F) is completely limited by mass transport of oxygen to the surface and carbon monoxide and dioxide away from it. Oxidation protection at high temperatures is discussed in the article "Oxidation-Resistant Carbon-Carbon Composites" in this Section.

Carbon-carbon composites can be attacked by strongly oxidizing acids, but are inert to most other acids and to all alkalies, salts, and organic solvents.

REFERENCES

1. W.V. Kotlensky, Deposition of Pyrolytic Carbons in Porous Solids, in *Chemistry and Physics of Carbon*, Vol 9, P.L. Walker, Jr. and P.A. Thrower, Ed, Marcel Dekker, 1973, p 173

2. J. Aveston, G. Cooper, and A. Kelly, Single and Multiple Fracture, in *Properties of Fiber Composites*, Paper 2, National Physical Laboratory, Nov 1971

3. E. Fitzer, The Future of Carbon/Carbon Composites, in *Proceedings of the Third Annual Materials Technology Conference, Solid Carbon Materials: Production and Properties*, M.H. Genisio Ed., Southern Illinois University, 1986, p 4

4. E. Fitzer and W. Hüttner, Structure and Strength of Carbon/Carbon Composites, *J. Phys. D, Appl. Phys.*, Vol 14, 1981, p 347

5. C.R. Thomas and E.J. Walker, Carbon-Carbon Composites as High Strength Refractories, in *High Temperature High Pressure*, Vol 10, 1979, p 79

6. J. Hill, C.R. Thomas, and E.J. Walker, Paper 119, in *Proceedings of the Second International Carbon Fibre Conference*, Plastics Industry, 1974, p 122

7. W. Hüttner, K. Kewscher, and M. Hunin-ger, in *Ceramics in Surgery*, P. Vincenzini Ed., Elsevier, 1982, p 225

8. A. Gkogkidis, Ph.D. Thesis, University of Karlsruhe, 1986

2

Alumina-Silica System

Robert H. Doremus
Rensselaer Polytechnic Institute
Troy, New York

INTRODUCTION

The alumina-silica system. including the end members of the pure oxides. is probably the most important binary oxide system both in technology and science. Alumina. silica. and aluminosilicate compounds are widely used high-temperature materials. are important in mineralogy and geology. are basic material in glasses. and have many specialty applications. In this review the processing. properties. and uses of the end-member compounds. silicon dioxide (SiO_2) and aluminum oxide (Al_2O_3). are discussed first. Then the compound mullite ($3Al_2O_3 \cdot 2SiO_2$). which is the only stable unhydrated compound in the alumina-silica system. is considered.

The phase diagram of the alumina-silica binary system is of great importance. but. until recently. conflicting diagrams have been put forward by different investigators [1-4]. especially in the mullite region. The work of Klug [5. 6] has resolved these difficulties. and a definitive phase diagram can now be constructed from his and earlier work. Methods for studying the phase diagram in the mullite region will be described: microstructures. sol-gel processing. and x-ray diffraction help to define the phase diagram and also provide insight into the structural and microstructural characteristics of the system and their relation to properties. Finally. hydrates in this system will be briefly discussed: they are important as minerals and raw materials for some of the unhydrated solids.

ALUMINA

Crystalline alumina is a highly valuable solid material because of its high melting point (2054°C), high hardness, high strength, and chemical stability [7, 8]. Some properties of alumina are given in Table 1. As a single crystal (sapphire), alumina is prized as a gemstone (sapphire or ruby, depending upon the impurities present) and for special applications such as watch bearings. Polycrystalline alumina is much less expensive to make and is widely used as a high-temperature material and in diverse applications. A translucent polycrystalline tube of alumina (Lucalox) is the arc tube for the yellow sodium vapor lamps that are replacing blue mercury lamps in many outdoor applications. These and other uses are summarized in Table 2.

The stable crystalline phase of alumina is α-Al_2O_3 with a hexagonal structure. The larger oxygen ions are close-packed in a hexagonal array, and the much smaller aluminum ions occupy two-thirds of the octahedral (six-coordinated to oxygen) interstitial sites in the oxygen lattice. A number of metastable crystalline phases (cubic "γ aluminas") are formed when alumina is made by crystallization from aqueous solution or from hydrated aluminas, such as boehmite (Al_2O_3·H_2O). These phases form as the boehmite or amor-

Table 1 Selected Properties of Alumina, Silicas, and Mullite

	α-Al_2O_3	α-Quartz	Vitreous silica	Mullite
Density, g/cm³	3.96	2.65	2.20	3.13
Melting temperature, °C	2054	1734 (cristobalite)		1890
Elastic modulus [GPa]	520	72	73	250
Coefficient of thermal expansion (25–1000°C), 10⁶/°C	8.5	12	0.5	5.5
Indentation hardness, GPa	20	8	8	12

Table 2

Compound	Uses
Alumina (Al_2O_3)	
Single-crystal (sapphire)	Gems, watch bearings, laser hosts, high-temperature windows
Polycrystalline	Refractories, high-temperature materials, lamp tubes, grinding pebbles, bearings, guides, nozzles, valves, radomes, cutting tools, polishing compounds, prostheses, armor plating, electronic substrates, spark plugs, laboratory ware
Silica (SiO_2)	
Single-crystal quartz	Oscillators, filters, frequency controls, optical windows
Vitreous	Crucibles, high-temperature components, lamp envelopes, optical fibers, electrical transducers and insulators, lenses, prisms, telescope mirrors
Mullite ($3Al_2O_3$·$2SiO_2$)	Refractories, crucibles, high temperature components, infrared windows

phous precipitated phases are dehydrated by heating to about 1000°C. At temperatures above 1000°C these metastable phases convert to α-Al_2O_3. The microstructure and electron diffraction in one step in this conversion are shown in Figure 1.

Alumina is made by the usual processing methods for crystalline ceramics [10]. A fine powder (approximately 0.2 to 5 μm in particle diameter) is pressed into the desired shape. usually including a "binder" of organic material. such as polyvinyl alcohol: then the pressed ware is dried and then fired at a high temperature (1500–1800°C). Often slow heating or a hold at intermediate temperature ("calcining") is provided to remove binder and traces of water and any other volatiles.

Some properties of the alumina depend strongly upon impurities in the starting powder. Many commercial aluminas contain impurities. such as oxides of silicon. calcium. magnesium. sodium. and potassium: these oxides melt at lower temperatures than alumina and form liquid at sintering temperatures. These liquids speed sintering to a dense material. but they degrade high-temperature strength and creep resistance. Creep is slow high-temperature deformation of a solid. The most common impurity is silica. and together with the
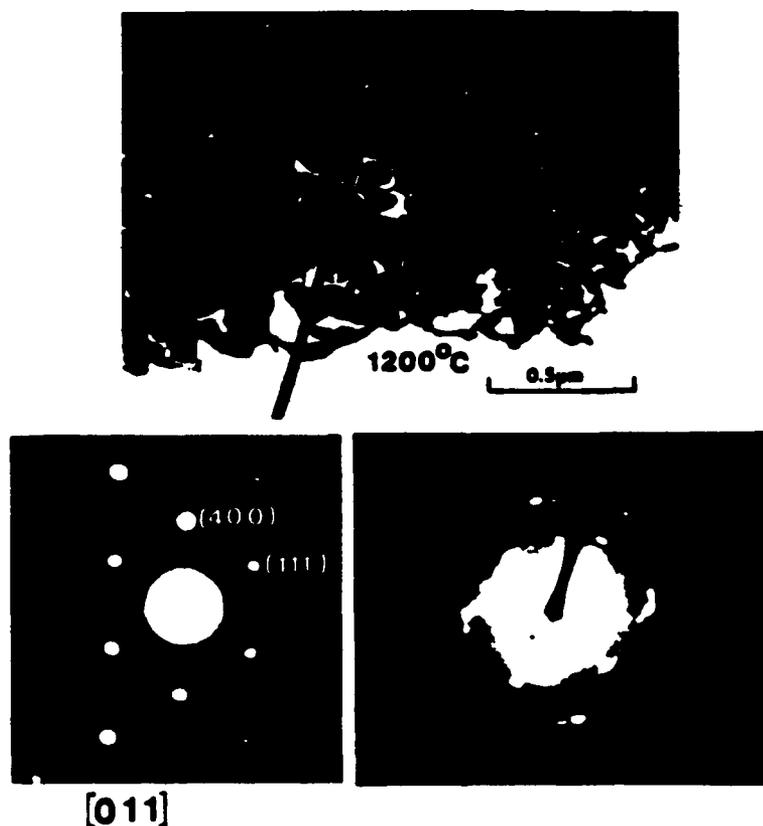
Figure 1 Transmission electron micrograph of a pellet of precipitated alumina sintered 2 h at 1200°C (top). Lower left. selected area electron diffraction pattern of 0.3 μm cubic γ-Al_2O_3 grain. Lower right. deformed diffraction pattern of polycrystalline matrix. (From Ref. 9.)

other oxides silica forms a glass upon cooling. This glass segregates to grain boundaries and can flow at high temperatures, leading to increased creep. Thus the impurity content of commercial alumina is a rough indicator of its high-temperature resistance to deformation: alumina brick. 96% alumina. and 99% alumina are typical commercial designations of increasing high-temperature stability.

The white, opaque appearance of most sintered ceramics results from light scattering from pores and second phases in them; most oxides show no intrinsic optical absorption in visible light. If the polycrystalline oxide is single-phase, reducing porosity can lead to a translucent solid; low porosity in alumina provides an optically acceptable arc tube in the sodium vapor Lucalox lamp.

SILICA

Silicon dioxide (SiO_2) has a variety of structural forms, as listed in Table 3. The naturally occurring form of most silica is crystalline α-quartz, which has a complex hexagonal structure. The high-temperature crystalline form of pure SiO_2 is cubic β-cristobalite. A small amount of impurity oxide, especially alkali oxide, stabilizes a third crystalline form, tridymite. Each of these crystalline forms has high- and low-temperature modifications β and α; the structural differences between these modifications are small. Most of the information in Table 3 is taken from Sosman [11]; in spite of its age this book is still a valuable source of information about silica. At pressures above atmospheric two additional, denser crystalline phases form. Amorphous or vitreous silica is easily formed by cooling molten silica, because its high viscosity inhibits crystallization.

The building block of silica structures is the silicon-oxygen tetrahedron. Each silicon atom is surrounded by four oxygen atoms; each oxygen atom is bonded by two silicons. This tetrahedral configuration is remarkably stable and forms the elemental unit of structure in all silicates. In the pure silicas of Table 3, these tetrahedra are bonded in a three-dimensional network, which has great chemical and mechanical durability. When the

Table 3 Structural Forms of Silica and Some of Their Properties

Form	Transition temp. (°C)	Melting temp. (°C)	Density (g/cm³)	Coefficient of thermal expansion/°C
α-Quartz	573		2.65	12
β-Quartz	867	1430	2.60	
α-Tridymite	163		2.28	21
β-Tridymite	1470	1670	2.30	
α-Cristobalite	273		2.31	10
β-Cristobalite		1734	2.21	
Vitreous silica			2.20	0.5
	Transition pressure at 25°C. kbar			
Coesite	30–40			
Stishovite	100			

crystalline silica melts, the three-dimensional network is retained, so that the molten silica has a structure close to the crystalline. The result is a low heat of fusion and low-energy differences between different structures, leading to the many structures listed in Table 3.

Single-crystal quartz for the applications listed in Table 3 is cut from natural crystals or made synthetically. Large, very pure natural quartz crystals are mined in Brazil. Synthetic quartz crystals are grown from alkaline aqueous solution at high temperature ($250–450°C$) and pressures (300 to 1000 atm or $3 (10)^7$ to 10^8 Pa).

Vitreous silica crucibles for melting semiconductors are made by arc melting very pure quartz sand. Ingots of vitreous silica are made by melting crushed natural quartz crystals or sand in crucibles of graphite, tungsten, or molybdenum in an inert or slightly reducing atmosphere. The melting temperature is $1800–2000°C$ to exceed the melting point of cristobalite ($1734°C$). The ingot is then cut up into desired shapes or drawn to other shapes, such as tubing or rods.

Very pure vitreous silica is made from vapor-phase oxidation or hydrolysis of silicon tetrachloride ($SiCl_4$). In one method the $SiCl_4$ is mixed with oxygen and natural gas, fed through a burner, and deposited on a substrate of preheated sand or on a rotating air-cooled mandrel of aluminum. A plasma torch can also be used.

Fibers of silica are pulled from a preformed silica rod or other convenient shape.

The softening temperature (viscosity of 10^6 Pa-s) of vitreous silica is about $1500°C$, so it must be heated to near this temperature to be worked. The glass transition temperature (viscosity of 10^{12} Pa-s) is about $1200°C$ for pure silica, but is reduced sharply by impurities, especially water. Above about $1350°C$ silica begins to vaporize by the reaction to silicon monoxide:

$$SiO_2 = SiO + \tfrac{1}{2} O_2 \qquad (1)$$

The SiO exists only in the vapor; it forms a mixture of SiO_2 and silicon on a solid surface.

Pure vitreous silica has a wide range of optical transparency from about 0.18 to $4 \, \mu m$. Its low coefficient of thermal expansion provides high resistance to thermal shock. The electrical conductivity and dielectric loss are extremely low. The elastic modulus of vitreous silica is unusual in that it increases with temperature increase and at very high strains.

Further information on vitreous silica is in Refs. 11–14.

MULLITE

The only stable unhydrated compound in the alumina-silica system is mullite ($3Al_2O_3 \cdot 2SiO_2$). Mullite has been widely used in refractory brick and other high-temperature applications. It is often made by heating natural clays such as kaolinite, which is a hydrated aluminosilicate:

kaolinite   mullite
$$3Al_2O_3 \cdot 2SiO_2 \cdot 2H_2O = 3Al_2O_3 \cdot 2SiO_2 + 4SiO_2 + 6H_2O \qquad (2)$$
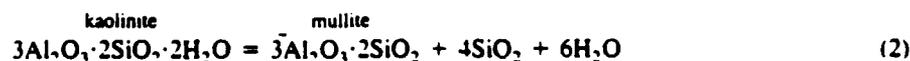
As mined, the kaolin includes impurities, especially oxides of alkali and alkaline earths and iron. Thus mullite made in this way is impure; because of the excess silica, a glassy silicate phase usually forms. This glassy phase flows at temperatures above about $1200°C$, limiting the usefulness of mullite made from the usual raw materials.

Mullite cannot be easily sintered to high density from mixed powders of silica and alumina; usually high porosity and a glassy silicate phase result. A dense, pure mullite can

be made by sol-gel methods. for example. from mixtures of colloidal. hydrated alumina. and tetraethyl silicate (see below) or aluminum and silicon alkoxides. This mullite has superior high-temperature properties; it shows much better creep resistance than does polycrystalline alumina at temperatures from 1400 to 1650°C [15. 16]. Other methods of making superior mullite-based ceramics show promise [17. 18]. In all these methods knowledge of the correct alumina-silica phase diagram. described in the next section. is invaluable in making dense. single-phase materials.

Mullite has a complex orthorhombic crystal structure containing chains of aluminum ions six- and four-coordinated to oxygen. and tetrahedra of silica [19]. Both silicon and aluminum ions can move into normally unoccupied tetrahedral sites. which is one reason for the solid-solution and nonstoichiometric phase boundaries (see below). The unit cell can be represented by the formula $Al_{(4-2x)}Si_{(2-2x)}O_{(10-x)}$. in which x is the number of oxygen vacancies per unit cell [19]. Values of x from 0.25 to 0.4 give mullite-alumina solid solutions from Al_2O_3 to SiO_2 ratios from 3 : 2 to 2 : 1. Mullite is chemically durable in acid metal slags and most gases at high temperatures. It has a low thermal expansion coefficient. giving it good thermal shock resistance. The value of mullite as a quality high-temperature material appears to have been underestimated in the past: it has excellent intrinsic properties. and the above and new methods of synthesis should make mullite to be one of the most important "advanced" high-temperature oxides.

PHASE DIAGRAM

An alumina-silica phase diagram constructed from recent work is given in Figure 2. The diagram from 0 to 70 wt% Al_2O_3 is from Aramaki and Roy [2] except for the eutectic temperature of 1587°C from Aksay and Pask [4]. The mullite-alumina liquidus line is from Horibe and Kuwabara [3]. and the mullite solubility lines and melting temperature are from Klug [5. 6]. There is a eutectic at about 7.6 wt% Al_2O_3. and mullite just melts incongru-
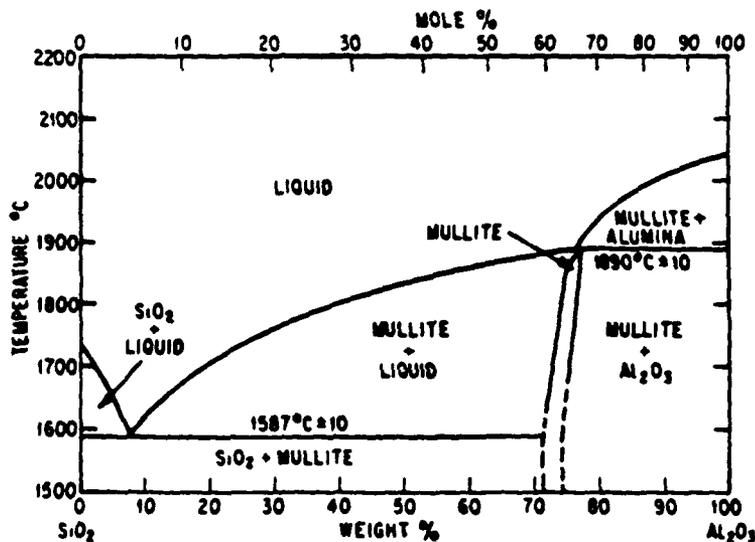
Figure 2   Alumina-silica phase diagram. (From Refs. 5 and 6.)

ently at 1890°C and 77.15% Al_2O_3. The peculiar mullite region is shown in detail in Figure 3. At high temperatures (above 1600°C) the stoichiometric composition $3Al_2O_3 \cdot 2SiO_2$ is unstable and decomposes into a solid solution mullite with dissolved alumina and liquid. There is a solid solution region about 2 wt% wide, ending in a peritectic reaction, with an unusual sloping of the mullite-liquid and mullite-alumina phase boundaries. The diagram contrasts with those of metallic alloys, which usually have solid solutions of the constituent elements, but little or no solid solutions of intermetallic compounds.

The sloping of the phase boundaries and the slow reaction to equilibrium in the mullite region, giving rise to easily formed metastable phase regions [4], have caused great difficulties and controversies in determining the mullite region of the diagram [5]. The solution was to approach equilibrium in different ways and to use microstructure studies, chemical microanalysis, and x-ray diffraction, and to make samples from sol-gel techniques [5, 6]. This work of Klug will be described in some detail because of the insights it gives into the characteristics of the alumina-silica system.
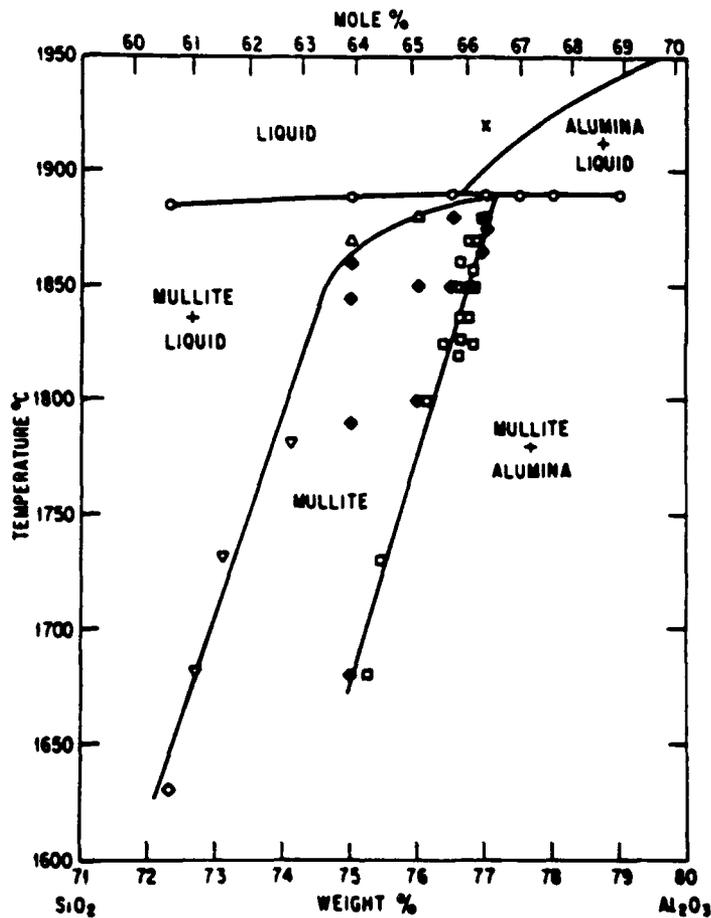
Figure 3 The mullite region of the alumina-silica phase diagram. ☐ calculated from the lever rule. ◆ single phase mullite. ☐ mullite plus glass. ☐ melting of mullite.

EXPERIMENTS OF KLUG [5, 6]

Homogeneous powders were made from a colloidal suspension of $Al_2O_3 \cdot H_2O$ and tetra-ethyl orthosilicate. These materials were made into a gel. broken up. and then heated to 800°C and held 12 h to remove hydrocarbons and water. The resulting powder was pressed into pellets and heated to 1325°C in air to convert it to mullite and to remove residual carbon. Then the samples were fired at higher temperatures to determine the equilibrium phase boundaries. To reduce silica loss. samples were wrapped in rhodium foil and fired in oxygen. leading to negligible weight loss. Sample compositions were checked with microprobe analysis.

The volume fraction of phases were determined with image analysis of sample micrographs, one of which is in Figure 4. There was no glassy phase in any of the samples containing between 76.5 and 78 wt% Al_2O_3 and heated at temperatures below 1890°. consistent with the phase diagram in Figure 3. There was very little porosity in any of the samples. The amount of alumina and mullite (by difference) in these samples were used with the lever rule to determine the points in Figure 3. Single-phase (mullite only) samples had compositions inside the solid solution region. These single-phase samples were translucent because of low pore. second phase. and glassy volumes, reducing light scattering to a minimum.
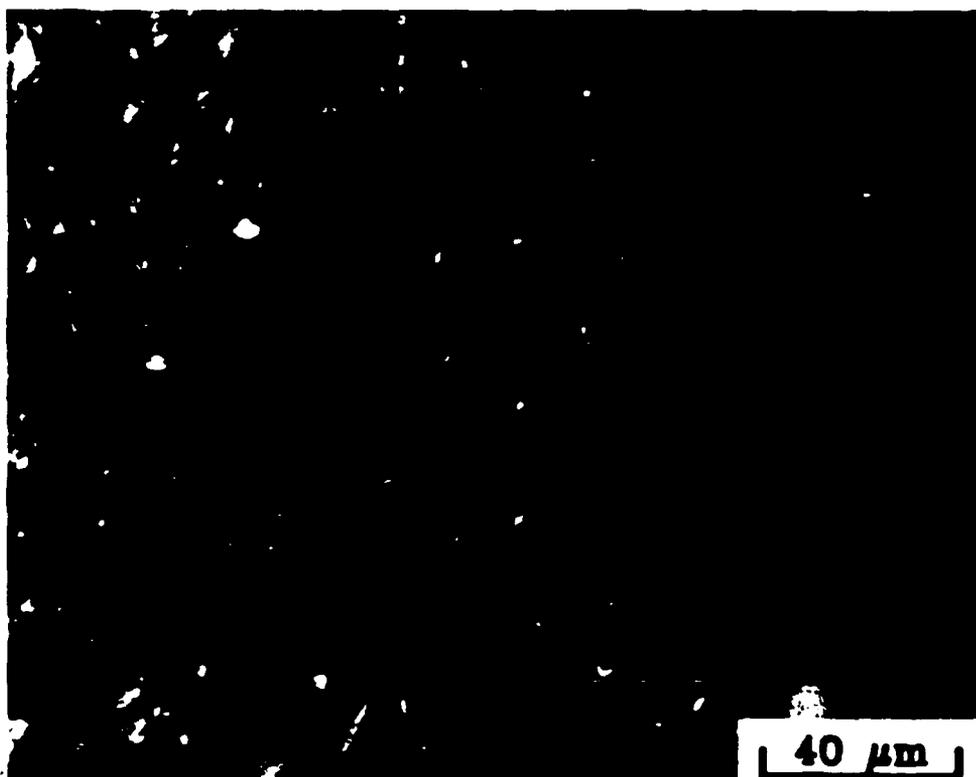
Figure 4   Optical micrograph. Nomarski contrast. 76.5 wt% Al_2O_3 after sintering at 1680°C for 144 h. Etched 5 min. in boiling. concentrated NaOH. 500×.

Half of each sample was crushed to 100-mesh powder for x-ray diffraction analysis. Lattice parameters of mullite were calculated from peak positions. and the amount of second-phase alumina was determined from the ratio of an alumina peak to the average of four mullite peaks. The amount of alumina agreed well with that calculated from the micrographs.

The melting point of mullite was determined in a special set of experiments. Samples were observed in the optical pyrometer as they were heated from 1880°C until they melted. Thirty-four samples of different overall compositions melted at 1890°C. The pyrometer temperature was checked with a thermocouple of tungsten 5% rhenium against tungsten 26% rhenium. Micrographs showed glassy phase as evidence of melting for samples heated above 1890°C. as shown in Figure 5.

Figure 5 Bright field optical micrograph of mullite (77% Al_2O_3) melted at 1895°C. The light particles are Al_2O_3. and the dark gray areas are glass. high in silica; the matrix is mullite. formed on cooling. 750×.

Single-phase mullite samples containing 76.5 wt% alumina were heated for long times at temperatures below the solid solution region; second-phase alumina precipitated in these samples onto the mullite grain boundaries, as shown in Figure 6. Then the sample was heated at 1880°C, and almost all of the precipitated alumina dissolved. Thus the precipitation and resolution of alumina was reversible, showing that equilibrium can be approached from both composition directions. There was negligible silica loss in these samples from microprobe analysis.

These results of Klug were used to construct the mullite region of the alumina-silica phase diagram in Figure 3 and were incorporated into the complete diagram in Figure 2.

HYDRATES AND MINERALS

Alumina forms two hydrates: $Al_2O_3 \cdot 3H_2O$ or $Al(OH)_3$ and $Al_2O_3 \cdot H_2O$ or $AlO(OH)$. Each of these compounds has two crystalline forms, α and γ, and their names are in Table 4. Bauxite is the mineral raw material for making aluminum, and is a mixture of these hydrates plus impurities such as clay (aluminosilicates) and iron oxides. The structures of these and other hydrates, as well as the unhydrated oxides, are described in Wells [20].

Three mineral aluminosilicates occur widely in nature and have the same formula

Figure 6 Optical micrograph. Nomarski contrast. Single-phase mullite. 76.5 wt% Al_2O_3, after heating at 1730°C for 48 h. Arrow shows Al_2O_3 precipitate. 500×.

Table 4 Hydrated Alumina and Aluminosilicates

Name	Chemical compound
Diaspore	α-Al_2O_3·H_2O
Boehmite	γ-Al_2O_3·H_2O
Bayerite	α-Al_2O_3·$3H_2O$
Gibbsite, Hydrargillite	γ-Al_2O_3·$3H_2O$
Kaolinite	Al_2O_3·$2SiO_2$·$2H_2O$
Halloysite	Al_2O_3·$2SiO_2$·$4H_2O$
Pyrophyllite	Al_2O_3·$4SiO_2$·H_2O

Al_2O·SiO_2; these are sillimanite, kyanite, and andalusite, each with a somewhat different structure. In these compounds one-half of the aluminum ions are six-coordinated, and the other half are four-, five-, or six-coordinated in sillimanite, andalusite, and kyanite, respectively. In kyanite, the densest, the oxygen atoms are in a close-packed cubic lattice. When these compounds are heated, they break down to the stable phase mullite plus silica.

Clays are hydrated aluminosilicates that occur naturally as many different compounds, with impurities and substitutions of ions common. Some clays that in the pure form contain only hydrated oxides of silicon and aluminum are listed in Table 4.

CONCLUDING REMARKS

The accurate determination of the mullite region of the alumina-silica system, shown in Figures 2 and 3, should lead to new applications of mullite ceramics because of their excellent mechanical and chemical properties. The traditional alumina and silica applications are being continuously expanded because of their superior high-temperature and optical properties. The alumina-silica system is of great importance and utility.

REFERENCES

1. N. L. Bowen and W. Grieg. *J. Am. Ceramic Soc.*. 7:238 (1924).
2. S. Aramaki and R. Roy. *J. Am. Ceramic Soc.*. 45:229 (1962).
3. T. Horibe and S. Kuwabara. *Bull. Chem. Soc. Japan*. 40:972 (1967).
4. J. A. Aksay and J. A. Pask. *J. Am. Ceramic Soc.*. 58:507 (1975).
5. F. J. Klug. Ph.D. Thesis. Rensselaer Polytechnic Institute. Troy. N.Y. (1984).
6. F. J. Klug. S. Prochazka. and R. H. Doremus. *J. Am. Ceramic Soc.*. 70:750 (1987).
7. W. H. Gitzen. "Alumina as a Ceramic Material." Am. Ceramic Soc.. Columbus. Ohio. 1970.
8. G. Richards. *Trans. J. Br. Ceramic Soc.*. 80:120 (1981).
9. S. V. Raman. R. H. Doremus. and R. M. German. *J. de Physique*. 47(2):4-225 (1986).
10. D. W. Rickerson. *Modern Ceramic Engineering*. Dekker. New York (1982).
11. R. B. Sosman. *The Properties of Silica*. Chem. Cat. Co.. New York (1927).
12. R. H. Doremus. in *Encyclopedia of Material Science and Engineering* (M. B. Bever. ed.). Pergamon. Oxford. p. 5257 (1986).
13. P. Danielson. in *Kirk Othmer Encyclopedia of Chemical Technology* 3rd ed.. Vol. 20. Wiley. New York. p. 782 (1982).
14. R. H. Doremus. *Glass Science*. Wiley. New York (1973).
15. P. A. Lessing. R. S. Gordon. and K. S. Mazdyonni. *J. Am. Ceramic Soc.*. 58:149 (1975).

16. A. Hynes and R. H. Doremus. unpublished results.

17. S. Kanzaki. H. Tabatu. J. Kumazawa. and S. Ohta. *J. Am. Ceramic Soc.*. 68:C-6 (1985).

18. Q. Yuan. J. Ton. and Z. Jin. *J. Am. Ceramic Soc.*. 69:265. 268 (1986).

19. C. W. Burnham. Yearbook of the Carnegie Inst.. Vol. 63. Carnegie Institute. Washington. D.C.. pp. 223. 227 (1964).

20. A. F. Wells. *Structural Inorganic Chemistry*. Oxford University Press. Oxford (1984).

Grain Growth in Mullite and a Mullite/Corundum Composite

A. P. HYNES, T. W. FOLMSBEE, JR. AND R. H. DOREMUS

ABSTRACT

The grain growth and microstructural changes in mullite and a mullite/α-Al$_2$O$_3$ composite were studied after heat treatments at 1423K, 1840K and 2048K, and compared with those noted after compressive creep tests. Grain growth of mullite in the matrix and composite was similar, and grain growth during creep tests was not significant. Grain growth coefficients ranged from 4.6E-2 to 3.0 μm^2/h, and a grain growth activation energy of 185 kJ/mol was calculated for the combined data of the matrix and composite. A calculation of grain boundary diffusion coefficient from the grain growth data indicates that a boundary diffusion mechanism is possible.

INTRODUCTION

Recent work on mullite plus corundum composites indicates that the incorporation of acicular corundum may inhibit creep relative to the monolithic material [1]. Since creep rate depends strongly on grain size and other microstructural features which may change with time at high temperature, it is useful to evaluate the evolution of the microstructure in order to predict and understand the high temperature mechanical properties such as creep.

Among the changes that occur at high temperatures, grain growth is among the most significant. Grain growth may be defined [2] as "the process by which the average grain size of strain free or nearly strain free material increases continuously during heat treatment". By this definition normal grain growth is distinguished from primary recrystallization, in which strain-free grains grow from a plastically deformed matrix, and from discontinuous grain growth, in which a few large grains grow in a fine-grained, strain-free matrix.

The driving force for grain growth is the reduction in surface energy that occurs as the total grain boundary area decreases. The driving force for grain growth and therefore the growth rate are often considered to be inversely proportional to grain size, d, resulting in the following grain growth equation:

Rensselaer Polytechnic Institute, Troy, NY 12180-3590.
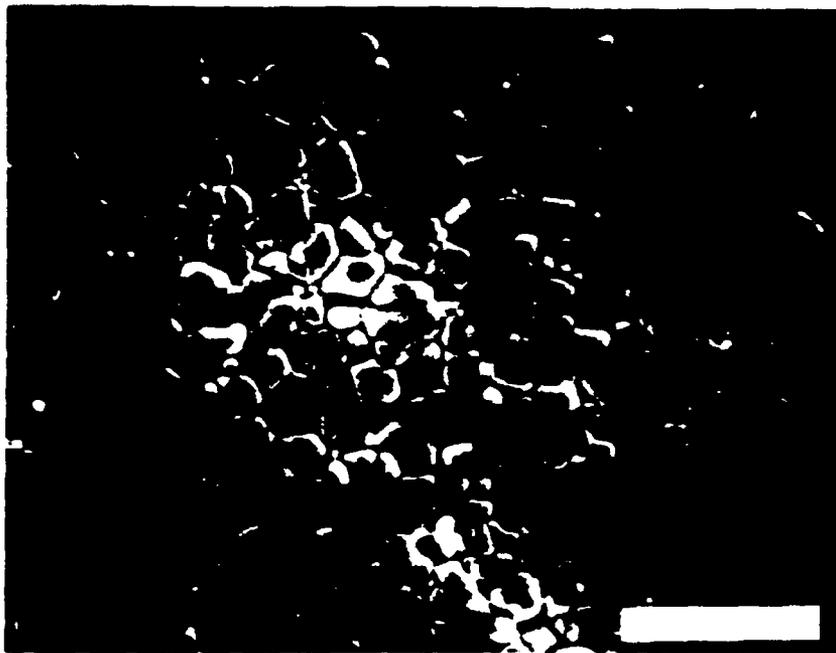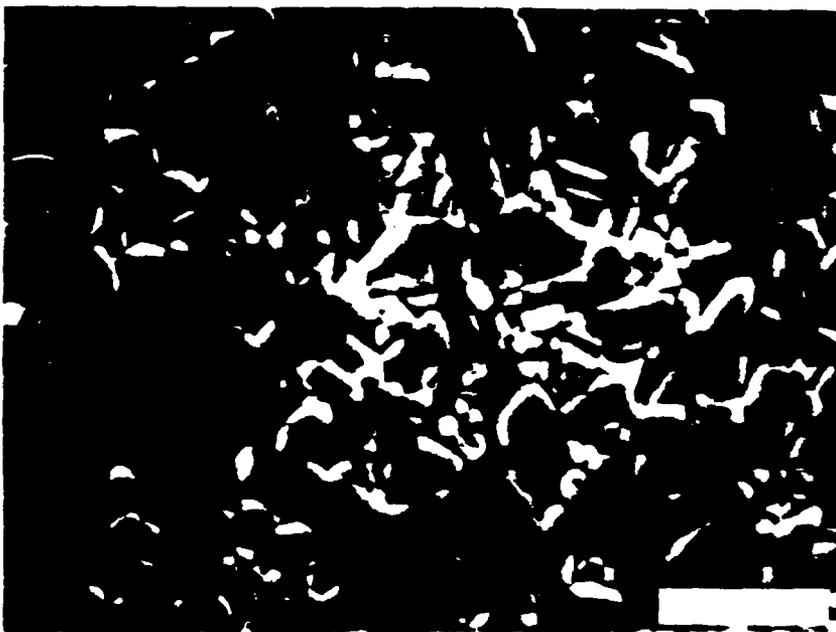
Fig. 1. SEM micrographs of mullite matrix: (a) after 1 h at 1423K. Bar is 4 μm. (b) after 31.6 at 2048K. Bar is 20 μm.

$$d^2 - d_0^2 = kt \qquad (1)$$

where d is the grain diameter at time t, d_0 is the initial grain diameter when time t is zero, and k is a growth coefficient. Plots of grain growth data as log of the grain diameter vs log time often give a straight line with slope between 0.1 and 0.6, and usually <0.5. The slope may be <0.5 because d and d_0 are not sufficiently different; alternately equation (1) may not be valid.

Grain boundary velocity (v_b) is the product of the grain boundary mobility (M) and the driving force (DF),and from a and from a simple derivation [3] considering two adjacent grains of diameter d_1 and d_2:

$$v_b = -4(\gamma)V_m M \ (1/d_1 - 1/d_2) \qquad (2)$$

where γ is the grain boundary surface energy, V_m is the molar volume, and mobility is given by:

$$M = D_b/\delta RT \qquad (3)$$

where D_b is the grain boundary diffusion coefficient, δ is the boundary width, R is the gas constant and T is the temperature. The grain boundary mobility is affected by space-charge atmospheres of lattice defects and solute segregation, precipitates and pores [2,3].

Grain growth occurs during high temperature creep testing, and creep rate depends on the microstructure and grain size. Many creep models predict strain rate dependencies on some integral power of grain size such as -1, -2 or -3 [4]. At temperatures where grain growth is significant, grain growth can reduce the creep rate, and this rate will not reach a steady state unless the rate of grain growth is negligible. In addition, calculations of the stress exponent [5] and creep activation energy will be in error.

EXPERIMENTAL PROCEDURE

The powders used for the matrix and composite samples were prepared by a sol-gel process that has been described elsewhere [1]. The powder compositions were 73 w/o Al_2O_3 for the matrix sample and 77 w/o Al_2O_3 for the mullite/corundum composite. The 73 w/o composition was single-phase mullite and the 77 w/o Al_2O_3 composition contained 10 w/o (8 v/o) α-Al_2O_3. The powders were cold-isostatically-pressed at $\approx$345 MPa, or uniaxially die pressed at $\approx$240 MPa, and then sintered in air according to the following schedule:

298K - 1598K	@100K/h	
1598K	hold 12 h	
1598K - 1873K	@100K/h	
1873K	hold 2 h	
1873K - 298K	furnace cool ($\approx$5 h)	
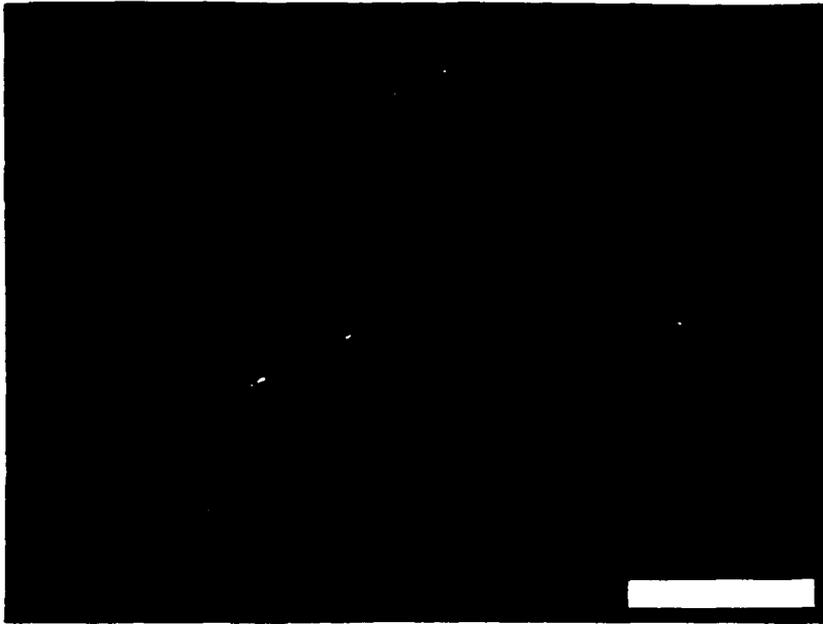
(a)

(b)

Fig. 2. SEM micrographs of mullite/corrundum composite:
(a) after 1 h at 1423K. Bar is 4 μm. (b) after 79.4 h at
1840K. Bar is 4 μm.

Samples were heat treated in air for 1-100h at 1423K, 1840K and 2048K and were examined with SEM following polishing through 1 μm diamond and thermal etching at 1773K for 2 h. The samples were sputter-coated with Au before SEM examination to avoid charging. The mean grain size of the crept and uncrept samples was measured by the linear intercept method with a digitizing pad, and is reported as the inverse of the specific surface area. Histograms of the grain size distributions were plotted. Micrographs were taken at 0° tilt. A line spacing was chosen that did not overlap a grain twice, and a minimum of 100 points were taken per sample.

The grain size data was fit to equation (1) and the growth coefficient, k, was calculated.

The density of the crept and uncrept samples was determined by the Archimedes method with distilled water.

Dead-load uniaxial compression creep tests were performed at temperatures of 1323-1723K and stresses of 10-100 MPa in air with equipment and methods that have been described previously [1]. The change in mean grain size and density for the crept mullite and mullite/corundum composites were calculated. During a few creep runs, small pieces cut from the same sintered body as the creep sample were placed in the furnace on the platen next to the creep sample. Thus these small pieces of mullite experienced the same temperature history as the creep sample, but without the load. The grain sizes and densities of these samples were measured after the creep run and compared with those of the crept samples.

RESULTS

The mullite grains in all the samples were polygonal, approximately equiaxed and had slightly curved or straight grain boundaries, as shown in Figure 1. Grain boundary curvature increased with grain size. The aspect ratio of the corundum grains decreased slightly at the three temperatures tested with increasing time. A typical decrease was from ¯9 after 1 h hold to ¯4 after 80 h 1423K. Changes in porosity were not observed in SEM, and density was essentially unchanged at 2.99 g/cc for the matrix and 3.04 g/cc for the composite. Small pores were occasionally observed in the centers of mullite grains in both the matrix (single-phase mullite) and the composite at all of the temperatures and times tested, except at 2048K. The most pronounced change in the microstructure with heat treatment time was the grain growth of the mullite in both the matrix and composite samples.

The grain sizes and densities did not increase significantly during creep tests. The average increase in grain size was 0.15μm and the average increase in density was ¯1% TD for both the single phase mullite and the composite.

The initial mean mullite grain size in both the single-phase mullite and the composite was 0.3-1.0 μm and a typical standard deviation was 0.5 μm. Grain size distributions in mullite have been reported to be log-normal [6], but many of the distributions measured here had a tail at the smallest grain sizes.

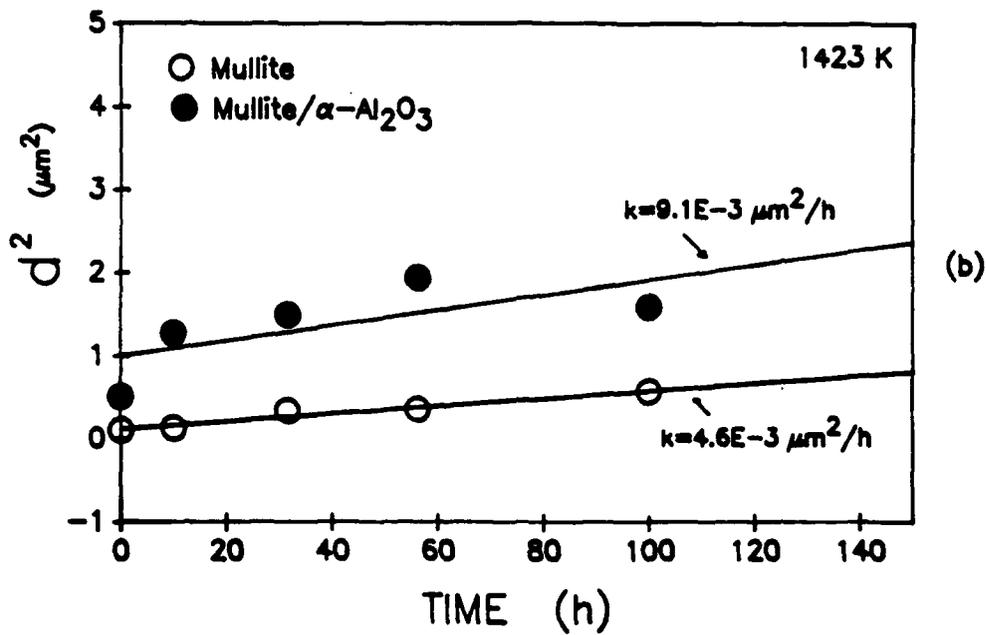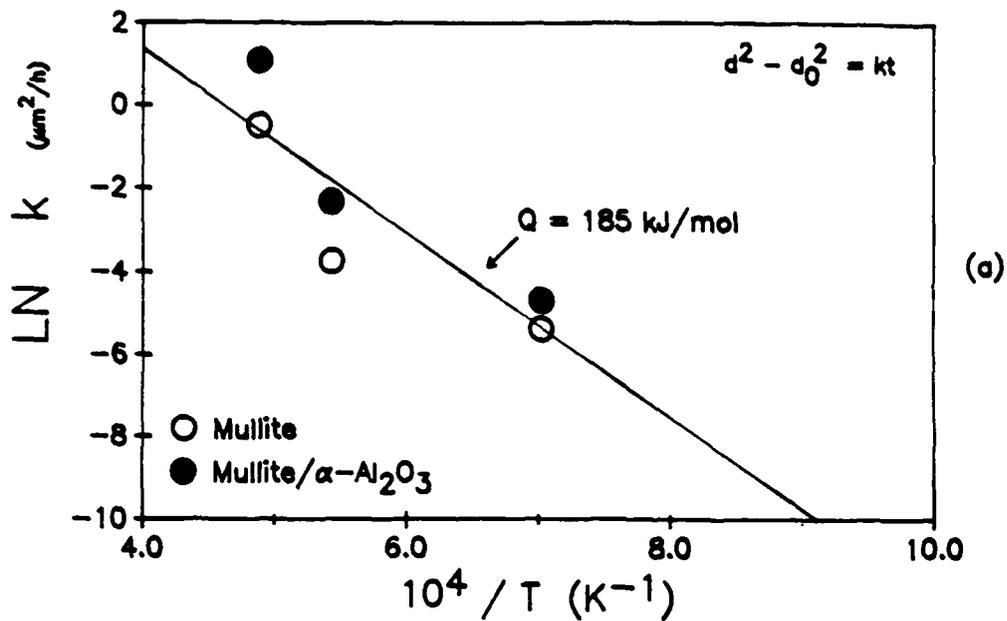The grain growth of the matrix was similar to that of the

Fig. 3. (a) Grain growth exponent, k, as a function of temperature. (b) Grain growth in mullite matrix and mullite/corrundum composite as a function of time at 1423K.

composite, except at 2048K. The grain growth as a function of
time is shown in Figures 3 and 4.   The apparent grain growth
activation energy for the single-phase mullite and composite
data, combined as shown in Figure 3(a) is 185 kJ/mol. At 2048K
the composite growth rate was significantly faster than that of
the single-phase mullite (3.0 versus 0.6 μm^2/h).   The grain
growth constants (k in equation [1]) for the matrix were:
4.6E-3, 2.4E-2 and   6.2E-1 μm^2/h at 1423K, 1840K and 2048K
respectively.   For the composite the constants were: 9.1E-3,
1.9E-2 and 3.0 μm^2/h at 1423K, 1840K and 2048K respectively. If
the observed grain growth rates were constant to 100 h, after
a 100 h heat treatment the mullite grain size in the matrix
would have increased from an initial 0.5 μm to 1.2 μm at
1423K, to 2.0 μm at 1840K, and to 8.4 μm at 2048K. In the
composite after 100 h, the mullite grain size would have
increased to 1.5 μm at 1423K, to 1.9 μm at 1840K and to 18 μm
at 2048K.

The velocity v_b at a particular grain diameter d was calcu-
lated from k with the relation v_b=k/2d from equation (1). Then
the mobility was calculated from equation (2) and the grain
boundary diffusion coefficient from equation (3), from the
equation:

$$D_b = k\delta RT/8(\gamma)V_m \qquad (4)$$

The parameters in these calculations were: γ=0.3 J/m^2, V_m =
2.84E-5 m^3/mol, T=2048K, and k=1.72E-16 m^2/s. The resulting
boundary diffusion coefficient of 1.3E-18 m^2/s can be compared
with the interdiffusion coefficient of 1.6E-15 m^2/s in mullite
[7] at 2026K.

DISCUSSION
The grain growth rates in the single-phase mullite and the
mullite/α-Al$_2$O$_3$ composite are so low that the grain size only
increases by a factor of 2 during 100 h at 1423K and by a factor
of 3 at 1840K.   Thus an initial creep rate of 1E-7 s^{-1} would
decrease by a factor of $\approx$30 to 3.1E-9 s^{-1} over 100h at 1840K if
creep rate has a 1/d^3 dependence and all other factors remained
the same. If the grain size exponent is -1, the creep rate only
decreases by a factor of 3 to 2.9E-8 s^{-1}. The grain size de-
pendence of the creep of mullite has not been clearly estab-
lished. Measured values of the exponent range from -1 to -3
[8,9], so over a 100h period at temperature less than 1840K
(1567C) the change in creep rate due to grain growth is unlikely
to be more than a factor of 30 lower than the initial creep
rate.

The measured grain growth rates in the single-phase mullite
and the composite are similar for the temperatures and times
tested with the exception of the composite data at 2048K which
is approximately 80% faster than the single-phase mullite at the
same temperature. The similarity of grain growth constants
indicates that the rate-controlling processes in the two materi-
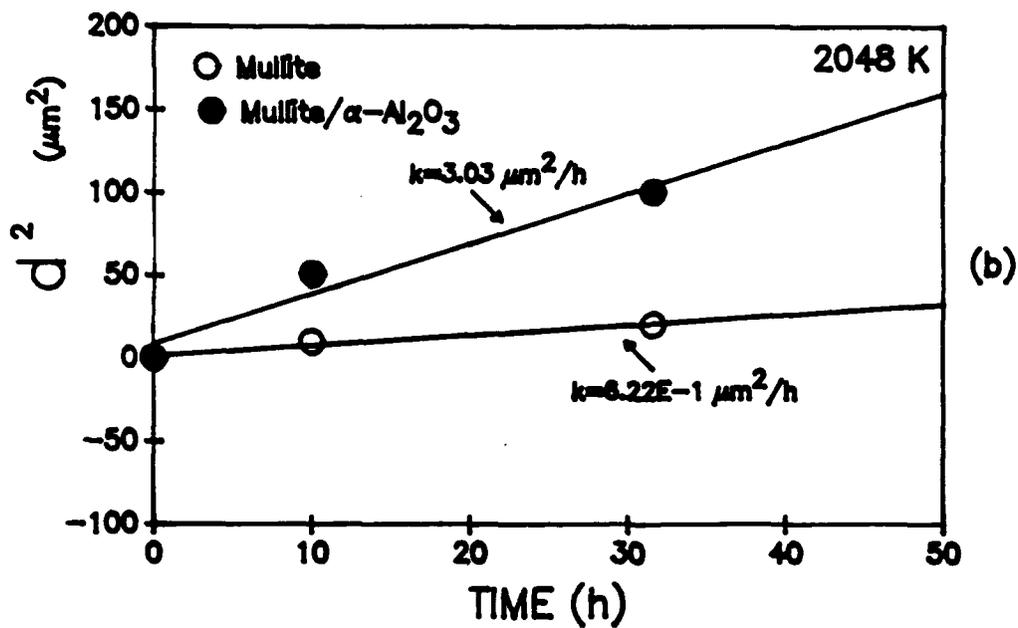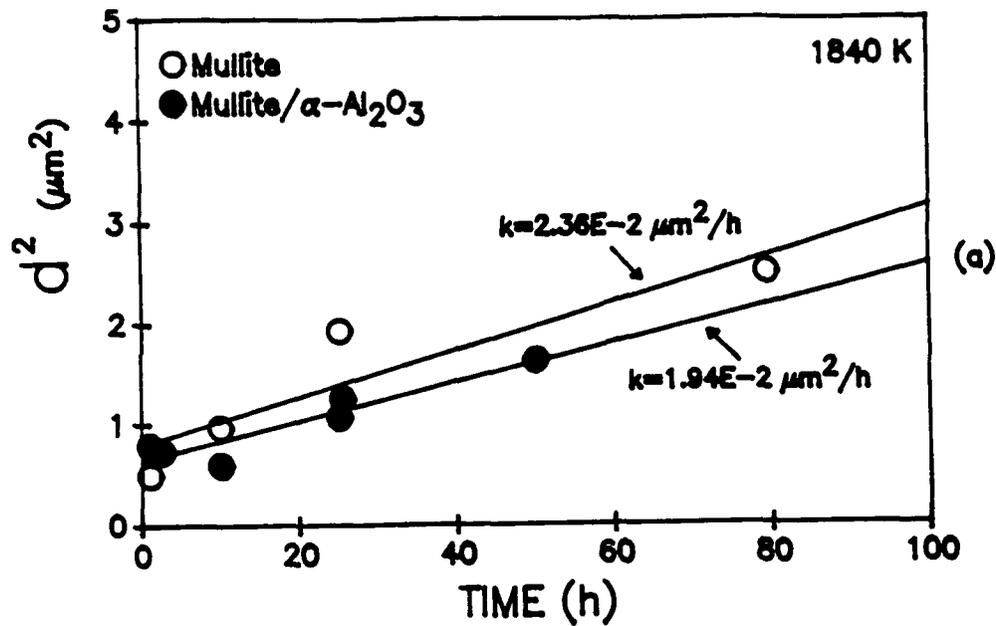als may be the same over the temperature region tested.

Fig. 4. Grain growth in mullite matrix and mullite/corundum composite as a function of time: (a) 1840K. (b) 2048K.

The grain boundary diffusion coefficient calculated from the grain growth data is 3 orders of magnitude lower than that of the lattice diffusivity measured by Aksay. Thus diffusion may be rate-controlling process for grain growth.

The grain growth activation energy of 185 kJ/mol calculated from the grain growth runs is considerably lower than the 698 kJ/mol measured by Aksay [7] for the activation energy of interdiffusion in mullite. Although creep mechanisms in mullite are still a matter of debate, activation energies calculated from creep data range from ≈375-1000 kJ/mol, and cluster around 650-750 kJ/mol [8,9], the vicinity of the the mullite diffusion activation energy. The activation energy for grain boundary diffusion is usually lower than that for lattice diffusion. In Ag, the activation energy for boundary diffusion is about half that of lattice diffusion [9]. If the interdiffusion was controlled by lattice diffusion, the present grain growth results are consistent with grain growth controlled by grain boundary diffusion.

ACKNOWLEDGEMENTS

REFERENCES
1. Hynes, A.P., and Doremus, R.H., to be published, "High Temperature Compressive Creep of Polycrystalline Mullite".
2. Kingery, W.D., Bowen, H.K., and Uhlmann, D.L., 1976, Introduction to Ceramics, Wiley-Interscienc Pub..
3. Doremus, R.H., 1985, Rates of Phase Transformations, Academic Press.
4. Cannon, W.R., and Langdon, T.G., 1983, "Review Creep of Ceramics", J. Mater. Sci., Vol. 18, p. 1.
5. Chokshi, A.H. and Porter, J.R., 1986, "Analysis of Concurrent Grain Growth During Creep of Polycrystalline Alumina", J. Am. Ceram. Soc., Vol.69, No. 2, p.C-37.
6. Lee, C., 1988, "Microstructure and Grain Growth of Mullite", M.S. Thesis, R.P.I..
7. Aksay, I.A., 1973, "Diffusion and Phase Relationship Studies in the Alumina-Silica System", PhD.Thesis, Univ. Calif., Berkeley.
8. Ohnishi, H., Maeda,K., Nakamura, Y., and Kawanami, T., 1990, "High Temperature Mechanical Properties of Mullite Ceramics", pp.605-612 in Mullite and Mullite Matrix Composites, Proc. First Int. Conf. Mullite, Nov. 9-10,1987, JAPAN, Ceramic Transactions, Vol.6, Ed. S. Somiya, R.F. Davis and J.A. Pask, American Ceramic Society, Westerville, OH.
9. Ashizuka, M., Okuno, T., and Kubota, Y., 1989, "Creep of Mullite Ceramics", Yogyo Kyokaishi, Vol. 97, No. 6, p. 662.
10. Reed-Hill, R.E., 1973, Physical Metallurgy Principles. 2nd edition.

MICROSTRUCTURE AND GRAIN GROWTH OF MULLITE

PREPARED BY THE SOL-GEL METHOD

by

Carolyn Lee

A Thesis Submitted to the Graduate

Faculty of Rensselaer Polytechnic Institute

in Partial Fulfillment of the

Requirements for the Degree of

MASTER OF SCIENCE

Approved:

_____

Robert H. Doremus
Thesis Advisor

Rensselaer Polytechnic Institute
Troy, New York

December 1988

CONTENTS

LIST OF TABLES

LIST OF FIGURES

ACKNOWLEDGEMENT

ABSTRACT

The microstructural development of mullite produced by a sol-gel method was observed with the aid of a scanning electron microscope. Modelling equations of log grain size, density, and hardness were derived as a function of heat treatment temperature and time, and mullite composition. The grain sizes within each sample were found to be lognormally distributed.

1. INTRODUCTION

Mullite has long been used in refractory materials in multi-phase form. The more recent advent of single phase mullite produced by sol-gel methods has made it more attractive for use in high temperature structural composites and other applications.

The microstructure of a material controls the properties of that material. If the grain structure can be predicted for a processing schedule, then the properties of the material can also be predicted and optimized. In this study, the effects of composition and heat treatment temperature and time on the microstructure of mullite were observed. The grain size distribution was found to be lognormal in samples processed under various conditions. Data from various samples were used to model grain size, density, and hardness as functions of the processing parameters.

2. HISTORICAL REVIEW

2.1 Ceramic Composites

Ceramic composites have recently gained much attention for their potential use in structural components at high temperatures above 1500°C.

A composite is a combination of two or more components existing as separate phases, put together in such a way that the properties of the components complement each other. Generally a composite consists of a high strength, high stiffness reinforcement material embedded within a continuous matrix material. The matrix acts as a binder, protecting the reinforcement material and transferring loads and stresses.

The reinforcement material may be in the from of small equiaxed particles called particulates, flat particles called flakes, or high length to diameter particles called fibers. These fibers may be continuous or chopped. Two other classes of composites are laminar composites, in which layers of single components are bonded together along a two dimensional area, and filled composites, in which the matrix has many channels or cells filled with the second component. In these cases, it is arbitrary as to which component is called the matrix. [1] [2]

Ceramics are inorganic compounds in with the interatomic bonds are ionic or covalent. Because of the nature of these bonds, ceramics tend to have high melting points, and are very hard, but brittle. They are attractive for high temperature uses because they are electrical and thermal insulators, and are generally more resistant to high temperature and chemical attack than metals and polymers. [1] [3]

The brittleness of ceramics limits its use as a monolithic solid. Adding whiskers improves toughness by inhibiting crack growth and dissipating energy along the fiber/matrix interface. The high aspect ratio of the whiskers also improves high temperature creep resistance.

2

The most common ceramics are oxides, nitrides, carbides, and borides. Of these, silicon nitride (Si_3N_4), silicon carbide (SiC), stabilized cubic zirconia (ZrO_2), hafnium oxide (HfO_2), alumina (Al_2O_3), mullite ($3Al_2O_3 * 2SiO_2$), and cordierite ($2MgO * 2Al_2O_3 * 5SiO_2$) are considered good choices for ceramic matrix materials. [4]

Oxide ceramics are especially resistant to environmental attack at high temperatures. They resist further oxidation and also reduction to suboxides or metals. Silicon carbide and silicon nitride are stable at high temperatures in neutral or reducing atmospheres. However, in oxidative atmospheres their surfaces oxidize to silica (SiO_2). This oxide layer provides some protection from additional oxidation up to 1700°C when the silica starts to flow, exposing the matrix material to further oxidation. [1]

2.2 Mullite

Mullite is the only crystalline phase in the aluminosilicate system (SiO_2-Al_2O_3) which is stable at both room temperature and high temperatures under normal atmospheric pressure. It has a nominal composition of $3Al_2O_3 * 2SiO_2$, but exists over a solid solution range of 65 to 83.6 weight percent Al_2O_3. [5] Mullite has an orthorhombic crystal structure with a structural formula of $Al_2(Al_{2+2x} Si_{2-2x})O_{10-x}$, where x is the number of oxygen vacancies per unit cell. The value of x varies from .17 to .59 (according to Cameron). [6] The $SiO_2 \cdot Al_2O_3$ binary phase diagram is shown in Figure 1. [7]

Mullite is much used in refractories, advanced ceramics and structural ceramics because of its many good properties. It has low thermal expansion, low thermal and electrical conductivity, good thermal shock resistance, and good chemical and thermal stability. It also has low creep, good toughness and strength, and high temperature mechanical stability. Finally, high purity mullite can be made from cheap raw materials. [5]
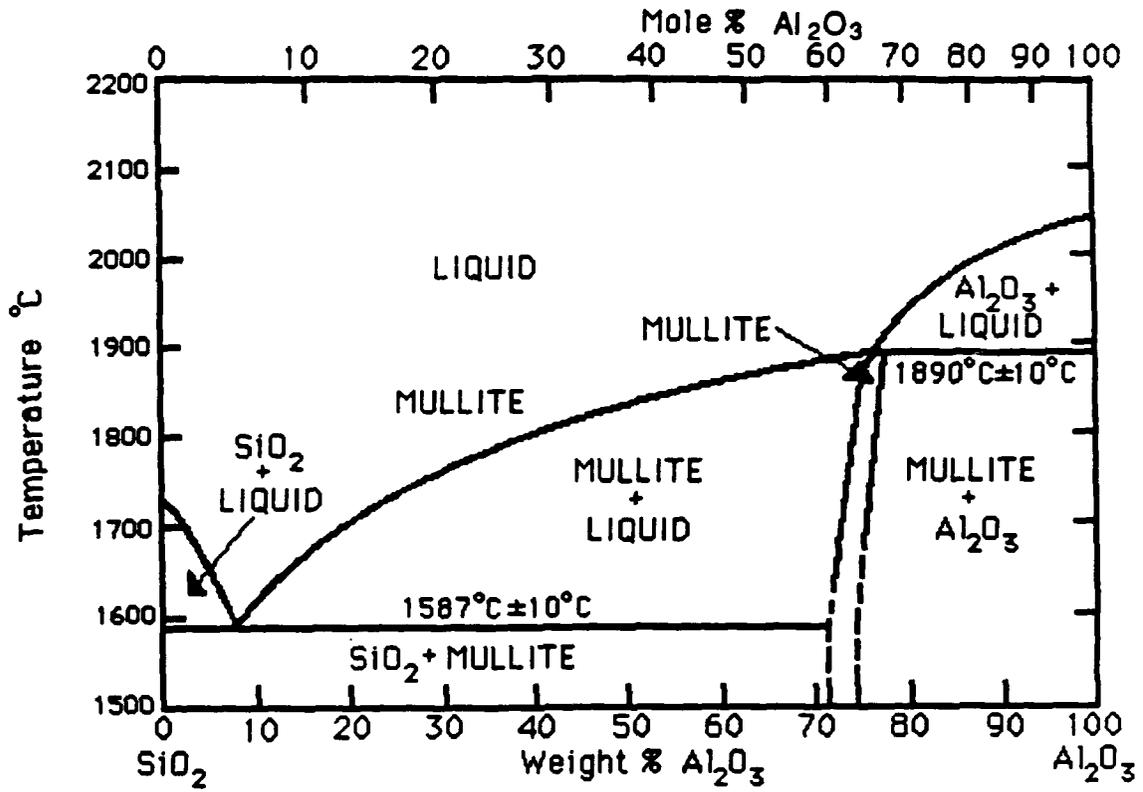
Figure 1

SiO$_2$ - Al$_2$O$_3$ Binary Phase Diagram

Until recently, mullite has been produced mainly by conventional solid state sintering of powders and clays containing alumina (Al_2O_3) and silica (SiO_2). Because of the difficulties in creating homogeneous starting mixtures, the formation of mullite from silica and alumina powders requires long range interdiffusion, and thus requires high temperatures (1700-1800°C) and long processing times. Mullite synthesized in this fashion often contains silica glass at the grain boundaries and sometimes also α-alumina particles. [8]

Silica at the grain boundaries lowers the corrosion resistance of mullite and degrades its high temperature strength and creep resistance. [9] Because of this, emphasis has been placed on homogeneous mixing of Al_2O_3 and SiO_2, and high purity, fine grained starting powders. [10]

A number of wet chemical methods of powder preparation are currently being studied to solve this problem. Among them are sol-gel methods, chemical co-precipitation, hot-petroleum drying, and polymer decomposition. These methods are generally more costly than conventional methods, but the impurities are more easily controlled and a much more homogeneous powder can be produced. These can be processed into chemically and structurally homogeneous solids with improved properties. [11]

In this study, a sol-gel process is used to achieve homogeneous mixing on the molecular level. This intimate mixing of Al and Si ions also permits firing at lower temperatures and shorter times than by conventional methods. [5]

2.3 Microstructural Studies

The study of microstructures is very important to materials science and engineering. The mechanical, chemical and electrical properties of a material with a given overall chemical composition may vary significantly depending upon its microstructure. Understanding and control of microstructure is important to acheiving

the desired properties.

Microstructure is the internal arrangement of a material on a microscopic scale, including the number of material phases present (including porosity), the relative amounts of these phases, the distribution of phases, and the geometric characteristics of these phases, such as size, size distribution, shape and orientation. [12]

There are various techniques of studying microstructure. Early studies employed optical microscopes to look at surfaces with reflected light or to observe thin sections of materials with transmitted light. However, the resolution of the image obtainable with a microscope is limited by the wavelength of light used. Optical microscopes are limited to a resolution of 2000Å, or a magnification of 1000x.

Higher resolutions and magnifications can be obtained with an electron microscope which uses high energy electrons with very small wavelengths to produce images. Transmission electron microscopes (TEM) typically have resolutions of around 5Å with magnifications up to 100,000x, but require samples or replicas less than 1μm in thickness. Scanning electron microscopes (SEM) provide a wide range of magnifications from 20x to 50,000x with resolutions down to 40Å . Since it is not necessary to have a smooth surface with SEM, surface features and fracture surfaces may be studied.

In SEM, a focussed electron beam sweeps or "scans" the specimen surface causing the emission of secondary electrons which are collected and amplified to produce an image on the screen of a cathode ray tube. Because the sample is bombarded with electrons, the surface of an electrically insulating specimen, such as a ceramic, must be coated with a thin layer of gold or carbon to prevent electrostatic charging.

2.4 Grain Growth

Grain growth is the process by which the average grain size in strain free or nearly strain free material increases during heat treatment. This is accomplished by grain boundary movement.

The driving force for grain boundary movement is the reduction of grain boundary area. Grains are single crystals. Within the grain, the interatomic spacing is such that the free energy is at a minimum. At grain boundaries, the interatomic spacings vary (both greater and smaller) from that within the crystallites, thus the free energy is higher there. [13]

To reduce the total free energy in the material, grain boundaries tend to migrate from larger grains to smaller ones, lowering the total grain boundary area. Thus the average grain size increases as larger grains grow at the expense of smaller grains which shrink and disappear. [14]

The velocity of a grain boundary can be expressed as

$$V = MF, \tag{2.1}$$

where M is the boundary mobility and F is the driving force.

$$F = \gamma S_V = 2\gamma/L, \tag{2.2}$$

where γ is the interfacial energy of the grain boundary, S_V is the grain boundary area per unit volume, and L is the mean linear intercept.

If it is assumed that the grain boundary movement has an activation energy about the same as for the self diffusion of the material, Q_b, then the mobility can be expressed as

$$M = M_\bullet\, e^{-Q_b/RT}, \tag{2.3}$$

where R is the universal gas constant and T is the temperature in degrees Kelvin.

Assuming the rate of grain boundary disappearance is proportional to the grain boundary velocity, the mobility, interface energy and grain size distribution is independent of average grain size $\bar{G}$, (i.e. $\bar{G} \propto \bar{L}$,) and grain growth continues indefinitely, we find the the grain boundary velocity is

$$V \propto \frac{d\bar{G}}{dt} = \frac{AM\gamma}{\bar{G}}, \tag{2.4}$$

where A is a geometric constant and t is time. Upon integration, this becomes

$$\bar{G}^2 - \bar{G}_0^2 = AM\gamma t \tag{2.5}$$

or

$$\bar{G}^2 - \bar{G}_0^2 = AM_0\gamma\, e^{-Q_b/RT}\, t. \tag{2.6}$$

In experimental work it is common to assume $\bar{G}_0$ to be neglible, and to plot $\log\bar{G}$ vs $\log t$. [13] Experimental results can usually be represented by empirical equations of the form

$$\bar{G} = K\, e^{-Q/RT}\, t^n. \tag{2.7}$$

Equation (2.6) predicts $n = \frac{1}{2}$ while experimentally it is found that $0.1 < n < 0.6$. [15]

Dispersions of a second phase, including pores, impede grain boundary movement. For a grain boundary to move away from an inclusion or pore, new grain boundary area equal to the cross-sectional area of the inclusion must be formed.

When the restraining force is balanced against the driving force, growth will stop. The limiting grain size is found to be

$$G_l = \frac{d}{f}, \tag{2.8}$$

where d is the average inclusion diameter and f is the volume fraction of inclusions. [13]

During grain growth, as the average grain size $\bar{G}$ approaches G_1, the driving force for grain growth goes to zero. Burke suggested that this be taken into account by modifying equation (2.3) to read

$$\frac{d\bar{G}}{dt} = AM\gamma \ (\ 1/\bar{G} \cdot 1/G_1 \ ). \tag{2.9}$$

It was found that this equation agreed with experimental grain growth results obtained in high purity lead.

The above discussion assumes that the average inclusion diameter remains constant, and that grain growth will stop when the average grain size $\bar{G}$ reaches G_1. However, during heat treatment the inclusions or pores may gradually coalesce so that the value of G_1 increases. Lifshitz and Slyozov predict a $t^{1/3}$ dependence of particle size with time. [13] This should lead to a grain growth law of

$$\bar{G} = Kt^{1/3}. \tag{2.10}$$

2.5 Grain Size Measurement

Grain size and grain size distribution is normally determined by the mean intercept method. A polished planar section of the sample is photographed using an electron microscope and a set of lines is drawn or superimposed on the photograph. The average chord length (mean intercept length) of the particles intersecting the the lines gives a convenient measurement for characterizing particle size.

For spherical particles or rods of uniform size, the mean intercept length is directly related to the particle radius r, by the following equations. [14]

$$L = \frac{4}{3} \ r \ \text{for spheres} \tag{2.11}$$

$$\bar{L} = 2r \ \text{for rods} \tag{2.12}$$

For space filling grains, the mean intercept length also gives the grain boundary area per unit volume, S_V.

$$S_V = 2P_L = \frac{2N}{L} = \frac{2}{L}, \tag{2.13}$$

where P_L is the number of grain boundary intersections per unit length of test line, and N is the number of intersections on a test line of total length, L. [14]

The grain size in metals and ceramics is usually found to have a lognormal distribution. Grain size distribution can be estimated from the intercept length distribution provided certain assumptions are made. If the grains are assumed to be spherical and the distribution can be represented by a discontinuous distribution, then the following equation can be used to estimate the distribution of grain diameters.

$$N(D)_{D=L} = \frac{2n(L)}{\pi L^2} - \frac{2}{\pi L} \frac{dn(L)}{dL}, \tag{2.14}$$

where $N(D)$ is the number of spheres of diameter D per unit volume, and $n(L)$ and $dn(L)/dL$ are the magnitude and slope at L of the continuous distribution curve of chord lengths. [13]

A method of determining grain size distribution, assuming the particles are ellipsoidal in shape with identical axial ratios is detailed in the literature. [16]

2.6 Experimental Design

There are many methods of designing an experiment to measure the effects of a number of factors (or variables) on some property or quantity of interest. One common design is the symmetric factorial design in which a small integral number, p, of levels is chosen for each of k factors, and all p^k combinations of these levels are run. The results of such an experiment may be used to estimate the effects and interactions of the various factors on the response of interest.

Supposing the functional relationship between the response of interest and the k quantitative experimental variables can be approximated by a general polynomial of degree d. A design appropriate for estimating each of the $(k+d)!/k!d!$ constants of such a polynomial would be called a design of order d. A p-level factorial design can be used to estimate a polynomial of no more than p-1 degrees.

An experimental design using N runs to estimate each of L constants is said to have a redundancy factor or $R=N/L$ This factor can not be less than unity. For example, a three level factorial in four variables used as a second order design requires $3^4=81$ runs to estimate 15 constants, and thus has a redundancy factor of $81/15 = 5.4$.

In cases where the experimental error is small, it is not necessary to have a large number of observations to acheive the desired precision. A large redundancy factor would then be a waste of resources and time. A small redundancy factor may be obtained by using incomplete factorial designs.

An incomplete factorial design is an design in which not all, but only a subset, of the factorial combinations are used. It is particularly useful if the subset of factorial combinations is chosen in such a way that a second order rotatable design is produced.

Suppose in a 3-level design the levels are coded in standardized units such that the three values taken by each of the k variables, $x_1, x_2, \ldots x_k$, are -1, 0 and 1. Suppose also that the results of interest can be estimated by the method of least squares to fit a second order polynomial of the form

$$\hat{y} = b_0 + \sum_{i=1}^{k} b_i x_i + \sum_{i=1}^{k} \sum_{j=1}^{k} b_{ij} x_i x_j. \qquad (2.15)$$

A second order rotatable design is one such that the variance of $\hat{y}$ is constant for all points equidistant from the center of the design. (i.e. for all points where $\rho = (\sum_{i=1}^{k} x_i^2)^{1/2}$ is the same.) This type of design ensures that the variance of $\hat{y}$ is reasonably constant

throughout the region of k space covered by the design. Various incomplete factorial designs are detailed in the literature. [17]

3. EXPERIMENTAL PROCEDURES

3.1 Sample Preparation

A mullite precursor was provided by Anne Hynes of Dr. Doremus' group in the Materials Engineering department of Rensselaer Polytechnic Institute. The precursor was made by a sol-gel method based on aluminum alkyoxide (AlO(OH)) and tetraethylorthosilicate (TEOS).

An AlO(OH) dispersion was made by slowly adding AlO(OH) to a solution made by mixing 6ml of concentrated HNO_3 per liter of water. The dispersion was stirred for 12 hours before letting it stand overnight to let any large aggregates or agglomerates to settle to the bottom. The colloidal dispersion was decanted and the sediment discarded. The dispersion was then stirred again and a small amount was removed for gravimetric analysis to determine the amount of AlO(OH) per gram of dispersion.

TEOS was added to the AlO(OH) dispersion in proportions designed to result in the desired weight ratio of Al_2O_3 to SiO_2. TEOS is immiscible with water and at low pH hydrolizes to form a hydrated silica and alcohol. As the TEOS slowly hydrolized, the mixture was stirred rapidly to prevent the TEOS from segregating, and to ensure a uniform dispersion of silica.

The mixture was flocculated into a gel by adding NH_4OH to increase the pH, and then freeze thawed and filtered to remove the water. The filter cake was repeatedly washed with methanol to remove even more water and was dried under heat lamps. If much water was left in the gel, the highly polar water molecules and the strong capillary forces would have resulted in a highly aggregated powder. [7]

The dried powder was calcined at a heating rate of 600°C/hr with a hold at 800°C for 18 hrs to remove any remaining hydrocarbons.

Powders produced in this manner were received from Anne Hynes with compositions to result in mullite with approximately 72, 73, and 74 w/o Al_2O_3.

13

The powders were pressed into pellets 1.27mm in diameter and 0.1 to 0.2 mm in height at 30,000psi so that there were 5, 12, and 5 pellets of 72, 73, and 74 w/o Al_2O_3, respectively. The pellets were heat treated at 1325°C for 12 hours with a heating rate of 100°C/hr to convert the precursor powders into mullite. The pellets were then annealed at various temperatures and times as detailed in Table 1.

Temperature is coded on an inverse scale such that

$$\frac{1}{T(K)} = 5.339 \text{ x } 10^{-4} - 0.2706 \text{ x } 10^{-4}A. \qquad (3.1)$$

So for factor A, a value of $-\sqrt{2}$ corresponds to 1475°C, -1 corresponds to 1510°C, 0 corresponds to 1600°C, 1 corresponds to 1700°C, and $\sqrt{2}$ corresponds to 1745°C.

Time is coded on a log scale such that

$$\log t = 2.303 + 1.609B \qquad (3.2)$$
$$\text{or } t = 10 \text{x } 5^B. \qquad (3.3)$$

For factor B, a value of $-\sqrt{2}$ corresponds to 1 hour 1 minute, -1 corresponds to 2 hours, 0 corresponds to 10 hours, 1 corresponds to 50 hours, and $\sqrt{2}$ corresponds to 97 hours 23 minutes.

Composition is coded linearly such that for factor C, a value of -1 corresponds to 72 w/o Al_2O_3, 0 corresponds to 73 w/o Al_2O_3, and 1 corresponds to 74 w/o Al_2O_3.

Experiments have shown that grain growth can usually be represented by an empirical equation of the form found in Equation 2.7. Taking the log of this equation gives

$$\log \bar{G} = \log K + (-Q/RT) + n \log t, \qquad (3.4)$$

which is of the form

Table 1

Experimental Design

Sample #	A Temp	B Time	C Comp
1	-1	-1	0
2	-1	0	-1
3	-1	0	1
4	-1	1	0
5	0	-1	-1
6	0	-1	1
7	0	1	-1
8	0	1	1
9	1	-1	0
10	1	0	-1
11	1	0	1
12	1	1	0
13	0	0	0
14	0	0	0
15	0	0	0
16	$-\sqrt{2}$	0	0
17	$\sqrt{2}$	0	0
18	0	$-\sqrt{2}$	0
19	0	$\sqrt{2}$	0

$$\hat{y} = b_0 + b_1 \frac{1}{T} + b_2 \log t, \tag{3.5}$$

where $b_0 = \log K$, $b_1 = \frac{-Q}{R}$, and $b_2 = n$.

A second order polynomial of the form in Equation 2.15 will be fit to the experimental data. This will give the constants b_0, b_1, and b_2 mentioned above, and will also reveal any interaction terms between the variables.

3.2 Scanning Electron Microscopy

An Amray AMR 1000 scanning electron microscope was used to examine samples. The mullite pellets were mounted on polishing blocks with hot wax and polished on a 600 grit silicon carbide wheel, followed by polishing on $9\mu m$ and $1\mu m$ diamond wheels with decreasing pressure. The samples were examined under an inverted light microscope to make sure there were no scratches. The samples were then removed from the polishing blocks and cleaned with acetone. Next the samples were etched in boiling sodium hydroxide (NaOH) for 1.5 to 10 minutes to reveal the grain boundaries.

The samples were mounted on aluminum SEM stubs with low resistance carbon paint and sputter coated with gold to prevent the sample from charging under the electron beam. An Ernest Fullam, Model EMS-76M sputter coater was used at a setting of $25\mu A$ and 5 minutes to get the desired gold coat.

The samples were examined in the scanning electron microscope at 20 kV with a 100 micron aperture and a working distance of 8mm. Micrographs of the samples were then taken using a Polaroid camera at magnifications between 625x and 25,000x.

3.3 Measurement of Microstructural Features

The average linear intercept method was used to determine grain size. This was done with the aid of an IBM PC/XT and a Houston Instrument TG 1011 digitizing pad.

Each micrograph was placed under a transparency with 10 parallel lines drawn on it. The chord lengths of the grains intersecting the lines were digitized and stored into files in the PC, with a computer program taking into account the magnifications of the micrographs. The number of grains sampled for each heat treatment ranged from 91 to 1952 grains.

The files containing the chord lengths for the various heat treatments were transferred to an IBM 3081D mainframe operating under the Michigan Terminal System (MTS). The SAS statistical package was used to find the average chord length (mean linear intercept) and to convert the chord lengths to log values which were then averaged to find the mean grain diameter. and standard deviation of the log of the chord lengths. The Kolmogorov D statistic was used to test the goodness of fit of the sample grain size distribution and log grain size distribution with a normal distribution.

The Kolmogorov D statistic is defined as

$$D = \text{least upper bound of } |F(x) - F_N(x)|, \tag{3.6}$$

the greatest absolute difference between $F(x)$ and $F_N(x)$, where $F(x)$ is the continuous cumulative distribution function of a random variable, x,

$$F(x) = \text{Prob } \{ X \leq x \}, \tag{3.7}$$

and $F_N(x)$ is the empirical distribution function for a sample of size N. $F_N(x)$ is a step function with N steps of height $1/N$. [18]

The Kolmogorov D statistic is useful because the probability distribution of D_N is independent of the shape of the distribution function, $F(x)$. For large N, the probability distribution of D_N is given by the relationship

$$\lim_{N \to \infty} \text{Prob } \{ D_N < \frac{z}{N} \} = 1 - 2 \sum_{j=1}^{\infty} (-1)^{j-1} e^{-2j^2 z^2} = L(z). \tag{3.8}$$

The function, $L(z)$ has been tabulated by Smirnov. [19] Equation 3.8 makes it possible to determine the probability that the calculated value, D, comes from a large random sample of a population with a distribution function $F(x)$.

3.4 Density Measurement

The densities of the mullite samples were measured using the Archemedes' Principal with distilled water as the displacement medium. A Mettler balance was used with an attachment for density measurement. The automatic stability detection setting was set to "1" and the integration time set to "3". The balance was calibrated with the built-in calibrator and the density measurement attachment was put in place.

First each sample was weighed dry, and then each sample was weighed twice while immersed in distilled water that had been sitting for several days. (This allows any gasses trapped in the water to diffuse out.) The water temperature was measured before and after all the weighings so that the density of the water could be more accurately determined.

The density of each sample was calculated using the following formula

$$\rho_{mullite} = \frac{m_{dry}}{m_{dry} - m_{wet}} \, \rho_{H_2O} \, , \qquad (3.9)$$

where $\rho_{mullite}$ is the density of the sample, m_{dry} is the weight of the sample in air, m_{H_2O} is the weight of the sample immersed in water, and ρ_{H_2O} is the density of the distilled water.

The two calculated densities for each sample were then averaged and recorded.

3.5 Hardness Measurement

Sample hardness was determined on the Vicker's DPH scale. A Leco M-400 Hardness Tester was used to press a small equiaxed diamond indenter perpendicularly against a highly polished surface of the mullite with a load of 200 grams for 10

seconds, leaving a pyramid shaped dent in the surface.

Five such dents were made in each sample and their widths measured along the two diagonals. Using a lookup chart, the hardness corresponding to each width was found for 10 seconds under a 200 gram load. The ten resulting values for each sample were then averaged and recorded.

4. EXPERIMENTAL RESULTS

The grain size results of each of the samples as determined by the linear intercept method are given in Table 2 along with the processing parameters. The results included are the mean and standard deviation of the intercept lengths, $\bar{L}$, and the mean and standard deviation of the natural log of the intercept lengths. The density and hardness of each of the samples are tabulated in Table 3.

The mean log intercept lengths of the samples are plotted against an inverse temperature scale and a log time scale in a 3-dimensional scatter plot in Figure 2 with the various shapes of the data points representing the various mullite compositions. Similar plots for density and hardness are included in Figures 3 and 4, respectively.

As expected, the log of the grain size increases nearly linearly with log time and decreases linearly with inverse temperature. It is also found that grain size increases with increasing alumina content in the mullite.

The density and hardness of the mullite increases with processing time, but this increase becomes less marked at higher temperatures where near theoretical density is more quickly reached. Unlike grain sized, density and hardness do not increase with increasing processing temperatures at longer processing times, but actually start to decrease with increasing temperatures. The composition of the mullite appears to have little effect on the density attained, but an increase in alumina content increases hardness.

A micrograph and a histogram of the log grain size of each of the 19 samples are included in Figures 5 through 23. Micrographs and histograms are also included for samples of nominally 72, 73 and 74 w/o Al_2O_3 which were not heat treated beyond the calcining at 12 hours at 1325°C. These are shown in Figures 24, 25 and 26, respectively.

20

Table 2

Mean and Standard Deviation of Chord Lengths and Log Chord Lengths

Sample #	Temp (°C)	Time (hrs)	Comp (w/o Al$_2$O$_3$)	$\bar{L}$ (μm)	$\sigma(\bar{L})$ (μm)	$\overline{Log(L)}$	$\sigma(Log(L))$
1	1510	2	73	0.286	0.126	-1.33	0.41
2	1510	10	72	0.340	0.139	-1.16	0.40
3	1510	10	74	0.527	0.267	-0.75	0.47
4	1510	50	73	2.061	1.725	0.44	0.73
5	1600	2	72	0.405	0.185	-1.00	0.45
6	1600	2	74	0.677	0.281	-0.47	0.41
7	1600	50	72	2.060	0.929	0.62	0.49
8	1600	50	74	4.110	1.984	1.28	0.54
9	1700	2	73	1.938	0.926	0.53	0.52
10	1700	10	72	1.448	0.976	0.19	0.60
11	1700	10	74	4.032	2.112	1.27	0.52
12	1700	50	73	8.928	5.520	2.00	0.64
13	1600	10	73	0.916	0.514	-0.24	0.56
14	1600	10	73	0.863	0.511	-0.30	0.56
15	1600	10	73	1.670	0.884	0.39	0.49
16	1475	10	73	0.265	0.102	-1.40	0.37
17	1745	10	73	4.495	2.760	1.31	0.63
18	1600	1.04	73	0.632	0.369	-0.61	0.57
19	1600	97.4	73	5.449	4.443	1.46	0.70
72	0	0	72	0.495	0.237	-0.81	0.47
73	0	0	73	0.241	0.087	-1.48	0.35
74	0	0	74	0.209	0.075	-1.63	0.35

Table 3

Density and Hardness Data

Sample #	Temp (°C)	Time (hrs)	Comp (w/o Al_2O_3)	Density (g/cc)	Hardness (Vicker's DPH)
1	1510	2	73	2.63	469
2	1510	10	72	2.94	698
3	1510	10	74	2.88	1162
4	1510	50	73	3.16	1322
5	1600	2	72	2.79	1102
6	1600	2	74	2.93	900
7	1600	50	72	3.06	1204
8	1600	50	74	3.02	1296
9	1700	2	73	3.12	1232
10	1700	10	72	3.03	1134
11	1700	10	74	3.05	1316
12	1700	50	73	3.12	1255
13	1600	10	73	3.17	1134
14	1600	10	73	3.16	825
15	1600	10	73	3.05	1179
16	1475	10	73	2.47	673
17	1745	10	73	2.96	1214
18	1600	1.04	73	2.80	1025
19	1600	97.4	73	3.11	1376
72	0	0	72	2.70	444
73	0	0	73	2.54	269
74	0	0	74	2.70	659
Alumina	0	0	99.8	3.80	1860

Samples heated treated below 1600°C for less than 50 hours were not very well sintered. The particles are mostly round in shape and there is considerable open porosity.

Samples that were heated at higher temperatures and times were closer to theoretical density. Their grains were faceted, and there was little open porosity. In many of the 73 w/o Al_2O_3 mullite samples with average grain sizes above 1 micron, microstructure varied from region to region. There were areas containing large, nearly equiaxed grains, and areas with smaller rod shaped grains with aspect ratios of 1.5:1 to 6:1. The smaller elongated grains appeared to occur in the more porous sections of the sample.

In the 74 w/o Al_2O_3 mullite sample heated at 1600°C for 50 hours, there was a bimodal distribution of grain sizes. Pockets of small grains were found among much larger grains. In the 72 w/o Al_2O_3 mullite sample heated at 1700°C for 10 hours, there was a bimodal distribution of grain sizes. Here the smaller grains were more evenly interspersed among the larger grains.

It was also noted that samples heated at 1700°C and above, samples heated for 50 hours or more, and samples of 74 w/o Al_2O_3 required longer etch times (i.e. 5 or more minutes) to reveal grain boundaries.

Equations modelling the mean log grain size, density and hardness were derived according to the analysis given by Box. [17] The modelling equations with the coded variables are as follows:

$$\overline{Log(L)} = -0.05 + 0.848A + 0.826B + 0.335C + 0.120A^2 + 0.340B^2 - 0.18C^2 -$$
$$0.07AB + 0.167AC - 0.032BC \qquad (4.1)$$

LOG GRAIN SIZE
(microns)

▼ 72 w/o Al $_2$O$_3$ composition

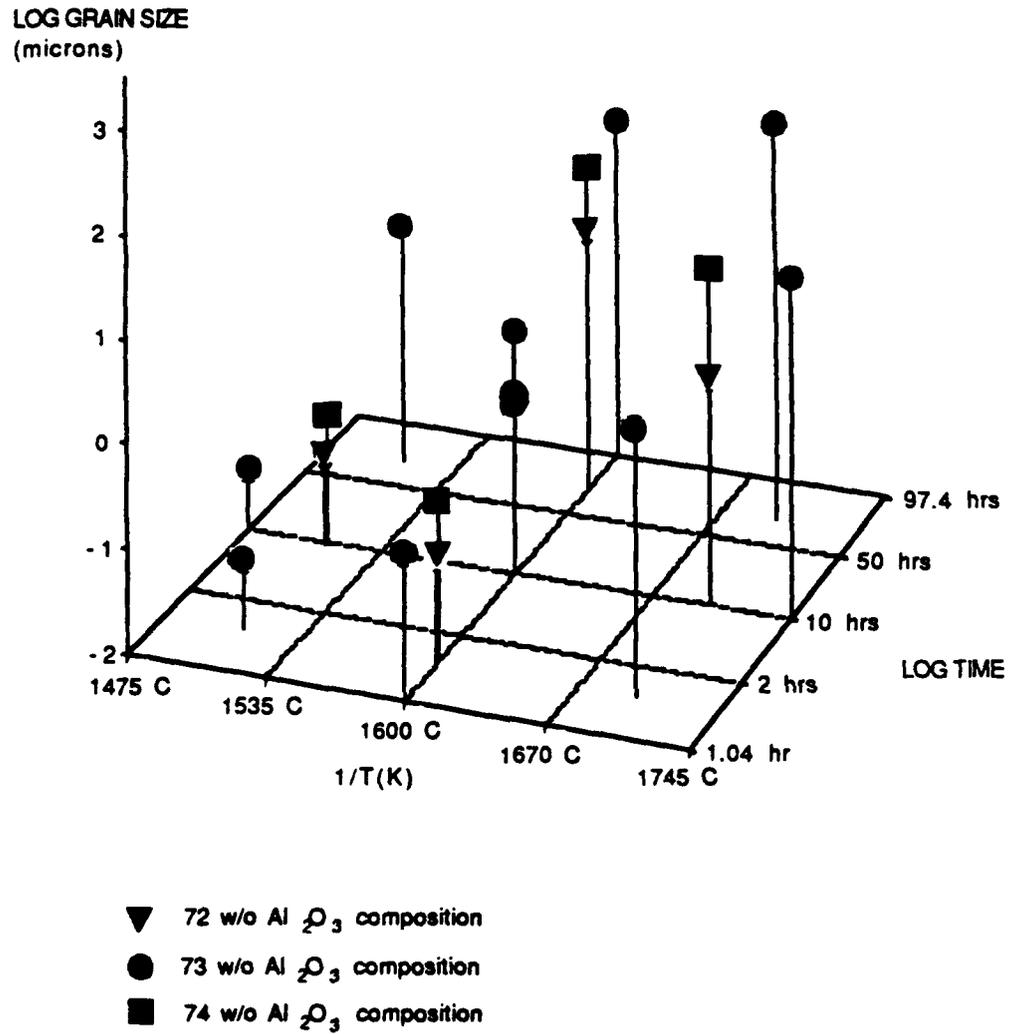● 73 w/o Al $_2$O$_3$ composition

■ 74 w/o Al $_2$O$_3$ composition

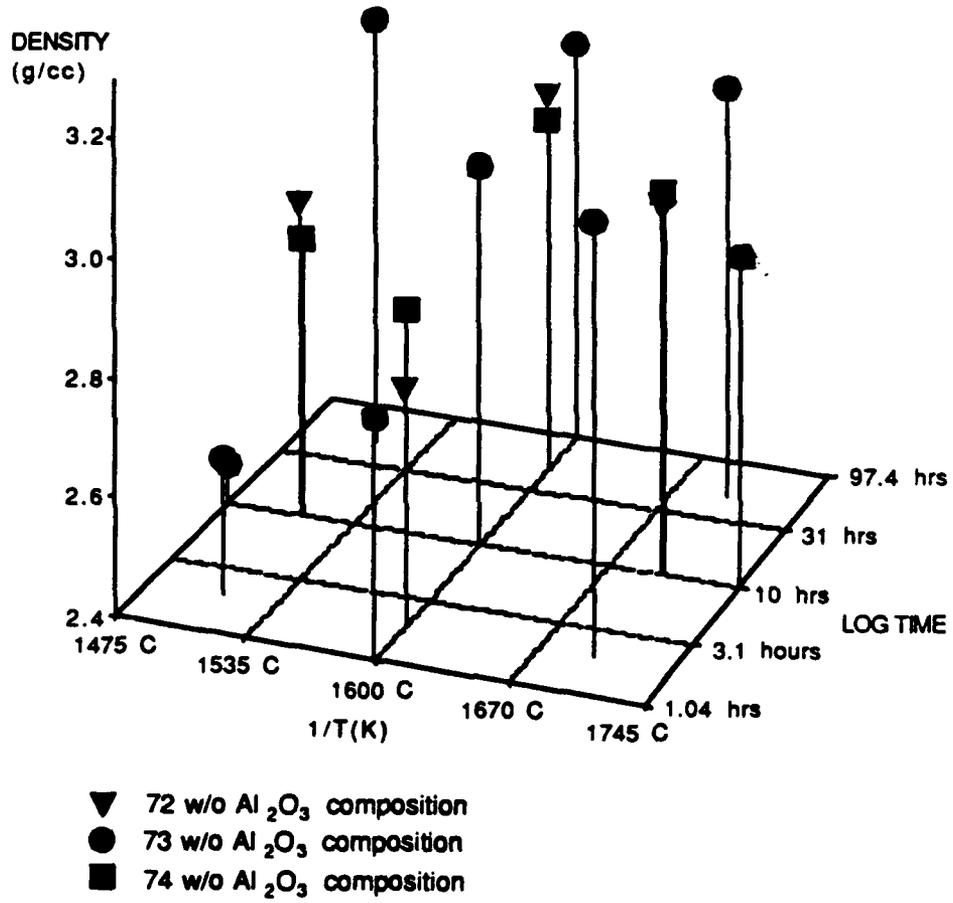Figure 2

Log Grainsize Data vs 1/T(K) and Log time

Figure 3

Density data vs 1/T(K) and Log time
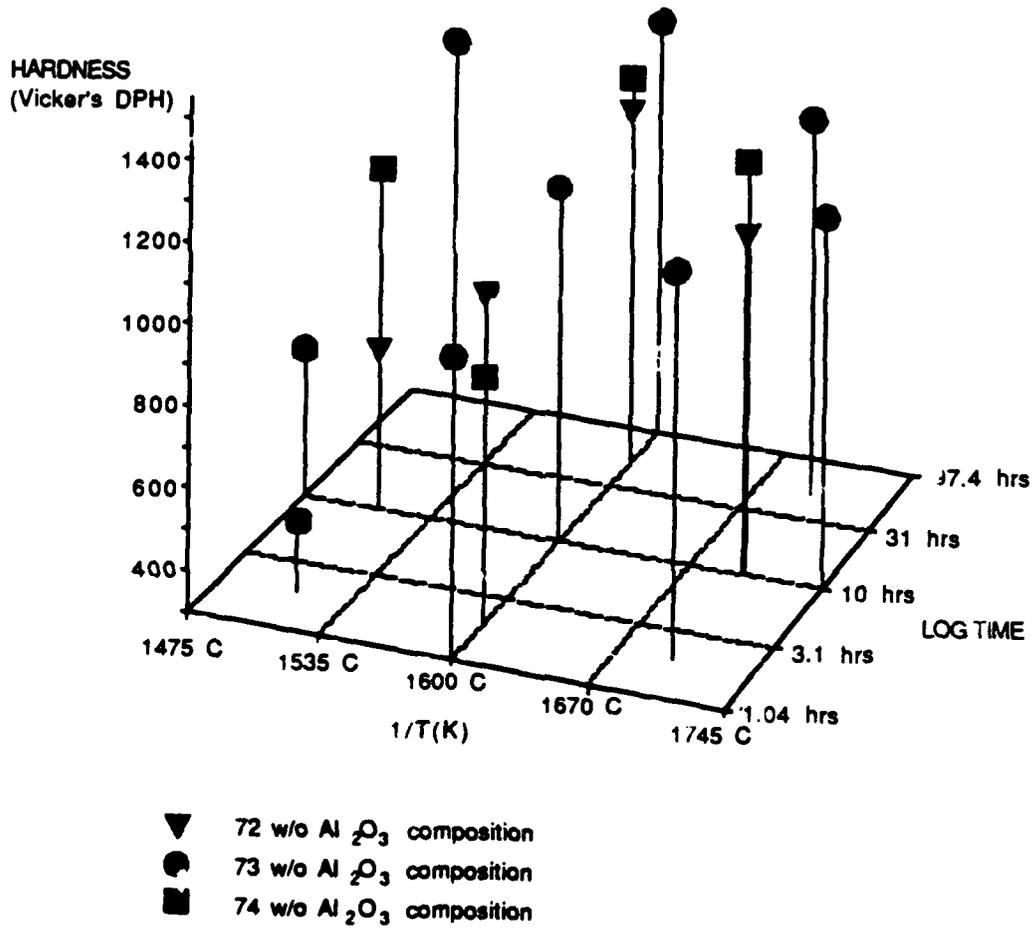
Figure 4

Hardness data vs 1/T(K) and Log time
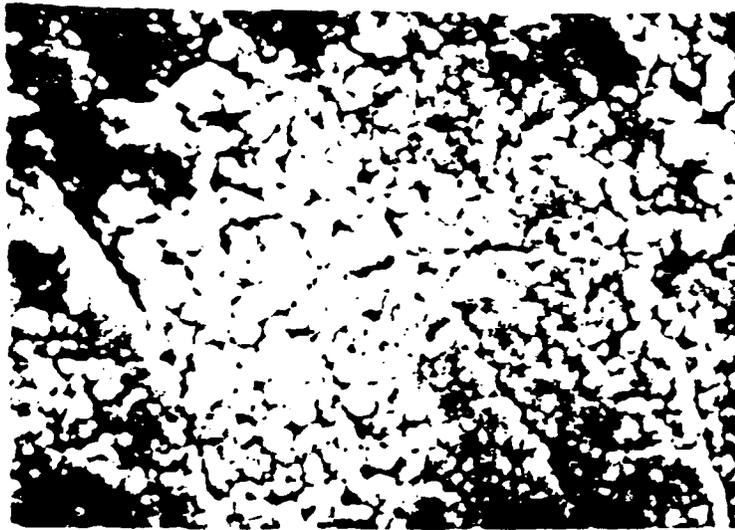
Magnification 12,500x

Figure 5. Micrograph and histogram of Sample 1,
73 w/o Al_2O_3 mullite heat treated at 1510 C for 2 hours.

Magnification 12,500x

Log Grain Size

Figure 6. Micrograph and histogram of Sample 2
72 w/o Al_2O_3 mullite heat treated at 1510 C for 10 hours

Magnification 12,500x

Figure 7. Micrograph and histogram of Sample 3
74 w/o Al_2O_3 mullite heat treated at 1510 C for 10 hours

Magnification 6,250x

Figure 8. Micrograph and histogram of Sample 4
73 w/o Al_2O_3 mullite heat treated at 1510 C for 50 hours

Magnification 12,500x

Figure 9. Micrograph and histogram of Sample 5
72 w/o Al$_2$O$_3$ mullite heat treated at 1600 C for 2 hours

Magnification 6,250x
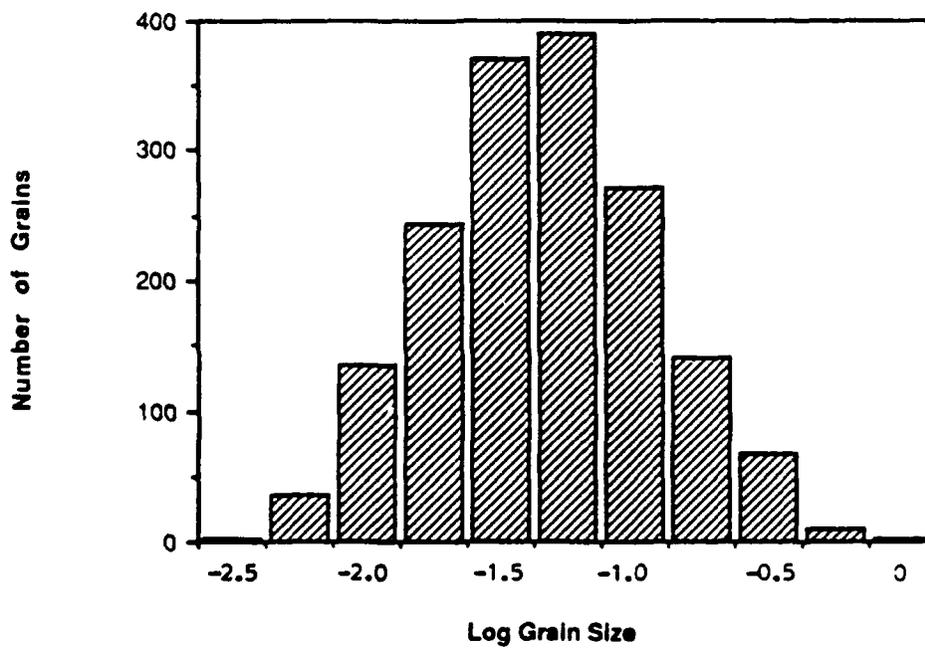

Figure 10. Micrograph and histogram of Sample 6
74 w/o Al$_2$O$_3$ mullite heat treated at 1600 C for 2 hours

Magnification 2,800x
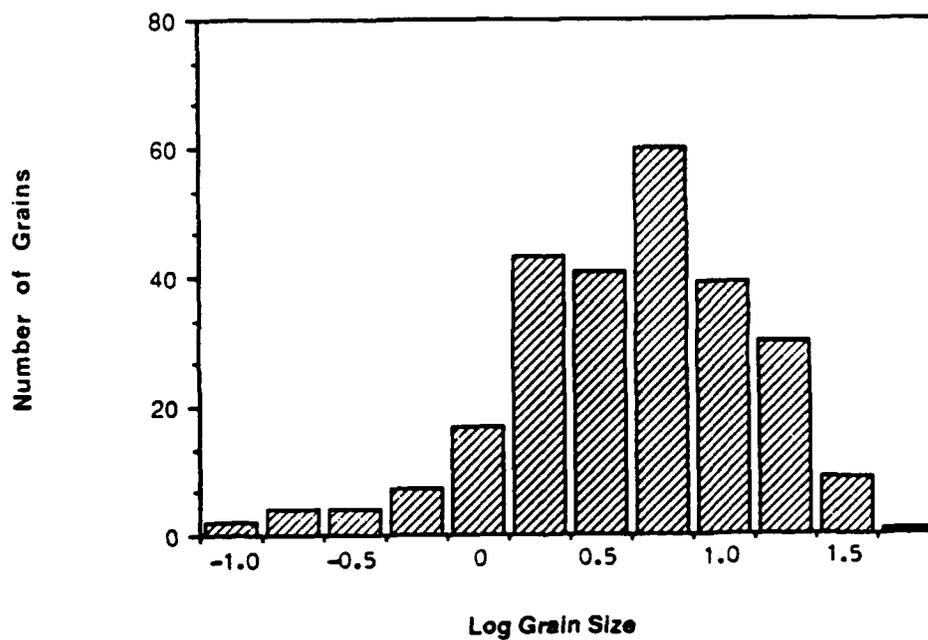
Figure 11. Micrograph and histogram of Sample 7
72 w/o Al_2O_3 mullite heat treated at 1600 C for 50 hours
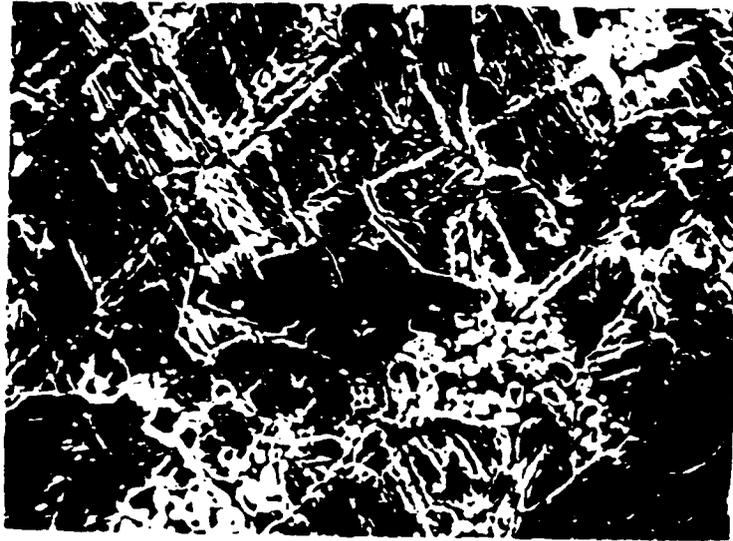
Magnification 2,500x
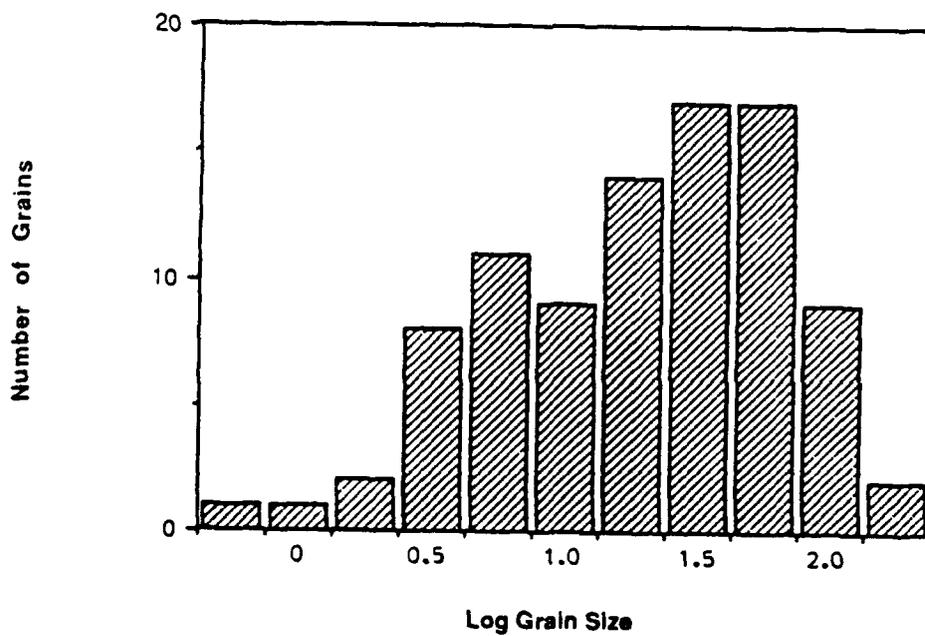
Figure 12. Micrograph and histogram of Sample 8
74 w/o Al_2O_3 mullite heat treated at 1600 C for 50 hours
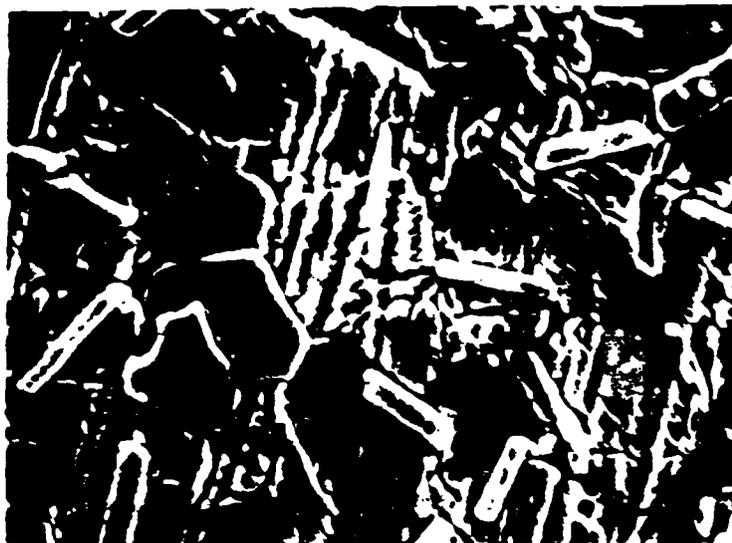
Magnification 6,250x
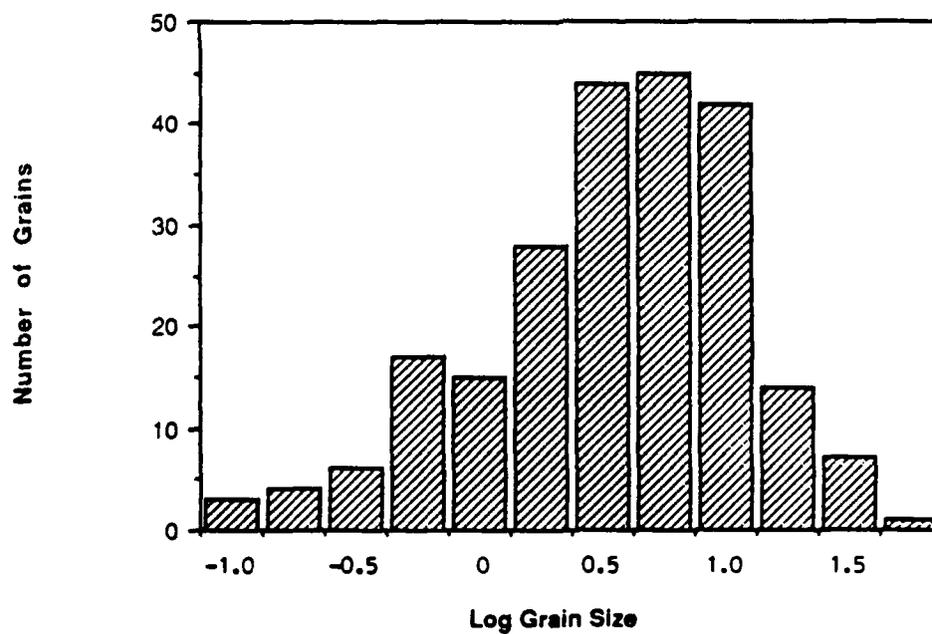
Figure 13. Micrograph and histogram of Sample 9
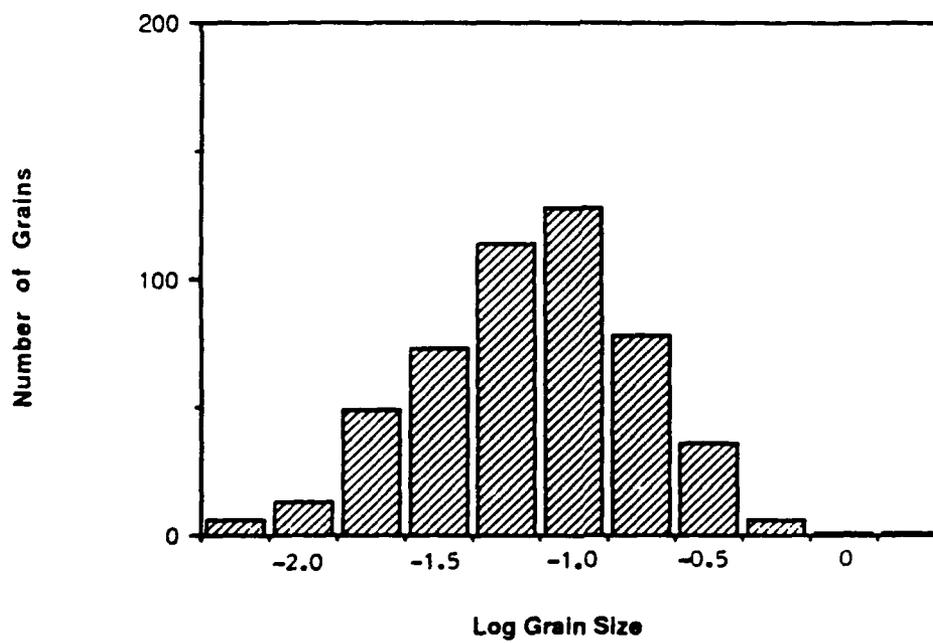73 w/o Al$_2$C, mullite heat treated at 1700 C for 2 hours
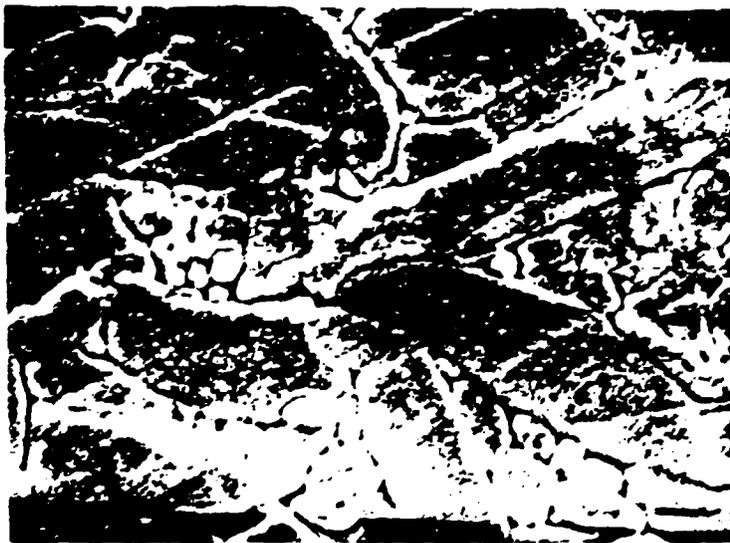
Magnification 6,250x
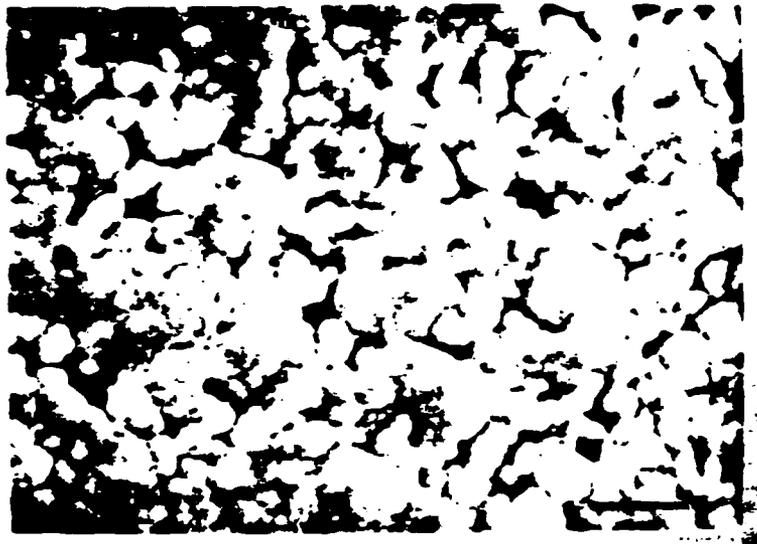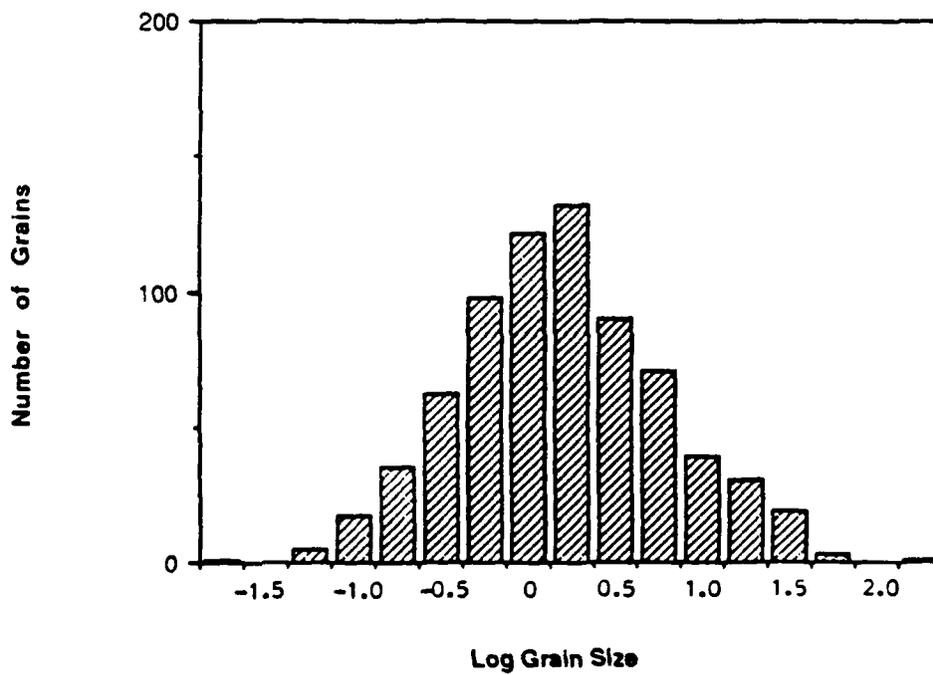

Figure 14. Micrograph and histogram of Sample 10
72 w/o Al_2O_3 mullite heat treated at 1700 C for 10 hours
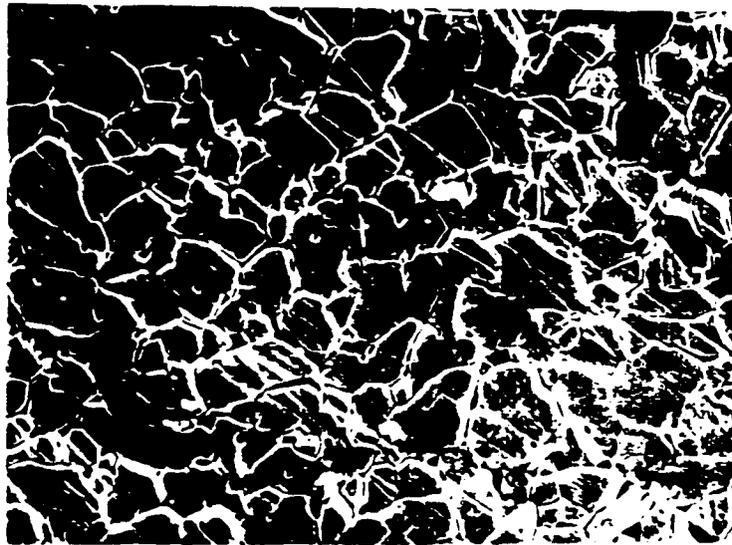
Magnification 1,250x
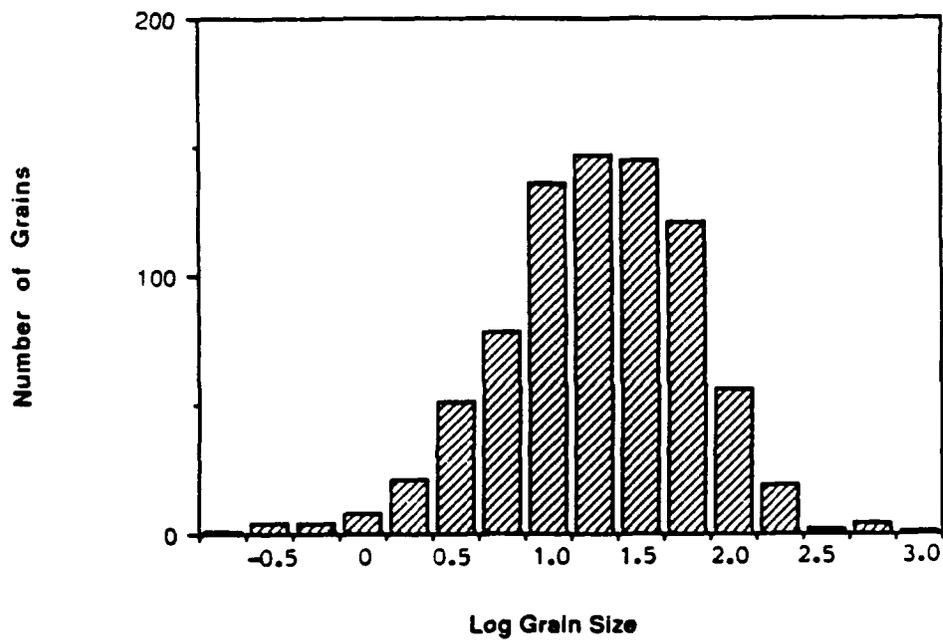
Figure 15. Micrograph and histogram of Sample 11
74 w/o Al_2O_3 mullite heat treated at 1700 C for 10 hours

Magnification 2,500x
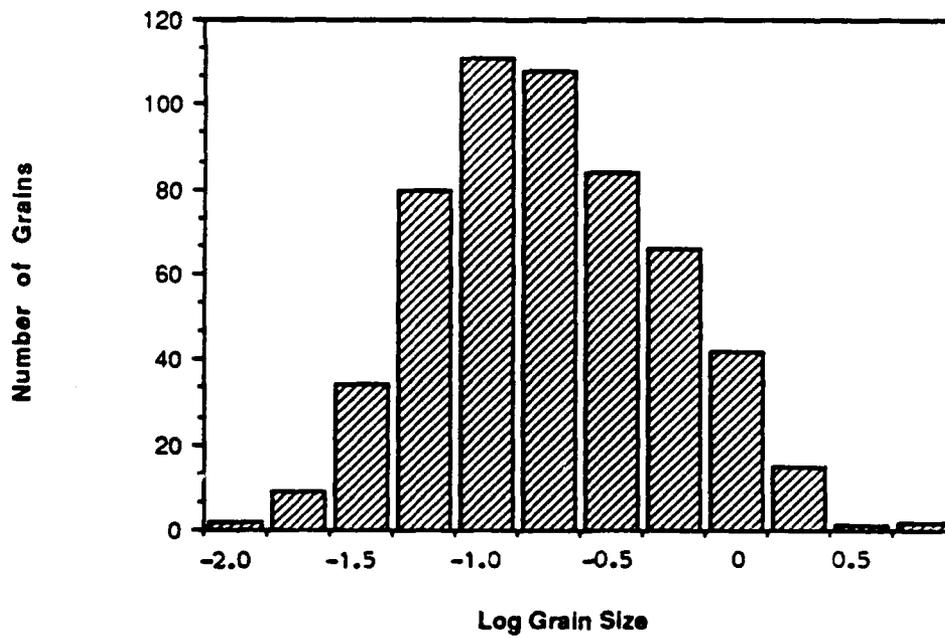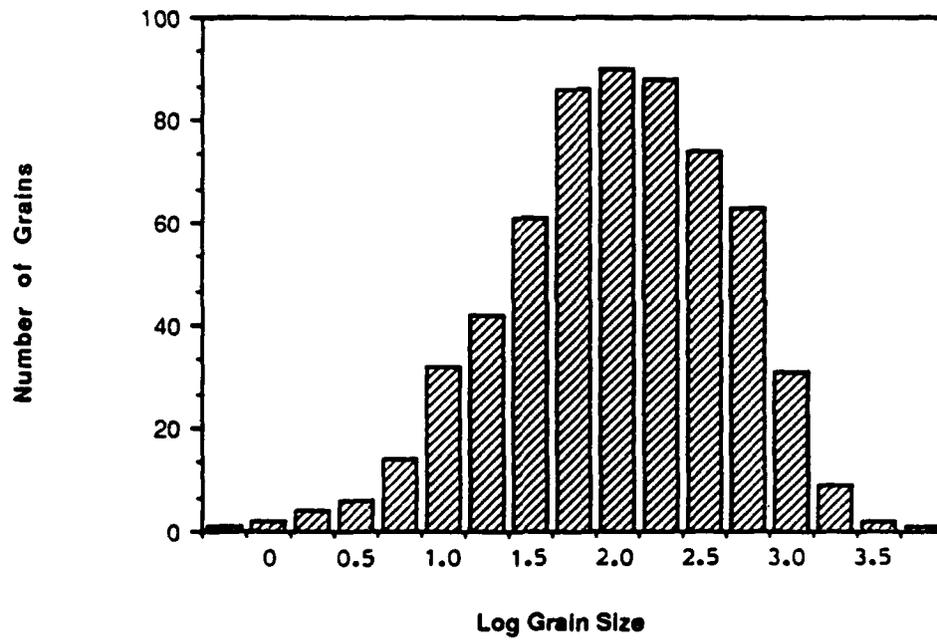

Figure 16. Micrograph and histogram of Sample 12
73 w/o Al_2O_3 mullite heat treated at 1700 C for 50 hours
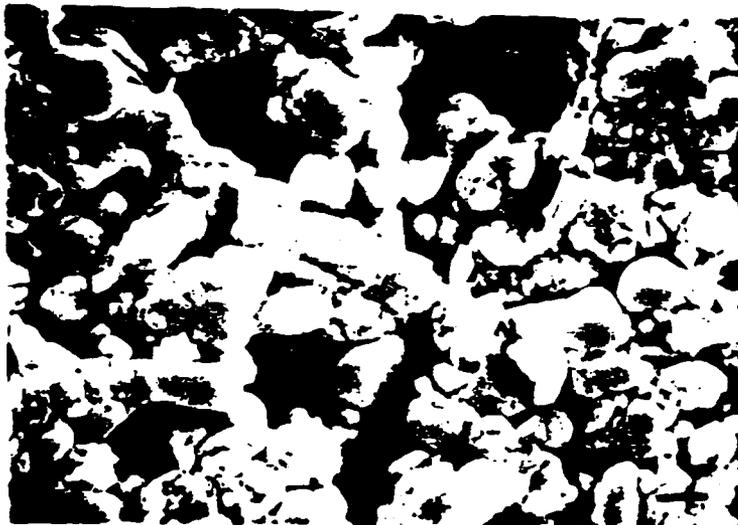
Magnification 6,250x
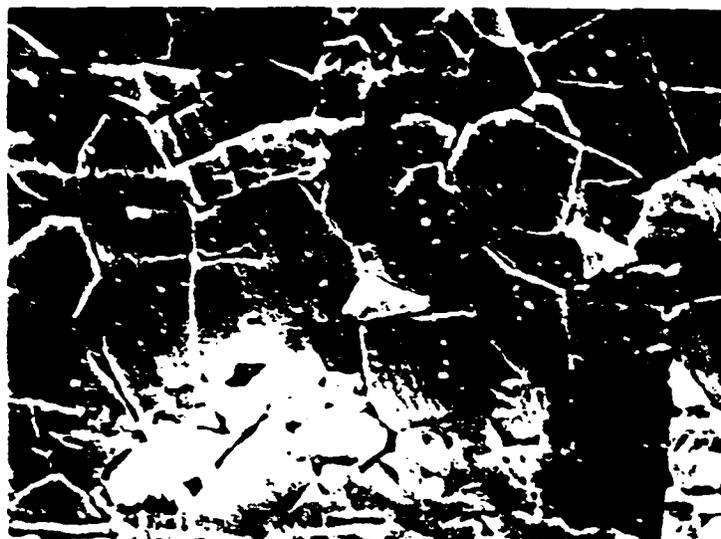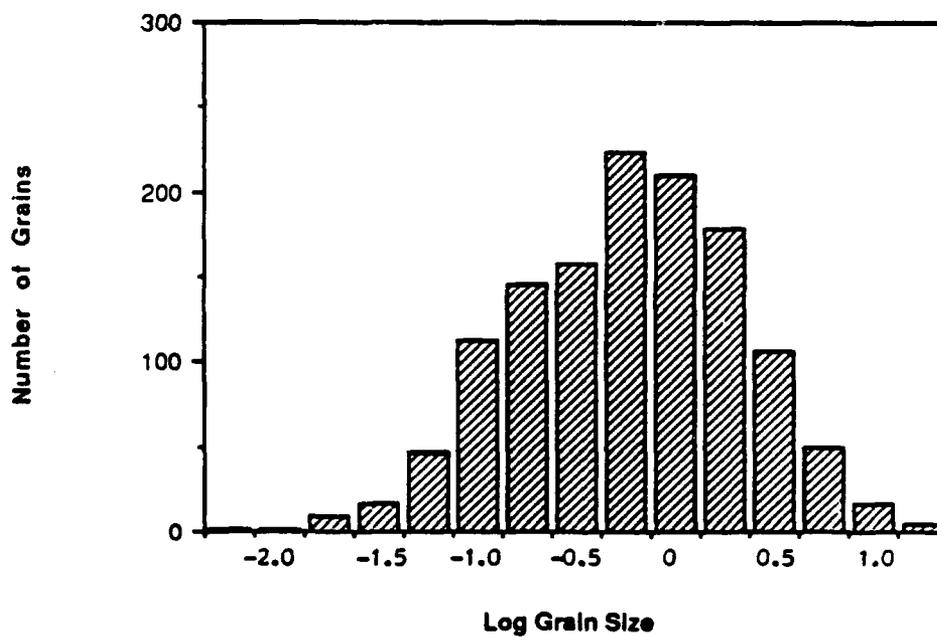

Figure 17. Micrograph and histogram of Sample 13
73 w/o Al_2O_3 mullite heat treated at 1600 C for 10 hours

Magnification 6,250x

Number of Grains

Log Grain Size
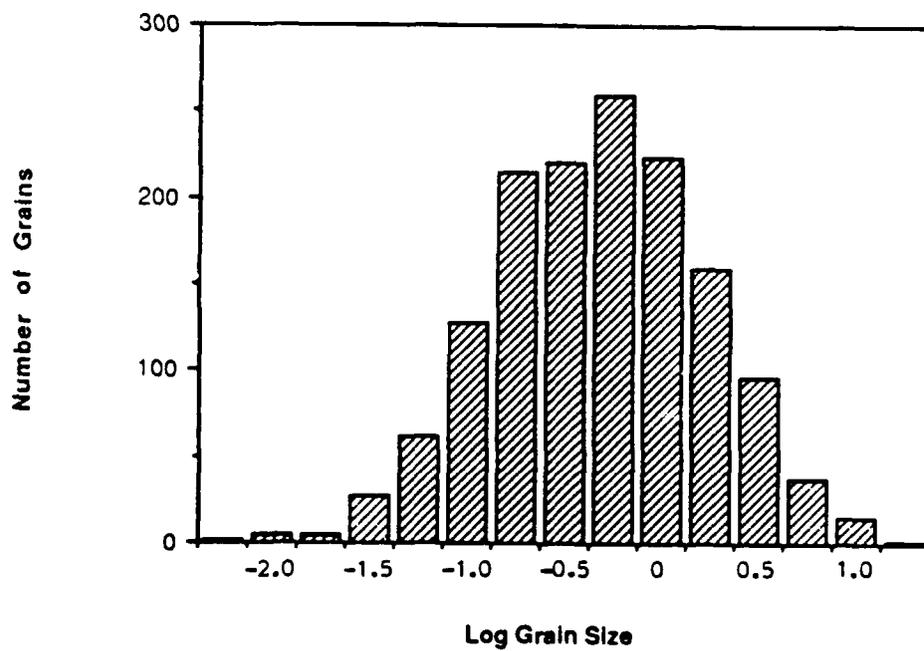
Figure 18. Micrograph and histogram of Sample 14
73 w/o Al$_2$O$_3$ mullite heat treated at 1600 C for 10 hours
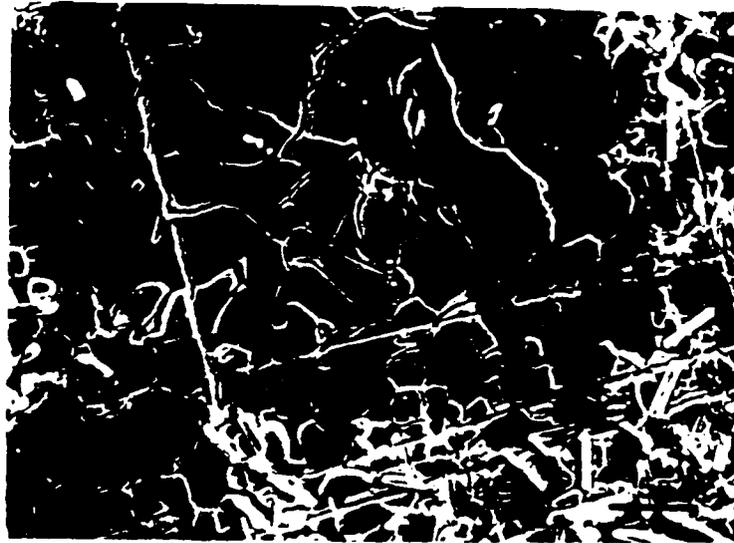
Magnification 2,400x
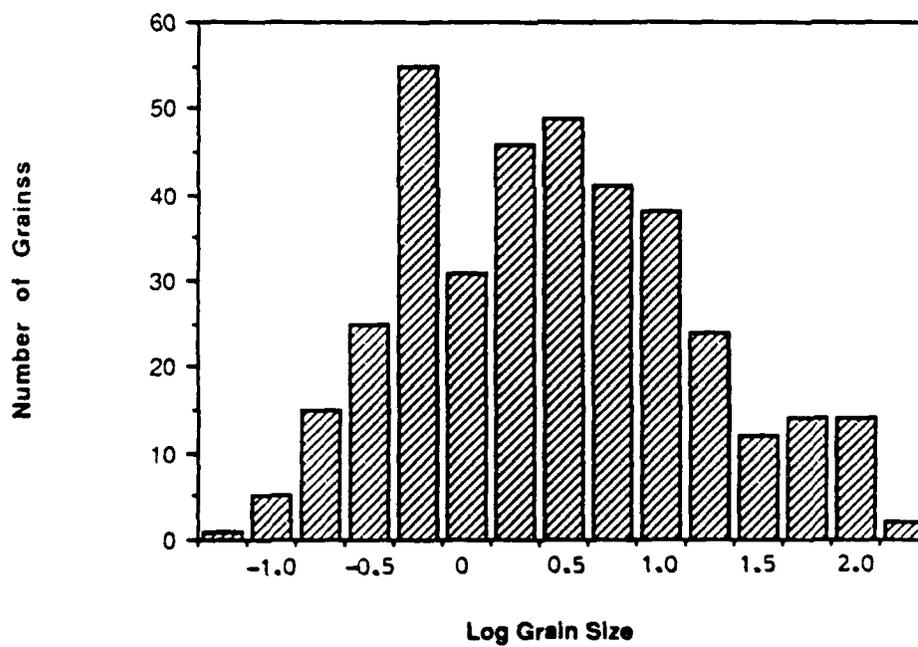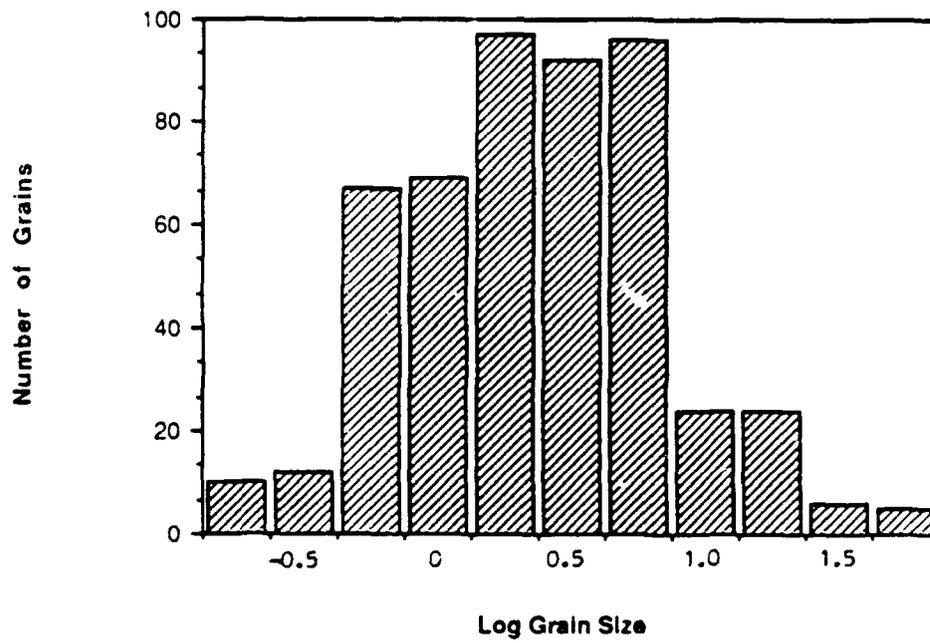

Figure 19. Micrograph and histogram of Sample 15
73 w/o Al_2O_3 mullite heat treated at 1600 C for 10 hours
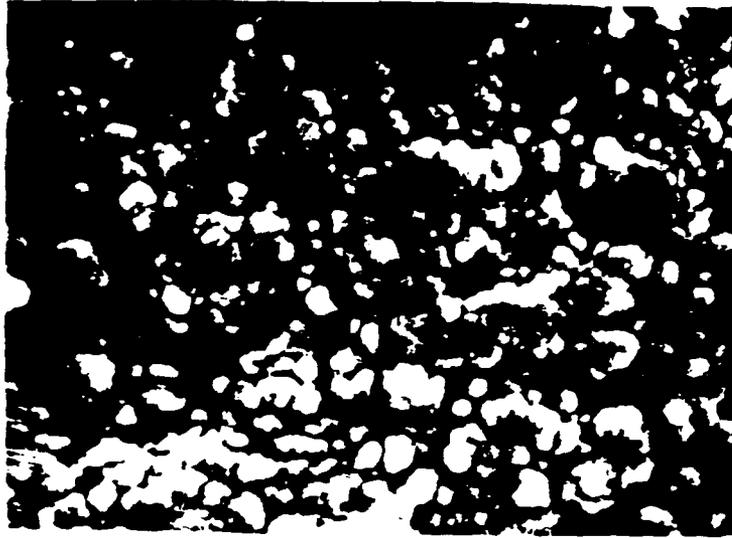
Magnification 12,500x
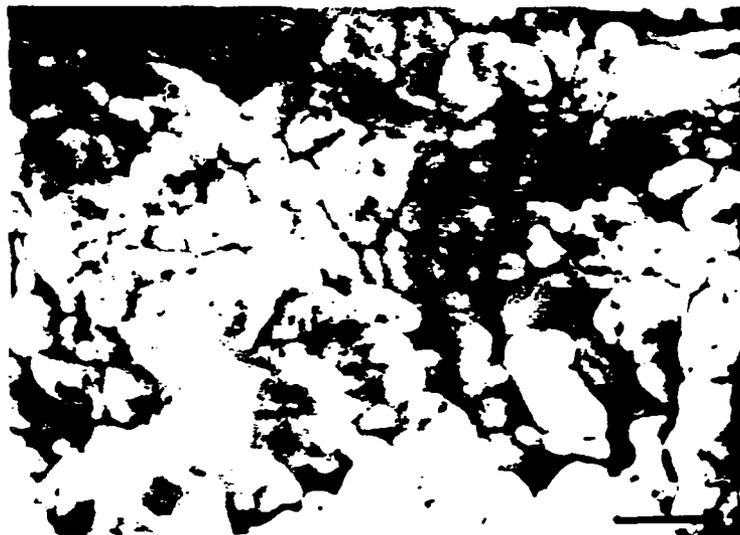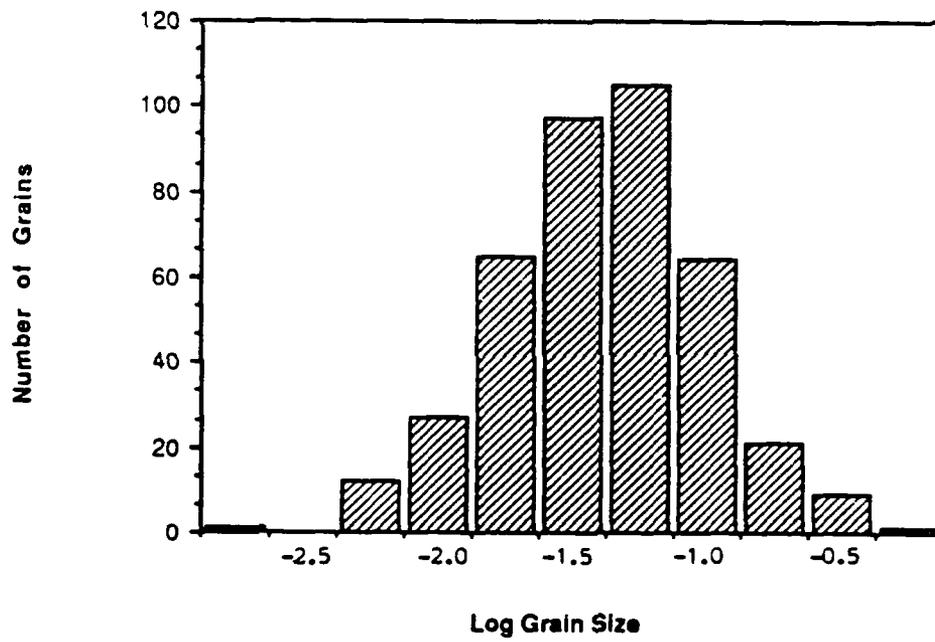

Figure 20. Micrograph and histogram of Sample 16
73 w/o Al_2O_3 mullite heat treated at 1475 C for 10 hours
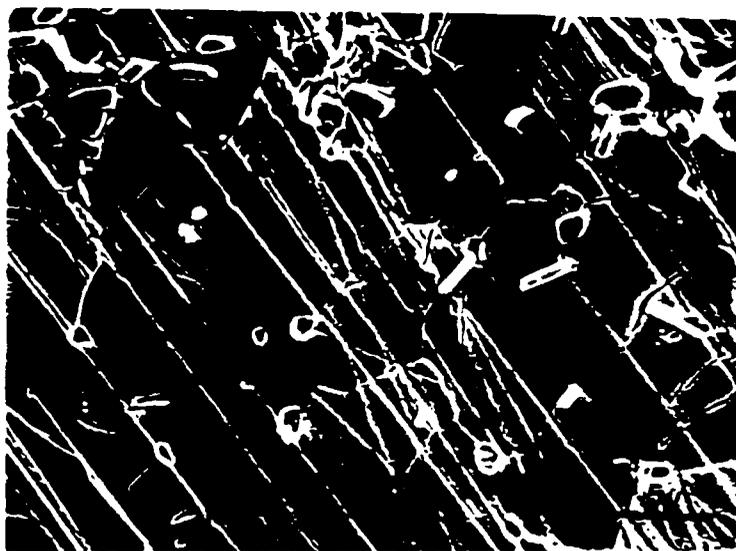
Magnification 2,500x
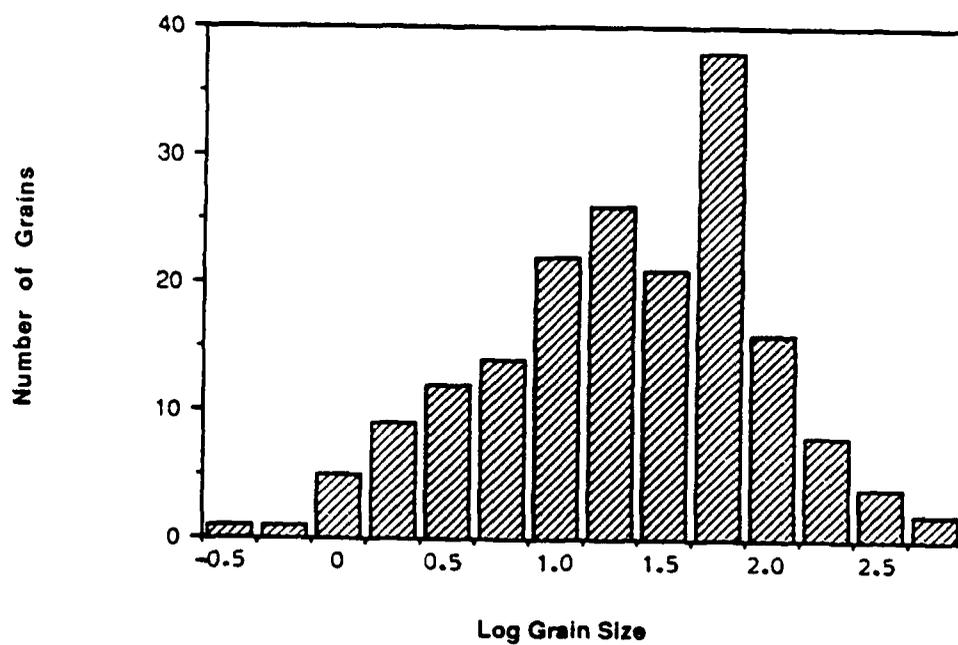
Figure 21. Micrograph and histogram of Sample 17
73 w/o Al_2O_3 mullite heat treated at 1475 C for 10 hours
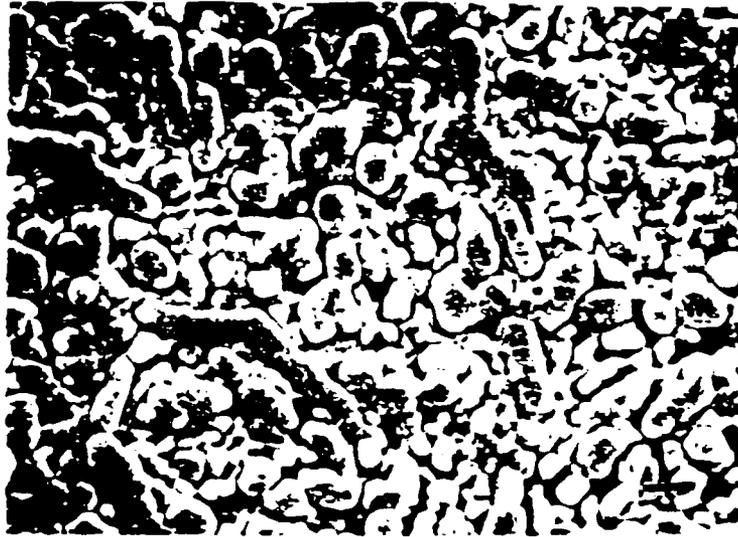
Magnification 6,250x
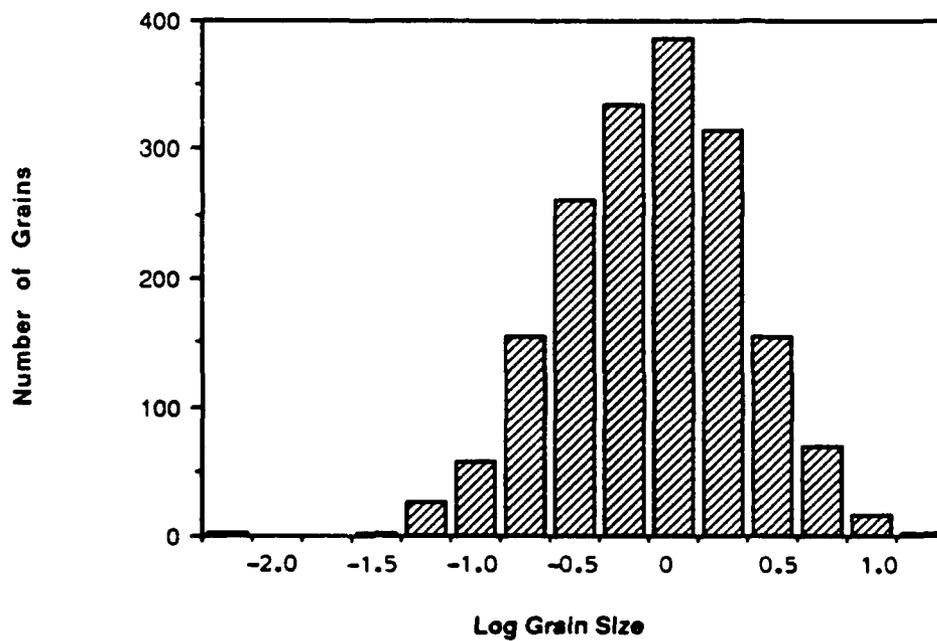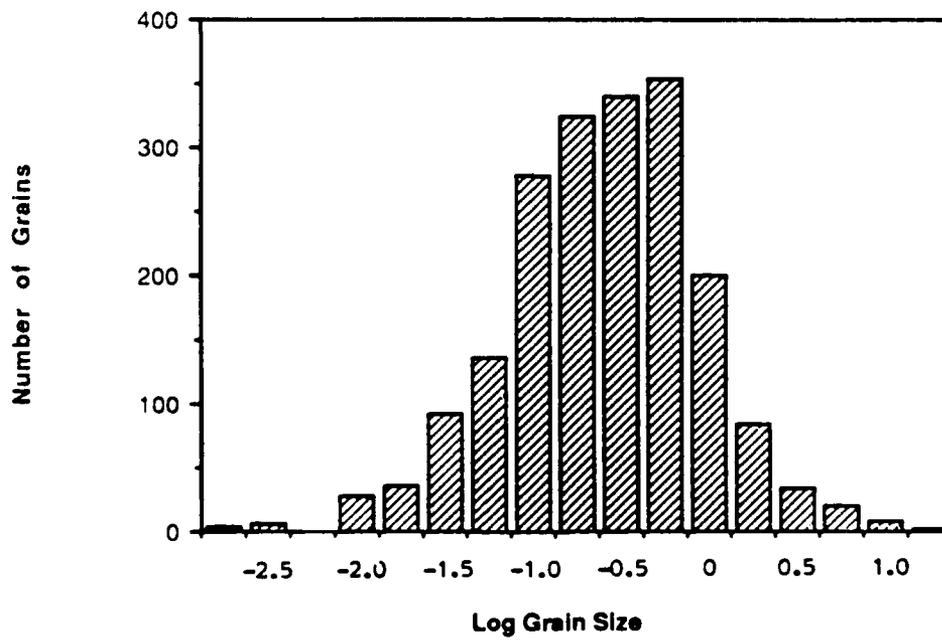

Figure 22. Micrograph and histogram of Sample 18
73 w/o Al$_2$O$_3$ mullite heat treated at 1600 C for 1.04 hours
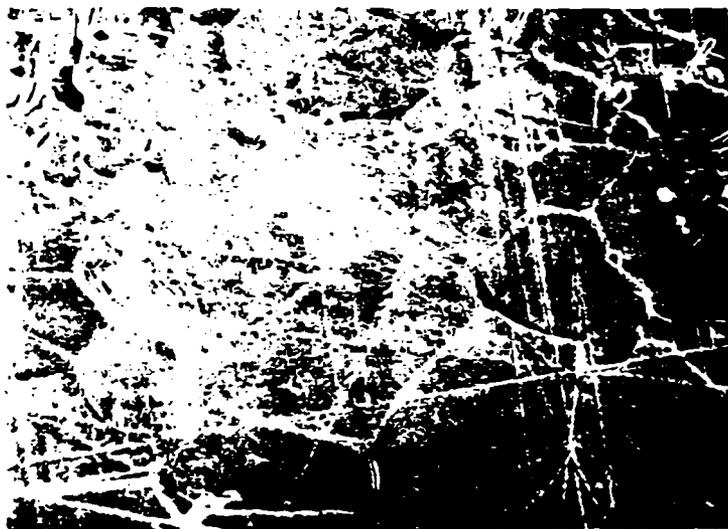
Magnification 1,250x
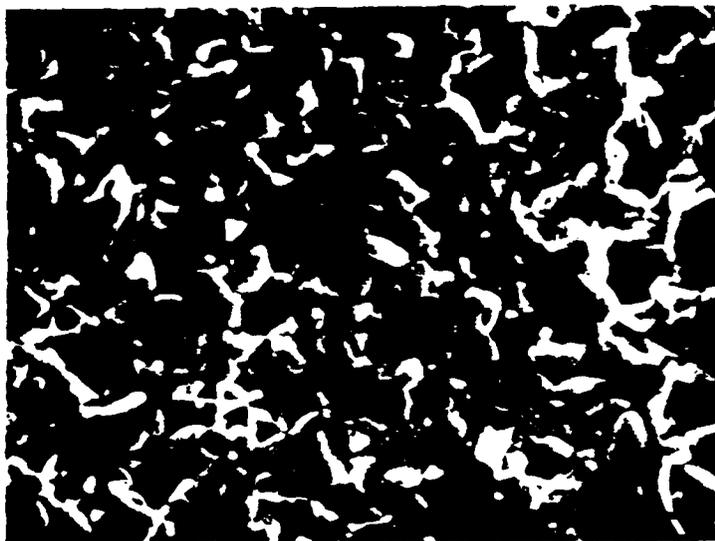

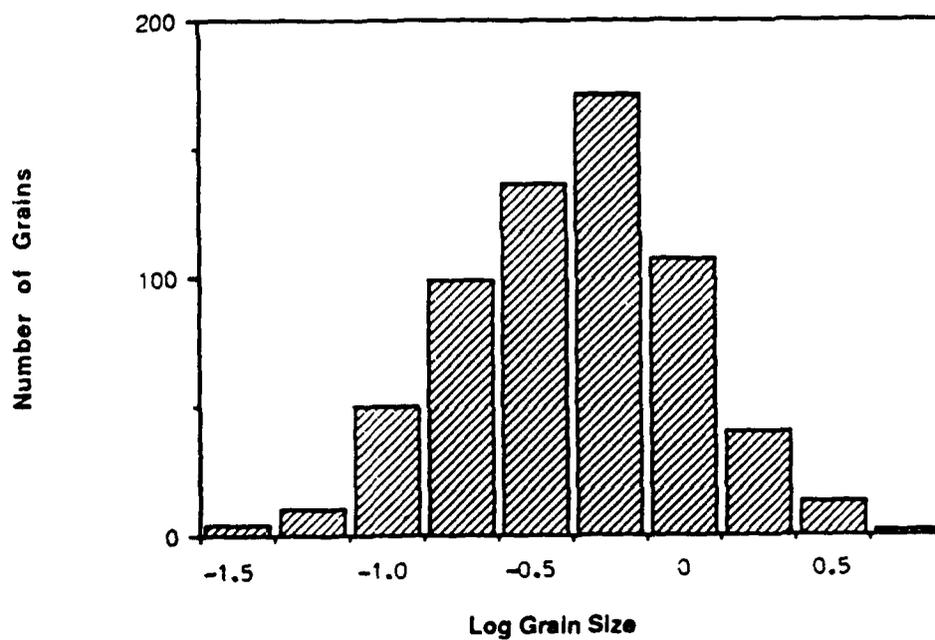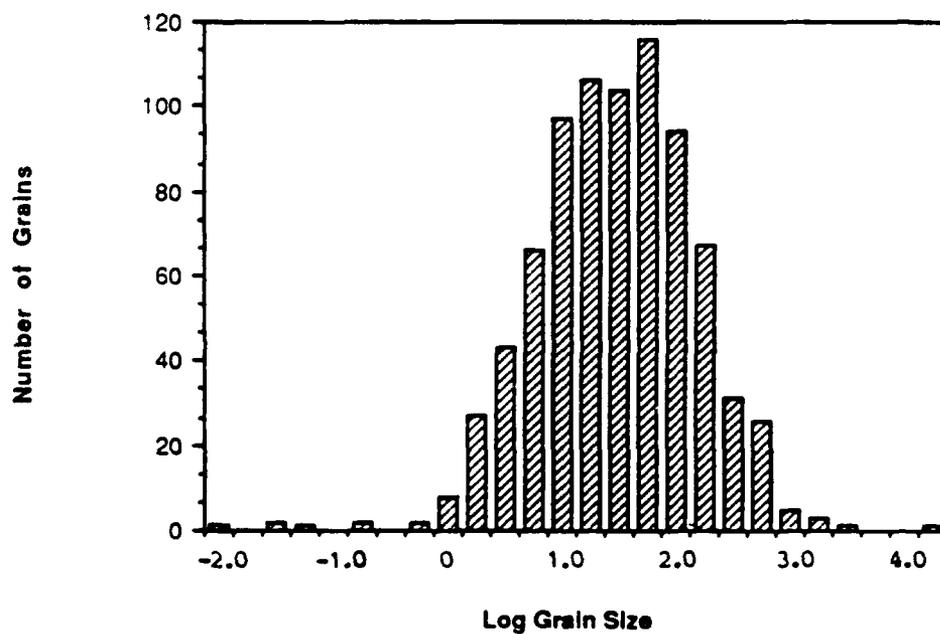Figure 23. Micrograph and histogram of Sample 19
73 w/o Al₂O₃ mullite heat treated at 1600 C for 97.4 hours
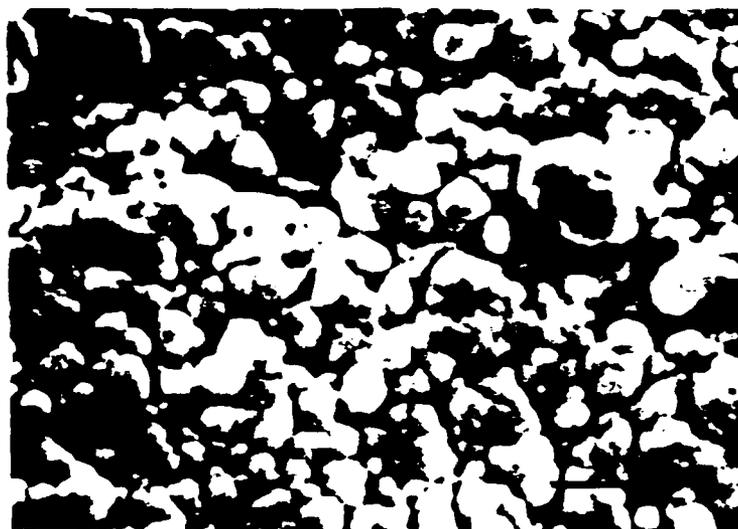
Magnification 12,500x
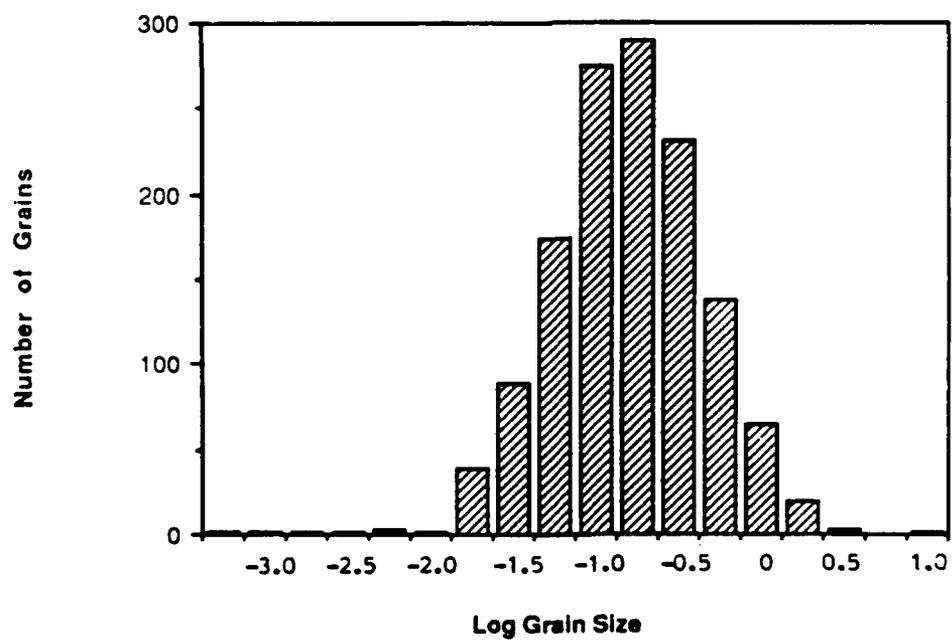
Figure 24. Micrograph and histogram of Sample 72
72 w/o Al_2O_3 mullite calcined, but not further heat treated.

Magnification 12,500x

Log Grain Size
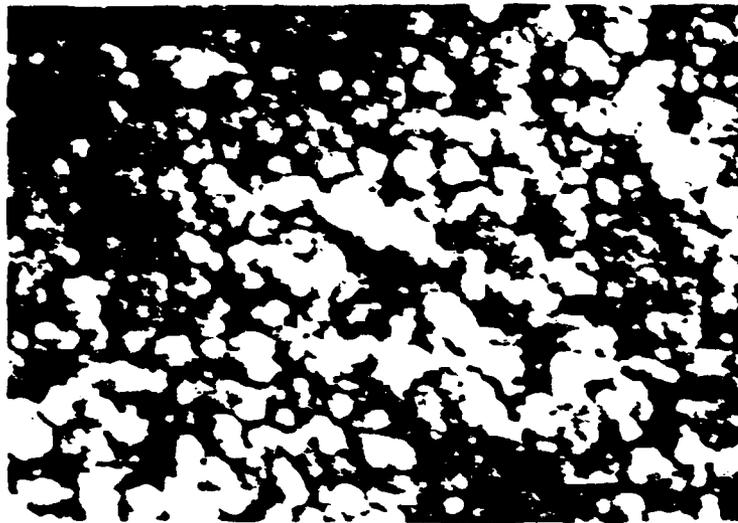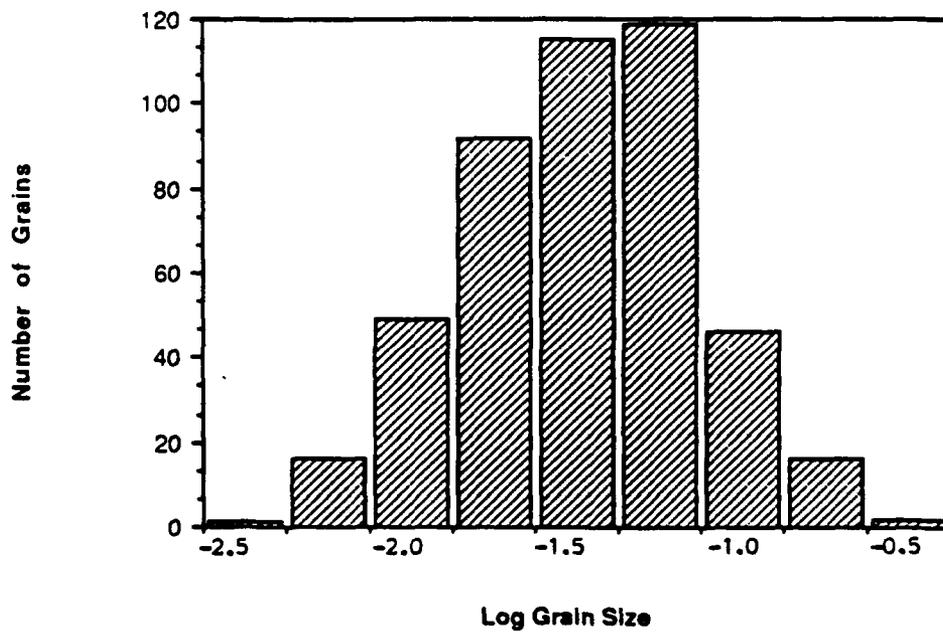
Figure 25. Micrograph and histogram of Sample 73
73 w/o $Al_2 O_3$ mullite calcined, but not further heat treated.
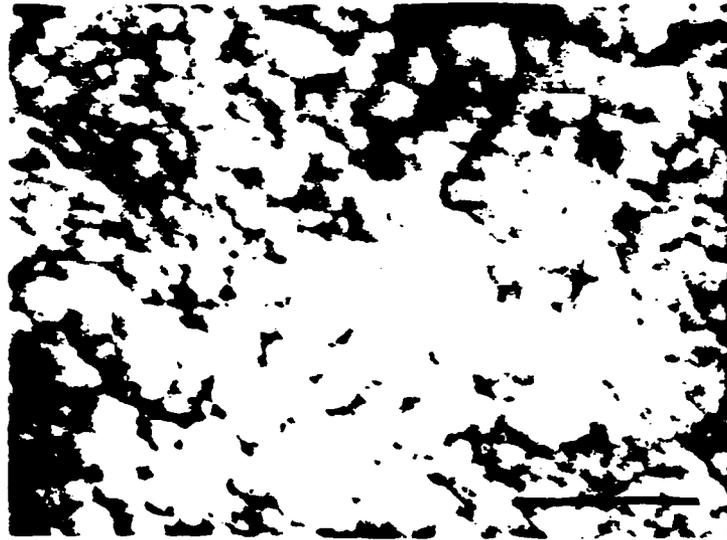
Magnification 25,000x
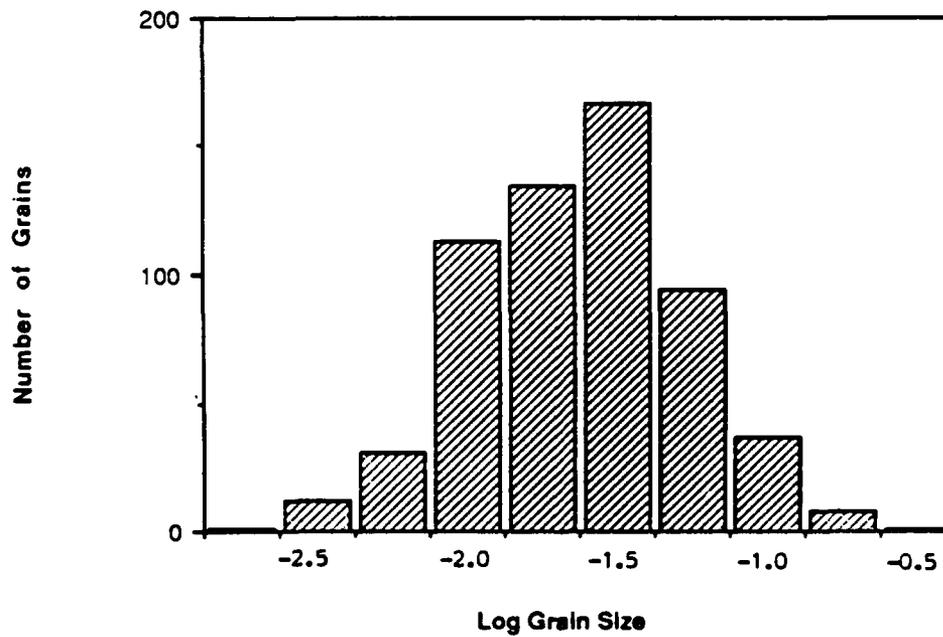
Figure 26. Micrograph and histogram of Sample 74
74 w/o Al_2O_3 mullite calcined, but not further heat treated.

$$\rho = 3.126 + 0.088A + 0.111B + 0.007C - 0.04A^2 - 0.07B^2 - 0.10C^2 - 0.13AB +$$

$$0.02AC - 0.04BC \qquad (4.2)$$

$$Hardness = 1046 + 161A + 172B + 67C - 12.2A^2 + 35.75B^2 + 43.75C^2 - 207AB -$$

$$70.5AC + 73.5BC. \qquad (4.3)$$

For the 73 w/o Al_2O_3 composition, $C=0$, so the C, C^2, AC, and BC terms drop out. The resulting equations are shown as a 3-dimensional plot in Figures 27 through 29. The slope, n of the function with log time appears to increase with time.

Assuming the squared terms are neglible, the modelling equations in their uncoded form are

$$\overline{Log(L)} = -8.955 - 31337 \left(\frac{1}{T}\right) + 0.5132(\log t) + 0.335(\text{composition}) \qquad (4.4)$$

$$\rho = 4.19 - 3251 \left(\frac{1}{T}\right) + 0.069 (\log t) + 0.007 (\text{composition}) \qquad (4.5)$$

$$Hardness = -915 - 6 \times 10^6 \left(\frac{1}{T}\right) + 107 (\log t) + 67 (\text{composition}). \qquad (4.6)$$

At the 73 w/o Al_2O_3 composition, the equation becomes

$$Log(\bar{L}) = 15.5 - 31337 (1/T) - 0.513 \log t, \qquad (4.7)$$

which is in the same form as Equation 3.5. This equation can be converted to the same form as Equation 2.7 as discussed in Section 2.1 of the Experimental Procedures. The equation becomes

$$\bar{L} = 5 \times 10^6 e^{-260(\text{KJ/mole-K})/RT} t^{0.51}. \qquad (4.8)$$

Thus the constants for equation 3.5 are
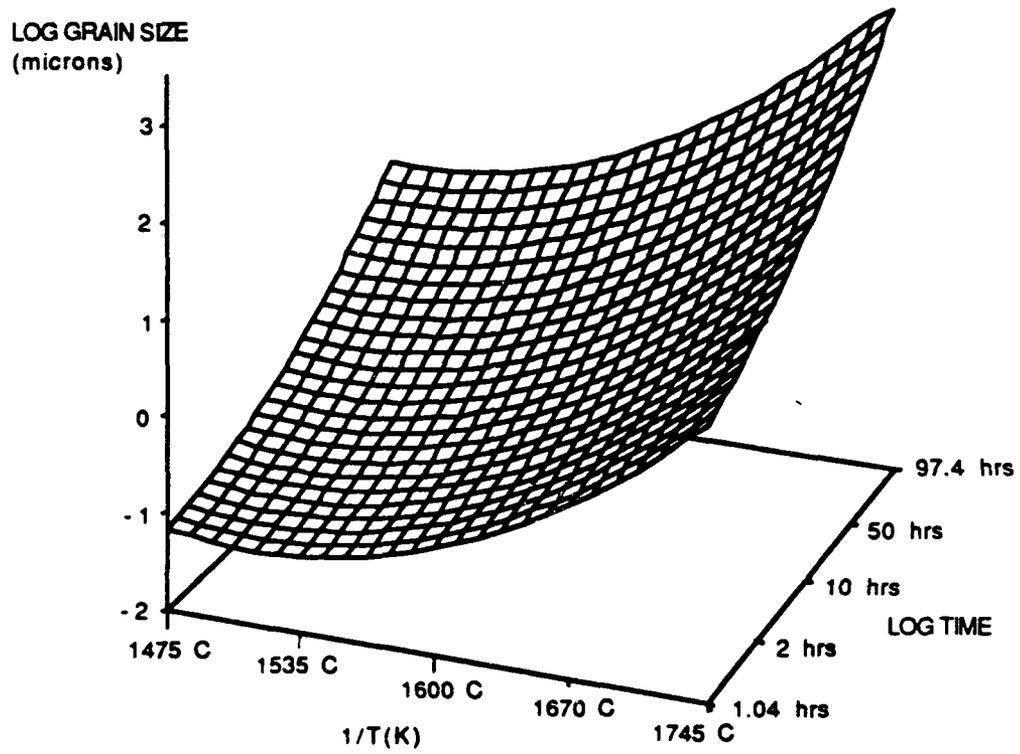
Figure 27

Predicted Log Grain Size vs 1/T(K) and Log time for 73w/o Al$_2$O$_3$ mullite
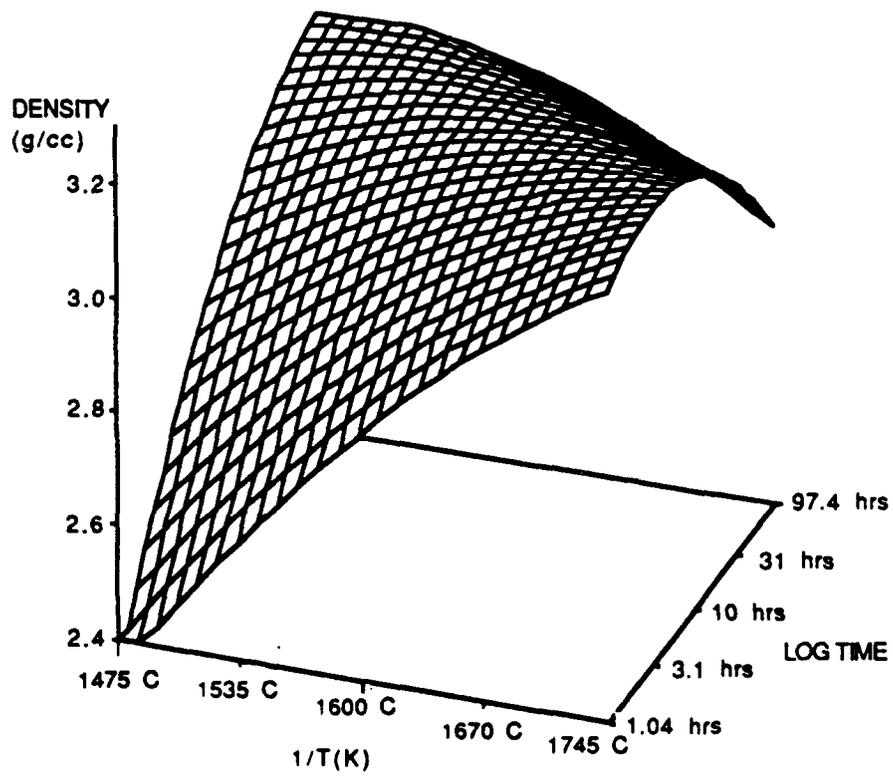
Figure 28

Predicted Density vs 1/T(K) and Log time
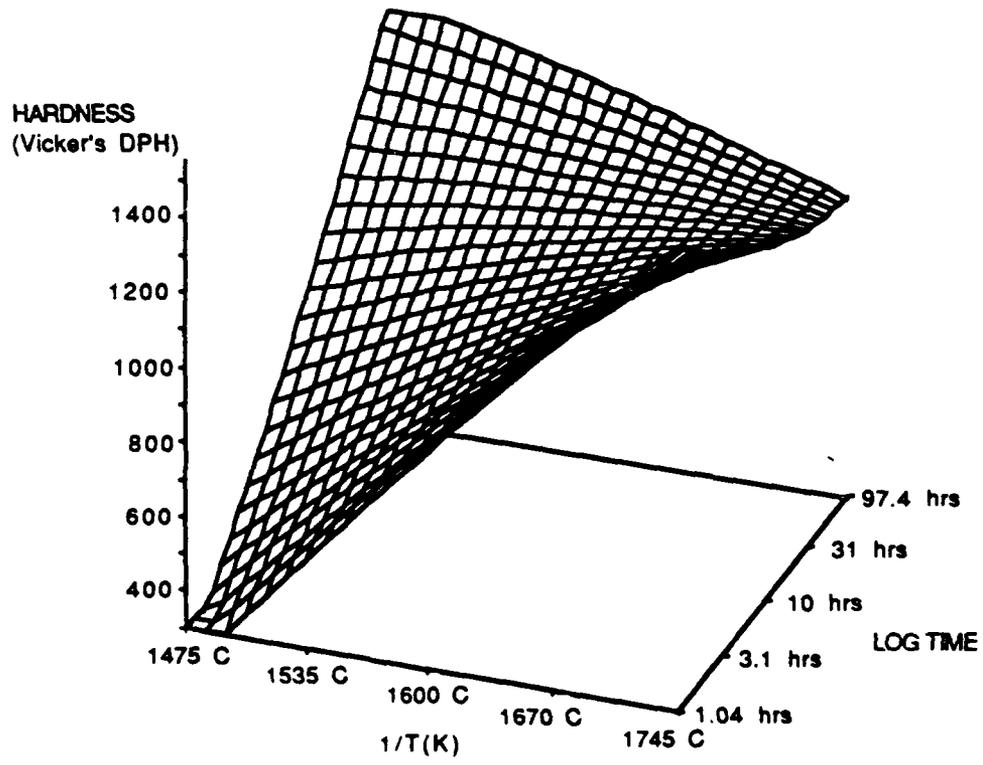
Figure 29

Predicted hardness vs 1/T(K) and Log time

$$n = 0.51$$

$$Q = 260 \text{ KJ/mole-K}$$

$$K = 5 \times 10^6.$$

Log grain size is plotted against log time for each composition and heat treatment temperature in Figure 30. A line is fitted to each set of data points. The slope of each line is the value of n for that particular temperature and composition. The values of n are found to range from 0.45 to 0.55 with a mean of 0.50 and a standard deviation of 0.04. There is no clear trend of n increasing or decreasing with temperature or composition.

A Kolmogorov D test statistic was calculated for each sample to determine goodness of fit with a normal and lognormal distribution as explained in the experimental procedures section. Table 4 lists the skewness of the sample distribution, the Kolmogorov D statistic and the probability of obtaining a D statistic that value or higher from a random sample of a population with a normal distribution. These values are included for both the grain size distributions and the log grain size distributions.

The probability of the D value being consistent with a normal distribution was less than 0.01 for all samples except sample 8 which was 74 w/o Al_2O_3 mullite heated 50 hours at 1600°C, indicating that the distributions are not normal. The probability of the D value being consistent with a lognormal distribution ranged from less than 0.01 to greater than 0.15. Samples 4, 7, 9, 13, and 18 had probability values less than 0.01, indicating that these distributions were not lognormal. Samples 16, 19, and 73 had probability values greater than 0.15, indicating that those distributions were very close to being lognormal.

The skewness of the sample grain size distributions range from 0.53 to 4.44. The skewness of the sample log grain size distributions range from -0.63 to 0.30. These statistics show that the grain size distribution des not match a normal distribution, but

□   Log GS

○   LGS 1510,73

●   LGS 1700,73
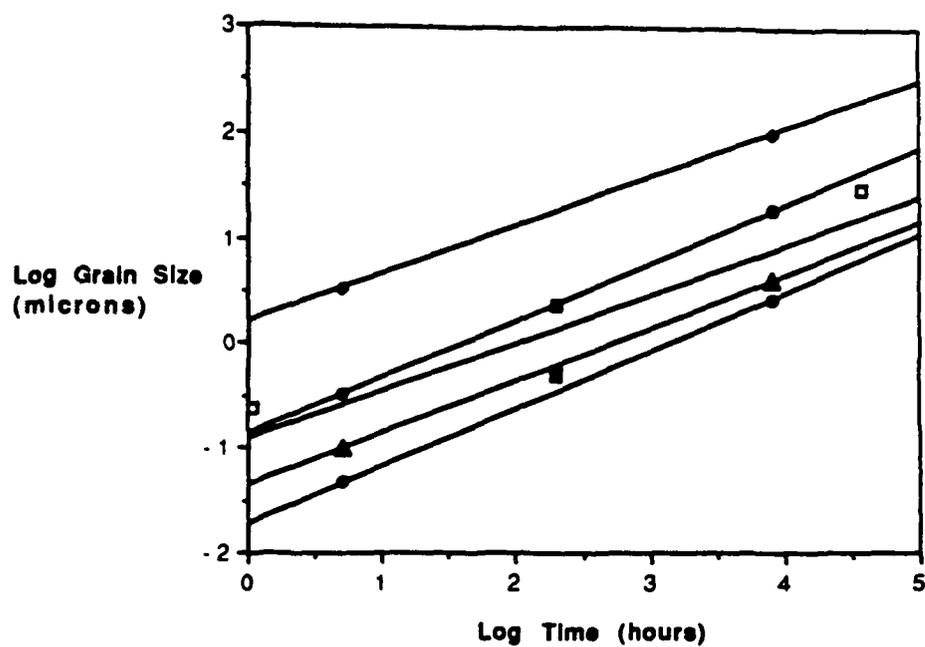
▲   LGS 1600,72

●   LGS 1600,74

□ Log GS = - 0.91190 + 0.45628 Log time
         R^2 = 0.793

○ Log GS = - 1.7111 + 0.54986 Log time
         R^2 = 1.000

● Log GS = 0.21353 + 0.45666 Log time
         R^2 = 1.000

▲ Log GS = - 1.348ა + 0.50326 Log time
         R^2 = 1.000

% Log GS = - 0.84675 + 0.54365 Log time
         R^2 = 1.000

Figure 30

Log Grainsize vs Log time by temperature and composition

Table 4

Distribution Statistics

Sample #	Normal			Lognormal		
	Skewness	D	Prob > D	Skewness	D	Prob > Π
1	1.55	0.090	<0.01	0.128	0.020	0.113
2	1.39	0.084	<0.01	-0.101	0.035	0.125
3	1.59	0.117	<0.01	0.167	0.038	0.046
4	1.87	0.165	<0.01	0.297	0.057	0.010
5	1.16	0.096	<0.01	-0.135	0.020	0.076
6	1.04	0.092	<0.01	-0.142	0.040	0.051
7	0.68	0.082	<0.01	-0.633	0.070	0.010
8	0.53	0.084	0.11	-0.477	0.096	0.037
9	0.77	0.092	<0.01	-0.552	0.082	0.010
10	2.05	0.153	<0.01	0.183	0.034	0.034
11	1.69	0.095	<0.01	-0.346	0.036	>0.015
12	1.38	0.099	<0.01	-0.333	0.038	0.031
13	1.28	0.095	<0.01	-0.203	0.040	0.010
14	1.47	0.102	<0.01	-0.142	0.025	0.030
15	1.65	0.098	<0.01	0.081	0.039	0.056
16	1.19	0.100	<0.01	-0.024	0.037	>0.150
17	2.76	0.112	<0.01	-0.312	0.071	0.028
18	2.12	0.100	<0.01	-0.460	0.040	0.010
19	4.44	0.146	<0.01	-0.313	0.025	>0.150
72	1.67	0.095	<0.01	-0.313	0.024	0.072
73	0.97	0.074	<0.01	0.040	0.031	>0.150
74	1.10	0.081	<0.01	-0.060	0.033	0.121

more closely matches a lognormal distribution.

Hardness is plotted against density for each compostion in Figure 31, and a line fitted to each set of data points. The figure shows that there is an increase in hardness with density. There is considerable scatter of the data about the lines and the coefficients of determination, R^2, ranges from 0.466 to 0.797, indicating that other factors beside density have a significant effect on hardness. The slope of the lines appear independent of composition. The hardness and density of pure alumina falls along the hardness vs density curve for mullite.
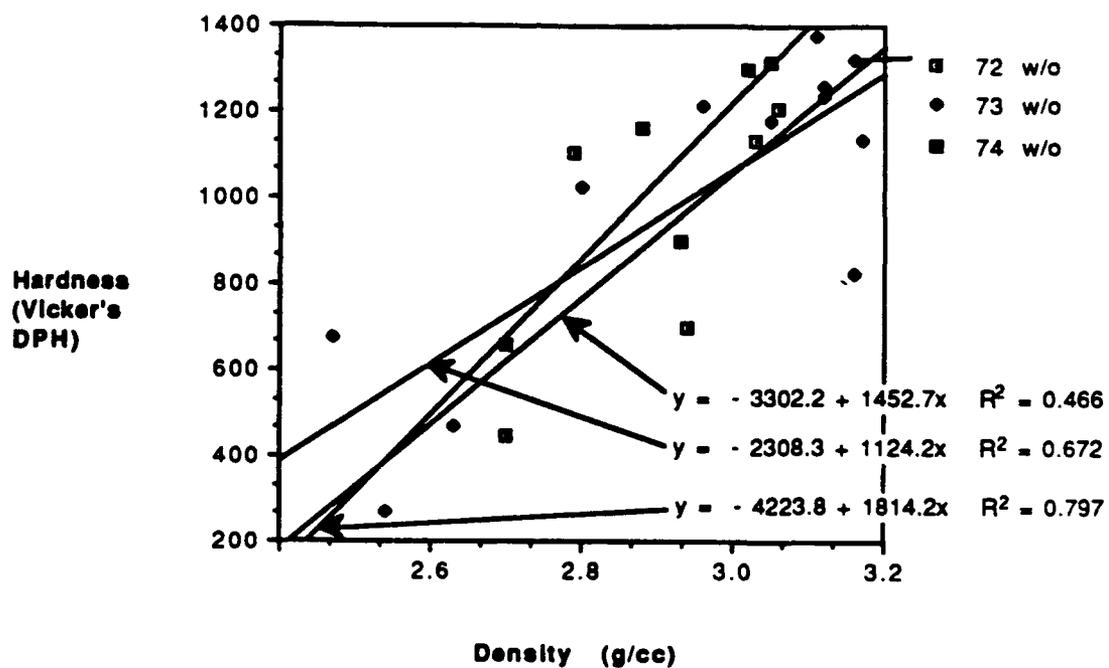
Figure 31

Hardness vs Density by Composition

temperatures. This may be because pores trapped within the grains of the higher temperature samples can not reach the surface of the samples as easily and quickly as pores located at the higher energy grain boundaries.

Certain samples had a bimodal distribution of grain sizes with small grains in porous regions of the samples and large grains in denser regions of the samples. This indicates that the starting powder may not have been completely homogeneous. In future studies more care should be taken to ensure that the samples remain homogenous throughout all the processing procedures.

15. Doremus, R.H., *Rates of Phase Transformations*, Academic Press, Inc., New York, 1985.

16. DeHoff, R.T., "The Determination of the Size Distribution of Ellipsiodal Particles from Measurements Made on Random Plane Sections", *AIME Trans.*, 224 , p. 474-477, 1962.

17. Box, G.E.P. and Behnken, D.W., "Some New Three Level Designs for the Study of Quantitative Variables", *Technometrics*, 2, p. 455-475, 1960.

18. Birnbaum, Z.W., "Numerical Tabulation of the Distribution of Kolmogorov's Statistic for Finite Sample Size", *American Statistical Association Journal*, 47, p. 425-434, 1952.

19. Smirnov, N., "Table for Estimating the Goodness of Fit of Empirical Distributions", *Annals of Mathematical Statistics*, 19, p. 279-281, 1948.

Preparation of Silicon Carbide/Aluminum Nitride Ceramics Using Organometallic Precursors

Corinna L. Czekaj,* Michael L. J. Hackney, William J. Hurley, Jr.,*·*
Leonard V. Interrante,* and Gary A. Sigel*

Departments of Chemistry and Materials Engineering, Rensselaer Polytechnic Institute,
Troy, New York   12180

Paul J. Schields and Glen A. Slack*

General Electric Research and Development Center, Schenectady, New York   12301

Solid solutions of 2H-SiC/AlN can be prepared at temperatures less than 1600°C by rapid pyrolysis ("hot drop") of mixtures of [(Me$_3$Si)$_{0.86}$((CH$_2$=CH)MeSi)$_{1.0}$(MeHSi)$_{0.35}$]$_n$ (VPS) or [MeHSiCH$_2$]$_n$ (MPCS) with [R$_2$AlNH$_2$]$_3$, where R = Et, i-Bu or simply by slow pyrolysis of the precursor mixture in the case of [Et$_2$AlNH$_2$]$_3$. In contrast, slow pyrolysis of mixtures of VPS or MPCS with [i-Bu$_2$AlNH$_2$]$_3$ yields a composite of 2H-AlN and 3C-SiC at 1600°C, which transforms into a single 2H-SiC/AlN solid solution on heating to 2000°C. The influences of the nature of the precursor and processing conditions on the structure, composition, and purity of the SiC/AlN materials are discussed. [Key words: silicon carbide, precursors, aluminum nitride, solid solutions, pyrolysis.]

I. Introduction

THE prospect of alloying SiC with other covalently bonded refractory materials, such as AlN, to achieve microstructural control or alter properties has been previously noted and realized under certain conditions.[1-16] However, because of the high melting points and low solid-state diffusivities which are characteristic of these materials, currently available ceramic processing methods, such as sintering or hot-pressing, are of limited practical value as a means of obtaining chemically and microstructurally homogeneous materials in useful final form.

A constraint on the use of SiC in high-temperature applications is the existence of cubic (β-SiC, 3C), hexagonal (α-SiC, 2H, 4H, 6H), and rhombohedral ("α-SiC," 15R, 21R) polytypes of SiC having one or more phase transformations between 1400° and 2200°C. These phase transformations often result in undesirable changes in microstructure, including exaggerated grain growth.[1] AlN is a good candidate for solid solution formation with, and phase stabilization of, SiC because its only form is isostructural with the wurtzite (hexagonal 2H) form of SiC and is closely lattice matched. In addition, the presence of 1% to 10% AlN in hot-pressed SiC samples has been reported to reduce grain size and improve microstructural uniformity.[1] The potential to vary properties such as band gap (SiC, 2.3 eV; AlN, 6.0 eV), thermal conductivity, and thermal expansion over the range of SiC/AlN solid solution compositions makes this system attractive for electronic applications.[2]

SiC/AlN composite and solid-solution materials with a wide compositional range have been prepared by several traditional processing routes. For example, Rafaniello and co-workers prepared SiC/AlN powder by carbothermal reduction of mixtures of alumina, silica, and carbon in a nitrogen atmosphere at 1625°C. Samples of the powder were subsequently hot-pressed under argon at 70 MPa and temperatures of 1950° to 2300°C. At temperatures below 2100°C, bulk materials of 15 to 75 wt% AlN were inhomogeneous mixtures of SiC/AlN solid solutions of different compositions, whereas samples hot-pressed at 2300°C are homogeneous, single-phase 2H materials. Annealing samples at 1700°C that had been hot-pressed at 2100° to 2300°C resulted in phase separation within individual grains, suggesting a miscibility gap.[3]

Ruh and Zangvil have also obtained composite and solid-solution materials, over the complete compositional range, by hot-pressing mixtures of β-SiC and AlN under vacuum at 35 MPa and temperatures of 1700° to 2300°C.[4-7] Recently, these authors proposed a phase diagram for the SiC/AlN system, based on analytical electron microscopy studies of local equilibria among adjacent phases in hot-pressed samples and diffusion couples.[7] At temperatures above 2100°C and compositions from 24 to 100 wt% AlN, a single 2H solid-solution phase exists. At temperatures less than 1950°C and compositions from approximately 10 to 90 wt% AlN, 2H is the stable phase; however, a miscibility gap exists, such that SiC- and AlN-rich 2H phases were observed. The phase boundaries in this diagram are in general agreement with one calculated by Safaraliev and co-workers, who suggest that the polytype structure is largely dependent on phase composition and that 2H solid solutions should predominate at compositions >20 wt% AlN.[8]

Tsukuma and co-workers have prepared single-phase 2H materials by sintering mixtures of Si$_3$N$_4$ and Al$_4$C$_3$ under 10 MPa of argon.[9] Zangvil and Ruh suggest that this phase is a solid solution of SiC/AlN based on the lattice parameters.[10] Recently, Sugahara[13] and Mitomo[14] have extended the work of Jack[11] and Cutler[12] on the preparation of SiC/AlN solid solutions and mixtures by carrying out the carbothermal reduction of montmorillonite–PAN intercalation compounds and sol–gel-derived SiO$_2$ and Al$_2$O$_3$, respectively. Solid solutions of SiC/AlN have also been prepared by the vapor deposition of Al and N into a porous SiC body[15] and by chemical vapor deposition of AlN and SiC on 6H-SiC and α-Al$_2$O$_3$.[16]

Several general observations regarding the formation and microstructure of SiC/AlN solid solutions emerge from these studies. First, it is difficult to prepare homogeneous single-phase SiC/AlN solid solutions at temperatures less than 2100°C. Second, large gradients in composition typically exist within solid solutions and individual grains. Finally, the microstructure and composition of the resulting materials are

through the small septum and reactor septum in one operation. The precursor mixture was dropped onto the heated stage of the reactor, over a 15-min period, at a rate of 0.2 cm³/min. A white solid was observed immediately on addition. After 2 h of heating under an ammonia atmosphere, nitrogen gas was introduced into the system and heating continued for 4 h. The reactor was cooled to room temperature while purging with nitrogen, and transferred to a nitrogen-filled glove box. The white solid was removed from the reactor and transferred into a tungsten boat in a quartz tube for further heating to 1000°C.

III. Subsequent Sample Annealing

The solid SiC- and AlN-containing pyrolysis products of both procedures were handled under nitrogen and stored in a glove box. To improve crystallinity of the products, further heating at 1400° to 1600°C in a nitrogen atmosphere was employed. Boron nitride boats were used to minimize carbon contamination. X-ray powder diffraction, electron microprobe, and chemical analysis were used in the characterization of the crystalline products. Thermal gravimetric analyses (TGA) of the organometallic precursors were carried out under an atmosphere of nitrogen.* A special Lexan glove box was designed and built to house the TGA equipment so as to allow the handling of air-sensitive precursors under an inert atmosphere.

IV. Results

Eight separate experiments were carried out in which $[(Me_3Si)_x((CH_2=CH)MeSi)_y(MeHSi)_z]_n$ (VPS) or $[MeHSiCH_2]_n$ (MPCS) were mixed with $[Et_2AlNH_2]_3$ or $[i\text{-}Bu_2AlNH_2]_3$ and processed by the copyrolysis, or "hot-drop," approach. Elemental analysis data obtained for the black solids obtained from these pyrolyses after heating to 1000°C are summarized in Table I. Independent oxygen analyses were obtained for selected samples and also appear in Table I. From these data, ratios of Si:Al, Al:N, and Si:C were calculated and are listed in Table II.

Fourier transform infrared (FT-IR) studies on these samples indicated little or no residual C–H or N–H groups remained after heating to 1000°C. At this stage, XRD patterns showed little evidence for crystallinity.

SEM data of all pyrolysis products showed highly agglomerated, irregularly shaped particles varying in size from 1 to 20 μm. No attempts have been made to optimize product morphology by tailoring processing conditions. TEM analyses of both the 600° and 1000°C products of the hot-drop pyrolysis of a mixture of VPS with $[Et_2AlNH_2]_3$ showed no discernible features. SAD analyses of these materials confirmed their noncrystalline nature.

X-ray powder diffraction (XRD) data for the sample prepared by the hot-drop approach, and subsequently heated to 1400° to 1600°C to improve crystallinity, indicated the formation of SiC/AlN solid solutions for all precursor combinations. Consider, for example, the XRD data for the pyrolysis product of VPS and $[Et_2AlNH_2]_3$, shown in Fig. 2. There is evidence for at least two major solid solution compositions between end-members of α-SiC and AlN. Heating the samples to 1800°C improved crystallinity but did not introduce any new diffraction lines.

The existence of two separate solid solution phases is corroborated by electron microprobe, TEM, and SAD analyses of a sample prepared by the hot-drop pyrolysis of a mixture of VPS and $[Et_2AlNH_2]_3$, followed by heating to 1800°C under nitrogen. Electron microprobe indicates a nonuniform distribution of Si and Al within and between individual grains, with Si:Al ratios varying from 0.62 to 0.82. TEM analyses indicate two morphologies—fine-grained, aluminum-rich flakes and thin, silicon-rich plates, as shown in Fig. 3. Energy dispersive X-ray spectra indicate Si:Al ratios in the range of 1:10 and 2.5:1, respectively. There are large compositional variations between particles; however, all particles exhibit wurtzite diffraction patterns, as observed by SAD.[31]

XRD analyses of copyrolyzed samples heated to 1400° to 1600°C indicated that SiC/AlN solid solution formation is precursor-dependent. The pyrolysis products of mixtures of VPS or MPCS with $[Et_2AlNH_2]_3$ are SiC/AlN solid solutions; thus, XRD patterns typical of the hexagonal 2H structure were observed with diffraction lines that fall between those of the α-SiC and AlN end-member compositions. In contrast, XRD data for the pyrolysis products of mixtures of VPS or MPCS with $[i\text{-}Bu_2AlNH_2]_3$ are mixtures of β-SiC and AlN, as illustrated in Fig. 4. Heating the samples to 2000°C under argon resulted in the transformation of the mixture of β-SiC and 2H-AlN to a single-phase 2H-SiC/AlN solid solution.[21]

Thermal gravimetric analyses involved heating mixtures of VPS or MPCS with $[Et_2AlNH_2]_3$ or $[i\text{-}Bu_2AlNH_2]_3$, at 5°C/min, in a nitrogen atmosphere. As summarized in Table III, the precursor mixtures have a higher ceramic yield than would be predicted based on ceramic yields of individual precursors. This increase in ceramic yield is particularly pronounced in the case of mixtures of MCPS with the organoaluminum amide precursors.

V. Discussion

Low-temperature pyrolysis products, prepared by slowly heating mixtures of VPS or MPCS with $[i\text{-}Bu_2AlNH_2]_3$ to 1000°C under nitrogen flow, contained mixtures of 3C-SiC and 2H-AlN. Heat-treating these products to 1500°C improved the crystallinity of the sample but did not promote solid solution formation. This suggests that, under the reaction conditions and heating rates employed, the organometallic precursors may decompose independently of one another to provide an intimate mixture of SiC and AlN. This would be understandable in the context of the widely different decomposition characteristics of these two precursor systems and the

---

Table I. Elemental Analyses of SiC/AlN Materials Treated at 1000°C

| Precursor	Method*	Element (%)				
		Si	C	Al	N	O†
VPS, [Et₂AlNH₂]₃	HD	39.62	17.17	27.24	15.79	0.18
VPS, [i-Bu₂AlNH₂]₃	HD	40.21	18.47	25.76	14.96	0.59
VPS, [Et₂AlNH₂]₃	CP	32.15	16.06	33.18	17.27	1.34
VPS, [i-Bu₂AlNH₂]₃	CP	29.87	17.63	33.17	17.24	3.05
MPCS, [Et₂AlNH₂]₃	HD	41.35	19.71	24.62	14.23	0.09
MPCS, [i-Bu₂AlNH₂]₃	HD	39.89	17.02	26.31	15.12	2.66
MPCS, [Et₂AlNH₂]₃	CP	29.72	17.86	33.19	17.26	3.01
MPCS, [i-Bu₂AlNH₂]₃	CP	30.42	16.91	33.20	17.23	2.24
Theoretical yields		34.64	14.76	33.19	17.23	0.00

*HD is "hot drop," CP is copyrolysis. †Determined by difference.
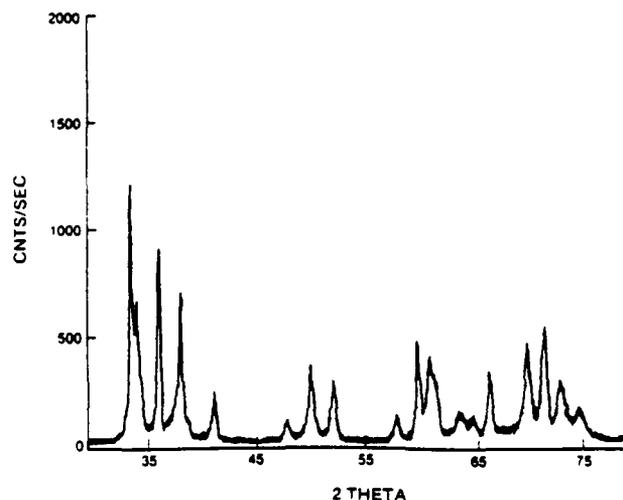
Fig. 4. X-ray powder diffraction data for SiC/AlN material prepared from MPCS and [*i*-Bu₂AlNH₂]₃ by the copyrolysis procedure, after heat treatment to 1500°C.

2*H*-SiC/AlN solid solution can be prepared by heat-treating samples at temperatures greater than 2000°C.

An interesting question is the role of ammonia in the copyrolysis and hot-drop processes. It is generally accepted that ammonia serves two functions: to remove carbon from the product and to enrich the sample in nitrogen.[32] Ammonia is employed in our processes while the precursor mixture is heated to 350°C in the copyrolysis experiments and during the first 2 h of the hot-drop experiments. The original intent of these experimental procedures was to ensure adequate conversion of the organoaluminum amide precursor to AlN. Independent studies of the conversion of VPS under ammonia to Si₃N₄ demonstrate that ammonia does indeed facilitate carbon removal.[33] Removal of carbon by reactions with ammonia seems to occur more effectively under the conditions of the hot-drop experiment. Preliminary results indicate that the temperature employed in these experiments is a critical factor in determining the proportion of carbon in the product and that at temperatures above ca. 650°C essentially all of the carbon is eliminated to form Si₃N₄/AlN mixtures.

Ongoing studies of the gas phase and solid pyrolysis products of both processes, as a function of temperature, precursor system, and atmosphere, should provide more information on the mechanisms of carbon removal and 2*H*-SiC/AlN solid solution formation.

VI. Conclusions

Solid solutions of 2*H*-SiC/AlN can be prepared at temperatures less than 1600°C by the rapid pyrolysis ("hot-drop") of mixtures of VPS or MPCS with [R₂AlNH₂]₃, where R = Et, *i*-Bu simply by slow pyrolysis of the precursor mixture in the case of [Et₂AlNH₂]₃. In contrast, slow pyrolysis of mixtures of VPS or MPCS with [*i*-Bu₂AlNH₂]₃ yields a composite of 2*H*-AlN and 3*C*-SiC at 1600°C, which transforms into a single 2*H*-SiC/AlN solid solution on heating to 2000°C. This

Table III. TGA Data for SiC/AlN Solid Solutions as a Function of Composition

SiC:AlN ratio	Yield (wt%)			Improvement in yield
	Theoretical	Calculated from known yields*	Experimental	
3:1	61.4	24.5	50.7	2.07
9:1	65.6	21.3	33.4	1.57
19:1	67.0	20.2	19.7	None

*Assuming quantitative conversion of [Et₂AlNH₂]₃ to AlN and a ceramic yield of SiC from MPCS of 20%.

suggests that both the nature of the precursors and the processing conditions are significant in determining the composition and structure of the SiC/AlN materials. Finally, the use of ammonia during the pyrolysis processes assists in carbon removal.

References

[1] W. Rafaniello, M. R. Plichta, and A. V. Virkar, "Investigation of Phase Stability in the System SiC–AlN," *J. Am. Ceram. Soc.*, **66** [4] 272–76 (1983).
[2] L. D. Bensten, D. P. H. Hasselman, and R. Ruh, "Effect of Hot-Pressing Temperature on the Thermal Diffusivity/Conductivity of SiC/AlN Composites," *J. Am. Ceram. Soc.*, **66** [3] C-40–C-41 (1983).
[3] W. Rafaniello, K. Cho, and A. V. Virkar, "Fabrication and Characterization of SiC–AlN Alloys," *J. Mater. Sci.*, **16** [12] 3479–88 (1981).
[4] R. Ruh and A. Zangvil, "Composition and Properties of Hot-Pressed SiC–AlN Solid Solutions," *J. Am. Ceram. Soc.*, **65** [5] 260–65 (1982).
[5] R. Ruh and A. Zangvil, "Hot-Pressed SiC–AlN Mixtures: Compositions and Properties of Solid Solutions"; presented at the 83d Annual Meeting of the American Ceramic Society. Washington, DC, May 5–9, 1981 (Basic Science Division, Paper No. 115-B-81).
[6] A. Zangvil and R. Ruh, "Solid Solutions and Composites in the SiC–AlN and SiC–BN Systems," *Mater. Sci. Eng.*, **71**, 159–64 (1985).
[7] A. Zangvil and R. Ruh, "Phase Relationships in the Silicon Carbide–Aluminum Nitride System," *J. Am. Ceram. Soc.*, **71** [10] 884–90 (1988).
[8] G. K. Safaraliev, G. K. Salchank, Y. M. Tairov, and V. F. Tsvetkov, "Criteria for the Formation of Solid Solutions Based on Silicon Carbide," *Inorg. Mater. (Engl. Transl.)*, **22** [11] 1610–11 (1987).
[9] K. Tskuma, M. Shimidu, and M. Koizami, "A New Compound SiCAl₄N₄C₃ with the Wurtzite Structure in the System Si₃N₄–Al₄C₃," *J. Mater. Sci. Lett.*, **1** [1] 9 (1982).
[10] A. Zangvil and R. Ruh, "The Si₃Al₄N₄C₃ and Si₃Al₅N₅C₃ Compounds as SiC–AlN Solid Solutions," *J. Mater. Sci. Lett.*, **3** [3] 249–50 (1984).
[11] I. B. Cutler, P. D. Miller, W. Rafaniello, D. P. Thompson, and H. K. Jack, "New Materials in the Si-C-Al-O-N and Related Systems," *Nature (London)*, **275**, 434–35 (1978).
[12] I. B. Cutler, and P. D. Miller, "Solid Solution and Process for Producing a Solid Solution," U.S. Pat. No. 4141740, Feb. 27, 1979.
[13] Y. Sugahara, K.-I. Sugimoto, H. Takagi, K. Kuroda, and C. Kato, "The Formation of SiC–AlN Solid Solution by the Carbothermal Reduction Process of Montmorillonite," *J. Mater. Sci. Lett.*, **7** [8] 795–97 (1988).
[14] M. Mitomo, H. Tsutumi, and Y. Kishi, "Preparation of a Composite Powder System SiC–AlN," *J. Mater. Sci. Lett.*, **7** [11] 1151–53 (1988).
[15] G. Ervin, Jr., "Silicon Carbide–Aluminum Nitride Refractory Composites," U.S. Pat. No. 3492153, Jan. 27, 1970.
[16] S. A. Nurmagomedov, A. N. Pikhtin, V. N. Ruzbegaev, G. K. Safaraliev, Y. M. Tairov, and V. F. Tsvetkov, "Synthesis and Study of Epitaxial Layers of (SiC)₁₋ₓ/(AlN)ₓ Wide-Gap Solid Solutions," *Pis' ma Zh. Tekn. Fiz.*, **12**, 1403 (1986).
[17] D. R. Uhlmann, B. J. Zelinski, and G. E. Wnek, "The Ceramist as Chemist—Opportunities for New Materials," *Mater. Res. Soc. Symp. Proc.*, **32**, 59–71 (1984).
[18] L. V. Interrante, L. E. Carpenter, II, C. Whitmarsh, W. Lee, M. Garbaukas, and G. L. Slack, "Studies of Organometallic Precursors to Aluminum Nitride," *Mater. Res. Soc. Symp. Proc.*, **73**, 359–65 (1986).
[19] F. C. Sauls, L. V. Interrante, and Z. Jiang, "Me₃AlNH₃ Formation and Pyrolytic Methane Loss: Thermodynamics, Kinetics, and Mechanism"; unpublished work.
[20] W. R. Schmidt, L. V. Interrante, P. S. Marchetti, R. H. Doremus, and T. K. Trout, "Pyrolysis Chemistry of an Organometallic Precursor to Silicon Carbide"; unpublished work.
[21] M. L. J. Hackney, L. V. Interrante, G. A. Slack, and P. J. Schields, "Organometallic Precursors to Siₓ,Al,C,N, Ceramics"; pp. 99–111 in Ultrastructure Processing of Advanced Ceramics. Edited by J. D. Mackenzie and D. R. Ulrich. Wiley, New York, 1988.
[22] L. V. Interrante, C. L. Czekaj, M. L. J. Hackney, G. A. Sigel, P. J. Schields, and G. A. Slack, "An Investigation into the Preparation, Properties, and Processing of SiC/AlN Solid Solutions from Organometallic Precursors," *Mater. Res. Soc. Symp. Proc.*, **121**, 465–70 (1988).
[23] T. J. Clark and R. E. Johnson, "Fabrication of SiC–AlN Alloys," U.S. Pat. No. 4687657, Aug. 18, 1987.
[24] J. F. Janik, E. N. Duesler, and R. T. Paine, "Reactions of Tris(trimethylsilyl)aluminum and Ammonia. Formation, Structure, and Thermal Decomposition of [(Me₃Si)₂AlNH₃]₃," *Inorg. Chem.*, **26** [26] 4341–45 (1987).
[25] R. T. Paine, J. F. Janik, and C. Narula, "Synthesis of AlN and AlN/SiC Ceramics from Polymeric Molecular Precursors," *Mater. Res. Soc. Symp. Proc.*, **121**, 461–64 (1988).
[26] C. L. Schilling, Jr., J. P. Wesson, and T. C. Williams, "Polycarbosilane Precursors for Silicon Carbide," *Am. Ceram. Soc. Bull.*, **62** [8] 912–15 (1983).
[27] B. A. Bishop, M. S. Spotz, W. E. Rhine, H. K. Bowen, and J. R. Fox, "Sintering of Silicon Carbide Prepared from Polymeric Precursors"; pp. 856–63 in Ceramic Transactions, Vol. 1, Ceramic Powder Science. Edited by G. L. Messing, E. R. Fuller, Jr., and H. Hausner. American

Ceramic Society, Westerville, OH, 1988.

[28]V. G. Fritz and H. Frohlich, "Reactions of Chlorine Containing Carbosilanes with LiAlH₄," *Z. Anorg. Allg. Chem.*, 382 [1] 9–25 (1971).

[29]V. G. Fritz, "Building Carbosilanes from Methyl Silanes," *Z. Anorg. Allg. Chem.*, 460 [1] 115–43 (1980).

[30]S. Yajima, K. Okamura, J. Hayashi, and M. Omori, "Synthesis of Continuous SiC Fibers with High Tensile Strength," *J. Am. Ceram. Soc.*, 59 [7–8] 324–27 (1976).

[31]R. P. Miller, J. G. Lee, and I. B. Cutler, "The Reduction of Silica with Carbon and Silicon Carbide," *J. Am. Ceram. Soc.*, 62 [2] 147–49 (1979).

[32]G. T. Burns and G. Chandra, "Pyrolysis of Preceramic Polymers in Ammonia: Preparation of Silicon Nitride Powders," *J. Am. Ceram. Soc.*, 72 [2] 333–37 (1989).

[33]W. R. Schmidt, W. J. Hurley, Jr., L. V. Interrante, P. S. Marchetti, and R. H. Doremus, "Chemistry of the Conversion of a Vinylic Polysilane to Silicon Nitride"; unpublished work.   □

GAS PHASE DECOMPOSITION OF AN ORGANOMETALLIC
CHEMICAL VAPOR DEPOSITION PRECURSOR TO AlN:
[Al(CH3)2NH2]3

CARMELA C. AMATO*, JOHN B. HUDSON** AND LEONARD V. INTERRANTE*
*Rensselaer Polytechnic Institute, Dept. of Chemistry, Troy, NY 12180
**Rensselaer Polytechnic Institute, Dept. of Materials Engineering, Troy, NY 12180

ABSTRACT

A novel technique for probing chemical vapor deposition reaction mechanisms is presented. A conventional hot-wall Pyrex reactor is coupled to a molecular beam apparatus. Preliminary results of the decomposition of an organometallic precursor to AlN, [Al(CH3)2NH2]3, indicate a decomposition temperature between 200 and 270°C. The mass spectrum of the precursor at 100°C provides evidence for the existence of a trimer-dimer equilibrium of the precursor at this temperature.

INTRODUCTION

Organometallic chemical vapor deposition (CVD) has been instrumental in many areas, including: materials science, metallurgy, chemistry and electronics[1]. The experimental studies that have been pursued for many years have centered on properties of the deposited film and optimization of growth conditions[2]. Work has recently begun aimed at understanding the chemical processes and mechanisms which occur during the film growth process in a CVD system[3].

The formation of solid materials by CVD involves a wide range of chemical processes, taking place in several regions of the CVD reactor. If the process requires mixing two or more reactants, association reactions can take place in the gas phase. In all cases, if the gas phase is heated prior to encountering the surface on which growth is to take place, gas phase pyrolysis or reactions on the heated wall surface may occur. There will certainly be surface reactions on the growth surface, and there may be further gas phase or surface reactions among the primary gas phase products in the region beyond the growth surface.

In order to characterize completely the chemistry of the CVD process it is necessary to set up systems in which each of these processes can be studied independently, so that their impact on the overall deposition process may be assessed. We have begun a program of study aimed at this complete characterization process for the case of the deposition of refractory materials such as SiC, AlN and Si3N4, from organometallic precursors. In each case the precursor has been synthesized to contain both of the elements to appear in the final product. We are thus dealing with a single precursor system, and the question of gas phase association reactions does not arise. All of the other reaction processes listed above, however, must be accounted for.

We are at present pursuing two lines of approach. In the one case, we have developed a system which involves impinging the precursor on the desired growth surface in an ultrahigh vacuum system, which excludes gas phase reactions. A variety of surface science techniques is used to characterize both the chemistry of the growing film and the gas phase reaction products. This system separates the reaction process at the growth surface from the other gas phase or wall surface reactions.

The second system under study is essentially a hot-wall CVD reactor, with a gas inlet system, coupled to a differentially pumped mass spectrometer. A description of the apparatus is included in the experimental section. This system is being used to study gas phase pyrolysis reactions and reactions on the surface of the hot wall of the reactor; that is, those processes

occurring prior to the point at which the precursor flow encounters the growth surface. In this paper we report the initial results obtained using the AlN precursor: [Al(CH3)2NH2]3.

AlN has several properties which make it an attractive candidate for materials applications. It is highly refractory and chemically resistant. It has a large band gap (6.2eV) and a high thermal conductivity (3.2W/cmK). Its thermal expansion coefficient is closely matched to Si, and it is a piezoelectric material. These properties make it an important material for Si-based integrated circuits, optoelectronic devices and surface acoustic wave devices[4].

The organometallic precursor to AlN is prepared according to the following scheme. which has previously been reported by Interrante and coworkers[5]:

$$3 \text{ AlMe}_3 \ + \ 3 \text{ NH}_3 \longrightarrow 3 \text{ H}_3\text{N:AlMe}_3 \xrightarrow[-3 \text{ CH}_4]{\Delta}$$
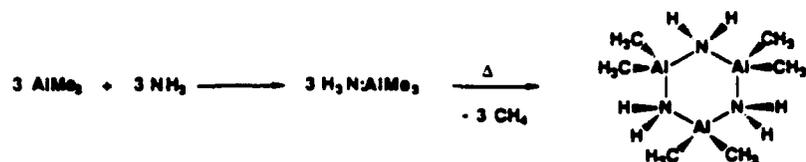
The compound exists as a cyclic trimeric species in the solid state[5] and has a vapor pressure of approximately one torr at 70°C. This relatively high vapor pressure makes it a good candidate for use as a CVD precursor. In fact, stoichiometric AlN thin films on Si have been achieved with this precursor using a hot wall reactor at temperatures between 600 and 800°C[6]. An Auger depth profile of these films reveals a one-to-one ratio of aluminum to nitrogen and an oxygen concentration of less than five percent[6].

EXPERIMENTAL

The apparatus built in this study is shown schematically in Figure 1. It consists, in short, of the inlet half of a hot-wall CVD reactor interfaced through a sampling system to a quadrupole mass spectrometer. The precursor is contained in a heated stainless steel bubbler.
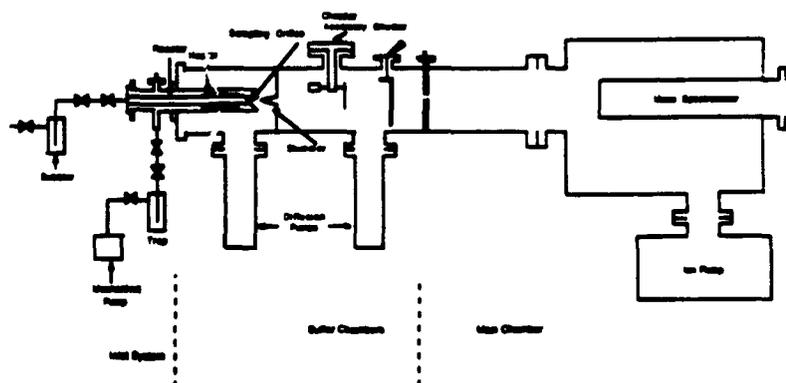
Figure 1. Schematic of the CVD reactor coupled to a differentially pumped mass spectrometer

been obtained which indicate the presence of a trimer-dimer equilibrium in solution at elevated temperatures, with a positive ΔH for the formation of the dimer from the trimer[7]. Hence, it would not be unreasonable to speculate that the cracking pattern in Figure 2 is that of a trimer-

Table I. Possible mass peak assignments

dimer equilibrium which is shifted essentially completely toward the dimer as a result of maintaining the precursor at 100°C.

Figure 3 is the temperature profile of the mass 115 peak obtained by increasing the temperature of the reactor from 100°C to 400°C over a period of approximately two hours.
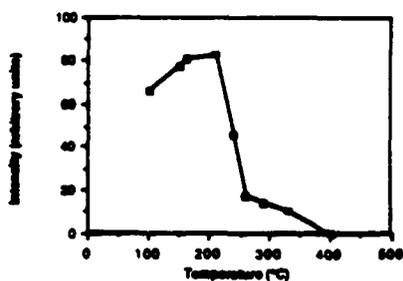
Figure 3. Temperature profile of mass 115 peak

Decomposition of the precursor occurs between the temperatures 200 and 270°C; by 400°C the mass 115 peak completely disappears. The mass 57 and 131 peaks also track this temperature
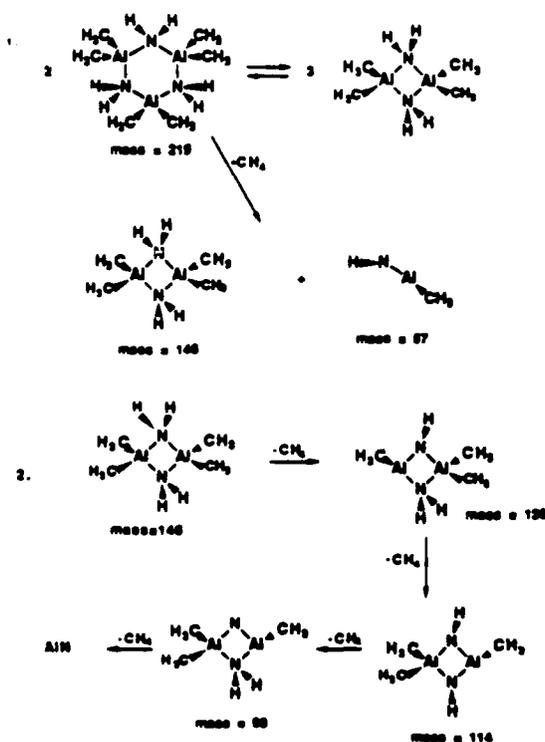
Figure 4. Mechanistic speculation relating to mass spectral cracking pattern

profile. The implication of this is that all three species, mass 57, 115 and 131, are derived from the same species in the mass spectrometer ion source. Given the above information it is possible to offer Schemes 1 and 2 in Figure 4 as mechanistic speculations for the decomposition of the precursor as it flows through the heated Pyrex tube. First, the precursor may exist in rapid trimer-dimer equilibrium. Alternatively, the precursor may already begin to decompose at 100°C by releasing methane and generating a dimeric species as well as a species of mass 57, which is also present in our spectrum. This mechanism is postulated because previous results of Interrante and coworkers[6] reveal methane as a by-product of the CVD process. At the present time a high background signal at low mass numbers prevents us from identifying whether or not methane is one of the decomposition products. Scheme 2 depicts a decomposition of the dimeric species to AlN by way of successive methane elimination. It is interesting that the intermediate species in this pathway have masses which correspond to those observed in our spectra at various temperatures. (Some proposed species may have masses which differ by one mass unit from those observed as a result of proton transfer reactions occurring after electron impact). Alternatively, the peaks corresponding to these masses in our spectra may result from the dimer by fragmentation of the corresponding

molecular ion in the mass spectrometer. Efforts to distinguish these and other possible decomposition pathways are currently in progress.

CONCLUSION

It has been demonstrated that the coupling of a CVD reactor to a molecular beam apparatus provides a novel technique with which to elucidate CVD mechanisms. Current research efforts are being directed toward the detailed study of the temperature dependence of the trimer-dimer equilibrium and the role of these species in the CVD process. Isotopically substituted analogues of the precursor have been prepared to help determine the structure of the species which give rise to the peaks observed in our mass spectra.

Also, the question still remains as to whether any or all of the species observed during the decomposition are a result of purely gas phase pyrolysis or a result of gas interactions with the Pyrex reactor. In order to address this issue, it is planned to repeat the above experiments with the addition of a flow of inert carrier gas through the reactor. Provided that laminar flow conditions are maintained, the inert gas will inhibit reaction of the precursor with the surface of the reactor walls.

ACKNOWLEDGEMENTS

REFERENCES   .

1. G.B. Stringfellow, Organometallic Vapor Phase Epitaxy: Theory and Practice, (Academic Press, Inc., Boston, MA 1989), p.1.

2. R. Messier, MRS Bulletin 13, 11, 18 (1988).

3. (a)F. Lee, A.L. Backman, R. Lin, T.R. Gow and R.I. Masel, Surface Science 216, 173 (1989). (b)B.E. Bent, R.G. Nuzzo and L.H. Dubois, J. Am. Chem. Soc. 111, 1634 (1989).

4. L.V. Interrante, L.E. Carpenter, C. Whitmarsh, W.Lee, M. Garbauskas and G.A. Slack in Better Ceramics Through Chemistry III, edited by (Maters. Res. Soc. Proc. 73, Pittsburgh, PA 1988) pp. 359-366.

5. L.V. Interrante, G.A. Sigel, M. Garbauskas, C. Hejna and G.A. Slack, Inorg. Chem. 28, 252 (1989).

6. L.V. Interrante, W. Lee, M. McConnell, N. Lewis and E. Hall, J. Electrochem. Soc. 136, 472 (1989).

7. F.C. Sauls, C.L. Czekaj and L.V. Interrante, submitted for publication.

Synthesis and Structure of a Highly Branched Polycarbosilane Derived from (Chloromethyl)trichlorosilane

Chris K. Whitmarsh and Leonard V. Interrante*

Chemistry Department, Rensselaer Polytechnic Institute, Troy, New York 12180

Received August 29, 1990

A highly branched hydridopolycarbosilane has been prepared by Grignard coupling of (chloromethyl)trichlorosilane, followed by reduction with lithium aluminum hydride. Trapping studies show that the initial step in the polymerization is a nearly quantitative formation of the Grignard compound Cl_3SiCH_2MgCl. This Grignard compound undergoes head-to-tail (Si–C) coupling almost exclusively, and due to its trifunctional $SiCl_3$ "tail", a complicated, branched, polycarbosilane polymer results, which contains the following structural units: $SiCl_3CH_2$–, $-SiCl_2CH_2$–, $>SiClCH_2$–, and $>SiCH_2$–. The chloropolycarbosilane undergoes side reactions with ether, leading to incorporation of small amounts of ethyl and ethoxy functionality. During the reduction step the ethoxy groups are eliminated, yielding a polymer with the approximate formula $[SiH_{1.8}Et_{0.1}CH_2]_n$, which has been characterized by ^1H, ^{13}C, and ^{29}Si NMR, IR, GPC, and elemental analysis. This polymer is of interest as a precursor to near-stoichiometric silicon carbide.

Introduction

Highly branched silicon-containing polymers have been previously reported in conjunction with studies on silicon carbide precursors. Schilling et al.[1] have investigated several systems in which various mixtures of Me_3SiCl, Me_2SiCl_2, and $H_2C=CHSi(Me)Cl_2$ were treated with potassium, resulting in the formation of complicated, branched polysilanes. The branching was induced by reaction of the vinyl groups with potassium, leading to formation of $SiCH_2CHSi_2$ units in the polymer. Baney[2] has prepared polymers composed of complicated arrangements of fused polysilane rings. These polymers are prepared by treating mixtures of partially chlorinated disilanes of the general formula $Me_{6-x}Cl_xSi_2$ ($x = 2-4$) with Bu_4PCl at elevated temperatures. Kriner[3] reported the formation of polymeric byproducts during the "reverse Grignard" reaction of (chloromethyl)dichloromethylsilane employed to prepare various cyclic carbosilane compounds. These

byproducts were presumably branched polycarbosilanes but were not investigated in any detail.

We report herein the characterization of a novel polycarbosilane with a highly branched structure. Due to the complex nature of this polymer, precise naming is difficult. The polymer isolated from the initial Grignard coupling reaction and its $LiAlH_4$-reduced analogue will be referred to as chloropolycarbosilane and hydridopolycarbosilane, respectively. The theoretical "average" formulas for these polymers would be $[SiCl_2CH_2]_n$ and $[SiH_2CH_2]_n$; however, due to their highly branched nature and side reactions with the ether solvent, the actual structures are much more complicated. The hydridopolycarbosilane is potentially useful as a precursor to silicon carbide ceramics, as it has nearly at 1:1 Si:C ratio and undergoes facile thermal cross-linking reactions leading to high ceramic yields.

Experimental Section

General Procedures. All manipulations involving air-sensitive materials were carried out in oven-dried glassware by using standard inert-atmosphere techniques.[4] Solvents were distilled under nitrogen from appropriate drying agents.[5] Magnesium powder (No. 50 mesh) was reground by using a modified pepper

(1) (a) Schilling, C. L., Jr.; Wesson, J. P.; Williams, T. C. *J. Polym. Sci., Polm. Symp.* 1983, 70, 121. (b) Schilling, C. L., Jr. U. S. 4,414,403 and 4,472,591. (c) Schilling, C. L., Jr.; Williams, T. C. *Polym. Pre. Pr.* 1984, 25, 1.

(2) (a) Baney, R. H.; Gaul, J. H.; Hilty, T. K. *Emergent Process Methods for High Temperature Ceramics. Mater. Sci. Res.* 1984, 17, 253. Baney, R. H.; Gaul, J. H.; Hilty, T. K. *Organometallics* 1983, 2, 860. Baney, R. H. U. S. 4,310,481, 4,310, 482, and 4,310, 651.

(3) Kriner, W. A. *J. Org. Chem.* 1964, 29, 1601.

(4) Shriver, D. F.; Drezdon, M. A. *Manipulation of Air-sensitive Compounds*, 2nd ed.; Wiley: New York, 1986.

(5) Gordon, A. S.; Port, R. A. *The Chemist's Companion*; Wiley: New York, 1977.

grinder, under nitrogen, before use. Other commercially available reagents were used as received, unless otherwise specified. ^{1}H, ^{13}C, and ^{29}Si NMR spectra were run on a Varian XL-200 spectrometer using benzene-d_6 or toluene-d_8 as solvents. Spectra were referenced to residual protons in the solvent, as TMS often interfered with sample peaks. IR spectra were taken, as neat films, between salt plates on a Perkin-Elmer 298 spectrometer. GC analyses were performed on a Shimadzu GC-9A gas chromatograph equipped with a Shimadzu C-R3A recorder–integrator unit. Unless otherwise specified, samples separated satisfactorily by using the following parameters: 6-ft SE-30 column, 100–250 °C at 15 °C/min, INJ and TCD at 275 °C, He at 45 cm³/min. Elemental analyses were carried out by either Schwarzkopf Microanalytical Laboratory, Galbraith Laboratories Inc., or LECO Corp.

Preparation of Chloropolycarbosilane. Dry ether (1 L) and 30 g of magnesium powder (1.25 mol) were added to a 2-L, three-neck flask equipped with a reflux condenser, mechanical stirrer, and a nitrogen inlet. The reaction was started by addition of 5–10 mL of (chloromethyl)trichlorosilane to the flask, followed by intermittent heating with a heat-gun without stirring. Once the reaction was started, a 50 °C water bath was employed.[6] The remainder of the Cl₃SiCH₂Cl (126 mL, 1.0 mole total) was added over about 8 h by using a syringe. After the addition was complete, a highly air-sensitive, dark brown solution, containing small amounts of magnesium chloride and excess magnesium was obtained. This solution was heated under reflux for 3–5 days, causing a gradual color change to brownish yellow as large amounts of MgCl₂ precipitated. Due to the large volume of solid which formed, addition of more ether was required to maintain a sufficiently fluid consistency. The ether solution of the product was removed by using a cannula fitted with a gas diffuser frit to prevent clogging. The resulting solution of chloropolycarbosilane was stripped of ether under vacuum with the aid of the 50 °C water bath. A yellow-brown, moisture-sensitive, highly viscous oil was obtained in 45–50% yield (based on an assumed "average" formula [SiCl₂CH₂]ₙ). IR (cm⁻¹): 2980 (s), 2930 (m), 2900 (m), 1440 (m), 1385 (m), 1345 (m), 1290 (w), 1260 (m), 1160 (m), 1100–1030 (vs, b), 965 (s), 815–755 (vs. b). All NMR peaks are complex multiplets or broad [ppm (relative integral)]: ^{1}H 0.2–1.5 (25), 1.9–2.3 (1.0), 3.6–4.1 (3.6); ^{13}C{^{1}H} 8–24 (major portion, several multiplets), 29–33, 56–61; ^{29}Si{^{1}H} –20 to –12.5; –6 to +2 (both minor), 2–10, 13–28 (both major). Anal. Calcd for [SiCl₂CH₂]ₙ: C, 10.63; H, 1.77; Si, 24.80; Cl, 62.80. Calcd for [SiCl₁.₇Et₀.₁₅OEt₀.₁₅CH₂]ₙ (the best approximation based on NMR integration): C, 16.94; H, 2.09; Si, 24.7; Cl, 53.16; O, 2.1. Calcd for [SiCl₁.₁Et₀.₁₅OEt₀.₃₅CH₂]ₙ (the best approximation based on the observed elemental analyses): C, 34.7; H, 4.45; Si, 27.7; Cl, 38.57; O, 5.54. Found: C, 21.90; H, 4.14; Si, 22.30; Cl, 37.34.

Reduction of Chloropolycarbosilane. Typically, about 0.5 mol (56 g) of chloropolycarbosilane in 500 mL of ether was transferred to a 1-L, three-neck flask equipped with a reflux condenser, magnetic stirrer and nitrogen inlet and cooled to 10 °C by using an ice/water bath. LiAlH₄, 12.3 g (0.33 mol, 30% excess) suspended in 200 mL of ether was added over 30 min, via cannula or syringe, with rapid stirring. The resulting light gray suspension was refluxed overnight under nitrogen. The large excess of LiAlH₄ was employed due to uncertainty in the amount of Si–Cl in the polymer.

Aqueous Workup of Crude Hydridopolycarbosilane. Initially, dilute HCl (about 3 M) was added dropwise to the rapidly stirred LiAlH₄/polymer slurry under nitrogen. An oil bubbler allowed the byproduct gases to escape. After the reaction became sluggish, the remainder of about 1 L of the acid was poured in, resulting in the dissolution of the lithium and aluminum salts. (If large amounts of unreacted LiAlH₄ are present, this process can be expedited by allowing the slurry to settle and transferring the liquid portion to another flask for hydrolysis.) The ether layer was separated and again washed with dilute HCl, and the ether was stripped off to yield a cloudy, yellow oil. This oil was redissolved in pentane to drive out small amounts of emulsified

water and residual aluminum complexes. After settling, the pentane solution was easily separated from the residue, dried, and passed through a 0.5-μm syringe filter, and the solvent was stripped off, under vacuum, with warming to 60 °C. A viscous, transparent, pale yellow oil was obtained in about 85% yield (or 40% overall, from Cl₃SiCH₂Cl) on the basis of the assumed "average" formula [SiH₂CH₂]ₙ for the hydridopolycarbosilane. This polymer is not pyrophoric, and appears to be reasonably air-stable.[7] IR (cm⁻¹): 2950 (m), 2920 (m), 2870 (m), 2140 (vs), 1450 (w), 1350 (m), 1250 (w), 1040 (s), 1040 (s), 930 (vs), 830 (s), 760 (vs). All NMR peaks are complex multiplets or broad [ppm (relative integral)]: ^{1}H –0.4 to –0.05, –0.05 to +0.3 [16 (total)], 0.85–1.15 (3), 1.55–1.8 (1), 3.55–3.85, 3.85–4.1, 4.1–4.3 [13.3 (total)]; ^{13}C{^{1}H} –12 to +9 (major portion), 12.5–16, 23–26; ^{29}Si{^{1}H} –66 to –53 (4 large singlets and small multiplets), –39 to –26, –14 to –8, 0.0–5 (all complicated multiplets); ^{29}Si(^{1}H coupled) –73 to –45 [several overlapping quartets, J_{Si-H} about 200 Hz (other multiplets became more complicated)]; ^{29}Si{^{1}H} (DEPT, multiplicity = 1.5) –66 to –53, –14 to –8 (positive); –39 to –26 (negative). Anal. Calcd for SiH₂CH₂ (the theoretical "average" formula): C, 27.27; H, 9.09; Si, 63.63. Calcd for [SiH₁.₈₅Et₀.₁₅CH₂]ₙ (the best approximation from NMR integration): C, 32.3; H, 9.54; Si, 58.1. Calcd for [SiH₁.₁Et₀.₀₂₅CH₂]ₙ (the best approximation from C and H analyses): C, 28.07; H, 7.36; Si, 63.9. Found: C, 28.26; H, 7.36; Si, 48.71; Cl, 1.63; O, 0.02.

Gel Permeation Chromatography (GPC) Analysis of Hydridopolycarbosilane. GPC of the reduced polymer was performed on a Waters 600 solvent delivery system, 410 RI detector, and 745 data-processing unit. Waters Ultrastyragel columns of 100-, 500-, and 10000-Å porosity were kept at 40 °C. Helium-sparged HPLC grade toluene at a flow rate of 0.6 mL/min was used as the eluant. Molecular weights were obtained from a 15-point calibration curve by using polystyrene standards from 200 to 470000 amu. A wide MW distribution of 300 to about 50000 amu, with the majority of the polymer falling between 300 and 3000 amu was observed. The M_n (750), M_w (5200), and polydispersity of 6.9 reflect the broad MW distribution of this polymer.

Nonaqueous Workup of Hydridopolycarbosilane. The crude, reduced mixture was stripped of as much ether as possible under vacuum with heating to 50 °C. The resulting solids were extracted with pentane and allowed to settle, and the clear, yellow pentane solution was transferred by cannula to remove the polymer from the lithium and aluminum salts. The solution remained clear yellow during removal of the solvent under vacuum; only a gradual increase in viscosity was observed. Finally, an extremely viscous, yellowish, air-sensitive polymer was recovered in about 85% yield. The IR spectrum of this material was identical with that from the aqueous workup, except for two additional peaks: 1930 (w), 670 (w) cm⁻¹, respectively. ^{1}H NMR (ppm): C–H peaks –0.6 to +1.2 (broad, complex); Si–H peaks

(6) The onset of the reaction is signaled by the formation of a blackish coating on the Mg; the addition of more than 10% of the Cl₃SiCH₂Cl prior to the initiation of a self-sustaining reaction with the Mg should be avoided, as a violent exotherm can result.

(7) The hydridopolycarbosilane, when left exposed to air as a film between salt plates about 2 h, showed no significant changes on rerunning the IR spectrum.

(8) Petrarch Systems Catalog S-7 (Silicon Compounds Register and Review) 1987, p 176.

(9) (a) Webb, G. A., Ed. *Annual Reports on NMR Spectroscopy*; Academic: New York, 1983; Vol. 15, pp 235–289. (b) Harris, R. K.; Mann, B. H., Eds. *NMR and the Periodic Table*; Academic: New York, 1978; pp 310–334. (c) Schraml, J.; Bellama, J. M. In *Determination of Organic Structure by Physical Methods*; Nachod, E. C., Zuckerman, J. J., Randall, E. W., Eds; Academic Press: New York, 1976; Vol. 6, p 202. (d) Harris, R. K.; Kimber, B. J. *J. Magn. Reson.* 1975, 17, 174.

(10) (a) Silverstein, R. M.; Bassler, G. C.; Morril, T. C. *Spectrometric Identification of Compounds*, 4th ed.; Wiley: New York, 1981. (b) Smith, A. L. *Analysis of Silicones*; John Wiley & Sons: New York, 1974; pp 248–280.

(11) Subjecting a 1:2 mixture of Me₃SiCH₂Cl and Me₃SiCl to Grignard coupling conditions showed that the Grignard reagent prefers to couple with the Si–Cl group rather than the SiCH₂Cl group. The compounds Me₃SiCH₂SiMe₃ and Me₃SiCH₂CH₂SiMe₃ were formed in a ratio of 33:1 confirmed by GC and ^{1}H NMR spectroscopy. Due to the large amount of –SiCl₃ groups present, the probability for head–head coupling should be even less in the chloropolycarbosilane. In addition, no Si–Si bonded compounds were observed.

(12) (a) Selin, T. G.; West, R. *Tetrahedron* 1959, 5, 97. (b) Steudel, W.; Gilman, H. *J. Am. Chem. Soc.* 1960, 82, 6219. (c) Gerval, P.; Frainnet, E.; Lain, G.; Moulines, F. *Bull. Soc. Chim. Fr.* 1974, 7–8 (2), 1548.

3.6–3.9, 3.9–4.1, 4.1–4.3 (3 separate regions); 2.8:1 integration ratio for the C–H vs Si–H regions. Anal. Calcd for SiH_2CH_2: C, 27.27; H, 9.09; Si, 63.63. Found: C, 20.88; H, 5.82; Si, 34.51; Al, 6.64.

Preparation of Deuteriopolycarbosilane. Chloropolycarbosilane (5.02 g, 0.0444 mol as $[SiCl_2CH_2]_n$) was reduced with 1.165 g of $LiAlD_4$ (0.0277 mol) by using a scaled-down version of the procedure employed for preparation of hydridopolycarbosilane. Reduction was followed by aqueous/HCl workup as described previously. The product was a pale yellow, viscous liquid similar to hydridopolycarbosilane. IR (cm^{-1}): 2960 (m), 2920 (m), 2870 (m), 2840 (m), 2120 (vw), 1540 (vs), 1450 (w), 1350 (m), 1250 (m), 1035 (s), 940 (w), 890 (w), 750–850 (s, b), 675 (vs). ^{1}H NMR (ppm, all peaks relatively broad singlets): 1.7, 1.05, −0.4 to +0.6.

Preparation of Chloro- and Hydridopolycarbosilane in Ether-d_{10}. Chloropolycarbosilane was prepared as previously described but on a smaller scale, with the substitution of magnetic stirring due to the small quantities of reactants used. Cl_3SiCH_2Cl (3 mL) was added dropwise by syringe over about 1 h to 5 g of ether-d_{10} and 1.05 g of Mg powder. Gentle heating was required to initiate the reaction. When addition was complete the resulting brownish solution was refluxed for 3 days to complete the polymerization. The ether was removed under vacuum, and the resulting solids were extracted with about 20 mL of dry pentane. On evaporation, the chloropolycarbosilane was recovered as a nearly clear, viscous, moisture-sensitive liquid. If the formula $[SiCl_2CH_2]_n$ is assumed for this polymer, a 46.7% yield was obtained. Hydridopolycarbosilane was prepared from this chloropolycarbosilane by $LiAlH_4$ reduction followed by the aqueous workup procedure as previously described. A nearly clear, viscous oil was obtained in 87% yield, assuming the formula $[SiH_2CH_2]_n$. Chloropolycarbosilane (ether-d_{10}): IR (cm^{-1}) 2960 (m), 2930 (m), 2875 (w), 2210 (m), 2095 (w), 1450 (w), 1400 (w), 1350 (m), 1265 (m), 1185 (m), 1110 (sh), 1075 (s), 1045 (sh), 945 (m), 795 (vs); ^{1}H NMR (ppm) −0.1 to +1.8 (complex multiplet); ^{2}D NMR (ppm) 1.1 (asymmetric singlet), 2.0, 3.6 (all broad). Hydridopolycarbosilane (ether-d_{10}): IR (cm^{-1}) 2950 (w), 2920 (m), 2890 (w), 2205 (m), 2140 (vs), 1350 (m), 1250 (w), 1115 (w), 1050 (vs), 940 (vs), 850 (vs), 765 (vs); ^{1}H NMR (ppm) 0.0 (broad), 3.7, 4.1 (broad), minor peaks at 0.9, 1.35, 4.65, 4.9; ^{2}D NMR (ppm) 0.60, 1.1 (2:3 ratio).

Reduction of Solid Residue from Chloropolycarbosilane Preparation. The residual solids from the chloropolycarbosilane preparation, after two ether extractions, were suspended in about 1 L of dry ether. The amount of reducible material remaining in the residue was unknown, so $LiAlH_4$ was added until the yellowish slurry assumed a light gray color, suggesting excess $LiAlH_4$ was present. This slurry was allowed to reflux overnight. The "aqueous workup" was performed in the same manner as that for the soluble fraction of polymer. Vigorous foaming during the initial dropwise addition of 3 M HCl to the crude product showed that an excess of $LiAlH_4$ was present. This process recovered variable amounts of additional hydridopolycarbosilane corresponding to 10–25% of the theoretical yield. The IR and NMR of this product was similar to that from the soluble fractions of the chloropolycarbosilane. GPC was also quite similar; the majority of the polymer falling between 400 and 3400 amu, with M_n = 681.

Trapping of Chlorocarbosilane Oligomers as Methoxy Derivatives. (Chloromethyl)trichlorosilane (0.5 mol, 63 mL) was added to Mg powder as in the preparation of chloropolycarbosilane, except that the resulting brown solution was refluxed for only $^1/_2$ h before transferring, by cannula, to well-stirred cooled excess methanol. After the resulting white solids settled, a pale yellow solution was separated. Removal of the excess methanol gave a liquid/solid mixture, which was extracted with hexane and distilled under N_2. The major components were identified as $[MeO]_3SiMe$ and $[MeO]_3SiCH_2Si[OMe]_2CH_2Cl$ by boiling point and/or NMR data. A yellow, oily liquid, a mixture of higher weight oligomers, accounting for about 25% of the crude mixture, remained behind. $[MeO]_3SiMe$: 105–110 °C (lit. 103 °C).[8] $[MeO]_3SiCH_2Si[OMe]_2CH_2Cl$: 150–160 °C. ^{1}H NMR (all singlets) [ppm (number of protons)]: $[MeO]_3SiMe$ −0.28 (3) $(SiCH_3)$, 3.37 (9) (OCH_3); $[MeO]_3SiCH_2Si[OMe]_2CH_2Cl$ 0.103 (2) $(SiCH_2Si)$, 2.6 (2) (CH_2Cl), 3.42 (15) (OCH_3).

Preparation of Hydridopolycarbosilane Oligomers. Using 0.25 mol of Cl_3SiCH_2Cl (31.5 mL) the initial brown solution was

prepared as before and allowed to reflux for 1 h. The solution was reduced by addition of 30% excess $LiAlH_4$ as a suspension in ether and allowed to stir overnight. After aqueous/HCl workup and solvent removal, about 8 mL of light yellow liquid was recovered. Distillation of this product under N_2 yielded only about 0.25 mL of liquid before undergoing a rapid exothermic cross-linking reaction, with much gas evolution, to form a white foamlike glassy solid. The fraction obtained was found by GC to be 80% one component, identified by NMR as $H_3SiCH_2Si[H]_2CH_2Cl$. The remaining 20% consisted of several related compounds in quantities too small to separate and characterize in detail. $H_3SiCH_2Si[H]_2CH_2Cl$: 75–85 °C; ^{1}H NMR [ppm (number of protons)]: −0.4 (2) $(SiCH_2Si)$, sextet; 2.46 (2) $(-CH_2Cl)$, triplet; 3.6 (3) $(-SiH_3)$, triplet; 3.87 (2) $(-SiH_2-)$, overlapping triplet of triplets (nearly a quintet).

Results and Discussion

Part I: Chloropolycarbosilane. Investigations of the chloropolycarbosilane by NMR spectroscopy were performed in order to identify the functional units present. In the ^{1}H NMR spectrum (Figure 1A) a broad, complex peak is seen near 1 ppm. This peak is consistent with an assignment to the protons of methylene units between many slightly different $SiCl_x$ functionalities, which are a result of the extensive branching of the polymer. The corresponding carbons for these methylene groups are believed to be the origin of the several complex peaks observed between 8 and 25 ppm in the $^{13}C\{^1H\}$ NMR spectrum (Figure 2). Several groups of overlapping peaks are seen in the range 2–28 ppm in the ^{29}Si NMR spectrum (Figure 3). These groups are attributed to $>SiCH_2-$, $>SiClCH_2-$, $-SiCl_2CH_2-$, and $SiCl_3CH_2-$ units in the polymer.[9] Additional peaks are observed in the NMR spectra of this polymer, indicating that other functional groups are present as well. The ^{1}H NMR spectrum (Figure 1A) shows a smaller, broad peak at 3.8 ppm, which is assigned to the $-OCH_2-$ protons of ethoxy groups. The peaks due to the methyl protons for these ethoxy groups would lie near 1 ppm and presumably are buried under the carbosilane methylene peak. ^{1}H NMR analysis of a sample of the chloropolycarbosilane prepared in ether-d_{10} (Figure 1B) did not exhibit the peak at 3.8 ppm, and the peak near 1 ppm showed distinct changes. In addition, ^{2}D NMR of the same sample (Figure 4A) exhibits the missing peaks, demonstrating that the ether was the source of these ethoxy groups. The asymmetric shape of the peak at 1 ppm in Figure 4A is attributed to Si–Et groups, also introduced by the reaction with the ether solvent. This will be discussed in more detail later, as the ethyl groups are more easily seen in the hydridopolycarbosilane where interference in the ^{1}H NMR spectrum due to $-CH_3$ portion of the $-OEt$ groups is no longer present. The carbons from the $-OCH_2-$ of ethoxy groups presumably give rise to the peaks between 56 and 61 ppm seen in the ^{13}C NMR spectrum of the chloropolycarbosilane. The corresponding methyl carbon peaks would be buried under those due to Si–CH_2–Si in the polymer chain. The ^{29}Si NMR spectrum (Figure 3) shows smaller upfield multiplets from +2 to −6 and −17.5 to −20 ppm, strongly suggestive that oxygen, in addition to chlorine, is bound to silicon.[9] In addition to Si–OEt, these upfield peaks could result from the presence of Si–Si bonding in the polymer. Small peaks from 1.9 to 2.3 and 29 to 33 ppm in the ^{1}H and ^{13}C NMR spectra, respectively, have been assigned to unreacted chloromethyl end groups in this polymer. The infrared spectrum of this polymer shows medium-intensity bands at 1385 and 1160 cm^{-1}, which are consistent with CH_2Cl groups on silicon.[10]

The IR data (Figure 5A) also support the conclusion that ethoxy substitution has occurred during the preparation

Figure 1. Proton NMR spectra of polycarbosilanes: chloropolycarbosilane prepared in ether (A) and in ether-d_{10} (B); hydridopolycarbosilane prepared in ether (C), in ether-d_{10} (D), and in ether but reduced with LiAlD₄ (E). The singlets near 7 ppm are protons in C_6D_6 solvent. The fine structure in some samples is attributed to the presence of oligomers.

of the chloropolycarbosilane. Peaks of medium intensity at 965 and 1160 cm⁻¹ are consistent with the presence of SiOEt groups.[10] The strong, broad band between 1000 and 1120 cm⁻¹ also can result from Si–OR functionality in addition to the expected Si–CH₂–Si carbosilane "backbone" units of the polymer.[10] The major differences found in the IR spectrum of the chloropolycarbosilane prepared in ether-d_{10} (Figure 5B) were changes in, or disappearance of certain peaks in the C–H region and the appearance of new C–D peaks at 2090 and 2210 cm⁻¹. These changes are consistent with the presence of deuterated –OEt and –Et groups in the polymer.

Scheme I. Proposed Routes for Formation of Products Based on Methanol Trapping Experiments[a]
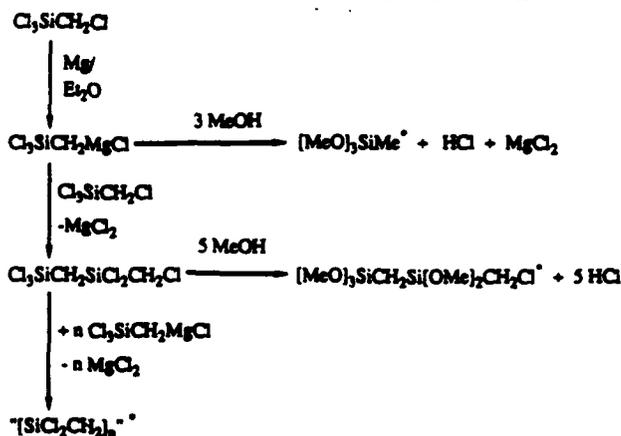
[a] Asterisks indicate those compounds that were actually observed.

The IR, NMR, and other experimental results indicate that the chloropolycarbosilane consists of the following "units" randomly assembled:
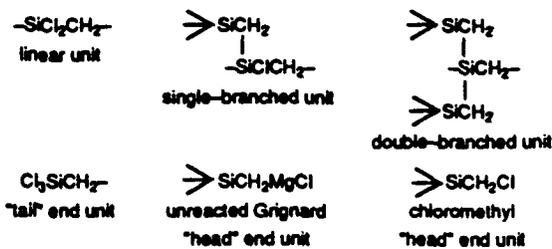
In addition, chlorine (on silicon) in any of these groups can be replaced with either –OEt or –Et.

The experimental results suggest that the formation of the chloropolycarbosilane proceeds in the following manner. Due to the complexity of the system, the side reactions will be discussed separately.

Slow addition of Cl₃SiCH₂Cl to refluxing Mg/ether was found to initially yield a dark, air-sensitive solution which, on extended reflux, gradually produced large amounts of MgCl₂ and a brownish yellow, viscous, moisture-sensitive polymer. The initial dark solution was suspected to contain the Grignard reagent, Cl₃SiCH₂MgCl, and was further investigated by quenching a freshly made batch with excess methanol before significant polymerization had occurred. On distillation, the principal compound obtained (about 80% of the volatiles) was [MeO]₃SiMe, the expected product from reaction of Cl₃SiCH₂MgCl with excess MeOH. Smaller amounts (about 17%) of [MeO]₃SiCH₂Si[OMe]₂CH₂Cl were recovered. Compounds suggestive of head to head coupling, such as [MeO]₃SiCH₂CH₂Si[OMe]₃, were not observed. No [MeO]₃SiCH₂Cl (from unreacted Cl₃SiCH₂Cl) was recovered, suggesting that the reactant was either converted to the Grignard reagent, or coupled with it to form Cl₃SiCH₂SiCl₂CH₂Cl before the methanol was added. Proposed pathways explaining the formation of the observed compounds are outlined in Scheme I.

These results suggest that most of the Cl₃SiCH₂Cl is quickly converted to the corresponding Grignard reagent. Some of this Grignard reagent couples with Si–Cl of unreacted Cl₃SiCH₂Cl to form the dimeric intermediate compund Cl₃SiCH₂SiCl₂CH₂Cl. The corresponding reduced compound, H₃SiCH₂SiH₂CH₂Cl, was recovered from the LiAlH₄ "quench" of a batch of the Cl₃SiCH₂MgCl that
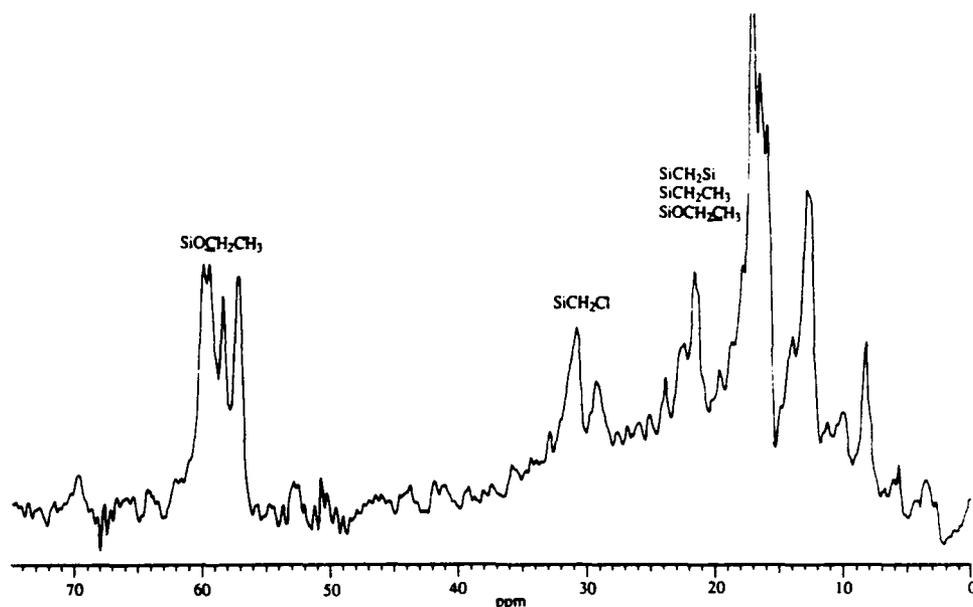
Figure 2. $^{13}C\{^1H\}$ NMR spectrum of chloropolycarbosilane.
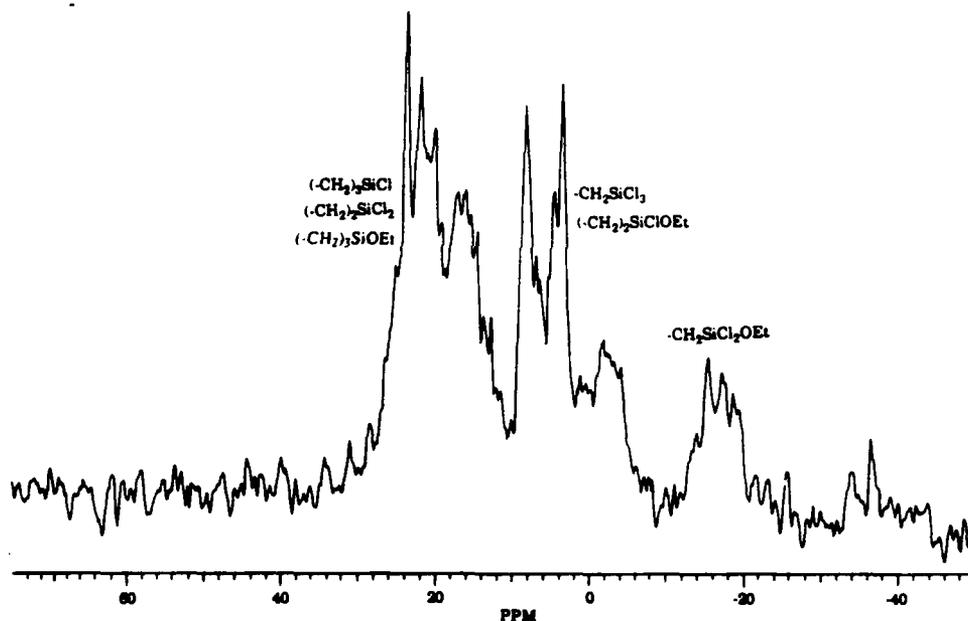
Figure 3. $^{29}Si\{^1H\}$ NMR spectrum of chloropolycarbosilane.

had been allowed to reflux for about 1 h (the chloromethyl group does not reduce as easily as SiCl). Any H_3SiCH_2Cl or H_3SiMe (from Cl_3SiCH_2Cl or Cl_3SiCH_2MgCl, respectively) would have escaped as gases along with the hydrogen formed during the aqueous workup step. The head-to-tail self-coupling of the Grignard reagent (Cl_3Si-CH_2MgCl) appears to be relatively sluggish, as most of it could be trapped with methanol to give $[MeO]_3SiMe$. In fact, the initial Grignard solution must be refluxed for a considerable time before visible amounts of $MgCl_2$ are formed.

The trifunctional $SiCl_3$ "tail", monofunctional $-CH_2MgCl$ "head", and strong bias toward head-to-tail coupling[11] give this polymer system several interesting features. Up to three Grignard head-end groups can couple to each $SiCl_3$ site on the growing polymer. With the addition of each new monomer, another $SiCl_3$ site is formed. Continuation of this process results in a polymer exhibiting extensive branching, limited only by steric effects. Due to the branching, this polymer is characterized by a relatively large number of $SiCl_3$ "tail" functionalities. Only one "CH_2" end group exists for each polymer molecule, as all others are employed in linking the carbosilane polymer together. If no side reactions occur, the extent of branching does not affect the theoretical 2:1 Cl:Si ratio for this polymer. This theoretical Cl:Si ratio can be justified in that the monomer contains three chlorine sites on each silicon ($-SiCl_3$) and one CH_2Cl group (which becomes the Grignard functionality). If all of the Grignard reagent couples with Si–Cl groups, there will be 2 equiv of Si–Cl remaining regardless of the extent of branching. Branching of this polymer can be described by the relationships: X = T + L + S + D and T = 2D + S + 1 (where X = total units, T = "tail" units (Cl_3SiCH_2-), L = "linear" units ($-SiCl_2CH_2-$), S = "single-branched" units ($>SiClCH_2-$), and D = "double-branched" units ($>SiCH_2-$). An example
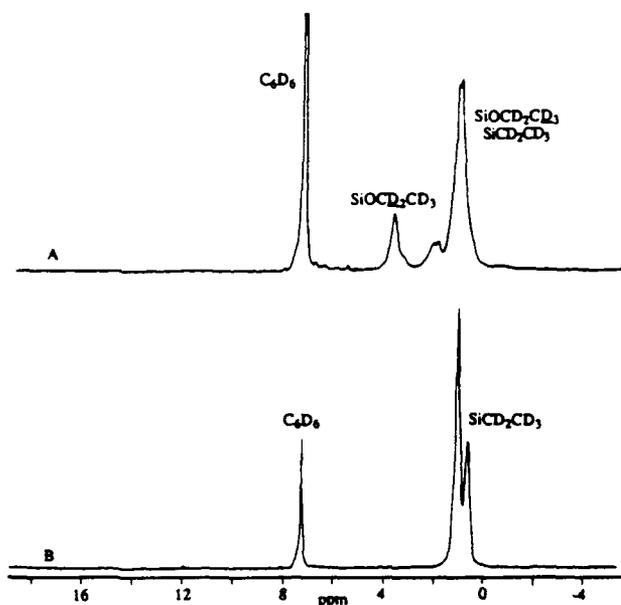
Figure 4. ^{2}D NMR spectra of polycarbosilanes prepared in ether-d_{10}: chloropolycarbosilane (A) and hydridopolycarbosilane (B). A small amount of C_6D_6 was added to the benzene solvent as an internal reference.
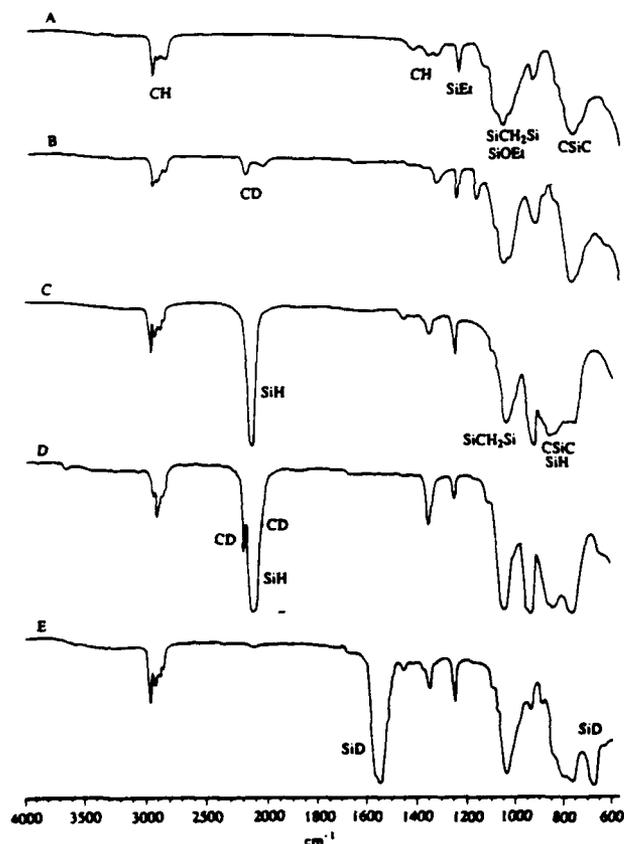
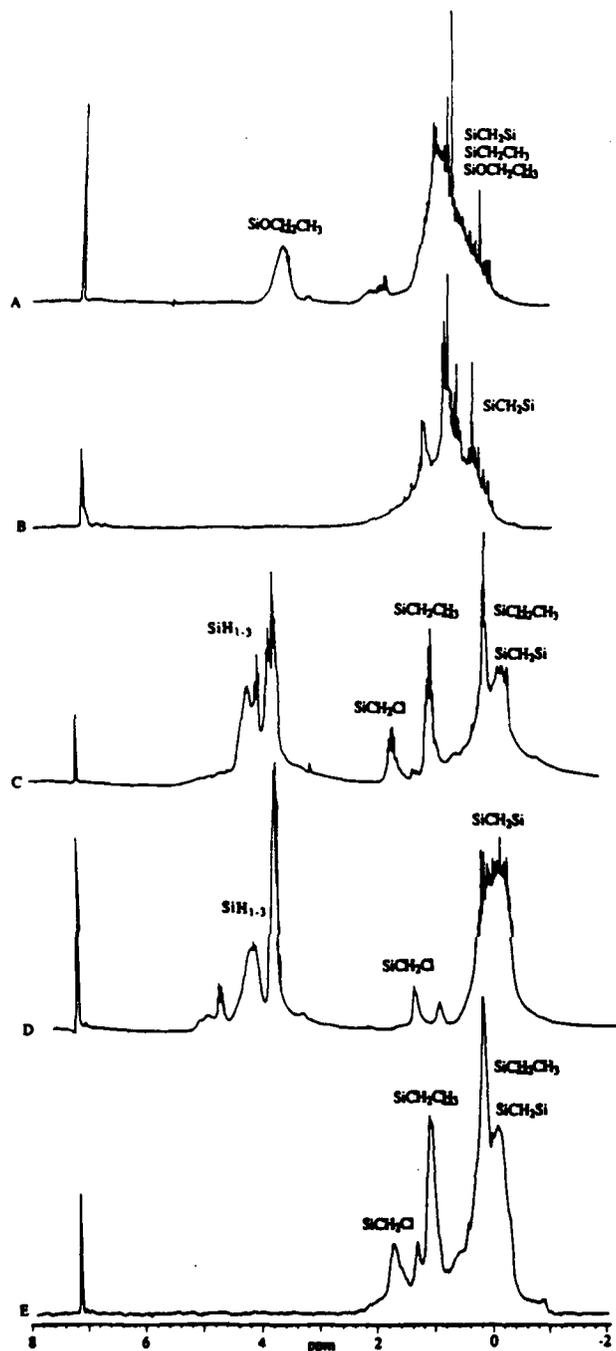**Figure 5.** IR spectra of polycarbosilanes: chloropolycarbosilane prepared in ether (A) and in ether-d_{10} (B); hydridopolycarbosilane prepared in ether (C), in ether-d_{10} (D), and in ether but reduced with LiAlD$_4$ (E).

of how the highly branched structure of chloropolycarbosilane develops is given in eq 1. It is important to note that this head–tail coupling process does not cause cross-linking of the branched polymer. For this system, cross-linking would require species with two head-end groups. Cross-linking by direct formation of Si–Si bonding
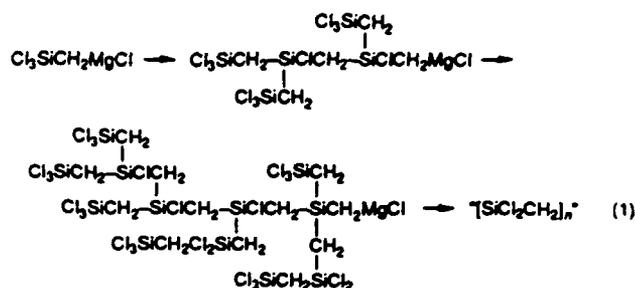
by magnesium dechlorination has not been observed, except in the case of phenyl- or aryl-substituted silanes.[12]

The actual chloropolycarbosilane system is found to be considerably more complex, as side reactions are found to occur. In addition to the previously described groups, NMR and IR data indicate that both Si–OEt and Si–Et functionalities are present. Elemental analysis of chloropolycarbosilane shows both a low chlorine and high carbon and hydrogen content for the expected "$[SiCl_2CH_2]_n$," average formula. This is consistent with ^{1}H, ^{13}C and ^{29}Si NMR and IR results, which suggest, in addition to SiCl$_x$, there are significant amounts of Si–OEt and Si–Et functionalities in the chloropolycarbosilane. Precedent for the cleavage of ethers by halosilanes to form alkoxysilanes is well established, having been known for over 100 years.[13] For iodosilanes the reaction is often quantitative.[14] Chlorosilanes are less active, but react similarly,[15] moreover, the extended reflux employed to effect coupling of the Grignard reagent would be expected to increase the extent of ether cleavage.

The formation of the Si–Et functionality is less obvious, it appears to originate from magnesium reacting with EtCl, a product of the side reactions,[15] to form ethyl magnesium chloride, which couples with the Si–Cl functionality to form SiEt groups. These ethyl groups were shown to originate from the diethyl ether used as solvent. When chloropolycarbosilane is prepared by using Et$_2$O-d_{10} during the Grignard coupling step, the incorporation of SiEt-d_5, (and OEt-d_5) groups occurs. When the polymer is reduced, the usual "ethyl" peaks are not seen in the proton in the proton NMR spectra. These ethyl groups can be seen in the ^{2}D NMR of the same sample, confirming the previous observation. These side reactions are outlined in eqs 2–4.

$$Si\text{–}Cl + Et_2O \rightarrow Si\text{–}OEt + Et\text{–}Cl \qquad (2)$$

$$Et\text{–}Cl + Mg/Et_2O \rightarrow Et\text{–}MgCl/Et_2O \qquad (3)$$

$$Et\text{–}MgCl/Et_2O + Si\text{–}Cl \rightarrow Si\text{–}Et + MgCl_2 \qquad (4)$$

It is difficult to propose an exact formula for the chloropolycarbosilane due to its complexity. Factors such as the rate of addition of Cl_3SiCH_2Cl, concentration, temperature, and length of reflux may have significant effects on the degree of branching, molecular weight, and stochiometry of this polymer. However, the "average" formula appears to be $[SiCl_{1.7}OEt_{0.15}Et_{0.15}CH_2]_n$. This formula represents the best agreement between ^{1}H, ^{13}C and ^{29}Si NMR and IR spectra and literature precedent. If the elemental analysis data are given priority, a considerably different formula, corresponding approximately to $[SiCl_{1.1}Et_{0.15}OEt_{0.35}CH_2]_n$, is obtained. In order to estimate this formula for the chloropolycarbosilane, it was presumed

(13) Friedel, C. *Ber. Dtch. Chem. Ges.* **1872**, *5*, 327.

(14) (a) Jung, M. E.; Lyster, M. A. *J. Org. Chem.* **1977**, *42*, 3761. (b) Keinan, E.; Perez, D. *J. Org. Chem.* **1987**, *52*, 4846.

(15) (a) Kipping, F. S.; Murray, A. G. *J. Chem. Soc.* **1927**, 2735. (b) Schwartz, R.; Kuchen, W. *Chem. Ber.* **1956**, *89*, 12. (c) Kibbel, H. U.; Schott, G. *Z. Anorg. Allg. Chem.* **1968**, *362*, 81.

Table I. ¹H, ¹³C, and ²⁹Si NMR Chemical Shift Values (ppm) for the Series [Me₃SiCH₂]ₓSiH₄₋ₓ (x = 1–4)[17a]

	compd (R = Me₃SiCH₂–)			
	RSiH₃	R₂SiH₂	R₃SiH	R₄Si
		¹H NMR		
SiCH₂Si	–0.40	–0.26	–0.19	–0.11
Si–Me	0.02	0.07	0.10	0.14
Si–H	3.70	4.05	4.29	–
		¹³C NMR		
SiCH₂Si	–8.86	–1.25	3.39	8.58
Si–Me	–0.235	0.906	1.15	1.65
		²⁹Si NMR		
Si–H	–65.1	–38.7	–17.3	14.5
Si–Me	1.81	1.13	0.66	–0.54

that the C, H, and Cl analyses were reasonably accurate. The silicon analysis was not employed for this estimation as it was found to be very low for all of the compounds studied.[16] The formula obtained from elemental analysis is considered to be less reliable in that it suggests a large amount of Si–Si bonding, which in not supported by literature precedent.[12] It also assumes that the C, H, and Cl analyses of the carbosilane are accurate, which is not justified by prior observations on analogous systems.[16]

The molecular weight of the chloropolycarbosilane was not determined by GPC, as even traces of water in the solvent required would cause cross-linking, seriously affecting the results. The MW of this polymer can be indirectly estimated from the GPC of the hydridopolycarbosilane, which is not highly moisture-sensitive. This value was found to be about 15.4 units (vide infra), corresponding to a molecular weight of about 1700 amu, if the "average" repeat unit, [SiCl₁.₇OEt₀.₁₅Et₀.₁₅CH₂], for the chloropolycarbosilane is accurate.

Part II: Hydridopolycarbosilane (from Aqueous Workup). The IR spectrum of the hydridopolycarbosilane (Figure 5C) is consistent with the proposed highly branched structure: [SiHₓCH₂]ₙ (where x = 0–3). Strong peaks at 2140, 930, 830, and 760 cm⁻¹ confirm the presence of SiH, SiH₂, and SiH₃ groups.[10] The disappearance of the peaks at 1160 and 960 cm⁻¹ and the narrowing of the band near 1060 cm⁻¹ are consistent with the reduction of Si–OR groups to Si–H. The absence of the characteristic peak for SiCH₂CH₂Si between 1120 and 1180 cm⁻¹ indicates that little or no head-to-head coupling has occurred.[10]

The ¹H NMR spectrum of the hydridopolycarbosilane (Figure 1C) consists of complex multiplets and broad peaks, as expected on the basis of its highly branched structure. The two groups of peaks centered at –0.2 and 0.15 ppm are attributed to the various SiCH₂Si environments and the SiCH₂– (of the Si–Et) functionality.[10b,17] Any Si–Me functionality in the polymer from reduced CH₂Cl end groups would also appear in this region. The peak near 1 ppm is consistent with the "–CH₃" protons of ethyl groups on silicon. Residual chloromethyl functionalities not reduced by LiAlH₄ treatment appear as a peak of 1.65 ppm. This peak underwent a small upfield shift when the polymer was reduced, as would be expected for the replacement of the electron-withdrawing chlorine at-
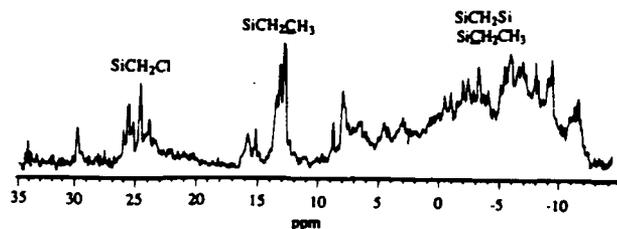
Figure 6. ¹³C{¹H} NMR spectrum of hydridopolycarbosilane.

oms on silicon by hydrogen. The three groups of peaks at 3.7, 3.95, and 4.2 ppm closely match the values for the SiH₃, SiH₂, and SiH groups, respectively, in the series of compounds [Me₃SiCH₂]ₓSiH₄₋ₓ (x = 1–3)[17a] (Table I).

It is difficult to verify by proton NMR spectroscopy that all the Si–OEt functionalities in the chloropolycarbosilane are eliminated during reduction, as the resonances in the ¹H NMR spectrum due to Si–H and Si–OCH₂– tend to overlap. The interference due to the Si–H protons was eliminated by performing the reduction using LiAlD₄. The ¹H NMR spectrum of the resulting deuteriopolycarbosilane (Figure 1E) shows no peaks in the 3–5 ppm region, indicating that reduction of the Si–OEt functionality in the polymer is complete. The peaks near 0.2 and 1.0 ppm, for the CH₂ and CH₃ of Si–Et, respectively, and the peak for residual CH₂Cl were not affected. The infrared spectrum of the deuteriopolycarbosilane (Figure 5E) is similar to that for the corresponding hydrido polymer except for those peaks due to Si–H groups. The Si–H stretching peak normally found at 2130 cm⁻¹ moved to 1540; the Si–H bending bands at 940 and 820 moved to 675 and below 600 cm⁻¹, respectively.

The peaks seen in the proton NMR spectrum of the hydridopolycarbosilane at 0.15 and 1.0 ppm were suspected to be due to ethyl groups from ether solvent being incorporated into the polymer during the Grignard coupling procedure. Proton NMR analysis of a sample of the chloropolycarbosilane prepared in ether-d₁₀ and then reduced with LiAlH₄ (Figure 1D) showed that these peaks nearly disappeared.[18] ²D NMR analysis of this same polymer sample (Figure 4B) shows these ethyl peaks as the only deuterated functionality present. The infrared spectrum of this polymer (Figure 5D) showed distinct changes in the C–H stretching region that were consistent with the proton NMR results. The Et-d₅-substituted polymer shows new peaks at 2205 and 2070 cm⁻¹ (due to the C–D functionality) with corresponding decreases in the C–H peaks at 2950 and 2850 cm⁻¹. Some of the weaker peaks in the C–H bending region near 1400 cm⁻¹ disappeared, presumably shifting to lower frequency, where they are obscured by the strong Si–CH₂–Si deformation or Si–H bands.

The data from the ¹³C NMR spectrum of the reduced polymer (Figure 6) are consistent with assignments from the ¹H spectra. Due to the numerous Si–CH₂–Si environments, the major feature is a broad, complicated multiplet extending from –12 to +8 ppm. These NMR chemical shift values are comparable to those for the "model" compounds given in Table I. A small group of peaks at 25 ppm is attributed to residual SiCH₂Cl functionality not completely reduced by the LiAlH₄. A second small group of peaks, near 13 ppm is assigned to the "–CH₃" carbon of ethyl groups on silicon. The "CH₂" carbons

(16) (a) Bacqué, E.; Pillot, J. P.; Birot, M.; Dunogués, J. *Macromolecules* **1988**, *21*, 30. Patai, S., Rappoport, Z., Eds. *The Chemistry of Organic Silicon Compounds*; Wiley: New York, 1989; Chapter 6. (c) Wu, H. J.; Interrante, L. V. *Chem. Mater.* **1989**, *1*, 564.

(17) (a) Fritz, G.; Maas, J.; Hornung, A. *Z. Anorg. Allg. Chem.* **1980**, *460*, 115. (b) Fritz, G.; Göts, N. *Z. Anorg. Allg. Chem.* **1970**, *370*, 171. (c) Fritz, G.; Grobe, J.; Kummer, D. *Adv. Inorg. Chem. Radiochem.* **1965**, *7*, 349. (d) Fritz, G.; Buhl, H. J.; Kummer, D. *Z. Anorg. Allg. Chem.* **1964**, *327*, 165. (e) Interrante, L. V.; Whitmarsh, C. K., submitted for publication in *J. Organomet. Chem.*

(18) Slight changes in the SiH region of this NMR spectrum are most likely due to differences in the degree of branching compared with other batches rather than any exchange reaction, as no peaks were seen in the Si–H region in the ²D NMR spectrum.
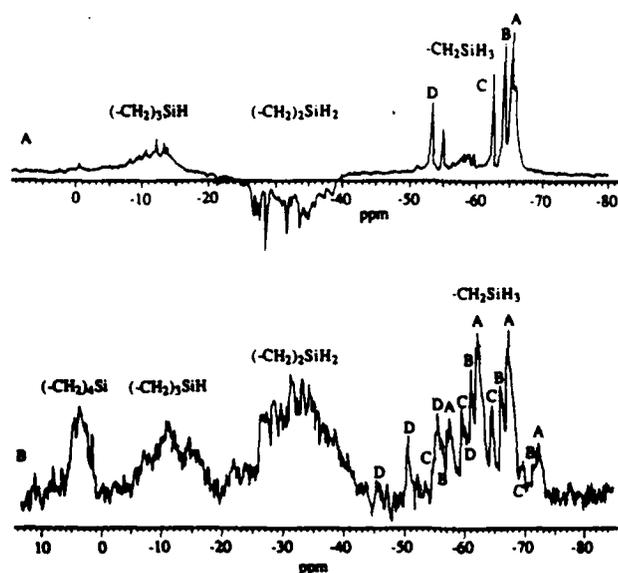
Figure 7. ^{29}Si{^{1}H} NMR spectra of hydridopolycarbosilane: (A) DEPT (multiplicity = 1.5); (B) proton coupled. Letters indicate sets of quartets ($^1J_{Si-H} \approx 200$ Hz) arising from SiH$_3$ end groups.

Figure 8. GPC of hydridopolycarbosilane, M_n = 747, M_w = 5200 vs polystyrene.

of the Si–Et groups are presumably buried under the Si–CH$_2$–Si multiplet. Peaks observed near 60 ppm in the ^{13}C NMR spectrum of the chloropolycarbosilane (assigned to the –OCH$_2$– carbons of SiOEt groups) are not seen in the reduced polymer, again suggesting that the ethoxy groups are eliminated during reduction.

The decoupled ^{29}Si DEPT NMR spectrum (multiplicity of 1.5) of the hydridopolycarbosilane (Figure 7A) shows that the groups of peaks between –8 and –14 ppm and several resolved singlets ranging from –53 to –66 ppm have odd numbers of hydrogens, whereas those between –26 and –39 have an even number. This is consistent with assignments as >SiHCH$_2$–, SiH$_3$CH$_2$–, and –SiH$_2$CH$_2$– polymer functionalities, respectively, using information from the NMR spectra of the model compounds^{17e} (Table I). The complexity of these NMR spectra reflects the branched structure of the polymer. The >SiCH$_2$– units do not appear on this NMR spectrum, as only silicons bearing hydrogens respond under these conditions. The coupled ^{29}Si NMR spectrum (Figure 7B) shows several clearly discernible, overlapping quartets with typical Si–H coupling constants of about 200 Hz. The coupled ^{29}Si NMR spectrum gives little information about the other Si–H functionalities because the peaks are so complicated.

The molecular weight distribution by GPC of the hydridopolycarbosilane (Figure 8) shows a very broad MW distribution, with most of the polymer falling between 450 and 3000 amu, but tailing off up to 50 000 amu to give a large polydispersity value of 6.95. The M_w for this polymer is 745, corresponding to about 15.4 repeat units as SiH$_{1.86}$Et$_{0.15}$CH$_2$, the approximate formula suggested by NMR and IR spectroscopy. The actual MW distribution could be considerably different from this, as this polymer is not very similar to the polystyrene standards employed.

NMR integration values show the actual "average" formula for the reduced polymer to be approximately [SiH$_{1.86}$Et$_{0.15}$CH$_2$]$_n$, about one ethyl group for every seven repeat units. As with the chloropolycarbosilane, the elemental analyses disagree; suggesting a formula closer to [SiH$_{1.1}$Et$_{0.05}$CH$_2$]$_n$. Due to the problems in obtaining good elemental analyses on preceramic compounds,^{16} this disagreement is not surprising. Low hydrogen content for this type of polymer could also result from several causes, such as Si–Cl, Si–Et, or Si–OEt substitution, in addition to Si–Si
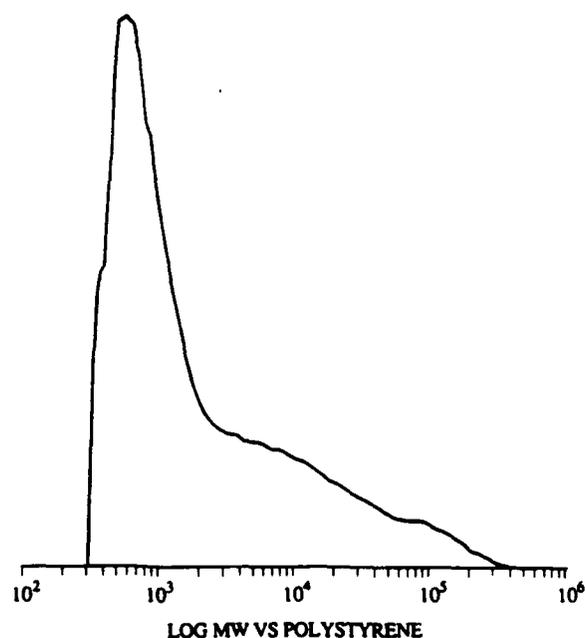
or Si–O–Si bonding. The presence of residual Si–Cl groups in the reduced polymer is unlikely, due to the reduction and aqueous workup procedure. Indeed, analysis of the hydridopolycarbosilane found only 1.63% chlorine, which appears to exist as residual chloromethyl groups seen in the proton NMR of the polymer. From the M_w of this polymer and approximate repeat unit weight, the chloromethyl end groups would result in about 2.6% chlorine content. The analysis of 1.63% seems reasonable, as partial reduction of these groups is achieved. The presence of oxygen-containing groups, such as Si–OEt or Si–O–Si, in this polymer is rendered unlikely by the results of oxygen analyses, which indicated only about 0.2% oxygen.^{19} In addition, proton and deuterium NMR studies indicated complete reduction of the SiOEt functionality. This is consistent with previous observations that alkoxy groups on silicon, even when surrounded by bulky groups, as in the case of [1-naphthyl]$_3$Si–OEt, are converted to the corresponding silanes by LiAlH$_4$ in high yield.^{20} Alkyl-substituted alkoxysilanes react similarly.^{21} It is difficult to detect any Si–O–Si in the polymer by ^{29}Si NMR spectroscopy as peaks due to SiH interfere. In addition, the strong Si–CH$_2$–Si deformation band obscures the Si–O–Si region in the IR spectrum of this polymer.

There is little evidence to suggest Si–Si bonding in the hydridopolycarbosilane. There is no precedent for magnesium-induced Si–Si bond formation, except for phenyl- (or aryl-) substituted chlorosilanes.^{12} Previous work by others^{22} showed that Cl$_3$Si–SiCl$_3$ gave silane gas on reduction with excess LiAlH$_4$. This suggests that if any Si–Si bonding is present in the chloropolycarbosilane, it could also undergo reduction to Si–H. The high solubility of the reduced polymer in pentane suggests that either Si–Si bonding does not form, or that it is eliminated during reduction, since formation of Si–Si bonding during the coupling reaction would lead to cross-linking. The pres-

(19) Oxygen analysis for this compound was performed by LECO; values ranged from 0.01 to 0.02% for three trials.

(20) Gilman, H.; Brannen, C. G. J. Am. Chem. Soc. 1951, 73, 4640.

(21) Emeléus, H. J.; Smythe, L. E. J. Chem. Soc. 1958, 609.

(22) (a) Gutowski, H. S.; Stejskal, E. O. J. Chem. Phys. 1954, 22, 939. (b) Finholt, A. E.; Bond, A. C. Jr.; Wilzbach, K. E.; Schlesinger, H. I. J. Am. Chem. Soc. 1947, 69, 2692.

ence of Si–Si bonding in the hydridopolycarbosilane is difficult to confirm by ²⁹Si NMR spectroscopy, as the Si–Si regions overlap with Si–H regions.

The formation of Si–Si bonding in the reduced polymer (with loss of hydrogen) after isolation, but prior to the sample analysis, could account for the low hydrogen content by elemental analysis. Samples of the reduced polymer have been observed to gradually increase in viscosity, eventually becoming rubbery and insoluble, and develop pressure when stored in sealed containers exposed to light. This is consistent with cross-linking through Si–Si bond formation and hydrogen loss.

The ethyl groups, as expected, are not affected by the reduction and remain in the hydridopolycarbosilane. Residual Grignard end groups in the chloropolycarbosilane, if any, would be converted to a magnesium aluminum hydride complex during the reduction.[23] Subsequent aqueous acid workup would result in the corresponding hydrocarbon end group, as shown in reactions 5 and 6.

$$>SiCH_2MgCl + LiAlH_4/Et_2O \rightarrow$$
$$>SiCH_2MgAlH_4 + LiCl \quad (5)$$

$$>SiCH_2MgAlH_4 \xrightarrow{\text{excess HCl/H}_2\text{O}}$$
$$>SiMe + MgCl_2 + H_2 + Al^{3+} + Cl^- \quad (6)$$
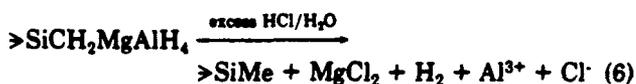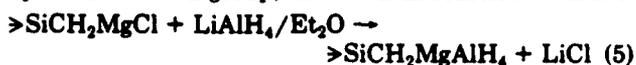
Part III: Hydridopolycarbosilane (from Nonaqueous Workup). The polymeric products from the nonaqueous workup are tacky, yellow solids which, unlike those prepared by aqueous workup, rapidly develop a whitish

coating on exposure to air. The IR spectrum of this polymer is similar to that from the aqueous workup, except for two additional peaks at 1930 and 670 cm⁻¹. These peaks, in addition to elemental analysis showing 6.64% aluminum, suggest that residual Al–H_x functionality is present.[24] LiAlH₄ itself is insoluble in the pentane used to extract the polymer from the residue and therefore not likely to be a contaminant. Furthermore, the polymer had a transparent yellow color with no sign of suspended solid.[25]

The ¹H NMR spectrum of this polymer contains a broad, complex peak between –0.6 and +1.5 ppm, on which is superimposed a narrower peak between 0.8 and 1.1 ppm. The Si–H peaks are similar to those of the polymer derived from the aqueous workup, appearing at 3.6–3.9, 3.9–4.1, and 4.1–4.3 ppm. Their integration ratio with respect to the Si–CH₂Si protons is considerably below the approximately 1:1 ratio seen for the polymer derived from the aqueous workup. Difficulty in separating byproducts of LiAlH₄ reductions of polymeric halosilanes by nonaqueous methods has been previously observed.[16a]

(23) Gaylord, N. G. *Reduction With Complex Metal Hydrides*; Interscience: New York, 1956; p 70.

(24) These peaks are observed when the IR spectrum of LiAlH₄ was run in Nujol.

(25) The possibility of a colloidal suspension of the LiAlH₄ in the polymer cannot be excluded.

PREPARATION OF NANOCRYSTALLINE COMPOSITES BY PYROLYSIS OF ORGANOMETALLIC PRECURSORS

L. V. Interrante*,@, W. J. Hurley, Jr.*, W. R. Schmidt*, D. Kwon,@ and R. H. Doremus,* Departments of Chemistry@ and Materials Engineering,* Rensselaer Polytechnic Institute, Troy, NY 12180-3590

P. S. Marchetti and G. E. Maciel, Department of Chemistry, Colorado State University, Fort Collins, CO 80523

ABSTRACT

Nanocrystalline composite ceramic powders were obtained by the pyrolysis of organometallic precursors to AlN, BN, SiC, Si_3N_4, and TiN. Both mixtures of known precursors to the individual ceramic components and specially prepared single-component precursors were employed to obtain binary composites of the type, SiC/AlN, Si_3N_4/AlN, Si_3N_4/BN, AlN/BN, and TiN/BN.

The powders obtained by heating the precursors to 1000^0C all appeared to be amorphous based on XRD patterns, although some nm-size crystallites were observed by TEM. Annealing in N_2 at 1600^0C produced a homogeneous distribution of nanocrystallites of the respective components.

This paper details the preparation of the precursor systems, the methodology employed for their pyrolysis, and the results of microstructural studies of the ceramic powders. The potential benefits of this approach to homogeneous, nanocrystalline, ceramic composites are discussed.

INTRODUCTION

Organometallic precursors to ceramics are receiving increasing attention in the context of high temperature structural composites [1]. Key reasons for the interest in these systems include the potential for 1) improved control over composition, phase distribution and homogeneity; 2) lower processing temperatures; 3) finer-grained materials; and 4) the generation of continuous fiber, films and other useful forms through solution or melt processing.

Following the successful development of Nicalon "SiC" fiber in Japan over 10 years ago [2], a variety of other covalent ceramic fibers have been obtained by using polymeric precursors [3]. In addition, such precursors have been employed to obtain fiber-reinforced ceramic matrix composites by liquid phase infiltration [4] and thin films on fibers and other substrates by solution deposition followed by pyrolysis [5]. In the course of this work, several examples of precursors to mixed ceramic phases have been identified [6 - 8]. Detailed studies of the mixed-phase ceramic products derived from these precursors have been limited and, in general, the use of organometallic precursors as a source of nanocrystalline composites has not received particular attention.

The high temperature stability, strength, and hardness of much Si_3N_4, SiC, BN, TiN and AlN have made these materials of much interest as components of cutting tools, bearings and rotors, turbine engines, and high temperature composites. Various mixtures of these ceramics have been found to exhibit properties that are superior to those of the separate component ceramics. For example, the addition of AlN to SiC was reported to reduce grain size, improve microstructural uniformity, and vary thermal conductivity and expansion in hot-pressed samples [9]. In this case, the formation of a solid solution with the $2H$ structure over a broad range of AlN/SiC compositions was evidenced by TEM/SAD studies of samples obtained by hot-pressing AlN/SiC mixtures. Recently, such solid solutions were obtained by pyrolysis of organometallic precursors [6]. Similarly, the additions of AlN to BN [10], BN to Si_3N_4 [11], and TiN to BN [12] have been found to result in improved toughness, sinterability, and other specific property improvements. Our work on the Si_3N_4/BN system has evidenced a marked decrease in the activation energy for surface area reduction of precursor-derived amorphous Si_3N_4 powder in the presence of BN, while at the same time crystallization of the Si_3N_4 at 1600^0C was inhibited [13].

The recent discovery of ductility and even superplasticity for nanocrystalline ceramics and ceramic composites has generated considerable interest from both a theoretical and practical perspective [14 - 16]. The ready availability of such superplastic ceramic materials could permit the fabrication of complex parts via simple net shape forming processes, such as sinter forging or extrusion [14,15]. In addition, improvements in sinterability and resulting mechanical properties relative to conventionally prepared material have been observed [16].

The first observation of superplasticity in covalent ceramics is credited to Wakai and co-workers [17] who prepared a

follow standard practice in organometallic chemistry [20] and have been described in detail in our earlier publications [6].

All ceramic products were handled in the glovebox due to their high surface area and affinity for moisture, except when preparing samples for X-ray diffraction, microscopy, and surface area determination. In the latter cases, the exposure to air was minimized as much as possible.

Electron microscopy samples of finely ground ceramic materials were prepared by passing Cu grids through a suspension of the powder in nitrocellulose/1 % amyl acetate, which was sonicated to break apart agglomerates. The grids were then lightly coated with C and/or Au to prevent charging in the electron beam. X-Ray diffraction measurements were made between $2\theta = 15 - 80@$. TGA experiments were carried out in flowing, prepurified N_2 or NH_3 with a heating rate of $10^0C/min$.

Precursors

Diethylaluminum amide, $[Et_2AlNH_2]_3$, was used as the precursor to AlN and prepared from the reaction of triethylaluminum with NH_3 [6]. A vinylic polysilane (VPS) (Union Carbide Corp. Y-12044) of approximate composition, $[[(SiMe_3)]_{0.32}[Si(CH=CH_2)Me]_{0.35}[Si(H)Me]_{0.18}[SiMe_2]_{0.07}[CH_2SiMe]_{0.08}]_n$, with n ca. 50, and a branched methylhydridopolycarbosilane (MPCS), $[MeHSiCH_2]_n$, were used as the polymeric precursors to SiC [6]. VPS was also used as a source of Si_3N_4 [21].

Single-component precursors to AlN/BN, TiN/BN, and Si_3N_4/BN composite powders were employed. The precursor to AlN/BN was prepared by refluxing a 1:1 (B:Al) molar ratio of tris-ethylaminoborane $(EtNH)_3B$ with diethylaluminum amide at 100°C for 2 h and cooling to room temperature [22]. This reaction yielded a viscous, turbid liquid which was used directly for the pyrolysis experiments described below. After pyrolysis the resulting white ceramic product was found to have a 1:2 ratio of B:Al, presumably due to loss of some of the $(EtNH)_3B$ reagent during pyrolysis. The TiN/BN precursor was prepared by the reaction of a 3:1 molar ratio of $(MeNH)_3B$ and tetrakis-dimethylaminotitanium, $(Me_2N)_4Ti$, at room temperature.

After several hours, the initially liquid reaction mixture converted to a dark red solid with little overall loss in weight. The Si_3N_4/BN precursor was prepared by refluxing

---

nanocrystalline Si_3N_4/SiC composite containing yttria and alumina, using a Si-C-N powder which was obtained from the vapor-phase reaction of $[Si(CH_3)_3]_2NH$ with NH_3. The resultant material exhibited superplastic elongation up to 150% in tension at 1600°C. An alternative approach to Si_3N_4-based superplastic ceramics was taken by Chen and co-workers [15] who used a nanocrystalline composite consisting mostly of a fine-grained, equiaxed, α'-sialon.

Based on this prior work, superplastic ceramics are apparently best realized with powders which have ultrafine (<500 nm), equiaxed grains, and a fairly uniform grain size distribution. This microstructure must also be stable under the conditions of the superplastic deformation. A second phase may be needed to inhibit crystal growth and enhance grain boundary diffusion.

Fabrication of nanocrystalline composites of covalent ceramic materials is problematic using conventional powders and processing techniques because: 1) the grain sizes and grain size distributions typically obtained by most powder production methods are too large; 2) the ability to control the purity and crystalline form of the product is limited; and 3) mixing two or more ceramic powders to form a composite which is homogeneous at the nanoscale level is often difficult if not impossible. Moreover, nanocrystalline, high-surface area powders, prepared typically by vapor phase and laser-initiated gas reactions, are expensive and difficult to handle, pack, and process without introducing impurities [18].

In the case of oxide ceramics, sol-gel processing of mixed metal alkoxides has provided an effective alternative to these other methods of preparing homogeneous, nanocrystalline composites [19]. In much the same way, the pyrolysis of appropriately designed organometallic precursors may provide a better general route to nanocrystalline covalent ceramic composites, while also enabling the preparation of new types of mixed-phase, ceramic fibers and matrices. We report here preliminary results of our efforts to develop organometallic precursor routes to nanocrystalline composite materials containing Si_3N_4, SiC, AlN, BN and TiN.

EXPERIMENTAL PROCEDURE

General

All precursor handling and preparation was done in a N_2-filled glovebox or with Schlenk techniques. The procedures used for precursor synthesis, handling, and characterization

1,3,5-trimethyl-1,3,5-trivinylcyclotrisilazane with trimethylamine borane adduct, $BH_3:N(CH_3)_3$, in toluene for up to 12 hours and removing the solvent under vacuum. Reactions were performed using Si/B ratios of 9, 3, and 1.

Preparation of Precursor Mixtures

Homogeneous liquids consisting of various ratios of VPS/[Et$_2$AlNH$_2$]$_3$ and MCPS/[Et$_2$AlNH$_2$]$_3$ were prepared by thoroughly mixing the respective liquid precursors. Precursors to Si$_3$N$_4$/BN composites were also obtained by mixing VPS with poly(borazinylamine) (PBZA), a known precursor to BN [23], in 1:1 and 10:1 weight ratios, as detailed elsewhere [7]. Except in the case of VPS/[Et$_2$AlNH$_2$]$_3$ where a small amount of a gas, identified as mainly ethane, was evolved, no obvious reaction of these precursor mixtures was observed prior to their use in the pyrolysis experiments.

For the preparation of the Si$_3$N$_4$/AlN composites, a large batch of the VPS/[Et$_2$AlNH$_2$]$_3$ mixture was initially prepared by mixing 34.3 g of VPS with 2.83 g of the aluminum amide. This was calculated to give a 95% Si$_3$N$_4$/ 5% AlN by weight composite after pyrolysis, based on the known ceramic yield of the separate precursors [6].

Pyrolysis of Precursors

Direct Pyrolysis (Procedure A)

Except as noted below, precursors mixtures were typically heated at 1-5°C/min in molybdenum foil boats to 1000°C in NH$_3$.

Samples were held at the desired temperature for 6-14 h and annealed at 1600°C in N$_2$ for 4 h.

Hot Drop Si$_3$N$_4$/AlN (Procedure B)

A quartz reaction vessel [6a] was maintained at 500°C while flowing (0.05 SCFH) NH$_3$ gas through it. Roughly 1/3 of the VPS/[Et$_2$AlNH$_2$]$_3$ mixture, prepared as described above, was loaded into a gas-tight, plastic syringe, equipped with a needle, which then was transferred from the glovebox and pierced through the septum on the reaction vessel. The viscous liquid mixture was "dropped" onto the heated surface at a rate of 1 drop every 5-10

sec. After complete addition of the mixture, the highly porous, white solid product was allowed to cool and collected in the glove box. Subsequent conversion to ceramic was carried out by direct pyrolysis as noted abo...

Preheating Followed by Pyrolysis Si$_3$N$_4$/AlN (Procedure C)

Approximately 1/3 of the VPS/[Et$_2$AlNH$_2$]$_3$ mixture was first heated at 140-150°C for 1 h in the glovebox and allowed to cool to room temperature. The resulting material was a tacky, gum-like solid. Subsequent heating to 1000°C was carried out in a tube furnace in flowing NH$_3$ (0.3-0.4 SCFH) employing the following schedule: heating to 140°C in 1 h, holding at 140°C for 1 h, heating to 1000°C in 6 h with a 14 h hold at 1000°C. The sample was then furnace cooled in N$_2$.

RESULTS

SiC/AlN

The results of our studies of the VPS/[R$_2$AlNH$_2$]$_3$ and MCPS/[R$_2$AlNH$_2$]$_3$ (where R = i-Bu or Et) precursor systems to SiC/AlN solid solutions and composites have been detailed elsewhere [6]. Based on the XRD data and TEM/SAD studies, both nanocrystalline composites of 2H AlN and β-SiC and 2H solid solutions of SiC/AlN were identified as products of the pyrolyses depending on the specific pyrolysis procedure and precursor combinations employed. In either case, after annealing the powders at 1600°C, the crystallite sizes were less than 500 nm and typically on the order of 10-50 nm.

Si$_3$N$_4$/AlN

Application of the three different pyrolysis procedures in NH$_3$ (see Experimental Procedures A, B, and C) to the VPS/[Et$_2$AlNH$_2$]$_3$ mixture yielded, after the 1000°C heating stage, tan powders which were apparently amorphous by XRD. However, TEM/SAD studies of these samples indicated small regions of nanosized crystallites in a matrix of predominantly amorphous material. After annealing to 1600°C, the powders were still white and consisted mainly of nanocrystalline α- and β-Si$_3$N$_4$ based on TEM/SAD and XRD results.

yellow liquid (Si/B = 9) to white, semi-solid pastes (Si/B = 3 and 1), and were soluble in aromatic hydrocarbon solvents. The char yields for the products pyrolyzed to 1100^{0}C in NH_3 were 40%, 20% and 20%, and were 52%, 40%, and 42% in N_2, for Si/B = 9, 3, and 1, respectively. The separate reactants gave 0% char yields when pyrolyzed under the same conditions. Analysis of the Si/B = 9 NH_3 pyrolysis product, after annealing at 1600^{0}C in N_2, gave: Si 54.2%, N 32.6%, B 2.8%, C <0.5%.
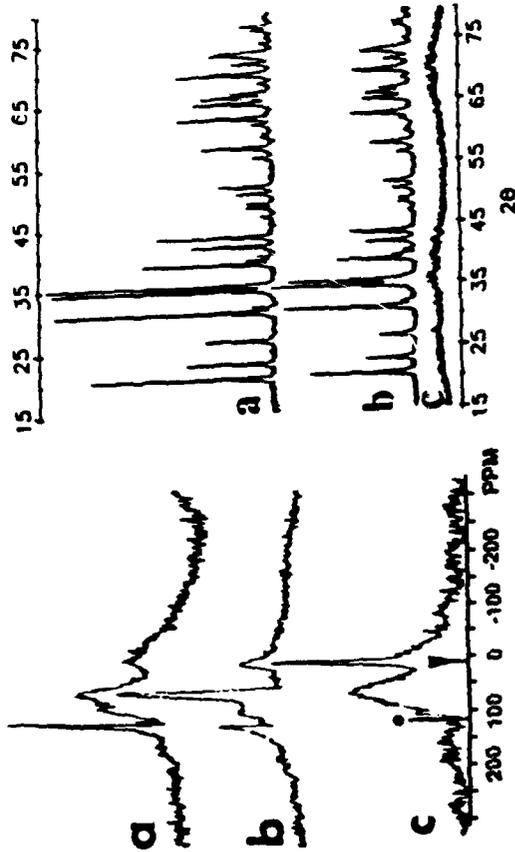
Figure 1. ^{27}Al solid state NMR spectra of Si_3N_4/AlN a) Hot drop (Procedure B), b) linear ramp (Procedure A), and c) preheated mixture (Procedure C); all heated to 1600^{0}C. ● = AlN, ▼ = Al_2O_3

Figure 2. XRD patterns of a) VPS-derived Si_3N_4, b) VPS/PBZA-Si_3N_4/BN, and c) single component precursor Si_3N_4/BN, following NH_3 pyrolysis and 1600^{0}C anneal.

The IR spectrum of the liquid polymer (Si/B = 9) showed a decreased intensity of the vinyl stretch at 3050 cm^{-1} relative to the N-H stretch at 3390 cm^{-1} compared to the spectra of the starting silazane and a new band at 1300-1360 cm^{-1} assigned to B-N and/or B-C. The ^{1}H, ^{13}C, and ^{11}B NMR spectra also showed a reduction in relative intensity of the peaks due to the vinyl groups and new peaks attributed to the CH_2CH_2B group.

The major difference in these powders was that the relative distribution of α/β-Si_3N_4 significantly varied among the three samples. The sample pyrolyzed in the "hot drop" apparatus (Procedure B) exhibited the most α, the one pyrolyzed in the furnace by using a linear temperature ramp (Procedure A) contained a mixture of α and β, whereas the sample held at 140-150°C prior to pyrolysis (Procedure C) exhibited essentially all β-Si_3N_4.

The crystallites exhibited two distinct shapes; blocky, equiaxed and rod-like, elongated shapes. The rod-like crystals exhibited a β-Si_3N_4-like electron diffraction pattern. The typical grain size in these materials was 40-80 nm.

Solid state ^{27}Al NMR showed that the Al environments are different in the three samples (Figure 1). The "hot drop" sample (Procedure B) gave a sharp resonance at 114.3 ppm, indicative of AlN_4 tetrahedra found in h-AlN, a broad peak between 100-40 ppm, which may be Al(O, N)$_{4-6}$ type species and a weaker feature near 15 ppm, which may be indicative of AlO_6 octahedra such as those in Al_2O_3 [24]. The sample derived from Procedure A exhibits a lower intensity 114.3 resonance, a sharper peak of enhanced intensity near 70 ppm, and a more intense 15 ppm peak. Finally, the sample obtained by Procedure C exhibits virtually no AlN_4, a broad peak due to multicoordinated Al(O,N) environments, and a strong peak at 15 ppm which is close in appearance and position to that exhibited by Al_2O_3.

Si_3N_4/BN

Composites derived from VPS/PBZA mixed precursors have been described previously [7]. IR spectral data corroborate the presence of both BN and Si_3N_4 in all samples; however, the XRD data indicate that, in close analogy to the results obtained using added h-BN powder [13], crystallization of the Si_3N_4 was inhibited in the presence of the BN precursor. Thus for the 1:1 VPS:PBZA samples, even after heating to 1600°C, only a very weak pattern indicative of α-Si_3N_4 was observed on a background of the broad peaks typical of turbostratic BN. On the other hand, for the 10:1 wt. % VPS:PBZA mixture significant crystallization of the Si_3N_4 was evident after the 1600°C anneal by XRD.

The products obtained from reactions of the methylvinylsilazane and the borane adduct ranged from a pale

with the 3-6 nm particle size observed by TEM (Figure 4).

Figure 4. Dark field transmission micrograph of TiN/BN composite.

Figure 3. Dark field transmission micrograph of AlN/BN composite.

The Si_3N_4/BN composites derived from the single-component precursor had IR spectra that were similar to those obtained from the mixed precursors. However, in this case the XRD patterns of samples heated to $1000^{\circ}C$ and $1600^{\circ}C$ show only broad features which are typical of nanocrystalline or amorphous materials. Distinguishable XRD patterns were only observed after heating the samples to $1750-1800^{\circ}C$ for at least 2 hours. These indicated that a mixture of $\alpha-Si_3N_4$ (major), $\beta-Si_3N_4$ (minor), and t-BN (minor) was present.

Figure 2 compares the XRD patterns of Si_3N_4 from VPS alone [21], Si_3N_4/BN from 10/1 wt. % VPS/PBZA [7], and Si_3N_4/BN from the 9:1 Si:B single-component precursor, after heating to $1600^{\circ}C$ for 4 hr. Crystal sizes were calculated from the XRD peak widths to be ca. 40 nm for the VPS-Si_3N_4 and 30 nm for the VPS/PBZA-Si_3N_4, which are in agreement with TEM measurements.

TEM examination of the $1600^{\circ}C$ composite powder derived from the single-component precursor showed mainly featureless particles with a few nm-sized crystals of Si_3N_4. The Si_3N_4 grain size in this sample was substantially smaller than either the VPS-derived Si_3N_4 or that obtained by pyrolysis of VPS/PBZA.

AlN/BN

The single component precursor to this composite yields a white solid in 40% char yield after pyrolysis in NH_3 to $1000^{\circ}C$.

The IR spectrum of the $1000^{\circ}C$ sample shows features characteristic of both the B-N and Al-N bonding in the respective ceramic materials [22,24]. The XRD pattern of the $1000^{\circ}C$ sample confirms the presence of partially crystalline AlN. Further heating of the composite to $1600^{\circ}C$ improves the crystallinity of the AlN and reveals two broad peaks indicative of t-BN at $2\theta=25^{\circ}$ (002) and 42° (100, 101) [25]. TEM of the $1000^{\circ}C$ material shows AlN grains which are uniformly sized (5-10 nm) and homogeneously dispersed in a matrix of t-BN (Figure 3).

TiN/BN

Following pyrolysis in NH_3 to $1000^{\circ}C$, this composite was obtained in 30% char yield as a dark brown solid. The XRD pattern exhibits broad characteristic peaks for TiN at $2\theta=37^{\circ}$ (111), 43° (200), 62° (220) and t-BN at $2\theta=25^{\circ}$ and 42° (buried under TiN peak). The TiN peak width was used to calculate a particle size of ca. 3 nm, which is in good agreement
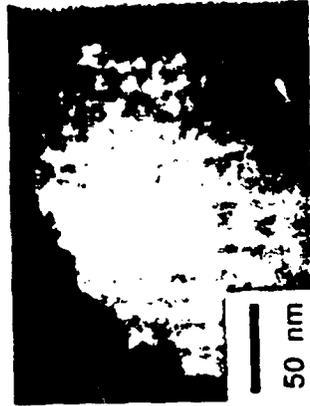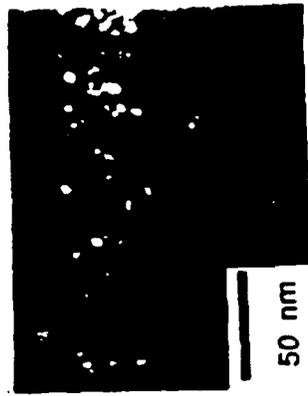
DISCUSSION

Preliminary results of this investigation have shown that both mixtures of precursors to the separate ceramics and single-component precursors in which the metals (or metalloids) of interest are precombined in a common structure can be used to obtain homogeneous, nanocrystalline composites containing SiC, Si_3N_4, AlN, BN, and TiN. However, it is also clear from these studies that the choice of precursor systems and also the pyrolysis procedure can have a profound effect on the composition and microstructure of the ceramic end product. For example, we have found that a sequence of NH_3 and N_2 treatments yields SiC/AlN materials from mixed organosilicon and organoaluminum precursors, whereas heating the same precursor mixtures in NH_3 alone gives Si_3N_4/AlN mixtures [6c]. For the SiC/AlN system, variations in the pyrolysis procedure (i.e., using a rapid pyrolysis vs. a slow temperature ramp) and in the precursor source were employed to obtain either a nanoscale mixture of β-SiC and 2H-AlN or a 2H-SiC/AlN solid solution [6]. The difference in the products appears to be related to the different rates of solidification of the two initially liquid precursors and the need to maintain an atomically mixed Si/Al precursor during conversion to the ceramic phases. Rapid pyrolysis apparently aids in maintaining such a mixture as does reaction between the precursors prior to their conversion to solids.

The utility of chemical interactions between the precursor sources, as a means of limiting the degree of phase separation in

their microstructure. Moreover, the [...] of these nanocrystalline (or amorphous) ceramic powder mixtures to monolithic ceramic objects, or the direct use of the precursors to prepare fibers, matrices or coatings, represent major steps to be surmounted before the full potential of this approach can be adequately assessed. Efforts to resolve these and other key issues relating to the application of organometallic precursors to the fabrication of composite materials are currently in progress in our laboratories.

ACKNOWLEDGEMENTS

$Joel 100CXII
$Phillips 1710W Automated Powder Diffractometer, equipped with a monochromator
$$Perkin Elmer Series 7 Thermal Analysis System
$$Galbraith Laboratories, Inc.

REFERENCES

1. M. Peuckert, T. Vaahs, and M. Bruck. "Ceramics From Organometallic Polymers", Adv. Mater., V 2 (9) (1990), P. 398.

2. J. Tanaka, "Development of silicon carbide fiber application". Chem. Econ. Eng. Rev., V 12 (1980). P. 40.

3. see, for example: J. Lipowitz, H.A. Freeman, H.A. Goldberg. R.T. Chen, E.R. Prack. "Structure and Properties of Ceramic Fibers from Polymeric Precursors", Mater Res Soc Symp Proc, V 73 (1986), p.489; K. Okamura, M. Sato, Y. Hasegawa, "Silicon Nitride Fibers and Silicon Oxynitride Fibers by the Nitridation of Polycarbosilane", Ceram. Int., V 13 (1987), p.55; K.J.L. Paciorek and R.L. Kratzer, "Boron Nitride Preceramic Polymer Studies". Ceram. Eng. Sci. Proc., V 9 (1988), P. 993; J. Bolt and F.N. Tebbe, "Aluminum Nitride Fibers: Sintering and Microstructure". In Proceedings of Advances in Ceramics, V 26, H.M. O'Bryan, K. Niwa, W. Young, and M.S. Yan, Eds.; Amer. Ceram. Society; in press.

the product ceramic, is also suggested by the results of our studies of the two different precursor routes to Si_3N_4/BN composites. The use of a mixture of the poly(borazinylamine) and VPS was found to yield appreciably larger grain sizes for the Si_3N_4 crystallites in the t-BN matrix as compared to the single-component, boron and silicon-containing precursor. The limited miscibility and different decomposition temperatures of the PBZA and VPS precursors are clearly not conducive to obtaining a homogeneous ceramic mixture after pyrolysis. On the other hand, in the case of the single-component precursor, NMR and IR data indicate that the BH_3 reacts with the vinyl groups on the silazane during the toluene reflux, presumably leading to an ethylene-bridged borosilazane polymer containing a homogeneous distribution of B and Si atoms [27]. This atomic-level distribution of B and Si is apparently maintained to an appreciable extent during the subsequent pyrolysis of this polymer to the ceramic composite.

The ability to control the composition and phase distribution of the ceramic products through variations in the pyrolysis procedure is also illustrated by the results of the study of the 95% Si_3N_4/5% AlN system. In this case, the proportion of α- to β-Si_3N_4, obtained on annealing the initially obtained amorphous powder at 1400-1600°C, appears to depend on the heating rate used for pyrolysis of the precursor mixture. As the precursor mixture is held for a longer time period between ca. 100°C and 200°C, the proportion of β-Si_3N_4 seems to increase, whereas rapid pyrolysis by dropping the precursor mixture onto a very hot surface yields almost entirely the α-phase. Based on solid state ^{27}Al NMR results (Figure 1), the proportion of β-Si_3N_4 correlates with the amount of Al that has been converted to AlO_x species, presumably by reaction of the organoaluminum amide with adventitious sources of oxygen in the initial polymer or in the environment prior to its conversion to AlN. Alumina is known to catalyze the α to β transition in Si_3N_4 [28] and the presence of these AlO_x species in the mixture may be effective in promoting the crystallization of the β-form from the initial amorphous phase.

This work has provided ample evidence for the potential utility of the "precursor pyrolysis" approach as a means of generating nanophase composites of a wide range of covalent ceramic materials. However, it is also clear that much remains to be learned about the detailed nature of these materials and the role of precursor structure and chemistry in determining

10. J. R. Morris and R. A. Tanzilli, "Aluminum Nitride-Boron Nitride Composite Article and Method of Making Same", US Patent 4,666,873 (1987).

11. K. S. Mazdiyasni and R. Ruh, "High/Low Modulus Si_3N_4-B Composite for Improved Electrical and Thermal Shock Behavior", J. Am. Ceram. Soc., V 64 [7] (1981). p. 415.

12. H. Shimoda, "Sintered Hard Alloys for Cutting Tools" Japanese Patent 61,179,847, (August 1986).

13. a) V. Sukumar, M. S. Thesis, "Effect of Boron Nitride on the Coarsening of Silicon Nitride", Rensselaer Polytechnic Institute December 1989. b) V. Sukumar, W. R. Schmidt, R. H. Doremus, and L. V. Interrante, "Effect of Boron Nitride on the Coarsening of Silicon Nitride", Mat. Letters, V 9 [4] (1990), p. 117.

14. Y. Maehara and T. G. Langdon, "Review - Superplasticity in Ceramics", J. Mater. Sci., V 25 [5] (1990), p. 2275.

15. I.-W. Chen and L.A. Xue. "Development of Superplasti Structural Ceramics", J. Am. Ceram. Soc., V 73 [9] (1990), p. 2585.

16. J. Eastman and R. Siegel, "Nanophase Synthesis Assemble Materials from Atomic Clusters", Res. & Devel. (1989) (January) p. 56.

17. F. Wakai, Y. Kodama, Sakaguchi, N. Murayama, K. Izaki, and K Niihara, "A Superplastic Covalent Crystal Composite", Nature, 344 (1990). p. 421.

18. G. W. Kriechbaum and P. Kleinschmit, "Superfine Oxide Powder: - Flame Hydrolysis and Hydrothermal Synthesis", Adv. Mater. [10] (1989). p. 330.

19. R. Roy, "Ceramics by the Solution-Sol-Gel Route", Science, V 238 (1987), p. 1664; D.R. Ulrich, "Chemical Processing of Ceramics", Chem. & Engr. News, (1990) [January 1], p. 28; A. Clearfield, A.M. Gadalla, W.H. Marlow, and T.W. Livingston, "Synthesis of Ultrafine Grain Ferrites", J. Am. Ceram. Soc., V 72 [10] (1989). p. 1789.

20. R.B. King, "Organometallic Syntheses, V 1 Transition-Metal Compounds", (1965) Academic Press, NY.

21. W. R. Schmidt, V. Sukumar, W. J. Hurley, Jr., R. Garcia, L. V. Interrante, and R. H. Doremus, "Silicon Nitride Derived from

4. W.S. Coblenz, C.H. Wiseman, P.B. Davis, R.W. Rice, "Formation of Ceramic Composites and Coatings Utilizing Polymer Pyrolysis", in Emergent Process Methods High-Technol Ceram., Mater. Sci. Res., V 17 (1984), p. 271; R.P. Boisvert and R.J. Diefendorf. "Polymer Precursor SiC Matrix Composite", Ceram. Eng. Sci. Proc., V 9 [7-8], Am. Ceram. Soc.(1988). p. 873.

5. J.S. Beck, C.R. Albani, A.R. McGhie, J.B. Rothman, and L. Sneddon, "Dibromoborane-Dimethyl Sulfide: A Simple Molecular Precursor for the Formation of Bulk Powders and Fiber Coatings of Boron Nitride", Chem. Mater., V 1 (1989), p. 433. ; R.T. Paine, C.K. Narula, R. Schaeffer, and A.K. Datye. "Formation of Boron Nitride Coatings on Metal Oxides", Chem. Mater., V 1 (1989). p. 486; 2. Jiang and L.V. Interrante, "N,N'-Bis(triethylaluminio)-ethylenediamine and N,N'-Bis(trimethylaluminio)ethylenediamine -Derived Organometallic Precursors to Aluminum Nitride: Syntheses, Structures, and Pyrolyses", Chem. Mater., V 2 (1990), p. 439.

6. a) C. L. Czekaj, M. L. J. Hackney, W. J. Hurley, Jr., L. V. Interrante, G. A. Sigel, P. J. Shields, and G. A. Slack. "Preparation of Silicon Carbide/Aluminum Nitride Ceramics Using Organometallic Precursors", J. Am. Ceram. Soc., V 73 [2] (1990). p. 352; b) L.V. Interrante, C.L. Czekaj, M.L.J. Hackney, G.A. Sigel, P.J. Shields, and G.A. Slack, "An Investigation into the Preparation, Properties, and Processing of SiC/AlN and Si_3N_4/AlN Solid Solutions from Organometallic Precursors", Mat. Res. Symp. Proc., V 121 (1988), p. 465; c) M.L.J. Hackney, L.V. Interrante, G.A. Slack, and P.J. Shields, "Organometallic Precursors to $Al_wSi_xN_yC_z$ Ceramics", Ultrastructure Processing of Advanced Ceramics, J. D. Mackenzie and D. R. Ulrich, editors, John Wiley and Sons, New York (1988). p. 99.

7. W. R. Schmidt, W.J. Hurley, Jr., V. Sukumar, R. H. Doremus, and L. V. Interrante, "Polymer Derived Si_3N_4/BN Composites", Mat. Res. Soc. Symp. Proc., V 171 (1990). p.79.

8. D. Seyferth and H. Plenio, "Borasilazane Polymeric Precursors for Borosilicon Nitride", J. Am. Ceram. Soc., V 73 [7] (1990), p. 2131.

9. a) A. Zangvil and R. Ruh, "Phase Relationships in the Silicon Carbide - Aluminum Nitride System", J. Am. Ceram. Soc., V 71 [10] (1988). p. 884; b) W. Rafaniello, M. R. Plichta, and A. V. Virkar, "Investigation of Phase Stability in the System SiC-AlN". J. Am. Ceram. Soc., V 66 [4] (1983), p. 272.

an Organometallic Polymeric Precursor: Preparation and Characterization", *J. Am. Ceram. Soc.*, V 73 [8] (1990). p. 2412.

22. D. Kwon, W. R. Schmidt, L. V. Interrante, P. S. Marchetti, and G. E. Maciel, "Preparation and Microstructure of Organometallic Polymer Derived AlN-BN Composites", Proceedings of the Symposium on "Inorganic Polymers and Oligimers", IUPAC 33rd Symposium on Macromolecules, Montreal, Canada, July 1990, Kluwer Publ. Co., in press.

23. C. K. Narula, R. Schaeffer, R. T. Paine, A. Datye, and W. F. Hammetter, "Synthesis of Boron Nitride Ceramics from Poly(borazinylamine) Precursors", *J. Am. Chem. Soc.*, V 109 (1987), p. 5556.

24. R.A. Nyquist and R.O. Kagel, Infrared Spectra of Inorganic Compounds, Academic Press, NY (1971); C. K. Narula, R. Schaeffer, A.K. Datye, T.T. Borek, B.M. Rapko, and R. T. Paine, "Synthesis of Boron Nitride Ceramics from Oligimeric Precursors Derived from 2-(Dimethylamino)-4,6- dichloroborazine", *Chem. Mater.*, V 2 (1990). p. 384.

25. J. Thomas, N.E. Weston, and T.E. O'Connor, "Turbostratic Boron Nitride. Transformation to Ordered-layer-lattice Boron Nitride", *J. Am. Chem. Soc.*, V 84, p. 4619.

26. R. Dupree, M. H. Lewis, and M. E. Smith, "Structural Characterization of Ceramic Phases with High-Resolution [27] Al NMR", *J. Appl. Cryst.*, V 21 (1988), p. 109.

27. Another possible pathway for polymer formation which produces B-N-Si bonds by a reaction involving the -N-H + -B-H groups is suggested by the work of Seyferth and Plenio on the related borane + methylsilazane precursor to "borosilicon nitride" [Ref. 8]. This reaction is less likely in our system due to steric effects induced by the vinyl + methyl substitution on Si [see Ref. 8].

28. T. Fukuhara, "Effect of Nitrogen on the α/β Phase Conversion in Silicon Nitride", *J. Am. Ceram. Soc.*, V 68 [9] (1988). C226.

SYNTHESIS AND PYROLYSIS CHEMISTRY OF POLYMERIC PRECURSORS TO SiC AND Si_3N_4

L.V. INTERRANTE, C.K. WHITMARSH, T.K. TROUT, W.R. SCHMIDT,
Department of Chemistry
Rensselaer Polytechnic Institute,
Troy, NY 12180-3590.

ABSTRACT

A commercial vinylic polysilane has been used to obtain both SiC and Si_3N_4 by pyrolysis in N_2 and NH_3, respectively. The polymer-to-ceramic conversion process was studied by GPC, TGA/DTA, elemental analyses, FTIR, solid state NMR (^1H, ^{13}C and ^{29}Si), XRD, BET surface area measurements, and analysis of the gaseous decomposition products, providing a detailed picture of the cross-linking process and the evolution of the ceramic products.

In pursuit of alternative precursors to SiC and Si_3N_4, a novel branched polycarbosilane of the approximate composition $[SiH_{2-x}Et_xCH_2]$ (where x = 0.15) was obtained by the Grignard coupling of chloromethyltrichlorosilane followed by reduction with $LiAlH_4$; cleavage of diethylether by the chlorosilane was identified as the source of the ethyl groups in the final hydridopolycarbosilane. This polycarbosilane yields partially crystalline SiC ceramic on pyrolysis to 1000 °C in N_2. Annealing of this product at 1400-1600 °C results in further crystallization of β-SiC. Preliminary studies of the polymer-to-ceramic conversion process in N_2 by GPC, TGA, FTIR and NMR methods indicate that cross-linking occurs by H_2 elimination and Si-Si bond formation and that the 1000 °C product has a much lower proportion of free carbon than the corresponding ceramic derived from the vinylic polysilane.

1. INTRODUCTION

A wide range of organosilicon polymers have been studied over the last 15 years as potential precursors to SiC [1]. Several of these systems have found commercial use as sources of SiC fibers and as ceramic binders. A common feature of these precursors is that they generally contain a higher proportion of carbon to silicon than is

243

demanded by the 1:1 stoichiometry of SiC, requiring the elimination of the excess organic functionality during pyrolysis and thereby lowering the potential char yield of SiC. Moreoever, the pyrolytic conversion of such precursors to SiC is rarely accomplished cleanly, which leads to the incorporation of substantial quantities of excess carbon in the ceramic product. It has recently been shown that some of these same organosilicon polymers can be used as sources of Si_3N_4 by carrying out the pyrolytic conversion in NH_3 [2].

Most of the available precursors are obtained as highly crosslinked polymers of uncertain and often variable structure and composition, which causes difficulties in controlling physical properties that are appropriate for processing as well as for maintaining a uniform and consistent ceramic composition and microstructure. Furthermore, pyrolytic conversions in an inert atmosphere or in ammonia were followed by complete analysis of the intermediate and final products in only a few cases [3]. A detailed understanding of the relevant chemical processes involved in either case is still lacking.

Work in our laboratory has been directed towards three main goals: (1) the elucidation of the polymer-to-ceramic conversion process for selected organosilicon polymers in sufficient detail to enable the intelligent selection of both precursors and functionalities appropriate to particular processing objectives; (2) the synthesis and characterization of new precursors to SiC and Si_3N_4; (3) the application of polymeric precursors to the preparation of ceramic nanocomposites and ultrastructures containing two or more components (e.g., SiC and AlN).

In this paper we will summarize the key results of our investigation of the polymer-to-ceramic conversion process for a commercial vinylic polysilane and then describe the synthesis of a new polycarbosilane and the preliminary results of the study of its pyrolysis in N_2.

2. RESULTS AND DISCUSSION

2.1. STUDIES OF THE PRECURSOR TO CERAMIC CONVERSION OF VINYLIC POLYSILANE.

Our initial efforts to characterize the conversion process for polymeric organosilanes have focused on a detailed study of a vinylic polysilane (VPS) [Union Carbide, Y-12044] [4]. Based on our solution and solid state NMR studies of VPS, an approximate composition,
$[[(SiMe_3)]_{0.32}[Si(CH=CH_2)Me]_{0.35}[Si(H)Me]_{0.18}[SiMe_2]_{0.07}[CH_2SiMe]_{0.08}]_n$
was derived for the sample that we obtained from Union Carbide. This polymer has been widely employed as a precursor to silicon carbide [1d-e, 4] and has been used recently as the matrix source in SiC/SiC ceramic composites [5]. VPS is obtained by sodium-induced coupling of a mixture of chloromethyl-, chloromethylhydrido- and chloromethylvinyl-silanes [4] and is known to give a carbon-rich silicon carbide ceramic

on pyrolysis [4b,6]. Preliminary studies of the thermosetting process known to occur at around 225 °C have been carried out by Lee and Hench [7] while Bowen and coworkers monitored the increasing crystallinity of the resulting ceramic with increasing temperature from 1000 °C to 2100 °C [6]. Solid solutions and composites of SiC and Si_3N_4 with AlN or BN have been prepared by copyrolysis of VPS with organoaluminum amides [8a] or a polymeric precursor to boron nitride [8b].

We have carried out studies on the pyrolysis of VPS under both N_2 [9] and NH_3 [2d,10] with TGA/DTA, and have examined the intermediate and final solid products by elemental analyses, FTIR, solid state NMR (^{1}H, ^{13}C and ^{29}Si), and XRD, as well as the gaseous products by gas chromatography, mass spectrometry and FTIR. The main chemical differences between the conversion of VPS under N_2 and NH_3 begin to appear only above ca. 250 °C, where substantial changes in the nature of the solid products are seen by solid state NMR, IR and other methods. The detected gaseous decomposition products appear to be basically the same for the two atmospheres, consisting of trimethysilane and lesser amounts of hydrocarbons and other methylsilanes. Moreover, the general shape of the TGA curves for the pyrolysis in N_2 and NH_3 are quite similar (Figure 1), although pyrolysis in NH_3 causes larger weight losses from 50-150 °C and 300-600 °C, which results in a 15% lower char yield than in N_2. The ceramic products obtained at 1000 °C are
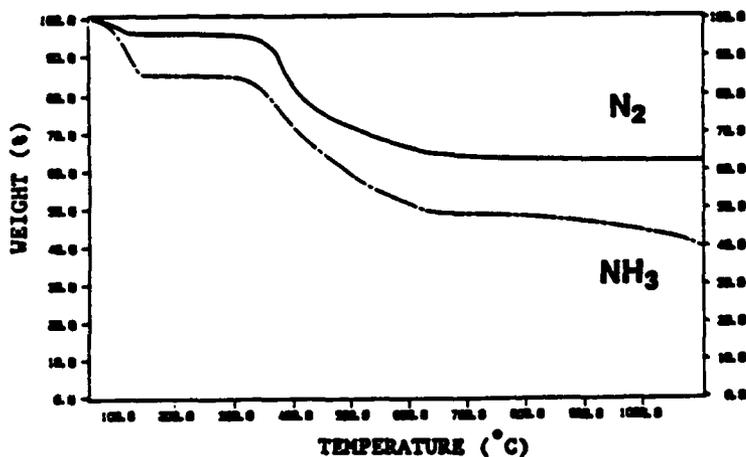
Figure 1. TGA curves for VPS heated in N_2 and NH_3 at a rate of 5 °C/min.

substantially different, consisting of C-rich, partially crystalline β-SiC in the case of N_2 and essentially pure, partially crystalline α-Si$_3$N$_4$ when NH$_3$ is used. In both cases the polymer undergoes extensive crosslinking between ca. 100 and 250 °C, resulting in the formation of a translucent glassy solid. The chemistry occuring in this temperature regime appears to be essentially independent of the atmosphere and to consist of both direct vinyl coupling (presumably radical initiated) and hydrosilation, with a greater proportion of direct vinyl coupling relative to hydrosilation. This conclusion was reached on the basis of solid state ^{13}C and ^{1}H NMR measurements utilizing the CRAMPS technique, and FTIR, where a plot of the ratio of the vinyl C-H to the Si-H stretching frequency intensities vs temperature shows a sharp drop in the same temperature region as the observed solidification of the polymer (120-200 °C).

On heating above 300 °C in N_2, the yellowish glassy solid was transformed into a black solid by 600 °C, resulting in a major fraction of the overall 35-40 % weight loss observed by TGA to 1000 °C. As suggested by the results of the IR, NMR studies and the gas product analysis, the chemistry occurring in this region appears to be quite complex, involving extensive homolytic bond cleavage and, presumably, radical chain reactions. Both the IR and NMR data suggest that extensive methylene insertion into the Si-Si bonds occurs above 300 °C, adding substantially to the small amount of Si-CH$_2$-Si units initially present in the polymer. A similar reaction has been proposed in the case of tne conversion of poly(dimethylsilanes) to Yajima's polycarbosilane [11]. The major gaseous product (ca. 90% of the total amount) in the region of maximal weight loss (300-750 °C) is trimethylsilane, suggesting that extensive chain scission, presumably by homolytic Si-Si bond cleavage, occurs during decomposition of the polymer. Significant amounts of C_1 to C_4 hydrocarbons and Me$_x$SiH$_{4-x}$ (x = 1 - 4) were also observed among the gaseous products, indicating that rearrangement of H and alkyl groups on Si probably occurs as well as radical cleavage and coupling reactions.

The IR and NMR spectra of the solids isolated at various temperatures during the decomposition show the gradual conversion of the polymer to a preceramic SiC. Thus the IR and ^{1}H CRAMPS spectra confirm the decreasing concentration of hydrogen with increasing pyrolysis temperature. The ^{13}C NMR demonstrate the coalescence of the various Si$_x$-C$_y$ units to a single peak representing the SiC$_4$ units in SiC and the development, above 400 °C, of a separate peak at lower field due to excess carbon. ^{1}H -> ^{13}C cross polarization NMR experiments indicate that even after heating to 1000 °C, a significant hydrogen concentration remains in the ceramic, which may serve to complete bonding saturation around carbon and Si centers. Preliminary ESR studies of the 1000 °C sample suggests that there is also a significant concentration of free radicals which are probably associated with incompletely bonded C or Si sites. Elemental analysis indicates that the H concentration is ca. 0.5 % and that there is a 17 % excess carbon than in stoichiometric SiC.

As was observed previously [6], further heating to 1600-1900 °C is

required to fully crystallize the SiC. An XRD pattern consistent with that of partially crystalline β-SiC was obtained for the 1000 $^\circ$C N_2 pyrolysis product of VPS. Further crystallization occurred after annealling this powder to 1600 $^\circ$C.

The main differences in chemistry that occur during pyrolysis in NH_3 start to appear above 250 $^\circ$C. The graph of the elemental compositions of the solids isolated after pyrolysis in NH_3 for 10 h at the indicated temperature (Figure 2), shows that nitrogen begins to appear in significant amounts in the solids at 400 $^\circ$C, and by 650 $^\circ$C it has virtually replaced the carbon that was present in the original polymer. The 1000 $^\circ$C product was found to contain only 1.8 % carbon; after annealing this solid at 1600 $^\circ$C under N_2 the analysis corresponds reasonably well to stoichiometric Si_3N_4. Both the IR and NMR spectra
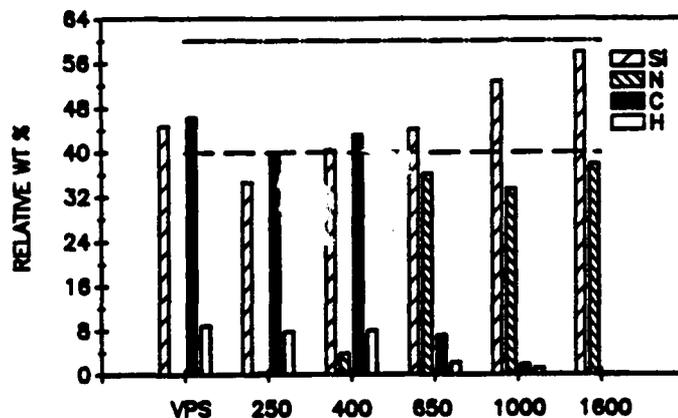
Figure 2. Elemental Analyses for solids isolated during pyrolysis of VPS in NH_3 to 1000 $^\circ$C and annealed in N_2 at 1600 $^\circ$C. Lines indicate theoretical levels of Si and N in stoichiometric Si_3N_4.

(^{13}C and ^{29}Si) show corresponding changes in this region that are consistent with the introduction of NH_x groups and loss of C-H functionality. The solid state ^{13}C MAS NMR spectrum of the 400 $^\circ$C sample shows a broad peak centered near 5 ppm, whereas the spectra obtained for the 650 and 1000 $^\circ$C samples show no peaks above background. In the ^{29}Si NMR spectra, very broad resonances are observed for the 250 and 400 $^\circ$C samples, suggesting a large number of different Si environments. By 650 $^\circ$C these peaks have coalesced into a single, relatively sharp peak near -45 ppm, indicative of a SiN_4 environment analogous to that in the amorphous and crystalline forms of Si_3N_4 [12].

The 1000 °C product is already partially crystalline by TEM/SAD and has an effective surface area of 250 m²/gm based on BET measurements with N_2 adsorption. This solid crystallizes to high purity α-Si_3N_4 on heating above 1400 °C with a considerable (90%) reduction in the surface area [2d].

The detailed nature of the chemical reactions occuring in the presence of NH_3 in the 250-650 °C region remains to be fully determined; however, our TGA and gas analysis results suggest that one of the roles of NH_3 is to facilitate the elimination of silanes and hydrocarbons, possibly by acting as an efficient source of hydrogen and a radical trap. The introduction of N presumably occurs by nucleophilic attack of NH_x species on Si, allowing elimination of the C-containing substituents as simple hydrocarbons.

2.2. SYNTHESIS OF NEW POLYCARBOSILANE PRECURSORS

Our efforts to synthesize new SiC polymer precursors have focused on the preparation of polycarbosilane polymers by two main reaction pathways: (1) ring opening polymerization (ROP) of disilacyclobutanes, and (2) Grignard coupling of chlorocarbosilanes. In the former case, 1,3-dimethyl- and 1,3-tetramethyl-1,3-disilacyclobutane were converted to high molecular weight polycarbosilanes by ROP with the aid of a platinum catalyst [13]. As was previously known [14], the fully methylated polycarbosilane gave a negligible char yield on pyrolysis in N_2; however, the $[SiMe(H)CH_2]_n$ polymer derived from the dimethyldisila-cyclobutane gave a low yield of amorphous SiC on pyrolysis to 1000 °C, which could be increased by increasing the molecular weight of the polymer or by holding at 400 °C to allow cross-linking by hydrogen elimination and Si-Si bond formation [13].

The second approach to polycarbosilane precursors to SiC has involved the preparation of a highly branched polymer of the approximate composition "SiH_2CH_2" by Grignard coupling of chloromethyltrichloro-silane [Cl_3SiCH_2Cl] followed by reduction with $LiAlH_4$ [15].

$$Cl_3SiCH_2Cl \xrightarrow[\text{reflux, 5d}]{Mg, Et_2O} \text{"}[SiCl_2CH_2]_n\text{"} \xrightarrow[\text{2] } H_2O/HCl]{\text{1] } LiAlH_4/Et_2O} \text{"}[SiH_2CH_2]_n\text{"} \tag{1}$$
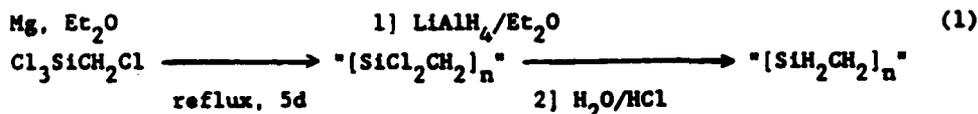
This process was followed in detail by trapping intermediates with methanol, isolating low molecular weight reduced products, and by carrying out selected model reactions with monofunctional chlorosilanes. Reactions employing $LiAlD_4$ and D_{10}-ether were also performed in order to characterize the various functional groups on Si which were introduced during the Grignard coupling reaction and the subsequent reduction. The key features of the coupling reaction are an almost exclusive occurance of "head-to-tail" coupling (i.e., C to Si) and extensive branching at Si

due to the trifuctional nature of the Si "tail". The result is a complex arrangement of $-SiCH_2-$, $=SiCH_2-$ and $\equiv SiCH_2-$ units, along with Cl_3Si- and $-CH_2Cl$ end groups. Due to the propensity for "head-to-tail" coupling and the 1:1 ratio of C to Si atoms, there is little or no crosslinking; thus, the polymers are viscous oils which are largely soluble in hydrocarbon solvents.

A further level of complexity is introduced by the chlorosilane-induced cleavage of the diethylether solvent during the course of the Grignard coupling reaction. This reaction is carried out under ether reflux for several days to build up the molecular weight of the polymer. Under these conditions the following ether-cleavage reaction occurs [16], leading to the substitution of -OEt groups onto the Si-Cl sites and the formation of EtCl.

$$\equiv SiCl \ + \ Et_2O \ \longrightarrow \ SiOEt \ + \ EtCl \qquad (2)$$
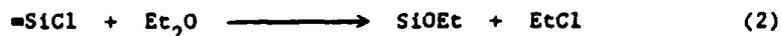
In the presence of Mg this EtCl forms a Grignard reagent which also reacts with the Si-Cl groups.

$$EtCl \ + \ Mg/Et_2O \ \longrightarrow \ EtMgCl/Et_2O \qquad (3)$$

$$EtMgCl/Et_2O \ + \ \equiv SiCl \ \longrightarrow \ \equiv SiEt \ + \ MgCl_2 \ + \ Et_2O \ (4)$$

Conclusive evidence for these reactions has been obtained from ^{2}D-NMR measurements carried out on the product isolated from the Grignard reaction conducted in D_{10}-ether. Based on NMR integrations, the level of -OEt and -Et introduction into the initial chloropolycarbosilane was estimated to be on the order of one Et and one OEt group per 13.3 SiCl sites, resulting in the following average composition for this polymer, $[SiCl_{1.7}Et_{0.15}OEt_{0.15}CH_2]$.

Fortunately, after reduction with $LiAlH_4$ the -OEt groups are efficiently reduced along with the remaining Si-Cl functionalities, leading to a somewhat less complicated and apparently oxygen-free hydridopolycarbosilane with the average formula, $[SiH_{1.85}Et_{0.15}CH_2]$. Again, isotopic labeling along with a full characterization of the polycarbosilane product by ^{1}H, ^{13}C, and ^{29}Si NMR (including Si DEPT) and IR spectroscopy were used to assign the average formula and to characterize the various structural units in the polymer. The assignment of the broad peaks in the NMR spectra of this polycarbosilane was aided by the synthesis of a series of "model compounds" of the type, $[Me_3SiCH_2]_xSiH_{4-x}$ (x = 1 - 4), which simulated the local environment around Si in the polymer [17].

The molecular weight distribution of a sample of this

polycarbosilane was determined by gel permeation chromatography using polystyrene standards. A very broad MW distribution was found, with most of the polymer falling between 450 and 3000 amu, but tailing off gradually to 80,000 amu to give a large polydispersity value of 6.95. The M_w for this polymer was 745, corresponding to about 15.4 repeat units as $SiH_{1.85}Et_{0.15}CH_2$.

At the intermediate "chloropolycarbosilane" stage the polymer is readily susceptible to structural modification through the reaction of the Si-Cl groups with Grignard or lithium reagents. A preliminary attempt to add vinyl groups at this stage led to the preparation of a 10 %-substituted vinylic hydridopolycarbosilane after reduction which was found to undergo facile crosslinking via Pt-catalyzed hydrosilation at 150 $^{\circ}$C.

2.3. CROSSLINKING AND PYROLYSIS OF THE "SiH_2CH_2" POLYMER

The SiH_2CH_2 polymer was obtained from these reactions as a pale yellow, reasonably air-stable oil which gradually solidified on standing over several months with the generation of a gas (later identified as H_2). This solidification process is accelerated by heating the neat polymer and proceeds rapidly above about 150-200 $^{\circ}$C (the rate of solidification appears to depend markedly on the molecular weight of the polymer, increasing with increasing molecular weight). Based on GPC, NMR and IR analysis of the polymer during solidification, a crosslinking reaction involving elimination of H_2 from Si-H and Si-Si bond formation was evidenced.

Further heating to 1000 $^{\circ}$C resulted in the formation of a black solid which was poorly crystalline by XRD. Annealing at 1600 $^{\circ}$C gave β-SiC as the only crystalline product. Efforts to obtain an accurate elemental analysis are still in progress. However, as is indicated by the comparison of the ^{13}C NMR spectra (Figure 3) and the TGAs in air (Figure 4) of the 1000 $^{\circ}$C pyrolysis products obtained from the above polycarbosilane and the Union Carbide vinylic polysilane, the polycarbosilane-derived product appears to have much less free carbon. Moreover, as is suggested by the IR spectra in Figure 5 obtained for the 1000 $^{\circ}$C powder before and after reaction with oxygen for an extended period at 1200 $^{\circ}$C, the proportion of Si-O groups in the ceramic initially obtained from the pyrolysis must be very low indeed. The overall ceramic yield observed for this polycarbosilane was found to depend greatly on the heating rate used in the TGA experiment, as well as the degree of polymerization of the polymer. Char yields from 58 to 76 % were observed for the "high molecular weight" products at a heating rate of 10 $^{\circ}$C/min. Holding at temperatures from ca. 80 to 200 $^{\circ}$C to effect crosslinking resulted in improved char yields, with overall weight losses from initial polymer to SiC ceramic of less than 20%. This is close to the theoretical yield of 83%, assuming the polymer formula $[SiH_{1.85}Et_{0.15}CH_2]_n$ and "SiC" as the product.
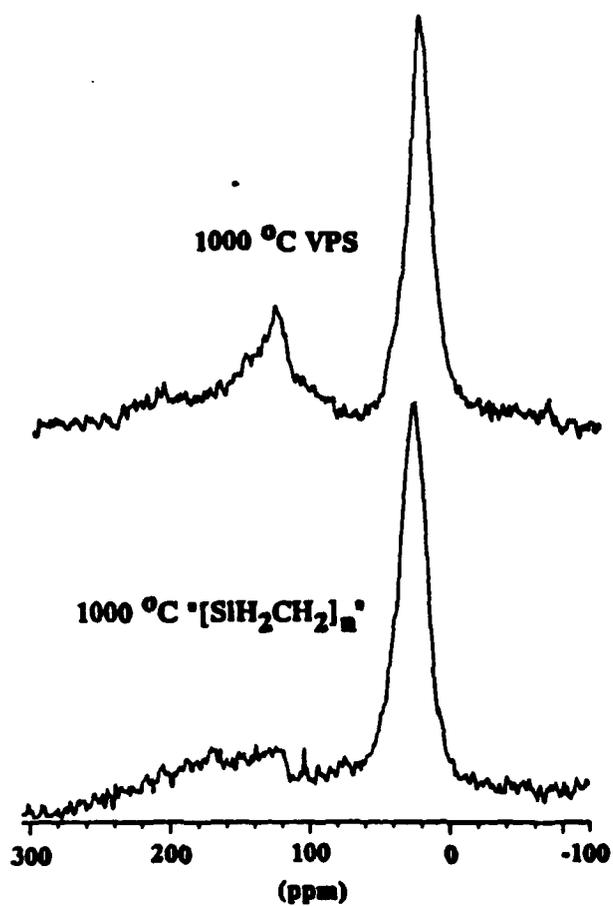
Figure 3. Solid state ^{13}C NMR spectra of ceramic products derived from VPS and "[SiH$_2$CH$_2$]"$_n$ at 1000°C in N$_2$.
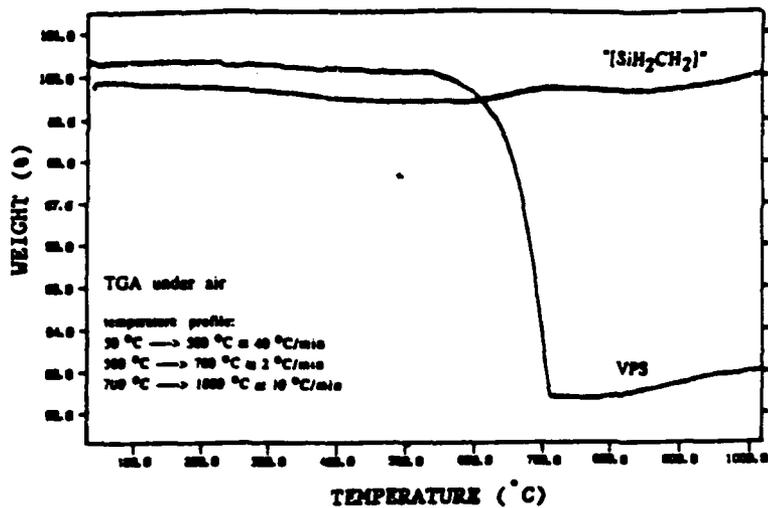
Figure 4. TGA (in air) of ceramic products derived from VPS and "[SiH$_2$CH$_2$]$_n$" at 1000°C in N$_2$.
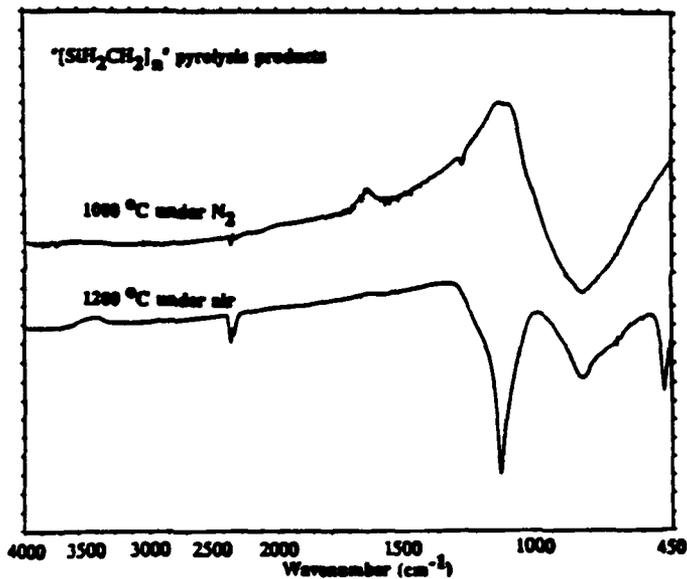
Figure 5. IR spectra of ceramic prepared from "[SiH$_2$CH$_2$]$_n$" at 1000° before and after oxidation in air at 1200°C.

Based on these observations it is clear that this polymer shows considerable promise for use as a SiC precursor. A variety of potential applications in the area of ceramic composites and nanostructures are currently under investigation. In addition, our efforts to fully characterize the pyrolysis process and the SiC product are continuing along with further work on the synthesis and structural modification of the polymer.

3. ACKNOWLEDGEMENT

4. REFERENCES

1. a) Yajima, S.; Hasegawa, Y.; Hayashi, J.; Iimura, M. J. Mater. Sci. (1978), 13, 2569-2576. b) West, R.; Nozue, I.; Zhang, X-H.; Trefonas, P. Polym. Preprints (American Chemical Society, Div. Polym. Chem.) (1984), 25[1], 4. c) West, R.; David, L. D.; Djurovich, P. I.; Yu, H.; Sinclair, R. Am. Ceram. Soc. Bull. (1983), 62[8], 899. d) Schilling, C. L. Jr.; Williams, T. C.; Wesson, J. P. U. S. Patent 4,414,403, Nov. 8, 1983. e) Schilling, C. L. Jr.; Williams, T. C. U. S. Patent 4,472,591, Sept. 18, 1984. f) Okamura, K.; Sato, M.; Matsuzawa, T.; Hasegawa, Y., Ch. 37 in Ultrastructure Processing of Advanced Ceramics, ed., Mackenzie, J. D.; Ulrich, D. R., 1988, Wiley: New York, 501. g) Lipowitz, J.; LeGrow, G. E.; Lim, T. F.; Langley, N. Ceram. Eng. Sci. Proc. (1988), 9[7-8], 931. h) Kumar, K. J. Polym. Sci. C: Polym. Letters, (1988), 26, 25-32.

2. a) Okamura, K.; Sato, M.; Matsuzawa, T.; Seguchi, T.; Kawanishi, S. Ceram. Eng. Sci. Proc. (1988), 9[7-8], 909. b) Okamura, K.; Sato, M.; Hasegawa, Y. Ceram. Int. (1987), 13, 55-61. c) Nakaido, Y.; Otani, Y.; Kozakai, N.; Otani, S. Chem. Soc. Jpn. Chem. Letters (1987), 705. d) Schmidt, W. R.; Sukumar, V.; Hurley, W. J. Jr.; Garcia, R.; Interrante, L. V.; Doremus, R. H.; Renlund, G. M. J. Am. Ceram. Soc. (1990),73[8], 2412. e) Seyferth, D. L'actualit'e chimique, (1986, March), 71.

3. a) Carlsson, D. J.; Cooney, J. D.; Gauthier, S.; Worsfold, D. J. J. Am. Ceram. Soc. (1990), 73[2], 237-241. b) Hasegawa, Y.; Iimura, M.; Yajima, S. J. Mater. Sci. (1980), 15, 720-728. c) Hasegawa, Y. J. Mater. Sci. (1989), 24, 1177-1190. d) Poupeau, J. J., Abbe, D.; Jamet, J. in Emergent Process Methods for High-Technology Ceramics, Materials Science Research Vol. 17, ed., Davis, R. F.; Palmour, H. III; Porter, R. L., 1984, Plenum Press: New York, 287. e) Laffon, C.; Flank, A. M.; LaGarde, P.; Bouillon, E. Physica B (1989), 158, 229-230.

4. a) Schilling, C. L. Jr.; Williams, T. C. Polym. Preprints (American Chemical Society Div. Polym. Chem.), (1984), 25[1], 1. b) Schilling, C.

254

L. Jr. Brit. Polym. Jr. (1986), 18[6], 355.

5. Boisvert, R. P.; Diefendorf, R. J. Ceram. Eng. Sci. Proc. (1988), 9[7-8], 873-880.

6. Bishop, B. A.; Spotz, M. S.; Rhine, W. E.; Bowen, H. K.; Fox, J. R. Ceramic Trans. Vol. 1, Part B, Ceramic Powder Science, 1988, American Ceramic Society: Westerville, OH, 856.

7. Lee, B. J.; Hench, L. L. Mat. Res. Soc. Symp. Proc. Vol. 73 "Better Ceramics Through Chemistry II", 1986, Materials Research Society, 815.

8. a) Czekaj, C. L.; Hackney, M. L. J.; Hurley, W. J. Jr.; Interrante, L. V.; Sigel, G. A.; Schields, P. J.; Slack, G. A. J. Am. Ceram. Sci. (1990), 73[2], 352-357. b) Schmidt, W. R.; Hurley, W. J. Jr.; Sukumar, V.; Doremus, R. H.; Interrante, L. V. Mat. Res. Soc. Symp. Proc. Vol. 171. "Polymer Based Molecular Composites", 1990, Materials Research Society, 79.

9. Schmidt, W. R.; Interrante, L. V.; Doremus, R. H.; Trout, T. K.; Marchetti, P. S.; Maciel, G. E. "Pyrolysis Chemistry of an Organometallic Precursor to Silicon Carbide", Chem. Mater. (1990) in press.

10. Schmidt, W. R.; Hurley, W. J. Jr.; Marchetti, P. S.; Interrante, L. V.; Doremus, R. H.; Maciel, G. E. "Pyrolytic Conversion of a Vinylic Polysilane to Silicon Nitride", to be published.

11. Yajima, S. Phil. Trans. R. Soc. Lond. A, (1980), 294, 419.

12. Carduner, K. R.; Carter, R. O. III; Milberg, M. E.; Crosbie, G. M. Anal. Chem. (1987), 59, 2794-2797.

13. Wu, H-J; Interrante, L.V. Chem. Mater. (1989), 1, 564-568.

14. Levin, G.; Carmichael, B.J. J. Polym. Sci. (part A-1), (1968), 6, 1.

15. Whitmarsh, C.; Interrante, L.V., "Synthesis and Characterization of a Highly Branched Polycarbosilane Derived from Chloromethyltrichloro-silane", submitted to Organometallics.

16. a) Kipping, F.S.; Murray, A.G. J. Chem. Soc. London, (1927), 2735. b) Schwartz, R.; Kucher, W. Chem. Ber. (1956), 89, 12. c) Kibbel. H.U.;Schott, G. Z. Anorg. Allg. Chem. (1968), 362, 81.

17. Whitmarsh, C.; Interrante, L.V., "Synthesis and Characterization of Mono-, Bis-, Tris-, and Tetrakis[Trimethylsilylmethyl]silane", submitted to Organometallics.

Synthesis and characterization of mono-, bis-, tris- and tetrakis(trimethylsilylmethyl)silanes: $(Me_3SiCH_2)_xSiH_{4-x}$ $(x = 1-4)$

Chris K. Whitmarsh and Leonard V. Interrante

Chemistry Department, Rensselaer Polytechnic Institute, Troy, New York 12180 (USA)

(Received March 15th, 1991)

Abstract

The mono-, bis-, tris-, and tetrakis(trimethylsilylmethyl)silanes, $(Me_3SiCH_2)_xSiH_{4-x}$ $(x = 1-4)$, have been prepared for use as "models" of the various Si-centered functional units in a complex, highly branched polycarbosilane polymer of the approximate composition, "$(SiH_2CH_2)_n$". These compounds have been characterized by GC, IR, ^1H, ^{13}C, ^{29}Si NMR, MS, and elemental analysis. The IR and NMR data for this series of compounds show distinct trends on increasing substitution, which are related to the structural differences within the series.

Introduction

We are currently investigating the structure of highly branched carbosilane polymers with extensive Si–H substitution as potential precursors to SiC ceramics [1]. Although there is considerable information available on NMR spectral assignments for siloxanes, polysilanes, and alkyl/aryl silanes [2], relatively little data exists on carbosilanes with one or more Si–H groups. Due to the highly branched nature of the polymers we have obtained [1], the ^1H, ^{13}C, and ^{29}Si NMR spectra consist of broad and/or highly complex groups of peaks. In order to more fully understand both the structure and the polymerization process for this system, it is desirable to confirm unambigously the NMR assignments. For this purpose, we have prepared a series of compounds of the general formula: $(Me_3SiCH_2)_xSiH_{4-x}$ (where $x = 1-4$) for use as "models" for the various functional units present in the polycarbosilane. In the course of the preparation of these compounds certain modifications in existing synthetic methodology were employed that may have general utility in organosilicon chemistry.

$Me_3SiCH_2SiH_3$, was previously isolated by Fritz, et al. [3–6], and more recently has been investigated as a CVD precursor for silicon carbide films [7]. Daniels et al. [8] employed Me_3SiCH_2Br and $HSiCl_3$ to prepare the dichloro derivative, $Me_3SiCH_2SiHCl_2$. Sommer et al. [9] have prepared $Me_3SiCH_2SiCl_3$ by substituting

$SiCl_4$ for $HSiCl_3$. Neither of these compounds were reduced to $Me_3SiCH_2SiH_3$. The second compound of the series. $(Me_3SiCH_2)_2SiH_2$. does not appear to have been previously prepared. although the derivatives. $(Me_3SiCH_2)_2SiHCl$ [8] and $(Me_3SiCH_2)_2SiCl_2$ [9]. and several related compounds have been reported [3–6]. One of these compounds. $Me_3SiCH_2SiH_2SiHMe_2$. is sufficiently similar that the relevant ^1H NMR assignments are comparable [3]. The remaining compounds of the series. $(Me_3SiCH_2)_3SiH$ and $(Me_3SiCH_2)_4Si$. have been previously reported in conjunction with studies on the properties of silicon compounds bearing bulky substituents [8–10].

The three previously known compounds of this series were prepared 30–40 years ago. before the advent of modern spectroscopic methods. and in general. they have not been re-investigated. For most of these compounds. IR. MS. and ^1H NMR data do not exist: in addition. there have been no ^{13}C or ^{29}Si NMR studies. The availability of the complete series now permits a detailed analysis of the effect of structural variations on the NMR and IR spectra.

Experimental section

Solvents were distilled from appropriate drying agents [11] immediately before use whenever air. or moisture-sensitive. materials were involved. Air-sensitive materials were manipulated using oven dried glassware and standard inert atmosphere techniques [12]. Reagents were typically > 97% pure. and were used as received unless otherwise specified. Boiling points are uncorrected. Infrared spectra were taken as films between NaCl plates on a Perkin–Elmer 298 spectrometer using medium slit and 12 min. scan time. Gas chromatograms were run on a Shimadzu GC9-A equipped with a CR3-A recorder-integrator unit. Unless otherwise specified. components separated satisfactorily using the following parameters: column. SE-30 X 6Ft: INJ. TCD. 300°C: oven. 100–250°C @ 15°C/min: carrier gas. He @ 45 cc/min. NMR spectra were obtained on a Varian XL-200 using C_6D_6 as solvent. The sample concentration was approximately 20%. ^1H and ^{13}C NMR spectra were referenced to residual protons in the solvent. as TMS tended to interfere with the Me-Si peaks in the samples. ^{29}Si NMR spectra were referenced by running a sample of TMS and setting the peak to 0 ppm immediately prior to running the actual sample. Any slight drifting of this setting is relatively insignificant compared to the ^{29}Si peak widths. Gated decoupling was employed except when coupled ^{29}Si spectra were desired. The mass spectrum of $Me_3SiCH_2SiH_3$ was studied using a Hiden Analytical Ltd. model HAL 201 mass spectrometer (EI. 77 eV) with a modified sample introduction system due to its volatility. In the case of EI − MS only the major and/or molecular ion peaks are listed. Mass spectra of the other compounds were obtained using a Hewlett–Packard 5987A GC/MS system in the direct insertion mode under CI conditions (isobutane or methane at 70 eV). Elemental i nalyses were performed by either Schwarzkopf Microanalytical Laboratory or Galbraith laboratories.

Preparation of Me_3SiCH_2MgCl

Me_3SiCH_2MgCl was prepared essentially as in reference 8. by the reaction of Me_3SiCH_2Cl with #50 mesh Mg powder in ether under nitrogen.

Preparation of mono-, bis-, and tris(trimethylsilylmethyl)silanes

The compounds $Me_3SiCH_2SiH_3$, $(Me_3SiCH_2)_2SiH_2$, and $(Me_3SiCH_2)_3SiH$ were prepared by slowly adding an ether solution of 0.437 mole of Me_3SiCH_2MgCl (based on the amount of Me_3SiCH_2Cl used) to a stirred solution containing 15 g (0.111 mol) of trichlorosilane in 100 mL of ether, and allowing it to boil under reflux overnight [13*]. The resulting solution was found by GC to contain a mixture of the di-, and tri-substituted compounds, as well as a large amount of unreacted Grignard reagent. Addition of excess trichlorosilane (25 mL) and further refluxing, produced a mixture of $Me_3SiCH_2SiHCl_2$, $(Me_3SiCH_2)_2SiHCl$, and $(Me_3SiCH_2)_3$-SiH, in approximately equal quantities by GC. The crude mixture was separated from $MgCl_2$ by cannula transfer, then stripped of solvent and excess $HSiCl_3$. The resulting mixture was redissolved in ether and reduced with 1.4 g (0.037 mole 50% excess) $LiAlH_4$ suspended in ether. After workup with approximately 4 M HCl (about 750 mL), the ether layer was separated and the most of the solvent removed under vacuum. $Me_3SiCH_2SiH_3$ was distilled from this mixture under nitrogen at ambient pressure. $(Me_3SiCH_2)_2SiH_2$, and $(Me_3SiCH_2)_3SiH$ were isolated by vacuum distillation. $Me_3SiCH_2SiH_3$; purity: 98.4% (by GC), b.p. 81–84°C @ 1 ATM. (Lit. 90–91°C [7]). MS (EI, 77 eV): 118 [M^+], 117, 103, 73 [Me_3Si^+], 59, 45 [$CH_2SiH_3^-$], 43 [$MeSi^+$, or CH_2SiH^+]. Elemental analysis [14*]: Found: C, 40.76; H, 11.66. $C_4H_{14}Si_2$ calc.: C, 40.68; H, 11.86%. IR (cm^{-1}): 2950s, 2895m, 2140vs, 1410w, 1350w, 1250s, 1045vs, 965w, sh, 940vs, 840vs, 785m, 755m, 695m, 675m. $(Me_3SiCH_2)_2SiH_2$; purity: 94.6% (by GC), B.p. 40–46°C @ 0.5 mmHg. MS [DIP, CI, (isobutane)] 204 [M], 202 [$M-2$], 188 [$M-16$]. Elemental analysis: Found: C, 47.02; H, 11.83. $C_8H_{24}Si_3$ calc.: C,47.06; H, 11.77%. IR (cm^{-1}): 2950s, 2895m, 2120s, 1415w, 1350w, 1245s, 1040s, 995w, 955s, 880m,sh, 835vs, 765s, 690m, 660m. $(Me_3SiCH_2)_3SiH$; purity: 91.3% (by GC), b.p. 78–84°C @ 0.5 mmHg. (Lit. 110–12°C @ 10 mmHg). MS [DIP, CI, (isobutane)]: 290 [M], 274 [$M-16$]. Elemental analysis: Found: C, 48.36; H, 11.53. $C_{12}H_{34}Si_4$ calc.: C, 49.65; H, 11.72%. IR (cm^{-1}): 2950vs, 2895m, 2090m, 1405w, 1350w, 1245vs, 1040vs, 995w, 955vw, 860sh, 830vs, 770vs, 685m, 660m.

Preparation of tris(trimethylsilylmethyl)silane [(Me₃SiCH₂)₃SiH] using CuCN catalyst

$HSiCl_3$ (0.25 mole) was added, dropwise, to 1 mole of Me_3SiCH_2MgCl in 500 mL of ether with rapid stirring and cool water bath. After the addition was complete, the mixture was allowed to reflux for 2 days during which much $MgCl_2$ precipitated. The crude product was separated from the $MgCl_2$ and found by GC to consist of a 2:1 ratio of $(Me_3SiCH_2)_2SiHCl$ and $(Me_3SiCH_2)_3SiH$, respectively, and unreacted Grignard reagent. Addition of Me_3SiCH_2MgCl (0.25 mol), and refluxing for 1 day, resulted in a 1:1 product ratio (by GC). CuCN catalyst [15] (0.3 g) was added, the color changed from pale yellow to black in a few minutes, and reflux was continued overnight. GC of the crude product showed almost quantitative conversion to $(Me_3SiCH_2)_3SiH$. Subsequent aqueous workup (as previously described) and vacuum distillation, gave the desired product $(Me_3CH_2)_3SiH$, in 65% yield (91.3% purity by GC). IR and ^1H NMR spectra of this compound matched those of $(Me_3SiCH_2)_3SiH$ produced without use of CuCN.

---

* Reference number with asterisk indicates a note in the list of references.

Preparation of tris[trimethylsilylmethyl]bromosilane [(Me₃SiCH₂)₃SiBr]

Preparation of $(Me_3SiCH_2)_3SiBr$, involved a variation on the procedure used by Daniels and Post [8]. A 100 mL single-neck flask with nitrogen inlet was charged with 0.16 mole $(Me_3SiCH_2)_3SiH$ and 50 mL of dry benzene. The temperature was maintained at approximately 10°C with a cool water bath. Bromine (0.18 mole, 1.1 eq.) was added, dropwise, over about 2 h, with stirring. The bromine was immediately decolorized until approximately 90% had been added. An oil bubbler allowed the by-product, HBr, to escape. After stirring overnight at 20°C, the contents were purged with nitrogen to drive out HBr, excess Br_2, and most of the benzene. The product, $(Me_3SiCH_2)_3SiBr$, was isolated in 73.2% yield (93.2% pure by GC) by vacuum distillation. B.p. 89–94°C @ 0.5 mmHg (Lit. 110°C @ 1.8 mmHg [8]). IR (cm⁻¹) 2950s, 2895m, 1400w, 1350w, 1245vs, 1060vs, 1000w, 835vs, 775vs, 690m, 665w.

Conversion of (Me₃SiCH₂)₃SiBr to (Me₃SiCH₂)₄Si

A 500 mL 3-neck flask fitted with reflux condenser and nitrogen atmosphere was charged with 31.9 g of $(Me_3SiCH_2)_3SiBr$ (0.086 mole), 0.25 mole of Me_3SiCH_2MgCl in 300 mL of ether, and 0.3 g of CuCN as catalyst. After 4 days reflux, the "aqueous workup" was performed as described above. The crude product was a mixture of tetrakis(trimethylsilylmethyl)silane $[(Me_3SiCH_2)_4Si]$ and tris(trimethylsilylmethyl) silanol [from hydrolysis of unreacted $(Me_3SiCH_2)_3SiBr$], in an approximately 2:1 ratio, respectively (by GC). Repeated vacuum distillation failed to give complete separation. A 60/37% mixture (by GC) of $(Me_3SiCH_2)_4Si$ and $(Me_3SiCH_2)_3SiOH$ was treated with excess $LiAlH_4$ and subjected to aqueous workup. Resulting in a mixture of $(Me_3SiCH_2)_3SiH$ and $(Me_3SiCH_2)_4Si$. This mixture was separable by vacuum distillation, giving the desired compound $(Me_3SiCH_2)_4Si$ in 94.7% purity (by GC). B.p. 96–97°C @ 0.5 mmHg. MS (CI methane DIP): M, $M - 14$, $M - 86$, $M - 174$, Me_3Si (73). Elemental analysis: Found: C, 47.90; H, 11.30. $C_{16}H_{44}Si_5$ calc.: C, 51.06; H, 11.70%. IR (cm⁻¹): 2950s, 2895m, 1405w, 1350w, 1250s, 1055s, 990w, 835vs, 780s, 690m, 670w.

Results and discussion

Syntheses

The purpose of this study was to more fully characterize the series of compounds represented by the general formula $[Me_3SiCH_2]_xSiH_{4-x}$ ($x = 1$–4), particularly with respect to their NMR and IR spectra. Although large quantities were not needed, samples of each member of the series were required. It was found that a modification to the procedure of Daniels and Post [8] produces the first three compounds of the series in one preparation (eq. 1).

$$HSiCl_3 \xrightarrow{\underset{Et_2O,\ Reflux}{Me_3SiCH_2MgCl}}$$

$$(Me_3SiCH_2)_2SiHCl + (Me_3SiCH_2)_3SiH + excess\ Me_3SiCH_2MgCl \xrightarrow{excess\ HSiCl_3}$$

$$HSiCl_3 + Me_3SiCH_2SiH_3 + (Me_3SiCH_2)_2SiHCl + (Me_3SiCH_2)_3SiH$$

$$\xrightarrow[\substack{2)\ Et_2O,\ LiAlH_4 \\ 3)\ HCl,\ H_2O}]{1)\ Vac.\ (-HSiCl_3,\ Et_2O)} Me_3SiCH_2SiH_3 + (Me_3SiCH_2)_2SiH_2$$
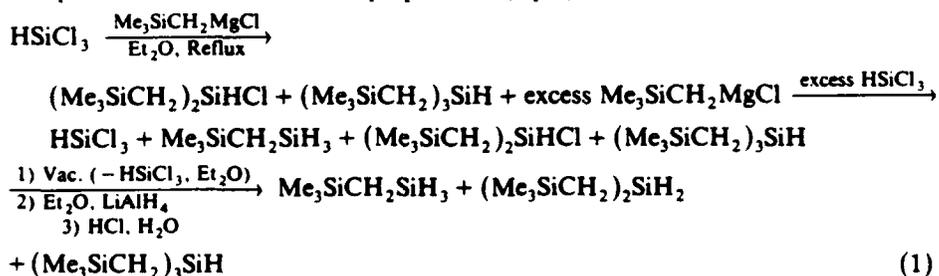
$$+ (Me_3SiCH_2)_3SiH \hspace{4cm} (1)$$

After the initial reflux, the crude mixture contained approximately equal quantities of the di- and tri-substituted compounds due to the rather sluggish formation of $(Me_3SiCH_2)_3SiH$. Addition of excess trichlorosilane to the reaction mixture at this stage not only formed the desired mono-substituted compound, but served to eliminate any remaining Grignard reagent prior to the $LiAlH_4$ reduction. Unreacted trichlorosilane was stripped off before the reduction of the crude products to avoid the formation of pyrophoric silane gas. Due to large boiling point differences, the components were easily separated after the final workup.

Using an alternative approach, $(Me_3SiCH_2)_3SiH$ was prepared in high yield by the use of CuCN [15] as catalyst, as shown in eq. 2.

$$HSiCl_3 \xrightarrow[\substack{2)\ CuCN.\ Reflux \\ 3)\ H_2O/HCl}]{1)\ Et_2O.\ excess\ Me_3SiCH_2MgCl} (Me_3SiCH_2)_3SiH \tag{2}$$
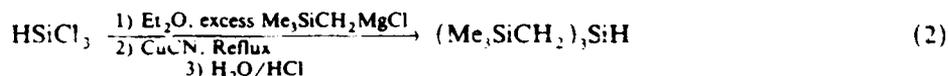
In this case, the CuCN was not added until the $HSiCl_3$ had already been partially reacted, as the initial substitution is highly vigorous and exothermic. Even with only a single extraction (to isolate the crude products from $MgCl_2$) before CuCN addition, yields of 65% were achieved. These results were comparable to those obtained by employing the more active lithium reagent Me_3SiCH_2Li (71%), and much better than the uncatalysed Grignard reaction (18.6%) [8].

The exact nature of the catalytic effect is not completely understood, but CuCN has been reported to greatly increase the yield of reactions involving bulky Grignard reagents with chlorosilanes [15]. The use of Si–H-containing chlorosilanes as substrates for this catalytic process does not appear to have been previously reported. Our results suggest that the scope of the CuCN-catalysed reactions can be extended to include sterically hindered, Si–H bearing compounds.

The compound $(Me_3SiCH_2)_3SiH$ was found to be a convenient intermediate in the preparation of $(Me_3SiCH_2)_4Si$. The procedure is outlined in equations 3 and 4.

$$(Me_3SiCH_2)_3SiH + 1.1\ eq.\ Br_2 \xrightarrow[10°C]{C_6H_6} (Me_3SiCH_2)_3SiBr + HBr \tag{3}$$

$$[Me_3SiCH_2]_3SiBr + excess\ Me_3SiCH_2MgCl \xrightarrow[2)\ H_2O]{\substack{1)\ Et_2O.\ reflux. \\ cat.\ CuCN}} (Me_3SiCH_2)_4Si$$

$$+ MgCl_2 \tag{4}$$
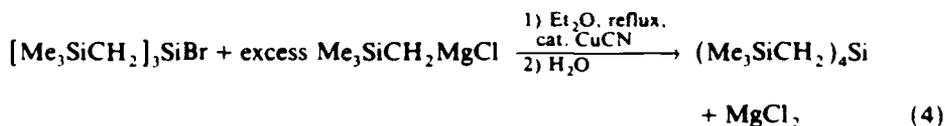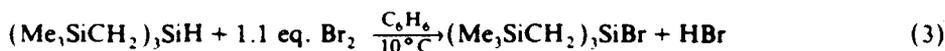
The bromination of $(Me_3SiCH_2)_3SiH$, in CCl_4 followed by aqueous ammonium hydroxide workup, has been previously reported [8], however yields of only about 20% were obtained. Presumably, a large portion of the product was hydrolysed. It was found in this study that using benzene as solvent and omitting the aqueous workup enabled, after purification, a yield of 73.2% to be achieved. Difficulties were encountered with the final substitution step as, despite the use of excess Grignard reagent, CuCN and an extended reflux period, the reaction did not go to completion. Subsequent aqueous workup formed $(Me_3SiCH_2)_3SiOH$ from the unreacted $(Me_3SiCH_2)_3SiBr$. Direct separation of this mixture by distillation was not successful, however, after treatment of the crude mixture with $LiAlH_4$ the silanol was quantitatively converted to $(Me_3SiCH_2)_3SiH$. The boiling points of the resulting mixture were now sufficiently different to give good separation of the desired compound: $(Me_3SiCH_2)_4Si$.

Characterization and properties

The series of compounds, $(Me_3SiCH_2)_xSiH_{4-x}$ (where $x = 1-4$), are clear, watery liquids. Even the first member of the series, $Me_3SiCH_2SiH_3$, is sufficiently stable to be briefly handled in air without any evidence of decomposition or fuming [14].

The only compound of this series for which infrared spectral data has been previously reported is tris(trimethylsilylmethyl)silane [8]. The IR spectra for this series of compounds are found to be quite similar, as they are dominated by the Me_3SiCH_2-based bands. The most notable change is a decrease in the relative intensity of the Si–H stretch vs C–H stretch as the number of Me_3SiCH_2- groups increases from 1 to 3, due to the considerable change in the ratio of Si–H to C–H for the series. This increased substitution is also associated with a shift of the Si–H stretch from 2140 to 2090 cm^{-1}. The SiH stretching and bending modes observed for this series of compounds are very similar to published IR data for the series Ph_xSiH_{4-x} (where $x = 1-3$) [16c].

Prior NMR studies of these compounds are rather limited. No ^{13}C or ^{29}Si spectra have been reported and ^{1}H NMR data are incomplete, although related silicon compounds have been investigated [3-6]. The proton NMR spectrum of the compound $Me_3SiCH_2SiH_3$ has been previously reported by others, however, there are disagreements regarding the chemical shift values. The SiH_3 group has been assigned values of 4.47 [4], 4.15 [7] and 3.53 [3] ppm. None of the values agreed well with our result of 3.7 ppm obtained using a ca 20% solution in C_6D_6. Differences in the chemical shifts for the methyl and methylene protons were also significant. A solvent or concentration effect was suspected as multiplicities and coupling constants were in agreement. Attempts to confirm concentration effects were made by increasing the portion of $Me_3SiCH_2SiH_3$ in C_6D_6 from ca 3 to 25%. The results showed only minor changes in the chemical shifts [(SiCH$_2$Si) -0.44 to -0.40, (SiMe$_3$) -0.12 to -0.005, (SiH$_3$) 3.72 to 3.69, respectively]. The magnitude of the concentration effect appears to be too small to to explain the wide variation in chemical shifts reported for the SiH_3 group. In addition, minimal differences in chemical shift data for the compound $H_2C(SiH_3)_2$ (neat vs CCl$_4$) and for the compound $(Me_3SiCH_2)_3SiH$ (C_6D_6 vs CCl$_4$) (Table 1) suggest that solvent effects are not very important.

The proton NMR spectrum of $(Me_3SiCH_2)_2SiH_2$ has not been reported; however, the compound, $Me_3SiCH_2SiH_2CH_2SiHMe_2$, isolated in small amounts from the pyrolysis products of trimethylsilane, gave very similar chemical shifts [4]. Published ^{1}H NMR chemical shifts for $(Me_3SiCH_2)_3SiH$ [10] agree with our results within 0.1 ppm for all peaks, but the coupling constants were not given. No prior NMR data for $(Me_3SiCH_2)_4Si$ has been reported.

The NMR chemical shift and coupling constant data for these compounds are collected in Table 1 and 2, respectively. Examination of the NMR data (Table 1) shows that the central silicon, the Si–H, and the methylene groups (both carbons and hydrogens) in the series of compounds, $[Me_3SiCH_2]_nSiH_{4-n}$, all have significant, progressive, downfield shifts corresponding to the number of Me_3SiCH_2-groups. The chemical shifts in the ^{29}Si NMR spectra of the series $(Me_3SiCH_2)_xSiH_{4-x}$ are comparable to those of the corresponding methyl series [2a-d] Me_xSiH_{4-x} (which lack the steric crowding of the Me_3Si- functionalities). The silicon chemical shifts in these compounds move progressively downfield as Si–H is replaced with Me_3SiCH_2 (or Me), presumably due to the higher electro-

Table 1

^{1}H. ^{13}C. and ^{29}Si NMR chemical shift values for the series $(Me_3SiCH_2)_xSiH_{4-x}$ $(x = 1-4)$ and some related compounds [a]

Compound/ref.	^{1}H			^{13}C		^{29}Si	
	SiCH$_2$Si	Si–Me	Si–H	SiCH$_2$Si	Si–Me	Si–H	Si–Me
Me$_3$Si.CH$_2$SiH$_3$							
This study	−0.40	0.02	3.70	−8.86	−0.235	−65.1	1.81
3 (CCl$_4$)	[b]	[b]	4.47	[b]	[b]	[b]	[b]
4 (CCl$_4$?)	[b]	0.09	3.53	[b]	[b]	[b]	[b]
7 (C$_6$D$_6$)	−0.05	0.15	4.15	[b]	[b]	[b]	[b]
H$_2$C(SiH$_3$)$_2$							
7 (neat, −20 °C)	−0.10	[b]	3.69	−21.03	[b]	[b]	[b]
6 (CCl$_4$, 20%)	−0.08	[b]	3.63	[b]	[b]	[b]	[b]
H$_2$Si[CH$_2$SiH$_3$]$_2$							
6 (CCl$_4$, 20%)	−0.03	[b]	3.65	[b]	[b]	−69.04 [c]	[b]
(Me$_3$SiCH$_2$)$_2$SiH$_2$							
This study	−0.26	0.076	4.05	−1.25	0.906	−38.7	1.13
Me$_3$SiCH$_2$SiH$_2$CH$_2$SiHMe$_2$							
4 (CCl$_4$?)	−0.17	0.09	3.88	[b]	[b]	[b]	[b]
H$_2$Si(CH$_2$SiH$_3$)$_2$							
6 (CCl$_4$, 20%)	−0.03	[b]	3.95	[b]	[b]	−30.44 [c]	[b]
(Me$_3$SiCH$_2$)$_3$SiH							
This study	−0.19	0.10	4.29	3.39	1.15	−17.3	0.66
10 (CCl$_4$)	−0.10	0.02	4.20	[b]	[b]	[b]	[b]
(Me$_3$SiCH$_2$)$_4$Si							
This study	−0.11	0.14	[b]	8.58	1.65	14.5	−0.54

[a] For this study, NMR spectra were run in benzene-d_6 (ca 20%). expected peak multiplicities and integration values were seen in all cases. Conditions for spectra of compounds done by others are given when known. Nuclei of interest when not obvious are indicated in italics. [b] Not applicable. or not reported in reference. [c] Si chemical shifts for H$_2$Si(CH$_2$SiH$_3$)$_2$ are from ref. 2a. presumably run in a deuterated solvent.

negativity of carbon vs hydrogen. The nearly identical values observed for the two series of compounds, suggest that neither steric factors, not the Me$_3$Si– functionalities, are very important in determining the ^{29}Si chemical shifts for these compounds. Chemical shifts for the –SiMe$_3$ groups, which are more remote from the central silicon, show only moderate downfield shifts for ^{1}H, and ^{13}C, and slight upfield shifts for ^{29}Si.

Coupling constants obtained from the ^{1}H, ^{13}C, and ^{29}Si NMR of these, and some related compounds are collected in Table 2. The new values obtained appear to be consistent with the published values for the related compounds. The sequential replacement of Si–H by Me$_3$SiCH$_2$– groups causes definite trends in the coupling constants of this series of compounds. The ^1J(SiH) value decreases from 194.7 to 181.1 Hz as the number of Me$_3$SiCH$_2$– groups increases from 1 to 3. The coupling constants for the trimethylsilyl groups [^1J(CH) and ^1J(SiC)] show only small decreases in value progressing from Me$_3$SiCH$_2$SiH$_3$ to (Me$_3$SiCH$_2$)$_4$Si. This is consistent with the chemical shift data for these groups (Table 1) that show relatively small, but systematic, changes with increasing substitution of Me$_3$SiCH$_2$– on Si, suggesting that the trimethylsilyl groups are only slightly affected by steric crowding. The ^1J(CH) coupling constants for the methylene units show a more

Table 2

Coupling constants for the series. $[Me_3SiCH_2]_xSiH_{4-x}$ ($x = 1-4$) and some related compounds [a]

Compound/ref.	$^1J(SiH)$	$^1J(H_3C)$	$^1J(H_2C)$	$^1J(H_3CSi)$	$^1J(H_2CSi)$	$^2J(H_2CSi)$	$^3J(HCSiH)$
$Me_3SiCH_2SiH_3$							
This study	194.7	118.5	113.5	51.25	42.75	9.7	4.6
3	b	b	b	b	b	b	4.4
4	b	b	b	b	b	b	4.5
7	b	b	b	b	b	b	4.3
$HC_2(SiH_3)_2$							
2c	195.4	b	118.6	b	43.94	b	4.7
$H_2Si(CH_2SiH_3)_2$							
2c (SiH$_3$)	199.0	b	b	b	b	(H_3SiCH_2)	4.5
(SiH$_2$)	196.5	b	b	b	b	(H_2SiCH_2)	4.2
$(Me_3SiCH_2)_2SiH_2$							
This study	187.7	117.6	112.5	50.80	43.35	8.9	4.4
$(Me_3SiCH_2)_3SiH$							
This study	181.1	117.0	105.0	50.75	43.95	8.6	3.8
$(Me_3SiCH_2)_4Si$							
This study	b	117.0	108	50.60	43.30	8.0	–

[a] Coupling constants were obtained from the appropriate NMR spectra as follows: $^3J(HSiCH)$, ^1H; $^1J(HC)$, ^{13}C; $^1J(CSi)$, $^{13}C\{^1\}$; $^1J(HSi)$, and $^2J(HCSi)$. ^{29}Si. [b] Not applicable, or not reported in original reference.

pronounced dependence, decreasing from 113.5 to 105.0 Hz as the number of Me_3SiCH_2 groups increases from 1 to 3. The corresponding $^1J(SiC)$ couplings undergo a slight increase from 42.75 to 43.95 Hz. The compound $(Me_3SiCH_2)_4Si$ shows slightly anomalous behavior, with values of $^1J(CH)$ of 108 and $^1J(SiC)$ of 43.30 Hz respectively. Values for the $^2J(HCSi)$ coupling ranged from 9.7 to 8.0 Hz as the number of Me_3SiCH_2- groups increased from 1 to 4. Typical values for this coupling range from about 6 to 9 Hz [2c]. The values for the $^3J(HSiCH)$ couplings of the series of compounds, $(Me_3SiCH_2)_xSiH_{4-x}$, decreased from 4.6 to 3.8 Hz on increasing substitution. These values are found to be consistent with literature data for related systems.

Existing mass spectral data [5,10] (EI) and results from this study (EI and CI) suggests that for this series of compounds the parent molecular ion becomes less stable as the number of Me_3SiCH_2- groups increases. One possible explanation may be that the additional crowding resulting from the increase in the number of Me_3SiCH_2- groups facilitates fragmentation of the molecule. Alternatively, the larger molecules may absorb energy more efficiently in the mass spectrometer. Significant peaks at m/e $M - 86$, $M - 87$ are seen in most cases (CI), suggesting the loss of $Me_2Si(CH_2-)_2^+$, or $Me_3SiCH_2-^+$. For $(Me_3SiCH_2)_2SiH_2$, a fragment at m/e $M - 2$ is observed, consistent with facile loss of the SiH_2 hydrogens. Compounds with several Si–H bonds have been found to give complex groups of peaks in the mass spectra by this mechanism [5].

Acknowledgements

References

1 C.K. Whitmarsh and L.V. Interrante. Organometallics, 10 (1991) 1336.
2 (a) R.K. Harris and B.E. Mann (Eds.). NMR and the Periodic Table, Academic Press, New York, 1978; (b) G.A. Webb (Ed.), Annual Reports on NMR Spectroscopy, Vol. 15, Academic Press, New York, p. 235-289; (c) J. Schraml and J.M. Bellama, in E.C. Nachod, J.J. Zuckerman and E.W. Randell (Eds.), Determination of Organic Structure by Physical Methods, Vol. 6, p. 202, Academic Press, New York, 1976; (d) R.K. Harris and B.J. Kimber, J. Magn. Reson., 17 (1975) 174.
3 G. Fritz, J. Maas and A. Hornung, Z. Anorg. Allg. Chem., 460 (1980) 115.
4 G. Fritz and N. Götz, Z. Anorg. Allg. Chem., 375 (1970) 171.
5 G. Fritz, J. Grobe and D. Kummer, Adv. Inorg. Radiochem., 7 (1965) 349.
6 G. Fritz, H.J. Buhl and D. Kummer, Z. Anorg. Allg. Chem., 327 (1964) 165.
7 H. Schmidbauer and J. Ebenhöch, Z. Naturforsch. B, 41 (1986) 1527.
8 B.F. Daniels and H.W. Post, J. Org. Chem., 22 (1957) 748.
9 L.H. Sommer, R.M. Murch and F.A. Mitch, J. Am. Chem. Soc., 76 (1954) 1619.
10 G.D. Homer and L.H. Sommer, J. Am. Chem. Soc., 95 (1973) 7700.
11 A.J. Gordon and R.A. Ford, The Chemist's Companion, Wiley, New York, 1972.
12 D.F. Shriver and M.A. Drezdon, The Manipulation of Air-sensitive Compounds, 2nd ed., Wiley, New York, 1986.
13 This procedure is somewhat modified from that used in ref. 8.
14 *CAUTION.* During an attempt to obtain a C, H analysis, the compound $Me_3SiCH_2SiH_3$ exploded with sufficient violence to burst the combustion tube of the analyzer. It is suggested that any experiments involving the heating to decomposition of large quantities of this, (or related) compounds in the presence of air or oxygen be approached with caution.
15 P.J. Lennon, D.P. Mack and Q.E. Thompson, Organometallics, 8 (1989) 112.
16 (a) R.M. Silverstein, G.C. Bassler and T.C. Morrill, The Spectrometric Identification of Organic Compounds, 4th ed., Wiley, New York, 1981; (b) A.L. Smith, Analysis of Silicones, John Wiley & Sons, New York, 1974, p. 248-280; (c) N.B. Colthup, L.H. Daly and S.E. Wiberly, Introduction to Infrared and Raman Spectroscopy, Academic Press, New York, 1964, p. 295 and 400.

SILICON CARBIDE-ALUMINUM NITRIDE SOLID SOLUTIONS BY PYROLYSIS OF

ORGANOMETALLICS

L. V. Interrante[*], W. R. Schmidt[+], S.N. Shaikh[*], and R. Garcia[+],

Departments of Chemistry[*] and Materials Engineering[+], Rensselaer

Polytechnic Institute, Troy, NY 12180-3590

P. S. Marchetti and G. E. Maciel, Department of Chemistry, Colorado State

University, Fort Collins, CO 80523

ABSTRACT

SiC/AlN solid solutions and nanocomposites were prepared both by
pyrolysis of single-component polymeric precursors derived from the
reaction of cyclotrisilazanes with triethylaluminum and by copyrolysis of
mixed organosilicon and organoaluminum precursors. The evolution of the
final crystalline ceramic phases from the preceramic products of these
pyrolyses was studied by XRD, TEM/EDS, and solid state ^{27}Al and ^{13}C magic
angle spinning NMR spectroscopy, providing a detailed picture of the
precursor-to-ceramic conversion process. The results of these studies are
discussed in the context of the SiC/AlN phase diagram and the chemistry
occuring during the conversion process.

INTRODUCTION

The SiC/AlN system has been the subject of much interest and
investigation over at least the past 10 years [1-11]. This interest is due

in part to the opportunity presented through solid solution formation to modify the properties of the component ceramic phases in particular ways: for example, the band gap, the thermal conductivity, thermal expansion, the hardness, the fracture toughness and the creep rate can be varied in a controlled manner [1-6]. But perhaps even more noteworthy is the prospect of effecting specific desired changes in the microstructure of the resultant ceramic product relative to that of the component ceramics. In particular, SiC occurs as various polytypes (3C, 2H, 4H, 6H, etc.) and undergoes phase transformations between these polytypes that can lead to exaggerated grain growth on temperature cycling. This is believed to be one of the reasons for the precipitous losses in strength that have been observed for polymer precursor-derived SiC fibers above 1400°C [8]. Unlike SiC, AlN has only one stable phase, which is isostructural and closely lattice matched to the wurtzite (hexagonal 2H) form of SiC. The addition of as little as 1-10 % AlN in hot-pressed SiC samples is reported to reduce grain size and improve microstructural uniformity [1-5]. Alloying AlN with SiC appears to stabilize the 2H structure which then resists structural transformation at high temperatures.

Ruh and Zangvil have published a tentative phase diagram for the SiC/AlN system that suggests the existence of a wurtzite-type 2H solid solution over a wide range of temperatures and compositions [7]. At temperatures above ca. 2100°C, a single 2H solid solution phase exists from about 23 % AlN to 100 % AlN. At temperatures less than ca. 1950°C and compositions from ca. 10 to 90 wt% AlN, 2H is the stable form; however, a miscibility gap exists, such that SiC- and AlN-rich 2H phases were observed.

The use of organometallic precursors to prepare SiC/AlN solid

solutions has received relatively little attention. A patent has claimed the production of such solid solutions by pyrolysis of a mixture of a polycarbosilane and a poly(N-alkylaminoalane) under an inert atmosphere; however, a detailed characterization of the products of these reactions was not reported nor was the precursor-to-ceramic conversion process studied [9]. Paine and coworkers have evidenced, by X-ray powder diffraction and infrared spectroscopy, the formation of partially crystalline 2H SiC/AlN on pyrolysis of trimethylsilyl-substituted aluminum amide and imide in vacuo at 930°C [10].

The use of such organometallic precursor routes in the preparation and processing of these ceramic phases offers several potential advantages, including the prospect for: 1) improved control over composition, phase distribution and homogeneity; 2) lower processing temperatures; 3) finer-grained materials; and 4) the generation of useful final forms through solution or melt processing. In the particular case of SiC/AlN solid solutions, the high melting or infusible characteristics of these materials, along with the attendant low solid state diffusivities, render the production of the solid solution phases extremely difficult by the usual powder processing methods. Moreover, processing these solid solutions into continuous fiber, coatings, or ceramic matrices would clearly be problematic if not impossible.

In the context of our general interest in the design, synthesis and pyrolysis of organometallic precursors to specific phases and nanocrystalline composites in the Si-C-Al-O-N system, we have pursued the use of both single-component precursors and mixed organosilicon/ organoaluminum systems to prepare SiC/AlN solid solutions. Our initial work employing both a vinylic polysilane (VPS) and

3

methylhydridopolycarbosilane (MPCS) as SiC sources, in copyrolysis with organoaluminum amides, yielded both 2H solid solutions and 3C-SiC/2H-AlN composites, depending on the AlN source employed [11].

We report here the results of both further copyrolysis experiments with diethylaluminum amide $[Et_2AlNH_2]_3$, employing a new polycarbosilane as the SiC source, and our pyrolysis studies of single-component precursors derived from the interaction of cyclotrisilazanes and triethylaluminum. Preliminary results from the latter study were recently reported at the 2nd International Ceramic Science and Technology Congress [12].

The SiC precursor source that was employed in the present studies was a new polycarbosilane of the approximate composition, $[SiH_{1.85}Et_{0.15}CH_2]_n$, prepared by Grignard coupling of chloromethyltri....osilane [13]. Our studies of this precursor indicate a near-quantitative conversion to apparently stoichiometric SiC on confined pyrolysis in N_2 to $1000^\circ C$ [14]. It has a highly branched structure with $Si(C)H_3$, $Si(C)_2H_2$, $Si(C)_3H$, and $Si(C)_4$ microenvironments, and undergoes rapid crosslinking on heating to $150\text{-}250^\circ C$ (or slowly at room temperature) to form a glassy, insoluble solid. It is unusual in that it gives SiC with little or no free carbon on pyrolysis; this precursor was used in the present study to provide better compositional control of the final solid solution product.

EXPERIMENTAL PROCEDURE

General

All precursor handling and preparation was done in a N_2-filled glovebox or with Schlenk techniques. The procedures used for precursor

synthesis, handling, and characterization follow standard practice in organometallic chemistry [15] and have been described in detail in our earlier publications [11].

Transmission electron microscopy[s] samples of finely ground ceramic materials were prepared by dropping a suspension of the powder in hexane onto carbon-coated nylon grids and blotting away excess solvent. X-Ray diffraction measurements were made between $2\theta=10-80^{o}$[@]. TGA experiments were carried out in flowing, prepurified N_2 or NH_3 with a typical heating rate of $10^{o}C/min$[@@]. A special Lexan glove box was designed and built to house the TGA equipment so as to allow the handling of the air-sensitive precursors under an inert atmosphere. Annealing of $1000^{o}C$ pyrolyzed ceramics was performed from $1600-1800^{o}C$ in N_2 for 2h at the desired temperature in a two-chamber H_2-protected, molybdenum wound tube furnace.

Solid state ^{13}C and ^{27}Al NMR studies were performed at the Colorado State University Regional NMR Center. High-speed MAS NMR spectroscopy was carried out at 14.0 T on a Bruker AM-600 spectrometer using a high-speed MAS probe built in-house and tuned to 156.38 MHz [16-18]. Samples were spun in 4.5 mm O.D. cylindrical Vespel rotors at a speed of 12-14 kHz. Single pulse excitation using a 90 degree (2.3 μs) solids pulse was employed [19,20]. A 1.0s recycle delay was used in all cases. 1K data blocks (512-10,000 scans) were acquired using a 100 kHz spectral width and then zero filled to 4kB before Fourier Transformation using 50 Hz line broadening. ^{27}Al chemical shifts were referenced to aqueous 1M $Al(NO_3)_3$ (0.0 ppm). ^{13}C MAS NMR were acquired on a modified NT-100 spectrometer using cylindical Kel-F rotors [18] and an MAS probe built in-house and tuned to 25.27 MHz. Single pulse excitation using a 45 degree (2.5 μs) pulse was employed along with high power proton decoupling during data

5

acquisition. 1kB data blocks (30,000-40,000 transients) were acquired

using a 12 KHz spectral width and a 5.0s recycle delay. The resulting data

were zero filled to 4kB and Fourier Transformed with 100 Hz line

broadening. Carbon chemical shifts were referenced to liquid

tetramethylsilane (TMS) whose chemical shift was taken to be 0.0 ppm.

Precursors

Diethylaluminum amide, $[Et_2AlNH_2]_3$, was used as the precursor to AlN

and prepared from the reaction of triethylaluminum with NH_3 as reported

previously, except that dry hexane was used as the solvent [21]. The

polycarbosilane, $[SiH_{1.85}Et_{0.15}CH_2]_n$ (HPCS), was obtained from the reaction

of Cl_3SiCH_2Cl with Mg in diethylether [13]. The small amount of Et

substitution arises from ether cleavage by the chlorosilane under extended

reflux.

The single-component precursors to SiC/AlN were prepared under N_2 by

direct reaction of either 1,3,5-trimethyl-1,3,5-trivinylcyclotrisilazane

(TMTVTS) or 1,1',3,3',5,5'-hexamethylcyclotrisilazane (HMTS) with

triethylaluminum [12]. Reactions were performed using Si/Al molar ratios

of 9, 3, and 1. Following the exothermic evolution of ethane, clear,

water-like (Si/Al=9) or viscous (Si/Al=3,1) liquids were obtained. Heating

these liquid products at 200-300°C produced viscous melts which solidified

to yellowish glasses on cooling. Fibers could be drawn from these melts

and converted to ceramic fibers by heating them rapidly to 1000-1400°C in

N_2 or NH_3. In this manner, short lengths of a black ceramic fiber (10-100

μm in diameter) were obtained from hand-drawn precursor fiber heated in N_2.

6

Preparation of Precursor Mixtures

A homogeneous liquid containing a 2.1:1 molar (1:1 by weight) ratio of $HPCS/[Et_2AlNH_2]_3$ was prepared by thoroughly mixing the respective liquid precursors in a N_2-filled glove box. This mixture was proportioned for copyrolysis, hot-drop and TGA experiments.

Pyrolysis of Precursors

Copyrolysis of Mixture (Procedure A)

A *ca.* 10 g portion of the precursor mixture was transferred to a molybdenum boat and then loaded into a fused silica tube, equipped with roto-flow valves, in a glovebox. The fused silica tube was inserted into a programmable tube furnace and connected to gas inlet and outlet lines without exposure of the tube contents to the atmosphere. Initial pyrolysis was conducted in an NH_3 atmosphere, using a commercial purifier to remove residual O_2 and H_2O vapor from the anhydrous NH_3 source. The furnace temperature was increased, while flowing NH_3 through the furnace (0.2-0.4 scfh), from 25°C to 200°C in 1h, followed by a hold at 200°C for 4h, and then an increase to 300°C over 0.5h, with a hold at this temperature for another 4h. At this point the gas flow was switched from NH_3 to prepurified N_2 and the temperature was raised to 1000°C over 3.5h. After a 5h hold at 1000°C, the tube was furnace-cooled to room temperature and removed to the glove box for sample retrieval.

Hot Drop of Mixture (Procedure B)

A portion of the precursor mixture was transfered to a 5ml syringe fitted with a needle whose tip was covered with a small rubber septum. A fused silica reactor [11] was heated to 485°C in a sand bath with a constant stream of NH_3 (0.05 scfh) flowing through an inlet tube which extended to near the bottom of the reactor. The needle of the syringe was then pierced through a septum on the reaction vessel and the liquid mixture was "dropped" onto the heated bottom surface at a rate of 1 drop every 5-10s. White fumes were observed during the addition and the temperature of the reactor had increased to 510°C by the end of the addition. After complete addition of the mixture, the reaction vessel was flushed with N_2, cooled under N_2 flow, and transferred into the glovebox for sample collection. Subsequent heating to 1000°C was carried out in a molybdenum boat in the fused silica furnace tube as described in Procedure A after the switch from NH_3 to N_2 gas.

Pyrolysis of Single-Component Precursors (Procedure C)

Typically, 10-15 g portions of these precursors were loaded in the glovebox into the sealed furnace tube as described in Procedures A and B. The samples were directly pyrolyzed in flowing (0.05-0.1 scfh) N_2 by heating from 25°C to 1000°C in 10h, holding at 1000°C for an additional 10h, and cooling to ambient temperature. Samples were retrieved in the glovebox.

RESULTS

Copyrolysis of HPCS/Et$_2$AlNH$_2$ Pr. ~ursor Mixture

TGA results for the mixture of the HPCS and [Et$_2$AlNH$_2$]$_3$ precursors
(Figure 1) indicate a sizeable increase in char yield for the mixture as
compared to those of the individual precursors alone. Essentially the same
results were obtained by heating at a constant rate of 10°C/min in N$_2$ or
under conditions which simulated that of the bulk copyrolysis runs, i.e.,
5°C/min to 200°C under NH$_3$, hold for 2h at 200°C, heating to 400°C at
10°C/min, then switching to N$_2$ for the final heating to 1000°C. In either
case, the overall weight loss to 1000°C is only 6-10% more than that
expected for a quantitative conversion of the mixture to SiC and AlN,
whereas the individual precursors both gave char yields which were on the
order of 27-30% under the same conditions (10°C/min, under N$_2$) [22].

XRD data (Figure 2) for the 1000°C samples obtained by either
pyrolysis procedure A or B indicate little or no crystallinity, whereas
after the 1600°C anneal the crystallinity has obviously increased, although
the crystallite sizes are apparently still quite small. By 1800°C the 2H
XRD pattern is clearly seen for all pyrolysis products.

TEM/EDS analyses performed on the ceramic powders derived from
pyrolysis procedures A and B showed a significant difference in overall
composition, despite the fact that these samples were derived from the same
initial precursor mixture (Si/Al=2.1). Whereas the copyrolysis samples
(procedure A) appeared to contain more Si than Al (Si/Al= ca. 3-10), the
samples obtained from the hot drop appeared to be richer in Al (Si/Al= ca.
0.2-0.5). After the 1000°C pyrolysis, both samples were largely amorphous;

9

after the 1600°C anneal, blocky crystallites of 10-50 nm were observed. Further annealing at 1800°C produced some slightly larger crystallites (50-500 nm), although most crystals were 20-50 nm in size; no grain sizes above 1μm were observed. As we observed previously for our precursor-derived SiC/AlN solid solution products [11], there appeared to be two distinct types of particles in these samples, an extremely fine-grained (<10 nm), material which was quite high in Al content and the larger blocky crystallites which were richer in Si than Al, but appeared to contain a significant proportion of both elements.

Single-component Precursor

The char yields for the single-component precursors, pyrolyzed in N_2 to 1000°C, ranged from 35-75%, increasing as the ratio of Si/Al decreased from 9 to 1, $i.e.$, as the amount of Al increased in the polymer [12], and also when the vinyl/methyl-substituted silazane, TMTVTS, was used instead of the methyl-substituted compound, HMTS (Figure 3). In all cases, the resulting ceramics were black glassy solids.

XRD indicated that all materials pyrolyzed to 1000°C were poorly crystalline. Heating to 1600-1800°C under N_2 induced crystallization, with the XRD patterns comparable to those obtained for the mixed-precursor ceramics and consistent with expectations for a 2H solid solution [12].

Solid state ^{27}Al and ^{13}C NMR results for the TMTVS-derived ceramic products are shown in Figures 4 and 5, respectively. The ^{27}Al spectra show a single, broad peak (with broad side bands) which sharpens somewhat and shifts to lower shielding as the temperature is increased from 1000°C to 1800°C. The peak at 113.2 ppm in the spectrum for the 1800°C sample is

10

consistent with that observed at 114.3 ppm for the AlN derived from pyrolysis of the $[Et_2AlNH_2]_3$ precursor alone. The ^{13}C spectra have rather low signal-to-noise ratios; the presence of graphitic carbon from 180-100 ppm [23] is not seen in the 1600°C or 1800°C samples. Carbidic carbon (20 ppm) [23,24] is seen in both of these samples.

DISCUSSION

In our earlier studies of SiC/AlN solid solution formation by pyrolysis of mixed organometallic precursors, it was found that either 2H solid solutions or nanoscale composites of β-SiC and 2H AlN could be obtained, depending on the AlN precursor and the pyrolysis procedure employed. [11]. The use of $[i\text{-}Bu_2AlNH_2]_3$ as the AlN source led to a composite ceramic when a gradual copyrolysis was employed; on rapid heating (hot drop) or through the use of $[Et_2AlNH_2]_3$ as the AlN source, a 2H solid solution was obtained.

Two SiC sources were employed in our earlier work, a methylpolycarbosilane $[MeHSiCH_2]_n$ (MPCS) and a vinylic polysilane $[(vinyl)_xMe_yH_zSi]_n$ (VPS). Both polymers contain a considerable excess of carbon, relative to the unit Si/C ratio in SiC and, as was suggested by the elemental analyses, some of this excess carbon remains in the final ceramic products, presumably as free C.

In the present study, we have focused on the use of $[Et_2AlNH_2]_3$ as the AlN source for the mixed-precursor pyrolysis and, in order to avoid the introduction of excess carbon, we have employed a new precursor (HPCS) to SiC that has a near stoichiometric ratio of Si/C=1 [13]. HPCS is a highly branched polycarbosilane of the composition, $[SiH_{1.85}Et_{0.15}CH_2]_n$, that is

11

known to undergo crosslinking by elimination of H_2 between SiH_n groups on heating between 100-300°C [14]. Thus, in our copyrolysis experiments, the temperature of the mixture of this precursor with $[Et_2AlNH_2]_3$ was held at 200°C for several hours to avoid the loss of volatile carbosilane oligomer fractions in HPCS. However, as is suggested by our TGA study of this mixture (Figure 1) even under the relatively rapid pyrolysis conditions (10 °C/min) employed in this TGA experiment, the overall char yield of the mixture is substantially enhanced relative to that of the individual precursors when studied under the same conditions alone. We conclude that a reaction between these two precursors occurs during the heating of the mixture between 200-500°C, which renders the precursors involatile and fixes the relative positions of Si and Al in the mixture during the subsequent pyrolysis. This would explain the observation that a 2H SiC/AlN solid solution is obtained as the eventual product of this pyrolysis.

The precise nature of the reaction between these two precursors is presently unknown; however, it is expected that Si-based radicals are formed by thermolysis of the Si-H bonds in the polycarbosilane near 200°C. These radicals can be trapped by the organoaluminum amide, which could lead to Si-N-Al linkages between these two precursors. Alternately, a reaction involving the relatively protonic (N)-H hydrogen atom of the organoaluminum amide and the relatively hydridic (Si)-H of the polycarbosilane could eliminate H_2 to form Al-N-Si bonds directly [25]. Efforts to test this hypothesis of Al-N-Si linkage formation in the heated polymer mixture are currently underway using solid state NMR spectroscopy. In any event, it is clear that the copyrolysis of this precursor mixture can be used to prepare an apparently homogeneous SiC/AlN solid solution in high yield.

Preliminary studies of this solid solution by using TEM/EDS and solid state ^{27}Al NMR spectroscopy suggest that, on annealing between 1600 and 1800°C, phase separation occurs to yield at least two distinct 2H solid solution phases. A similar situation was observed in our earlier studies [11] as well as in our investigation of the single-component precursors (see below). This is presumably a manifestation of the miscibility gap in the SiC/AlN phase diagram in the temperature regime where crystallization of the solid solution actually occurs [7].

The single-component precursors to SiC/AlN solid solutions are polyaluminosilazanes derived from the reaction of cyclotrisilazanes of the type $[RR'SiNH]_3$ (R = Me; R' = Me, vinyl) with Et_3Al. A reaction occurs at room temperature between these compounds, releasing ethane and presumably forming Si-N-Al bridges between at least partially intact silazane rings [20]. The substantial increase in viscosity that occurs on mixing the two liquid precursors, along with the eventual solidification on heating to form an insoluble glass, suggests a condensation polymerization process that eventually proceeds to form a three-dimensional network structure. In the case of the vinyl-substituted silazane, TMTVTS, IR spectra suggest that vinyl polymerization occurs along with Si-N-Al bond formation, contributing to the establishment of a network structure. It was found that, at an appropriate point in this thermally induced polymerization process, fibers could be hand drawn from the melt of the TMTVTS + Et_3Al polymer. These were successfully converted to amorphous ceramic fiber by heating rapidly in either N_2 or NH_3. In the latter case, a mixture of β-Si_3N_4 and AlN is the eventual crystalline product on thermally annealing at 1600°C, whereas under N_2 the only crystalline phase observed by XRD [12] is the 2H SiC/AlN solid solution. Based on the unusually high TGA yield observed for the

13

TMTVTS-derived polymer relative to the HMTS-derived polymer in particular (Figure 3), it is anticipated that the final ceramic product also contains a considerable amount of excess carbon.

The ^{27}Al and ^{13}C NMR data on the TMTVS-derived ceramic products (Figures 4 and 5) indicate that the final Al and C environments after crystallization at 1800°C are similar to those in AlN and SiC, respectively; however, a closer examination of these spectra show a broadening that is not found in the pure phases, suggesting a distribution of environments. The substantial peak shifts that are observed in these spectra following the annealing of the 1000°C sample at 1600°C and finally 1800°C, indicate further that a marked change in the local environment has occurred as this material crystallized. The initial ^{27}Al peak position observed for the amorphous 1000°C product is consistent with an environment which contains both N and C. After heating to 1600°C and then 1800°C, the Al peak shifts to lower fields, approaching the 114.0 ppm position found for AlN. Similarly, the ^{13}C peak, which starts out with a value appropriate to graphitic carbon, shifts towards the position expected for C in SiC.

These observations are, in general, consistent with expectations based on the phase diagram for SiC/AlN which indicates a miscibility gap in this temperature regime, with AlN- and SiC-rich solid solution phases separating out on crystallization. Further NMR studies (including ^{29}Si NMR) of these solid solutions are planned, along with a full investigation of the homogeneous 2H solid solution phase which is anticipated on crystallization of the 1000°C material above 2000°C.

ACKNOWLEDGEMENTS

REFERENCES

1. W. Rafaniello, K. Cho, and A. V. Virkar, "Fabrication and Characterization of SiC-AlN Alloys", J. Mater. Sci., 16 [12] 3479-3488 (1981).

2. R. Ruh and A. Zangvil, "Composition and Properties of Hot-Pressed SiC-AlN Solid Solutions", J. Am. Ceram. Soc., 65 [5] 260-265 (1982).

3. L. D. Bentsen, D. P. H. Hasselman and R. Ruh, "Effect of Hot-Pressing Temperature on the Thermal Diffusivity/Conductivity of SiC/AlN Composites", J. Am. Ceram. Soc., 66 [3] C40-C41 (1983).

4. W. Rafaniello, M. R. Plichta, and A. V. Virkar, "Investigation of Phase Stability in the System SiC-AlN", J. Am. Ceram. Soc., 66 [4] 272-276 (1983).

5. A. Zangvil and R. Ruh, "Solid Solutions and Composites in the SiC-AlN and SiC-BN Systems", Mater. Sci. Eng., 71, 159-164 (1985).

6. Z.C. Jou, S.Y. Kuo, and A.V. Virkar, "High Temperature Creep in Polycrystalline AlN-SiC Ceramics", J. Mater. Sci., 21, 3015-3018 (1986).

7. A. Zangvil and R. Ruh, "Phase Relationships in the Silicon

Carbide-Aluminum Nitride System", J. Am. Ceram. Soc., 71 [10] 884-890 (1988).

8. K. Okamura, "Ceramic Fibers From Polymer Precursors", Composites, 18 [2] 107-120; L. Sawyer, M. Jamieson, D. Brikowski, M. Ishaq Haider, and R.T. Chen, "Strength, Structure, and Fracture Properties of Ceramic Fibers Produced from Polymeric Precursors: Base-Line Studies", J. Am. Ceram. Soc., 70 [11] 798-810 (1987).

9. T.J. Clark and R.E. Johnson, "Fabrication of SiC-AlN Alloys", US Patent 4,687,657, August 18, 1987.

10. R.T. Paine, J.F. Janik, and C. Narula, "Synthesis of AlN and AlN/SiC Ceramics from Polymeric Molecular Precursors", Mat. Res. Soc. Symp. Proc., 121, 461-464 (1988).

11. (a) C. L. Czeckaj, M. L. J. Hackney, W. J. Hurley, Jr., L. V. Interrante, G. A. Sigel, P. J. Shields, and G. A. Slack, "Preparation of Silicon Carbide/Aluminum Nitride Ceramics Using Organometallic Precursors", J. Am. Ceram. Soc,, 73 [2] 352-357 (1990); b) L.V. Interrante, C.L. Czekaj, M.L.J. Hackney, G.A. Sigel, P.J. Shields, and G.A. Slack, "An Investigation into the Preparation, Properties, and Processing of SiC/AlN and Si_3N_4/AlN Solid Solutions from Organometallic Precursors", Mat. Res. Symp. Proc., 121, 465-470 (1988); c) M.L.J. Hackney, L.V. Interrante, G.A. Slack, and P.J. Shields, "Organometallic Precursors to $Al_wSi_xN_yC_z$ Ceramics", Ultrastructure Processing of Advanced Ceramics, J. D. Mackenzie and D. R. Ulrich, editors, John Wiley and Sons, New York (1988), p. 99-111.

12. W.R. Schmidt, W. J. Hurley, Jr., R.H. Doremus, L. V. Interrante and P.S. Marchetti, "Novel Polymeric Precursors to Si-C-Al-O-N Ceramic Composites", Proceedings, Symposium on Ceramic, Polymer and Metal Matrix Composites, 2nd Intl. Ceramic Science and Technology Congress, Orlando, FL,

Nov. 12-15, 1990, to be published in the Ceramics Transactions Series.

13. C. Whitmarsh and L.V. Interrante, "Synthesis and Characterization of a Highly Branched Polycarbosilane Derived from Chloromethyltrichlorosilane", Organometallics, in press.

14. L.V. Interrante, C. Whitmarsh, T.K. Trout and W.R. Schmidt, Synthesis and Pyrolysis Chemistry of Polymeric Precursors to SiC and Si_3N_4", Kluwer Academic Publishers, Dordrecht, NATO Workshop on Organometallic Polymers with Special Properties", Cap D'Agde, France, Sept. 10-15, 1990, in press.

15. R.B. King, "Organometallic Syntheses, Volume 1, Transition-Metal Compounds", (1965) Academic Press, NY.

16. S.F. Dec and G.E. Maciel, "High-Speed MAS NMR Spectra of Quadrupolar Nuclides at High Magnetic Fields", J. Magn. Reson. 87, 153-159 (1990).

17. S.F. Dec, R.A. Wind, G.E. Maciel and F.E. Anthonio, "High-Speed Magic Angle Spinning", J. Magn. Reson. 70, 355-359 (1986).

18. R.A. Wind, F.E. Anthonio, M.J. Duijvestijn, J. Smidt, J. Trommel and G.M.C. De Vette, "Experimental Setup for Enhanced ^{13}C NMR Spectroscopy in Solids Using Dynamic Nuclear Polarization", J. Magn. Reson. 52, 424-434 (1983).

19. E. Fukushima and S.B.W. Roeder, "Experimental Pulse NMR - A Nuts and Bolts Approach", Addison-Wesley, Reading, PA (1981) 106-112.

20. D.E. Woessner, "Observation of Effects of Hydration on CP/MAS NMR Measurements on Quadrupolar Nuclei", Z. Phys. Chem. Neue Folge 152, 51-58 (1987).

21. L.V. Interrante, L.E. Carpenter II, C. Whitmarsh, W. Lee, M. Garbauskas and G.A. Slack, "Studies of Organometallic Precursors to Aluminum Nitride", Mat. Res. Soc. Symp. Proc., 73, 359-366 (1986).

22. Depending on the preparation conditions employed, char yields from ca.

17

25-60% have been observed for the HPCS polycarbosilane when heated in flowing N_2 at 10^3C/min (Reference 14). The particular batch employed in this work had a 27% char yield under these conditions, although after holding at ca. 200°C, as was done in the bulk copyrolysis experiments, the overall char yield is increased to 60-80%.

23. D.T. Haworth and C.A. Wilkie, "The Solid State ^{13}C NMR Spectra of Some Carbides", J. Inorg. Nucl. Chem. 1978, 40, 1689.

24. a) G.W. Wagner, B.-K. Na and M.A. Vannice, "High-Resolution Solid-State NMR of ^{29}Si and ^{13}C in β-SiC", J. Phys. Chem., 93 [13], 5061 (1989); b) K.R. Carduner, S.S. Shinozaki, M.J. Rokosz, C.R. Peters, T.J. Whalen, "Characterization of β-Silicon Carbide by Silicon-29 Solid State NMR, Transmission Electron Microscopy, and Powder X-ray Diffraction", J. Am. Ceram. Soc. 73(8) 2281 (1990).

25. S. N. Borisov, M. G. Voronkov, and E. Ya. Lukevits, "Organosilicon Heteropolymers and Heterocompounds", Plenum Press: New York (1970).

Figure Captions

Figure 1. TGA curves for the pyrolysis of 2.1:1 molar (1:1 by weight) mixtures of HPCS/$[Et_2AlNH_2]_3$ in N_2 or N_2/NH_3. TGA under N_2 run at $10^{\circ}C/min$. For the N_2/NH_3 run, conditions simulating the copyrolysis were employed (see text). The sum of the char yields for the individual precursors are noted along with the theoretical yield of SiC + AlN.

Figure 2. XRD powder patterns for ceramics obtained by a) Copyrolysis/Procedure A, and b) Hot Drop/Procedure B for HPCS/$[Et_2AlNH_2]_3$.

Figure 3. TGA curves for the N_2 pyrolysis of a) TMTVS and b) HMTS single-component precursors. Heating rate was $10^{\circ}C/min$.

Figure 4. Solid state ^{27}Al MAS NMR spectra for TMTVS (Si/Al-3) samples pyrolyzed to $1000^{\circ}C$ and annealed at $1600^{\circ}C$ and $1800^{\circ}C$ in N_2. Peak positions are noted. Spectra of $[Et_2AlNH_2]_3$ samples that were heated to $1000^{\circ}C$ and $1600^{\circ}C$ are shown for comparison. Spinning side bands (*) are seen as small, broad bands on each side of the main peak.

Figure 5. Solid state ^{13}C MAS NMR spectra for TMTVS (Si/Al-3) samples pyrolyzed to $1000^{\circ}C$ and annealed at $1600^{\circ}C$ and $1800^{\circ}C$ in N_2.

Figure 1
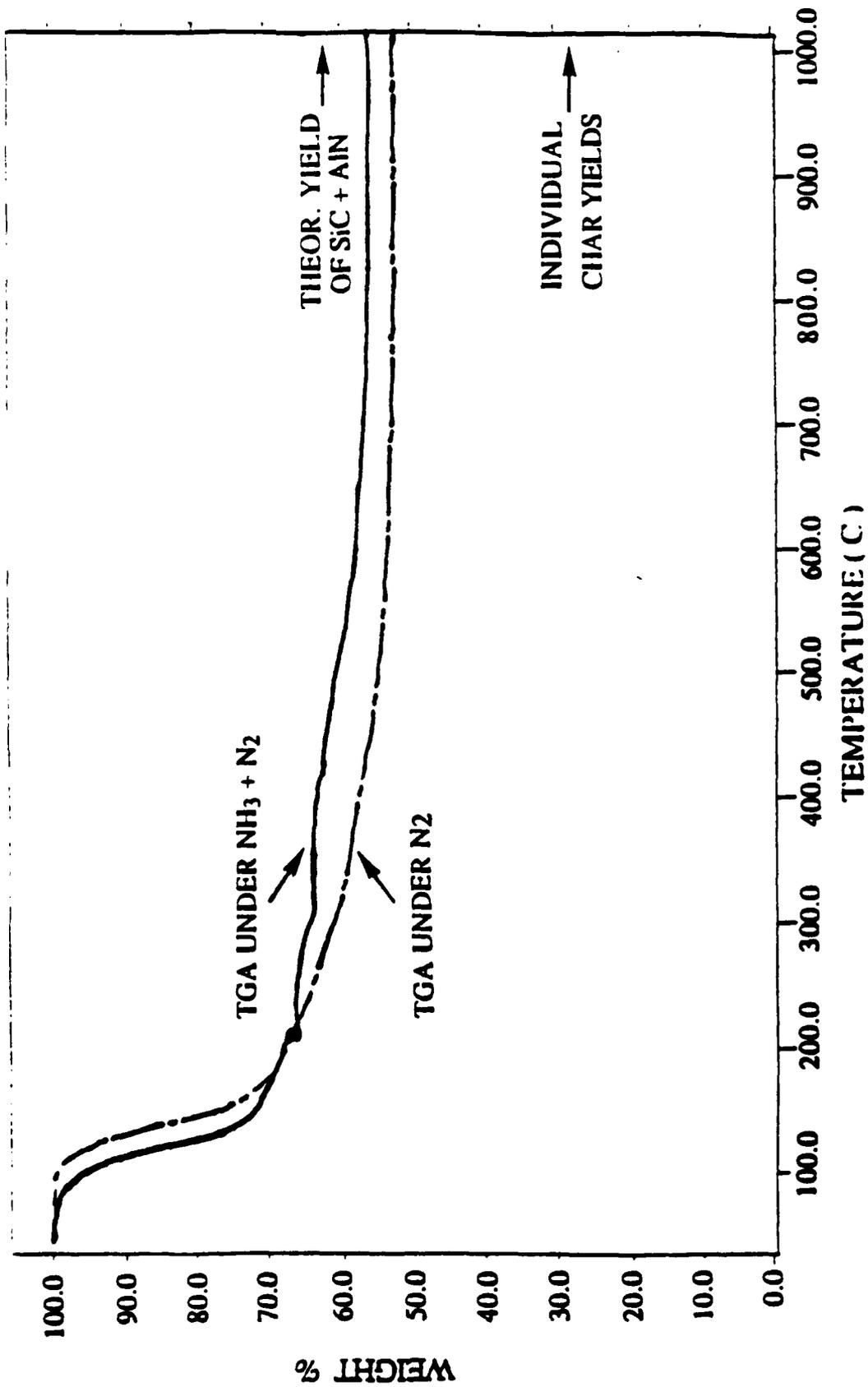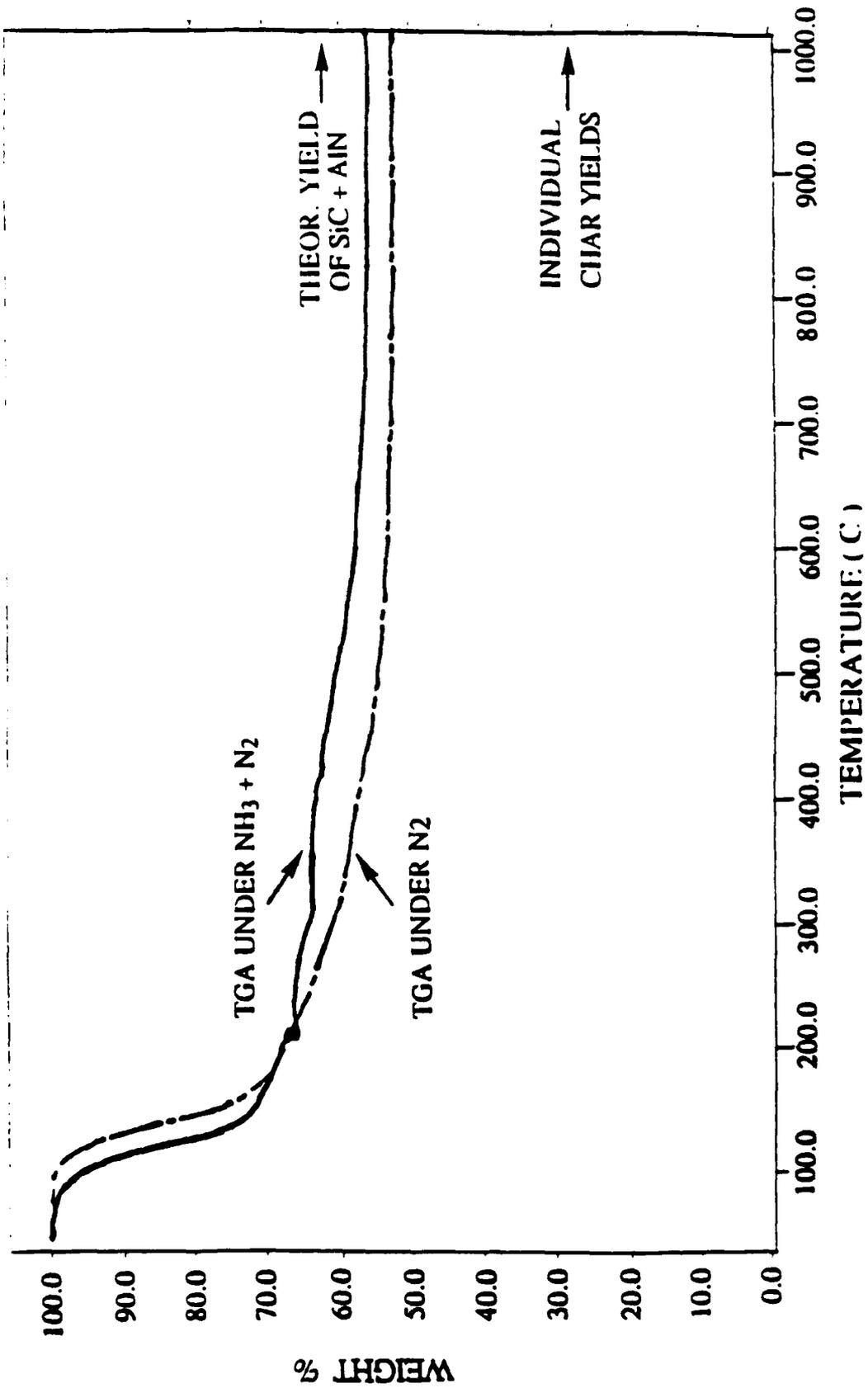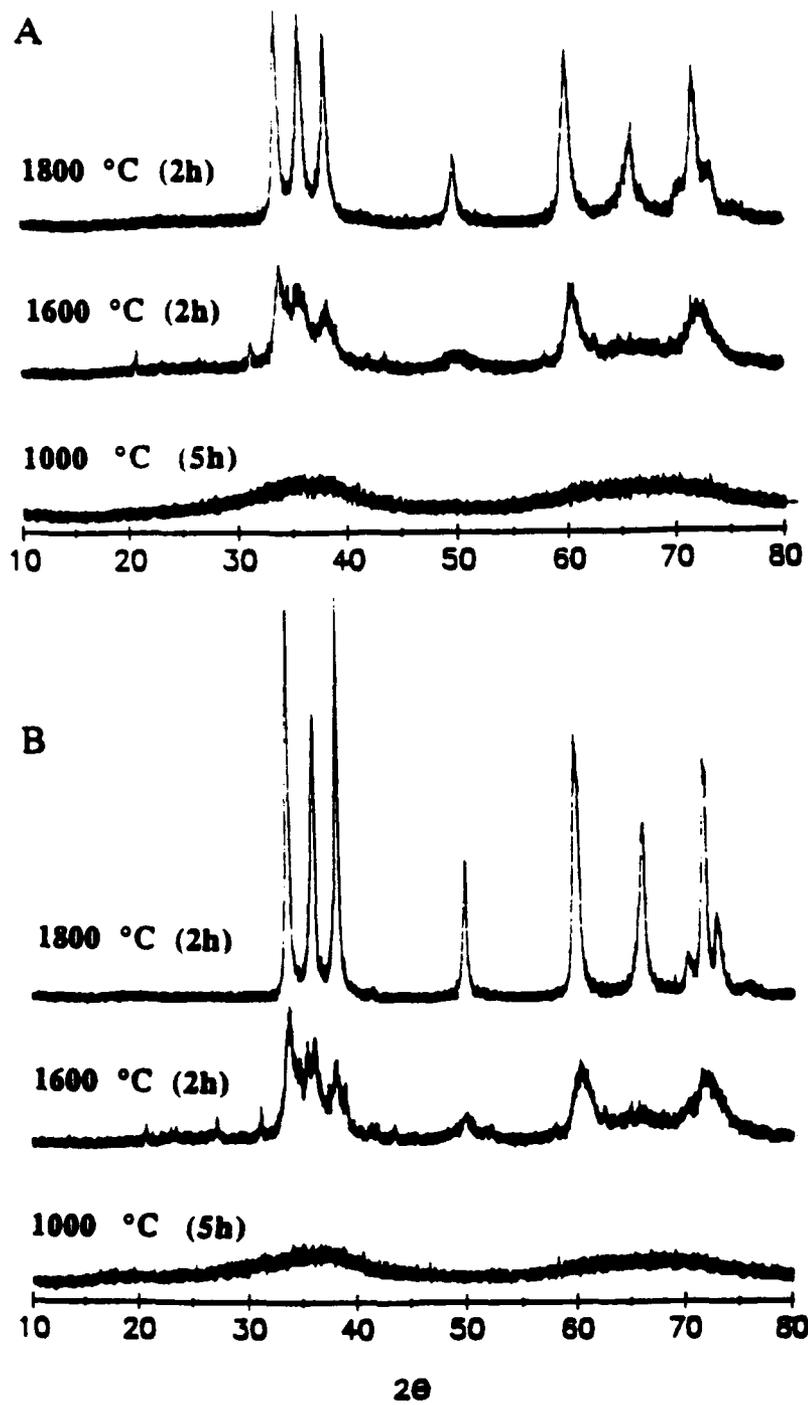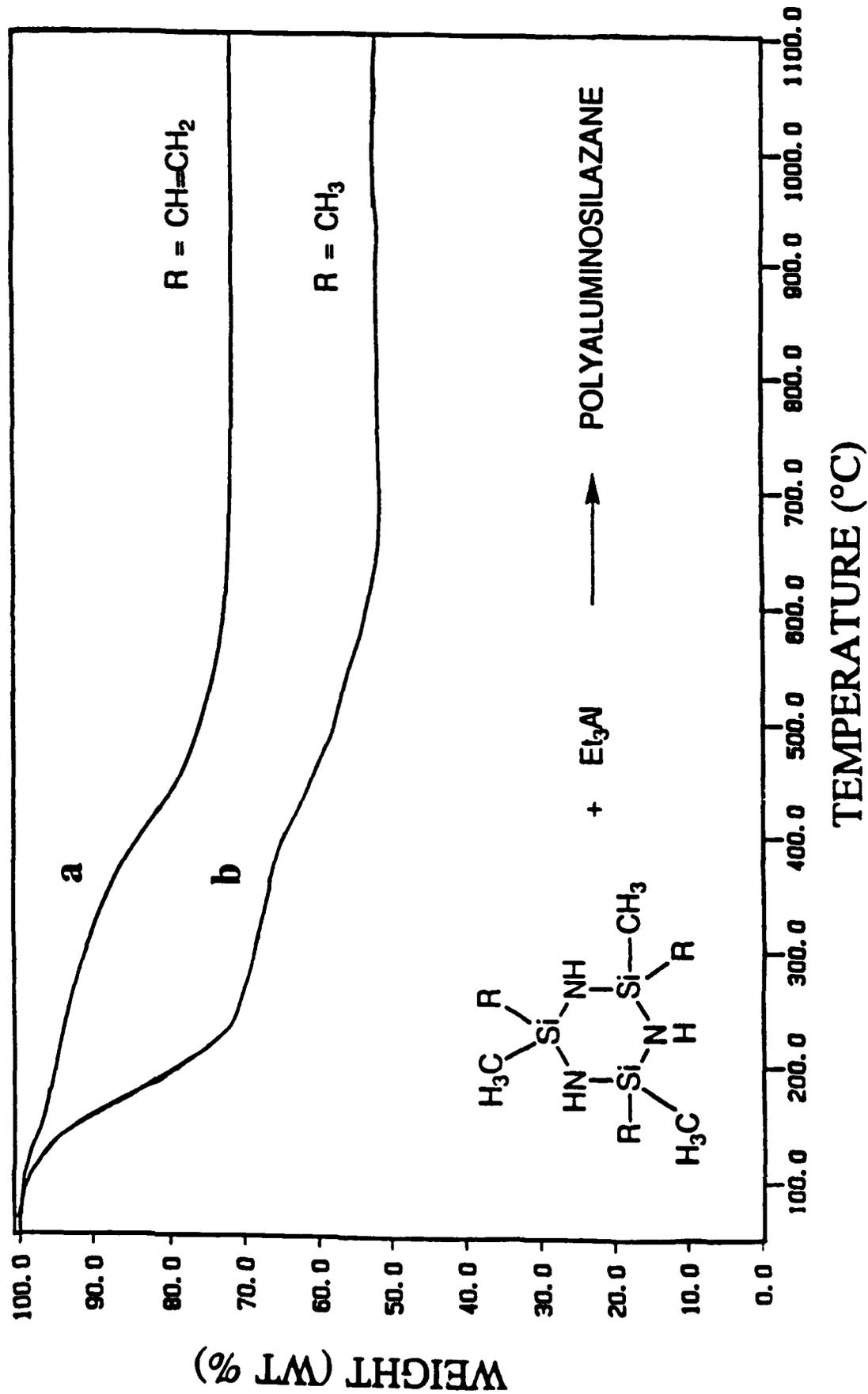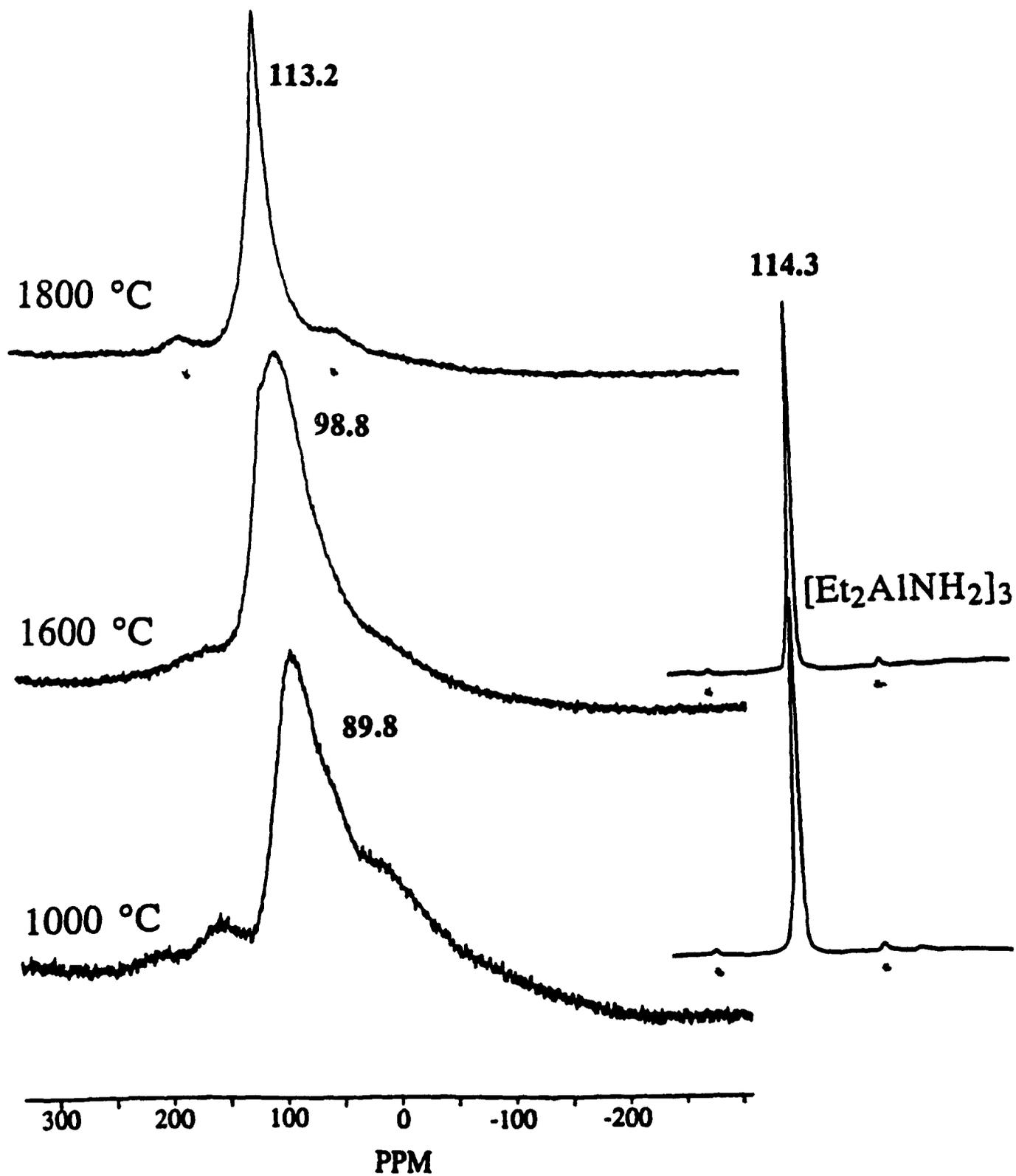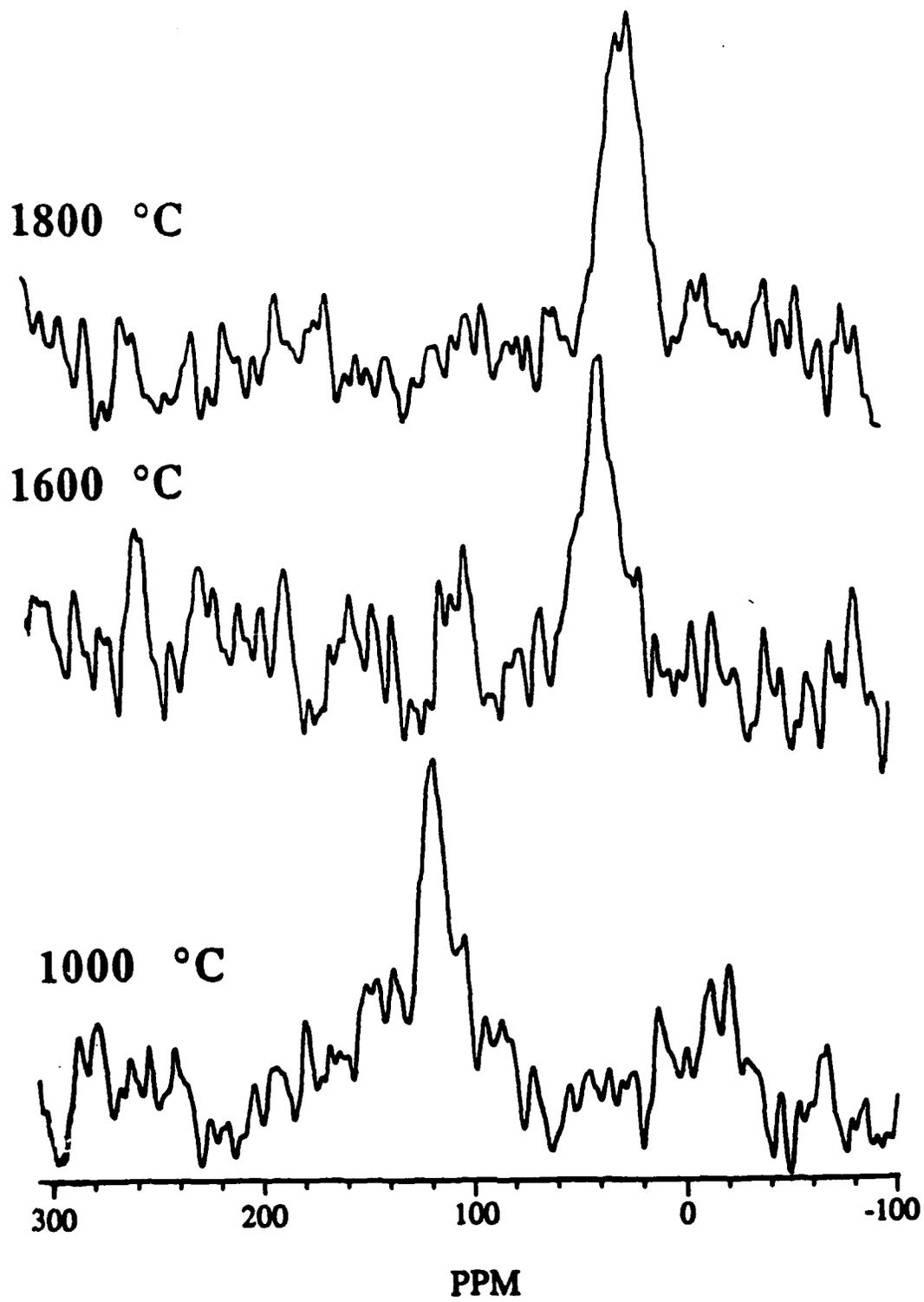
WEIGHT %

TEMPERATURE (C)

TGA UNDER NH₃ + N₂

TGA UNDER N2

THEOR. YIELD
OF SiC + AlN

INDIVIDUAL
CHAR YIELDS

Figure 2

A

1800 °C (2h)

1600 °C (2h)

1000 °C (5h)

10   20   30   40   50   60   70   80

B

1800 °C (2h)

1600 °C (2h)

1000 °C (5h)

10   20   30   40   50   60   70   80

2θ

Figure 4

Figure 5

1800 °C

1600 °C

1000 °C

300   200   100   0   -100

PPM

Preparation of Poly(dichlorosilaethylene) and Poly(silaethylene) via Ring-Opening Polymerization[1]

Hui-Jung Wu and Leonard V. Interrante*

Department of Chemistry, Rensselaer Polytechnic Institute, Troy, New York 12180

Received October 31, 1991

Polymeric precursors to SiC that have the requisite properties for fiber spinning, preparation of SiC coatings, etc., and that will produce this ceramic product in high yield and purity on pyrolysis have been the subject of much attention during the past ca. 10 years.[2,3] In this context, polymers that possess a nominal 1:1 ratio of Si to C and that undergo pyrolysis so as to preserve this 1:1 stoichiometry have been of particular interest.[3] The general rule-of-thumb in this search for high-yield SiC precursors has been that linear polymers exhibit a low ceramic yield due to thermally induced "chain-unzipping" processes that lead to volatile, low molecular weight fragments and, consequently, that cross-linked structures are a virtual requirement for suitable precursors.[4]

Our recent work on linear poly(silapropylene) obtained via ring-opening polymerization (ROP) of 1,3-dichloro-1,3-dimethyl-1,3-disilacyclobutane has suggested that the presence of H attached to Si in linear polycarbosilanes may provide an effective thermosetting mechanism for overcoming this depolymerization tendency.[5] We now report an extension of this ROP process that permits the preparation of high molecular weight, linear poly(silaethylene), $(-SiH_2CH_2-)_n$, a polymer that exhibits remarkably high ceramic yields on pyrolysis to 1000 °C. This paper also reports the basic NMR and IR characterization data for this silicon analogue to polyethylene.

Prior reports of the preparation of poly(silaethylene) have been limited to the claim, in a patent, that the synthesis of this polymer was accomplished by the ring-opening polymerization of disilacyclobutane.[6] However, other than its conversion to SiC in 85% ceramic yield, no basic characterization data for this polymer was given nor was the yield of the ROP reaction specified. Indeed, it is well-known in silicon chemistry that the Si–H bond is easily activated by the Pt catalysts employed in this patent, and it appears likely that the polymer so obtained would be extensively cross-linked by Si–Si interchain bonding.[7] Our attempts to repeat this preparation have resulted in an extremely low conversion efficiency (20%) with even lower yields of hydrocarbon-soluble polymer (8%) whose IR and NMR spectra indicate branching at Si.

We have found that 1,1,3,3-tetrachloro-1,3-disilacyclobutane (I) is a much more satisfactory starting point for the preparation of poly(silaethylene) and that high yields of a high molecular weight precursor to this polymer can be obtained by ROP of I. Moreover, this intermediate, poly(dichlorosilaethylene) (II), $(-SiCl_2CH_2-)_n$, is a novel polymer in its own right that holds considerable potential as a precursor to a wide range of new substituted polycarbosilanes.

Poly(dichlorosilaethylene) (II) was prepared by ROP of I catalyzed by chloroplatinic acid or a platinum–divinyltetramethyldisiloxane complex in benzene as described in detail elsewhere.[1] ^1H NMR: 1.17 ppm. $^{13}C\{H\}$ NMR: 18.03 ppm. $^{29}Si\{H\}$ NMR: 18.5 ppm.

Direct reduction of this product in benzene leads to the corresponding poly(silaethylene) (III) as a hydrocarbon-soluble, viscous liquid.[1] Gel permeation chromatography
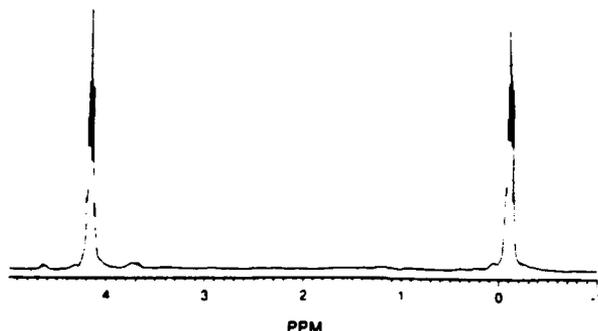
Figure 1. ^1H NMR spectrum of poly(silaethylene), $(-SiH_2CH_2-)_n$.

indicated a monomodal molecular weight distribution (M_n = 12 300, M_w = 33 000 vs polystyrene). The quintets observed in the ^1H NMR spectrum of this polymer (Figure 1) at 4.158 and –0.098 ppm and their 1:1 integration ratio are consistent with the expected structure, $(-SiH_2CH_2-)_n$.[8] The ^{29}Si NMR spectrum of III showed the proper splittings when coupled with the protons and gave one major singlet at –34.4 ppm when proton decoupled. A small peak at –62.3 ppm was attributed to the end group –SiH$_3$ and another even smaller peak at –12.3 ppm was presumed to be due to –SiH. The ^{13}C NMR spectrum showed one major singlet at –9.21 ppm as expected for the –CH$_2$– group and another small peak at –4.85 ppm due to the –CH$_3$ end group. Elemental analysis of this polymer is consistent with the expected structure. (Found: C, 27.21; H, 9.09. Calcd: C, 27.27; H, 9.09.)

The IR spectrum of III indicates well-defined narrow absorption bands at 1046, 950, 851, and 760 cm^{-1}. This is in contrast to the branched hydridopolycarbosilane prepared in our laboratory by Grignard coupling of trichloro(chloromethyl)silane followed by reduction with LiAlH$_4$, which shows broad absorption in the 1050–750-cm^{-1} region.[3a]

The TGA study of III in N$_2$ gave a remarkably high ceramic yield (calcd, 90.9; obsd, 87). Weight loss started at about 100 °C, and there was almost no weight loss after 600 °C. The infrared spectrum of the ceramic product obtained after pyrolysis to 1200 °C showed only one absorption at 823 cm^{-1}, consistent with the formation of SiC.[9] The powder X-ray diffraction study of the ceramic product, obtained after pyrolysis to 1000 °C in N$_2$ and holding at that temperature for 1 h, indicated the formation of β-SiC. The average crystallite size of this material, calculated by the line broadening of the XRD pattern, was 2.5 nm.[10] This represents an unusually low crystallization temperature for SiC obtained from organometallic precursors[2,3] and suggests, along with the observed weight loss, a high level of purity for the SiC so obtained. Further heating under N$_2$ at 1800 °C for 2 h, resulted in a sharpening of the XRD pattern, indicating an increase in the average crystallite size to 24.3 nm.

These results, along with those obtained in our earlier study of poly(silapropylene),[5] show clearly that an initially cross-linked structure is by no means a requirement for high ceramic yields. The studies suggest further that high molecular weight linear polycarbosilanes, when substituted with H on Si, can undergo relatively facile thermally-induced cross-linking prior to, or accompanying, chain scission. The mechanism for this cross-linking process is currently under study; however, it is perhaps notable that the decomposition of methylsilanes (Me_nSiH_{4-n}, n = 1–4)

is also facilitated by increasing substitution of H on Si.[11] In this case 1,1-H_2 elimination from the methylsilanes with n = 1 and 2 leads to a silylene (=Si:) intermediate. This highly reactive species is known to insert into Si–H or even C–H bonds;[12] thus in a condensed polymer, cross-linking and branching would be expected to result from the attack of such silylene species on adjacent polymer chains. Even in the case of polycarbosilanes such as poly-(silapropylene), which have only one H per Si, H transfer from Si to the adjacent C atom, accompanied by Si–C bond scission,[11] could generate such silylene species with a similar consequence in terms of interchain cross-linking and/or branching.

References and Notes

(1) This work was presented in the Polymer Chemistry Division program at the 4th International Chemical Congress in New York in Aug 1991, and a brief description of the preparation method has appeared in the proceedings (*Polym. prepr. (Am. Chem. Soc., Div. Polym. Chem.)* **1991**, *32* (3), 588–589).

(2) Yajima, S.; Hasegawa, Y.; Hayashi, J.; Iimura, M. J. *J. Mater. Sci.* **1978**, *13*, 2569–2576. West, R.; David, D. D.; Djurovich, P. I.; Yu, H.; Sinclair, R. *Am. Ceram. Soc. Bull.* **1987**, *62*, 899–903. Schilling, C. L.; Wesson, J. P.; Williams, T. C. *Am. Ceram. Soc. Bull.* **1983**, *62*, 912–915. Ijadi-Maghsoodi, S.; Pang, Y.; Barton, T. J. *J. Polym. Sci., Part A: Polym. Chem.* **1990**, *28*, 955–965. Boury, B.; Corriu, R. J. P.; Leclercq, D.; Mutin, P. H.; Planeix, J.-M.; Vioux, A. *Organometallics* **1991**, *10*, 1457–1461. Seyferth, D.; Lang, H. *Organometallics* **1991**, *10*, 551–558.

(3) (a) Whitmarsh, C. K.; Interrante, L. V. *Organometallics* **1991**, *10*, 1336–1344. (b) Zhang, Z.-F.; Babonneau, F.; Laine, R. M.; Mu, Y.; Harrod, J. F.; Rahn, J. A. *J. Am. Ceram. Soc.* **1991**, *74*, 670–673.

(4) Wynne, K. J.; Rice, R. W. *Annu. Rev. Mater. Sci.* **1984**, *14*, 297–334. Seyferth, D. In *Inorganic and Organometallic Polymers*; Zeldin, M., Wynne, K., Allcock, H. R., Eds.; ACS Symposium Series 360; American Chemical Society: Washington, DC, 1988; Chapter 3, pp 21–42.

(5) Wu, H. J.; Interrante, L. V. *Chem. Mater.* **1989**, *1*, 564–568.

(6) Smith, T. L. U.S. Patent 4,631,179, Dec 23, 1986.

(7) Yamamoto, K.; Okinoshima, H.; Kumada, M. *J. Organomet. Chem.* **1970**, *23*, C7-8. Seyferth, D. In *Inorganic and Organometallic Polymers*; Zeldin, M., Wynne, K., Allcock, H. R., Eds.; ACS Symposium Series 360; American Chemical Society: Washington, DC, 1988; Chapter 3, pp 21–42.

(8) Whitmarsh, C. K.; Interrante, L. V. *J. Organomet. Chem.* **1991**, *418*, 69–77.

(9) Hasegawa, Y.; Okamura, K. *J. Mater. Sci.* **1983**, *18*, 3633–3648.

(10) Cullity, B. D. *Elements of X-Ray Diffraction*, 2nd ed.; Addison-Wesley: London, 1978; pp 100–102.

(11) O'Neal, H. E.; Ring, M. A. *Organometallics* **1988**, *7*, 1017–1025. Neudorfl, P. S.; Lown, E. M.; Safarik, I.; Jodhan, A.; Strausz, O. P. *J. Am. Chem. Soc.* **1987**, *109*, 5780–5789. Ring, M. A.; O'Neal, H. E.; Rickborn, S. F.; Sawrey, B. A. *Organometallics* **1983**, *2*, 1891–1894. Davidson, I. M. T.; Ring, M. A. *J. Chem. Soc., Faraday Trans. 1* **1980**, *76*, 1520–1525.

(12) Gano, D. R.; Gordon, M. S.; Boatz, J. A. *J. Am. Chem. Soc.* **1991**, *18*, 6711–6718. Tang, T. N. In *Reactive Intermediates*; Abramovitch. R. A., Ed.; Plenum Press: New York, 1982; Vol. 2, Chapter 4, pp 297–366. Gaspar, P. P. In *Organosilicon and Bioorganosilicon Chemistry: Structure, Bonding, Reactivity and Synthetic Application*; Sakurai, H., Ed.; IUPAC: Oxford, U.K., 1985; Chapter 7, pp 87–98.

PREPARATION OF NON-OXIDE CERAMICS BY PYROLYSIS OF ORGANOMETALLIC PRECURSORS

LEONARD V. INTERRANTE[§], WAYDE R. SCHMIDT[§], PAUL S. MARCHETTI[¥], and GARY E. MACIEL[¥], [§]Department of Chemistry, Rensselaer Polytechnic Institute, Troy, NY 12180-3590; [¥]Department of Chemistry, Colorado State University, Fort Collins, CO 80523.

INTRODUCTION

Chemical processing routes to advanced ceramic materials are gaining importance as a convenient approach to control the stoichiometry, purity, microstructure and final form of the ceramic products [1]. The pyrolytic conversion of organometallic molecules and polymers is one such chemical processing route that has been widely applied in ceramic fiber technology [1,2], in coating processes [1,2], and in the sintering of bulk ceramic objects [3]. Despite these advances in practical applications, there is a continuing need in this area for a better fundamental understanding of the chemistry involved during the precursor-to-ceramic conversion process and for the development of new precursors which yield the desired ceramic(s) in high yield and purity.

The recent discovery of superplasticity for nanocrystalline SiC/Si_3N_4 obtained by pyrolysis of a methylsilazane [4], along with the potential advantages afforded by nanocrystalline materials in terms of mechanical, optical, and electronic properties [5], has focused attention on the preparation of these materials by pyrolysis of molecular precursors. Finally, the prospect of developing ceramic powders and/or films with controlled nanoporosity for use as catalysts, catalyst supports and as gas separation media offers additional incentive to develop further the range of processes and new systems available through polymer precursor pyrolysis [6].

This paper focuses on our own efforts over the past ca. 10 years to explore polymer/molecular precursor pyrolysis as a route to both known and potentially new non-oxide ceramic compositions with unique properties.

Organometallic Precursor Routes to AlN

Our efforts in this area began with an attempt to obtain AlN powder in high yield and purity from organoaluminum-ammonia derivatives. These experiments led to a process for AlN powder production that employs Et_3Al and NH_3 as the Al and N sources, respectively (Scheme I), and which gives a high surface area, pure AlN powder in nearly quantitative yield at a low net

$$R_3Al \;+\; NH_3 \;\longrightarrow\; R_3Al{:}NH_3$$

$$R_3Al{:}NH_3 \;\longrightarrow\; R_2AlNH_2 \;+\; RH$$

Scheme I

$$R_2AlNH_2 \;\longrightarrow\; RAlNH \;+\; RH$$

$$RAlNH \;\xrightarrow{\;NH_3\;}\; AlN \;+\; RH$$
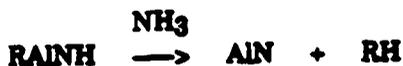
materials cost [7]. A key step in this procedure is the use of an NH_3 atmosphere in the final stage of conversion to promote loss of residual alkyl groups as volatile hydrocarbons, thereby yielding stoichiometric AlN with both C and O contents less than 0.1 wt. % and negligible amounts of other impurities. This is to be contrasted with alternative processing methods that start with Al or Al_2O_3 where control of product stoichiometry and/or C and O content is problematic.

The use of Me_3Al as the Al source in this same sequence of reactions involving NH_3 yields $[Me_2AlNH_2]_3$ as a crystalline intermediate. This compound is relatively volatile and serves as an excellent single-source precursor for AlN CVD yielding high quality, polycrystalline AlN films at relatively low deposition temperatures (ca. 500 °C) compared to alternative mixed Al and N

precursor systems, such as AlX$_3$ (X = Cl, Br) or Me$_3$Al and NH$_3$ [8]. In this case, the loss of C from the growing AlN surface is relatively efficient, leading to low levels of C incorporation in the product films even without the use of additional NH$_3$ as a co-reactant.

These applications of the R$_3$Al + NH$_3$ system as a source of AlN powder and thin film have been aided and enhanced by our continuing studies of the chemistry represented in the sequence of reactions shown in Scheme I. This work has included kinetic studies of the Me$_3$Al:NH$_3$ decomposition to [Me$_2$AlNH$_2$]$_3$, which provided the first indirect evidence for a trimer (T) <=> dimer (D) <=> monomer (M) equilibrium for the Me$_2$AlNH$_2$ product species [9]. The existence of at least the T <=> D equilibrium in hydrocarbon solution was evidenced in further NMR studies of the R = Me, Et, i-Bu and t-Bu derivatives which yielded the respective ΔH and ΔS values [10]. Our isolation of the trimeric form of the [(t-Bu)$_2$AlNH$_2$]$_3$ compound led to a crystal structure study that revealed a novel planar arrangement for the (AlN)$_3$ six-membered ring [11]. In this study, the factors that determined the relative stabilities of the dimer and trimer forms for the [R$_2$AlNH$_2$]$_n$ compounds, as well as the conformation of the [R$_2$AlNH$_2$]$_3$ ring system, were noted and discussed [11]. A subsequent theoretical study indicated a probable planar structure for the monomeric Me$_2$AlNH$_2$ species and led to a prediction of its bond lengths and angles [12]. Time of flight studies of the [Me$_2$AlNH$_2$]$_3$ system have recently confirmed the existence of dimeric and trimeric forms in the vapor phase [13]; however, the corresponding monomeric form currently remains elusive.

An alternative solution-based route to AlN films and coatings which employs a mixture of R$_3$Al and ethylenediamine (en) has also been investigated yielding, in the case of the 2:1 R$_3$Al:en system, a soluble polymeric intermediate [(R$_2$Al)$_2$(en-2H)]$_n$ which was used to make AlN films on Si [14]. Again, a detailed study of the chemistry involved in the conversion of the xR$_3$Al:en (x = 2,1) adducts to polymeric products was carried out which has revealed a series of novel aluminum/(en-2H) cluster intermediates on thermolysis of the 1:1 adducts [15].

Precursors to SiC and Si$_3$N$_4$

Our efforts to synthesize new SiC precursors were prompted by the problem of excess C in SiC derived from most of the organosilicon polymers that are currently employed as precursors. These precursors typically contain a 2/1 or greater ratio of C/Si initially, and the excess C is not eliminated cleanly as hydrocarbons on pyrolysis. Residual carbon can lead to decreased oxidative stability for the resulting SiC ceramics, as well as excessive creep and other undesireable effects on the microstructure and/or properties. Moreover, in the presence of oxygen derived from curing, handling, and/or partial oxidation of the precursors or from oxide components in a composite, loss of CO$_x$ species becomes a significant problem for these materials beyond about 1200 °C [16].

For these reasons, we have directed our attention to the preparation of polycarbosilanes that have a nominal "SiH$_2$CH$_2$" composition and have explored two approaches to such polymers that yield structurally quite different products having either highly branched or linear -Si-CH$_2$-Si- backbones. Both polymers were found to have high ceramic yields after thermal processing and gave near-stoichiometric SiC on pyrolysis in N$_2$.

The first approach developed employs Mg as a coupling agent and Cl$_3$SiCH$_2$Cl as the starting material. The resultant "chloropolymer" (nominally, "[SiCl$_2$CH$_2$]") was converted to the hydridopolycarbosilane (HPCS) "[SiH$_2$CH$_2$]" by reduction with LiAlH$_4$. A side reaction with the diethylether solvent leads to the incorporation of a small amount of ethyl groups, giving the actual formula, [SiH$_{1.85}$Et$_{0.15}$CH$_2$] [17].

A structural analysis of this polymer by solution NMR methods has revealed a complex, highly branched structure, resulting from the ternary functionality of the Cl$_3$Si end of the monomer unit. Despite this branching, the polymer is not appreciably crosslinked and remains liquid and highly soluble in hydrocarbon solvents. This "[SiH$_2$CH$_2$]" polymer undergoes crosslinking through loss of H$_2$ above ca. 200 °C. Additional crosslinking by thermal treatment produces a gel at 200 °C (12 hrs) and an insoluble rubber at 400 °C (2 hrs), which have significantly increased ceramic yields (53% and 91%, respectively) on pyrolysis in N$_2$ to 1000 °C (Figure 1), as compared to the initially isolated, untreated polymer (30-40% ceramic yield) [18].
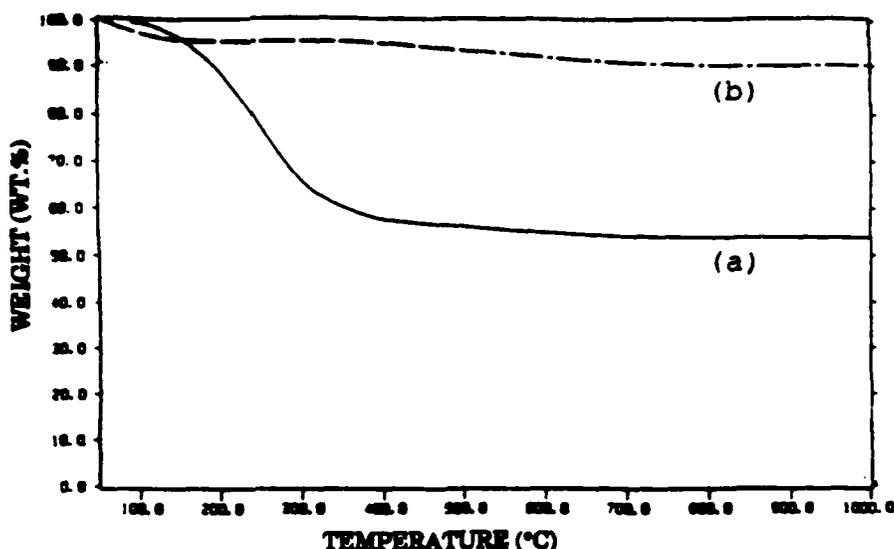
Figure 1. TGA curves for highly branched hydridopolycarbosilane (HPCS) after thermal crosslinking a) 200 °C (12 hrs), b) 400 °C (2 hr).

We have used this polymer to obtain amorphous "SiC" coatings on glassy carbon substrates and C fiber that inhibit oxidation of these substrates at 600 °C in air. Adherent coatings have also been applied to various metal surfaces, including C-steels. These coatings can be applied as polymer solutions through dip or spin coating techniques, followed by pyrolysis to 1000 °C in N_2. We have also used this hydridopolycarbosilane to prepare particulate and fiber-reinforced SiC/SiC composites by liquid phase impregnation. The advantages over alternative precursors for SiC include the effective elimination of excess C and O, thereby providing a SiC product that is more thermally and oxidatively stable than those obtained using alternative precursors [19]. This polymer also does not require a catalyst or an oxidation step for thermosetting and exibits a high ceramic yield of essentially pure SiC.

The second approach that we have developed to obtain a "[SiH$_2$CH$_2$]" polymer involves the ring-opening polymerization (ROP) of tetrachlorodisilacyclobutane, [SiCl$_2$CH$_2$]$_2$ [20]. The resultant "chloropolymer" is again reduced to the hydridopolymer with LiAlH$_4$. In this case, however, the product polycarbosilane is a high molecular weight linear polymer with [SiH$_2$CH$_2$]$_n$ as the actual repeat unit. This polymer is also a liquid a room temperature, is soluble in hydrocarbons, and undergoes pyrolysis under N_2 to give stoichiometric SiC in yields approaching the theoretical value (up to 91%) by 1000 °C. This polymer is currently available only in small quantities by a relatively low yield process and is not expected to be competitive in the short term with the branched "[SiH$_2$CH$_2$]" polymer as a source of SiC for practical applications.

Both of these synthetic methods are fundamentally new approaches for preparing useful polymeric precursors to SiC. These polycarbosilanes undergo a novel, thermally-induced crosslinking process that involves elimination of H_2 from SiH$_n$ groups on the polymer backbone. They show considerable promise as high yield precursors to stoichiometric SiC and, in the case of the branched polymer, as a viable source of SiC coatings and matrices for composites.

In addition to these ongoing investigations of the pyrolysis of our own "SiH$_2$CH$_2$" polymers, we have carried out parallel studies of a commercial polysilane of the approximate composition,

$$[[Si(Me_3)]_{0.32}[Si(CH=CH_2)Me]_{0.35}[Si(H)Me]_{0.18}[SiMe_2]_{0.07}[CH_2SiMe_3]_{0.08}]_n$$

obtained from Union Carbide (Y-12044) [19,21]. This liquid polymer provides a predominantly polysilane (-RR'Si-)$_n$ chain structure with reactive vinyl and H groups for possible thermosetting through radical coupling of the vinyl groups and hydrosilylation. It is known to yield a C-rich (ca. 17 wt.% excess C) SiC on pyrolysis in N$_2$ or other inert atmospheres. We have studied the crosslinking process and the evolution of the SiC network structure in this polymer by a combination of methods, but of particular value has been the use of solid state NMR methods, where the Si, C and even H environments in the precursor were followed through the different stages of the thermal conversion process [21]. The chief conclusion in the case of the pyrolysis in N$_2$ was that cleavage of the end groups from the polymer backbone to give R$_3$Si$^\bullet$ radicals at relatively low temperature is a key step in both the thermosetting and the initial part of the polymer conversion process, during which the -Si-Si- backbone converts to -Si-CH$_2$-Si- via a radical-initated -CH$_2$ insertion process [21].

Following other studies in which NH$_3$ has been used to convert polycarbosilanes and polysilazanes to Si$_3$N$_4$, we have found that the vinylic polysilane and our "SiH$_2$CH$_2$" polymer can be used to obtain high surface area powders of largely amorphous Si$_3$N$_4$ at 1000 °C [22]. The Si$_3$N$_4$ eventually crystallizes with reduction in surface area on further heating above 1200 °C; however, below this temperature, in the absence of certain impurities such as B or BN [23], this high surface area Si$_3$N$_4$ is relatively stable and conceivably could be used as a catalyst support [6].

We have recently completed a detailed study of the chemistry occurring during the conversion of this vinylic polysilane to Si$_3$N$_4$ in NH$_3$ that has included esr and dynamic nuclear polarization, as well as solid state NMR measurements on the intermediate and final solid products [24]. A key difference here with respect to the analagous conversion in N$_2$, in addition to the eventual loss of all C and its replacement by N, is the relatively low spin concentrations for the samples pyrolyzed in NH$_3$ (Figure 2). Whereas the "inert" atmosphere pyrolysis generates a significant concentration of paramagnetic centers and unpaired spins in the solid products, in NH$_3$ the unpaired spins are effectively quenched, presumably by radical transfer processes involving NH$_3$ (Scheme II).

$$NH_3 \ + \ ^\bullet Si{\lessgtr} \ \ (\text{or } R^\bullet) \ \ \longrightarrow \ \ NH_2^\bullet \ + \ HSi{\lessgtr} \ \ (\text{or } RH)$$

Scheme II

$$NH_2^\bullet \ + \ ^\bullet Si{\lessgtr} \ \ \longrightarrow \ \ {\gtrless}Si\text{-}NH_2$$
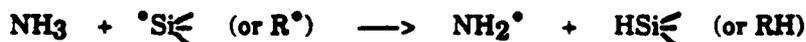
The resultant NH$_2$$^\bullet$ radicals generated can couple with Si-based radical sites on the polymer backbone. This process, along with nucleophilic attack of NH$_3$ directly on the backbone Si atoms of the polymer, are believed to be responsible for the efficient removal of C, as hydrocarbons, and its replacement by NH$_x$ species. Condensation processes that eliminate NH$_3$ and silylamine species then lead to the extended -Si-N- network structure of Si$_3$N$_4$ [24].

A study of the condensation polymerization and pyrolysis of silicon tetradiethylamide, [Si(NEt$_2$)$_4$], was also carried out with the aid of solid state ^{29}Si, ^{13}C, and ^{1}H (CRAMPS) NMR spectroscopy [25]. Among the key observations here was that the initial SiN$_4$ bonding of the precursor was maintained throughout the conversion of the tetraamide to the polymeric silazane and then to the amorphous preceramic product at 800 °C, albeit with the formation of a considerable amount of free C by-product. On heating further to 1500-1600 °C, this amorphous "silicon nitride" plus C mixture is converted under an Ar atmosphere largely to SiC and N$_2$(g), whereas under one atmosphere of N$_2$, crystalline α-Si$_3$N$_4$, along with free C, are the main products.
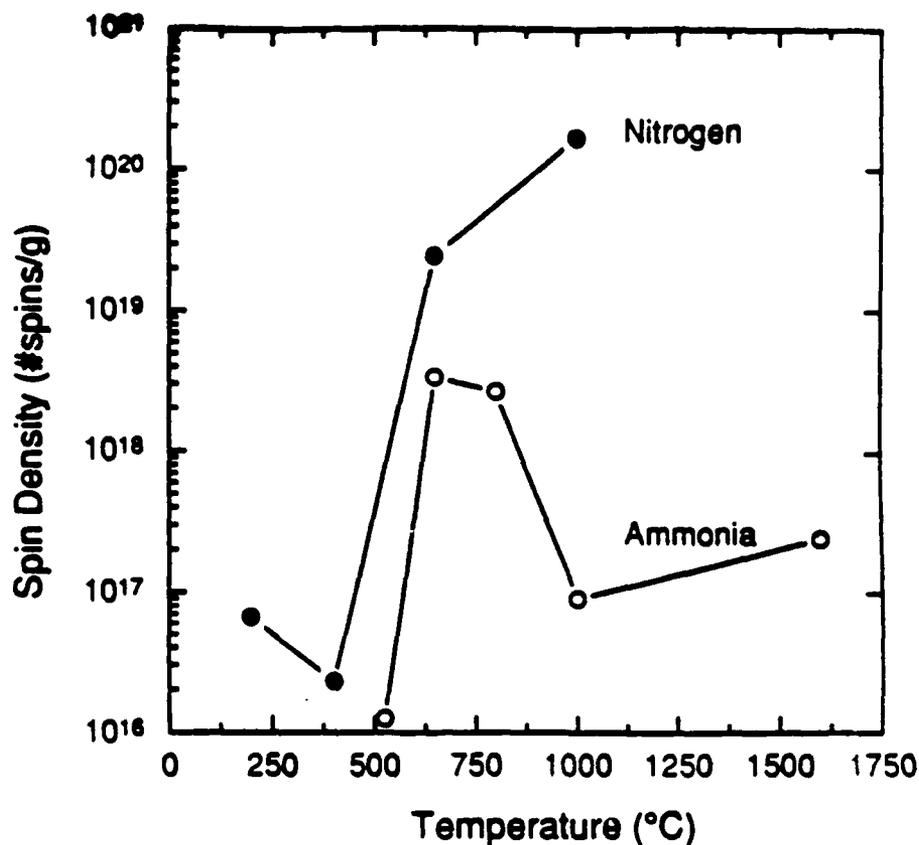
Figure 2. Spin densities as a function of temperature for solids isolated by pyrolysis of the vinylic polysilane in either nitrogen or ammonia.

Preparation of AlN/SiC Solid Solutions and Ceramic Nanocomposites Using Organometallic Precursors

We have found that both homogeneous solid solutions and nanoscale composite mixtures of SiC with AlN can be obtained on pyrolysis of mixtures of the polycarbosilanes or polysilane (as the SiC source) and dialkylaluminum amides (as the AlN precursor) and that the ceramic yield of the polycarbosilane is greatly enhanced in the presence of the AlN precursor [26].

In this work the use of miscible liquid precursors to both AlN and SiC allowed the attainment of molecular-level homogeneity in the initial precursor mixture. Subtle differences in the extent to which this molecular-level homogeneity was maintained after pyrolysis of the precursor mixture were evidenced by X-ray diffraction studies and solid state ^{27}Al and ^{29}Si NMR spectroscopy. Figure 3 shows a series of X-ray diffraction patterns of a 50/50 mole % mixture of the completely miscible liquid HPCS and [Me$_2$AlNH$_2$]$_3$ precursors which were pyrolyzed gradually to 1000 °C (GP) (Fig. 3a) or rapidly pyrolyzed at 500 °C (RP) prior to further heating (Fig. 3b). These samples were further heated in N$_2$ to temperatures as high as 1800 °C to crystallize the solid solution. In both cases the X-ray diffraction patterns obtained at 1800 °C are consistent with expectations for the 2H solid solution [26,27]; however, the sharper lines exhibited by the rapidly pyrolyzed sample suggest that the crystallinity is somewhat higher in this case as compared to the gradually pyrolyzed sample. These XRD patterns contrast markedly with that

obtained on pyrolysis, and subsequent annealing at 1800 °C, of the HPCS polymer alone. In this case the diffraction pattern is consistent with expectations for the cubic 3C form of SiC.

A

1800 °C (2h)

1600 °C (2h)

1000 °C (5h)

| 10 | 20 | 30 | 40 | 50 | 60 | 70 | 80 |

B

1800 °C (2h)

1600 °C (2h)

1000 °C (5h)

| 10 | 20 | 30 | 40 | 50 | 60 | 70 | 80 |

2θ
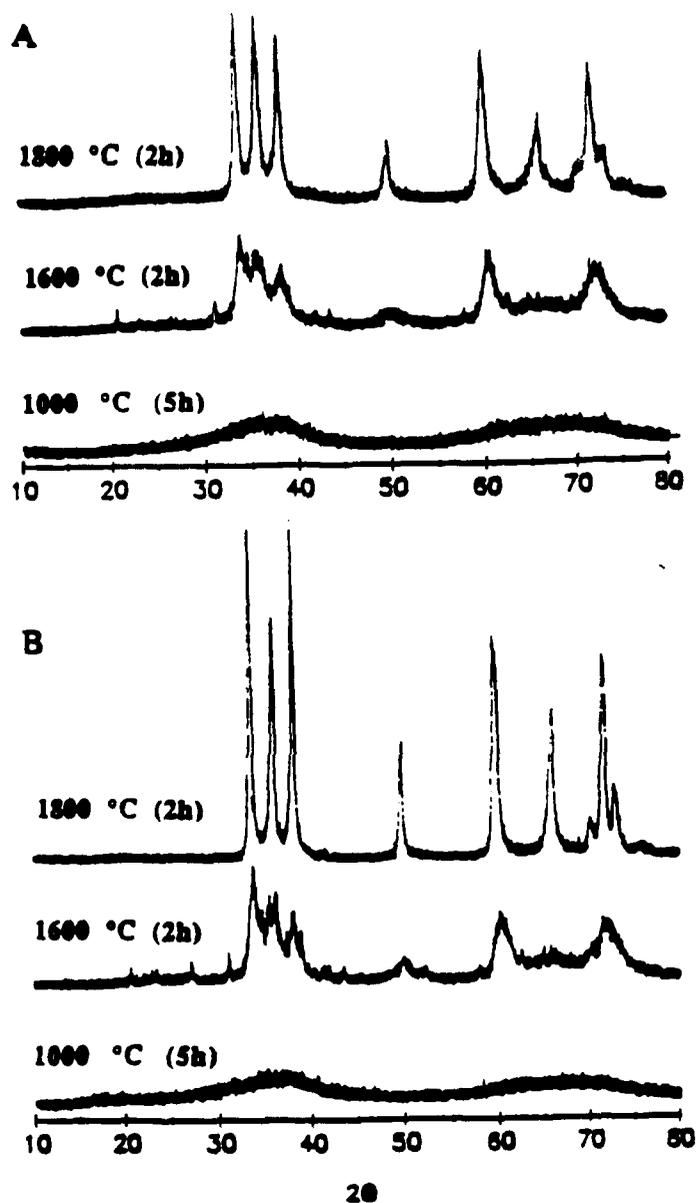
Figure 3. X-ray diffraction patterns of a) gradually pyrolyzed (GP) and b) rapidly pyrolyzed (RP) SiC/AlN precursor mixture.

The solid state NMR spectra of the solid solution samples (Figures 4-6) show the effects of the miscibility gap in the SiC/AlN solid solution below 1950 °C [27]. Thus, both 1000 °C samples show spectra consistent with expectations for "averaged" $Al(Si)N_xC_y$ environments whereas, after crystallization of these samples at 1600-1800 °C, the the Al and Si NMR peaks shift to chemical shift values more nearly representative of the "pure" components, AlN and SiC. On the other hand, there are clearly differences in these spectra that support the presumption of solid solution

formation and suggest further that the processing method employed plays a role in determining the atomic-level homogeneity of the crystallized SiC/AlN solid solution phases obtained. In particular, after heating to 1000 °C the gradually pyrolyzed (GP) sample exhibits a two-peak ^{27}Al NMR spectrum, with one relatively sharp peak close to the expected position for pure AlN (Figure 4). This suggests that partial phase separation occurs during the slow heating of the precursor mixture, as would be expected on the basis of the lower thermal stability of [Et$_2$AlNH$_2$]$_3$ relative to HPCS [26]. Moreover, in the ^{29}Si NMR spectrum obtained for the rapidly pyrolyzed (RP) sample after heating to 1800 °C, the main Si peak is broader and shifted to a more shielded position relative to that observed for the corresponding GP sample (Figures 5 and 6). These data suggest that on an atomic level, the crystallized solid solution phases are slightly different, with the RP sample exhibiting a greater degree of homogeneity and a more "solid-solution like" ^{29}Si NMR spectrum.
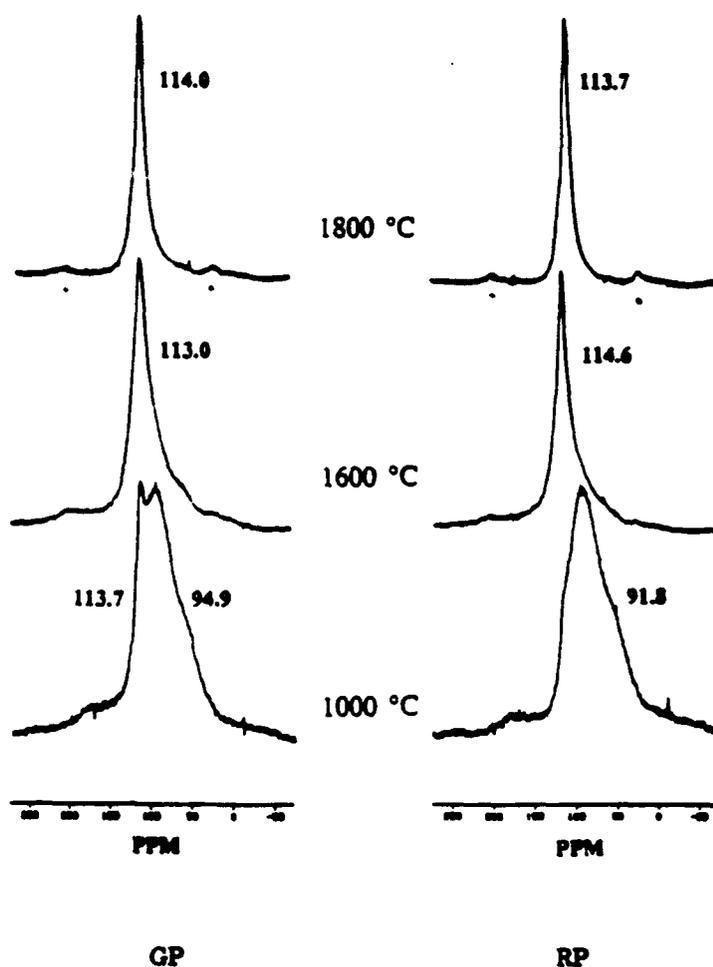
Figure 4. Solid state 27Al MAS NMR spectra of the gradually pyrolyzed (GP) or rapidly pyrolyzed (RP) HPCS/[Et2AlNH2]3 precursor mixture.

Despite these subtle processing-dependant differences in composition and homogeneity and the presence of a miscibility gap in the phase diagram, the successful generation of $2H$ solid solutions of SiC and AlN from HPCS and [Me$_2$AlNH$_2$]$_3$ mixtures represents a significant advance in ceramic processing by polymer precursor pyrolysis. This opens up the possibility of using liquid phase, thermally curable precursors such as HPCS not only as a source of SiC coatings and matrices for ceramic composites, but also for the preparation of other mixed-component ceramic
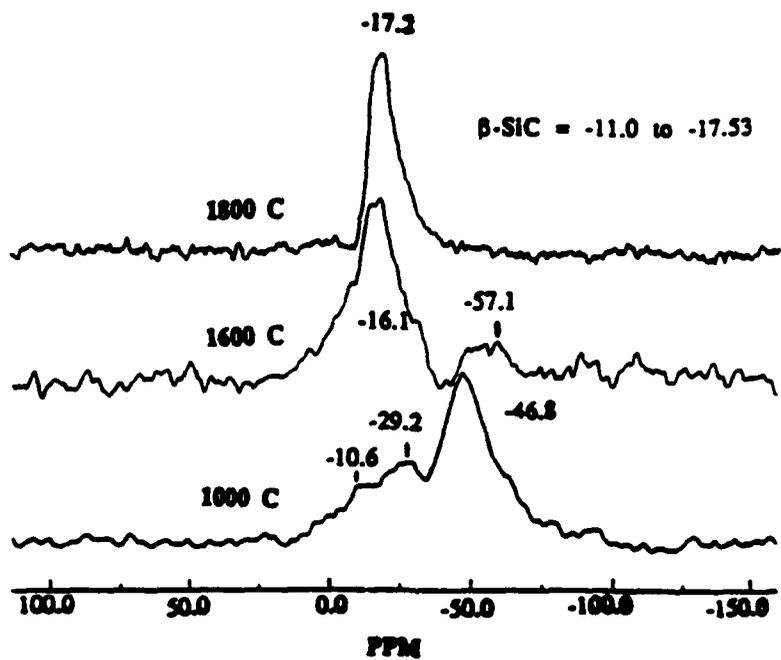
Figure 5. Solid state 29Si MAS NMR spectra of a gradually pyrolyzed HPCS/[Et2AlNH2]3 precursor mixture.
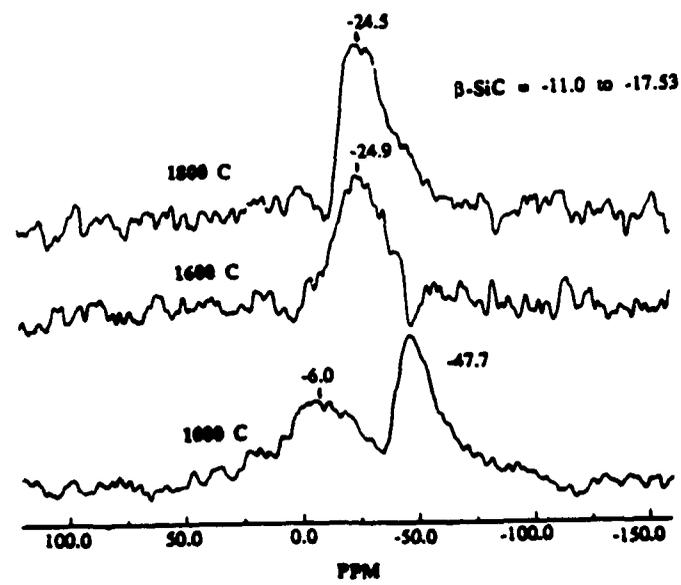
Figure 6. Solid state 29Si MAS NMR spectra of a rapidly pyrolyzed HPCS/[Et2AlNH2]3 precursor mixture.

systems that may be more advantageous than SiC alone. In particular, in the case of SiC/AlN, the alloying of SiC with AlN has been reported to improve its microstructural stability, inhibiting the exaggerated grain growth that is known to contribute to the loss of strength typically observed for commercial "SiC" fibers at high temperatures (1200-1800 °C) [27]. The SiC/AlN solid solution has also been reported to have superior strength and oxidation resistance compared to either SiC or AlN alone [28].

We have also explored the use of both precursor mixtures and specially designed single-component precursors to prepare nanocrystalline composites of AlN/SiC, AlN/Si3N4, BN/Si3N4, AlN/BN, and BN/TiN [29]. We have demonstrated that such precursors can be used to obtain extremely fine-grained (typically less than 100 nm), homogeneously mixed composite powders of these crystalline ceramic phases. Moreover, these fine-grained mixtures resist coarsening during exposure to temperature in excess of 1500 °C. Such mixed-phase ceramics may be useful as matrices for SiC-reinforced composites, in applications requiring superplasticity, or as tough monolithic materials in their own right.

ACKNOWLEDGEMENTS

REFERENCES

1. a) K. J. Wynne and R. W. Rice, *Annu. Rev. Mater. Sci.*, 14 (1984) 297; b) D. R. Ulrich, "Chemical Processing of Ceramics", *Chemical and Engineering News*, Jan. 1 (1990) 28; c) D. Segal, Chemical Synthesis of Advanced Ceramic Materials, Cambridge University Press: New York, (1989).

2. H. E. Fischer, D. J. Larkin, and L. V. Interrante, *MRS Bull.*, 26[4] (1991) 59-65; b) T. P. Cooke, *J. Am. Ceram. Soc.*, 74[12] (1991) 2959.

3. a) S. T. Schwab and C. R. Blanchard-Ardid, *Mat. Res. Soc. Symp. Proc.*, 121 (1988) 581; b) W. H. Atwell, G. T. Burns, and G. A. Zank, "Silicon Carbide Preceramic Polymers as Binders for Ceramic Powders", in Inorganic and Organometallic Oligomers and Polymers, J. F. Harrod and R. M. Laine, eds., Kluwer Academic Publishers, (1991) 147-159.

4. F. Wakai, Y. Kodama, S. Sakaguchi, N. Murayama, K. Izaki, and K. Niihara, *Nature*, 344[29 March] (1990) 421.

5. a) Y. Maehara and T. G. Langdon, *J. Mat. Sci.*, 25 (1990) 2275; b) I.-W. Chen and L. A. Xue, *J. Am. Ceram. Soc.*, 73[9] (1990) 2585; b) R. W. Siegel, *MRS Bull.*, 25[10] (1990) 60.

6. a) R. W. Chorley and P. W. Lednor, *Adv. Mater.*, 3[10] (1991) 474; b) S. Yamanaka, *Ceram. Bull.*, 70[6] (1991) 1056.

7. L. V. Interrante, L. E. Carpenter II, C. Whitmarsh, and W. Lee, *Mat. Res. Soc. Symp. Proc.*, 73 (1986) 359.

8. L. V. Interrante, W. Lee, M. McConnell, N. Lewis and E. Hall, *J. Electrochem. Soc.*, 136[2] (1989) 472-478.

9. F. C. Sauls, L. V. Interrante and Z. Jiang, *Inorg. Chem.*, 29 (1990) 2989-96.

10. F. C. Sauls, C. L. Czekaj, and L. V. Interrante, *Inorg. Chem.*, 29[23] (1990) 4688-4692.

11. a) L. V. Interrante, G. A. Sigel, C. Hejna and M. Garbauskas, *Inorg. Chem.*, 28 (1989) 252-257; b) L. V. Interrante, G. A. Sigel, C. Hejna and M. Garbauskas, *Phosphorus, Sulfur and Silicon*, 41 (1989) 325-334.

12. M. M. Lynam, L. V. Interrante, C. H. Patterson, and R. P. Messmer, *Inorg. Chem.*, 30 (1991) 1918-1922.

13. a) C. C. Amato, J. B. Hudson and L. V. Interrante, *Mat. Res. Soc. Symp. Proc.*, 168 (1990) 119-124; b) C. C. Amato, J. B. Hudson, and L. V. Interrante, *Mat. Res. Soc. Symp. Proc.*, 204 (1991) 135-140.

14. Z. Jiang and L. V. Interrante, *Chem. Mater.*, 2 (1990) 439-446.

15. Z. Jiang, L. V. Interrante, D. Kwon, F. S. Tham, and R. Kullnig, *Inorg. Chem.*, 30 (1991) 995-1000.

16. a) D. J. Pysher, K. C. Goretta, R. S. Hodder, Jr., and R. E. Tressler, *J. Am. Ceram. Soc.*, 72[2] (1988) 244; b) Z.-F. Zhang, F. Babonneau, R. M. Laine, Y. Mu, J. F. Harrod, and J. A. Rahn, *J. Am. Ceram. Soc.*, 74[3] (1991) 1670.

17. C. Whitmarsh and L. V. Interrante, *Organometallics*, 10 (1991) 1336-1344.

18. C.-Y. Yang and L. V. Interrante, "Thermally and Chemically Induced Crosslinking of a Hydridopolycarbosilane for Optimization of Silicon Carbide Yield", submitted to *Polymer Preprints*.

19. L. V. Interrante, C. K. Whitmarsh, T. K. Trout, and W. R. Schmidt, "Synthesis and Pyrolysis Chemistry of Polymeric Precursors to SiC and Si3N4", Kluwer Academic Publishers, Dordrecht, (1991); Proceedings, NATO Workshop on Organometallic Polymers with Special Properties, Cap D'Agde, France, Sept. 10-15, 1990.

20. a) H.-J. Wu and L. V. Interrante, "Preparation of A Linear Polycarbosilane via Ring-Opening Polymerization", Polymer Preprints, 4th Chem. Congress, NY, Aug. 1991; b) H.-J. Wu and L. V. Interrante, *Macromolecules*, 25 (1992) 1840.

21. W. R. Schmidt, L. V. Interrante, R. H. Doremus, T. K. Trout, P. S. Marchetti, and G. E. Maciel, *Chem. Mater.*, 3 [2] (1991) 257-267.

22. W. R. Schmidt, V. Sukumar, W. J. Hurley, Jr., R. Garcia, R. H. Doremus, and L. V. Interrante, *J. Am. Ceram. Soc.*, 73[8] (1990) 2412.

23. V. Sukumar, W. R. Schmidt, R. Garcia, R. H. Doremus and L. V. Interrante, *Mater. Letters*, 9 (1990) 117-120.

24. W. R. Schmidt, P. S. Marchetti, L. V. Interrante, W. J. Hurley, Jr., R. H. Lewis, R. H. Doremus, and G. E. Maciel, "Ammonia-Induced Pyrolytic Conversion of a Vinylic Polysilane to Silicon Nitride", submitted to *Chem. Mater.*

25. D. M. Narsavage, L. V. Interrante, P. S. Marchetti, and G. E. Maciel, *Chem. Mater.*, 3[4] (1991) 721.

26. a) C. L. Czekaj, M. L. Hackney, W. J. Hurley, Jr, L. V. Interrante and G. A. Sigel, *J. Am. Ceram. Soc.*, 73[2] (1990) 352-357; b) L. V. Interrante, W. R. Schmidt, S. N. Shaikh, R. Garcia, P. S. Marchetti, and G. Maciel, "Silicon Carbide Aluminum Nitride Solid Solutions by Pyrolysis of Organometallics", Proc. 5th Intl. Conf on Ultrastructure Processing of Ceramics, Glasses, Composites, Ordered Polymers and Advanced Optical Materials, Series E: Applied Sciences, Vol. 206, J. Wiley and Sons, publs., (1991) 243-254.

27. a) A. Zangvil and R. Ruh, *J. Am. Ceram. Soc.*, 71[10] (1988) 884; b) R. Ruh and A. Zangvil, *J. Am. Ceram. Soc.*, 65[5] (1982) 260; c) W. Rafaniello, M. R. Plichta, and A. V. Virkar, *J. Am. Ceram. Soc.*, 66[4] (1983) 272; d) W. Rafaniello, K. Cho, and A. V. Virkar, *J. Mater. Sci.*, 16[12] (1981) 3479.

28. G. Ervin, Jr., US Patent 3,492,153, Jan. 27, 1970.

29. a) D. Kwon, W. R. Schmidt, L. V. Interrante, P. Marchetti, and G. Maciel, "Preparation and Microstructure of Organometallic Polymer Derived AlN-BN Composites", Inorganic and Organometallic Oligomers and Polymers, J.F. Harrod and R.M. Laine, eds., Kluwer Academic Publishers, (1991) 191-197; b) W. R. Schmidt, W. J. Hurley, Jr., V. Sukumar, R. H. Doremus, and L. V. Interrante, *Mat. Res. Soc. Symp. Proc.*, 171 (1990) 79-84; c) L. V. Interrante, W. J. Hurley, Jr., W. R. Schmidt, D. Kwon, R. H. Doremus, P. S. Marchetti, and G. Maciel, "Preparation of Nanocrystalline Composites by Pyrolysis of Organometallic Precursors", Proceedings, Symposium on Composites, American Ceramic Society Meeting, Orlando, FL, Nov. 1990, Advanced Composite Materials-Ceramic Transactions, Vol. 19, M.D. Sacks, ed. American Ceramic Society: Westerville, Ohio, (1991) 3-17; d) W. R. Schmidt, W. J. Hurley, Jr., R. H. Doremus, L. V. Interrante, and P. S. Marchetti, "Novel Polymer Precursors to Si-C-Al-O-N Ceramic Composites", Proceedings, Symposium on Composites, American Ceramic Society Meeting, Orlando, FL, Nov. 1990, Advanced Composite Materials-Ceramic Transactions, Vol. 19, M.D. Sacks, ed. American Ceramic Society, Westerville: Ohio, (1991) 19-25.

Poly(silaethylene) the "Silaethylene" Analog of Polyethylene and a High Yield Precursor To SiC

Hui-Jung Wu and Leonard V. Interrante*
Department of Chemistry
Rensselaer Polytechnic Institute
Troy, NY 12180

Introduction

Our prior work on the ring-opening polymerization of 1,1,3,3-tetrachloro-1,3-disilacyclobutane to give poly(dichloro-silnethylene) and the subsequent reduction of this polymer to poly(silaethylene) provide, for the first time, a feasible synthetic route to this novel analog of polyethylene.[1] In contrast to the earlier approach, which started directly from 1,3-disilacyclobutane,[2] this new method yields a high molecular weight (Mw=32800; Mn=10800) linear polymer that is soluble in hydrocarbon solvents and which shows the expected double quintet ^{1}H NMR spectrum for the (-SiH$_2$CH$_2$-)n repeat unit. In our earlier report of the synthesis of this polymer, we noted that it undergoes pyrolysis in high yield (up to 87%) to form nanocrystalline SiC by 1000°C. This observation contrasts with the general supposition in ceramic precursor chemistry that linear polymers invariably give low ceramic yields due to loss of volatile species via "backbiting", and that a prerequisite for a high ceramic yield precursor is an initially crosslinked polymer.[3]

We now report the results of a comparative study of the pyrolysis of poly(silaethylene) and its methyl-substituted derivatives, poly(silapropylene) and poly(silabutylene) as well as some of the basic physical properties of this novel silicon analog of polyethylene.

Experimental

All manipulations were carried out in oven-dried glassware under nitrogen following standard inert-atmosphere techniques.[4] All solvents were distilled from appropriate drying agents under a nitrogen atmosphere prior to use.[5] The reagents employed were available commercially unless otherwise indicated.

Preparation of poly(silnethylene) was carried out as described.[1a] Gases evolved during pyrolysis were analyzed by connecting an evacuated quartz tube which contained the polymer to a mass spectrometer. The quartz tube was then heated to 1000°C at 3°C/min. and the gaseous species evolved were monitored by the mass spectrometer. The measurement of the melting point of poly(silaethylene) was carried out by placing a sealed capillary tube containing the polymer in a stirred ethanol bath and then adjusting the temperature of the bath by adding powered dry ice.

Results and Discussion

Linear polyethylene is well known for its great tendency to crystallize and, to a large extent, its mechanical and other physical properties depend on its crystallinity.[6] It is a solid at room temperature and undergoes a melting transition at 141°C.[7] In contrast, the mono-silicon analog of polyethylene, poly(silaethylene), is a liquid at room temperature and does not crystallize until cooled below ca. 1°C. When this polymer was slowly cooled to 4°C, a white opaque gel was observed. A white solid was obtained when the sample was further cooled to 1°C. On slow warming, this solid began to melt at 5°C and became a viscous liquid at 12°C. The lower T_m of poly(silaethylene) than that of polyethylene may be due to the appreciable difference in the effective van der Waals radii of the -SiH2- and -CH2- groups, leading to a higher entropy crystallization. Further studies of this transition, and of the solid phase obtained below 5°C, are currently in progress.

The results of a comparative TGA study carried out on poly(silaethylene) and its mono-and dimethyl-derivative poly(silapropylene) and poly(silabutylene), are shown in Figure 1.[8] These three polymers show different thermal decomposition onset temperatures, with the parent poly(silaethylene) undergoing significant weight loss beginning near around 300°C, whereas the monomethyl-derivative poly(silapropylene), begins to decompose rapidly by 420°C and the dimethyl-derivative, poly(silabutylene) persists to around 450°C before undergoing rapid depolymerization. On the other hand, the yield of the ceramic product left after pyrolysis varies in the inverse order, with poly(silabutylene) essentially completely vaporizing by ca. 550°C. If we assume that the decomposition of poly(silabutylene) represents the onset temperature of thermolysis for the SiC backbone, it is apparent that this process becomes rapid by around 500°C. In the case of the Si-H containing polymers this process is apparently preceeded by some sort of thermally-induced cross-linking process. This process was studied in more detail in the case of poly(silaethylene) by mass spectrometric analysis of the gaseous products released as a function of temperature.

No gaseous species were detected by mass spectrometry below 300°C, suggesting that the small amount of weight loss observed below this temperature represents loss of volatile oligomers. Beyond ca. 300°C, the evolution of H$_2$ in significant quantity was detected, which continues as the major gaseous byproduct throughout the remainder of the total weight loss observed between 300 and ca. 700°C. This loss of H$_2$ seems to have a bimodal distribution with respect to the sample temperature, with a apparent minimum near 525°C. We are currently studying the SiD$_2$CH$_2$ analog of this polymer in order to determine whether this bimodal H$_2$ loss might reflect the preferential loss of H$_2$ from Si initially, followed by thermolysis of the remaining CH$_x$ groups.

Other gases detected in much smaller concentrations were methane, C$_2$ hydrocarbons, methylsilane, dimethylsilane and 1,3-disilacyclobutane. The evolution of these gases became measurable only beyond 400°C and, in the case of methane reached a maximum at ca. 550°C, whereas the other gases were detected only between 400 and 500°C.

The observation of significant H$_2$ loss beyond 300°C from poly(silaethylene) suggests that loss of H$_2$ from SiH$_2$ groups by some sort of radical or concerted molecular (or intermolecular) process may be operative. The difference in the thermal stabilities of the above three polymers is reminescent of the results of earlier studies of the thermal decomposition of the methylsilanes, Me$_{4-n}$SiH$_n$, where Me$_2$SiH$_2$ decomposes at a significant rate by 600°C, whereas Me$_3$SiH is stable to around 620°C and SiMe$_4$ only exhibits significant decomposition beyond ca. 700°C.[9] In addition to the cleavage of SiH to form Si radical species, which is highly surface dependant,[10] the loss of H$_2$ and alkanes from organosilanes containing SiH groups is known to proceed by reactions involving 1,1- or 1,2-elimination to form silylene species.[11] Either type of reaction in the case of poly(silaethylene) would generate Si-based reactive species that could cause interchain coupling,[1] resulting in extensive crosslinking of the polymer prior to the temperature at which interchain Si-C cleavage becomes significant. This would lead to high ceramic yields of essentially pure SiC, as was observed for poly(silaethylene).

Studies of the poly(silaethylene)-to-SiC conversion which employ both IR and solid state NMR spectroscopy are currently underway and will be reported in the presentation.

References

1 (a) Wu, H.-J.; Interrante, L.V. *Polym. Prepr.* **1991**, 32(3), 588. (b) Wu, H.-J.; Interrante, L.V. *Macromol.* **1992**, 25, 1840.

2 Smith, T.L. US Patent 4,631,179, Dec. 23, **1986**.

3 Wynne, K.J.; Rice, R.W. *Ann. Rev. Mater. Sci.* **1984**, 14, 297-334. Seyferth, D. in " *Inorganic and Organometallic Polymers* " Zeldin, M.; Wynne, K.; Allcock, H.R. Eds. ACS Symposium Series 360, ACS: Washington D.C. **1988** Chapter 3, pp 21-42.

4 Shriver, D.F.; Drezdzon, M.A. *"Manipulation of Air Sensitive compounds"* 2nd ed.; Wiley: New York, **1988**.

5 Gordon, A.J.; Ford, R.A. *"The Chemist's Companion"* Wiley: New York, **1977**

6 Elias, H.G. *"Macromoles: Structure and Properties"* 2nd.; Plenum: New York, **1984**, pp 428-431.

7 Lewis, O.G. *"Physical Constants of Linear Homopolymers"* Springer-Verlag: New York, **1968**.

8 Wu, H.-J.; Interrante, L.V. *Chem. Mater.* **1989**, 1, 564.

9 Fritz, G.; Matern, E. *"Carbosilanes, Synthesis and Reactions"*, Springer-Verlag: Berlin, **1986**.

10 Davidson, I.M.T.; Ring, M.A. *J. C. S. Faraday I*, **1980**, 76, 1520. Neudorfl, P.S.; Strausz, O.P. *J. Phys. Chem.* **1978**, 82(2), 241.

11 O'Neal, H.E.; Ring, M.A. *Organomet.* **1988**, 7, 1017. Ring, M.A.; O'Neal, H.E.; Rickborn, S.F.; Sawrey, B.A. *Organomet.* **1983**, 2, 1891.

12 Gano, D.R.; Gordon, M.S.; Boatz, J. A. *J. Am. Chem. Soc.* **1991**, 18, 6711-6718. Tang, T.N. in *"Reactive Intermediates"*, Vol. 2, Abramovitch, R.A. ed. Plenum press, NewYork, **1982**, Chapter 4, pp 297-366. Gaspar, P.P. in *"Organosilicon and Bioorganosilicon Chemistry: Structure, Bonding, Reactivity and Synthetic Application"*, Sakurai, H. ed. IUPAC, Oxford, UK, **1985**, Chapter 7, pp 87-98.
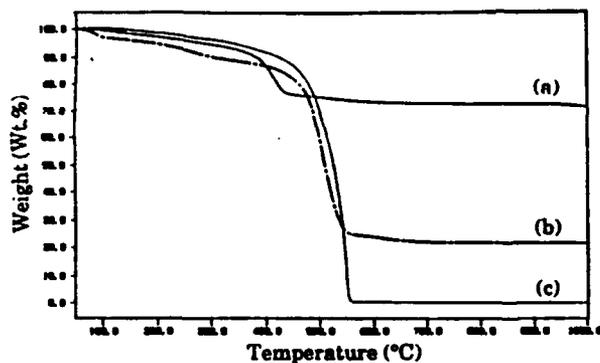
Figure 1. TGA Plots of (a) Poly(silaethylene), (b) Poly(silapropylene), (c) Poly(silabutylene).

M E M O R A N D U M

TO: Joseph M. LoGiudice, Director   **DATE:** June 26, 1989
           Office of Contracts and Grants

FROM: Prof. L. v. Interrante

SUBJECT: Disclosure of Invention

     As required under **ARTICLE II** of the Institute's Patent Polic:
as amended March 8, '.957, I am enclosing a Disclosure of Invention entit

     The invention was made under one or more of the following
circumstances:

1. In connection with sponsored research Project No. 5-24182 .
   (Attach Disclosure)   DARPA/ONR No. N0014-86-K-0770

2. In connection with any agreement of any type which gives or
   may give any party any rights whatsoever in the invention.

   If so, please identify the agreement and, if possible, attach
   a copy.

3. On my own time as follows:

   a) Consulting (describe):

   b) Other   (describe):

   c) Use of Institute time, materials, or facilities (describe):
      NMR spectrometers (CHEM)
      XRD Facility (MAT)

4. In connection with Institute activities:

     Please attach a full description of the invention, including
necessary sketches and drawings.
     Attached is a draft of a paper to be submitted for publication shortly.

DISCLOSURE OF INVENTION

.

INVENTOR(S): [Full Names]__Christopher Kenneth Whitmarsh and

Leonard Vincent Interrante

TITLE(S) OR POSITION(S):__Research Assistant, Professor

2. TITLE OF INVENTION:__Carbosilane Polymer Precursors to Silicon Carbide

3. DATES AND PLACES OF INVENTION:

   a) Conception by inventor(s)____3/6___19_87_ at __RPI - Cogswell Lab 12:
     First reaction of Cl_3SiCH_2Cl + mg in Et_2O NMR, IR of crude $[SiCl_xCH_2]_n$

   b) First sketch or drawing on ___3/16___19 87_ at _RPI - Cogswell Lab 121_
     First $LiAlH_4$ reduction of $[SiCl_xCH_2]_n$

   c) First written description on ___3/19__19_87_ at _RPI - Cogswell Lab 121_
     First characterization of $[SiH_xCH_2]$ (by NMR)

   d) Disclosure to others: [full names]

     1. _____ on_____19____

     2. _____ on_____19____

   e) Other proof of conception:_____

   f) First working model on _____NA_____19____ filed_____

   g) First test or operation on ___NA_____19____ filed_____

4. THIS SHEET PREPARED BY:__Leonard V. Interrante-

                 ON:__June 2, 1989

ATTACH ADDITIONAL SHEETS IF NECESSARY.

Director,
Office of Contracts and Grants

It is my understanding that I will be notified in writing as to the action which the Institute intends to take in the disposition of this invention.

SIGNATURE(S) OF INVENTOR(S):

Chris W. Whitmarsh
(signed)

[signature]
(signed)

_____
(signed)

_____
(date)

June. 23, 1989
(date)

_____
(date)

ENDORSEMENT

To the best of my knowledge the above information is correct except as follows:_____

_____

_____

_____

[signature]
Department Chairperson

_7/10/89_
Date

RENSSELAER POLYTECHNIC INSTITUTE

Troy, New York 12180

INVENTION QUESTIONNAIRE

I. **Descriptive**

1. Title of Invention_____ Carbosilane Polymer Precursors to Silicon
   Carbide Ceramics _____

2. Brief description. Is this invention a new process, composition of
   matter, a device, or one or more products? A new use for, or an
   improvement to, an existing product or process?_This invention consists_
   of a new hydrido-polycarbosilane of branched structure approximated by the formula
   $[SiH_xCH_2]_n$ and variations of this polymer for improved crosslinking properties such
   as $[SiH_xCH_2]_{n-z} . [SiH_{x-1}(Vi)CH_2]_z$ which give good yields of SiC on pyrolysis
   (see attached sheet)
   _____

   Use additional sheets to elaborate, or attach descriptive materials.

3. From the description, pick out and expand on novel and unusual features
   How does the invention differ from present technology? What problems
   does it solve, or what advantages does it possess?_____
   Precursor has 1:1 Si to C ratio, (no extra carbon), low oxygen content, and
   only hydrogen substitution. Up to ~91% ceramic yield is possible (actual yields
   ~ 60-75% so far) (see attached sheet)
   _____

4. If not indicated previously, what are possible uses for the invention?
   In addition to immediate applications, are there other uses that might
   be realized in the future?_____
   A variety of applicatons for manufacture of SiC fiber, matrix of composites,
   ceramic binder, etc. (see attached sheets)

Does the invention possess disadvantages or limitations? Can they be overcome? How? Chloromethyl-trichlorosilane [Cl_3SiCH_2Cl], the precursor for the polymer is relatively expensive. The molecular weight of polymers formed by coupling processes is relatively low compared to typical free radical or ring opening processes _____ (see attached sheet)

6. Enclose sketches, drawings, photographs and other materials that help illustrate the description. [Rough artwork, flow sheets, Polaroid photographs and penciled graphs are satisfactory as long as they tell a clear and understandable story.] (see attached sheet for diagram)

II. Other Pertinent Data

1. Are there publications-theses, reports, preprints, reprints, etc. pertaining to the invention? Please list with publication dates, and attach copies insofar as possible. Include manuscripts for publication (submitted or not), news releases, feature articles and items from internal publications. A paper will be submitted for publication in J. Mat. Chem. describing preparation, characterization and conversion to SiC, but is not ready as of yet. A number of internal progress reports discuss the preparation, characterization, and/or conversion to SiC of this precursor.

2. Are laboratory records and data available? Give reference numbers an physical location, but do not enclose. The preparation characterization, conversion to SiC and relevant spectra, analysis reports, etc. described in lab notebook (Cogswell 121)

3. Are related patents or other publications known to the inventor? Ple list. US Pat. No. 4,631,179 Smith,J.C. process for the production of SiC by the pyrolysis of polycarbosilane polymer. Patent appears to cover the process o ring opening polymerization of 1,3,disilacyclobutane ($H_2Si \frown SiH_2$) by various catalysts (mainly, H_2PtCl_6) in hydrocarbon solvents to yield a viscous liquid or clear "cake" "shown to have a linear structure" and pyrolysis under Ar at 900°C

4. Date, place and circumstances of first public disclosure. SiC in ~85% yi Two DARPA meetings, department seminar, talks to visiting professors, Glen Slack (GE), Larry Snedden (U.Penn), and others

5. Any commercial interest shown at this stage? Name companies and specific persons if possible. Unknown

a). Do you know of other qualified firms? Please list. _____
General Electric Co., AKZO Chemicals, Inc., Enichem.

...lymer precursor to silicon carbide ceramics.

...ction is a new branched polymeric precursor of formula $[SiH_xCH_2]_n$ to branching; x=0,1,2, or 3 if end groups]. On pyrolysis this polymer ...ds silicon carbide in >60% ceramic yield depending on crosslinking pro-...dure. The polymer is made by slow addition of chloromethyl-trichlorosilane ...o refluxing ether and magnesium powder under nitrogen atmosphere, followed by extensive refluxing to drive the coupling reaction to completion. The product at this stage is branched, primarily head-tail coupled polymer of the formula $[SiCl_xCH_2]_n$. Subsequent reduction with lithium aluminum hydride/ether yields the final polymer $[SiH_xCH_2]_n$ (due to branching; x=0, 1,2, or 3 if end group).

3. Currently existing polymeric precursors for silicon carbide contain large excesses of carbon, usually as alkyl substitution on silicon, but occasionally in the polymer backbone as well. These groups do not completely eliminate as hydrocarbon gases during pyrolysis, resulting in significant excess carbon in the ceramic products. In addition, many commercial precursor systems for silicon carbide are prepared, crosslinked, or pyrolysed in such a manner that large amounts of oxygen are incorporated, resulting in product containing silica (SiO_2) as impurity. It is well known that both carbon and silica seriously degrade the desirable refractory properties of silicon carbide. This new carbosilane precursor contains a one to one ratio of carbon to silicon with only hydrogen substitution. Since only hydrogen has to be eliminated, up to ~91% ceramic yield is possible, and potential excess carbon is eliminated. Typically, if no special crosslink-ing procedure is performed, about 60% ceramic yield is observed (TGA/N_2) due to some depolymerization before direct thermal crosslinking (via Si-Si bonds) occurs. In addition to thermal methods, crosslinking can be achieved by hydrosilation using difunctional vinyl compounds or alkyenes and a suitable catalyst such as H_2PtCl_6.

The "chloro" compound ($[SiCl_xCH_2]_n$) is useful precursor to a variety of derivatives via Grignard or organolithium reagents before the reduction step. For example reaction of $[SiCl_xCH_2]_n$ with ~5% vinylmagnesium bromide before reduction yields a viscous liquid polymer with pendent vinyl groups in addition to the usual Si-H functionality which was readily crosslinked by heating with chloroplatinic acid. The product was an insoluble, infusible, pale yellow, glassy solid which gave 75% ceramic yield (85% theo.) on pyrolysis (TGA/N_2).

4. Potential applications for this polymer precursor include:

   a. Preparation of high strength, refractory SiC fiber for composites by spinning, crosslinking, then pyrolysis in N_2 or other nonreactive atmos-phere.

   b. Formation of matrix of composites by 1 or more cycles of: impregnation of various ceramic or metal fibers, crosslinking, pyrolysis.

   c. Ceramic binder via mixing polymer with various ceramic or metal powders or whiskers, crosslinking, pyrolysis.

   d. Strengthening of porous hotpressed, sintered or bonded ceramics by 1 or more cycles of: vacuum or pressure assisted impregnation, and refiring.

   e. Direct injection molding of polymeric pre-ceramic objects, with or without ceramic or metal powder or whiskers as filler; crosslinking and pyrolysis to monolithic ceramic parts with complicated, near-net shapes.

...re of polymer with a suitable precursor for another ceramic (AlN, ...BN, Si_3N_4, etc.) to facilitate the production of solid solutions, ...new phases, not readily obtainable by current powder processing technology.

By modification of the "chloro" polymer $(SiCl_xCH_2)_n$ with suitable side groups:
1. preparation of polymeric nonlinear optical materials
2. preparation of heat resistant polymers or elastomers

5. **Potential drawbacks of the system:**

The precursor for the polymer [chloromethyl-trichlorosilane; Cl_3SiCH_2Cl] is relatively expensive ($\sim$\$80/100g) but cost should drop if large scale production is developed. The polymerization method (Grignard coupling) tends to be limited to lower mw than typical organic type polymerizations. This may be a limitation for some types of applicatons, however, even this lower mw polymer can be quite viscous, and resistant to depolymerization on heating.

AKZO

April 23, 1992

Dr. Leonard V. Interrante
Rensselaer Polytechnic Institute
Department of Chemistry
Troy, New York 12180-3590

Re: Patent Application ACR 5621
Whitmarsh, Interrante

Dear Len:

We have just been informed of the allowance of claims to the polycarbosilane compositions described in the above application and to their process of manufacture. A sample of the allowed independent claims is reproduced on the attached sheet. Please circulate copies of this letter to the appropriate Rensselaer personnel who should know of this event. We plan to pay the issue fee in about two months and the patent should issue two to three months after that.

Separate divisional applications could be filed on: (1) the isolation of the crude poly(halocarbosilane) and treatment with a second Grignard coupling process; (2) reduction of the poly(halo-carbosilane) with a reducing agent; and (3) crosslinking of the polycarbosilane precursor with hydrosilation catalyst. However, in view of the claims which were allowed, we, at Akzo, are inclined not to support the expense for such additional filings. Conceivably, Rensselaer could undertake to retain outside counsel to pursue such additional cases if such additional protection is deemed necessary.

Very truly yours,

Richard

Richard P. Fennelly
Senior Patent Attorney

RPF/mjw

Attachment

cc: J. H. Burk
J. Vleggaar
F. A. Via

Interrante

Submitted by the Akzo Company or
behalf of Rensselaer Polytech. Inst.

1   ACR 5621 US   7/90

CARBOSILANE POLYMER PRECURSORS
TO SILICON CARBIDE CERAMICS

BACKGROUND OF THE INVENTION

Silicon carbide (SiC) is one of several advanced ceramic
5   materials which are currently receiving considerable attention
as potential replacements for metals in engines, and as
structural components in aerospace vehicles. Ceramics, such
as SiC, have the potential to outperform currently available
super alloys in terms of density, corrosion resistance, and
10   service temperature. Ideally these ceramics would be in the
form of tough composites, or, for certain less demanding
applications, monolithic objects. Unfortunately, these
extremely hard, non-melting ceramics are difficult to process
by conventional forming, machining, or spinning equipment.

15   Polymeric precursors to ceramics, such as SiC, afford a
potential solution to these problems as they would allow the
use of conventional processing operations prior to conversion
to a ceramic form. A ceramic precursor should be moldable or
spinnable, crosslinkable, and give a substantially pure
20   ceramic product in high yields upon pyrolysis. Unfortunately,
it is difficult to simultaneously achieve all of these goals.
Currently, available SiC precursor systems tend to be lacking
in one or more of these areas.

Yajima (se J. of Mater. Sci. 13 (1978), pp. 2569-2576)
25   has prepared a preceramic polymer by a thermally induced
methylene insertion reaction of readily prepared, but
intractable, poly[dimethylsilane]. The resulting, tractable,
polymer is only approximately represented by the formula
[SiHMeCH$_2$]$_n$, as significant amounts of unreacted SiMe$_2$ units,
30   complex rearrangements, and branching are observed. Yajima's
polymer has been employed to prepare "SiC" fiber. However, it
contains twice the stoichiometric amount of carbon, and must
be treated with various crosslinking agents that introduce
contaminants. This results in a final ceramic product that
35   contains significant amounts of excess carbon and silica which

greatly degrade the high temperature performance of the fiber.

Similar problems have been encountered in efforts to employ various other polysilanes as precursors to SiC fiber and monolithic ceramic objects. All of these precursors have

5   C/Si ratios considerably greater than one, and undergo a complex series of often ill-defined thermal decomposition reactions which, in general, lead to incorporation of excess carbon. The existence of even small amounts of carbon at the grain boundaries within SiC ceramics has been found to have a

10   detrimental effect on the strength of the ceramic, contributing to the relatively low room-temperature tensile strengths typically observed for precursor-derived SiC fibers.

The application of linear polycarbosilanes of the type $[R_2SiCH_2]_n$, where R = H and/or hydrocarbon groups, as SiC

15   precursors has received much less attention, presumably because of the expected low ceramic yield due to chain "unzipping" reactions. Indeed, studies of high molecular weight $[Me_2SiCH_2]_n$ polymers have indicated virtually complete volatilization on pyrolysis under an inert atmosphere to

20   $1000^\circ C$. Recent work by the present inventors herein on the related $[MeHSiCH_2]_n$ polymer suggests that the introduction of Si-H groups leads to crosslinking reactions upon pyrolysis and subsequently higher ceramic yields. However, a significant loss of volatile organosilane by-products as well as

25   hydrocarbons upon pyrolysis was still evident.

Schilling (see Ceramic Bulletin, Vol. 26, No. 8, 1983 pp. 912-915), and others have also investigated predominately linear polycarbosilanes prepared via potassium dechlorination of chloro-chloromethyl-dimethylsilane. The resulting polymers

30   have not been fully characterized, but probably contain significant amounts of Si-Si and CH_2-CH_2 in the polymer backbone. Polycarbosilanes with various substituents on silicon have been made by ring opening polymerization [ROP] of various 1,3-disilacyclobutanes by treatment with

35   chloroplatinic acid and related catalysts. Although the mechanism for the ROP process is not well understood, the polymers typically obtained are highly linear and have

characteristically higher molecular weights. The major drawback to ROP-derived systems is the difficulty in preparing the cyclic precursors in reasonable yield from readily available starting materials.

5   The formation of carbosilane polymers with pendent methyl groups was reported by Kriner as by-products during the "reverse-Grignard" reaction of chloromethyl-dichloro-methylsilane to prepare carbosilane rings. These polymers were presumably branched, although they were not investigated 10 in any detail.

      In a recent patent (U.S. Patent No. 4,631,179), Smith describes the ring opening polymerization of 1,3-disilacyclobutane by chloroplatinic acid. The resulting polymer is claimed to be linear. Ceramic yields of up to 85% 15 were reported. Little information is given concerning the characterization of this polymer, or the resulting ceramic products. In addition, the preparation of the cyclic monomer, $[SiH_2CH_2]_2$ is not discussed at all. This compound is typically available only by rather tedious preparative routes 20 and only in modest yields at best. Hence, this precursor system is, at present, not commercially practical.

      U.S. Patent No. 4,923,716 to D. W. Brown et al. describes the chemical vapor deposition of silicon carbide using a "single molecular species" which provides reactive fragments 25 containing both silicon and carbon atoms in equal number. Cyclic structures of up to five units containing silicon and carbon are mentioned.

SUMMARY OF THE INVENTION

      The present invention relates to the preparation of 30 carbosilane polymer precursors, of the structure to be described in greater detail below, by the reaction of a polyhalocarbosilane of the formula $[SiX_xCH_2]_n$, where n can range from about __ to about __ and X preferably being chlorine with a suitable reducing agent, such as an alkali 35 metal aluminum hydride (e.g., lithium aluminum hydride). The

which can be crosslinked by hydrosilation (e.g., treatment
with H_2PtCl_6 at 150°C) or thermally. The crosslinking
reaction allows one to "set up" the polymer during or after
processing as might be needed for fiber synthesis or SiC
5   matrix formation.

1. Polycarbosilane compositions of matter comprising the repeat units $[SiR_xCH_2]$ and $[SiR_{x-1}(CH=CH_2)CH_2]$, where R is hydrogen and x is from 0 to 3 and 1 to 3, respectively.

2. A process for forming polycarbosilane compositions comprising the repeat unit $[SiR_xCH_2]$, where R is hydrogen and x ranges from 0 to 3 which employs, as starting materials, a halomethylcarbosilane of the type $X_{4-x}Si(CH_2X)_x$, where X is halo and x is from 0 to 3, and which comprises a Grignard coupling reaction of the halomethylcarbosilane with magnesium to form a poly(halocarbosilane) followed by reduction of the poly(halocarbosilane).

3. Substantially non-cyclic, branched polycarbosilane precursors for silicon carbide having a substantially 1:1 silicon to carbon stoichiometry which are comprised of the repeat units $[SiH_3CH_2-]$, $[-SiH_2CH_2-]-$, $[=SiHCH_2-]$, and $[\equiv SiCH_2-]$.

4. Substantially non-cyclic, branched polycarbosilane precursors for silicon carbide which are comprised of the repeat units $[SiR_xCH_2]$ and $[SiH_{x-1}(CH=CH_2CH_2]$, where R is hydrogen and x can range from 0 to 3 and 1 to 3, respectively. --

EXAMPLES

All manipulations involving air-sensitive materials were carried out in oven-dried glassware using standard inert atmosphere techniques. Solvents were distilled, under

5   nitrogen, from appropriate drying agents. Magnesium powder [#50 mesh] was reground using a modified pepper grinder, under nitrogen, before use. Other commercially available reagents were used as received, unless otherwise specified. ^1H, ^{13}C, and ^{29}Si NMR were run on a Varian XL-200 using D_6-benzene or

10 D_8-toluene as solvents. IR spectra were taken, as neat films, between salt plates on a Perkin-Elmer 298 spectrometer. Gas chromatographic analyses were performed on a Shimadzu GC-9A equipped with a Shimadzu C-R3A recorder-integrator unit. Unless otherwise specified, samples separated satisfactorily

15 using the following parameters: 6Ft. SE-30 column, 100-250°C @ 15°C/min., INJ & TCD @ 275°C, He @ 45cc/min. Elemental analyses were carried out by either Schwarzkopf Microanylitical Laboratory, Galbraith Laboratories Inc., or LECO Corporation.

20 In these Examples, the Grignard coupling of chloromethyl-trichloro-silane followed by reduction with lithium aluminum hydride has been investigated by ^1H, ^{13}C, ^{29}Si NMR, IR, GPC and various trapping experiments in order to characterize both the intermediate "chloro-polymer" and

25 "reduced polymer". For simplicity these branched polymers have been represented by the formulas; "$[SiCl_2CH_2]_n$" and "$[SiH_2CH_2]_n$" respectively, although it will be shown that their structure is actually somewhat more complicated. The reduced polymer incorporates extensive Si-H functionality and

30 a nominal 1:1 silicon to carbon ratio. On heating, direct thermal crosslinking is observed, leading to high ceramic yields of a black, ceramic product found to contain b-SiC by X-ray diffraction.

EXAMPLE 1

Preparation of "Chloro-polymer" $[SiCl_2CH_2]_n$:

Dry ether (1L) and 30g magnesium powder (1.25 mole) were added to a 2L, three neck (3N), round bottom (RB) flask
5   equipped with a reflux condenser, a mechanical stirrer, and a nitrogen inlet. Chloromethyl-trichlorosilane (126 ml, 1.0 mole) was added over about 8 hours using a syringe, at a suitable rate to maintain a vigorous reaction. Initially, a few drops of methyl iodide were added to the mixture to start
10 the reaction. A warm water bath (50°C) was also employed, as necessary, to help maintain the reaction rate. After the addition was complete, a highly air-sensitive, dark brown solution, containing only small
amounts of magnesium chloride and excess magnesium was
15 obtained. Continued reflux, for 2-5 days, caused a gradual color change, to brownish-yellow, as large amounts of $MgCl_2$ precipitated. Due to the large volume of solid which formed, addition of more ether was required to maintain a reasonably fluid consistency. Since the $MgCl_2$/Mg solids would not settle
20 out, and the material clogged during all attempts at filtration, the $[SiCl_xCH_2]_x$ material was separated in a nitrogen-filled glove-bag by pouring the slurry onto oven-dried fiberglass cloth placed over a suitable container. Careful squeezing allowed rapid removal of 80-90% of the
25 solids. The remaining solids rapidly settled from the resulting yellow ether solution of $[SiCl_2CH_2]_n$ material, allowing separation by canulla transfer. The solution was stripped of ether under vacuum with the aid of a 50°C water bath to yield $[SiCl_xCH_2]_n$ material, a dark yellow-brown,
30 mildly air-sensitive, viscous oil, in 45-50% yield (based on an assumed "average" formula $[SiCl_2CH_2]_n$).

IR: $[cm^{-1}]$ 2980s, 2930m, 2900m, 1440m, 1385m, 1345m, 1290w, 1260m, 1160m, 1100->1030vs, 965s, 815->755vs. NMR, decoupled, ppm vs TMS, all peaks were complex multiplets or broad.

^{1}H   0.2->1.5/(25), ·1.9->2.3/(1.0), 3.6->4.1/(3.6)
ppm/(Integration)

^{13}C   8->24 (major portion, several multiplets), 29->33,
56->61

^{29}Si   -20-> -12.5, -6->2 (both minor), 2->10, 13->28 (major)

Elemental Analysis:

   Calculated for $[SiCl_2CH_2]_n$; the theoretical "average" repeat
unit: C:10.63, H:1.77, Si:24.80, Cl:62.80

   Calculated for $[SiCl_{1.26} O_{0.44/2}Et_{0.14}OEt_{0.16}CH_2]_n$
(Approximate formula suggested by NMR, IR studies, actual
analysis). C:21.89, H:3.99, Si:31.92, O:7.07, Cl:37.34

   Found values: C:21.09, H:4.14, Si:22.30, Cl:37.34[12]

Reduction of " $[SiCl_xCH_2]_n$" to " $[SiH_xCH_2]_n$":

      Typically, about 1/2 mole of $[SiCl_xCH_2]_n$ (as $[SiCl_2CH_2]_n$)
in 500 ml ether was transferred to a 1L, 3N, RB flask equipped
with reflux condenser, magnetic stirrer, nitrogen inlet, and
cool (10°C) water bath. About 12.3 g $LiAlH_4$ (1.3 mole H$^-$, 30%
excess). suspended in 200 ml ether, was added over 30 minutes,
via canulla or syringe, with rapid stirring. The resulting
light grey suspension was refluxed overnight under nitrogen.
The large excess of $LiAlH_4$ was employed due to the uncertainty
in the amount of Si-Cl functionality in the polymer.

EXAMPLES 2-3

Workup of Crude $[SiH_xCH_2]_x$:

EXAMPLE 2

Aqueous workup:

5   Initially, approximately 3M HCl was added, dropwise, to
the rapidly stirred $LiAlH_4$/polymer slurry from Example 1.
After the reactivity lessened, about 1 liter of the acid was
poured in, resulting in the dissolution of the lithium and
aluminum salts. The ether layer was separated, again washed

10   with dilute HCl, and the ether was stripped off to yield a
cloudy, yellow oil. This oil was redissolved in pentane to
drive out small amounts of emulsified water and residual
aluminum complexes. After settling, the transparent yellow
pentane solution was easily separated from the residue and

15   stripped of solvent, under vacuum, with warming to 75°C. A
viscous, transparent, pale yellow polymer was obtained in
about 85% yield (or 40% overall, from Cl_3SiCH_2Cl) based on the
assumed formula $[SiH_2CH_2]_n$ for $[SiH_xCH_2]_n$.

IR (cm^{-1}) 2950m, 2920m, 2870m, 2140vs, 1450w, 1350m, 1250w,

20   1040s, 930vs, 830s, 760vs.
NMR, decoupled, (ppm vs TMS) all peaks are complex multiplets
or broad.
^1H -0.4-> -0.05, -0.05->0.3, 3.55->3.85, 3.85->4.1, 4.1->4.3
^{13}C -12->9, (major portion), 12.5->16, 23->26.

25   ^{29}Si -66-> -53 (4 large singlets and small multiplets), -39->
-26, -14-> -8, 0.0->5, (all complicated multiplets).
^{29}Si (coupled) -73-> -45 several overlapping quartets,
J_{Si-H} about 200 Hz., other multiplets become more complicated.
^{29}Si (decoupled, DEPT, mult.=1.5) -66-> -53, -14-> -8;

30   (positive) -39-> -26; (negative).

Elemental Analysis:
Calculated for SiH_2CH_2; theoretical "average" formula:

C:27.27, H:9.09, Si:63.63, Cl: 0, O: 0   Calculated for
$[SiH_{1.53}Et_{0.14}CH_2]_n$ (Approximate formula suggested by NMR, IR, studies, and elemental analyses).

C:32.26, H:8.19, Si:58.8

5   Found: C:28.26, H:7.36, Si:48.71, Cl:1.63, O:0.02*

       * Oxygen analyses by LECO. The values ranged from 0.01%
to 0.02% for three trials.

Gel Permeation Chromatographic analysis (GPC) of $[SiH_xCH_2]_n$:

       GPC of the reduced polymer was performed on a Waters 600
0   solvent delivery system, 410 RI detector and 745 data
processing unit. Waters Ultrastyragel columns of 100, 500,
and 10,000 Å porosity were kept at 40°C. Helium-sparged
toluene at a flow rate of 0.6 ml/min was used as the eluent.
Molecular weights were obtained from a 15 point calibration
5   curve by using polystyrene standards from 200 to 470,000 amu.
A wide MW distribution of 300->80,000 amu, with the majority
of the polymer falling between 300-3000 amu was observed. The
MW_n (750), MW_w (5200) and polydispersity (6.9) reflect the
broad MW distribution of this polymer.

EXAMPLE 3

Non-aqueous Workup:

The crude, reduced mixture was stripped of as much ether as possible, under vacuum, with heating to 50°C. The
5   resulting solids were extracted with pentane, allowed to settle, and the clear, yellow pentane solution was transferred by cannula to remove the polymer from the lithium and aluminum salts. The solution remained clear yellow during removal of the solvent under vacuum, only a gradual increase in viscosity
10 was observed. Finally an extremely viscous, yellowish, air-sensitive polymer was recovered in about 85% yield. The IR spectrum of this material was identical to that from the aqueous workup, except for two additional peaks: 1930w, 670w cm^{-1} respectively.

15 ^1H NMR, decoupled, (ppm vs TMS)
    -0.6->1.2 (broad), 0.8->1.1 (superimposed, less broad peak)
    3.6->3.9, 3.9->4.1, 4.1->4.3 (3 adjacent broad peaks)
    integration ratio 2.8:1 for the two sets of broad peaks
20 (for C-H and Si-H, respectively).

Elemental Analysis:
Calculated for SiH_2CH_2:   C:27.27, H:9.09, Si:63.63, Al: 0
Found: C:20.88, H:5.82, Si:34.51, Al:6.64

EXAMPLE 4

Preparation of $[SiD_xCH_2]_n$:

"Chloro-polymer" (5.02 g, 0.0444 mole as $[SiCl_2CH_2]_n$) was reduced with 1.165 g of $LiAlD_4$ (0.111 mole D^-) using a scaled down version of the procedure employed for $[SiH_xCH_2]_n$. The reduction was followed by the aqueous/HCl workup previously described. The product was a pale yellow, viscous liquid similar to $[SiH_xCH_2]_n$.

IR (cm^{-1}) 2960m, 2920m, 2870m, 2840m, 2120vw, 1540vs, 1450w, 1350m, 1250m, 1035s, 940w, 890w, 750->850s, 675vs.

^1H NMR ppm vs TMS, all peaks relatively broad singlets. 1.7, 1.05, -0.4->0.6

EXAMPLE 5

Preparation of "$[SiH_xCH_2]_n$" Using D_{10} Ether.

The "chloro-polymer" was prepared as previously
described, but on a smaller scale, using a 250 ml 3-neck RB
5   flask, 3g Mg powder, 3g of D_{10} ether, 40 ml dry pentane, and
one small drop of MeI. Slow addition of 11.5 ml (0.091 mol)
of Cl_3SiCH_2Cl over about 2 hours (with initial heating to
start the reaction) resulted in a brownish solution. This
mixture was refluxed for about 3 days to complete the
10   polymerization. The resulting "chloro-polymer" was reduced by
direct addition of 3g (0.08 mol) of $LiAlH_4$ powder to the crude
products over about 1 hour, and the mixture was allowed to
stir for 4 hours. Additional non-deuterated ether (20 ml) was
then added, and the mixture was allowed to stir at room
15   temperature for several days. After the reduction was
complete, the grayish slurry was allowed to settle. The
yellowish ether layer was transferred by syringe to a 500 ml
RB flask fitted with septum and an oil bubbler. The residual
$LiAlH_4$ was killed by the dropwise addition of 3M HCl while
20   swirling the contents in the flask. Once the reaction slowed
sufficiently, 250 ml of 3M HCl was poured in, and the mixture
was swirled for several minutes before being transferred to a
separatory funnel. The resulting, yellow, ether layer was
washed once more with 250 ml of the dilute acid before
25   transfer to a 50 ml RB flask. Ether and pentane were removed
by warming (50°C) while flushing with nitrogen for a few
minutes. The resulting polymer was redissolved in an equal
amount of pentane to drive out any remaining water or aluminum
salts. The polymer solution was separated from a small amount
30   of water, and stripped of pentane by flushing with nitrogen
while warming to about 50°C. The polymer was obtained as a
viscous transparent, yellow oil similar in appearance to that
from the preparation described earlier.

IR (cm^{-1}) 2950w, 2920m, 2890w, 2205m, 2140vs, 1350m, 1250w,
35   1115w, 1050vs, 940vs, 850vs, 765vs.

^{1}H NMR (ppm vs TMS)   0.0 broad, major, 0.9 minor, 1.35 minor, 3.7 major, 4.1 major, 4.65 minor, 4.9 minor.

EXAMPLE 6

Reduction of Solid Residue from $[SiCl_xCH_2]_n$ Preparation:

After two ether extractions, the residual solids from the "chloro-polymer" preparation were returned to the 2 liter, 3
5   neck flask, in a nitrogen-filled glove bag, and about 1 liter of dry ether was added. The amount of reducible material remaining in the residue was unknown, so $LiAlH_4$ was added until the yellowish slurry assumed a light grey color suggesting excess $LiAlH_4$ was present. This slurry was allowed
10   to reflux overnight. The "aqueous work-up" was performed in the same manner as that for the soluble fraction of polymer. Vigorous foaming during the initial dropwise addition of 3M HCl to the crude product showed that an excess of $LiAlH_4$ was present. The presence of large amounts of $MgCl_2$ does not
15   appear to affect the reduction process as it reacts with $LiAlH_4$ to form $Mg(AlH_4)_2$ which has the same reducing properties as $LiAlH_4$. The remainder of the isolation procedure was substantially identical to that for the soluble "chloro-polymer" reduction products. This process recovers
20   variable amounts of additional reduced polymer corresponding to 15-25% of the theoretical yield. The IR and NMR of this product was similar to that from the soluble fractions of the "chloro-polymer". GPC was also quite similar; the majority of the polymer falling between 400 and 3400 amu, with Mn = 681.

EXAMPLE 7

Trapping of Oligomers as Methoxy Derivatives

Chloromethyl-trichlorosilane (0.5 mole, 63 ml) was added
to magnesium powder as in the preparation of $[SiCl_xCH_2]_n$,
5   except that the resulting brown solution was refluxed for only
30 min. before transferring, by canulla, to well stirred,
cooled excess methanol. After the resulting white solids
settled, a pale yellow solution was separated. Removal of the
excess methanol gave a liquid/solid mixture, which was
10 extracted with hexane, and distilled under N_2. The major
components were identified as $(MeO)_3SiMe$, and
$(MeO)_3SiCH_2Si(OMe)_2CH_2Cl$ by boiling point and/or NMR data. A
yellow, oily liquid, a mixture of higher weight oligomers,
accounting for about 25% of the crude mixture remained behind.

15 $(MeO)_3SiMe$ Bp. 105-110°C, (103°C Lit.)
$(MeO)_3SiCH_2Si(OMe)_2CH_2Cl$ Bp. 150-160°C
^1H NMR: All singlets, (No. of protons @ ppm) reference: TMS.
$(MeO)_3SiMe$:   3@-0.28 $(SiCH_3)$, 9@3.37 (OCH_3)
$(MeO)_3SiCH_2Si(OMe)_2CH_2Cl$:
20   2@0.103 $(SiCH_2Si)$, 2@2.6 (CH_2Cl), 15@3.42
(OCH_3)

EXAMPLE 8

Preparation of $[SiH_xCH_2]_n$ Oligomers.

Using 0.25 mole of Cl_3SiCH_2Cl (31.5 ml) the initial, brown solution was prepared, as above, and allowed to reflux

5   for one hour. The solution was reduced by addition of 30% excess $LiAlH_4$ as a suspension in ether and was allowed to stir overnight. After aqueous/HCl workup and solvent removal, about 8 ml of light yellow, watery liquid was recovered. Distillation of this product, under N_2, yielded only about

10   0.25 ml of liquid before undergoing a rapid, exothermic, cross-linking reaction, with much gas evolution, to form a white, foam-like, glassy solid. The fraction obtained was found by GC to be 80% one component, identified by NMR as $H_3SiCH_2Si(H)_2CH_2Cl$. The remaining 20% consisted of several

15   related compounds in quantities too small to separate and characterize in detail.

$H_3SiCH_2Si[H]_2CH_2Cl$ Bp 75-85°C
^{1}H NMR (No. of protons @ ppm vs TMS, multiplicity): 2 @ -0.4 sextet (overlapping triplet of quartets) $(SiCH_2Si)$, 2 @ 2.46

20   triplet $(-CH_2Cl)$, 3 @ 3.6 triplet $(-SiH_3)$, and 2 @ 3.87 overlapping triplet of triplets (nearly a quintet) $(-SiH_2-)$.

EXAMPLE 9

Model Coupling Reaction of Me_3SiCH_2Cl With Me_3SiCl:

A mixture of Me_3SiCH_2Cl (0.1 mol) and excess Me_3SiCl (0.2 mol) in 100 ml of dry ether was refluxed for three days under

5   nitrogen until no further reaction was evident. The resulting $MgCl_2$ was allowed to settle, and the ether layer separated. The solvent and excess Me_3SiCl were stripped off under vacuum giving the crude products. GC of this crude material, in addition to small amounts of residual solvent and Me_3SiCl,

10   gave 85.7% of $Me_3SiCH_2SiMe_3$, the expected product from the Grignard reagent (Me_3SiCH_2MgCl), formed in situ, reacting with Me_3SiCl. Only 2.56% of $Me_3SiCH_2CH_2SiMe_3$ (from Me_3SiCH_2MgCl reacting with Me_3SiCH_2Cl) was observed. In addition, 0.087% of Me_3SiOEt was observed, the retention time being confirmed

15   with an actual sample. No observable amounts of $Me_3SiCH_2SiMe_3$ (which would arise from direct dechlorination of Me_3SiCl by magnesium) were detected. The data below is only for $Me_3SiCH_2SiMe_3$ as the other components were present in quantities too small to characterize.

20   GC: 85.7% $Me_3SiCH_2SiMe_3$, 2.56% $Me_3SiCH_2CH_2SiMe_3$, 0.087% Me_3SiOEt Bp @ 760mmHg $Me_3SiCH_2SiMe_3$ 130-131°C, (132°C lit.) IR (cm^{-1}) 2950m, 2895w, 1420w, 1250m, 1055m, 840s, 690w. NMR: ^1H: $Me_3SiCH_2SiMe_3$ (ppm vs TMS): 0.045 (SiMe), -0.345 (SiCH$_2$)

25   ^{13}C (DEC.): 1.106 (CH$_3$Si), 4.025 (SiCH$_2$Si) ^{29}Si: 0.319

EXPERIMENTAL RESULTS: ·

The product of the Grignard coupling reaction was a dark, viscous, mildly air-sensitive polymer. The trifunctional nature of the silicon end of the initial monomer (Cl_3SiCH_2Cl) suggested that the polymeric products would exhibit a complicated branched structure. Investigations of this polymer by ^1H, ^{13}C, and ^{29}Si NMR were performed in order to identify the functional units present. In the ^1H NMR spectrum, a broad, complex peak was seen near 1 ppm. This peak was consistent with an assignment to the protons of methylene units between many slightly different $SiCl_x$ functionalities which were the result of the extensive branching of the polymer. The corresponding carbons for these methylene groups are believed to be the origin of the several complex peaks observed between 8 and 25 ppm in the ^{13}C NMR spectrum. Several groups of complex multiplets were seen in the range of 2->28 ppm in the ^{29}Si NMR spectrum. These peaks are attributed to $[-CH_2]_{4/2}Si$, $[-CH_2]_{3/2}SiCl$, $[-CH_2]_{2/2}SiCl_2$, and $[-CH_2]_{1/2}SiCl_3$ units in the polymer. At first it would appear that these units represent only four kinds of silicon, however, differences in local environments due to the complex branching of this polymer result in very complex multiplets, even when decoupled. Additional peaks were observed in the NMR spectra of this polymer, indicating that other functional groups are present as well. The ^1H NMR spectrum also showed a smaller, broad peak at 3.8 ppm, which was assigned to the $-OCH_2-$ protons of ethoxy groups. The peaks due to the methyl protons for these ethoxy groups would lie near 1 ppm and presumably were buried under the carbosilane methylene peak. In the ^{13}C NMR spectrum, the carbons from the $-OCH_2-$ are deemed to give rise to the peaks between 56 and 61 ppm. Again, the corresponding methyl carbon peaks would be buried under those due to $Si-CH_2-Si$ in the polymer chain. The ^{29}Si NMR spectrum showed smaller up-field multiplets at 2-> -6, and -17.5-> -20 ppm, strongly suggestive that oxygen is bound to silicon, in addition to chlorine. Silicon compounds with only

alkyl and chlorine functionalities generally do not go up-field of 0 ppm in the ^{29}Si NMR. In addition to Si-OEt, these up-field peaks might result from Si-Si, or Si-O-Si bonding present in the polymer.

5   The IR data also support the conclusion that ethoxy substitution has occurred during the preparation of the "chloro-polymer". A peak of medium intensity at 1160 cm^{-1} was consistent with the C-O functionality of SiOEt. The strong, broad band between 1000 and 1120 cm^{-1} was suggestive of Si-OR

10   and/or Si-O-Si functionality in addition to the Si-CH$_2$-Si deformation band from the carbosilane "backbone" of the polymer. The peak at 960 cm^{-1} was also characteristic of the presence of Si-OEt groups.

        Thus, evidence from several sources (^{1}H, ^{13}C, ^{29}Si NMR

15   and IR) suggests that ethoxy groups and other Si-O-functionality is present, in addition to chlorine, as substituents on silicon in this "chloro-polymer". In addition to this data, integration values from the ^{1}H NMR of the "chloro-, and reduced polymers, and elemental analysis,

20   suggest the approximate "average" formula, $[SiCl_{1.26})O_{0.44/2}OEt_{0.16}Et_{0.14}CH_2]_n$, for the "chloro-polymer". The ^{1}H NMR of the reduced polymer shows ethyl groups that are obscured in the NMR of the corresponding "chloro-polymer" due to overlap with the methylene groups.

25   Small peaks at 1.9->2.3 and 29->33 ppm, in the ^{1}H, and ^{13}C NMR respectively, have been assigned to unreacted chloromethyl end groups in the polymer. The infrared spectrum of this polymer showed medium-intensity bands at 1385 and 1160 cm^{-1} which were consistent with CH$_2$Cl groups on silicon.

30   Reduction of this branched, chloro-polycarbosilane $[SiCl_xCH_2]_n$ with LiAlH$_4$/ether to form the corresponding hydrido-polycarbosilane has been investigated by two routes differing in the final work-up. Aqueous workup involved treatment of the crude reduction products with dilute HCl and

35   separation of the polymer in ether. The non-aqueous method consisted of stripping the ether from the crude reduction products, under vacuum, yielding sticky solids that were

re-extracted with pentane to separate the polymer. The aqueous workup was easier to perform, but involved the potential risk of oxygen incorporation into the polymer. Samples of polymer resulting from both methods of workup were characterized.

$[SiH_xCH_2]_n$ BY AQUEOUS WORKUP:

The product from the aqueous workup was a highly viscous, yellow oil that, despite extensive Si-H functionality, appeared to be relatively stable to air exposure. The IR spectrum of this polymer was consistent with the proposed, highly branched, structure: $[SiH_xCH_2]_n$ (where x=0,1,2,3). Strong peaks at 2140, 930, 830, and 760 cm^{-1} confirmed the presence of SiH, SiH_2, and SiH_3 groups. The disappearance of the bands at 1160 and 960 cm^{-1}, and the narrowing of the $SiCH_2Si$ absorption due to loss of C-O and Si-O functionality in the polymer suggested the reduction of Si-OR and Si-O-Si groups to Si-H. The absence of the characteristic peak for $SiCH_2CH_2Si$ between 1120-1180 cm^{-1} indicated that little or no head-to-head coupling was present.

The ^1H NMR spectrum of the reduced polymer, suggestive of a branched structure, consisted of complex multiplets and broad peaks. Two groups of peaks centered at -0.2, and 0.15 were attributed to the various $SiCH_2Si$ environments, as well as the $SiCH_2-$ of Si-Et functionality. Any Si-Me functionality in the polymer would also be deemed to appear in this region. The peak near 1 ppm was consistent with the "-CH_3" protons of ethyl groups on silicon. Residual chloromethyl functionality not reduced by $LiAlH_4$ treatment appeared as a peak at 1.65 ppm. This peak underwent a small up-field shift when the polymer was reduced, as would be expected for the replacement of the electron-withdrawing chlorine atoms on silicon by hydrogen. The three groups of peaks at 3.7, 3.95, and 4.2 ppm closely matched the values for the SiH_3, SiH_2, and SiH groups of a series of "model" compounds; $[Me_3SiCH_2]_xSiH_{4-x}$ where X = 1->3, respectively.

The resonances due to Si-H and $-OCH_2-$ groups in the proton NMR tended to overlap, rendering verification that all the Si-OEt on the "chloro-polymer" was reduced difficult. This problem was avoided by performing the reduction of the

5   "chloro-polymer" using $LiAlD_4$. For the resulting deutero-polymer "$[SiD_xCH_2]_n$", ^1H NMR showed no peaks in the $Si-H/OCH_2$ region (3.5->4.3 ppm). Apparently neither functionality exists in sufficient quantity to be observed, suggesting that reduction of Si-OEt functionality in the

10   polymer was complete, or very nearly so. The peaks near 0.1 and 1.0 ppm, for the CH_2 and CH_3 of Si-Et, respectively, and the peak for residual CH_2Cl, were not affected.

The infrared spectrum of the deutero-polymer was similar to that for the hydrido-polymer except for changes in the

15   position of the peaks for the Si-H functionality as follows: $[cm^{-1}]$ 2130/1540, 940/675, 820/below 600. Only small peaks at 2120, 940, and 890 cm^{-1} were seen, due to traces of Si-H in the deutero-polymer.

In order to confirm that the peaks seen in the proton NMR

20   at 0.1 and 1.0 ppm were actually due to ethyl groups from the ether being incorporated during the Grignard coupling reaction, the preparation of the "chloro-polymer" was run in a D_{10} diethyl ether/pentane mixture followed by a slightly modified $LiAlH_4$ reduction, and aqueous workup. The proton NMR

25   of this polymer showed only small peaks for SiEt functionality (probably from residual protons in the ether, or slight proton exchange during the preparation) indicating that the ethyl groups originated from the ether during the coupling reaction. The only other significant difference in the proton NMR was

30   the greater relative amount of SiH_3 (3.7 ppm; free end groups) versus SiH_2/SiH (4.1, 4.3 ppm; in-chain/branched groups) suggesting that the molecular weight of the D_5-Et substituted polymer was somewhat lower than with a typical preparation. This was most likely a result of poorer solvating ability of

35   the mixed D_{10}-ether/pentane solvent required for this preparation. The infrared spectrum of this polymer showed distinct changes in the C-H stretch region that were

consistent with the proton NMR results. The D_5-Et substituted
polymer shows new peaks at 2205 and 2070 cm^{-1} (due to C-D
functionality) with corresponding decreases in the C-H peaks
at 2950 and 2850 cm^{-1}. Some of the weaker peaks in the C-H

5   bending region near 1400 cm^{-1} also shifted to lower wave
numbers presumably lying buried under the strong Si-CH$_2$-Si
deformat'on, or Si-H bands.

The data from the ^{13}C NMR of the reduced polymer were
consistent with assignments from the ^{1}H spectra, the major

10   feature being a broad, complicated multiplet extending from
-12 to 8 ppm, covering the same range as the peaks arising
from the methylene carbons between silicons of the "model"
compounds for the reduced polymer. A small group of peaks at
25 ppm was attributed to residual SiCH$_2$Cl functionality not

15   completely reduced by the LiAlH$_4$. A second small group of
peaks, near 13 ppm was assigned to the "-CH$_3$" carbon of ethyl
groups on silicon. The "CH$_2$" carbons of the Si-Et groups were
presumably buried under the Si-CH$_2$-Si multiplet. Peaks
observed near 6$\bigcirc$ ppm in the ^{13}C NMR spectrum of the

20   chloro-polymer (assigned to the -OCH$_2$- carbons of SiOEt
groups) were not seen in the reduced polymer, again,
indicating that the ethoxy groups were eliminated during
reduction.

The decoupled ^{29}Si "DEPT" NMR spectrum (multiplicity of

25   1.5), of the reduced polymer: [SiH$_x$CH$_2$]$_n$, showed that the
groups of peaks around -8-> -14 and several resolved singlets
at -53-> -66 ppm had odd numbers of hydrogens, whereas those
between -26 and -39 had an even number. This was consistent
with assignments as [-CH$_2$]$_{3/2}$SiH, [-CH$_2$]$_{1/2}$SiH$_3$ and

30   [-CH$_2$]$_{2/2}$SiH$_2$ polymer functionalities, respectively, using
information from the NMR spectra of the "model" compounds.
The complexity of these NMR spectra reflected the branched
structure of the polymer, which can contain many slightly
different environments for each type of silicon. Presumably,

35   the CH$_2$SiH$_3$ groups were better resolved, because, as end
groups, they are less affected by the surrounding,
complicated, polymer environment. The [-CH$_2$]$_{4/2}$Si units did

not appear on this NMR spectrum, as only silicons bearing
hydrogens respond under these conditions. The coupled ^{29}Si
NMR showed several, clearly discernable, overlapping quartets
with typical Si-H coupling constants of about 200 Hz. The
5   superimposed, fine splitting of the SiH$_3$ quartets by adjacent
methylenes, as seen in the "model" compounds, was not
completely resolved in the polymer due to the increased width
of the peaks. Coupled ^{29}Si NMR gave little information about
the other Si-H functionalities because the peaks were so
10   complicated.

Elemental analysis for the reduced polymer showed a small
amount of chlorine (1.63%), from the residual chloromethyl
groups. The carbon value was close to that expected for
$[SiH_2CH_2]_n$, however, the hydrogen value was somewhat low. The
15   possibility that there were unreduced oxygen-containing
groups, such as Si-OEt or Si-O-Si, in this polymer was
rendered unlikely by the results of oxygen analyses which
indicated that the oxygen content of the polymer was only
about 0.02%.

20   The ^{1}H NMR integration values for the reduced polymer,
obtained soon after isolation, gave a nearly 1:1 Si-H to C-H
ratio, suggesting that formation of Si-Si bonding in the
reduced polymer with loss of hydrogen had occurred before the
sample was analyzed. Samples of the reduced polymer have been
25   observed to gradually increase in viscosity, and develop
pressure when stored in sealed containers which is consistent
with this hydrogen loss. The silicon value obtained from the
elemental analysis was significantly lower than would be
expected for the $[SiH_{1.86}Et_{0.14}CH_2]_n$ formula; however, there
30   is substantial evidence from prior literature reports that the
silicon analysis, as typically performed, is unreliable for
many carbosilane compounds. The well-characterized
$[Me_3SiCH_2]_xSiH_{4-x}$ "model" compounds were no exception, giving
silicon values up to 30% low.

35   Molecular weight distribution by GPC of the reduced
polymer showed a very broad MW distribution with most of the
polymer falling between 450 and 3000 amu, but tailing off up

to 80,000 amu vs polystyrene to give a large polydispersity value of 6.95. The M_w for this polymer was 745, corresponding to about 15 repeat units as $SiH_{1.86}Et_{0.14}CH_2$ (suggested by NMR, IR, and elemental analysis). The actual MW distribution

5   could be considerably different from this, as the reduced polymer was not very similar to polystyrene. A rough estimate of the number of repeat units in the reduced polymer could also be obtained from examination of the "chloro-polymer" by comparing the proton NMR integration values for $SiCH_2Cl$

10   ("head" end groups) vs $SiCH_2Si$ (all other polymer units). The $SiCH_2$ Si peak for the "chloro-polymer" also included the methyl protons of the ethoxy groups, for which it is corrected by subtracting a 1.5 multiple of the $-OCH_2-$ integration value. The resulting, corrected $Si-CH_2-Si$ peak also contained all of

15   the Si-Et protons. The correction factor for the ethyl group protons was also obtained from the "average formula; $[SiH_{1.86}Et_{0.14}CH_2]_n$ for the reduced polymer, determined by the ^1H NMR integrations. One ethyl group per 7 CH_2 units corresponded to a ratio of 5 to 14 for the overlapping CH_2 &

20   CH_3 [of Et] and $Si-CH_2-Si$ that made up the peak in the ^1H NMR. Applying the factor 14/19 to the $Si-CH_2-Si$ integration value of the "chloro-polymer" [after subtraction for the "CH_3" of Si-OEt] gave the actual integration value for $Si-CH_2-Si$ functionality alone. After comparing with CH_2Cl integration,

25   the value obtained by this method for the average number of repeat units (as $SiH_{1.86}Et_{0.14}CH_2$) in the polymer was about 13.5. It is important to note that since Si-Si and Si-O-Si bonding in the polymer does not affect the $SiCH_2Cl$ to $SiCH_2Si$ ratio, the molecular weight values obtained reflected only the

30   effects of $Si-CH_2-Si$ bonding, hence any crosslinking was ignored for the MW value obtained be this method.

$[SiH_xCH_2]_n$ FROM NON-AQUEOUS WORKUP:

       The polymeric products from the non-aqueous workup were tacky, yellow, solids which, unlike the aqueous workup

35   version, rapidly developed a whitish coating on exposure to

air. The IR spectrum of this polymer was similar to that from the aqueous workup, except for two additional peaks at 1930 and 670 cm^{-1}. These peaks suggested that residual $Al-H_x$ functionality was present. $LiAlH_4$ itself, is insoluble in

5   pentane (which was used to extract the transparent, yellow polymer from the residue) and therefore not likely to be a contaminant.

The ^{1}H NMR spectrum of this polymer contained a broad, complex peak between -0.6 and 1.5 ppm, on which was

10 superimposed a narrower peak between 0.8 and 1.1 ppm. The differences in the $SiCH_2Si$ region of the NMR spectrum from that of the aqueous-workup polymer, suggested the presence of some additional species in the non-aqueous product.
The Si-H peaks were similar to those of the aqueous-workup

15 polymer, appearing at 3.6-3.9, 3.9-4.1, and 4.1-4.3 ppm. Their integration ratio (^{1}H NMR) was considerably below the approximately 1:1 ratio with methylene protons which was seen for the polymer derived from the aqueous work-up.

DISCUSSION OF EXPERIMENTAL RESULTS: PART A, "CHLORO-POLYMER" $[SiCl_xCH_2]_n$.

The IR, NMR, and other experimental results for the
"chloro-polymer" appear to be consistent with the following
5   hypotheses regarding the generation of the polymer structure.
Evidence for proposed side-reactions will be discussed
separately.

Slow addition of Cl_3SiCH_2Cl to refluxing Mg/ether was
found to yield, initially, a dark, highly air-sensitive
10   solution which, on extended reflux, gradually produces large
amounts of $MgCl_2$ and a dark, brownish-yellow, viscous, mildly
air-sensitive polymer. The initial dark solution was
suspected to be the Grignard reagent; (Cl_3SiCH_2MgCl), and was
further investigated by quenching a freshly-made batch with
15   excess methanol before significant polymerization had
occurred. On distillation, the principal compound of interest
(about 80%) was $(MeO)_3SiMe$ which as the expected product from
reaction of Cl_3SiCH_2MgCl with excess MeOH. Smaller amounts,
about 17%, of $(MeO)_3SiCH_2Si(OMe)_2CH_2Cl$ were also recovered.
20   This compound appears to originate from Cl_3SiCH_2MgCl coupling
with unreacted Cl_3SiCH_2Cl to form $Cl_3SiCH_2Si(Cl_2)CH_2Cl$ before
methanolysis. About 3% of $(MeO)_3SiCH_2Si(OMe)_2Me$ was observed,
which could result from either conversion of the previous
compound to the corresponding Grignard, or from head-tail
25   coupling of two $Cl_3SiCH_2 MgCl$ species before the addition of
methanol. Compounds suggestive of head to head coupling, such
as $(MeO)_3SiCH_2CH_2Si(OMe)_3$, did not exist in sufficient
quantity to be observed.

These results suggest that most of the Cl_3SiCH_2Cl was
30   quickly converted to the corresponding Grignard reagent (the
dark colored species). Some of this Grignard reagent couples
with Si-Cl of unreacted Cl_3SiCH_2Cl to form the observed
dimeric intermediate compound; $Cl_3SiCH_2Si(Cl_2)CH_2Cl$. The
corresponding reduced compound; $(H_3SiCH_2SiH_2CH_2Cl)$, was
35   recovered from the $LiAlH_4$ "quench" of a batch of the
Cl_3SiCH_2MgCl that had been allowed to reflux for about one

hour. Any H_3SiCH_2Cl, or H_3SiMe (from Cl_3SiCH_2Cl, and Cl_3SiCH_2MgCl respectively) would have escaped as gases. The coupling process of Cl_3SiCH_2MgCl with unreacted Cl_3SiCH_2Cl must be fairly rapid as no $(MeO)_3SiCH_2Cl$ was recovered. The

5   head-tail coupling of the Grignard reagent; (Cl_3SiCH_2MgCl) with itself appears to be relatively sluggish, as most of it could be trapped with methanol, and even though Cl_3SiCH_2MgCl is the most abundant species present, only traces of the corresponding dimeric compound, $Cl_3SiCH_2Si(Cl_2)CH_2MgCl$, were

10 observed. We deem that the initial sluggishness of the Cl_3SiCH_2MgCl self-coupling reaction arose because the silicon is surrounded by three chlorines, the electron-rich Grignard carbon, and presumably coordinated ether as well, such that the usual mechanism of nucleophilic attack on silicon was

15 inhibited by unfavorable steric and/or electronic effects. Potential pathways explaining the formation of the observed compounds are outlined in Fig. 1.

Since the reactivity of the $SiCl_3$ "tail" of Cl_3SiCH_2MgCl to coupling was inhibited, it appeared that the major

20 mechanism of polymer growth was by successive attack of Cl_3SiCH_2MgCl, or oligomers with Grignard "head" end-groups, at the Si-Cl sites of the initial dimeric compounds, $Cl_3SiCH_2SiCl_2CH_2Cl$, primarily, and, to a lesser extent $Cl_3SiCH_2SiCl_2CH_2MgCl$. The $SiCl_3$ of these dimers would be far

25 enough from the Grignard site, if any, that the deactivation effect would be no longer operative. As each new group attached to the growing polymer, the Grignard functionality was lost, and the Si-Cl groups now behaved approximately like ordinary alkyl-chlorosilanes such as $MeSiCl_3$ or Me_2SiCl_2,

30 allowing further polymerization to continue.

The strong tendency toward head-tail coupling ($-CH_2MgCl/Cl_3Si-$) for the Grignard coupling reaction was demonstrated by the model coupling reaction of Me_3SiCH_2Cl and Me_3SiCl. For this system, even with the presence of excess

35 Me_3SiCl, the ratio of head-tail product, $Me_3SiCH_2SiMe_3$, to head-head compound, $Me_3SiCH_2CH_2SiMe_3$ was 33:1. For the polymer system, the "tail" functionality was $-SiCl_3$ which

would be considerably more reactive to Grignards, than
Me_3SiCl, therefore greatly reducing the extent of head-head
coupling in the actual polymer system. No observable amount
of $Me_3Si-SiMe_3$ was obtained during this coupling reaction

5   indicating that the direct dechlorination of Si-Cl groups,
with subsequent formation of Si-Si linkages did not occur.
This appears to be consistent with other studies that showed
that one or more phenyl groups attached to silicon were
required for the formation of Si-Si bonding by Mg.

10   The trifunctional $SiCl_3$ "tail", monofunctional $-CH_2MgCl$
"head", and strong bias towards head-to-tail coupling, as
shown by the $Me_3SiCH_2Cl/Me_3SiCl/Mg$ model coupling experiment,
gave this polymer system several interesting features. Up to
three Grignard head-end groups can couple to each $SiCl_3$ site

15   on the growing polymer. With the addition of each new
monomer, another $SiCl_3$ site was formed. Continuation of this
process resulted in a polymer exhibiting extensive branching,
limited only by steric effects. Due to the branching, this
polymer was characterized by a relatively large number of

20        $SiCl_3$ "tail" functionalities. Only one "CH_2" end group
existed for each polymer, as all others were employed in
linking the carbosilane polymer together. If no side
reactions occurred, the extent of branching should not have
affected the theoretical 2:1 Cl to Si ratio for this polymer.

25   This theoretical Cl to Si ratio could be justified in that the
monomer contained three chlorine sites on each silicon
($-SiCl_3$), and one CH_2Cl group (which becomes the Grignard
functionality). If all of the Grignard coupled with Si-Cl
groups, there would be two equivalents of Si-Cl remaining;

30   however, branching would increase the ratio of "tail" units
($Cl_3Si(CH_2-]_{1/2}$), and branched units ($ClSi(CH_2-]_{3/2}$,
$Si(CH_2]_{4/2}$ to linear units ($Cl_2Si(CH_2-]_{2/2}$) in the polymer.
        If head-to-head coupling ($-CH_2MgCl<->ClCH_2-$) occurred,
the maximum theoretical molecular weight that could be

35   achieved would rapidly decrease. This would result because
there would be just enough head end groups to couple all of
the monomers (one per monomer). If any were wasted through

head-to-head coupling,. the system would essentially run out of
head end groups before polymerization was complete.   In
actuality, for this system, unreacted chloromethyl groups were
seen in the NMR, suggesting that sterics were the limiting

5   factor.   In addition, the $Me_3SiCH_2Cl/Me_3SiCl/Mg$ model coupling
reaction strongly suggested that head-to-head coupling was
negligible.

It is important to note that this head-tail coupling
process, in itself, should not cause crosslinking of the

10   branched polymer.   Since polymerization was head-tail,
crosslinking would require species with two head end groups.
However, the low recovery rate (about 50%) for the
"chloro-polymer" suggests that at least some crosslinking may
have occurred in this system.   The possible origin of such

15   crosslinking will be discussed later.   The potential polymer
"building blocks" that are to be expected as the
polymerization progresses are illustrated below:

```
              \                          \
              -SiCH2                      -SiCH2
            /   |2                      /   |2
20    '              -SiClCH2-                  SiCH2-
  -SiCl2CH2-           |                 \   |
     |                                   -SiCH2
                                         /
```
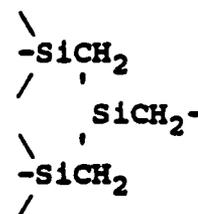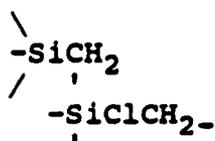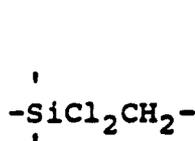
25   Linear unit   single branched unit   double branched unit

Cl_3SiCH_2- $\backslash$ $-SiCH_2MgCl$ / $\backslash$ $-SiCH_2Cl$ /

"Tail" end group   Unreacted Grignard   Chloromethyl

                         "head" end group   "head" end group

The actual "chloro-polymer" system was found to be considerably more complex, as several side reaction were found to occur. In addition to the above groups, NMR and IR data indicate that several other functionalities were present:

$-SiCH_2-$ $-SiCH_2-$ $-SiCH_2-$

   OEt   O   Et

                    $-SiCH_2-$
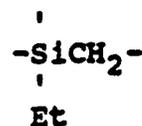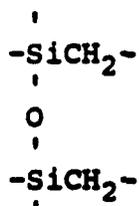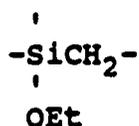
Elemental analysis of the "chloro-polymer" showed the chlorine content to be significantly low for the expected $[SiCl_2CH_2]_n$ average formula. This is consistent with ^{1}H, ^{13}C, ^{29}Si, NMR and IR results which suggest in addition to $SiCl_x$, there were significant amounts of Si-OEt, Si-Et and possibly Si-O-Si functionalities in the "chloro-polymer". The carbon and hydrogen values were considerably higher than expected for the assumed "average" formula $[SiCl_2CH_2]_n$. This was also consistent with both Si-OEt and/or Si-Et functionalities in the polymer. Precedent for this kind of side reaction is well established, the cleavage of ethers by halosilanes to form alkoxy silane and/or siloxanes has been known for many years. For iodosilanes the reaction is often quantitative. Chlorosilanes are less active, but react similarly; moreover, the extended reflux employed to effect coupling of the Grignard reagent would be expected to increase the extent of ether cleavage. The formation of Si-Et functionality is less obvious, it appears to originate from magnesium reacting with

EtCl, a product of the side reactions, to form ethyl Grignard which couples with Si-Cl functionality to form SiEt groups. These ethyl groups have been shown to originate from the ether. When the reduced polymer was prepared using D_{10}-Et_2O

5   during the Grignard coupling step prior to reduction, the incorporation of SiEt-D_5 groups resulted in almost complete disappearance of the "ethyl" peaks in the proton NMR except for residual "CH_2" and "CH_3" protons. These side reactions have been outlined in reactions 2-5:

10   Si-Cl + Et_2O ----------> Si-OEt + Et-Cl   2

Si-OEt + Si-Cl ---------> Si-O-Si + Et-Cl   3

Et-Cl + Mg/Et_2O --------> Et-MgCl   4
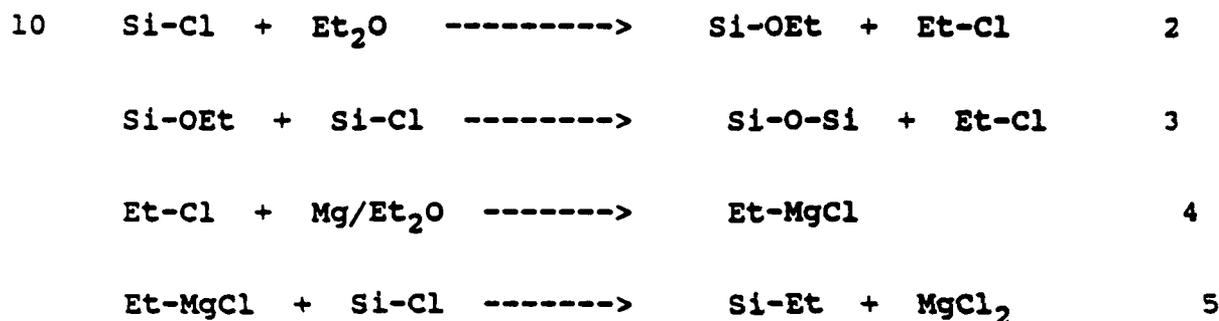
Et-MgCl + Si-Cl --------> Si-Et + $MgCl_2$ 5

Another potential cause of the low chlorine content of
15   the "chloro-polymer" could be direct dechlorination of Si-Cl functionality by magnesium to form Si-Si bonding. However, all reported couplings of halosilanes by magnesium required at least one or more phenyl/aryl substituents on the reactant compounds. Ether cleavage was often the only observed result
20   when these functionalities were lacking. The absence of Me_3Si-$SiMe_3$ in the products of the Me_3SiCH_2Cl/Me_3SiCl/Mg model coupling reaction, and the formation of small amounts of Me_3SiOEt, suggest that magnesium does not induce significant Si-Si bond formation in alkyl substituted chlorosilanes.
25   Either Si-O-Si or Si-Si coupling, even to a relatively modest extent, would tend to crosslink the polymer causing it to become insoluble. This may explain the relatively low yield (50%) for extraction of the "chloro-polymer" from the residual magnesium chloride. If the residual solids, after
30   extraction, were treated similarly to the "chloro-polymer" (reduced with excess $LiAlH_4$ followed by H_2O/HCl workup) 15-25% additional reduced-polymer was recovered. If the solids

contained insoluble, Si-O-Si, or Si-Si crosslinked "chloro-polymer", treatment with excess $LiAlH_4$ would not only reduce the Si-Cl groups, but convert both the Si-O-Si, and Si-Si to Si-H as well. This would destroy the crosslinking,
5 rendering the polymer soluble, and recoverable.

It is difficult to propose an exact formula for this polymer system at the "chloro-" stage as both determination of the theoretical, and the actual composition are subject to error. However, the "average" formula
10 $[SiCl_{1.26}O_{0.44/2}OEt_{0.16}Et_{0.14}CH_2]_n$ has been assigned. This formula is in good agreement w h the ^{1}H, ^{13}C, and ^{29}Si NMR, IR spectra, elemental analysis, and literature precedent. In addition, it accounts for the difficulty in isolating all of the "chloro-polymer" from the MgCl solids by extraction, and
15 the recovery of additional polymer when the solids are reduced by $LiAlH_4$.

The molecular weight of the "chloro-polymer " is difficult to measure directly as even traces of water in the solvent required would cause crosslinking, seriously affecting
20 the results. The molecular weight of this polymer can be indirectly estimated by two methods; The average number of repeat units obtained from the GPC of the corresponding reduced polymer, which is not highly moisture sensitive (as described later) can be corrected for the heavier "average"
25 repeat unit for the "chloro-polymer" (described above). A value of approximately 1500 amu is found. The ratio of chloromethyl ("head" end groups) to methylene (in chain units) from integration of the ^{1}H NMR spectrum can be used to estimate the average number of repeat units giving a value of
30 1400 amu. Both of these methods only count carbosilane bonding in the polymer and are therefore approximate. The effects due to Si-O-Si linkages between polymers was ignored. The first method bases the molecular weight on that of the reduced polymer where the Si-O-Si linkages have been
35 destroyed. The second method also ignores these effects since Si-O-Si linkages do not affect the ratio of $-CH_2Cl$ to $Si-CH_2-Si$ in the ^{1}H NMR spectrum.

PART 2 REDUCED POLYMER:

The reduced polymer is considerably less complicated than its "chloro-polymer" precursor. NMR results of the reduced polymer, and suitable "model" compounds, confirmed the presence of $(-CH_2)_{1/2}SiH_3$, $(-CH_2)_{2/2}SiH_2$, $(-CH_2)_{3/2}SiH$, and $(-CH_2)_{4/2}Si$ functionalities; where the 1/2 factor represents the sharing of the CH_2 functionalities between silicons in the carbosilane backbone of the polymer. The SiEt functionality was retained in the reduced polymer. However, the Si-OEt, and any Si-Si or Si-O-Si groups present in the "chloropolymer" were reduced to Si-H along with Si-Cl. These results appear to be consistent with previous work where $Cl_3Si-SiCl_3$, $Cl_3Si-O-SiCl_3$, and $H_3Si-O-SiH_3$ all gave silane gas on reduction with excess $LiAlH_4$ in ether or THF. It has also been observed that alkoxy groups on silicon, even when surrounded by relatively bulky groups, as in the case of [1-naphthyl]$_3$ Si-OEt, are readily converted to the corresponding silanes by $LiAlH_4$. Alkyl-substituted alkoxy silanes react similarly. In addition, residual Grignard end groups remaining in the "chloro- polymer", if any, would be converted to a magnesium aluminum hydride complex during the reduction. Subsequent aqueous acid workup would result in the corresponding hydrocarbon end group as shown in reactions 7 and 8.
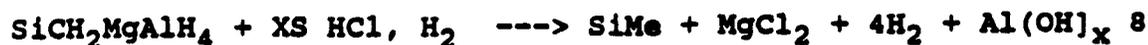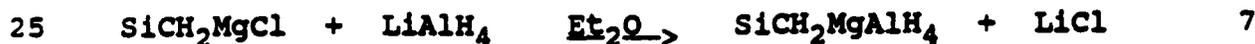
$$SiCH_2MgCl + LiAlH_4 \xrightarrow{\;Et_2O\;} SiCH_2MgAlH_4 + LiCl \qquad 7$$

$$SiCH_2MgAlH_4 + XS\ HCl,\ H_2 \longrightarrow SiMe + MgCl_2 + 4H_2 + Al(OH]_x \quad 8$$

NMR integration values show the actual "average" formula for the reduced polymer to be approximately $[SiH_{1.86}Et_{0.14}CH_2]_n$, or about one ethyl group per seven "average" $[SiH_2CH_2]$ repeat units.

The molecular weight value obtained by GPC of the reduced polymer (745 amu) is about 15 repeat units (as $[SiH_{1.86}Et_{0.14}CH_2]$). This method takes into account any

effects on the molecular weight due to crosslinking processes
so long as the polymer remains soluble.

The similarity of the values for molecular weight of the
reduced polymer by the two methods, suggests little or no
Si-O-Si or Si-Si bonding existed in the reduced polymer, as
one method ignores any crosslinking, the other does not. This
is in agreement with the high solubility of the reduced
polymer in pentane, the absence of protons from Si-OCH$_2$- in
the LiAlD$_4$-reduced polymer and the elemental analyses which
indicated a very low oxygen content (0.02%). All suggest that
reduction of Si-OEt, Si-O-Si, and any Si-Si is complete, or
very nearly so, in the reduced polymer.

However, the elemental analysis also gives a low hydrogen
value for the reduced polymer. This could be the result of
slow loss of hydrogen from the polymer, at room temperature,
to give Si-Si bonding after isolation. It has been observed
that samples of the reduced polymer slowly increase in
viscosity and generate gaseous by-products (presumably
hydrogen) after storage for several weeks The reduced polymer
is found to crosslink on heating, presumably by the same
process.

From the ^{1}H NMR, differences in peak shape and
integration values suggest that the reduced polymer prepared
by non-aqueous workup appears to contain a significant amount
of Al-H$_x$ protons, bound to the polymer, having approximately
the same chemical shift as the Si-CH$_2$-Si protons.

Elemental analysis of this product indicated the presence
of over 6% aluminum. In total, these results are consistent
with the incorporation of significant amounts of Al-H in the
polymeric product obtained from the non-aqueous workup. This
may be in the form of AlH$_x^{-[3-x]}$ species: either bound,
complexed, or trapped, within the polymer. Difficulty in
separating by-products of LiAlH$_4$ reductions of polymeric
halosilanes by non-aqueous methods has been previously
observed.

The reduced, branched, polycarbosilane polymer
represented by the "average" formula, [SiH$_{1.86}$Et$_{0.14}$CH$_2$]$_n$, on

heating under nitrogen, began to evolve gases and formed a
"gel" at about 200°C. GC/FTIR showed these gaseous
by-products were predominantly hydrogen, with smaller amounts
of methane, ethane, ethylene, propene, and mixed

5   methylsilanes. In addition, small amounts of volatile,
oligomeric hydridosilanes were produced. These results
suggest that some depolymerization occurred before extensive
crosslinking (presumably via Si-Si bond formation) occurred.
Continued heating to about 450°C gave a pale yellow, hard,

10   glassy solid with the evolution of more hydrogen and much
lesser amounts of hydrocarbons and silanes than in the earlier
stages of pyrolysis. Further heating yielded a shiny, hard,
black ceramic. TGA of the reduced polymer to 1200°C showed
about 60% ceramic yield without any special crosslinking

15   procedures. The theoretical yield is about 83%, assuming the
polymer formula, $[SiH_{1.86}Et_{0.14}CH_2]_n$, as suggested by NMR, IR
and elemental analysis. If the polymer is subjected to
heating at the crosslinking temperature prior to pyrolysis,
higher yields may be realized. Powder X-ray diffraction of

20   the black ceramic product formed at 1000°C, under N , showed
it to be nearly amorphous. Material heated to 1600°C for five
hours (under N_2) gave a XRD pattern consistent with
expectations for β-SiC.

        The Examples set forth herein, the Experimental Results,
25   and the discussion of those Experimental results are presented
to describe certain embodiments of the instant process and
should not be construed in a limiting sense for that reason.
The scope of protection sought is set forth in the claims
which follow.

We Claim:

1.   A process for forming a polycarbosilane precursor
for silicon carbide which comprises the reaction of a
polyhalocarbosilane with a reducing agent.

5   2.   A process as claimed in Claim 1 wherein the reducing
agent is lithium aluminum hydride.

3.   A process as claimed in Claim 1 wherein the
polyhalocarbosilane is a polychlorocarbosilane.

4.   A process as claimed in Claim 1 wherein the
10   polyhalocarbosilane is formed by reaction of a trihalo-
halomethylsilane with a Grignard coupling agent.

5.   A process as claimed in Claim 4 wherein the trihalo-
halomethylsilane is trichloro-chloromethylsilane.

6.   A process as claimed in Claim 4 wherein the Grignard
15   coupling agent comprises a mixture of magnesium metal and an
alkyl iodide.

7.   A process as claimed in any of Claims 1-6 wherein
the polyhalocarabosilane is modified by adding a vinyl group
to the polymer backbone.

20   8.   Branched polycarbosilane, substantially non-cyclic
precursors for silicon carbide having a substantially 1:1 Si
to C stoichiometry which comprise the repeating units

$$[H_2SiCH_2] \ [SiCH_2] \ [SiH_3CH_2].$$

9.   Precursors as claimed in Claim 8 formed by any of
25   the processes of Claims 1-6.

10.   Precursors as claimed in Claim 8 which contain
terminal -SiH$_3$ groups.

11.   Branched polycarbosilane, substantially non-cyclic
precursors for silicon carbide containing the repeating units:

$$[SiH_xCH_2] \; [SiH_{x-1}CH_2]$$
$$Ch=CH_2]$$
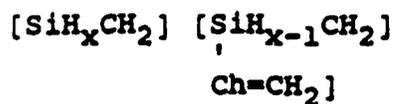
where x can range from __ to __.

CARBOSILANE POLYMER PRECURSORS
TO SILICON CARBIDE CERAMICS

ABSTRACT OF THE DISCLOSURE

Grignard coupling of trichloro-chloromethylsilane,
5   followed by reduction with lithium aluminum hydride, can be
employed to prepare a complex, branched polycarbosilane with
extensive Si-H functionality and a nominal 1:1 silicon to
carbon ratio. Direct pyrolysis of polycarbosilane material to
1000°C under nitrogen without any specific crosslinking
10   procedure, yields a black ceramic product. Annealing at
1600°C indicates ß-SiC as the crystalline phase present.

* * * * *

Cl$_3$SiCH$_2$Cl

Mg/
Et$_2$O

Cl$_3$SiCH$_2$MgCl $\xrightarrow{\text{3 MeOH}}$ [MeO]$_3$SiMe + HCl + MgCl$_2$

Cl$_3$SiCH$_2$Cl

-MgCl$_2$

Cl$_3$SiCH$_2$SiCl$_2$CH$_2$Cl $\xrightarrow{\text{5 MeOH}}$ [MeO]$_3$SiCH$_2$Si[OMe]$_2$CH$_2$Cl + 5 HCl

Cl$_3$SiCH$_2$MgCl

-MgCl$_2$

Mg/
Et$_2$O

Cl$_3$SiCH$_2$SiCl$_2$CH$_2$MgCl $\xrightarrow{\text{5 MeOH}}$ [MeO]$_3$SiCH$_2$Si[MeO]$_2$Me

+ 4 HCl + MgCl$_2$

+n Cl$_3$SiCH$_2$MgCl
$\xrightarrow{\hspace{3cm}}$ "[SiCl$_x$CH$_2$]$_n$"
-n MgCl$_2$
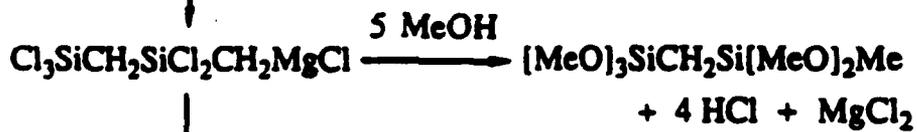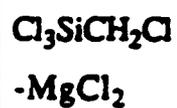
Compressive Creep of MoSi$_2$ Matrix and Composite

A. P. HYNES, M. S. WILENSKI AND R. H. DOREMUS

ABSTRACT

The creep of monolithic MoSi$_2$ matrix and a Nb-particulate composite were contrasted in uniaxial compression measurements from 1323-1724K and 10-100 MPa. Nb-particulate composites crept more rapidly than the matrix under all conditions tested. The composite creep rate decreased with time, and that of the matrix was linear with time within experimental error. The apparent creep activation energies were 232 kJ/mol for the matrix and 119 kJ/mol for the composite at 1667K. The stress exponents of the matrix and composite were 1.2 and 2.0 respectively. The flow of glass at the grain boundaries controlled the matrix deformation and the deformation of Nb contributed to the time-dependent, rapid creep of the composite.

INTRODUCTION

Recently [1-7] MoSi$_2$ has been tested as an advanced structural material because it has several promising characteristics such as: high melting point (2293 ±20K), excellent hot corrosion resistance, and oxidation resistance. The density (6.31 gm/cc) is below that of the Ni-based superalloys (~8 gm/cc). MoSi$_2$ undergoes a brittle-ductile transition at 1200-1300K and thus offers the prospect of toughness, but also unfortunately creep, at high temperatures. MoSi$_2$ has a tetragonal crystal structure and limited active slip systems below the ductile-brittle transition temperature. Thus in order to be useful as a high temperature structural material, the high temperature strength and creep resistance must be improved, as well as the low temperature toughness. In addition, the behavior in reducing atmospheres must be evaluated.

Published information on the creep behavior of either unreinforced MoSi$_2$ or MoSi$_2$ composites is quite limited. In one study, Bose [7,8] found creep rates from ~10E-8s^{-1} to ~10E-6s^{-1} at 20-100 MPa at 1473K for a MoSi$_2$ matrix without glass and with a grain size of 30 μm. In a second study Sadananda et al [1,2] found creep rates of ~5E-8 to 1E-6S^{-1} at 1473K and 60-200 MPa for a MoSi$_2$ matrix containing glass with a grain size of 10-35 μm. The addition of 20 v/o SiC whiskers reduced the creep rate of

Rensselaer Polytechnic Institute, Troy, NY 12180-3590.

$MoSi_2$ significantly, although at least some of the reduction is due to the elimination of the glassy phase from the composite. Sadananda et al determined apparent creep activation energies of 430 kJ/mol for the monolithic material at 1373-1573K and 590 kJ/mol from 1473- 1723K for the composite at 20 MPa stress. The stress exponent was ≈3 for the matrix at ≈20-100 MPa and 1473-1673K [2].

Although ductile microphases can decrease the creep resistance, they should improve the fracture resistance relative to the matrix; continuous ductile fiber may improve creep resistance as well. Meschter and Schwartz [6] have surveyed the available metals for ductile reinforcement on the basis of melting point, availability, cost and thermodynamic compatibility with $MoSi_2$. They found the most promising pure metals to be Nb and Ta. Although Nb reacts more rapidly with $MoSi_2$ than Ta does [6], Nb has the advantage of a higher melting temperature, a lower elastic modulus, lower density and a lower cost.

It was a goal of the project to improve the fracture resistance of $MoSi_2$, and thus a ductile metal reinforcement was chosen. Despite concerns about reactivity, Nb was selected over Ta as likely to be superior on balance for the reasons listed above. As a preliminary study until coated Nb-wire-reinforced composite samples were available, the creep behavior of dispersed particulate-Nb composite was evaluated relative to the monolithic (matrix) material.

EXPERIMENTAL PROCEDURE

Sample Preparation

The matrix samples were prepared by loading loose powder (Starck, Grade C) into a Nb can and hot-isostatically pressing (HIP) at 1873K for 2 h at 170 MPa. The composite powders of target composition 75 w/o $MoSi_2$-25 w/o Nb (79 v/o $MoSi_2$-19 v/o Nb) were mixed in a turbula mixer, then cold-isostatically-pressed at 240 MPa and hot isostatically pressed at 1773K for 2 h at 170 MPa.

The pressed compacts were sectioned, cut by EDM into right circular cylinders 3.18 mm (1/8") diameter x 6.35 mm (1/4") high. The sides of the cylinders were polished through various grits from 600 grit SiC through 1200 grit SiC, and the ends were polished parallel through 1 μm diamond paste for creep testing.

Characterization

The phase compositions were determined by X-ray diffraction, electron microprobe and stereology of scanning electron micrographs (SEM). The $MoSi_2$ and SiO_2 phase contents of the matrix were also calculated from the $MoSi_2$ powder lot analysis. Electron microprobe analyses were performed on the monolithic and composite crept and uncrept samples. The microprobe analyses used elemental Mo, Si and Nb standards and the ZAF analysis technique, and were run at 20 kV. Phase analysis of the $MoSi_2$ matrix, of the composite and of the as-received $MoSi_2$ powder were made with an X-ray diffractometer equipped with CuK_α radiation and operated at 40 kV. The diffractometer calibration was

checked before each run with a standard.

The microstructures of the uncrept and crept samples were examined with SEM after polishing through 1 μm diamond paste and thermal etching at 1773K for 2 minutes. Backscattered compositional imaging highlighted the variation in chemical composition. The grain size of the crept and uncrept samples was measured by the linear intercept method with a digitizing pad, and is reported as the inverse of the specific surface area. A minimum of 100 points were taken per sample.

The density of the crept and uncrept samples was determined by the Archimedes method with distilled water.

Vickers hardness was measured using a 1000 gm load for 10s at room temperature in air on samples freshly polished through 1 μm diamond paste. For the matrix and composite, twenty measurements were made per sample, and 5 measurements each were made on the reaction zone and the Nb particles.

Creep Equipment, Procedure and Analysis

Dead-load uniaxial compression creep tests were performed at temperatures of 1323-1724K (1050-1450C) and stresses of 10-100 MPa in air with equipment and methods that have been described previously [9]. The data acquisition is via PC and can be remotely accessed by modem. Two types of experiments were performed: (1) change in stress at constant temperature, and (2) change in temperature at constant stress. Tests were run in order of increasing load and temperature in order to minimize the effects of transients.

Trial least-squares fits were made to several equations to find a satisfactory fit for for the strain-time data of the matrix and composite. The steady-state creep rates for the matrix and the creep rates at 0.5% strain for the composite were calculated from these fits. The apparent creep activation energies were calculated from the slope of the creep rate vs reciprocal temperature plots. Stress exponents were calculated from the log-log slope of the strain rate vs stress plots.

RESULTS
Chemical and Phase Composition

The lot analysis supplied with the MoSi₂ powder showed that excess Si was present over that required to form stoichiometric MoSi₂. Consequently we expected a significant volume fraction of SiO₂ glass. A phase which was chemically and topographically distinct (after thermal etching) from the matrix was identified at the grain boundaries and inside the grains of the MoSi₂, as shown in Figure 1. This phase was identified by microprobe as an SiO₂ phase and the composition was pure SiO₂ within the microprobe detection limits. In the matrix, the SiO₂ content was calculated to be 9.7 v/o (3.6 w/o) from the lot analysis, and was measured to be 10.2 v/o from stereology. The lot analysis calculation assumed that all the excess Si over the stoichiometric amount needed for MoSi₂ was oxidized to SiO₂ glass. MoSi₂ was the only phase detected by X-ray diffraction in the as-received powder and in the pressed uncrept matrix, so the SiO₂ phase detected optically and by SEM is SiO₂ glass.
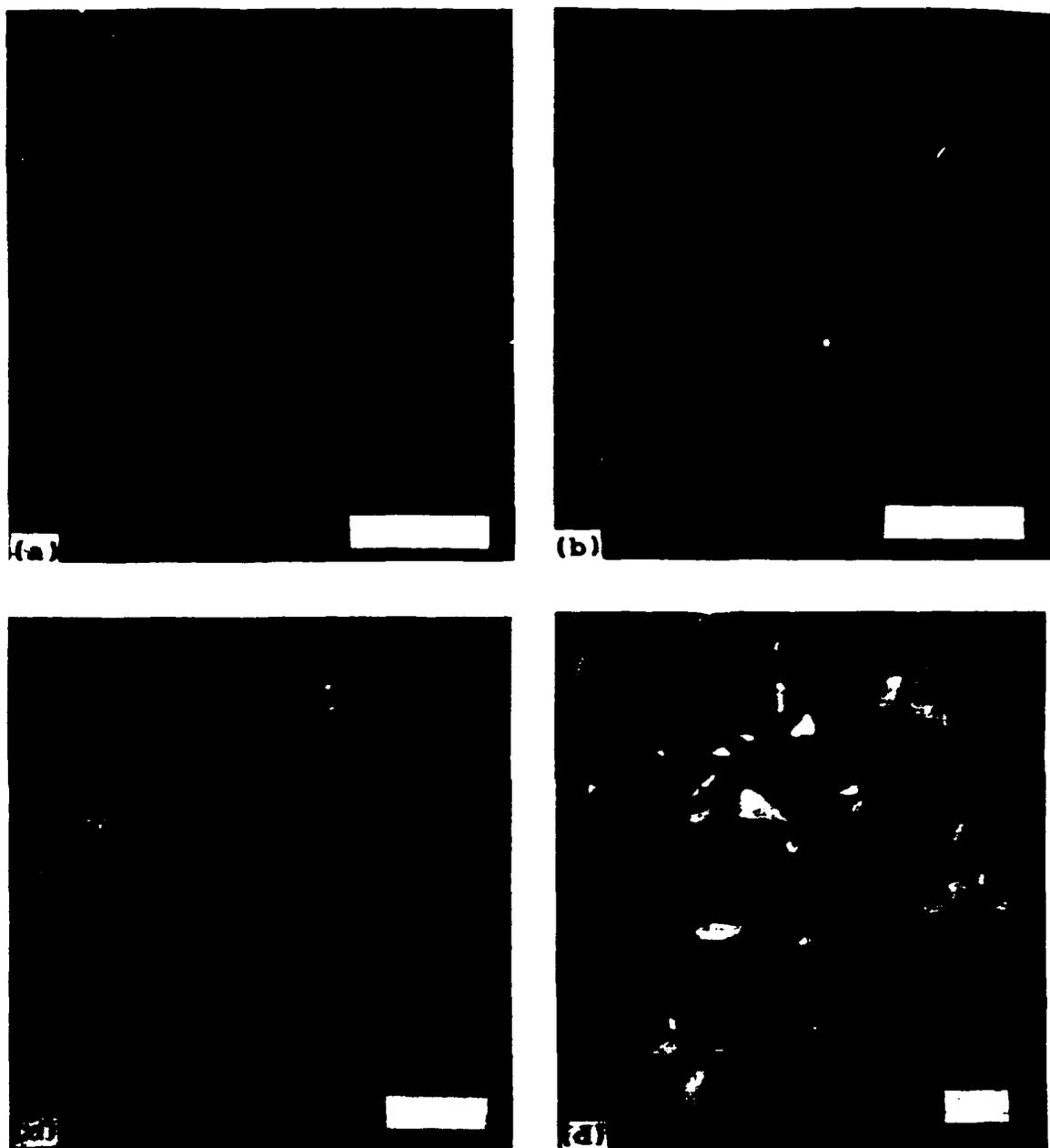
Fig. 1. Matrix and composite microstructures: (a) SEM micro-
graph showing topographic contrast between SiO_2 glass and $MoSi_2$
in matrix. (b) same area showing chemical contrast.
(c) optical micrograph of uncrept matrix. (d) optical micro-
graph of uncrept composite. Bar is 10 μm in (a) and (b);
75 μm in (c) and 150 μm in (d).

The glass was calculated to be 7.8 v/o of the composite from the lot analysis, assuming the target starting composition. The glass was present in the matrix and the composite both before and after creep. In addition to the $MoSi_2$, Nb and glass, the composite samples both before and after creep contained a reaction layer around the Nb particles samples as shown in Figure 2. The thickness of the reaction layer did not increase significantly during creep. The composition of the reaction layer was 84.6 w/o Nb-15 w/o Si according to microprobe spot analysis, which corresponds to Nb_5Si_3. An elemental analysis by microprobe, in the form of a step scan across the reaction zone, found Nb, Mo, Si and O (˜5 w/o) in the reaction zone, as shown in Figure 2. The step scan results for an uncrept sample were essentially identical to those of a crept sample. The following phases were identified in the composite by X-ray diffraction: $MoSi_2$, Nb, Mo_5Si_3, Nb_5Si_3 and Nb_3Si. Low intensity (<50 counts/s) diffraction peaks at d-spacings of 1.920 and 1.910 Å could not be assigned.

The composite consisted of 8 v/o unreacted Nb, 20 v/o reaction zone and 72 v/o matrix (including glass) according to stereographic measurements. From the target composite composition and accounting for the SiO_2 phase, the target 19 v/o Nb in the composite was met.

Although the as-prepared uncrept samples were shiny and metallic gray in color, the monolithic samples were a dull gray color after creep. The outer surfaces of the composite samples were covered with a yellowish-green powder after creep. The powder was easily scraped off for X-ray diffraction, which detected the following phases: $MoSi_2$, α-SiO_2, Nb_2O_5, $Nb_{12}O_{29}$, Nb and MoO_3.

Microstructure and Physical Properties

The microstructure of the matrix samples consisted of approximately-equiaxed $MoSi_2$ grains with well-dispersed elongated stringers of the SiO_2 glass at the grain boundaries and within the grains. The average grain size was 23 μm in the uncrept monolithic samples and 24 μm in the composite. Creep testing did not change the grain sizes significantly.

The Nb particles were irregularly shaped, and randomly distributed and oriented in the composite. The microstructures of the matrix and composite are shown in the optical micrographs of Figure 1 and the SEM micrograph of Figure 2. The grain boundaries showed a pronounced curvature. After creep the microstructure of the matrix showed an increase in SiO_2 segregation at the grain boundaries. The microstructure of the composite appeared essentially unchanged during creep.

The densities of the uncrept monolithic and composite samples were ˜5.93 and ˜6.33 gm/cc, or ˜100 %TD for both the matrix and composite on the basis of the phases $MoSi_2$, SiO_2 glass and Nb, and assuming 9.7 v/o SiO_2 glass in the matrix. For the composite, this is a slight overestimate of the theoretical density, since it does not account for the reaction zone.

The hardness of the composite was 10.0 ±1.0 GPa (1024 VHN) and that of the matrix was 8.7 ±0.4 GPa (889 VHN). The hardness
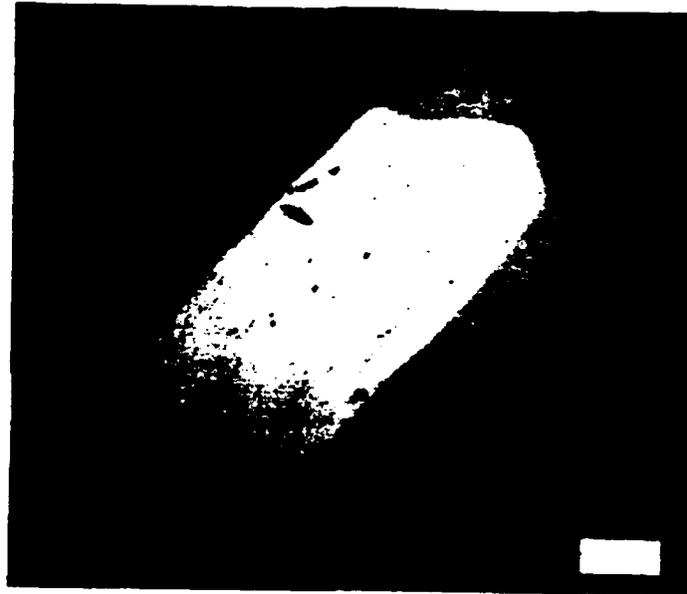
(a)
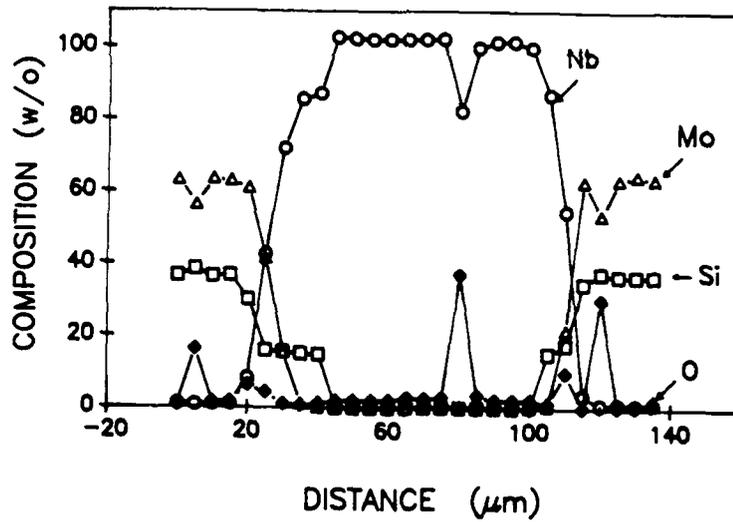
(b)

Fig. 2. Composite showing reaction zone between Nb and MoSi$_2$: (a) micrograph showing Nb particle with reaction zone. Bar is 25 μm. (b) compositional profile across micrograph shown in (a).

of the Nb particles in the composite was 3.6 ±0.8 GPa (366 VHN) and that of the reaction layer between the Nb and $MoSi_2$ was 10.9 ±1.2 GPa (1113 VHN).

Creep

The creep rate of the $MoSi_2$/Nb composite was significantly faster than that of the $MoSi_2$ matrix under all conditions tested. The creep rates of the monolithic material and the composite are shown as a function of temperature and stress in Figure 3.

The shape of the strain-time curves for the matrix and composite differed significantly. Except for short transients at the start of a new test condition, the matrix creep curve was linear with time for the test durations observed, within the measurement and fitting error. In contrast, the composite samples exhibited a creep rate that continuously decreased with time under all conditions tested. A few tests which were run to high strain (>10%) exhibited an accelerating creep rate prior to failure and these results are not reported here. None of the strain-time data for composites could be satisfactorily fit to a straight line. Consequently the strain rate was calculated from the derivative of the expression fit to the strain-time data, evaluated at 0.5% strain.

Several expressions were examined on test sets of data to evaluate their suitability for the composite. Polynomials with integral exponents give unsatisfactory fits. Log-log plots of the data did not yield time exponents which were consistently valid for a number of test conditions. Polynomial expressions in $t^{1/3}$ were examined and fit the data well, Expressions of the form:

$$a_0 + a_1 t^{1/2} + a_2 t \qquad (1)$$

were also examined, and gave a better fit than the other expressions in almost all cases on the basis of the sum of the squares of the residuals. Consequently expression (1) was used to calculate the strain rate at 0.5% strain for the composite data, and this data is plotted in Figure 3.

The apparent creep activation energies are 232 kJ/mol for the $MoSi_2$ matrix and 119 kJ/mol for the $MoSi_2$/Nb composite at 10 MPa. The stress exponents are 1.4 for the matrix and 2.0 for the $MoSi_2$/Nb composite at 1667K (1394C).

DISCUSSION

The flow of glass at the grain boundaries is known to control the creep rate in a variety of materials, and the elimination of a glassy grain boundary phase decreases the creep rate [10]. If the flow of the glass at grain boundaries controls the creep rate, elimination of the glass by use of purer starting powders or by crystallization of the SiO_2 glass should decrease the creep rate of the matrix.

The stress dependence measured for the matrix, n=1.4, is lower than that measured by Sadananda (n=3) [2], but in the range typically observed for ceramics (n=1-3) [10]. A stress exponent of 1.4 is close to the Newtonian exponent of 1.0
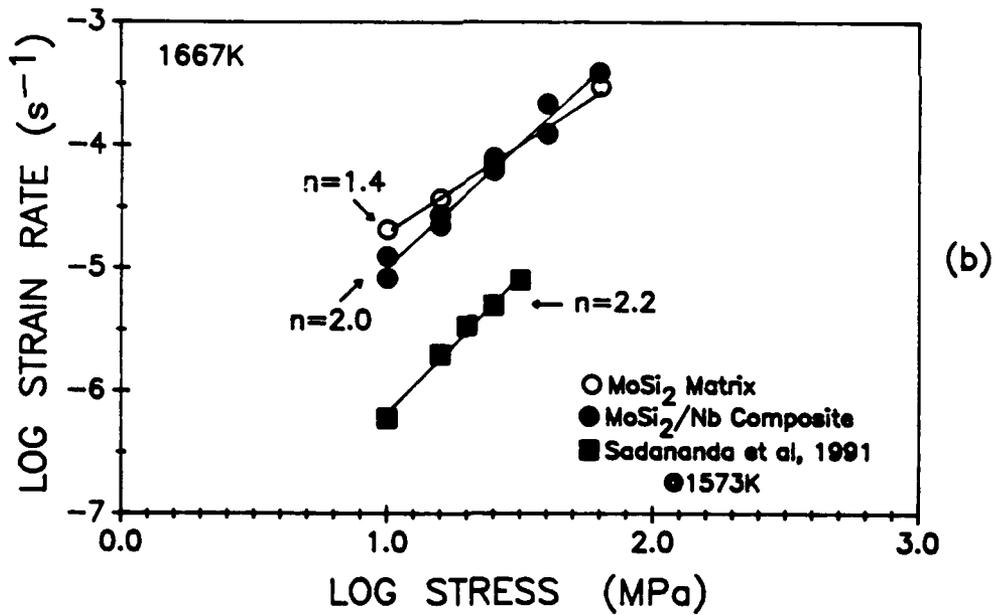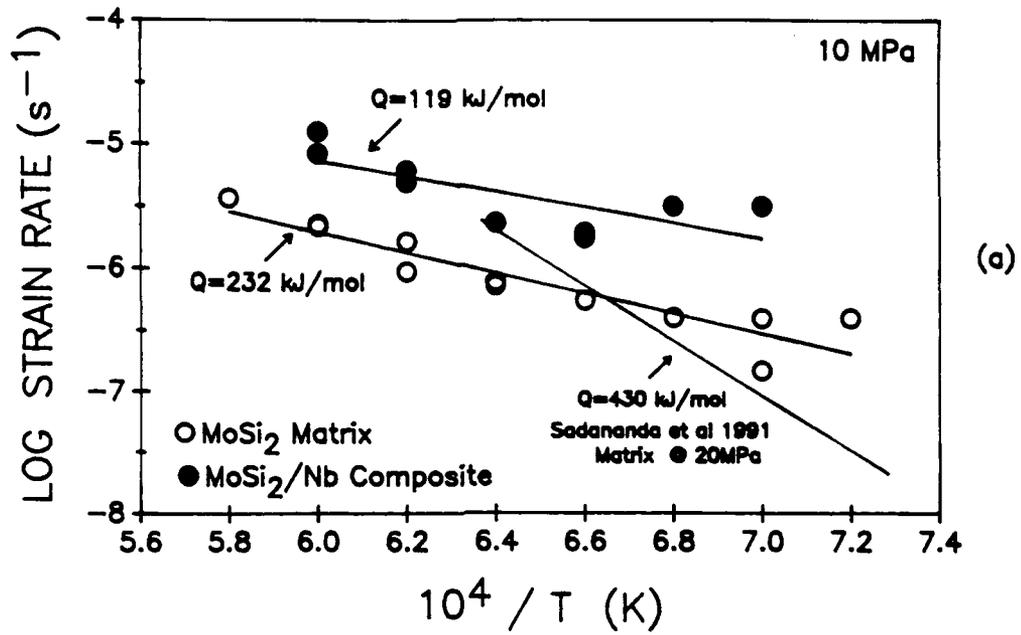
Fig. 3. Creep data: (a) creep rate as a function of temperature. (b) creep rate as a function of stress.

598

expected for viscous flow. Slight deviations from Newtonian behavior are usually attributed to interface limitations.

The matrix creep rates measured in the present work are on the same order of magnitude as those reported by Sadananda et al [1,2] over the same temperature range, at similar stresses (10 MPa versus 20 MPa) and for material of similar grain size. The exact amount of glass in the samples of Sadananda was not reported, so small differences in the creep rates may be due to differences in the glass content or composition.

The activation energy for viscous flow in fused SiO_2 is higher (711 kJ/mol) than the observed activation energy for flow in the matrix (232 kJ/mol). Small amounts of alkali oxides or hydroxyl groups can lower the activation energy slightly. For example, 0.1 w/o hydroxyl ion only lowers the viscosity of fused silica to ⁻500 kJ/mol [11]. Consequently the presence of such impurities may have lowered the activation energy of the grain boundary glass, but it is unlikely to lower it to the low value observed here. The matrix activation energy found here is significantly lower than that reported by Sadananda (430 kJ/mol) [2]. The activation energies for diffusion in $MoSi_2$ are unavailable.

The matrix may have softened slightly during testing because of the increased segregation of the SiO_2 glass to the grain boundaries during the test. The tests were run in order of increasing temperature, which could produce an activation energy lower than that of the matrix containing SiO_2 glass in a static microstructure.

Sadananda et al [2] found dislocation subboundaries in their crept matrix samples. Plastic flow inside the grains and a lower total glass content in their samples could account for the fact that they obtained a higher activation energy and a higher stress exponent than that measured here.

The fast creep rates of the $MoSi_2$/Nb composite mean that it is not attractive for high temperature structural applications. The Nb is responsible for the faster creep rate, and for the time-dependent strain rate, either due to the creep of the Nb particles themselves or because of the deformation of the reaction zone. Meschter [6] had suggested that a Nb particulate composite might have low toughness due to the formation of a brittle $(Mo,Nb)_5Si_3$ reaction zone with a weak interface which does not permit ductile-phase crack bridging. No cracking was observed at the reaction zone, and neither the particles nor the reaction zone were visibly deformed.

Niobium's creep rate is strongly time-dependent, exhibiting a $t^{1/3}$ dependence [12]. The creep rate of the composite is also time dependent, and was found to fit equation (1) which contains a $t^{1/2}$ term and a term linear with time. A term in $t^{1/3}$ plus a linear time term also gave good fits. The $MoSi_2$/Nb creep may be the sum of the linear $MoSi_2$ deformation and the time dependent Nb (and possibly reaction zone) creep.

The minimum creep rate of Nb (⁻200 μm grain size) is on the same order as the creep rates of the $MoSi_2$ matrix for the same temperature and stress range. The creep rate of the $MoSi_2$/Nb composite is faster than the minimum Nb creep rate. Nb creep

rates at small strains, such as measured in this work, are faster than that creep rates measured at large strains, so the faster creep rates of the composite relative to the matrix may be caused by the very rapid initial creep rate of the Nb.

Niobium has a stress exponent of 7.2 [12], so Nb could contribute to higher stress exponent of the composite (2.0) relative to the matrix (1.4). The stress exponent in the present work is slightly lower than the value of ~3 reported by Sadananda [2] for comparable stresses and temperatures.

On the other hand, the creep activation of Nb calculated from the minimum creep rates is 162 kJ/mol which is lower than the $MoSi_2$ matrix value of 232 kJ/mol. If the Nb deformation controls the creep rate, one might expect the composite's activation energy (119 kJ/mol) to be smaller than that of the matrix, but not smaller than that of Nb as is observed here.

ACKNOWLEDGEMENTS

REFERENCES

1. K. Sadananda, H. Jones, J.Feng, J.J.Petrovic, A.K. Vasuderan, "Creep of Monolithic and SiC Whisker Reinforced $MoSi_2$", to be published.
2. K. Sadananda, private communication, 3/91.
3. T.C. Lu, A.G. Evans, R.J. Hecht, R. Mehrabian, Abstract #25-C-91F, 15th Ann. Conf. Compos. Adv. Ceram., Jan. 13-16, 1991, Cocoa Beach, FL.
4. P.J. Meschter, "Oxidation Kinetics of $MoSi_2$ and $MoSi_2$ Reinforcement Mixtures", in High Temp. Intermetallics IV., MRS Conf. Proc. published as vol.213, ed. L.Johnson, J.Stiegler, D.Pope, in press.
5. J.J. Petrovic, R.E. Honnell, T.E. Mitchell, "ZrO_2 Reinforced $MoSi_2$ Matrix Composites", Abstract #24-C-91F, 15th Ann. Conf. Compos. Adv. Ceram., Jan. 13-16, 1991, Cocoa Beach, FL.
6. P.J. Meschter, D.S. Schwatrz, "Silicide-Matrix Materials for High Temperature Applications", J.O.M., Nov, 1989, 52-55.
7. S. Bose, "Creep of Molybdenum Dilicide", Abstract #41-C-91F, 15th Ann. Conf. Compos. Adv. Ceram., Jan. 13-16, 1991, Cocoa Beach, FL.
8. S. Bose, private communication, 3/91.
9. A.P. Hynes, R.H. Doremus, "High Temperature Compressive Creep of Polycrystalline Mullite", to be published.
10. W.R. Cannon, T.G. Langdon, "Review Creep of Ceramics", J.Mater. Sci., 18(1983)1.
11. R.H. Doremus, Glass Science, Wiley-Interscience Pub., 1973, p.106.
12. J.B. Conway, P.N. Flagella, "Creep Rupture Data for the Refractory Metals to High Temperatures", G.E. Report #R-69-NSP-9, 1969.

journal

Mullite Processing, Structure, and Properties

J. Am. Ceram. Soc. 74 [10] 2469-75 (1991)

High-Temperature Compressive Creep of Polycrystalline Mullite

Anne P. Hynes* and Robert H. Doremus*

Department of Materials Engineering, Rensselaer Polytechnic Institute, Troy, New York 12180-3590

Aluminosilicates of three compositions with mullite as the major phase were synthesized by a sol-gel process and characterized with bulk and microchemical analyses and microstructural observation. An apparatus for measuring the compressive creep up to 1900 K with a sensitivity of ± 1 μm was constructed and used to measure the creep of single-phase mullite, mullite with second-phase glass, and mullite with second-phase corundum. Measurements in air at stresses of 15 to 100 MPa and temperatures of 1471 to 1724 K determined that samples with second-phase glass crept more rapidly than single-phase mullite or mullite with second-phase corundum. The apparent creep activation energies determined at 100 MPa were 742 kJ/mol for the mullite containing glass, 819 kJ/mol for the single-phase mullite, and 769 kJ/mol for the mullite with second-phase corundum. The stress exponents determined at 1724 K were 1.6 for the mullite plus glass, 1.5 for the single-phase mullite, and 1.2 for the mullite with α-Al$_2$O$_3$. The creep behavior of the aluminosilicates containing glass were consistent with rate control by the viscous flow of the glass and the measured creep rates were in good agreement with creep rates calculated from a model by Dryden. The creep behavior of the completely crystalline aluminosilicates was consistent with rate control by diffusional creep. [Key words: creep, aluminosilicates, mullite, corundum, glass.]

I. Introduction

MULLITE is a well-known refractory and an uncommon mineral, named for the Island of Mull, Scotland.[1] The compositional bounds of mullite extend from 3Al$_2$O$_3\cdot$SiO$_2$ to 3Al$_2$O$_3\cdot$SiO$_2$ (3:2 and 2:1 mullites).[2] Mullite has several attractive characteristics as an advanced structural material, such as chemical stability with oxygen at high temperature. Assessment of the high-temperature mechanical properties including creep behavior is critical to determining its suitability.

Mullite has traditionally been derived from the decomposition of clays or minerals such as kyanite, resulting in a product that contains glass and impurity oxides, which can degrade the high-temperature properties. However, a number of workers[3-8] have developed methods of producing fine, pure, glass-free, and/or stoichiometric mullite powder. Most of the older work on the creep of mullite dealt with refractories containing glass and other phases and therefore is not directly relevent. There has been a recent flurry of interest in mullite's mechanical properties[6-8,10,11,13-16,18,29,30] after the intriguing work by Lessing *et al.*[6] on a sol-gel mullite which found a creep rate lower than that of alumina at the same grain size, stress, and temperature. Creep work to date has been mainly in flexure,[9-12] although three groups have reported work in

compression[13-15] and one oral report was made of creep in tension.[16] A wide range of activation energies from 357 to 1051 kJ/mol have been found for various aluminosilicate compositions at stresses of 0.2 to 300 MPa.[9-15] Stress exponents close to 1.0 have been reported in several studies, although a range from 0.6 to 2.0 have been reported.[9-15,29] Grain size exponents of 1 to 3.7 have been determined over testing temperatures of 1450 to 1788 K.[11,13,29,30]

Compression tests were chosen for the present work because flexural tests present special difficulties in interpretation[18,19] and tension tests require relatively large samples and/or expensive machining. Their main inconvenience is friction at the platens, which leads to inhomogeneous deformation and barreling. These effects become more pronounced at higher strains, so the strain was maintained at less than 5%. Significant scatter in creep results obtained by different laboratories on material which is nominally the same may occur for a myriad of reasons, including small differences in sample composition, microstructure, processing or in the test procedures themselves. Therefore, the samples were extensively characterized and the characterizations and procedures described in detail.[20,21] In the present work, three mullite compositions were produced by sol-gel methods and tested: one single-phase, one containing glass, and one containing second-phase corundum. The mullites were characterized by X-ray diffraction, chemical and physical analyses, and microstructural observation. The results of creep tests on sintered samples between 15 and 100 MPa and temperatures of 1471 to 1724 K are reported here. Subsequent reports will deal with the creep of single-crystal mullite and mullite creep literature.

II. Experimental Procedure

The main points of the experimental procedure are noted here. Additional information about the equipment, test procedure, and sample preparation is found elsewhere.[20,21]

(1) Equipment

A high-temperature compressive creep tester was built for this work, capable of applying loads of 35 to 300 lb (15 to 400 MPa) in air at temperatures between 1300 and 1900 K, and measuring the deflection accurately to 1 μm. Factors such as frame rigidity, freedom from vibration, transducer noise, drift and calibration, and temperature control were considered in the design. The transducer measured only the sample shortening. The tests were constant-load, and the load was applied as dead load. Data aquisition is computer-controlled* and can be accessed via a modem[†] by a remote personal computer.[‡]

(2) Sample Preparation

Aluminosilicate powders of three compositions in the vicinity of mullite were synthesized with slight variations[21] from a procedure detailed elsewhere.[22] The primary starting

---

components were $Si(OC_2H_5)_4$[3] and $Al_2O_3 \cdot 1.3H_2O$.[4] The dried powder was either uniaxially cold pressed at 276 MPa (40 ksi) into flat 12.7 mm (0.5 in.) diameter pellets for analyses or isostatically cold pressed at 310 to 345 MPa (45 to 50 ksi) into cylindrical pellets to be used as creep samples The pellets were sintered in air according to the following schedule: 298–373 K at 300 K/h; 373–1598 K at 100 K/h; 1598 K, hold 12 h; 1598–1873 K at 100 K/h; 1873 K hold 2 h; 1873–298 K at 100 K/h (furnace cool).

Creep samples consisting of right circular cylinders 5 to 8 mm high and either 3 or 4 mm in diameter were cut** from the pellets. The ends of the sample were polished parallel with a special polishing jig, and the sides were polished to 600-μm SiC.

(3) Testing Procedure

The weight of the load train (3 to 10 MPa stress) was applied to the sample, then the furnace was heated to 1473 K over 3 to 4 h and equilibrated overnight. Two types of experiments were performed: (1) change in stress at constant temperature and (2) change in temperature at constant stress. Tests were made in order of increasing stress and temperature to reduce the effects of transients. A minimum of 0.3% strain, and usually 0.4% to 0.5% strain, was measured at each condition. The total strain for one sample was usually <3% and never exceeded 5%. For a temperature increase, the temperature setpoint was increased with the load on the sample, and the data collection commenced as soon as the temperature reached the setpoint. For a stress increase, a jack was used to support the weight while bricks were added to the platform. The amount of time required to change temperatures or stresses was usually less than 3 min and was no more than 7 min in any instance.

High-temperature deflection tests were also made without a sample in order to evaluate equipment transients resulting from a change to new conditions. A small piece of the SiC platen material was placed between the platens during these runs.

(4) Data Analysis

Stress was calculated as engineering stress from the initial area and the weight applied. No correction was made to the stress for the change in cross-sectional area during the run. Strain was calculated as true strain from the initial height and the calibration relation between deflection and voltage. The log of the strain rate was plotted versus strain to determine the onset of the apparent steady-state creep. The creep rate was determined by a straight-line fit to the true-strain vs. time data within this latter region.

No correction was made to the creep for the nearly undetectable ($\leq 0.2 \mu$m) increase in grain size that occurred during some of the creep runs. This point is covered further in the Results and Discussion sections.

Since the samples contained $\leq 1\%$ porosity by stereology, and since no change in density due to creep was detected, no porosity correction was made to the creep data.

(5) Characterization Techniques

The chemical compositions of the powders and the phase compositions of the sintered compacts were determined by several techniques. The density, grain size, and microstructure of the uncrept and crept samples were evaluated. In addition, characterization of the powders' appearance in SEM, phase content, and BET surface area was performed.

Chemical composition was determined by plasma emission spectroscopy,[††] electron microprobe,[‡‡] and X-ray fluorescence

(XRF).[§§] Phase composition was determined by (1) X-ray diffraction[¶¶] and transmission electron microscopy (TEM)[***] with electron diffraction; (2) the lever rule, using the chemical composition and the phase diagram;[††] and (3) stereology of scanning electron micrographs (SEM). Phase analysis of sintered creep samples and of powder heat-treated at 373 to 1873 K used an X-ray diffractometer equipped with $CuK\alpha$ radiation. The surface area of unpressed (uncompacted) powders heat-treated between 298 and 1873 K was measured with a sorptometer[***] using N_2 absorption. The microstructure of calcined powder, and that of the uncrept and crept samples, were examined with an SEM[‡‡‡] following polishing through 1-μm diamond and thermal etching at 1773 K for 2 h. The grain size of crept and uncrept samples was measured by the linear intercept method with a digitizing pad,[§§§] and is reported as the inverse of the specific surface area. Longitudinally sectioned transmission electron microscopy specimens were prepared by mechanically thinning, dimpling, and ion beam milling. The density of crept and uncrept samples was determined by the Archimedes method with distilled water and was compared with the point-counting of pores in SEM micrographs. Vickers hardness was measured[¶¶¶] at room temperature in air with a load of 10 g on samples freshly polished through 1-μm-diamond paste.

III. Results

(1) Uncrept Samples

The BET surface area of the uncompacted powders decreased from ~360 m^2/g "as-dried" to 10–20 m^2/g after a 2-h hold at 1873 K. The surface area of the three compositions was the same.

As shown in the X-ray diffractograms of Fig. 1, boehmite was found in the dried gel. After heat treatment at 1598 K, the trace exhibited a well-defined mullite pattern, and the peaks became sharper after the sintering step at 1873 K. Mullite was identified in all three compositions, and corundum in the 77 wt% composition after heat treatment at 1598 K. No other crystalline phases were observed by X-ray diffraction.

The un-heat-treated powder and the powders heated up to 1273 K had a botryoidal appearance. The powder subsequently heated to 1873 K for 2 h was relatively smooth.

The chemical and phase compositions and some microstructural properties of the sintered samples are shown in Table I. The average chemical compositions were 67.7(8), 73.0(5), and 77.0(4) wt% Al_2O_3. The results from different techniques agreed within experimental error. The 68 wt% composition contained 3 to 8 wt% glass (assuming the eutectic glass composition) and the 77 wt% composition contained 10 wt% α-Al_2O_3 according to both the phase diagram[††] and stereology. An estimate of the chemical homogeneity is obtained from the standard deviation of the microprobe results, assuming the density to be uniform on the scale of the beam size (~20 μm). The single-phase polycrystalline sample was the least homogeneous, with a standard deviation of ± 2.3 wt% Al_2O_3. The homogeneity of the other two compositions was similar, with microprobe standard deviations of 0.9 to 1.0 wt% Al_2O_3.

The hardnesses were 9.2 to 9.6 GPa for the three compositions.

TEM and electron diffraction revealed mullite in all three sintered compositions. The grain boundaries of the 68 wt% composition were surrounded by a glassy phase and elongated

[†]99+%, Aldrich Chemical Co., Milwaukee, WI.
[‡]CATAPAL B Boehmite, 99.5+%, VISTA Chemical, Houston, TX.
[**]Model 360 disk cutter, South Bay Technology, Temple City, CA.
[†]Galbraith Laboratories, Knoxville, TN.
[‡‡]JEOL 733 Superprobe, JEOL Ltd., Peabody, MA.

[§§]Rigaku 3370 spectrophotometer with Rh target, Rigaku, Japan.
[¶¶]Philips APD 3520 diffractometer, Philips, Mahwah, NJ.
[***]Philips model CM12, Philips.
[***]Multipoint Brunnauer, Emmett, Teller (BET) Sorptometer, No. QS10, Quantichrome Corp, Syosset, NY.
[‡‡‡]AMRAY 1000 scanning electron microscope, AMRAY, Bedford, PA.
[§§§]Houston Instruments #1011, Austin, TX.
[¶¶¶]LECO Model M400 indenter, St. Joseph, MI.
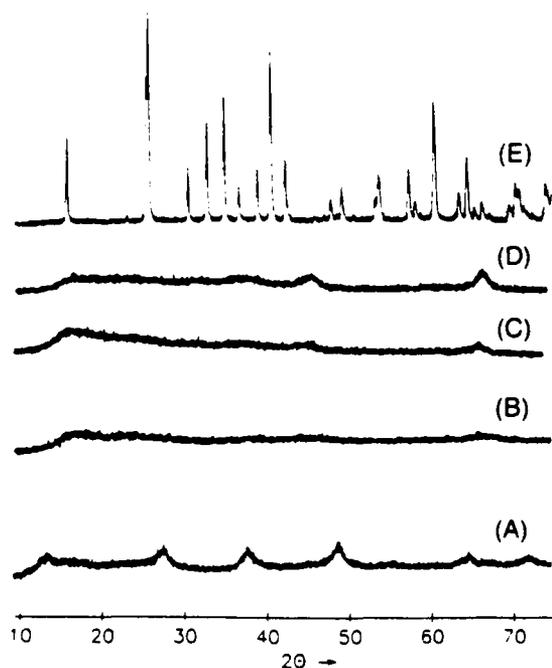
Fig. 1. X-ray diffraction trace of powder after heating at various temperatures. (A) unheated gel, (B) 773 K for 1 h, (C) 1273 K for 1 h, (D) 1273 K for 12 h, (e) 1873 K for 2 h.

corundum grains were identified in the 77 wt% composition. No other phases were observed by electron diffraction. Glass was not found in the 73 or 77 wt% compositions at the triple points or grain boundaries at a scale of 10 nm. Small faceted pores or pockets which may have originally been filled with glass were observed by TEM and SEM in the center of approximately 5% of the grains of all three compositions. The pores or glass pockets were typically found in the largest grains. Intergranular porosity was occasionally observed.

According to the Archimedes method, the densities were 98% theoretical for the 68 and 73 wt% compositions and 97% theoretical for the 77 wt% composition. By stereology, however, the densities were higher; ≤1% porosity was measured by point counting, and the latter measurement should be more accurate.

Typical microstructures of uncrept samples obtained with SEM are shown in Fig. 2 and TEM micrographs are shown in Fig. 3. The mullite grains in the 68 wt% composition were smooth, rounded, surrounded by glass and had an average mullite grain size of 0.96 μm. The mullite grains in the 73 and 77 wt% compositions were mostly equiaxed, with rare elongated grains. The average mullite grain sizes were 0.74 and 0.82 μm, respectively. The standard deviation of the grain sizes ranged from 0.15 to 0.40 μm. The grain boundaries in the 73 and 77 wt% compositions were smooth, and either flat or very slightly curved. In the 77 wt% composition, the intergranular corundum grains were approximately 5 μm long and 0.5 to 1.0 μm in diameter. TEM of the uncrept samples revealed dislocations in some grains, often associated with the intragranular defect.

Table I. Some Chemical and Microstructural Properties

Al$_2$O$_3$ (wt%)		Phases present	Amount second phase	Average mullite grain size (μm)
Nominal composition	Chemical analysis*			
68	67.7(8)	m + g	5.9 ± 2.5	0.96
73	73.0(5)	m	0.0	0.74
77	77.0(4)	m + α	10.5 ± 2.5	0.82

*Average of results of XRF, microprobe, and phase emission spectroscopy. m = mullite, g = glass, α = corundum. †Calculated from phase diagram.
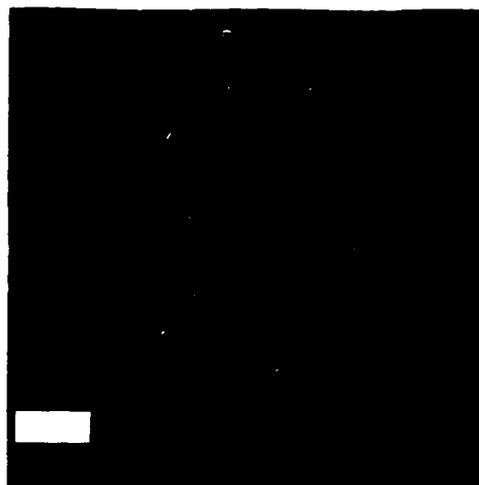
(A)
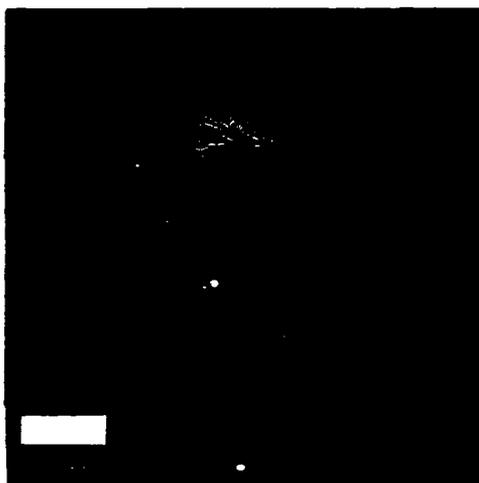
(B)
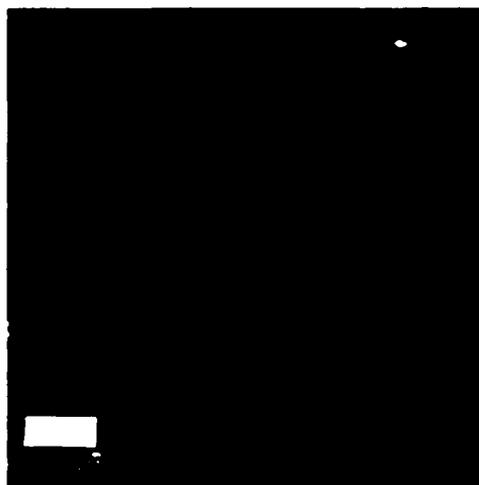
(C)

Fig. 2. SEM Micrographs of uncrept samples (A) mullite plus glass, (B) single-phase mullite, (C) mullite plus α-Al$_2$O$_3$.

(2) Crept Samples

A change in density due to creep was not detected. The average grain sizes for a given composition either did not change or increased slightly during the creep tests. Typi-

(A)

(B)

(C)

Fig. 3. TEM micrographs of samples: (A) uncrept 68 wt% Al₂O₃ composition showing glass at grain boundaries and triple point, (B) crept 73 wt% Al₂O₃ composition showing grain boundary, (C) crept 77 wt% Al₂O₃ composition showing elongated corundum grain.

cal increases (determined by averaging all samples of a given composition) were on the order of 0.1 μm. These results are consistent with other grain growth and densification measurements.

Pronounced microstructural changes due to creep were not detected with SEM. In TEM, crept samples exhibited somewhat higher dislocation densities than the corresponding uncrept samples, but dislocation densities were low. In all three compositions, the dislocation densities were highest in the largest grains and were associated with the pores or glass in these grains. Dislocations were not found in the mullite grains surrounding the corundum grains in the 77 wt% composition, as shown in Fig. 3(C). Intergranular separations were occasionally observed between the corundum and adjacent mullite grains. Neither cavitation nor change in grain shape was observed in any of the samples. Evidence of grain boundary sliding was seen in the 68 wt% composition, but was not observed in the 73 ot 77 wt% compositions. It is possible that these microstructural changes were not observed because of the low total strain (<5%) experienced by the samples.

(3) Creep Results

A short, initial stage of rapid compression was observed in most experiments, except at the highest temperatures, before the creep rate reduced to an apparent linear creep rate, as shown in Fig. 4. These "steady-state" creep rates are plotted as a function of temperature and stress in Figs. 5 and 6, respectively.

The creep rates for the 68 wt% composition were faster than those of the 73 and 77 wt% compositions, which were very similar to one another.

The apparent activation energy for each composition was determined from a plot of the natural log of the true strain rate vs reciprocal temperature, as shown in Fig. 5. The activation energies at 100 MPa were 742 kJ/mol for the 68 wt% composition, 819 kJ/mol for the 73 wt% composition, and 769 kJ/mol for the 77 wt% composition.

The stress exponents at 1724 K were determined from a plot of logarithm of the true strain rate vs logarithm of stress to be 1.6, 1.5, and 1.2 for the 68, 73, and 77 wt% compositions, respectively, as shown in Fig. 6.

A relatively large initial transient due to the application of >200 kg is shown in Fig. 4(C); the initial transients due to a change in temperature at constant load were much smaller. These initial transients match well with the initial transients measured in the high-temperature deflection tests that were made without a sample, and thus are associated primarily with the equipment. However, a subtle nonlinearity was sometimes found in the apparent linear region, as in the apparent linear region of Fig. 4(C). Even in cases where the strain–time data in the "linear" region could be fitted with a straight line yielding a correlation coefficient of ≥0.99, a comparison of the residuals from a straight line fit and from other expressions for strain, such as the Andrade expression plus a linear term, or a polynomial in $t^{1/2}$ or $t^{1/3}$ revealed a small degree of nonlinearity. This nonlinearity consisted of a steadily decreasing creep rate and was only detectable in the longer creep tests.

IV. Discussion

At a particular temperature and stress, the creep rates of the three different compositions were within a factor of 10 of one another. The apparent creep activation energies, stress exponents, and strain–time dependencies of the three compositions were similar. The samples containing glass crept about an order of magnitude faster than the samples without glass. The presence of the elongated corundum particles caused only a very minor reduction of the creep rate relative to the single-phase material. These observations suggest that the same mechanisms may be rate-controlling in the three compositions.

(A)

(B)

(C)
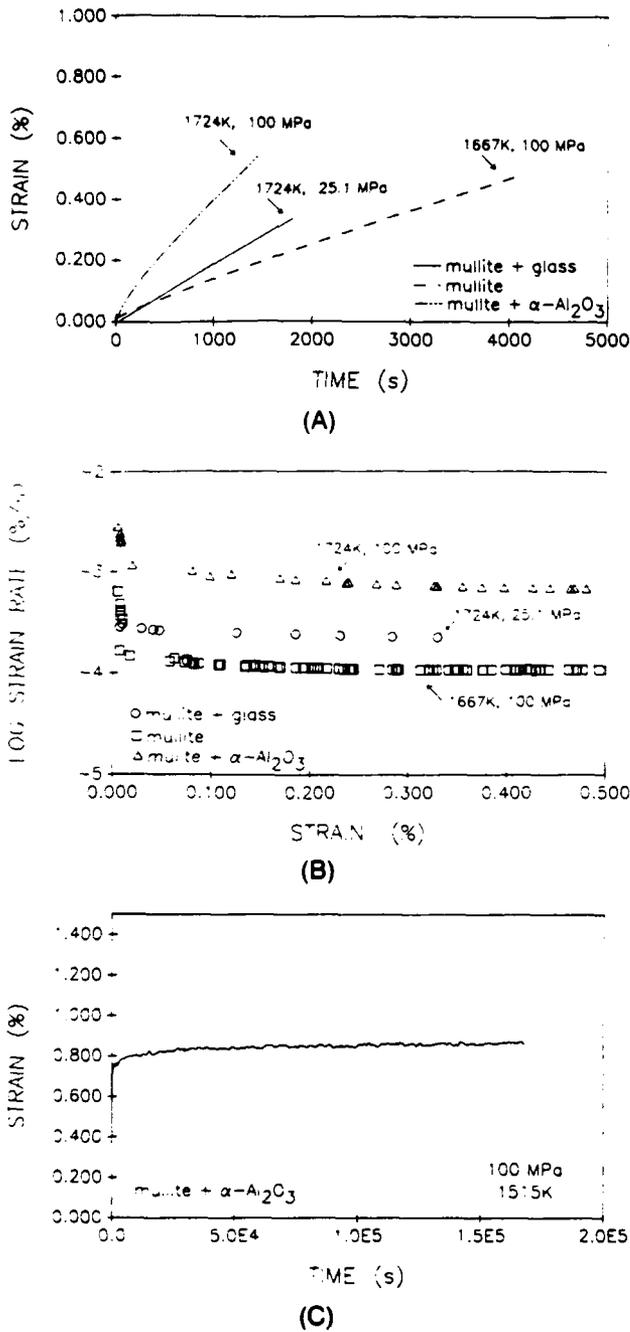
Fig. 4. Examples of (A) true strain vs time, (B) true strain rate vs strain, and (C) strain vs time showing a large initial transient due to load applications and an apparent steady-state creep region containing a small amount of grain growth.

Certain creep mechanisms can be tentatively eliminated in the present results. Mechanisms requiring extensive cavitation or requiring substantial grain deformation as in power-law creep seem unlikely because such deformation was not observed. Some dislocations were formed around defects inside crept grains, and a few dislocations were observed at the grain boundaries after creep, but these were not nearly extensive enough to support models requiring dislocation motion and plastic deformation inside the grains. In addition, the stress exponents measured here do not support dislocation creep models, for which $n \approx 3$ to 5.[25]

In the glass-containing samples, grain boundary sliding was observed within the glassy boundary phase of the crept samples. Where mullite grain boundaries were offset, the gap was
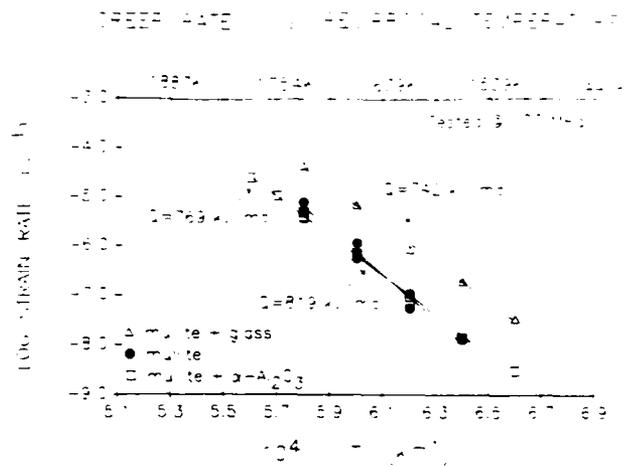
Fig. 5. True strain rate as a function of reciprocal temperature at 100 MPa.

filled with glass. The lack of internal mullite grain deformation, the stress exponents close to 1, and the microstructural evidence suggest a viscous flow mechanism. Dryden[26] and Drucker[27] have treated the viscous deformation of hard circular or hexagonal grains surrounded by a viscous grain boundary phase. They find that the effective viscosity, n_{eff} of the material is inversely proportional to the cube of the volume fraction, f, of the boundary phase:

$$n_{eff} \propto n_i/f^3 \qquad (1)$$

where n_i is the intrinsic viscosity of the grain boundary phase. The shear strain rate and shear stress are related by

$$\dot{\gamma} = \tau/n_{eff} \qquad (2)$$

The composition of the grain boundary phase is uncertain because the final sintering hold was at 1873 K, just above the eutectic temperature (1860 ± 10 K) but the creep tests were made well below the eutectic temperature. The fine scale of the microstructure makes microprobe analysis difficult. If in equilibrium above the eutectic temperature, 5.9 ± 2.5 wt% (8.1 vol%) of glass of the eutectic composition (≈ 7 wt% Al_2O_3) is present according to the phase diagram. If the samples were in equilibrium at the test temperature, 3.9 ± 2.0 wt% (5.4 vol%) of SiO_2 glass would be present.

The creep rates for Dryden's model were calculated for pure SiO_2 glass and for glass of the eutectic composition (by extrapolation of the viscosity data of Urbain[28] to lower temperatures) at several volume fractions. The measured creep rates and some of the predicted rates are plotted in Fig. 7. As may be seen in Fig. 7, the experimental data match well with the use of 4 vol% of the SiO_2 glass. This volume fraction is in agreement with that calculated for equilibrium below the eu-
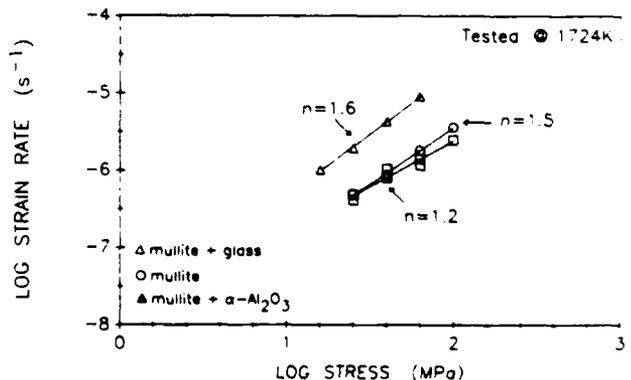
Fig. 6. True strain rate as a function of stress at 1724 K.
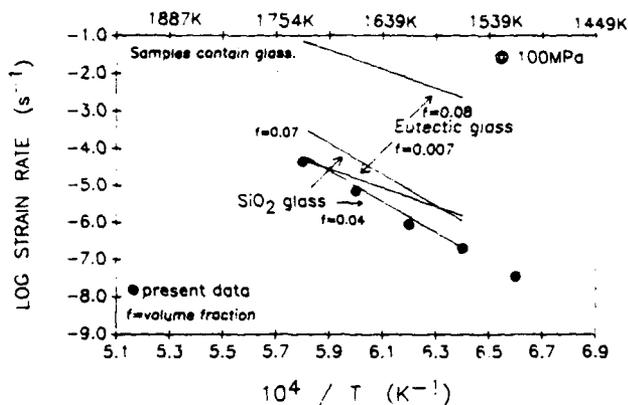
Fig. 7. Comparison of present creep results for samples containing mullite and glass with strain rates calculated from Dryden's model. Calculated creep rates are for either SiO_2 glass or glass of the eutectic composition (~7 wt% Al_2O_3).

Fig. 8. Comparison of present creep results for glass-free samples with strain rates calculated according to Dryden's model and a diffusional creep model.

tectic temperature from the chemical composition and phase diagram, within experimental error. Eight volume percent of the eutectic composition glass gives a creep rate several orders of magnitude higher than the experimental results. To match the experimental data at 1724 K, only 0.7 vol% of the eutectic glass could be present.

The activation energy for viscous flow in fused SiO_2 glass is ≈711 kJ/mol,[31] which is roughly comparable to the creep activation energy (742 kJ/mol) measured here. The activation energy of the eutectic glass is estimated to be ≈ 482 kJ/mol from Urbain's data.[28]

According to Dryden's model of perfect hexagons, the creep rate is independent of grain size, since the creep rate depends only on the dimensions of the boundary layer, and thus on the volume fraction of glass. For a given volume fraction of glass there can be only one boundary layer width (*h*) and length (*l*) which determines the volume fraction of glass. In a real material, for a given volume fraction of glass, the dimensions of the boundary layer depend on the grain size distribution and on the arrangement of these grains in the microstructure. In these samples we observed that the standard deviation of the grain size increases with an increase in the mean grain size. On average the ratio *l/h* will increase as the grain size increases. The rate at which two grains can be squeezed together is proportional to the cube of the inverse aspect ratio *h/l*. Thus if *h/l* increases linearly with grain size, the creep rate will depend on the cube of the grain size. Ohnishi *et al.*[11] have reported a grain size exponent of 3 in their measurements on a 68 wt% Al_2O_3 composition containing mullite and glass.

In summary, the microstructural observations, stress exponent, activation energy, grain size dependence, and the magnitude of the creep rates are consistent with control by a viscous flow mechanism for the samples containing glass. The use of SiO_2 glass viscosity gives a better fit to the data than the eutectic glass viscosity for the volume fraction present.

Although the creep parameters for the samples with and without glass are similar, Dryden's model does not give a good fit to the experimental data for the glass-free compositions, unless the thickness of the viscous boundary layer is on the order of ~1 nm, as shown in Fig. 8. To test whether Dryden's model could be applied to these compositions, we assumed that the grain boundary consists of a layer with viscosity equal to that of a glass of the 2:1 mullite composition (~60 mol% Al_2O_3), and used the experimental creep values to calculate the boundary layer thickness of ~1 nm on a 1 μm diameter spherical grain.

As was the case for the samples containing glass, the measured creep activation energies were significantly higher (≈790 kJ/mol) than that estimated from Urbain's data (482 kJ/mol).
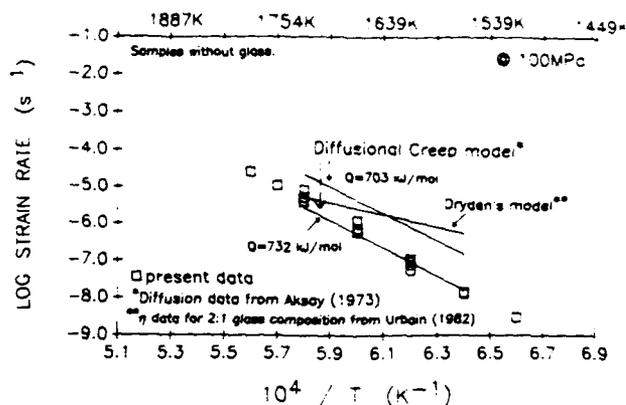
Another model which is consistent with the observed stress dependence and microstructural observations is diffusional creep. In diffusional creep, the strain rate[25] is

$$\dot{\varepsilon} = 14\sigma\Omega D_{eff}/d^2kT \tag{3}$$

where Ω is the "molecular volume" of mullite (2.24 × 10^{-28} m³), σ is the stress, *d* is the grain size, *k* is Boltzmann's constant, *T* is temperature, and D_{eff} is the effective diffusion coefficient. The diffusional creep model was tested for fit by extrapolating a diffusion coefficient into the lower temperatures of the creep tests and using it as the effective diffusion coefficient. D_{eff}. Few diffusion measurements are available for mullite. Klug[22] has calculated an effective diffusion coefficient of Al_2O_3 in mullite from α-Al_2O_3 precipitation experiments to be 3.0 × 10^{39} exp[(−2000 kJ/mol)/RT] m²/s. Aksay[23] measured the interdiffusion coefficient of mullite to be 3.23 × 10^3 exp[(−703 kJ/mol/RT]. The use of the diffusion coefficient measured by Klug as an effective diffusivity in Eq. (3) results in a creep rate orders of magnitude smaller than the measured creep rates. As shown in Fig. 8, use of the interdiffusion coefficient measured by Aksay[23] with the activation energy of 703 kJ/mol gives creep rates which are about a factor of 3 higher than the experimental values. However, the calculated and experimental creep rates are within experimental error with the use of an activation energy of 732 (703 + 29) kJ/mol.

The large difference in activation energies obtained by Klug and Aksay is remarkable. Klug's precipitation experiment primarily involved lattice diffusion, so perhaps the measurement by Aksay reflects a strong component of grain boundary diffusion.

Although the magnitude of the experimentally measured creep rate is within the predicted range of diffusional creep, the apparent creep activation energy of ~790 kJ/mol for the glass-free samples is either somewhat higher or significantly lower than that of the available diffusion data. The measured stress dependence is greater than the value of one expected for diffusional creep, indicating possible interface control. Cavitation, which could produce *n* > 1, was not observed in the glass-free samples.

The grain size exponents (*p* = 1 to 3) which have been reported[11,13,30] for single-phase mullite and mullite containing corundum are insufficient to distinguish between the application of a Dryden-type model and diffusional creep. In addition to more microstructural observations of crept samples, more data are needed on diffusion of the various species through the lattice and grain boundaries in mullite and on the activation energy of viscous flow of glasses of these compositions in order to distinguish between these models.

The small decrease in creep rate observed in the apparent steady-state region is consistent with that due to grain growth. For example, in the sample shown in Fig. 4(C), the expected[32]

increase in grain size of ~0.2 μm could account for the observed decrease in creep rate from 7×10^{-3} to 5×10^{-3} s^{-1} over a period of 33 h, assuming a grain size exponent of 2 to 3.

V. Summary

Three aluminosilicate compositions were synthesized, characterized, and creep tested: a 68 wt% Al$_2$O$_3$ composition containing mullite and glass; a 73 wt% Al$_2$O$_3$ composition consisting of single-phase mullite; and a 77 wt% Al$_2$O$_3$ containing mullite plus corundum. Stress exponents from 1.2 to 1.6 and apparent activation energies from 742 to 819 kJ/mol were determined from compression tests conducted in air with creep apparatus built for this work.

References

[1]W. A. Deer, R. A. Howie, and J. Zussman; p. 37 in *An Introduction to the Rock Forming Minerals*, 13th ed. Longman Group Ltd., Harlow, Essex, England, 1982.

[2]P. H. Ribbe, "Kyanite, Andalusite and Other Aluminum Silicates"; pp. 189-214 in *Reviews in Minerology*, Vol. 5. *Orthosilicates*, 2d ed. Edited by P. H. Ribbe. Mineralogical Society of America, Washington, DC, 1982.

[3]K. S. Mazdiyasni, "Preparation and Characterization of Mullite Powders from Alkoxides and Other Chemical Routes"; pp. 243-54 in Ceramic Transactions, Vol. 6. *Mullite and Mullite Matrix Composites*. Proceedings of the First International Conference on Mullite, Nov. 9-10, 1987, Japan. Edited by S. Somiya, R. F. Davis, and J. A. Pask. American Ceramic Society, Westerville, OH, 1990.

[4]B. E. Yoldas, "Mullite Formation from Aluminum and Silicon Alkoxides"; pp. 255-62 in Ceramic Transactions, Vol. 6. *Mullite and Mullite Matrix Composites*. Proceedings of the First International Conference on Mullite, Nov. 9-10, 1987, Japan. Edited by S. Somiya, R. F. Davis, and J. A. Pask. American Ceramic Society, Westerville, OH, 1990.

[5]M. D. Sacks, H. Lee, and J. A. Pask, "A Review of Powder Preparation Methods and Densification Procedures for Fabricating High Density Mullite"; pp. 167-208 in Ceramic Transactions, Vol. 6. *Mullite and Mullite Matrix Composites*. Proceedings of the First International Conference on Mullite, Nov. 9-10, 1987, Japan. Edited by S. Somiya, R. F. Davis, and J. A. Pask. American Ceramic Society, Westerville, OH, 1990.

[6]T. Kumazawa, S. Ohta, S. Kanzaki, and H. Tabata, "Influence of Powder Characteristics on Microstructure and Mechanical Properties of Mullite Ceramics"; pp. 401-12 in Ceramic Transactions, Vol. 6. *Mullite and Mullite Matrix Composites*. Proceedings of the First International Conference on Mullite, Nov. 9-10, 1987, Japan. Edited by S. Somiya, R. F. Davis, and J. A. Pask. American Ceramic Society, Westerville, OH, 1990.

[7]C. K. Yoon and I. W. Chen, "Superplastic Flow of Mullite-Zirconia Composites"; pp. 567-77 in Ceramic Transactions, Vol. 6. *Mullite and Mullite Matrix Composites*. Proceedings of the First International Conference on Mullite, Nov. 9-10, 1987, Japan. Edited by S. Somiya, R. F. Davis, and J. A. Pask. American Ceramic Society, Westerville, OH, 1990.

[8]M. Mizuno, M. Shiraishi, and H. Saito, "Microstructure and Bending Strength of Highly Pure Mullite Ceramics"; pp. 413-24 in Ceramic Transactions, Vol. 6. *Mullite and Mullite Matrix Composites*. Proceedings of the First International Conference on Mullite, Nov. 9-10, 1987, Japan. Edited by S. Somiya, R. F. Davis, and J. A. Pask. American Ceramic Society, Westerville, OH, 1990.

[9]P. A. Lessing, R. S. Gordon, and K. S. Mazdiyasni, "Creep of Polycrystalline Mullite," *J. Am. Ceram. Soc.* **58** [3-4] 149 (1975).

[10]M. Ashizuka, T. Okuno, and Y. Kubota, "Creep of Mullite Ceramics," *Yogyo Kyokaishi* **97** [6] 662-68 (1989).

[11]H. Ohnishi, K. Maeda, T. Nakamura, and T. Kawanami, "High Temperature Mechanical Properties of Mullite Ceramics"; pp. 605-12 in Ceramic Transactions, Vol. 6. *Mullite and Mullite Matrix Composites*. Proceedings of the First International Conference on Mullite, Nov. 9-10, 1987, Japan. Edited by S. Somiya, R. F. Davis, and J. A. Pask. American Ceramic Society, Westerville, OH, 1990.

[12]R. A. Penty and D. P. H. Hasselman. "Creep Kinetics of High Purity, Ultra-Fine Grain Polycrystalline Mullite," *Mater. Res. Bull.* **7** [10] 1117-24 (1972).

[13]P. C. Dokko, J. A. Pask, and K. S. Mazdiyasni, "High Temperature Mechanical Properties of Mullite Under Compression," *J. Am. Ceram. Soc.* **60** [3-4] 150-55 (1977).

[14]R. D. Nixon, S. Chevacharoenkul, R. Davis, and T. N. Tiegs, "Creep of Hot-Pressed SiC Whisker Reinforced Mullite"; pp. 579-603 in Ceramic Transactions, Vol. 6. *Mullite and Mullite Matrix Composites*. Proceedings of the First International Conference on Mullite, Nov. 9-10, 1987, Japan. Edited by S. Somiya, R. F. Davis, and J. A. Pask. American Ceramic Society, Westerville, OH, 1990.

[15]R. Torrecillas, H. Gros, G. Fantozzi, J. S. Moya, and S. de Aza, "Processing-Microstructure-Mechanical Properties Relationships in Mullite-Zirconia Composites"; Abstract 2-F-90P. Symposium F: Mullite Processing, Structure and Properties, Pacific Coast Regional Meeting of the American Ceramic Society, Oct. 24-26, 1990, Seattle, WA.

[16]T. Kumazawa, S. Ohta, S. Zanzaki, and H. Tabata, "Influence of Powder Characteristics on Microstructure and Mechanical Properties of Mullite Ceramics"; 1st International Workshop on Mullite, Abstract MP-14, Nov. 9-10, 1987, Tokyo, Japan.

[17]P. C. Smith and R. E. Moore, "High Temperature Compressive Creep of Mullite," Abstract 15-R-71P. *Am. Ceram. Soc. Bull.* **50** [9] 803-804 (1971).

[18]K. Jakus and S. M. Wiederhorn, "Creep Deformation of Ceramics in Four-Point Bending," *J. Am. Ceram. Soc.* **71** [10] 832-36 (1988).

[19]D. F. Carroll and S. M. Wiederhorn. "High Temperature Creep Testing of Ceramics," *Int. J. High Tech. Ceram.*, **4**, 227-41 (1988).

[20]A. P. Hynes, E. Muzzi, and R. H. Doremus. "High Temperature Compressive Creep Apparatus"; unpublished work.

[21]A. P. Hynes, "Creep Study of Single Crystal and Polycrystalline Mullite"; Ph.D. Thesis Rensselaer Polytechnic Institue, Troy, NY, to be completed 1991.

[22]F. J. Klug, "Alumina-Silica Phase Equilibria in the Mullite Region", Ph.D. Thesis. Rensselaer Polytechnic Institute, Troy, NY, 1984.

[23]I. A. Aksay, "Diffusion and Phase Relationship Studies in the Aluminum-Silica System"; Ph.D. Thesis. University of California, Berkeley, CA, 1973.

[24]A. P. Hynes and R. H. Doremus. "High Temperature Compressive Creep of Single Crystal and Polycrystalline Mullite"; Abstract 9-F-90P. Symposium F: Mullite Processing, Structure and Properties. Pacific Coast Regional Meeting of the American Ceramic Society, Oct. 24-26, 1990, Seattle, WA.

[25]W. R. Cannon and T. G. Langdon. "Review Creep of Ceramics Part 2," *J. Mater. Sci.*, **23**, 1-20 (1988).

[26]J. R. Dryden, D. Kucerovsky, D. S. Wilkinson, and D. F. Watt, "Creep Deformation Due to a Viscous Grain Boundary Phase," *Acta Metall.*, **37** [7] 2007-15 (1989).

[27]D. C. Drucker; p. 795 in *High-Strength Materials*. Edited by Y. F. Zackay Wiley, New York, 1965.

[28]G. Urbain, Y. Bottinga, and P. Ruhel. *Geochim. Cosmochim. Acta.* **46**, 1061 (1982).

[29]Y. Okamoto, H. Fukudome, K. Hayashi, and T. Nishikawa, "Creep Deformation of Polycrystalline Mullite," *J. Eur. Ceram. Soc.*, **6**, 161-68 (1990).

[30]M. Ashizuka, T. Honda, and Y. Kubota, "Effect of Grain Size on Creep in Mullite Ceramics," *J. Ceram. Soc. Jpn.*, **99** [4] 292-95 (1991).

[31]R. H. Doremus. *Glass Science*; p. 106. Wiley, New York, 1973.

[32]A. P. Hynes, T. W. Folmsbee, and R. H. Doremus. "Grain Growth in Mullite and Mullite/Corundum Composites," *Proc. Am. Soc. Compos.*, in press.   □

FIBER PROCESSING AND PROPERTIES

A high-temperature fibre testing facility

Edgar Lara-Curzio and S S Sternstein†

Center for Composite Materials and Structures, Rensselaer Polytechnic Institute
Troy, NY 12180, USA

Abstract. A multiple-unit fibre tester with a controlled environment and fully computerized data acquisition and control has been designed and constructed to study the thermomechanical behaviour of fibres at high temperatures. High temperatures are achieved by a self-resistance heating technique, strains are estimated from displacement measurements using LVDTs, while temperature is measured using a two-colour infrared pyrometer. In the determination of displacements 0.25 μm can be resolved, while temperature stability can be achieved over long periods of time. The temperature difference between the hottest and coldest points in the hot zone was minimized to 30 °C at 1500 °C by combining appropriate values of gas flow rates and fibre gauge lengths. Examples of creep and thermal expansion measurements are presented for SCS-6 SiC fibres over the temperature interval of 900–1500 °C.

1. Introduction

In the quest for more efficient energy-conversion systems a need has been created for materials capable of retaining their strength, stiffness and environmental stability at higher and higher temperatures. However, there are only a handful of materials with melting temperatures above 2500 °C and most of them are either carbides, nitrides or oxides [1]. Although some of these candidates offer many outstanding properties for high-temperature structural applications, their use is limited in part because they are brittle in nature, leading often to catastrophic failure.

The recent availability of continuous high-performance fibres provides a promising alternative in achieving damage-tolerant structural materials through their use as reinforcements in composite materials. But to understand and then predict the overall deformation of composite materials it is first necessary to understand the individual responses of the different phases under the same thermomechanical conditions that structural applications will eventually impose.

Data are required from both the scientific and engineering points of view. For the former it is important to obtain information on the materials' structure–properties relations to improve their performance, whereas for the latter, even the most sophisticated composite algorithms require accurate input data. In the case of fibres, data on their thermomechanical behaviour at high temperatures are scarce and often misleading.

Since high-temperature structural applications will impose temperatures in excess of 1500 °C, in addition to a high melting point, creep resistance and service life are without a doubt the most limiting requirements for

† Author to whom correspondence should be sent.

any candidate material. However, the need for long-duration creep data and the inherent difficulties encountered in the testing of single fibres pose a requirement for relatively inexpensive testing procedures, making a multiple-unit testing apparatus highly desirable.

Different approaches have been followed for the mechanical testing of fibres at high temperatures, ranging from the use of commercial machines and special designs [2–6], to simple and ingenious techniques [7–10]. The main consideration in the design of equipment for high-temperature mechanical testing of fibres is the heating procedure, although the stressing mechanism, deformation and temperature measurements, environment, stability and control are also important considerations.

Two approaches have been used to achieve high temperatures in the evaluation of stiffness, strength, fatigue, dynamic properties, relaxation and creep for fibres: (i) hot-wall systems and (ii) self-resistance heating. Although most of the results reported in the literature on fibre testing at high temperatures have been obtained while the fibre is exposed at high temperatures [2, 4, 5, 7–18], some results refer to ambient tests on samples that have been previously exposed to extreme conditions [19–21].

(i) *Hot-wall systems.* Because it is desirable to avoid the interference of grip deformation in the determination of strains, most tests are carried out with the fibre grips held at room temperature, which in a heated-wall system results in a semi-parabolic temperature profile along the fibre. Creep measurements on boron, alumino-silicate and SiC fibres have been reported using this approach [7, 9, 11, 15]. The obvious problems with this approach are the need to correct for non-uniform temperature distributions and the difficulty in determining gauge lengths. Several different properties have been reported

under these circumstances but no details have been presented on the necessary corrections for the lack of uniform temperature distributions in stiffness and creep measurements, for example [15]. An algorithm to extract isothermal properties from parabolic temperature distributions was recently developed and applied to correct measurements of the dynamic in-phase and loss moduli of SiC fibres up to 1600 °C [4].

(ii) *Self-resistance heating*. This approach has been used to test carbon, tungsten, boron and SiC fibres [5, 14, 16, 18] and is limited to electrically conductive fibres. The main attributes of this heating procedure are well defined isothermal gauge lengths, cold grips and the ability to perform very fast temperature changes. However, the dependence of temperature control on the structural changes in the fibre can be a major disadvantage. For example, changes in the cross section and therefore in electrical resistance can lead to the formation of hot spots, or regions of localized heating. This is a common problem in the testing of filaments susceptible to oxidation in aggressive environments, or samples which undergo necking before failure. Another disadvantage of this approach is that arcing can occur when the specimens break and the electric circuit is suddenly opened, melting and/or evaporating the specimen near and at the two fracture surfaces and preventing any fractographic examination. When arcing has become a major problem, special circuits have been designed to shut off the current just prior to failure [22].

In this report, a multiple-unit apparatus in which the self-resistance heating technique has been used to achieve high temperatures for the thermomechanical evaluation of ceramic fibres is described. First, an overall description of the apparatus is presented in section 2, including a detailed description of a representative unit. Section 3 describes the data acquisition and control process, and details of the operation and some examples of experimental results are presented in section 4. Finally, section 5 includes a summary and comments on the attributes and limitations of the equipment.

2. The apparatus

An overall block diagram for the high-temperature fibre testing facility (HTFTF) is shown in figure 1, and each of the major components is described below.

2.1 Mechanical design

2.1.1. Mounting frame. The apparatus consists of six independent single-fibre units (refer to figure 2) arranged in a semicircle and mounted on a stiff frame. The frame consists of a rigid steel plate 101.6 × 64.8 × 1.9 cm and two aluminium platforms separated by five columns of adjustable height.

Paper-reinforced phenolic blocks are used to mechanically support and electrically isolate the units' endcaps from the frame. The frame is supported by six

pneumatic spring mounts (Barry Controls model SLM-1) and kept inside a rectangular acrylic plastic box to avoid the hazards of high voltages.

2.1.2. Single-fibre units. Each of the six single-fibre units resembles a parallel vertical flow reactor used for the CVD coating of fibres and consists of two identical end-caps and one 2.54 cm diameter quartz tube (see figure 2). Each end-cap, 7.5 × 7.5 × 5.0 cm in size, has a system of internal channels to allow for water cooling and a small internal cylindrical cavity connected to an external manometer. The cavities are filled with mercury to provide electrical contact between the end-caps and the fibres while working at the same time as a sealant to prevent gases from leaking out of the units. The fibres pass through two perfectly aligned 0.0254 cm diameter holes located on the top and bottom of the mercury receptacles at the centre of the end-caps. The large angle of contact of mercury coupled with the small size of the holes prevents mercury from dripping. A cross section of the end-cap is presented in figure 3.

2.2. Heating procedure

High temperatures are achieved by applying a high DC voltage at the end-caps using a programmable high-voltage power supply (Kepco BHK 500-0.4M). The voltage and current specifications of the power supply will depend on the electrical properties of the fibres. In the case of composite SCS-6 SiC fibres composed of a pyrolytic graphite-coated glassy carbon substrate, a β-SiC sheath and a carbon-rich coating, the fibres behave like a network of four resistors in parallel where most of the current will be flowing through the pyrolytic graphite layer and the outside coating (see figure 4). A transport analysis in which radiation and bimodal convection are considered was developed to predict the power requirements and the temperature distribution inside a unit of the HTFTF using these fibres. The analysis was extremely useful in determining the required specifications of voltage and current of the power supplies. Details of the analysis can be found elsewhere [23].

2.3. Measurements and electronic circuitry

Displacements are measured using linear variable differential transducers (LVDT) (Shaevitz model 200 DC-D) with the LVDT core attached to the bottom end of the fibres. Figure 5 describes the arrangement. The temperature is read using a two-colour pyrometer with a 4–20 mA linear output (Mikron 77 78 series) and a 700–2000 °C temperature range. The sensor is focused at the fibre surface using a fibre optic lens assembly that enables temperature measurements on a 0.0127 cm spot at a 5 cm focus distance. The lens assembly is mounted onto a rotating table (DAEDAL 20501-P) controlled by a programmable positioner (DAEDAL MC5001-MS-23) that allows a 0.0002° travel for each microstep in the motor. This approach serves two purposes: it allows for multiple simultaneous experiments
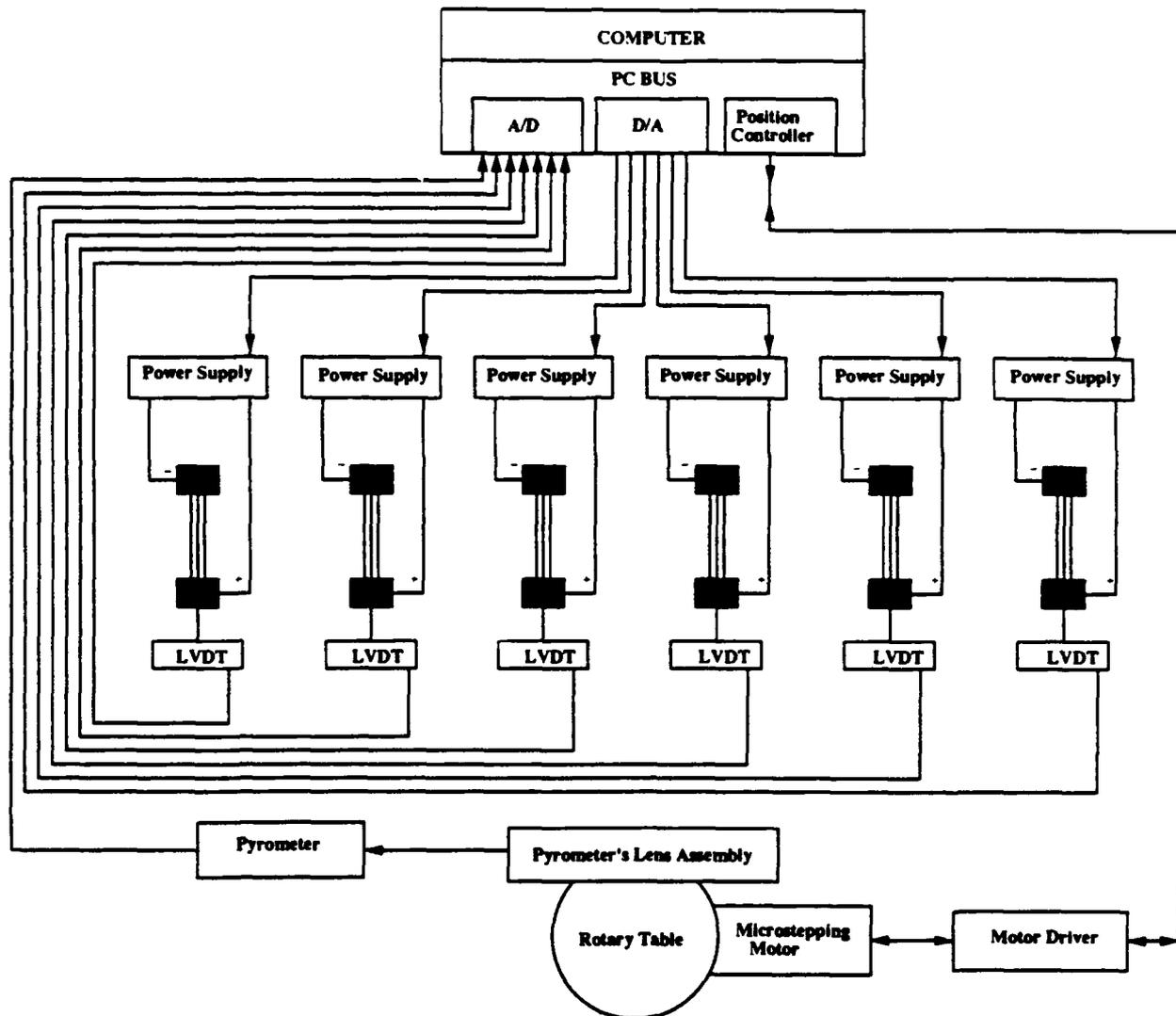
Figure 1. Schematic diagram of the multiple-unit high temperature fibre testing facility.

with only one temperature-measuring device, while providing extreme precision for focusing the lens assembly on very small spot sizes. The MC5001-MS-23 contains a board that occupies one slot in the PC, one single-axis motor driver and a 10 000 steps/revolution microstepping motor.

Voltage signals from the LVDTs are connected to an analogue termination panel (Intelligent I/O® IQ-110T) where noise filtering is carried out. The 4–20 mA signal from the temperature readings is passed through a 500 Ω resistor in the termination panel and also filtered. The termination panel is connected to a 12-bit resolution A/D converter module (Intelligent I/O® IQ-102M-1) which is mounted onto a carrier with 32 bits of digital I/O (Intelligent I/O® IQ-101C-2), which in turn plugs directly into an expansion slot in a PC (ZEOS® 386 20 MHz). Connected also to the carrier are a counter, timer, pulse generator module (Intelligent I/O® IQ-107M-1) and an eight-channel 12-bit D/A module (Intelligent I/O® IQ-121M-1A), with the latter connected externally to a second termination panel from which connections are

made to the rear panel of the high-voltage power supplies for the closed-loop temperature control. In this application the power supplies work simply like operational amplifiers, in which 0–10 V signals are linearly scaled into 0–500 V outputs (figure 6).

3. Data acquisition and control

Data acquisition and control is accomplished with in-house-developed software written using Turbo Pascal® v.5.0, and interfaced to the commercial packages Labtech Notebook (NB) and Labtech Notebook Real Time Access (RTA). Two types of experiment have been performed: thermal expansion measurements and creep. For the first the pyrometer is dedicated to one unit only, whereas for creep experiments the pyrometer is shared by all units. Both thermal expansion and creep experiments are described in detail below.
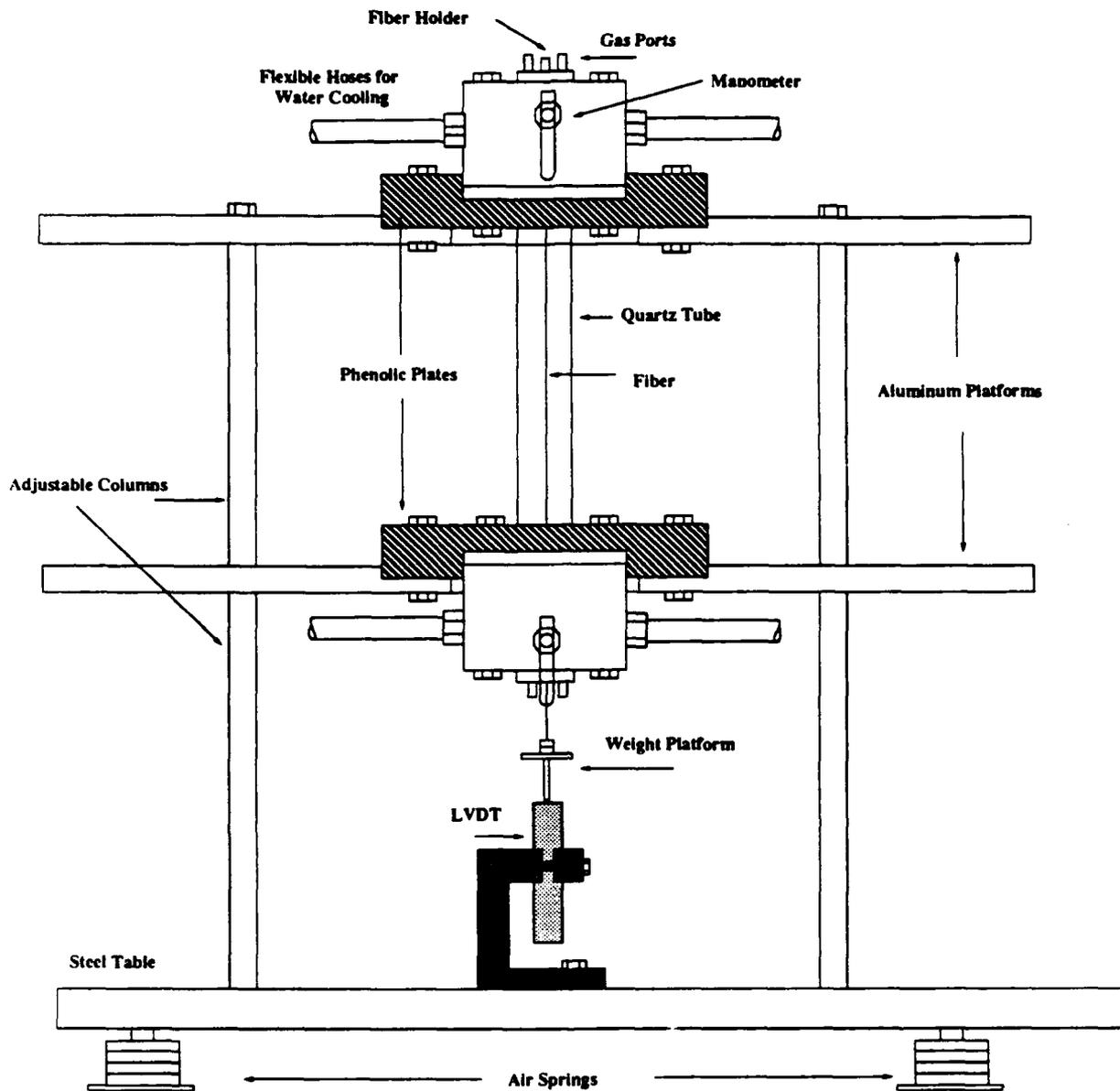
Figure 2. Detailed illustration of a single-fibre unit showing the end-caps for electrical contact with the fibre and the displacement and load assembly. Not drawn to scale.

3.1. Thermal expansion measurements

Labtech Notebook is an integrated software package for data acquisition, control, monitoring and data analysis, in which the conditions for an experimental run are saved as a group of channels. Eight channels are required to carry out thermal expansion measurements. A brief description of the operations performed by each channel is given below and presented schematically in figure 7.

Channel 1 is an analogue input channel sampling the filtered signal from the LVDT. The signal is then echoed into channel 2 in which strains are calculated. The calculation includes multiplication by the calibration factor of the LVDT and subtraction of an offset value obtained at the start of the experiment.

For the pyrometer, similar operations are performed. After passing the 4–20 mA signal through a 500 Ω

resistor to scale it into 2–10 V voltages, the signal is then filtered and sampled by an analogue input channel at a rate of 3 Hz considering that the time of response of the pyrometer is only 300 ms. Temperature is calculated by using two channels in cascade, in which the formula given below is evaluated:

$$\text{temperature} = T_1 + (T_2 - T_1)\frac{(V/R) - 4}{16}. \tag{1}$$

T_1 and T_2 are the lower and upper limits of the pyrometer's range (700 and 2000 °C respectively), R is the resistor installed in the termination panel (500 Ω) and V is the filtered voltage across the resistor.

For temperature control, a closed-loop PID control algorithm built inside NB is used, in which the 0–10 V
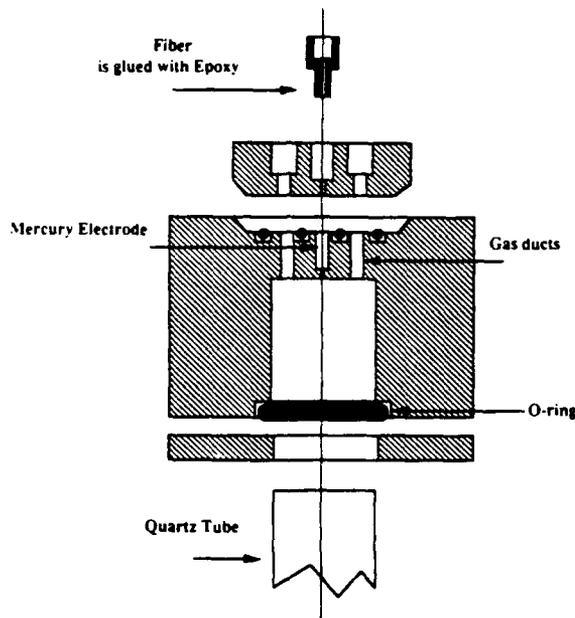
Figure 3. Cutaway view of the end-cap and fibre upper end fixture.
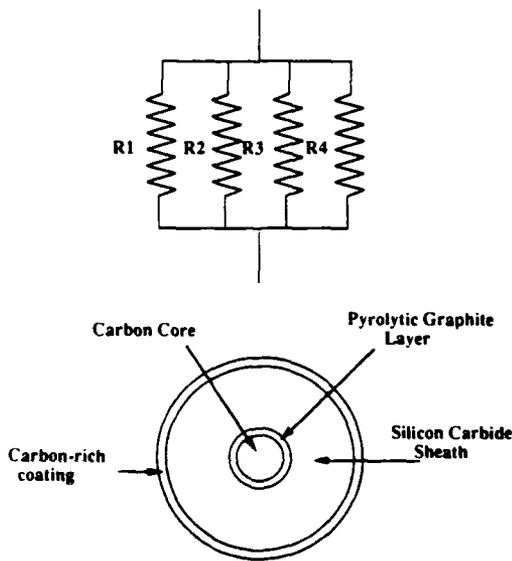
Figure 4. Illustration of the four-layer structure of Avco SCS-6 silicon carbide fibre and the parallel resistance model.

Figure 5. Fibre lower end fixture showing the load platform and LVDT core mounting arrangement. Total weight of the assembly is 10.2 g.
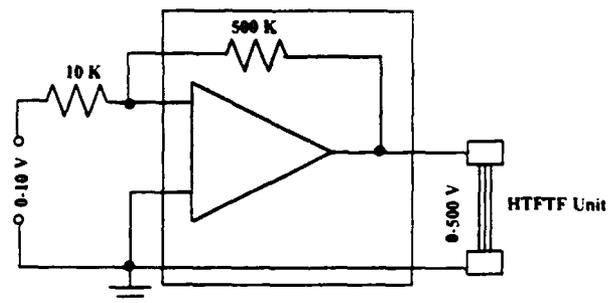
Figure 6. Operational amplifier representation of the programmable power supply employed for resistive heating of the fibre.

output sent to the power supply is estimated from

$$\text{output}\,(t) = P\,(\text{error}\,(t)) + I \int \text{error}\,(t')\,dt'$$

$$+ D\,\frac{d\,(\text{error}\,(t))}{dt} \tag{2}$$

where the error term is calculated by subtracting the value of the actual temperature from the desired set point. To keep a record of the time–temperature–power requirements relation during the test, the 0–10 V output

to the power supply is echoed into an additional channel. All channels operate synchronized with channel 6 – a time channel – to keep track of the history of the test. Groups of data containing time, strain, temperature and the output signal to the power supply are recorded at a prescribed rate into a data file for post-test analysis.

RTA allows the stand-alone application operating in
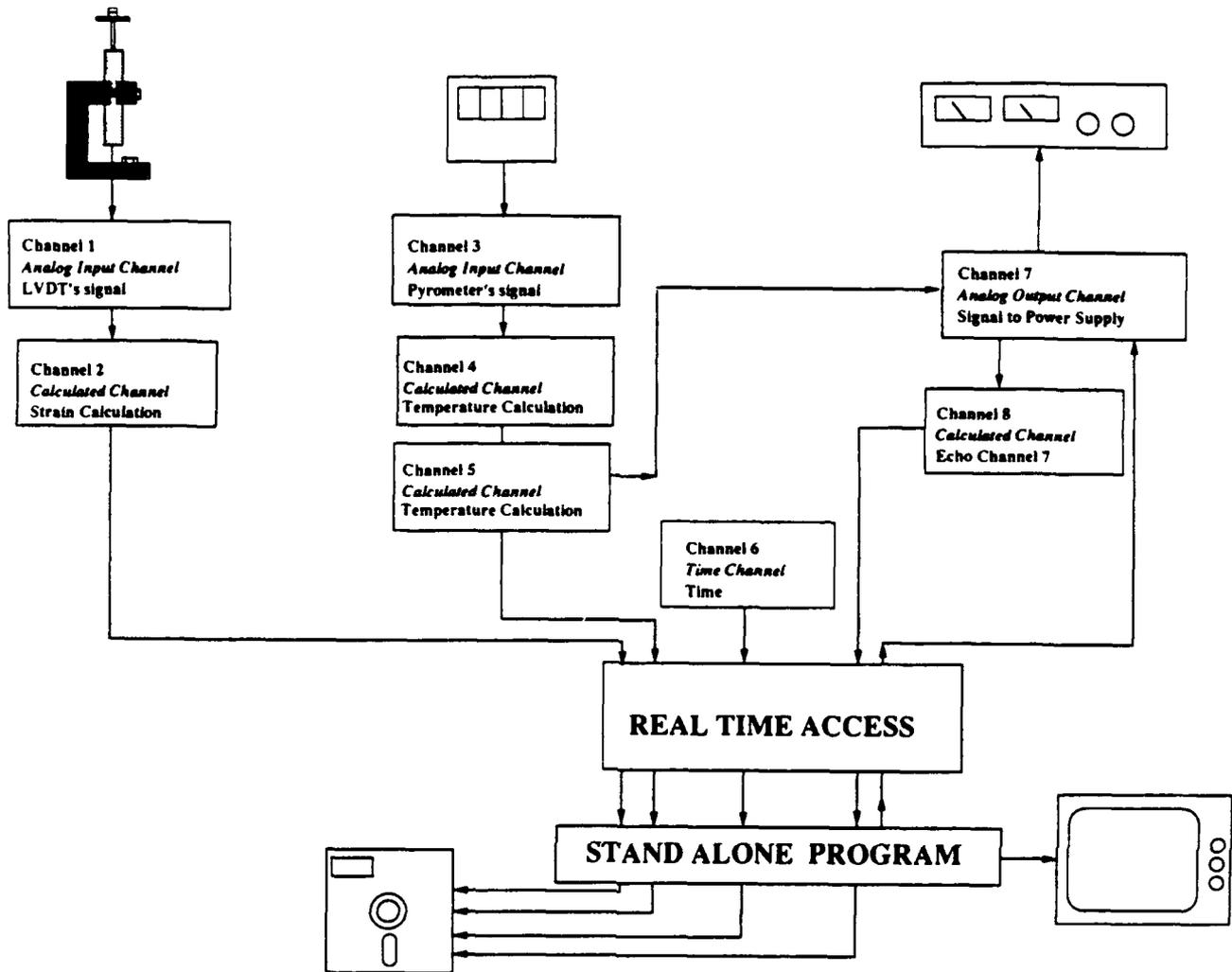
Figure 7. Schematic representation of the data acquisition and control procedure for a thermal expansion experiment.

the foreground to communicate with NB in the background, in a way similar to acquiring data from a DOS device, to access real-time data being acquired simultaneously by NB and buffered in RAM. Access to the control channel is also provided through RTA to change any of the PID constants and/or the set point. Figure 8 shows a simple thermal history of a thermal expansion experiment.

3.2. Creep experiments

In contrast to thermal expansion measurements, creep experiments require a more elaborate data acquisition and control scheme because the pyrometer must be shared by all units. To simplify the presentation, the operation of HTFTF with only three units will be addressed. Figure 9 presents a brief description of the operations performed by each channel while figure 10 shows a flow chart describing a creep experiment.

NB requires 24 channels to carry out a simultaneous creep experiment with three units. For each unit, similarly to the thermal expansion measurements, two channels – synchronized with one time channel – are
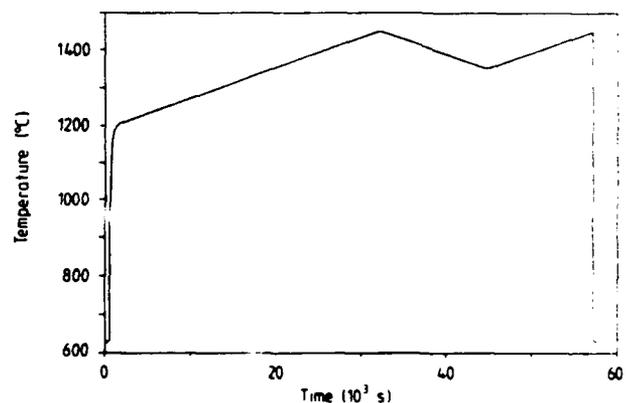
Figure 8. Example thermal history for a thermal expansion experiment showing the linear ramp program followed by a rapid quench in 2 s.

dedicated to sampling the displacements and calculating the strains, and pairs of time–strain values for each of the units are recorded into different files. For all units, the sampling of displacements is carried out on continuous
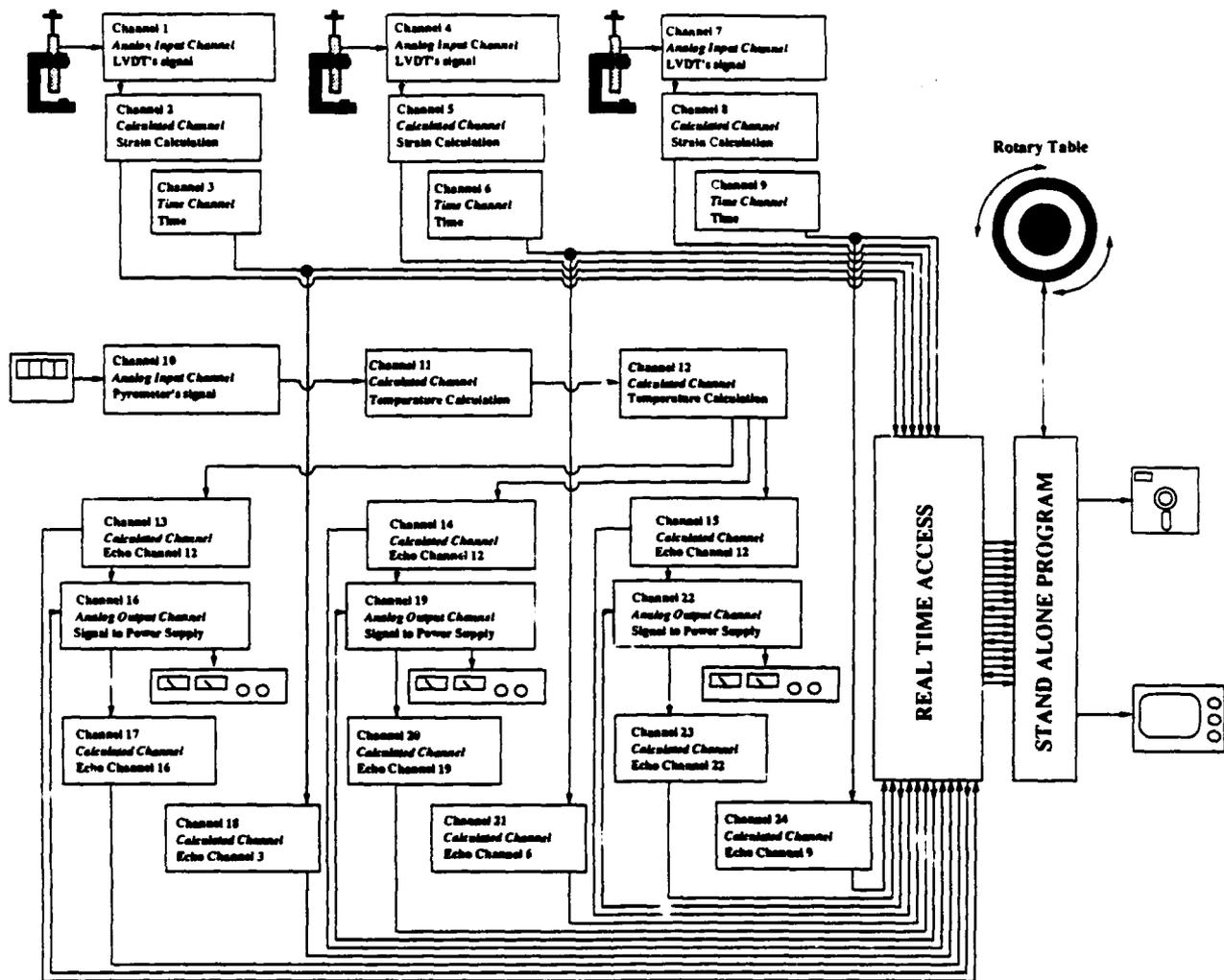
Figure 9. Schematic representation of the data acquisition and control procedure for three simultaneous creep experiments.

bases at rates typically between 3 and 7 Hz. For long-duration tests, strains are calculated and stored at much slower rates varying from 0.1 to 0.001 Hz, although whenever mechanical and/or thermal loading/unloading takes place, or when much faster changes in the displacements are expected, data can be stored at faster rates.

In addition to analogue filtering of the displacement and temperature signals, further filtering can be accomplished by incorporating an additional channel in the NB set-up to perform a moving average of the input signals at a rate equal to the sampling rate.

For temperature measurements three channels in succession are needed; one for data acquisition and two for temperature calculations. The signal from the channel containing the value of the temperature is echoed and synchronized with a PID control channel for the fibre unit on which the pyrometer is being focused. To record the temperature–power requirement history for each unit, the output signal to the power supply is echoed and synchronized with the temperature measurements and with a time mark duplicated from the calculation of strains, and sent subsequently into a second data file. Abnormalities in the

power requirement history may be indicative of structural changes or surface oxidation as reflected in the fibre resistance. Although the temperature control in each unit is intermittently switched between PID and open-loop, the advantage of this approach resides in the fact that, during post-test data analysis, a correlation can be established between temperature, strain and output signals to the power supply because they have been labelled with the same time signature.

A special routine was developed to focus precisely the lens assembly of the pyrometer at the centre of each fibre. This routine consists in scanning with the pyrometer across the fibre in discrete steps to construct a function of the form $T(x)$, where T is the temperature at the x position in absolute coordinates, and with the centre of the fibre providing the largest temperature reading, i.e. $\max(T(x))$. At the end of the scan, the lens assembly is positioned at x' where $T(x') = \max(T(x))$ and the PID algorithm for temperature control begins to operate.

Although the thermal inertia of the fibres is practically zero, the system is extremely stable, allowing us to remove the pyrometer and to operate the power supplies in open-
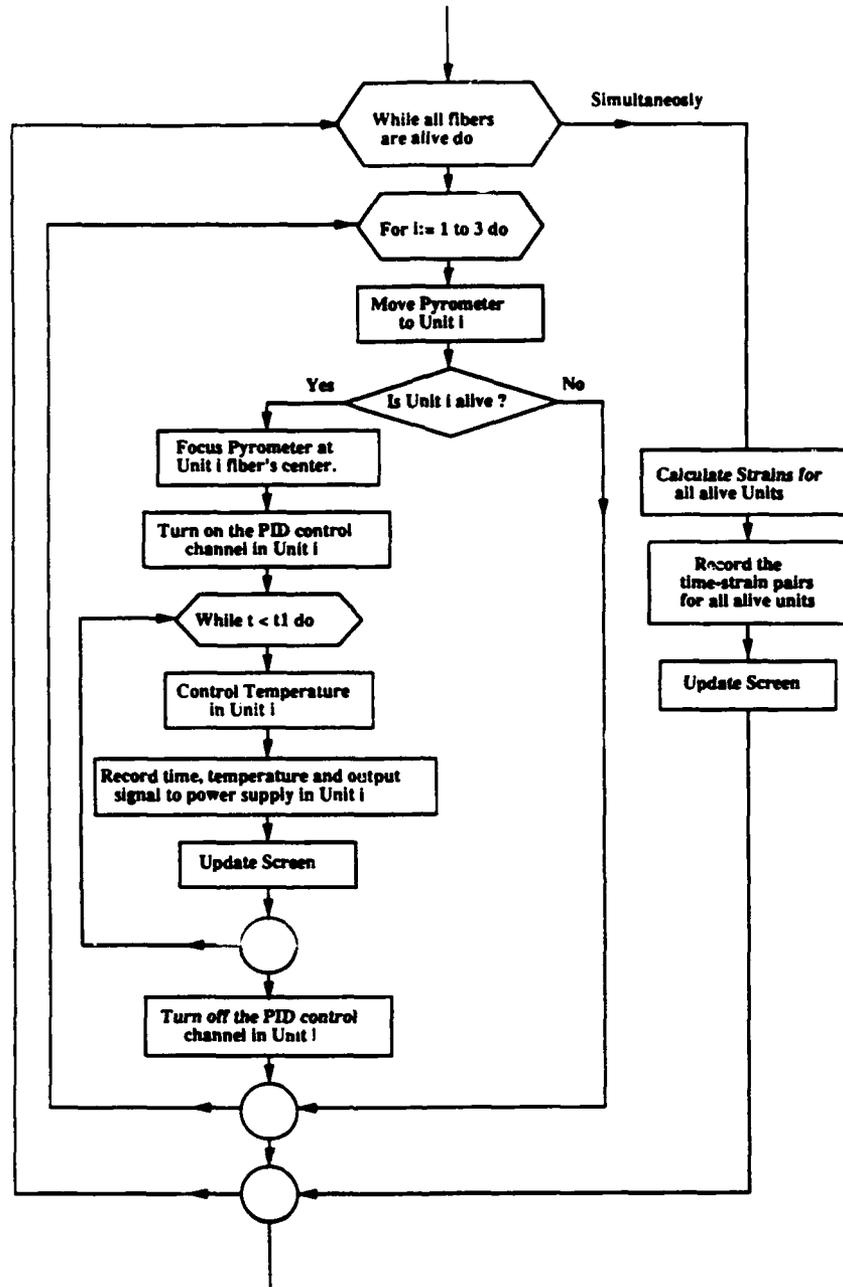
Figure 10. Logical flow chart for the simultaneous acquisition of creep data and control of temperature for three simultaneous creep experiments.

loop control maintaining a constant output across the fibre for long periods of time (e.g. hours) without undergoing temperature changes larger than 2 °C at 1500 °C. Time periods ranging from 1 to 25 min have been used in the routine controlling the position of the pyrometer's lens assembly.

4. Operation

The results presented below were obtained using a gauge length of 37.5 cm. This value was chosen to optimize the resolution in the strain calculations and also to minimize the temperature gradient resulting from the convection of hot rising gases inside the unit. For a volumetric flow of 5 cm^3 s^{-1} the maximum temperature difference between the hottest and coldest points was found to be 30 °C at 1500 °C. Argon 99.99% pure was used in all runs. To ensure an oxidation-free environment, prior to entering the unit the gas is passed through a moisture/oxygen getter consisting of heated titanium sponge maintained at 900 °C. However, despite these precautions, thin layers of silica start to appear on the fibre's surface at 1500 °C. Temperature measurements are made at two thirds of the fibre's length (25 cm from the bottom). Although the lower limit of the

pyrometer's range is 700°C, temperature readings can only be registered above 850 °C because the fibre emissivity – which was found to be close to 0.8 [23] – is less than 0.99. Although calibration of the pyrometer is traceable to NIST standards, we have found that a good way to ensure calibration is through thermal expansion measurements in the temperature range of interest.

Strains are calculated simply as

$$\varepsilon = \frac{\Delta L}{L_0} \qquad (3)$$

where L_0 is the gauge length and given as the distance between the mercury electrodes. The system offers the capability to resolve 0.25 μm in the displacements, with the resolution being limited by the A/D converter and noise levels. Different gauge lengths can be achieved by changing the height of the adjustable columns of the frame, but with the 37.5 cm gauge length resolution is translated into $6.6 \times 10^{-5}\%$ strain. The approach used to measure displacements, in which the LVDT core is attached to the bottom of the fibre is limited to fibres with large cross sections. In the case of SCS-6 SiC fibres with a 142 μm diameter, the weight of the attachment is translated into a stress of only 6 MPa, which for practical purposes is negligible. For fibres with smaller cross sections, a different approach should be adopted to determine axial displacements.

For creep experiments, the fibres are stressed using lead discs of different weights mounted onto the weight platform shown in figure 5. For SCS-6 SiC fibres, weights in excess of 1 kg have been used in creep experiments. Stresses are calculated assuming the entire cross section of the fibres carry the load.

Figure 11 shows thermal expansion measurements on SCS-6 SiC fibres using a heating/cooling rate of 15 °C min^{-1}. The upper part of the curve corresponds to the heating part of the cycle. It is interesting to note the anomalous thermal expansion behaviour of these fibres in the region of 1375 °C. Details of this behaviour and the probable responsible mechanism can be found
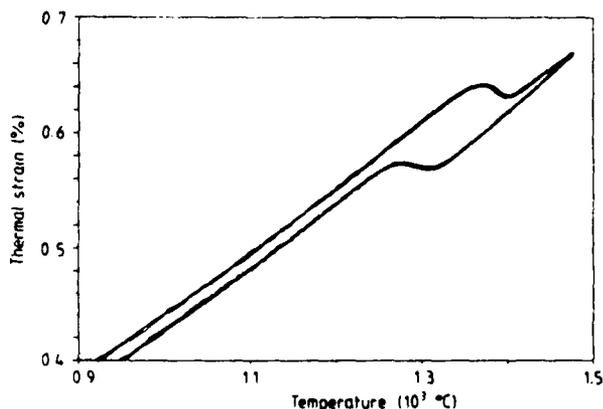
elsewhere [24]. In the plot, three different cycles are presented for the same fibre, showing the degree of reproducibility and the smooth nature of the measurements. For practical purposes, any heating and or cooling rate can be imposed on these fibres. Figure 8 shows a simple thermal history for thermal expansion measurements in which a fast quenching of almost 1450 °C in 2 s was included. Similarly, because of the negligible thermal inertia of the fibres, temperatures as high as 1800 °C have been reached in less than 5 s from room temperature.

Figure 12 shows a two cycle creep–creep recovery experiment. First the sample was taken to the test temperature (1200 °C) and held there for 1 h to achieve steady state conditions. Then the fibre was mechanically loaded with 500 MPa and allowed to creep for three hours. At the end of this period, the mechanical load was removed while the temperature was increased by 100 °C allowing the fibre to undergo a 10 h creep recovery, at the end of which the temperature was lowered to its original value and the process repeated.

Creep–creep recovery experiments were devised to quantify the thermally activated characteristics of the creep recovery process, and it was found that SCS-6 SiC fibres exhibit anelastic creep at temperatures up to 1375 °C. A model based on the composite structure of the fibres has been developed and proposed to explain their creep behaviour. Some of the predictions of the model are: anelastic creep, the existence of equilibrium creep strains and monotonically decreasing creep rates. Details of the model and comparisons with experimental measurements can be found elsewhere [25].

Creep measurements have been extended for spans of time in excess of 200 h. Figure 13(a) shows a long-term creep test along with a curve predicted by the composite model, while figure 13(b) shows the thermal history for this test. It is worth noticing the stability

Figure 11. Typical thermal strain versus temperature result for an Avco SCS-6 fibre subjected to a linear up and down ramp of temperature versus time. The graph shows three repeated experiments on the same fibre.
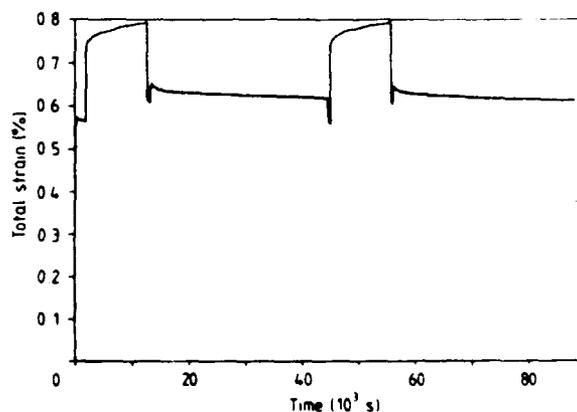
Figure 12. Typical total strain versus time for an Avco SCS-6 fibre subjected to the following treatment: (1) temperature was ramped to 1200 °C and held for one hour at no load; (2) at 1200°C, a load of 500 MPa was applied for 3 h; (3) the fibre was unloaded and allowed to recover for 10 h at 1300 °C; (4) temperature was lowered to 1200 °C and the creep experiment repeated; (5) recovery at no load was repeated at 1300 °C.
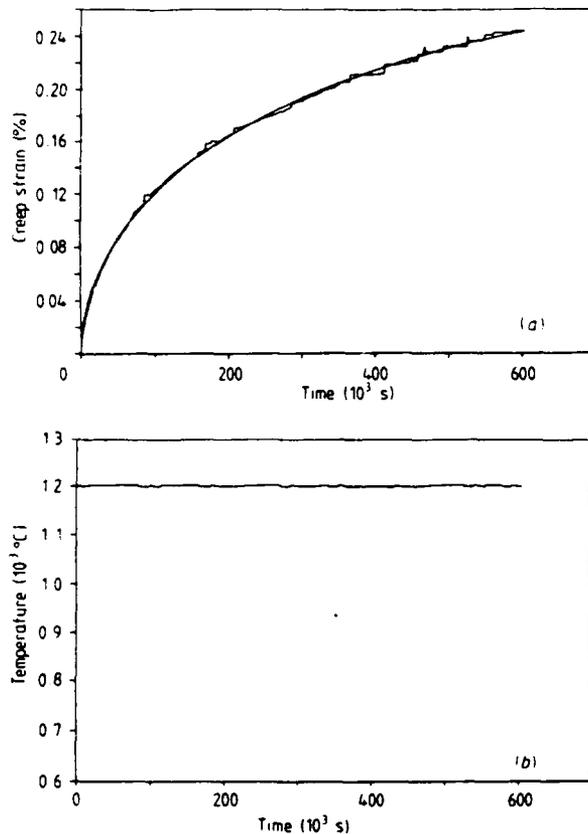
Figure 13. (a) Typical creep strain (total strain minus thermal and immediate elastic strains) versus time behaviour for an Avco SCS-6 fibre at 1200 °C and 400 MPa. (b) Thermal history for the creep curve shown in (a).

frame. For a guage length of 37.5 cm, resolution is translated into $6.6 \times 10^{-5}\%$ strain. Temperatures are measured using a two-colour infrared pyrometer having a response time of 300 ms in the temperature range of 700–2000 °C. By mounting the lens assembly of the pyrometer on a rotary table, the pyrometer can be shared by all six units, allowing for multiple simultaneous creep experiments. Although the thermal inertia of the fibres is very small, the system is thermally very stable, and temperature can be controlled to within 1 °C at 1500 °C for very long periods of time. Almost isothermal hot zones have been achieved with differences of 30 °C at 1500 °C between the hottest and coldest points along the hot zone.

For SCS-6 SiC fibres, testing has been limited to 1500 °C, above which, regardless of the installation of a heated titanium sponge oxygen/moisture getter, evaporation of the outside coating on the fibres takes place, reducing their diameter, creating regions of localized heating (hot spots) and forming thin layers of silica which, because they have a much lower emissivity, can create problems with the temperature-reading process. On occasion, failure has been accompanied by arcing, evaporating the fracture surfaces of the fibres.

of the strain and temperature measurements over long periods of time.

For most of the tests that have ended with fibre failure, fracture has been traced to the hottest point, located approximately less than 10 mm below the mercury electrode in the upper end-cap. On occasion, failure has been accompanied by short-duration arcing, evaporating the fracture surfaces of the fibre and sputtering the products on the inside walls of the quartz tube.

5. Summary and conclusions

A multiple-unit fibre tester was designed and built to study the thermomechanical behaviour of fibres up to 2000 °C. The system consists of six independent units in which data acquisition and control are fully computerized. A self-resistance heating technique, limited to electrically conductive fibres, was employed to achieve high temperatures. LVDTs were used in the determination of axial displacements for the calculation of strains by attaching the lower end of the fibre to the core of the LVDT, although this approach is limited to fibres with large cross sections. Resolution in the determination of displacements is 0.25 μm, and different gauge lengths can be obtained with the adjustable columns of the

References

[1] Hillig W B 1985 Prospects for ultra-high-temperature ceramic composites *General Electric Technical Information Series* report no 85CRD152

[2] Veltri R D and Galasso F 1971 Apparatus for measuring the high temperature strength of filaments *Rev. Sci. Instrum.* **42** 369–70

[3] Sviridovskii Y M and Volynets Y M 1983 A machine for micromechanical tests at high temperatures *Zavod. Lab.* **49** 80–3

[4] Beale J W 1989 Dynamic characterization of SCS-6 SiC fibres *MSc Thesis* Rensselaer Polytechnic Institute, Troy, NY

[5] Crane R L and Krukonis V J 1975 Strength and fracture properties of a silicon carbide filament *Ceram. Bull.* **54** 184–8

[6] Bunsell A R, Hearle J W S and Hunter R D 1971 An apparatus for fatigue testing of fibres *J. Phys. E: Sci. Instrum.* **4** 868–72

[7] Prewo K M 1974 Anelastic creep of boron fibers 1974 *J. Comp. Mater.* **8** 411–4

[8] DiCarlo J A 1976 Anelastic deformation of boron fibers *Scr. Metall.* **10** 115–9

[9] Hickling H, Thomas D H and Briggs J 1981 High temperature behavior of alumino-silicate ceramic fibers *Sci. Ceram.* **11** 397–403

[10] DiCarlo J A and Williams W 1980 Dynamic modulus and damping of boron silicon carbide and alumina fibers *Ceram. Eng. Sci. Proc.* **1** 671–93

[11] Ellison E G and Boone D H 1967 Some mechanical properties of boron–tungsten boride filaments *J. Less-Common Met.* **13** 103–11

[12] Veltri R D and Galasso F 1971 High-temperature strength of boron, silicon-carbide-coated boron, silicon carbide, stainless steel, and tungsten fibers *J. Am. Ceram. Soc.* **54** 319–20

[13] McHenry K D and Tressler R E 1975 Elevated temperature strength of silicon carbide-on-carbon filaments *J. Comp. Mater.* **9** 73–6

[14] Ahmad I, Hill D N and Heffernan W 1975 Silicon carbide filaments as reinforcements for high temperature alloy matrices *ICCM Proc. Int. Conf. Composite Mater.* vol 1 (New York: American Institute of Mechanical Engineers) pp 85–102

[15] Simon G and Bunsell A R 1984 Creep behaviour and structural characterization at high temperatures of nicalon SiC fibres *J. Mater. Sci.* **19** 3658–70

[16] DiCarlo J A 1986 Creep of chemically vapor deposited SiC fibers *J. Mater. Sci.* **21** 217–24

[17] Pysher D J, Goretta K C, Hodder R S and Tressler R E 1989 Strengths of ceramic fibers at elevated temperatures *J. Am. Ceram. Soc.* **72** 284–8

[18] Mehalso R M 1974 CVD of boron on a carbon monofilament substrate: a study of residual stresses and deposition kinetics *PhD Thesis* Rensselaer Polytechnic Institute, Troy, NY

[19] Randon J L, Slama G and Vignes A 1973 SiC fibers with improved mechanical properties: study of thermal stability *Proc. 3rd. Int. Conf. on Silicon Carbide, Miami Beach, 17–20 September 1973* (University of South Carolina Press) pp 386–93

[20] Marr S L and Ko F K 1989 Thermomechanical properties of tungsten core SiC monofilament *21st Int. SAMPE Conf., September 25–28, 1989* (Society for the Advancement of Material and Process Engineering) pp 879–91

[21] Hwan L, Suib S and Galasso F 1989 Silicon carbide-coated boron fibers *J. Am. Ceram. Soc.* **72** 1259–61

[22] Mehan R L and Sturgeon L F 1974 The use of interrupted resistance heating to perform elevated temperature tensile tests *Rev. Sci. Instrum.* **45** 1022–5

[23] Lara-Curzio E and Sternstein S S 1988 A transport analysis in the high temperature fiber testing facility *Internal Report* (HiTASC Program at Rensselaer. DARPA/ONR)

[24] Lara-Curzio E and Sternstein S S 1991 On the anomalous thermal expansion of CVD SiC fibers (to be published)

[25] Lara-Curzio E and Sternstein S S 1991 Creep analysis of a composite SiC fiber (to be published)

THERMOELASTIC ANALYSIS OF COMPOSITE CVD SiC FIBERS

Edgar Lara-Curzio & S. S. Sternstein*

Center for Composite Materials and Structures, Rensselaer Polytechnic Institute, Troy, New York 12180, USA

Abstract

A thermoelastic model has been developed for the prediction of the state of stress of composite fibers when subjected to thermomechanical loads. The model is based on a system of four infinitely long and perfectly bonded concentric cylinders. Predictions are presented for composite fibers produced by chemical vapor deposition (CVD), and in particular for the SCS-6 fiber, for which it is found that neglecting the strains that the substrate experiences during CVD in the calculations, can lead to severe underestimates of the magnitude of the predicted residual stresses. Relationships are established between the predicted state of stress and experimentally observed changes of strength with temperature, stress thresholds in creep and structural defects such as debonding at the interfaces for the SCS-6 filter.

1 INTRODUCTION

Ceramic materials offer some outstanding properties for structural applications at elevated temperatures. For example, they are strong and stiff having at the same time low densities, low coefficients of thermal expansion and resistance to aggressive environments. Despite these qualities, their use in high-performance applications has been limited in part because they are inherently brittle, often leading to catastrophic failure.

Of the limited techniques available to eliminate or lessen the lack of toughness of ceramics, the incorporation of reinforcing continuous fibers provides the best alternative for using ceramics in high-temperature structural applications. Among the filaments commercially available today, CVD SiC fibers have produced some of the most promising results in terms of mechanical, thermal and environ-

mental performance. Although their large diameter and large stiffness will most probably limit their use to applications requiring parts with simple geometries, these composite fibers provide an ideal model system worthy of study to set guidelines toward the development of a much needed new generation of fibers capable of retaining superior mechanical, thermal and environmental stability at higher and higher temperatures.

One of the characteristics of fibers produced by chemical vapor deposition (CVD) is the existence of a complicated state of stress created in part by the thermal expansion mismatch of the substrate and the deposit and the high temperatures required for their production. The objective of this paper is to provide expressions for the estimation of such state of stress when these CVD composite fibers are subjected to tensile and thermal loads. Although the analysis developed in this paper is material and scale insensitive, the predictions to be presented address the case of the SCS-6 fiber (Textron Specialty Materials. Lowell, MA 01851). Estimates of the magnitude and nature of the residual stresses are also presented, because they are important in the understanding of subjects such as failure modes, crack propagation, high temperature hardening, stress thresholds for creep, etc. Some of these subjects have been extensively addressed for CVD Boron Fibers,[1-10] and identified as important in CVD SiC fibers.[11]

2 THE SYSTEM

The SCS-6 fiber is manufactured by chemical vapor deposition in a two-step process with a 37 μm diameter glassy carbon monofilament as substrate.[12-14] This carbon filament, originally developed at the Great Lakes Carbon Corporation,[15-17] is produced at 1100°C by the spinning, oxidation and carbonization of a sulfur-doped carbonaceous pitch from petroleum or coal tar origin. The final product has a very smooth surface with occasional anomalies which can result in areas of irregular deposition, creating stress rising regions limiting the strength of the fiber.

The high temperatures required for deposition are

achieved with resistance heating techniques by passing an electric current through the substrate. The first step in the manufacture of these fibers consists of depositing a 1·5 μm thick layer of highly oriented pyrolytic graphite while the substrate is being stretched to ensure uniform deposition. This thin graphitic layer enhances the electrical conductivity and smooths the surface of the substrate, working at the same time as a buffer coating having a wave propagation velocity less than that of carbon and the deposit, effectively isolating the sheath from shocks originating in the carbon core. This was the solution to prevent the so called 'string of lights' effect, observed during the initial attempts to manufacture boron fibers and associated with a series of breaks in the substrate whenever it was unable to accommodate itself to the dimensional and structural changes that amorphous boron undergoes during chemical vapor deposition.[18,19]

When depositing the pyrolytic graphite coating on the carbon filament, the reactor is maintained at temperatures in excess of 1800°C. At lower temperatures pyrolytic graphite can not be formed, while at higher temperatures the carbon substrate begins to evaporate producing a net loss of material.[19]

In the second step of the deposition process, the pyrolytic graphite coated substrate is exposed to a mixture of polycarbosilane and hydrogen gases. The former decompose to form heavily faulted radially-aligned columnar grains of mostly β-SiC with the octahedral planes preferentially aligned parallel to the deposition surface.[20,21] Although the polycarbosilane gases used have a 1:1 carbon to silicon ratio, e.g. methyltrichlorosilane, there is a tendency for the deposition of carbon. It was found that hydrogen additions act as a catalyst for the deposition of SiC, although at 1300°C it can cause deposition of excess silicon[20] with a final product which is not 100% stoichiometric. Temperature control during deposition is critical, and the process calls for a peak deposition temperature of about 1300°C. Higher temperatures promote grain coarsening and a reduction of excess silicon which results in a decrease in the strength of the fibers. It has been suggested[22-24] that melting of this excess silicon is responsible for the anomalous thermal expansion behavior of these fibers in the neighborhood of 1375°C (as discussed in relation to Fig. 17, below). Although this argument is not conclusive, this anomalous behavior has a tremendous impact on the state of stress of the fiber with the creation of additional internal stresses, and increases in the creep resistance of these fibers have been observed after heat treatments beyond this temperature.[25]

If the fiber were to be removed from the reactor at this point and tested, its ultimate tensile strength would be approximately 1·5 GPa. By adding a rich

amorphous carbon coating of approximately 3 μm in thickness, the exposed grain boundaries of the SiC sheath are sealed, nearly doubling the fiber strength.[26-28] This additional coating has also been found to be ideal for tailoring matrix/fiber interfaces in metal matrix composites.

3 STRESS ANALYSIS

The system of interest is presented in Fig. 1 and consists of an infinitely long assembly of four perfectly bonded concentric cylinders with diameters $2r_1$, $2r_2$, $2r_3$ and $2r_4$, where $r_1 < r_2 < r_3 < r_4$. A plane strain model is presented, which implies that plane cross-sections will remain plane after deformation. All components are assumed isotropic except for the pyrolytic graphite layer.

Because the problem is axisymmetric, the circumferential component of displacement in each layer is zero. The compatibility and equilibrium equations for a cylindrical differential element, require that:

$$\varepsilon_r = \varepsilon_\theta + r\frac{d\varepsilon_\theta}{dr} = \frac{d}{dr}(r\varepsilon_\theta) \tag{1}$$

$$\sigma_r = \sigma_\theta + r\frac{d\sigma_\theta}{dr} = \frac{d}{dr}(r\sigma_\theta) \tag{2}$$

and

$$\sigma_\theta = \sigma_r + r\frac{d\sigma_r}{dr} = \frac{d}{dr}(r\sigma_r) \tag{3}$$

Combination of eqns (2) and (3) gives

$$r\frac{d}{dr}\left(\frac{1}{r}\frac{d}{dr}(r^2\sigma_r)\right) = 0 \tag{4}$$
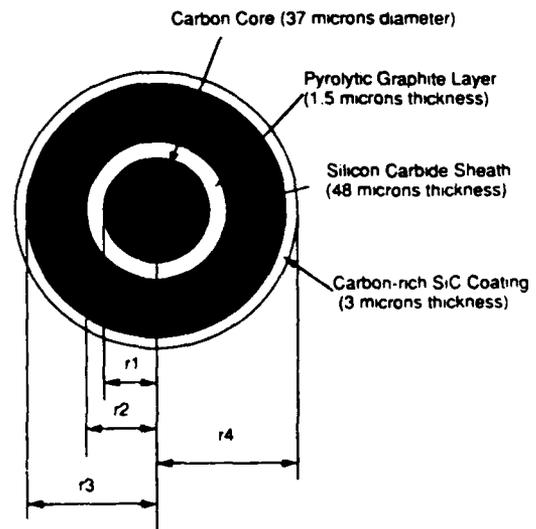
Fig. 1. Cross-sectional representation of the SCS-6 silicon carbide fiber.

which after integration, yields solutions of the form:

$$\sigma_r = A - \frac{B}{r^2} \tag{5}$$

$$\sigma_\theta = A + \frac{B}{r^2} \tag{6}$$

where A and B are integration constants which have different values for each of the four phases. The boundary conditions to be applied to the second, third and fourth phases are:

$$\sigma_r^G(r = r_1) = -P_1 \quad \sigma_r^G(r = r_2) = -P_2$$

$$\sigma_r^S(r = r_2) = -P_2 \quad \sigma_r^S(r = r_3) = -P_3$$

$$\sigma_r^M(r = r_3) = -P_3 \quad \sigma_r^M(r = r_4) = 0$$

where P_1, P_2 and P_3 are the interface normal stresses and the superscripts G, S and M refer to the pyrolytic graphite layer, the SiC sheath and the outer carbon rich coating, respectively. With reference to eqns (5) and (6), the value of the constant B for the carbon core (phase 1) is zero, and this phase is subjected to uniform radial and tangential stresses given by:

$$\sigma_r^C(r) = -P_1 \quad 0 \leq r \leq r_1 \tag{7}$$

$$\sigma_\theta^C(r) = -P_1 \quad 0 \leq r \leq r_1 \tag{8}$$

The constants A and B can be eliminated from eqns (5) and (6), as applied to each phase, in favor of the unknown interface normal stresses and result in the following equations for the radial and tangential stresses:

$$\sigma_r^G(r) = \frac{P_1 r_1^2 - P_2 r_2^2}{r_2^2 - r_1^2} + \frac{r_1^2 r_2^2 (P_2 - P_1)}{r^2 (r_2^2 - r_1^2)} \quad r_1 \leq r \leq r_2 \tag{9}$$

$$\sigma_\theta^G(r) = \frac{P_1 r_1^2 - P_2 r_2^2}{r_2^2 - r_1^2} - \frac{r_1^2 r_2^2 (P_2 - P_1)}{r^2 (r_2^2 - r_1^2)} \quad r_1 \leq r < r_2 \tag{10}$$

$$\sigma_r^S(r) = \frac{P_2 r_2^2 - P_3 r_3^2}{r_3^2 - r_2^2} + \frac{r_2^2 r_3^2 (P_3 - P_2)}{r^2 (r_3^2 - r_2^2)} \quad r_2 \leq r \leq r_3 \tag{11}$$

$$\sigma_\theta^S(r) = \frac{P_2 r_2^2 - P_3 r_3^2}{r_3^2 - r_2^2} - \frac{r_2^2 r_3^2 (P_3 - P_2)}{r^2 (r_3^2 - r_2^2)} \quad r_2 \leq r < r_3 \tag{12}$$

$$\sigma_r^M(r) = \frac{P_3 r_3^2}{r_4^2 - r_3^2} + \left(1 - \frac{r_4^2}{r^2}\right) \quad r_3 \leq r \leq r_4 \tag{13}$$

$$\sigma_\theta^M(r) = \frac{P_3 r_3^2}{r_4^2 - r_3^2} + \left(1 + \frac{r_4^2}{r^2}\right) \quad r_3 \leq r < r_4 \tag{14}$$

Deformation compatibility requires that the radial displacements at the interfaces (or the tangential strains) be the same for the phases meeting there. The requirements of uniform axial strain and deformation compatibility are written mathematically as:

$$\varepsilon_z^C - \varepsilon_{zo}^C = \varepsilon_z^G = \varepsilon_z^S = \varepsilon_z^M \tag{15}$$

and

$$\varepsilon_\theta^C - \varepsilon_{\theta o}^C = \varepsilon_\theta^G \quad \text{at} \quad r = r_1 \tag{16}$$

$$\varepsilon_\theta^G = \varepsilon_\theta^S \quad \text{at} \quad r = r_2 \tag{17}$$

$$\varepsilon_\theta^S = \varepsilon_\theta^M \quad \text{at} \quad r = r_3 \tag{18}$$

The terms with subscript 'o' in eqns (15) and (16) represent the elastic strains introduced in the substrate during the fabrication process. This occurs when the substrate is stretched in order to keep it straight during deposition. These terms are given by:

$$\varepsilon_{zo}^C = \frac{F_o}{A^C E^C} + \int_{T_1}^{T_2} \alpha^C(T)\, dT \tag{19}$$

$$\varepsilon_{\theta o}^C = -\frac{F_o \nu^C}{A^C E^C} + \int_{T_1}^{T_2} \alpha^C(T)\, dT \tag{20}$$

where we have designated T_1 as the reference temperature for the carbon core, T_2 as the temperature for the deposition of the pyrolytic graphite layer and F_o as the axial load applied to the substrate to keep it straight during deposition.

Assuming that the carbon core, the SiC layer and the carbon outer layer are isotropic, and that the graphite layer has a turbostratic structure, the elastic constitutive equations for the four phases at a temperature T' are given as follows:

$$\begin{bmatrix} \varepsilon_r^C \\ \varepsilon_\theta^C \\ \varepsilon_z^C \end{bmatrix} = \begin{bmatrix} \frac{1}{E^C} & -\frac{\nu^C}{E^C} & -\frac{\nu^C}{E^C} \\ & \frac{1}{E^C} & -\frac{\nu^C}{E^C} \\ & & \frac{1}{E^C} \end{bmatrix} \begin{bmatrix} \sigma_r^C \\ \sigma_\theta^C \\ \sigma_z^C \end{bmatrix} + \int_{T_1}^{T'} \begin{bmatrix} \alpha^C(T) \\ \alpha^C(T) \\ \alpha^C(T) \end{bmatrix} dT \tag{21}$$

$$\begin{bmatrix} \varepsilon_r^G \\ \varepsilon_\theta^G \\ \varepsilon_z^G \end{bmatrix} = \begin{bmatrix} \frac{1}{E_r^G} & -\frac{\nu_{r\theta}^G}{E_r^G} & -\frac{\nu_{rz}^G}{E_r^G} \\ & \frac{1}{E_\theta^G} & -\frac{\nu_{\theta z}^G}{E_\theta^G} \\ & & \frac{1}{E_z^G} \end{bmatrix} \begin{bmatrix} \sigma_r^G \\ \sigma_\theta^G \\ \sigma_z^G \end{bmatrix} + \int_{T_2}^{T'} \begin{bmatrix} \alpha_r^G(T) \\ \alpha_\theta^G(T) \\ \alpha_z^G(T) \end{bmatrix} dT \tag{22}$$

$$\begin{bmatrix} \varepsilon_r^S \\ \varepsilon_\theta^S \\ \varepsilon_z^S \end{bmatrix} = \begin{bmatrix} \frac{1}{E^S} & -\frac{\nu^S}{E^S} & -\frac{\nu^S}{E^S} \\ & \frac{1}{E^S} & -\frac{\nu^S}{E^S} \\ & & \frac{1}{E^S} \end{bmatrix} \begin{bmatrix} \sigma_r^S \\ \sigma_\theta^S \\ \sigma_z^S \end{bmatrix} + \int_{T_3}^{T'} \begin{bmatrix} \alpha^S(T) \\ \alpha^S(T) \\ \alpha^S(T) \end{bmatrix} dT \tag{23}$$

$$\begin{bmatrix} \varepsilon_r^M \\ \varepsilon_\theta^M \\ \varepsilon_z^M \end{bmatrix} = \begin{bmatrix} \frac{1}{E^M} & -\frac{\nu^M}{E^M} & -\frac{\nu^M}{E^M} \\ & \frac{1}{E^M} & -\frac{\nu^M}{E^M} \\ & & \frac{1}{E^M} \end{bmatrix} \begin{bmatrix} \sigma_r^M \\ \sigma_\theta^M \\ \sigma_z^M \end{bmatrix} + \int_{T_3}^{T'} \begin{bmatrix} \alpha^M(T) \\ \alpha^M(T) \\ \alpha^M(T) \end{bmatrix} dT \tag{24}$$

where the indices indicate: C, carbon core, r, θ and z are the cylindrical polar coordinates, T_3 is the

temperature for the deposition of SiC and the outer carbon coating and T' is the temperature of interest. Also, because of the uniform axial strain condition imposed in eqn (15), the principal stresses are the only non-vanishing stresses. For the pyrolytic graphite layer, $v_{r\theta} = v_{rz}$, $E_z = E_\theta$, and

$$v_{zr} = \frac{E_z}{E_r} v_{rz}$$

Substituting eqns (21)–(24) into the six equations (15)–(18) we obtain:

$$-\frac{v^C}{E^C}(\sigma_r^C + \sigma_\theta^C) + \frac{\sigma_z^C}{E^C} + \int_{T_1}^{T'} \alpha^C(T)\,dT - \varepsilon_{oz}^C$$

$$= -\frac{v_{zr}^G}{E_z^G}\sigma_r^G - \frac{v_{z\theta}^G}{E_z^G}\sigma_\theta^G + \frac{1}{E_z^G}\sigma_z^G + \int_{T_2}^{T'} \alpha_z^G(T)\,dT$$

$$(25)$$

$$-\frac{v^C}{E^C}(\sigma_r^C + \sigma_\theta^C) + \frac{\sigma_z^C}{E^C} + \int_{T_1}^{T'} \alpha^C(T)\,dT - \varepsilon_{oz}^C$$

$$= -\frac{v^2}{E^S}(\sigma_r^S + \sigma_\theta^S) + \frac{1}{E^S}\sigma_z^S + \int_{T_1}^{T'} \alpha^S(T)\,dT \qquad (26)$$

$$-\frac{v^S}{E^S}(\sigma_r^S + \sigma_\theta^S) + \frac{1}{E^S}\sigma_z^S + \int_{T_1}^{T'} \alpha^S(T)\,dT$$

$$= -\frac{v^M}{E^M}(\sigma_r^M + \sigma_\theta^M) + \frac{1}{E^M}\sigma_z^M + \int_{T_1}^{T'} \alpha^M(T)\,dT \qquad (27)$$

$$-\frac{v_{\theta r}^G}{E_\theta^G}\sigma_r^G + \frac{1}{E_\theta^G}\sigma_\theta^G - \frac{v_{\theta z}^G}{E_\theta^G}\sigma_z^G + \int_{T_2}^{T'} \alpha_\theta^G(T)\,dT$$

$$= -\frac{v^S}{E^S}\sigma_r^S + \frac{1}{E^S}\sigma_\theta^S - \frac{v^S}{E^S}\sigma_z^S + \int_{T_1}^{T'} \alpha^S(T)\,dT \qquad (28)$$

$$-\frac{v^S}{E^S}\sigma_r^S + \frac{1}{E^S}\sigma_\theta^S - \frac{v^S}{E^S}\sigma_z^S + \int_{T_1}^{T'} \alpha^S(T)\,dT$$

$$= -\frac{v^M}{E^M}\sigma_r^M + \frac{1}{E^M}\sigma_\theta^M - \frac{v^M}{E^M}\sigma_z^M + \int_{T_1}^{T'} \alpha^M(T)\,dT \qquad (29)$$

The enforcement of the uniform axial strain condition on the anisotropic graphite layer produces an expression for the radial position-dependent axial stress given by:

$$\sigma_z^G(r) = \left\{ \frac{2v^C E_z^G}{E^C} + \frac{1}{(r_2^2 - r_1^2)}\left[r_1^2(v_{zr}^G + v_{z\theta}^G) \right.\right.$$

$$\left.\left. + \frac{r_2^2 r_1^2(v_{z\theta}^G - v_{zr}^G)}{r^2} \right] \right\} P_1$$

$$- \left\{ \frac{1}{(r_2^2 - r_1^2)}\left[r_2^2(v_{zr}^G + v_{z\theta}^G) + \frac{r_2^2 r_1^2(v_{z\theta}^G - v_{zr}^G)}{r^2} \right] \right\} P_2$$

$$+ \frac{E_z^G}{E^C}\sigma_z^C - E_z^G \varepsilon_{oz}^C + E_z^G \int_{T_1}^{T'} \alpha^C(T)\,dT$$

$$- E_z^G \int_{T_2}^{T'} \alpha_z^G(T)\,dT \qquad (30)$$

Axial equilibrium is established with the expression given below when an axial load of magnitude F is imposed on the fiber:

$$A_1\sigma_z^C + 2\pi\int_{r_1}^{r_2} r\sigma_z^G(r)\,dr + A_3\sigma_z^S + A_4\sigma_z^M = F \qquad (31)$$

A_i being the appropriate cross-sectional areas. Arranging eqns (25)–(29) and (31) we obtain a 6×6 linear system of equations (eqn (32)) with the interfacial normal stresses and the axial stresses as unknowns, and with matrix $\Omega[6 \times 6]$ and vector $\Psi[6 \times 1]$ containing the physical properties of the system as well as the applied conditions for temperature and mechanical load. The elements of both the matrix Ω and the vector Ψ are given in Appendix A. The advantage of solving the problem this way is that the expressions for the interface normal stresses, which are extremely useful in a number of micromechanical analyses for composite structures, become available immediately. The solution for the system is straightforward and predictions for the state of stress in the fiber for different temperatures and stress levels are presented in Section V.

$$\begin{bmatrix} P_1 \\ P_2 \\ P_3 \\ \sigma_z^C \\ \sigma_z^S \\ \sigma_z^M \end{bmatrix} = [\Omega][\Psi] \qquad (32)$$

4 MATERIAL PROPERTIES

The validity of the predictions will depend strongly on the assumptions and values of the properties used in the calculations. Because of the proprietary nature of the fabrication process for this fiber we were unable to obtain information on the thermomechanical properties of the pyrolytic graphite layer and the outer carbon-rich coating, and certain assumptions on their properties have been made. Attempts to isolate a single carbon core with its pyrolytic graphite layer from the fiber for mechanical testing were not successful. The values for Young's moduli, Poisson's ratios and coefficients of thermal expansion presented in Table 1 have been reported for the carbon core,

Table 1. Material properties

Material	E(GPa)	v	$\alpha(10^{-6}/°C)$	Ref. temp.
Carbon core	41·37[16] 34·48[17]	0·24[4]	10·0[11] 13·0(800–1200)[16] 35·0(1200–1500)[16]	1100°C[16]
SiC	413·7[30]	0·17[30]	5·0[11] 3·2(20°C)[31] 5·1(1000°C)[31]	1300°C[11]
Pyrocarbon	80·0[29]	0·3[32]	8·8[29]	1300°C[26]

Table 2. Material properties for pyrolytic graphite

E_r	E_θ	E_z	v_{rz}	v_{qz}	α_r	α_θ	α_z
7 GPa	175 GPa	175 GPa	0·075	0·036	$28 \times 10^{-6}/°C$	$1·8 \times 10^{-6}/°C$	$1·8 \times 10^{-6}/°C$

β-SiC and amorphous pyrocarbon. As described in Section II, the deposition of the pyrolytic graphite layer is at temperatures in excess of 1800°C, with the final product having a highly oriented structure in which the basal planes are aligned parallel to the deposition surface ('onion skin'). It is only in pyrolytic graphite with this extreme preferred orientation where we can find anisotropic properties comparable with those of single crystals.[29] In this respect, we should expect a very stiff structure with a small CTE on the basal planes but very compliant and with a large CTE perpendicular to them.

For perfect single crystals of graphite the entire compliance matrix in cylindrical coordinates is given below:[33]

$$\begin{bmatrix} 33·2 \times 10^{-12} & -2·5 \times 10^{-12} & -2·5 \times 10^{-12} \\ & 1·11 \times 10^{-12} & -0·04 \times 10^{-12} \\ & & 1·11 \times 10^{-12} \end{bmatrix} [Pa]^{-1}$$

The values for the Young's moduli and Poisson's ratios contained in this matrix are: $E_r = 30·1$ GPa, $E_\theta = E_z = 900$ GPa, $v_{rz} = 0·075$, $v_{\theta z} = 0·036$, but more realistic values for the polycrystalline PG layer in these fibers are presented in Table 2[32] with a reference temperature of 1800°C.[19] The elastic properties of the external carbon-rich coating were obtained using the rule of mixtures by averaging the properties of SiC and those of amorphous pyrocarbon. The thermal expansion coefficient for this coating was approximated by:[34]

$$\alpha^M = \frac{E^{SiC}\alpha^{SiC}\phi^{SiC} + E^C\alpha^C\phi^C}{E^{SiC}\phi^{SiC} + E^C\phi^C} \tag{33}$$

where ϕ^{SiC} and ϕ^C are the volume fractions of SiC and pyrocarbon, 40 and 60% respectively.

In the calculations, the temperature dependence of the elastic properties has been considered as follows:[35]

$$E(T) = E_o \left(1 - \left(\frac{T}{T_m}\right)^3\right) \tag{34}$$

where E_o is the Young's modulus at room temperature and T_m the melting point. In the case of carbon and SiC, T_m is the sublimation temperature at ambient pressure. Values for the axial Young's modulus of the fiber predicted by this composite model are in excellent agreement with experimental measurements of the modulus up to 1600°C.[25,36] Figure 2 shows the temperature dependence of the moduli for the different phases which are the values used in the calculations.
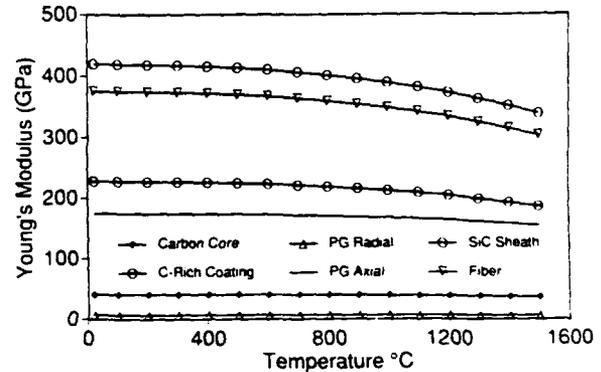
Fig. 2. Temperature dependence of the Young's modulus for the different phases in the fiber. These values were used in the calculations.

The recommended operating tension for the carbon monofilament when wound from the original shipping packages is 16 g[16] and this value was used to calculate F_o for the evaluation of eqns (19) and (20).

5 RESULTS AND DISCUSSION

The first step was an evaluation of the importance of the straining of the carbon substrate during fabrication. Figure 3 shows the predicted interface normal stresses as a function of temperature when the stretching of the carbon substrate has been taken into account in the calculations. In this case both normal interface stresses around the PG layer are positive and decrease in magnitude with temperature, whereas the normal interface stress between the SiC sheath and
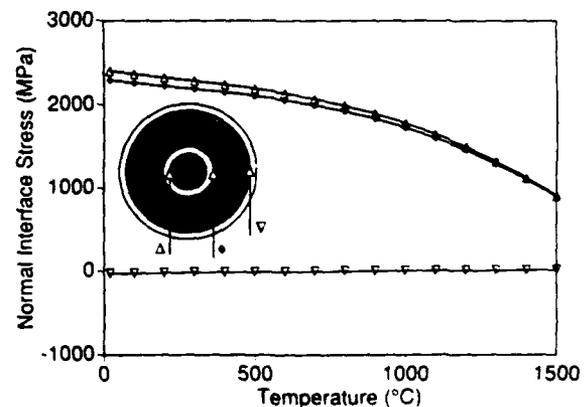
Fig. 3. Temperature dependence of the predicted interface normal stresses. The stretching of the carbon substrate during fabrication has been taken into account in the calculations.
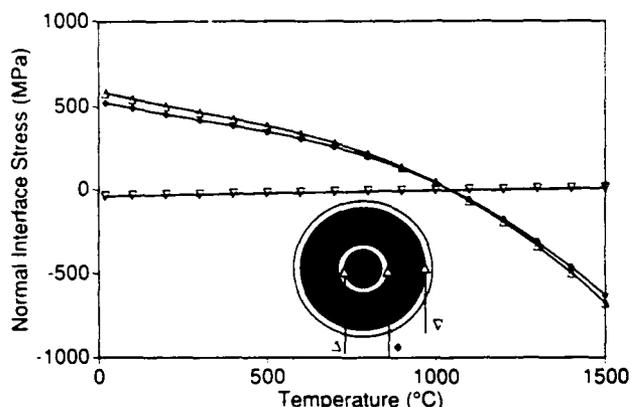
Fig. 4. Temperature dependence of the predicted interface normal stresses when stretching of the carbon substrate during fabrication has been neglected.

the outside coating is compressive, very small in magnitude and changes very little with temperature. Clearly, the radial interface stresses at both sides of the PG layer are quite high (Fig. 3), and it is unlikely that such stress levels can be achieved or sustained without debonding occurring at either the carbon substrate/PG layer interface, or the PG layer/SiC interface, or both. As shown later (Figs 12(a) and 12(b)), this conclusion is consistent with the observation of interfacial debonding in this fiber system. Additional evidence of debonding has been presented elsewhere.[37] Figure 4 shows that neglecting the straining of the carbon substrate in the calculations produces large underestimates in the predicted normal interface stresses at both boundaries of the PG layer. For this case both normal interface stresses around the PG layer are positive at room temperature and decrease continuously with temperature becoming compressive above 1000°C. As expected, there is little effect of considering the straining of the carbon substrate in the prediction of the normal interface stress between the SiC sheath and the outside coating.
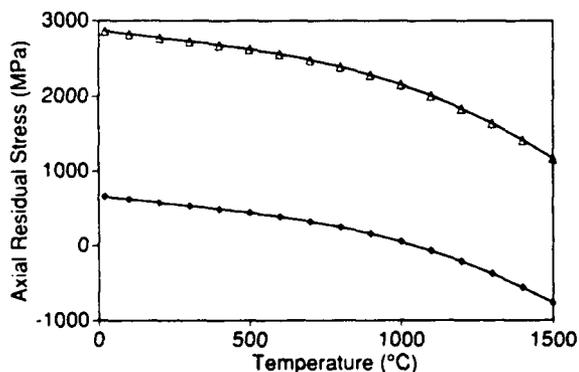
Fig. 5. Temperature dependence of the axial residual stress in the carbon substrate. Open symbols show the predictions when the stretching of the carbon core has been taken into account in the calculations.

The influence of straining the carbon substrate during deposition is most critical in the prediction of the axial stresses. In Fig. 5, the temperature dependence of the predicted axial residual stress in the carbon substrate is presented, and shows that this stress is severely underestimated when the straining of the substrate during fabrication has been ignored. The predicted decrease with temperature of the axial residual stress in the substrate can be related to experimental observations of increase of strength with temperature at 1000°C,[11] taking into account that fracture usually originates at the carbon core (Fig. 6).

Of the elastic properties used in the calculations, the values of the two independent Poisson's ratios needed to model the PG layer are the least known quantities. A parametric analysis for Poisson's ratios different from those presented in Table 2, revealed that both the axial and tangential stress distributions across the PG layer are extremely sensitive to the choice of values, as observed in Fig. 7 for the average axial residual stress. However, the influence of the value of the PG Poisson's ratios on the predicted radial stress distribution across the PG layer and the overall stress distribution in the rest of the fiber is nominal except when both $v_{z\theta}$ and $v_{r\theta}$ become larger than 0·05 and 0·1 respectively. This is illustrated for example in Figs 8 and 9 for the normal interface stress

Fig. 6. Scanning electron micrograph of the composite SCS-6 silicon carbide fiber showing the brittle nature of the fracture surface. Fiber diameter is 142 μm.
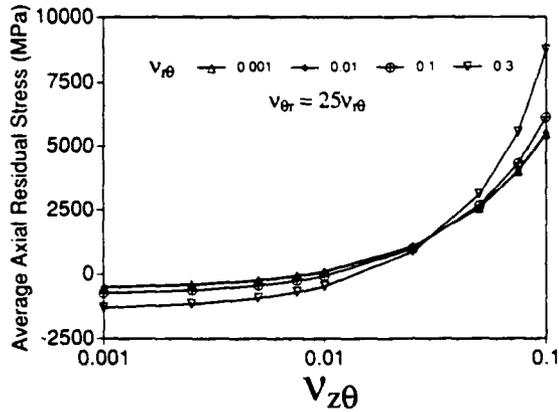
Fig. 7. Effect of the two independent Poisson's ratio values for turbostratic PG on the predicted average axial residual stress in the PG layer, where the average is defined as $\frac{1}{2}(\sigma_z^G(r_1) + \sigma_z^G(r_2))$.

Fig. 8. Effect of the two independent PG Poisson's ratios on the normal interface residual stress at the carbon-substrate/PG layer interface. This stress is almost insensitive for $v_{z\theta}$ and $v_{r\theta}$ smaller than 0·05 and 0·1 respectively.
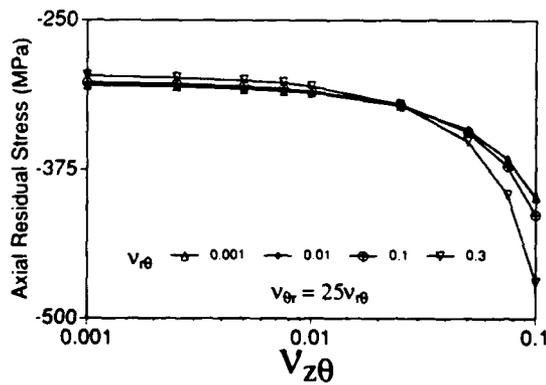
Fig. 9. Effect of the two independent PG Poisson's ratios on the axial residual stress in the SiC sheath. This stress is almost insensitive for $v_{z\theta}$ and $v_{r\theta}$ smaller than 0·05 and 0·1 respectively.

Fig. 10. Predicted temperature dependence of the axial residual stress in the SiC sheath. Open symbols show the predictions when stretching of the carbon core has been taken into account in the calculations.

at the substrate-PG layer interface and the axial residual stress in the SiC sheath respectively.

In Figs 10 and 11 the temperature dependence of the residual axial and hydrostatic stresses in the SiC sheath are compared with predictions made when straining of the substrate has been neglected. As in the case for the carbon substrate, neglecting the straining of the carbon substrate during fabrication produces large underestimates in the prediction of these stresses. Because they are compressive up to 1500°C, the predicted axial and hydrostatic residual stresses can be associated to experimentally observed thresholds of 200 MPa for creep deformation at 1100°C.[25] At this moment, further time-dependent deformation studies are under way to extend the understanding of the deformation mechanisms in these fibers and their relation to residual stresses.

An indication of the influence of residual stresses on the integrity of the fiber is evident in Figs 12(a) and 12(b), where debonding at the carbon-substrate/pyrolytic-graphite interface is shown for an
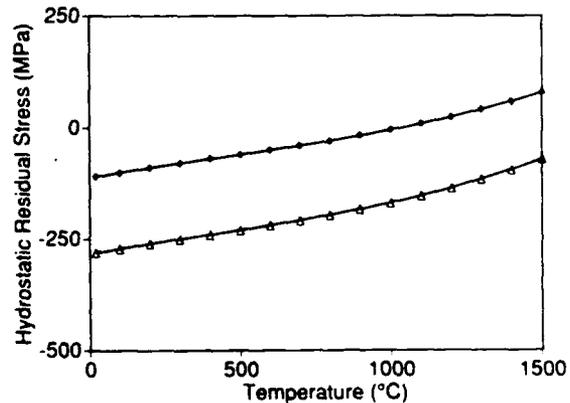
Fig. 11. Temperature dependence of the predicted hydrostatic residual stress in the SiC sheath. Open symbols represent predictions when stretching of the carbon core has been taken into account in the calculations.

Edgar Lara-Curzio, S. S. Sternstein

(a)

(b)
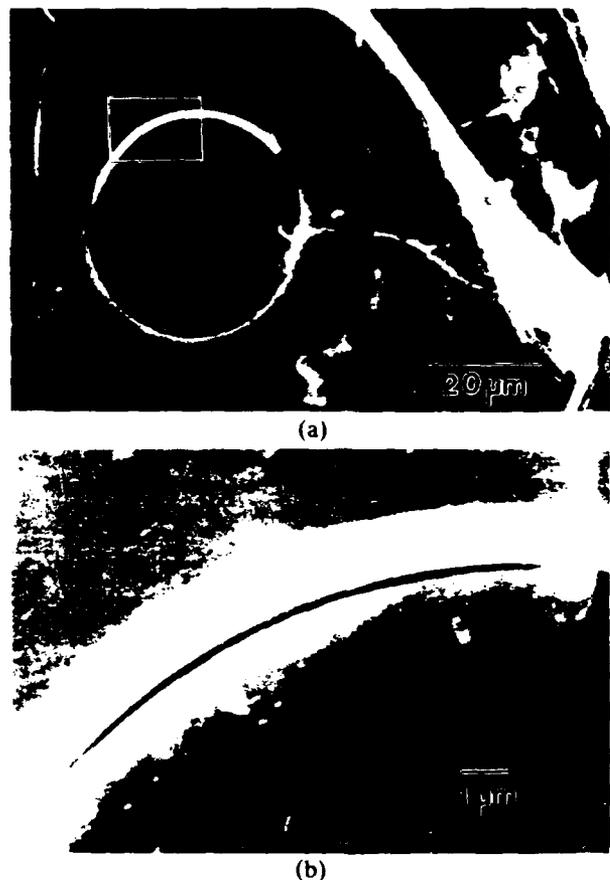
Fig. 12.(a) Scanning electron micrograph of a typical fracture surface of an as-received SCS-6 SiC. (b) Magnification of the carbon-substrate/pyrolytic-graphite layer interface from Fig. 12(a). Evidence of debonding is visible at this interface as a result of the large tensile normal interface stress.

as-received fiber. This phenomenon can be understood from the nature of the state of stress at this interface at room temperature, where there exists a tensile interface stress of almost 2·5 GPa (Fig. 13). The severity of this state of stress is a direct consequence of first, the large degree of anisotropy in

Fig. 14. Radial distribution of the predicted tangential residual stress across the fiber for different temperatures.

the pyrolytic graphite layer and second of the high temperatures required to deposit this layer. Similar results have been observed in highly anisotropic CVD graphite coatings.[29]

Another interesting observation is the nature of the tangential stresses across the SiC sheath (Fig. 14). For all the temperatures studied in this report the tangential stresses in the SiC sheath are always compressive, which in turn could explain why radial cracks are almost never observed in these fibers. Evidence of radial cracks in these fibers has been reported[23] only when the fibers have been incorporated into a composite and subjected to a high temperature fabrication schedule, changing in turn the internal stress distribution of the fiber.

Figure 15 presents the axial residual stress across the fiber while Fig. 16 shows the axial stress distribution when a load of 10 N, equivalent to 631 MPa is applied to the fiber. It is important to notice the large stresses carried by both the PG layer and carbon substrate, although most of the load is supported by the SiC sheath. Also, the axial stress in both the carbon core and the outside coating decrease in magnitude with temperature in contrast to the

Fig. 13. Radial distribution of the predicted radial residual stress across the fiber for different temperatures.
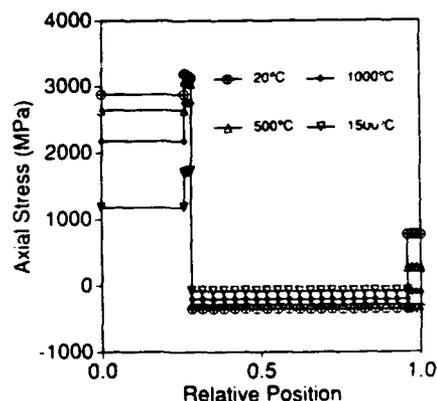
Fig. 15. Radial distribution of the predicted axial residual stress across the fiber for different temperatures.
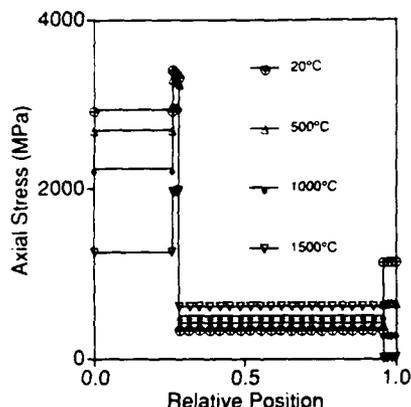
Fig. 16. Radial distribution of the predicted axial stress across the fiber for different temperatures when a uniform stress of 631 MPa has been applied to the fiber.

behavior observed in the SiC sheath. In regard to the outside coating, the model predicts tensile tangential and axial stresses at room temperature, which decrease in magnitude with temperature and that become compressive above 1000°C. The presence of this coating producing a compressive axial stress in the SiC sheath is in good part responsible for the large tensile strengths observed in these fibers.

The comparison between measured values of thermal expansion and those predicted by the model is extremely good up to the critical point when the fiber shrinks on heating (Fig. 17). In this figure the continuous curves are experimental measurements obtained using Rensselaer's high temperature fiber testing facility[38] at a heating/cooling rate of 15°C/min, while the data points correspond to the predictions by the residual stress model. The agreement up to 1350°C should not be surprising because the overall thermal expansion behavior will be dominated by the behavior of the SiC sheath.
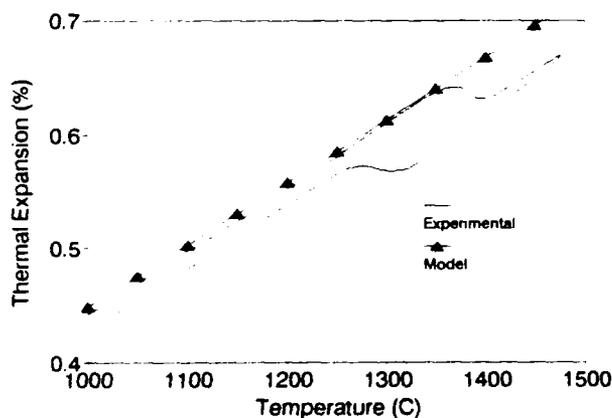
Fig. 17. Overall thermal expansion behavior of the SCS-6 SiC fiber as a function of temperature both on heating and cooling. The continuous curve represents continuous measurements made at a rate of 15°C/min using Rensselaer's High Temperature Fiber Testing Facility,[17,38] whereas the data points represent the model predictions.

It has been suggested that the anomalous thermal behavior of these fibers in the neighborhood of 1375°C could be understood in terms of melting of the free silicon and its increase in density upon melting at 1415°C.[22,23] One of the arguments that has been used to explain the depression of 40°C in the melting point is based on the theory of first-order phase transitions. For silicon, its melting temperature can be lowered by applying a compressive hydrostatic stress. The magnitude of the depression can be found using Clapeyron's equation:

$$\Delta T = \frac{T_m \Delta v \Delta P}{\Delta H_{fusion}} \tag{35}$$

For the 9% volume change that silicon exhibits upon melting[39] and a heat of fusion of 1.41×10^6 J/kg[40] the required hydrostatic stress to depress the melting point of silicon by 40°C is of the order of 1·11 GPa.

Although the magnitude of the hydrostatic stress in the SiC sheath that the present thermoelastic analysis predicts is approximately one tenth of this value at 1375°C (Figs 11), one effect that this model doesn't consider is the possible presence of excess silicon forming very small clusters where surface tension effects become important and where large stresses are not uncommon. Recent experiments[37] have demonstrated the kinetic nature of this anomalous behavior when shifts of almost 20°C toward lower temperatures were observed in the critical points of the thermal expansion curve when slower heating and cooling were used. A thermodynamic–mechanical model, which incorporates the results from this residual stress analysis, has been proposed to predict both quantitatively and qualitatively the anomalous thermal expansion behavior of this fiber including its kinetic nature.[37]

6 CONCLUSIONS

A thermoelastic analysis has been developed to estimate the state of stress of a composite fiber when subjected to thermomechanical loads. The structure is modeled as an infinitely long assembly of four perfectly bonded concentric cylinders, and although the model is insensitive to scale and/or material properties, the case of composite fibers produced by CVD was addressed and in particular the case of the SCS-6 fiber. Because of the proprietary nature of the manufacturing process for this fiber, assumptions were made in regard to the reference fabrication temperatures and the value of the mechanical properties for the different constituents in the fiber.

It was found that large differences in the prediction of the axial residual stresses and normal interface stresses result when the straining of the substrate during CVD fabrication is neglected in the calcula-

tions. This omission always leads to underestimates of the residual stresses. Values for the predictions of the normal interface stress at the SiC-carbon rich coating are almost insensitive to this consideration.

The fact that the predicted axial residual stress in the carbon substrate is tensile and decreases with temperture, can be associated with experimentally observed increases in strength up to 1000°C, taking into account that most failures originate at the carbon substrate.

It was found that the stress distribution in the pyrolytic graphite layer follows a complex pattern due in part to its large degree of anisotropy. A parametric analysis revealed that both the tangential and axial residual stresses in this layer are very sensitive to the values used in the calculations for the two independent Poisson's ratios needed to model turbostratic structures. It was also shown that all other predicted stresses in the fiber are much less sensitive to the choice of these values except when $v_{z\theta}$ and $v_{r\theta}$ become larger than 0·05 and 0·1 respectively.

The predicted axial and hydrostatic residual stresses in the SiC sheath are compressive and decrease in magnitude with temperature. This prediction has been associated with observed thresholds for creep deformation at high temperatures and with the high tensile strength of these fibers. Also the nature of the residual tangential stress in the SiC sheath is always compressive and decreases in magnitude along the radius toward the outer layers of the fiber as well as with temperature. This prediction is in agreement with the experimental observation that radial cracks in the SiC sheath are never observed, except when the fiber is incorporated into a composite and subjected to a high temperature manufacturing schedule, at which point the stress distribution inside the fiber has been altered.

The effect of the large residual radial stresses at the carbon-surface/PG layer, and PG-layer/SiC sheath interfaces has been identified with structural defects in the fiber, such as debonding. The origin of these large stresses can be traced to the large degree of anisotropy of the PG layer and to the high temperature required for its deposition in order to obtain its highly oriented structure.

The predicted hydrostatic stress in the SiC sheath at 1375°C is almost one-tenth the magnitude of the stress required to explain the anomalous thermal expansion behavior of the SCS-6 fiber at this temperature using the theory of first order transformations.[37]

ACKNOWLEDGEMENTS

REFERENCES

1. Behrendt, D. R., *Longitudinal Residual Stresses in Boron Fibers.* NASA TM-X-73402.
2. Behrendt, D. R., *Residual Stresses in Boron/Tungsten and Boron/Carbon Fibers.* NASA TM-X-73616.
3. Behrendt, D. R., *Some Properties of an Advanced Boron Fiber.* NASA TM-79065.
4. Behrendt, D. R., *Calculation of Residual Principal Stresses in CVD Boron on Carbon Filaments.* NASA TM-81456.
5. Adler, R. P. I. & Hammond, M. L., Macrostructural integrity of vapor-deposited boron and silicon carbide filament. *Appl. Phys. Letters*, **14** (1969) 11,354.
6. Kreider, K. G. & Prewo, K. M., The transverse strength of boron fibers. *Comp. Mater., Test. Design.* ASTM STP 497, 1972, 539 pp.
7. Layden, G. K., Fracture behavior of boron fibers. *J. Mater. Sci.*, **8** (1973) 1581.
8. Vega-Boggio, J. & Vingsbo, O., Tensile strength and crack nucleation in boron fibers. *J. Mater. Sci.*, **11** (1976) 273.
9. Vega-Boggio, J. & Vingsbo, O., Radial cracks in boron fibers. *J. Mater. Sci.*, **12** (1977) 2519.
10. Wawner, F. E. & McCoy, J. W., The origin of the 'crack tip' mode of failure in boron filaments. *J. Mater. Sci.*, **24** (1989) 2305.
11. McHenry, K. D. & Tressler, R. E., Elevated temperature strength of silicon carbide-on-carbon filaments. *J. Comp. Mater.*, **9** (1975) 73.
12. *Continuous Silicon Carbide Metal Matrix Composites.* AVCO Specialty Materials, Product Information.
13. DeBolt, H. E., Krukonis, V. J. & Wawner, F. E., High strength, high modulus SiC filament via CVD. In *Silicon Carbide-1973*, ed. R. C. Marshall, J. W. Faust & C. E. Ryan. University of South Carolina Press, 168 pp.
14. Crane, R. L. & Krukonis, V. J., Strength and fracture properties of SiC filament. *Ceram. Bull.*, **54**(2) (1975) 184.
15. Joo, L. A., Martin, W. & McKee, J. A., Process for Vapor Deposition on Glassy-Carbon Substrate. US Patent 3,811,927, 21 May, 1974.
16. McKee, J. A. & Joo, L. A., New carbon monofilament substrate for CVD. In *Proceedings of the 3rd International Conference on CVD*, ed. F. A. Glaski. ANS, Hinsdale, IL, 1972, p. 536.
17. Mehalso, R. M., CVD of boron on a carbon monofilament substrate—A study of residual stresses and deposition kinetics. PhD Thesis, Rensselaer Polytechnic Institute, Troy, New York, 1974.
18. DeBolt, H. E., Krukonis, V. J., Neff, R. M. & Wawner, F. E., CVD of boron on a carbon monofilament substrate. In *Materials Review for '72*, Vol. 17. SAMPE, 1972, pp II-B-TWO.
19. DeBolt, H. E., Carbon filament coated with boron and method of making same. US Patent 4,142,008, 27 Feb., 1979.
20. Diefendorf, R. J. & Weiss, J. R., CVD SiC for high temperature and structural applications. In *Silicon Carbide—1973*, ed. R. C. Marshall, J. W. Faust & C. E. Ryan. University of South Carolina Press, 80 pp.
21. Wawner, F. W., Teng, A. Y. & Nutt, S. R., Microstructural characterization of SiC SCS filaments. *SAMPE Quarterly.* (April 1983) 39.
22. DiCarlo, J. A., Creep of CVD SiC fiber. *J. Mater. Sci.*, **21** (1986) 217.
23. Brun, K. M. & Borom, M. P., Thermomechanical properties of chemically vapor deposited silicon carbide filaments. *J. Am. Ceram. Soc.* **72**(10) (1989) 1993.

24. Kern, E. L., Hamill, D. W., Deem, H. W. & Sheets, H. D., Thermal properties of beta-silicon carbide from 20 to 2000°C. *Mater. Res. Bull.*, **4** (1969) S25–32.
25. Lara-Curzio, E. & Sternstein, S. S., High temperature time-dependent deformation of composite CVD SiC fibers (to be published).
26. Cornie, J. A., Suplinskas, R. J. & DeBolt, H., Surface enhancement of silicon carbide filament for MMC. ONR Contract N000014-79-C-0691, 1981.
27. Martineau, P., Lahaye, M., Pailler, R., Naslain, R., Couzi, M. & Cruege, F., SiC filament/titanium matrix composites regarded as model composites. *J. Mater. Sci.*, **19** (1984) 2731.
28. Kotchick, D. M. & Tressler, R. E., Surface damage and environmental effects on the strain-rate sensitivity of the strength of sapphire and silicon carbide filaments. *J. Mater. Sci.*, **10** (1975) 608.
29. Fitzer, E. & Heym, M., High-temperature mechanical properties of carbon and graphite (review). *High Temp-High Pressures*, **10** (1978) 29–66.
30. Gulden, T. D., Mechanical properties of polycrystalline β-SiC. *J. Am. Ceram. Soc.*, **52**(11) (1969) 585.
31. Li, Z. & Bradt, R. C., Thermal expansion of the cubic (3C) polytype of SiC. *J. Mater. Sci.*, **21** (1986) 4366.
32. Diefendorf, R. J., High temperature advanced structural composites at Rensselaer Polytechnic Institute, Troy, New York. Program Review by ONR/DARPA 10 and 11 April, 1990.
33. Bokros, J. C., Deposition, structure and properties of pyrolitic carbon. In *Chemistry and Physics of Carbon*, Vol. 5, ed. P. L. Walker, 1969, p. 1.
34. Shapery, R. A., Thermal expansion coefficients of composite materials based on energy principles. *J. Comp. Mater.*, **2** (1968) 380.
35. Hillig, W. B., Prospects for ultra-high-temperature ceramic composites. G.E. CRD Technical Information Series, Report 85CRD152, August 1985.
36. Beale, J. W., Dynamic characterization of SCS-6 fibers. MSc Thesis, Rensselaer Polytechnic Institute, Troy, New York, 1989.
37. Lara-Curzio, E. & Sternstein, S. S., The anomalous thermal expansion behavior of chemically vapor deposited silicon carbide fibers. *J. Am. Ceram. Soc.* (in press).
38. Lara-Curzio, E. & Sternstein, S. S., A high temperature fiber testing facility. *Meas. Sci. Technol.*, **2** (1991) 358–68.
39. Logan, R. A. & Bond, W. L., Density change in silicon upon melting. *J. Appl. Phys.*, **30**(3) (1959) 322.
40. Cotterill, R. M., Jensen, E. J. & Kristensen, W. D., Melting: theories and recent computer simulations. In *Anharmonic Lattices, Structural Transitions and Melting*, ed. T. Riste. Noordhoof-Leiden, 1974, pp. 405–39.

APPENDIX A

$$\Omega_{11} = \frac{2v^C}{E^C} \quad \Omega_{12} = \frac{2v^S r_2^2}{E^S(r_3^2 - r_2^2)} \quad \Omega_{13} = -\frac{2v^S r_3^2}{E^S(r_3^2 - r_2^2)}$$

$$\Omega_{14} = \frac{1}{E^C} \quad \Omega_{15} = -\frac{1}{E^S}$$

$$\Omega_{16} = 0 \quad \Omega_{21} = 0 \quad \Omega_{22} = -\left(\frac{2v^S r_2^2}{E^S(r_3^2 - r_2^2)}\right)$$

$$\Omega_{23} = 2r_3^2\left(\frac{v^S}{E^S(r_3^2 - r_2^2)} + \frac{v^M}{E^M(r_4^2 - r_3^2)}\right) \quad \Omega_{24} = 0$$

$$\Omega_{25} = \frac{1}{E^S} \quad \Omega_{26} = -\frac{1}{E^M}$$

$$\Omega_{31} = \frac{v^C - 1}{E^C} + \frac{1}{E_\theta^G}\left(\frac{2v^C v_{\theta z}^G E_z^G}{E^C} - \frac{r_1^2 + r_2^2}{r_2^2 - r_1^2}\right)$$

$$\times (1 - v_{z\theta}^G v_{\theta z}^G) - v_{\theta r}^G - v_{zr}^G v_{\theta z}^G)$$

$$\Omega_{32} = \frac{2r_2^2(1 - v_{z\theta}^G v_{\theta z}^G)}{E_\theta^G(r_2^2 - r_1^2)} \quad \Omega_{33} = 0$$

$$\Omega_{34} = \frac{1}{E^C}\left(\frac{v_{\theta z}^G E_z^G}{E_\theta^G} - v^C\right) \quad \Omega_{35} = 0 \quad \Omega_{36} = 0$$

$$\Omega_{42} = \frac{1}{E_\theta^G}\left(\frac{(r_1^2 + r_2^2)(v_{z\theta}^G v_{\theta z}^G - 1)}{r_2^2 - r_1^2} + v_{zr}^G v_{\theta z}^G + v_{\theta r}^G\right)$$

$$- \frac{1}{E^S}\left(v^S + \frac{r_2^2 + r_3^2}{r_3^2 - r_2^2}\right) \quad \Omega_{43} = \frac{2r_3^2}{E^S(r_3^2 - r_2^2)}$$

$$\Omega_{44} = -\frac{E_z^G v_{\theta z}^G}{E^C E_\theta^G} \quad \Omega_{45} = \frac{v^S}{E^S} \quad \Omega_{46} = 0$$

$$\Omega_{51} = 0 \quad \Omega_{52} = \frac{2r_2^2}{E^S(r_3^2 - r_2^2)}$$

$$\Omega_{53} = \frac{1}{E^S}\left(v^S - \frac{r_2^2 + r_3^2}{r_3^2 - r_2^2}\right) - \frac{1}{E^M}\left(v^M + \frac{r_3^2 + r_4^2}{r_4^2 - r_3^2}\right)$$

$$\Omega_{54} = 0 \quad \Omega_{55} = -\frac{v^S}{E^S} \quad \Omega_{56} = \frac{v^M}{E^M}$$

$$\psi_1 = \int_{T_3}^{T'} \alpha^S(T)\, dT - \int_{T_1}^{T'} \alpha^C(T)\, dT + \varepsilon_{0z}^C$$

$$\psi_2 = \int_{T_3}^{T'} (\alpha^M(T) - \alpha^S(T))\, dT$$

$$\psi_3 = \frac{v_{\theta z}^G E_z^G}{E_\theta^G} \int_{T_2}^{T'} \alpha_z^G(T)\, dT + \int_{T_2}^{T'} \alpha_\theta^G(T)\, dT$$

$$- \left(\frac{v_{\theta z}^G E_z^G}{E_\theta^G} + 1\right) \times \int_{T_1}^{T'} \alpha^C(T)\, dT + \frac{E_z^G v_{\theta z}^G}{E_\theta^G}\varepsilon_{0z}^C - \varepsilon_{0\theta}^C$$

$$\psi_4 = \int_{T_3}^{T'} \alpha^S(T)\, dT - \int_{T_2}^{T'} \alpha_\theta(T)\, dT - \frac{v_\theta^z E_z^G}{E_\theta^G}\int_{T_2}^{T'} \alpha_z^G(T)\, dT$$

$$\psi_6 = \int_{T_3}^{T'} (\alpha^M(T) - \alpha^S(T))\, dT$$

A Methodology for the Elevated Temperature Characterization of High Performance Fibers

E. LARA-CURZIO[1] AND S. S. STERNSTEIN[2]

ABSTRACT

A methodology is presented for studying the thermomechanical behavior of fibers at elevated temperatures. Emphasis is given to the importance and sensitivity of mechanical spectroscopy measurements as a tool for investigating deformation mechanisms. Selected experiments include thermomechanical tests in a wide span of the time domain (dynamic measurements, creep and thermal expansion response) as well as analytical structural characterization. This approach will only be useful if realistic modeling can be developed to establish links between microstructure, macrostructure and properties. As an example an overview of the characterization of the SCS-6 SiC fiber at high temperatures is presented.

INTRODUCTION.

The need for structural materials in energy conversion systems - e.g. nuclear reactors and jet engines- capable of withstanding extreme conditions of stress, environment and temperature has shifted attention from the improvement of superalloys to the potential development of ceramic matrix composites which offer the capability of retaining stiffness and strength at higher temperatures with substantially lower densities. Of all possible reinforcements, continuous fibers offer the best alternative to improve the damage tolerance, fracture toughness and resistance to creep of ceramics. However, there is only a limited number of fibers commercially available today and they behave in a way that will prevent them from being used in advanced structural applications. For example, silicon-oxy-carbide fibers begin to decompose at temperatures as low as 1100°C, graphite fibers can not survive in aggressive environments beyond 600°C without protective coatings, tungsten fibers are heavy and very reactive, CVD SiC fibers with carbon substrates exhibit an anomalous thermal expansion behavior in the neighborhood of 1375°C and possess large diameters, whereas CVD SiC fibers with a tungsten substrate readily react resulting in a severe drop in strength at temperatures beyond 1100°C.

These limitations have prompted work on their improvement and in the development of new filaments, calling in turn for screening procedures and a methodology

1 Graduate Research Assistant, Dept. of Matls. Eng., RPI, Troy, NY 12180
2 Professor, Dept. of Matls. Eng., RPI, Troy, NY 12180

for their characterization. The results from the characterization studies will be useful both as input parameters for the design of composite structures and/or for the improvement of the filaments. Some of the relevant properties that need to be evaluated include the temperature dependence of stiffness and strength, the resistance to creep, the thermal expansion response, environmental stability and how these properties relate to the micro and macro structures. For the latter, complementary studies should include compositional and microstructural characterization using spectroscopy, the power of the analytical electron microscope and other techniques such as XRD and high temperature DSC/TGA.

Furthermore, the development of constitutive equations and deformation models that incorporate the effects of the manufacturing process to simulate and predict the behavior of these filaments under a given set of conditions of stress, temperature, environment and time is of utmost importance.

In this paper, a general methodology is presented for the characterization of fibers at elevated temperatures. The case of the SCS-6 SiC fiber will be addressed showing the advantages and limitations of some analytical techniques and highlighting the importance of mechanical spectroscopy for characterization. In this particular case, the sensitivity of thermal expansion measurements was proved to be far superior for detecting a phase transformation compared to any of the conventional characterization techniques.

EXPERIMENTAL APPROACH.

Figure 1 shows the areas where characterization is needed. The links in the diagram indicate for example that physical and mechanical models should be developed based on the results of thermomechanical tests and microstructural observations, but also that further tests and observations should be designed to test the validity of the models.

In the physical area, it is necessary to determine basic macrostructural properties such as diameter, uniformity, fracture surface morphology, interfaces in composite structures, density, etc. Microstructural features include grain size, crystallographic structure, texture, etc. Some of the techniques for diameter determination include laser diffraction and direct measurements using the optical or electron microscope. Density measurements could be achieved by X-ray diffraction methods or a combination of hydrostatic and dilatometric measurements. The fracture morphology provides information on the degree of brittleness of the fiber and the regions where crack initiation takes place. These observations can then be used to evaluate the validity of residual stress and damage propagation analyses for example. Microstructural characterization can be achieved mostly with X-ray and TEM analyses.

Compositional analysis can be carried out by combining techniques such as XRD, the electron microprobe, Raman and Auger spectroscopy. Some of the limitations of these techniques are that they are unable to detect or identify phases present in less than 3% concentration and because of the rather large size of the probe compared to the average grain size in polycrystalline materials, the results are only averages over large sections. In this case the analytical electron microscope and the measurement of SAD patterns of very

small regions provide the most powerful tool for phase identification. However there are situations in which even this technique is limited because transparency requirements during sample preparation could sometimes introduce additional artifacts and tamper with the evidence.

Figure 2 shows the X-ray spectra for pulverized SCS-6 SiC fibers after a heat treatment in air at elevated temperatures. Notice the appearance of a silica peak indicating that oxidation had taken place. It is also interesting to observe that the microstructure is heavily faulted because of the presence of several reflections from α-SiC planes in this mostly β-SiC fiber. The graphite reflections arise from the pyrolytic graphite coating deposited around the carbon substrate. Although dislocation motion is limited in ceramics because of the large value of the Pierls stress, the presence of stacking faults could enhance gliding and climbing promoting in turn deformation. A detailed description of the manufacturing process and the general features of the fiber can be found in [1]. Figure 3 shows a scan across the fiber using the electron microprobe. The spot size of the beam was 1 μm approximately. Considering that the average grain size in this fiber is of the order of 50 nm, this technique, as well as Raman and Auger spectroscopy are limited if detailed analysis of the grain boundaries or change in composition form grain to grain is intended, although effective averages for composition can be obtained readily. Although it might seem that the composition across the fiber changes from carbon-rich to silicon-rich it should be mention that these fluctuations are perhaps outside the resolution of these measurements

Some fibers undergo recrystallization and phase transitions at high temperatures and new phases could be formed if the samples are exposed to aggressive environments. Also loss or gain of weight is a common occurrence at high temperatures in aggressive environments. In this case simultaneous TGA/DTA provide valuable information as the system absorbs or releases heat while temperature is increased or decreased at a prescribed rate and as the material gains or losses weight. Figure 4 shows a typical DSC scan at a rate of 20°C/min for a SCS-6 fiber. The temperatures indicated in the graph are small deviations from the base line. However, despite the sensitivity of some of these instruments, if small reactions are the subject of the study, they could easily get lost in the noise and fluctuations inherent in these measurements at temperatures above 1300°C. It is believed that the faint signal at 1376°C is related to the anomalous thermal expansion behavior exhibited by this fiber but it is so weak that no quantitative analysis was possible.

Mechanical spectroscopy has proved to be an invaluable tool for the sensitive measurement of parameters intimately related to the microstructure of the material. For example there exist dynamic techniques capable of resolving 1 part in 5000 of the out of phase dynamic modulus. A detailed monitoring of the out-of-phase modulus with temperature can provide information on the way the material dissipates energy, for example through the formation of a new phase, by the disruption of an interface or by friction. Also, this method offers the possibility of determining the temperature dependence of the elastic modulus as shown in Figure 5 and compared to other forms of SiC. The major limitation for applying this technique is that hot wall furnaces with open

ends should be used to avoid the frictional interference of the fiber grips with the furnace, implying that a way must be devised to extract isothermal properties from a collection of tests at different temperatures with variable gauge lengths. Examples of this procedure can be found elsewhere[1,2].

Dilatometry in the form of axial and radial thermal expansion measurements not only provides information on the continuous change of the material as temperature is changed, but if the measurements are sensitive, volume changes associated with phase transformations can be detected.

This is the case for the SCS-6 SiC fiber. Because of the manufacturing conditions, it is likely that non-stoichiometric silicon is present in the fiber. Upon melting, this excess silicon increases its density forcing the fiber to contract in the neighborhood of 1375°C on heating, and to expand on cooling at around 1300°C upon solidification. Compositional studies were unable to detect the small amount of silicon (approximately 1% volume) necessary to produce the effect shown in Figure 6. It can be observed that the sensitivity of the dilatometric measurements is large enough to reproduce this phenomenon repeatedly on the same fiber after three cycles. New techniques have been devised to measure simultaneously the radial and axial thermal expansion response of fibers incorporating diffraction techniques in the High Temperature Fiber Testing Facility[3]. This is useful because in a number of manufacturing processes, the products show a large degree of anisotropy in the thermal expansion behavior and other mechanical properties. Details of the measurements and the nature of the anomalous thermal expansion behavior can be found in [3,4].

Creep is perhaps the most limiting factor for using a material at high temperatures in structural applications and it is one phenomenon where the relationships between structure, properties and thermomechanical response are most evident. The size of the grains, the formation of glassy phases at the grain boundaries, a heavily faulted structure, the existence of residual stresses etc, are all strongly linked to the deformation mechanisms controlling the rate of deformation of the material. Creep experiments in single filaments are difficult and expensive because of their long duration and because of the small dimensions of individual fibers.

Figure 7 shows the typical creep response of a SCS-6 SiC fiber at 1200°C and 400 MPa along with the curve predicted by a composite model which was developed to analyze the time-dependent deformation of this composite fiber. Both the creep and thermal expansion measurements presented in this paper were obtained in the High Temperature Fiber Testing Facility[3].

MODELING.

Data acquisition although important is far more useful when models capable of establishing links between the micro and macrostructure of the fiber and its properties are developed. For example, three models have been developed to analyze the deformation under stress and temperature as a function of time of the SCS-6 SiC fiber.

The first model was created to study the internal state of stress of the fiber after fabrication, taking into account that the fiber possesses a composite structure and that high temperatures are necessary for its manufacture. Although the analysis assumed that all the phases behaved in a perfectly elastic manner, the model was capable of predicting the large stresses responsible for producing debonding at some of the fiber interfaces. Figure 8 shows a scanning electron micrograph of the carbon-pyrolytic graphite layer interface in which debonding is evident while Figure 9 shows the radial residual stress across the fiber. From this set of curves can be observed the large value of the normal interface stress at the carbon-pyrolytic graphite interface. Also, other predictions of the model have been linked to observed increases of strength with temperature and stress thresholds for creep. Further details can be found elsewhere[5].

The second model deals with the anomalous thermal expansion behavior of this fiber in the neighborhood of 1375°C on heating and around 1300°C on cooling and its kinetic nature. The model takes into account the lack of stoichiometry of the fiber and the likely presence of small clusters of excess silicon dispersed according to a distribution law. The model incorporates the thermodynamic effect of size in melting and successfully predicts the anomalous behavior on both heating and cooling. Figure 10 shows the predicted thermal expansion response on heating according to this model. Details of the analysis can be found in a recent report[4]. Also at this moment, attempts are under way to detect experimentally the existence of these silicon clusters in the fiber to validate the model.

The third model was developed to address the composite structure of this fiber and the influence of this structure on the time dependent deformation under stress. This is important because if the fiber is analyzed as a single entity, then activation energies and other parameters (e.g. stress exponents, etc) that can be extracted from a family of creep curves would be just fitting parameters without clear physical meaning. Furthermore, the anelastic behavior of this fiber is most likely related to its composite structure and not to some relaxation mechanism as previously suggested[6]. Figure 7 shows the predictions of the composite creep model along with an experimental creep curve at 1200°C and 400 MPa. Some of the predictions of the model include monotonic decreases in the creep rate, the existence of equilibrium strains after long times and the complete recovery of the creep deformation. This implies that there exists a stress transfer mechanism from the creeping phases to the elastic ones during creep and vice versa during recovery. Although the entire fiber might be subjected to a constant stress level during creep, the creeping phases will be subjected to a non-constant decreasing stress. Details of the model will be the subject of an upcoming report[7].

One of the ways deformation mechanisms are identified is by determining the activation energy controlling the rate of deformation. In the case of fibers, activation energies can be obtained from dynamic viscosity measurements[2], creep[7], and in the case of the the anomalous thermal expansion behavior, from heating-isothermal holding experiments[8]. Once again, special attention should be paid to the interpretation of these

parameters in composite systems in which more than one phase is undergoing deformation. Many times the sources of deformation based on activation measurements can be corroborated through microstructural observations, of events such as dislocation motion, grain boundary sliding, cavitation, etc.

SUMMARY.

Using the example of the SCS-6 SiC fiber, a systematic methodology for the characterization of advanced fibers for high temperature structural applications was presented. The main ideas behind this methodology include the evaluation of the thermomechanical behavior using mechanical spectroscopy and the study of the microstructural evolution as a function of stress, time, environment and temperature. The use of realistic physical models is necessary if an understanding of the deformation mechanisms is intended and if improvement in the mechanical behavior of the filaments is sought. Furthermore, the model predictions should be tested experimentally against samples with special features relevant to the characteristics of the model whenever possible. Special care should be taken during the interpretation of the results and specially of parameters such as activation energies, for example. The way they are obtained and the assumptions that were made for their calculation should be considered with special attention for composite fibers.

ACKNOWLEDGEMENTS.

REFERENCES.

1.- Beale, J., Lara-Curzio, E., and Sternstein, S.,S.,' High Temperature Deformation Studies on CVD SiC Fibers,' 35th International SAMPE Symposium. Anaheim, April 2-5 1990. Society for the Advancement of Material and Process Engineering, 1990. pp.1193-1204.

2.- Beale, J.W., "Dynamic Characterization of SCS-6 SiC Fibers," M.Sc. Thesis, Rensselaer Polytechnic Institute, Troy, NY 12180, 1989

3.- Lara-Curzio, E., and Sternstein, S., S., 'A High Temperature Fiber Testing Facility,' Meas. Sci. Technol.2 (1991) 358-368.

4.- Lara-Curzio, E., and Sternstein, S., S., 'On the Anomalous Thermal Expansion of CVD SiC Fibers,' Submitted to J. Am. Ceram. Soc. (1991).

5.- Lara-Curzio, E., and Sternstein, S., S., 'Thermoelastic Analysis of Composite Fibers,' Submitted to Comp. Sci. and Tech, (1991).

6.- DiCarlo, J. A., 'Creep of Chemically Vapor Deposited SiC Fibers', J. Mat.Sci, 21 (1986) 217-224.

7.- Lara-Curzio, E., and Sternstein, S. S., 'Creep Analysis of a Composite SiC Fiber,' To be published.

8.- Lara-Curzio, E., and Sternstein, S., S., 'Kinetics of the Anomalous Thermal Expansion of CVD SiC Fibers,' To be published.
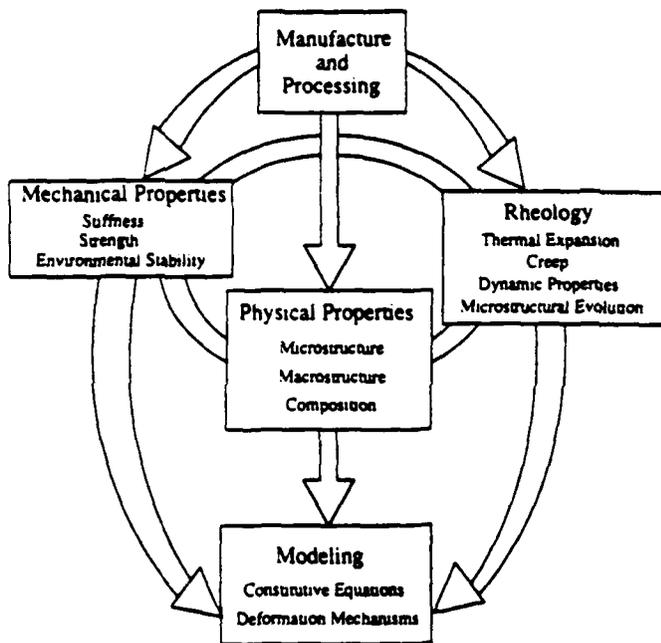
Fig. 1 Schematic diagram showing the areas where characterization and analysis is needed for the thermomechanical and structural characterization of high performance fibers
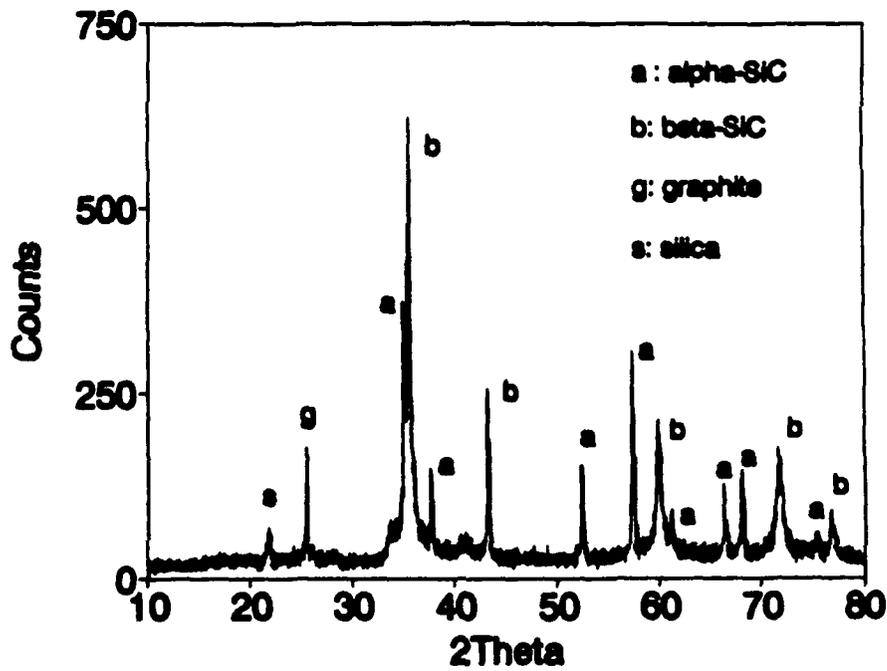
Fig.2 X-ray spectra of pulverized SCS-6 fibers after a heat treatment at high temperatures. Oxidation is evident from the presence of a silica peak. Also the reflections from alpha-SiC planes indicate that the microstructure is heavily faulted
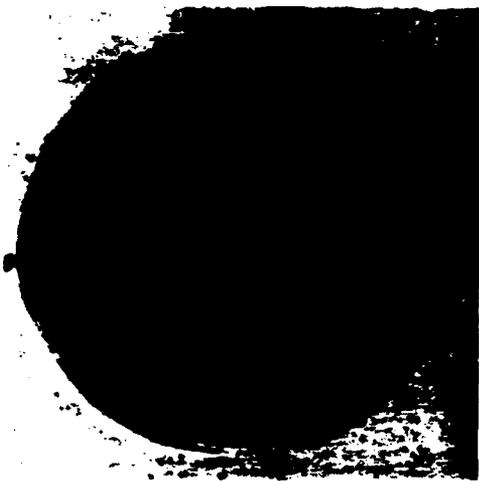
Fig.3.a. Cross sectional area of the SCS-6 SiC fiber. Total diameter is 142 microns.
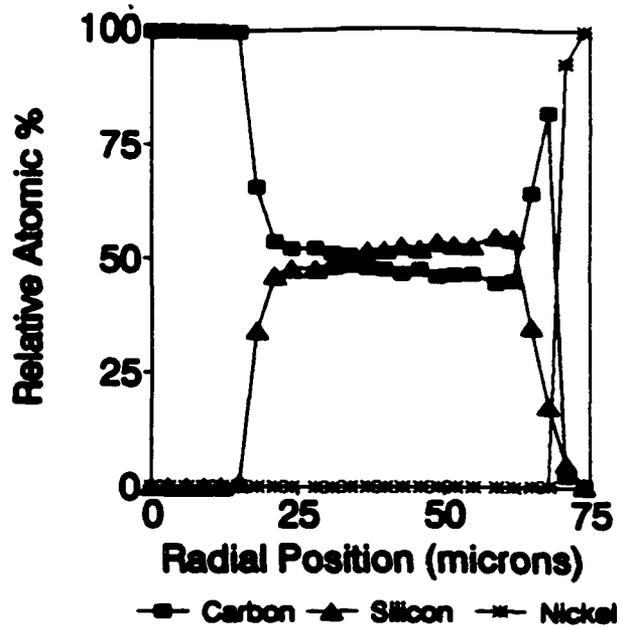
Fig.3.b. Electron microprobe scan across the fiber in Fig. 3.a. Probe size : 1.0 micron
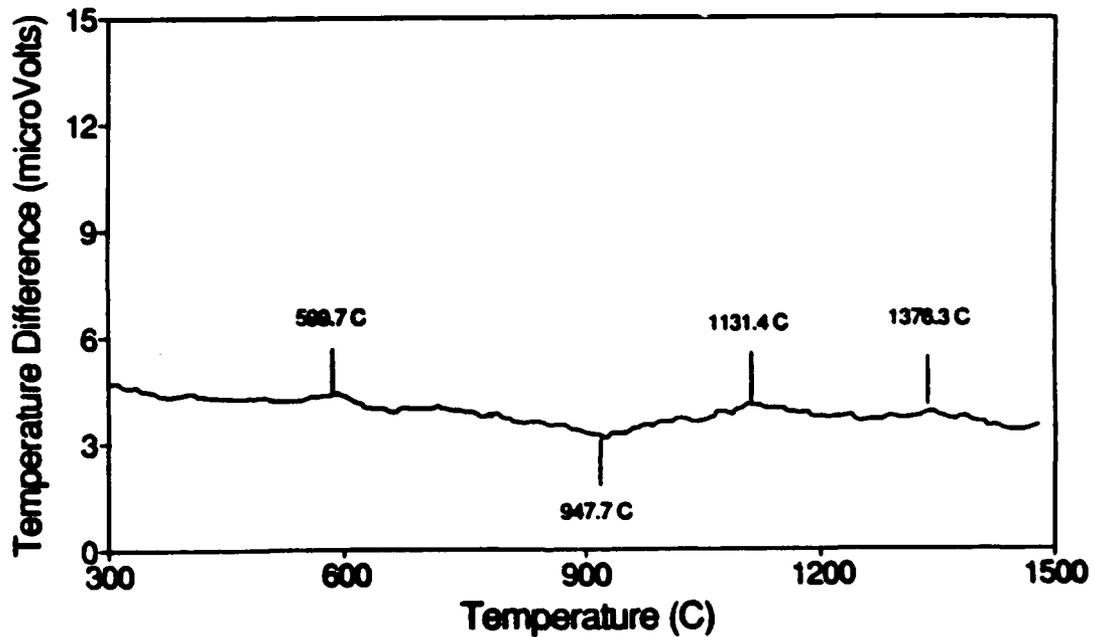
Fig.4 DSC result for SCS-6 fibers. The temperatures indicated are small deviations from the base line. No quantitative analysis was possible. Heating rate: 20°C/min.
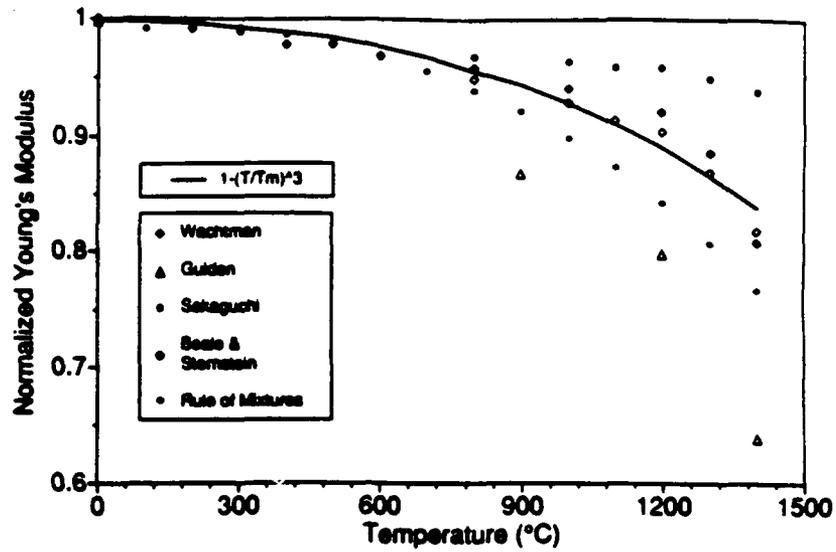
Fig.5 Temperature dependence of the elastic modulus of SCS-6 SiC fibers
from dynamic measurements (Beale & Sternstein) compared to other forms
of SiC along with the prediction of the rule of mixtures based on the composite
structure of the fiber
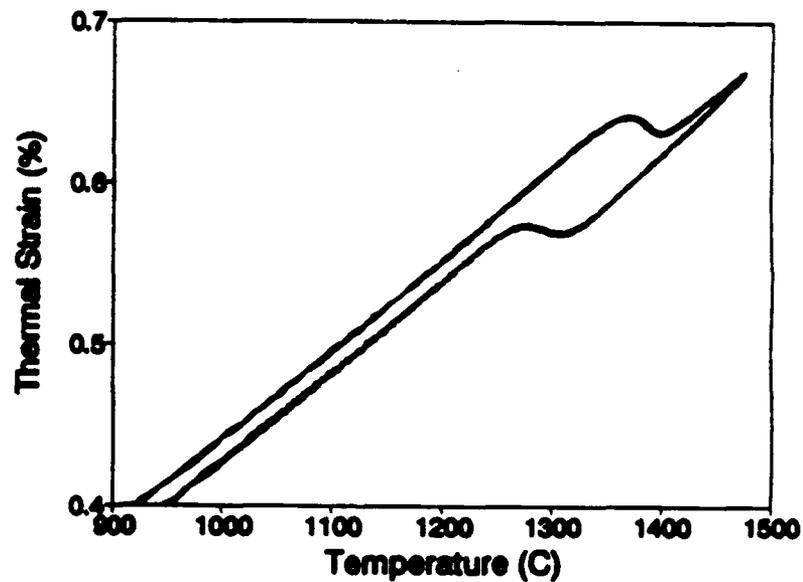
Fig. 6 Thermal expansion response of a SCS-6 SiC fiber. Three different curves are
presented indicating the degree of reproducibility and the smooth nature of the
measurements. The results were obtained using Rensselaer's High Temperature
Fiber Testing Facility.
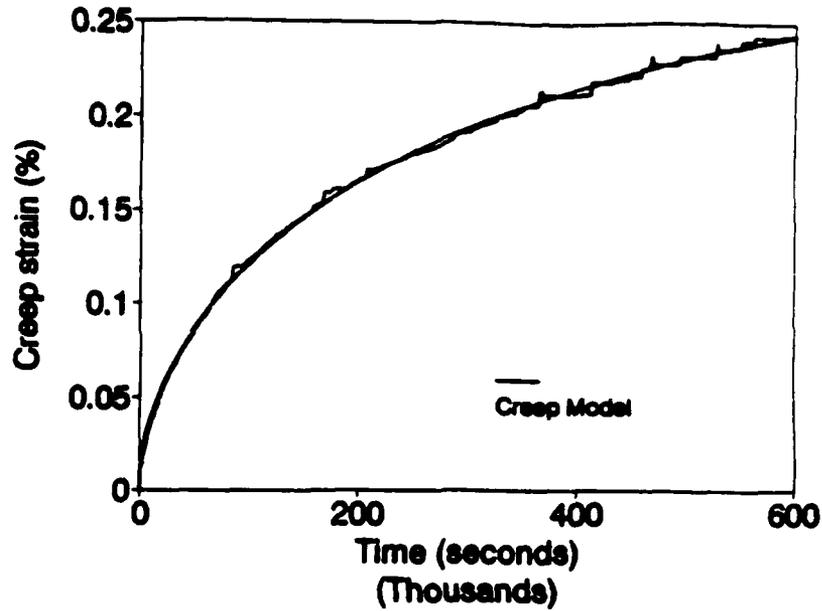
Fig.7 Creep response of a SCS-6 SiC fiber at 1200°C and 400 MPa and predictions of the creep model. The creep behavior is anelastic arising from the fiber's composite structure. The results were obtained using Rensselaer's High Temperature Fiber Testing Facility
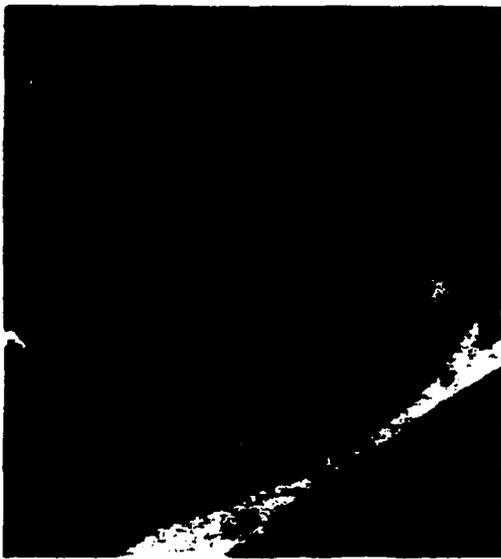
Fig. 8.a Scanning electron micrograph of a typical SCS-6 fiber fracture surface. Carbon core diameter is 37 microns.

Fig.8.b. Magnification of Fig. 8. a. showing the debonded region at the carbon core-pyrolytic graphite interface.
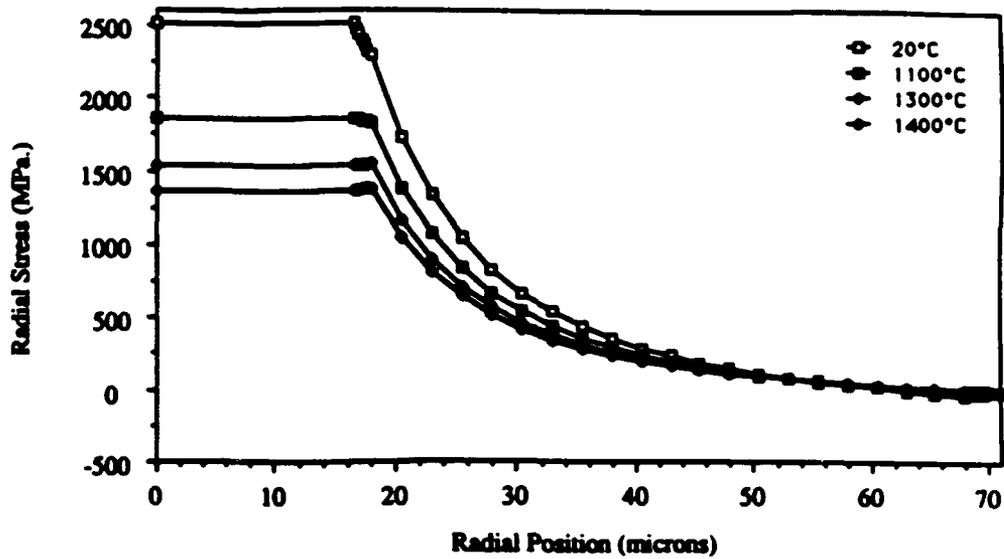
Fig. 9 Radial residual stress across the SCS-6 fiber at different temperatures. The results were obtained using a four-phase composite model which incorporates the effects of straining the carbon substrate during chemical vapor deposition.
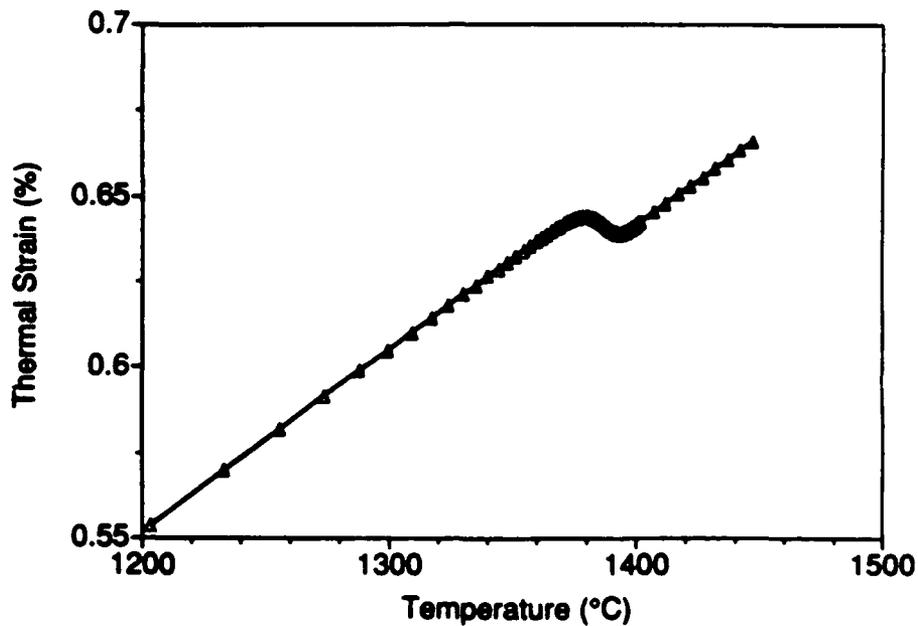
Fig. 10 Thermal expansion response according to the composite model developed to predict the effective thermal expansion behavior of systems containing non-stoichiometric silicon. The model incorporates the thermodynamic effect of particle size on the melting of excess silicon.

CHARACTERIZATION OF FIBERS AT HIGH TEMPERATURE

Sanford S. Sternstein, Edgar Lara-Curzio, and John Beale
Center for Composite Materials and Structures
Rensselaer Polytechnic Institute
Troy, New York 12180

INTRODUCTION

Thermal characterization of the constituent mechanical properties is an essential step in the development of advanced high temperature composites. The limited database on engineering properties of candidate materials for both fibers and matrices is a major factor which hinders the screening of potentially successful composite systems prior to their actual development or fabrication. Many advances in the micromechanics of composite materials cannot be fully utilized as a result of incomplete or reliable data on essential properties such as coefficient of thermal expansion (CTE), creep behavior, modulus or strength. Modeling studies provide not only a means to screen viable materials systems prior to actual fabrication, but also provide a means to supplement, validate and/or substitute for extensive long term testing of the final composite system.

In this paper, two new instruments are described which were specifically developed to provide extensive and reliable data on single fibers at elevated temperatures. The first instrument is designed to measure complex dynamic modulus over a broad range of both frequency and temperature. The dynamic technique is especially useful for measuring anelastic processes which occur at very short relaxation times, too short to be meaningfully measured by creep experiments. Thus, dynamic measurements provide information pertaining to material response for rapid changes in stress levels. In addition, the dynamic method is far more sensitive than creep in determining the presence of small levels of anelastic response, and is therefore a highly sensitive probe for evaluating small changes in structure-property relations or mechanisms of deformation resulting, for example, from changes in fiber processing or subsequent heat treatments.

The second instrument has been designed to measure creep and CTE on several single fiber samples simultaneously. This instrument provides for an inert sample atmosphere and an unusually long and isothermal gauge length with exceptionally stable high temperature control. The creep data span a time scale from several seconds to an arbitrary upper limit. Owing to the exceptionally long isothermal gauge length, the creep data directly reflect the sample behavior without corrections, as opposed to the dynamic modulus data which must be deconvoluted as a result of the sample temperature distribution. The creep and dynamic data are complementary and combine to render anelastic data on single fibers over a range of more than eight decades of time scale.

DYNAMIC MODULUS APPARATUS

A schematic of this apparatus test frame is shown in Figure 1. The typical test sample is approximately 46 cm long, although provisions have been made to employ samples ranging from ca. 20 cm to 64 cm in length in order to evaluate the "machine compliance" correction factor. Heating is accomplished by a hollow SiC tube about 30 cm long which surrounds the fiber. The ends of the fiber are cold gripped outside of the heating tube, with one end connected to a load cell and the other end connected to a linear motor employing an externally mounted spring steel suspension. Massive copper end blocks which are water cooled are fitted with special conducting strips that provide electrical contact with the SiC heating tube. An LVDT (linear variable differential transformer) is mounted in parallel with the lower sample grip and linear motor.

An electrical current as high as 120 amps is passed through the SiC heater via the copper end blocks. This current is obtained from a massive transformer whose secondary windings have been impedance matched to the nominal resistance of the heater, which varies significantly with temperature and goes as low as 0.1 ohms at ca. 700 C after which the resistance rises with temperature. The primary of the transformer is fed from an SCR controlled by a PID temperature controller using a Pt/Pt-10% Rh thermocouple located at midplane in the heating tube and adjacent to the fiber. The high currents required for initial heating and the minimum in the heater's resistance posed several control difficulties which were subsequently overcome by the impedance matching of the transformer and special snubber circuits across both the primary and secondary windings. Without these precautions, the lifetime of the temperature controller was found to be alarmingly small and costly.

The linear motor is driven by a DC coupled power amplifier with the sinusoidal drive signal superposed on a static signal to provide for a tensile preload on the fiber at all times (including the bottom of the sine wave). The sinusoidal drive signal originates in an instrument called the Dynalyzer (Ref. 1, and available from IMASS, Accord, Mass.), which is also used to process the load and displacement signals and recover the in-phase (or elastic) and out-of-phase (or loss or viscous) components of the dynamic modulus. Special signal processing techniques in the Dynalyzer eliminate errors in phase measurements due to the DC signal component and also due to noise and harmonics in the load and displacement signals.

Measurements on Avco SCS-6 SiC fibers have been performed from room temperature to 1600 C. At room temperature, the dynamic loss factor (ratio of out-of-phase to in-phase components of the dynamic modulus) was found to be less than 0.0005, indicating virtually perfect elastic response, as expected. It should be noted that such resolution requires identical phase matching of the frequency response of the load and displacement amplifiers, which is not easy due to the fact that the load cell is a strain gauge and the displacement transducer is an LVDT. We have achieved near perfect phase matching of these two amplifiers from DC to 1000 Hz. Thus, it is safely concluded that any differential phase response observed is

due to the actual sample anelastic behavior and is not an artifact associated with the processing electronics.

The heated wall method used for the dynamic modulus apparatus produces a parabolic temperature distribution from grip to grip as expected from theory. Accordingly, algorithms have been developed to deconvolute both the in-phase and out-of-phase measurements so as to obtain data which represents isothermal behavior of the sample. The corrected data agree well with available literature data on SiC, and will be discussed at length.

No apparatus is ideally stiff. The actual compliance of the present apparatus has been measured by comparing modulus data obtained on elastic samples (SCS-6 at room temperature) of various gauge lengths and extrapolating on a reciprocal length plot to infinite length. All data presented have been corrected for machine compliance.

CREEP APPARATUS

A multi-station creep apparatus which is fully computerized is described in detail elsewhere (Ref. 2). Briefly, the apparatus consists of six independent creep stations. Each fiber is encased in a 2.5 cm Pyrex tube which also serves as an environmental chamber, generally purged with Argon. The single fiber samples are heated by passing a current directly through each sample. A closed loop servo temperature control is implemented by means of a two wavelength optical pyrometer which sends the temperature of each fiber to a computer which then implements a PID loop and outputs a DC control signal to a high voltage power supply (for each fiber). The optical pyrometer is mounted on a precision rotary table containing a digital stepping motor, used to precisely align the field of view of the pyrometer with each fiber.

The temperature of each fiber can be programmed to ramp at precise rates ranging from less than 1 to greater than 1000 °C per minute for CTE experiments, or held constant (for creep experiments). Experiments have shown that temperature can be controlled to within 1 °C for indefinite times (e.g., of the order of a month) at temperatures of 1400 °C. The gauge length of 38 cm is uniform to within 30 °C (max. - min.) at 1400 °C. Therefore, no corrections are required as with the dynamic modulus apparatus. Loads are applied to each fiber by means of a weight and platform attached to one end of each fiber. The motion of each platform is monitored using an LVDT, which transmits its signal to the computer, which also serves as a data logger. Incremental strains as small as 0.000066 % can be reproducibly resolved.

RESULTS

Extensive dynamic modulus measurements on Avco SCS-6 fibers have been obtained and reported elsewhere (Ref. 3). The thermal gradient corrected and normalized (to the room temperature value) in-phase (elastic) moduli, at one Hz, for several SCS-6 samples are shown vs. temperature in Fig. 2. The room temperature

value used for normalization is 374 GPa. The data represent samples run under a variety of load and thermal test histories. The onset of a marked change in the rate of change of modulus with temperature at ca. 1300 °C is noteworthy. The corresponding (simultaneously measured) values for the thermally corrected out-of-phase (loss) moduli vs. temperature, also at one Hz., are shown in Fig. 3. These data are not normalized, since the room temperature value is close to zero (less than 0.05 GPa). From linear anelasticity theory, it is easy to show that the real part of the complex dynamic viscosity is equal to the imaginary (or loss) part of the complex dynamic modulus divided by the frequency of measurement (in radians per sec). Figure 4 shows the data for one of the load/temperature histories plotted as real (in-phase) dynamic viscosity vs. temperature for three test frequencies. The lack of convergence of the three frequency curves indicates that a Non-Newtonian process is involved. Slope measurements on these curves gives an activation energy for the process as will be discussed in the presentation.

Data obtained on the creep apparatus run at a constant heating/cooling rate of 15 °C is shown in Fig. 5. Several repetitions of the heating and cooling cycles on a single sample are shown. During the heating cycle, at 1373 °C the fiber undergoes a contraction while during the cooling cycle, an expansion occurs at 1307 °C. These contraction and expansion values are rate dependent, and a possible explanation will be presented. Creep results at several loads and temperatures will also be given.

REFERENCES

1) S. S. Sternstein, "Transient and Dynamic Characterization of Viscoelastic Solids", in Polymer Characterization: Spectroscopic, Chromatographic, and Physical Instrumental Methods, Clara D. Craver, Editor, ACS Advances in Chemistry Series, No. 203 (1983).

2) E. Lara-Curzio and S. S. Sternstein, "A High Temperature Fiber Testing Facility", Meas. Sci. and Technol. 2 (1991), pp. 358-368.

3) J. Beale, "High Temperature Dynamic Mechanical Characterization of AVCO SCS-6 SiC Fibers", M. S. Thesis, Rensselaer Polytechnic Institute, Troy, N. Y., Dec. (1989)
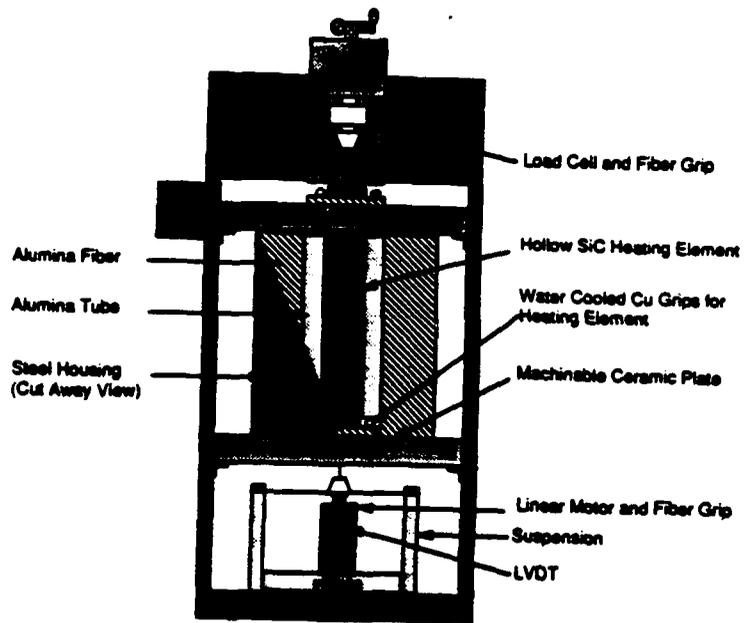
Figure 1
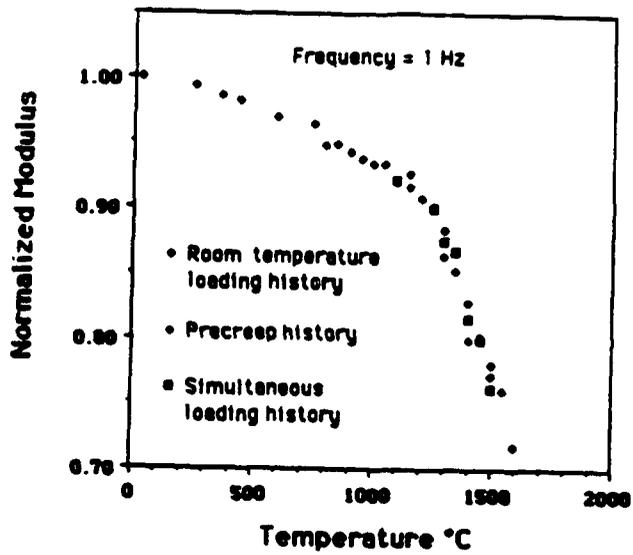
Figure 2
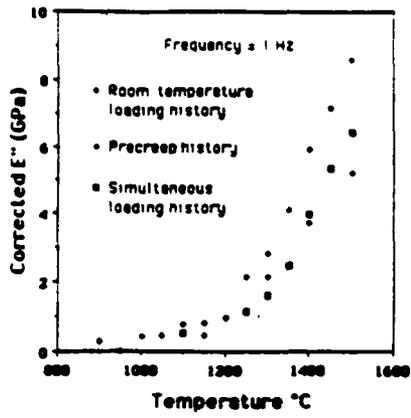
Figure 3
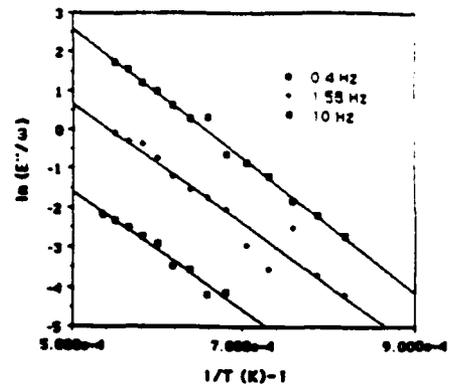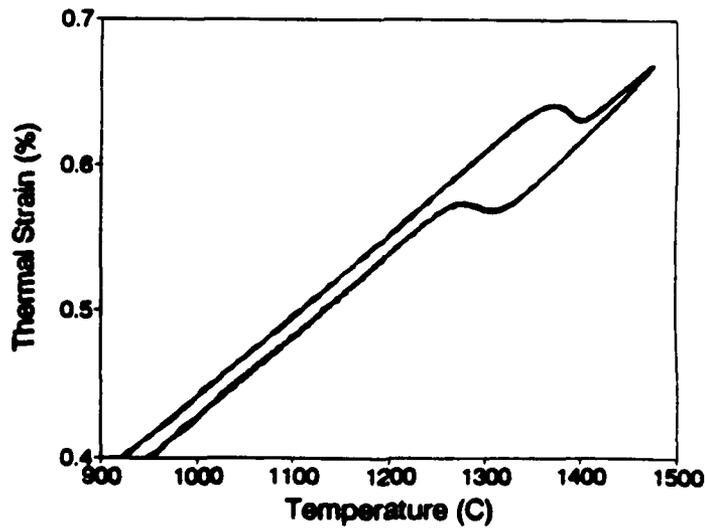
Figure 4

Figure 5

HIGH TEMPERATURE DEFORMATION STUDIES ON
CVD SILICON CARBIDE FIBERS

J. Beale, E. Lara-Curzio, and S. S. Sternstein

Center for Composite Materials and Structures

Rensselaer Polytechnic Institute, Troy, N. Y.

ABSTRACT

The composite structure of SiC fibers produced by chemical vapor deposition is reviewed briefly in order to illustrate the complex mechanical behavior which such fibers can exhibit. A new apparatus for studying the creep behavior of fibers is described in which virtually isothermal gage lengths can be achieved at temperatures up to 1600 C. A second apparatus for measuring complex dynamic moduli from 0.1 to 25 Hz for temperatures to 1600 C is also presented. Loss (imaginary) modulus values greater than 1 part in 2000 of the storage (real) modulus can be measured. Example data are presented for a variety of loading histories, temperatures and stress levels. A new algorithm for the correction of non isothermal mechanical data is used to compute isothermal dynamic moduli values to 1600 C. It is found that anelastic processes occur both dynamically and in creep at temperatures as low as 1100 C. Activation energies for dynamic loss mechanisms are presented.

1. INTRODUCTION

The low fracture toughness of ceramic materials is a major obstacle to their increased usage in high temperature structural (load bearing) applications. A number of techniques including second phase dispersions, transformation toughening and fiber reinforcement have been considered to increase toughness. The tremendous potential offered by continuous fiber reinforcement has led to considerable interest in the properties of reinforcing fibers and the role of the fiber/matrix interface in producing enhanced toughness, ceramic matrix composites. To better understand and predict the global mechanical properties of the composite, it is necessary to first understand and characterize the properties of the constituent phases. This paper focuses on one of the more promising high temperature reinforcing fibers, namely SiC fibers produced by chemical vapor deposition (CVD)

2. THE FIBER - A COMPOSITE STRUCTURE

SiC fibers appear to have substantial promise as a high temperature reinforcement. However, issues such as failure modes, crack propagation resistance, residual stresses and creep have already been identified as important to the intended application (1,2,3). Avco SiC fibers are available commercially and are the material chosen for this study. These fibers are manufactured by a CVD process which involves a complex series of steps that serve to produce a fiber that is itself a composite, thereby complicating the interpretation of deformation mechanisms and behavior of the fiber.

A glassy carbon fiber about 33 um in diameter is used to provide a continuous feed substrate on which to deposit SiC by CVD. The carbon fiber is heated electrically using mercury electrodes. However, to provide a smooth flaw free surface for enhanced electrical conductivity and avoid the "light bulb effect", the carbon fiber is first coated with a highly oriented pyrolytic graphite layer about 1 um in thickness. This layer is deposited at about 2500 C. A similar process is used in the production of Boron fibers (4).

The coated carbon fiber is then exposed to a mixture of silane and hydrogen gases at about 1300 C, which produces beta SiC in columnar grains with the {111} planes preferentially oriented parallel to the deposition surface (5,6). At this stage the fiber has a diameter of ca. 140 um. Although the silane gases used have a 1:1 Si to C ratio, there is a tendency for the deposition of excess carbon. This is detrimental to the strength of the SiC fiber. The use of hydrogen suppresses carbon deposition and results in excess silicon (5), which may be responsible for the shrinkage of SiC fibers at ca. 1400 C as noted by DiCarlo (2).

The final step is to deposit a surface coating on the fiber which serves to reduce susceptability to surface damage and promote compatability with the matrix with which the fiber will be used. In our studies, Avco SCS-6 fibers were used for which the surface treatment is a carbon rich coating with a variable SiC content. The coating is ca. 2 um thick.

The composite structure of the fiber and the widely different mechanical properties of the various layers suggest that a simple creep model for the fiber is inappropriate and that a composite averaging scheme must be employed. Also, the disparate thermal properties of the layers implies that residual thermal stresses may be a significant factor in the analysis of high temperature mechanical data.

3. EXPERIMENTAL

Creep and recovery experiments were performed using a specially constructed apparatus permitting six simultaneous creep experiments. Each unit resembles a tubular CVD reactor consisting of two water cooled aluminum end caps with internal mercury receptacles for making electrical contact with the fiber. The sample chamber is simply an 18 mm dia. pyrex tube without insulation. An inert atmosphere of Argon is maintained at all times. The lower end of the fiber is connected to a LVDT displacement transducer using a lightweight platform on which the desired creep loads may be placed.

Temperatures are measured using a two wavelength optical pyrometer which is incorporated into a computerized data acquisition and control system. Thermal control is achieved by closed loop control of a DC power supply which varies the current passing through the fiber specimen. The gauge length of the fiber is about 350 mm. This system has the advantage of producing a nearly uniform temperature along the entire gage length, typically with a variation of less than 50 C occuring within 10 mm of the end caps. The control of temperature throughout 90% of the sample is typically 1 C at an operating temperature of 1500 C.

Measurements of complex dynamic modulus (in phase and out of phase components) were also performed on a special apparatus consisting of a linear motor, DC coupled power amplifier, precision phase matched load and dispacement amplifiers, a heated wall SiC heating element and a dynamic mechanical analyzer capable of resolving phase angles as small as 1/5000 (out of phase to in phase modulus ratio). This apparatus exhibited the expected parabolic temperature profile common to heated wall cylindrical chambers. Temperature control to about 2 C could be maintained.

This apparatus allows independent control of the static and dynamic force amplitudes thereby maintaining a positive (non buckling) force on the fiber at all temperatures. Dynamic modulus measurements were made over a frequency range of 0.1 to 25 Hz. The major advantage of complex dynamic measurements over creep is the high sensitivity with which small levels of anelastic behavior can be detected in relatively short times. Thus, these measurements are an exceedingly useful complement to the creep results, especially at short timescales (less than 1 sec.) for which creep results are subject to large errors due to the precise loading history (which is never a perfect step function).

A new algorithm has been developed which provides a computational procedure by which the modulus data obtained at various temperatures can be deconvoluted to obtain the thermal gradient corrected modulus data. In other words, it is possible to calculate the isothermal gage length data from the parabolic profile data. Corrected data are presented below.

Three different fiber loading histories were used in the dynamic modulus measurements, as follows:

(1) Room Temperature Loading History (RTH) for which a static load of 300 MPa was applied to the sample at room temperature, the temperature was ramped to each value and held for 10 minutes and the dynamic load then applied. A single sample was therefore tested at many temperatures. Two dynamic load amplitudes, 180 and 244 MPa were used and tests above 1400 C were conducted for 30 min. to check for time dependence of the dynamic results.

(2) Simultaneous Loading History (SH) for which a sample was tested at a single temperature. The unloaded sample was brought to the desired temperature and held for 10 min. after which the static load of 300 MPa and the dynamic load (from 110 to 300 MPa) were applied simultaneously. Data were collected for a period of 1 hr. to determine time dependence.

(3) Precreep History (PCH) for which the unloaded sample was brought to the desired test temperature and held for 30 min after which the static load of 300 MPa was applied for another 30 min before dynamic testing. Time dependence of the dynamic results were checked for 30 min at various frequencies and amplitudes. This history effectively gave minimal creep during the dynamic testing.

4. RESULTS AND DISCUSSION

Due to space limitations, a synopsis of the experimental results will be presented here. The in phase (or storage or real) component of the dynamic modulus is a measure of the elastic behavior of the fiber, whereas the out of phase (or imaginary or loss) component is a measure of the viscous response. Results from the RTH for the real component of the modulus (E') are shown in Fig 1 where both the measured and temperature gradient corrected values are shown at both 1 and 10 Hz, all relative to the room temperature value (which we determined dynamically to be 374 GPa). As expected, the 10 Hz values are slightly higher than the 1 Hz values at temperatures greater than 1100 C, and indistinguishable below that. The temperature corrected values exhibit a marked increase in temperature dependence above about 1100 C, with the value of modulus at 1600 C falling to about 70 % of its room temperature value.

Room temperature normalized, temperature gradient corrected values of E' for all three loading histories are shown in Fig 2. Clearly, insofar as the real modulus is concerned there is effectively no dependence on the particular loading history. However, it should be noted that the SH results represent the terminal data, that is, the results obtained after 1 h.

The imaginary, or loss, component of the modulus, E'', is shown in Fig 3 for the RTH at 10 Hz. Once again, it is apparent that the temperature gradient correction is quite significant. It is noteworthy that there is a smooth and continuous increase in loss modulus which begins below 1200 C, and not relatively abruptly at 1400 C as we might of expected if the melting of excess Si at grain boundaries was responsible for the loss mechanism. Results for the loss modulus obtained from all three loading histories are shown in Fig 4, where it is seen that the RTH gives the highest values of loss, suggestive of the most damage among the three histories. The PCH gives the lowest loss at temperatures above 1350 C, which suggests that the creep prior to dynamic testing may result in some strain hardening and a loss of internal mobility.

Additional tests and histories are required to determine the mechanism(s) responsible for the softening of the real modulus and onset of the loss modulus both at about 1100 C and higher. However, it seems clear that the melting of excess Si is not the rate controlling process for dynamic loads, and some other mechanism must be sought.

Activation energies for whatever mechanisms are responsible for the energy dissipation associated with the loss moduli are obtained by plotting the log of E''/ω (where ω is the frequency in rad/s) vs. reciprocal absolute temperature. These plots yielded straight lines, the slopes of which are used to compute the activation energy. The ratio E''/ω is often referred to as the real component of the dynamic viscosity. The results are frequency and history dependent as follows: for the RTH, the activation energies range from 140 KJ/mol at 0.4 Hz to 124 KJ/mol at 10 Hz; for the PCH, 185 KJ/mol at 0.1 Hz to 134 KJ/mol at 10 Hz. The activation energy for dislocation controlled creep in SiC at a stress of 182 MPa and temperatures above 1400 C has been determined by Carter and Davis to be 176 KJ/mol (7). This value is intended only as one example for a possible loss mechanism, namely dislocation motion.

The dynamic moduli results emphasize short relaxation time behavior. The longer relaxation time mechanisms are conveniently studied using creep histories. A 600,000 s creep curve obtained at 1200 C and 400 MPa is shown in Fig 5 which presents only the anelastic component of the creep strain (the immediate elastic deformation has been subtracted from the total creep strain). This creep curve is misleading in that it is not at all obvious as to whether or not the creep process will eventually terminate. The same data are shown in Fig 6 using log coordinates and indicate the beginning of a slight reduction in creep rate at long times. The necessity for obtaining extended creep time data on the SiC fibers is evident. What is most striking about these results and the dynamic data is that the anelastic processes appear to cover a range of timescales in excess of 7 decades (from 10 Hz or 0.016 s/rad to 600,000 s). A log creep curve at 1450 C and 500 MPa is shown in Fig 7, which should be compared to Fig 6. Note that the same level of anelastic creep is achieved in about 1/100 of the time at

1450 C.

Creep and creep recovery data at temperatures to 1500 C and with several stress levels have been obtained, but detailed presentation is beyond the scope of the present paper. Some of our conclusions are as follows:

(1) Below 1150 C and for stress levels below 200 MPa, there is no detectable creep. The occurrence of a threshold stress for creep may be due to residual thermal stresses in the composite fibers. A model for these thermal stresses has been formulated.

(2) Creep occurring below 1400 C is completely recoverable as demonstrated by elevated creep recovery experiments and multiple cycle creep tests. A model has been formulated for the composite fiber creep behavior which assumes that the carbon core behaves elastically while the SiC sheath is anelastic and/or inelastic. This model predicts that, even for inelastic SiC behavior, the fiber will behave anelastically due to the backstress imposed by the elastic carbon core. While the consequences of this model are currently under investigation, it is clear that the creep behavior of Avco SCS-6 and similar composite fibers requires additional analysis and interpretation.

(3) The reversible shrinkage of Avco SCS-6 fibers at ca. 1400 C (we measure 1375 C) may be due to the combined effects of the melting of free silicon and the residual fabrication thermal stresses. However, free silicon melting cannot account for the dynamic loss modulus and creep behavior observed at 1200 C.

(4) The combined dynamic and creep data suggest that several deformation mechanisms may be active in these fibers and additional structural and modeling studies are required to fully understand these processes.

5. REFERENCES

1) K. D. McHenry and R. E. Tressler, J. Composite Mat., 9, 73 (1975)
2) J. A.DiCarlo, J. Materials Sci., 21, 217 (1986)
3) R. L. Crane and V. J. Krukonis, Ceramic Bulletin, 54(2), 184 (1975)
4) H. E. DeBolt, "Carbon Filament Coated with Boron and Method of Making Same", U. S. Patent 4,142,008, Feb 27, 1979
5) R. J. Diefendorf and J. R. Weiss, "CVD SiC for High Temperature and Structural Applications" in Silicon Carbide - 1973, R. C. Marshall, J. W. Faust and C. E. Ryan Eds., Univ. of S. C. Press, 80 (1973)
6) F. W. Wawner, A. Y. Teng and S. R. Nutt, SAMPE Quarterly, April 1983, 39
7) C. H. Carter and R. F. Davis, J. Amer. Ceramics Soc., 67(11), 733 (1984)

6. ACKNOWLEDGEMENTS
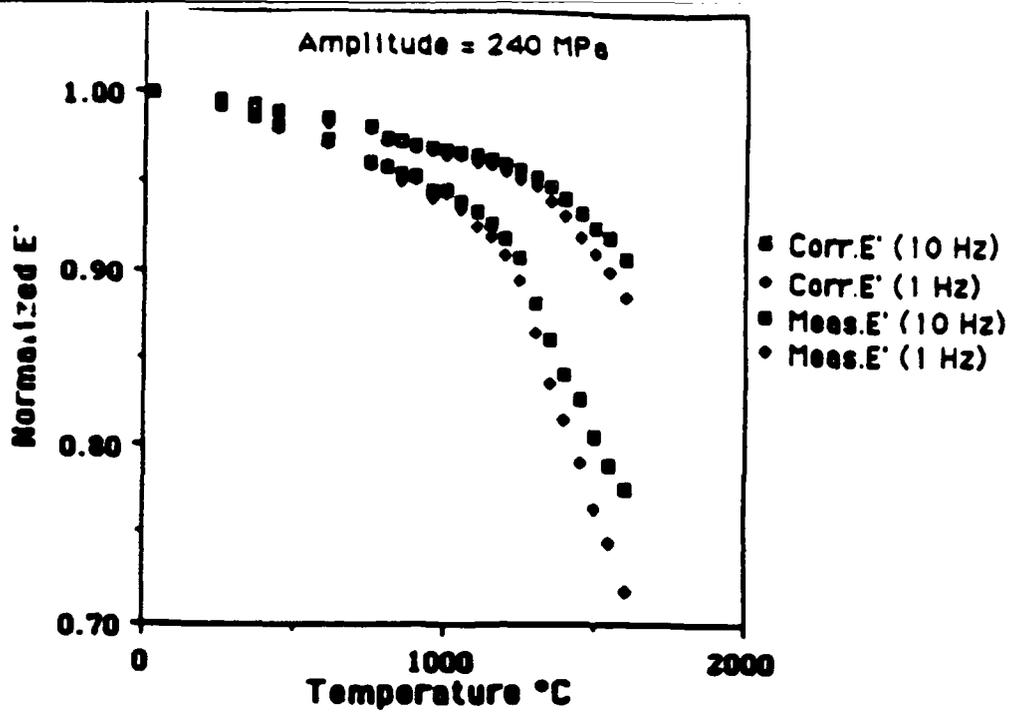
Figure 1. Comparison of the measured and temperature gradient corrected values for in-phase (real) modulus at 1 Hz and 10 Hz for the room temperature loading history. Moduli are normalized by the room temperature value.
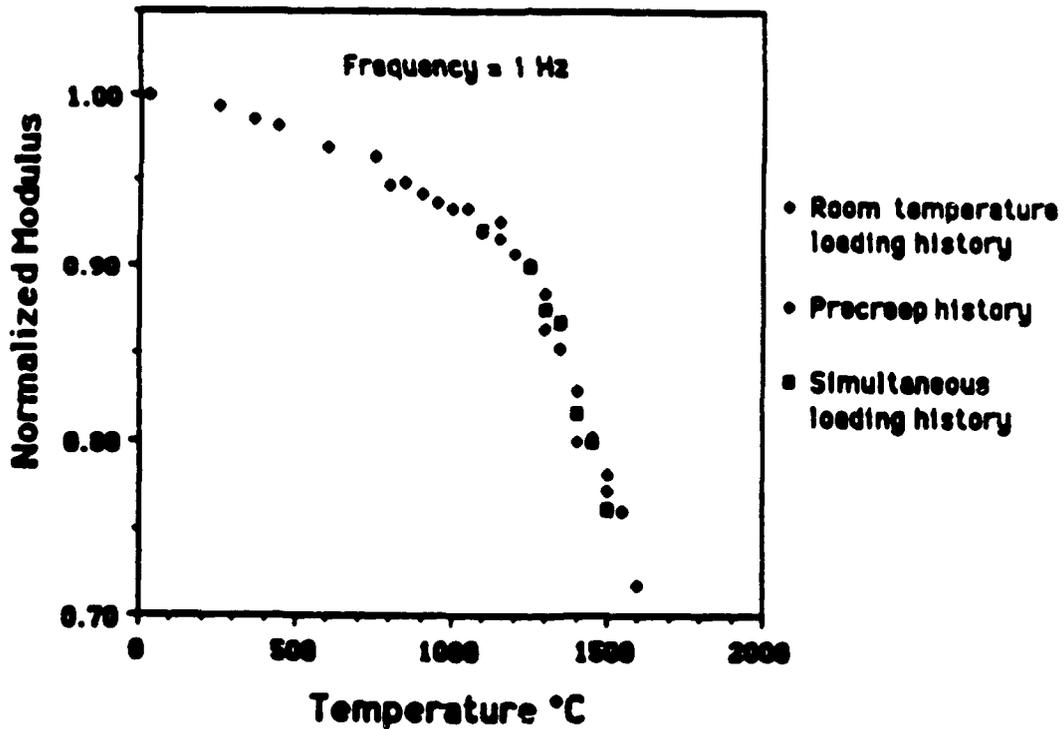
Figure 2. Comparison of temperature corrected in-phase moduli at 1 Hz for the three loading histories studied.
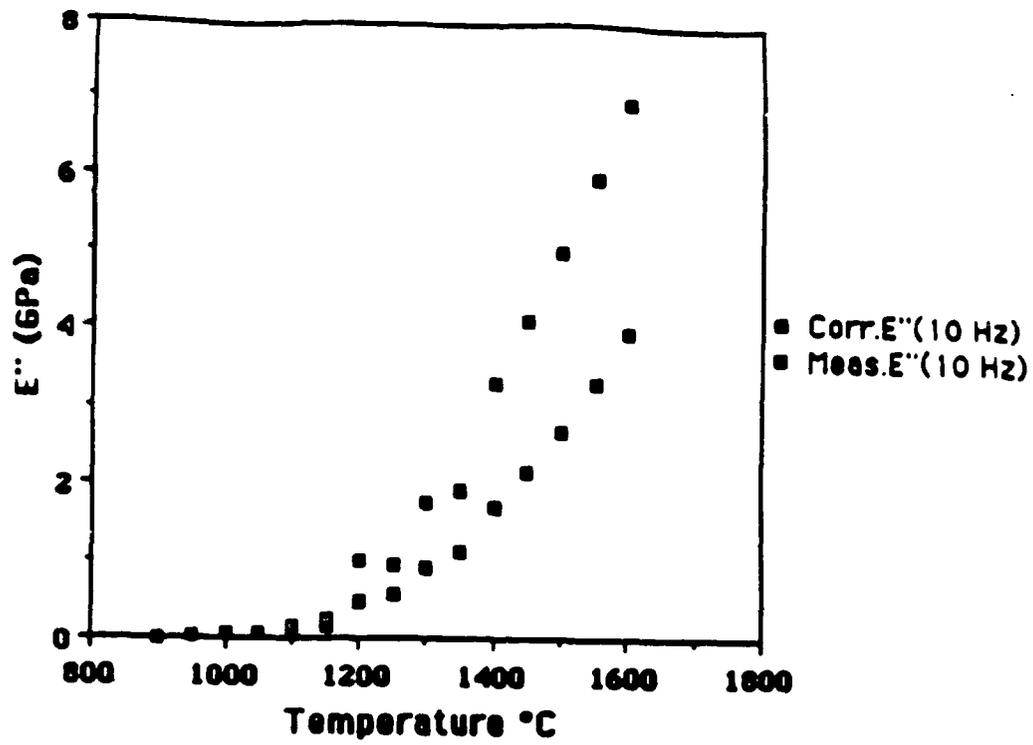
Figure 3. Comparison of the measured and temperature corrected values for out-of-phase (loss) modulus at 10 Hz for the room temperature loading history.
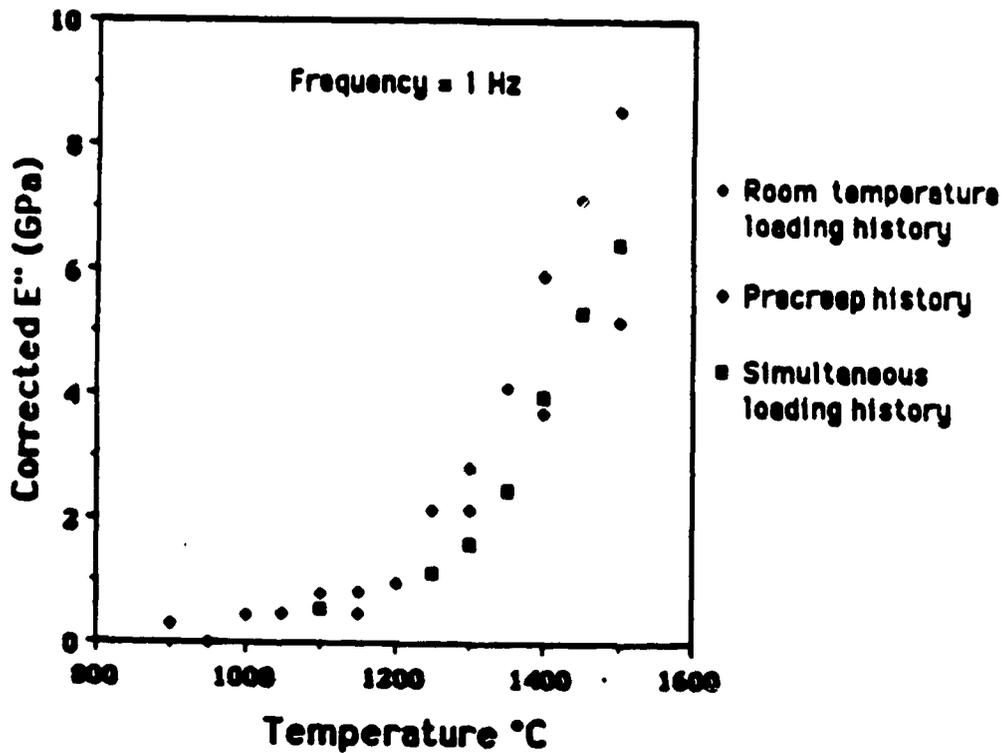
Figure 4. Comparison of the temperature corrected out-of-phase moduli at 1Hz for the three loading histories.
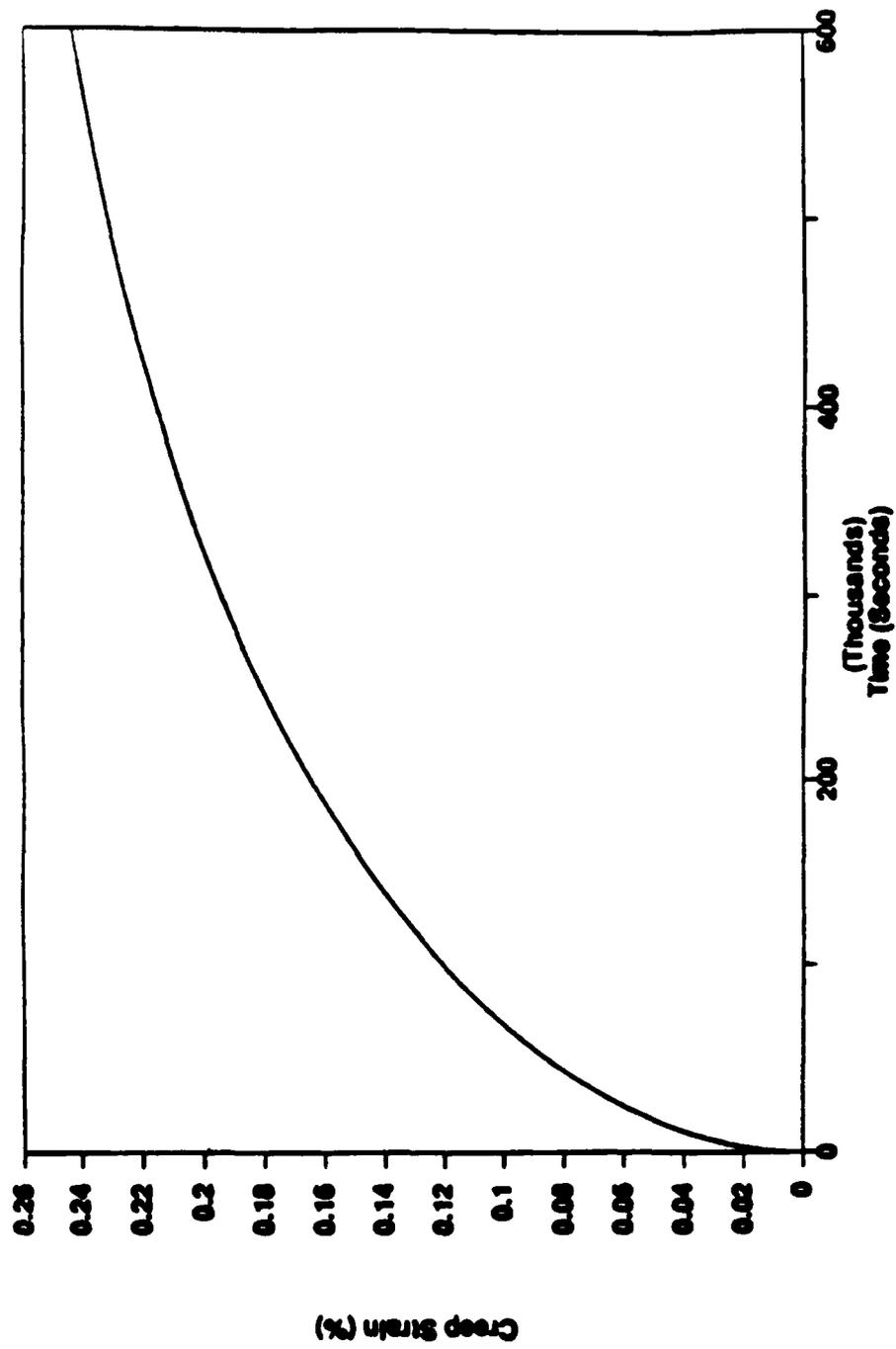
Figure 5. Typical creep curve showing the anelastic component of strain vs. time for a stress of 400 MPa and temperature of 1200 C with an Argon atmosphere.
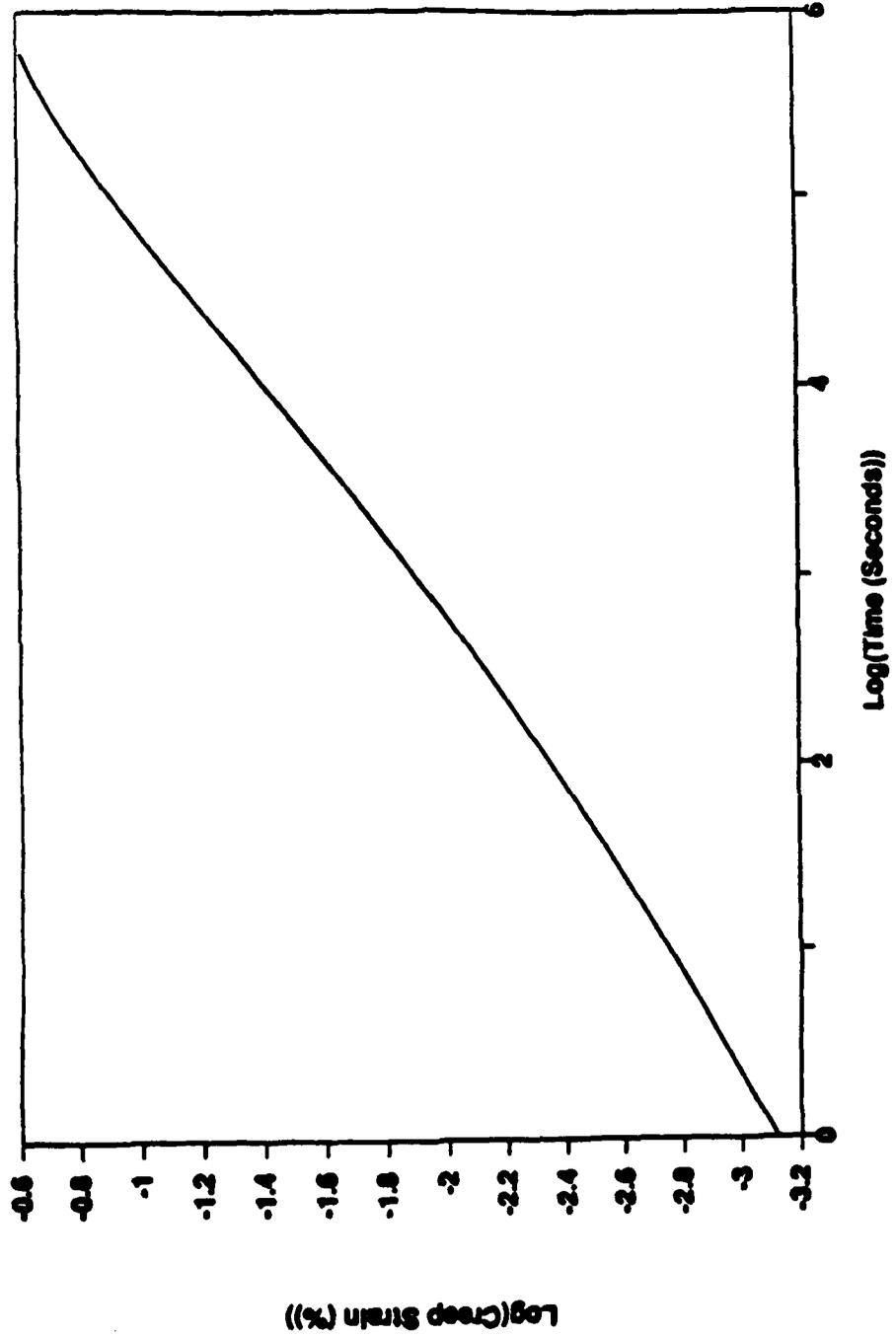
Figure 6. A log-log representation of the data shown in Figure 5. Note the slight reduction in creep rate at long times.
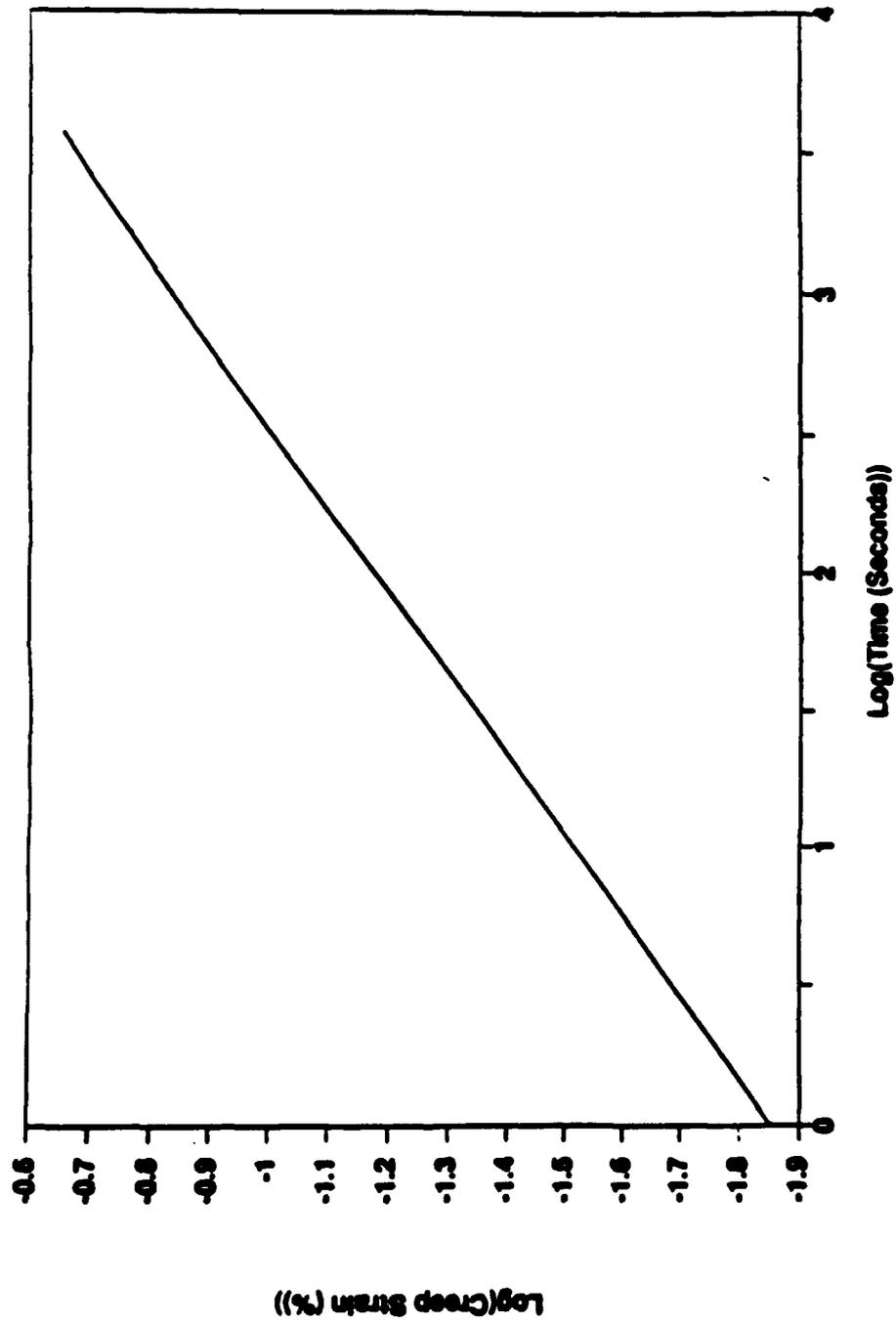
Figure 7. Anelastic component of strain vs. time for a stress of 500 MPa and temperature of 1450 C with an Argon atmosphere.

Carbon/Graphite Fibers

Russell J. Diefendorf, Rensselaer Polytechnic Institute

THE ELEMENT CARBON has two low-density allotropes, graphite and diamond, both of which have strong covalent bonding between the carbon atoms. Graphite has a hexagonal structure in which the strong sp^2 bonding in the hexagonal-layer planes generates the highest absolute modulus, highest specific modulus (modulus/density), and highest theoretical tensile strength of all known materials (see Tables 1 and 2). However, the weak, dispersive bonding between planes produces a low shear modulus and cross-plane Young's modulus that is detrimental to fiber properties (Ref 2). Diamond, with a cubic crystallographic structure, possesses the next highest absolute and specific modulus and does not suffer from a low shear modulus, as does graphite (Ref 3). Diamond or diamondlike carbon fibers have not yet been made, but could have great applicability, especially for compressively loaded structures.

This article deals with carbon and graphite fibers that are based on the graphene- (hexagonal-) layer networks present in graphite. Graphene is the accepted term used by the International Committee for the Characterization and Terminology of Carbon. If these graphene-layer planes stack with three-dimensional order, the material is defined as graphite (Ref 4). Because the bonding between planes is weak, disorder frequently occurs as rotation and/or translation such that only the two-dimensional ordering in the layers is present. This material is defined as carbon (Ref 4). In earlier literature, two-dimensionally ordered structures were referred to as turbostratic

graphite. Historical usage continues, and the term graphite fibers often is applied, improperly, to carbon fibers, which only have two-dimensional ordering.

Carbon and graphite fibers offer the highest modulus and highest strength of all reinforcing fibers. The fibers do not suffer from stress corrosion or stress rupture failures at room temperature, as glass and organic polymer fibers do. At high temperatures, the strength and modulus are outstanding compared to other materials. Finally, aggressive development of new processes promises significant improvements in the performance/cost ratio.

Carbon Fiber Processes

Carbon fibers have been made inadvertently from natural cellulosic fibers such as cotton or linen for thousands of years. However, it was Thomas Edison who, in 1878, purposely took cotton fibers and later, bamboo, and converted them into carbon in his quest for incandescent lamp filaments (Ref 5). Interest in carbon fibers was renewed in the late 1950s when synthetic rayons in textile forms were carbonized to produce carbon fibers for high-temperature

missile applications (Ref 6-8). All these fibers had low elastic moduli (≤ 50 GPa, or 7×10^6 psi).

All continuous carbon fibers produced to date have started with organic precursors that were subsequently converted to carbon fibers. Discontinuous carbon whiskers have been produced by vapor-liquid-solid (VLS) growth from an iron catalyst and a hydrocarbon gas (Ref 9, 10). High-modulus carbon fibers (≥ 200 GPa, or 30×10^6 psi) require that the stiff graphene layers be aligned approximately parallel to the fiber axis. (The low shear modulus between the planes significantly decreases fiber stiffness for off-axis layers.) Commercial processes develop this orientation by plastic deformation. This preferred orientation, which can be introduced in the precursor fibers, will be at least partially preserved upon conversion to carbon (Ref 11-14) and also may be introduced into the carbon fiber by high-temperature deformation (Ref 15, 16).

Three different precursor materials are used at present to produce carbon fibers: rayon, polyacrylonitrile (PAN), and isotropic and liquid crystalline pitches. Rayon and isotropic

Table 1 Theoretical properties of graphite and diamond

	Tensile modulus		Tensile strength		Density, g/cm³	Specific modulus	Specific strength
	GPa	10⁶ psi	GPa	10⁶ psi			
Graphite(a)	1020	150	150	20	2.26	451	66
Diamond	20	3	90	15	3.51	177	25

(a) Parallel to basal plane. Source: Ref 1-3

Table 2 Properties of carbon fibers: polyacrylonitrile precursor fibers

Properties	Standard grades				New grades					
	Low modulus		High modulus		Low modulus		Intermediate modulus		High modulus	
Axial										
Tensile modulus, GPa (10⁶ psi)	230	(30)	390	(55)	230	(35)	270	(40)	320	(45)
Tensile strength, GPa (10⁶ psi)	3.3	(0.48)	2.4	(0.35)	4.5	(0.65)	5.3-6.8	(0.77-0.99)	5.5	(0.80)
Elongation at break, %	1.4		0.6		2.0		2.0-2.5		1.8	
Thermal conductivity, W/m · K (Btu · in./h · ft² · °F)	8.5	(59)	70	(490)	7	(50)				
Electrical resistivity, µΩ · m (µΩ · cm)	18	(1800)	9.5	(950)	18	(1800)				
Coefficient of thermal expansion at 21 °C (70 °F), 10⁻⁶ K	-0.7		-0.5							
Transverse										
Tensile modulus, GPa (10⁶ psi)	40	(6)	21	(3)						
Coefficient of thermal expansion at 50 °C (120 °F), 10⁻⁶ K	10	(2)	7	(1)						
Bulk										
Density, g/cm³	1.76		1.9		1.8		1.8		1.8	
Filament diameter, µm (µin.)	7.8	(280-310)	7	(280)	5-6	(200-240)	6	(240)	4	(160)
Carbon assay, %	92-97		100		92-97		96		96	
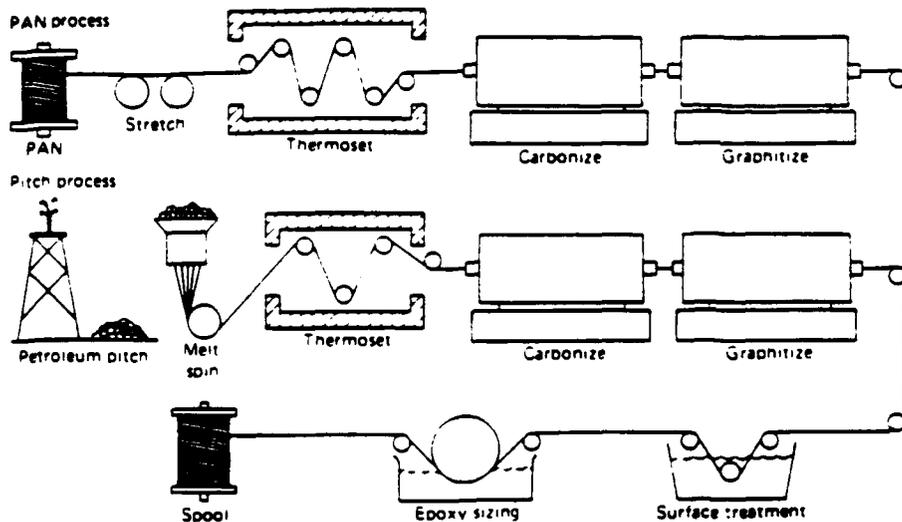
Fig. 1 The processing sequence for polyacrylonitrile (PAN) and mesophase pitch-based precursor fibers shows the similarities for the two processes. Highly oriented polymer chains are obtained in PAN by hot stretching, while high orientation in pitch is a natural consequence of the mesophase (liquid crystalline) order.

Fig. 3 The modulus of a carbon fiber is determined by the preferred orientation, microstructure, and elastic constants. The relationship between modulus and preferred orientation for a pitch-based carbon fiber is shown.

Fig. 2 The preferred orientation of the graphene planes is determined by the heat treatment temperature and the precursor type. Source: Ref 2, 23

Fig. 4 The undulating ribbon structure of the graphene layers for a PAN-based carbon fiber with a 400 GPa (60 × 10⁶ psi) modulus. The ribbons at the surface have lower amplitude than in the core. There are about 20 graphene layers in the ribbons in the core and about 30 near the surface.

pitch precursors are used to produce low-modulus carbon fibers (≤50 GPa, or 7 × 10⁶ psi) (Ref 6, 16-19). Both rayon-based and isotropic pitch-based carbon fibers can be strained at high temperature to increase fiber modulus but this process is not used commercially at present (Ref 15, 16). Higher modulus carbon fibers (≥200 GPa, or 30 × 10⁶ psi) are made from PAN or liquid crystalline (mesophase) pitch precursors (Fig. 1). In both cases, an oriented precursor fiber is spun, slightly oxidized to thermoset the fibers, and carbonized to temperatures above 800 °C (1400 °F) to produce a carbon fiber (Ref 11-14, 20). The fiber modulus increases with heat treatment to temperatures from 1000 to 3000 °C (1830 to 5430 °F), although not uniformly with temper-

ature. The exact relation depends on the precursor (Ref 2, 21). Fiber strength usually maximizes at an intermediate temperature (1500 °C, or 2730 °F) for PAN and some pitch precursor fibers, but continuously increases for most mesophase pitch precursor fibers (Ref 2, 21).

Carbon Fiber Microstructures

The axial preferred orientation of the graphene layers determines the modulus of the fiber, while both axial and radial textures, as well as flaws, affect fiber strength. The orientation of the graphene layers at the fiber surface affects wetting and the strength of the interfacial bond to the matrix. The following sections describe axial and radial textures, illustrate a model of a three-dimensional carbon fiber, and describe the consequences of these microstructures on fiber performance.

Axial Structure. An overall measure of preferred orientation of graphene planes with respect to the fiber axis is obtained by x-ray diffraction (Ref 22). The full width at half maximum of the graphene-layer diffraction (0002) is useful for describing preferred orientation. The effect of heat treatment temperature on the preferred orientation of PAN and mesophase pitch-based carbon fibers is shown in Fig. 2. The trend for PAN is similar to that for mesophase pitch, but the curve is shifted about 400 °C (750 °F) higher. The relation between preferred orientation and fiber modulus for the mesophase pitch-based fiber is illustrated in Fig. 3. For a carbon fiber with a modulus of 220 GPa (30 × 10⁶ psi), about two-thirds of the graphene layers are aligned within about 15° of the fiber axis. Correspondingly, the orientation improves for a 400-GPa (60 × 10⁶-psi) fiber such that two-thirds of the layers fall within about 6° of the fiber axis. A PAN-based fiber shows similar behavior, except that it is
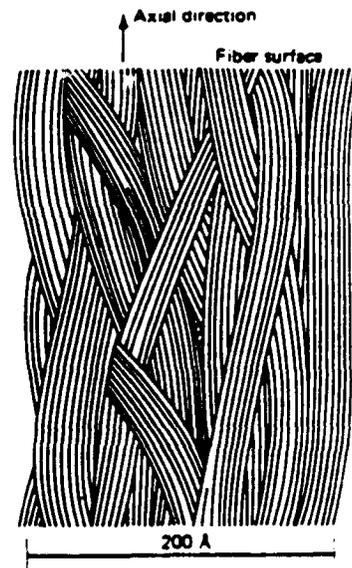
more difficult to obtain preferred orientations below 10° and a modulus greater than 400 GPa (60 × 10⁶ psi), whereas at least one mesophase pitch-based fiber has a modulus of 827 GPa (120 × 10⁶ psi). Transmission electron microscopy (TEM) has revealed, at lattice resolution, that the structure looks like wrinkled ribbons (Ref 23-25), as shown in Fig. 4. Lower-resolution TEM shows that for pitch-based fibers of 220 GPa (30 × 10⁶ psi), ribbons are typically about 16 layer planes thick, essentially continuous, and parallel to the fiber axis (Ref 26-30). The amplitude of the undulation is greater than the wavelength. As modulus is increased, the ribbons thicken and the amplitude of the undulation decreases.

Radial Structure. Radial texturing increases with axial preferred orientation. In contrast to axial structure, radial structure depends substantially on precursor type and processing (Ref 23, 26-30). Mesophase pitch-based fibers can have the graphene planes showing radial.
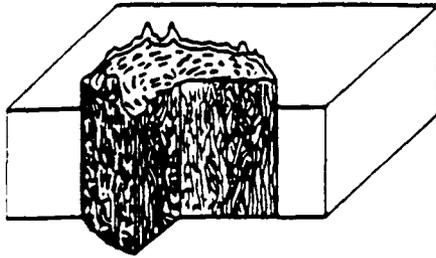
Fig. 5 A 400-GPa (60 × 10⁶ psi) PAN-based fiber. Source: Ref 26

onion-skin, or highly contorted planes with no overall transverse preferred orientation (Ref 31). However, most commercial pitch-based fibers have a radial preferred orientation. PAN-based fibers can have contorted graphene planes, or onion-skin structures. Low-modulus PAN-based fibers (≤350 GPa, or 50 × 10⁶ psi) now have a highly contorted transverse graphene-layer structure; higher-modulus fibers have a thin, highly oriented, onion-skin surface layer 50 to 100 × 10⁻⁹ m (1950 to 3950 × 10⁻⁹ in.) thick about a randomly oriented, contorted layer core (Ref 32).

Three-Dimensional Structure. A schematic model of a 400-GPa (60 × 10⁶-psi) PAN-based fiber is shown in three dimensions in Fig. 5. The axial orientation is higher at the surface than in the core. The ribbons are randomly, radially oriented in the core, with an onion-skin orientation at the fiber surface. A gradient in axial preferred orientation from skin to core produces a compressive axial stress at the surface after cool-down from processing temperatures. This stress makes the fiber insensitive to surface abrasion. Lower-modulus fibers do not have the preferred orientation gradient and beneficial residual stress.

Consequences of Structure on Properties. The increase in radial texture with increasing fiber modulus has some deleterious consequences (Ref 33). First, the onion skin that develops on the surface of a higher-modulus PAN-based fiber gives poor bonding to the matrix. The essentially basal plane char-

acter of very high modulus fibers is difficult to wet. As the fiber modulus increases, the surface becomes smoother, thereby decreasing mechanical interlocking, and the highly oriented surface layer becomes weak in shear. Second, microcracking occurs with the fiber upon cooldown from the processing temperature because of the anisotropy of thermal expansion both parallel and perpendicular to the graphene planes. The fracture surface of the fibers becomes rougher, especially when a strong radial texture develops, because microcracking causes decoupling between the undulating ribbons. Also, the fiber strength decreases. For high-modulus PAN-based fibers (≥400 GPa, or 60 × 10⁶ psi), the onion-skin structure and the axial gradient in preferred orientation place the fiber surface in axial and hoop compression and in radial tension, upon cool-down. These compressive surface stresses and the onion-skin microstructure protect the fiber from strength degradation due to surface abrasion. Other fibers are sensitive to surface abrasion. Finally, as better orientation develops, the interaction or tangling between ribbons decreases, and the shear modulus drops, making the fiber susceptible to compressive microbuckling at low compressive loads. Very highly oriented carbon and organic fibers both suffer from this problem.

Fiber Properties. Commercially available high-modulus carbon fibers are available from a number of manufacturers in an array of yarns and tows with differing moduli, strengths, cross-sectional areas and shapes, twists, plies, and number of fiber ends. They may be purchased in continuous lengths, or chopped to dimension. The diversity of physical properties is one of the benefits of carbon fibers, but is also a problem because complete evaluation is expensive. Certain generalizations can be made about the types of fibers available. First, fibers produced from mesophase pitch-based and PAN-based fibers have quite different combinations of properties and, hence, applications. At present, they cannot be considered interchangeable. Second, there are generally four classes of carbon fiber, based on moduli: low, intermediate, high, or ultrahigh. Unfortunately,

these categories are not like the specifications for alloys. Although fibers made by different manufacturers may be similar, they may not behave identically in all respects. Subtle differences in precursor types and carbon fiber processes can significantly affect the behavior of the carbon fiber in a composite. Moreover, improvements in fibers from different manufacturers have tended to splinter the categories. Third, the fiber selections that make up a particular manufacturer's grade, but have different numbers of fibers, are usually, but not always, based on the same precursor. In addition, while the fibers may be considered to have the same properties, the fiber count or twist may affect composite properties. Finally, because it is not realistic to list all the different manufacturers' fiber properties, general properties for each major category of carbon fibers are presented in Tables 2 to 4.

Bulk Properties. The carbon content of low-modulus PAN-based carbon fibers (≤300 GPa, or 45 × 10⁶ psi) is significantly below 100% because of retained nitrogen. High-modulus PAN-, rayon-, and pitch-based carbon fibers are essentially 100% carbon.

The density of carbon fibers, which increases with increasing modulus, varies from 80 to 94% and 86 to 100% of theoretical for PAN- and pitch-based fibers, respectively. The fractional density for rayon-based fibers is about 68% and increases to as high as 94% for higher-modulus fibers.

Finally, the diameters of present reinforcement grade carbon fibers are in the range of 4 to 10 μm (160 to 390 μin.). The trend has been toward smaller fiber diameters to attain improved tensile strength and processing speeds. However, the compressive and transverse properties of composites made with smaller-diameter fibers do not increase proportionally with tensile properties, and can contribute to failure in compression caused by buckling at lower loads.

Axial Properties. Of the commercially available carbon fibers, those made from PAN precursor provide the highest strain at failure, but only at lower moduli (≤300 GPa, or 45 ×

Table 3 Properties of carbon fibers: mesophase pitch precursor fibers

Properties	Standard grades						New grades			
	Low modulus		High modulus		Very high modulus		Low modulus		High modulus	
Axial										
Tensile modulus, GPa (10⁶ psi)	160	(25)	380	(55)	725	(110)	225	(35)	380	(55)
Tensile strength, GPa (10⁶ psi)	1.4	(0.20)	1.7	(0.25)	2.2	(0.32)	3.1	(0.45)	3.1	(0.45)
Elongation at break, %	0.9		0.4		0.3					
Thermal conductivity, W·m⁻¹·K⁻¹ (Btu·in·h⁻¹·ft⁻²·°F⁻¹)			100	(690)	520	(3600)				
Electrical resistivity, μΩ·m (μΩ·cm)	13	(1300)	7.5	(750)	2.5	(250)				
Coefficient of thermal expansion at 21 °C (70 °F), 10⁻⁶/K			−0.9		−1.6					
Transverse										
Tensile modulus, GPa (10⁶ psi)			21	(3)						
Coefficient of thermal expansion at 50 °C (120 °F), 10⁻⁶/K			7.8							
Bulk										
Density, g/cm³	1.9		2.0		2.15		2.05		2.15	
Filament diameter, μm (μin.)	11	(430)	10	(390)	10	(390)	8	(310)	5	(310)
Carbon assay, %	97+		99+		99+		99+		99+	

The data in this table was obtained from technical data sheets from Great Lakes Carbon Corp., BASF Structural Materials Inc., Amoco Corp., Hercules Corp., Fiber Materials Inc., Stackpole Fibers Co., Polycarbon, and Ashland Petroleum Co.

Table 4 Properties of carbon fibers: low-modulus rayon and isotropic pitch precursor fibers

Properties	Rayon precursor		Isotropic pitch precursor	
Axial				
Tensile modulus. GPa (10⁶ psi)	41	6	55	8
Tensile strength. GPa (10⁶ psi)	1 0	(0 15)	0 7	0 10
Elongation at break. %	2.5		1 4	
Electrical resistivity. μΩ · m (μΩ · cm)	20	(2000)	30	(3000)
Bulk				
Density. g·cm³	1 6		1 6	
Filament diameter. μm (μin)	8.5	(330)	10	(390)
Carbon assay. %	99		98	

10⁶ psi). In general. at least 1.5% strain at failure is required for secondary composite structure and 2% or better for primary structure. The newer PAN precursor grades of carbon fiber achieve 2% strain at failure and can provide slightly higher stiffness as well. The newer grades also provide much higher strength and specific strength. which is attractive for nonstiffness-critical structures such as pressure vessels. The advantages of mesophase pitch-based fibers are that they can be made in ultrahigh-modulus grades (≥600 GPa. or 90 × 10⁶ psi). which are desirable for stiffness-critical but lightly loaded structures.

Carbon fibers increase in modulus by about 10% when highly loaded (Ref 34). However. the fibers show complete elastic recovery upon unloading (Ref 35) and do not appear to degrade because of mechanical fatigue or show stress rupture at temperatures below 2000 °C (3650 °F). as glass or aramid fibers do at or near room temperature (Ref 36-38). High-temperature mechanical properties depend on the maximum heat treatment temperature and the inherent mechanical properties of graphite. Measurements performed above the heat treatment temperature of the fiber will cause changes in microstructure and properties. The moduli and strength of carbon fibers are essentially constant up to temperatures of 1000 °C (1830 °F) for fibers given a higher heat treatment temperature. There is a drop of about 30% in modulus at 1900 °C (3450 °F). Above 2200 °C (3990 °F). creep becomes appreciable (Ref 39).

The coefficients of thermal expansion (CTEs) are slightly negative and become more negative with increasing modulus. This contraction. which is due to layer bending. can be combined with the positive coefficient of the matrix to produce a material with a near-zero CTE over a temperature range of several hundred degrees. At higher temperatures. (>700 °C. or 1290 °F). the CTE for all carbon fibers is positive. Zero-CTE metal matrix composites require the more negative CTE and very high modulus fibers (≥650 GPa. or 95 × 10⁶ psi) that are only available in mesophase pitch-based carbon fibers. Both high-modulus PAN- or pitch-based fibers can be used with zero-CTE resin matrix composites because of the lower matrix modulus.

Thermal conductivity and electrical resistivity depend on preferred orientation. crystallite

size. and purity (Ref 40). All three increase with increasing heat treatment temperatures. Thermal conductivity can equal or exceed that of copper in the very high modulus. commercially available pitch-based fibers. Thermal conductivities that are several times higher have been made in the laboratory and should become available in the future. The electrical conductivity of carbon fibers varies with precursor type and heat treatment temperature. and is 1/40 or less that of copper for commercial 230-GPa (35 × 10⁶-psi) fibers (Fig. 6). The fiber precursor is important for low heat treatment temperature. but to a lesser extent for high-temperature heat treatment. The relatively high conductivity of carbon fibers can cause electrical failures. Free-floating carbon fibers. which could be produced during composite manufacture. can be a problem in shorting out electrical equipment. and must be protected against.

Transverse Properties. While property measurements parallel to the fiber axis are easy to make. transverse property measurements on an 8-μm (315-μin.) fiber are nearly impossible. Values in Table 2 were derived from composite measurements and theory (Ref 41, 42). As can be seen. the fibers are anisotropic with a relatively low transverse modulus and a positive transverse CTE.

Interfacial Bonding

Carbon fibers are not wet by molten metals and are difficult to wet with resins. especially the higher-modulus fibers (Ref 43. 44). Surface treatments. which increase the number of active chemical groups and sometimes roughen the fiber surface. have been developed for the more mature resin matrix composites. Carbon fibers are commonly shipped with an epoxy size. which usually prevents fiber abrasion. improves handling. and provides an epoxy matrix compatible interface. Special surface treatments and sizes have been developed for other resins. especially polyimides and thermoplastics. and should be specified. Fiber and matrix interfacial bond strengths approach the strength of the neat matrix resin for lower-modulus carbon fibers (Ref 45). Higher-modulus PAN-based fibers (≥400 GPa. or 60 × 10⁶ psi) show substantially lower interfacial bond strengths (Ref 45). Failure in high-modulus fiber occurs in its surface layer.
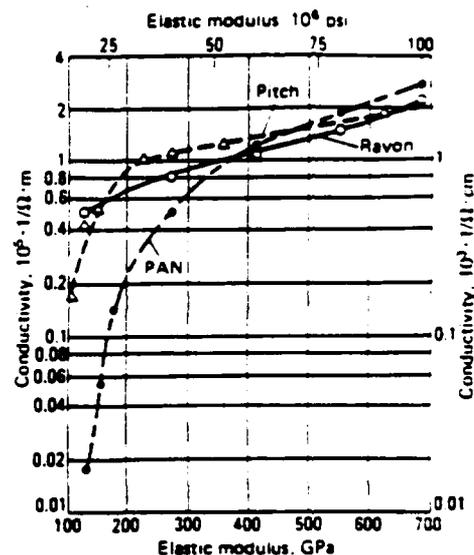
Fig. 6 The conductivity of carbon fibers increases with fiber modulus (heat treatment temperature). These data have been collected by laboratory heat treatments of fibers and may differ from conductivity measured on commercially produced fibers

in much the same way failure occurs within the fiber for aramids (Ref 46).

Environmental Interaction

Carbon fibers are not affected by moisture. atmosphere. solvents. bases. and weak acids at room temperature (Ref 47). However. oxidation becomes a problem at elevated temperature. For low-modulus PAN-based fibers and high-modulus PAN- or pitch-based fibers. the threshold for oxidation for extended operating times is 350 °C (660 °F) and 450 °C (840 °F). respectively (Ref 48). Oxidation is catalytic at these low temperatures. and somewhat improved oxidation resistance can be expected with higher-purity fibers and resins in the future (Ref 49).

Carbon fibers react with molten aluminum and titanium and must be protected by a barrier coating (Ref 50). While carbon does not react with nickel. a small amount of solution dissolution can occur (even in the solid state). which degrades the fibers (Ref 51-53). Reactions occur with most oxides in the 1200 to 1500 °C (2190 to 2730 °F) range. and in the 1600 to 1700 °C (2910 to 3090 °F) range for zirconia (ZrO₂). hafnia (HfO₂). and thoria (ThO₂) (Ref 54).

REFERENCES

1. O.L. Blakslee. D.G. Procter. E.J. Seldin. G.B. Spence. and T Weng. Elastic Constants of Compression Annealed Pyrolytic Graphite. *J. Appl. Phys.*. Vol 41. 1970. p 3373
2. G.D. D'Abate and R.J. Diefendorf. The Effect of Heat on the Structure and Prop-

erties of Mesophase Precursor Carbon Fibers, in *Proceedings of the 17th Biennial Conference on Carbon.* American Carbon Society, 1985, p 390

3. R. Berman, *The Properties of Diamond.* J.E. Field, Ed., Academic Press, 1979

4. *Carbon,* Vol 20 (No. 5), 1982, p 445-449

5. T. Edison, U.S. Patent 223,898, Jan 1880

6. C.E. Ford and C.V. Mitchell, U.S. Patent 3,107,152, Oct 1963

7. R. Bacon and M.M. Tang, Carbonization of Cellulose Fibers I. *Carbon,* Vol 2, 1964, p 211

8. R. Bacon and M.M. Tang, Carbonization of Cellulose Fibers II. *Carbon,* Vol 2, 1964, p 220

9. T.V. Hughes and C.R. Chambers, British Patent 405,480, June 1889

10. A. Oberlin, M. Endo, and T. Koyama, Filamentous Growth of Carbon Through Benzene Decomposition, *J. Cryst. Growth,* Vol 32, 1976, p 335

11. W. Johnston, L.N. Phillips, and W. Watt, British Patent 1,110,791, April and Dec 1964

12. W. Johnston, L.N. Phillips, and W. Watt, U.S. Patent 3,412,062, Nov 1968

13. L.S. Singer, Netherlands Patent 239490, April 1972

14. L.S. Singer, U.S. Patent 4,005,183, Jan 1977

15. R. Bacon and W.A. Schalamon, High Strength and High Modulus Carbon Fibers, in *Proceedings of the Eighth Biennial Conference on Carbon.* American Carbon Committee, 1967

16. H. Hawthorne, Structure and Properties of Strain-Graphitized Glassy Carbon Fibers, in *Proceedings of the First International Conference on Carbon Fibers.* Plastics Industry, 1971, p 81

17. W. Soltes, U.S. Patent 3,011,981, 1961

18. W. Abbott, U.S. Patent 3,053,775, 1962

19. S. Otani, The Fundamental of MP Carbon Fiber. *Carbon,* Vol 3, 1965, p 213

20. R.J. Diefendorf and D.M. Riggs, U.S. Patent 4,208,267, June 1980

21. R. Prescott and A. Standage, High Elastic Modulus Carbon Fibre. *Nature,* Vol 211, 1966, p 169

22. W. Ruland, The Relationship Between Preferred Orientation and Young's Modulus of Carbon Fibers. *Polymer Preprints,* Vol 9 (No. 2), Polymer Chemistry Division, American Chemical Society, 1968, p 1368

23. C.W. LeMaistre and R.J. Diefendorf. The Origin of Structure in Carbonized PAN Fibers. *SAMPE Q.,* Vol 4, 1973, p 1

24. R. Perret and W. Ruland, The Microstructure of PAN-Base Carbon Fibers, *J. Appl. Crystallogr.,* Vol 3, 1970, p 525

25. S.C. Bennett and D.J. Johnson, Structural Characterization of a High Modulus Carbon Fibre by High-Resolution Electron Microscopy and Electron Diffraction. *Car-*

bon, Vol 14, 1976, p 117

26. E.W. Tokarsky and R.J. Diefendorf, High Performance Carbon Fibers, *Polym. Eng. Sci.,* Vol 15 (No. 3), 1975, p 150

27. R.J. Diefendorf and E.W. Tokarsky, "The Relationships of Structure to Properties in Graphite Fibers, Part I," AFML-TR-72-133, Air Force Materials Laboratory, 1971

28. R.J. Diefendorf and E.W. Tokarsky, "The Relationships of Structure to Properties in Graphite Fibers, Part II," AFML-TR-72-133, Air Force Materials Laboratory, 1973

29. R.J. Diefendorf and E.W. Tokarsky, "The Relationships of Structure to Properties in Graphite Fibers, Part III," AFML-TR-72-133, Air Force Materials Laboratory, 1975

30. R.J. Diefendorf and E.W. Tokarsky, "The Relationships of Structure to Properties in Graphite Fibers, Part IV," AFML-TR-72-133, Air Force Materials Laboratory, 1975

31. D.M. Riggs, "The Characterization and Kinetic Mechanism of Mesophase Formation in High Molecular Weight Carbonaceous Materials and Its Relationship to the Concepts of Thermal and Catalytic Cracking," Ph.D. thesis, Rensselaer Polytechnic Institute, 1979

32. B.L. Butler and R.J. Diefendorf, Graphite Filament Structure, in *Proceedings of the Tenth Carbon Composite Technology Symposium,* American Society of Mechanical Engineers, 1970, p 109

33. K.J. Chen, C.W. LeMaistre, J.H. Wang, and R.J. Diefendorf, The Consequences of Residual Stress in High Modulus Carbon Fibers on Composite Performance, in *Polymer Preprints,* American Chemical Society, Vol 22 (No. 2), 1981, p 212

34. C.P. Beetz, Strain Induced Stiffening in Carbon Fibers, in *Proceedings of the 15th Biennial Conference on Carbon,* American Carbon Society, 1981, p 302

35. R.J. Diefendorf, unpublished data

36. J. Awerback and H.T. Hahn, Fatigue and Proof Testing of Unidirectional Graphite/Epoxy Composites, in *Fatigue of Filamentary Composite Materials,* STP 636, American Society for Testing and Materials, 1977, p 248

37. T.T. Chiao, C.C. Chiao, and R.J. Sherry, Lifetimes of Fiber Composites Under Sustained Tensile Loading, in *Proceedings of the 1977 International Conference on Fracture Mechanics and Technology,* 1977

38. R.J. Diefendorf, unpublished data

39. L.A. Feldman, High Temperature Creep Effects in Carbon Yarns and Composites, in *Proceedings of the 17th Biennial Conference on Carbon,* American Carbon Society, 1985, p 393

40. A.A. Bright and L.S. Singer, Electronic and Structural Characteristics of Carbon Fibers from Mesophase Pitch, in *Proceed-*

ings of the 13th Biennial Conference on Carbon, American Carbon Society, 1977, p 100

41. J.H. Helmer and R.J. Diefendorf, Transverse Properties of Carbon and Kevlar Fiber Composites, in *Proceedings of the 16th Biennial Conference on Carbon.* American Carbon Society, 1983, p 511

42. I.M. Kowalski, Determining the Transverse Modulus of Carbon Fibers, *SAMPE J.,* Vol 22 (No. 4), 1986, p 38

43. B.L. Butler, C.W. LeMaistre, and R.J. Diefendorf, The Structure of High Modulus Graphite Fibers, in *Eighth Annual Conference Proceedings,* Society of the Plastics Industry, 1973, p 21-C

44. J.B. Donnet and P. Ehrberger, Carbon Fibre in Polymer Reinforcement. *Carbon,* Vol 15, 1977, p 143

45. J.C. Goan and S.P. Prosen, *Interfacial Bonding in Graphite-Resin Composites,* STP 452, American Society for Testing and Materials, 1969, p 3

46. L.T. Drzal, Adhesion of Graphite Fibers in Epoxy Matrices: I. Role of Fiber Surface Treatment, *J. Adhesion,* Vol 16, 1982, p 1-30

47. N.C.W. Judd, The Chemical Resistance of Carbon Fibres and a Carbon Fibre/Polyester Composite, in *Proceedings of the First International Conference on Carbon Fibres.* Plastics Institute, 1971, p 258

48. D.W. McKee and V.J. Mimeault, Surface Properties of Carbon Fibers, in *Chemistry and Physics of Carbon,* Vol 8, Marcel Dekker, 1973, p 235

49. D.W. McKee, The Catalysed Gasification Reactions of Carbon, in *Chemistry and Physics of Carbon,* Vol 17, Marcel Dekker, 1981, p 1

50. W. Meyerer, D. Kizer, and H. Paul, Versatility of Graphite-Aluminum Composites, in *Proceedings of the 1978 International Conference on Composite Materials,* American Institute of Mining, Metallurgical, and Petroleum Engineers, 1978, p 141

51. P.W. Jackson and J.R. Marjoram, Recrystallization of Nickel-Coated Carbon Fibers, *Nature,* Vol 218, 1968, p 83

52. R.V. Sara, Fabrication and Properties of Graphite-Fiber Nickel-Matrix Composites, in *Proceedings 14th SAMPE Symposium,* Society for the Advancement of Material and Process Engineering, 1968, p II-4a-4

53. S. Sarian, Elevated Temperature of Carbon-Fibre, Nickel-Matrix Composites, Morphological and Mechanical Property Degradation. *J. Mater. Sci.,* Vol 8, 1973, p 251-260

54. R.M. Bushong, "Improved Graphite Materials for High-Temperature Aerospace Use, Vol II, Development of Graphite-Refractory Composites Technical Documentary Report," AFML ML-TDR-64-125, Air Force Materials Laboratory

CROSS-SECTIONAL AREA MEASUREMENT OF SINGLE CARBON FIBERS

S.-S. Tzeng and R.J. Diefendorf
Center for Composite Materials and Structures (CCMS)
Rensselaer Polytechnic Institute, Troy, NY 12180-3590

Introduction

Single fiber testing results in much scatter, especially in strength. Many factors affect strength. For example, internal flaws occurring within the gauge length may cause the strength to decrease[1], and neglecting the compliance due to the test machine will produce a lower modulus value. However, the precision of the strength and modulus measurements is mainly determined by the precision of the cross-sectional area measurement. Difficulties arise because of the tiny cross-section and also since not all the fibers have circular shape cross-section. T-300 fiber is a typical example with irregular cross-section.

There are three methods used to estimate the cross-section of the fibers : (1) optical microscopy, (2) electron microscopy, and (3) laser diffraction. Although microscopy is more suitable for complex cross-sections, the laser diffraction technique has better resolution[2] and is a much faster and better method for routine measurements of cross-sections without negative curvature. The measurement errors are analyzed for a non-circular cross-section based on an elliptical cross-section. Laser diffraction patterns for carbon and tungsten fibers are presented.

Model of Analysis

Chen and Diefendorf[3] suggested a polygon method for the calculation of the cross-sectional area of relatively circular fibers and found that five measurements(measured every 36 degrees) have minimum error. Using the polygon method and based on an elliptical cross-section, the errors are analyzed for different number of measurements made at equally spaced intervals.

The angle theta in the figures 1-5 represents the angle between long axis of the ellipse and the direction perpendicular to the laser beam. The errors for 1, 2, 3, 4, and 5 measurements are shown in figures 1-5. For one measurement which many people use, a 50% maximum error could occur when the ellipticity equals 1.5. In general, the larger the ellipticity, the worse the errors. From the results we can see that for 1 and 2(orthogonal) measurements, the errors are affected largely by angle theta , but for 5 measurements made at equal angular intervals around a fiber, the errors are almost independent of theta for p/q < 4. From the comparison of errors shown in fig. 6, we see that for 1 < p/q < 2 , 5 measurements are best with a minimum error(=0) at p/q = 1.5. This is the range of p/q most often observed. For p/q = 1 (circular), the values of 5 measurements will be equal, and the polygon approximation yields an error of -6% . From fig. 6 we also find that for 2 < p/q < 3, 3 measurements at

equal angular intervals have smaller errors, and the errors are also independent of angle theta . For p/q > 3, the errors are too large to be suitable for cross-sectional area calculation. If the shape of the approximate cross-section is known in advance, the number of measurements and method of calculation can be selected to improve the accuracy. However, the laser technique can not detect a reentrant shape, for example a dog-bone shape for some PAN-based fibers and the PAC-man shape for some pitch-based fibers. Also, sometimes the diffraction pattern is not good and hard to detect the minimum intensity.

Experimental Results and Discussions

The laser diffraction patterns for tungsten and carbon fibers using a photoresistor and CCD array are shown in figures 7-8. From the results of photoresistor in fig. 7, we can see that tungsten has smooth diffraction pattern which is close to the theoretical pattern[4], but the diffraction pattern for carbon fiber shows modulation. The resolution for both cases is smaller than 1000 micron, and compared with the 5.4cm distance between two minimum intensity locations of 6.66 micron T-300 fiber, we can obtain an accuracy better than 1.8%. Also when the distance between fiber and detector is closer, the resolution increases. Because of this precision, it appears possible to determine the Poisson's ratio directly. The diffraction patterns (fig. 8) for tungsten and carbon fibers using a higher resolution CCD array show the same result with carbon fiber's pattern having more modulation. Due to the resolution of the CCD array, the tungsten also has a little modulation. The reason for the modulation is probably due to surface roughness. By using the CCD detector, a large number of measurements can be done quickly, and the calculation of cross-sectional area will be very accurate. Also additional information can be obtained if the shape of cross-section is close to an ellipse. By fitting the equation of an ellipse, the morphology of the cross-section can be investigated[5].

Conclusions

The polygon approximation is good for small ellipticity. If the shape of the cross-section is close to an ellipse, more measurements must be done to improve the accuracy for high ellipticity. For cross-sections with a reentrant shape, the laser diffraction technique is not suitable for measurement of cross-sectional area.Due to surface roughness, the diffraction pattern for carbon fiber shows modulation and can be used to characterize surface roughness.The resolution appears enough to determine Poisson's ratio directly.

References

1. J. W. Johnson and D. J. Thorne, Carbon, 7(1969)659.
2. K. J. Chen and R. J. Diefendorf, Progress in Science and Engineering of Composites(T. Hayashi, K. Kawata, and S. Umekawa, editors) (1982)97-105.
3. K. J. Chen, Ph.D Thesis, Rensselaer Polytechnic Institute, 1984.
4. A. J. Perry, B. Ineichen, and B. Eliasson, J. Material Science, 9(1974)1376-1378.
5. P. Gagnaire, P. Delhaes, and A. Pacault, Ext. Abstr. of 18th Conference on Carbon, Worcester ,1987 p.432.
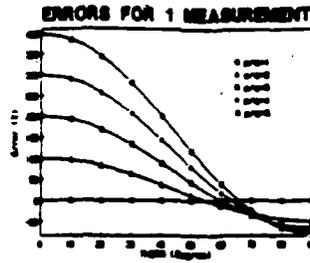
Figure 1.
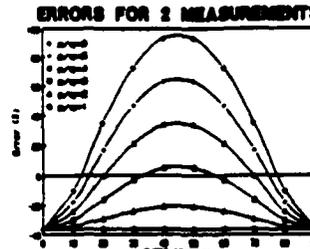
Figure 2.
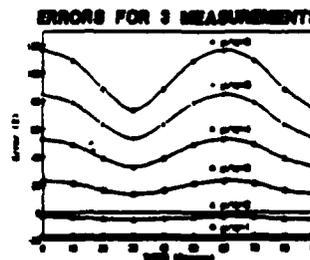
Figure 3.
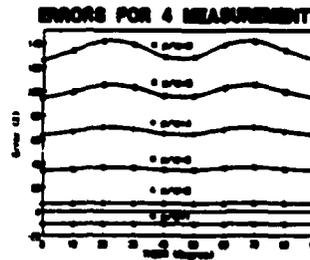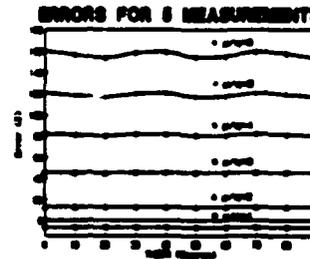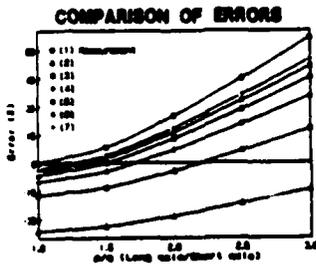
Figure 4.

Figure 5.

Figure 6.
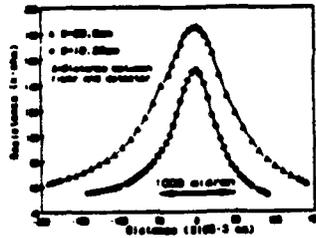
Figure 7. Laser diffraction pattern of photoresistor : (a)tungsten(b)carbon fiber
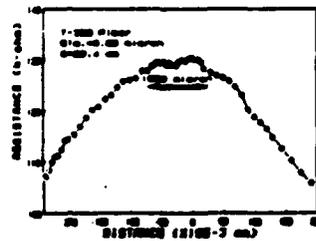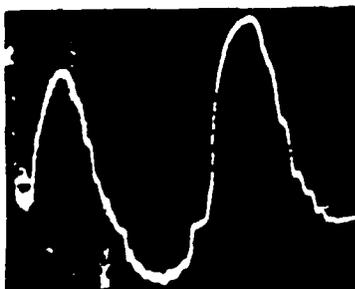
(a)
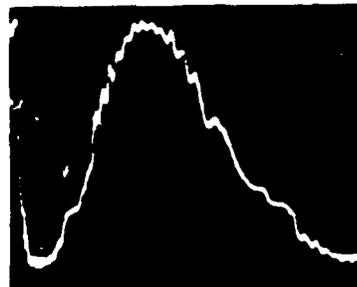
(b)

Figure 8. Laser diffraction pattern of CCD array : (a)tungsten (b)carbon fiber.

(a)

(b)

HIGH PERFORMANCE TITANIUM DIBORIDE FIBERS

R. J. Diefendorf and L. Mazlout

Materials Engineering Department
Rensselaer Polytechnic Institute

INTRODUCTION

The properties of more than 500 high melting materials were considered for fiber reinforcement. TiB_2 was chosen as a potential material for fiber reinforcement of intermetallic matrix composites. TiB_2 fibers can be produced using different methods, but the one most promising is the chemical vapor deposition (CVD) of TiB_2 by the hydrogen reduction of $TiCl_4$ and BCl_3. Also, TiB_2 can be deposited using a two-step process in which boron is deposited first and then titanium, which reacts with the already deposited boron to form titanium diboride. The results related to this experiment will be presented. Since some difficulties were encountered during the deposition, the deposition process was modeled with the purpose of solving these problems. The results of this modeling which lead to a new reactor design will be discussed.

- Introduction

- Experimental setup

- Modeling of the tube reactor

- Tube reactor design

- Chemical vapor deposition of TiB2

- Summary

FIBER SELECTION CRITERIA

The objective of our work consisted of finding and then producing a fiber reinforcement for composites for use at very high temperatures. More than 500 materials have been considered by investigating their properties, the most important of which are melting temperature, creep and stress rupture, specific modulus, coefficient of thermal expansion, volatility and environmental stability. Unfortunately, the data are not available for the properties of all materials. Therefore, our selection of materials is based on the available data and intuition. Missing data is insufficient to eliminate a material. Hence, if all known properties are "good", the material is considered for further studies. As a result of this survey, nine materials were considered for further studies. Finally, titanium diboride in pure or doped forms was selected out of these nine materials for initial fiber development.

* CREEP AND STRESS RUPTURE

* SPECIFIC MODULUS

* COEFFICIENT OF THERMAL EXPANSION

* VOLATILITY

* ENVIRONMENTAL STABILITY

HIGH MELTING COMPOUNDS

The chart below shows the elements and compounds with a melting point higher than 2200°C. Among these materials carbon and TiB_2 have the highest melting temperatures and lowest densities. While a number of other properties also must be acceptable, TiB_2 appears to meet the requirements although there is considerable scatter in the data.
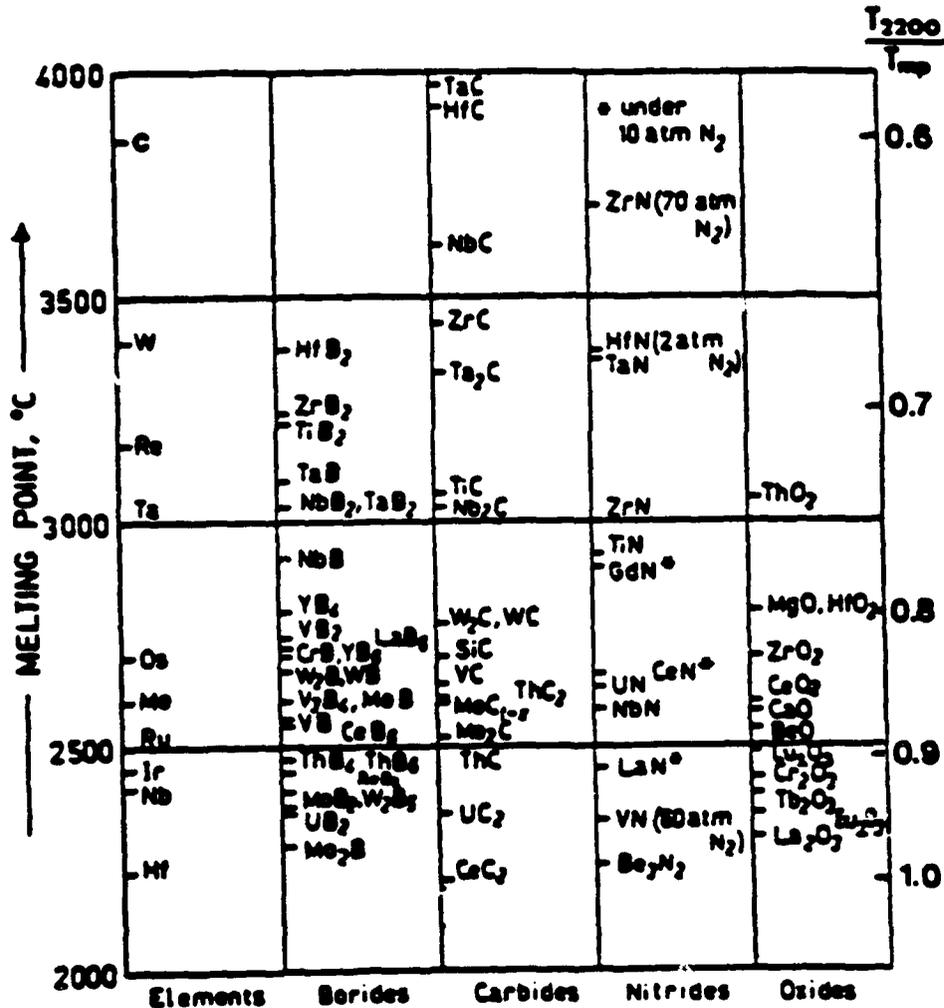
DETERMINING TiB$_2$ PROPERTIES

The properties of titanium diboride show enormous scatter. Part of this variation may be caused by preferred orientation. TiB$_2$ has a hexagonal structure which consists of alternating layers of boron and titanium. This type of structure leads to different properties in the "a" and "c" directions. Any preferred orientation generated during the production of TiB$_2$ such as by chemical vapor deposition will vary properties. A second problem is producing pure TiB$_2$. The TiB$_2$ domain in the phase diagram is narrow. An excess of boron over the stoichiometric ratio leads to boron precipitates while an excess of titanium leads to Ti$_3$B$_4$ precipitates within TiB$_2$. The stoichiometries measured by many investigators[1-3] ranges from TiB$_{1.89}$ to TiB$_{2.22}$. In addition, other impurities such as carbon and oxygen often have been formed by chemical analysis.
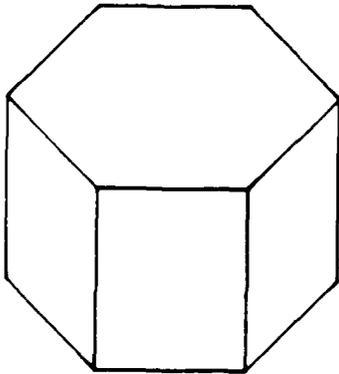
PREFERRED ORIENTATION
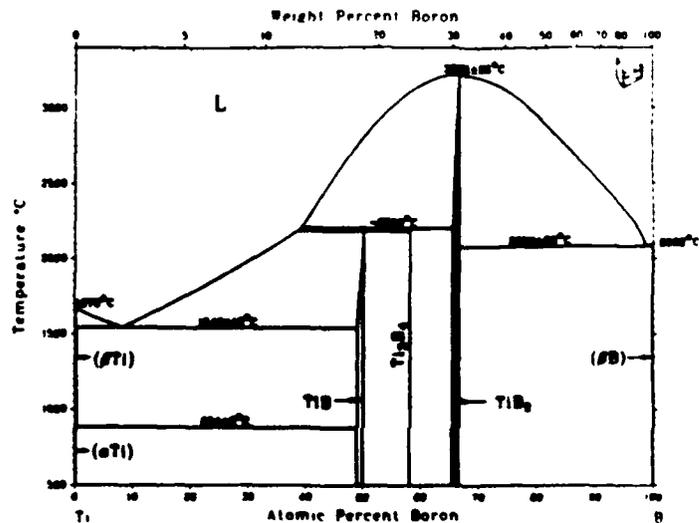
PHASE PURITY

PROPERTIES OF TiB$_2$

Some of the important properties of TiB$_2$ which led to its selection are tabulated below. The elastic modulus of 500 GPa$_4$ is easily obtained, but values as high as 810 GPa have been measured on CVD produced fiber using a tungsten substrate. The intermediate value of the coefficient of thermal expansion makes TiB$_2$ a potential reinforcement of both intermetallic and ceramic-matrix composites. Its good stability with many potential matrices makes it an attractive reinforcement. For example, as compared with SiC, TiB$_2$ was found to be very stable in contact with Ni$_3$Al.

The value of the electrical resistivity is very low. In the production of TiB$_2$ fibers by CVD, the substrate fiber, on which TiB$_2$ is deposited, is resistively heated generally. Since the electrical resistivity of TiB$_2$ is very low, large currents are required to keep the fiber at the desired temperature as deposition takes place. The difficulty caused by this property in producing TiB$_2$ fibers will be evident later.

MELTING TEMPERATURE	HIGH	(3225C)
DENSITY	LOW	(4.52g/cc)
MODULUS OF ELASTICITY	HIGH	(500GPa)
CREEP	LOW	(10^{-7}/SEC @ 1300-1500C)
THERMAL EXPANSION COEFFICIENT	MED	($7-8 \times 10^{-6}$/ C)
VOLATILITY	LOW	(Kp=10^{-6}@2000K)
REACTIVITY	LOW	(Al, Ni, Ti)
ELECTRICAL RESISTIVITY	LOW	(7microohm.cm)

DEPOSITION CONDITIONS AND RESULTS

The method adopted for depositing TiB_2 coatings was the two-step process. In the first step gas flow rates of 162 cc/min of BCl_3 and 1150 cc/min of hydrogen were fed into the tube reactor. The substrate fiber used was SCS-6 SiC fibers. Its temperature was held at 930°C for a period of one minute. In the second step the resulting fiber was heated up in a flowing gas of $TiCl_4$ and excess hydrogen. The reaction time was 75 seconds. The initially supplied power of 650 V and 250 mA changed indicating the deposition of a conducting material. The boron deposition rate at the conditions specified above was 2.9 micrometer/min. Finally, the TiB_2 deposition, or transformation, rate was about 0.3 micrometer/min. The strength of three different samples was measured using a loop test. By comparison with an uncoated SiC fiber it was found that the samples had the same strength. A SEM photograph of the produced fiber after it has been broken in a bend test is shown. The resulting TiB_2 coating is very uniform around and along the fiber. Because of the high electrical conductivity of TiB_2 the temperature of the fiber dropped as TiB_2 was deposited. As will be described later, a new tube reactor which can lead to deposition of thick TiB_2 coatings at constant temperature was designed.

RESULTS AND DISCUSSION

The figure shows the deposited coating at a magnification of 10,000X. The deposited coating consists of three layers. Qualitative analysis has been made on these three layers. The results from the top layer are shown in the next figure. Auger analysis was also performed on the very top layer. By considering the results obtained from a sample where only the first step was performed, i.e. only boron was deposited, the results can be summarized as follows. First, the very top titanium diboride layer has an appreciable amount of silicon and some traces of carbon and oxygen. Second, the middle dark layer is mainly boron and silicon with some traces of carbon. Third, the bottom bright layer is silicon rich containing an unidentifiable amount of boron and carbon.

QUALITATIVE ELEMENT IDENTIFICATION

SAMPLE ID:TiB2 COATING OUTSIDE

POSSIBLE IDENTIFICATION
   TI KA KB OR BA LA
   SI KA OR RB LA?
   NB LA OR AU LA MA

      PEAK LISTING
     ENERGY   AREA EL. AND LINE
1   1.736   5985 SI KA OR RB LA?
2   2.149   5824 AU MA
3   4.514   9990 TI KA
4   4.936   1262 TI KB
5   9.717   821 AU LA

RPI MATERIALS ENGINEERING   WED 13-NOV-87 22:23
Cursor: 0.000keV = 0
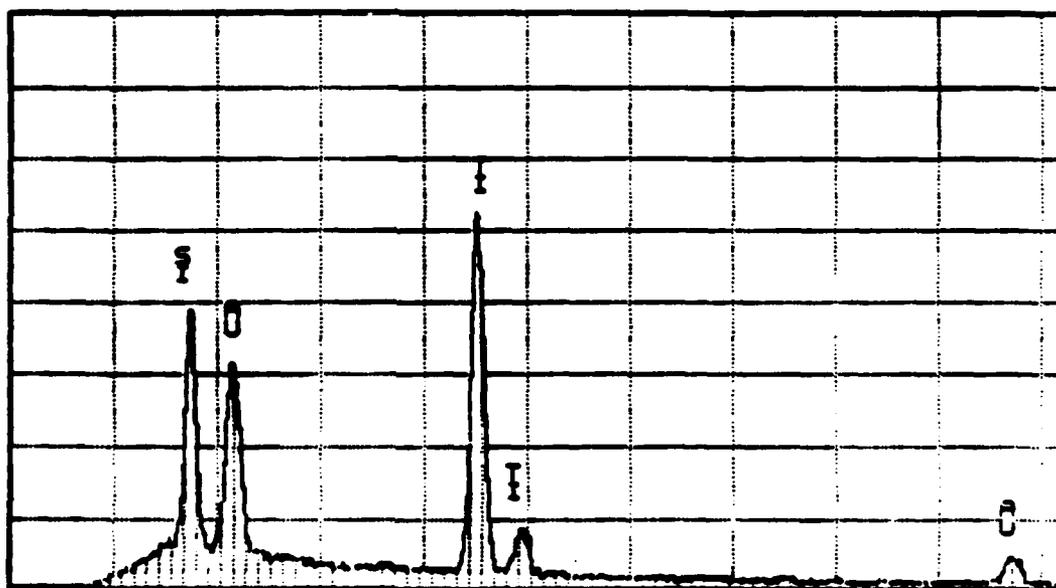
0.000
50   TiB2 COATING OUTSIDE   VFS = 2048 10.240

SUMMARY OF TiB$_2$ COATING WORK

Using the two-step process, TiB$_2$ could be deposited successfully on a SiC substrate. The very high electrical conductivity of TiB$_2$ made it impossible to deposit thick coatings. Silicon diffused throughout the coating, resulting in unpure TiB$_2$. The reactivity of these TiB$_2$ coatings with existing and potential matrix materials such as Ni$_3$Al will be studied. Also, the production of pure TiB$_2$ fibers using the one-step process will be performed.

* TiB$_2$ SUCCESSFULLY COATED

* TiB$_2$ COATING AS STRONG AS SCS-6
                                    SiC FILAMENT

* REACTIVITY STUDIES TO BE PERFORMED

CVD OF TiB$_2$ - PROBLEMS ENCOUNTERED

Four major problems were encountered during the deposition of TiB$_2$. Three of these were related to the design of the tube reactor and the fourth to the heating method. The first problem lead to fiber breaking soon after deposition started at the lower jewel of the top end-cap. There is relatively little gas flowing at this location, so that the fiber is relatively hot. The second problem was caused by the plugging of the inside jewels which prevented the substrate from being threaded into the tube reactor for continuous deposition. Finally, TiCl$_3$ was observed to deposit on the relatively cold tube wall which fouled up temperature measurement of the fiber.

- **Local heating: breaking of fiber.**

- **Plugging of the jewels: sticking of fiber.**

- **Deposition of TiCl$_x$ on tube walls.**

CVD OF TiB$_2$

The main problem encountered during the deposition of TiB$_2$ was the difficulty in depositing thick TiB$_2$ coatings. The cause for this is the high electrical conductivity of TiB$_2$, which is even a better conductor than elemental titanium. (The electrical resistivity of TiB$_2$ is 7 micro ohm-cm at room temperature and it increases linearly to about 50 micro ohm-cm at 1100°C.) Since the filament is generally resistance heated during deposition, the voltage and amperage requirements change from high voltage to high current as TiB$_2$ is deposited on the substrate. By contrast, deposition of silicon carbide and boron present a much lesser problem since they have much higher resistivities. The solution to this problem can be any or a combination of the following: 1) Multiple reactors can be used. The length of each reactor should be short enough so that a constant temperature may be achieved with a DC power supply having the appropriate voltage and amperage rating. 2) Alternate heating methods such as light or radio frequency heating external to the silica reactor can be used. 3) Finally, the heat losses can be minimized, which allows smaller power supplies to be used.

MAIN PROBLEM

— HIGH ELECTRICAL CONDUCTIVITY —

SOLUTIONS

* MULTIPLE REACTORS

* ALTERNATE HEATING METHODS

* MINIMIZE HEAT LOSS

HEAT TRANSFER MODELING - TUBE WALL TEMPERATURE

The effect of the deposition conditions and the process variables on the current, I, required to achieve a fiber temperature T_f, is required in minimizing the heat losses. The figure shows the control volume used to estimate the tube wall temperature, T_w. q_1 and q denote the heat transferred by conduction and radiation, and by convection. The heat radiated from the tube walls has been estimated to be about 2% of the convected heat, and hence it has been neglected. By equating the heat coming in to the heat going out of the control volume, T_w can be estimated by the expression shown below where ϵ, σ, k, and h are the fiber emissivity, the Stephan-Boltzman constant, the average thermal conductivity of the gas, and the convection coefficient, respectively.

HEAT BALANCE
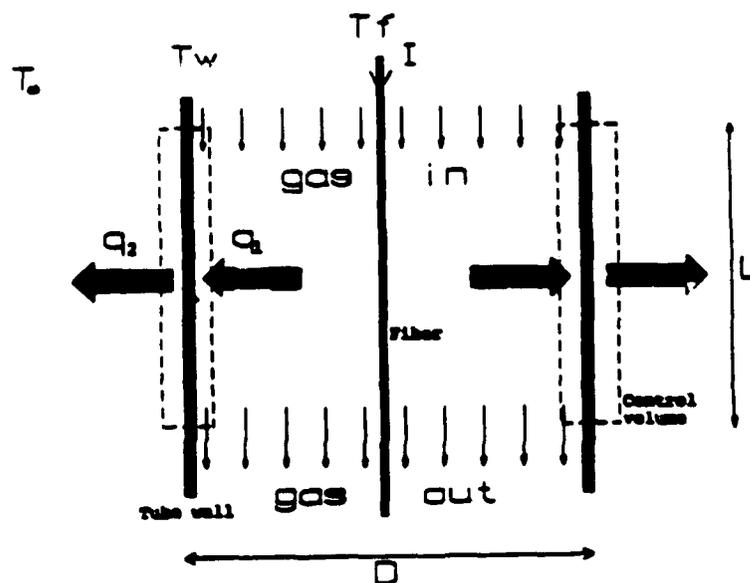
$$T_w = (T_\infty + mT_f + (\epsilon\sigma/h)\,T_f^4) / (1 + m) \qquad (1)$$

$$\text{where} \quad m = 2k / Dh$$

HEAT TRANSFER MODELING - POWER REQUIREMENT

The current required to heat up the fiber to a temperature T_f can be found by considering the control volume shown by the dotted line. The total heat entering the control volume is the sum of the heat supplied by the power supply, I^2R, and the heat carried by the gas at the inlet temperature T_o. The total heat leaving the control volume is the sum of the convected heat through the tube walls, q, and the heat carried out by the gas at the exit temperature T. Again, the radiated heat from the tube walls to the surroundings is negligible. The heat contribution of the gas is es ˙mat d from the heat capacity. The heat of the gas is esτ nated by $H(T) = N\{(T_f+2T_w)a/3-H(T_o)\}$ with a maximum error of 5.9% and 1.6% for nitrogen and hydrogen, respectively. N is the total gas flow rate and a is the constant in the heat capacity expression: $C_p = a+bT+cT^2+dT^4$. After equating the total heat in to the total heat out, the current can be expressed as given by the equation below, where R is the resistance of the fiber.

HEAT BALANCE
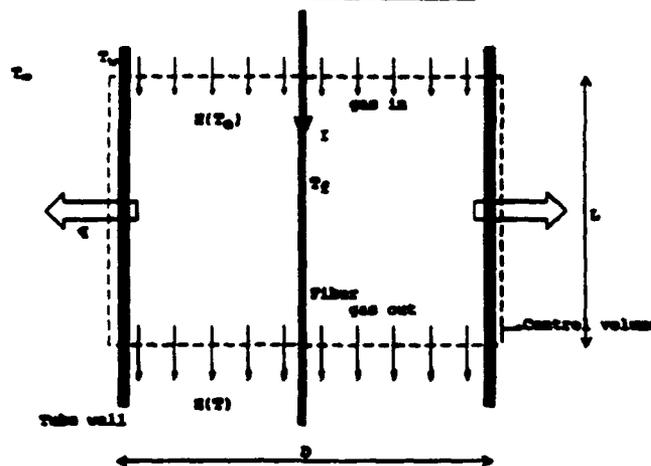
$$I = \sqrt{hπDL(T_w-T_o)/R + aN(T_f+2T_w)/3R - No/R}$$

(2)

CALCULATED VERSUS EXPERIMENTAL RESULTS

The equation derived for the current can be used to study the effect of process variables on the power requirement. The figure below compares the calculated to the measured current as a function of fiber temperature. The difference observed could be due to the heat transfer coefficient or to any of the assumptions made during the derivation of equation (2). One assumption was that the temperature gradient from the fiber surface to the tube wall was linear. In fact, near the fiber surface, the temperature drops faster than linearly. The estimated wall temperature which was higher than the measured value agrees with this argument. Hence, the effective convective coefficient will be different from the convective coefficient used in the calculations. Other assumptions such as those related to the heat loss at the end-caps and to the temperature drop across the tube wall are negligible. Using the effective convective coefficient, the calculated value is considered to be accurate enough to allow a better understanding of the heat transfer process.
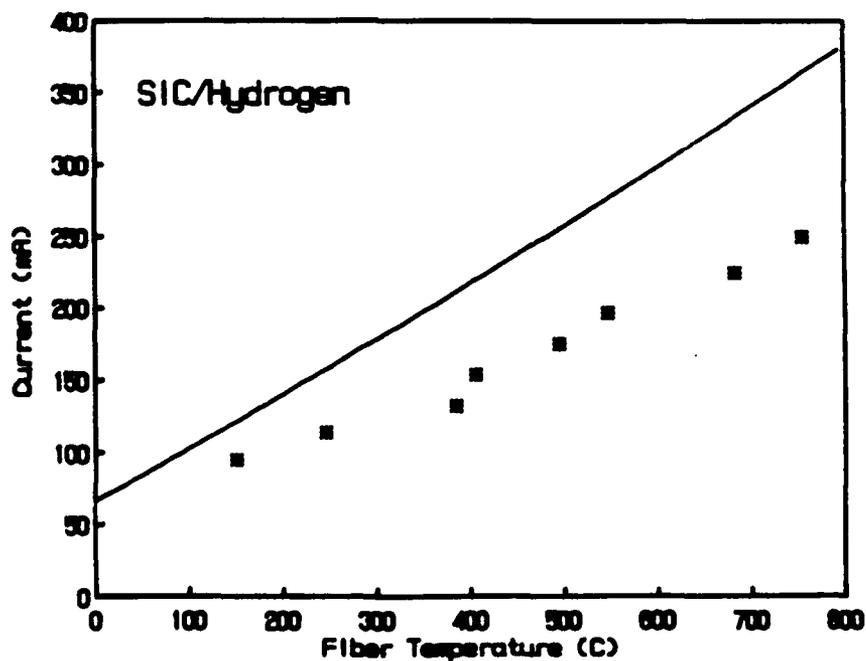
HEAT LOSSES

The figure shows how the current varies with fiber temperature for two different cases. The first one, represented by the solid line, is when there is no gas flowing through the reactor, i.e. all the heat is lost to the outside by convection from the tube wall. In the second case, represented by the dotted line, the convective coefficient is set to equal zero; i.e. the tube is totally insulated and the heat is lost through the flowing gas. By comparing these two curves it is easily seen that if the tube is insulated, then the power required to heat up the fiber to the desired temperature is decreased by at least a factor of eight. The consequence of this is that thick coatings of highly conductive materials can be deposited on a substrate more easily.
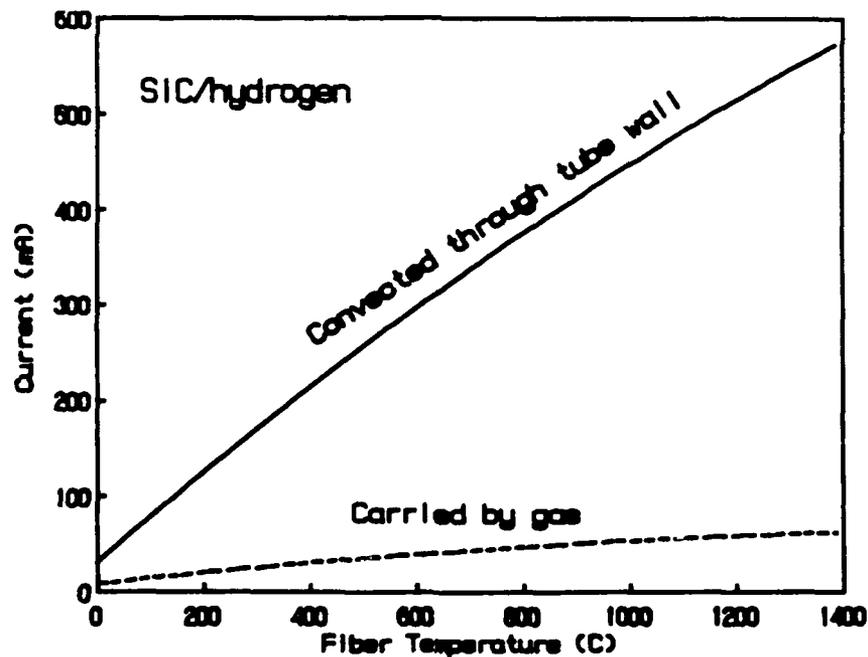
NEW REACTOR DESIGN

A schematic of a tube reactor chamber that can be
used to produce thick coatings of highly conductive materials
with less power is shown. The insulation on the outside of
the tube can be achieved by a vacuum. This should allow the
operator to monitor the temperature using an optical pyrometer.
This new design has other advantages as well. Since the
vacuum does not extend to the ends of the tube, the fiber
there will be relatively cooler than in the middle section,
hence the "hot spot" problem is minimized. Also, the level
of vacuum can be changed such that the inner tube wall is hot
enough to prevent undesired $TiCl_3$ deposition.
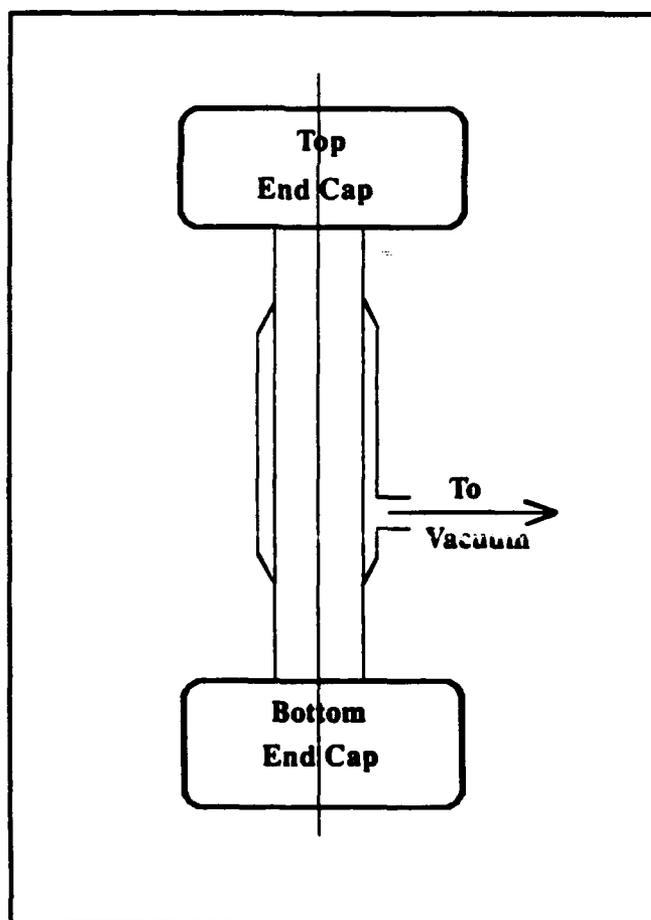
NEW REACTOR DESIGN (Cont'd.)

A diagram of the new end-caps designed to solve the problems encountered during earlier depositions is shown below. The new design is based on a concentric flow of a cooling gas such as hydrogen. This gas enters the end-cap at the top and flows around the mercury column, thus cooling it. It also prevents the reacting gases which enter the tube reactor at a lower inlet from getting near the small hole through which the fiber is threaded. Hence clogging of the hole and sticking of the fiber is avoided. The third function of the cooling gas is to cool the very top portion of the fiber as it exits from the mercury column to avoid a hot spot that may lead to fiber breakage.

NEW DESIGN

Cooling gas (H_2)

$H_2 + TiCl_4 + BCl_3$
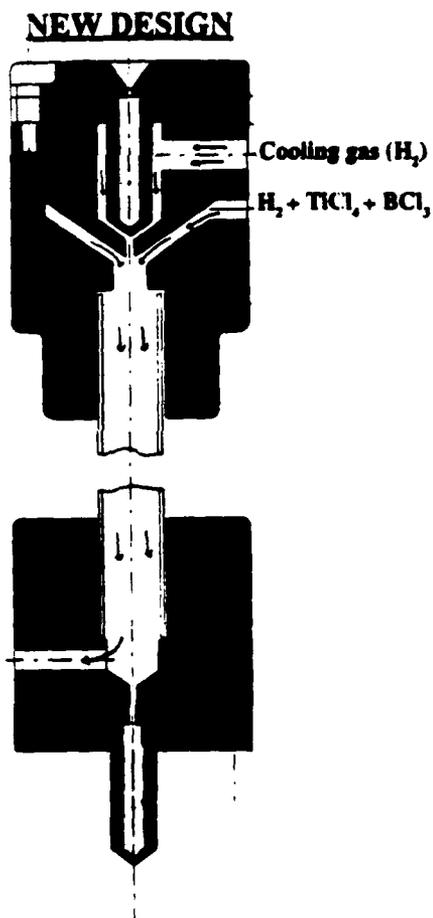
SUMMARY

A survey of the properties of over 500 materials lead to the conclusion that TiB_2 is one of the best reinforcing materials that can be used in composites for aerospace and high temperature applications. Also, due to its intermediate properties it can be used to reinforce metal as well as ceramic matrix composites. TiB_2 could be deposited successfully, although in unpure form, onto SCS-6 SiC fibers. Silicon was observed to diffuse throughout the coating. The strength of the TiB_2-coated fibers was at least of comparable magnitude to commercially available CVD SiC filament.

A better understanding of the heat transfer phenomenon during CVD was achieved by modeling the heat transfer process by a simple, but powerful model. The results of this modeling led to the design of a new tube reactor which solves problems encountered using the old reactor; namely (1) inability to deposit thick coatings, (2) breaking of the fiber during deposition, (3) sticking of the fiber to the end-caps, and (4) unwanted deposition of $TiCl_3$ on the tube wall.

* TiB2 is a potential reinforcement for

    - Metal matrix composites.

    - Ceramic matrix composites.

* TiB2 has been successfully deposited.

* Problems can be solved using the new reactor.

188

REFERENCES

1. J. R. Ramberg and W. S. Williams, "High Temperature Deformation of Titanium Diboride", J. Mater. Sci. <u>22</u> (1987) 1815-1826.

2. C. T. Lynch, S. A. Mersol, and F. W. Vahldiek, "The Microstructure of Single Crystal Titanium Diboride", J. Less-Common Metals, 10 (1966) 206-219.

3. R. Feurer, G. Constand, and C. Bernard, "Single Crystals with Compositions in the Range $TiB_{1.89}$-$TiB_{1.96}$ Prepared by Chemical Vapor Transport", J. Less-Common Metals, 67 (1979) 107-114.

BIBLIOGRAPHY

McLead, A. D., Haggerty, J. S., and Sadoway, D. R., "Electrical Resistivities of Monocrystalline and Polycrystalline TiB_2", J. American Ceramic Society, 67 No. 11 (1984) 705-708.

Mehalso, R. M. and Diefendorf, R. J., "Vapor Deposition of High Strength-High Modulus Boron on a Carbon Monofilament Substrate", 5th International Conference on Chemical Vapor Deposition, pp. 552-561.

Miller, G. H., "Method of Making Continuous Length Super-Conducting Wires Using Chemical Vapor Plating", IEEE Transactions on Magnetics, 17 No. 1 (1981) 1032-1035.

HIGH TEMPERATURE, ADVANCED STRUCTURAL COMPOSITE REINFORCEMENTS*

R. Judd Diefendorf**
Rensselaer Polytechnic Institute
Troy, NY 12180-3590, USA

Introduction

Improvements to high temperature alloys have been instrumental in improving the performance of aircraft gas turbine engines. Better materials have resulted in an increase in the past of 5° to 10°C per year in material temperature capability. However, the melting of nickel-base superalloys limits future performance increases with these materials. Improved thermal efficiency could be obtained running at higher turbine inlet temperatures and higher pressure ratios. Hence, the goal for a high temperature composite material which can operate in a combustion gas atmosphere.

Turbine blades must operate at high temperature with centrifugal stresses, gas flow induced stresses, as well as thermal stresses resulting from steady state temperature gradients, and transients in gas temperature and pressure. The moduli of elasticity govern the natural blade frequencies and influence the thermal stresses; the coefficients of thermal expansion cause blade growth, and contribute to thermal stress; the thermal conductivities affect the temperature gradients. Conceptually, the combined centrifugal, thermal, and gas-load stresses can be evaluated to define the lifetime based on stress-rupture, creep, and high cycle fatigue. Other phenomina which affect or determine lifetime are thermal fatigue, and low cycle fatigue. Finally, near-ambient conditions often are the most severe for brittle systems, as ceramics are less forgiving than at higher temperature. Therefore, the fracture toughness or damage tolerance of these materials is important at ambient temperature.

The turbine blade is subjected to combustion gases, and the surface must be resistant to oxidation/hot corrosion. Furthermore, the various materials in the composite should be compatible and ideally thermodynamically stable. The microstructures of the constituent materials also should be stable.

Listed below are the properties which are normally required for turbine design:

1) Tensile strengths and moduli
2) Creep
3) Stress-rupture
4) High and low cycle fatigue
5) Thermal cycle fatigue
6) Fracture toughness
7) Damage tolerance
8) Density
9) Coefficients of Thermal Expansion
10) Thermal Conductivities
11) Microstructural stability
12) Oxidation/hot corrosion.

All of these properties must be known over the temperatures, times and environments that the turbine blade would encounter during its service life. Composites also require extra testing because of their directionality. Obviously, the cost of testing many potential candidate systems up to 2000°C is high. The purpose of this paper is to consider reinforcement fibers, and their use in composite material systems. Unfortunately, necessary data for many of the materials with pure or controlled composition is not available, or if available, misleading. Hence, theory may provide better estimates of potential performance than experimental data.

Some criteria must be selected for comparing the reinforcing fibers. The values are calculated from the composite properties that probably would be required to replace superalloys. They are:

1) Tensile and compressive strength of 1.5 GPA minimum from room temperature to 1500C.

2) Tensile modulus of 70 GPA minimum from room temperature to 1500C.

3) Radial creep of <1% at 1500C under 130 MPA stress for 1000 hours.

4) A 1000 hour radial stress-rupture life at 1500C under a 130 MPA stress.

5) Out of plane shear strengths of 15 MPA from room temperature to 1500C.

6) Ability of composite and any coatings to withstand multiple cycling without probability of spallation of the coating or major damage to composite properties. (Particularly out-of-plane properties.)(A coefficient of thermal expansion consideration.)

31.4

7) A 1000 hour oxidation resistance at 1500C and better oxidation resistance at lower temperatures and normal engine cycles.

8) Microstructural stability at 1500C for 1000 hours.

9) Melting point over 2000C.

10) Low density if possible.

These are strigent requirements. Fibers will be noted if they approach these requirements, or if different processing or compositions might provide improvement.

I. Fiber Materials

The introduction enumerated the extensive set of properties necessary to evaluate the potential of a material as a fibrous reinforcement. Unfortunately, most of these properties are unknown for the majority of the materials. What is known for most materials is melting point, density, and crystal structure. For even as fundamental a property as modulus, only about ten percent of the values for the high melting intermetallic compounds are known. The question is then how can the potential of the materials be estimated from these simple data and first principles and known "rules of thumb"?

A. Melting Point

Over three hundred materials have melting points over 2200C. Figure 1 illustrates a portion of the total. While many materials have melting points over 2200C, only ten elements or simple compounds have a homologous temperature ($T°_K/T_{mp}$) of 0.7 or less for an operating temperature of 2200C at one atmospheric pressure. Carbon, tungsten, the carbides of hafnium, niobium, tantalum and zirconium, the borides of hafnium, zirconium and titanium, and tantalum nitride are the candidates. Of course, if the operating temperature were 1700C, then all the materials shown in Figure 1 have a homologous temperature of 0.7 or less.

Consideration of density for weight critical application decreases the number of potential materials substantially. Of the elements, only carbon has low density and a high melting point. Titanium diboride, berylium borides, boron nitride, titanium carbide, silicon carbide, titanium nitride, silicon nitride, berylium nitride, magnesium oxide berylium oxide and aluminum oxide, plus perhaps some rare earth borides are other candidates. Hence, out of over 300 high melting materials, only about twelve also have low density.

$$\frac{T_{2200}}{T_{mp}}$$

MELTING POINT, °C

4000 —

—TaC
—HfC

—C

* under
  10 atm N_2

—0.6

— ZrN (70 atm
            N_2)

— NbC

3500 —

—ZrC

—W

—HfB_2

—Ta$_2$C

HfN(2 atm
TaN N_2)

—0.7

—ZrB_2
—TiB_2

—Re

—TaB

—TiC

—NbB$_2$,TaB_2

—Nb$_2$C

Ta   ZrN   —ThO$_2$

3000 —

—NbB

—TiN
—GdN*

—YB_6
—VB_2 LaB_6

—W$_2$C, WC

—MgO, HfO$_2$ 0.8

—Cr B,YB_f

—SiC

—ZrO_2

—Os

—W$_2$B,WB

—VC

—Mo

—V$_3$B$_6$, Mo B

—MoC$_{l-x}$ ThC_2

—UN CeN*

—CeO_2

Ru

—VB CeB$_f$

—Mo$_2$C

—NbN

—CaO
—BeO

2500 —

—0.9

—Ir
—Nb

—ThB_4,ThB_6
          AoB

—ThC

— LaN*

—Cu$_2$O$_3$
—Cr$_2$O$_3$

—MoB$_2$,W$_2$B$_5$

—Tb$_2$O$_3$

—UB_2

—UC_2

— VN (60 atm
            N_2)

—La$_2$O$_3$ Eu$_2$O$_3$

—Hf

—Mo$_2$B

—Be$_3$N$_2$

—1.0

—CaC_2

2000 —

Elements   Borides   Carbides   Nitrides   Oxides

FIGURE 1:   Elements and Binary Compounds with Melting
            Points greater than 2200C.

B. Volatility

The rate of evaporation may be estimated from the Knudsen-Langmuir equation:

Rate = $1.5 \times 10^5 \alpha P_{eq}/(MT)^{\frac{1}{2}} gm/cm^2/min$

where

α = accommodation coefficient

P_{eq} = equilibrium vapor pressure

M = molecular weight of evaporating species.

The accommodation coefficient is usually near unity (0.1 to 1) for clean metals, but may be lower in ceramic systems (10^{-2} to 10^{-1}), especially if bonding states in the solid and gas phase are quite different. (Nitrogen in N_2 and galium nitride is an example.) An upper bound on the evaporation can be obtained by assuming $\alpha = 1$.

There are also many other mechanisms which may lead to material loss by volatility. For example, either reducing or oxidizing atmospheres may accelerate volatilization. However, the only candidate from the materials selected on the basis of melting point and density that is eliminated because of volatility is magnesium oxide, although aluminum oxide may lose excessive weight under highly reducing conditions.

C. Modulus and Strength

High melting point implies strong attractive bonds between atoms in the solid, and this would generally result in high modulus also. It has been mentioned previously that even room temperature moduli of these materials are frequently not known, much less elevated temperature moduli. A good theoretical method for calculating modulus, especially as a function of temperature, would be highly desirable. Surprisingly, there is relatively little literature dealing with modulus near the melting point of the material. Fortunately, for the high melting materials with low density the specific moduli are known and are desirably high.

These high moduli would also result in high strengths if the materials were perfect. The high strengths that can be achieved in these materials in fiber form, mean that strength is generally not a limiting factor.

D. Creep and Stress Rupture

High temperature creep and stress-rupture are the mechanical properties of greatest concern. Various equations for the different mechanisms for creep can be com-

bined to generate an Ashby deformation map. The equations
have the general form:

$$\dot{\varepsilon} = \frac{\alpha D G^a b^b}{kTd^d} s^c$$

where $\alpha, a.b, c, d$ = constants

   D = diffusion coefficient

   b = Burgers vector

   s = stress

   d = grain size.

Hence, to minimize creep, the material should be a single
crystal, oriented in the proper crystallographic direction,
with a complex crystal structure (large Burgers vector),
and low diffusion coefficient. Practically, this means
that creep will occur in simple crystal structures as low
as a homologous temperature of 0.45 or as high as 0.85 in
ordered complex crystal structures such as the intermetal-
lic compounds. For the simple crystal structures, it can
be estimated that the diffusion coefficient for the slower
diffusing species must be less than 10^{-10} cm/s to have an
acceptably low creep rate. As might be expected for meas-
urements made at high temperatures on materials of variable
stoichiometry, there is scatter in results. However, dif-
fusion parameters for the more attractive materials are
presented in Table I. All of these materials appear to
meet the diffusion criteria. However, only graphite has
acceptable creep resistance at 2200C if the samples are
polycrystalline. At lower temperatures, silicon carbide
and titanium diboride appear attractive. An oxide rein-
forcement would be desirable if one existed with sufficient-
ly low creep. Berylia appears to be inadequate, but sap-
phire, grown in the "c" axis direction, and stressed paral-
el to the "c" axis is sufficiently creep resistant to be
attractive for reinforcement. The difficulty will be to
keep the off fiber-axis stresses in the composite suffi-
ciently low to prevent the easy creep on the other crystal-
lographic planes from occurring.

     Thoria might have the desired high temperature
mechanical properties. Estimates of the diffusion coeffi-
cient indicate that creep would be sufficiently low and
stress-rupture life satisfactory with pure thoria at 2000C.
Thoria has not been made in filament form, but presumably
could be made by sol-gel or by processing a thorium salt
loaded rayon fiber. Short time strengths might be signifi-
cantly higher than bulk thoria artifacts. High CTE would
be a problem.

TABLE I: SELF-DIFFUSION PARAMETERS

System	D_0(cm/s)	Q(kcal/mole)	D_{2200}(cm/s)
$ZrC_{0.85}$-C	56	124	6.1E-10
ZrC-Zr	6.7E5	162	3.2E- 9
$HfC_{0.97}$-C	63	130	2.0E-10
HfC-Hf	1.5E8	183	9.9E- 9
NbC-C	0.5	102(73)	4.8E-10(1.8E-7)
NbC-Nb	1.2	107	4.2E-10
$TaC_{0.98}$-C	3.9(0.08)	119(64)	1.2E-10(1.8E-7)
TaC-Ta	25	122	4.1E-10
C	1.4E-8	71	7.4E-15
W	15.3	149.6	9.1E-13
ThO_2-O	5.7E-2	49.9	2.2E- 6
ThO_2-Th	0.35	149.5	2.1E-14

All the remaining potential reinforcements would have to be protected from oxidation. Only carbon, tungsten and silicon carbide are available in fiber form, although the other carbides could be presumably formed by reaction with carbon fibers or by chemical vapor deposition. Carbon fiber microstructure is stable at 2200C provided it has previously been heat-treated at 2200C or higher. Feldman has measured the high temperature creep of several types of carbon fibers. For a low modulus carbon fiber (WCA) made from rayon, the experimental rates followed the general creep equation:

$$\dot{\varepsilon} = A \sigma n_e - \Delta E/RT$$

where ΔE = 108 kcal/mole

n = 3.2 at 2200C but 1.9 at 2400C.

The creep rate is not directly quoted for WCA fiber but likely can be inferred as $\sim 10^{-9}$/sec at 2200C. A pitch fiber (UCC P-55) was observed to have a lower activation energy of 66 kcal/mole, but no creep data was published. Some first-stage creep and structural changes occur in carbons when they are heated above their maximum heat treatment temperature. The low activation energy for P-55 fibers may be associated with transient creep when the fiber is heated above its heat treatment temperature ($T \sim 2200C$). Although diffusion studies in graphite are complicated by

anisotropy, self diffusion in graphite is very low at 2200 C, which is consistent with the creep measurements regardless of what model is used.

Pure tungsten has a stress-rupture life of minutes at 2200C with a 60 MPa load. However, tungsten alloys with high rhenium content (20-30%) have five times the yield strength of pure tungsten at 2200C. Tungsten which has been dispersion hardened with thoria produces higher tensile strengths, and the best properties have been obtained with tungsten/rhenium alloys dispersion hardened with hafnium carbide. Similar improved alloys may prove adequate for short time applications.

The pure and mixed carbides of hafnium, niobium, tantalum and zirconium are the last group to be considered for reinforcements. They have simple crystal structures and soften at surprisingly low temperatures. The diffusion rates of all the carbides at 2200C are high enough that creep and stress-rupture would be problems assuming a 10 μ grain size. A 10 μ grain size is larger than desired for high strength fiber unless single crystal whiskers could be made, and a smaller grain size would aggravate the creep. Yield strengths for $NbC_{0.95}$ and $TiC_{0.75}$ are about 130 MPa at 2200C, with unspecified microstructure. The carbides generally are carbon deficient. Making carbides that are close to stoichiometry might decrease creep. However, carbon often precipitates at the grain boundaries on cool down, which would drastically reduce the strength.

Creep of course depends on grain size and purity. Most fibers that have been developed have a fine grain size or even amorphous structure so as to obtain high strength at room temperature. The fine grain size leads to enhanced creep and microstructural instability at high temperature. In the future, single crystal reinforcements, fibers with elongated grain structures, and controlled preferred orientation of the crystals in the fiber will probably have to be developed to achieve improved creep resistance. Some progress has been made. For example, the preferred orientation of the crystallities in silicon carbide filament, made by chemical vapor deposition, minimizes creep.

Phase purity is a major problem with at least two of the better potential reinforcing materials: silicon carbide and titanium diboride. The silicon/carbon phase diagram shows that silicon carbide is a line compound. Hence, unless one controls the deposition conditions extremely well when using chemical vapor deposition for producing silicon carbide filament, either excess carbon or silicon will codeposit. Excess carbon deposits as graphite at the grain boundaries of the silicon carbide crystals and an

extremely low strength fiber results. Therefore, manufacturers have selected conditions that give a silicon excess, which produces a high, room temperature strength. The high temperature properties are compromised, of course, by the presence of free silicon which can melt. The potential exists for producing silicon carbide filament with much improved creep resistance ($<10^{-9}$/sec at 1500C). The case with titanium diboride is similar in that titanium diboride has a limited solubility range and the adjacent compounds (B, Ti_3B_4) both melt at much lower temperatures.

Stress-rupture lives are much more difficult to predict because failure is likely to occur at a local flaw. However, the Charles model can be used to estimate diffusion controlled stress-rupture of polycrystalline materials. The Charles equation is:

$$e^{-RN} \left[\frac{N^3}{R} + \frac{3N^2}{R^2} + \frac{6N}{R^3} + \frac{6}{R^4} \right]$$

$$\approx 8D_s(\beta\sigma_{max})^4 \left(e^{-\frac{\beta\gamma/\zeta}{\zeta^2}} \right) t_f$$

where

$$R = \frac{\sigma_a}{\sigma_{max}}$$

σ_a = applied stress

σ_{max} = short time failure stress

$N = \beta\sigma_{th}$

$$\beta = \left(\frac{\partial \Delta G/RT}{\partial \sigma} \right)_T$$

σ_{th} = theoretical strength

D_s = Diffusion constant = $D_o e^{-\frac{\Delta H}{kT}}$

$\gamma = \gamma_{sv}$ surface energy

ζ = radius of crack tip.

For order of magnitude estimation, the slope parameter $N \approx \sigma_{th} V^*/kT$, where V^* is the activated volume. The theoretical strength may be estimated as $\sim 0.15E$, $V^*/T \sim (0.5\Omega)/(TM/2)$ $\sim \Omega/Tm$, and $\partial N/\partial T \sim \partial \sigma_{th}/\partial T \sim \partial E/\partial T$, where Tm is the melting point of the material, Ω is the atomic volume of the diffusing species, and E is the Young's modulus. Since in

both the stress rupture model and creep equations the dif-
fusion coefficient is a major factor, the same materials
appear to give the best performance.

In summary, creep and stress rupture are probably
the most restrictive limitations for selection of reinforce-
ment materials. For temperatures of 1500C, the list con-
sists of carbon, boron nitride, tungsten, silicon carbide,
and perhaps titanium diboride or sapphire.

E. Coefficient of Thermal Expansion

The coefficient of thermal expansion for the fiber,
matrix and oxidation protective coatings must be reasonably
matched ($|\Delta CTE| \sim 2 \times 10^{-6}/°C$) to prevent thermomechanical
damage upon processing or during the composite's lifetime.
The very low CTE of carbon fibers ($1-2 \times 10^{-6}/°C$ to 1000C)
parallel to the fiber axis, but moderate ($8 \times 10^{-6}/°C$) normal
to the fiber axis limits their use to low CTE matrices.
Conversely, the high CTE's ($>10 \times 10^{-6}/°C$) of some potential
intermetallic matrices require reinforcements such as
sapphire ($10 \times 10^{-6}/°C$) or perhaps TiB_2($7 \times 10^{-6}/°C$).

F. Chemical Compatibility

Chemical compatibility is generally estimated from
thermodynamic calculations. Normally, it is assumed that
the pair of materials selected for fiber and matrix are
satisfactory if they are thermodynamically stable or ther-
modynamically unstable but with slow kinetics. In reality,
even material systems that are thermodynamically stable can
be unsatisfactory. For example, both hafnium and titanium
diboride are thermodynamically stable with respect to nick-
el. Hence, the volume fractions in compacts of either haf-
nium diboride or titanium diboride in nickel were invari-
ant when the compacts were heat treated at high tempera-
ture. The grain size, however, coarsened substantially
with hafnium diboride, but not with titanium diboride.
Therefore, while hafnium diboride is thermodynamically
stable with nickel, it is not suitable as a reinforcement.

II. Conclusions

There is only one fiber reinforcement which is ade-
quate for short time air or inert atmosphere at 2200C: car-
bon. Operation in an oxidizing atmosphere but at tempera-
tures of 1500C or slightly above make silicon carbide the
material of choice. Decreasing the operating temperature
to 1450C for an oxidizing atmosphere may make "c" axis
single crystal sapphire or titanium diboride attractive.
In summary, while it would first appear that many materi-
als might be suitable for high temperature reinforcement,
the many simultaneous requirements limit the number to a

surprisingly few. Hopefully, some new materials will be identified which can be added to our present short list of fiber reinforcements.

CARBON FIBER MANUFACTURING

D. D. Edie and R. J. Diefendorf

Center for Advanced Engineering Fibers

Clemson University, Clemson, South Carolina 29634-0909, USA

INTRODUCTION

The high strength, superior stiffness and light weight of carbon fibers have made them the dominant reinforcing fiber used in high performance polymer matrix composites. However, brittle materials, such as ceramics and carbon, can be reinforced by the same fibers, creating a unique class of high temperature composite materials. When properly protected from oxidation, these carbon fiber / carbon matrix composites can withstand extended exposure to temperatures of up to 2500°C, making them attractive for many aerospace applications. In addition, because of their improved friction performance and high wear resistance, carbon/carbon materials are used in the high performance brakes of aircraft as well as racing cars, and the use of these carbon/carbon brakes in passenger cars and trucks is currently being evaluated.

At present, all commercial carbon fibers are produced by the thermal decomposition of various organic fiber precursors. By far the most popular precursor materials are fibers of polyacrylonitrile (PAN), cellulose (Rayon) and pitch (1). A proposed alternate process, which produces a discontinuous, high performance carbon fiber, is CVD vapor growth. This chapter will describe the similarities of these four fiber processes as well as discuss their differences.

MANUFACTURE OF PAN-BASED CARBON FIBERS

Today, approximately 90% of all commercially-produced carbon fibers are produced from a polyacrylonitrile (PAN) precursor fiber. Normally, polyacrylonitrile is copolymerized with a small amount of another monomer,

The rate at which the solvent is extracted from the polymer as it passes through the coagulation bath governs the final cross-sectional shape of the fiber. Thus, the temperature, concentration and circulation rate of the fluid in the coagulation bath all can effect the structure of a wet spun fiber. Rapid extraction of the solvent during coagulation allows the outer portion of the fiber to solidify before the solvent can diffuse out of the center of the fiber. The large concentration gradient across the fiber cross section makes the initial density of the center portion of a rapidly formed wet spun fiber much less than that of the fiber skin. As the solvent eventually diffuses out of the center of the fiber, the density of the inner portion of the fiber increases, causing the skin of the fiber to collapse and yielding a kidney bean (or dog-bone shape) fiber. However, PAN precursor fibers with a circular cross section and a minimum of internal voids can be produced by wet spinning if the rate of solvent extraction is properly controlled.

In another variation of solution spinning, the polymer solution is extruded into a hot gas environment. In this case, the temperature and composition of the gas must be carefully controlled to control the rate of solvent evaporation and, thus, control the fiber's structure. This process variation, called *dry spinning*, tends to produce an as-spun fiber with dog-bone shaped cross section.

Often, both wet and dry spun fibers are washed after fiber formation to remove the final traces of solvent. Then the fibers are passed through one or two stages where they are stretched to further align the polymer molecules parallel to the fiber axis. Finally, this fully-drawn PAN precursor fiber is dried and packaged.

treatment requirements. In addition, since the polymer content of the plasticized PAN is much higher than that of the solutions used in wet or dry spinning, coalescence during fiber formation is simplified. Thus, the cross-sectional structure of fibers formed by melt-assisted spinning should be more uniform.

Heat Treatment of PAN Precursor Fibers

Oxidation of PAN Precursor Fibers. The molecular orientation produced as the PAN precursor is drawn and stretched must be locked into place if the final mechanical properties of the carbon fiber are to be maximized. Commercially, this is accomplished by heating the PAN precursor fiber in air under tension at 220 to 270°C for a period which can vary from 30 minutes to as much as 7 hours (4). The exact temperature and time required for this thermosetting process depends upon the exact composition and diameter of the PAN precursor fiber. The primary reactions which occur during this step, called oxidation, are cyclization of the nitrile groups, the dehydration of saturated carbon-carbon bonds and, of course, oxidation. These reactions convert the PAN molecules into an infusible cyclized network of hexagonal carbon-nitrogen rings. Although many structures result, Figure 4 summarizes the functional groups most often observed.

Insert figure 4 about here

Commercially, the oxidation step is carried out in large furnaces such as that shown in Figure 5. Drive rolls are used to slowly pull the PAN precursor fiber through the oven under a controlled tension. If tension were not applied during the thermoset process, the polymer would relax to a

1000°C only smaller molecules, such as H_2 and N_2, are given off. Thus, carbonization is often conducted in two steps: precarbonization (heat treatment up to 1100°C) and carbonization (heat treatment at temperatures ranging from 1600 to 1800°C. Even though the carbon content of PAN is 54%, carbon loss during the heat treatment steps make the overall yield for converting PAN precursor fiber to carbon fiber about 40-45% (7).

It is the final heat treatment temperature, along with the degree of molecular orientation of the molecules in the thermoset precursor fiber, which govern the modulus of the final carbon fiber product. Like all brittle materials, the strength of the final carbon fiber is limited by flaws in its structure. Thus, the final carbon fiber strength can be influenced by the purity in the precursor fiber, the final carbonization conditions, and even the void content of the precursor fiber.

After final heat treatment, most PAN-based carbon fibers are given a surface treatment to improve their bonding with polymeric matrix materials. Although surface treatment results in some roughening of the surface, its primary effect is to increase the concentration of oxygenated groups on the fiber surface. This can be accomplished by various techniques, such as exposing the carbon fiber to gases (such as air or carbon dioxide) at elevated temperatures, submerging the fiber in sodium hyporchlorite or nitric acid solutions, or electrolytically etching the fiber. The principal goal of this process step is to increase the interfacial bond strength between the fiber and the matrix material and, thus, improve the interlaminar shear strength of the composite.

After being surface treated, a small amount of size (about 1% by weight) is added to improve the carbon fiber's wetability. Normally this

significantly improves its carbon yield, the cellulose precursor fiber is oxidized by heating it in air to temperatures as high as 400°C. Initially, as the fiber is heated, the physically adsorbed water is desorbed. As heating continues, additional water is evolved due to the reaction of hydroxyl groups in the cellulose. Finally, as the cellulose begins to decompose, CO_2, CO and water are given off and aromatization of the structure begins (7, 8). Because the cellulose polymer decomposes as it is stabilized, prestretching or stabilizing under tension (useful for PAN precursor fibers) is ineffective (9).

After being stabilized, cellulose precursor fibers are carbonized and graphitized in an inert atmosphere at temperatures similar to those used for PAN. However, since the cellulose molecules in the precursor fiber lose most of their axial orientation during pyrolysis, the fibers are strained at high temperature to increase the preferred orientation and improve the final mechanical properties. The filaments are quite plastic at high temperatures and can be stretched as much as 150%. When stretched 100% during graphitization at 2800°C, fibers with a modulus approaching 720 GPa can be formed (9). However, if the same fibers are graphitized at the same temperature, but not stretched, they attain a modulus of only 72 GPa.

The overall yield for converting the cellulose precursor fiber to carbon fiber ranges from 10 to 30%, compared to 40-45% for PAN precursor. This low yield is the direct result of the low carbon content of cellulose (44%) and the extensive decomposition which occurs during stabilization. This low conversion, especially when coupled with the expense of the stretch-graphitization, accounts for high cost of rayon-based carbon fibers.

the isotropic pitch. The solvent insoluble portion can be converted to an anisotropic pitch by heating to between 230 and 400°C for less than 10 minutes (12). The anisotropic, or oriented, phase is composed of stacked polynuclear aromatic hydrocarbon molecules. These molecules tend to be disc-like in shape with an average molecular weight of about 1000 (although the molecular weight can vary considerably). The molecular structure of the mesophase produced from coal-tar pitch is characterized by higher aromaticity, whereas petroleum-derived mesophase has a more open structure caused by its higher content of aliphatic side chains (13). Figure 8 shows the structure of a typical mesophase molecule. Initially, small spheres of mesophase form in the isotropic pitch when heated for a adequate time at a sufficiently high temperature. Upon further heating the concentration of mesophase spheres increases, causing them to collide and coalesce, creating a mosaic-like nematic liquid crystal structure (14).

Insert figure 8 about here

Mesophase products which have a high average molecular weight and no side groups or small molecular components to cause disordering often decompose before becoming fluid enough to flow. Because of this, the mesophase used to melt spin fibers is normally a mixture of high molecular weight molecules which still have a small number of side groups. Therefore, commercial mesophase precursors have certain characteristics of both mixtures and solutions: they soften over a range of temperatures and orient under an applied stress.

Numerous studies of mesophase pitches have found that, in general, their flow behavior is shear thinning at low shear rates but approaches

Because of the extreme temperature dependency of mesophase, fiber diameters can vary widely if the spinnerette temperature is not accurately controlled. Edie and Dunham showed that only a ±3.5°C variation in temperature across the face of the spinnerette can result in a ±15% variation in the diameter of the as-spun fibers (15). Their analysis also indicated that, even when process conditions during spinning are controlled, the tensile stress in the mesophase filament is nearly one-half of its ultimate strength.

Heat Treatment of Mesophase Precursor Fibers

Oxidation of Mesophase Precursor Fibers. After spinning, the pitch-based fiber must be thermoset, in a manner similar to the PAN process, in order to render it infusible. The exact temperature and time required depends on the chemical composition and diameter of the mesophase fiber. The temperature must be below the softening point of the mesophase in order to minimize any fiber-to-fiber sticking. However, higher temperatures increase the rate of the stabilization reactions, decreasing the time required for this step. Commercially, the temperature selected for stabilization is a compromise between minimizing the required time for this process step and maximizing the mechanical properties of the final carbon fiber. Typically, the as-spun mesophase fibers are heated to temperatures of approximately 300°C for a period ranging from 30 minutes to 2 hours to be adequately stabilized for final heat treatment. Since the as-spun mesophase fiber already possesses a high degree of molecular orientation, applying tension during stabilization is unnecessary.

are CH_4 and H_2. Like PAN precursor fibers, most of these gases are evolved below 1000°C. Thus, normally the stabilized mesophase fibers also are pre-carbonized for a few minutes at 900 to 1000°C. After precarbonization, they are carbonized or graphitized at the desired temperature. Here again, hydrogen is the principal gas evolved above 1000°C. While still not extremely strong, after oxidation the mesophase fiber can handled if the tow is sufficiently large. Thus, the ovens used to carbonize and graphitize mesophase fibers are similar to those used to process PAN precursor fibers.

The process used to surface treat and size mesophase pitch-based carbon fibers is similar to that employed for PAN-based fibers. However, since pitch-based fibers are less reactive to surface oxidation, more severe reaction conditions are employed during surface treatment.

Insert figure 11 about here

Isotropic Pitch-Based Carbon Fibers

Currently, a variety of carbon fibers is produced from isotropic pitch. However, unless these fibers undergo an expensive and difficult final stretch-graphitization step, their modulus is an order of magnitude less than that of mesophase pitch-based fibers. While they are useful for applications such as filtration, asbestos replacement and static dissipation, the poor mechanical properties of isotropic pitch-based carbon fibers limit them to non-structural applications. Therefore, the manufacturing of isotropic pitch-based carbon fibers not been included in this chapter, and the reader is referred to a review by Edie (15) for a detailed discussion of this process.

filaments makes them a potential carcinogen. Since pyrocarbon deposits with the basal planes parallel to the fiber surface, the fiber is highly oriented and has a high modulus. Figure 12 shows a schematic of this catalyst-induced growth of carbon fibers (19).

Insert figure 12 about here

Tibbetts and coworkers at General Motors used this growth technique to produce filaments with lengths of up to 30 cm in an atmosphere of methane and hydrogen (19). Several metals, including nickel, cobalt, iron-nickel powder, and Fe(NO$_3$)$_3$, have been employed as catalysts (19, 20, 21). Even though the feed stock (methane and hydrogen) was inexpensive and process temperatures of only 1000°C were employed, the batch nature of this process used for early studies made it uneconomical for commercialization.

To overcome the low productivity of the batch process, Koyama and Endo (22) recently patented a continuous method for producing vapor-grown fibers. In their process the catalyst particles are either incorporated in the feedstock or produced in the reactor by the decomposition of a organometallic. A simple schematic of the process is shown in Figure 13. The catalyst and hydrocarbon feed are introduced at the top of the heated reactor, and short fibers are continuously withdrawn from the bottom. Fiber lengthening and thickening can be continuously controlled by adjusting the carbon potential of the gas within the reactor. The technique, which could be considered fluidized catalytic growth, allows carbon filaments with varying length, diameter and physical properties to be continuously produced. If the thickening step can be accurately controlled and the

manufacturer are, normally, the result of changes in this temperature.

Insert figure 14 about here

The more perfect graphitic structure of mesophase pitch-based carbon fibers, compared to PAN-based carbon fiber accounts for their higher thermal conductivity. In fact, mesophase pitch-based fibers recently developed by Amoco Performance Products, Inc. exhibit a thermal conductivity which is three times that of copper.

SUMMARY

The precursor fibers used to produce current commercial carbon fibers are produced by melt, melt-assisted and solution spinning. Since it eliminates the problems of solvent recovery and produces a purer precursor fiber, melt spinning normally is the preferred fiber formation process. However, conventional melt spinning can not be used for polymers, such as PAN and cellulose, which degrade below their melt temperature. Nevertheless, melt-assisted spinning, a new process, permits PAN to be spun as a pseudo-melt. PAN-based and rayon-based precursor fibers are thermoset, carbonized and graphitized in similar equipment and at similar conditions. By comparison, its weak tensile strength prior to final heat treatment makes pitch-based carbon fibers much more difficult to handle. Because of this, special oxidation ovens are often employed for this product. Short vapor-grown carbon fibers represent the latest entry to the high performance fiber field. If health issues can be adequately addressed, some feel that these discontinuous filaments could become a truly low-cost reinforcement for composites.

REFERENCES

1. Diefendorf, R. J. and Tokarsky, E., High-Performance Carbon Fibers, _Polymer Engineering and Science_, Vol. 15, No. 3, pp 150-159 (1975)

2. Ram, M. J. and Riggs, J. P., U.S. Patent 3,657,409, April, 1972; *Process for the Production of Acrylic Filaments* assigned to Celanese Corporation.

3. Daumit, G. P. and Ko, Y. S., in: _High Tech - the Way into the Nineties_ (K. Brunsch, H. D. Golden and C. M. Herkert, eds.) pp 201-213, Elsevier Science Publishers B. V., Amsterdam (1986)

4. Delmonte, J., _Technology of Carbon and Graphite Fiber Composites_, van Nostrand Reinhold Company, New York, 1981.

5. Clark, A. J. and J. E. Bailey, _Nature_, Vol. 243, p 146 (1973)

6. Thorne, D. J., in: _Handbook of Composites. Vol. 1 - Strong Fibers_ (W. Watt and B. V. Perov, eds.) pp 475-494, Elsevier Science Publishers B. V., Amsterdam (1985) *Manufacture of Carbon Fibre from PAN*

7. Riggs, D. M., Shuford, R. J. and Lewis, R. W., in: _Handbook of Composites_ (G. Lubin, ed.) pp 196-271, Van Nostrand Reinhold Co., New York (1982)

8. Fitzer, E., in: _Carbon Fibers, Filaments and Composites_ (J. Figueiredo et al., eds.) pp 3-41, Kluwer Academic Publishers, Boston (1990). *Carbon Fibers: Present State + Future Expectations* *C. A. Bernardo, R. T. K. Baker, K. J. Hüttinger*

9. Bacon, R., in: _Chemistry and Physics of Carbon_ (P. L. Walker and P. A. Thrower, eds.) Vol. 9, p 2, Marcel-Dekker, Inc., New York (1973) *CARBON FIBERS FROM RAYON PRECURSORS*

10. Singer, L. S., U.S. Patent 4,005,183, January, 1977; assigned to Union Carbide Corporation *High Modulus, High Strength Carbon Fibre Produced from Mesophase Pitch,*

11. Singer, L. S. and Lewis, I. C., _Carbon_, Vol. 16, p 417 (1978)

12. Riggs, D. and R. J. Diefendorf, U.S. Patent 4,208,267, June, 1980; *FORMING OPTICALLY ANISOTROPIC PITCHES* assigned to Exxon Corporation

13. Fitzer, E., Kompalik, D., and Mayer, B., Influence of Additives on Pyrolysis of Mesophase Pitch, _Carbon '86_, Proceedings of the International Conference on Carbon, Baden-Baden, FRG, p 842 (1986). *DEUTSCHEN KERAMISCHEN GESELLSHAFT, BAD HONNEF*

LIST OF FIGURES

Figure 2

O_2, ~220-280°C

Polyacrylonitrile

$+ \ HCN + CO_2 + H_2O$

Figure 4

Oxidized PAN Supply Creel

Tension Control

Exhaust Gases

N_2

N_2

Carbon Fiber Wind-up

~800 - 1000°C

~1100 1700°C

Carbonization Furnace

Surface Treatment

Figure 6

Molecular Weight = 1178

C / H = 1.50

H_{arom} / H_{aliph} = 1.30

C_{arom} / C_{aliph} = 6.15

Figure 8
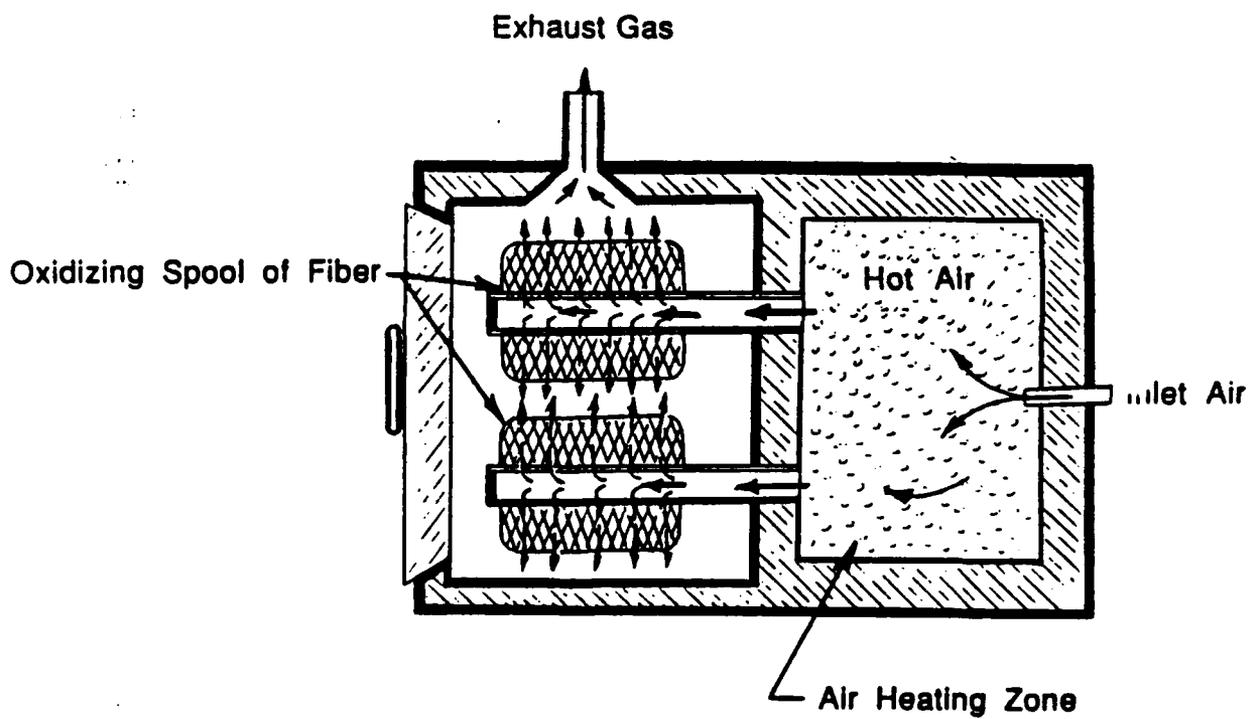
Figure 10

Catalyst
Particles

Filaments
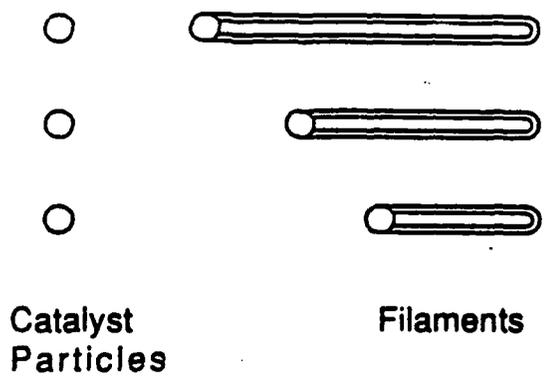
(a) Fiber Growth Stage
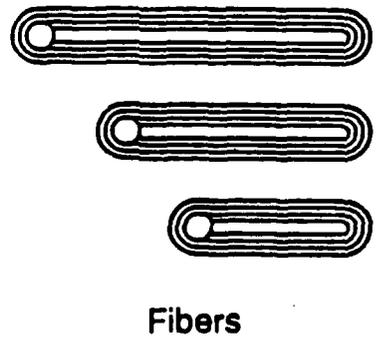
Fibers

(b) Fiber Thickening Stage

Figure 12
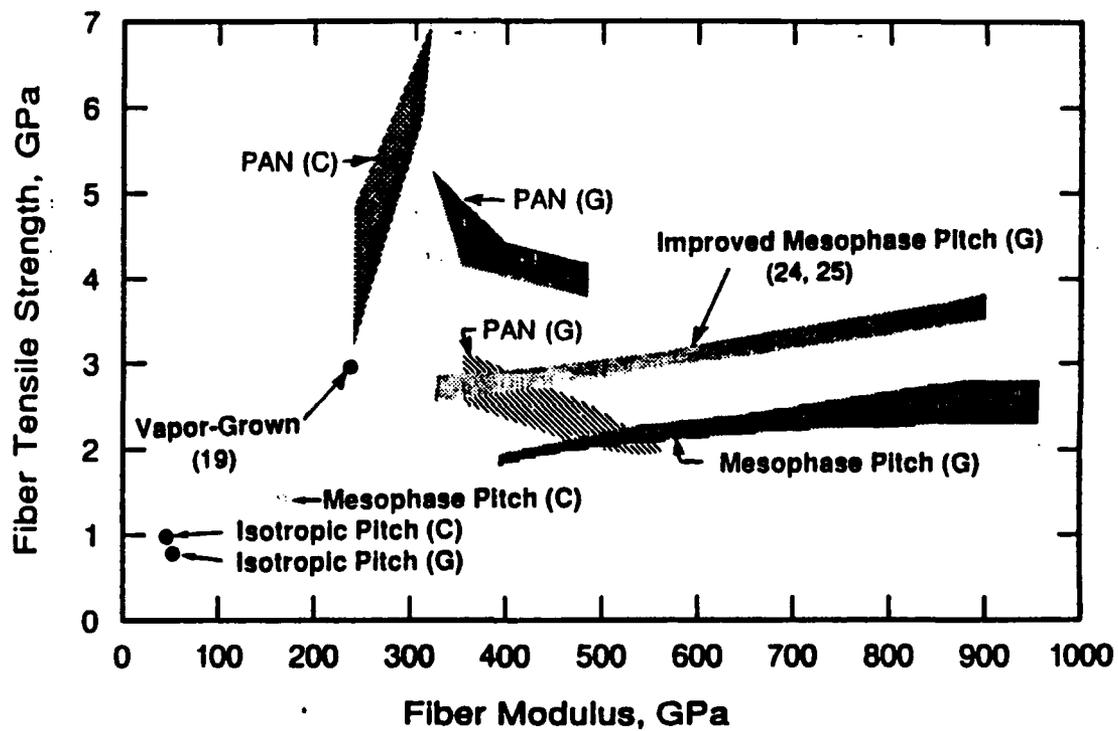
Figure 14

MODULUS OF MESOPHASE PITCH CARBON FIBERS

D. A. Kurtz*, G. D. D'Abate**, S. S. Tzeng and R. J. Diefendorf
Department of Ceramic Engineering
Clemson University
Clemson, South Carolina 29634-0907, U.S.A.

ABSTRACT

The modulus and axial preferred orientation of mesophase pitch fibers, in the
as-spun condition, were determined for a variety of spinning conditions.
Similar measurements were made after thermally annealing, oxidatively thermo-
setting, carbonizing, and heat treating the as-spun mesophase pitch fibers.
The relationship between the modulus and preferred orientation was analyzed
in terms of the elastic constants of graphite and a single disposable con-
stant. The magnitude of this constant determines the effective coupling
between the graphitic basal planes. This has direct consequences on proper-
ties, particularly compressive strength.

1. INTRODUTION

The production of high performance carbon fiber from mesophase pitches is of
commercial interest for use in fiber reinforced composites. Final fiber prop-
erties are highly dependent on the ability to axially orient the disc-shaped
mesophase pitch molecules in the precursor fiber. Past efforts to improve
axial molecular orientation often have concentrated on modifying the chemi-
cal composition of the precursor pitch. The subject of this paper deals pri-
marily with observing changes in axial preferred orientation (of the fiber)
and mechanical properties after melt spinning, annealing, stabilization (ther-
mosetting) and carbonization/graphitization.

2. EXPERIMENTAL

These studies were performed with a mesophase pitch made from the solvent
insoluble fraction of a heat treated cut of a catalytic cracker effluent.
This distillation cut, from 454C to 566C, was heat treated at 420C. The heat
treatment time was just short enough to prevent the first visible formation
of mesophase spheres. Then, the highest molecular weight species were removed
by precipitation with an addition of a small amount of an "antisolvent", tolu-
ene, so as to improve the rheology of the pitch for spinning. These insolu-
bles were filtered out of the pitch and a second precipitation with 80% tolu-

*ATM Inc., 520B Danbury Road, New Milford, Connecticut 06776, U.S.A.
**Michelin America's Research and Development Corp., Michelin Road, Green-
ville, South Carolina 29605, U.S.A.

ene/20% heptane antisolvent was performed and filtered to produce the insoluble mesophase pitch fraction used in these studies.

Melt spinning was performed under a variety of mass flow rates, temperatures, spinneret nozzle diameter and aspect ratios, and take-up rates. These fibers were annealed for various times up to seven hours at temperatures over the range 180C to 290C and then stabilized in air at 225C, 260C or 290C to thermo-set the fibers. The fibers were carbonized to 1000C or 1500C and then heat treated to temperatures as high as 2400C in argon.

The preferred orientation of the polynuclear aromatic rings or carbon basal planes with respect to the fiber axis was determined by x-ray diffraction using copper K_α radiation. A bundle of fibers was used to increase signal to noise ratio, and a drop of a wetting liquid was placed on the bundle, and allowed to dry to improve fiber collimation. The misorientation of fibers in the fiber bundle was generally, but not always, small enough to have negligible effect on the preferred orientations. Fiber misorientation was estimated by image analysis. Together with machine broadening and strain/crystallite broadening, variance subtraction was used to correct the observed half width:

$$S_o^2 = S_M^2 + S_C^2 + S_B^2 + S_F^2$$

where

S_o = observed peak half-width at half maximum intensity

S_M = machine broadening for preferred orientation

S_C = broadening due to crystallite size and strain

S_B = basal plane misorientation broadening within fiber

S_F = fiber-to-fiber misorientation broadening.

Generally, the corrections needed to obtain the basal plane orientation within the fibers were small compared to the experimental differences observed caused by processing. The interlayer spacing was estimated from the 002 diffraction line after correction for background and Lorentz polarization. Crystallite size was calculated from the Sherrer formula after using variance subtraction to correct for machine broadening.

Mechanical properties were measured on the various fibers. Single fiber laser diffraction, using scattering theory for analysis, was employed to determine fiber cross-sectional area. Early measurements relied on visual determination of diffraction minima. Later measurements were made using a 3456 element charge coupled device interfacing with a data acquisition board on an IBM AT computer. While fibers spun at high elongation rates were nearly circular, others were sufficiently non-circular that five "diameter" readings were made at 36° intervals, and the cross-section was calculated using a polygon approximation. An odd number of diameter measurements was made to eliminate problems with fibers which have nearly elliptical, two-fold symmetrical cross-sections. Five measurements were found to give an acceptably low error for the fibers measured. If all five diameter values fell within the scatter of the measurements, then a simple average was taken of the diameters, and the cross-section was calculated on the basis of a circle.

Carbon fibers many times have a non-linear stress/strain curve. Hence, the modulus of the fiber depends on the stress (or strain). The moduli are quoted for the initial part of the stress-strain curve, but the data acquisition also

159

allows for a second modulus to be measured at higher stresses over a range
specified by the tester. Average modulus over the whole stress range is also
calculated. Strain was not measured directly, but derived from cross-head
displacement and machine compliance (mostly caused by the load cell and fiber
grips). The normal assumption that the value for machine compliance is inde-
pendent of fiber type was found not to be true. However, the compliance
corrections to the modulus were small except for the carbon fibers heat
treated to above 2000C.

3. RESULTS AND DISCUSSION

3.1 Melt Spinning

The effect of some primary melt spinning parameters (V_L, W, d_o, T_o, m) on
molecular orientation was determined (Figure 1). Fiber take-up speed, V_L, was
varied from 91m/sec to 455m/sec with all other conditions remaining constant.
The increase in draw rate with increasing take-up winder speed was expected
to increase the as-spun preferred orienta-tion. However, in the case of this
particular mesophase pitch and spinning conditions, the opposite behavior is
observed (Figure 2). As the winding speed is increased, the preferred orien-
tation and stack height (Figure 3) decrease slightly. At least two explana-
tions are possible: 1) the increased density of disclinations which occur at
higher drawing rates, and/or, 2) the more rapid quenching of the fiber at
higher drawing rates freezes in the poorer orientation which is present at the
spinning temperature. The decrease in orientation with increasing temperature
is indicated in Figure 4 which shows hot stage measurements of optical activi-
ty versus temperature. Drawing, which occurs below the spinneret appears to
affect orientation by affecting the quench rate. The axial orientation of the
pitch has already occurred by the time it exits the spinneret.

Four groups of fiber were spun under different mass throughputs and draw
ratios (Table I). The purpose was to estimate the effects of capillary shear
rate and draw rate. If the preferred orientation and crystallite stack height
are plotted as a function of final fiber diameter, a similar trend is observed
as was noted with winding speed.

The modulus of the fibers made at various winding speeds was found to be con-
stant at 4.0GPA. This low value indicates that the modulus is determined

TABLE I
Spinning Parameters for T = 380C

	Group I	Group II	Group III	Group IV
Die Size (μm)	200	397	397	1588
Draw Ratio	17	8.6	20.3	26.8
Extrusion Pressure, (absolute) MPA	1.47	.17	.14	.10
Avg. Diameter, (μm)	12.0	46.0	19.6	59.2

mainly by molecule to molecule interactions rather than the stiffness of the
molecules themselves. This may explain why the increase in axial orientation
with decreased winding speed does not produce a change in modulus. The
strength of the fiber decreased with increasing diameter which was consistent

with its brittle fracture characteristic. Strength was 38MPA for 10μm diameter fibers and decreased to 16MPA for 50μm diameter fibers.

3.2 Annealing of As-spun Mesophase Pitch Fibers

Although annealing may not be an intended part of fiber processing, annealing often occurs during or prior to the stabilization (oxidation) of the mesophase pitch fiber. This is especially true for larger diameter fibers which are oxidized for longer periods of time often at or above the Tg of the unoxidized pitch. The center of these fibers often has a more coalesced mesophase microstructure than the original fiber or the more rapidly thermoset outer regions of the fiber. The annealing runs were performed over the temperature range of 180C to 290C on 10μm fibers made at high drawing rates. Most of the increase in axial preferred orientation occurred within the first 30 minutes at the glass transition (258C) temperature or above (Figure 5), but the time increased to 60 minutes at 210C and no change was observed at 180C. The final equilibrium preferred orientation was found to be the same, for a given annealing temperature, regardless of the initial preferred orientation produced by different quench rate conditions. Lower temperatures produced a larger orientation increase (except for 180C). The annealing temperature for where there would be no improvement in axial preferred orientation is close to the spinning temperature of 380C. Hence, unless quenching and dynamic orientation effects cancel changes in the orientation of the melt, drawing does not add any dynamic orientation. These results again agree with the variable take-up rate experiments. In this respect, this mesophase pitch behaves similarly to conventional small rod-like liquid crystal systems rather than linear high molecular weight polymers, which do show dynamic ordering. Crystallite stack height increased after annealing except for the 180C anneal. Both results are what might be expected from the change in preferred orientations. The crystallite stack heights increased from about 3.1nm to a plateau of about 3.6nm after about 30 minutes when the temperature was above Tg. Below Tg, at 210C for example, there was a rapid increase of .8nm during the first half-hour, and then a more gentle increase to 4.1nm over the next 2 hours. It is surprising that the stack height continued to increase at temperatures below Tg for longer times when the preferred orientation remained constant. However, local orientation and stack height may increase without a large change in overall preferred orientation when the overall preferred orientation is not extremely high.

In summary, axial preferred orientation can be increased by annealing. This improvement would likely lead to higher modulus in the final carbon fiber, if this improvement could be maintained through subsequent processing. Yet, it is unlikely that the higher modulus could be achieved unless the thermosetting process could be carried out at low temperatures.

3.3 Stabilization

A stabilization step is required in pitch fiber processing to render the fibers infusible so that carbonization can be carried out without fusion and loss of fiber morphology. Stabilization is normally performed in the 220C-300C range using oxygen containing atmospheres. One would like to maintain or improve preferred orientation as much as possible throughout stabilization. However, preferred orientation and infusibility are not the only factors to consider. Oxygen concentration profiles through the cross-section and dimen-

sional changes also affect the final properties.

Plots of axial preferred orientation and crystallite stack height as a function of thermosetting temperature and time for 10μm, high draw rate fibers are presented in Figures 6 and 7. For long times the apparent preferred orientation and crystallite stack height is decreasing for all temperatures. However, the preferred orientation for stabilization temperatures above Tg (260C, 290C), at the point where the fibers are sufficiently infusible to process is similar (36° full width). The oxidation performed at 225C produces a somewhat higher preferred orientation at the infusibility point. Carbon fibers made from 225C stabilized precursors have slightly higher moduli than those stabilized at 260C or 290C.

Fibers, annealed for 2 hours at 210C, were subsequently stabilized at 225C and compared to the unannealed samples. Figures 8 and 9 indicate that the difference in preferred orientation and crystallite stack height can be maintained to where the fibers are infusible.

3.4 Carbonization

To see if any of the orientation differences between annealed and unannealed fibers (stabilized at 225C for 20 hours) could be carried through to the carbonized product, both groups were heat treated in an inert atmosphere to 1000C. Mechanical properties for both groups are shown in Table II. Although the annealed group has a slightly higher modulus, significance testing shows no difference in diameter, strength, modulus or strain-to-failure.

TABLE II
Effect of Annealing on Carbonized Strength and Modulus

A - Annealed 2 hours at 200C
U - Unannealed
(Both groups stabilized for 20 hours at 225C and carbonized to 1000C.)

Diameter μm		Strength GPA		Modulus GPA		Strain-to-Failure %	
A	U	A	U	A	U	A	U
9.2	10.1	1.6	1.4	173	136	1.1	1.0
10.2	9.4	2.1	2.3	143	169	1.6	1.5
11.2	10.2	2.7	2.2	177	145	1.8	1.7
9.8	10.1	2.3	1.9	171	155	1.6	1.4
10.2	10.2	1.7	2.2	160	180	1.2	1.4
Av. 10.1	10.0	2.1	2..	165	157	1.5	1.4

3.5 Heat Treatment (Graphitization)

Mesophase pitch precursor fibers that had been carbonized to 1500C were heated in argon to temperatures from 1600C to 2400C with soak times of 1 to 30 minutes. The axial preferred orientation and crystallite stack height as a function of heat treatment temperature (for 5 minutes) are shown in Figure 10. Crystallite stack height increases rapidly above 2000C due to the increased mobility of carbon atoms, but the improvement in preferred orientation decreases. Since high preferred orientation is desired simultaneously with small crystallite stack height, a cross plot of reciprocal preferred orientation versus L_c was made. Data showed little scatter for different processing cycles from a single line. Hence there was no advantage of using a longer time at a lower temperature versus a shorter time at a higher temperature. Tensile strength and modulus increased smoothly with heat treatment temperature (Figure 11). The Reynolds and Sharp model[1] was used to relate preferred

162

orientation to modulus:

$$1/E = S_{11}\cos^4\bar{\varphi} + AS_{44}\sin^2\bar{\varphi}\cos^2\bar{\varphi}$$

where S_{11}, S_{44} - compliances of single crystal graphite

$\bar{\varphi}$ - average crystallite orientation.

A is a parameter which changes the model for deformation: A = 1 for the uniform stress model, and A = 0 for the uniform strain model. Basically, A was varied to fit the experimental data. A small value for A would indicate that coupling between the basal planes inhibits shear, while A = 1 would indicate single crystal behavior. (The other terms normally in the equation are negligible for high preferred orientations.) The value of A as a function of heat treatment temperature shows a sudden increase above 2000C (Figure 12). Fracture surfaces of fibers loaded in tension changed from a mirror-hackle surface to a rougher folded radial fracture surface above 2000C. The relative importance of crystal stack height versus preferred orientation could not be ascertained.   An increased stack height might be expected to increase A. While the equation for the modulus assumes a single off-axis orientation, a fiber is more closely approximated by assuming that each off-axis orientation is balanced by an orientation of equal magnitude but opposite direction because of symmetry. Just as in an angle-ply composite laminate, this increases the modulus significantly. The goal is to make a fiber where these oppositely oriented regions are close enough together to obtain tight coupling. Not only does tight coupling increase tensile modulus, but the same tightly curved basal planes provide better compressive strengths.

4. CONCLUSIONS

Overall axial molecular orientation will depend partly on "domain" orientation and on crystallite orientation mesophase pitch fibers. The axial orientation of these domains is nearly perfect as observed under polarized light. Hence, misorientation occurs on a more molecular level. Molecular axial preferred orientation appears to be most significantly affected by molecular structure and not the process modifications studied in this research. Axial molecular orientation is easily attained in the spinneret, and the actual orientation observed in the as-spun fiber is only modified by quench rate. Annealing the as-spun mesophase pitch fiber improves axial preferred orientation, which could be maintained through stabilization. However, the modulus of carbonized fibers show no improvement due to prestabilization annealing. Finally, heat treatment of carbonized fibers improves modulus; the same heat treatment decreases the coupling between basal planes. Consequences of this are twofold: 1) a higher preferred orientation is required for a given modulus and 2) tensile and compressive strengths will be lower. Since this coupling can be of geometrical origin as well as by direct chemical bonding, tighter basal plane curvatures introduced by spinning and pitch modification can be expected to produce improved fibers.

5. REFERENCE

1. W. N. Reynolds and J. V. Sharp, Carbon, 12, 103 (1974).

163
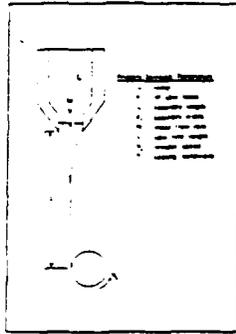
FIG. 1: Spinning parameters.
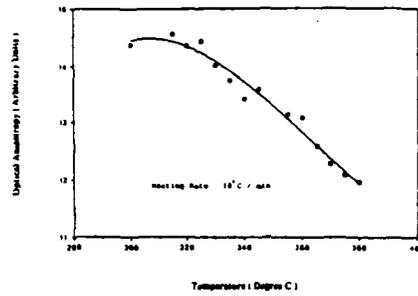
FIG. 4: Mesophase optical anisot-
ropy vs. temperature.
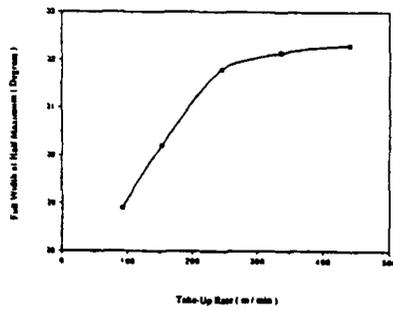
FIG. 2: Preferred orientation,
e, of as-spun mesophase
fibers vs. take-up speed.
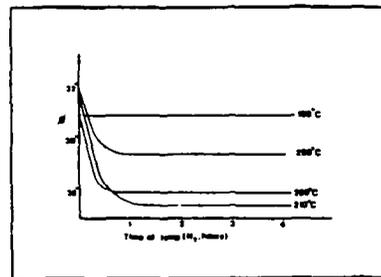
FIG. 5: Preferred orientation vs.
annealing time.
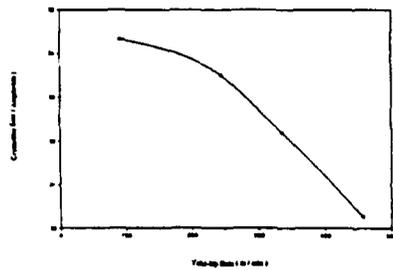
FIG. 3: Crystallite size, L_c,
of as-spun mesophase
fibers vs. take-up
speed.
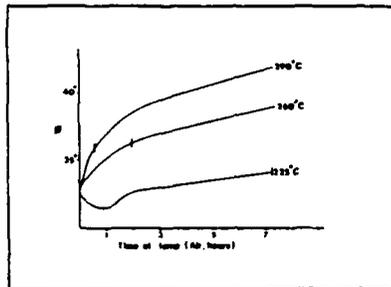
FIG. 6: Preferred orientation vs.
stabilization time and
infusibility point (+).

164
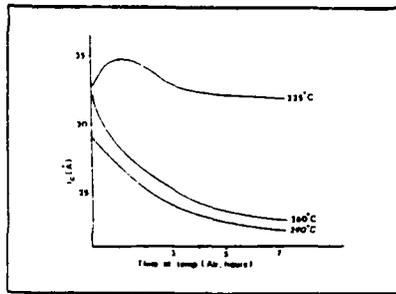
FIG. 7: Crystallite size vs. stabilization time.

FIG. 8: Preferred orientation vs. stabilization time annealed and non-annealed fibers.

FIG. 9: Crystallite size vs. stabilization time annealed and non-annealed fibers.
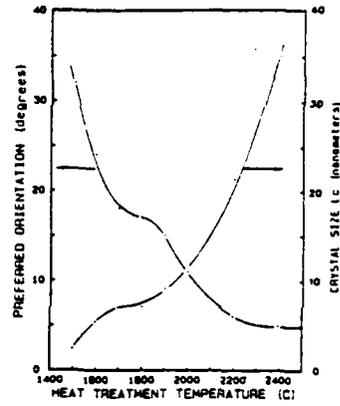
FIG. 10: X-ray diffraction parameters of heat-treated carbon fibers.
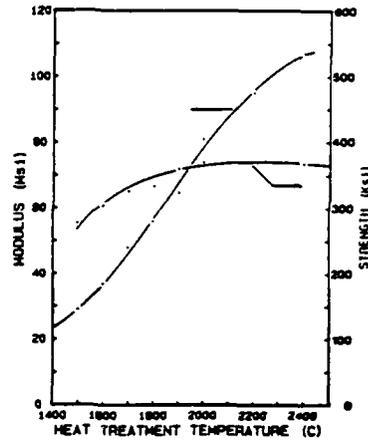
FIG. 11: Mechanical properties of heat-treated carbon fibers.
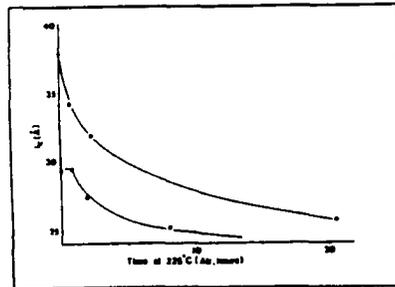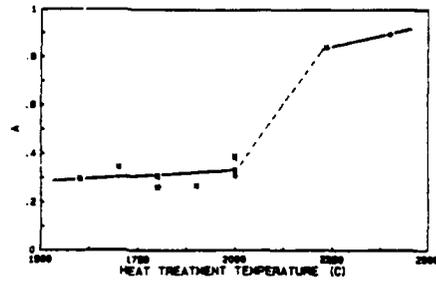
FIG. 12: Reynolds-Sharp "A" Parameter vs. heat treatment temperature.

165

FINAL REPORT

Transverse Thermal Expansion and Microstructure Studies of Carbon Fibers

Shinn-Shyong Tzeng

Department of Mechanical Engineering

March 31, 1992

1. INTRODUCTION

One of the advantages of composite materials is that engineers can tailor composite properties according to the specific requirements by placing the strong stiff fibers in the correct location, in the right orientation and with the right volume fraction. However, the modelling of thermomechanical behavior and physical properties of fiber-reinforced composite materials requires the knowledge of the elastic and thermal properties of both fiber and matrix phases as well as the interface between them.The properties of matrix can be measured from bulk materials using conventional methods. However, measurement of some of the fiber properties, especially the transverse properties presents a problem due to the tiny dimension of fibers. Moreover, the anisotropic nature of some fibers and the strong dependence of properties on the porosity complicate the problem since the measurement values scatter a lot and also vary depending on the direction of measurement. Carbon fibers are the most typical example since the graphite single crystal is one of the most anisotropic materials. In general, carbon fibers have been considered as a transversely isotropic material as shown in the transverse microtexture in Fig. 1(a)-(c). However, some more recent high modulus pitch-based carbon fibers show a microtexture (Fig.1(d)) which is not transversely isotropic and the transverse properties are expected to depend on the direction. For transversely isotropic materials five independent elastic constants are necessary to characterize the mechanical behavior. Until present, most of the measurements have been restricted to the axial elastic modulus, very few measurements on transverse Young's modulus and shear modulus and the axial Poisson's ratio have been reported[1,2]

For high temperature applications, the coefficient of thermal expansion (CTE) is an important parameter to be considered. Thermal residual stress in composite materials often occurs due to the mismatch of CTE between fiber and matrix and between fiber and coating. For ceramic-matrix composites, in general, the thermal expansion of the matrix should be either equal to or less than the fiber thermal expansion to prevent matrix cracking. The cracking results from tensile matrix stresses that are generated upon cooling down from higher processing temperature[3]. Residual stress is also observed within the single carbon fiber due to the anisotropy of CTE of graphite single crystal[4,5]. Two CTEs need to be measured in a transversely isotropic carbon fiber. The longitudinal CTE has been measured using LVDT[6] and other methods[7,11,12]. However, few measurements on transverse CTE have been reported[8-13] and the measured values are also more uncertain due to the experimental difficulty. For the anisotropic transverse microtexture, transverse CTE is expected to vary depending on the direction CTE is measured. This is confirmed by experiment in this report.

In this study, the transverse CTE of a single carbon fiber is measured by using a laser diffraction technique and a CCD(charge-coupled device) detector. The relationship between transverse CTE and microstructure is discussed.

2. REVIEW OF PAST WORK

As mentioned before, very few measurements on the transverse CTE of carbon fibers have been reported due to experimental difficulty. Three approaches were used in the past. They are : (1) derivation of fiber CTE from composite test data, (2) direct measurement in a transmission electron microscope fitted with a hot stage, and (3) a laser diffraction technique. Van Schooneveld and Diefendorf[13] measured the transverse CTE of unidirectional carbon/epoxy composites of different fiber volume fractions, then extrapolated to 100% volume fraction and obtained a value of 8.8 * 10⁻ /°C for T-300 carbon fibers. Wagoner et al [11,12] measured the elastic properties of fiber/epoxy unidirectional composites and then computed the properties of fibers by the composite cylindrical assemblage (CCA) model [14]. The above composite approaches are indirect and the reliability of the derived CTE value depends on the accuracy of measurement on the composite materials and on the validity of theoretical model. Since it is anticipated that the transverse CTE will be the function of microstructure, it is desirable to have a direct accurate measurement method which will minimize the sources of uncertainty and to relate the measured value to microstructure. Moreover, as mentioned before and shown in Fig.1(d), the transverse microtexture can not be considered always to be transversely isotropic. Therefore, the use of transversely isotropic theoretical model to derive the fiber properties is also not appropriate. However, the composite approach allows all the fiber properties to be computed, is self-consistent and tends to average the properties of all the fibers in the composite. Rozploch and Marciniak [8,9] carried out the measurement of transverse CTE with a transmission electron microscopy fitted with a furnace. The furnace temperature was calibrated against the resistance of the heating element and checked against the melting point of aluminum. The values they obtained (shown in Table 1) are larger compared to others [10-13], and some values are even greater than the CTE in c-axis of graphite single crystal which seems unreasonable. Sheaffer [10] measured the transverse CTE using the laser diffraction technique. The fiber was resistance heated in a vacuum environment, and the temperature was measured by a disappearing-filament-type micro-optical pyrometer. However, the data seem to scatter even for the same sample. From the comparison of data shown in Table 1, the data are not consistent for the different methods. For the single filament approach, the temperature measurement of fiber contributes to the source of scatter, and thermo-induced twist of fibers is noted and assigned to the scatter by all the authors.

3. THEORETICAL BACKGROUND

3.1 Thermal Expansion of Materials

Thermal expansion of a solid is a direct result of the anharmonic vibration of the crystal lattice. If the vibrations were purely harmonic the mean positions of the atoms would not change even though the atoms would vibrate with larger and larger amplitudes as the temperature increases. Using the quasi-harmonic approximation, Grüneisen [15] observed that for a large number of crystalline solids, the thermal expansion follows the following relationship known as "Grüneisen's rule":

$$\frac{3\alpha}{\chi_T} = \gamma \frac{C_v}{V} \quad (1)$$

where

  α = linear thermal expansion coefficient
  χ_T = isothermal compressibility of the solid
  V = volume
  C_v = specific heat
  γ = Grüneisen constant, generally in the vicinity of 2.

Since both γ and χ_T/V are weak functions of temperature, the value of α is nearly proportional to C_v at all temperatures, that is, at high temperature, α is nearly a constant and α will decrease to zero as the temperature tends to the absolute zero.

3.2 Thermal Expansion of Carbon Fibers

Structural studies of carbon fibers [16-20] indicated that carbon fibers have an undulating ribbon structure which consists of highly oriented crystallites of turbostratic graphite with the layer plane of the crystalline more or less parallel to the fiber axis. There has been an extensive research effort to relate the properties of polycrystalline materials in terms of the properties of the single crystal, and in general it involves an anisotropic factor[21]. Bacon [22] was the first person to estimate this anisotropic factor quantitatively by X-ray diffraction. The anisotropic function $I(\phi)$ is defined as, in the case of carbon fibers, the relative number of crystallites with their basal plane at an angle ϕ to the fiber axis. The anisotropic properties of polycrystalline materials then could be related to certain moments of $I(\phi)$, viz

$$I_n = \int_0^{\frac{\pi}{2}} I(\phi)\sin^n\phi\,d\phi, \quad \text{where } n=1,3,5. \tag{2}$$

By combining the ideas of Bacon [22] and Simmons [23] who introduces the constant A to take into account the porosity and state of internal stresses, Reynolds [21,24,25] suggests that the thermal expansion coefficients α and $\alpha_\perp$, parallel and perpendicular to the fiber axis, are given by

$$\alpha_{//} = A\left(1-\frac{I_3}{I_1}\right)\alpha_c + \left(1-A+\frac{AI_3}{I_1}\right)\alpha_a \tag{3}$$

$$\alpha_\perp = \frac{A}{2}\frac{I_3}{I_1}\alpha_c + \left(1-\frac{A}{2}\frac{I_3}{I_1}\right)\alpha_a \tag{4}$$

where

  α_c = CTE of single crystal graphite in c-axis,
  α_a = CTE of single crystal graphite in a-axis,
  I_1, I_3 = as defined in eq.(2),

and A is a parameter which takes into account the porosity and internal

stresses and is defined as

$$\alpha_v = 2\alpha_\perp + \alpha_{//} = A\alpha_c + (3-A)\alpha_a \qquad (5)$$

where α_v is volume CTE. From the X-ray diffraction measurement of preferred orientation (which will be discussed in a later section), the function $I(\phi)$ could be closely approximated by the function $\cos^r\phi$. It could be shown that

$$\frac{I_3}{I_1} = \frac{\int \cos^m\phi \sin^3\phi\, d\phi}{\int \cos^m\phi \sin\phi\, d\phi} = \frac{m+2}{m+3} \qquad (6)$$

Substitute Eq.(6) into Eq.(3) and Eq.(4), we have

$$\alpha_{//} = A\frac{1}{m+3}\alpha_c + (1-A\frac{1}{m+3})\alpha_a \qquad (7)$$

$$\alpha_\perp = \frac{A}{2}\frac{m+2}{m+3}\alpha_c + (1-\frac{A}{2}\frac{m+2}{m+3})\alpha_a \qquad (8)$$

where m could be considered as an index of preferred orientation.

The CTE of single crystal graphite both in c and a directions have been measured by several researchers [26-29] ,and the theory is developed by Kelly [30,31] using the Komatsu-Nagamiya [32] lattice dynamics and by Riley [33] following the approach of Gruneisen and Goens [34]. Using Morgan's analysis [35] and eq.(7) and eq.(8), the axial and transverse CTEs of both fiber and graphite single crystal as a function of temperature are computed and are shown in Fig. 2(a) and 2(b). As could be seen in Fig.2, the axial CTE of fibers is close to that of graphite single crystal, presumably because that the layer planes are more or less parallel to the fiber axis. However, the transverse CTE value between fiber and graphite crystal is quite different in terms of magnitude, with the number for fibers being much smaller. In eq.(8), transversely isotropy is assumed; therefore the value of transverse CTE is a combined contribution of graphite crystal in various orientations. For the temperature range between 200°C and 900°C, the transverse CTE of single crystal shows a decrease with temperature, while the transverse CTE of fibers shows a very small increase with temperature. The theoretical analysis of Kelly[31] indicates that the transverse CTE becomes constant above about 1000K at $-30*10^{-5}$ K^{-1} and he attributed the increase of transverse CTE at higher temperature observed experimentally to excitation of optical modes and perhaps to the softening of the interlayer interactions due to the large expansion of the spacing.

From eq.(7) and eq.(8), the axial and transverse CTEs of fibers are computed as a function of preferred orientation for 3 different A constants and are shown in Fig. 3(a) and 3(b). It is shown from Fig. 3(a) that the axial CTE is almost constant at higher preferred orientation and

is not affected by porosity (A constant). The transverse CTE is also a very weak function of preferred orientation at higher preferred orientation. However, the value will be affected by the porosity; a higher A constant produces a lower CTE as shown in Fig. 3(b).

3.3 Laser Diffraction Technique

Measurement of diameter of a thin wire using laser diffraction was reported as early as 1966 [36]. Fraunhofer diffraction was used to calculate the diameter from the spacing between two minimum intensity locations. It was pointed out by Perry et al [37] that the locations of minima calculated from Fraunhofer diffraction are slightly different from that calculated using a more complicated scattering theory [38]. However, the data show a lot of scatter and fail to confirm the difference experimentally. Perry et al showed that there is a difference of the order of $1/3$ μ between laser diffraction and the optical projection microscope with the laser value being the smaller, which is contrary to that predicted by scattering theory. More recently, Li and Tietz [39] compared the laser diffraction and SEM values which were calibrated using the NIST standard SRM484B. Their results showed that the laser diameter is about 5% larger than the corresponding SEM diameter. The two theories, Fraunhofer diffraction and scattering theory, which are used to interpret the laser diffraction phenomenon will be reviewed briefly in the following sections.

3.3.1 Fraunhofer Diffraction

Consider a rectangular slit, with dimensions d in width and 1 in length, in an opaque plate. A laser beam passes through the slit with normal incident angle as shown in Fig.4. According to Fraunhofer diffraction, the intensity $I(\theta)$ at the observation point will be [40]

$$I(\theta) = I_o \left(\frac{\sin\beta}{\beta} \right)^2 \qquad (9)$$

where
$\beta = (\pi d/\lambda)\sin\theta$,
λ = wavelength of the laser,
θ = angle between observation point and center point O,
I_o = intensity at the center of the diffraction pattern.

It can be shown that [40]

$$\sin\theta = \frac{n\lambda}{d} = \frac{\delta_n/2}{[S^2 + (\delta_n/2)^2]^{1/2}} \qquad (10)$$

where δ_n is the distance between the two nth minimum intensity nodes. Therefore the slit width can be calculated by

$$d = n\lambda \left[1 + \left(\frac{2S}{\delta_n} \right)^2 \right]^{1/2} \qquad (11)$$

If $S \gg \delta_n$, which is satisfied for the first minimum (n=1) if the distance S is large, then eq.(11) becomes

$$d = \frac{2\lambda S}{\delta_1} \qquad (12)$$

Using Babinet's principle [41], the diffraction intensity of a single slit is the same as its complementary screen : a rectangular bar with the same dimensions as the slit. The diffraction for this rectangular bar is used to approximate the diffraction of a single fiber. Therefore, the fiber diameter can be calculated by eq.(11) or eq.(12).

3.3.2 Scattering Theory

Assuming the fiber is a perfect cylinder with circular cross-section and has infinite refractive index (i.e. the fiber is totally reflecting), and if the incident laser beam is in TM mode and perpendicular to the fiber axis, then the far-field scattering intensity is given by [38]

$$\frac{I_{TM}}{I_o} = \frac{2}{k_o \pi s} \left| b_o + 2 \sum_{n=1}^{\infty} b_n \cos(n\theta) \right|^2 \qquad (13)$$

where
  I_o = intensity of the incident laser beam,
  k_o = $2\pi/\lambda$,
  θ = scattering angle,
  s = distance between fiber and detector,
  α = $\pi d_f/\lambda$,
  b_n = scattering coefficient = $J_n(\alpha)/H_n^{(2)}(\alpha)$,
  J_n = Bessel function of first kind of order n,
  $H_n^{(2)}$ = Hankel function of second kind of order n
      = $J_n - iY_n$,
  Y_n = Bessel function of second kind of order n.

In the later section, the diameter calculated from Fraunhofer diffraction will be compared to that from scattering theory and the experimental results.

4. EXPERIMENTAL SETUP AND PROCEDURES

4.1 Experimental Technique and Setup for Transverse CTE Measurement

There are a variety of methods developed to measure the CTE of a solid, for examples, the push-rod dilatometer, twin-telemicroscope method, optical interferometric techniques, X-ray diffraction etc. [42,43]. Although some of these methods are very accurate, they are not suitable for the measurement of fibers due to the tiny diameter of fibers. The laser diffraction technique, which has been used to measure the diameter of the fiber, seems to be a natural candidate to be considered and is proven to be a good one. Although the fiber diameter change is only 0.05 μ for a 500°C temperature change, for a 10 μ fiber with a CTE of 10*10⁻¹ /°C, it corresponds to a minimum intensity location shift of about 100μ for a 35 cm distance between fiber and detector which is large enough to be measured. In order to measure the intensity change over such short distances, a CCD (charge-coupled device) detector (Texas Instruments type TC104-1) is used. The CCD detector is very sensitive to light intensity and has 3456 sensor elements with a distance between pixels of 10.7 μ which allows the determination of locations in the micron range.

The design of the vacuum furnace is shown in Fig. 5. An optically polished square quartz cell, which was designed to be used for UV spectrophotometer, was used as the furnace body and the nickel-chromium wire with a diameter of 0.0126 in. was used for a heating element. The quartz cell was fitted into a vacuum chamber made of brass. The purpose of vacuum is to prevent the oxidation of carbon fibers at high temperature. The vacuum chamber is water cooled, and a K-type thermocouple with Inconel sheath was used and hooked up to a temperature controller to control the temperature. The "dum-dum", which is generally used as a sealing material for vacuum bags in the fabrication of composite laminates, was used as the sealing material between the quartz cell and vacuum chamber.

The single carbon fiber is mounted on a graphite piece as shown in Fig. 6 using alumina fiber based high temperature cement. Before testing, they were heated to 66.5 °C for 4 hours to cure the cement. Two holes were drilled in the graphite piece with one in 0 degree and another in 90 degree position which allowed the measurement of CTE in two directions perpendicular to each other. Small alumina tubes were put before the graphite piece for precise positioning. The length of the alumina tubes was adjusted carefully for the 0 and 90 degree graphite piece orientation to make sure that the fiber and the thermocouple were in the same position for both directions. A He-Ne laser with 20 milliwatt power was used. The signal from the CCD detector was offset and amplified, and a PC-AT personal computer was used for the data acquisition and processing.

4.2 X-Ray Diffraction

A Scintag XRD2000 X-ray diffractometer was used for wide-angle diffraction experiments. Either quartz or silicon was used as a standard. CuKα radiation was used and the Kβ radiation was removed using a single-channel pulse-height analyzer to increase the peak/background ratio. For the preferred orientation measurement, a transmission azimuthal stage was used which allows an intensity scan in the φ direction as shown in Fig.7. A well annealed graphite crystal was used as the standard to determine the instrumental broadening. The fiber bundle sample is mounted on an aluminum ring one inch in outside diameter which was then fitted into the

transmission stage. Special care was taken to align the fibers. For those fibers without surface treatment, alignment is not easy and small amount of epoxy resin was used to hold the fibers together. For preferred orientation measurement, the Bragg angle was determined first, and after fixing the incident X-ray beam and detector both at the Bragg angle, the azimuthal scan then provided the information about the orientation distribution of the graphite layer planes. The accuracy of determination of Bragg angle is not critical to the preferred orientation measurement, therefore, no correction procedures were made on the determination of Bragg angle. Shen [44] pointed out that there is a slightly difference in the preferred orientation when using the integrated intensity method instead of using the peak height method. For the integrated intensity method, the intensity versus 2θ scan is made at each ϕ angle and the peak area is measured instead of simply measuring the peak height at each ϕ angle as in peak height method. The difference is larger for higher modulus fibers and a difference as large as 2 degrees (8.9% error) in the preferred orientation was measured. However, the procedure is too time-consuming and not practical for large numbers of specimens.

4.3 Scanning Electron Microscopy

The transverse microtexture is investigated using a JEOL 848 scanning electron microscopy with a 15 kV or 20 kV accelerating potential. The sample was coated with a thin layer of gold using a sputtering apparatus under vacuum with a pressure of 0.069 torr to minimize charging effect. Different sputtering time was tried to reduce the thickness of gold coating in order to make sure that gold coating would not affect the observed microstructure.

4.4 Image Analysis

A Zeiss optical microscope with an image analysis system was used to measure the cross-sectional area of carbon fibers.

5. RESULTS AND DISCUSSIONS

5.1 Diameter Measurement of fiber materials

Strength measurement of carbon fibers often shows a lot of scatter. One of the reasons has been attributed to the error associated with fiber diameter measurement. In general, four techniques are used to determine the diameter or cross-sectional area of the fibers. They are : (1) SEM, (2) optical microscopy, (3) image analysis, and (4) laser diffraction. Although SEM could obtain quite accurate measurement, it requires tedious calibration and sample preparation procedures. It was pointed out by Lundgren et al [45] that optical measurements normally overestimate the value of diameter due to diffraction effects at the fiber edge. Also the resolution is lower in optical microscopy. Several difficulties are associated with image analysis. First, the fiber must be positioned perpendicular to the surface of epoxy mount, and the position also needs to be maintained during polishing. It is often difficult to determine the boundary between fiber and matrix which therefore over- or underestimates the fiber cross-sectional area. Also the edge of the fiber sometimes will chip off during polishing. In this case, the area is underestimated. Compared to the above three methods, laser diffraction technique is more convenient and the resolution is high enough to determine the transverse CTE which will be discussed in the later section. However, the accuracy of the technique has been questioned. As mentioned before, Perry et al

[37] pointed out the difference of diameter derived from the Fraunhofer diffraction approximation and scattering theory. However, the scatter of data fails to confirm that experimentally. Several reasons could attribute to the error, such as non-uniform diameter along the fiber axis, non-circular cross-section and non-clean surface due to other materials or particles attached which causes non-clean, overlapping or multiple diffraction patterns. Fig.8(a) and (b) show the experimental data of the variation of cross-sectional area and apparent diameter along the fiber axis. The area was measured using image analysis and the apparent diameter is calculated by assuming a circular cross-section. In the following section, Fraunhofer diffraction and scattering theory will be compared and comparison of experimental data with theories will be discussed.

5.1.1. Comparison of Fraunhofer Diffraction and Scattering Theory with Experimental data

Comparison of Fraunhofer diffraction and scattering theory as shown in Fig. 9 indicates that the minimum intensity locations are different between the two approaches, and as the distance away from the center of diffraction pattern increases, the difference also increases. Therefore, the diameter calculated from the Fraunhofer diffraction (eq.(11) or eq.(12)) will not be the same as the diameter from scattering theory, with the Fraunhofer diffraction diameter being larger. Numerical results for different diameter fibers show the percentage difference decreases with increasing fiber diameter as shown in Fig.10. It is noted that depending on eq.(11) or eq.(12) is used, the percentage error is also different as shown in Fig.10. The distance S between fiber and detector has very little effect on the results. The experimental data on P55x fibers are shown in Fig. 11 using the Fraunhofer approximation. Since the cross-section of the fiber is oval-shaped, five measurements made at every 36 degree around the fiber were made for each fiber sample, and polygon method was used to calculate the cross-sectional area [46,47]. The area calculated by using the average diameter of five measurements was also computed and compared to the polygon method. The results indicated that a simple average of diameters will overestimate the apparent diameter. The average error was 0.32 μm in this experiment. Although the image analysis also involves some error as mentioned before and not the same location on the fiber was measured in these two approaches, the diameter from polygon method is statistically larger than the diameter from image analysis as shown in Fig. 11 with an average 0.26 μm larger. From calculation using scattering theory, the diameter from Fraunhofer diffraction will be 0.35 μm larger. Recently, Li and Tietz [39] compared the laser diffraction and SEM values which were carefully calibrated using the NIST standard SRM484B. Their results also showed that the laser diffraction diameter using the Fraunhofer approximation is about 5% larger than the SEM diameter. Therefore, it seems to indicate that the diameter from scattering theory is closer to the true diameter although certain assumptions also are made in the scattering theory.

A more careful calculation using scattering theory indicates that the spacing between minimums is not equal to each other. The spacing is larger for higher order diffraction, that is, $\Delta\delta_2 > \Delta\delta_1 > \Delta\delta_0$ as shown in Fig.12. This was also confirmed by experiment and the result is shown in Table 2. Therefore, depending on which distance between minimums is used, the diameter calculated using Fraunhofer diffraction will be different. It is also noted that depending on whether eq.(11) or eq.(12) is used, the diameter calculated is also quite different as shown in Table 2. The diameter calculated using eq.(11) is increased for higher order

diffraction, however, the diameter calculated using eq.(12) is decreased for higher order diffraction. A more complete calculation for 3 different diameter fibers (4, 10, and 20 μm) using scattering theory indicated that the percentage error produced using eq.(11) and eq.(12) is different and in the opposite directions for higher order diffraction, i.e. eq.(11) results in a larger error and eq.(12) results in a smaller error for a higher order diffraction as shown in Fig. 13. The difference is larger for smaller diameter fibers. As shown in Fig. 13, the error is from +12.5% when using eq.(11) to -21.7% when using eq.(12) for a 4 μm diameter fiber when 4th minimum location is used.

As shown in Fig. 12, the distances δ_1, δ_2, etc, could not be measured precisely in the current experimental setup, therefore only eq.(12) could be used. Also only $\Delta\delta_1$ or $\Delta\delta_2$ will be measured instead of $\Delta\delta_2$ as shown in Fig. 12, which has advantage for a 10 μm fiber since the error percentage is more close to zero when using $\Delta\delta_1$ or $\Delta\delta_2$ as shown in Fig. 13. A closer look at the data of Li and Tietz [39] in which higher order diffraction was used seems quite consistent with the above analysis.

5.2 Transverse Microtexture

The transverse microtexture of Amoco P-series pitch-based carbon fibers was studied using SEM. Some of the results are shown in Fig.15. The mechanical properties of those fibers are shown in Table 3. It must be pointed out that the number is somewhat different from the results tested in our laboratory. The difference for P55 fibers is also shown in Table 3. In our measurement, four different gauge lengths (1, 2, 3, and 4 in) were used and at least ten samples were tested for each gauge length. Since the slope of stress-strain curve as shown in Fig.14 increases gradually, secant method was used to determine the modulus. From the modulus values for different gauge length, the compliance of the test machine was determined and the modulus corrected for machine compliance was deduced. Fig.15(a),(b),(d),(e),(f), and (g) were obtained from the bending fractured surfaces of fiber bundles. The fiber bundles had been set into epoxy resin and then broken by bending. Fig.15(c) and (h) were obtained from the tensile fractured surface of a single carbon fiber. In these cases, a single carbon fiber was mounted horizontally on the grip of a home-made single filament tensile testing apparatus and a glass slide was positioned underneath the fiber very closely but without touching the fiber. A few drops of glycerin was then applied onto the glass slide and covered the carbon fiber. The fiber was then broken by tension. The broken ends will be kept inside the glycerin after the testing. They were then removed, cleaned, and dried. A gold coating was applied for the observation in SEM. It was noted that the use of glycerin to catch the fractured ends does not affect the modulus and strength results. It was also noted that the broken locations vary from near the grip (few samples) to the center of the gauge length, presumably because of the flaw distribution and , in the case of grip failure, due to stress concentration.

As shown in Fig.15(a), no obvious transverse microtexture could be seen for P25 fibers which is more or less similar to that of PAN-based carbon fibers. Two kinds of transverse microtextures were observed in P55 fibers for two different batches of P55 fibers. The P55x fiber (Fig.15(c)) has an oriented-core microtexture, and the P55s fiber (Fig.15(b)) has a random structure in the core and a radial texture in the sheath. The particle-like structure in the Fig.15(c) is probably due to too much gold coating. An elliptical flaw near the surface can be seen in this tensile fracture surface, which happened quite frequently (around

5 out of 10 samples) in this particular batch of P55x fibers. Both surface and internal flaws were observed. Although the diameter distribution is particularly wide, ranging from 9 to 18 μ, for this batch of P55s fibers, the cross-section of all the fibers appears to be circular. However, the P55x fibers with an oriented-core microtexture show an elliptical shape cross-section. As will be shown in the later section, the P55s fibers, which has a more or less transversely isotropic microtexture, show about the same transverse CTE tested in two directions perpendicular to each other. However, the oriented-core microtexture of P55s fibers results in a high anisotropy of transverse CTE.

It has been reported that shrinkage during graphitization occurs preferentially along the c-axis and results in oriented-core fibers with an oval-shaped cross-section [48]. As the graphitization temperature increases, radial cracks in the as-spun fiber split and develop into a PAC-man shaped cross-section [48,49]. As shown in Fig.15(d),(e) and (f), as the fiber modulus increases, i.e. graphitization temperature increases, the microtexture becomes oriented-core structure, and the sheet-like structure is more developed. Also, the cross-section becomes oval-shaped with the oriented-core along the longer diameter of the cross-section. A schematic plot of the oriented-core structure after Fitz Gerald et al [50] is shown in Fig.16 which shows the basic characteristics although some variations in details may appear for different fibers as can be seen in Fig.15. If we define the ellipticity as the ratio of long diameter and short diameter, the ellipticity of those oriented-core fibers is in the range of 1.05-1.15. Obviously, these fibers are not transversely isotropic and anisotropy of transverse CTE was also observed in this study and will be discussed in the later section.

A crack through the oriented-core region and along the fiber axis can obviously be seen in Fig.15(f) of a P120x fiber. This indicates that the crack is more likely to propagate along the sheet-like structure, which is also why the fracture surface of the sheet-like structure is generally not flat, but has the sheet-like texture sticking out up and down out of the fracture surface as shown in Fig.15(e) and (f). For the lower modulus fiber, the sheet-like texture is not well developed and the fracture surface is relatively flat as shown in Fig.15(a) and (c) of P25 and P55 fibers. It is noted that the fracture surface on the compression side is flatter than that of tension side as shown in Fig.15(f) of a P120x fiber broken in bending. Crack propagation along the fiber axis parallel to the sheet-like texture is more pronounced in the tension failure than in the flexural failure as shown in Fig.15(h) of a P130x fiber failed in tension. This type of failure causes an unique fracture surface which is not only unflat but also has a protrusion with a length as long as several times fiber diameter. Again, for lower modulus fibers, the fracture surface is relatively flat as shown in Fig.15(c) of P55 fiber even though failed in tension. Although this sheet-like structure is the reason why pitch-based carbon fibers could achieve higher modulus, it is also why the strength is not increased proportional to the modulus since the crack could easily propagate across the width of a sheet, therefore the strength is more sensitive to any flaws and imperfections. A cross-section with the PAC-man shape was observed for some of the P130x fibers. As shown in Fig.15(g), the sheet-like texture is well developed, and the fiber has a radial texture. However, a closer look at the tip of the notch and following the texture of the sheet, it is noted that the split occurred from the oriented-core which also shrank more and has smaller spacing between sheets. A void also could be seen on the fracture surface.

5.3 X-Ray Diffraction

Both wide-angle X-ray diffraction and preferred orientation using an azimuthal transmission stage were studied for Amoco P-series pitch-based carbon fibers. Some of the results are shown in Fig. 17 and Fig. 18. The same fiber bundles which were mounted on an aluminum ring as described in section 4.2 were used for both studies. As shown in Fig. 17, it is obvious that when the modulus decreases, the (002) peak was shifted to the smaller diffraction angle, therefore the d-spacing between basal planes increases. Also the shape of (002) peak becomes broader as the modulus decreases, indicating the decrease of crystalline size. For low modulus P25 fibers, only a very broad (002) peak was observed, no (004) peak could be seen, due to very low crystallinity. Two examples of preferred orientation measurement were shown in Fig. 18(a) and (b) for P55x and P120 fibers. Obviously, the modulus increases as the preferred orientation increases. The relationship between fiber modulus and preferred orientation for Amoco P-series fibers is shown in Fig. 19. In Fig. 19, the preferred orientation is interpreted as the full width at half maximum intensity (FWHM) in the intensity distribution function $I(\phi)$. No corrections in FWHM were made in Fig.19.

5.4 Measurement of Transverse CTE

Transverse CTE of several carbon fibers were measured using a laser diffraction technique and two CCD detectors. The furnace design and experimental setup were shown in Fig. 5 and described in section 4.1. A single fiber was mounted onto a graphite piece (Fig.6) using an alumina fiber based high temperature cement only in one end since the incompatibility of CTE between graphite piece and the fiber will cause the fiber to buckle upon cooling down from high temperature if the fiber was mounted in both sides. The other advantage of mounting the fiber only in one side is that it also eliminates the transverse dimensional change of the fiber due to Poisson's effect which is a result of thermal stress due to the mismatch of CTE between fiber and graphite piece. This dimensional change could be as high as 10% compared to that due the thermal expansion under some experimental conditions, although some optimization could be made to reduce the error percentage. The disadvantage of mounting fiber only in one side is that the fiber position could be shifted or rotated due to the CTE mismatch among the fiber, graphite piece and alumina cement. This movement of fiber causes the shift or rotation of diffraction pattern, which turns out to be the source of experimental error, since the alignment between CCD and the diffraction pattern is very important due to the tiny photosensitive area of each CCD element (only 10.7*10.7 μm⁻). Fortunately, the error is not severe under some experimental conditions and could be corrected by using two CCD detectors on both sides of the diffraction pattern.

Since the experiment is sensitive to the fiber movement and any other movements of the furnace or CCD detectors, in order to make sure this does not happen during the thermal cycle, continuous heating is not adapted. Instead, each time the fiber was heated to certain temperature, it was cooled down to room temperature, and the room temperature diameter was measured to make sure that the room temperature diameter was not shifted between each heating cycle due to any movement or oxidation. It had been cited by several researchers [8,9,10] that twist occurs when the fiber was heated. If this is so, then it will show up on the diameter measurement at higher temperature if the fiber cross-section is elliptical. The room temperature diameter will also tend to vary between

each heating cycle. This seems to be not the case from our experiments, at least for most of the fibers.

As shown in Fig.12, the distance between the first pair minima δ_1 could not be measured very accurately because of the experimental setup. However, the change of δ_1 upon heating could be determined very precisely from two CCD detectors. For the diameter measurement, the distance between first and second minimum intensity locations $\Delta\delta_1$ (= $(\delta_2 - \delta_1)/2$) is measured. As shown in section 5.1.1, there is a slightly difference between $\Delta\delta_1$ and $\Delta\delta_1$, however, it could be corrected using scattering theory and has only small effect on the final CTE values. Therefore, the CTE with respect to the room temperature could be calculated from eq.(12) as :

$$\alpha = \frac{\Delta d}{d_o} = \frac{d_T - d_o}{d_o} = \frac{\dfrac{\lambda S}{\Delta\delta_{1T}}A_{1T} - \dfrac{\lambda S}{\Delta\delta_1}A_1}{\dfrac{\lambda S}{\Delta\delta_1}A_1} \qquad (14)$$

where
   d_T = diameter at temperature T,
   d_o = diameter at room temperature,
   λ = wavelength of laser,
   S = distance between fiber and CCD detector,
   A = correction factor for diameter using Fraunhofer diffraction
       eq.(12).

Since the diameter change is very small (in the range of 0.01 - 0.15 μm), $A_{1T} \approx A_1$. Therefore

$$\alpha = \frac{\Delta\delta_1 - \Delta\delta_{1T}}{\Delta\delta_{1T}} \qquad (15)$$

In the experiment, we measured $(\delta_1 - \delta_{1T})/2$ instead of $(\Delta\delta_1 - \Delta\delta_{1T})$ due to the much higher resolution in first minimum. However, the difference is small and also could be corrected using scattering theory and has very small effect on the final result. It must be noted that the distance between fiber and detector is not needed in order to calculate the CTE since it canceled out in eq.(14). This eliminates the error due to measurement of S. This error will become more pronounced at smaller distance S.

The result for a P75s fiber is shown in Fig. 20. In order to test the reproducibility of the experiment, several runs were made on the same fiber at same or different temperature. As shown in Fig. 20, the reproducibility in general is quite good considering the very small dimensional change and the experimental difficulties. A best-fit straight line was drawn through the data since the CTE is relatively constant for the temperature range tested as shown in Fig. 2(b). The fit of the data to a straight line in general is quite good, although some data at the same temperature show large scatter due to the movement of fiber as mentioned before. It must be noted that the data of run #b was taken from measurement of only one CCD detector, which are not accurate for most

experiments since the resolution of second minimum is not good compared to first minimum and the location of second minimum is also more likely to be affected by the rotation of the diffraction pattern. The CTE value for this particular P75s fiber is about $15.9*10^{-7}$ /$^\circ$C which is higher than $12.5*10^{-6}$ /$^\circ$C obtained by Wagoner et al [11,12] as shown in Table 1. The data of Wagoner et al is closer to the prediction by eq.(8) where the fiber is assumed to be transversely isotropic. However, this is not the case for P75s fibers as shown in the transverse microtexture in Fig. 15(d), and CTE anisotropy is expected. Therefore, it is not surprised that the high CTE value was obtained considering the high CTE anisotropy in the graphite single crystal. Moreover, the value is still quite low compared to the graphite crystal CTE in the c-axis ($\approx 27*10^{-7}$ /$^\circ$C) since the graphite layer planes are not all oriented in the same direction. The porosity in the fiber will also lower the transverse CTE value as shown in Fig. 3(b). Fig. 21 shows the result for a P120 fiber. The CTE value is about $5.7*10^{-7}$ /$^\circ$C which is much lower than that of P75s fiber. The data show more scatter compared to that of P75s fiber which is probably partly due to the low CTE value. Fig. 22 shows another result of a P120 fiber. The CTE was measured in two directions perpendicular to each other as described before. High CTE anisotropy was observed in this sample with one CTE about $6.16*10^{-5}$ /$^\circ$C and the other CTE about $17.^{7}3*10^{-6}$ /$^\circ$C. The anisotropy factor is 2.88. A result for P55x fiber which has an oriented-core microstructure is shown in Fig. 23. Although the data for 0 degree position runs show a lot scatter, the CTE anisotropy can still be distinguished easily. The CTE for 0 degree position is about $5.47*10^{-6}$ /$^\circ$C and the CTE for 90 degree position is about $13.88*10^{-6}$ /$^\circ$C. The anisotropy ratio is 2.54. Comparison of the results between P55x and P120 seems to indicate that as the modulus increases, the higher transverse CTE anisotropy is developed although current data are not enough to draw this conclusion. Also, the current experimental setup only allows the CTE measurement in two perpendicular directions, therefore Whether or not the anisotropy factor obtained is the highest value is a question. The P55s fiber which has about the same modulus, but with a transversely isotropic microtexture as shown in Fig. 15(b), was tested in order to compare with P55x fibers which have an oriented-core microstructure. The result is shown in Fig. 24. Although not identical, the P55s fiber shows very close transverse CTEs in both directions with one about $12.64*10^{-5}$ /$^\circ$C and the other about $11.47*10^{-7}$ /$^\circ$C. This is very consistent with the transversely isotropic microtexture and the values are also in excellent agreement with that obtained by Wagoner et al[11,12] as shown in Table 1. Fig. 25 shows the result for a P100 fiber tested in two locations along the fiber length. Two different CTE values were obtained. One is about $13.82*10^{-6}$/$^\circ$C and the other about $8.35*10^{-7}$ /$^\circ$C. Two possible reasons could be used to explain that. First, it is possible that a large void exists in one location which will decrease the CTE value. The other explanation is that the direction of transverse texture rotates along the fiber length.

It is predicted by eq.(8) that the transverse CTE is a very weak function of preferred orientation as shown in Fig. 3(b). However, no experiment was attempted due to the availability of fibers with the same transverse microstructure and different modulus. Also the void content is unknown which has appreciable effect on the CTE value. Assuming same porosity content and residual stress state, the fiber with a radial and a onion skin microstructure should have the same transverse CTE since the percentage of basal plane oriented in all directions is the same for both fibers. Again, no experimental confirmation was made due to the availability of samples with onion skin structure and the lack of knowledge of porosity and residual stress state.

6. CONCLUSIONS AND FUTURE WORK

Transverse coefficients of thermal expansion of carbon fibers were measured successfully using a laser diffraction technique and two CCD detectors. The measured value is well correlated to the transverse microtexture in a qualitative way. The CTE values of fiber with transversely isotropic microtexture are close to the value predicted by the Reynolds' model and could be predicted semiquantitatively if the constant A which takes into account of porosity and residual stress is known. More experiments are needed to draw a conclusion that whether or not the increase of modulus increases the transverse CTE anisotropy in high modulus pitch-based carbon fibers. An experimental setup which allows the rotation of the fiber is more desirable in this investigation. It is also more helpful in terms of modelling of transverse CTE. The effects of void content and residual stress on the transverse CTE remain a question due to the experimental difficulty in characterizing them, particular for a single fiber. Although small angle scattering has been used to characterize the microporosity, it is a macroscopic approach. Finally, experimental evidences indicate that the diameter from scattering theory is more likely to be the true diameter, while the diameter calculated from the Fraunhofer diffraction approximation is overestimated. A correction could be made for the diameter calculated from Fraunhofer diffraction approximation. However, more experimental support is necessary.

7. REFERENCES

[1]   Kawabata, S., in Proceedings of the Fourth Japan-US Conference on Composite Materials, Washington, D.C., pp.253-262, 1988.

[2]   Krucinska, I. and Stypka, T., Composites Sci. Tech., v41(1991)1-12.
[3]   Singh, R.N., American Ceramic Soc. Bulletin, v70(1991)55-56.
[4]   Chen, K.J., in Progress in Science and Engineering of Composites, Hayashi, T., Kawata, K., and Umekawa, S., Eds., pp.97-105, 1982.
[5]   Stevens, W.C., Wang, J.H., and Diefendorf, R.J., in Carbon'80, pp.598-602, W. Germany.
[6]   Butler, B., Duliere, S., and Tidmore, J., in Abst. of 10th Biennial Conf. on Carbon, pp.45-46, 1970.
[7]   Yasuda, E., Tanabe, Y., Machino, H., and Takaku, A., in Extended Abstracts of 18th Biennial Carbon Conference, pp.30-31, 1987.
[8]   Marciniak, W. and Rozploch, F., High Temperatures-High Pressures, v11(1979)709-710.
[9]   Rozploch, F. and Marciniak, W., High Temperatures-High Pressures, v18(1986)585-587.
[10]   Sheaffer, P.M., in Extended Abstracts of 18th Biennial Carbon Conference, pp.20-21, 1987.
[11]   Wagoner, G., Smith, R.E., and Bacon, R., in Extended Abstracts of 18th Biennial Carbon Conference, pp.415-416, 1987.
[12]   Wagoner, G. and Bacon, R., in Extended Abstracts of 19th Biennial Carbon Conference, pp.296-297, 1989.
[13]   Van Schooneveld, H.G. and Diefendorf, R.J., in Proceeding of the Baden-Baden Carbon Conference, p.606, 1980.
[14]   Hashin, Z., J. Appl. Mechanics, v46(1979)543.
[15]   Grüneisen, E., Handbuch der Physik, vol. X, pp.1-59, 1926, Springer Verlag, Berlin.
[16]   Tokarsky, E., Ph.D Thesis, RPI, 1973.
[17]   Johnson, D.J., in Chemistry and Physics of Carbon, vol.20, 1987.
[18]   Jain, M.K. and Abhiraman, A.S., J. Mat. Sci., v22(1987)278-300.
[19]   Diefendorf, R.J. and Tokarsky, E., Polymer Eng. Sci., v15(1975)150-159.
[20]   Dresselhaus, M.S., Dresselhaus, G., Sugihara, K., Spain, I.L., and Goldberg, H.A., Graphite Fibers and Filaments, Springer-Verlag, 1988.
[21]   Reynolds, W.N., Carbon, v6(1968)277-282.
[22]   Bacon, G.E., J. Appl. Chem., v6(1956)477.
[23]   Simmons, J.H.W., in Proceedings of the third Carbon Conference, p.559, 1959.
[24]   Reynolds, W.N., in Proc. 3rd International Conference on Industrial Carbons and Graphite, London, p.427, 1970.
[25]   Reynolds, W.N., in Chemistry and Physics of Carbon, vol.11, Walker, P.L. and Thrower, P.A., Eds., Marcel Dekker, Inc., New York, p.54, 1973.
[26]   Bailey, A.C. and Yates, B., J. Appl. Phys., v41(1970)5088.
[27]   Nelson, J.B. and Riley, D.P., Proc. Phys. Soc.(London), v57(1945)477-486.
[28]   Steward, E.G., Cook, B.P., and Kellet, E.A., Nature, v187(1960)1015.
[29]   Harrison, J.W., High Temperatures-High Pressures, v9(1977)211.
[30]   Kelly, B.T. and Walker, P.L., Carbon, v8(1970)211.
[31]   Kelly, B.T., Carbon, v29(1991)721-724.
[32]   Komatsu, K. and Nagamiya, I., J. Chem. Phys., v22(1954)1457.
[33]   Riley, D.P., Proc. Phys. Soc.(London), v57(1945)486.
[34]   Grüneisen, E. and Goens, E., Z. Phys., v29(1924)141.
[35]   Morgan, W.G., Carbon, v10(1972)73-79.
[36]   Koedam, M., Philips Tech. Review, v27(1966)1982.

[37] Perry, A.J., Ineichen, B., and Eliasson, B., *J. Mat. Sci.*, v9(1974)1376-1378.

[38] Kerker, M., <u>The Scattering of Light and Other Electromagnetic Radiations</u>, Academic Press, 1969.

[39] Li, C.T. and Tietz, J.V., *J. Mat. Sci.*, v25(1990)4694-4698.

[40] Charschan, S.S., Ed., <u>Lasers in Industry</u>, 1972.

[41] Young, M., <u>Optics and Lasers</u>, 2nd ed., 1984.

[42] Krishnan, R.S., Srinivasan, R., and Devanarayanan, S., <u>Thermal Expansion of Crystals</u>, 1979.

[43] Touloukian, Y.S., Kirby, R.K., Taylor, R.E., and Lee, T.Y.R., <u>Thermal Expansion-Nonmetallic Solids</u>, Thermophysical Properties of Matter, Vol. 13, 1977.

[44] Shen, T.H., MS Thesis, Rensselaer Polytechnic Institute, 1980.

[45] Lundgren, C.A., Davis, H.A., Neal, C.R., and Schmitz, P.H., in <u>Proceedings of International Conference of Fiber and Textile Science</u>, Institute of Textile Science, Ottawa, Canada, April 1991, pp.105-110.

[46] Chen, K.J., Ph.D thesis, RPI, 1984.

[47] Tzeng, S.S., MS thesis, RPI, 1990.

[48] White, J.L. and Buechler, M., in <u>Petroleum-Derived Carbons</u>, Bacha, J.D. *et al*, Eds., pp.62-84, 1986.

[49] Barr, J.B., Chwastiak, S., Didchenko, R., Lewis, I.C., Lewis, R.T., and Singer, L.S., *Applied Polymer Symposium*, No.29, pp.161-173, 1976.

[50] Fitz Gerald, J.D., Pennock, G.M., and Taylor, G.H., *Carbon*, v29(1991)139-164.

Fiber Type	Wagoner et al [11,12]		Van Schooneveld and Diefendorf [13]	Rozploch and Marciniak [8,9]	Sheaffer [10]
	Axial CTE	Transverse CTE			
P55	-1.37 -1.37	12.1 11.6			12.0 (+2.9)
P75	-1.49 -1.44	12.2 12.7			
P100	-1.48 -1.47	9.4 9.5			
T-50	-1.28 -1.17	6.6 6.8			
T-300X	-1.2	7.0			
T-300	-0.67 -0.67	8.9 8.8	8.6		
T-650	-0.84	7.8			
HM3000					10.9 (+0.8)
G50					13.1 (+0.7)
AS-1					12.5 (+1.2)
PAN(*)				T_{th}=1573K 22 18 19 17 T_{th}=1973K 41 40 34 31	
MPP				58 58 57	
T800				29.5 30.4 26.8 26.2	

* Refer to the original paper for detail.

Table 1. Coefficient of Thermal Expansion of Various Fibers.

	Distance from Scattering Theory (cm)	Diameter calculated from Fraunhofer Approximation (micron)		Distance from Experiment (cm)	Diameter Calculated from Fraunhofer Approx. Eq.(12)
		Eq(12)	Eq(11)		
Center					
	0.97	8.318	8.342		
1 min.					
	0.98	8.233	8.371	1.00687	8.01315
2 min.					
	1.005	8.028	8.408	1.03683	7.78160
3 min.					
	1.045	7.721	8.456	1.11387	7.24339
4 min.					
	1.095	7.368	8.527		
5 min.					
	1.175	6.867	8.604		
6 min.					

Table 2.   Comparison of Scattering Theory (8 micron fiber, S = 12.75 cm) and experiment.

Fiber	Modulus (GPa)	Strength (GPa)	Density (mg/m^3)
P25	170	1.3	na
P55	379	1.9	2.00
	428(*)	1.92(*)	na
P75	490	1.89	na
P75S	524	1.75	2.00
P100	765	2.41	2.16
P120S	827	2.2	2.18
P130x	923	2.87	2.19

(*) Tested in our laboratory.

Table 3.   Properties of Amoco P-series Fibers[50].

(a)

(b)

(c)

(d)
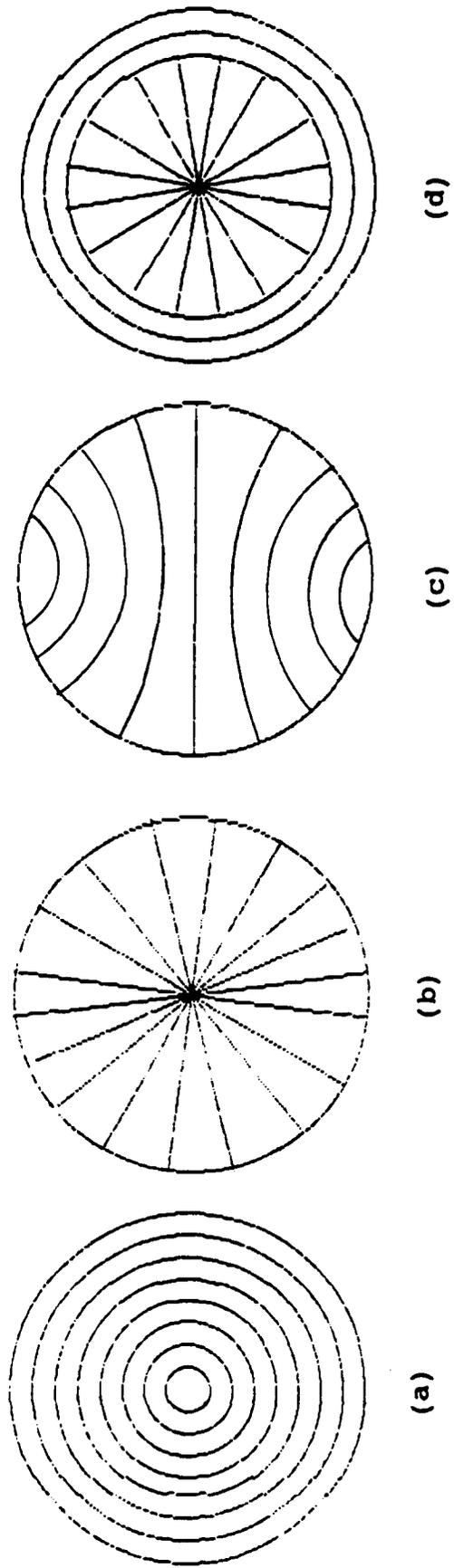
Fig. 1. Transverse Microstructure of Carbon Fibers.
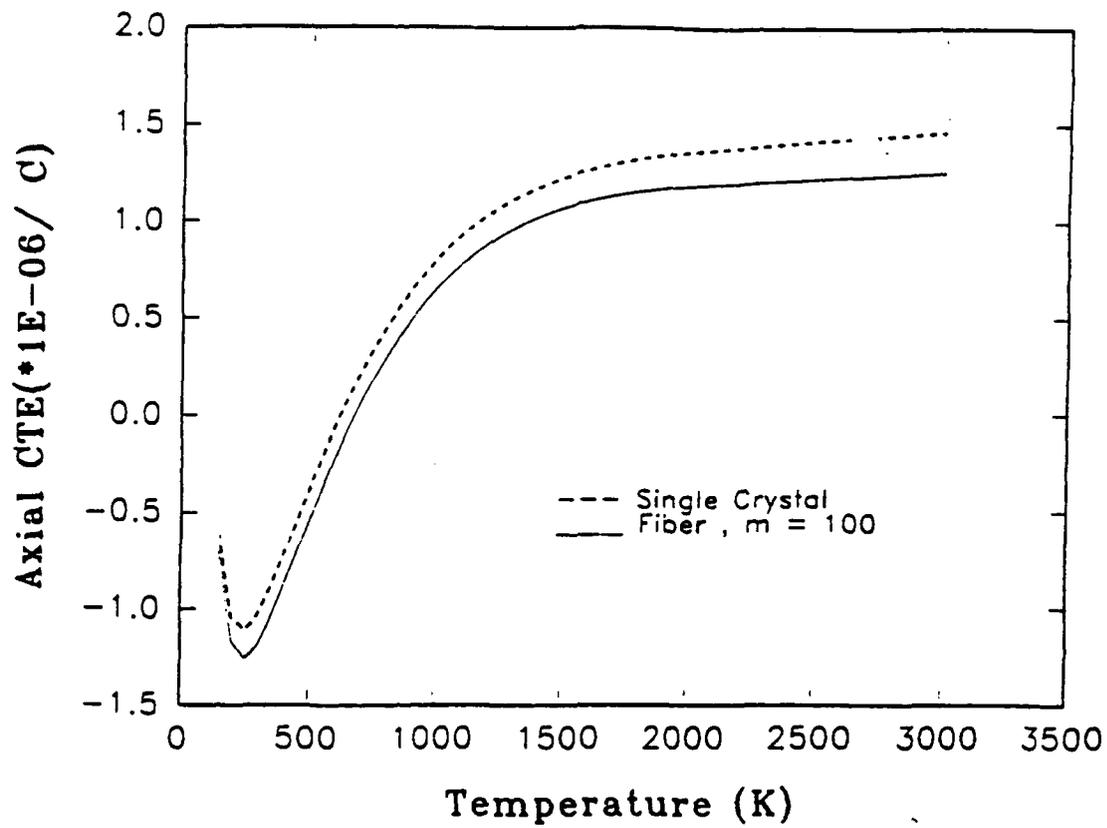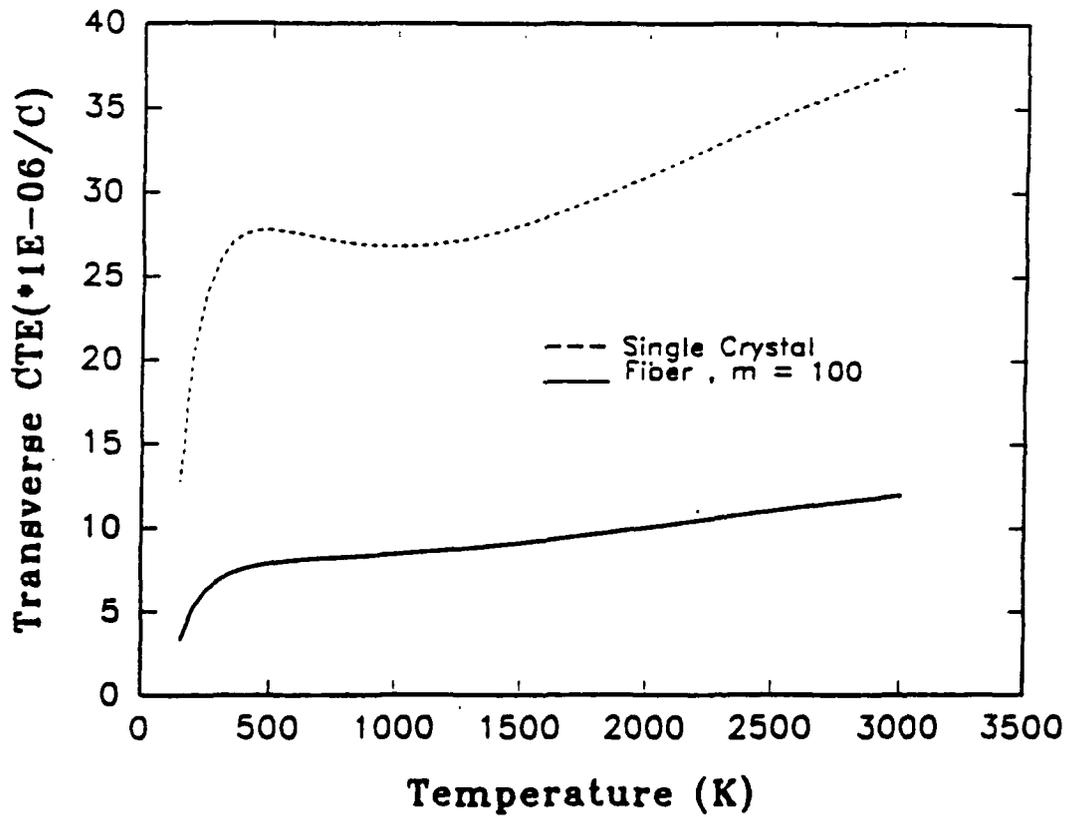
Fig. 2(a)   Axial CTE as a Function of Temperature.
    (b)   Transverse CTE as a Function of Temperature.
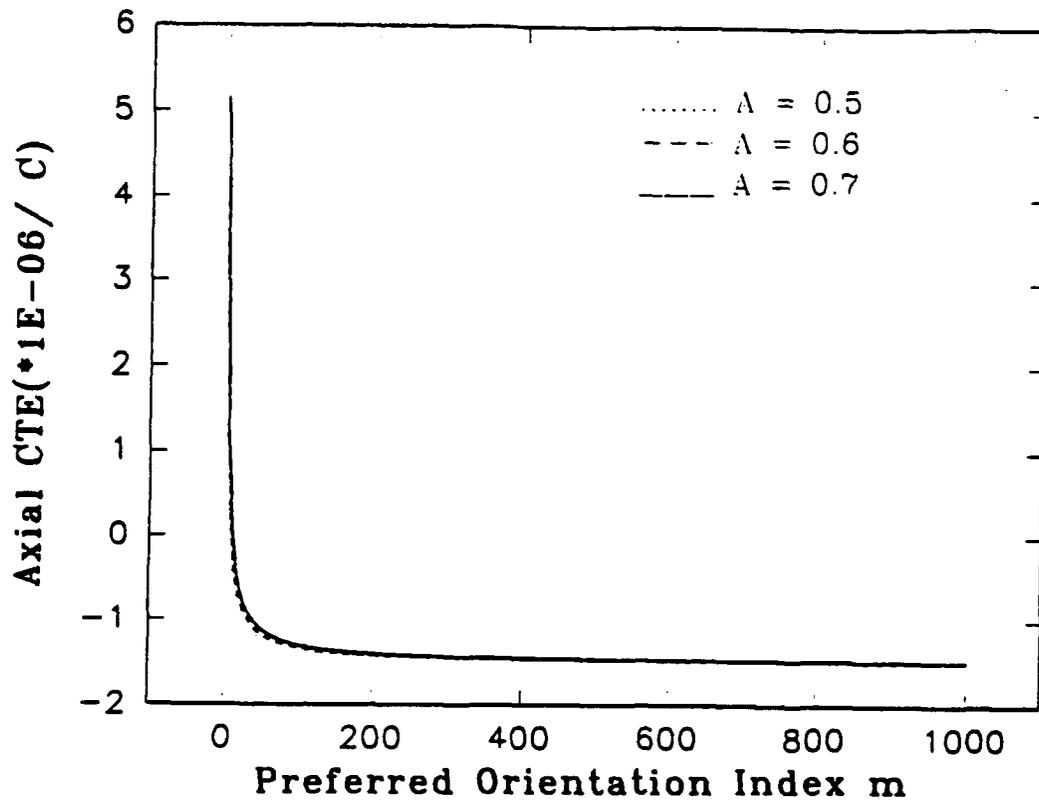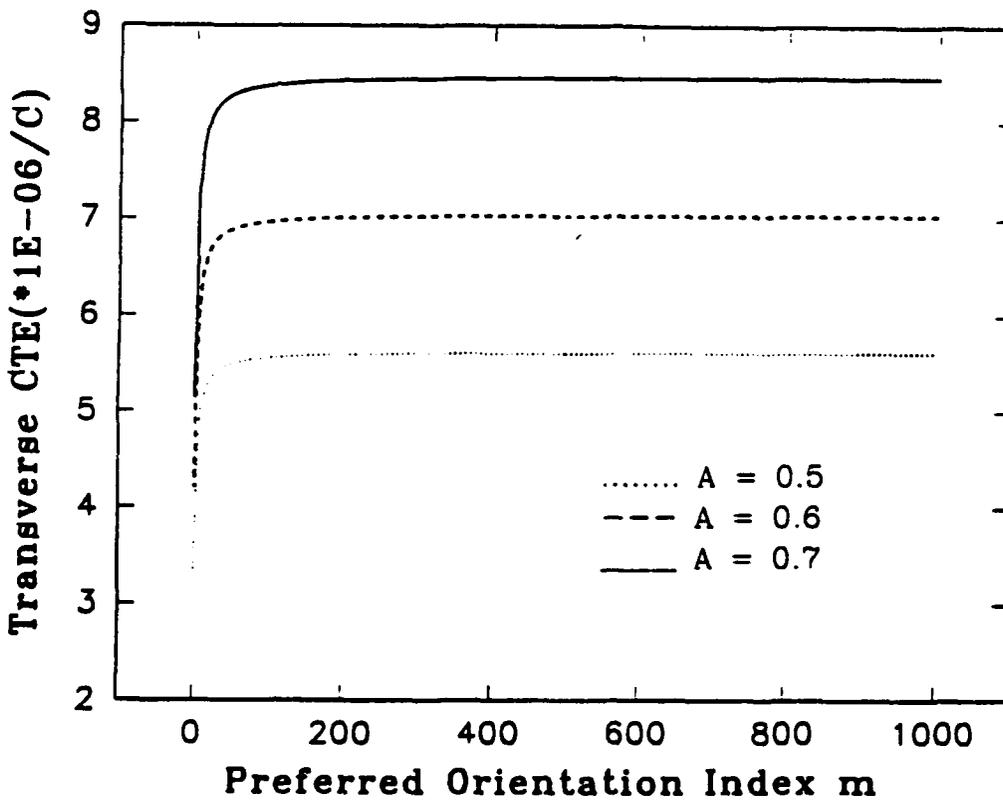
Fig. 3(a)   Axial CTE as a Function of Preferred Orientation.
     (b)   Transverse CTE as a Function of Preferred Orientation.

Fig. 4. Single Slit Fraunhofer Diffraction.
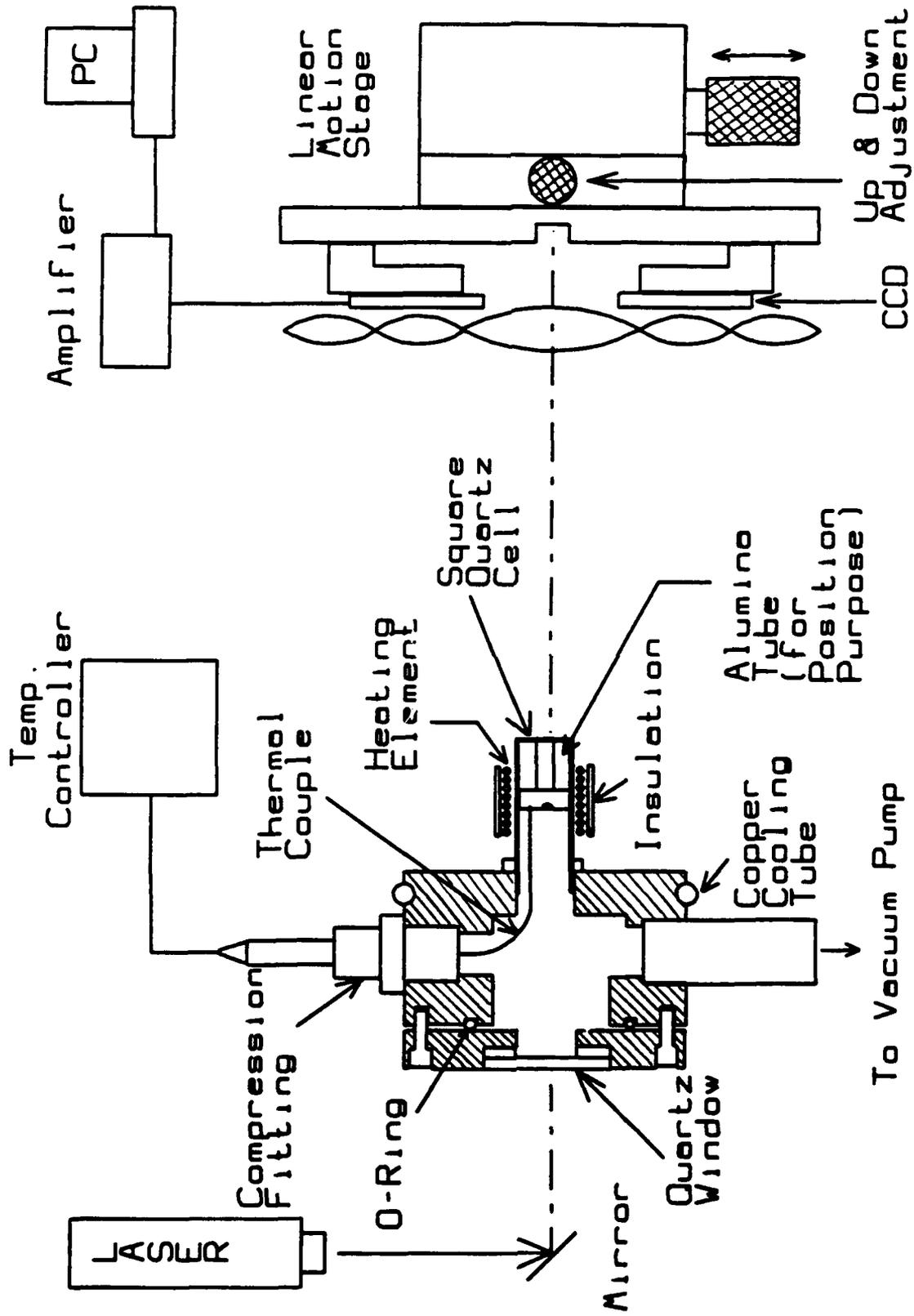
Fig. 5. Experimental Setup for Transverse CTE Measurement.
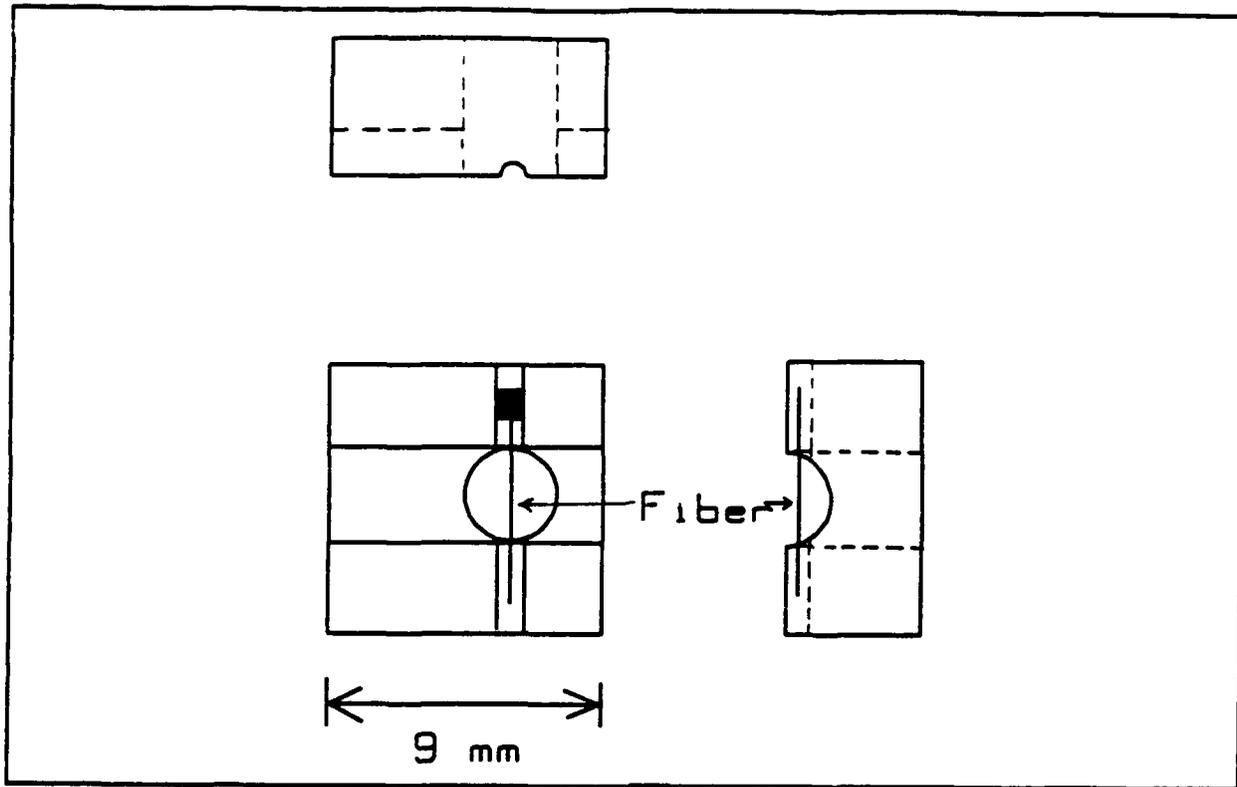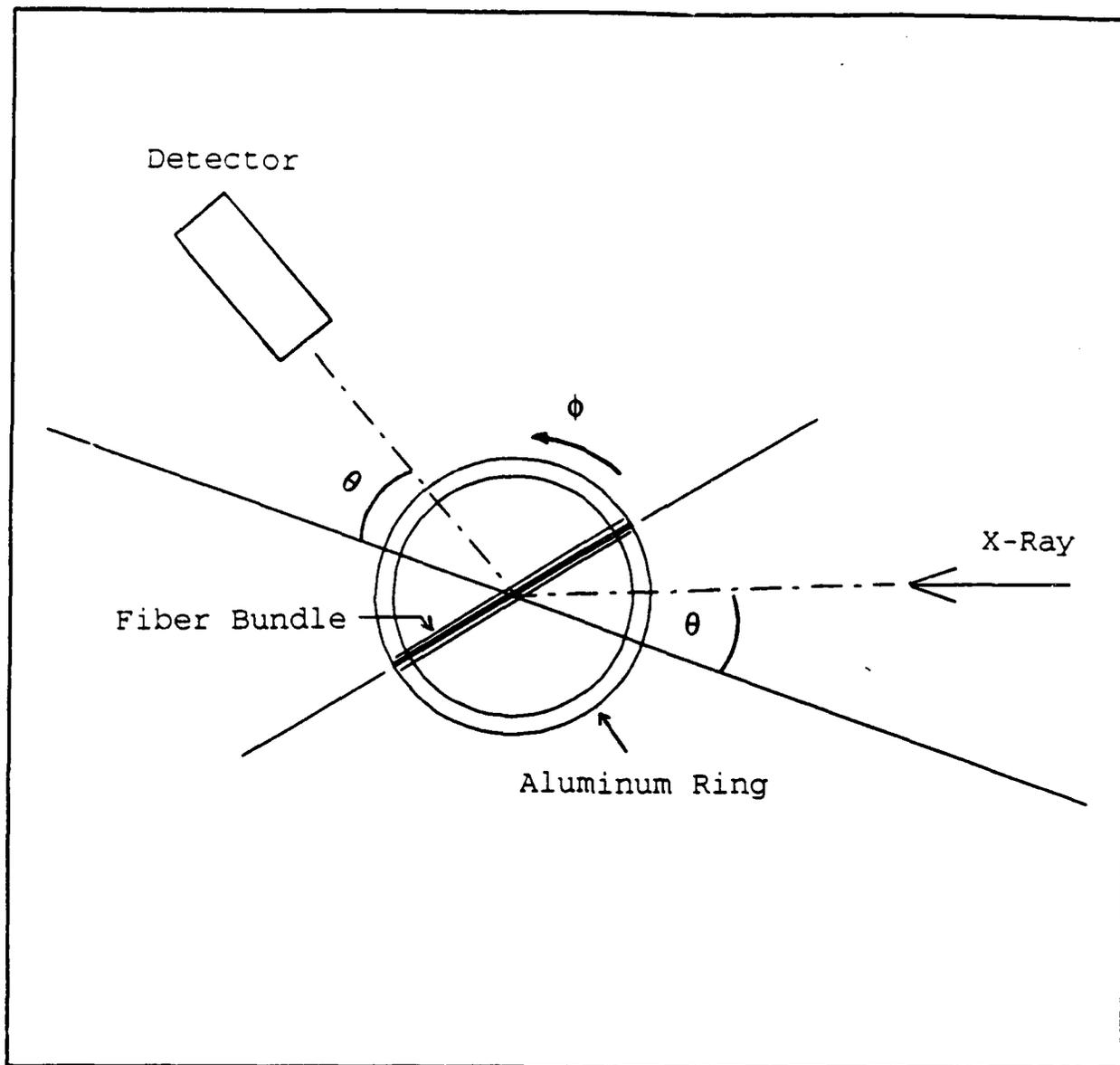
Fig. 6. A Graphite Piece Used for Fiber Mounting.
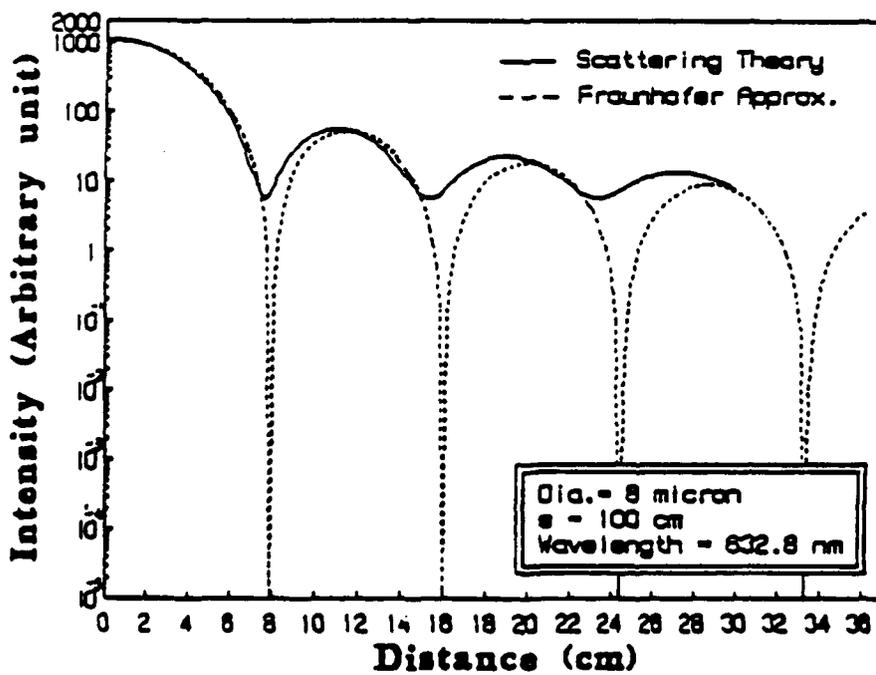
Fig. 7. Preferred Orientation Measurement by X-Ray
Diffraction.
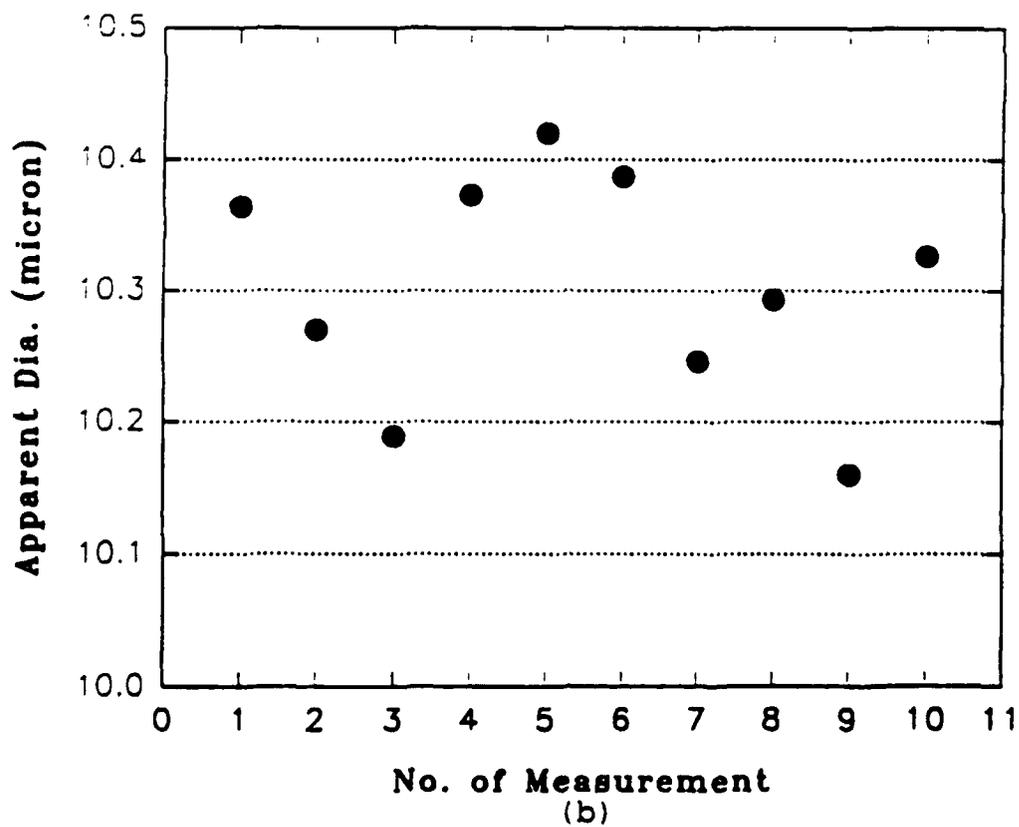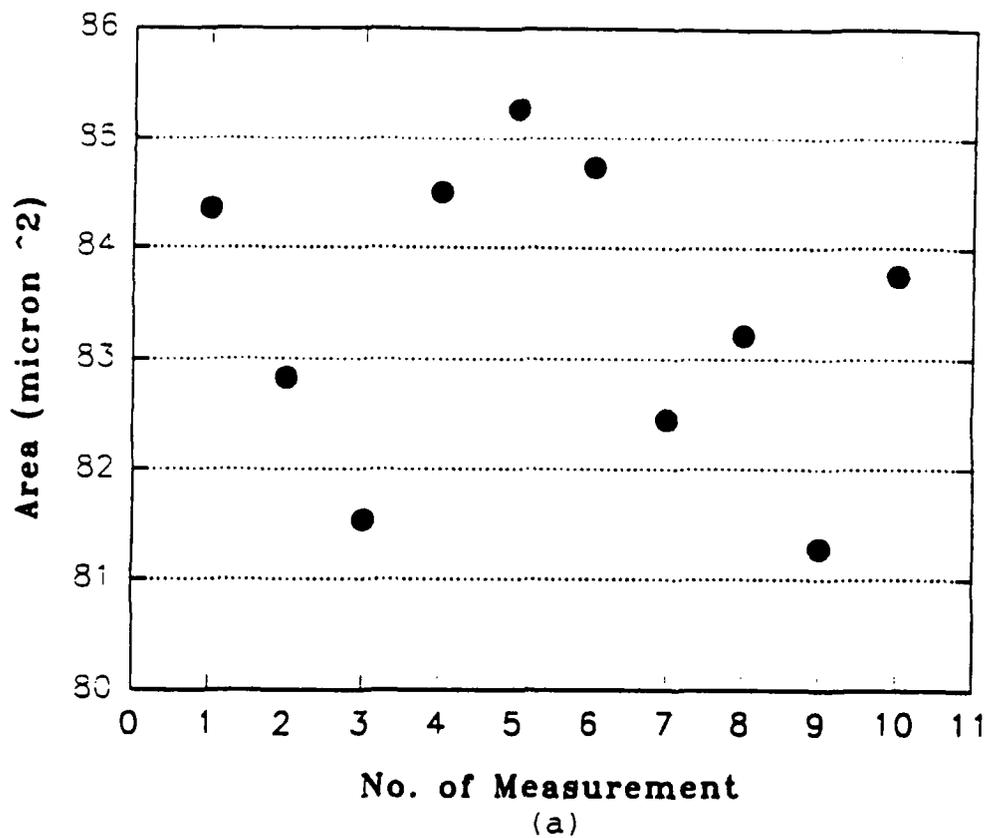
Fig. 8(a)   Variation of Cross-sectional Area along the Fiber Axis.
   (b)   Variation of Apparent Diameter along the Fiber Axis.
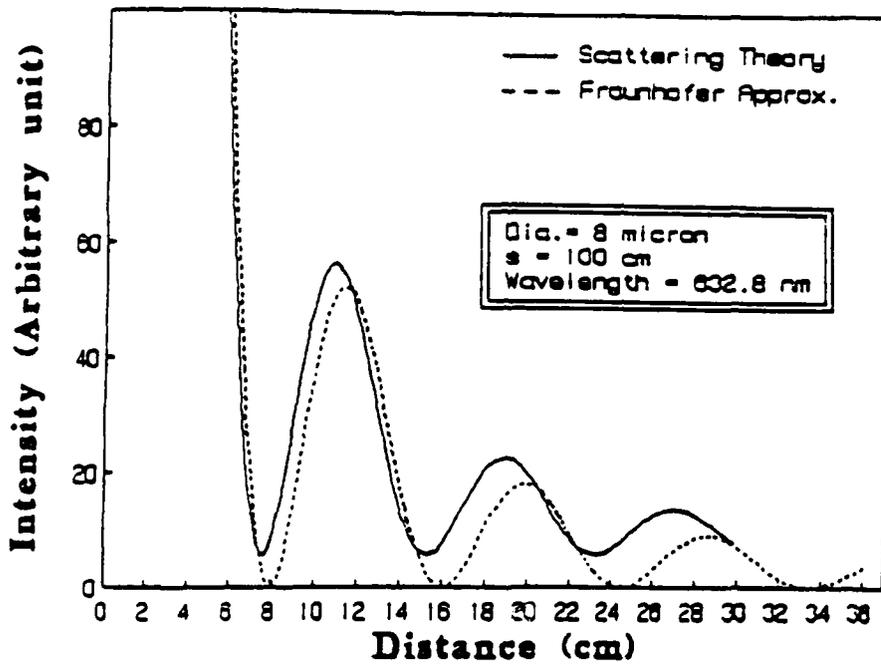
Fig. 9 (a)   Comparison Between Fraunhofer Diffraction
             and the Scattering Theory.
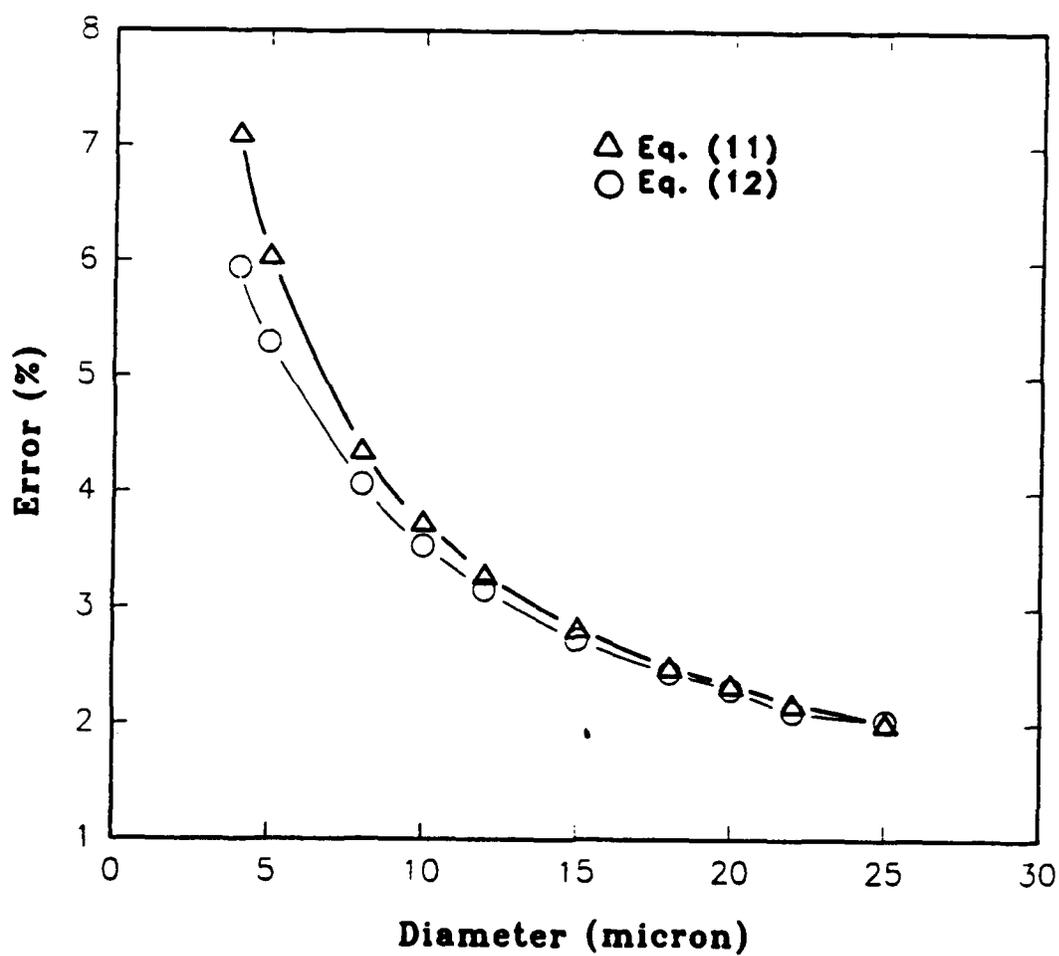   (b) As in (a) Except the Intensity Axis is in
             Log Scale.

Fig. 10. Percentage Error of Diameter Calculated from Fraunhofer Diffraction Approximation.
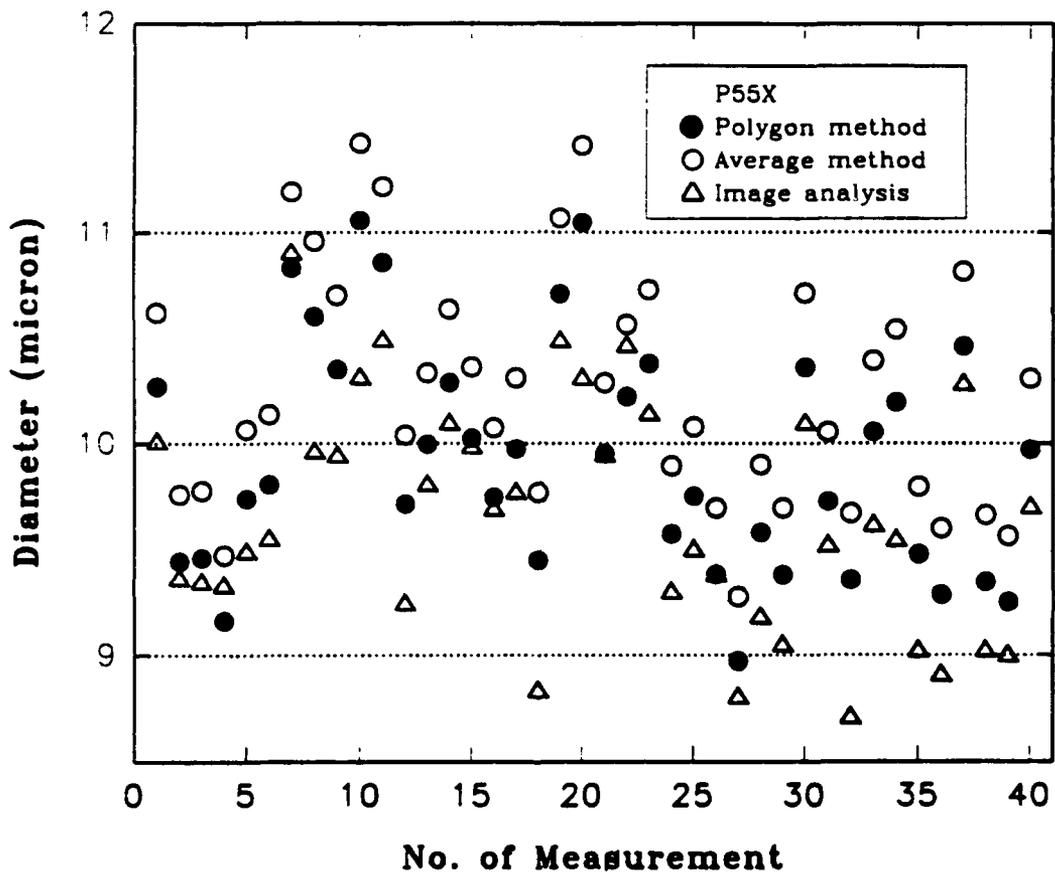
Fig. 11. Comparison of Diameter Measurement Using Laser Diffraction and Image Analysis.
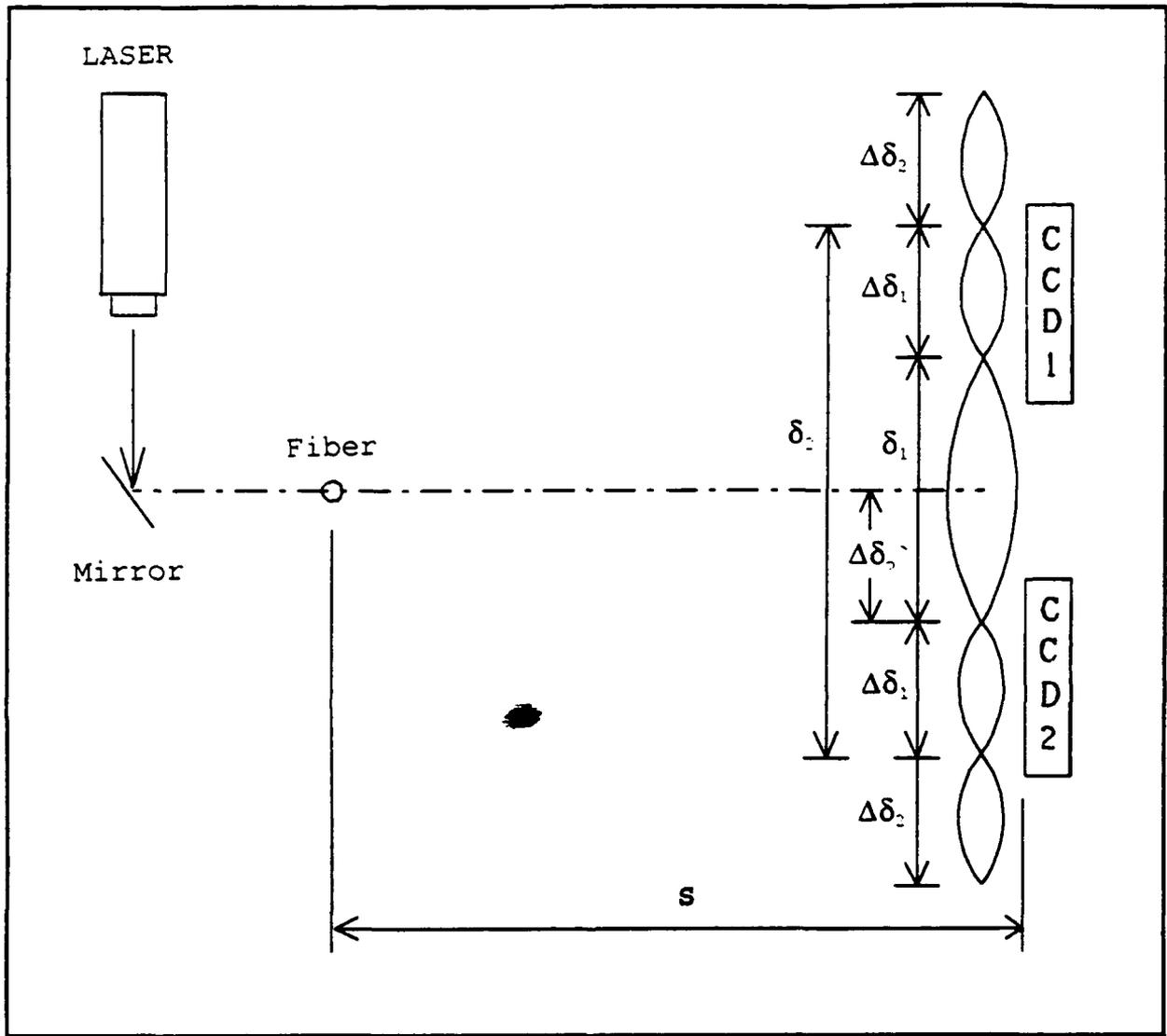
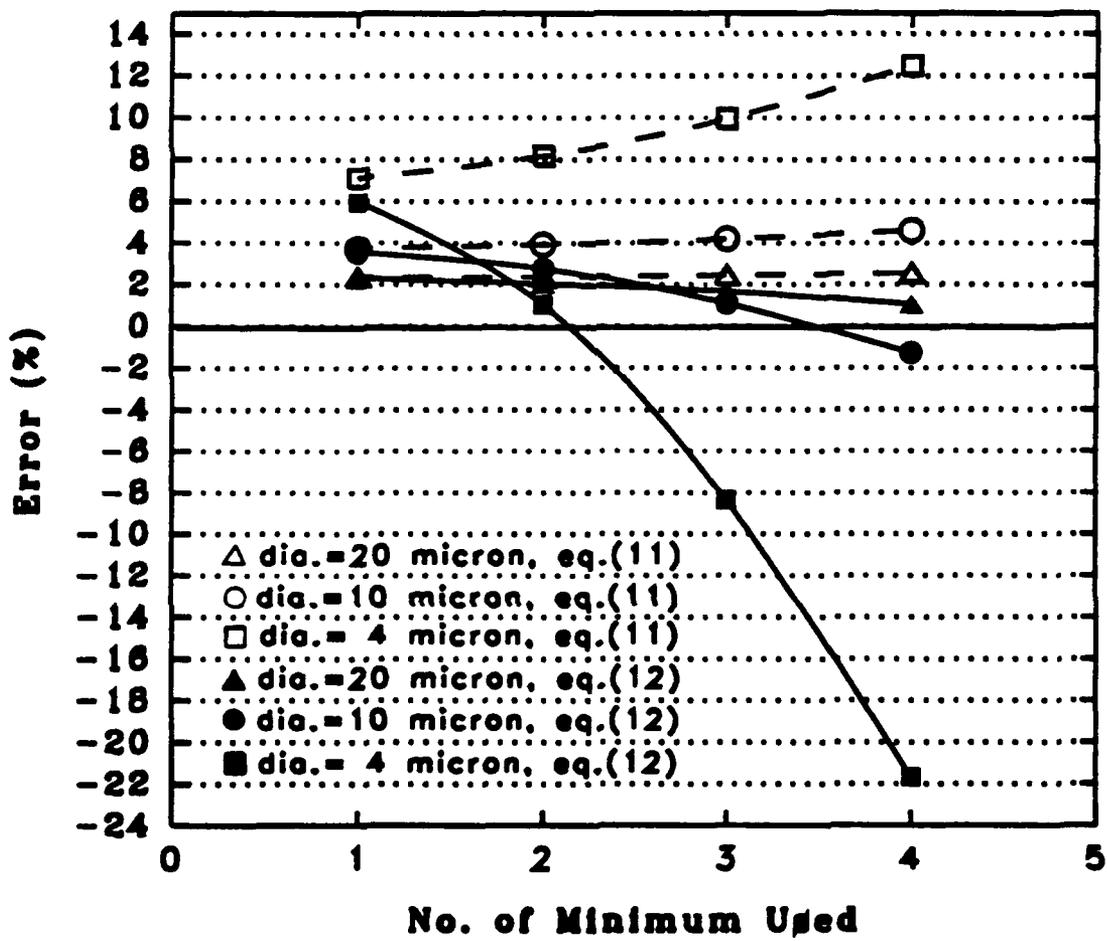Fig. 12. A Schematic Diagram of Laser Diffraction Experiment
Setup.

Fig. 13.   Percentage Error of Diameter Calculated from
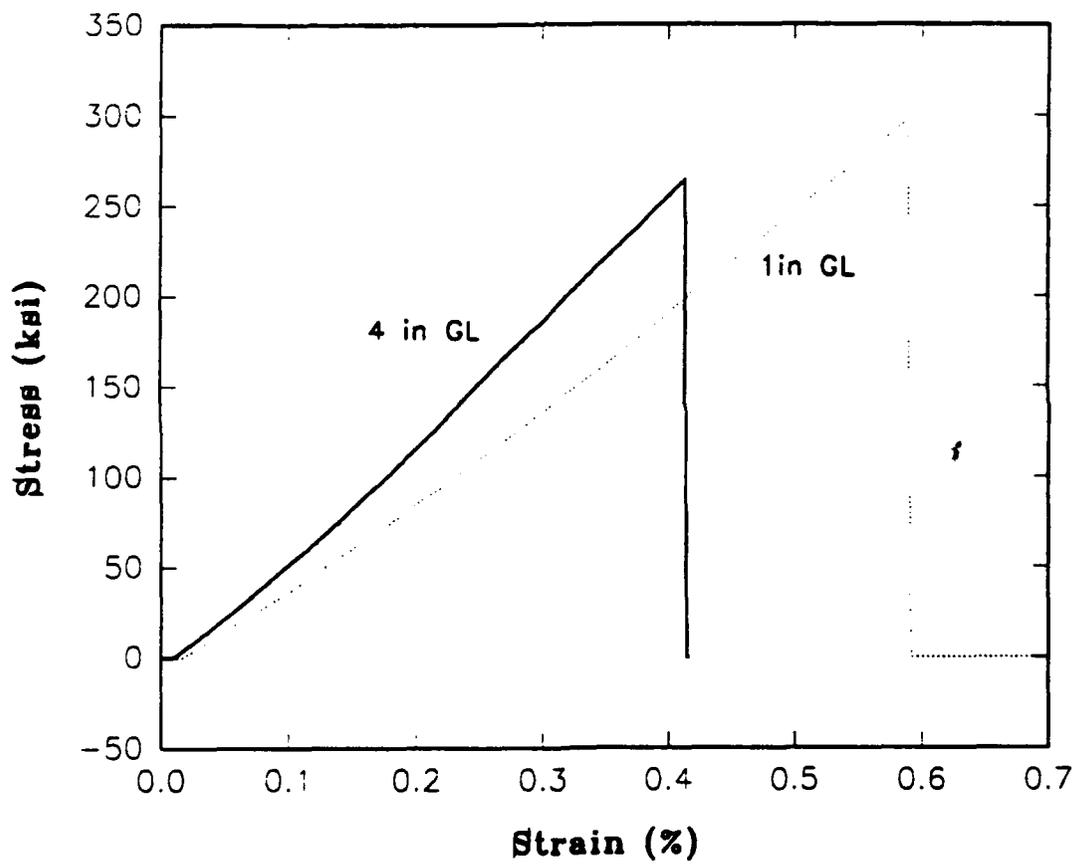Fraunhofer Diffraction Using Higher Order
Diffraction Minimum.

Fig. 14.   Stress–Strain Curve for P55x Fibers.

Fig. 15. SEM Photographs of Transverse Microstructure

                    (a) P25   (Flexural Failure)
                    (b) P55s   (Flexural Failure)
                    (c) P55x   (Tensile Failure)
                    (d) P75s   (Flexural Failure)
                    (e) P100   (Flexural Failure)
                    (f) P120x (Flexural Failure)
                    (g) P130x (Flexural Failure)
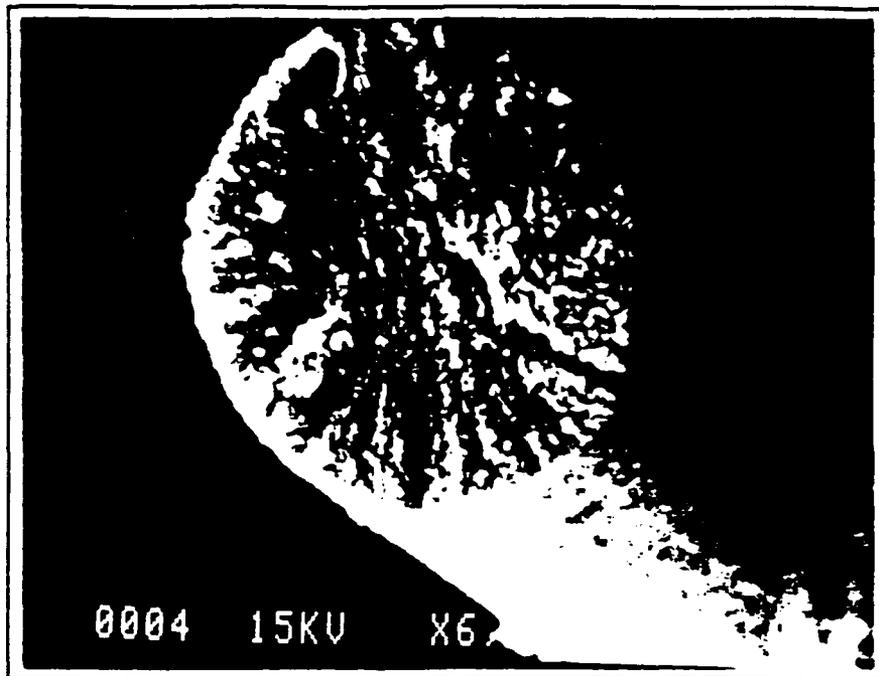   (h) P130x (Tensile Failure).

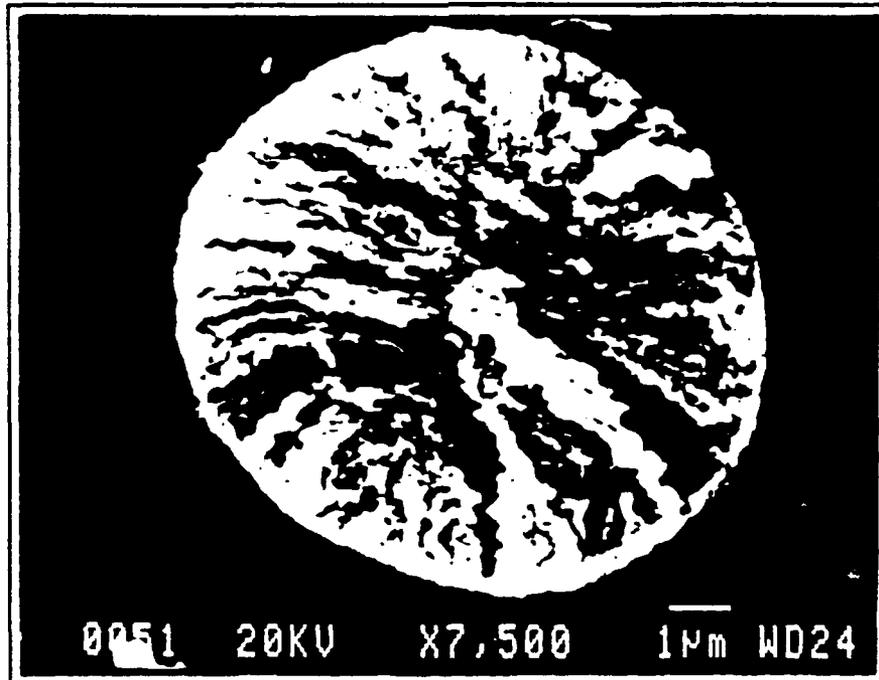(a) P25 (Flexural Failure)
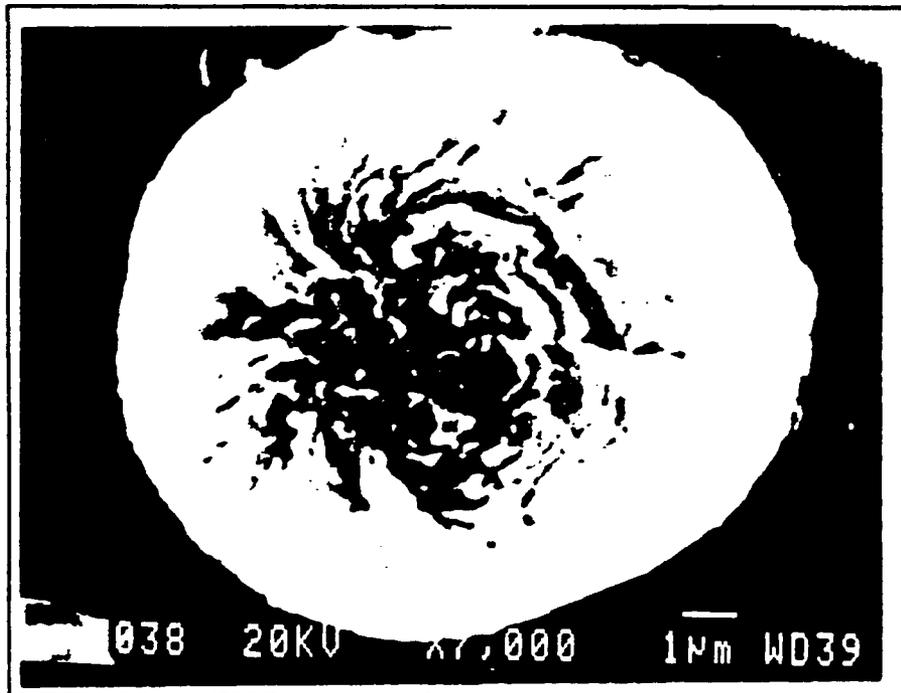
(b) P55s (Flexural Failure)

(c) P55x (Tensile Failure)

(d) P75s (Flexural Failure)

(e) P100 (Flexural Failure)
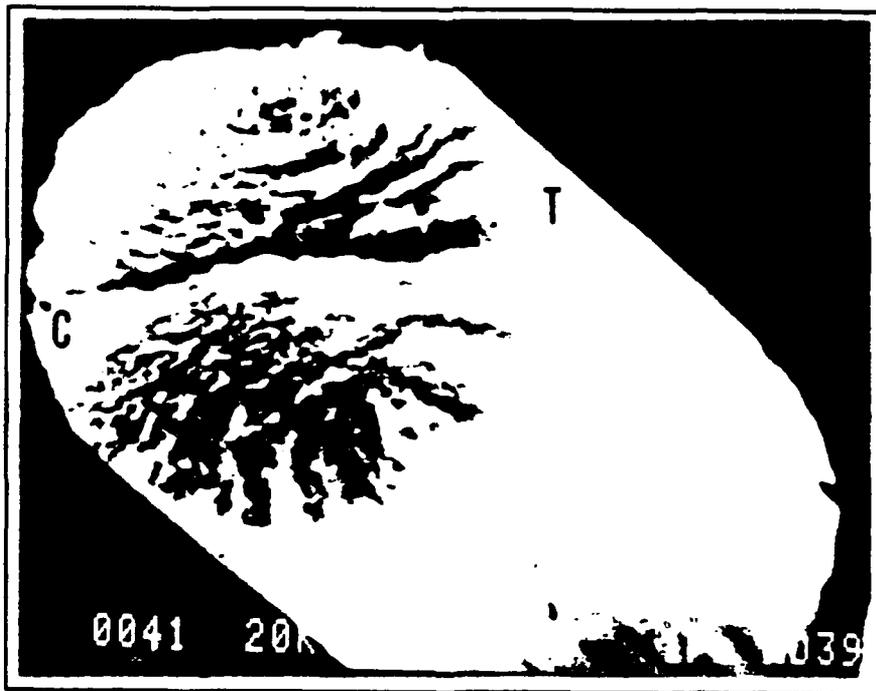
(d) P120x (Flexural Failure)
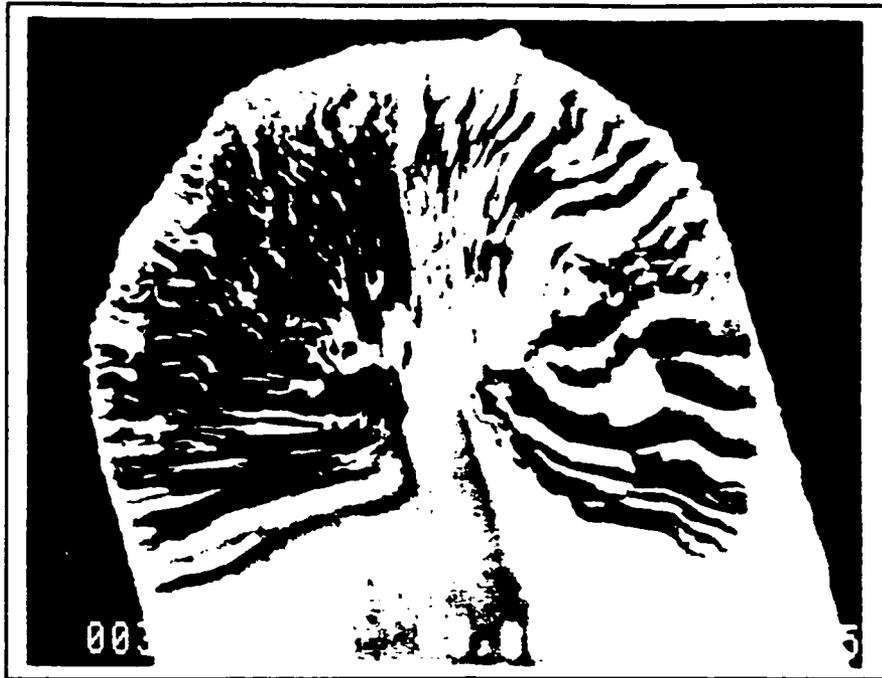
(g) P130x (Flexural Failure)
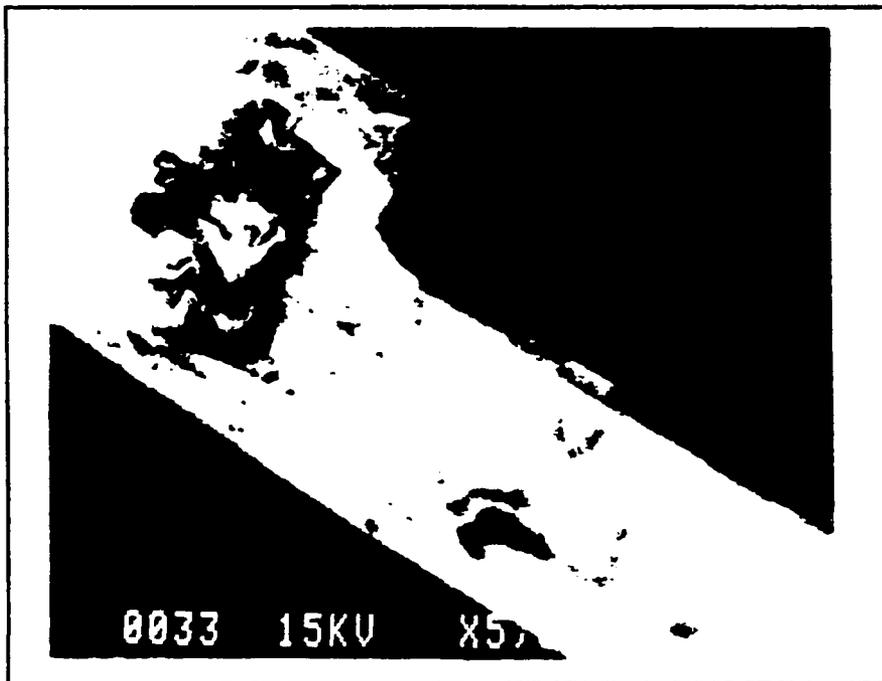
(h) P130x (Tensile Failure)
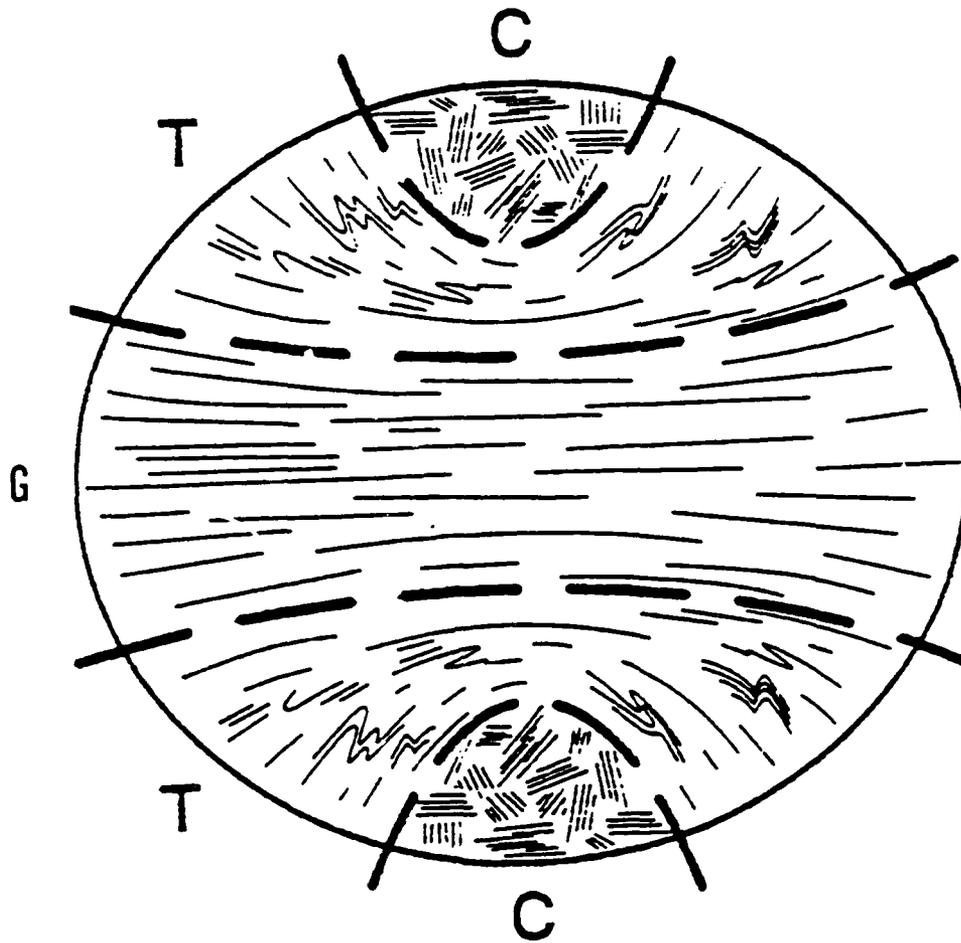
Fig. 16.   Schematic Transverse Microstructure of an
            Oriented-Core Fiber : C for Chaotic, G for
            Girdle, and T for Transitional Regions[50].
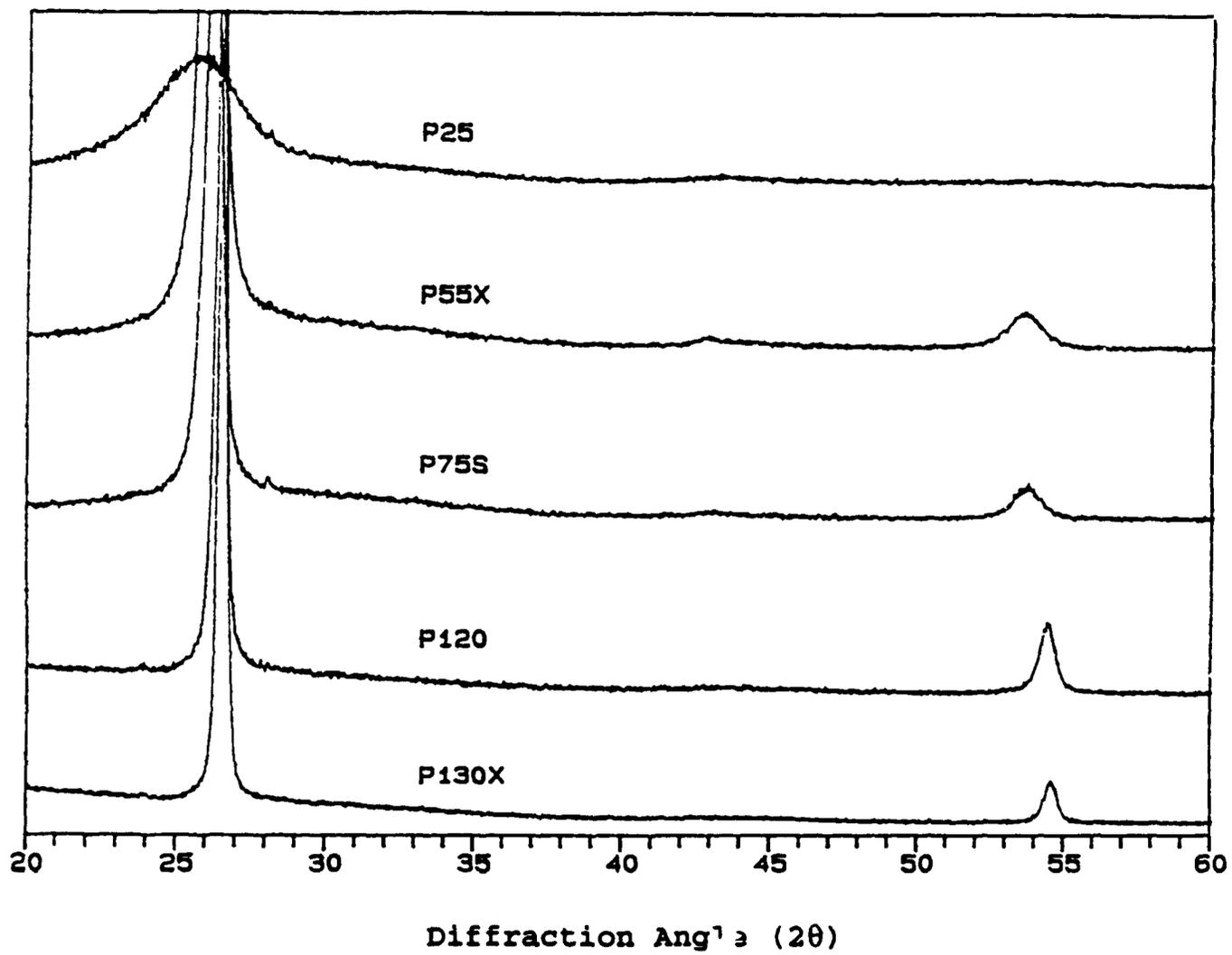
Fig. 17. X-Ray Diffractograms for Pitch-Based
Carbon Fibers.
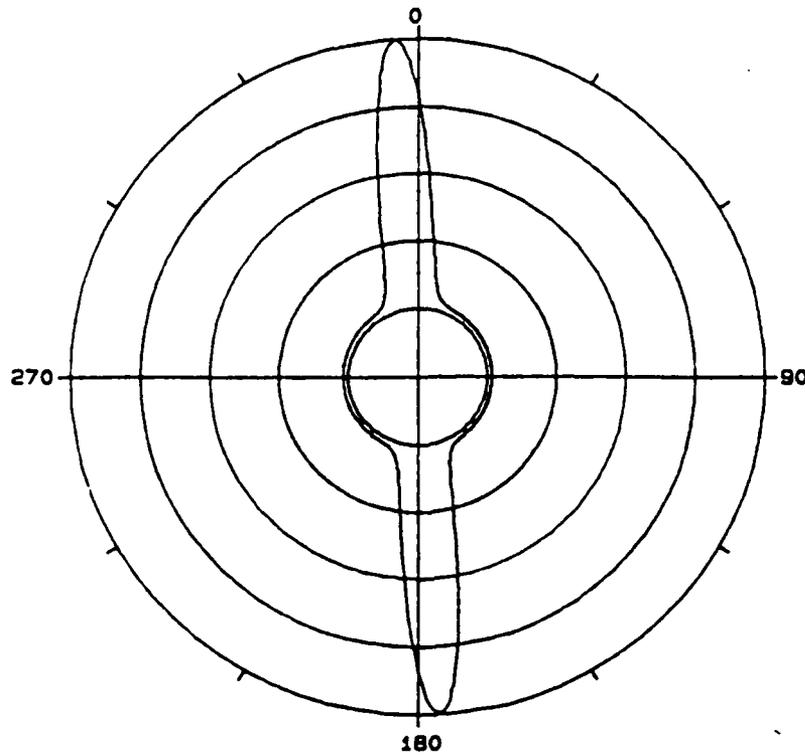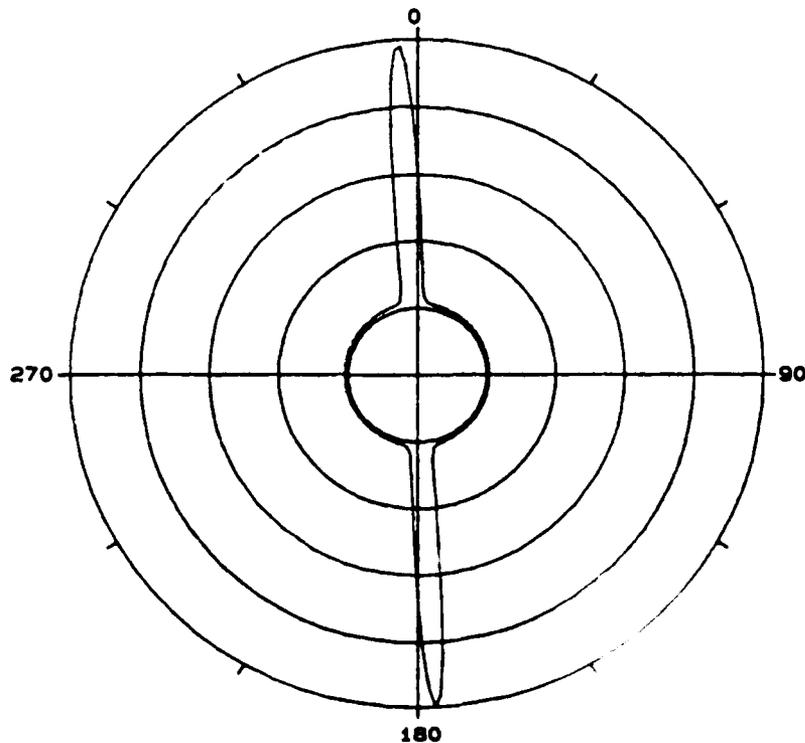
Fig. 18. Preferred Orientation Measurement of
(a) P55x Fiber
(b) P120 Fiber.
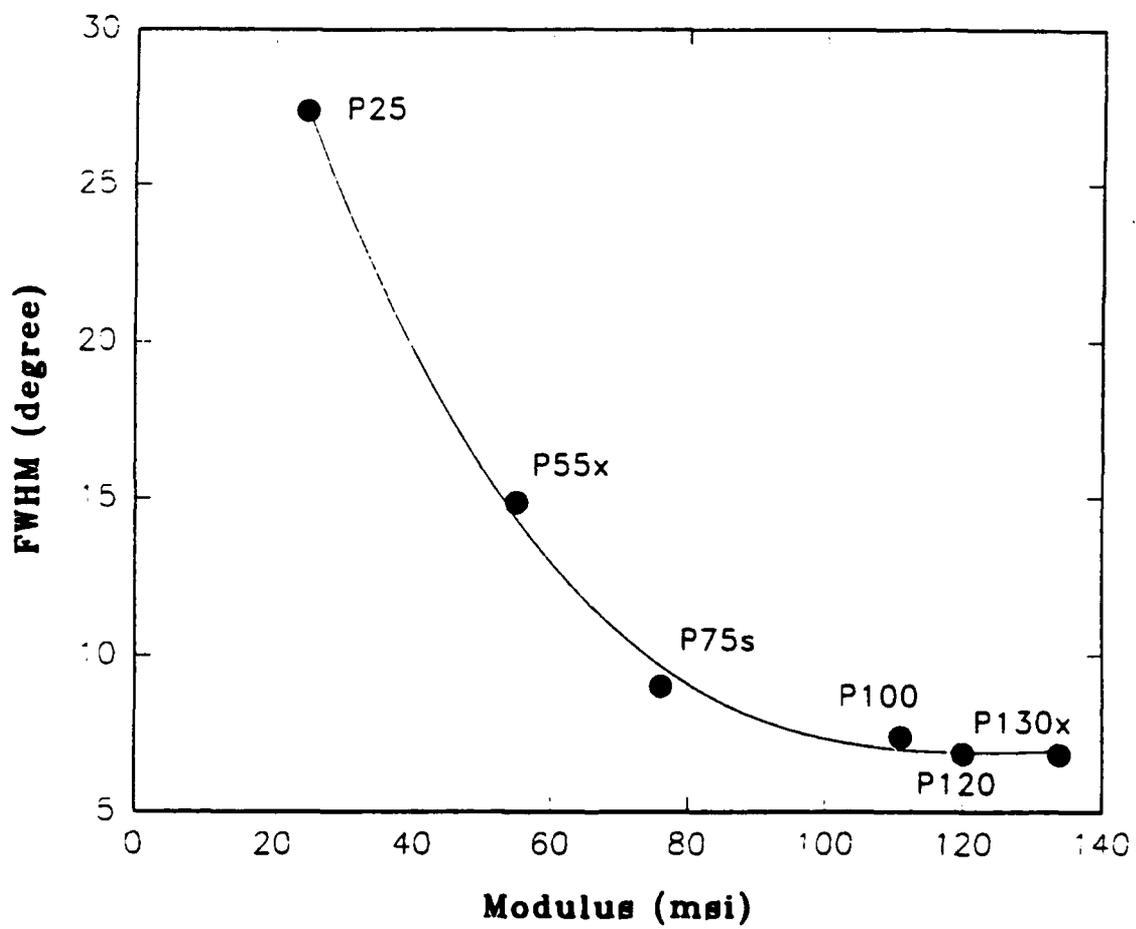
Fig. 19. Relationship between Modulus and Preferred Orientation.
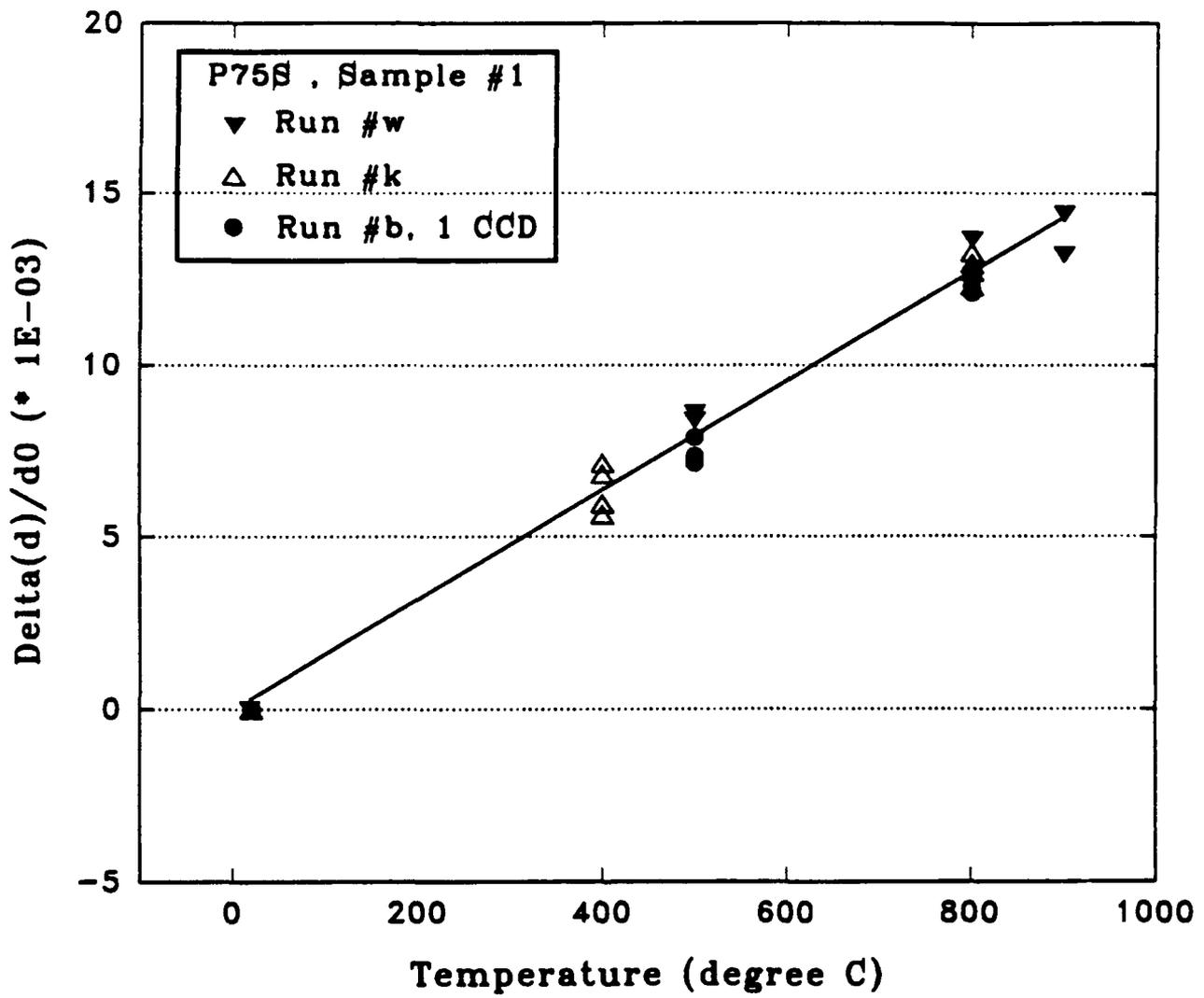
Fig. 20. Thermal Expansion of a P75s Fiber.
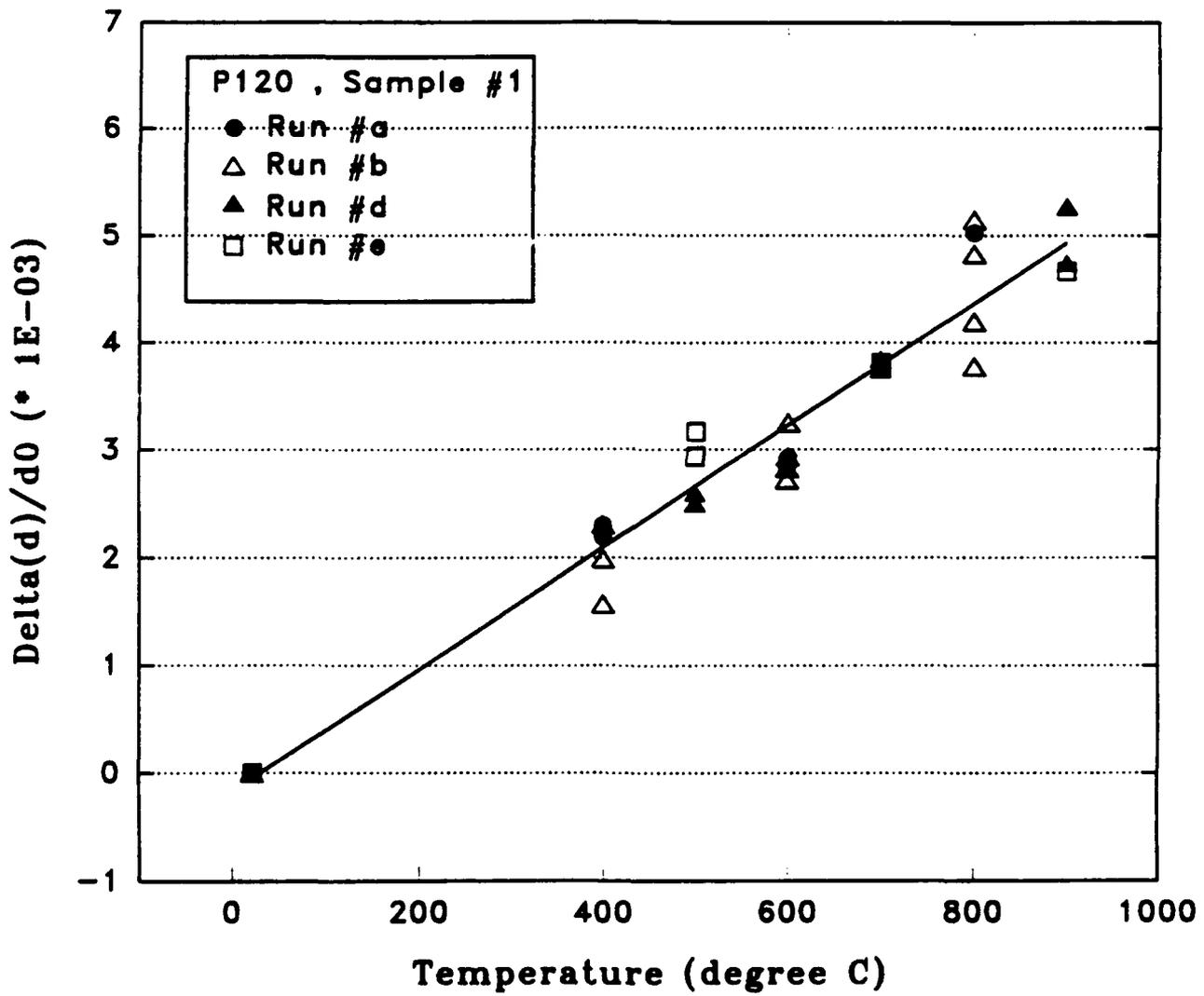
Fig. 21. Thermal Expansion of a P120 Fiber.
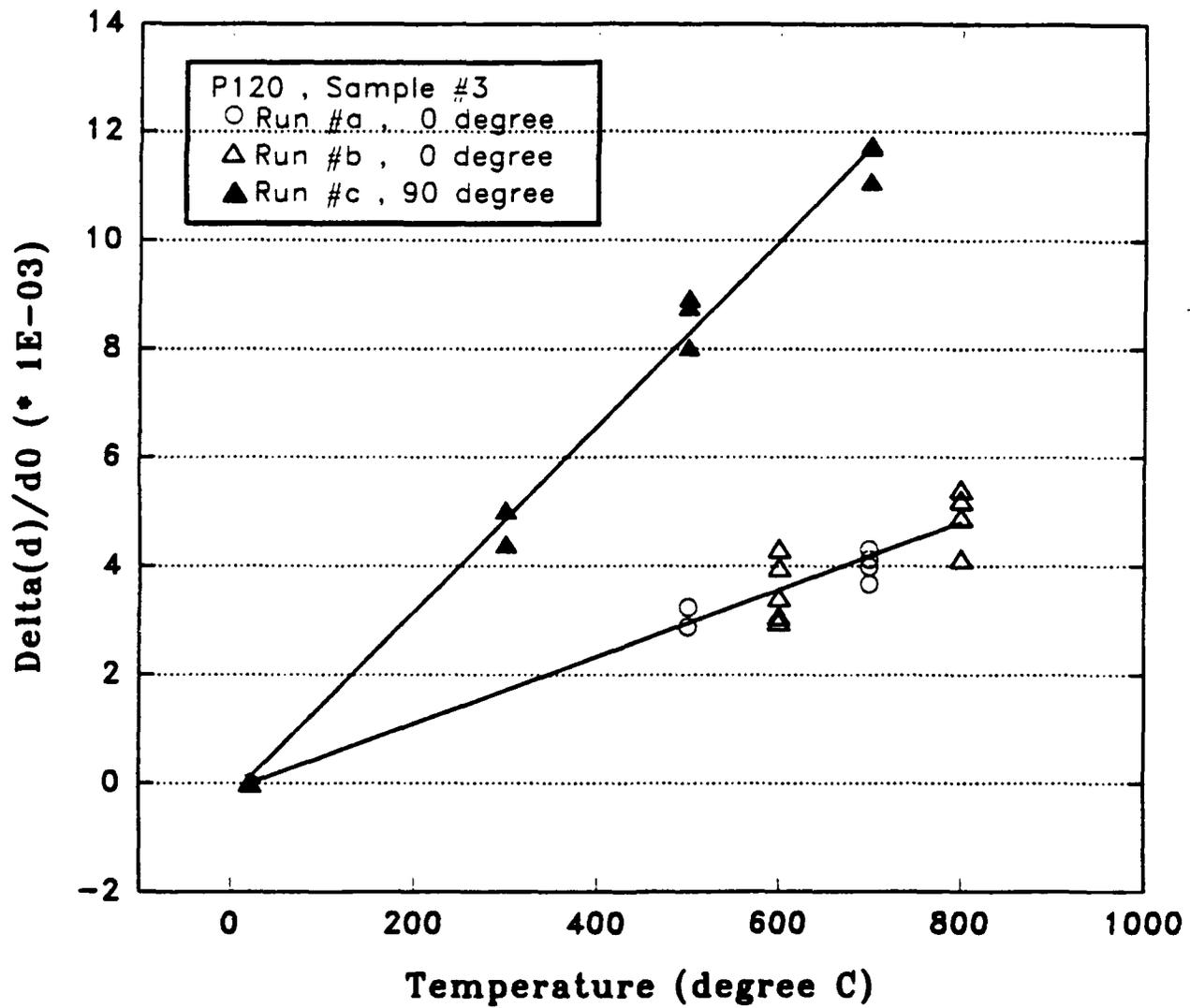
Fig. 22. Thermal Expansion of a P120 Fiber.
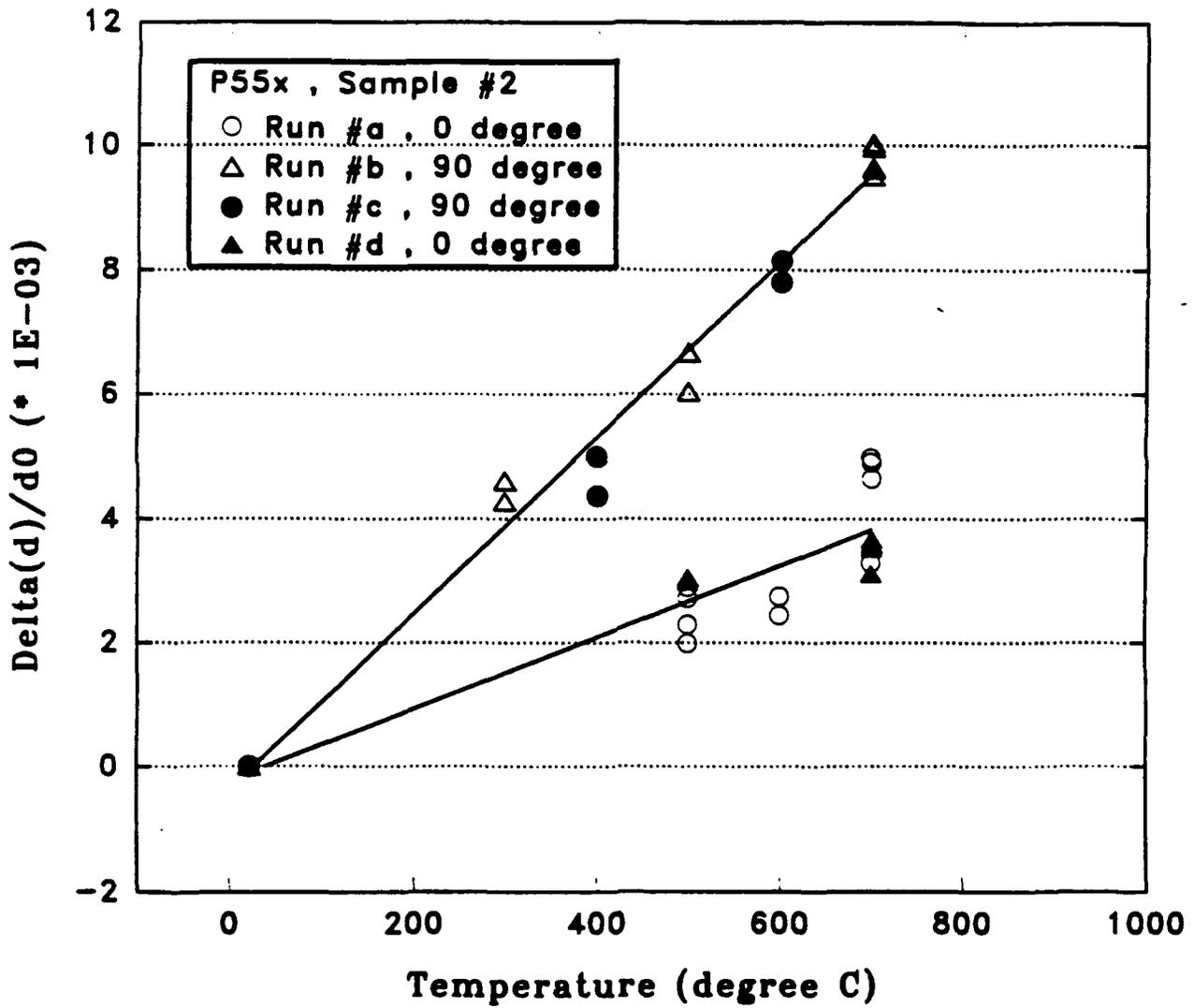
Fig. 23. Thermal Expansion of a P55x Fiber.
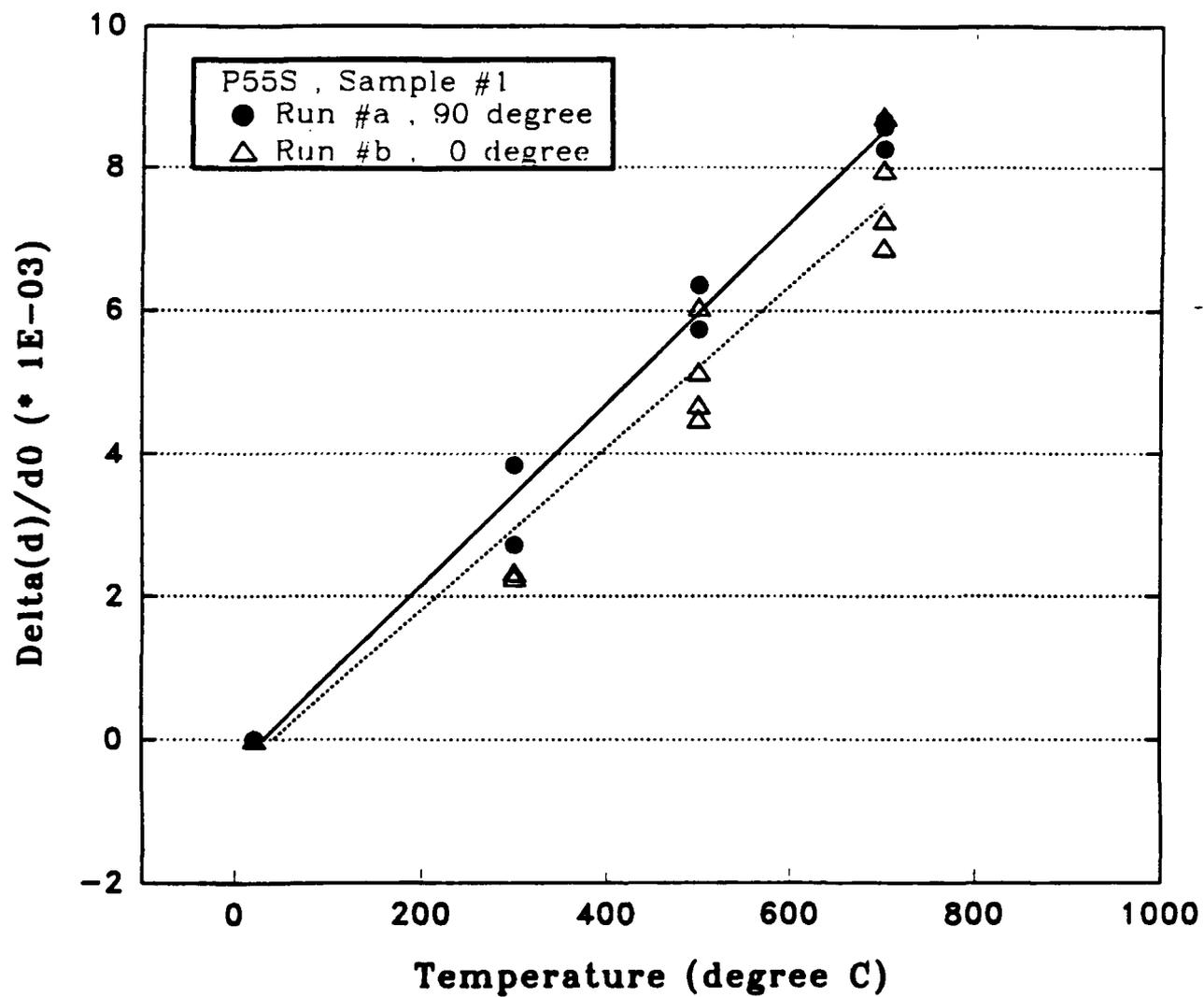
Fig. 24. Thermal Expansion of a P55s Fiber.
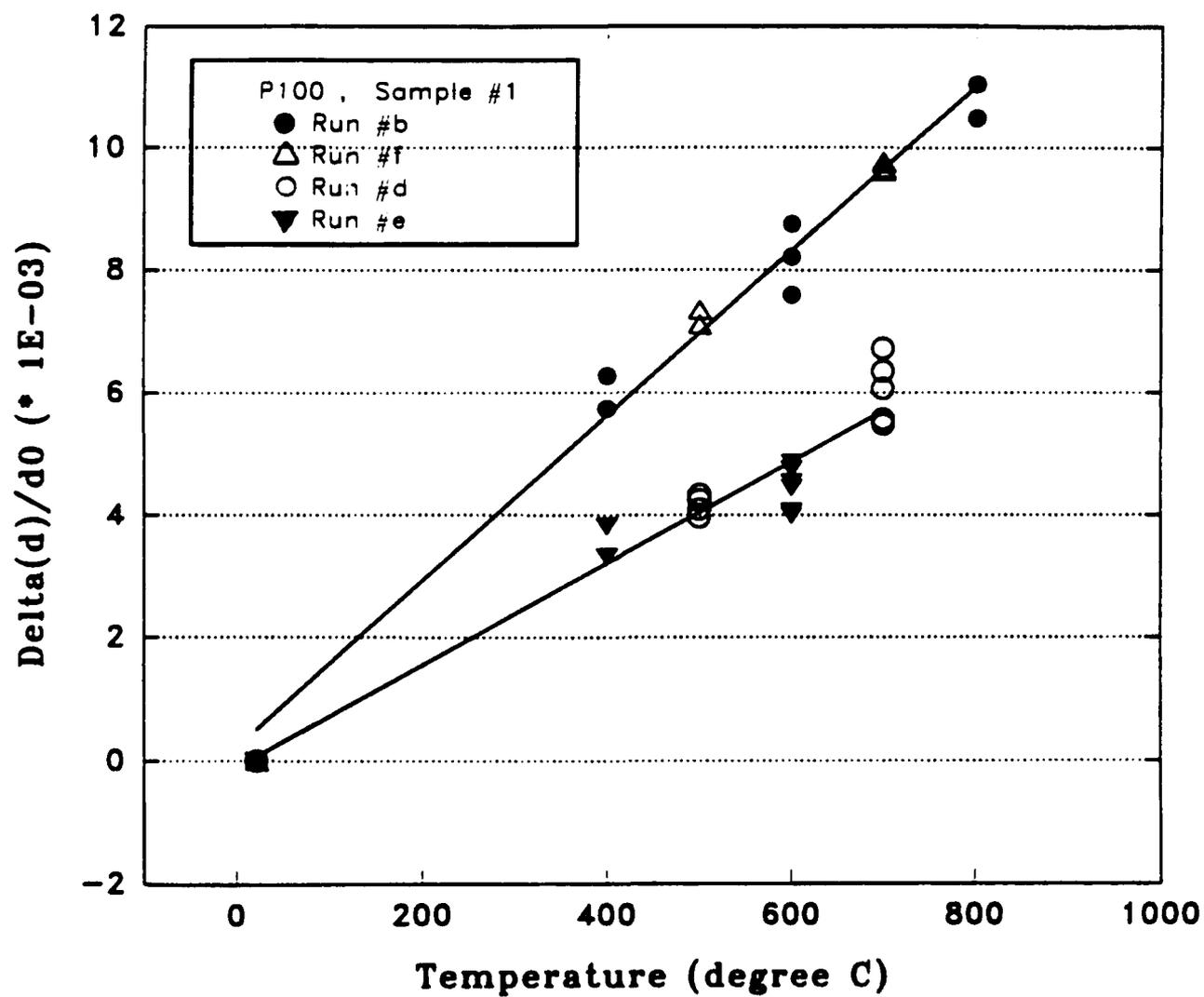
Fig. 25. Thermal Expansion of a P100 Fiber.

SIMPLIFIED DYNAMIC FINITE ELEMENT PROCESSING MODEL FOR THE CVD OF TiB$_2$ FIBERS

R. J. Diefendorf
Ceramic Engineering Department
Clemson University
Clemson, SC 29634-0907, USA

and

L. Mazlout
Advanced Innovative Technologies, Inc.
1223 Peoples Ave.
Troy, NY 12180, USA

Abstract

Titanium diboride appea   to be an attractive candidate for a high temperature reinforcing fiber for intermetallic matrix composites. Titanium diboride has high modulus, reasonably low density, a moderate thermal expansion coefficient and is thermodynamically compatible with a number of potential intermetallic matrices. However, there is considerable disagreement in the literature about its high temperature creep behavior. This work was performed to prepare TiB$_2$ fibers for evaluation of mechanical behavior using chemical vapor deposition. A simplified finite element, dynamic analysis model is used to describe the chemical vapor deposition of titanium diboride fibers in a cold wall reactor at atmospheric pressure. The gas mixture considered is titanium tetrachloride, boron trichloride, hydrogen, and hydrochloride. A description of the model and the computer program algorithm and subroutines are described. The application of this model to study the effect of deposition parameters on TiB$_2$ growth and the mechanism of rate limiting processes is discussed. For the mass transport rate limited process, the rate limiting mechanism changes from exhaustion of BCl$_3$ and TiCl$_4$ at high dilution, to slow BCl$_3$ and TiCl$_4$ diffusion at moderate concentrations, to slow HCl diffusion away from the fiber surface at high reaction concentrations.

Key words: Modeling, CVD, Titanium diboride, fibers, finite element.

1. Introduction

TiB$_2$ is a high temperature material with melting point near 3000°C. The retention of its room temperature strength and elastic modulus to temperatures as high as 1500°C[1] and the absence of any plastic deformation up to 1700°C[2-3] make it an excellent candidate for consideration as a creep resistant, high strength fiber. In addition, the relatively high CTE of TiB$_2$ of 8.7 X 10^{-6} °C^{-1} in the temperature range of 25 to 750°C[4] makes it an excellent match with low CTE metallics such as Inconel 903 and marginal with other higher CTE IMC matrices. In addition to physical compatibility, TiB$_2$ is chemically compatible with many intermetallics such as titanium aluminides, nickel aluminides, and molybdenum disilicide[5].

The properties of TiB$_2$ depend strongly on the process used and in the case of CVD on the process parameters and deposit quality. For example, the elastic modulus is reported to be as low as 261 GPa[6] and as high as 810 GPa[7]. Similarly the room temperature strength can be as high as 4.9GPa[7] for chemically vapor deposited TiB$_2$ and much lower for differently processed TiB$_2$[2,8-11]. A third example is the creep resistance. At General Atomic creep was registered at temperatures as low as 800°C while at Union Carbide creep was unmeasurable to 1450°C. Finally, the stability of chemically vapor deposited TiB$_2$ depends strongly on the deposition parameters.

These considerations highlight the importance of the processing method used to produce the fiber. Given the power and versatility of CVD, attempts to develop TiB$_2$ fibers were made only

2

represents a good medium for modeling and understanding what happens in the gas stream on a molecular level. The modeling is compared to experimental runs that were made to produce TiB_2 fibers. The results and discussion presented in this paper are geared towards widening this understanding so that process optimization is achieved with the least experimental tests. The structure and properties of the TiB_2 fiber will be presented in a subsequent paper.

2. Description of the model

The model consists of dividing the vertical reactor into equally sized horizontal disks from top to bottom, each extending from the fiber at its axis to the inside of the tube, Figure 1. Each of these disks is in turn divided into concentric rings, with the first ring located around the fiber and the last ring adjacent to the tube wall. Any cross section taken through the fiber axis would result in the same element architecture of Figure 1, regardless of the orientation θ. Therefore, the model is treated as a 2-D model. The reactant gases enter the reactor at the top and exit from the bottom. The following assumptions are made in this model:

a.   The gas flows with a uniform velocity across the tube, ie. plug flow.

b.   The fiber diameter is very small compared to the first ring diameter.

c.   The reactant gases are perfectly mixed as they enter the reactor.

4

temperature. The SOLVESYST subroutine then solves for the gas fluxes and the new gas concentrations.

The above steps covering all disks are repeated for a time period equal to the residence time of the fiber segment inside disk#1. Then the fiber is moved down the reactor through a step equals to the disk thickness, and the same procedure mentioned above is repeated. This goes on until the top fiber segment that started at disk#1 exits the reactor. At this stage, steady state conditions are assumed to have been established, and the program is ended. The following section describes the function of each subroutine in detail.

3.2. Subroutine FIBERTEMP

This subroutine calculates the fiber and tube wall temperatures given the fiber diameter, heating power, gas average thermal conductivity, convective heat coefficient (h) outside the tube, and tube diameter. The computations are based on two equations.

Fourier equation:

$$Q = \frac{2 \pi k L (T_f - T_v)}{\ln(\frac{D}{d})} \tag{1}$$

where Q = heat input to the fiber

k = gas average thermal conductivity

L = Heated fiber length

Substituting equation (2) and rearranging:

$$T_f = (1+m) \frac{\ln(\frac{D}{d})}{\ln(\frac{D}{d_{initial}})} (T_{f,initial} - T_{v,initial}) + T_\infty \qquad (3)$$

where d is the fiber diameter resulting in a fiber temperature T_f, $d_{f,initial}$ is the inlet fiber diameter which is equal to the substrate diameter, $T_{v,initial}$ is the wall temperature found from equation (2), and T_∞ is room temperature (293°K).

3.3. Subroutine TEMPGRAD

For a specific disk i, this subroutine calculates the temperature at each ring assuming an exponential temperature drop of 100(1-w)% of $(T_f - T_v)$ at a distance equal to fD/2 where w and f have assumed values of 0.5 and 0.1. w and f are scaling factors between 0 and 1. This translates into a 50% temperature drop a distance from the fiber equal to one tenth the tube radius. The governing equation is given by:

$$T_f = (T_f - T_v) \exp(2f\frac{r}{D \ln(w)}) + T_v \qquad (4)$$

where r is the radial distance from the fiber. This subroutine also calculates the distance, reff, from the fiber where the temperature equals 750°C -the thermodynamic temperature at which the Gibbs free energy of formation of TiB_2 from H_2, BCl_3, and $TiCl_4$

8

$$\nabla x_i = \sum_{j=1}^{n} \frac{1}{c \, D_{ij}} \, (x_i \, N_j - x_j \, N_i) \qquad (5)$$

where

n = number of gaseous species considered (n=4)

x_i = mole concentration of specie i (mol/m^3)

N_i = net flux of specie i relative to stationary coordinates ($mol/sec.m^2$)

c = total species concentration in the reactor (mol/m^3)

D_{ij} = Binary diffusion coefficient of species i and j (m^2/sec)

Subroutine DIFFCOEF calculates the diffusion coefficients D_{ij} as a function of ring temperature. In order to provide the program with a simple function of D_{ij} as a function of temperature to minimize computing time it was necessary to simplify equation (6) to a polynomial.

$$D_{ij} = D_{AB} = 0.0018583 \sqrt{\frac{1}{M_A} + \frac{1}{M_B}} \; \frac{T^{3/2} \, f_D}{P \, \sigma_{AB}^2 \, \Omega_D} \qquad (6)$$

where

D_{AB} = diffusivity (m^2/sec)

M_A = molecular weight of specie A

M_B = molecular weight of specie B

P = total pressure (1 atm)

σ_{AB} = collision diameter (Å) = $(\sigma_{AB} + \sigma_{AB})/2$

f_D = a small second order correction factor, which is close to

iii. Finally, the value of Ω_D, as a function of kT/e_o from the literature[13], is fit to the following equation:

$$\Omega_D = \frac{\exp(-0.105 \, \frac{kT}{e_o})}{0.28 + \frac{kT}{e_o}} - 0.0035 \, \frac{kT}{e_o} + 0.744 \qquad (9)$$

Tables 1 and 2 summarize the values of σ and e_o/k for the different species considered as well as the diffusivity of each one. Finally, subroutine DIFFCOEF calculates a modified diffusivity $K_{ij}=1/(2cD_{ij})$ which will be used by the subroutine SOLVESYST and will lead to further reduction in computing time.

3.6. Subroutine SOLVESYST

For the four gaseous species considered and diffusion between rings j and j+1 in disk i the Stephan-Maxwell equation (5) reduces to a set of four equations with four unknowns. To let the computer solve this system of equations for the unknowns N_1, N_2, N_3, and N_4 would increase the execution time drastically. Since this system involves only four equations it was solved analytically for N_i's.

The function of this subroutine is to calculate the amount of each specie transferred between the two adjacent rings during the time step TSTEP. TSTEP is calculated from real physical parameters, and hence it is not picked at random. The time the gas spends in each disk, TSPD, equals the total time the gas spends in the reactor divided by the number of disks. The total time is

12

rings across the deposition tube. The number of iterations required increases quadratically with the number of rings according to:

$$niter = 0.288 \, N_r^2 - 2.162 \, N_r + 12.77$$

In order to appreciate the length of time it takes the program to go through one run the real running time (not the CPU time) is plotted versus the number of rings for a fiber speed of 190m/min (7480in/min) in an IBM RISC Powerstation 320, Figure 4. To duplicate the experimental runs which are typically performed at fiber speeds around .28 m/min (11in/min) and a tube diameter of one inch -requiring 40 rings- 152 days of running time are needed. The same program with identical initial conditions was run on the University of California Cray supercomputer, and it was found to be only eleven times faster than the RISC workstation.

The times mentioned above are based on computational convergence. For physical convergence to be achieved even smaller elements (disks and rings) and a larger number of iterations must be used. This in turn increases the running time even further, and exponentially.

The above time constraints put obvious limitations on duplicating experimental runs. Therefore, the following section will focus mainly on the qualitative aspects of the results. Although, quantitative analysis with respect to species concentration gradients is possible.

concentrations occur in the top quarter of the tube. This matches perfectly with what was observed in all experiments, namely, more than 60% of the TiB_2 deposit occurs in the top quarter of the tube. A practical benefit from these conclusions is that one may inject BCl_3 and $TiCl_4$ at different locations along the tube to increase the deposition rate. However, experimental results[12] showed that turbulence must be avoided so that a smooth and strong coating deposits.

The results pertaining to the formation of HCl also give a good insight into the process characteristics. By looking at the HCl concentration profiles, at first look, one cannot rule out the possibility of HCl's diffusion away from the fiber being a rate limiting step in the deposition of TiB_2. The fact that curve 5 is above curve 1 across the entire tube, and especially near the fiber, suggests that HCl forms at a faster rate than it diffuses to the bulk stream. This build up may be preventing BCl_3 and $TiCl_4$ molecules from diffusing to the region surrounding the fiber. Hence, HCl diffusion would be the real limiting step. This argument cannot be correct because as the HCl concentration approaches uniformity, BCl_3 and $TiCl_4$ molecules still cannot diffuse to the fiber. Therefore, the initial net build up of HCl near the fiber must be caused by the fast TiB_2 deposition rate in the top quarter of the tube rather than by a low diffusion rate to the bulk stream.

The local minimum in hydrogen concentration at the inlet of the reactor suggests again that the hydrogen responds very fast to what happens near the fiber, but not fast enough for the molecules

16

Considering the ratio of fiber speeds of about 40 and the fact that most deposition occurs in the top quarter of the reactor, the final fiber diameter predicted by the model should be even smaller. This means that the model overestimates the overall deposition rate. There are a few reasons why this may be true. First, it is assumed that the thermodynamic efficiency is 100%. Second, this efficiency is valid at all temperatures inside the previously mentioned (section 3.3) cylinder of radius $reff$; ie. all the BCl_3 and $TiCl_4$ molecules satisfying the two-to-one ratio condition react to form TiB_2, regardless of how close to 750°C the temperature is. This problem can be fixed by integrating the SOLGASMIX program in the model. Finally, $TiCl_3$ which is a major by-product of the system has not been taken into account. The formation of large amounts of $TiCl_3$ and its deposition on the tube wall would decrease the effective titanium containing species that can diffuse to the fiber surface.

Although the model correctly predicted the increase in deposition rate with inlet temperature, it could not predict the increase in deposition rate observed experimentally at higher tube diameters. The reader is referred to elsewhere[12] for a detailed discussion of this point which is related to the geometry of the deposition tube.

5.3. Effect of B:Ti ratio

Figure 9 shows a plot of the average deposition rate (total deposit thickness divided by residence time) versus B:Ti ratio. As expected, on both sides of the stoichiometric B:Ti ratio the

BCl$_3$ and TiCl$_4$ diffusion at moderate concentrations, Figure 5.7, to a slow HCl diffusion away from the fiber surface at low hydrogen concentrations, Figure 11. The humps present in the HCl profiles at low dilution are indicative of resistance to HCl diffusion resulting from the highly concentrated gas mixture with BCl$_3$ and TiCl$_4$. The HCl concentration peaks at 18 mol/m^3 near the fiber at low dilution versus 1.2 mol/m^3 at high dilution. Although hydrogen concentration is lowered appreciably, its small size allows it to diffuse to the fiber surface relatively fast to replace the consumed hydrogen molecules, Figure 11.

6. Conclusion

The power of the developed model in describing qualitatively the rate limiting mechanisms at different conditions is substantiated by the consistency of the conclusions drawn from totally different experiments. However, the model fell short of predicting some aspects of the CVD process such as the codeposition of boron because of the lack of thermodynamic aspects that could have been added through integrating SOLGASMIX in the model. Unfortunately, the long execution times of the program at present made such a merge unpractical. Also, overestimating deposition rates could probably be fixed through considering other neglected important species such as TiCl$_3$. Finally, for the mass transport rate limited process, the rate limiting mechanism changes from exhaustion of BCl$_3$ and TiCl$_4$ at high dilution, to slow BCl$_3$ and TiCl$_4$ diffusion at moderate concentrations, to slow HCl diffusion away from the fiber surface at high reactant concentrations.

20

References

1. V. Mandorf, J. Hartwig, and E. J. Seldin, High temperature properties of titanium diboride, Proceedings, Cleveland, Ohio, April 26-27, 1961.

2. J. R. Ramberg and W. S. Williams, High temperature deformation of titanium diboride, *J. Mater. Sci.*, 22 (1987) pp. 1815-26.

3. W. S. Williams, C. Allison, and P. Mochel, Crystal chemistry and electron energy loss spectroscopy of titanium carbide precipitates in TiB_2, Science of Hard Materials, Plenum Press, New York, pp. 169-178, 1981.

4. F. J. Keihn, High temperature thermal expansion of certain group IV and group V diborides, *J. Am. Ceram. Soc.*, 50 (1967) pp. 81-4.

5. M. Singh and H. Weidemeyer, Rensselaer Polytechnic Institute, HiTASC ONR/DARPA Program, Internal Report, 1988.

6. F. W. Vahdiek, Electrical resistivity, elastic modulus, and debye temperature of titanium diboride, *J. Less-Common Metals*, 12 (1967) pp. 202-9.

7. G. H. Miller, Method of making continuous length superconducting wires using chemical vapor plating, IEEE

Gas in
$H_2 + BCl_3 + TiCl_4$

Ring #10

Ring #1

Disk #1

Tube wall

Fiber substrate and
TiB_2 deposit

Disk #20

Gas out
$H_2 + BCl_3 + TiCl_4 + HCl$
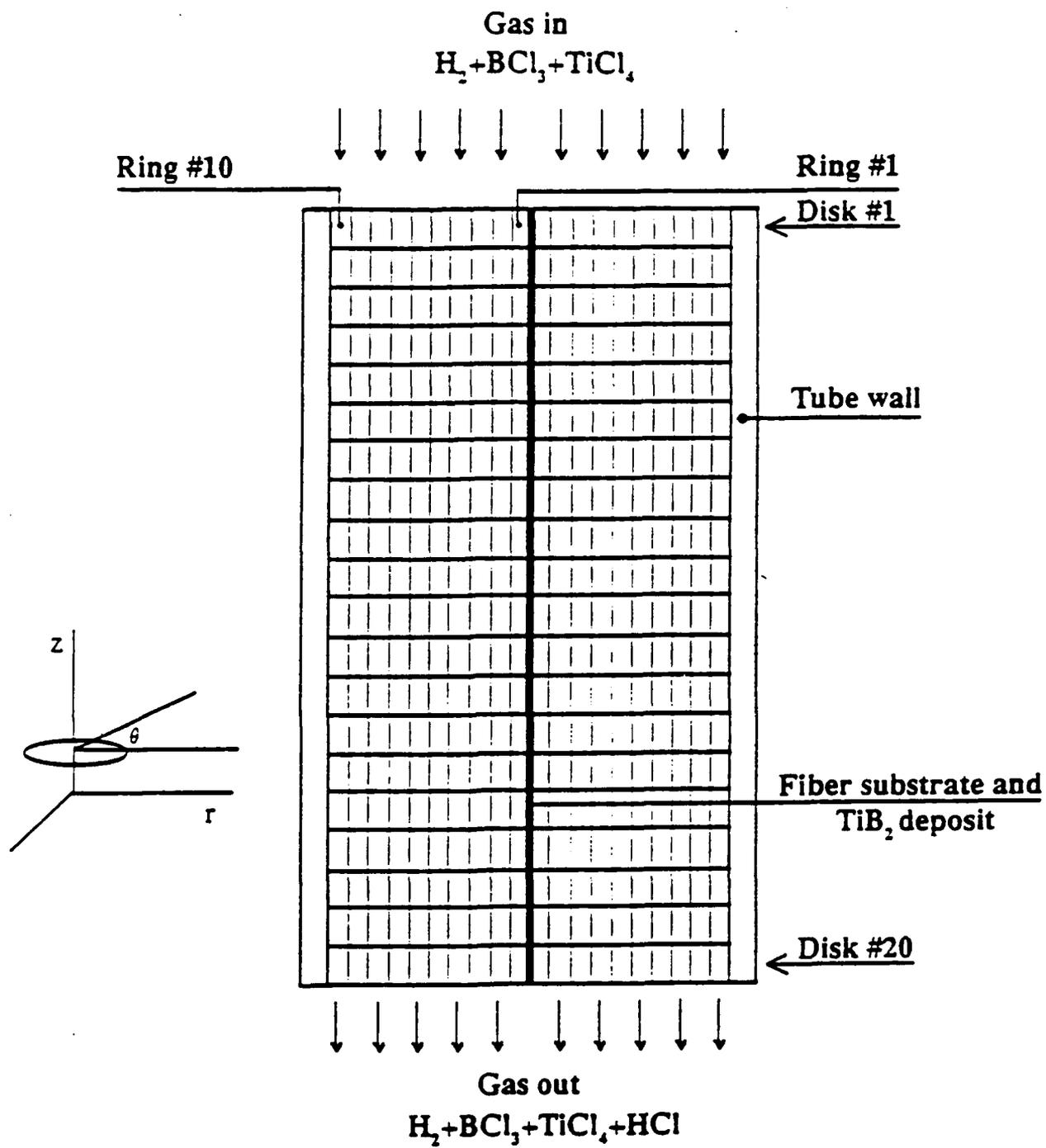
Figure 1. Finite element model showing a typical mesh.

Table 1. Summary of constants used for estimating diffusion coefficients.

	M	$\sigma(\text{Å})$	ε_o/k (°K)
H_2	2.002	2.827	59.7
BCl_3	117.191	5.127	337.7
$TiCl_4$	189.728	5.854*	495.3**
HCl	36.459	3.339	344.7

* Estimated from equation (7)
** Estimated from equation (8)

Table 2. Polynomial coefficients for the diffusivities.

$D_{ij} = aT^2 + bT + c$			
D_{ij}	a	b	c
D_{11}	5.626755×10^{-6}	0.005801	-0.866194
D_{12}	1.780123×10^{-6}	0.001998	-0.391606
D_{22}	1.998544×10^{-7}	0.000136	-0.031625
D_{44}	8.448708×10^{-7}	0.000564	-0.131764
D_{33}	1.192316×10^{-7}	0.000056	-0.013612
D_{13}	1.490630×10^{-6}	0.001553	-0.320206
D_{14}	3.016422×10^{-6}	0.00335	-0.663236
D_{23}	1.564553×10^{-7}	0.000089	-0.021344
D_{24}	4.256135×10^{-7}	0.000287	-0.066864
D_{34}	3.434855×10^{-7}	0.000194	-0.04645
$D_{ij} = D_{ji}$			
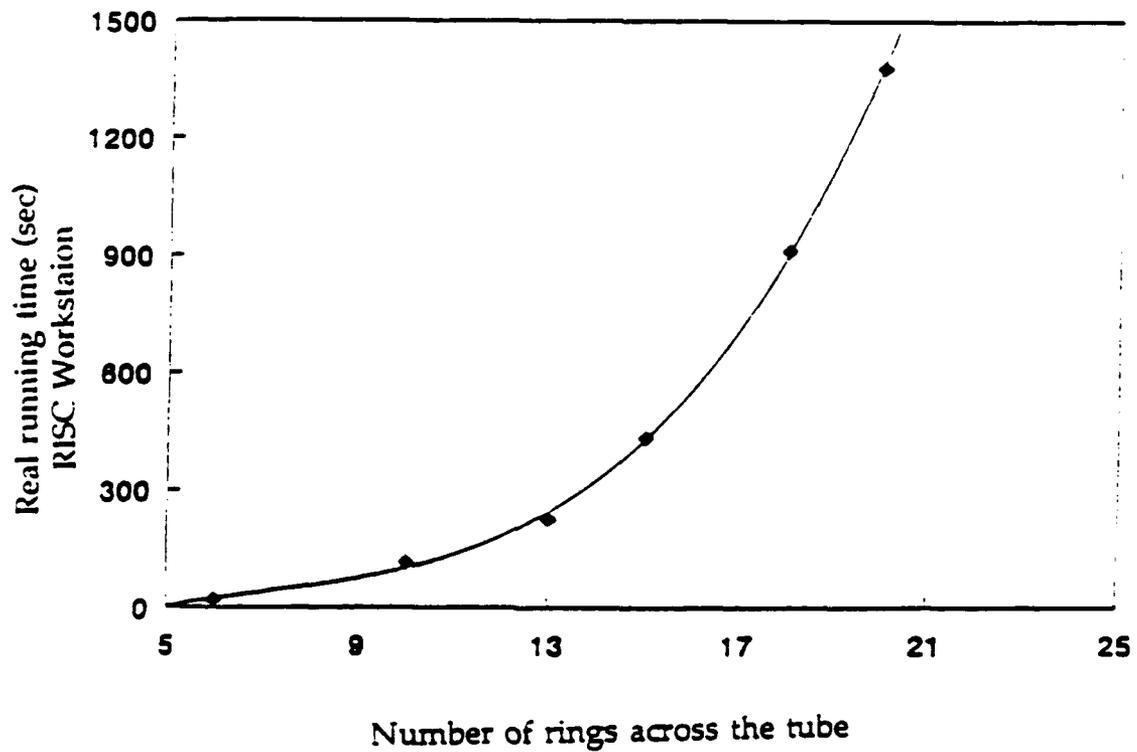
Figure 4. Exponentially increasing time with mesh size: 20 disks and 190 m/min fiber speed.
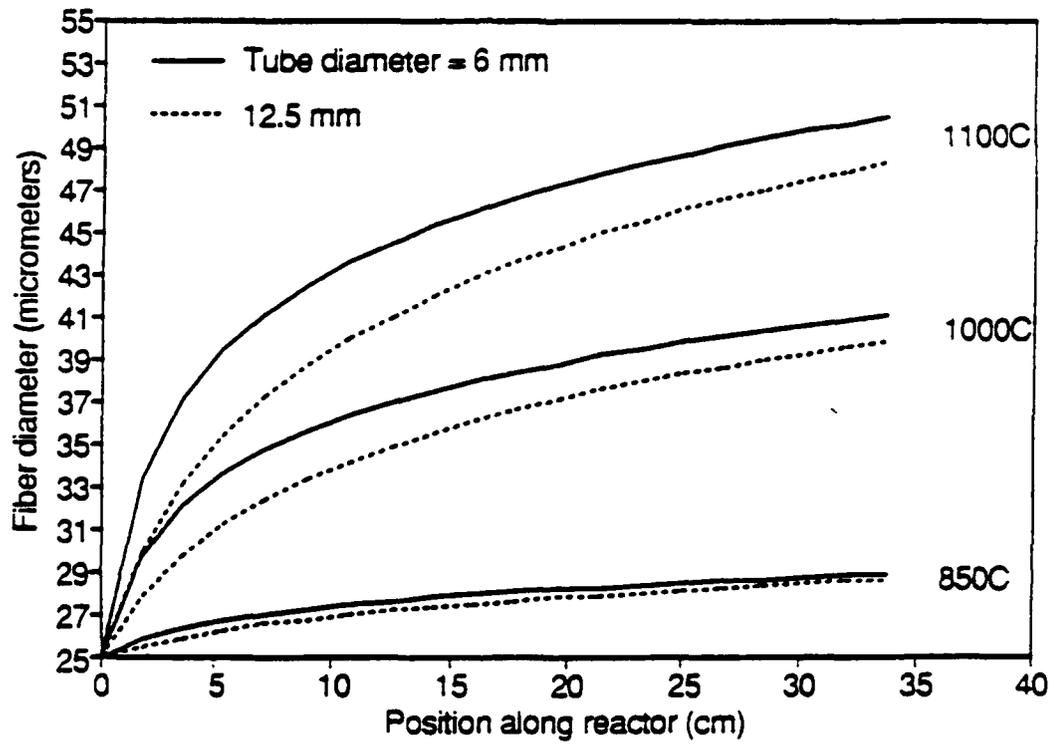
Figure 6. Effect of fiber inlet temperature and tube diameter on the deposition profile.
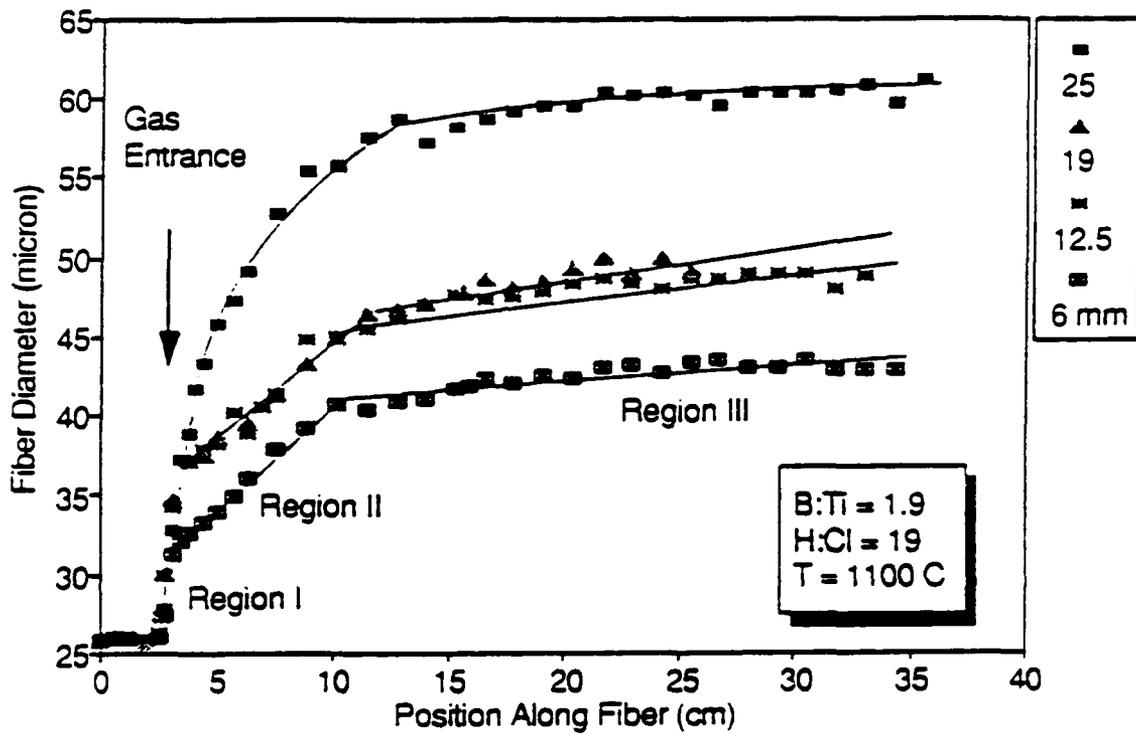
Figure 8. Experimental results showing the effect of deposition tube diameter on the deposition profile along the reactor length at T=1100C.
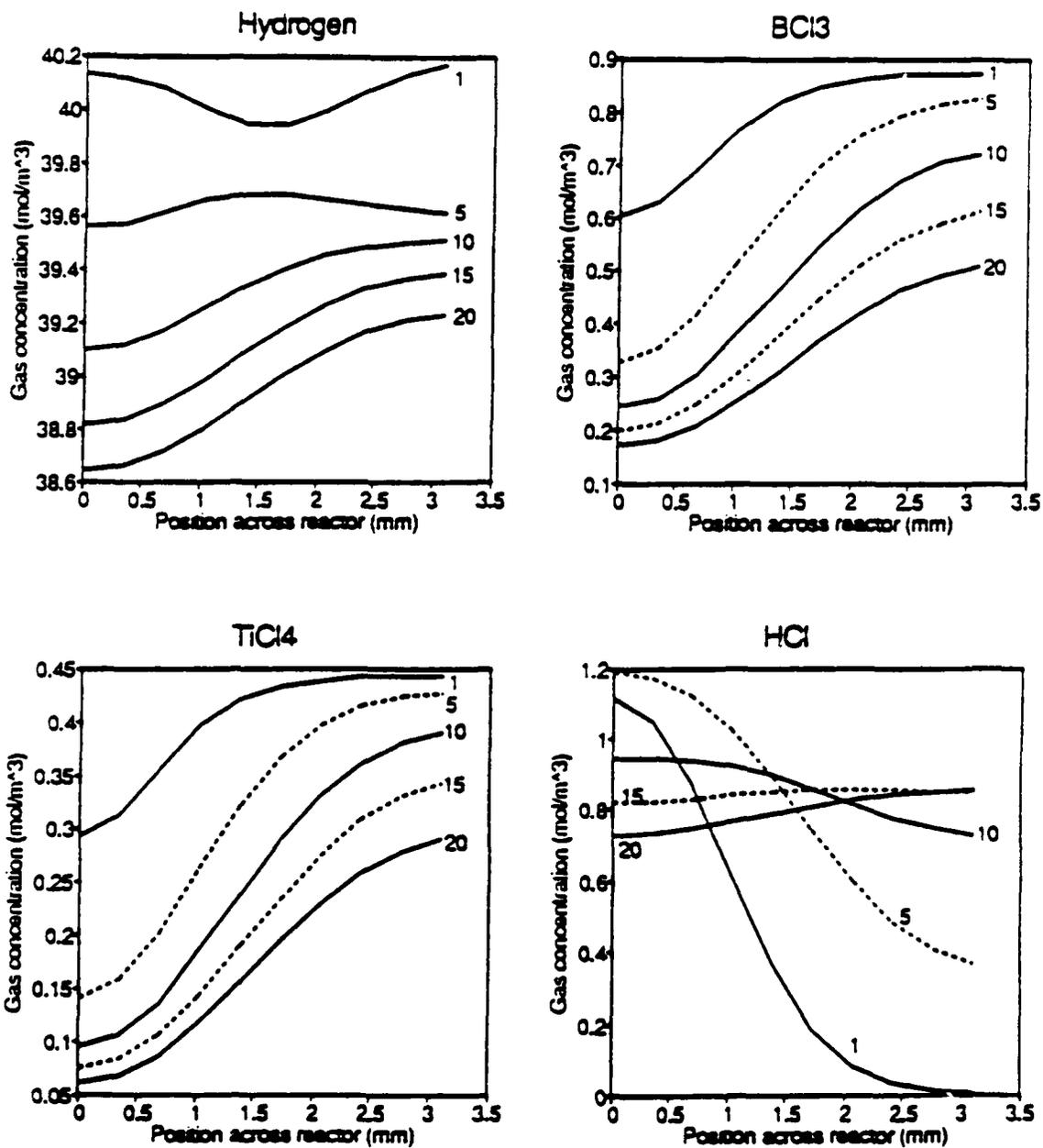
Figure 10. Concentration profiles of a diluted mixture in H_2 at H:Cl=40, inlet T=950C, tube dia.=6mm, B:Ti=2.0, total flow rate=500cc/min, mesh=20x10.

INTERFACES IN INTERMETALLIC
AND CERAMIC MATRIX COMPOSITES

Fiber Coatings Derived from Molecular Precursors

H. Eric Fischer, David J. Larkin, and Leonard V. Interrante

Introduction
Interphases in Fiber-Reinforced Composites

It is generally agreed that the mechanical performance of continuous fiber-reinforced composites will depend to a large extent on the nature of the interface between the fiber and the matrix.[1] In the case of many inorganic composites, compositional and/or morphological gradients can arise over an extended region between the matrix and reinforcing fiber as a result of processing conditions, mechanical forces, or chemical interactions. The term "interphase" has been applied to such a region.[2,3]

There have been numerous theoretical and experimental treatments of this subject in an effort to quantify the stress and strain in the interphase region, and to correlate the presence of such forces with the mechanical performance of the attendant composites.[4] Much of the experimental work has emphasized controlling the nature of the interphase through careful control of the processing conditions[5] or by the introduction of special interface layers, often by applying a coating to the reinforcing fiber prior to incorporating it into the matrix.[4,5c,6]

Coatings as divergent as metals,[7,8] ceramics, and pyrocarbon or silicon[8] have been applied to fibers incorporated into reinforced composites. Fibers have been coated to aid in the processing of composites, for example, by improving the ability of the matrix to wet the reinforcing fiber[8,9] or as a barrier layer providing protection from chemical or mechanical damage during incorporation into the matrix.[10] Coatings have also been em-ployed to effect the performance of composites under "in-use" conditions such as modification of the fiber to matrix bond[11] and as a reaction barrier to permit the use of composites in corrosive environments.[12] Coatings that have received particular attention in the literature are metals (e.g., Ni and Cu),[7] oxides (e.g., Al_2O_3, Y_2O_3, and ZrO_2),[13] and non-oxide ceramics[8,12a,14] (e.g., nitrides,[15a] carbides,[10b,16] and borides[15b]). A diverse array of methods have been employed to produce fiber coatings ranging from merely oxidizing the fiber surface[9] to the application of multilayer coatings using rf sputtering.[16]

This article will highlight precursors that permit application of coatings by thermal processing using simple apparatus and low pyrolysis temperatures. This includes both low-weight, volatile molecules suitable for MOCVD (metal-organic chemical vapor deposition) application and polymers which may be applied by dipping or spray coating their solutions.
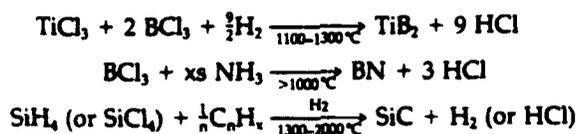
In some situations, plasmas or lasers have been used to facilitate deposition from these organometallics at low tem-peratures or to write lines on substrates for electronic applications. Considering the problems imposed by these methods (such as coating uniformity), the higher cost, and the relatively lesser need for such methods in fiber coating, no further discussion concerning such approaches will be presented here. Also excluded from this discussion are sol-gel approaches to metal oxides, which may employ organometallic systems as precursors but do not generally involve pyrolysis as the primary reaction pathway to the final ceramic material.

Factors Involved in Coating Fibers

Cranmer has briefly reviewed fiber coating and characterization techniques.[17] As noted in the Cranmer review, most of the work leading to carbide, boride, and nitride coatings employs conventional atmospheric pressure CVD processing. This typically involves mixing two or more gaseous reagents with a carrier gas. Examples of some of these processes are given here (in Scheme 1) in the form of simple stoichiometric equations. Although these equations express the mass balance of the relevant chemical processes, the actual chemical mechanisms and flow dynamics involved in applying such coatings are often quite complex. Control of the product (coating) in terms of the stoichiometry, homogeneity, and morphology is correspondingly problematic.

The reagents used in these coating schemes, or their gaseous byproducts, are often corrosive, poisonous or explosive, and the substrate temperatures involved generally exceed 1100°C. These factors limit the types of substrates that can be employed. Additionally, rigorous control of the reactant stoichiometry and other processing variables is required to maintain coating quality, which usually dictates elaborate reactor design and sophisticated control of the reagent gas flow rates. When such coating schemes are used, these requirements can add significantly to the cost of composite processing. Moreover, for coatings which have a significant thermal

$$TiCl_3 + 2\ BCl_3 + \tfrac{9}{2}H_2 \xrightarrow[1100-1300°C]{} TiB_2 + 9\ HCl$$

$$BCl_3 + xs\ NH_3 \xrightarrow[>1000°C]{} BN + 3\ HCl$$

$$SiH_4\ (or\ SiCl_4) + \tfrac{1}{n}C_nH_x \xrightarrow[1300-2000°C]{H_2} SiC + H_2\ (or\ HCl)$$

Scheme 1: Reaction schemes for gas phase chemistry leading to selected ceramic coatings.

expansion mismatch with respect to the fiber, deposition at such high temperatures can lead to high residual stresses at the fiber/coating interface on cooling to room temperature, resulting in coating failure or degraded mechanical performance for the composite.[3] There are alternatives to these "traditional" coating methods which address some of these problems.

"Nontraditional" Precursors as an Alternative Source of Metal and Ceramic Coatings

Increasingly, metal and ceramic coatings are being produced using monomolecular precursors. These precursors include both solution-applied, generally polymeric systems, as well as volatile molecular species for MOCVD. In most cases, thermal processing is used to convert the organometallic species to the final inorganic coating, sometimes with the aid of a reactive gas such as H_2 or NH_3.

Ideally, a metal or ceramic precursor is designed to contain the essential elements of the desired inorganic coating in the correct stoichiometric amounts, a "compositional core" of the precursor, surrounded or appended by "extraneous substituents" which impart desirable physical properties (such as volatility) to the molecule. The composition and structure of the precursor's "compositional core" are configured to resemble that of the product (coating) as much as possible. Ideally, the bonds between the elements of the "compositional core" in a precursor are stronger than those between this core and the "extraneous substituents." This affords precursors from which the substituents are easily lost, preferably as relatively stable, gaseous, molecular byproducts. In general, it is desirable to have byproducts which are volatile at temperatures significantly below the decomposition temperature of the precursor.

An example of such a system[18] can be seen in Figure 1, which highlights a precursor that has been used in the LPCVD (low-pressure chemical vapor deposition) deposition of AlN. The precursor is a volatile solid comprised of cyclohexane-like $[(CH_3)_2AlNH_2]_3$ molecules. These molecules have a central "core" consisting of a six-membered $[AlN]_3$ ring, much like that in the structure of AlN itself. This "core" is held together by fairly strong Al-N bonds and is appended by CH_3 and H "substituents" through relatively weaker bonds. The complex was found to decompose to h-AlN and CH_4 on heating above 500°C, which is well
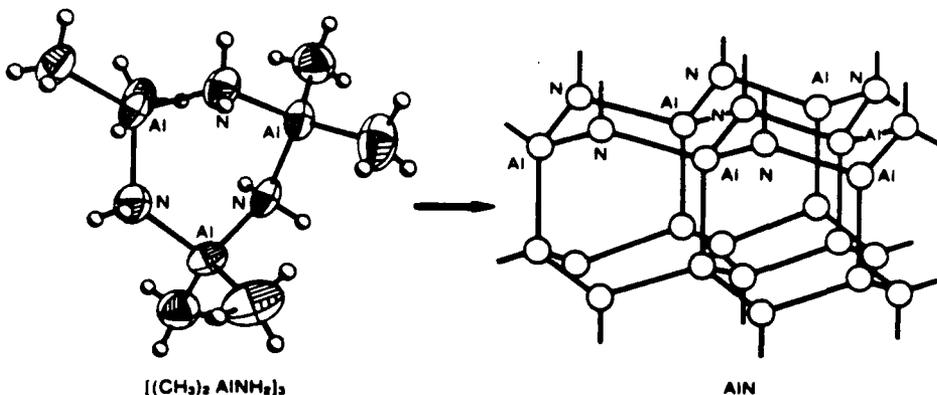

[(CH₃)₂ AlNH₂]₃

AlN

Figure 1: Structure of an organo-aluminum amine precursor and AlN.

below the temperature required for conventional CVD of AlN using trimethyl- or trichloro-aluminum and NH_3. It is also important to note that the decomposition byproduct, methane, is a small, gaseous molecule and is reasonably stable under the reaction conditions. These features all contribute to the production of a stoichiometric AlN film at a relatively low temperature with minimal contamination from the "extraneous substituents."

In many cases such idealized structural and bonding circumstances may not be as readily obtained, yet the use of organometallic or specially designed inorganic precursors can still provide relative advantages in processing temperature, stoichiometry control, and uniformity of coverage. We should point out that many of the coatings cited are not necessarily direct replacements for "traditional" methods of applying these materials in terms of crystalline modification, density, or coating purity. In some cases the "nontraditional" routes supply "superior" coatings, in others they are "inferior" when judged by these criteria. In many cases these and other questions relating to the utility of the coatings in inorganic composites have not been addressed. Since this article focuses on materials intended to be included in composites, the quality of coatings applied by these methods should more properly be judged by their ability to perform the desired function within that environment. In the majority of cases, even among coatings applied by traditional methods, the question of in-composite performance is at present unanswered.

Nontraditional Inorganic and Organometallic Precursors Applied to Coating Formation

We now present some examples from the recent literature of routes which have been employed to impart metallic and ceramic coatings using such nontraditional precursors. In some cases, fibers which have been coated using this type of chemistry have been incorporated into matrices. We do not intend an exhaustive review of the work being done in this area. Our aim is to give the reader a feeling for the scope and type of work which has been done, and to stimulate the imagination to the possibilities for future application in the processing of inorganic composites.

Deposition of Metals

Considering that metal carbonyls fall within the generally accepted definition of organometallics, metals are the earliest materials to have been deposited by MOCVD methods. The vapor transport of Ni by CO was discovered before the turn of the century, and both $Ni(CO)_4$ and $Fe(CO)_5$ can be used to deposit relatively pure metallic thin films of these metals by thermal CVD at quite low temperatures (35–250°C).[19] Most other binary transition metal carbonyls require relatively higher temperatures to decompose completely, generally yielding products which contain significant amounts of oxygen and/or carbon impurities upon pyrolysis.[20,21] Other volatile molecular species have been used to deposit these transition metals, often in the presence of H_2 as a reductant.[21]

Recent efforts to deposit metallic films using molecular precursors have been largely driven by the perceived needs of the electronic industry. In addition to tungsten, this work has largely centered on deposition of aluminum and copper, owing to their intrinsically low resistivities. Trialkylaluminum compounds have

been employed as Al CVD precursors for many years, particularly those which employ an alkyl group having a β-H available to facilitate elimination of an olefin from the complex. These complexes afford a relatively simple, inexpensive route to Al metal films, with tris-isobutylaluminum apparently affording the best quality Al films at the lowest temperatures (260°C).[22] Problems with surface roughness and the drive for even lower deposition temperatures have prompted the reinvestigation of trimethylaminealane [$(CH_3)_3N{:}AlH_3$] as a source of Al films.[31] This volatile alane (AlH_3) adduct decomposes readily and cleanly on a wide range of substrates at temperatures as low as 100°C to give smooth, relatively pure, and highly reflective films of Al with free trimethylamine and H_2 produced as byproducts.

Copper deposition has attracted much attention in the last few years and a variety of novel precursors have been used in both laser-assisted and thermal CVD of this material. The chief issues concerning Cu deposition have been the volatility of the precursor, the conductivity and surface morphology of the resultant film, and the selectivity towards different substrates. Among the systems investigated are various complexes of Cu[II] and Cu[I] such as (β-diketonate)$_2$Cu,[23] (η^5-C$_5$H$_5$)CuPR$_3$,[24] Cu$_4$(tert-butoxy)$_4$,[25] [Cu{OCH(CH$_3$)-CH$_2$N(CH$_3$)$_2$}$_2$],[26] and (β-diketonate) CuP(CH$_3$)$_3$.[27] The latter compounds are particularly interesting in that they reportedly decompose at 150–400°C via a disproportionation process to give elemental Cu films, free phosphine, and the bis-β-diketonate Cu[II] complex.[27] Moreover, Cu films deposited this way are reasonably pure and exhibit low electrical resistivity.

Organometallic precursors to noble metal coatings, particularly Pt and Au, have also received considerable attention recently, driven as well by their potential utility in electronics. Both solution deposition of polymeric complexes followed by laser or electron beam irradiation[28] and thermal LPCVD have been used to prepare thin films of these metals by pyrolysis. For the CVD approach, recent efforts have focused primarily on identifying volatile, yet reasonably stable precursors and on obtaining high conductivity films at as low a temperature as possible. As with copper, these metals are relatively easily obtained in the metallic form by reduction of higher oxidation state complexes. Reduction is often effected during pyrolysis by the attached organic ligands,

but this may be accompanied by thermolysis of the ligands to carbonaceous byproducts which can contaminate the metallic film and so influence its adhesion and other properties. Using hydrogen gas as a co-reductant is sometimes helpful in avoiding this contamination. As for most of the OMCVD precursors to metals and ceramics, few detailed studies of the reaction mechanisms relevant to these processes have appeared so far in the literature.

Specific examples of successful Pt CVD precursors include [Pt(CH$_3$)$_2$-(MeNC)$_2$](MeNC = methyl isonitrile) and [Pt(CH$_3$)$_2$(COD)] (COD = cyclooctadiene), which have been used to deposit Pt on silicon at 250°C.[29] In the presence of H_2, the carbon content of the Pt film was considerably reduced and the temperature of deposition lowered to 135–180°C. Similarly, gold has been deposited using [Au(CH$_3$)(P(CH$_3$)$_3$)$_3$] and [Au(CH$_3$)$_3$(P(CH$_3$)$_3$)] by LPCVD at 200°C.[30]

Deposition of Oxides

As with metal coatings, work on oxide CVD has been motivated largely by applications requiring oxide thin films as passive or active components in electronic devices. Recent interest in preparing thin films of the copper oxide superconductors by CVD has fueled particular interest in volatile precursors for CuO, BaO, and Y_2O_3.[31]
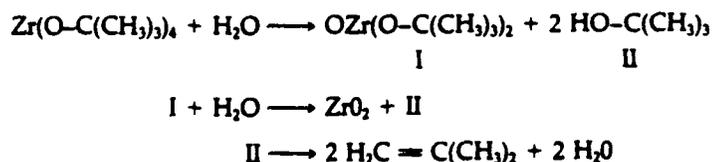
Molecular sources for these depositions are generally either alkoxides [M(OR)$_x$]$_n$ (where R = alkyl group) or β-diketonates [M{RC(O)CHC(O)R'}$_x$] (where R and R' can be various alkyl and perfluoroalkyl groups). The use of alkoxides as precursors for oxide ceramics has been recently reviewed.[32] The chief difficulty in using these compounds as MOCVD precursors is that they tend to form strongly associated

oligomeric or polymeric species with the -OR groups bridging two or more metal atoms. This can lead to low volatilities, although some oligomeric alkoxides (e.g., Al$_4$(OPr')$_{12}$[33] and Cu$_4$(OBu')$_8$[26]) are sufficiently volatile for CVD use. Oligomerization can sometimes be inhibited by increasing the steric bulk of the R group, e.g., through the use of the tertiary butoxy group, resulting in an increase in volatility.

Oligomerization is less of a problem for the β-diketonate complexes, where the monoanionic [β-diketonate]$^-$ ligand fills two coordination positions on the metal ion. Thus even with the relatively small acetylacetonate (MeC(O)CHC-(O)Me = acac) ligand, many of the neutral complexes are monomeric and sufficiently volatile for use in CVD.

When the simple acac complexes are not volatile enough below their decomposition temperatures, using fluorinated and/or bulky alkyl substituents as R and R' is often helpful in increasing volatility. For example, the ligands [Me$_3$CC(O)CHC(O)CF$_2$CF$_2$CF$_3$]–(fod), and [Me$_3$CC(O)CHC(O)CMe$_3$]–(thd) have been used to obtain volatile complexes of the rare earth elements and heavy metal ions such as Zr^{+4},[34] and several of these complexes have been subsequently employed as CVD precursors.[31,35] Even with these ligands, oligomerization still occurs with the Group IA and the heavier Group IIA metal complexes. Various neutral ligands, such as THF (tetrahydrofuran) and amines, as well as the free β-diketone ligand, have been used successfully in CVD studies to enhance the volatilities of some of these complexes.[36]

These two classes of precursors, the alkoxides and β-diketonates, have been used to produce a wide range of high purity, adherent metal oxide films. In general, an additional source of oxygen,

---

$$Zr(O{-}C(CH_3)_3)_4 + H_2O \longrightarrow OZr(O{-}C(CH_3)_3)_2 + 2\ HO{-}C(CH_3)_3$$
$$\qquad\qquad\qquad\qquad\qquad I \qquad\qquad\qquad\qquad\qquad II$$

$$I + H_2O \longrightarrow ZrO_2 + II$$

$$II \longrightarrow 2\ H_2C = C(CH_3)_2 + 2\ H_2O$$

Overall:

$$Zr(OC(CH_3)_3)_4 \xrightarrow{\text{cat H}_2O} ZrO_2 + 4\ H_2C = C(CH_3)_2 + 4H_2O$$
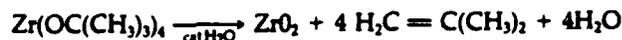
Reaction 1.

*Figure 2: (a) Uncoated and (b)
yttria-coated SCS-6 fiber after
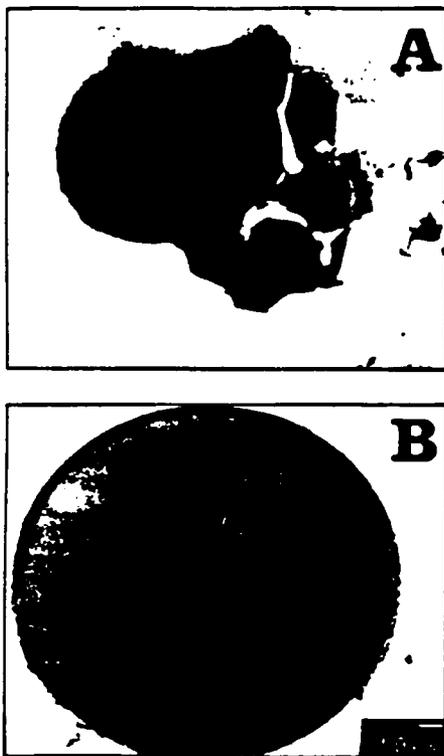incorporation into a Ni$_x$Al matrix.*

such as O$_2$ or H$_2$O, appears to be helpful in avoiding carbon contamination, especially in the case of the β-diketonates. Even when H$_2$O is not deliberately added, traces of water or even surface -OH groups appear to be sufficient to catalyze the thermal decomposition of certain alkoxides, leading to the rapid deposition of a metal oxide film.[37] An example of such a chain reaction decomposition for Zr(OBu')$_4$ is shown in Reaction I.

As examples of the many situations where these two classes of compounds have been used as CVD precursors, the CVD of alumina, zirconia, and yttria from their respective β-diketonate complexes: Al(acac)$_3$],[38] [Zr(thd)$_4$] and [Y(thd)$_3$],[35] and alumina, titania and silica from their alkoxides: [Al(OPr')$_3$],[33] [Ti(OEt)$_4$],[39] and [Si(OEt)$_4$][40] have been reported. Deposition temperatures vary from 250 to 800°C, with the β-diketonates generally requiring somewhat higher temperatures than the alkoxides. In all of these cases, source and inlet temperatures of ~120–200°C along with a carrier gas are required to maintain a sufficient rate of precursor introduction. Except

for Al(OPr')$_3$, all these processes add O$_2$ or H$_2$O to facilitate removing the ligand byproducts.

An application of this approach to prepare adherent Y$_2$O$_3$ films on SCS-6 SiC fiber for use as a barrier layer in the fabrication of SiC/Ni$_3$Al composites has been reported by Larkin, Interrante, and Bose.[41] In this work the β-diketonate complex Y(thd)$_3$ was decomposed in the presence of water vapor in a hot-wall CVD reactor to deposit high purity yttria coatings on short lengths of the SiC fiber at ~600°C. These coatings were found to survive composite fabrication by cold pressing followed by reactive sintering, when temperatures exceeding 1300°C were reached. This is illustrated in Figure 2, where an yttria-coated SCS-6 fiber cross section is compared with that of an uncoated fiber after reactive sintering of the Ni$_3$Al matrix. The coated fibers were also found to survive even after subsequent annealing for extended periods at 1000°C.

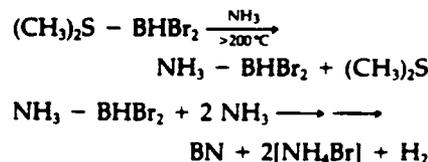## Non-Oxide Ceramics

Boron Nitride. Synthesis of boron nitride has received much attention, and both CVD and polymeric precursor routes exist for producing ceramic coatings. Recent reviews by Paine[42] and Sneddon[43] have covered this subject thoroughly, but some background information and several systems which have recently appeared in the literature will be highlighted here.

The classic boron nitride (BN) CVD precursor system, BCl$_3$/NH$_3$, forms the ceramic at substrate temperatures above 1100°C. Several CVD precursor systems combining diborane with NH$_3$ or borazines (particularly B-trichloroborazine)

have been examined, and these systems have been reported to give BN coatings at temperatures as low as 650°C.[42,44] The diborane route is thought to proceed to coatings through the formation of an intermediate borazine moiety,[44] although it has been pointed out that coatings obtained below 500°C from borazine precursors differ spectroscopically from those produced using diborane precursors.[42,45] These coatings are microcrystalline, and several reports claim that these routes produce h-BN at temperatures below 1000°C. The trichloroborazine precursor has been used by Singh to deposit BN on ceramic fibers prior to their incorporation in oxide matrices by hot pressing.[46a,46b]

In a singular example, Sneddon et al.[46] report a precursor which is neither a volatile molecule nor a polymer system. In this work, the dimethyl sulfide adduct of HB(Br)$_2$ was employed as a boron source. This material was solution coated onto a substrate, followed by reaction of the substrate coating with NH$_3$. This chemistry is thought to follow the reaction shown below, with formation of a BN$_x$H$_y$Br$_z$ intermediate followed by loss of NH$_4$Br leading to the BN coating.

$$(CH_3)_2S - BHBr_2 \xrightarrow{NH_3}{>200°C}$$

$$NH_3 - BHBr_2 + (CH_3)_2S$$

$$NH_3 - BHBr_2 + 2 NH_3 \longrightarrow \longrightarrow$$

$$BN + 2[NH_4Br] + H_2$$

Polymeric precursors to BN ceramics have been prepared largely by oligomerization reactions involving substituted borazines or boranes. In general, the
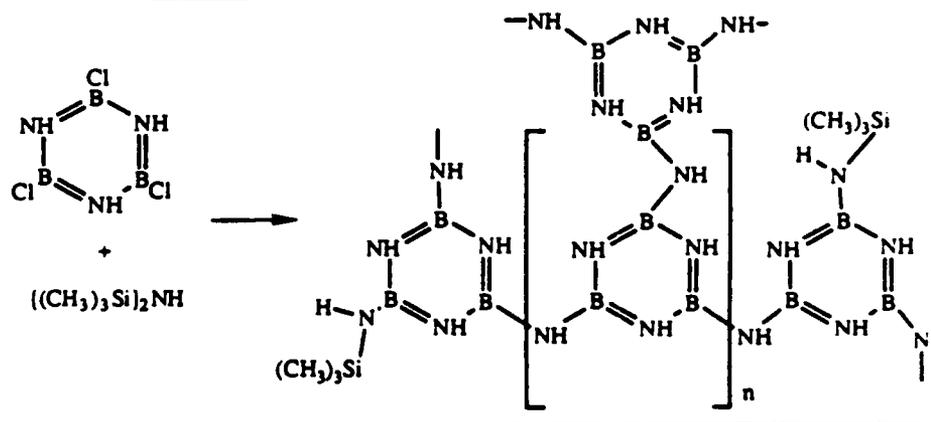
Reaction II.

polymers take the form of an alkyl chain with borazine structures pendant on it,[47] or as borazine structures that are linked directly[48] or through amino or alkyl amino moieties.[49]

Paine and co-workers, using the reaction shown in Reaction II, have produced a gel-like polymer which yields h-BN below 1000°C.[49,50] This material is insoluble in organic solvents, which might suggest that it is of limited use for coatings. However, treating this polymer with anhydrous liquid ammonia produces a clear solution that has been used to coat a number of substrates by dipping. Pyrolysis of the dip-coated substrates gave smooth, pore-free BN coatings.[49b]

Silicon Nitride. The "traditional" CVD precursor system to Si_3N_4 is the reaction of a silane/ammonia gas mixture at temperatures above 1000°C.[51] There have been few monomolecular precursors reported which are suitable for CVD of Si_3N_4, possibly owing to the great tendency of aminosilanes and silazanes to polymerize. A brief review of volatile precursors suitable for rf-enhanced CVD has been published by Beatty,[52] but most of the complexes mentioned either contain too much carbon or are too thermally stable to be used as precursors in a simple pyrolysis system. Gordon, Hoffman, and Riaz[53] recently reported on a family of aminosilanes of the type $H_xSi(N(CH_3)_2)_{4-x}$ from which they deposited Si_3N_4 films on silicon, vitreous carbon, boron, and quartz at temperatures as low as 600°C. Reasonably pure films are available from these precursors when thermolysis is carried out under an ammonia atmosphere.

Silicon nitride films can also be applied using polymeric precursors. Polysilazanes are well known as such precursors, and have the general formula [RR'SiNR"]$_x$ (R, R' and R" are H or alkyl moieties). Seyferth and Wiseman[52b] reported on the synthesis of these polymers and outlined the scope of work in this area. These materials decompose to the product (Si_3N_4) through the successive loss of alkyl moieties or H_2 and subsequent formation of additional Si-N bonds. In recent work, Blum et al.[54] reported the use of a polysilazane polymer ([$H_2SiN(CH_3)$]$_n$) to apply coatings to glass and aluminum substrates.

Other Nitrides. A general route for applying coatings of many metal nitrides, including Ti, Nb, and Zr, by the decomposition of organometallic complexes with the general structure $M(N(CH_3)_2)_x$, has been described.[55]

Although deposition temperatures as low as 250°C have been reported by this method, these films have a high level of carbon contamination at deposition temperatures below 800°C. For titanium, attempts have been made to design a suitable ligand system based on cyclic amines to permit conversion to the nitride by direct pyrolysis. However, the TiN films obtained proved to have significant carbon contamination.[56] Chemistry based on the metal tetraamines has recently been revived with the recognition that solution-phase transamination/dehydroamidation reactions of early transition metals may be mimicked in the heterogeneous chemistry occurring during thermolysis of tetraamino complexes when the thermolysis is carried out under ammonia. Reasonably pure films of various metal nitrides have been prepared using this approach. Thus Hoffman, Gordon, and co-workers[56,57] reported the deposition of Zr, Nb, V, Mo, Hf, Ga, and Ti nitride coatings by atmospheric pressure CVD in NH_3 at 200–400°C.

Interrante et al.[18] and Gladfelter[58] have reported monomolecular CVD precursors for aluminum nitride from alkylaluminum -amino and -azide complexes, respectively. These precursors have a cyclic structure of alternating Al and N atoms, and yield polycrystalline AlN films at temperatures as low as 500°C. Decomposition of this type of precursor was shown as an example in the Introduction to this article. Gladfelter also reported a precursor to GaN, $(GaH_2NH_2)_3$, which has a similar cyclic structure of alternating Ga and N atoms.[59] This material has given cubic GaN coatings at temperatures below 600°C.

Interrante and Jiang[60] have recently prepared AlN films from a polymeric precursor. This work is an extension of their efforts in developing a precursor suitable for CVD application of AlN.[18] The polymer is synthesized by employing a reaction between aluminum alkyls and ethylenediamine resulting in a complex structure thought to consist of aluminium amino heterocycles linked by ethylene bridges. Seibold and Russel report an alternative approach to the synthesis of AlN polymeric precursors[61] which employed electrochemical reduction of a primary monoamine at an aluminum electrode. The resulting polymeric precursor has not been fully characterized but has been used to coat NiCAlON fibers with AlN.

Silicon Carbide. Precursors to SiC suitable for CVD application have been

known for some time, generally based upon the high temperature reaction of H_xSiCl_{4-x} and a carbon source such as CH_4 or C_2H_4 in H_2.[8] Carbosilanes such as CH_3SiCl_3[64] have also been employed, but again high reaction temperatures are required and HCl is a byproduct. Monomolecular precursors suitable for CVD, and which decompose to SiC at temperatures below 1000°C, may be found in mono- and di-silacyclobutanes. These complexes are believed to decompose at lower temperatures than corresponding linear carbosilanes because they possess a significant amount of ring strain.[62] Recently, a substituted disilacyclobutane (structure follows) was employed as a precursor to SiC coatings on silicon.[63] Although the mechanism of decomposition leading to coatings is known to involve the loss of some carbosilane moieties, decomposition proceeds primarily with the loss of alkanes, principally methane, providing near stoichiometric SiC.[64]
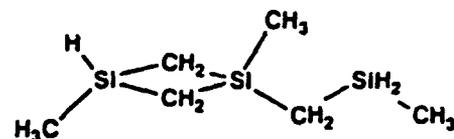
In some preliminary work, this precursor has been employed to apply a SiC coating to carbon fibers. During this work, it was observed that a SiC coating of less than ~500 Å applied this way noticeably improved the oxidation resistance of the fibers at 400°C.[64b] When this same procedure was employed to coat a glassy carbon substrate it was observed that the coating improved wetting of the substrate by molten glass, compared to uncoated glassy carbon samples, and also improved adhesion of the glass to the substrate upon cooling.

Among the well-studied polymeric precursors to SiC are various poly-alkylsilanes[65] and polycarbosilanes.[66] Numerous patents have appeared describing the use of such materials to coat a variety of fibers,[66c-n] but the composition and effectiveness of these coatings have not been reported.

Other Carbides. Films of TiC and B_4C deposited from organometallic precursors have been reported. Girolami[67] has examined tetraneopentyl titanium as a precursor to TiC, and Sneddon[63] has reported B_4C polymeric precursors. Girolami reports crystalline TiC films from his precursor at temperatures as low as 150°C. Sneddon's polymer, which is composed of pentaborane moieties pendant on a polyethylene chain,

has been reported to give amorphous B_4C under argon at 1000°C.

Borides. A family of precursors to borides of titanium, hafnium and zirconium have been prepared by Girolami et al.[68] These materials, tetrahydroborate (BH_4^-) adducts of the transition metals, have the general formula $[L_xM(BH_4)_{4-x}]$ (x=0,1). The hafnium and zirconium examples are binary compounds but the $Ti(BH_4)_4$ complex is unstable, so the dimethoxyethane (dme) stabilized complex $Ti(BH_4)_3(dme)$ was employed. These materials have been used to apply films of TiB_2, HfB_2 and ZrB_2 by LPCVD on glass, copper, aluminum, and steel at 250°C.

Mixed-Phase Ceramic Systems. Various studies have resulted in the preparation, deliberate or otherwise, of complex, generally amorphous or polyphasic ceramic films through MOCVD and polymer precursor pyrolysis. Examples include $SiC_xN_bO_c$[69] and TiC_xN_y[67b,70] phases, some of which have been examined for possible use as protective coatings for C/C composites.[71] Judging from some of the results described and our own largely unpublished observations, such films may offer special advantages as coatings for ceramic fibers incorporated into inorganic composites owing to their greater resistance to spalling during handling, phase transformations during thermal cycling, and/or to environmental degradation.

A key example is provided by the LPCVD of apparently amorphous TiC_xN_y films by using $Ti(bipy)_3$ at 370–520°C.[70] The excess C introduced by this precursor seems to inhibit crystal growth of the TiC (and TiN), requiring relatively high temperatures to produce observable crystallinity and leading to incompletely crystallized products even at 1200°C. Moreover, in a series of electrochemical experiments, amorphous TiC films deposited by MOCVD on quartz glass using $Ti(bipy)_3$ and $Ti(CH_2C(CH_3)_3)_4$ as precursors and electron beam vaporization (EBV) of TiC onto a liquid nitrogen cooled substrate were compared, along with polycrystalline TiC films deposited at high temperature from $TiCl_4$, CH_4, and H_2.[67b] It was found that the crystalline films were most easily corroded, followed by the high purity amorphous film from EBV. The coating obtained from the $Ti(bipy)_3$ was slightly more corrosion resistant than that from the neopentyl complex, but both performed signifi-

cantly better than either of the high purity coatings.

References

1. R.J. Kerans, R.S. Hay, N.J. Pagano, and T.A. Parthasarathy, *Ceram. Bull.* **68** (2) (1989) p. 429.
2. G.C. Papanicolaou, S.A. Paipetis, and P.S. Theocaris, *J. Colloid Polymer Sci.* **256** (7) (1978) p. 625; K.M. Prewo, in *Proc. Fourth Japan-U.S. Conference on Composite Materials* (Technomic, Lancaster, PA, 1989) p. 24–40.
3. R.S. Raghava, *J. Reinf. Plastics Comp.* **9** (1990) p. 151.
4. M.R. Piggott, *Carbon* **27** (5) (1989) p. 657; W.K. Tredway, K.M. Prewo, and C.G. Pantano, *Carbon* **27** (5) (1989) p. 717; A.S. Argon, V. Gupta, H.S. Landis, and J.A. Cornie, *Mat. Sci. Eng.* **A107** (1989) p. 41; M.K. Brun and R.N. Singh, *Adv. Ceram. Mater.* **3** (5) (1988) p. 506; T. Pradell, C. Olagnon, and E. Bullock, *J. Mater. Sci. Lett.* **9** (1990) p. 960; G.P. Tandon and N.J. Pagano, in *Proc. Fourth Japan-U.S. Conference on Composite Materials*, (Technomic, Lancaster, PA, 1989) p. 191; S.G. Fishman and A.M. Diness, *ibid.*, p. 209-215.
5. Y. Maniette and A. Oberlin, *J. Mater. Sci.* **25** (1990) p. 3864; S.D. Peteves, P. Tambuyser, P. Helbach, M. Audier, V. Laurent, and D. Chatain, *J. Mater. Sci.* **25** (8) (1990) p. 3765; K. Nishiyama, S. Umekawa, M. Yuasa, and I. Fukumoto, in *Proc. Fourth Japan-U.S. Conference on Composite Materials* (Technomic, Lancaster, PA, 1989) p. 776-788; C. Jones, C.J. Kiely, and S.S. Wang, *J. Mater. Res.* **4** (2) (1989) p. 327; **5** (7) (1990) p. 1435; S.J. Baker and W. Bonfield, *J. Mater. Sci.* **13** (1978) p. 1329.
6. R.N. Singh, *J. Am. Ceram. Soc.* **72**(9) (1989) p. 1764; R.N. Singh and M.K. Brun, *Adv. Ceram. Mater.* **3** (3) (1988) p. 235; R.P. Boisvert, R.K. Hutter, and R.J. Diefendorf, in *Proc. Fourth Japan-U.S. Conference on Composite Materials* (Technomic, Lancaster, PA, 1989) p. 789-798.
7. S. Abraham, B.C. Pai, K.G. Satyanarayana, and V.K. Vaidyan, in *Interfacial Phenomena in Composite Materials '89* edited by F.R. Jones (Butterworths, Boston, MA, 1989) p. 276-281.
8. L. Aggour, E. Fitzer, E. Ignotowitz, M. Sahebkar, *Carbon* **12** (1974) p. 358; *Vapor Deposition*, edited by C.F. Powell, J.H. Oxley, and J.M. Blocher (Wiley and Sons, New York, 1966).
9. H.H. Streckert, F.C. Montgomery, T.D. Tilley, B.K. Campion, and R.H. Heyn, in *Ultrastructure Processing of Advanced Ceramics*, edited by J.D. Mackenzie and D.R. Ulrich (Wiley & Sons, New York, 1988) p. 963-972.
10. H. Fukunaga and K. Goda, in *Proc. Fourth Japan-U.S. Conference on Composite Materials* (Technomic, Lancaster, PA, 1989) p. 653-660;

L. Hwan, S. Suib, *J. Am. Ceram. Soc.* **72** (7) (1989) p. 1259.
11. B. Rand, in *Interfacial Phenomena in Composite Materials '89*, edited by F.R. Jones (Butterworths, Boston, MA, 1989) p. 15-24. Also see references 1-8.
12. J.R. Strife, J.E. Sheehan, *Ceram. Bull.* **67** (2) (1988) p. 369; Y. Deslandes and F.N. Sabir, *J. Mater. Sci. Lett.* **9**(2) (1990) p. 200.
13. S.M. Sim, P-Y. Chu, R.H. Krabill, and D.E. Clark, in *Ultrastructure Processing of Advanced Ceramics*, edited by J.D. Mackenzie and D.R. Ulrich (Wiley & Sons, New York, 1988) p. 995-1010.
14. M. Peuckert, T. Vaahs, and M. Bruck, *Adv. Mater.* **2** (9) (1990) p. 398.
15. M. Okamoto, H. Yokoyama, and Y. Osaka, *Jpn. J. Appl. Phys.* **29** (5) (1990) p. 930; H. Vincent, M. Boubehira, J. Bouix, C. Bernar, and A. Roche, *J. Crystal Growth* **75** (1986) p. 504.
16. W. Weisweiler, E. Fitzer, G. Nagel, and H. Jager, *Thin Solid Films* **148** (1987) p. 93.
17. D.C. Cranmer, *Ceram. Bull.* **68** (2) (1989) p. 415.
18. L.V. Interrante, G.A. Sigel, M. Garbauskas, C. Hejna, and G.A. Slack, *Inorg. Chem.* **28** (2), (1989) p. 252; L.V. Interrante, W. Lee, M. McConnell, N. Lewis, and G.A. Slack, *J. Electrochem. Soc.* **136** (1989) p. 472.
19. L. Mond, C. Langer, and F. Quinke, *J. Chem. Soc. London* **57** (1890) p. 749; H.E. Carlton, and W.M. Goldberger, *J. Met.* **17** (1965) p. 611; R. Kaplan and N. Bottka, *Appl. Phys. Lett.* **41** (1982) p. 972; R. Kaplan, *J. Vac. Sci. Technol. A* **1** (1983) p. 551; J.S. Foord and R.B. Jackman, *Chem. Phys. Lett.* **112** (1984) p. 190.
20. S. Varma, Y.G. Kim, Z. Psenicnik, P.A. Dowben, and R.R. Birge, in *Protective Coatings: Processing and Characterization*, edited by R.M. Yazici (TMS, Warrendale, PA, 1989) p. 101-110.
21. P.A. Dowben, J.T. Spencer, and G.T. Stauf, *Mater. Sci. Eng.* **B2** (1989) p. 297; *Tungsten and Other Refractory Metals for VLSI Applications*, Vol. III, edited by V.A. Wells (Mater. Res. Soc., Pittsburgh, PA, 1988), and Vol. IV, edited by R.S. Blewer and C.M. McConica (1989).
22. M.J. Cooke, R.A. Heinecke, R.C. Stern, and J.W. Maes, *Solid State Technol.* **25** (12) (1982) p. 62; R.A. Levy and M.L. Green, *J. Electrochem. Soc.* **134** (1987) p. 37C.
23. F.A. Houle, C.R. Jones, T.H. Baum, C. Pico, and C.A. Kovac, *Appl. Phys. Lett.* **46** (1985) p. 204; C. Oehrand and H. Suhr, *Appl. Phys. A* **45** (1988) p. 151.
24. D.B. Beach, F.K. LeGoues, and C.K. Hu, *Chem. Mater.* **2** (1990) p. 216.
25. P.M. Jeffries and G.S. Girolami, *Chem. Mater.* **1** (1989) p. 8.
26. S.C. Geol, K.S. Kramer, M.Y. Chiang, and W. Buhro, *Polyhedron* **9** (1990) p. 611.
27. H.K. Shin, K.M. Chi, M.J. Hampden-Smith, T.T. Kodas, J.D. Farr, and M.F. Paffett, "Synthesis of New Copper(I) B-Diketonate Compounds For CVD of Copper" in *Chemical Perspectives of Microelectronic Materials — II*, edited by L.H. Dubois, L.V. Interrante,

M.E. Gross, and K.F. Jensen (Mater. Res. Soc. Symp. Proc., **204**, Pittsburgh, PA, 1991) p. 421.

28. L.V. Koplitz, C.K. Shuh, Y.J. Chen, R.S. Williams, and J.I. Zink, *Appl. Phys. Lett.* **53** (18) (1988) p. 1705.

29. R. Kumar, S. Roy, M. Rashidi, and R.J. Puddephat, *Polyhedron* **8** (1989) p. 551; S. Roy, R.J. Puddephat, and J.D. Scott, *J. Chem. Soc. Dalton Trans.* (1989) p. 2121.

30. R.J. Puddephat and I. Treuernicht, *J. Organomet. Chem.* **319** (1987) p. 129.

31. M. Nemoto and M. Yamanaka, *J. Mater. Res.* **5** (1990) p. 1; K. Wanatabe, H. Yamane, H. Kurasawa, T. Hirai, N. Kobayashi, H. Iwasake, K. Noto, and Y. Muto, *Appl. Phys. Lett.* **54** (1989) p. 575; A.P. Purdy, A.D. Berry, R.T. Holm, M. Fatemi, and D.K. Gaskill, *Inorg. Chem.* **28** (1989); A.D. Berry, R.T. Holm, M. Fatemi, D.K. Gaskill, R. Kaplan, and W.B. Fox, *J. Cryst. Growth.* **92** (1988) p. 344; J. Zhao, K.H. Dahmen, H.O. Marcy, L.M. Tonge, T.J. Marks, B.W. Wessels, and C.R. Kannewurf, *Phys. Lett.* **53** (1988) p. 1548.

32. D.C. Bradley, *Chem. Rev.* **89** (1989) p. 1317; C.C. Bradley, *Philos. Trans. R. Soc. Lond., Ser. A* **330** (1990) p. 167.

33. J. Saraie, J. Kwon, and Y. Yodogawa, *J. Electrochem. Soc.* **132**(4) (1985) p. 890.

34. R.E. Seivers, K.J. Eisentraut, C.S. Springer Jr., and D.W. Meek, in *Lanthanide/Actinide Chemistry, Advances in Chemistry Series*, Vol. 71 (American Chemical Society, 1967) p. 141-154; E.W. Berg and J.J. Chiang-Acosta, *Ann. Chim. Acta.* **40** (1968) p. 101; A.P. Purdy, A.D. Berry, R.T. Holm, M. Fatemi, and D.K. Gaskill, *Inorg. Chem.* **28** (1989) p. 2799.

35. K. Kamata, S. Matsumato, and Y. Shibata, *Yogyo Kyokaishi* **90** (1) (1982) p. 46; A.D. Berry, D.K. Gaskill, R.T. Holm, E.J. Cukauskas, R. Kaplan, and R.L. Henry, *Appl. Phys. Lett.* **52** (20) (1988) p. 1743; V.A. Varyukhin, V.Y. Vodzinskiy, V.A. Domrachev, B.I. Kozyrkin, V.V. Kutyreva, and O.N. Suvorova, in *Probl. Khim. Primen. Beta-Diketonatov Met.*, 1st edition, edited by V. Spitsyn (1982) p. 178-84.

36. S. Matsuno, F. Uchikawa, K. Yoshizaki, *Jpn. J. Appl. Phys.*, Part 2 **29** (6), (1990) L947; A.R. Barron, J.M. Buriak, L. Cheatham, and R. Gordon, in *Electrochemical Society 177th Meeting*, Abstract 943 HTS, Montreal, Quebec, Canada; T.H. Geballe, A. Sanjurjo, D. Hildenbrand, G. Craig, M. Zisk, J. Collman, S.A. Banning, and R.E. Sievers, *J. Appl. Phys.* **66** (1989) p. 444.

37. D.C. Bradley and M.M. Faktor, *Trans.*

Faraday Soc. **55** (1959) p. 2117.

38. A. Politychi and K. Hierber, in *Sci. Technol. Surf. Coat., NATO Adv. Study Inst.*, edited by B.N. Chapman and J.C. Anderson (Academic Publishing, London, 1972) p. 159-168.

39. C.C. Wang, K.H. Zaninger, and M.T. Duffy, *RCA Rev.* **31** (1970) p. 728.

40. B. Delperier, F. Maury, R. Calsou, R. Morancho, *Proc. 10th International Conf. on CVD* (Proc. Electrochemical Society, **87-88**, 1987) p. 1139-46.

41. D.J. Larkin, L.V. Interrante, and A. Bose, *J. Mater. Sci.* **5** (11) (1990) p. 2706.

42. R.T. Paine and C.K. Narula, *Chem. Rev.* **90** (1) (1990) p. 73.

43. M.G.L. Mirabelli, A. Lynch, L.G. Sneddon, *Solid State Ionics* **32/33** (1989) p. 655.

44. M.H. Rand and J.F. Roberts, *J. Electrochem. Soc.* **115** (4) (1968) p. 423, and references therein.

45. R.S. Pease, *Acta Crystallogr.* **5** (1952) p. 356.

46. J.S. Beck, C.R. Albani, A.R. McGhie, J.B. Rothman, and L.G. Sneddon, *Chem. Mater.* **1** (4) (1990) p. 433.

47. A.T. Lynch and L.G. Sneddon, *J. Am. Chem. Soc.* **111** (16) (1989) p. 6201.

48. P.J. Fazen, J.S. Beck, A.T. Lynch, E.E. Remsen, and L.G. Sneddon, *Chem. Mater.* **2** (2) (1990) p. 96.

49. C.K. Narula, R. Schaeffer, A.K. Datye, T.T. Borek, B.M. Rapko, and R.T. Paine, *Chem Mater.* **2** (4) (1990) p. 384; R.T. Paine, C.K. Narula, R. Schaeffer, and A.K. Datye, *ibid.* **1** (5) (1989) p. 486.

50. C.K. Narula, D.A. Lindquist, M. Fan, T.T. Borek, E.N. Duesler, A.K. Datye, R. Schaeffer, and R.T. Paine, *Chem Mater.* **2** (4) (1990) p. 377.

51. V.Y. Doo, D.R. Kerr, and D.R. Nichols, *J. Electrochem. Soc.* **115** (1) (1968) p. 61.

52. C.L. Beatty, in *Ultrastructure Processing of Ceramics, Glasses, and Composites*, edited by L.L. Hench and D.R. Ulrich (Wiley & Sons, New York, 1984) p. 272-91; D. Seyferth and G.H. Wiseman, *ibid.*, p. 265-71.

53. R.M. Fix, R.G. Gordon, D.M. Hoffman, *Chem. Mater.* **2** (3) (1990) p. 235.

54. Y.D. Blum, R.M. Platz, E.J. Crawford, *J. Am. Ceram. Soc.* **73** (1) (1990) p. 170; S.J. Lenhart, Y.D. Blum, R.M. Laine, *Corrosion* **45** (6) (1989) p. 503.

55. K. Sugiyama, S. Pac, Y. Takahashi, S. Motojima, *J. Electrochem. Soc.* **22** (11) (1975) p. 1545.

56. R.G. Gordon, D.M. Hoffman, and U. Riaz, *Chem. Mater.* **2** (5) (1990) p. 480; R.G. Gordon, D.M. Hoffman, and U. Riaz,

"Atmospheric Pressure Chemical Vapor Deposition of Main-Group Nitride Thin Films," in *Chemical Perspectives of Microelectronic Materials - II*, edited by L.H. Dubois, L.V. Interrante, M.E. Gross, and K.F. Jensen (Mater. Res. Soc. Symp. Proc. **204**, 1991), p. 95.

57. R.M. Fix, R.G. Gordon, D.M. Hoffman, *J. Am. Chem. Soc.* **112** (21) (1990) p. 7833; also see reference 56b.

58. D.C. Boyd, R.T. Haasch, D.R. Mantell, R.K. Schulze, J.F. Evans, and W.L. Gladfelter, *Chem Mater.* **1** (1) (1989) p. 119.

59. J.W. Hwang, S.A. Hanson, D. Britton, J.F. Evans, K.F. Jensen, and W.L. Gladfelter, *Chem. Mater.* **2** (3) (1990) p. 342.

60. Z. Jiang and L.V. Interrante, *Chem Mater.* **2** (4) (1990) p. 439.

61. M.M. Seibold and C. Russel, *J. Am. Ceram. Soc.* **72** (8) (1989) p. 1503; I. Teusel and C. Russel, *J. Mater. Sci.* **25** (8) (1990) p. 3531.

62. H.E. O'Neal and M.A. Ring, *J. Organomet. Chem.* **213** (1981) p. 419.

63. D.J. Larkin, L.V. Interrante, J.B. Hudson, and B. Han, in *Mater. Res. Soc. Symp. Proc.* **204** (1991) p. 141.

64. W. Lee, L.V. Interrante, C. Czekaj, J. Hudson, K. Lenz, and B. Sun, in *Mat. Res. Soc. Symp. Proc.* **131** (1989) p. 431; H.E. Fischer, L.V. Interrante, unpublished work.

65. S. Yajima, K. Okamura, J. Hayashi, and M. Omori, *J. Am. Ceram. Soc.* **59** (1976) p. 324; *Chem. Lett.* (1975) p. 1209.

66. C.L. Schilling Jr., *Br. Polym. J.* **18** (6) (1985) p. 355; C.L. Schilling Jr., J.P. Wesson, T.C. Williams, *J. Polym. Sci. Polym.* **70** (1983) p. 121; R.H. Baney, J.H. Gaul Jr., and T.K. Hilty, *Organometal.* **2** (1982) p. 859; L.M. Niebyiski, U.S. Patent 4,873,353 (1989); Katzman, U.S. Patent 4,737,382 (1988); R.H. Baney, Brit. U.K. Patent Appl., GB 2021545 (Dec. 5, 1979).

67. G.S. Girolami, J.A. Jensen, D.M. Pollina, W.S. Williams, A.E. Kaloyeros, and C.M. Allocca, *J. Am. Chem. Soc.* **109** (1987) p. 1579; C.M. Alloca, W.S. Williams, A.E. Kaloyeros, *J. Electrochem. Soc.* **134** (12) (1987) p. 3170.

68. J.A. Jensen, J.E. Gozum, D.M. Pollina, and G.S. Girolami, *J. Am. Chem. Soc.* **110** (5) (1988) p. 1643.

69. H. Du, B. Gallois, and K.E. Gonsalves, *Chem. Mater.* **1** (6) (1989) p. 569.

70. R. Morancho, G. Constant, and J.J. Ehrhardt, *Thin Solid Films* **77** (1981) p. 155.

71. R. Yazici, K. Gonsalves, and S. Han, in *Protective Coatings: Processing and Characterization*, edited by R.M. Yazici (TMS, Warrendale, PA, 1989) p. 91-100. □

Application of chemical vapor deposited yttria for the protection of silicon carbide fibers in a SiC/Ni₃Al composite[a]

D. J. Larkin and L. V. Interrante
Department of Chemistry, Rensselaer Polytechnic Institute, Troy, New York 12180-3590

A. Bose[b]
Department of Materials Engineering, Rensselaer Polytechnic Institute, Troy, New York 12180-3590

A CVD process has been developed for coating Textron-Avco SCS-6 SiC fiber with yttria. Both Y(fod)₃·H₂O and Y(thd)₃ (fod = 1,1,1,2,2,3,3-heptafluoro-7,7-dimethyl-4,6-octanedionato; thd = 2,2,6,6-tetramethyl-3,5-heptanedionato) were examined as potential Y₂O₃ CVD precursors. Analysis of the deposits by Auger spectroscopy indicated significant F and C incorporation in the case of Y(fod)₃·H₂O whereas, under appropriate conditions, Y(thd)₃ gave a deposit which was essentially free of C and other impurities. GCFTIR analysis of the volatile products of the CVD process indicated isobutylene, tetrafluoroethylene, 1,1-difluoroethylene, fluoroform, and fluoroethylene for Y(fod)₃·H₂O and mainly isobutylene and propylene for Y(thd)₃. The precursor Y(thd)₃ was chosen to deposit 1–2 μm of yttria on short lengths of silicon carbide fibers. The coated fibers were then incorporated into a nickel aluminide (Ni₃Al) matrix by reactive sintering, with yttria affording protection from the known SiC + 2Ni → Ni₂Si + C degradation process. The SiC/Ni₃Al composites, before and after annealing at 1000 °C for up to 100 h, were studied by using SEM and EMPA to determine the extent of reaction. With the exception of certain portions of the fibers that were inadequately coated with yttria, complete protection of the fibers was indicated.

I. INTRODUCTION

There has been considerable interest in ceramic fiber/intermetallic matrix composites.[1] This is, in part, due to the lower density and superior oxidation resistance of intermetallics versus that of many superalloys. The present study involves the use of a reactively sintered nickel aluminide (Ni₃Al) intermetallic matrix with Textron-Avco SCS-6 SiC fibers. The Textron-Avco SCS-6 fibers basically consist of chemically vapor deposited (CVD) silicon carbide on a pitch derived (ca. 40 μm diameter) carbon fiber substrate.

Silicon carbide fibers were chosen due to their high strength, good oxidation resistance, and availability. One major drawback is the fact that silicon carbide has been shown to react with nickel-based alloys at temperatures above 700 °C.[3,4] This reaction is dominated by the diffusion of nickel into the silicon carbide, and to a lesser extent diffusion of silicon into the matrix, leading to a reaction which forms various nickel silicides.[2,3,5] A stable barrier coating would therefore be necessary if these materials are to be used, in contact, at temperatures greater than 700 °C.

The work reported herein was carried out as an extension of the studies of R. L. Mehan and M. R. Jackson, using yttria as a reaction barrier.[6,7] They showed that sputtered yttria, on the surface of a silicon carbide disk, prevented reaction with a nickel-based alloy disk at 1000 °C. The application of yttria onto silicon carbide fibers by sputtering would be impractical, considering the size (140 μm in diameter) and shape of the fibers and the fact that sputtering is a 'line of sight' technique. Chemical vapor deposition (CVD), however, is not line of sight limited and has the potential of totally coating all of the exposed surfaces.

The metal β-diketonate complexes tris(2,2,6,6-tetramethyl-3,5-heptanedionato) yttrium(III) {Y(thd)₃} and tris(1,1,1,2,2,3,3-heptafluoro-7,7-dimethyl-4,6-octanedionato)-monoaquo yttrium(III) {Y(fod)₃·H₂O}, were chosen as potential precursors to yttria thin films due to their relatively high volatility and stability in the 140–200 °C temperature range.[8] Also, previous workers have reported on the use of such β-diketonate complexes in the CVD of various metal oxides.[9–11]

There also has been recent interest in producing the 1-2-3 superconductor (YBa₂Cu₃O₇₋ₓ) by MOCVD of the respective β-diketonate complexes of yttrium, barium, and copper.[12,13] All of these depositions were carried out in either an oxygen or water vapor enriched carrier gas flow and generally involve subsequent annealing of the films in oxygen at temperatures ⩾800 °C.

However, none of these papers has examined, in detail, the precursors' pyrolysis chemistry. A study of the pyrolysis chemistry is presented here along with an evaluation of the different coating compositions and morphologies that result from the application of these two precursors.

II. EXPERIMENTAL PROCEDURE

A. Preparation of the CVD precursors

Tris(2,2,6,6-tetramethyl-3,5-heptanedionato) yttrium(III) {Y(thd)$_3$} and tris(1,1,1,2,2,3,3-heptafluoro-7,7-dimethyl-4,6-octanedionato)-monoaquo yttrium(III) {Y(fod)$_3 \cdot$ H$_2$O} were prepared according to the procedures outlined previously.[8] The Y(thd)$_3$ was obtained as an air stable, white powder in ca. 70% yield and was purified by recrystallization from hexane and subsequent sublimation (1.5 Torr, 140 °C; mp = 171–2 °C).

The mass spectrum of the Y(thd)$_3$ precursor was determined using an HP-5987A GC/MS interfaced to an HP-2623A computer system. The sample was introduced into the system using a heated probe and then was subsequently decomposed using chemical ionization (using methane). The major peaks, with intensities relative to that of the peak at $m/z = 57$ ($I = 100$), were 455 ($I = 24.9$); 81 ($I = 15.1$); 581 ($I = 9.6$); 456 ($I = 6.9$); 55 ($I = 6.4$); 109 ($I = 6.0$); 127 ($I = 6.0$). The ($M + 1$) peak at $m/z = 639$ ($I = 2.0$) and the ($M+$) peak at $m/z = 638$ ($I = 2.2$) were also observed.

In the case of Y(fod)$_3 \cdot$ H$_2$O, the pinkish gummy solid obtained from the reaction procedure was recrystallized twice from methylene chloride (0 °C) and the resulting air stable white powder was further purified by vacuum sublimation. The melting point varied considerably from 60–118 °C, depending on the amount of hydration, which is in agreement with previous observations.[8]

B. CVD of yttria on SiC fibers

The SCS-6 SiC fiber (Textron-Avco Corp., Wilmington, MA) was taken from a continuous spool and broken into lengths of ca. 2 cm. The fiber segments were cleaned by successive immersions, with stirring, in acetone, methylene chloride, and hexane. The fibers were then placed onto an alumina boat, which was notched to support the fibers at two points (see Fig. 1), and then the assembly was loaded into a fused silica tube furnace. The furnace tube was heated to 630 °C (measured with an external thermocouple in contact with the silica outer surface). Approximately 0.5 g of precursor powder was loaded into the precursor vessel and the system was then evacuated to ca. 2.0 Torr. A (65–70 cc/min) flow of H$_2$O saturated N$_2$(g) was started through the precursor vessel. The precursor tempera-
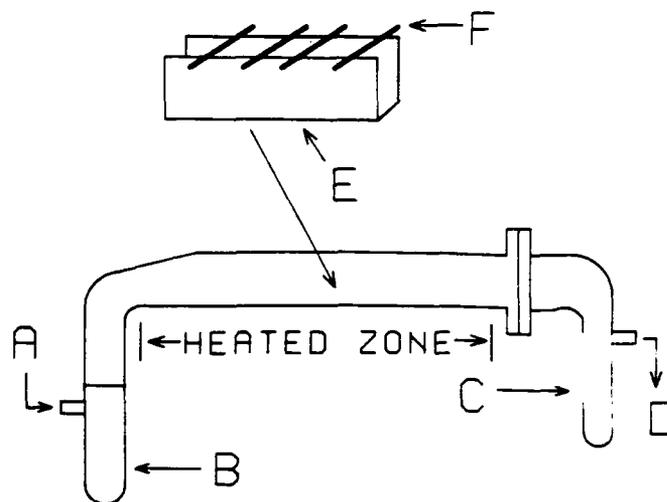

FIG. 1. The main components of the fused silica LPCVD reactor used to coat SCS-6 silicon carbide fibers with yttria include (A) carrier gas inlet, (B) precursor vessel, (C) liquid nitrogen-cooled trap, (D) connection to vacuum pump, (E) alumina support, and (F) silicon carbide fiber.

ture was increased to 150 °C and held at this point until ≥90% of the precursor had sublimed, while maintaining a dynamic vacuum of ca. 2 Torr. This resulted in an average deposition rate of 0.06 μm–0.1 μm/h. Typical coating thicknesses, estimated by using SEM, were from <0.5 μm to 2.0 μm. In the case of the experiments performed using dry N$_2$(g) as the precursor carrier gas, the volatile products were collected in the liquid N$_2$-cooled traps for later analysis by GCFTIR and NMR spectroscopy.

The GCFTIR spectra were obtained using a Varian 1500 GC (VZ-10 column) interfaced to a Perkin-Elmer 1800 FTIR equipped with a temperature controlled transfer line, Au-coated lightpipe, and a liquid nitrogen cooled MCT detector. A background spectrum was recorded before each run and electronically subtracted from subsequent product spectra. After backfilling w·dry N$_2$(g) to 1 atm and warming the isolated liquid-..traps, the pyrolysis gases were sampled using a gas-tight syringe. A Varian 200 MHz FTNMR was also used to help identify the volatile products. The nmr samples were prepared by bubbling the gases through benzene-d$_6$ contained in an nmr tube. The transfer of gases from the warmed LN$_2$-trap to the nmr tube was accomplished using a stainless-steel canula.

C. Fiber coating purity

Single crystal silicon wafer (100) pieces (cleaned in the same manner as the SiC fiber) were placed in front of and behind the alumina boat during deposition. The resulting coated silicon pieces were then analyzed for relative amounts of carbon, oxygen, fluorine, and yttrium using Auger electron spectroscopy (AES) with a

2 KeV electron beam. Argon$^+$, 5 KeV, was used as a sputtering source for depth profiling.

A Debye-Scherrer XRD analysis was performed on one of the CVD-yttria coated silicon carbide fibers using Cu K$_\alpha$ radiation with a Ni filter for a 12-h exposure.

D. Preparation of composites

Typically two to three 2 cm-long sections of CVD-yttria coated SiC fibers were laid up parallel to the longest direction of the composite sample and surrounded with a mixture of Ni (INCO, Carbonyl decomposition type 123) and Al (Balimet, helium atomized h-15 grade) powder (Ni:Al::3:1). This was pressed into a rectangular (3.0 × 1.5 × 0.5 cm) block using a static load of 330 MPa. The compact was then placed on alumina blocks and loaded into a resistively heated furnace (Lindberg, single zone) and evacuated to $<5 \times 10^{-6}$ Torr. The furnace was backfilled with argon and evacuated to $<5 \times 10^{-6}$ Torr a few times to remove oxygen. Then, while under vacuum, the temperature was raised to 200 °C and held for 1 h to remove any moisture, followed by a 30 °C/min ramp to 700 °C to initiate the reactive sintering process.

E. Electron microscopy

A JEOL 840 scanning electron microscope equipped with a backscattered electron (BSE) and secondary electron (SE) detector and also an energy dispersive x-ray (EDX) detector was used to obtain the electron micrographs and preliminary chemical information. A JEOL electron microprobe (EMP) was later employed for the more detailed elemental analysis using the wavelength dispersive detection (WD) mode. In addition to the normal SE, BSE, and EDX modes, this instrument also has an automated scanning WD capability controlled by a Tracor-Northern 5500 computer. This makes it possible to analyze successive points along a sample, which will be referred to as a *linescan*.

The composite samples were prepared for electron microprobe (EMP) studies by cutting (at the midsection) perpendicular to the fiber length with a diamond saw. They were then mounted in epoxy and ground with silicon carbide abrasives. After polishing with 0–1.0 μm diamond powder, the samples were sonicated in a water-based cleaning solution and then in methanol. The CVD-yttria coated fibers were broken in half to expose the fiber/coating interface for SEM imaging. All samples were carbon coated at $<5 \times 10^{-6}$ Torr, using a carbon evaporator.

The standards used for the Electron Microprobe study were silica (for Si K$_\alpha$ and O K$_\alpha$ x-rays); nickel (for Ni K$_\alpha$); yttria (for Y L$_\alpha$) from 99.99% powder (purchased from Alpha Products); and aluminum (for Al K$_\alpha$), all of which were similarly carbon coated.

III. RESULTS AND DISCUSSION

A. Precursor decomposition

In general, analysis of the volatile products that resulted from the pyrolysis of the YL$_3$ complexes indicated that the fragmentation of Y(fod)$_3$ was greater than that of Y(thd)$_3$, as evidenced by the number and relative amounts of the different gaseous byproducts detected. This is consistent with prior mass spectral studies,[14,15] which show less fragmentation for the thd-metal complexes as compared to the more numerous peaks and complex fragmentation of the metal complexes of the type ML$_x$ (where L = fluorinated β-diketone). Isobutylene, tetrafluoroethylene, 1,1-difluoroethylene, fluoroform, and fluoroethylene were detected by GCFTIR as the major volatile components of the trapped pyrolysis products from the Y(fod)$_3$ decomposition. These fluorinated hydrocarbons are not derived from simple fragments of the fod ligand, suggesting that extensive rearrangement accompanies fragmentation of the precursor on pyrolysis. This mobility of the fluorine atom was also suggested by the nature of the fragments observed in the prior mass spectrometry studies[14,15] of similar fluorinated β-diketonate complexes.
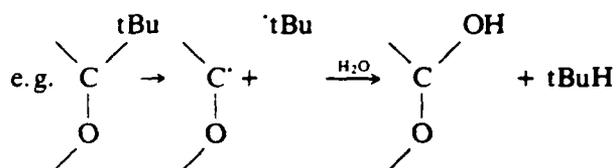
In contrast to Y(fod)$_3$, the pyrolysis of Y(thd)$_3$ yields two major volatile components, isobutylene and propylene. Also detected by using GCFTIR were propane, isobutane, n-butane, ethane, ethylene, methane, and carbon dioxide. The identity of isobutylene and propylene was confirmed by 200 MHz nmr spectroscopy using benzene-d$_6$ as the solvent and reference (using the residual protons at $\delta = 7.15$). In a negative ion mass spectrometry study of related M(thd)$_3$ compounds, Garnett et al. observed fragments which were attributed to the loss of a methyl radical, methane, a t-butyl radical, isobutylene, and isobutane.[15] Our mass spectrometric study of the Y(thd)$_3$ precursor revealed three major peaks with m/z ratios of 57 ($I = 100$), 455 ($I = 24.92$), and 581 ($I = 9.66$). These three peaks are consistent with a t-butyl ion (C$_4$H$_9^+$) for $m/z = 57$, Y(thd)$_2^+$ at $m/z = 455$, and the fragment ($m/z = 581$), possibly resulting from the loss of a (t-C$_4$H$_9$)$^+$ from Y(thd)$_3$. The loss of a t-butyl group on pyrolysis is also suggested by the observation of isobutane and isobutylene as gaseous products of the CVD using Y(thd)$_3$. Both gases could arise from a t-butyl radical which could either combine with a hydrogen atom from the ligand or lose hydrogen to another species.

Clobes has suggested a mechanism for the rearrangement of M(β-diketonate)$_x$ mass spectral fragmentation products which may account for our observation of CO$_2$(g) as one of the products of the thermal decomposition of Y(thd)$_3$.[16] This proposed mechanism starts with a fragment [LM(L-R)]$^+$ which has lost an initial β-diketonate ligand and an R group.

L-M-O — C^R $\longrightarrow$ L-M-O $^+$C^R $\xrightarrow{\text{rearrange}}$

O=$\overset{+}{C}$—C—H   O=C—C—H

H

L-M—O $\xrightarrow{-CO_2}$ L—M—C=C^+_R (Ref. 16)

H-C—C=O

‖

$^+$C$_R$

A similar process can be envisioned in the case of the thermal decomposition of Y(thd)$_3$ except that the initial species would be the radical (thd)$_2$Y(L*) instead of [LM(L*)]$^+$ {where L* = (thd)$^-$ ligand minus a t-butyl radical}. Evidence for the corresponding [(thd)$_2$Y(L*)]$^+$ species was obtained both in our chemical ionization (using methane) mass spectrometry experiments and also in other mass spectrometry studies of Y(thd)$_3$[16a,b] performed using electron ionization. It is interesting to note that CO$_2$ was not detected in the products from the pyrolysis of the Y(fod)$_3$ compound. This, in part, could be attributed to the greater fragmentation and reactivity of the Y(fod)$_3$ complex which would preclude the intramolecular rearrangement needed in this mechanistic scheme.

B. Oxide coating purity

Preliminary CVD studies employing the two different precursors were performed, using dry N$_2$(g) as the carrier gas and Si(100) as the substrate, in order to choose the best CVD precursor to yttrium oxide. In addition to volatility, the criteria that were used included the coating surface morphology and oxide purity as determined by using scanning electron microscopy and Auger electron spectroscopy, respectively.

By using SEM there was no clear difference in the surface morphologies of the coatings resulting from the decomposition of these two precursors. Both coatings were ca. 1 μm thick and had a very smooth surface morphology with the only obvious difference being in the color of the coating. The coating from the Y(thd)$_3$ precursor, deposited on silicon, appeared translucent white in color while deposition of the Y(fod)$_3$ precursor on silicon produced a coating which was distinctly darker. Auger electron spectroscopy of the dark coating obtained from the Y(fod)$_3$ precursor revealed gross carbon incorporation along with considerable fluorine contamination. Both impurities were uniformly distributed throughout the coating thickness, as determined by Auger depth profiling. This observation is consistent with previous mass spectrometry studies of similar fluorinated β-diketonate complexes, which indicate fluorine migration to the metal center. The two reported mechanisms involve either a fluorinated methyl radical or a fluorine radical migration to the metal cen-

ter.[14,15] This methyl radical migration is more likely to occur in the case of a fluorinated compound due to the carbon/carbon bond destabilization induced by the fluorine atom.[14] Auger electron spectroscopy of the translucent white coating produced by the decomposition of Y(thd)$_3$ indicated much less carbon impurity compared to the film produced from Y(fod)$_3$ (Fig. 2).

Therefore, although the fluorinated complex {Y(fod)$_3$ · XH$_2$O} was more volatile, the films produced from the CVD of this compound were unsatisfactory due to excess carbon and fluorine incorporation. In this case attempts to remove the excess carbon and fluorine, by using a N$_2$/H$_2$O(g) carrier gas, resulted in significant precursor decomposition before sublimation. This is most likely due to the smaller steric bulk of the fluorinated propyl groups of Y(fod)$_3$, making the compound reactive toward water vapor. In contrast, yttria was successfully applied using the MOCVD precursor

(a)

(b)

FIG. 2. Auger electron spectra of yttria coatings on silicon produced from the decomposition of (A) Y(thd)$_3$ and (B) Y(fod)$_3$ using dry N$_2$(g) as the carrier gas. The surfaces of both yttria coatings were etched for 8 min (using Ar$^+$ sputtering) prior to recording the spectra.

Y(thd)₃ without any significant decomposition, even when using N₂/H₂O(g) as a carrier gas, allowing control of the coating purity and morphology. This stability is in part due to the ability of the tertiary butyl groups to sterically hinder any additional coordination at the yttrium center.[8] Therefore, as a result of this preliminary study Y(thd)₃ was chosen as the precursor to be used for the deposition of yttria.

Measurements of the relative carbon content by Auger electron spectroscopy were also employed in efforts to optimize the CVD coating process. Yttria depositions on silicon were performed using the Y(thd)₃ precursor at different source temperatures, deposition rates, and gaseous environments while both the coating surface morphology (SEM) and the carbon content (AES) were monitored. An AES depth profile was performed once the best CVD conditions were found that provided a minimum of carbon contamination throughout the coating thickness with a smooth, crack-free surface morphology (Fig. 3). These CVD conditions were a ≤0.15 μm/h deposition rate (i.e., 1.5 μm over 10 h), 80 ccm flow of N₂(g) saturated with H₂O, dynamic pressure of ca. 1.5 Torr, and a 600 °C substrate temperature. An AES depth profile indicated that the coating was uniform in composition throughout the thickness. Water vapor has been used previously in the CVD of this compound in order to produce oxide films of higher purity.[9,12,13] The role of water vapor has not been determined; however, it could aid in the removal of the Hthd ligand, by hydrolysis, or it could serve as a source of H and OH in quenching the organic radical byproducts.

e.g.

$$\text{C} \underset{\text{O}}{\overset{\text{tBu}}{\diagup}} \rightarrow \text{C}^{\cdot} \underset{\text{O}}{\overset{\text{tBu}}{\diagup}} + \xrightarrow{H_2O} \text{C} \underset{\text{O}}{\overset{\text{OH}}{\diagup}} + \text{tBuH}$$

One of the coated fibers was analyzed by Debye-Scherrer XRD. This was done both to determine if the yttria was crystalline and to detect any yttrium oxycarbide (Y₂OC) that can form in the presence of excess carbon, as reported by Holcombe and Carpenter.[17] The observed lines were attributable only to yttrium oxide and β-silicon carbide. No yttrium oxycarbide or any other crystalline impurities were detected.

FIG. 3. (A) This ca. 1 μm thick yttria coating was obtained at 0.1 μm/h deposition rate and a dynamic pressure of 2.0 Torr using H₂O-saturated N₂(g) as a carrier gas. (a) Yttria coating, (b) carbon-rich layers of the SCS-6 SiC fiber, and (c) silicon carbide. (B) Lower magnification view of the yttria-coated SCS-6 silicon carbide fiber in (A), broken to reveal the coating.

C. Reactive sintering process

The Ni₃Al matrix was formed by reactively sintering an intimate mixture of nickel and aluminum powder.[18] Once initiated at about 650 °C, this highly exothermic reaction rapidly proceeds with the dissolution of the nickel into the molten aluminum, resulting in formation of the intermetallic compound Ni₃Al. In

fact, the exotherm is large enough to drive the reaction to completion along with a sharp increase in temperature to ≥1300 °C. As was verified by experiments carried out using uncoated silicon carbide fibers, at these temperatures the fiber can be totally consumed in only a few minutes.

D. Fiber/matrix reaction

Previous workers have indicated the occurrence of a gross reaction between silicon carbide and nickel or nickel base alloys at temperatures greater than about 700 °C.[2,3,5] The nickel and silicon seem to be the more active species which diffuse into the fiber and matrix, respectively. The nickel and silicon carbide react to

form free carbon (as graphite)[3] and nickel silicides such as Ni_2Si and Ni_3Si.[3,5,20-22] Mehan and Jackson[3] have reported on the reaction of the nickel base alloy, NiCrAl, with hot pressed silicon carbide. In their detailed study, they found δ-Ni_2Si and graphite as alternating layers on the silicon carbide side of the SiC/NiCrAl reaction couple. Our present results, as determined from electron microprobe analysis (EMPA) of a partially reacted SiC fiber/Ni_3Al sample, also indicate that the silicon carbide fiber has reacted to form a phase whose nickel-to-silicon ratio is consistent with Ni_2Si (vide infra).

All of the previously reported studies were performed using a nickel base preformed alloy where the reaction with silicon carbide was initiated by hot pressing the two components at temperatures ≤ 1150 °C. The reaction in the case of the SiC/Ni_3Al is further complicated by the fact that the Ni_3Al in this study is produced from the highly exothermic reaction between a mixture of nickel and aluminum powders. Since high temperatures (≥ 1300 °C)[19] are potentially reached before all of the reactants can be totally consumed, free elemental nickel as well as the Ni_3Al are both likely to be available for reaction with the silicon carbide. Therefore the two most likely reaction sequences that are possible would be:

$$SiC(s) + Ni_3Al(s) \rightarrow Ni_2Si(s) + C(gr) + NiAl(s)$$

and

$$2Ni(s) + SiC(s) \rightarrow Ni_2Si(s) + C(gr)$$

Furthermore, the reaction of silicon carbide is known to be most rapid with elemental nickel and slowest with the more complex and nickel deficient compounds.[3] The reaction between silicon carbide and different nickel compounds will be discussed further in the section dealing with the further heating of the composite.

E. Effect of yttria coatings

Coatings other than yttria have been tried, with limited or no success, for the protection of silicon carbide from nickel base alloys. Cornie and collaborators[23] have tried to protect silicon carbide filaments from reaction with a NiCrAlY matrix by using a CVD tungsten barrier coating on the fibers. They reported that there was limited success provided that the tungsten coating was defect-free and adequate in thickness.[23] However, this protection was lost after the tungsten had reacted with the NiCrAlY to form various intermetallic compounds.[23] Mehan and Jackson[6] have shown that a sputtered yttria coating was quite successful as an interface barrier provided there were no discontinuities in the yttria layer. Mehan and Jackson[6] also reported that even though the yttria spalls off after only one heating cycle, the resulting surfaces are modified and continue to provide protection from reaction. It

was proposed that the yttria may be reacting at the two interfaces and forming compounds such as the spinel Y_2SiO_5 and alumina at the ceramic and metal interfaces, respectively, which then serve as the reaction barriers.[6] This observation suggests the possibility that a Y_2O_3 coating on a SiC fiber could serve as both a protective layer and, after the initial processing step, as a weak interface. Whereas a strongly bound yttria coating on the silicon carbide fiber would be desirable during composite manufacture, once the fiber is incorporated into the matrix, the yttria coating could debond from the fiber (and matrix), allowing some desirable energy absorbing mechanisms, such as crack blunting and fiber pullout, to potentially occur. In support of this assumption, examination of the fracture surfaces of composite samples containing Y_2O_3-coated SCS-6 silicon carbide fibers in a reactively sintered Ni_3Al matrix indicated a significant degree of fiber pullout.[24]

In the present work, low pressure (1–2 Torr) chemical vapor deposition (CVD) was employed to obtain uniform Y_2O_3 coatings on all exposed surfaces of the silicon carbide fibers. Preliminary experiments with coatings of various thicknesses suggested the need for a minimum coating thickness. By comparison of composite samples that contained fibers with coatings of different thicknesses, it was found that fiber coatings ≥ 0.8 μm generally survived the reactive sintering (R.S.) step whereas the ≤ 0.6 μm coated fibers did not. The latter case will be discussed in detail first.

A typical yttria-coated fiber that did not survive the R.S. step (i.e., ≤ 0.6 μm coating) is shown in Fig. 4(B). This is believed to be mainly due to the small cracks typically observed by using SEM, in such coatings. The partially protected fiber can be compared to the results of an uncoated fiber in a reactively sintered nickel aluminide matrix [Fig. 4(A)]. Note that the only remaining part of the original uncoated fiber is the carbon core.

The EMPA results (Fig. 5) for the thinly coated silicon carbide fiber in Fig. 4(B) clearly indicate that it has reacted to form compound(s) containing mainly nickel, silicon, and carbon while retaining its original shape. The ratio of Ni to Si is 2:1 (at.%), in agreement with the results of both Refs. 2 and 3. As was shown by the essential replacement of the silicon carbide fiber by nickel silicide (Ni_2Si), the nickel seems to be the more active species, which diffuses into the fiber. Also by using EMPA it was determined that the dark precipitates (Fig. 5) were carbon, presumably graphite. Similar reaction products were observed by both Cornie et al.[23] as a result of incorporating silicon carbide filaments in a hot-pressed NiCrAlY matrix and also by Yang et al.[?] with SCS-6 SiC fibers in hot-pressed Ni_3Al. The surrounding matrix was also analyzed and found to contain

FIG 4 (A) An uncoated SCS-6 silicon carbide fiber in a reactively sintered nickel aluminide (Ni Al) matrix and (B) a silicon carbide fiber thinly coated with yttria (~0.6 μm) Note in (A) only the original carbon core remains unreacted
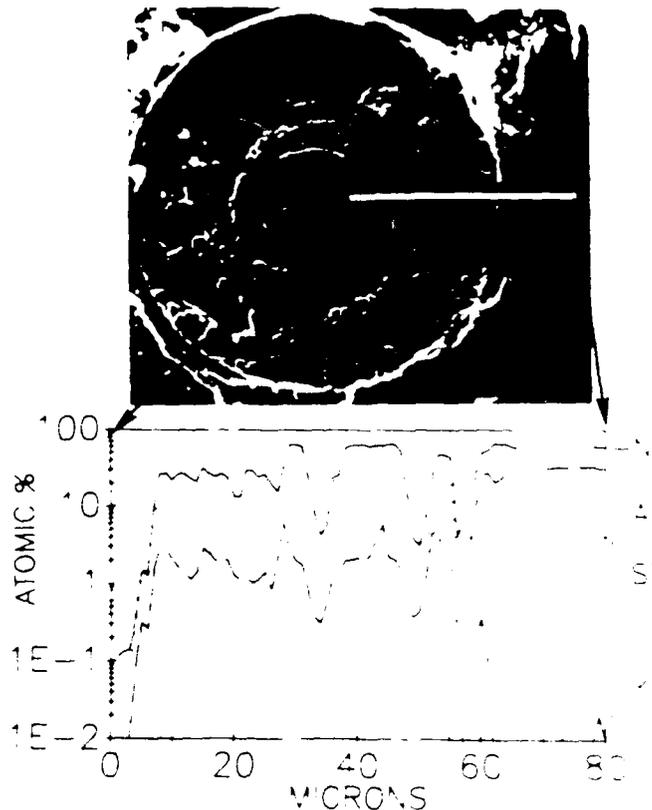

FIG 5 An electron microprobe profile showing that the thinly coated (with yttria) silicon carbide fiber in Fig 4(B) has reacted to form nickel silicides and carbon precipitates

silicon. as well as well-defined areas of nickel-deficient nickel aluminide (e.g., Ni₃Al). These areas were revealed by backscattered electron imaging (BSEI) of the matrix region (see Fig. 6). The dark-colored matrix area shown in Fig. 6(A) was found to have a Ni/Al ratio (at %) of ca. 58/31 by EMPA, whereas the surrounding, lighter area gave a Ni/Al (66/20) close to that expected for Ni Al. Other areas, closer to the original silicon carbide fiber region, were found which contained significant amounts of silicon. In general, the aluminum-rich (nickel deficient) areas were found to extend far (~70 μm) from the fiber whereas the silicon-containing regions were more confined to the matrix area close

(10 μm) to the fiber. This indicates that nickel is more mobile compared to silicon.

In contrast to the observations made on composites containing thinly coated silicon carbide fibers, the results typically obtained for the ≥0.8 μm thick yttria-coated fibers show no sign of a gross reaction between the fiber and the matrix. Also, the backscattered electron image shows none of the features in the matrix area that were very apparent in Fig. 6(A). It is also notable that there is good wetting of the yttria-coated fiber by the matrix [Fig. 7(B)] even though no pressure was applied during the reactive sintering step.

EMPA results of the fiber from Fig. 7 is shown in Fig. 8. A small amount of nickel has diffused into the silicon carbide fiber, ranging from 0.25% near the matrix down to 0.08% (at %) near the carbon core. Three linescans were performed on the fiber to verify that the diffusion was symmetrical. The results confirm that all components are in good contact and that the nickel had diffused in from the surrounding matrix. The aluminum concentration within the fiber area was below detectable limits, which also rules out any possible contamination by the matrix due to polishing. EMPA of the surrounding matrix also confirms the ab-

B

B
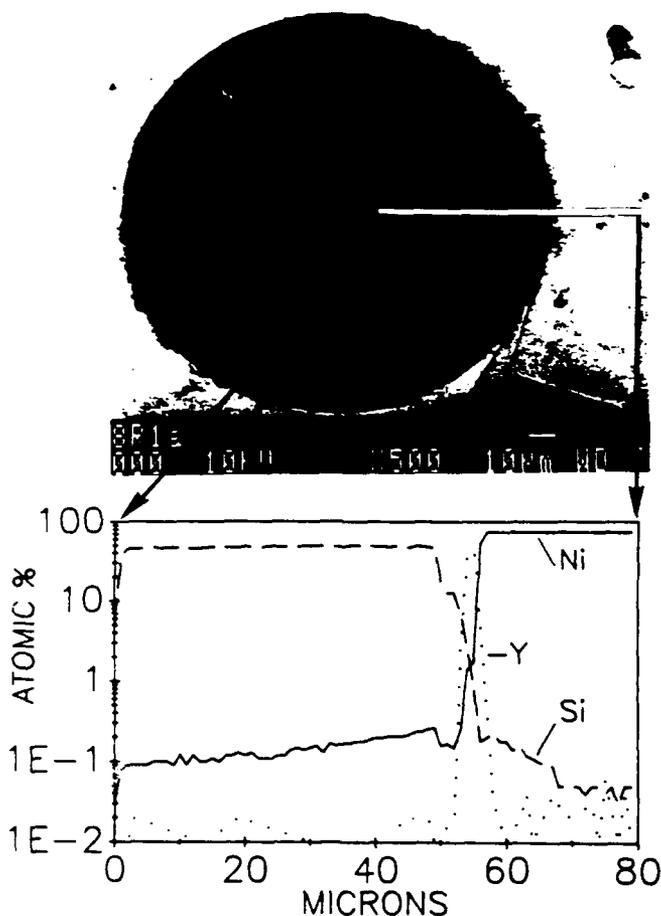
FIG. 8. Electron microprobe analysis from the carbon core of the yttria protected silicon carbide fiber to the Ni₃Al matrix. Note that the silicon diffuses less than the nickel.

difference in the coefficient of thermal expansion of these two sections of the fiber. Cracks in the yttria coatings at the intersection of these layers with the bulk silicon carbide fiber were typically observed during the examination of the ends of the coated fibers by SEM. The other area of observed reaction is associated with the inadequate coating of the fiber at the point of its contact with the modified alumina boat. This was verified by measurement of the distance between the fiber end and the point of contact with the boat in the CVD coating apparatus.

F. Oxygen analysis

The coated-fiber/matrix interface was also analyzed for oxygen by using EMPA. The analyses were then compared for the samples containing the unreacted versus the reacted fibers [Figs. 10(A) and 10(B), respectively]. The amount of oxygen detected, by using EMPA [Fig. 10(A)], on either side of the yttria layer was less than 1% (atomic) for the samples in which the fibers were unreacted. This EMPA [Fig. 10(A)] indicates that the oxygen is intimately associated with only the

yttria layer and not the surrounding nickel aluminide matrix or adjacent silicon carbide fiber. In contrast, Fig. 10(B) depicts an oxygen profile for the sample shown in Fig. 4(B) (reacted fiber), which indicates that a significant amount (>1 at.%) of oxygen was incorporated into the reacted fiber.

As is obvious from a comparison of Figs. 10(A) and 10(B), the fiber/yttria interface for the sample in which the fiber had reacted was not as clearly defined compared to the interface associated with the unreacted sample. This is presumably a direct result of the nickel diffusing into and reacting with the silicon carbide fiber during the reactive sintering of the matrix.

G. Effect of further heating (to 1000 °C)

Two composite samples, similar to the one shown in Fig. 7(B), were further heated in a nitrogen atmosphere to 1000 °C for 1 h. They were then analyzed using scanning and backscattered electron imaging. Since there was not any detectable reaction, they were reheated for an additional 10 h. Following this, the resulting samples were ground well below the surface exposed during the additional heating and then prepared for electron microprobe analysis, as previously described. Electron microprobe revealed that the nickel diffusion profile of the silicon carbide fiber was identical to that of the unannealed sample previously shown in Fig. 8. The backscattered electron image taken of the sample, after it was subjected to heating at 1000 °C for 11 h, did not reveal any evidence of inhomogeneities in the matrix surrounding the fiber.

Extended heating for a total of 100 h at 1000 °C also had no noticeable effect on the SiC fiber composite. This sample was then cut along the fiber axis to reveal the extent of protection provided by the yttria coating. Examining this longitudinal section using SEM and EMPA revealed that most (ca. 8.2 mm) of the 11 mm length of fiber displayed here was totally protected for 100 h at 1000 °C. Other sections, including the fiber end and the region near the fibers' point of contact with the alumina support, showed no obvious further reaction beyond that which was evident after the initial reactive sintering step.

Using the reaction rate data calculated for the NiCrAl/SiC couple,[3] we can compare the two situations that were performed experimentally. For the case of a reaction couple heated to 1000 °C for a period of ca. 11.0 h the silicon carbide is expected to react to a minimum depth of approximately 30 μm. If this temperature were held for a total time of 100 h, the reaction front would be expected to penetrate the silicon carbide fiber to ca. 1.2 cm. This suggests that the 70 μm radius silicon carbide fiber should be almost halfway consumed after being held for only 11 h at 1000 °C and completely consumed after 100 h at this temperature.
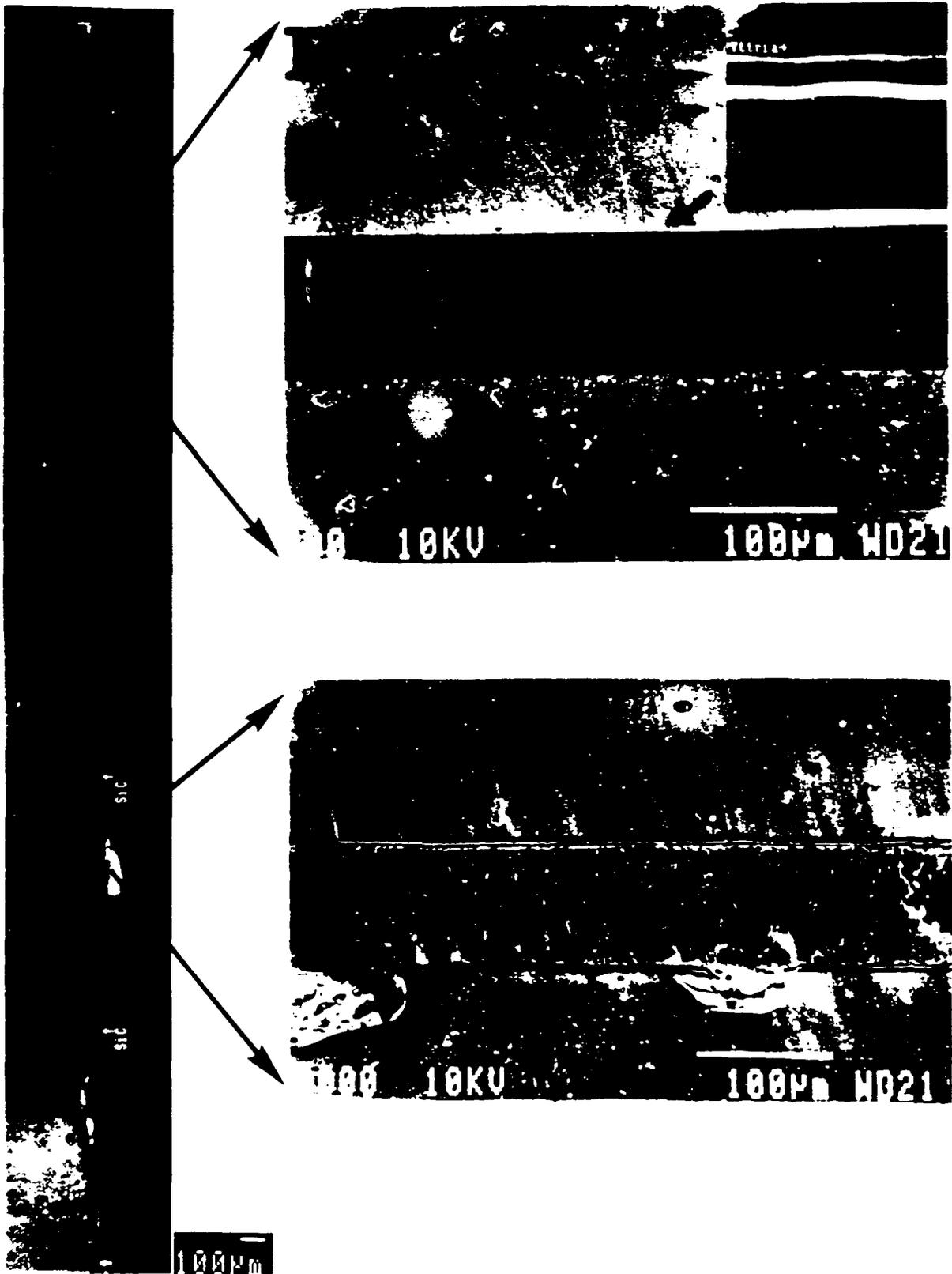
FIG. 9. Longitudinal section taken after the cross section of the original composite. (A) The overall view shows the two uncoated areas, one that was in contact with the alumina support and the fiber end. (B) Higher magnification of the typical section of the fiber, higher magnification of fiber-matrix interface shown in inset. (a) Nickel aluminide matrix and (b, c) the carbon-rich outer layers of the SCS-6 fiber. (C) Higher magnification view of an uncoated area of the fiber showing extensive reaction with the matrix.

(a)

(b)
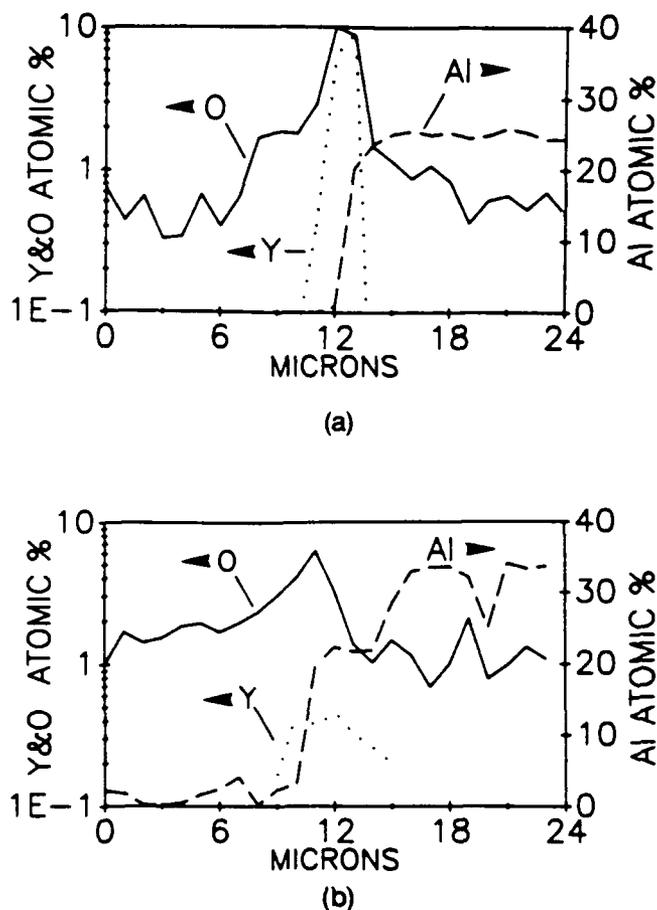
FIG. 10. Electron microprobe analysis of the oxygen distribution centered around the yttrium oxide coating for the sample shown in (A) Fig. 7 (unreacted fiber) and (B) Fig. 4(B) (reacted fiber).

IV. CONCLUSION

Of the two precursors examined as OMCVD precursors to yttria, $Y(fod)_3 \cdot XH_2O$ and $Y(thd)_3$, the nonfluorinated compound, $Y(thd)_3$, was found to give the highest quality yttria coatings.

The CVD-yttria coated SiC fibers survive the large exotherm produced by the reactive sintering of the nickel and aluminum powder in forming the Ni_3Al matrix. It was determined that significant reaction between the fiber and matrix occurs only at the areas on the fiber where the coating is cracked or too thin. The resulting pressureless sintered composite is shown, by SEM, to be free of major voids in the matrix and at the interfaces between the fiber, coating, and matrix. EMPA studies of reacted (inadequately coated) SiC fibers indicate that the nickel is more mobile compared to the silicon while carbon, yttrium, oxygen, and aluminum remain localized. The small amount of nickel diffusion detected after the reactive sintering of the matrix did not increase on further heating at 1000 °C for 11 h. It is suspected the majority of the nickel diffusion occurs while there is still free elemental nickel dur-

ing the reactive sintering step since free nickel would both react with[3] and diffuse into the silicon carbide more quickly. Except for the small amount of nickel diffusion detected after the reactive sintering step, the silicon carbide fiber underwent no further reaction with the surrounding Ni_3Al matrix even after heating at 1000 °C for 100 h.

ACKNOWLEDGMENTS

REFERENCES

[1]S. M. Jeng, W. Kai, C. J. Shih, and J-M. Yang, Mater. Sci. Eng. A114, 189–196 (1989) and refs. therein.

[2]J-M. Yang, W. H. Kao, and C.T. Liu, Metall. Trans. A 20A, 2459 (1989).

[3]M. R. Jackson, R. L. Mehan, A. M. Davis, and E. L. Hall, Metall. Trans. A 14A, 355 (1983).

[4]H. Addhoum and D. Broussaud, Mater. Sci. Eng. A109, 379–387 (1989).

[5]E. L. Hall, Y. M. Kouh, M. R. Jackson, and R. L. Mehan, Metall. Trans. A 14A, 781 (1983).

[6]R. L. Mehan, M. R. Jackson, and M. D. McConnell, J. Mater. Sci. 18 (11), 3195 (1983).

[7]R. L. Mehan and M. R. Jackson, Ceram. Eng. Sci. Proc. 3 (9–10), 484–503 (1982).

[8]R. E. Sievers, K. J. Eisentraut, C. S. Springer, Jr., and D. W. Meek, Lanthanide/Actinide Chemistry, Advances in Chemistry (ACS, 1967), Vol. 71, pp. 141–154.

[9]K. Kamata, S. Matsumato, and Y. Shibata, Yogyo Kyokaishi 90 (1), 46–47 (1982); A. D. Berry, D. K. Gaskill, R.T. Holm, E. J. Cukauskas, R. Kaplan, and R. L. Henry, Appl. Phys. Lett. 52 (20), 1743–1745 (1988); A. P. Purdy, A. D. Berry, R.T. Holm, M. Fatemi, and D. K. Gaskill, Inorg. Chem. 28, 2799–2803 (1989).

[10]L.V. Interrante, Z. Jiang, and D. J. Larkin, Chemistry of High Temperature Superconductors II, ACS Symposium Series 377, edited by D. L. Nelson and T. F. George, 168–180 (1988).

[11]V. A. Varyukhin, V. Yu. Vodzinskiy, G. A. Domrachev, B. I. Kozyrkin, V.V. Kutyreva, and O. N. Suvorova, Probl. Khim. Primen. Beta-Diketonatov Met., edited by V. Spitsyn, 1st ed., 178–184 (1982).

[12]J. Zhao, H. O. Marcy, L. M. Tonge, B.W. Wessels, T. J. Marks, and C. R. Kannewurf, Phys. C 159, 710–714 (1989).

[13]J. Zhao, K-H. Dahmen, H. O. Marcy, L. M. Tonge, B.W. Wessels, T. J. Marks, and C. R. Kannewurf, Solid State Commun. 69 (2), 187–189 (1989).

[14]C. Reichert, G. M. Bancroft, and J. B. Westmore, Can. J. Chem. 48, 1362 (1970).

[15]J. L. Garnett, I. K. Gregor, and M. Guilhaus, Org. Mass. Spec. 13 (10), 591 (1978).

[16]A. L. Clobes, M. L. Morris, and R. D. Koob, Org. Mass. Spec. 3, 1255 (1970).

[16a]E. M. Gavrishchuk, N. G. Dzyubenko, L. I. Martynenko, and P. E. Gaivoronskii, Zhur. Neorg. Khim. 28, 871 (1983).

[16b]J. D. McDonald and J. L. Margrave, J. Less-Common Metals **14**, 236 (1968).

[17]C. E. Holcombe·and D. A. Carpenter, J. Am. Ceram. Soc. **64**, C-82 (1981).

[18]A. Bose, B. H. Rabin, and R. M. German, Powder Metall. Int. **20** (3), 25–30 (1988).

[19]Yu. S. Naiborodenko, G.V. Lavrenchuk, and V. M. Filatov, Poroshk. Metall. **12** (240), 4 (1982).

[20]R. C. J. Schiepers, F. J. J. van Loo, and G. de With, J. Am. Ceram. Soc. **71** (6), C284 (1988).

[21]I. Ohdomari, S. Sha, H. Aochi, T. Chikyow, and S. Suzuki, J. Appl. Phys. **62** (9), 3747 (1987).

[22]C. S. Pai, C. M. Hanson, and S. S. Lau, J. Appl. Phys. **57** (2), 618 (1985).

[23]J. A. Cornie, C. S. Cook, and C. A. Anderson, NASA Contract Report, NASA-CR-134958.

[24]This was evidenced by the observation of protruding fiber ends and holes on the fracture surfaces of broken samples.

J. Mater. Res., Vol. 5, No. 11, Nov 1990

2717

INTERFACE STABILITY IN ALUMINIDE MATRIX COMPOSITES

John B. Hudson and Bing-Xi Sun
Materials Engineering Department
Rensselaer polytechnic Institute
Troy, NY 12180

corresponded to the "gross reaction layer" observed optically. The next layer out had an average composition of Ti_3Al. This layer was followed by a regime in which the aluminum content slowly dropped to zero, with a concomitant increase in titanium content toward the bulk composition. Oxygen concentrations could not be measured in this system.

More recently, Chamberlain [2] investigated this system by depositing titanium by electron beam evaporation, to a thickness of 200 nm, on a single crystal (111) sapphire surface and heat treating for 4.5 hours at 800 K. After heat treatment, the samples were analyzed by Auger electron spectrometry to determine the composition profile at the interface. The analysis involved monitoring the oxygen, titanium and aluminum Auger peaks as the film was removed by argon ion sputtering. The aluminum peak was monitored at high energy resolution to permit separation of contributions from metallic aluminum, and aluminum present as oxide. The resulting depth profiles showed a metallic aluminum layer at the interface, with oxidized aluminum restricted to the Al_2O_3 side of the interface. The final oxygen content of the titanium film was high, probably due to indiffusion of oxygen from the ambient atmosphere during heating.

In the present work, we have repeated the study of the Ti-Al_2O_3 interface, using methods similar to those of Chamberlain, and extended the work to $TiAl$-Al_2O_3, $TiTaAl_2$-Al_2O_3, Ta-Al_2O_3 and Y-Al_2O_3 interfaces, with the intent of determining the effect of interface composition on interfacial reactivity.

2. Experimental

The experimental interface samples were formed by sputter deposition of the appropriate metal or alloy onto α-Al_2O_3(1010) plates, $0.3cm^2$ in area, 1mm thick. The Al_2O_3 plates were ultrasonically cleaned prior to the deposition process, using successive baths of detergent water, distilled water, acetone and ethanol. Deposition was carried out in a dc magnetron sputtering system using metal targets of the desired final composition. Targets used included pure titanium, tantalum and yttrium obtained from Alfa Products Division of Johnson Matthey and TiAl and $TiTaAl_2$ alloy targets obtained from Pure Tech, Inc. No effort was made to compensate for differential sputter yields. The background pressure in the system prior to deposition was in the high 10^{-8} torr range. The experimental system permitted the preparation of as many as ten samples simultaneously. Film thicknesses varied from run to run in the 200 to 300 nm range, but were uniform within less than 10% for the samples of a given run.

After deposition, one or more samples from each run was reserved as an "as deposited" sample. The other samples were heat treated for various times and temperatures to induce interfacial reaction. The heat treating process was carried out in an ultrahigh vacuum system equipped with a small furnace, capable of temperatures up to 1200 K. During the heat treatment cycle, the pressure was maintained in the low 10^{-9} torr range, which avoided the introduction of oxygen through the free surface of the film.

Subsequent to the heat treatment, both the heat treated samples and the unheated reference samples were analyzed to determine the extent of interface reaction during heat treatment. Samples were first examined by Rutherford backscattering spectroscopy (RBS,) using 1.0 or 2.0 MeV He⁺ ions. Following this, the samples were examined by Auger surface analysis (AES) and depth profile analysis using argon ion sputtering. The extent of reaction and reaction products were determined by comparison of the backscattering spectra and Auger depth profiles for the heat treated and unheated samples.

In the Auger analysis, the sensitivity of the Auger spectrometer was standardized by adjusting the sensitivity to give a constant height for the molybdenum peaks from the molybdenum mask used to hold the samples in place. The absolute film thicknesses obtained from the backscattering spectra were used to standardize the depth scale.

3. Results and Discussion

Auger spectra taken in the course of a depth profile run, such as the one shown in Figure 1, indicated that the aluminum
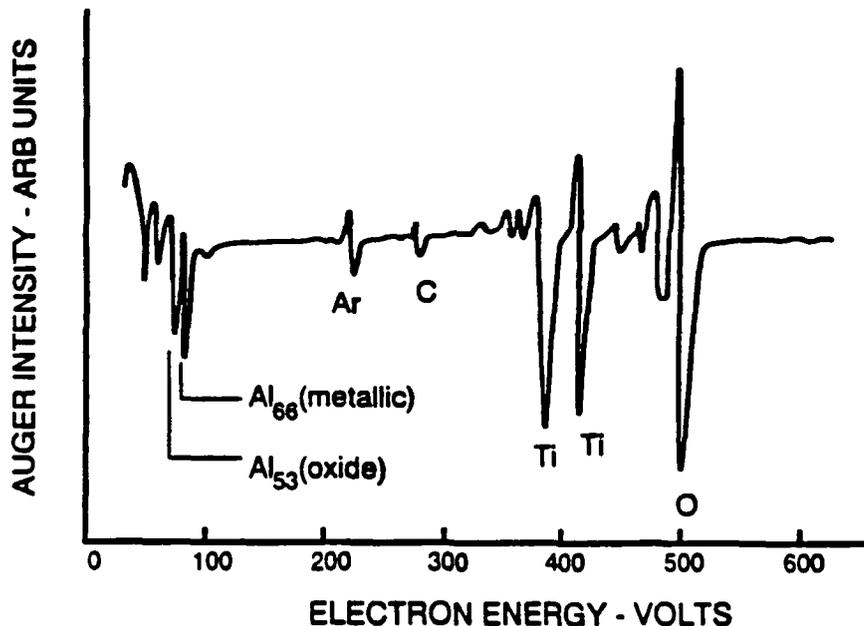
Figure 1. Auger spectrum of a Ti- Al_2O_3 thin film sample, after heat treatment, taken in the course of a depth profile measurement. The splitting of the aluminum peak near 60 eV into contributions from metallic and oxide species is evident.

Auger peak in the 60 eV region was split, showing contributions from both metallic aluminum and oxidized aluminum, Al^{3+}. Accordingly, all depth profile studies recorded these two contributions independently.

3.1 Titanium-Al_2O_3 Interface

RBS spectra obtained from as-deposited and annealed films

of titanium on sapphire are shown in Figures 2 and 3. These
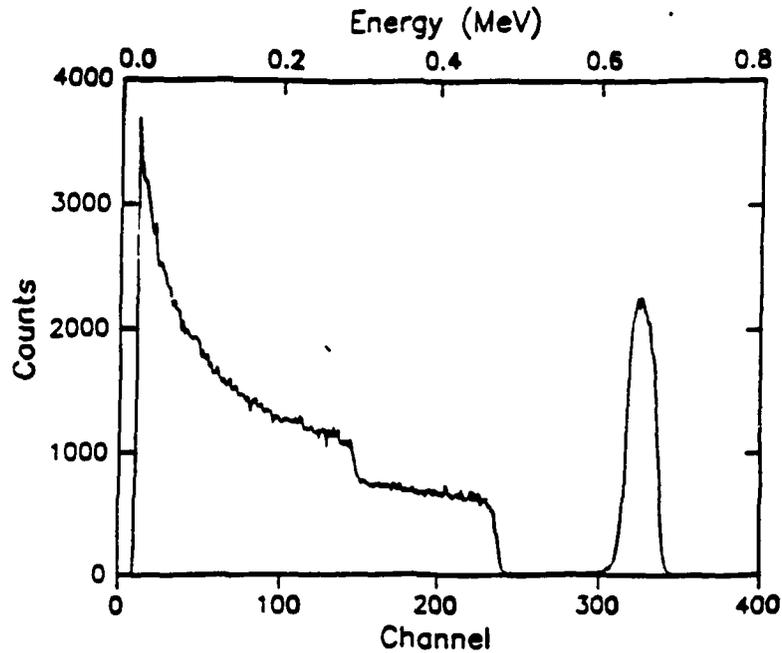
Figure 2. RBS spectrum of Ti-Al$_2$O$_3$ couple - as deposited.
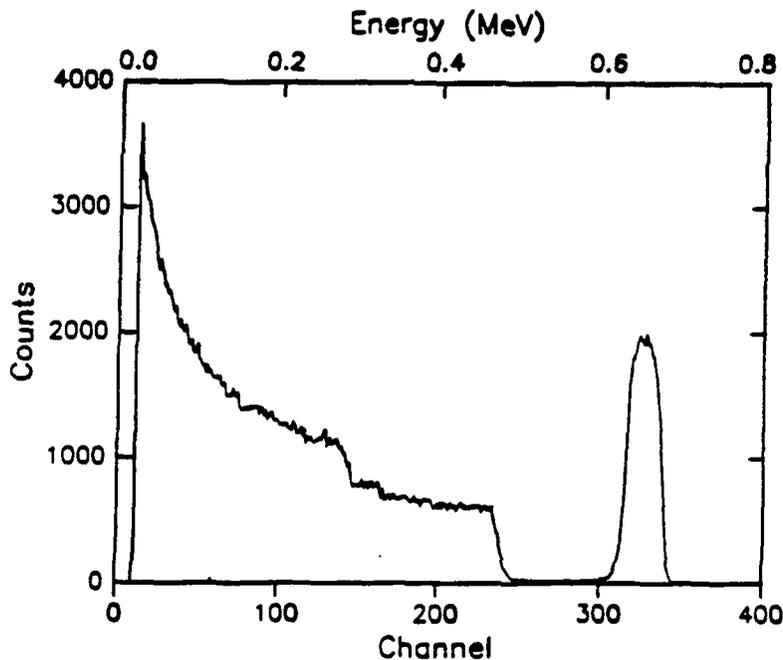
Figure 3. RBS spectrum of Ti-Al$_2$O$_3$ couple - after annealing for 8 hours at 550°C.

spectra differ in that the titanium peak (above channel 300) is wider but less intense for the annealed sample, and the oxygen edge (close to channel 150) and aluminum edge (close to channel 250) are less sharp, and show structure below the edge. These features are indicative of significant reaction at the interface. The extent of reaction is even more obvious in the corresponding Auger depth profiles, Figures 4 and 5. The

interface is clearly more diffuse for the annealed sample and there is a buildup of metallic aluminum (the Al_{66} peak) near the
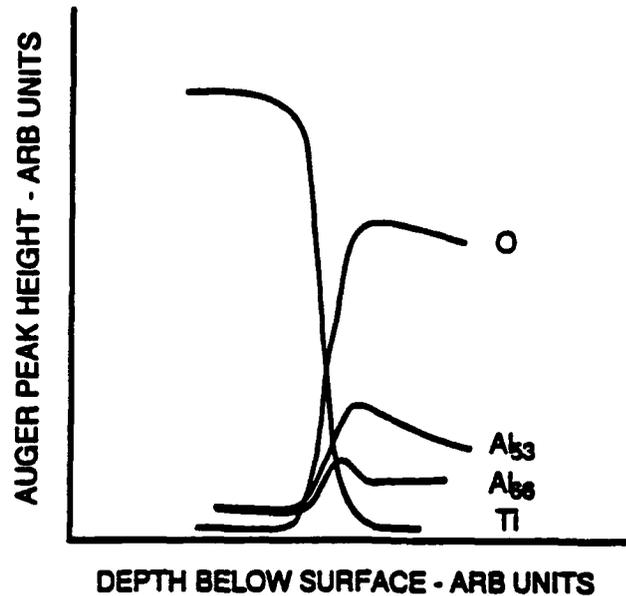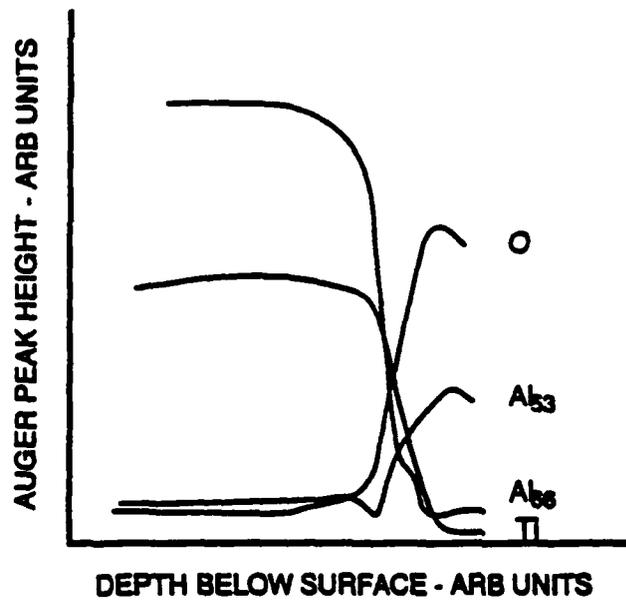

Figure 4. Auger dpeth profile study of a Ti-Al_2O_3 couple - as deposited
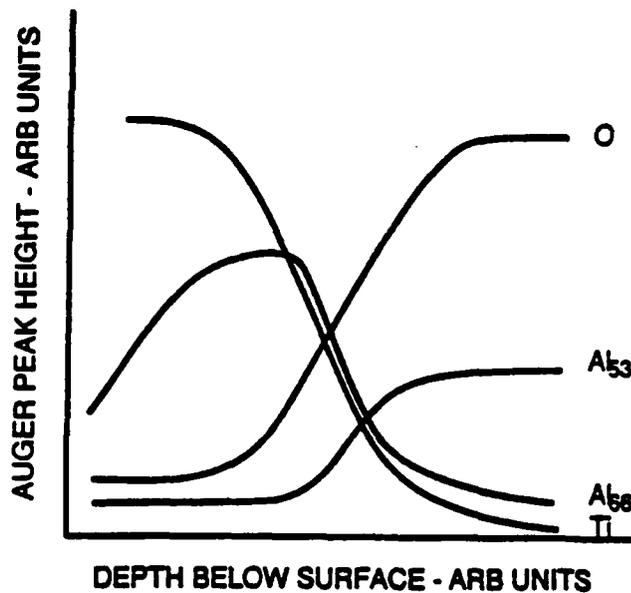
Figure 5. Auger depth profile study of a Ti-Al_2O_3 couple - after annealing for 8 hours at 550 °C.

interface. There is also significant diffusion of oxygen into the titanium. Note that these profiles show only the region close to the interface, not the whole thickness of the film. Far from the interface the profile showed only titanium and a small amount of oxygen.

These results are similar to those observed previously by Tressler et al [1] and Chamberlain [2]. Thermodynamic analysis of the Ti-Al_2O_3 system, in which titanium aluminide was

considered as a possible reaction product, led to the results
shown in Table 1.

Table 1

Reaction		ΔG (cal/mol)
Al_2O_3 + 7/2Ti	$3/2TiO_2$ + 2TiAl	+ 21000
Al_2O_3 + 13/5Ti	$3/5Ti_3O_5$ + 2TiAl	+4100
Al_2O_3 + 4Ti	Ti_2O_3 + 2TiAl	-4700
Al_2O_3 + 5Ti	3TiO + 2TiAl	-23000

Note that the general trend is that the reactions become
thermodynamically more favorable as the oxidation state of the
titanium in the oxide product decreases.

3.2 TiAl- Al_2O_3 Interface

RBS spectra obtained from TiAl films on Al_2O_3 are shown
superimposed in Figure 6. In this figure, the lack of
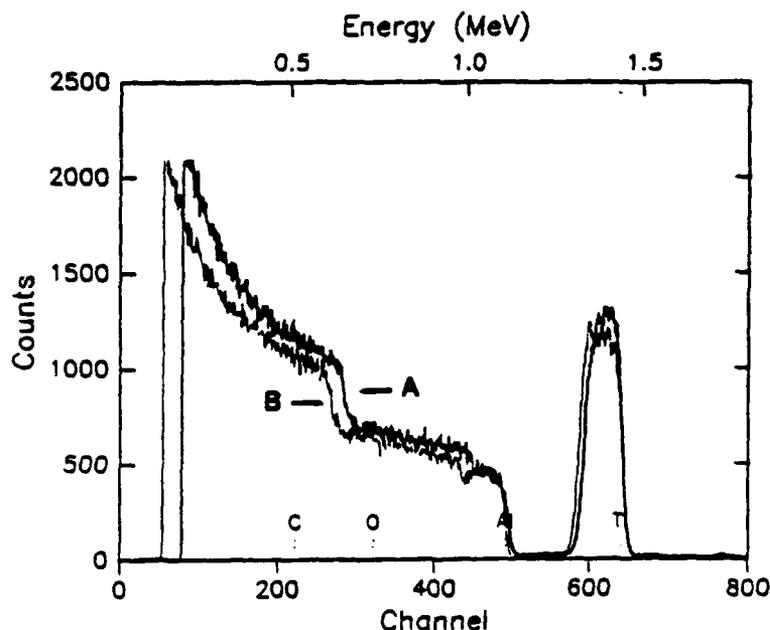
Figure 6.   RBS spectra of TiAl-Al_2O_3 couples: A, as
deposited. B, after annealing 24 hours at 850°C.

correspondence of the Al and O edges in the two cases arises
form a calibration problem in the RBS system. The feature of
greatest interest in this figure is the slight dip in the Al
peak at the film-substrate interface.   This may indicate
preferential diffusion of titanium into and aluminum away from
the interface, similar to the results observed by Tressler et
al [1]. The Auger depth profiles of this interface are shown
in Figures 7 and 8. Again the interface has become more
diffuse as a result of the annealing process, but the extent of
interdiffusion is much less here than in the case of the Ti-
Al_2O_3 interface, and there is no obvious increase in the Al_{66}
peak near the interface. Note that the annealing temperature

is much higher in this case - 810°C as compared to 550°C for the Ti-Al$_2$O$_3$ case - indicating a much lower reaction rate.

Figure 7.   Auger depth profile study of a TiAl-Al$_2$O$_3$ couple - as deposited.
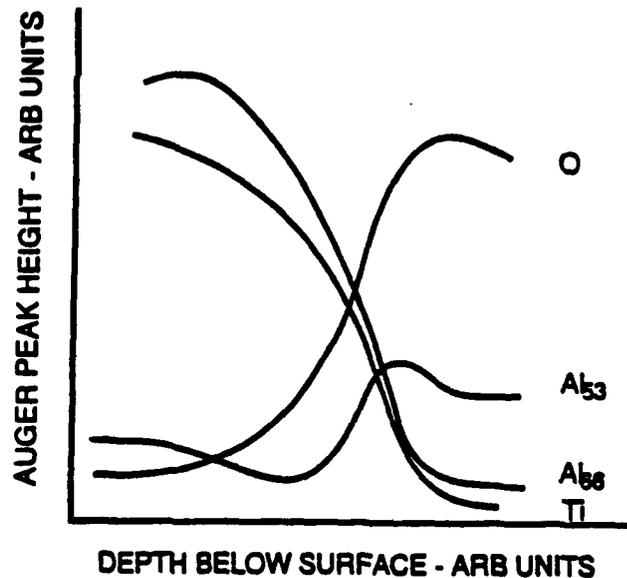
Figure 8.   Auger depth profile study of a TiAl-Al$_2$O$_3$ couple - after annealing for 24 hours at 810°C.

3.3   TiTaAl$_2$-Al$_2$O$_3$ Interface

RBS spectra for annealed and as-deposited films in this case are shown superimposed in Figure 9. Here, aside from the offset associated witt the RBS system calibration, the two spectra are indistinguishable. The Auger depth profiles, shown in Figures 10 and 11, show some increase in interface width, but significantly less than either of the previous cases.

3.4 Yttrium-Al$_2$O$_3$ Interface

A few measurements were made of the interfacial reactions of yttrium films on Al$_2$O$_3$. This was done to investigate the possibility of using Y$_2$O$_3$ as a barrier layer to reduce the
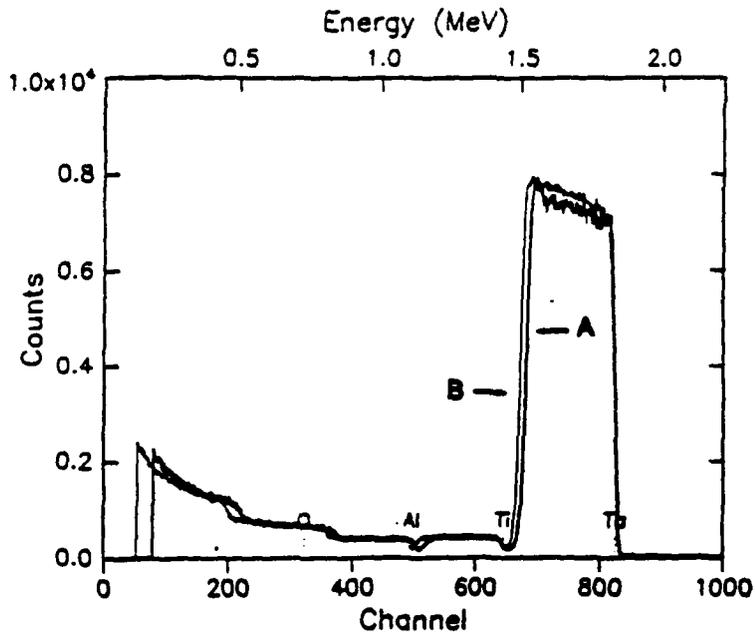
Figure 9. RBS spectra of TiTaAl$_2$-Al$_2$O$_3$ couples: A, as deposited. B, after annealing 24 hours at 850°C.

DEPTH BELOW SURFACE - ARB UNITS
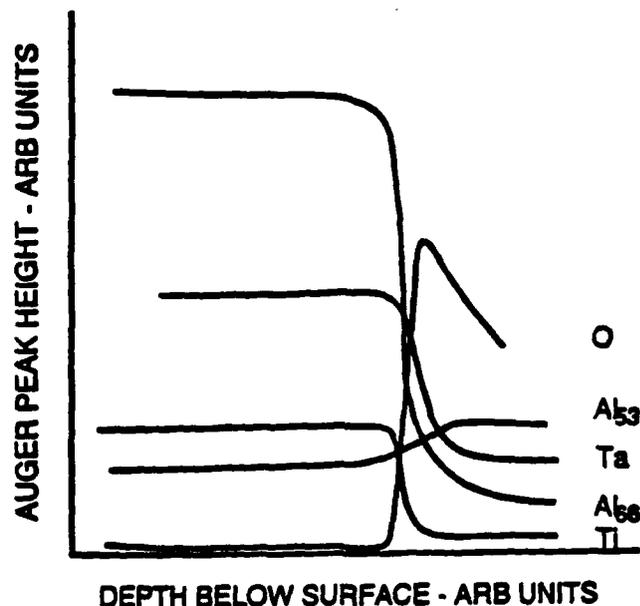
Figure 10. Auger depth profile study of TiTaAl$_2$-Al$_2$O$_3$ couple - as deposited.

reactivity of the titanium-Al$_2$O$_3$ interface. As shown in Figure 12, the RBS spectra in this case indicate extensive interfacial reaction, even for relatively short, low temperature anneals, with the formation of interfacial layers of yttrium oxides and
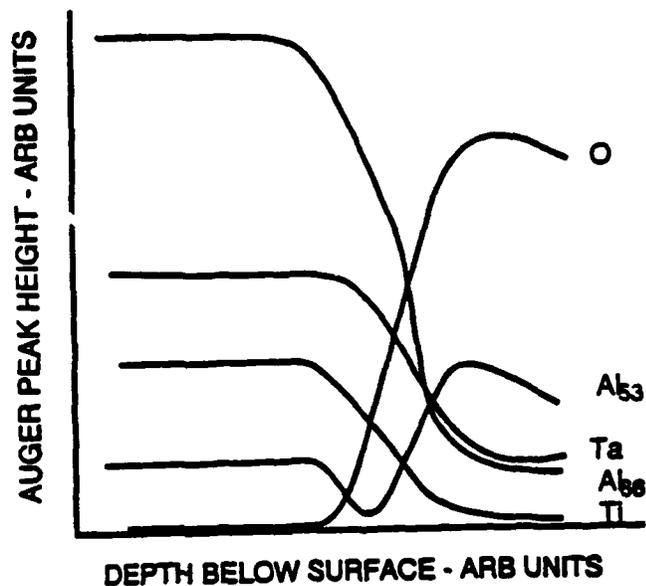
Figure 11. Auger depth profile study of $TiTaAl_2-Al_2O_3$ couple - after annealing 8 hours at 810°C.

yttrium aluminum oxides, with aluminum diffusing as far as the surface of the film. It is clear that if Y_2O_3 is to be used as a barrier layer, it will have to be deposited as the oxide.
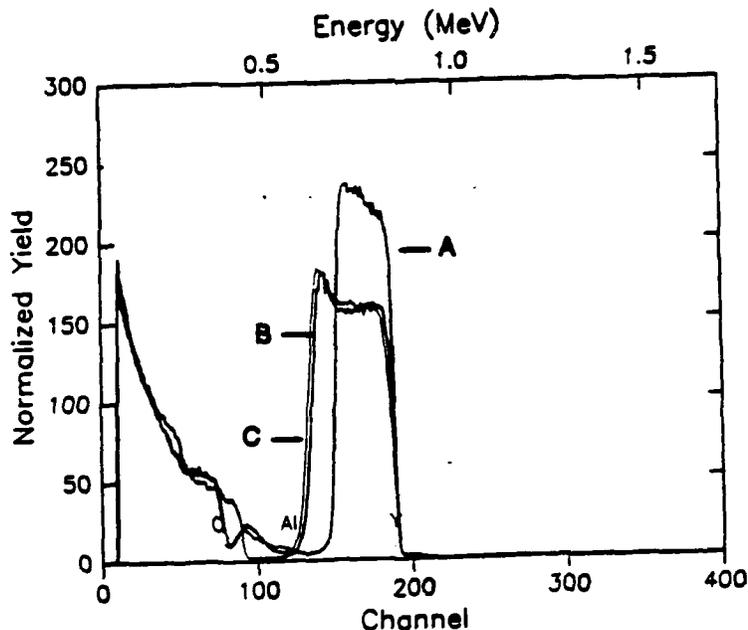
Figure 12. RBS spectra of $Y-Al_2O_3$ couple: A, as deposited, B, after annealing 4 hours at 550°C. C, after annealing 8 hours at 550°C.

3.4 Tantalum-Al_2O_3 Interface

A set of measurements made with pure tantalum films on Al_2O_3 indicated negligible interfacial reaction, as expected on thermodynamic grounds.

4. Conclusions

The results obtained clearly indicate that the titanium-Al_2O_3 interface is highly reactive, even at relatively low temperatures.

Use of intermetallic matrixes such TiAl or $TiTaAl_2$ greatly reduces the tendency toward interfacial reactions, with the interface stability increasing with the addition of tantalum.

The use of Y_2O_3 as a barrier layer is suggested on thermodynamic grounds. Present results with yttrium are inconclusive, due to our inability to deposit the oxide using available equipment.

Tantalum films are unreactive with Al_2O_3. and might, if thick enough, serve as a barrier layer in a titanium matrix system.

References

1. R. E. Tressler, T. L. Moore and R. E. Crane. J. of Materials Sci. 8,151, (1973).

2. M. B. Chamberlain. J. Vac. Sci. Technol. 15, 240, (1978).

HOLLOW CATHODE SPUTTER DEPOSITION OF TITANIUM ONTO CARBON FIBER TOWS

Bryan Lagos and John B. Hudson
Materials Engineering Department
Rensselaer Polytechnic Institute
Troy, NY 12180

Abstract

Two cylindrical hollow cathode magnetron (CHCM) sputtering systems were constructed to reactively sputter coatings of refractory materials onto carbon fibers in order to protect these fibers within a matrix environment. Because of the inherent cylindrical symmetry in this type of cathode, cylindrical objects such as carbon fibers are naturally given an even coating on their outer surfaces. Using this type of cathode, it was possible to deposit thin films of titanium onto carbon rods at high sputter deposition rates. The addition of nitrogen to the inert sputter gas atmosphere was used to produce non-stoichiometric coatings of the refractory compound TiN_x. Plasma leakage in the cathode had the added benefit of bombarding substrates with the sputtering plasma, resulting in electrostatic charging that could spread fibers within a carbon fiber tow. Under this condition it was possible to evenly coat each fiber within a bundle with titanium.

Part I: Introduction

In order to alleviate interface problems that occur when carbon fibers are incorporated into the matrix material of composites, thin films of various materials are deposited onto the fibers prior to their insertion into the matrix material. These interface problems arise from a combination of effects resulting from the differences between the two materials, including poor wetting of the carbon surface by the matrix material, reactions between the fiber and matrix material, and differences in the coefficient of thermal expansion of the two materials.[1-4] Thin films or thick films can act as functionally

gradient coatings and diffusion barriers and hence can alleviate some of these problems. As well as protecting the fiber during the process of combining the fiber with the matrix, coatings may promote the wetting and bonding of the fiber with the matrix. We have constructed and tested a cylindrical hollow cathode magnetron (CHCM) sputtering cathode[6-9] for coating carbon fibers. This paper deals with the sputtering of titanium and the reactive sputtering of TiN as a prelude to the sputtering of refractory metal borides. All hardware and techniques developed herein for working with Ti and TiN easily lend themselves to adaptation to a metal-boride sputtering system.

Part II: Experimental Apparatus

Two seperate CHCM sputtering cells were designed and built in our laboratory. These were operated within two separate vacuum systems. Schematic views of the first and second sputtering systems with their associated cathodes are shown in Figures 1, 2 and 3, 4 respectively.

Each CHCM was powered by a 0.8 Amp, 250 Volt D.C. power supply. The cathode bodies were constructed of copper to ensure efficient cooling of the target surface. The target area of each cathode consisted of a sheet of titanium rolled into a cylinder with a diameter of approximately one inch, and a length of one inch. The cathode in each design was insulated from the anodes by two annular ceramic inserts cut from machinable ceramic. The anodes were constructed of stainless steel and iron in the first and second CHCMs respectively. Although a solenoid coil originally surounded the first cathode to produce a

magnetic field for magnetron operation, the solenoid was soon replaced with two solid annular-shaped ceramic magnets, placed at the ends of the CHCM assembly. This same magnet configuration was used for the second cathode.

The sputter chamber used in conjunction with the first cathode was evacuated by the multi-stage pumping system illustrated in Figure 1. All components in the high vacuum parts of the system were made from 304 stainless steel and are joined using copper gasket technology. The system was used to achieve base pressures in the 10^{-9} range. Sample introduction and movement between the cathode and oven was achieved via a magnetic coupling system that transferred both translational and rotational motion to the substrates. Gas flow into the system was regulated by two piezoelectric mass flow controllers.

The sputter chamber used in conjunction with the second CHCM is shown in Figure 3. This system was also constructed of stainless steel using copper gasket technology and could achieve base pressures in the 10^{-9} range. The sample manipulator indicated in Figure 3 could place samples within the main chamber by use of a stainless steel rod that slid within a differentially pumped chamber.

V: Procedures and Results

A Preliminary Testing of Cathode I and Version I of the Sputtering System.

As an initial test of the first sputtering system, titanium was deposited onto a 3 inch long segment of copper wire (2 mm. in diameter)

at a pressure of 200 mtorr of Argon with no gas flow. After the solenoid coil magnetron established a magnetic field, the power supply to the cathode (version 1) was turned on, producing a power of approximately 85 watts. The resulting plasma was not contained entirely within the cathode cavity since each of the two cathode openings emitted dim jets of plasma. After five minute presputter, the copper wire was inserted into the cathode for fifteen minutes. An AES depth profile of the titanium coating is shown in Figure 5. This figure shows the large amount of carbon and oxygen contaminants contained within the film.

In an attempt to identify the cause of the contamination of the Ti film by carbon and oxygen, an experiment identical to that above was performed, except this time argon was slowly bled into the chamber while being removed by the turbopump. The pressure was maintained at 200 mtorr. After a 5 minute presputter, the copper wire substrate was inserted into the cathode for a period of two minutes. An AES depth profile of this material is shown in Figure 6. This deposition obviously resulted in a much purer film, indicating that sputtering with a flow of gas through the system could create higher purity films than sputtering with no such flow.

In order to demonstrate the ability of the cathode cell to coat carbon substrates, several three inch long rods (1/8 inch diameter) of pressed vitreous carbon were individually introduced into the deposition chamber in a series of experiments. Argon was bled into the chamber through one of the two piezoelectric gas leak valves throughout the experiments. Argon pressure was maintained at 250 mtorr by the pumping action of the turbopump. The cathode power was 112 watts. After a 15 minute presputter, the rod was inserted into the cathode for 2 minutes.

When the carbon rod was removed from the cathode, it appeared to glow red for several seconds, indicating a surface temperature in excess of 700 °C. This high substrate temperature was observed for all depositions performed on carbon substrates using version I of the cathode. Upon removal of the rod from the chamber, AES was again performed on the Ti coatings. Figures 7a and 7b show the results of the AES study on one rod, indicating a relatively pure deposited film. Metallographic techniques were used to obtain a thickness measurements as high as 1.5×10^{-4} cm for these titanium film depositions and a resulting sputtering deposition rate was 7500 Angstroms/minute.

B Sputtering of TiN using the First Sputtering System and Version I of the Cathode.

Coatings of TiN_x were deposited onto a carbon rods in the following manner. Rod were cleaned ultrasonically using the same procedures mentioned previously, and were loaded into the sample introduction chamber. Each rod was then brought into the main chamber and was baked out in the oven at 475 °C for 1 hour. The gas pressure was then adjusted to a pressure of 250 mtorr, with a partial pressure of 20% N_2 in Argon. The magnetron coil was turned on and the plasma was lit with a power of 135 watts. After a 10 minute presputter, the carbon rod was then inserted for a two minute sputter run. The AES depth profile analysis of a resulting film is shown in Figure 8. The films appeared to be a very dark black-reddish color with gold sparkling highlights, indicating that the films were nitrogen deficient.

In order to quantify the AES spectra taken of TiN$_x$, a "standard" was obtained from Mark Wittmer at IBM Yorktown Heights. The standard consisted of a 200 Angstrom thick layer of TiN$_x$ on a silicon wafer. Here x is approximately equal to 1. The exact value of x is not known; however, the film stoichiometric ratio was assumed to be close to 1:1 because of the observed characteristic gold TiN color. An AES spectrum and depth profile are shown in Figures 9 and 10.

Utilizing the AES spectrum of this standard, it was possible to determine the N/Ti ratio of the two sputtered TiN$_x$ films. Using the Auger results of the Ti film in Figure 7a and the Auger analysis process of Laimer et al.[10] and the equation:

$$(N/Ti)_{Sample} = [(N/Ti)_{TiN-Std}/K_{TiN-Std}] \times [I_{Sample}(383eV)/I_{Sample}(418eV) - k_{Ti-Std}].$$

(1)

[where $k_{Ti-Std} = (383eV/I(418eV)$ and $k_{TiN-Std} = I(383eV)/I(418eV)$] a ratio of N/Ti equalled to 0.56 was obtained for the average TiN$_x$ sample. A piece of the Ti sheet that was used to construct the cathode was used as a Ti standard (see Figure 11). All numerical values for peak heights used in these calculations are tabulated in Table 1.

It was also possible to use the TiN standard to calculate a rough sputter deposition rate for the first TiN$_x$ sample, assuming that the sputtering rates of TiN and TiN$_x$ are approximately equal. Knowing that the standard film thickness is 200 Angstroms and that 30 minutes (see Figure 11) were required to sputter down to the silicon substrate, one can calculate a sputter rate of 6.7 Angstroms/min. Noting from Figure 8 that approximately 80 minutes were required to sputter through the TiN$_x$

coating, one can calculate a film thickness of 530 Angstroms. This gives a sputter deposition rate of 240 Angstroms/min.

C Preliminary Testing of Cathode II and the Second Sputtering System

The first deposition attempted in the new configuration was Ti deposition onto a carbon rod. The rod was cleaned using the usual cleaning procedure and was brought into the sputtering chamber. The system was backfilled with argon to a pressure of 225 mtorr. The cathode was presputtered for 10 minutes at a power of 90 watts. There were no jets of plasma emanating from the cathode as was noted for the earlier cathode configuration, indicating that the new, stronger magnetic field confined the plasma more effectively than the old. Finally the carbon rod was inserted into the cathode for a 5 min. deposition. After the 5 min. deposition, the rod was removed from the system and a piece was prepared for Auger analysis. Auger results are shown in Figures 12 and 13. Although the Auger analysis indicates a high degree of purity in the upper layers of the Ti film, there is a large amount of carbon present in the lower regions of the film. This is an indication that the plasma is not being effectively confined to the cathode walls and is causing sputtering of carbon from the surface of the carbon rod, to be later redeposited as carbon within the film. As the deposition proceeded, the amount of carbon available decreased and as a result, the film slowly changed to pure titanium.

D Titanium Deposition onto Carbon Fiber Tows

The second group of depositions attempted with this system were titanium depositions onto carbon fiber tows. The fiber bundles consisted of approximately 1000 fibers of AKZO 5(C) Fortafil fibers, a PAN based

fiber with no surface treatment. The average fiber diameter was 7 microns. The fiber bundles were tied to a carbon rods using tantalum wire. A bundle was brought into the sputtering system in the same manner described above. After pumping to a base pressure of 6×10^{-8}, the chamber was backfilled to a pressure of 400 mtorr argon. The cathode was presputtered for 10 minutes prior to the 30 minute (approx.) depositions.

Upon removal, the fibers seemed to have bowed away from one another, as shown in Figure 14. This bowing is evidence of the electrostatic repulsion that results from the "charging" of the fibers within a plasma. Samples of the coated fibers were cleaved and placed into a Jeol JSM-840 electron microscope. A photograph of one of the fibers is shown in Figure 15 and an Auger depth profile is presented in Figure 16. This figure indicates again that resputtered carbon was integrated into the sputtered films, forming a titanium carbide material. The shape of the Auger carbon peak supportes this conclusion by showing a small positive excursion accompanied by a large negative excursion. This peak shape indicates the presence of a carbon compound, rather than elemental carbon.

Given a coating thickness of approximately 1 micron as evidenced in the SEM photograph, one arrives at a deposition rate of approximately 420 Angstroms/min onto each fiber within a tow containing perhaps 1000 fibers. There is also indication of a reaction zone at the fiber/coating interface on the order of 0.5 microns in thickness. This indicates that in spite of the increased plasma containment produced by the refinements made in the cathode, substrates still see excessive plasma bombardment, resulting in substrate heating. Given a coating thickness of

approximately 1 micron, as shown in the SEM photograph, one arrives at a deposition rate of approximately 360 Angstroms/min onto each fiber within a tow containing perhaps 1000 fibers.

Part VI: Discussion

The results obtained above indicate that a number of successes in sputtering have been achieved. Relatively pure films of titanium can be deposited on carbon at deposition rates from 1700 Ang./min. to as high as 7500 Ang./min. These rate agree roughly with those given by Thornton[6] for a generalized metal. Relatively pure films of TiN_x can also be produced, but the stoichiometries of these films have thus far been seriously nitrogen deficient. Depositon rates, though, have been relatively high, approximately 240 Ang./min. This value agrees closely with that of Ihsaan and Pourrezaei,[12] who reported a deposition rate of 260 Ang./min.

The results obtained above, however, also indicate a number of problems that must be overcome in order to produce pure stoichiometric TiN (or any other reactively sputtered compound) films at high deposition rates. These problems stem from four factors that can be corrected to some degree. These are (1) residual gas incorporation into the depo::ited film, (2) nitriding of the target, (3) a magnetic field that fails to contain the sputtering plasma completely, and (4) the low wattage of the power supply.

1. Residual Gas

In the initial sputtering experiment, when Ti was deposited onto copper in a static argon atmosphere, there was a great deal of carbon

and oxygen contamination within the deposited film. Although a second deposition using an argon flow reduced the amount of contamination, a small concentration of residual gases was still incorporated into the film. Increasing the argon flow, then, should reduce the amount of contamination further. Coupling an argon flow increase with an increased nitrogen flow in a reactive sputter deposition would have the double effect of not only producing purer films, but also of making the control of TiN_x film stoichiometry more precise.[12-15] In these experiments we have attempted to keep pumping speeds as high as possible in order to bring about both of these effects during TiN_x deposition.

The high pumping speeds (those near the full pumping capacity of the turbomolecular pump) seem to have been effective. TiN_x film stoichiometries were constant throughout their entire thicknesses, as is shown in the AES depth profile in Figure 8. These profiles also indicate a very low level of film contamination.

2. Nitriding of the target

The observed nitriding of the target during TiN_x deposition is probably the main reason for the observed low deposition rate. Although the rate reported above is consistent with the observations of other researchers, it should be possible to increase the sputtering rate by sputtering without a poisoned target. Nitriding would normally be avoided by decreasing the partial pressure of N_2, but this would create films that are even further from the desired stoichiometry. Here the cause of target nitridation might be the excessive temperatures attained at the target, as indicated by the grain growth features noted on the titanium target sheet. The high temperature is probably caused by poor thermal contact between the titanium sheet and the water cooled copper

body of the cathode. Although version II of the cathode seemed to reduce this heating effect, it was not entirely eliminated, as some grain growth (though to a lesser degree) was observed on the cathode titanium sheet. A more effective method of attaching the titanium to the copper body of the cathode should be employed if further TiN depositions are to be attempted.

3. Magnetic Field

The fact that the magnetic field was insufficient to confine the plasma discharge effectively is indicated by two observations in version I of the cathode. The first of these is the fact that carbon substrates were noted to be glowing red when removed from the cathode. This is an expected result if a plasma bombards the carbon rod with an intense flux of ions. We can conclude that the electrons that generate the plasma were not being confined to the region just inside the walls of the cathode, but rather was allowed to permeate throughout the entire cathode cavity. The bombardment of the substrate by high energy argon ions and electrons was then responsible for the substrate heating. An inadequate magnetic field is also partially responsible for inhibiting the deposition rate. The lack of plasma confinement results in fewer titanium atoms being sputtered from the cathode surface and depositing on the substrate.

A second observation that indicates that the magnetic field did not effectively contain the plasma was the existence of plasma outside of the cathode. This observation is indicative of a sputtering condition where electrons are allowed to reach the centerline region of the cathode. Instead of colliding with the anode, the electrons pass out through the center hole of the anode and excite a plasma in the region

outside the cathode cavity. The shape of the plasma existing outside the cathode, a jet extending outside each anode hole for several inches, is consistent with this hypotheses.

Although the magnetic field intensity was measured outside the vacuum system to be 100 Gauss within the solenoid coil, this measurement had to be made without the cathode inserted. Originally it was not known to what degree the copper, stainless steel and machinable ceramic shielded the cathode cavity from the magnetic field. Since these materials are not ferromagnetic, they should reduced the field intensity within the cathode to a great extent. Doubling the field strength seemed to confine the plasma more effectively within the cathode and did increase the deposition rate substantially, but some plasma still escaped.

In version II of the sputter cell, the magnetic field was confined to the cathode cavity much more effectively. The solid magnets and other modifications effectively contained all the plasma within the cathode with no visible plasma escaping. This did not, however, greatly effect deposition rates and did seem to add a new problem -- that of sputtering material from the substrate to the cathode surface, for later incorporation into the deposited film. It can be deduced from these observations that the problem with version II of the cathode is not the strength of the field, but the shape. The two magnets that formed the magnetron produce field lines like those in Figure 30a. This field configuration would tend to confine the plasma within the cavity, but not necessarily to the walls of the cell. The effect of such a field shape would be to allow heavy bombardment of the substrates by

electrons, and to lower the deposition rate, two effects which have been observea.

A possible solution to this problem was described at the very end of section IV. The addition of a backstrap to the cathode, as described in section IV should redefine the magnetic field shape as that shown in Figure 30b. The backstrap redirects the magnetic flux to form a return path for the field through a feromagnetic material, effectively linking together the fields of the two magnets into one. It is unfortunate that this modification could not be properly tested before writing of this thesis.

4. Power Supply

The D.C. power supply used in these experiments was inadequate. Higher voltages than could be produced with this supply were necessary in order to sputter at lower pressures. Although plasmas could be produced in the 200-600 mtorr range, these pressures are generally too high to sputter efficiently. Atoms ejected from the target surface encounter gas atoms, lose energy, and are deflected, resulting in a decreased deposition rate. Pressures on the order of 10 mtorr or less are usually the most efficient for depositing material quickly.[64] It is at these pressures that the balance between the number of atoms impinging on the substrate to produce sputtered atoms and the number of gas atoms that block depostion usually results in the most efficient deposition rate. Because of the low voltages associated with this power supply, plasmas simply could not be ignited below the 200 mtorr range.

Acknowledgments

[1] J.M. Liu, *App. Phys. Lett.* 48, (1986) 469.

[2] L. Aggour, E. Fitzer, M. Heym, E. Ignatowitz, *Thin Solid Films*, 40 (1977) 97.

[3] W. Wieswieler, E. Fitzer, G. Nagel, and H. Jager, *Thin Solid Films*, 148 (1987) 93.

[4] T. A. Chernyshova, L. I. Kobelova, *J. Mater. Sci.*, 20 (1984) 3524.

[5] M. Ihsan, K. Pourrezaei, *J. Vac. Sci. Technol. A*, 8 n. 3 (1990) 1304.

[6] J.A. Thornton, A.S. Penfold, "Cylindrical Magnetron Sputtering" in Thin Film Processes, ed. by J.L. Vossen, W. Kern, Academic Press, Inc. 1978, pp. 76.

[7] N. Kumar, K. Pourrezaei, M. Ihsan, *J. Vac. Sci. Technol. A*, 6 no. 3 (1988) 1772.

[8] J.A. Thornton, *Thin Solid Films*, 80 (1981) 1.

[9] J.A. Thornton, *Metal Finishing*, May (1979) 45-49, 83.

[10] J. Laimer, H. Stori, P. Rodhammer, *J. Vac. Sci. Technol. A*, 7 (1989) 2952.

[11] M. Ihsan, K. Pourrezaei, *J. Vac. Sci. Technol. A*, 8 n. 3 (1990) 1304.

[12] S. Berg, H.O. Blom, T. Larsson, C. Nender, *J. Vac. Sci. Technol. A*, 5 n. 2 (1987) 202.

[13] T. Larsson, H.O. Blom, C. Nender, S. Berg, *J. Vac. Sci. Technol. A 6* n. 3 (1988) 1832.

[14] S. Berg, T. Larsson, C. Nender, H.O. Blom, *J. Appl. Phys, 63* n. 3 (1988) 887.

[15] S. Berg, H.O. Blom, M. Moradi, C. Nender, T. Larsson, J. Vac. Sci Technol. A 7 n. 3 (1989) 1225.

Sample	Ti low E (cm.)	Ti/N (cm.)	Ti high E (cm.)
TiN Standard	--	10.1	4.6
Ti Standard (sheet)	7.4	--	9.8
TiN Sample 1	--	13.6	6.7
TiN Sample 2	--	9.0	4.4

Table 1. Various peak-to-peak Auger intensities used to calculate the ratio N/Ti.

.
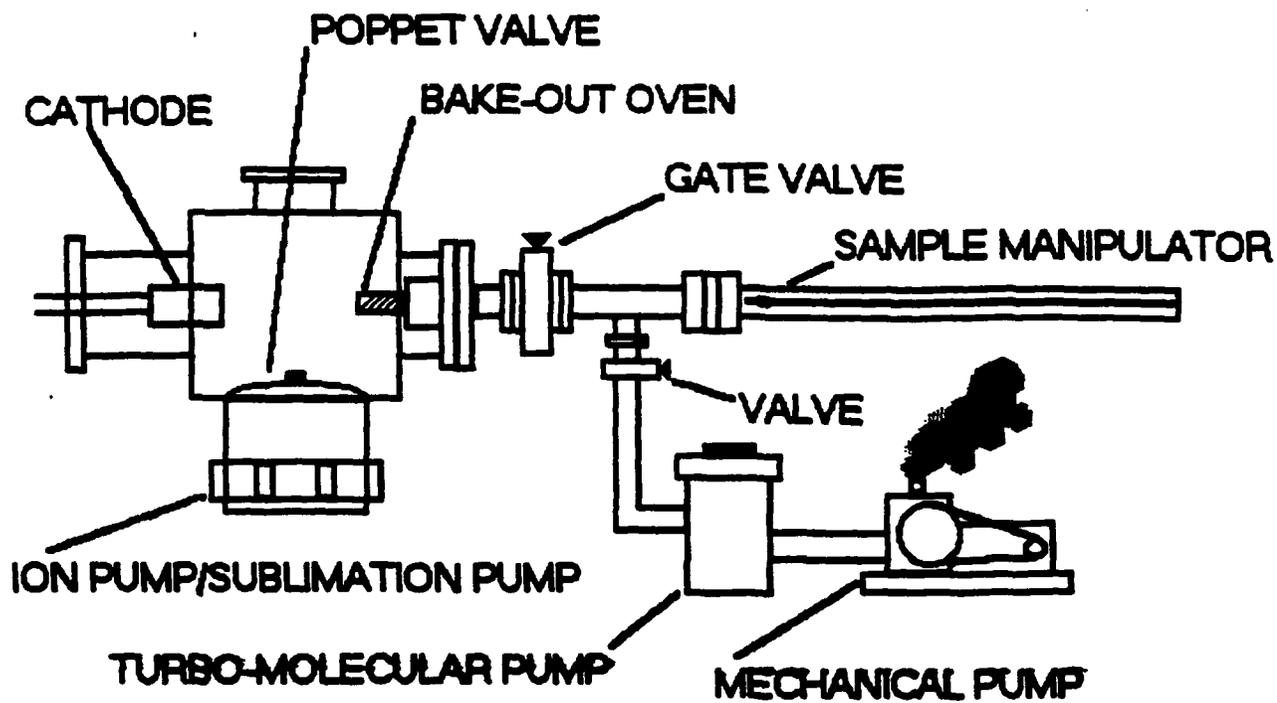
Figure 1. Pump configuration of version I system.

SPUTTERING CATHODE
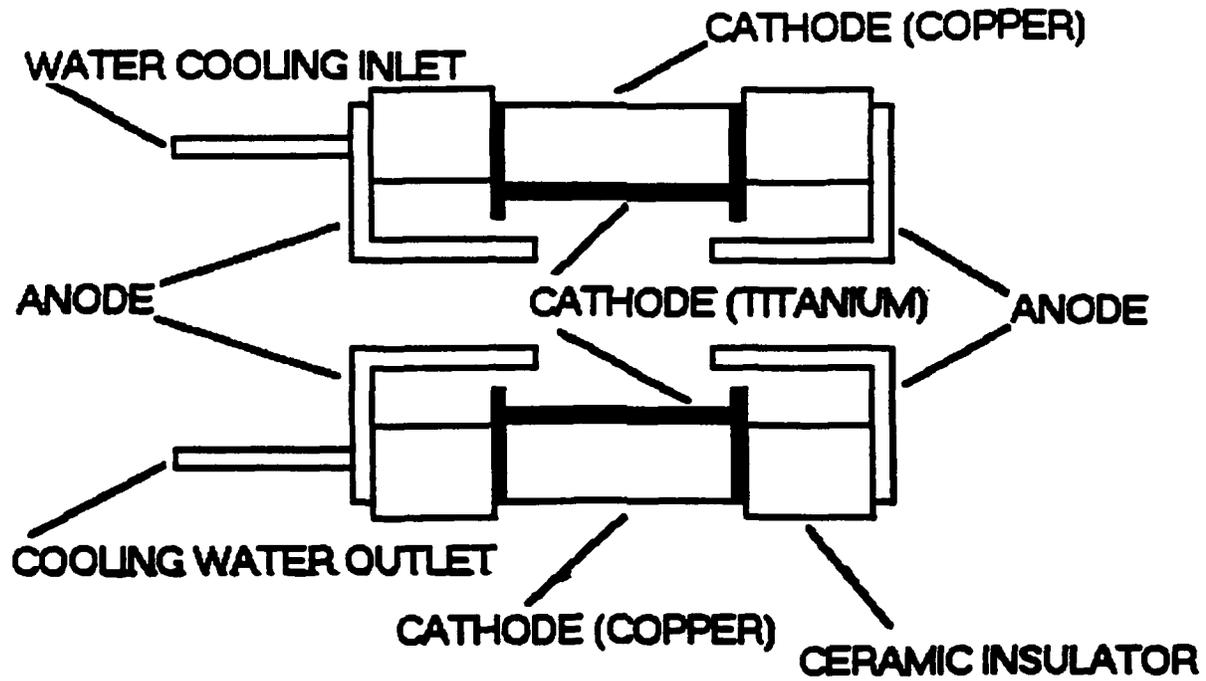
Figure 2. Original cathode configuration.

Cath l. B 14 ;0

fig 2
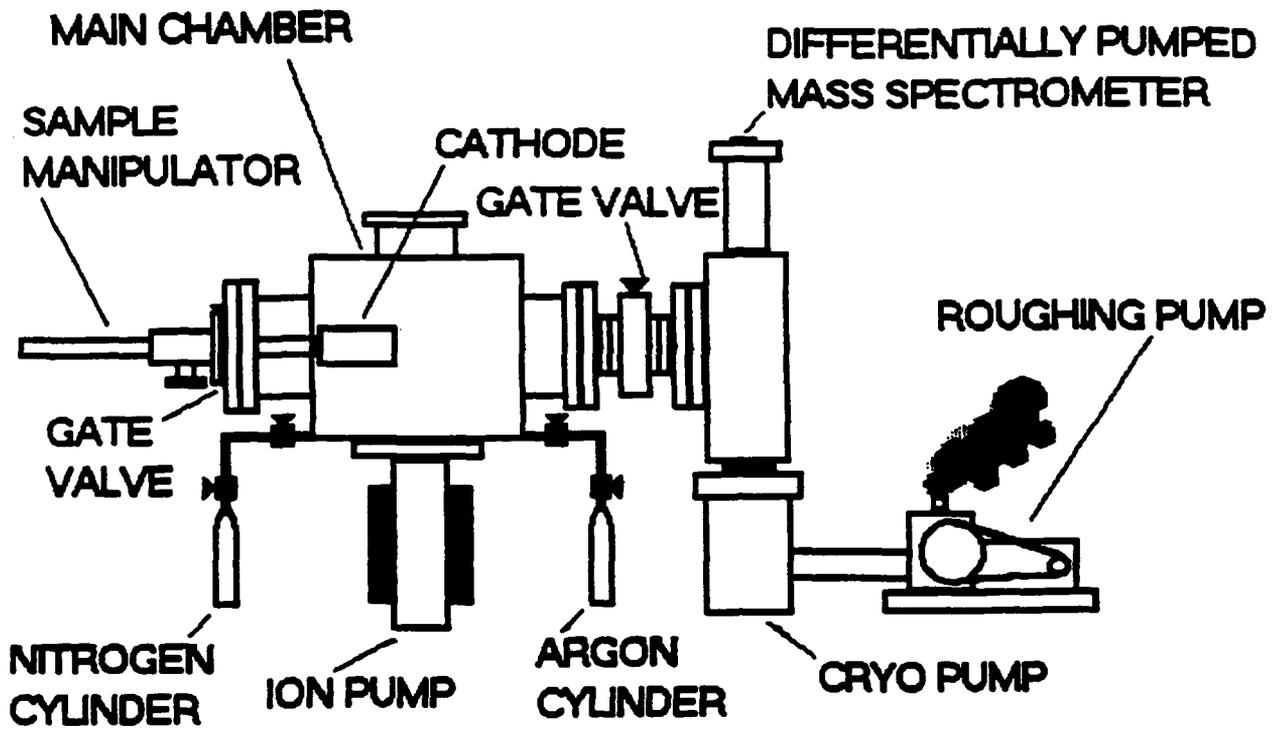
Figure 3. Version II of the sputtering system.
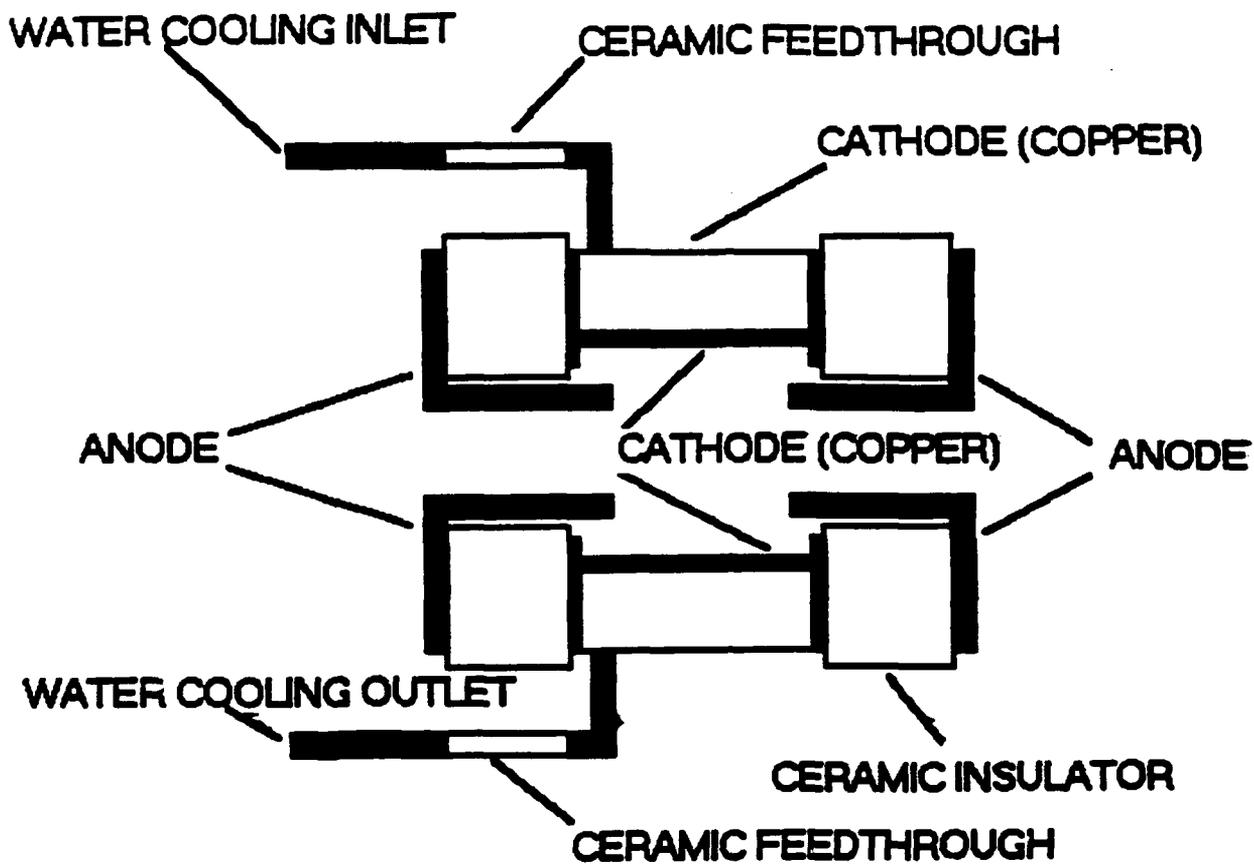
Figure 4. Version II cathode configuration.

CuT4 2.BMP

fig 4
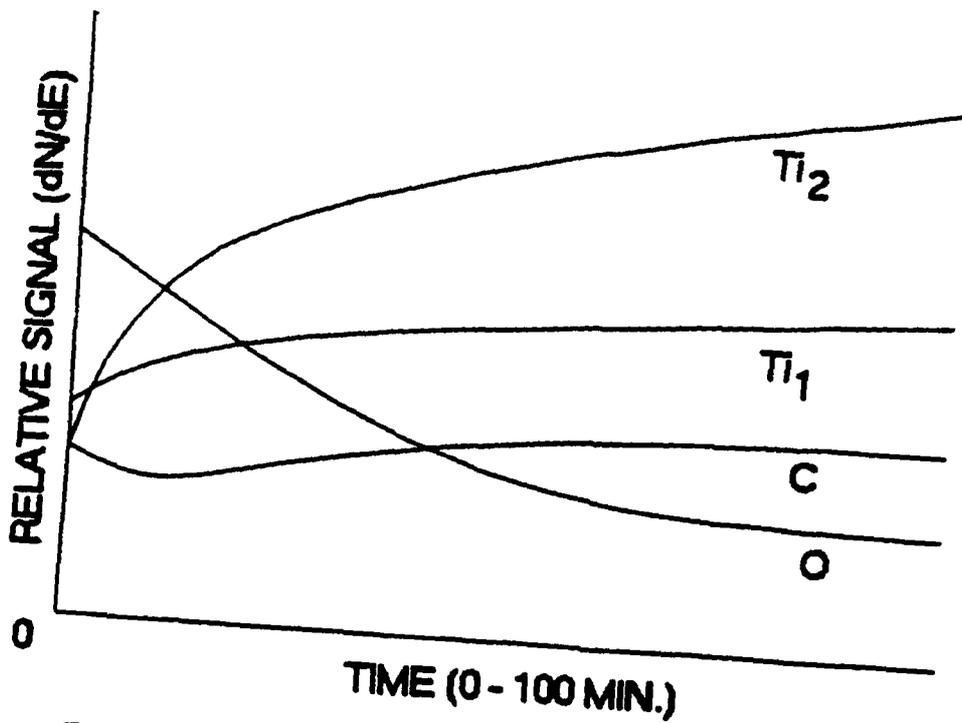
Figure 5. This Auger depth profile clearly shows large amounts of carbon and oxygen contamination within the film at the surface as well as deeper within the film.
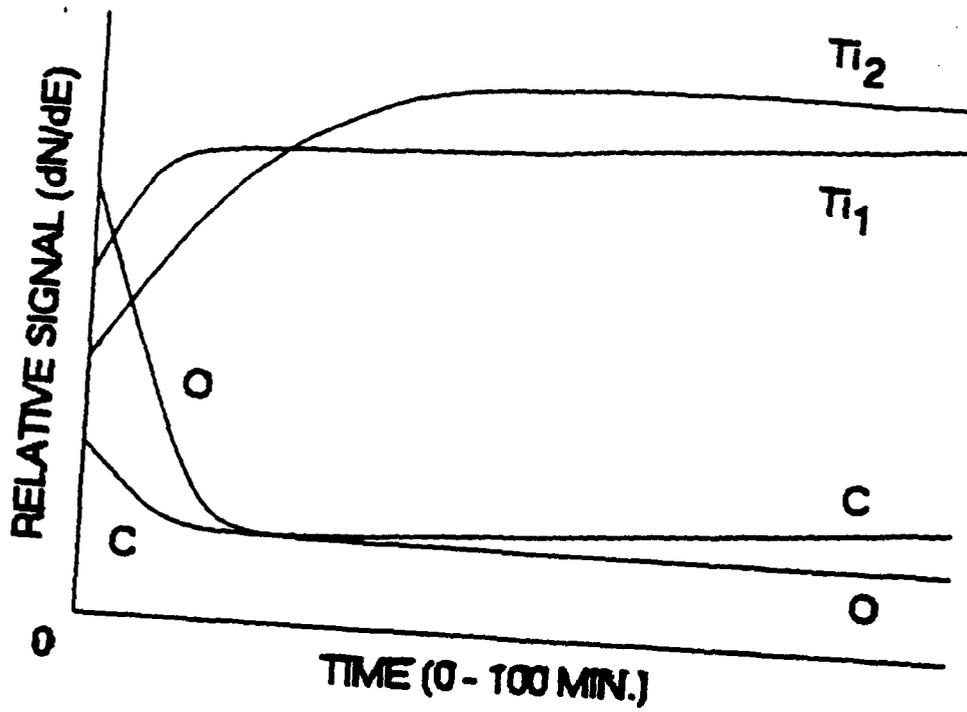
Figure 6. Here we see a substantial decrease in carbon contamination. The elemental fractions are also much more consistent.

fig 6
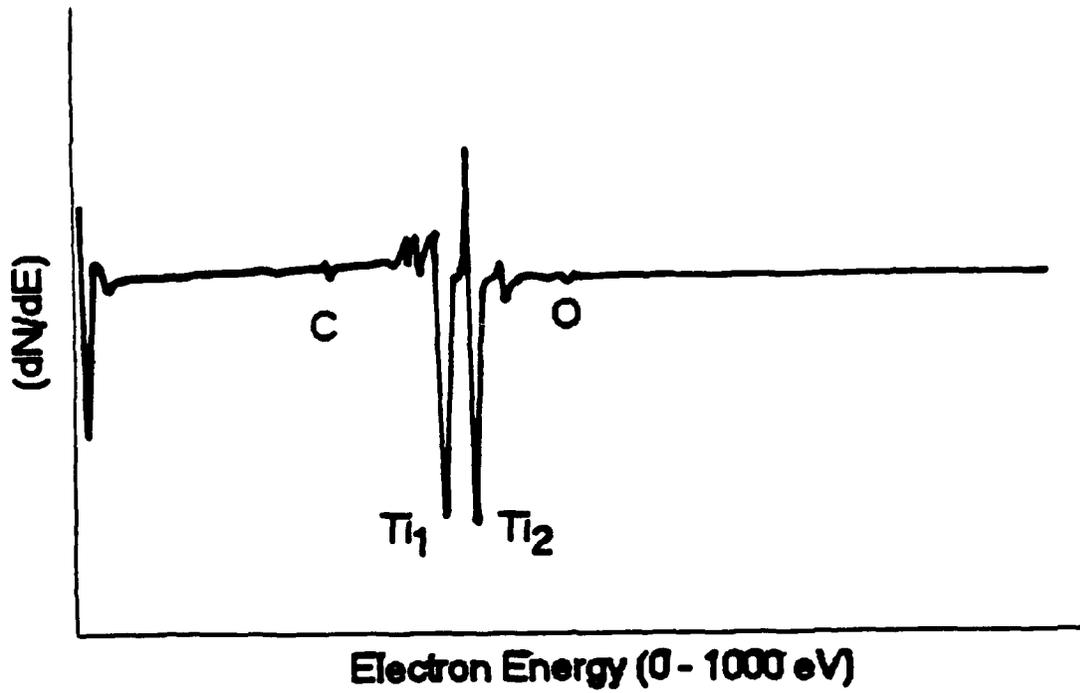
Figure 7a. AES of Ti on carbon. This is a highly pure film. Carbon and oxygen peaks are almost non-existent.

fig 7a
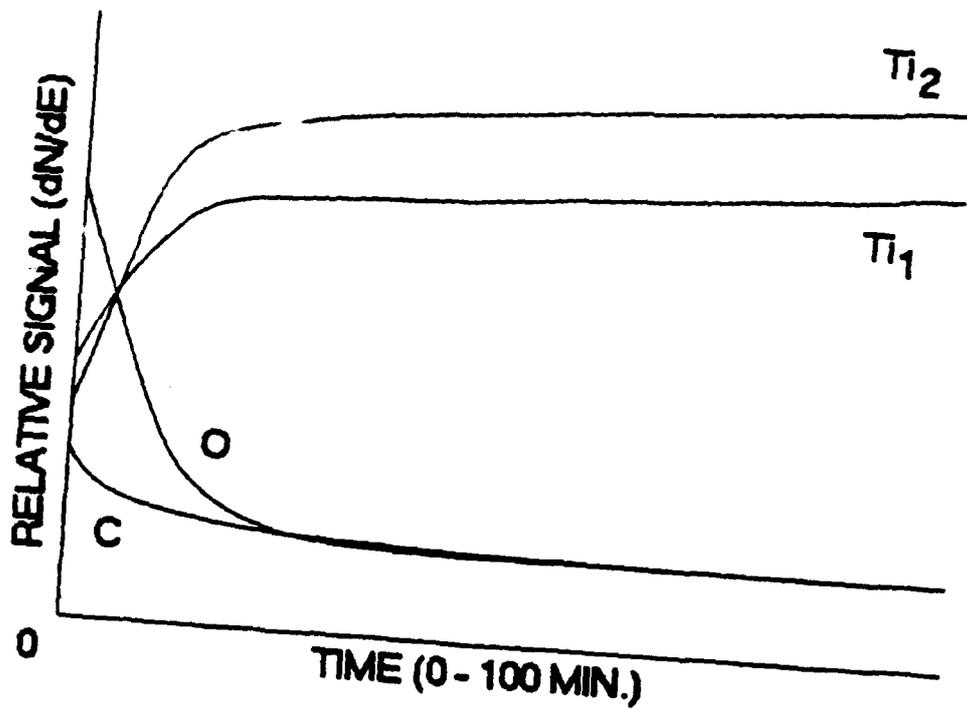
Figure 7b. Depth profile of Ti on Carbon. Note purity and consistency.
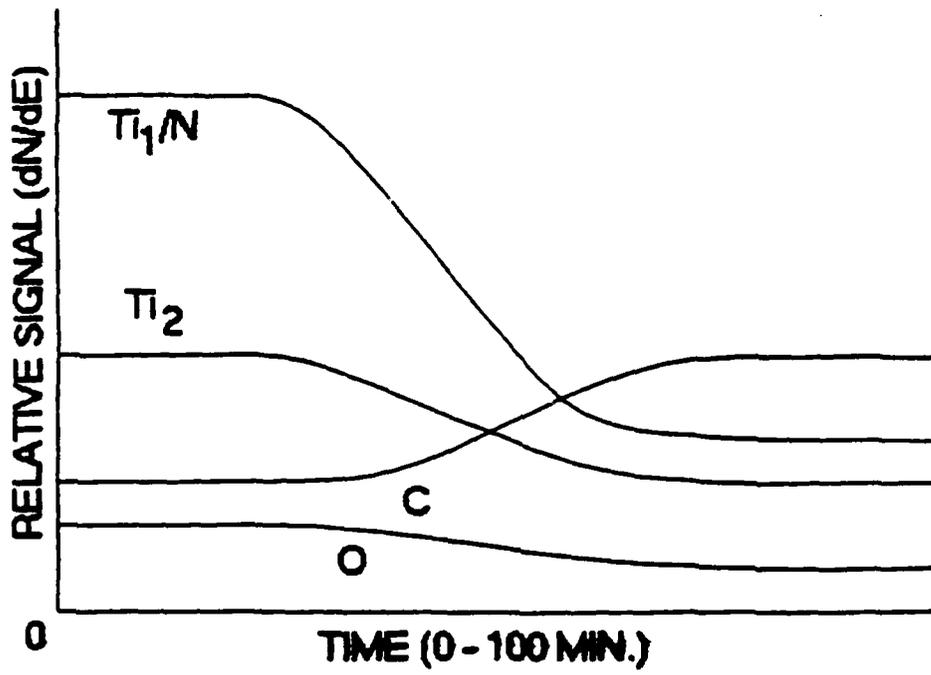
Figure 8. Depth profile of TiN_x.

fig 8
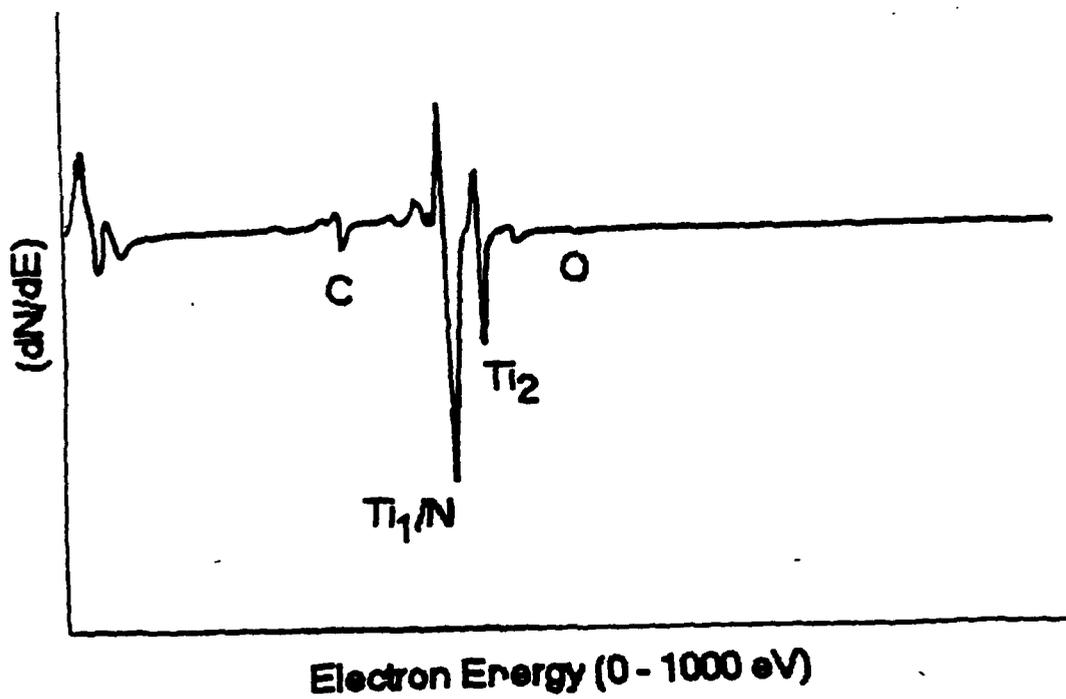
Figure 9. AES spectrum of TiN "standard".

fig 7
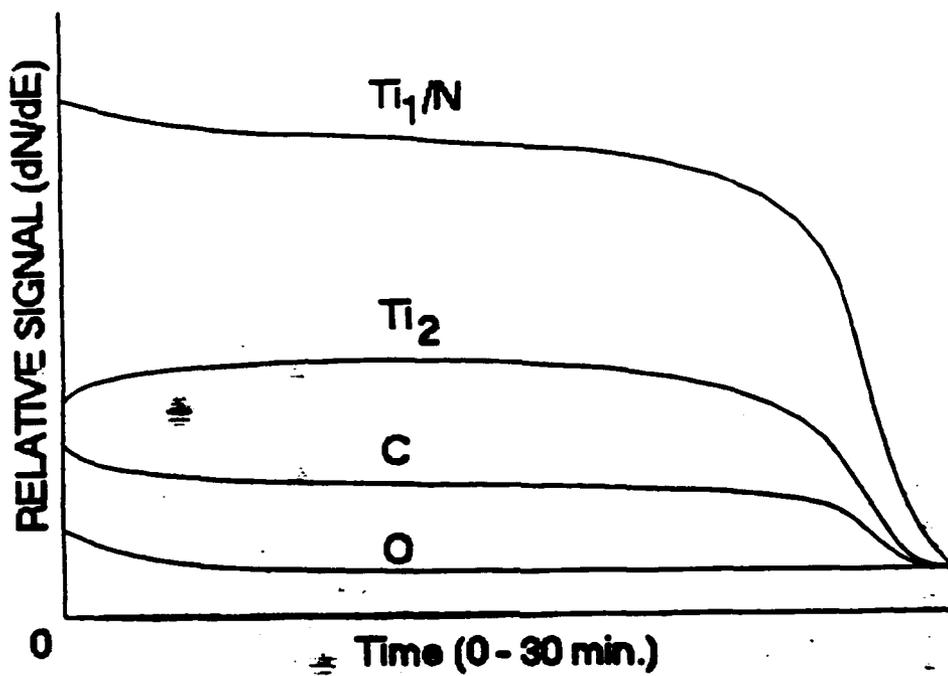
Figure 10. Depth profile of TiN "standard".

fig 10
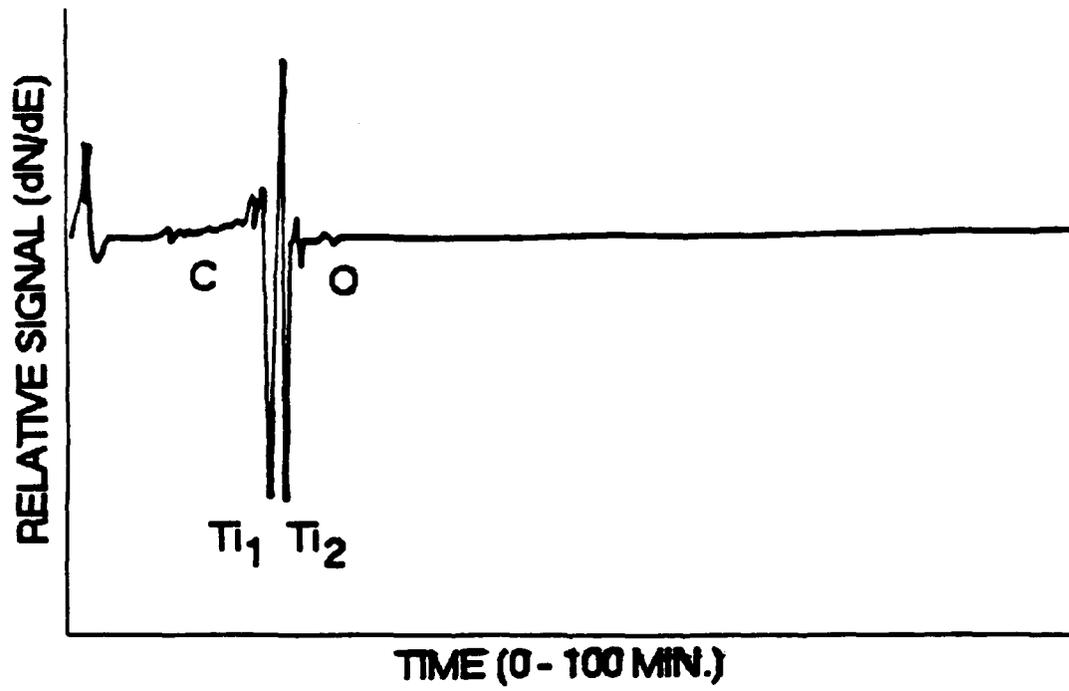
Figure 11. Auger spectrum of Ti from cathode sheet material.
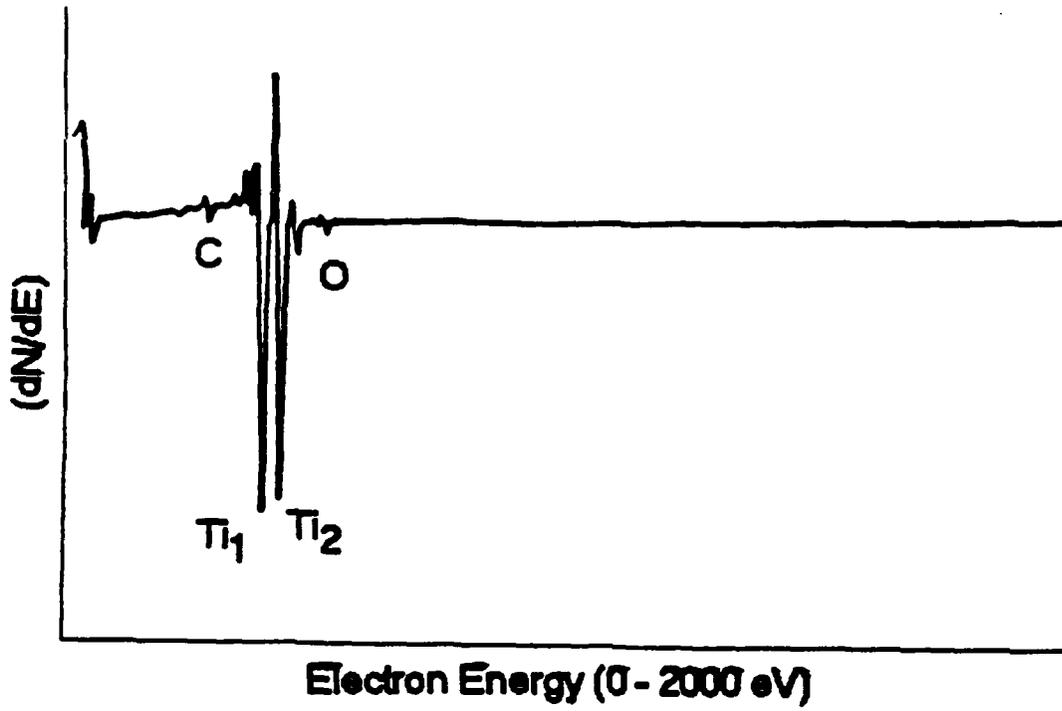
Figure 12. Auger spectrum of titanium deposited by the second cathode.
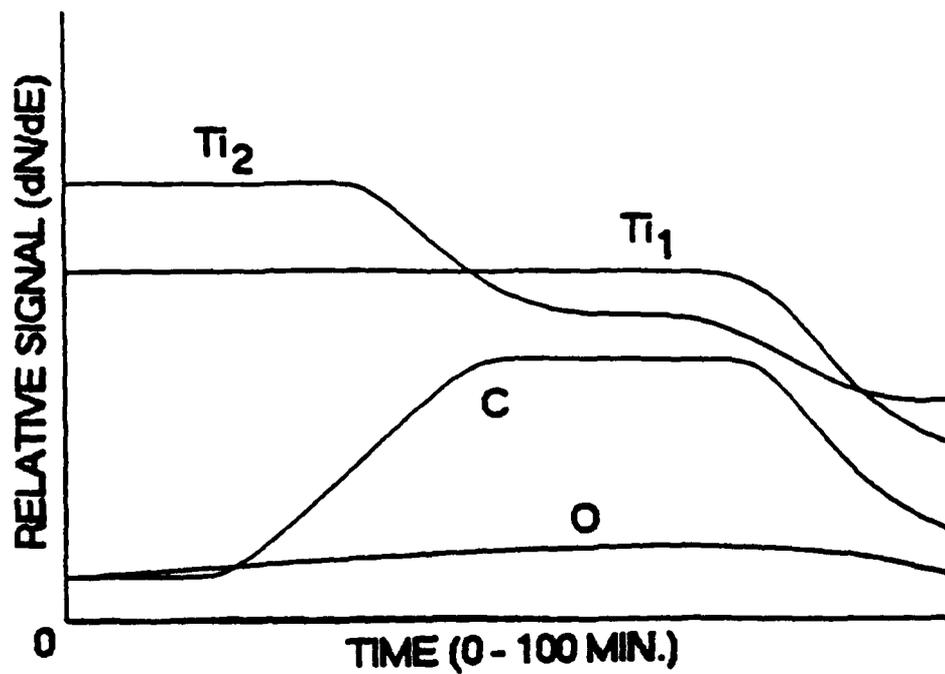
Figure 13. Auger depth profile of Ti on carbon rod. The carbon content increased with depth, indicating initial carbon sputtering from substrate.

Fig 13

Carbon Fibers Spread Due to Electrostatic Repulsion

Tantalum Wire

Carbon Rod
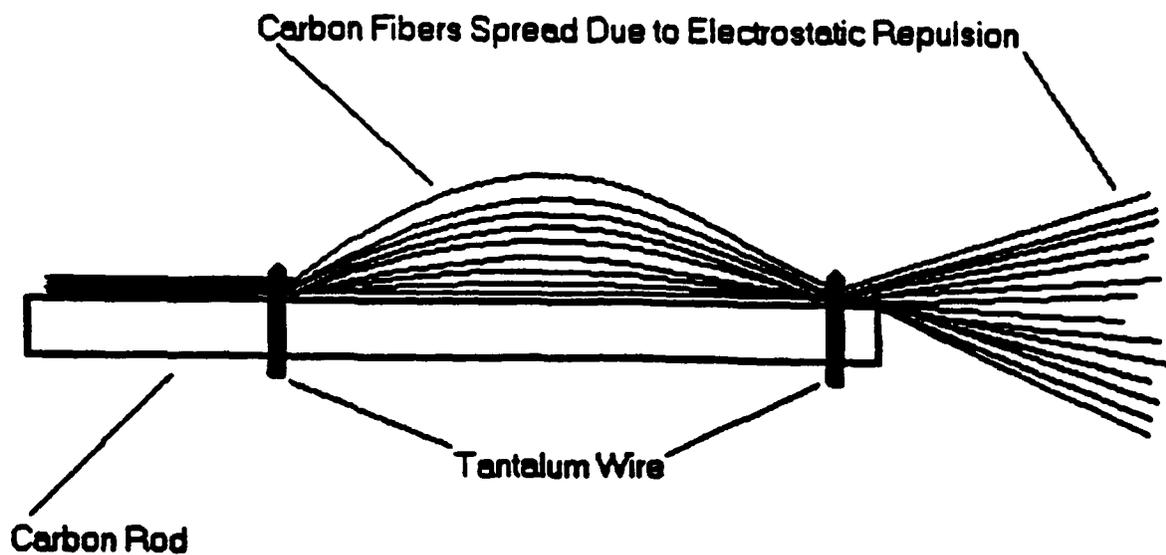
Figure 14. Carbon fiber spreading. This figure shows the orientation of fibers within the cathode during deposition. The portion of the fibers between the tantalum holding wires remained bowed after removal from the sputtering system.
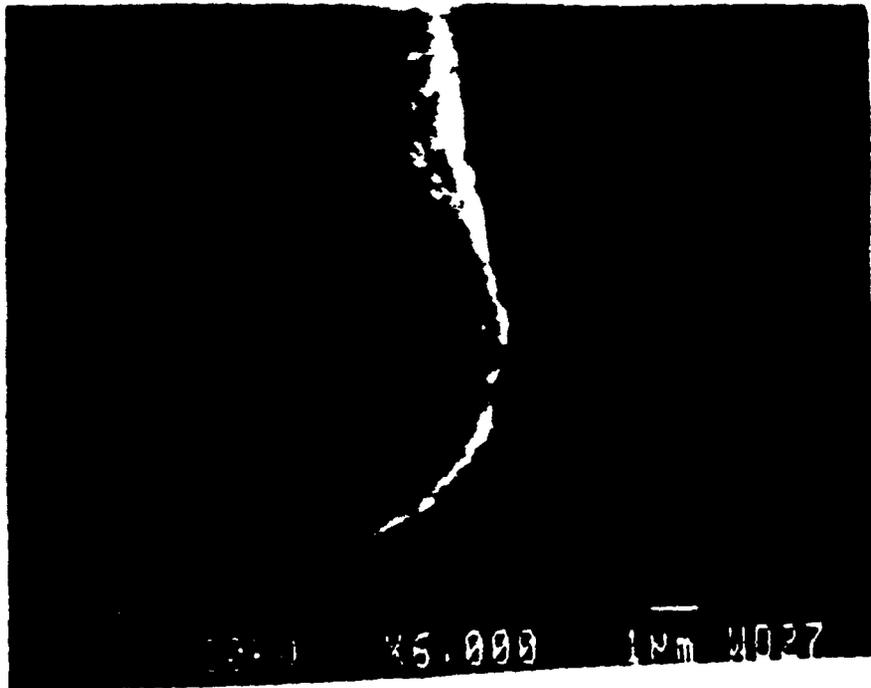
Figure 15. SEM photo of the cross section of a Ti coated carbon fiber.
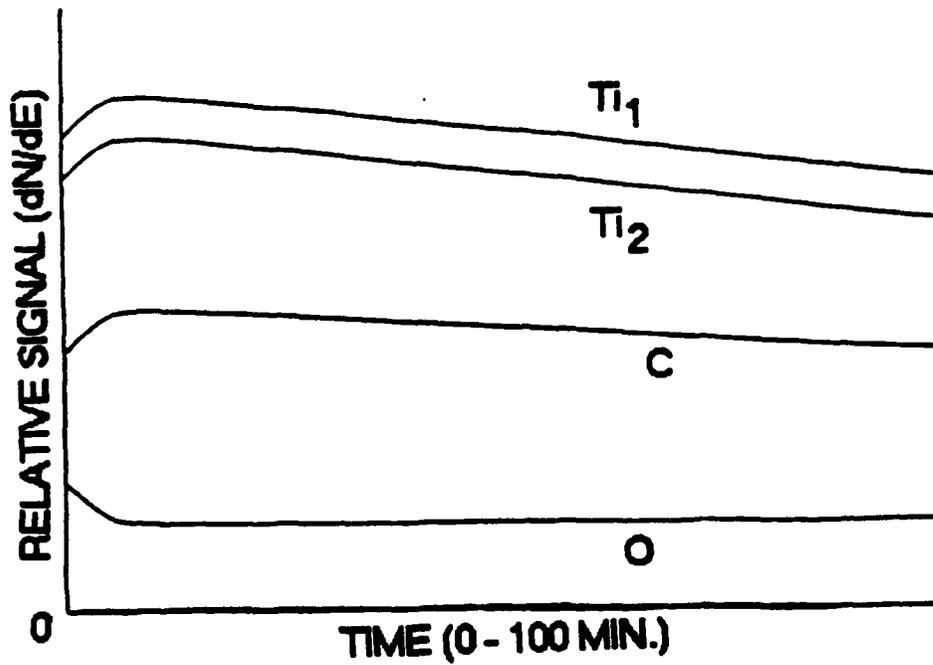
Figure 16. Auger of Ti deposited onto carbon rod holding carbon fibers.

fig 16

journal

Chemical Interactions in Diboride-Reinforced Oxide-Matrix Composites

Mrityunjay Singh* and Heribert Wiedemeier

Department of Chemistry, Rensselaer Polytechnic Institute, Troy, New York 12180-3590

Thermochemical analyses of interfacial reactions in titanium, zirconium, and hafnium diboride reinforced oxide-matrix composites have been carried out to evaluate the chemical compatibility. The chemical reactivity of these diborides with oxygen and the high volatility of $B_2O_3(l)$ at reduced oxygen pressures are concerns during processing and operating conditions. The thermochemical stability and the vaporization behavior of $B_2O_3(l)$ are discussed in terms of partial pressures of dominant gaseous species of the boron-oxygen system at 1700 and 2300 K. The TiB_2/ZrO_2 and TiB_2/HfO_2 systems are thermodynamically stable in a limited oxygen pressure range. The TiB_2/Al_2O_3 system is stable, but the reactions in this system may apparently be accompanied by formation of gaseous products (B_2O_3, AlO, Al_2O, and lower boron oxides) in the presence of elemental oxygen. These thermochemical considerations are very useful in evaluating the effectiveness of oxides as diffusion barrier coatings on diboride reinforcements. [Key words: matrix, reinforcement, borides, oxides, composites.]

I. Introduction

CERAMIC materials are emerging as a new generation of high-temperature materials for aerospace and other structural applications. This use of ceramics is mainly due to a combination of their excellent properties such as hardness, stiffness, corrosion and heat resistance, and relatively low density. The mechanical properties, i.e., fracture toughness, creep resistance, and thermal shock resistance, of these materials are further improved by the addition of certain reinforcements. Diborides (Ti, Zr, and Hf) have a great potential for high-temperature applications because of their superior mechanical properties at elevated temperatures and their high melting points.[1,2] A comparative study of the high-temperature compression behavior of a variety of materials by Ramberg and Williams[2] indicated that titanium diboride is potentially useful for elevated-temperature applications. However, these diborides are very susceptible to considerable oxidation at elevated temperatures. They oxidize readily to form B_2O_3, which has a melting point of 723 K and vaporizes rapidly above 1400 K. Several reports in the literature[3-8] deal with the oxidation behavior of these borides in the temperature range 1100 to 2100 K. In order for these compounds to be used as reinforcement materials at high temperatures, the matrix and the diborides must be chemically compatible in that temperature range. Among the criteria for the selection of oxides as matrix materials are their relatively high melting points. But

on the other hand, diffusion of oxygen in some matrices can lead to the oxidation of the diboride reinforcements.

The chemical compatibility of titanium diboride in some oxide matrices was investigated by Krylov,[9] Vedula et al.,[10,11] and Stadlbauer et al.[12] Weddell[13] investigated the chemical compatibility of some non-oxide/oxide constituents for high-temperature composites. Typical processing and operating temperatures for these oxide matrix composites are in the range 1100 to 2300 K.

The main objectives of the present communication are the evaluation of the environmental stability and chemical interactions of titanium, zirconium, and hafnium diborides in the oxide matrices TiO_2, ZrO_2, HfO_2, and Al_2O_3. The thermochemical behavior of B_2O_3 at various oxygen partial pressures and at high temperatures has been discussed. These considerations are very useful in the evaluation of chemical stabilities of diboride constituents. A detailed analysis of the chemical stabilities coupled with interfacial reactions is required for the selection of thermodynamically stable and chemically compatible diboride/oxide combinations for high-temperature composites.
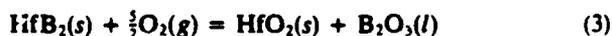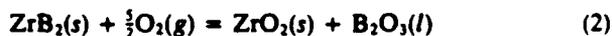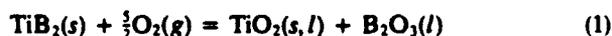
II. Thermochemical Considerations

Detailed knowledge of the thermodynamics and kinetics of composite systems is necessary to determine quantitatively the chemical reactivity between various constituents, their interface composition, and properties. The thermochemistry of the chemical reactions which yield desired interfaces and of those which may impede or prevent certain reactions must be known. Thermochemical modeling in general is very useful in determining the direction and extent of potential reactions, the actual occurrence of which is also governed by kinetic considerations. In addition, these data are also valuable in estimating the lifetime of the composites under different environmental conditions.

For the present calculations, thermochemical data from JANAF,[14] Barin and Knacke,[15] and of Shick[16] have been used. Gibbs free energy changes ($\Delta G°$) and equilibrium constants (K) are calculated for reactions over a temperature range 1100 to 2300 K.

III. Results and Discussion

(1) Chemical Interactions

The chemical reactivity of titanium, zirconium, and hafnium diborides with elemental oxygen has been evaluated here. Oxidation studies of these borides[3-8] indicate that the following predominant reactions occur in these systems:

$$TiB_2(s) + \tfrac{5}{2}O_2(g) = TiO_2(s,l) + B_2O_3(l) \quad (1)$$

$$ZrB_2(s) + \tfrac{5}{2}O_2(g) = ZrO_2(s) + B_2O_3(l) \quad (2)$$

$$HfB_2(s) + \tfrac{5}{2}O_2(g) = HfO_2(s) + B_2O_3(l) \quad (3)$$

A plot of the equilibrium oxygen partial pressures (P_{O_2}) vs reciprocal temperature for these reactions is given in Fig. 1. The oxygen partial pressure values for reactions (2) and (3)
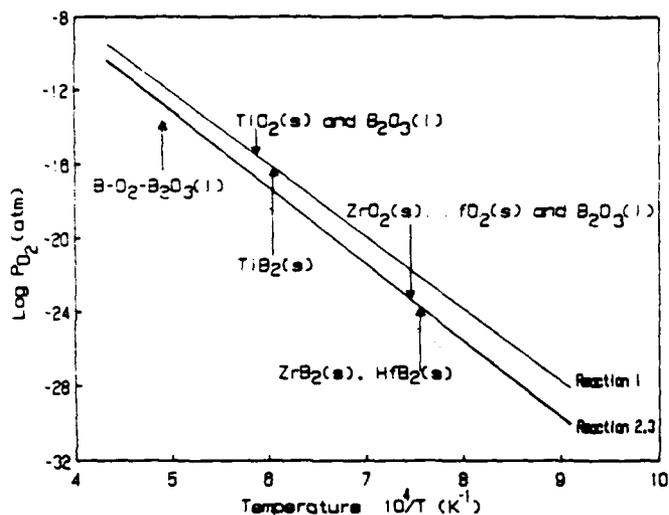
Fig. 1. Equilibrium oxygen pressures for the oxidation of TiB$_2$, ZrB$_2$, and HfB$_2$ as a function of temperature according to equilibria (1) to (3). The dotted line represents equilibrium oxygen partial pressures for the B–O–B$_2$O$_3$(l) system.

are numerically slightly different. Based on the magnitude of the equilibrium oxygen partial pressures, the oxidation of these diborides is thermodynamically practically complete at the temperatures (1100 to 2300 K) considered here. However, owing to kinetic reasons only small amounts of products may form as a pure phase or in solid solution with the diborides for oxygen pressures at or above the equilibrium values. At lower than equilibrium pressures, these diborides are stable.

In spite of their reactivity with elemental oxygen, some of these diborides are being used as reinforcements for high-temperature composites. The chemical interactions of the TiB$_2$/ZrO$_2$, TiB$_2$/HfO$_2$, and ZrB$_2$/HfO$_2$ systems in the temperature range 1100 to 2300 K are therefore of practical interest. Information about the chemical compatibility of the above systems is contained in Fig. 1, which is based on reactions (1) to (3). The results of Fig. 1 show that the TiB$_2$/ZrO$_2$, TiB$_2$/HfO$_2$, and ZrB$_2$/HfO$_2$ systems are thermodynamically stable only at very low oxygen partial pressures. Under actual processing and operating conditions such low partial pressures are not attainable. Thus, thermodynamically the above diborides are not stable and will oxidize at elevated temperatures. However, the oxidation of these systems is strongly affected by kinetic limitations of the oxidation processes. The oxide layer formed on the surface of diborides prevents or reduces the further oxidation of these materials. These kinetic limitations are the basis for the observed stability of these systems.
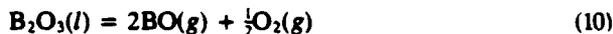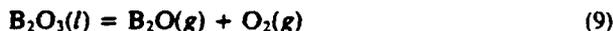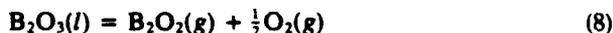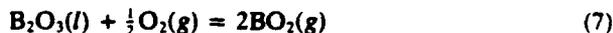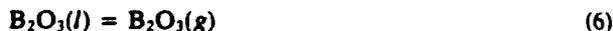
The chemical compatibility of the TiB$_2$/Al$_2$O$_3$ system is also limited by the stability of the boride constituent according to Fig. 1. The experimental investigations by Krylov,[9] Vedula *et al.*,[10,11] and Stadlbauer *et al.*[12] showed no observable interactions for the TiB$_2$/Al$_2$O$_3$ system at higher temperatures. As shown above in this work for the metal borides and earlier for alumina,[17] in the presence of elemental oxygen and at elevated temperatures the TiB$_2$/Al$_2$O$_3$ system may interact to form gaseous products such as B$_2$O$_3$, AlO, Al$_2$O, and other lower boron oxides. Under these conditions, B$_2$O$_3$(l) may react with alumina according to the reactions

$$9Al_2O_3(s) + 2B_2O_3(l) = 9Al_2O_3 \cdot 2B_2O_3(s) \tag{4}$$

$$2Al_2O_3(s) + B_2O_3(l) = 2Al_2O_3 \cdot B_2O_3(s) \tag{5}$$

at higher temperatures. These reactions are thermodynamically quite favorable.

It has been observed experimentally that at lower temperatures (1200 to 1400 K) the oxide scale consists of an inner layer of oxides (TiO$_2$, ZrO$_2$, and HfO$_2$) with an outer glassy

layer of B$_2$O$_3$(l). Because of the small atomic radius of boron, its diffusion to the surface of the oxidizing specimen is more extensive than the diffusion of the metal atom. This is accompanied by a simultaneous improvement of the protective properties of the scale, and metal borates can form in subsequent stages of the oxidation at higher temperatures. Two processes which occur at the reaction interface are the formation of condensed metal oxides and the vaporization of boron as B$_2$O$_3$(g). The initial reaction product B$_2$O$_3$(l) diffuses through the oxide layer to the outer surface and vaporizes.[6] This is schematically shown in Fig. 2. At temperatures above 1400 K, the high volatility of B$_2$O$_3$ causes the B$_2$O$_3$ layer to disappear. The formation of B$_2$O$_3$, under processing and operating conditions of the diboride-reinforced oxide-matrix composites, makes the control of the stoichiometry of the system difficult. At typical processing and operating temperatures (1100 to 2300 K), boron losses can occur either by evaporation[18] or by formation of gaseous boron suboxides and of other boron-containing gaseous species.[19] Therefore, knowledge of the vaporization behavior of B$_2$O$_3$ at different temperatures and under different environmental conditions is required in order to reduce the loss of boron. Because a large number of gaseous species may exist in the boron–oxygen system, it is necessary to determine the predominant boron oxide species at the temperature of interest. The computation of the equilibrium vapor pressures of gaseous species over B$_2$O$_3$(l) at 1700 and 2300 K as a function of oxygen partial pressures is based on the following equilibria:

$$B_2O_3(l) = B_2O_3(g) \tag{6}$$

$$B_2O_3(l) + \tfrac{1}{2}O_2(g) = 2BO_2(g) \tag{7}$$

$$B_2O_3(l) = B_2O_2(g) + \tfrac{1}{2}O_2(g) \tag{8}$$

$$B_2O_3(l) = B_2O(g) + O_2(g) \tag{9}$$

$$B_2O_3(l) = 2BO(g) + \tfrac{1}{2}O_2(g) \tag{10}$$

$$B_2O_3(l) = 2B(g) + \tfrac{3}{2}O_2(g) \tag{11}$$

A similar set of reactions can be written for the gaseous species in equilibrium with B(s). From the partial pressure diagram of the B–O system at 1700 K (Fig. 3) it is apparent that at oxygen pressures of about 10^{-10} atm or higher (1 atm ≈ 10^5 Pa), B$_2$O$_3$ and BO$_2$ are the predominant vapor species. However, at oxygen pressures lower than about 10^{-10} atm, B$_2$O$_2$ and BO are also important. A similar trend in the partial pressures of vapor species is observed at oxygen pressures above and below about 10^{-5} atm at 2300 K shown in Fig. 4. The actual relative amounts of B$_2$O$_3$(g), BO$_2$(g), and other species produced during oxidation may also depend on kinetic factors and have to be determined experimentally. The change in the partial pressures of the gaseous species (Figs. 3 and 4) is obvious from the fixed equilibrium constants of reactions (6) to (11) at 1700 and 2300 K, respectively, and from the change of the oxygen partial pressure. The equilibrium oxygen pressures for the oxidation of borides, based on reactions (1) to (3), are 1 to 2 orders of magnitude higher (Fig. 1) than the oxygen pressures at the invariant points of Figs. 3
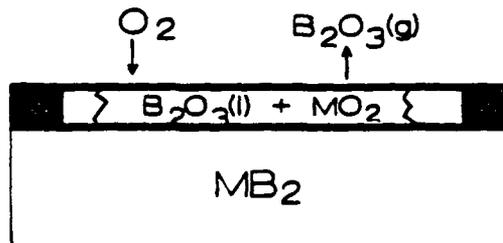

Fig. 2. Schematic representation of the oxidation of metal (Ti, Zr, and Hf) diborides.
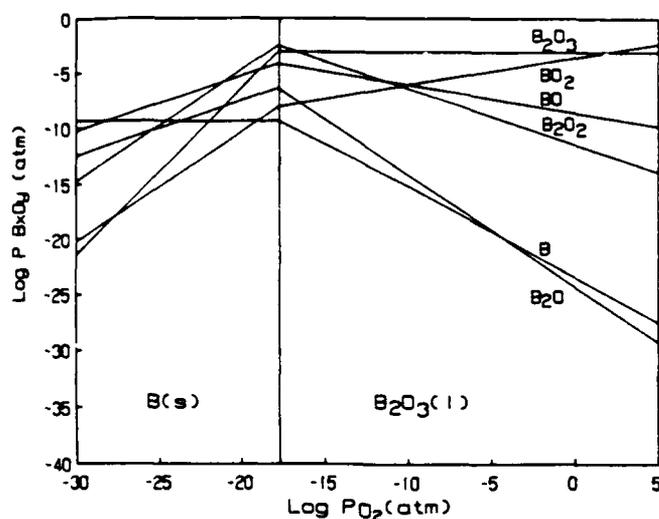
Fig. 3. Equilibrium vapor pressures (log P) of different species of the boron–oxygen system as a function of oxygen partial pressures at 1700 K.

and 4. Over a wide range of oxygen pressures, the dominating vapor species (Figs. 3 and 4) at both temperatures is $B_2O_3(g)$. The relatively high vapor pressures of boron oxides at these temperatures, even at very low oxygen pressures, may lead to a considerable loss of material.

Assuming congruent vaporization according to the dominant reaction (6) and based on the Hertz–Knudsen equation,[20] maximum vaporization rates of $B_2O_3(l)$ were computed in the temperature range 1000 to 2000 K. The corresponding mass loss rates of B_2O_3 as a function of temperature are given in the form of a linear equation

$$\log rate = 9.48 - 1.958 \times 10^4/T \tag{12}$$

where the mass loss rate is in $g \cdot cm^{-2} \cdot s^{-1}$ and T is in kelvins. Under present conditions and at higher temperatures, the predicted mass losses of B_2O_3 are significant and would lead to the depletion of the boride phase.

(2) Reactions of Oxides with Carbon

It is well-known that metal oxides react with carbon to form metal carbides at elevated temperatures.[21,22] Under processing conditions carbon from the heating elements of the furnace or from the graphite dies may react with these materials with
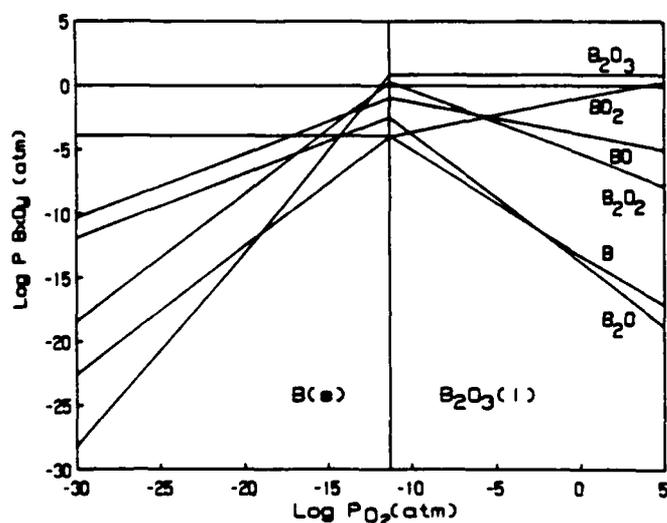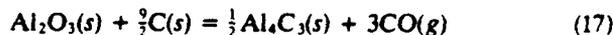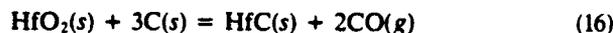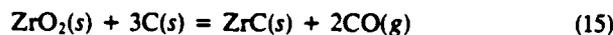
formation of carbides. This process may involve a combination of solid–gas phase reactions as discussed in the literature.[23] Based on reaction (13), the equilibrium partial pressures of oxygen may be very low. An upper value can be estimated by assuming an upper limit of 10^{-3} atm for the partial pressure of carbon monoxide. Based on this assumption, the equilibrium oxygen partial pressures are computed to be about 10^{-22} atm at 1700 K and about 7.6×10^{-21} atm at 2300 K. For TiO_2, ZrO_2, HfO_2, and Al_2O_3 the interactions with carbon are given by the equilibria (14) to (17).

$$C(s) + \tfrac{1}{2}O_2(g) = CO(g) \tag{13}$$

$$TiO_2(s) + 3C(s) = TiC(s) + 2CO(g) \tag{14}$$

$$ZrO_2(s) + 3C(s) = ZrC(s) + 2CO(g) \tag{15}$$

$$HfO_2(s) + 3C(s) = HfC(s) + 2CO(g) \tag{16}$$

$$Al_2O_3(s) + \tfrac{9}{2}C(s) = \tfrac{1}{2}Al_4C_3(s) + 3CO(g) \tag{17}$$

A plot of the equilibrium partial pressures of carbon monoxide (P_{CO}) versus reciprocal temperature for the above reactions is given in Fig. 5. It is evident from Fig. 5 that the CO partial pressures due to reactions (14) to (17) are quite high at temperatures between 1500 and 2000 K. This temperature range is generally used for the processing of these composites.

The calculations for the chemical interactions of carbon with alumina, titania, zirconia, and hafnia show that carbon monoxide overpressures may be required to reduce the extent of these reactions at higher temperatures. The formation of various oxycarbides, e.g., Al_2OC, Al_4O_4C, TiO_xC_y, ZrO_xC_y, and others, has also been reported in the literature. Thermodynamic data for these compounds are not readily available, but these phases, if present, will straddle the MeO_x–C–O_2–MeC_y equilibria. These compounds have not been considered in the present analysis. Of all the oxides considered here, the reaction of TiO_2 with carbon is thermodynamically most favorable at all temperatures (Fig. 5). Alumina is the most stable of these oxides with respect to interaction with carbon according to reaction (17).

IV. Conclusions

Thermochemical computations of chemical interactions of titanium, zirconium, and hafnium diborides with elemental oxygen indicate that the formation and subsequent vaporization of B_2O_3 considerably affect the stability of these materials at temperatures above 1100 K. The very low oxygen partial pressures required to prevent the oxidation of these diborides are practically unattainable. However, owing to kinetic limi-
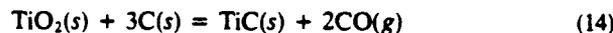

Fig. 4. Equilibrium vapor pressures (log P) of different species of the boron–oxygen system as a function of oxygen partial pressures at 2300 K.
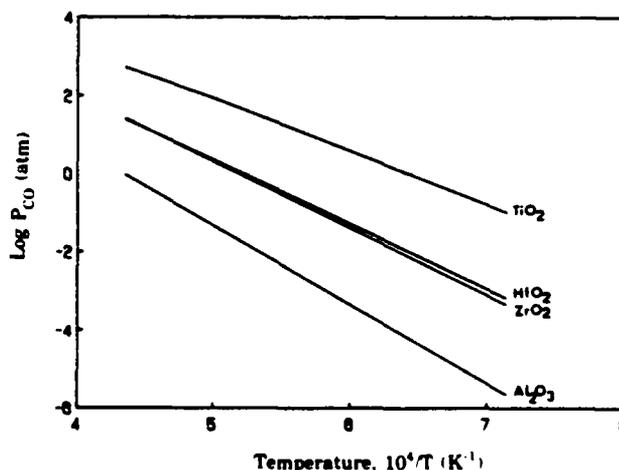

Fig. 5. Equilibrium vapor pressures of CO for the reaction of carbon with TiO_2, ZrO_2, HfO_2, and Al_2O_3 as a function of temperature (equilibria (14) to (17)).

tations, the oxide layers formed on the surface of these materials prevent or reduce further oxidation. The TiB_2/ZrO_2, TiB_2/HfO_2, ZrB_2/HfO_2, and TiB_2/Al_2O_3 systems are stable at very low oxygen partial pressures. Another concern in the processing of these composites is the reaction of the oxides with carbon. The partial pressures of carbon monoxide for the reaction of TiO_2 and carbon are higher than those of the corresponding reactions of carbon with ZrO_2, HfO_2, and Al_2O_3.

References

[1] J. S. Haggerty and D.W. Lee, "Plastic Deformation of ZrB_2 Single Crystals," *J. Am. Ceram. Soc.*, **54** [8] 572–76 (1971).

[2] J. R. Ramberg and W.S. Williams, "High Temperature Deformation of Titanium Diboride," *J. Mater. Sci.*, **22**, 1815–26 (1987).

[3] W. C. Tripp, H. H. Davis, and H. C. Graham, "Effect of an SiC Addition on the Oxidation of ZrB_2," *Am. Ceram. Soc. Bull.*, **52** [8] 612–16 (1973).

[4] W. C. Tripp and H. C. Graham, "Thermogravimetric Study of the Oxidation of ZrB_2 in the Temperature Range of 800 to 1500°C," *J. Electrochem. Soc.*, **118** [7] 1195–99 (1971).

[5] A. K. Kuriakose and J. L. Margrave, "Oxidation Kinetics of Zirconium Diboride and Zirconium Carbide at High Temperatures," *J. Electrochem. Soc.*, **111** [7] 827–31 (1964).

[6] R. J. Irving and I. G. Worseley, "The Oxidation of Titanium Diboride and Zirconium Diboride at High Temperatures," *J. Less Common Met.*, **16** [9] 103–12 (1968).

[7] J. B. Berkowitz-Mattuk, "High-Temperature Oxidation III. Zirconium and Hafnium Diborides," *J. Electrochem. Soc.*, **113** [9] 908–14 (1966).

[8] L. Kaufman, E.V. Clougherty, and J. B. Berkowitz-Mattuck, "Oxidation Characteristics of Hafnium and Zirconium Diboride," *Trans. Metall. Soc. AIME*, **239**, 458–66 (1966).

[9] Yu. I. Krylov, "Composite Materials Based on the System $TiB_2–Al_2O_3$,"

Izv. Akad. Nauk SSSR. Neorg. Mater., **12** [9] 1684–85 (1976).

[10] K. Vedula, A. Abada, and W. S. Williams, "Potential for Diboride Reinforcement of Oxide Matrix Composites," *Mater. Res. Soc. Symp. Proc.*, **125**, 61–69 (1988).

[11] J. Rigney, A. Abada, and K. Vedula, "Hot Pressing of Diboride Reinforced Oxide Matrix Composites," *Adv. Mater. Manuf. Processes*, **3** [3] 391–406 (1988).

[12] W. Stadlbauer, W. Kladnig, and G. Gritzner, "Al_2O_3–TiB_2 Composite Ceramics," *J. Mater. Sci. Lett.*, **8**, 1217–20 (1989).

[13] J. K. Weddell, "Screening Investigations of Pairs of Materials for 1650–2200°C Composites," Abstract No. 516, 176th Meeting of the Electrochemical Society, Hollywood, FL, October 15–20, 1989.

[14] D. R. Stull and H. D. Prophet, "JANAF Thermochemical Tables," 2d ed., National Bureau of Standards Publication No. NBS 37, 1971.

[15] I. Barin and O. Knacke, *Thermochemical Properties of Inorganic Substances*. Springer-Verlag, New York, 1973; Suppl., 1977.

[16] H. L. Shick *Thermodynamics of Certain Refractory Compounds*, Vol. II. Academic Press, New York, 1966.

[17] M. Singh and H. Wiedemeier, "Thermochemical Modeling of Interfacial Reactions in Intermetallic and Ceramic Matrix Composites"; pp. 303–309 in *Interfacial Phenomena in Composite Materials '89*. Butterworths, London, U.K., 1989.

[18] M. G. Inghram, R. F. Porter, and W. A. Chupka, "Mass Spectroscopic Study of Gaseous Species in the $B–B_2O_3$ System," *J. Chem. Phys.*, **25** [3] 498–500 (1956).

[19] A. W. Searcy and C. E. Myers, "The Heat of Sublimation of Boron and the Gaseous Species of Boron–Boric Oxide System," *J. Phys. Chem.*, **61** [7] 957–60 (1957).

[20] R. H. Lamoreaux, D. L. Hildenbrand, and L. Brewer, "High Temperature Vaporization Behavior of Oxides II. Oxides of Be, Mg, Ca, Sr, Ba, B, Al, Ga, In, Tl, Si, Ge, Sn, Pb, Zn, Cd, and Hg," *J. Phys. Chem. Ref. Data*, **16** [3] 419–43 (1987).

[21] K. L. Komarek, A. Coucoulas, and N. Klinger, "Reactions Between Refractory Oxides and Graphite," *J. Electrochem. Soc.*, **110** [7] 783–91 (1963).

[22] F. J. Klug, W. D. Pasco, and M. P. Borom, "Microstructure Development of Aluminum Oxide: Graphite Mixture during Carbothermic Reduction," *J. Am. Ceram. Soc.*, **65** [12] 619–24 (1982).

[23] J. K. Walker and C. K. Saha, "Formation of a Surface Carbide Layer during Sintering of Titanium Diboride," *J. Am. Ceram. Soc.*, **71** [4] C-207–C-209 (1988).   ◻

Thermochemical modelling of interfacial reactions in molybdenum disilicide matrix composites

H. WIEDEMEIER, M. SINGH
Department of Chemistry, Rensselaer Polytechnic Institute, Troy, NY 12180, USA

The thermal and environmental stabilities of molybdenum disilicide have been evaluated using thermochemical modelling. The chemical reactivity of molybdenum disilicide with oxygen indicates that various molybdenum compounds and silica are formed, depending on oxygen pressures. The structure and properties of the silica films play an important role in the oxidation reaction and the reactions of water vapour (moisture) with molybdenum disilicide at high temperatures. The thermodynamic stabilities of various potential reinforcements, e.g. carbon, silicon carbide, silicon nitride, alumina, and some refractory compounds (borides, carbides, and oxides of titanium, zirconium and hafnium) in molybdenum disilicide matrix have been evaluated. Based on the results of thermochemical computations, SiC, Si_3N_4, TiC, ZrC, HfC, TiB, TiB_2, ZrB_2, HfB_2, ZrO_2 and HfO_2 were found to be stable, but carbon and TiO_2 were found to be unstable in $MoSi_2$. The $Al_2O_3/MoSi_x$ system was found to be stable below 1800 K. At temperatures above 1800 K, significant mass losses could occur due to the high vapour pressures of gaseous species (Al_2O, SiO). These thermodynamic predictions are in agreement with available experimental data.

1. Introduction

Intermetallic compounds based on silicides have interesting properties at elevated temperatures. Among these silicides, molybdenum disilicide is quite attractive owing to its high melting point (2283 K), low density, and good oxidation resistance. Berkowitz-Mattuk *et al.* [1-3] and Chang [4] have investigated the oxidation behaviour of molybdenum disilicide. At lower temperatures this material exhibits oxidative degradation called the "pest degradation". This phenomenon is affected by porosity and does not occur for dense materials. At higher temperatures, a self-healing protective silica layer is formed. This film yields usable lifetimes in excess of 2000 h at 1923 K. The stability of the protective layer also depends on the volatilization of the simultaneously formed molybdenum trioxide. It has been observed that the oxidation without the molybdenum trioxide volatilization causes fast intergranular oxidation with severe material damage. The extreme brittleness of molybdenum disilicide at room temperature has prevented its use as an elevated temperature structural material. Schlichting [5] reviewed the available data on the molybdenum silicides and reported some of the problems and their prospects for use as high-temperature structural materials. Umakoshi *et al.* [6] reported that in $MoSi_2$ single crystals, a brittle to ductile transition occurs around 1273 K.

It has been pointed out by various authors [7-12] that molybdenum disilicide matrix composites, reinforced with fibres or whiskers, have great potential for high-temperature and aerospace applications. In addition, toughening and strengthening of molybdenum disilicide have been achieved by silicon carbide, alumina, zirconia and titanium carbide reinforcements. Molybdenum disilicide matrix can also be alloyed with other refractory silicides to improve mechanical properties and oxidation resistance. But interfacial reactions between different constituents occurring under processing and/or operating conditions are of major concern in these composites.

In the present work, thermodynamic stabilities of some ceramic reinforcements, e.g. refractory metal (titanium, zirconium and hafnium) borides, carbides, and oxides, carbon, silicon carbide, silicon nitride, and alumina in molybdenum disilicide ($MoSi_2$) matrix have been evaluated. The environmental stability of molybdenum disilicide under different processing and application conditions is discussed. A detailed analysis of the chemical stabilities and interfacial reactions is required for the selection of thermodynamically stable and chemically compatible reinforcement matrix combinations.

2. Alloying and reinforcement materials

Suitable reinforcements for molybdenum disilicide are required to improve its low-temperature toughness and high-temperature strength and creep resistance. In addition, some alloying elements/compounds are also desirable to improve the mechanical properties

TABLE I Relevant physicochemical properties of some refractory silicides

Material	Melting point (K)	Density (g cm^{-3})	CTE[a] (10^6 $^\circ$C^{-1})	Crystal structure
MoSi$_2$	2303	6.24	8.25	Tetragonal
WSi$_2$	2433	9.86	7.90	Tetragonal
NbSi$_2$	2203	5.66	11.7	Hexagonal
TaSi$_2$	2473	9.1	8.9	Hexagonal
Mo$_5$Si$_3$	2450	8.24	6.7	Tetragonal
W$_5$Si$_3$	2643	14.5	—	Tetragonal
Nb$_5$Si$_3$	2753	7.16	7.3 (along a) 4.6 (along c)	Tetragonal
Ta$_5$Si$_3$	2773	13.4	6.3 (along a) 6.6 (along c)	Tetragonal
Ti$_5$Si$_3$	2403	4.32	11.0	Hexagonal

[a] Coefficient of thermal expansion.

TABLE II Relevant physiochemical properties of some potential ceramic reinforcement

Material	Melting point (K)	Density (g cm^{-3})	Crystal structure
C	3925	2.25	Cubic
SiC	3100	3.21	Hexagonal
Si$_3$N$_4$	2173	3.19	Cubic
Al$_2$O$_3$	2318	3.97	Cubic
TiC	3413	4.9	Cubic
ZrC	3693	6.7	Cubic
HfC	4173	12.6	Cubic
TiB	2453	5.09	Orthorhombic
TiB$_2$	3253	4.5	Hexagonal
ZrB$_2$	3373	6.1	Hexagonal
HfB$_2$	3523	10.5	Hexagonal
TiO$_2$	2109	4.17	Tetragonal
ZrO$_2$	2973	6.0	Cubic
HfO$_2$	3031	10.0	Cubic

and oxidation resistance. Some relevant physicochemical properties of selected refractory silicides, which may be useful for the alloying of molybdenum disilicide matrix, are given in Table I. Some of these silicides (Table I) also have great potential as high-temperature matrices. The corresponding properties of potential ceramic reinforcements are given in Table II.

3. Thermochemical considerations
A critical aspect in the thermochemical modelling is the identification of possible product compounds and the reliability of available thermodynamic data. Owing to the lack of thermodynamic data for ternary and higher order phases of these materials, only binary compounds are considered here. Thermodynamic data for binary compounds have been taken from Barin and Knacke [12] and JANAF [13] tables. The temperature range considered for the environmental stability is 1000–1900 K and for the chemical compatibility computations is 1300–1900 K.

4. Results and discussion
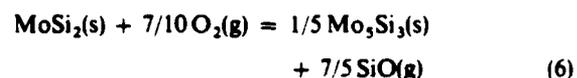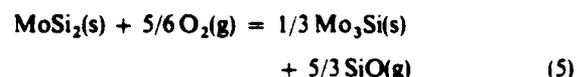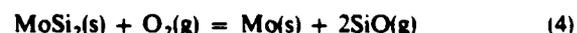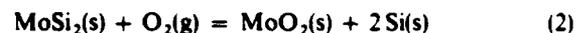### 4.1. Thermal and environmental stability
The thermal decomposition of molybdenum disilicide has been investigated by Blair et al. [14]. The de-

composition and vaporization under vacuum conditions at high temperatures (1800–2500 K) proceeds with formation of the following intermediate phases: $MoSi_2 \rightarrow Mo_5Si_3 \rightarrow Mo_3Si \rightarrow Mo$. The equilibrium vaporization reaction is given by

$$MoSi_2(s) = Mo(s) + 2 Si(g) \qquad (1)$$
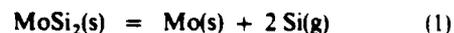
The partial pressures of silicon for Reaction 1 at 1900 and 2100 K are 0.33×10^{-6} and 0.69×10^{-5} atm, respectively. These data indicate that at temperatures around 2100 K and under vacuum conditions, mass losses of molybdenum disilicide can occur as a result of Reaction 1.

In addition, molybdenum disilicide reacts with oxygen and moisture. The oxidation processes of this material may proceed by three different mechanisms, namely, selective oxidation of the metal component, selective oxidation of silicon, and total oxidation. The chemical reactions of molybdenum disilicide with oxygen leading to silicon monoxide and other compounds (Reactions 4–8), the so-called "active" oxidation, considered are as follows:

$$MoSi_2(s) + O_2(g) = MoO_2(s) + 2 Si(s) \qquad (2)$$

$$MoSi_2(s) + 3/2 O_2(g) = MoO_3(l,g) + 2Si(s) \qquad (3)$$

$$MoSi_2(s) + O_2(g) = Mo(s) + 2SiO(g) \qquad (4)$$

$$MoSi_2(s) + 5/6 O_2(g) = 1/3 Mo_3Si(s) + 5/3 SiO(g) \qquad (5)$$

$$MoSi_2(s) + 7/10 O_2(g) = 1/5 Mo_5Si_3(s) + 7/5 SiO(g) \qquad (6)$$

$$MoSi_2(s) + 5/2 O_2(g) = MoO_3(l,g) + 2SiO(g) \qquad (7)$$

$$MoSi_2(s) + 2 O_2(g) = MoO_2(s) + 2 SiO(g) \qquad (8)$$

A plot of the silicon monoxide partial pressures, P_{SiO}, versus temperature is given in Fig. 1. From Fig. 1 it is seen that the silicon monoxide pressures of Reactions 7 and 8 leading to the formation of metal oxides are many orders of magnitude higher than those of the other reactions where selective oxidation of silicon takes place (Reactions 4–6). The formation of the molybdenum oxides shifts the equilibrium of Reactions 7 and 8 more towards the products. In all cases, an oxygen partial pressure of 0.2 atm has been used in these computations.
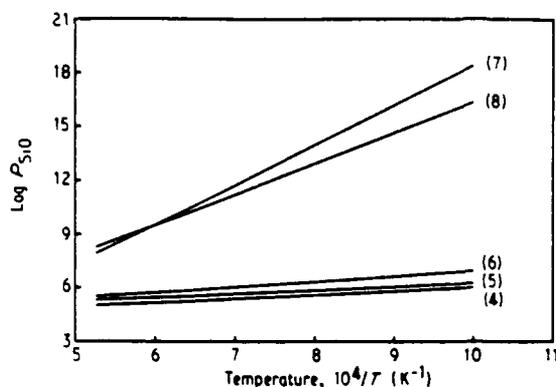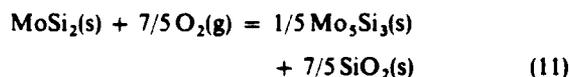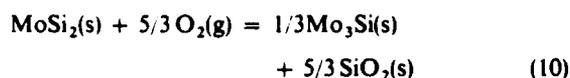
Figure 1 Partial pressures of silicon monoxide due to Reactions 4-8 (P_{O_2} = 0.2 atm) as a function of temperature.

Other oxidation reactions, the so-called "passive" oxidation, in which silica and different molybdenum compounds are formed, are the following:

$$MoSi_2(s) + 2O_2(g) = Mo(s) + 2SiO_2(s) \qquad (9)$$

$$MoSi_2(s) + 5/3 O_2(g) = 1/3Mo_3Si(s)$$
$$+ 5/3 SiO_2(s) \qquad (10)$$

$$MoSi_2(s) + 7/5 O_2(g) = 1/5 Mo_5Si_3(s)$$
$$+ 7/5 SiO_2(s) \qquad (11)$$

$$MoSi_2(s) + 7/2 O_2(g) = MoO_3(l,g) + 2SiO_2(s) \qquad (12)$$

$$MoSi_2(s) + 3O_2(g) = MoO_2(s) + 2SiO_2(s) \qquad (13)$$

The equilibrium oxygen pressures for the oxidation of $MoSi_2$ to various molybdenum-containing compounds and SiO_2 are given in Fig. 2. At a given temperature, the dominant reaction is determined by the oxygen partial pressure. Experimental observations by various authors [1–5] indicate that the growth of silica layers in $MoSi_2$ is determined by the rate of diffusion of silicon from the reaction interface through the lower silicide, and by the diffusion of the reacting species through the oxide layers where the formation of new layers of SiO_2 occurs. The state of the SiO_2 layer is decisive for the progress of these reactions. The results in Fig. 2 are consistent with the above observations.
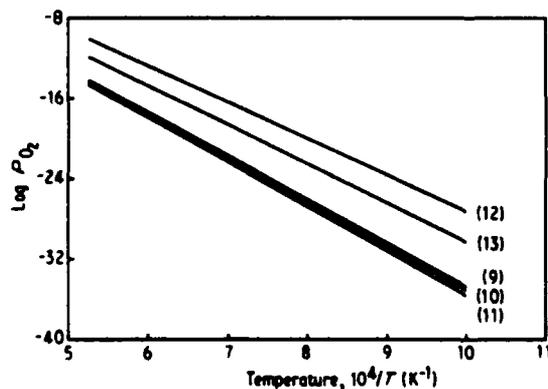
The chemical stability and the oxidation behaviour of molybdenum disilicide in water vapour has been investigated by Nechiporenko *et al.* [15] in the temperature range 1273–1873 K. According to these authors the rate of oxidation follows a parabolic law and silica is the reaction product. The following reactions are considered:

$$MoSi_2(s) + 5H_2O(g) = MoO_3(l,g) + 2SiO(g)$$
$$+ 5H_2(g) \qquad (14)$$

$$MoSi_2(s) + 7.5H_2O(g) = 1.5Mo_5Si_3(s)$$
$$+ 7.5SiO(g) + 7.5H_2(g) \qquad (15)$$

$$MoSi_2(s) + 7H_2O(g) = MoO_3(l,g) + 2SiO_2(s)$$
$$+ 7H_2(g) \qquad (16)$$

$$MoSi_2(s) + 14/5H_2O(g) = 1.5Mo_5Si_3(s)$$
$$+ 7.5SiO_2(s) + 14.5H_2(g) \qquad (17)$$
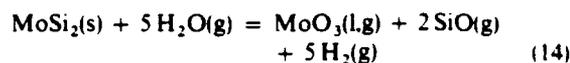
A plot of the total pressures of the product gaseous species of the above reactions versus temperature at P_{H_2O} = 10 atm, is given in Fig. 3. The hydrogen partial pressures for the reactions leading to the formation of SiO_2 (Reactions 16 and 17) are a few orders of magnitude higher than the total product pressures for Reactions 14 and 15. These two sets of reactions have opposite trends. In Reactions 14 and 15 the sum of the partial pressures of the product species increases with increasing temperature. On the other hand, for Reactions 16 and 17, the sum of the partial pressures decrease with increasing temperature which is due to the reverse reaction of the solid oxide products with hydrogen at higher temperatures. Experimental investigations [15] suggest that the formation of an oxide film is mainly due to Reaction 16. The MoO_3 has a very high vapour pressure at 1100 K and vaporizes leaving behind an SiO_2 film. In addition, other reactions also take place by diffusion of reacting species through the silica layer and with formation of lower silicides. The properties of the oxide films play an important role in the reaction of molybdenum disilicide with water vapour.

As discussed earlier, in a number of oxidation reactions of $MoSi_2$, silica and lower molybdenum silicides are formed. These molybdenum silicides react with
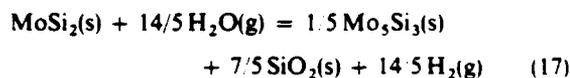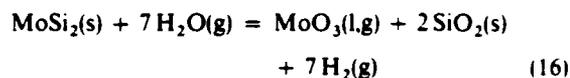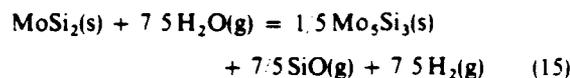

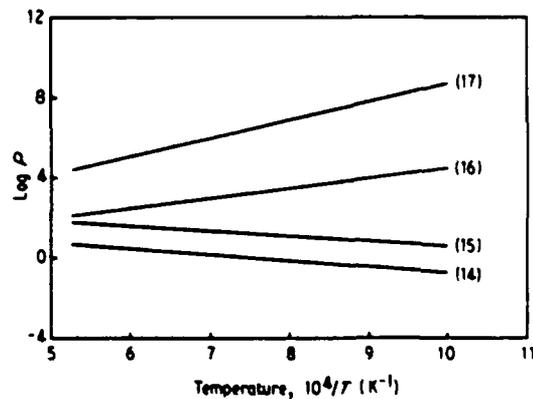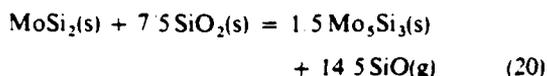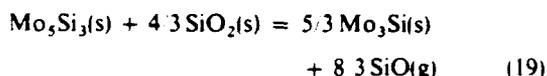*Figure 2* Equilibrium partial pressures of oxygen for Reactions 9–13 as a function of temperature.

Figure 3 The sum of the equilibrium partial pressures of the product gaseous species at P_{H_2O} = 10 atm of Reactions 14–17 as a function of temperature.

silica at higher temperatures according to the following reactions:

$$Mo_3Si(s) + SiO_2(s) = 3\,Mo(s) + 2\,SiO(g) \qquad (18)$$

$$Mo_5Si_3(s) + 4\,3\,SiO_2(s) = 5\,3\,Mo_3Si(s)$$
$$+ 8\,3\,SiO(g) \qquad (19)$$

$$MoSi_2(s) + 7\,5\,SiO_2(s) = 1\,5\,Mo_5Si_3(s)$$
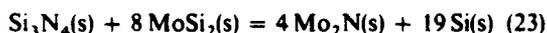$$+ 14\,5\,SiO(g) \qquad (20)$$

A plot of the silicon monoxide partial pressures versus temperature is given in Fig. 4. The silicon monoxide partial pressure increases as the metal to silicon ratio of the reactant Mo_xSi_y component decreases. The results in Fig. 4 indicate that at higher temperatures considerable mass losses via $SiO(g)$ vaporization may occur for the above reactions.

4.2. Chemical compatibility

One of the requirements for the use of reinforcing phases for high-temperature composites is that, ideally, they should coexist with the matrices. The protective coatings on the reactive reinforcements may not be very useful at higher temperatures. Thermochemical computations of the compatibility of various reinforcements in molybdenum disilicide are presented in the following sections.

The chemical reactions of carbon, silicon carbide and silicon nitride with molybdenum disilicide considered are

$$C(s) + 1/2\,MoSi_2(s) = Mo(s) + SiC(s) \qquad (21)$$

$$SiC(s) + 2\,MoSi_2(s) = Mo_2C(s) + 5\,Si(s) \qquad (22)$$

$$Si_3N_4(s) + 8\,MoSi_2(s) = 4\,Mo_2N(s) + 19\,Si(s) \qquad (23)$$

The Gibbs free energy change, $\Delta G°$, for Reaction 21 is $-6.9\,kcal\,mol^{-1}$ at 1300 K and $-11.5\,kcal\,mol^{-1}$ at 1900 K. These data indicate that the $C/MoSi_2$ system is reactive. On the other hand, the chemical reactions of silicon carbide and silicon nitride with molybdenum disilicide (Reactions 22 and 23) have Gibbs free energy changes, $\Delta G°$, of 64.4 and 326.3 kcal mol^{-1} at 1300 K and 52.1 and 263.1 kcal-mol^{-1} at 1900 K, respectively. These data indicate
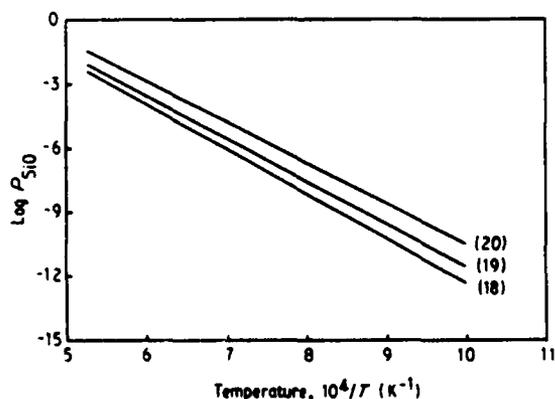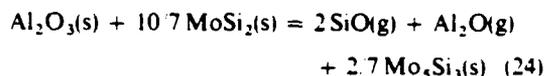
that silicon carbide and silicon nitride are stable with molybdenum disilicide in the temperature range 1300–1900 K.

The chemical reaction of alumina with molybdenum disilicide is

$$Al_2O_3(s) + 10\,7\,MoSi_2(s) = 2\,SiO(g) + Al_2O(g)$$
$$+ 2\,7\,Mo_5Si_3(s) \qquad (24)$$

The $\Delta G°$ values for the above reaction are 165.5 kcal mol^{-1} at 1300 and 91.6 kcal mol^{-1} at 1900 K. The partial pressures of gaseous species (Al_2O and SiO), reach critical limits (about 10^{-4} atm) at 1800 K. Thus, the $Al_2O_3/MoSi_2$ system could loose appreciable amounts of silicon and aluminium above 1800 K according to Reaction 24.

Using the same approach, chemical reactivities of other potential reinforcements with molybdenum disilicide have been computed. The thermodynamically stable reinforcements in molybdenum disilicide matrix are TiB, TiB_2, ZrB_2, HfB_2, TiC, ZrC, HfC, ZrO_2 and HfO_2. An unstable reinforcement is TiO_2.

5. Conclusions

Thermochemical data indicate that molybdenum disilicide reacts with oxygen and water vapour at high temperatures. In "active" oxidation processes, silicon monoxide pressures of the reactions including also the formation of metal oxides are many orders of magnitude higher than those of other reactions. The "passive" oxidation reactions are controlled by the state of the silica layer and the oxygen partial pressures. The structure and properties of the silica films play an important role in the reactions of molybdenum disilicide with water vapour. In addition, molybdenum silicides (Mo_3Si, Mo_5Si_3 and $MoSi_2$) also react with silica at higher temperatures. Thermodynamic stabilities of various ceramic reinforcements in molybdenum disilicide matrices have been computed in the temperature range 1300–1900 K. Based on these results, compatible reinforcements are SiC, Si_3N_4, TiC, ZrC, HfC, TiB, TiB_2, ZrB_2, HfB_2, ZrO_2 and HfO_2. On the other hand, carbon and TiO_2 are reactive. The $MoSi_2/Al_2O_3$ system is stable below 1800 K. At temperatures above 1800 K, significant mass losses could occur due to the high vapour pressures of gaseous species.

Figure 4 Partial pressures of silicon monoxide of Reactions 18–20 as a function of temperature.

References
1. J. B. BERKOWITZ-MATTUK, E. BLACKBURN and E. J. FELTEN, Trans. TMS-AIME 233 (1965) 1093.
2. J. B. BERKOWITZ-MATTUK and R. R. DILS, J. Electrochem. Soc. 112 (1965) 583.

3. J. B. BERKOWITZ-MATTUK, M. ROSSETTI and D. W. LEE, *Metall. Trans.* **1** (1970) 479.

4. Y. A. CHANG, *J. Mater. Sci.* **4** (1969) 641.

5. J. SCHLICHTING, *High Temp.-High Press.* **10** (1978) 241.

6. Y. UMAKOSHI, T. HIRANO, T. SAKAGAMI and T. YAMANE, *Scripta Metall.* **23** (1989) 87.

7. F. D. GAC and J. J. PETROVIC, *J. Amer. Ceram. Soc.* **68** (1985) C 200.

8. W. S. GIBBS, J. J. PETROVIC and R. E. HONNEL, *Ceram. Engng Sci. Proc.* **8** (1987) 645.

9. P. J. MESCHTER and D. S. SCHWARTZ, *J. Metals* **11** (1989) 52.

10. C. B. LIM, T. YANO and T. ISEKI, *J. Mater. Sci.* **24** (1989) 4144.

11. J.-M. YANG, W. KAI and S. M. JENG, *Scripta Metall.* **23** (1989) 1953.

12. I. BARIN and O. KNACKE, "Thermochemical Properties of Inorganic Substances" (Springer Verlag, New York, 1973, Supplement 1977).

13. D. R. STULL and H. R. PROPHET, "JANAF Thermochemical Tables", 2nd Edn (National Bureau of Standards NBS 37, Washington DC, 1971).

14. G. R. BLAIR, H. LEVIN and R. E. O'BRIAN, *J. Amer. Ceram. Soc.* **48** (1965) 430.

15. E. P. NECHIPORENKO, V. S. PETUKHOV and V. S. ANTIPOV, *Izvest. Akad. Nauk. SSSR Neorg. Mater* **10** (1974) 1027.

Interface Manipulation in Ceramic Matrix Composites for Improved Mechanical Performance

R. P. BOISVERT, R. K. HUTTER AND R. J. DIEFENDORF

ABSTRACT

One unfortunate characteristic of ceramic matrix composites is the catastrophic failure which occurs when good bonding exists between the fiber and matrix. A crack which originates in the matrix (or fibers) can transverse the entire cross section due to the lack of any crack deflecting or energy absorbing mechanisms. This limits the performance of the composite to the constituent which has the largest flaw or the lowest failure strain. In many ceramic composite systems the matrix is the limiting component and therefore the potential high strength of the fibers can never be realized. To improve the fracture behavior of brittle/brittle systems, the interface between the load bearing element and the matrix should be controlled. Optimum interface tailoring would provide for transfer of all the load to the fibers, but with the prevention of catastrophic crack propagation. In this work, the brittle failure in these systems was altered by controlling the fiber/matrix interface with a suitable barrier layer or by multilayering the matrix thereby introducing several barriers to prevent propagation of matrix cracks.

INTRODUCTION

Ceramics in bulk form generally have high elastic moduli, but suffer from low strengths and hence very low strains to failure due to flaws inherent in the normal processing. In fibrous form, where flaws are comparatively much smaller and less prevalent, high strengths as well as high moduli can be achieved. However, no matter what the form of these one component systems, they are linearly elastic to failure and and possess very little work of fracture, or "toughness".

R.P. Boisvert,Graduate Research Assistant,Materials Engineering
Rensselaer Polytechnic Institute, Troy, NY 12180-3590
R.K. Hutter, Graduate Research Assistant, Materials Engineering
presently with E.I. Dupont, Wilmington, Delaware.
R.J. Diefendorf, Professor of Materials Engineering,
Rensselaer Polytechnic Institute, Troy, NY 12180-3590

Considerable materials development has been placed on trying to combine fibrous and bulk ceramics to form ceramic/ceramic composites. These materials have the potential advantage of increasing strain to failure and "toughness" through transfer of stress to the high strength reinforcement and the creation of energy absorbent fracture mechanisms.

The fracture behavior of ceramic matrix composites is different from polymer matrix, and metal matrix composites, due to the characteristics of the individual constituents. The role of the matrix in polymer matrix composites is simply to transfer load to the reinforcement, which has the desirable properties, and to hold the fibers in place. Fracture is generally governed by the brittle, lower strain to failure fibers when the load is applied parallel to the fibers. In ceramic/ceramic systems the strain to failure of the matrix is typically lower than that of the fibers. Hence, instead of the fiber initiating failure as in the polymeric composite, the ceramic matrixes will fail before the fibers. If perfect coupling exists between fiber and matrix, the composite is found to catastrophically fail at the failure strain of the matrix thereby limiting the strength and work of fracture of the composite. Therefore, various fracture control techniques must be employed during the fabrication of certain ceramic matrix composites to obtain strong and reliable brittle matrix composites.

Two different ceramic composite processing techniques were utilized in studying the effects of placing carbon interface layers within the composite. The first method involved chemically vapor depositing SiC on Nicalon SiC fibers. Initially no carbon layer was placed on the fibers. In this situation the matrix was found to control the strength, which when calculated using Weibull theory had excellent agreement with experimental results. When a thin carbon layer was deposited on the fiber surface before SiC infiltration, composite strengths were found to be fiber controlled. Carbon was chosen for the interfacial layer as a model system because of its weak layered structure and inertness to SiC.

The alternate composite processing technique utilized pyrolysis of an organometallic polymer, polyvinylsilane(PVS), to form a SiC matrix material with Nicalon SiC fibers as reinforcement. Similar results were found for these composites when a carbon coating was placed on the fiber surface via a carbon polymeric precursor before composite fabrication. Increased composite performance can also be obtained by multilayering the ceramic matrix.

EXPERIMENTAL
Chemical Vapor Deposition

For a quantitative measure of the effect that a carbon interfacial layer could have in a ceramic/ceramic system, single bundles of Nicalon SiC fibers, C.V.D. infiltrated with varying amounts of SiC matrix, were tensile tested with and without a carbon interface. The single bundle approach was taken due to the ease in making samples and close simulation of

the real composite. Three classes of samples were made; strong interfaced(S.I.), weak interfaced(W.I.), and carbon interfaced(C.I.). Strong interfaced composites were prepared by first removing the sizing present on the filaments by heat treatment in a vacuum to high temperatures followed by deposition of SiC. Carbon interfaced specimens were prepared by; (1) remove sizing, (2) deposit carbon, and (3) infiltrate with SiC. The weak interfaced samples were actually made inadvertently due to a very fast heat-up and infiltration start which probably did not completely burn off the sizing on the "as received" Nicalon SiC fibers before SiC began depositing.

The chemical vapor deposition technique can be utilized under a wide range of operating conditions (eg; pressure, temperature, concentration, etc.). However, the process controlling parameters and mechanisms of reaction change along with these conditions. The furnace used throughout the course of this study consisted of a resistance heated graphite element held under vacuum. The reactant gases used to deposit SiC consisted of a mixture of hydrogen and methyltrichlorosilane in a ratio of 4:1. The deposition pressure was between 1-10 torr with an operating temperature of 1200°C. Various times were used to increase the quantity of deposited material. Carbon interfacial layers were deposited via a mixture of methane and hydrogen at 1300°C and a pressure between 1-10 torr. These micro composites were subsequently tensile tested. Due to the small strain to failure and brittleness of these materials, special consideration was necessary in specimen gripping and alignment in the tensile testing machine. After testing, the sample cross-sectional area was deduced by image analysis. The reader is referred to reference [1] for a detailed description of the experimental procedure.

Organometallic Precursors

Due to the difficulties in utilizing chemical vapor deposition in producing large scale ceramic structures, an alternate processing technique utilizing an organometallic precursor was used in producing ceramic matrix composites. The polymeric precursor, polyvinylsilane, developed by Schilling, et. al. [2], provides an efficient thermal crosslinking mechanism via the vinyl and SiH groups contained in its chemical structure. A vacuum bag process can be used to form laminates of various sizes and complex shapes. SiC whiskers are added to polyvinylsilane to form the matrix mixture used during the vacuum bag processing. This filler is needed to control shrinkage and microcracking that occurs during pyrolysis. These "green" bodies are subsequently pyrolyzed to form the ceramic matrix composite. Reimpregnation of pyrolyzed structures is necessary due to shrinkage which occurs during pyrolysis because of the moderate ceramic yields and density differences between initial polymer and final ceramic. The results stated in this article are based on composites which were fabricated utilizing Nicalon in the form of eight harness satin weave as

the reinforcement. The reader is referred to references [3], [4], and [5] for a more detailed description of composite fabrication.

During pyrolysis of polyvinylsilane, mechanical and chemical bonding occur between the matrix and reinforcing phase. This bonding leads to catastrophic failures, and low toughness in composite specimens. Carbon coatings were placed on Nicalon SiC fibers prior to lamination in an attempt to improve the mechanical performance. The coatings were deposited from solutions of Ashland 240 pitch and the toluene insolubles of a heat treated Ashland 240 pitch and then pyrolyzed. Fiber sizing was removed on all reinforcement utilized prior to composite fabrication. Coating uniformity was dependent on solvent type and solution concentration.

To increase the number of crack stopping interlayers, ceramic composite specimens were impregnated with a carbon polymeric precursor between polysilane densifications. Various cuts and concentration of Ashland 240 pitch were used as the carbon precursor. Mechanical testing was performed on a three point bend fixture.

RESULTS AND DISCUSSION
Chemical Vapor Deposition

Nicalon SiC bundle strength was determined before infiltration by testing specimens which were heat treated to 1200°C under vacuum for 1 hour. This served to remove the sizing found on the fibers and give them a similar thermal treatment at the infiltration temperature. By using the average fiber diameter of 12 m for the 500 filament bundle, the strength was found to be 1.46GPa.

The strength data for the infiltrated bundles, plotted as a function of fiber volume fraction for the three types of samples produced (strong interfaced(S.I.), weak interfaced(W.I.), carbon interfaced(C.I.)) is shown in figure 1. The data for the strongly coupled case indicates poor strength with the infiltration of even the slightest amount of SiC. Strength appears to continue decreasing with increasing amounts of matrix, but at a much slower rate. In contrast, the carbon interfaced and weak interfaced strengths appear to fall along a linearly decreasing curve but with much higher values.

By using Weibull theory to calculate the matrix strength as a function of volume, the composite strength, when governed by the strength of the matrix(i.e., strong interfaced case), can be predicted. The predicted values of composite strength are shown plotted over the experimental data in figure 1. Excellent agreement is seen between the matrix controlled theory and the strongly coupled composite strength. Hence, flaws in the low strain to failure matrix are propagating directly through the fiber reinforcement to cause failure. The plateau region of the curve gives an approximation of the inherent strength of the C.V.D. deposited SiC matrix in fiber filled composites(~55MPa).

For the weak interfaced and carbon interfaced samples, the fiber controlled strength can be predicted approximately by

multiplying the heat treated bundle strength by the fiber volume fraction plus the contribution from the matrix. The strength of the ceramic composite will never fall below that of the matrix. The excellent agreement between predicted values of composite strength and experimental data is shown plotted in figure 1.

The implications of these results are significant for the usefulness of real SiC ceramic composites. For volume fractions of about 50%, decoupling fibers could increase unidirectional composite tensile strength by over five times. Multidirectional reinforcement also benefits from this decoupling as will be shown in the following section. The greatest advantage gained for these composites is that the largest flaw in the matrix will not control the overall material strength. Since the fibers are carrying the load near the failure stress, their flaw distribution should be controlling.

Typical load-displacement curves for the three types of single bundle samples are shown in figure 2. These plots are taken directly from the strip chart recorder on the test machine, and represent the load carried by the sample versus the displacement of the machine's crosshead. Strain to failure and modulus values cannot be accurately assessed from these curves due to the high compliance in the system. However, the curves do indicate relative differences between samples. All specimens with strong interfaces exhibited a linearly elastic response followed by brittle failure. Samples with carbon interfaces and weak interfaces exhibited a slope change at the matrix failure strain, without catastrophic failure. A "tail section" was noticed in several curves indicating a graceful fracture with possibly the occurrence of fiber pull-out.

A final observation on the load-displacement characteristics is the variation in failure load between carbon coated samples. Theoretically, no matter what the fiber volume fraction is, the ultimate failure load of the specimens should be the same, assuming the same number of fibers exist in all samples. However, samples with increased carbon coating thickness failed at lower loads. The experimental results show that very little carbon is necessary for decoupling systems. This could be very significant for the processing of these types of materials, since control of the interfacial coating thickness could be crucial to the materials performance.

Scanning Electron Microscopy was used to view the fracture surfaces. The completely brittle failure of the strong interfaced composites is confirmed by the flat fracture surface. Samples with carbon at the fiber matrix interface had fibrous fracture surfaces which confirms that matrix failure did not destroy the reinforcement. The presence of pull-out can also be used to explain the tail section which occurred in the load-deflection curves.

Organometallic Precursors

Low fiber/matrix coupling has been shown to be capable of drastically improving the mechanical performance of chemically vapor deposited ceramic matrix composites. This same idea has

been tested on ceramic matrix composites which were processed utilizing an organometallic precursor called polyvinylsilane. The carbon interfacial layers for this situation were deposited via a carbon polymeric precursor. Depending on the type of precursor used and the application procedure, a range of composite performance can be expected. The mechanical behavior of the composite is found to be dependent on the structure of the carbon interfacial layer. A previous article[5] has reviewed the general characteristics of such composites, therefore this paper is going to focus on the stress/strain behavior of these ceramic matrix composites.

Composites fabricated with no carbon interfacial layer have a linear-elastic response curve up to the failure strain of the matrix when tested in a three point bend apparatus. Brittle failure occurs at the matrix failure strain. Cracks originate in the low-strain-to-failure matrix and propagate unimpeded through the entire cross section. The chemical and mechanical bonding which develops between the Nicalon reinforcement and matrix during processing provides a non-obstructed path for the passage of such matrix cracks. Table I list the failure strains for these composites as you increase the number of densifications.

A variety of different coating solutions were used in trying to develop a suitable crack stopping layer between the fiber and reinforcement. Mesophase forming pitches produced coatings which dramatically affected the performance of these composites. Load deflection curves were linear-elastic up to the failure strain of the composite for all specimens which contained a carbon coating. In contrast to the uncoated specimens, non-catastrophic failure occurred at this strain resulting in a tougher composite. Table I list failure strains for a variety of composites prepared with different pitches. No indication of matrix cracking, such as a change in deflection curve slope, occurs before the composite failure strain is reached, therefore a potential rise in the matrix microcrack yield strain results due the presence of the fiber coating.

The technique of multilayering the matrix with alternating carbon and polysilane impregnations has been shown [3],[5] to improve the strength and toughness of ceramic matrix composites. Load-deflection curves for such composites are linear elastic up to the matrix failure strain. This point can coincide with the ultimate composite failure strain or it can be substantially below that value(Table II). In selected composites the matrix is found to fail at the same strain level as uncoated composites. Composite failure does not occur at this point. The composite can be loaded to still higher stress levels, whereas in the previous two cases once the matrix failure strain is achieved composite failure occurs. In some instances matrix failure strain coincides with the ultimate failure strain. These composites have an enhanced matrix microcrack yield strain over all previous cases. Table III outlines the failure strains for composites with increasing number of carbon interlayers. No tremendous improvement in performance is immediately obvious when the number of interlayers is increased above two.

CONCLUSION

Decoupling of fibers from the matrix in SiC/SiC composites results in substantial improvements in material strength and work of fracture. C.V.D. applied carbon is an effective interfacial decoupling material. Thick C.V.D. carbon coatings may degrade fiber properties, and hence, overall composite performance. The effectiveness of a carbon coating applied via a polymeric precursor is dependent on the type used and processing parameters employed. Significant improvements in matrix microcrack yield strain are gained for composites with carbon coatings on reinforcing fibers and multilayered matrixes.

ACKNOWLEDGEMENT

REFERENCES

1. C.L. Shilling and T. C. Williams, Polym. Prepr. (Am. Chem. Soc., Div. Polym. Chem.), 25(1), 1 (1984).

2. R. K. Hutter, MS Thesis, Rensselaer Polytechnic Institute, December, 1985.

3. R. P. Boisvert, MS Thesis, Rensselaer Polytechnic Institute, May, 1988.

4. R. P. Boisvert and R. J. Diefendorf, presented at the ACS 12th Annual Conference on Composite Materials and Structures, Cocoa Beach, Fl, 1988.

5. R. P. Boisvert and R.J. Diefendorf, presented at the Materials Research Society Spring Meeting, Reno, Nevada, 1988.
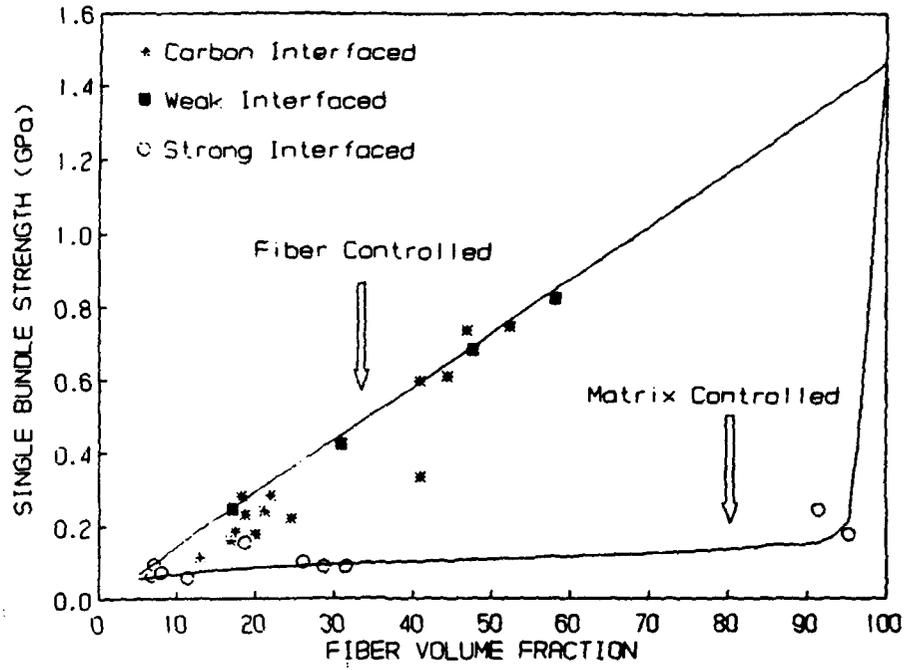
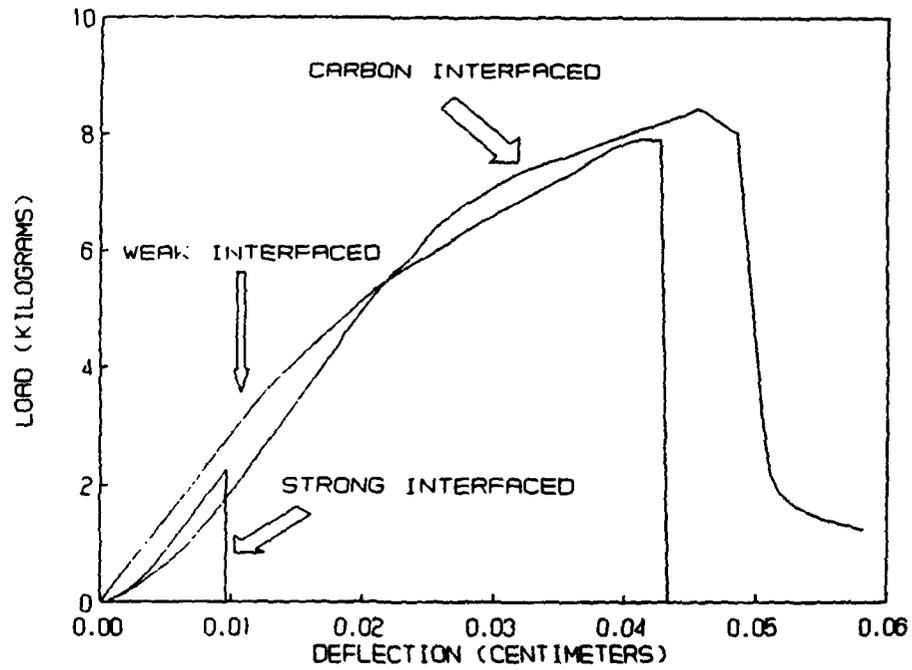**FIGURE 1** Chemically Vapor Deposited, Nicalon Single Bundle Strength Comparison.

FIGURE 2 Chemically Vapor Deposited, Nicalon Single Bundle Load-Deflection Curve Comparison.

TABLE I
Failure Strain for Coated and Non-coated Nicalon Reinforced(Eight Harness Satin Weave) Composites.

Number PVS Impregnations	1	2	3	4	5
No Fiber Coating					
Failure Strain	.0017	.0015	.0012	.0011	.0010
Flexural Strength(MPa)	52.3	56.7	61.2	63.2	59.7
Fiber Coating: A240 in Trichlorobenzene (0.01gm/cm^3)					
Failure Strain	-	.0041	.0021	.0022	-
Flexural Strength(MPa)	-	73.1	91.7	112.4	-
Fiber Coating: Toluene Insolubles A240 in TCB(0.0075gm/cm^3)					
Failure Strain	-	.0046	.0035	.0040	.0029
Flexural Strength(MPa)	-	128.2	128.2	157.2	126.2
Fiber Coating: CPTI in TCB(0.01gm/cm^3)					
Failure Strain	-	.0041	.0028	.0022	.0021
Flexural Strength(MPa)	-	95.8	93.1	93.1	104.8

TABLE II
Nicalon Reinforced(Eight Harness Satin Weave) Composites Multilayered Matrix with Carbon Coated Reinforcement

Number Carbon and PVS Impreg.	1	2	3	4	5
Fiber Coating:Toluene Insolubles A240 in TCB(0.0075gm/cm^3) Carbon Impregnation:Toluene Insolubles A240 in TCB(0.01gm/cm^3)					
ϵ_{matrix} *	.0030	.0036	.0050	.0051	-
$\epsilon_{f,composite}$ **	.0043	.0068	.0059	.0058	-
Flexural Strength(MPa)	98.6	186.2	213.7	234.4	-
Fiber Coating:CPTI in TCB(0.01gm/cm^3) Carbon Impregnation:CPTI in TCB(0.05gm/cm^3)					
ϵ_{matrix}	-	-	.0045	.0016	.0041
$\epsilon_{f,composite}$	-	-	.0072	.0084	.0075
Flexural Strength(MPa)	-	-	160.6	235.1	291.0
Fiber Coating:CPTI in TCB(0.01gm/cm^3) Carbon Impregnation:CPTI in TCB(0.1gm/cm^3)					
ϵ_{matrix}	-	-	.0025	.0015	.0029
$\epsilon_{f,composite}$	-	.0051	.0040	.0040	.0051
Flexural Strength(MPa)	-	106.9	122.7	144.8	199.3

* Indicates strain at which load-deflection curve deviates from linearity.

** Indicates strain at which there is a non-recoverable load drop, resulting in composite failure.

TABLE III

Results on Varying the Number of Carbon Impregnations in Nicalon Reinforced(Eight Harness Satin Weave) Composites

Number of PVS and Carbon Impregnations	5 PVS/ 1 Carb	5 PVS/ 2 Carb	5 PVS/ 3 Carb	5 PVS/ 4 Carb	5 PVS/ 5 Carb
Fiber Coating:CPTI in TCB(0.01gm/cm^3) Carbon Impregnation:CPTI in TCB(0.05gm/cm^3)					
ϵ_{matrix}	-	.0043	.0050	.0043	.0041
$\epsilon_{f,composite}$	.0048	.0069	.0067	.0065	.0075
Flexural Strength(MPa)	175.1	232.4	213.7	213.7	291.0
Fiber Coating:CPTI in TCB(0.01gm/cm^3) Carbon Impregnation:CPTI in TCB(0.10gm/cm^3)					
ϵ_{matrix}	.0015	.0024	.0024	.0015	.0024
$\epsilon_{f,composite}$	.0041	.0051	.0051	.0051	.0051
Flexural Strength(MPa)	174.4	215.1	207.5	203.4	199.3

Number of PVS and Carbon Impregnations	4 PVS/ 1 Carb	4 PVS/ 2 Carb	4 PVS/ 3 Carb	4 PVS/ 4 Carb
Fiber Coating:CPTI in TCB(0.01gm/cm^3) Carbon Impregnation:CPTI in TCB(0.05gm/cm^3)				
ϵ_{matrix}	.0040	.0055	.0042	.0017
$\epsilon_{f,composite}$	.0064	.0071	.0070	.0084
Flexural Strength(MPa)	177:9	207.5	204.8	235.1
Fiber Coating:CPTI in TCB(0.01gm/cm^3) Carbon Impregnation:CPTI in TCB(0.1gm/cm^3)				
ϵ_{matrix}	.0019	.0012	.0022	.0015
$\epsilon_{f,composite}$	.0033	.0037	.0039	.0040
Flexural Strength(MPa)	137.2	152.4	141.3	144.8